

# **COMPUTATIONAL METHODS IN SURFACE AND COLLOID SCIENCE**

# **SURFACTANT SCIENCE SERIES**

FOUNDING EDITOR

**MARTIN J. SCHICK**

*1918–1998*

SERIES EDITOR

**ARTHUR T. HUBBARD**

*Santa Barbara Science Project*

*Santa Barbara, California*

ADVISORY BOARD

**DANIEL BLANKSCHTEIN**

*Department of Chemical Engineering  
Massachusetts Institute of Technology  
Cambridge, Massachusetts*

**ERIC W. KALER**

*Department of Chemical Engineering  
University of Delaware  
Newark, Delaware*

**S. KARABORNI**

*Shell International Petroleum  
Company Limited  
London, England*

**CLARENCE MILLER**

*Department of Chemical Engineering  
Rice University  
Houston, Texas*

**LISA B. QUENCER**

*The Dow Chemical Company  
Midland, Michigan*

**DON RUBINGH**

*The Proctor & Gamble Company  
Cincinnati, Ohio*

**JOHN F. SCAMEHORN**

*Institute for Applied Surfactant  
Research  
University of Oklahoma  
Norman, Oklahoma*

**BEREND SMIT**

*Shell International Oil Products B.V.  
Amsterdam, The Netherlands*

**P. SOMASUNDARAN**

*Henry Krumb School of Mines  
Columbia University  
New York, New York*

**JOHN TEXTER**

*Strider Research Corporation  
Rochester, New York*

1. Nonionic Surfactants, *edited by Martin J. Schick* (see also Volumes 19, 23, and 60)
2. Solvent Properties of Surfactant Solutions, *edited by Kozo Shinoda* (see Volume 55)
3. Surfactant Biodegradation, *R. D. Swisher* (see Volume 18)
4. Cationic Surfactants, *edited by Eric Jungermann* (see also Volumes 34, 37, and 53)
5. Detergency: Theory and Test Methods (in three parts), *edited by W. G. Cutler and R. C. Davis* (see also Volume 20)
6. Emulsions and Emulsion Technology (in three parts), *edited by Kenneth J. Lissant*
7. Anionic Surfactants (in two parts), *edited by Warner M. Linfield* (see Volume 56)
8. Anionic Surfactants: Chemical Analysis, *edited by John Cross*
9. Stabilization of Colloidal Dispersions by Polymer Adsorption, *Tatsuo Sato and Richard Ruch*
10. Anionic Surfactants: Biochemistry, Toxicology, Dermatology, *edited by Christian Gloxhuber* (see Volume 43)
11. Anionic Surfactants: Physical Chemistry of Surfactant Action, *edited by E. H. Lucassen-Reynders*
12. Amphoteric Surfactants, *edited by B. R. Bluestein and Clifford L. Hilton* (see Volume 59)
13. Demulsification: Industrial Applications, *Kenneth J. Lissant*
14. Surfactants in Textile Processing, *Arved Datyner*
15. Electrical Phenomena at Interfaces: Fundamentals, Measurements, and Applications, *edited by Ayao Kitahara and Akira Watanabe*
16. Surfactants in Cosmetics, *edited by Martin M. Rieger* (see Volume 68)
17. Interfacial Phenomena: Equilibrium and Dynamic Effects, *Clarence A. Miller and P. Neogi*
18. Surfactant Biodegradation: Second Edition, Revised and Expanded, *R. D. Swisher*
19. Nonionic Surfactants: Chemical Analysis, *edited by John Cross*
20. Detergency: Theory and Technology, *edited by W. Gale Cutler and Erik Kissa*
21. Interfacial Phenomena in Apolar Media, *edited by Hans-Friedrich Eicke and Geoffrey D. Parfitt*
22. Surfactant Solutions: New Methods of Investigation, *edited by Raoul Zana*
23. Nonionic Surfactants: Physical Chemistry, *edited by Martin J. Schick*
24. Microemulsion Systems, *edited by Henri L. Rosano and Marc Clausse*
25. Biosurfactants and Biotechnology, *edited by Naim Kosaric, W. L. Cairns, and Neil C. C. Gray*
26. Surfactants in Emerging Technologies, *edited by Milton J. Rosen*
27. Reagents in Mineral Technology, *edited by P. Somasundaran and Brij M. Moudgil*
28. Surfactants in Chemical/Process Engineering, *edited by Darsh T. Wasan, Martin E. Ginn, and Dinesh O. Shah*
29. Thin Liquid Films, *edited by I. B. Ivanov*
30. Microemulsions and Related Systems: Formulation, Solvency, and Physical Properties, *edited by Maurice Bourrel and Robert S. Schechter*
31. Crystallization and Polymorphism of Fats and Fatty Acids, *edited by Nissim Garti and Kiyotaka Sato*

32. *Interfacial Phenomena in Coal Technology*, edited by Gregory D. Botsaris and Yuli M. Glazman
33. *Surfactant-Based Separation Processes*, edited by John F. Scamehorn and Jeffrey H. Harwell
34. *Cationic Surfactants: Organic Chemistry*, edited by James M. Richmond
35. *Alkylene Oxides and Their Polymers*, F. E. Bailey, Jr., and Joseph V. Koleske
36. *Interfacial Phenomena in Petroleum Recovery*, edited by Norman R. Morrow
37. *Cationic Surfactants: Physical Chemistry*, edited by Donn N. Rubingh and Paul M. Holland
38. *Kinetics and Catalysis in Microheterogeneous Systems*, edited by M. Grätzel and K. Kalyanasundaram
39. *Interfacial Phenomena in Biological Systems*, edited by Max Bender
40. *Analysis of Surfactants*, Thomas M. Schmitt
41. *Light Scattering by Liquid Surfaces and Complementary Techniques*, edited by Dominique Langevin
42. *Polymeric Surfactants*, Irja Piirma
43. *Anionic Surfactants: Biochemistry, Toxicology, Dermatology*. Second Edition, Revised and Expanded, edited by Christian Gloxhuber and Klaus Künstler
44. *Organized Solutions: Surfactants in Science and Technology*, edited by Stig E. Friberg and Björn Lindman
45. *Defoaming: Theory and Industrial Applications*, edited by P. R. Garrett
46. *Mixed Surfactant Systems*, edited by Keizo Ogino and Masahiko Abe
47. *Coagulation and Flocculation: Theory and Applications*, edited by Bohuslav Dobiáš
48. *Biosurfactants: Production • Properties • Applications*, edited by Naim Kossaric
49. *Wettability*, edited by John C. Berg
50. *Fluorinated Surfactants: Synthesis • Properties • Applications*, Erik Kissa
51. *Surface and Colloid Chemistry in Advanced Ceramics Processing*, edited by Robert J. Pugh and Lennart Bergström
52. *Technological Applications of Dispersions*, edited by Robert B. McKay
53. *Cationic Surfactants: Analytical and Biological Evaluation*, edited by John Cross and Edward J. Singer
54. *Surfactants in Agrochemicals*, Tharwat F. Tadros
55. *Solubilization in Surfactant Aggregates*, edited by Sherril D. Christian and John F. Scamehorn
56. *Anionic Surfactants: Organic Chemistry*, edited by Helmut W. Stache
57. *Foams: Theory, Measurements, and Applications*, edited by Robert K. Prud'homme and Saad A. Khan
58. *The Preparation of Dispersions in Liquids*, H. N. Stein
59. *Amphoteric Surfactants: Second Edition*, edited by Eric G. Lomax
60. *Nonionic Surfactants: Polyoxyalkylene Block Copolymers*, edited by Vaughn M. Nace
61. *Emulsions and Emulsion Stability*, edited by Johan Sjöblom
62. *Vesicles*, edited by Morton Rosoff
63. *Applied Surface Thermodynamics*, edited by A. W. Neumann and Jan K. Spelt
64. *Surfactants in Solution*, edited by Arun K. Chattopadhyay and K. L. Mittal
65. *Detergents in the Environment*, edited by Milan Johann Schwuger



66. Industrial Applications of Microemulsions, *edited by Conxita Solans and Hironobu Kunieda*
67. Liquid Detergents, *edited by Kuo-Yann Lai*
68. Surfactants in Cosmetics: Second Edition, Revised and Expanded, *edited by Martin M. Rieger and Linda D. Rhein*
69. Enzymes in Detergency, *edited by Jan H. van Ee, Onno Misset, and Erik J. Baas*
70. Structure–Performance Relationships in Surfactants, *edited by Kunio Esumi and Minoru Ueno*
71. Powdered Detergents, *edited by Michael S. Showell*
72. Nonionic Surfactants: Organic Chemistry, *edited by Nico M. van Os*
73. Anionic Surfactants: Analytical Chemistry, Second Edition, Revised and Expanded, *edited by John Cross*
74. Novel Surfactants: Preparation, Applications, and Biodegradability, *edited by Krister Holmberg*
75. Biopolymers at Interfaces, *edited by Martin Malmsten*
76. Electrical Phenomena at Interfaces: Fundamentals, Measurements, and Applications, Second Edition, Revised and Expanded, *edited by Hiroyuki Ohshima and Kunio Furusawa*
77. Polymer-Surfactant Systems, *edited by Jan C. T. Kwak*
78. Surfaces of Nanoparticles and Porous Materials, *edited by James A. Schwarz and Cristian I. Contescu*
79. Surface Chemistry and Electrochemistry of Membranes, *edited by Torben Smith Sørensen*
80. Interfacial Phenomena in Chromatography, *edited by Emile Pefferkorn*
81. Solid–Liquid Dispersions, *Bohuslav Dobiáš, Xueping Qiu, and Wolfgang von Rybinski*
82. Handbook of Detergents, *editor in chief: Uri Zoller*  
Part A: Properties, *edited by Guy Broze*
83. Modern Characterization Methods of Surfactant Systems, *edited by Bernard P. Binks*
84. Dispersions: Characterization, Testing, and Measurement, *Erik Kissa*
85. Interfacial Forces and Fields: Theory and Applications, *edited by Jyh-Ping Hsu*
86. Silicone Surfactants, *edited by Randal M. Hill*
87. Surface Characterization Methods: Principles, Techniques, and Applications, *edited by Andrew J. Milling*
88. Interfacial Dynamics, *edited by Nikola Kallay*
89. Computational Methods in Surface and Colloid Science, *edited by Małgorzata Borówka*

## ADDITIONAL VOLUMES IN PREPARATION

Adsorption on Silica Surfaces, *edited by Eugène Papirer*

Fine Particles: Synthesis, Characterization, and Mechanisms of Growth, *edited by Tadao Sugimoto*

Nonionic Surfactants: Alkyl Polyglucosides, *edited by Dieter Balzer and Harald Luders*

# COMPUTATIONAL METHODS IN SURFACE AND COLLOID SCIENCE

edited by

Małgorzata Borówko

*Maria Curie-Skłodowska University  
Lublin, Poland*



MARCEL DEKKER, INC.

NEW YORK • BASEL

**ISBN: 0-8247-0323-5**

This book is printed on acid-free paper.

**Headquarters**

Marcel Dekker, Inc.  
270 Madison Avenue, New York, NY 10016  
tel: 212-696-9000; fax: 212-685-4540

**Eastern Hemisphere Distribution**

Marcel Dekker AG  
Hutgasse 4, Postfach 812, CH-4001 Basel, Switzerland  
tel: 41-61-261-8482; fax: 41-61-261-8896

**World Wide Web**

<http://www.dekker.com>

The publisher offers discounts on this book when ordered in bulk quantities. For more information, write to Special Sales/Professional Marketing at the headquarters address above.

**Copyright © 2000 by Marcel Dekker, Inc. All Rights Reserved.**

Neither this book nor any part may be reproduced or transmitted in any form or by any means, electronic or mechanical, including photocopying, microfilming, and recording, or by any information storage and retrieval system, without permission in writing from the publisher.

Current printing (last digit):  
10 9 8 7 6 5 4 3 2 1

**PRINTED IN THE UNITED STATES OF AMERICA**

# Preface

Interfacial systems are frequently encountered in a large variety of phenomena in biology and industry. A few examples that come to mind are adsorption, catalysis, corrosion, flotation, osmosis, and colloidal stability. In particular, surface films are very interesting from a cognitive point of view. Surface science has a long history. For many years, natural philosophers were curious about interfacial phenomena because it was quite clear that matter near surface differs in its properties from the same matter in bulk. Decades of patient analysis and laboratory experiments gave only an approximate picture of a situation at the interface, which follows from a great complexity of investigated systems. However, much of the progress in science consists of asking old questions in new, more penetrating, and more wide-ranging ways.

One of the scientific advances that shaped history during the 20th century is the revolution in computer technology. It has given a strong impetus to the development of mathematical modelling of physical processes. The powerful new tools are vehemently accelerating the pace of interfacial research. We can easily carry out calculations that no one had previously imagined. Computer simulations have already had quite impressive achievements in surface science, so it seems timely to write a monograph summarizing the results.

The existing books cover the simple, rather than the advanced, theoretical approaches to interfacial systems. This volume should fill this gap in the literature. It is the purpose of this volume to serve as a comprehensive reference source on theory and simulations of various interfacial systems. Furthermore, it shows the power of statistical thermodynamics that offers a

reliable framework for an explanation of interfacial phenomena. This book is intended primarily for scientists engaged in theoretical physics and chemistry. It should also be a useful guide for all researchers and graduate students dealing with surface and colloid science.

The book is divided into 18 chapters written by different experts on various aspects. In many areas of contemporary science, one is confronted with the problem of theoretical descriptions of adsorption on solids. This problem is discussed in the first part of the volume. The majority of interfacial systems may be considered as fluids in confinement. Therefore, the first chapter is devoted to the behavior of confined soft condensed matter. Because quantum mechanics is a paradigm for microscopic physics, quantum effects in adsorption at surfaces are considered (Chapter 2). The theory of simple and chemically reacting nonuniform fluids is discussed in Chapters 3 and 4. In Chapters 5 and 6, the current state of theory of adsorption on energetically and geometrically heterogeneous surfaces, and in random porous media, is presented. Recent molecular computer-simulation studies of water and aqueous electrolyte solutions in confined geometries are reviewed in Chapter 7. In Chapter 8, the Monte Carlo simulation of surface chemical reactions is discussed within a broad context of integrated studies combining the efforts of different disciplines. Theoretical approaches to the kinetic of adsorption, desorption, and reactions on surfaces are reviewed in Chapter 9.

Chapters 10 through 14 examine the systems containing the polymer molecules. Computer simulations are natural tools in polymer science. This volume gives an overview of polymer simulations in the dense phase and the survey of existing coarse-grained models of living polymers used in computer experiments (Chapters 10 and 11). The properties of polymer chains adsorbed on hard surfaces are discussed in the framework of dynamic Monte Carlo simulations (Chapter 12). The systems involving surfactants and ordering in microemulsions are described in Chapters 13 and 14.

Chapters 15 through 17 are devoted to mathematical modeling of particular systems, namely colloidal suspensions, fluids in contact with semi-permeable membranes, and electrical double layers. Finally, Chapter 18 summarizes recent studies on crystal growth process.

I hope that this book will be useful for everyone whose professional activity is connected with surface science.

I would like to thank A. Hubbard for the idea of a volume on computer simulations in surface science and S. Sokołowski for fruitful discussions and encouragement. I thank the authors who contributed the various chapters. Finally, R. Zagórski is acknowledged for his constant assistance.

*Małgorzata Borówko*

# Contents

*Preface*      iii

*Contributors*      vii

1. Structure and Phase Behavior of Confined Soft Condensed Matter      1  
*Martin Schoen*
2. Quantum Effects in Adsorption at Surfaces      77  
*Peter Nielaba*
3. Integral Equations in the Theory of Simple Fluids      135  
*Douglas Henderson, Stefan Sokolowski, and Małgorzata Borówko*
4. Nonuniform Associating Fluids      167  
*Małgorzata Borówko, Stefan Sokolowski, and Orest Pizio*
5. Computer Simulations and Theory of Adsorption on Energetically and Geometrically Heterogeneous Surfaces      245  
*Andrzej Patrykiewicz and Małgorzata Borówko*
6. Adsorption in Random Porous Media      293  
*Orest Pizio*
7. Water and Solutions at Interfaces: Computer Simulations on the Molecular Level      347  
*Eckhard Spohr*

8.	Surface Chemical Reactions	387
	<i>Ezequiel Vicente Albano</i>	
9.	Theoretical Approaches to the Kinetics of Adsorption, Desorption, and Reactions at Surfaces	439
	<i>H. J. Kreuzer and Stephen H. Payne</i>	
10.	Computer Simulations of Dense Polymers	481
	<i>Kurt Kremer and Florian Müller-Plathe</i>	
11.	Computer Simulations of Living Polymers and Giant Micelles	509
	<i>Andrey Milchev</i>	
12.	Conformational and Dynamic Properties of Polymer Chains Adsorbed on Hard Surfaces	555
	<i>Andrey Milchev</i>	
13.	Systems Involving Surfactants	631
	<i>Friederike Schmid</i>	
14.	Ordering in Microemulsions	685
	<i>Robert Holyst, Alina Ciach, and Wojciech T. Gózdź</i>	
15.	Simulations of Systems with Colloidal Particles	745
	<i>Matthias Schmidt</i>	
16.	Fluids in Contact with Semi-permeable Membranes	775
	<i>Sohail Murad and Jack G. Powles</i>	
17.	Double Layer Theory: A New Point of View	799
	<i>Janusz Stafiej and Jean Badiali</i>	
18.	Crystal Growth and Solidification	851
	<i>Heiner Müller-Krumbhaar and Yukio Saito</i>	
	<i>Index</i>	933

# Contributors

**Ezequiel Vicente Albano, Ph.D.** Instituto de Investigaciones Fisicoquímicas Teóricas y Aplicadas, Universidad Nacional de La Plata, La Plata, Argentina

**Jean Badiali, Ph.D.** Structure et Réactivité des Systèmes Interfaciaux, Université P. et M. Curie, Paris, France

**Małgorzata Borówko, Ph.D.** Department for the Modelling of Physico-Chemical Processes, Maria Curie-Skłodowska University, Lublin, Poland

**Alina Ciach, Ph.D.** Institute of Physical Chemistry, Polish Academy of Sciences, Warsaw, Poland

**Wojciech T. Gózdź, Ph.D.** Institute of Physical Chemistry, Polish Academy of Sciences, Warsaw, Poland

**Douglas Henderson, Prof.** Department of Chemistry and Biochemistry, Brigham Young University, Provo, Utah

**Robert Hołyst, Ph.D.** Institute of Physical Chemistry, Polish Academy of Sciences, Warsaw, Poland

**Kurt Kremer, Ph.D.** Max-Planck-Institut für Polymerforschung, Mainz, Germany



**H. J. Kreuzer, Dr.rer.nat., F.R.S.C.** Department of Physics, Dalhousie University, Halifax, Nova Scotia, Canada

**Andrey Milchev, Ph.D., Dr.Sci.Habil.** Institute for Physical Chemistry, Bulgarian Academy of Sciences, Sofia, Bulgaria

**Florian Müller-Plathe, Ph.D.** Max-Planck-Institut für Polymerforschung, Mainz, Germany

**Heiner Müller-Krumbhaar, Prof. Dr.** Institut für Festkörperforschung, Forschungszentrum Jülich, Jülich GMBH, Germany

**Sohail Murad, Ph.D.** Department of Chemical Engineering, University of Illinois at Chicago, Chicago, Illinois

**Peter Nielaba, Prof. Dr.** Department of Physics, University of Konstanz, Konstanz, Germany

**Andrzej Patrykiewicz, Ph.D.** Department for the Modelling of Physico-Chemical Processes, Maria Curie-Skłodowska University, Lublin, Poland

**Stephen H. Payne** Department of Physics, Dalhousie University, Halifax, Nova Scotia, Canada

**Orest Pizio, Ph.D.** Instituto de Química de la Universidad Nacional Autónoma de México, Coyoacán, México

**Jack G. Powles, Ph.D., D.es.Sc.** Physics Laboratory, University of Kent, Canterbury, Kent, England

**Yukio Saito, Ph.D.** Department of Physics, Keio University, Yokohama, Japan

**Friederike Schmid, Dr.rer.nat.** Max-Planck-Institut für Polymerforschung, Mainz, Germany

**Matthias Schmidt, Dr.rer.nat.** Institut für Theoretische Physik II, Heinrich-Heine-Universität Düsseldorf, Düsseldorf, Germany

**Martin Schoen, Dr.rer.nat.** Fachbereich Physik – Theoretische Physik, Bergische Universität Wuppertal, Wuppertal, Germany

**Stefan Sokołowski, Ph.D.** Department for the Modelling of Physico-Chemical Processes, Maria Curie-Skłodowska University, Lublin, Poland

**Eckhard Spohr, Ph.D.** Department of Theoretical Chemistry, University of Ulm, Ulm, Germany

**Janusz Stafiej, Ph.D.** Department of Electrode Processes, Institute of Physical Chemistry, Polish Academy of Sciences, Warsaw, Poland

# 1

## Structure and Phase Behavior of Confined Soft Condensed Matter

**MARTIN SCHOEN** Fachbereich Physik—Theoretische Physik,  
Bergische Universität Wuppertal, Wuppertal, Germany

I.	Introduction	2
II.	Equilibrium Theory of Confined Phases	3
	A. Thermodynamics	3
	B. Symmetry and homogeneity of thermodynamic potentials	11
	C. Statistical physics	16
III.	Monte Carlo Simulations	21
	A. Stochastic processes	22
	B. Implementation of stress-strain ensembles for open and closed systems	24
	C. The Taylor-expansion algorithm for “simple” fluids	26
	D. Orientationally biased creation of molecules	28
IV.	Microscopic Structure	29
	A. Planar substrates	29
	B. The transverse structure of confined fluids	41
	C. Nonplanar substrates	45
V.	Phase Transitions	49
	A. Shear-induced phase transitions in confined fluids	49
	B. Liquid-gas equilibria in confined systems	56
	References	66

## I. INTRODUCTION

In many areas of contemporary science and technology one is confronted with the problem of miniaturizing parts of the system of interest in order to control processes on very short length and time scales [1]. For example, to study the kinetics of certain chemical reactions, reactants have to be mixed at a sufficiently high speed. By miniaturizing a continuous-flow mixer, Knight et al. have recently shown that nanoliters can be mixed within microseconds, thus permitting one to study fast reaction kinetics on time scales unattainable with conventional mixing technology [2]. The importance of designing and constructing microscopic machines gave rise to a new field in applied science and engineering known as "microfabrication technology" or "microengineering" [3]. A central problem in the operation of such small mechanical machines is posed by friction between movable machine parts and wear. Lubricants consisting of, say, organic fluids can be employed to reduce these ultimately destructive phenomena. Their functioning depends to a large extent on the nature of the interaction between the fluid and the solid substrate it lubricates [4,5]. In the case of micromachines the lubricant may become a thin confined film of a thickness of only one or two molecular layers. The impact of such severe confinement is perhaps best illustrated by the dramatic increase of the shear viscosity in a hexadecane film of a thickness of two molecular layers, which may exceed the bulk shear viscosity by four orders of magnitude [6].

Understanding the effect of confinement on the phase behavior and materials properties of fluids is therefore timely and important from both a fundamental scientific and an applied technological perspective. This is particularly so because the fabrication and characterization of confining substrates with prescribed chemical or geometrical structures on a nano- to micrometer length scale can nowadays be accomplished in the laboratory with high precision and by a variety of techniques. For example, by means of various lithographic methods [3,7] or wet chemical etching [8] the surfaces of solid substrates can be endowed with well-defined nanoscopic lateral structures. In yet another method the substrate is chemically patterned by elastomer stamps and, in certain cases, subsequent chemical etching [9–12].

The development of a host of scanning probe devices such as the atomic force microscope (AFM) [13–17] and the surface forces apparatus (SFA) [18–22], on the other hand, enables experimentalists to study almost routinely the behavior of soft condensed matter confined by such substrates to spaces of molecular dimensions. However, under conditions of severe confinement a direct study of the relation between material properties and the microscopic structure of confined phases still remains an experimental challenge.

Computer simulations, on the other hand, are ideally suited to address this particular question from a theoretical perspective. Generally speaking, computer simulations permit one to pursue the motion of atoms or molecules in space and time. Since the only significant assumption concerns the choice of interaction potentials, the behavior of condensed matter can be investigated essentially in a first-principles fashion. At each step of the simulation one has instantaneous access to coordinates and momenta of all molecules. Thus, by applying the laws of statistical physics, one can determine the thermomechanical properties of condensed matter as well as its underlying microscopic structure. In many cases the insight gained by computer simulations was and is unattainable by any other theoretical means. Perhaps the most prominent and earliest example in this regard concerns the prediction of solid–fluid phase transitions in hard-sphere fluids at high packing fraction [23].

However, because of limitations of computer time and memory required to treat dense many-particle systems, computer simulations are usually restricted to microscopic length and time scales (with hard-sphere fluids, which may be viewed as a model for colloidal suspensions [24] (this volume, chapter by M Schmidt), and Brownian dynamics [25] as two prominent exceptions). This limitation can be particularly troublesome in investigations of, say, critical phenomena where the correlation length may easily exceed the microscopic size of the simulation cell. In confinement, on the other hand, a phase may be physically bound to microscopically small volumes in one or more dimensions by the presence of solid substrates so that computer simulations almost become a natural theoretical tool of investigation by which experimental methods can be complemented. It is then not surprising that the study of confined phases by simulational techniques is still flourishing [26], illustrated here for one particular aspect, namely the relation between microscopic structure and phase transitions in confined fluids. In Sec. II an introduction to equilibrium theory of confined phases will be given. Sec. III is devoted to formal and technical aspects of computer simulations. In Sec. IV the microscopic structure of confined phases will be analyzed for a number of different systems. The chapter concludes in Sec. V with a description of phase transitions that are unique to phases in confined geometry.

## **II. EQUILIBRIUM THEORY OF CONFINED PHASES**

### **A. Thermodynamics**

#### **1. Experiments with the Surface Forces Apparatus**

The force exerted by a thin fluid film on a solid substrate can be measured with nearly molecular precision in the SFA [27]. In the SFA a thin film is

confined between the surfaces of two cylinders arranged such that their axes are at right angles [27]. In an alternative setup the fluid is confined between the surface of a macroscopic sphere and a planar substrate [28]. However, crossed-cylinder and sphere–plane configurations can be mapped onto each other by differential-geometrical arguments [29]. The surface of each macroscopic object is covered by a thin mica sheet with a silver backing, which permits one to measure the separation  $h$  between the surfaces by optical interferometry [27]. The radii are macroscopic so that the surfaces may be taken as parallel on a *molecular* length scale around the point of minimum distance. In addition, they are *locally* planar, since mica can be prepared with atomic smoothness over molecularly large areas. This setup is immersed in a bulk reservoir of the same fluid of which the film consists. Thus, at thermodynamic equilibrium temperature  $T$  and chemical potential  $\mu$  are equal in both subsystems (i.e., film and bulk reservoir). By applying an external force in the direction normal to both substrate surfaces, the thickness of the film can be altered either by expelling molecules from it or by imbibing them from the reservoir until thermodynamic equilibrium is re-established, that is, until the force exerted by the film on the surfaces equals the applied normal force. Plotting this force per radius  $R$ ,  $F/R$ , as a function of  $h$  yields a damped oscillatory curve in many cases (see, for instance, Fig. 1 in Ref. [30]).

In another mode of operation of the SFA a confined fluid can be exposed to a shear strain by attaching a movable stage to the upper substrate (i.e., wall) via a spring characterized by its spring constant  $k$  [6,31,32] and moving this stage at some constant velocity in, say, the  $x$  direction parallel to the film–wall interface. Experimentally it is observed that the upper wall first “sticks” to the film, as it were, because the upper wall remains stationary. From the known spring constant and the measured elongation of the spring, the shear stress sustained by the film can be determined. Beyond a critical shear strain (i.e., at the so-called “yield point” corresponding to the maximum shear stress sustained by the film) the shear stress declines abruptly and the upper wall “slips” across the surface of the film. If the stage moves at a sufficiently low speed the walls eventually come to rest again until the critical shear stress is once again attained so that the stick–slip cycle repeats itself periodically.

This stick–slip cycle, observed for all types of film compounds ranging from long-chain (e.g., hexadecane) to spheroidal [e.g., octamethylcyclotetrasiloxane (OMCTS)] hydrocarbons [21], has been attributed by Gee et al. [30] to the formation of solid-like films that pin the walls together (region of sticking) and must be made to flow plastically in order for the walls to slip. This suggests that the structure of the walls induces the formation of a solid film when the walls are properly registered and that this film “melts” when

the walls are moved out of the correct registry. As was first demonstrated in Ref. 33, such solid films may, in fact, form in “simple” fluids between commensurate walls on account of a template effect imposed on the film by the discrete (i.e., atomically structured) walls. However, noting that the stick–slip phenomenon is general, in that it is observed in every liquid investigated, and that the yield stress may exhibit hysteresis, Granick [21] has argued that mere confinement may so slow mechanical relaxation of the film that flow must be activated on a time scale comparable with that of the experiment. This more general mechanism does not necessarily involve solid films which can be formed only if the (solid-like) structure of the film and that of the walls possess a minimum geometrical compatibility.

2. The Fluid Lamella

For a theoretical analysis of SFA experiments it is prudent to start from a somewhat oversimplified model in which a fluid is confined by two parallel substrates in the  $z$  direction (see Fig. 1). To eliminate edge effects, the substrates are assumed to extend to infinity in the  $x$  and  $y$  directions. The *system* in the thermodynamic sense is taken to be a lamella of the fluid bounded by the substrate surfaces and by segments of the (imaginary) planes  $x = 0$ ,  $x = s_x$ ,  $y = 0$ , and  $y = s_y$ . Since the lamella is only a virtual construct it is convenient to associate with it the computational cell in later practical

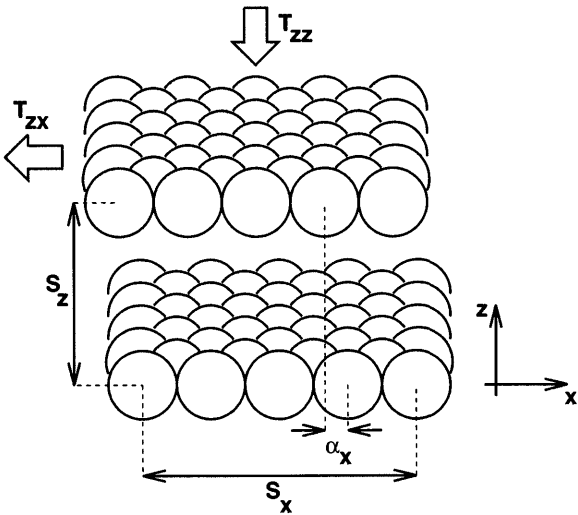


**FIG. 1** Schematic of two atomically structured, parallel surface planes (from Ref. 134).

applications (see Secs. IV, V). It is assumed that the lower substrate is stationary in the laboratory coordinate frame, whose origin is at  $\mathbf{0}$ , and that the substrates are identical and rigid. The crystallographic structure of the substrate is described by a rectangular unit cell having transverse dimensions  $\ell_x \times \ell_y$ . In general, each substrate consists of a large number of planes of atoms parallel with the  $x$ - $y$  plane. The plane at the film-substrate interface is called the *surface plane*. It is taken to be contained in the  $x$ - $y$  plane. The distance between the surface planes is  $s_z$ . To specify the transverse alignment of the substrates, registry parameters  $\alpha_x$  and  $\alpha_y$  are introduced. Coordinates of a given atom (2) in the upper surface plane ( $z = s_z$ ) are related to its counterpart (1) in the lower surface plane ( $z = 0$ ) by

$$\left. \begin{aligned} x^{[2]} &= x^{[1]} + \alpha_x \ell_x \\ y^{[2]} &= y^{[1]} + \alpha_y \ell_y \\ z^{[2]} &= z^{[1]} + s_z \end{aligned} \right\} \quad (1)$$

Thus the extensive variables characterizing the lamellar system are entropy  $S$ , number of fluid molecules  $N$ ,  $s_x$ ,  $s_y$ ,  $s_z$ ,  $\alpha_x \ell_x$ , and  $\alpha_y \ell_y$ .

Gibbs's fundamental relation governing an infinitesimal, reversible transformation can be written

$$d\mathcal{U} = TdS + \mu dN - dW_{\text{mech}} \quad (2)$$

where the mechanical work can be expressed as

$$-dW_{\text{mech}} = \sum_{s_\alpha} \left( \frac{\partial \mathcal{U}}{\partial s_\alpha} \right)_{S, N, \{s_\beta\}_{\beta \neq \alpha}} ds_\alpha = \sum_\alpha' \sum_\beta' A_\alpha T_{\alpha\beta} ds_\beta \quad (3)$$

The primes denote restricted summations over Cartesian components ( $\alpha, \beta = x, y, z$ ),  $ds_\alpha$  is a displacement in the  $\alpha$  direction,  $A_\alpha$  is the area of the  $\alpha$ -directed face of the lamella, and  $T_{\alpha\beta}$  is the average of the  $\beta$ -component of the stress applied to  $A_\alpha$ . Note that if the force exerted by the lamella on  $A_\alpha$  points outward,  $T_{\alpha\beta} < 0$ . Thus,  $dW_{\text{mech}}$  is the mechanical work done *by* the system *on* the surroundings. Terms involving diagonal and off-diagonal elements of the stress tensor  $\mathbf{T}$  in Eq. (3) respectively represent the work of compressing and shearing the lamella. Note that because the substrates are rigid they cannot be compressed or sheared. This is the reason for the absence of the four off-diagonal contributions involving  $T_{xz}$ ,  $T_{yz}$ ,  $T_{xy}$ , and  $T_{yx}$ .

To introduce area  $A \equiv A_z$  as an independent variable, the transformation

$$\left. \begin{aligned} A &= s_x s_y \\ R &= s_x / s_y \end{aligned} \right\} \quad (4)$$



is introduced. In terms of these new variables Eq. (2) becomes

$$d\mathcal{U} = TdS + \mu dN + \gamma' dA + \gamma'' AdR + T_{zz}Ads_z + T_{zx}Ad(\alpha_x \ell_x) + T_{zy}Ad(\alpha_y \ell_y) \quad (5)$$

where the interfacial tensions  $\gamma'$  and  $\gamma''$  are defined by

$$\gamma' = \left( \frac{\partial \mathcal{U}}{\partial A} \right)_{S, N, R, s_z, \alpha_x, \alpha_y} = \frac{(T_{xx} + T_{yy})s_z}{2} \quad (6)$$

$$A\gamma'' = \left( \frac{\partial \mathcal{U}}{\partial R} \right)_{S, N, A, s_z, \alpha_x, \alpha_y} = A \frac{(T_{xx} - T_{yy})s_z}{2R} \quad (7)$$

Note that the definition of  $R$  is arbitrary. However, the present choice seems simplest and has a transparent physical interpretation. The work done by the system in an infinitesimal reversible transformation at constant  $S$ ,  $N$ ,  $A$ ,  $s_z$ ,  $\alpha_x \ell_x$ , and  $\alpha_y \ell_y$  is given by

$$dW = T_{xx}s_y s_z ds_x + T_{yy}s_x s_z ds_y = (T_{xx} - T_{yy})s_y s_z ds_x = \gamma'' AdR \quad (8)$$

because  $ds_y = -s_y s_x^{-1} ds_x$ . It is then clear that the fourth term in Eq. (5) is the net work done by the lamella as its shape ( $R = s_x/s_y$ ) is changed at fixed area.

To recast the thermodynamic description in terms of independent variables that can be controlled in actual laboratory experiments (i.e.,  $T$ ,  $\mu$ , and the set of strains or their conjugate stresses), it is sensible to introduce certain auxiliary thermodynamic potentials via Legendre transformations. This chapter is primarily concerned with

$$\Phi := \Omega - T_{zz}As_z \quad (9)$$

where the grand potential is given by

$$\Omega(T, \mu, A, R, s_z, \alpha_x \ell_x, \alpha_y \ell_y) := \mathcal{U} - TS - \mu N =: \mathcal{F} - \mu N \quad (10)$$

and  $\mathcal{F}$  is the free energy. The exact differential of the grand potential follows as

$$d\Omega = -SdT - Nd\mu + \gamma' dA + \gamma'' AdR + T_{zz}Ads_z + T_{zx}Ad(\alpha_x \ell_x) + T_{zy}Ad(\alpha_y \ell_y) \quad (11)$$

where Eqs. (5) and (10) have also been employed. Other relevant potentials can be obtained by suitable Legendre transformations of  $\mathcal{F}$  or  $\Omega$  with respect to, say,  $T_{zz}$ ,  $T_{zx}$ , or  $T_{zy}$  (see Sec. V A1).

Conditions for thermodynamic equilibrium of the lamella can be derived by considering the lamella plus its environment as an *isolated* supersystem. Assuming the entropy of the supersystem to be fixed, one knows that the

internal energy must be minimum in a state of thermodynamic equilibrium. In mathematical terms, an infinitesimal virtual transformation that would take the system from this state must satisfy

$$\delta(\mathcal{U} + \tilde{\mathcal{U}}) \geq 0 \quad (12)$$

$$\delta(\mathcal{S} + \tilde{\mathcal{S}}) \geq 0 \quad (13)$$

where  $\delta\mathcal{U}$  is given in Eqs. (2), (3) and  $\delta\tilde{\mathcal{U}}$  by

$$\delta\tilde{\mathcal{U}} = \tilde{T}\delta\tilde{\mathcal{S}} + \tilde{\mu}\delta\tilde{N} + \sum_{\alpha}' \sum_{\beta}' A_{\alpha} \tilde{T}_{\alpha\beta} \delta\tilde{s}_{\beta} \quad (14)$$

and the tilde refers to environmental variables. Viewing the environment as virtual pistons, displacements  $\delta\tilde{s}_{\alpha}$  of the boundary between them and the lamella satisfy the equation  $\delta\tilde{s}_{\alpha} = -\delta s_{\alpha}$ . Moreover, because the supersystem is materially closed,  $\delta\tilde{N} = -\delta N$ . From these two conditions and Eqs. (12)–(14), the equilibrium conditions

$$\left. \begin{aligned} \tilde{T} &= T \\ \tilde{\mu} &= \mu \\ \tilde{T}_{\alpha\beta} &= T_{\alpha\beta} \end{aligned} \right\} \quad (15)$$

are deduced. Now suppose the lamella is subject to thermal, mechanical, and chemical reservoirs that maintain temperature, normal stress, and chemical potential fixed at the values  $\tilde{T}$ ,  $\tilde{T}_{zz}$ , and  $\tilde{\mu}$ . Assume also that the “complementary” strains  $A$ ,  $R$ ,  $\alpha_x \ell_x$ , and  $\alpha_y \ell_y$  are kept fixed. Then one has, from Eqs. (12) and (14)

$$\delta\mathcal{U} + \tilde{T}\delta\tilde{\mathcal{S}} + \tilde{\mu}\delta\tilde{N} + \sum_{\alpha}' \sum_{\beta}' A_{\alpha} \tilde{T}_{\alpha\beta} \delta\tilde{s}_{\beta} = \delta[\mathcal{U} - \tilde{T}\mathcal{S} - \tilde{\mu}N - A\tilde{T}_{zz}s_z] \geq 0 \quad (16)$$

Because of Eqs. (9), (10), and (15) this is equivalent to  $\delta\Phi \geq 0$ ; that is, when the lamella is at equilibrium at fixed  $T$ ,  $\mu$ ,  $A$ ,  $R$ ,  $T_{zz}$ ,  $\alpha_x \ell_x$ , and  $\alpha_y \ell_y$ ,  $\Phi$  is minimum.

### 3. Derjaguin's Approximation

To make contact with the SFA experiment one has to realize that the confining surfaces are only locally parallel. Because of the macroscopic curvature of the substrate surfaces,  $T_{zz}$  becomes a local quantity which varies with the vertical distance  $s_z = s_z(x, y)$  between the substrate surfaces (see Fig. 2). Since the sphere–plane arrangement (see Sec. II A1) is immersed in bulk fluid at pressure  $P_{\text{bulk}}$ , the total force exerted on the sphere by the film in

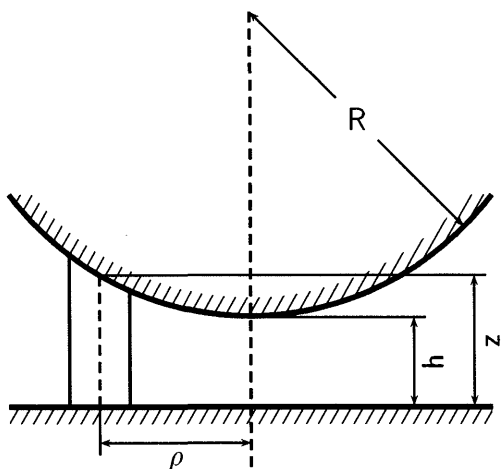


**FIG. 2** Side view of film confined between a sphere of macroscopic radius  $R$  and a planar substrate surface. The shortest distance between two points located on the surface of the sphere and of the substrate, respectively, is denoted by  $h$  (from Ref. 48).

the  $z$  direction can be expressed as

$$F(h; \mu, T) = - \int dx \int dy [T_{zz}(s_z(x, y); \mu, T) + P_{\text{bulk}}(\mu, T)] \quad (17)$$

which depends on the (bulk) thermodynamic state specified by  $T$  and  $\mu$ . This solvation, or depletion, force plays a vital role in the context of binary mixtures of colloidal particles of different sizes [34] (this volume, chapter by M. Schmidt). Because of their practical importance for colloid–polymer mixtures [35], depletion forces in binary hard-sphere mixtures have recently received a lot of attention and have been studied by a range of methods, including integral equations based upon sophisticated hypernetted chain closure approximations [36–41], density functional theory [42,43], virial expansion [44], and computer simulation [45–47].

To evaluate the integral in Eq. (17), it is convenient to transform from cartesian to cylindrical coordinates (see Fig. 2) to obtain

$$\begin{aligned} F(h) &= - \int_0^{2\pi} d\phi \int_0^R \rho d\rho [T_{zz}(s_z) + P_{\text{bulk}}] = 2\pi \int_0^R \rho d\rho f(s_z) \\ &= 2\pi \int_h^{h+R} ds_z (R - s_z + h) f(s_z) \end{aligned} \quad (18)$$

where the arguments  $\mu$  and  $T$  have been dropped to simplify notation and the far right side follows from  $s_z = h + R - \sqrt{R^2 - \rho^2}$  (see Fig. 2) [48]. In Eq. (18)

$$\begin{aligned} f(s_z) &:= -T_{zz}(s_z) - P_{\text{bulk}} = -\frac{1}{A} \left( \frac{\partial \Omega}{\partial s_z} \right)_{T, \mu, A} + \left( \frac{\partial \Omega_{\text{bulk}}}{\partial V} \right)_{T, \mu} \\ &=: -\frac{1}{A} \left( \frac{\partial \Omega^{\text{ex}}}{\partial s_z} \right)_{T, \mu, A} \end{aligned} \quad (19)$$

which follows from Eq. (11) (fixed  $R, \alpha_x \ell_x, \alpha_y \ell_y$ ) and a similar expression for the bulk reservoir

$$d\Omega_{\text{bulk}} = -S_{\text{bulk}} dT - N_{\text{bulk}} d\mu - P_{\text{bulk}} dV \quad (20)$$

where  $V$  is the bulk volume. In Eq. (19) the excess grand potential  $\Omega^{\text{ex}} := \Omega - \Omega_{\text{bulk}}$  is also introduced. Assuming  $V = A s_z$ , the far right side of Eq. (19) obtains because the bulk phase is isotropic. Furthermore, note that  $f(s_z(\rho))$  vanishes in the limit  $s_z \rightarrow \infty$  because of [49]

$$\lim_{s_z \rightarrow \infty} T_{zz}(s_z) = -P_{\text{bulk}} \quad (21)$$

so that  $f(s_z)$  may be interpreted as the *excess normal* pressure exerted on the sphere by the fluid. In Eq. (19),  $F(h)$  still depends on the curvature of the substrate surfaces through  $R$ . Experimentally, one is normally concerned with measuring  $F(h)/R$  rather than the solvation force itself [27], because for macroscopically curved substrate surfaces this ratio is independent of  $R$ . This can be rationalized by realizing that  $T_{zz}(s_z) + P_{\text{bulk}}$  vanishes on a microscopic length scale much smaller than  $R$ . The upper integration limit in Eq. (19) may then be taken to infinity to give

$$\frac{F(h)}{2\pi R} = \int_h^\infty ds_z f(s_z) = -\frac{1}{A} \int_h^\infty ds_z \left( \frac{\partial \Omega^{\text{ex}}}{\partial s_z} \right)_{T, \mu, A} = \frac{\Omega^{\text{ex}}(h)}{A} =: \omega^{\text{ex}}(h) \quad (22)$$

because  $\Omega^{\text{ex}}$  vanishes in the limit  $s_z \rightarrow \infty$  according to the definition in Eq. (19). In Eq. (22) we introduce  $\omega^{\text{ex}}(h)$  as the *excess* grand potential per unit area of a fluid confined between two *planar* substrate surfaces separated by a distance  $h$ . The far right side of Eq. (22) is known as the Derjaguin approximation (see Eq. (6) in Ref. 29). As pointed out recently by Götzelmann et al. [43], the Derjaguin approximation is exact in the limit of a macroscopic sphere (i.e., if  $R \rightarrow \infty$ ), which is the only case of interest here. A rigorous proof can be found in the appendix of Ref. 50. A similar “Derjaguin approximation” for shear forces exerted on curved substrates has recently been proposed by Klein and Kumacheva [51].

Eq. (22) is a key expression because it links the quantity  $F(h)/R$  that can be determined directly in SFA experiments to the local stress  $T_{zz}$  available from computer simulations (see Sec. IV A 1). It is also interesting that differentiating Eq. (22) yields

$$\frac{1}{2\pi} \frac{d}{dh} \frac{F(h)}{R} = \frac{d\omega^{\text{ex}}(h)}{dh} = T_{zz}(h) + P_{\text{bulk}} = -f(h) \quad (23)$$

Eq. (23) is particularly useful because it relates a derivative of experimentally accessible data directly to the stress exerted locally on the macroscopically curved substrates at the point  $(0, 0, s_z = h)$  (see Fig. 2, Secs. IV A 2, IV A 3).

## B. Symmetry and Homogeneity of Thermodynamic Potentials

An important issue in the thermodynamics of confined fluids concerns their symmetry which is lower than that of a corresponding homogeneous bulk phase because of the presence of the substrate and its inherent atomic structure [52]. The substrate may also be nonplanar (see Sec. IV C) or may consist of more than one chemical species so that it is heterogeneous on a nanoscopic length scale (see Sec. V B 3). The reduced symmetry of the confined phase led us to replace the usual compressional-work term  $-P_{\text{bulk}}V$  in the bulk analogue of Eq. (2) by individual stresses and strains. The appearance of shear contributions also reflects the reduced symmetry of confined phases.

### 1. Atomically Smooth Substrates

The simplest situation is one in which a planar substrate lacks any crystallographic structure. Then the confined fluid is homogeneous and isotropic in transverse  $(x, y)$  directions. All off-diagonal elements of  $\mathbf{T}$  vanish,  $T_{xx} = T_{yy} = T_{\parallel}$ , and Eq. (5) simplifies to

$$d\mathcal{U} = T dS + \mu dN + \gamma' dA + T_{zz} A ds_z \quad (24)$$

By symmetry,  $\gamma' \neq f(A)$  at fixed  $T$ ,  $\mu$ , and  $s_z$ . Hence, under these conditions one can formally integrate Eq. (24) to obtain

$$\mathcal{U} = TS + \mu N + \gamma' A \quad (25)$$

taking the zero of  $\mathcal{U}$  to correspond to zero interfacial area. From Eqs. (6), (10), and (25) one gets

$$\Omega = T_{\parallel} A s_z \quad (26)$$

which is the analogue of the bulk relation  $\Omega = -P_{\text{bulk}} V$ . From Eq. (9) it is straightforward to realize that

$$\Phi = (T_{\parallel} - T_{zz}) A s_z \geq 0 \quad (27)$$

is a nontrivial quantity (because in general  $T_{\parallel} \neq T_{zz}$ ), whereas its bulk analogue vanishes trivially because  $T_{\parallel} = T_{zz} = -P_{\text{bulk}}$  on account of the higher symmetry of bulk phases reflected by Eq. (21) [52]. From Eqs. (10), (24), and (25), the Gibbs–Duhem equation

$$0 = S dT + A d\gamma' + N d\mu - T_{zz} A ds_z \quad (28)$$

follows immediately.

## 2. The Two-dimensional Ideal Gas in an External Potential

While the smooth substrate considered in the preceding section is sufficiently realistic for many applications, the crystallographic structure of the substrate needs to be taken into account for more realistic models. The essential complications due to lack of transverse symmetry can be delineated by the following two-dimensional structured-wall model: an ideal gas confined in a periodic square-well potential field (see Fig. 3). The two-dimensional lamella remains rectangular with variable dimensions  $s_x$  and  $s_y$  and is therefore not subject to shear stresses. The boundaries of the lamella coinciding with the  $x$  and  $y$  axes are anchored. From Eqs. (2) and (10) one has

$$d\mathcal{F} = -S dT + \mu dN + T_{xx} s_y ds_x + T_{yy} s_x ds_y \quad (29)$$

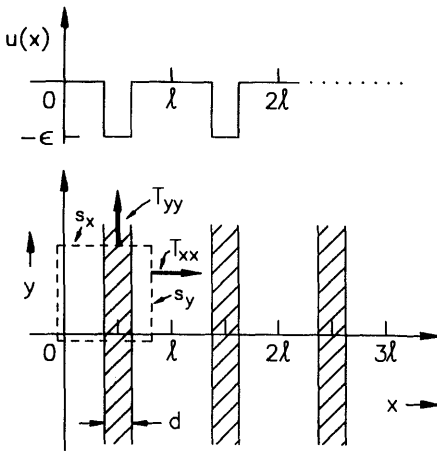


**FIG. 3** Schematic of the two-dimensional square-well potential  $u(x)$  of depth  $\epsilon$ , width  $d$ , and period  $\ell$  (from Ref. 48).

for the free energy of the ideal gas under these premises. From standard textbook considerations one also knows the statistical-physical expression [53]

$$\mathcal{F} = -\beta^{-1} \ln \mathcal{Q} \quad (30)$$

where  $\beta = 1/k_B T$  ( $k_B$  is Boltzmann's constant). The canonical partition function  $\mathcal{Q}$  can be written more explicitly as  $\mathcal{Q} = q^N/N!$  where the atomic partition function is given by

$$\begin{aligned} q &= q(T, s_x, s_y) = \frac{\mathcal{Z}_1}{\Lambda^2} = \Lambda^{-2} \int_0^{s_x} dx \int_0^{s_y} dy \exp[-\beta u(x)] \\ &= \frac{s_y}{\Lambda^2} \int_0^{s_x} dx \exp[-\beta u(x)], \end{aligned} \quad (31)$$

where  $\mathcal{Z}_1$  is the single-atom configurational integral, and  $\Lambda$  is the thermal de Broglie wavelength. The far right side of Eq. (31) follows immediately because the potential energy of a molecule in the present two-dimensional ideal gas does not depend on its  $y$  coordinate (see Fig. 3).

The configuration integral depends on  $s_x$  in a piecewise fashion. For  $s_x$  in the  $n$ th period of the potential, that is for  $(n-1)l < s_x \leq nl$  ( $n \in \mathbb{N}$ ), one obtains

$$\begin{aligned} \mathcal{Z}_1 &= s_y(n-1)\{l + [\exp(\beta\epsilon) - 1]d\} \\ &+ s_y \begin{cases} s_x - (n-1)l; & s_x \in \mathcal{I}_1 \\ \exp(\beta\epsilon)[s_x - (n-1)l] - [\exp(\beta\epsilon) - 1](l-d)/2; & s_x \in \mathcal{I}_2 \\ s_x - (n-1)l + [\exp(\beta\epsilon) - 1]d; & s_x \in \mathcal{I}_3 \end{cases} \end{aligned} \quad (32)$$

where

$$\begin{aligned} \mathcal{I}_1 &= \left[ (n-1)l, (2n-1)\frac{l}{2} - d/2 \right] \\ \mathcal{I}_2 &= \left[ (2n-1)\frac{l}{2} - \frac{d}{2}, (2n-1)\frac{l}{2} + \frac{d}{2} \right], \end{aligned}$$

and

$$\mathcal{I}_3 = \left[ (2n-1)\frac{l}{2} + \frac{d}{2}, nl \right]$$

From Eqs. (29)–(31) one has

$$\left. \begin{aligned} T_{xx} &= -\frac{Nk_B T}{\mathcal{Z}_1 s_y} \left( \frac{\partial \mathcal{Z}_1}{\partial s_x} \right)_{T, s_y} \\ T_{yy} &= -\frac{Nk_B T}{\mathcal{Z}_1 s_x} \left( \frac{\partial \mathcal{Z}_1}{\partial s_y} \right)_{T, s_x} \\ \mu &= -k_B T \ln(\mathcal{Z}_1 / \Lambda^2 N) \end{aligned} \right\} \quad (33)$$

With the help of Eq. (32) the first two expressions can be written explicitly as

$$T_{xx} = -P_{\text{bulk}} \begin{cases} 1; & s_x \in \mathcal{I}_3 \\ \exp(\beta\epsilon); & s_x \in \mathcal{I}_2 \\ 1; & s_x \in \mathcal{I}_3 \end{cases} \quad (34)$$

and

$$\begin{aligned} T_{yy} &= -\frac{P_{\text{bulk}}}{s_x} (n-1) \{ l + [\exp(\beta\epsilon) - 1]d \} \\ &\quad - \frac{P_{\text{bulk}}}{s_x} \begin{cases} s_x - (n-1)l; & s_x \in \mathcal{I}_1 \\ \exp(\beta\epsilon)[s_x - (n-1)l] - [\exp(\beta\epsilon) - 1](l-d)/2; & s_x \in \mathcal{I}_2 \\ s_x - (n-1)l + [\exp(\beta\epsilon) - 1]d; & s_x \in \mathcal{I}_3 \end{cases} \end{aligned} \quad (35)$$

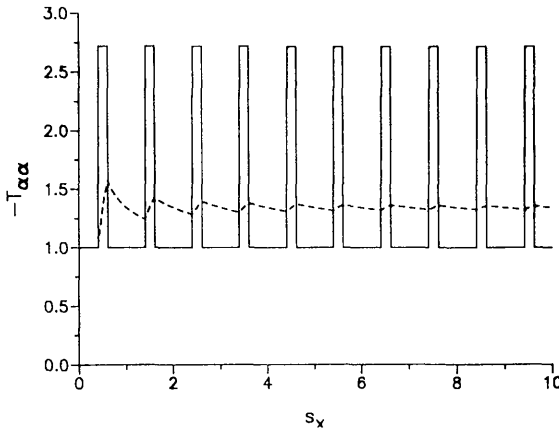
where  $P_{\text{bulk}} = \beta^{-1} \exp(\beta\mu) / \Lambda^2$  is the pressure of the two-dimensional ideal bulk gas in thermodynamic equilibrium with the confined fluid.

Fig. 4 displays plots of  $-T_{xx}$  and  $-T_{yy}$  versus  $s_x$ . From these it is clear that both stresses are functions of the size of the lamella. The most significant consequence of this is that, unlike Eq. (24), Eq. (29) cannot be integrated at fixed  $T$ ,  $\mu$ , and  $s_y$  in general to yield an expression analogous to Eq. (25) without additional equations of state, that is  $T_{xx} = T_{xx}(s_x)$ ,  $T_{yy} = T_{yy}(s_x)$ . In other words, a Gibbs–Duhem equation corresponding to Eq. (28) does not obtain for the present two-dimensional structured-wall model. The same conclusion holds for more realistic three-dimensional structured-wall models [54]. The lack of a Gibbs–Duhem equation for general thermodynamic transformations is a direct consequence of the additional reduction of the confined fluid’s symmetry caused by the discrete atomic structure of the substrate (see Sec. II B 1).

### 3. Coarse-grained Thermodynamics

While a Gibbs–Duhem equation does not exist for general transformations  $ds_\alpha \rightarrow ds'_\alpha$ , a specialized (i.e., “coarse-grained”) Gibbs–Duhem equation





**FIG. 4** Plots of  $-T_{xx}$  (—) and  $-T_{yy}$  (---) versus  $s_x$  for the ideal gas confined to the two-dimensional periodic square-well potential depicted in Fig. 3. Distance is measured in units of the period  $l$ ; stress in units of the pressure of the bulk ideal gas at the given  $T$  and  $\mu$  ( $d/l = 0.20$ ) (from Ref. 54).

may be derived for cases in which the transverse dimensions of the lamella are changed only discretely, that is, in such a way that the surface plane at the fluid–wall interface of the lamella always comprises an integer number  $n$  of unit cells in both  $x$  and  $y$  directions so that

$$\left. \begin{aligned} s_x &= n\ell_x \\ s_y &= n\ell_y \end{aligned} \right\} \quad (36)$$

Thus, the exchange of work between the lamella and its surroundings is effected on a coarse-grained length scale defined in units of  $\{\ell_x, \ell_y\}$ . Eliminating  $s_x$  and  $s_y$  in Eq. (11) in favor of  $n$  gives

$$d\Omega = -S dT - N d\mu + 2T_{\parallel} a s_z n dn + T_{zz} a n^2 ds_z \quad (37)$$

where work contributions due to shear and deformations of the shape of the lamella are neglected for simplicity. In Eq. (37),  $a := \ell_x \ell_y$  is the unit-cell area and

$$T_{\parallel}(T, \mu, n, s_z) = \frac{1}{2} [T_{xx}(T, \mu, n\ell_x, n\ell_y, s_z) + T_{yy}(T, \mu, n\ell_x, n\ell_y, s_z)] \quad (38)$$

is the “mean” stress applied transversely on the  $n \times n$  lamella. If  $T$ ,  $\mu$ , and  $s_z$  are fixed,  $T_{xx}$  and  $T_{yy}$  are periodic in  $s_x$  and  $s_y$ , having periods  $\ell_x$  and  $\ell_y$ , respectively. Thus, for the restricted class of transformations

$n \rightarrow n' = n \pm m$  ( $n, m$  integer),  $T_{\parallel}$  is constant provided  $n$  and  $n'$  are sufficiently large for intensive properties to be independent of the (microscopic) size of the lamella. Under these conditions Eq. (37) can be integrated to get

$$\Omega = T_{\parallel} a s_z n^2, \quad \text{fixed } T, \mu, s_z \quad (39)$$

Eq. (39) may be differentiated subsequently to give

$$d\Omega = 2T_{\parallel} a s_z n \, dn + a n^2 d(T_{\parallel} s_z) \quad (40)$$

Equating the expressions for  $d\Omega$  given in Eqs. (37) and (40) and rearranging terms yields the coarse-grained Gibbs–Duhem equation

$$0 = S \, dT + N \, d\mu + a n^2 d(T_{\parallel} s_z) - a n^2 T_{zz} \, ds_z \quad (41)$$

which permits one to define the (transverse) isothermal compressibility  $\kappa_{\parallel}$

$$\frac{N^2}{A s_z} \kappa_{\parallel} = \left( \frac{N}{a n^2} \right)^2 \frac{1}{s_z} \left( \frac{\partial(a n^2)}{\partial T_{\parallel}} \right)_{T, N, s_z} = \left( \frac{\partial N}{\partial \mu} \right)_{T, n, s_z} \quad (42)$$

where  $A = n^2 a$  as detailed in Ref. 55. Note that a similar definition is prevented for general transformations  $ds_{\alpha} \rightarrow ds'_{\alpha}$  according to the discussion in Sec. II B 2.

## C. Statistical Physics

### 1. Stress–Strain Ensembles for Open and Closed Systems

To achieve a description of confined soft condensed matter at the molecular level one has to resort to the principles of statistical physics. To make contact with, say, SFA experiments it is convenient to introduce statistical physical ensembles depending explicitly on a suitable set of stresses and strains. For simplicity, the lamella is treated quantum mechanically, following the procedure originated by Schrödinger [56] and extended by Hill [53] and McQuarrie [57], so that its energy states are formally discrete. The energy eigenvalues  $E_j(N, A, R, s_z, \alpha_x \ell_x, \alpha_y \ell_y)$  are implicit functions of the number of fluid molecules, extent and shape of the lamella, and the registry of the substrates, which control the external field acting on the fluid molecules. Index  $j$  signifies the collection of quantum numbers necessary to determine the eigenstate uniquely. The ensemble comprises an astronomical number  $\mathcal{N}$  of systems each in the same macroscopic state, which, as an example, is taken to be specified by the set  $\{T, \mu, A, R, \alpha_x \ell_x, \alpha_y \ell_y\}$  of ensemble parameters. Since the ensemble is isolated, it satisfies the

following constraints:

$$\left. \begin{aligned} \sum_j \sum_N \sum_{s_z} n_{jNs_z} &= \sum_{jNs_z} n_{jNs_z} = \mathcal{N} \\ \sum_{jNs_z} n_{jNs_z} E_j &= \hat{E} \\ \sum_{jNs_z} n_{jNs_z} N &= \hat{N} \\ \sum_{jNs_z} n_{jNs_z} s_z &= \hat{s}_z \end{aligned} \right\} \quad (43)$$

where  $n_{jNs_z}$  is the number of systems having  $N$  molecules between substrates separated by  $s_z$  and occupying eigenstate  $j$ . It is assumed that the isolated ensemble has fixed total energy  $\hat{E}$ , fixed total number of molecules  $\hat{N}$ , and fixed total volume  $A\hat{s}_z$ . The total number of ways of realizing a given distribution  $\mathbf{n} = \{n_{jNs_z}\}$  over the allowed “superstates” characterized by triplets  $(j, N, s_z)$  is  $W(\mathbf{n}) = \mathcal{N}! / \prod_j \prod_N \prod_{s_z} n_{jNs_z}!$ . Since the number of systems is extremely large, the most probable distribution, denoted by  $\mathbf{n}^*$ , overwhelms all others. It is found by maximizing  $W(\mathbf{n})$  subject to the constraints [see Eqs. (43)]. The result for the probability of a system’s occupying superstate  $(j, N, s_z)$  is

$$P_{jNs_z} = n_{jNs_z}^* / \mathcal{N} = \mathcal{X}^{-1} \exp[-\lambda_1 E_j - \lambda_2 N - \lambda_3 s_z] \quad (44)$$

where the partition function

$$\mathcal{X} = \sum_{jNs_z} \exp[-\lambda_1 E_j - \lambda_2 N - \lambda_3 s_z] \quad (45)$$

and the set of Lagrangian multipliers  $\{\lambda_1, \lambda_2, \lambda_3\}$  are determined through equivalence of thermodynamic and statistical expressions as follows.

The statistical expression for the internal energy is simply  $\langle \mathcal{U} \rangle = \sum_{jNs_z} P_{jNs_z} E_j$ , from which its exact differential follows as

$$d\langle \mathcal{U} \rangle = \sum_{jNs_z} (E_j dP_{jNs_z} + P_{jNs_z} dE_j) \quad (46)$$

$E_j$  can be obtained from Eq. (44) so that  $dE_j$  can be replaced. One

eventually obtains

$$\begin{aligned}
 d\langle \mathcal{U} \rangle = & -\lambda_1^{-1} \sum_{jNs_z} [\ln P_{jNs_z} + \lambda_2 N + \lambda_3 s_z + \ln \mathcal{X}] dP_{jNs_z} \\
 & + \sum_{jNs_z} P_{jNs_z} \left[ \left( \frac{\partial E_j}{\partial A} \right)_{N, s_z, R, \alpha_x \ell_x, \alpha_y \ell_y} dA + \left( \frac{\partial E_j}{\partial R} \right)_{N, s_z, A, \alpha_x \ell_x, \alpha_y \ell_y} dR \right. \\
 & \left. + \left( \frac{\partial E_j}{\partial (\alpha_x \ell_x)} \right)_{N, s_z, A, R, \alpha_y \ell_y} d(\alpha_x \ell_x) + \left( \frac{\partial E_j}{\partial (\alpha_y \ell_y)} \right)_{N, s_z, A, R, \alpha_x \ell_x} d(\alpha_y \ell_y) \right]
 \end{aligned} \quad (47)$$

At the molecular level one may interpret  $(\partial E_j / \partial A)_{N, s_z, R, \alpha_x \ell_x, \alpha_y \ell_y}$  as the interfacial tension of the system in superstate  $(j, N, s_z)$ . Similar meaning can be attached to the other partial derivatives of  $E_j$  appearing in Eq. (47). Invoking also the principle of conservation of probability ( $\sum_{jNs_z} dP_{jNs_z} = 0$ ), Eq. (47) can be recast as

$$\begin{aligned}
 d\langle \mathcal{U} \rangle = & -\lambda_1^{-1} d \left( \sum_{jNs_z} P_{jNs_z} \ln P_{jNs_z} \right) - \frac{\lambda_2}{\lambda_1} d\langle N \rangle - \frac{\lambda_3}{\lambda_1} d\langle s_z \rangle \\
 & + \left\langle \frac{\partial \mathcal{U}}{\partial A} \right\rangle dA + \left\langle \frac{\partial \mathcal{U}}{\partial R} \right\rangle dR + \left\langle \frac{\partial \mathcal{U}}{\partial (\alpha_x \ell_x)} \right\rangle d(\alpha_x \ell_x) \\
 & + \left\langle \frac{\partial \mathcal{U}}{\partial (\alpha_y \ell_y)} \right\rangle d(\alpha_y \ell_y)
 \end{aligned} \quad (48)$$

Following the lengthy argument by Hill [53], one identifies

$$\mathcal{S} = -k_b \sum_{jNs_z} P_{jNs_z} \ln P_{jNs_z} \quad (49)$$

Then a comparison of the microscopic Eq. (48) with its macroscopic counterpart Eq. (5) allows one to identify the Lagrangian multipliers as

$$\left. \begin{aligned} \lambda_1 &\equiv \beta = 1/k_B T \\ \lambda_2 &= -\beta \mu \\ \lambda_3 &= -\beta T_{zz} A \end{aligned} \right\} \quad (50)$$

Therefore, from Eq. (44) one obtains

$$\ln P_{jNs_z} = -\beta E_j + \beta \mu N + \beta T_{zz} A s_z - \ln \mathcal{X} \quad (51)$$

Upon substitution into Eq. (49), this yields

$$-\beta^{-1} \ln \mathcal{X} = \langle \mathcal{U} \rangle - T \mathcal{S} - \mu \langle N \rangle - T_{zz} A \langle s_z \rangle = \Phi \quad (52)$$

where the far right side is obtained by comparing the statistical expression in Eq. (52) with the thermodynamic Eqs. (9) and (10). By exactly the same approach one can also derive statistical-physical expressions for other mixed stress-strain ensembles [58,59]. Finally, from Eq. (45) one has for the partition function

$$\begin{aligned}\mathcal{X} &= \sum_{s_z} \exp(\beta T_{zz} A s_z) \sum_N \exp(\beta \mu N) \mathcal{Q}(T, N, A, R, s_z, \alpha_x \ell_x, \alpha_y \ell_y) \\ &= \sum_{s_z} \exp(\beta T_{zz} A s_z) \Xi(T, \mu, A, R, s_z)\end{aligned}\quad (53)$$

where  $\mathcal{Q} := \sum_j \exp(\beta E_j)$  is the canonical-ensemble partition function and  $\Xi = \exp(-\beta \Omega)$  is its counterpart in the grand canonical ensemble. Since this chapter is exclusively concerned with classical systems,  $\mathcal{Q}$  is replaced by its classical analogue

$$\mathcal{Q}_{\text{class}} = \frac{\mathcal{Z}(T, N, A, R, s_z \alpha_x \ell_x, \alpha_y \ell_y)}{N! \Lambda^{3N}} = \frac{1}{N! \Lambda^{3N}} \int_{V^N} d\mathbf{r}^N \exp[-\beta U(\mathbf{r}^N)] \quad (54)$$

for the special case of spherically-symmetric molecules where  $\mathcal{Z}$  is the configuration integral,  $\Lambda := (h^2 \beta / 2\pi m)^{1/2}$  is the thermal de Broglie wavelength ( $h$  is Planck's constant and  $m$  the molecular mass). The limiting expression  $\mathcal{Q}_{\text{class}}$  can be derived from the quantum mechanical  $\mathcal{Q}$  within the framework of the Kirkwood and Wigner theory [53]. In the classical limit one has to replace the quantum mechanical  $P_{jNs_z}$  by the analogous probability density distribution

$$f(\mathbf{r}^N; T, \mu, T_{zz}) = \frac{1}{N! \Lambda^{3N}} \frac{\exp\{\beta[\mu N + T_{zz} A s_z - U(\mathbf{r}^N)]\}}{\mathcal{X}_{\text{class}}} \quad (55)$$

where  $U(\mathbf{r}^N)$  is the configurational energy of the system and  $\mathcal{X}_{\text{class}}$  is the classical counterpart of  $\mathcal{X}$  obtained by replacing  $\mathcal{Q}$  in Eq. (53) by  $\mathcal{Q}_{\text{class}}$  (see also this volume, chapter by Nielaba).

## 2. Correlation Functions

Since we shall also be interested in analyzing the confined fluid's microscopic structure it is worthwhile to introduce some useful structural correlation functions at this point. The simplest of these is related to the instantaneous number density operator

$$\rho(\mathbf{r}) = \sum_{i=1}^N \delta(\mathbf{r}_i - \mathbf{r}) \quad (56)$$

where  $\delta$  is the Dirac delta function. The mean value of  $\rho$  is given by

$$\begin{aligned}
 \langle \rho(\mathbf{r}) \rangle &= \sum_{N, s_z} \sum_{i=1}^N \prod_{k=1}^N \int_V d\mathbf{r}_k f(\mathbf{r}^N; T, \mu, T_{zz}) \delta(\mathbf{r}_i - \mathbf{r}) \\
 &= \sum_{N, s_z} \sum_{i=1}^N \prod_{k \neq i}^N \int_V d\mathbf{r}_k f(\mathbf{r}_1, \mathbf{r}_2, \dots, \mathbf{r}_i = \mathbf{r}, \dots, \mathbf{r}_N; T, \mu, T_{zz}) \\
 &= \sum_{i=1}^N P^{[1]}(\mathbf{r}_i = \mathbf{r})
 \end{aligned} \tag{57}$$

where  $P^{[1]}(\mathbf{r}_i = \mathbf{r})$  is the probability of the center of mass of molecule  $i$  being at  $\mathbf{r}$  regardless of the positions of the other molecules (and regardless of orientation, see Sec. IV A 3). Since the molecules are equivalent,  $P^{[1]}$  is independent of  $i$  and the summation on  $i$  in Eq. (57) can be performed explicitly to yield

$$\langle \rho(\mathbf{r}) \rangle = NP^{[1]}(\mathbf{r}) =: \rho^{[1]}(\mathbf{r}). \tag{58}$$

In general,  $\rho^{[1]}(\mathbf{r})$  is a function of the *vector* position of the point of observation  $\mathbf{r}$ . However, if one is concerned mainly with the inhomogeneity of the confined fluid in the normal ( $z$ ) direction, the average over the interfacial area is adequate. Averaging yields

$$\rho^{[1]}(z) = A^{-1} \int_0^{s_x} dx \int_0^{s_y} dy \rho^{[1]}(\mathbf{r}) \tag{59}$$

to which we shall henceforth refer simply as the local density.

The translational microscopic structure of the confined fluid is partially revealed by correlations in the number density operator, given by

$$\begin{aligned}
 \langle \rho(\mathbf{r}) \rho(\mathbf{r}') \rangle &= \sum_{i=1}^N \langle \delta(\mathbf{r}_i - \mathbf{r}) \delta(\mathbf{r}_i - \mathbf{r}') \rangle + \sum_{i=1}^N \sum_{j \neq i}^N \langle \delta(\mathbf{r}_i - \mathbf{r}) \delta(\mathbf{r}_j - \mathbf{r}') \rangle \rho^{[1]}(\mathbf{r}) \\
 &= \rho^{[1]}(\mathbf{r}) \delta(\mathbf{r} - \mathbf{r}') + \sum_{N, s_z} \sum_{i=1}^N \sum_{j \neq i}^N \prod_{k \neq i, j}^N \\
 &\quad \times \int_V d\mathbf{r}_k f(\mathbf{r}_1, \dots, \mathbf{r}_i = \mathbf{r}, \dots, \mathbf{r}_j = \mathbf{r}', \dots, \mathbf{r}_N; T, \mu, T_{zz})
 \end{aligned} \tag{60}$$

where the “self-term” gives no new information beyond the mean density. Again invoking the equivalence of fluid molecules, we recognize the cross-term in Eq. (60) as the pair distribution function

$$\rho^{[2]}(\mathbf{r}, \mathbf{r}') = N(N-1)P^{[2]}(\mathbf{r}, \mathbf{r}') \tag{61}$$

which is related to the mean local density through the pair correlation function by

$$\rho^{[2]}(\mathbf{r}, \mathbf{r}') = \rho^{[1]}(\mathbf{r})\rho^{[1]}(\mathbf{r}')g^{[2]}(\mathbf{r}, \mathbf{r}'). \quad (62)$$

In general,  $g^{[2]}$  is a six-dimensional function of the position of reference  $(x, y, z)$  and observed  $(x', y', z')$  molecules. However, to be consistent with the approximation for the local density [see Eq. (59)], we take  $g^{[2]}$  to be a function only of the normal coordinate ( $z$ ) of the reference molecule and the cylindrical coordinates  $\rho_{12}$  and  $z_{12}$  of the observed molecule (2) relative to the reference molecule (1), where the distance vector between the two  $\mathbf{r}_{12} = \rho_{12} + z_{12}\hat{e}_z$  and  $\hat{e}_z$  is the unit vector in the  $z$  direction (see Sec. IV B).

### III. MONTE CARLO SIMULATIONS

A key problem in the equilibrium statistical-physical description of condensed matter concerns the computation of macroscopic properties  $O_{\text{macro}}$  like, for example, internal energy, pressure, or magnetization in terms of an ensemble average  $\langle O \rangle$  of a suitably defined microscopic representation  $O(\mathbf{r}^N)$  (see Sec. IV A 1 and V A 1 for relevant examples). To perform the ensemble average one has to realize that configurations  $\mathbf{r}^N := \{\mathbf{r}_1, \mathbf{r}_2, \dots, \mathbf{r}_N\}$  generally differ energetically so that a certain probability of occurrence is associated with each configuration. Therefore, to compute the correct value  $\langle O \rangle$ ,  $O(\mathbf{r})$  needs to be multiplied by the relevant probability density function  $f(\mathbf{r}^N; \mathbf{X})$ , where  $\mathbf{X}$  is a set of thermodynamic state variables (for example,  $T$ ,  $\mu$ , and a combination of stresses and strains).

Analytically, the computation of ensemble averages along this route is a formidable task, even if microscopically small representations of the system of interest are considered, because  $f(\mathbf{r}^N; \mathbf{X})$  is generally a very complicated function of the spatial arrangement of the  $N$  molecules. However, with the advent of large-scale computers some forty years ago the key problem in statistical physics became tractable, at least numerically, by means of computer simulations. In a computer simulation the evolution of a microscopically small sample of the macroscopic system is determined by computing trajectories of each molecule for a microscopic period of observation. An advantage of this approach is the treatment of the microscopic sample in essentially a first-principles fashion; the only significant assumption concerns the choice of an interaction potential [25]. Because of the power of modern supercomputers which can literally handle hundreds of millions of floating point operations per second, computer simulations are nowadays

viewed as “a third branch complementary to the ... two traditional approaches” [60]: theory and experiment.

There are basically two different computer simulation techniques known as molecular dynamics (MD) and Monte Carlo (MC) simulation. In MD molecular trajectories are computed by solving an equation of motion for equilibrium or nonequilibrium situations. Since the MD time scale is a physical one, this method permits investigations of time-dependent phenomena like, for example, transport processes [25,61–63]. In MC, on the other hand, trajectories are generated by a (biased) random walk in configuration space and, therefore, do not *per se* permit investigations of processes on a physical time scale (with the “dynamics” of spin lattices as an exception [64]). However, MC has the advantage that it can easily be applied to virtually all statistical-physical ensembles, which is of particular interest in the context of this chapter. On account of limitations of space and because excellent texts exist for the MD method [25,61–63,65], the present discussion will be restricted to the MC technique with particular emphasis on mixed stress-strain ensembles.

If one wishes to compute  $\langle O \rangle$  numerically by means of MC one immediately realizes that this requires the *a priori* unknown function  $f(\mathbf{r}^N; \mathbf{X})$  according to which the random walk in configuration space has to be carried out. However, if the random walk is carried out in a biased way as a Markov process it turns out that only the ratio  $f(\mathbf{r}_{m+1}^N; \mathbf{X})/f(\mathbf{r}_m^N; \mathbf{X})$  is relevant to generate a new configuration ( $m+1$ ) from a given old one ( $m$ ). The subsequent discussion will show that  $f(\mathbf{r}_{m+1}^N; \mathbf{X})/f(\mathbf{r}_m^N; \mathbf{X})$  is computationally accessible. Because this scheme generates configurations with the correct probability of occurrence,  $O_{\text{macro}}$  can be computed via the simple expression

$$O_{\text{macro}} = \lim_{M \rightarrow M_{\text{max}}} \langle O \rangle = \lim_{M \rightarrow M_{\text{max}}} \frac{1}{M} \sum_{m=1}^M [O(\mathbf{r}_m^N)]' \quad (63)$$

where the prime is attached as a reminder that the summation is restricted to configurations generated according to their importance (*importance sampling*) and  $M_{\text{max}}$  should be large enough [usually,  $M_{\text{max}} \approx \mathcal{O}(10^6\text{--}10^9)$  is sufficient, depending on the particular physical situation and quantity of interest]. However, before turning to practical aspects of MC, a brief introduction to Markov processes seems worthwhile because it rarely appears in the literature.

## A. Stochastic Processes

Let  $y(t)$  be a random process, that is a process incompletely determined at any given time  $t$ . The random process can be described by a set of probability distributions  $\{P_n\}$  where, for example,  $P_2(y_1 t_1, y_2 t_2) dy_1 dy_2$  is the



probability of finding  $y_1$  in the interval  $[y_1, y_1 + dy_1]$  at  $t = t_1$  and in the interval  $[y_2, y_2 + dy_2]$  at another time  $t = t_2$ . Thus the set  $\{P_n\}$  forms a hierarchy of probability distributions describing  $y(t)$  in greater detail the larger  $n$  is.

The simplest random process is completely stochastic so that one may write, for example,  $P_2(y_1 t_1, y_2 t_2) = P_1(y_1 t_1)P_1(y_2 t_2)$ . However, here we are concerned with a slightly more complex process known as the Markov process, characterized by

$$P_2(y_1 t_1, y_2 t_2) = P_1(y_1 t_1)K_1(y_1 t_1 | y_2 t_2) \quad (64)$$

where  $K_1(y_1 t_1 | y_2 t_2)$  is the *conditional* probability of finding  $y$  in the interval  $[y_2, y_2 + dy_2]$  at  $t = t_2$  *provided*  $y = y_1$  at an earlier time  $t = t_1$  ( $t_1 < t_2$ ). Some important properties are the following:

1. Normalization, that is  $\int K_1(y_1 t_1 | y_2 t_2) dy_2 = 1$ .
2.  $\int P_1(y_1 t_1) K_1(y_1 t_1 | y_2 t_2) dy_1 = P_1(y_2 t_2)$ .
3. Perhaps most importantly, a Markov process has a “one-step memory”; that is, to find  $y$  in the interval  $[y_n, y_n + dy_n]$  at  $t = t_n$  depends only on the realization  $y = y_{n-1}$  at the immediately preceding time  $t = t_{n-1}$  but is independent of all earlier realizations  $\{y_m t_m\}$ ,  $1 \leq m \leq n-2$ . Mathematically, this can be cast as  $K_{n-1}(y_1 t_1, \dots, y_{n-1} t_{n-1} | y_n t_n) = K_1(y_{n-1} t_{n-1} | y_n t_n)$ .
4. Stationarity, that is  $P_1(y_1 t_1) = P_1(y_1)$  and  $P_2(y_1 t_1, y_2 t_2) = P_2(y_1, y_2; t_2 - t_1)$ .

Consider now

$$P_2(y_{n-2} t_{n-2}, y_n t_n) = \int P_3(y_{n-2} t_{n-2}, y_{n-1} t_{n-1}, y_n t_n) dy_{n-1} \quad (65)$$

and assume that  $y(t)$  is a Markov process. Then

$$\begin{aligned} P_3(y_{n-2} t_{n-2}, y_{n-1} t_{n-1}, y_n t_n) &= P_1(y_{n-2} t_{n-2}) K_1(y_{n-2} t_{n-2} | y_{n-1} t_{n-1}) \\ &\quad \times K_2(y_{n-2} t_{n-2}, y_{n-1} t_{n-1} | y_n t_n) \\ &\stackrel{(3)}{=} P_1(y_{n-2} t_{n-2}) K_1(y_{n-2} t_{n-2} | y_{n-1} t_{n-1}) K_1(y_{n-1} t_{n-1} | y_n t_n) \end{aligned} \quad (66)$$

Because of Eqs. (64) and (66), Eq. (65) can be rewritten as

$$K_1(y_{n-2} t_{n-2} | y_n t_n) = \int K_1(y_{n-2} t_{n-2} | y_{n-1} t_{n-1}) K_1(y_{n-1} t_{n-1} | y_n t_n) dy_{n-1} \quad (67)$$

Alternatively, because of property (4), this last expression can be cast as

$$K_1(y_{n-2} | y_n; t + \tau) = \int K_1(y_{n-2} | y_{n-1}; t) K_1(y_{n-1} | y_n; \tau) dy_{n-1} \quad (68)$$

where  $t := t_{n-1} - t_{n-2}$  and  $\tau := t_n - t_{n-1}$ . Equation (68) is known as the Chapman-Kolmogoroff equation.

Suppose a small characteristic time interval  $\tau_c$  exists such that  $y_{n-1}$  changes without strongly affecting  $K_1(y_{n-2}|y_n; t)$  so that the latter may be expanded in a Taylor series as

$$K_1(y_{n-2}|y_n; t + \tau_c) = K_1(y_{n-2}|y_n; t) + \tau_c \frac{\partial K_1(y_{n-2}|y_n; t)}{\partial t} + \dots \quad (69)$$

From Eqs. (68) and (69) one gets

$$\frac{\partial K_1(y_{n-2}|y_n; t)}{\partial t} = \int K_1(y_{n-2}|y_{n-1}; t) \frac{K_1(y_{n-1}|y_n; t)}{\tau_c} dy_{n-1} - \frac{1}{\tau_c} K_1(y_{n-2}|y_n; t) \quad (70)$$

To proceed it is convenient to define the transition probability per time interval  $\tau_c$  as

$$\phi(y_{n-1}|y_n) = \lim_{\tau \rightarrow \tau_c} \frac{1}{\tau} K_1(y_{n-1}|y_n; \tau) \quad (71)$$

which satisfies

$$\int \phi(y_{n-1}|y_n) dy_{n-1} = \int \phi(y_n|y_{n-1}) dy_{n-1} \stackrel{(1)}{=} \lim_{\tau \rightarrow \tau_c} \frac{1}{\tau} = \frac{1}{\tau_c} \quad (72)$$

With Eqs. (71), (72), and  $t = t' - t_{n-2}$  ( $dt = dt'$ ) one may multiply both sides of Eq. (70) by  $P_1(y_{n-2}t_{n-2})$  and integrate over  $dy_{n-2}$  to obtain (see properties 1, 2, and 4)

$$\frac{\partial P_1(y_n t')}{\partial t'} = \int [P_1(y_{n-1} t') \phi(y_{n-1}|y_n) - \phi(y_n|y_{n-1}) P_1(y_n t')] dy_{n-1} \quad (73)$$

For stationary situations  $\partial P_1(y_n t') / \partial t' = 0$  and Eq. (73) is then satisfied by

$$\Pi := \frac{P_1(y_{n-1})}{P_1(y_n)} = \frac{\phi(y_n|y_{n-1})}{\phi(y_{n-1}|y_n)} \quad (74)$$

where  $\Pi$  is the probability for the transition  $n-1 \rightarrow n$ . Equation (74) reflects microscopic reversibility and is a special formulation of the *principle of detailed balance*.

## B. Implementation of Stress-Strain Ensembles for Open and Closed Systems

Consider now, as an illustration, a confined fluid in material and thermal contact with a bulk reservoir and under fixed normal stress  $T_{zz}$ . For simplicity we assume the substrates to be in fixed registry  $\alpha_x = \alpha_y = 0$  and the

fluid to consist of “simple” molecules having only (three) translational degrees of freedom. Under these premises one has (see Sec. II C 1) [66]

$$\begin{aligned}
 \langle O \rangle &= \sum_N \int ds_z \int_{\tilde{V}^N} d\tilde{\mathbf{r}}^N f(\tilde{\mathbf{r}}^N; T, \mu, T_{zz}) O(\tilde{\mathbf{r}}^N) \\
 &= \mathcal{X}_{\text{class}}^{-1} \sum_N \frac{\exp(BN)}{N!} A^N \int ds_z \exp(\beta T_{zz} A s_z) s_z^N \int_{\tilde{V}^N} d\tilde{\mathbf{r}}^N \\
 &\quad \times \exp[-\beta U(\tilde{\mathbf{r}}^N)] O(\tilde{\mathbf{r}}^N)
 \end{aligned} \tag{75}$$

where  $(x_i, y_i, z_i) \rightarrow (\tilde{x}_i = s_x^{-1} x_i, \tilde{y}_i = s_y^{-1} y_i, \tilde{z}_i = s_z^{-1} z_i), i = 1, \dots, N$  so that the integration is carried out over the unit-cube volume  $\tilde{V}$ . The summation over  $s_z$  [see Eq. (53)] has been replaced by an integral, and the dimensionless quantity  $B$  is defined by

$$B := \beta\mu - \ln(\Lambda^3 / A s_z). \tag{76}$$

The MC method can be implemented by a modification of the classic Metropolis scheme [25,67]. The Markov chain is generated by a three-step sequence. The first step is identical to the classic Metropolis algorithm: a randomly selected molecule  $i$  is displaced within a small cube of side length  $2\delta_r$  centered on its original position

$$\mathbf{r}_{i,m+1} = \mathbf{r}_{i,m} + \delta_r(\mathbf{1} - 2\xi) = \mathbf{r}_{i,m} + \delta_r \tag{77}$$

where  $\mathbf{1} = (1, 1, 1)$  and  $\xi$  is a vector whose three components are pseudo-random numbers distributed uniformly on the interval  $[0, 1]$ . During the MC run  $\delta_r$  is adjusted so that 40–60% of the attempted displacements are accepted. With the identification  $f(\tilde{\mathbf{r}}_m^N; T, \mu, T_{zz}) \equiv P(y_n)$  one obtains

$$\Pi_1 = \min\{1, f(\tilde{\mathbf{r}}_{m+1}^N; T, \mu, T_{zz}) / f(\tilde{\mathbf{r}}_m^N; T, \mu, T_{zz}) = \exp(-\beta\Delta U)\} \tag{78}$$

from Eqs. (55) and (74) because  $N_m = N_{m+1}$  and  $s_{z,m+1} = s_{z,m}$ , where  $\Delta U := U(\tilde{\mathbf{r}}_{m+1}^N; s_z) - U(\tilde{\mathbf{r}}_m^N; s_z)$  is the change in configurational energy associated with the process  $\tilde{\mathbf{r}}_m^N \rightarrow \tilde{\mathbf{r}}_{m+1}^N$ . An efficient way to compute  $\Delta U$  is detailed below in Sec. III.C.

In the second step it is decided with equal probability whether to remove ( $\Delta N = -1$ ) a randomly chosen molecule or to create ( $\Delta N = +1$ ) a new one at a randomly chosen point in the system (see also Sec. III D). From Eqs. (55) and (74) the transition probabilities for addition (“+”) and subtraction (“−”) are given by

$$\Pi_2 = \min\{1, f(\tilde{\mathbf{r}}_{m+1}^{N\pm 1}; T, \mu, T_{zz}) / f(\tilde{\mathbf{r}}_m^N; T, \mu, T_{zz}) = \exp(r_{\pm})\} \tag{79}$$

where

$$r_{\pm} = \pm B \mp \ln N \mp \beta U_{\pm} \tag{80}$$

Since only one molecule is added to (or removed from) the system,  $U_{\pm}$  is simply the interaction of the added (or removed) molecule with the remaining ones. If one attempts to add a new molecule,  $N$  is the number of molecules *after* addition, otherwise it is the number of molecules *prior* to removal. If a cutoff for the interaction potential is employed, long-range corrections to  $U_{\pm}$  must be taken into account because of the density change of  $\pm 1/A s_z$ . Analytic expressions for these corrections can be found in the appendix of Ref. 33.

In the third and final step the substrate separation is changed according to

$$s_{z,m+1} = s_{z,m} + \delta_{s_z}(1 - 2\xi) \quad (81)$$

and the coordinates of fluid molecules are scaled via  $z_{m+1} = z_m s_{z,m+1}/s_{z,m}$ . Because  $N$  is held constant the transition probability associated with this step is

$$\Pi_3 = \min\{1, f(\mathbf{r}_{m+1}^{N'}; T, \mu, T_{zz})/f(\mathbf{r}_m^{N'}; T, \mu, T_{zz}) = \exp(r_{s_z})\} \quad (82)$$

where

$$r_{s_z} := -\beta(\Delta U - T_{zz} A \Delta s_z) + N \ln(s_{z,m+1}/s_{z,m}) \quad (83)$$

$\Delta s_z := s_{z,m+1} - s_{z,m}$  and the same comments concerning corrections to  $\Delta U$  apply as in step 2. On each pass through the three-step sequence the number of attempts in steps 1, 2, and 3 is chosen to be  $N$ ,  $N$ , and 1, respectively, in order to realize a comparable degree of events in each of the steps. Because the third step moves all  $N$  molecules at once, and the first two affect only one molecule at a time, the sought balance is roughly achieved. The algorithm described here can easily be amended by additional steps if, for example, one is interested in situations in which the shear stress(es) is (are) also among the controlled parameters so that  $\alpha_x$  (and  $\alpha_y$ ) may vary too [58,59]. Applying the analysis of Wood [68] to each step of the algorithm separately, one can verify that the resulting transition probabilities indeed comply with the requirements of a Markov process as stated in Eq. (74).

### C. The Taylor-expansion Algorithm for “Simple” Fluids

According to Allen and Tildesley, the standard recipe to evaluate  $\Delta U$  in step one of the algorithm described in Sec. III B involves “computing the energy of atom  $i$  with *all the other atoms before and after the move* (see p. 159 of Ref. 25, italics by the present author) as far as “simple” fluids are concerned. The evaluation of  $\Delta U$  can be made more efficient in this case by realizing that for short-range interactions  $U$  can be split into three contributions

$U = U_1 + U_2 + U_3$  corresponding to three different spatial zones, where  $U_1$  is the configurational energy between atom  $i$  and  $N_1$  neighboring molecules located in a primary zone immediately surrounding  $i$ . Similarly,  $U_2$  refers to interactions between  $i$  and  $N_2$  molecules in a secondary zone adjacent to the primary zone and, last but not least,  $U_3$  refers to interactions between  $i$  and the remaining molecules in an outermost tertiary zone whose upper limit is identical with the potential cutoff by which the computational burden is reduced already in conventional implementations. Savings of computer time depend on the sizes of the three zones (i.e., the values of  $N_1, N_2, N_3$ ) and different degrees of sophistication with which the three terms are treated. It turns out that a sphere of radius  $r_1$  centered on  $\mathbf{r}_i$  can be associated with the primary zone. The secondary zone can be a spherical shell of thickness  $\Delta r = r_2 - r_1$  (bulk fluid) or a cylindrical shell of the same thickness but infinite height (confined fluid, slit geometry). If  $r_2$  is sufficiently large one may assume  $\Delta U_3 = U_3(\mathbf{r}_{i,m+1}) - U_3(\mathbf{r}_{i,m}) \simeq 0$  because  $|\delta_r|$  [see Eq. (77)] is small compared with typical distances corresponding to tertiary-zone interactions. Thus,  $N_3$  interactions are entirely neglected during the course of the simulation. For the secondary zone one assumes that  $\Delta U_2 = U_2(\mathbf{r}_{i,m+1}) - U_2(\mathbf{r}_{i,m})$  is not entirely negligible but small enough to be approximated by a Taylor expansion

$$\Delta U_2 \approx \frac{\partial U_2(\mathbf{r}_{i,m})}{\partial \mathbf{r}_{i,m}} \cdot \delta_r = -\mathbf{F}_2(\mathbf{r}_{i,m}) \cdot \delta_r \quad (84)$$

truncated after the first nonvanishing term, where  $\mathbf{F}_2$  is the total force exerted on  $i$  in the initial configuration  $m$  by the  $N_2$  atoms in the secondary zone. For the primary zone no simplifying assumptions can be made because  $U_1$  will strongly depend on  $\delta_r$ . Thus, on the basis of these assumptions,  $\Delta U$  in Eq. (78) can be written explicitly as

$$\Delta U \simeq U_1(\mathbf{r}_{i,m+1}) - U_1(\mathbf{r}_{i,m}) - \mathbf{F}_2(\mathbf{r}_{i,m}) \cdot \delta_r \quad (85)$$

It is clear that Eq. (85) is numerically reliable provided  $\delta_r$  is sufficiently small. However, a detailed investigation in Ref. 69 reveals that  $\delta_r$  can be as large as some ten percent of the diameter of a fluid molecule. Likewise,  $r_1$  should not be smaller than, say, the distance at which the radial pair correlation function has its first minimum (corresponding to the nearest-neighbor shell). Under these conditions, and if combined with a neighbor list technique, savings in computer time of up to 40% over conventional implementations are measured for the first (canonical) step of the algorithm detailed in Sec. III B. These are achieved because, for pairwise interactions, only  $N_1 + N_2$  contributions need to be computed here *before*  $i$  is moved ( $U_1$  and  $\mathbf{F}_2$ ), and only  $N_1$  contributions need to be evaluated *after*  $i$  is displaced

by  $\delta_r(U_1)$  where some efficiency is inevitably lost because the computation of forces is numerically more demanding than the computation of energies. A much larger number of  $2(N_1 + N_2 + N_3)$  such terms must be evaluated conventionally.

## D. Orientationally Biased Creation of Molecules

If fluid molecules have rotational degrees of freedom the algorithm outlined in Sec. IIIB must be modified in various respects. First, in addition to random displacements in step 1, the molecule is rotated randomly by a small angle increment  $\Delta\psi \in (-\psi_{\max}, \psi_{\max})$  around an axis chosen at random from the three axes of the Cartesian coordinate system. A rotation attempt is again accepted with the probability given in Eq. (78) where now  $\Delta U$  refers to the change in configurational energy associated with the rotation attempt. During the course of a simulation  $\psi_{\max}$  is adjusted to preserve an overall acceptance ratio of 40–60%.

For a removal attempt a molecule is selected irrespective of its orientation. To enhance the efficiency of addition attempts in cases where the system possesses a high degree of orientational order, the orientation of the molecule to be added is selected in a biased way from a distribution function. For a system of linear molecules this distribution, say,  $g(|\hat{\mathbf{u}} \cdot \hat{\mathbf{n}}|)$ , depends on the unit vector  $\hat{\mathbf{u}}$  parallel to the molecule's symmetry axis (the so-called microscopic director [70,71]) and on the macroscopic director  $\hat{\mathbf{n}}$  which is a measure of the average orientation in the entire sample [72]. The distribution  $g$  can be chosen in various ways, depending on the physical nature of the fluid (see below). However,  $g(|\hat{\mathbf{u}} \cdot \hat{\mathbf{n}}|)$  must be normalized to one [73,74]. In other words, an addition is attempted with a preferred orientation of the molecule determined by the macroscopic director  $\hat{\mathbf{n}}$  of the entire simulation cell. The position of the center of mass of the molecule is again chosen randomly. According to the *principle of detailed balance* the probability for a realization of an addition attempt is given by [73]

$$\Pi_+ = \min\{1, g^{-1}(|\hat{\mathbf{u}}_+ \cdot \hat{\mathbf{n}}|) \exp(r_{\pm})\} \quad (86)$$

whereas

$$\Pi_- = \min\{1, g(|\hat{\mathbf{u}}_- \cdot \hat{\mathbf{n}}|) \exp(r_{\pm})\} \quad (87)$$

for a removal attempt, where  $r_{\pm}$  is given in Eq. (80). However,  $B$  has to be replaced by  $B'$  defined analogously as (linear molecules only)

$$B' = \beta\mu - \ln\left(\frac{2m\Lambda^5}{VI}\right) \quad (88)$$

where  $I$  is the moment of inertia. Quantities  $\hat{\mathbf{u}}_+$  and  $\hat{\mathbf{u}}_-$  are the microscopic directors of the film molecule to be added to or removed from the film. Biased addition is indispensable if, for example, the confined fluid is a liquid crystal in thermodynamic equilibrium with a nematic bulk phase (see Sec. IV A 3). In this case  $g(|\hat{\mathbf{u}} \cdot \hat{\mathbf{n}}|)$  is identified as the orientational distribution function of film molecules, which is computed as a histogram averaged over all configurations preceding the actual one; if the thermodynamic state of the bulk liquid crystal is isotropic,  $g(|\hat{\mathbf{u}} \cdot \hat{\mathbf{n}}|) = 1$  is a suitable choice. One realizes from Eqs. (86), (87) that in this case one recovers Eq. (79).

## IV. MICROSCOPIC STRUCTURE

### A. Planar Substrates

#### 1. Molecular Expressions for the Normal Stress

Within the framework of Monte Carlo simulations, the relation between measurable quantities and the microscopic structure of confined phases can now be examined. An example of such a measurable quantity is the solvation force  $F(h)/2\pi R$  (see Sec. II A 1). From a theoretical perspective and according to the discussion in Sec. II A 3 its investigation requires the stress  $T_{zz}(s_z)$  exerted normally by a confined fluid on *planar* substrates [see Eqs. (19) and (22)]. Using Eqs. (11) and (53) one can derive a molecular expression for  $T_{zz}$  from

$$\begin{aligned} AT_{zz} &= \left( \frac{\partial \Omega}{\partial s_z} \right)_{T, \mu, A, R} = -\frac{1}{\beta \Xi} \sum_N \frac{\exp[\beta \mu N]}{N! \Lambda^{3N}} \left( \frac{\partial \mathcal{Z}}{\partial s_z} \right)_{T, \mu, A, R} \\ &= -\frac{1}{\beta \Xi} \sum_N \cdots \left( \frac{\partial \mathcal{Z}}{\partial s_z} \right)_{T, \mu, A, R} \end{aligned} \quad (89)$$

for “simple” fluids, where the shorthand notation is introduced to represent the weighted sum over  $N$ . Depending on how the partial derivative of  $\mathcal{Z}$  is worked out, two mathematically different but physically equivalent expressions for  $T_{zz}$  obtain. The first of these is obtained by following the procedure of Hill [53] and transforming variables according to  $z_i \rightarrow \tilde{z}_i = z_i s_z^{-1}$  ( $i = 1, \dots, N$ ) to obtain

$$T_{zz} = -\frac{1}{A\beta\Xi} \sum_N \cdots \frac{\partial}{\partial s_z} \left[ s_z^N \prod_{i=1}^N \int_0^{s_x} dx_i \int_0^{s_y} dy_i \int_0^1 d\tilde{z}_i \exp(-\beta U) \right] \quad (90)$$

assuming that

$$\begin{aligned}
 U &= \sum_{i=1}^{N-1} \sum_{j=i+1}^N u_{ff}(r_{ij}) + \sum_{k=1}^2 \sum_{i=1}^N u_{fs}(r_{ij}^{[k]}) \\
 &=: U_{FF} + \sum_{k=1}^2 U_{FS}^{[k]} =: U_{FF} + U_{FS}
 \end{aligned} \tag{91}$$

where  $u_{ff}$  is the fluid–fluid interaction potential (corresponding, for example, to the Lennard–Jones (12,6) potential) and the fluid–substrate interaction depends on the distance between a fluid molecule and a substrate atom. Scaling in Eq. (90) affects  $U_{FF}$  through the argument

$$r_{ij} = [(x_i - x_j)^2 + (y_i - y_j)^2 + s_z^2(\tilde{z}_i - \tilde{z}_j)^2]^{1/2} \tag{92}$$

and  $U_{FS}$  because of  $r_{ij}^{[k]} := |\mathbf{r}_i - \mathbf{r}_j^{[k]}|$  for a fluid molecule located at  $\mathbf{r}_i$  and a wall atom at  $\mathbf{r}_j^{[k]}$  [see Eqs. (1)]. According to the product rule, the differentiation in Eq. (90) yields three terms grouped as  $T_{zz} = T_{zz,FF} + T_{zz,FS}$  where

$$\begin{aligned}
 T_{zz,FF} &= -\frac{\langle N \rangle}{\beta A s_z} + \frac{1}{2 A s_z \Xi} \sum_N \cdots \int_{V^N} d\mathbf{r}^N \exp(-\beta U) \sum_{i=1}^{N-1} \sum_{j=i+1}^N u'_{ff}(r_{ij}) \frac{z_{ij}^2}{r_{ij}} \\
 &= -\frac{\langle N \rangle}{\beta A s_z} + \frac{1}{A s_z \Xi} \sum_N \cdots \int_{V^N} d\mathbf{r}^N \exp(-\beta U) W_{zz,FF} \\
 &= -\frac{\langle N \rangle}{\beta A s_z} + \frac{\langle W_{zz,FF} \rangle}{A s_z}
 \end{aligned} \tag{93}$$

and

$$\begin{aligned}
 T_{zz,FS} &= \frac{1}{2 A s_z \Xi} \sum_N \cdots \int_{V^N} d\mathbf{r}^N \exp(-\beta U) \sum_{k=1}^2 \sum_{i=1}^N u'_{fs}(z_{ij}^{[k]}) \frac{z_{ij}^{[k]2}}{r_{ij}^{[k]}} \\
 &= \frac{1}{A s_z \Xi} \sum_N \cdots \int_{V^N} d\mathbf{r}^N \exp(-\beta U) W_{zz,FS} = \frac{\langle W_{zz,FS} \rangle}{A s_z}
 \end{aligned} \tag{94}$$

In Eqs. (93) and (94)  $W_{zz}$  is an element of Clausius’s virial matrix [53] and  $u'$  is the derivative of  $u$  with respect to its argument. Therefore Eqs. (93) and (94) are termed “virial” expressions henceforth.

A different expression for  $T_{zz}$  can be obtained directly from Eq. (89) without transforming coordinates. It is then convenient to recast the



configuration integral as [75]

$$\mathcal{Z} = \int_0^{s_z} dz_1 g_1(z_1) := \int_0^{s_z} dz_1 \int_0^{s_x} dx_1 \int_0^{s_y} dy_1 \prod_{i=2}^N \int_0^{s_x} dx_i \int_0^{s_y} dy_i \int_0^{s_z} dz_i \times \exp[-\beta(U_{FF} + U_{FS})]. \quad (95)$$

Applying Leibniz's rule for the differentiation of a parameter integral [76], it follows from Eqs. (89) and (95) that

$$\begin{aligned} \frac{\partial \mathcal{Z}}{\partial s_z} &= \int_0^{s_z} dz_1 \frac{\partial g_1}{\partial s_z} + \underbrace{\frac{1}{2} g_1(z_1 = s_z)}_{=0} \\ &= \int_0^{s_z} dz_1 \frac{\partial g_1}{\partial s_z} =: \int_0^{s_z} dz_1 \frac{\partial}{\partial s_z} \int_0^{s_z} dz_2 g_2(z_1, z_2) \end{aligned} \quad (96)$$

because  $U$  becomes infinitely large if  $z_1 = s_z$  on account of the divergence of  $u_{fs}$  at this point. In Eq. (96),  $g_2$  is defined analogously to  $g_1$  in Eq. (95) and the above argument may be repeated  $N - 1$  times, to obtain finally

$$T_{zz} = -(A\Xi)^{-1} \sum_N \cdots \int_{V^N} d\mathbf{r}^N \exp(-\beta U) \frac{\partial U_{FS}}{\partial s_z} = \frac{\langle F_z^{[1]} \rangle - \langle F_z^{[2]} \rangle}{2A} \quad (97)$$

where  $F_z^{[k]} := -\partial U_{FS}^{[k]} / \partial s_z$  is the total force exerted by the film on substrate  $k$ . Equation (97) is therefore termed the “force” expression henceforth. The far right side of Eq. (97) is a statement of mechanical stability of the confined fluid. Virial and force expressions provide a useful test of internal consistency of a computer simulation and should agree within a few percent (see, for example, Table II in [77]).

## 2. Stratification

To illustrate the relationship between the microscopic structure and experimentally accessible information, we compute pseudo-experimental solvation-force curves  $F(h)/R$  [see Eq. (22)] as they would be determined in SFA experiments from computer-simulation data for  $T_{zz}$  [see Eqs. (93), (94), (97)]. Numerical values indicated by an asterisk are given in the customary dimensionless (i.e., reduced) units (see [33,75,78] for definitions in various model systems). Results are correlated with the microscopic structure of a thin film confined between plane parallel substrates separated by a distance  $s_z = h$ . Here the focus is specifically on a “simple” fluid in which the interaction between a pair of film molecules is governed by the Lennard–Jones (12,6) potential [33,58,59,77,79–84]. A confined “simple” fluid serves as a suitable model for approximately spherical OMCTS molecules confined

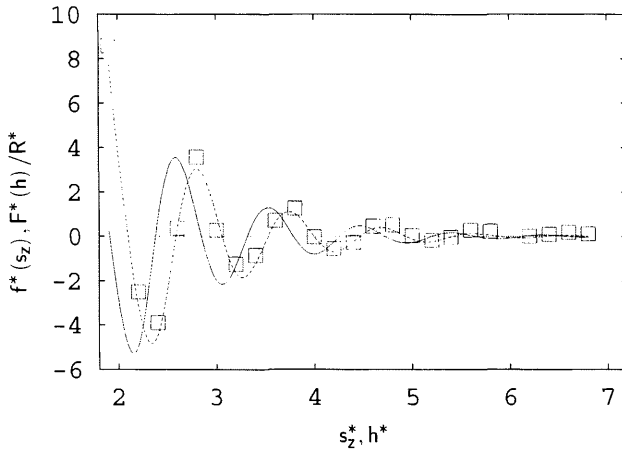


**FIG. 5** The excess pressure  $f(s_z)$  ( $\square$ , dashed line) and the solvation force per radius  $F(h)/R$  (full line) as functions of  $s_z$  and  $h$ , respectively, for a confined fluid composed of “simple” molecules (from Ref. 48).

between mica surfaces, which is perhaps the most thoroughly investigated system in SFA experiments [27,30]. Because OMCTS is chemically inert and electrically neutral, the influence of charges on the mica surfaces can safely be ignored.

Plots of  $f(s_z)$  and  $F(h)/R$  versus  $s_z$  and  $h$ , respectively, are shown in Fig. 5. The oscillatory decay of both quantities is a direct consequence of the oscillatory dependence of  $T_{zz}$  on  $s_z$ , which has also been investigated by integral equation approaches of varying sophistication [36,85–89]. As can be seen in Fig. 5, zeros of  $f(s_z)$  correspond to successive extrema of  $F(h)/R$  because of Eq. (22). In actual SFA experiments the only portions of the  $F(h)/R$  curve generally accessible are those where  $d[F(h)/R]/dh < 0$ . Regions where  $d[F(h)/R]/dh > 0$  are inaccessible, because  $\omega^{\text{ex}}(h)$  would decrease upon compression of the film [see Eq. (23)]. However, structural changes accompanying the variation of  $F(h)/R$  in the accessible regimes are rather obscure, as can be inferred from Fig. 6 where plots of the local density are presented. On account of Eq. (23) accessible portions of the pseudo-experimental curve can be related to the local stress at the point  $(0, 0, s_z = h)$  of minimum distance between the surfaces of the macroscopic sphere and the planar substrate (see Fig. 2). By correlating the local stress  $T_{zz}(h)$  with the film’s local structure at  $(0, 0, h)$  via  $\rho^{[1]}(z; s_z = h)$ , one can establish a direct correspondence between pseudo-experimental data (i.e.,  $F(h)/R$ ) and local microscopic structure of the film.

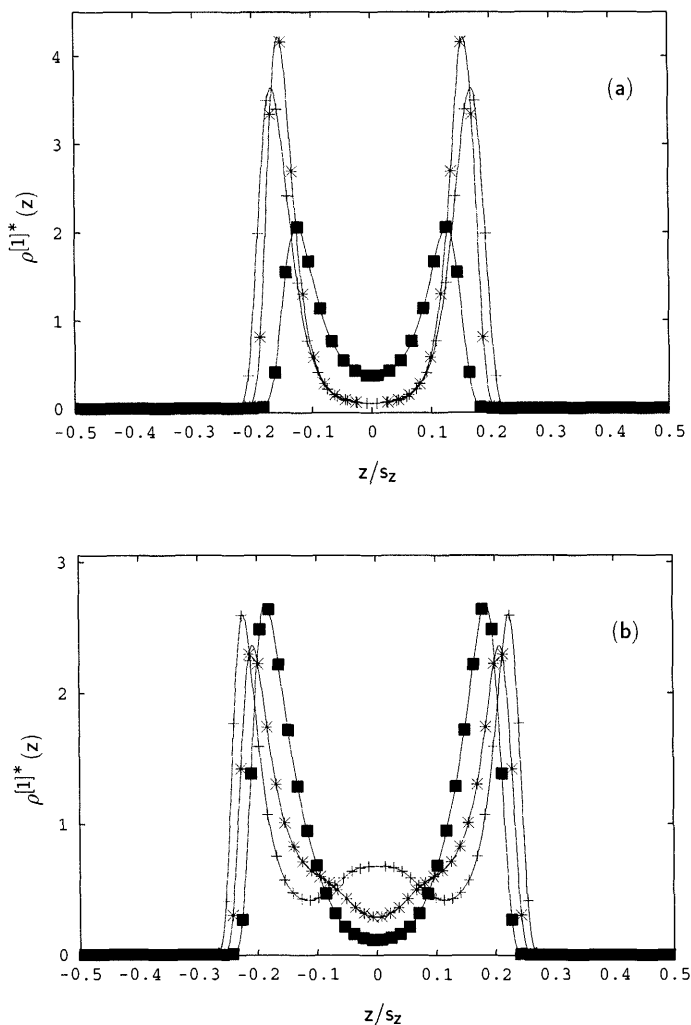


**FIG. 6** The local density  $\rho^{[1]}(z; s_z)$  as a function of  $z/s_z$  for a “simple” fluid confined by planar substrates. (a)  $s_z^* = 2.60$  (■),  $s_z^* = 2.80$  (\*),  $s_z^* = 3.00$  (+); (b)  $s_z^* = 3.20$  (■),  $s_z^* = 3.40$  (\*),  $s_z^* = 3.55$  (+); (c)  $s_z^* = 3.80$  (■),  $s_z^* = 4.00$  (\*) (from Ref. 48).

Plots of a sequence of local densities  $\rho^{[1]}(z; s_z = h)$  in Fig. 6 over the range  $2.60 \leq h^* \leq 4.00$  illustrate this correlation. In an actual SFA experiment  $2.59 \leq h^* \leq 3.06$  and  $3.53 \leq h^* \leq 4.00$  are accessible portions of the solvation-force curve whereas  $3.06 < h^* < 3.53$  demarcates the inaccessible range

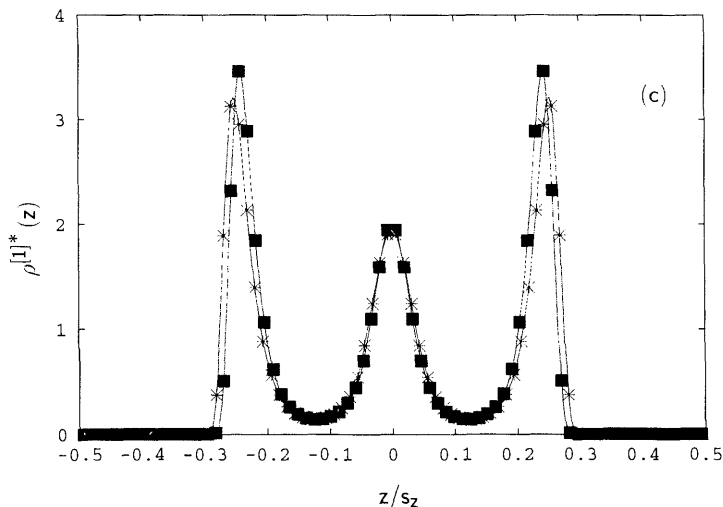


FIG. 6 Continued.

because here  $d[F(h)]/dh > 0$ . Plots in Figs. 6(a) and 6(c) show that in the experimentally accessible regions the film consists locally of two and three strata, respectively. For  $h^* = 2.60$  the film is locally compressed ( $F(h) > 0$ ) whereas it is stretched for  $h^* = 3.00$  ( $F(h) < 0$ ). Under compression the film appears to be less stratified, as is reflected by smaller heights of less well separated peaks of  $\rho^{[1]}(z; s_z = h)$  compared with the other two curves in Fig. 6(a). For  $h^* = 2.80$ ,  $F(h) \approx 0$  and  $T_{zz}(s_z = h)$  has almost assumed a minimum value, indicating that for this particular value of  $h$  film molecules are locally accommodated most satisfactorily between the surfaces of the macroscopic sphere and the planar substrate. It is therefore not surprising that peaks in  $\rho^{[1]}(z; s_z = h)$  are taller for  $h^* = 2.80$  compared with the two neighboring values of  $h$  [see Fig. 6(a)].

In the next accessible region ( $3.53 \leq h^* \leq 4.00$ ) the film consists of three molecular strata for which the most pronounced structure is observed for  $h^* \simeq 3.80$ , corresponding to a point at which  $F(h)/R$  nearly vanishes [see Fig. 6(c)]. As before [see Fig. 6(a)] this is reflected by the peak height in the contact strata (i.e., the strata closest to the substrate) whereas inner portions of the film remain largely unaffected. Plots of  $\rho^{[1]}(z; s_z = h)$  in the inaccessible regime in Fig. 6(b) show that here the film undergoes a local reorganization characterized by the vanishing (appearance) of a whole stratum. The reorganization is gradual, as one can see in the plot of  $\rho^{[1]}(z; s_z = h)$  for  $h^* = 3.4$ , where two shoulders appear at  $z/s_z \simeq \pm 0.1$ .

Stratification, as illustrated by the plots in Fig. 6, is due to constraints on the packing of molecules next to the wall and is therefore largely determined by the repulsive part of the intermolecular potential [55]. It is observed even in the absence of intermolecular attractions, such as in the case of a hard-sphere fluid confined between planar hard walls [42,90–92]. For this system Evans et al. [93] demonstrated that, as a consequence of the damped oscillatory character of the local density in the vicinity of the walls,  $T_{zz}$  is a damped oscillatory function of  $s_z$ , if  $s_z$  is of the order of a few molecular diameters, which is confirmed by Fig. 5.

For one-dimensional confined hard-rod [49,94,95] and Tonks–Takahashi fluids [49,96,97] the close relationship between stratification and the oscillatory decay of  $T_{zz}(s_z)$  has been demonstrated analytically. On the basis of a density-functional approach Iwamatsu [98] has recently analyzed the solvation force in various experimental systems. In the context of dielectric media the analogue of the solvation force between planar walls [ $f(s_z)$  in the current notation] is known as the Casimir force. It arises because the walls modify the spectrum of electromagnetic fluctuations between them such that the vacuum energy of the electromagnetic field becomes size- and shape-dependent [99].

### 3. Orientational Effects

In the other model system the film consists of (soft) ellipsoidal Gay–Berne molecules [78,100–102]. Depending on the thermodynamic state, bulk phases consisting of Gay–Berne molecules can be either isotropic or nematic [103]. The Gay–Berne fluid is therefore a suitable model for liquid crystals, which are currently intensively studied in SFA experiments [104–110] because of their importance in such diverse fields as, say, display technology [111] and lubrication [112]. Here the only case considered is that of a confined Gay–Berne fluid in thermodynamic equilibrium with a nematic bulk phase [102,113]. Parameters of the fluid–substrate intermolecular potential parameters are chosen so that a homeotropic anchoring of fluid molecules to the substrate surface is favored (i.e., fluid molecules in the vicinity of the substrate surface are preferentially ordered normal to the surface). The “nematic” Gay–Berne film between homeotropically anchoring substrates may be viewed as a rough model for a film of (dimers of) 4′-n-octyl-4-cyanobiphenyl (8CB) molecules confined between hydrophobic substrate surfaces consisting of mica coated with dihexadecyldimethyl ammonium acetate (DHDA) monolayers [107].

As in the case of a “simple”-fluid film, the normal component of the stress tensor is a damped oscillatory function of substrate separation (see Fig. 7). Over the range  $4.0 \leq s_z \leq 16.75$ ,  $f(s_z)$  exhibits four maxima separated by a distance  $\Delta s_z \simeq 3.2$ , which is slightly smaller than the large diameter of a film

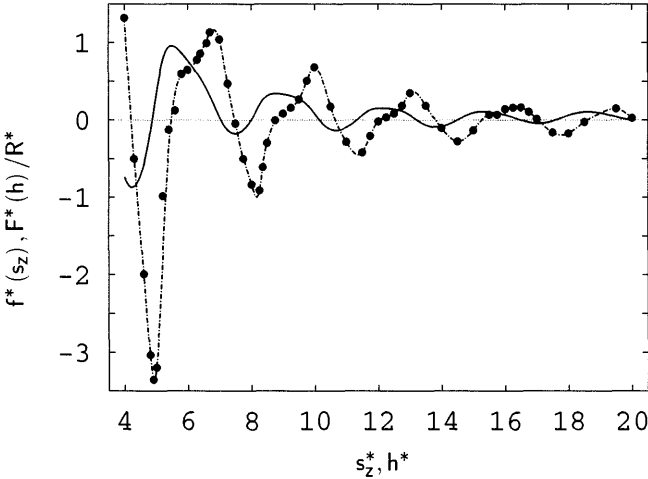


**FIG. 7** Same as Fig. 5, but for a “nematic” Gay–Berne film confined between homeotropically anchoring substrates (from Ref. 48).

molecule [102]. In analogy with results for confined “simple” fluids (see Sec. IV A 2), it is plausible to associate oscillations in  $f(s_z)$  with the formation of molecular strata parallel with the walls. Fig. 7 also shows that  $f(s_z)$  oscillates around zero in the limit of large  $s_z$  [see Eqs. (19), (21)] as it should [49].

However,  $f(s_z)$  also exhibits shoulders at characteristic values of  $s_z$  separated by the same distance  $\Delta s_z^* \approx 3.2$  as the maxima. Portions of  $f(s_z)$  between neighboring minima (i.e.,  $s_z^* < 6.80$ ,  $6.80 \leq s_z^* \leq 10.00$ ,  $10.00 \leq s_z^* \leq 13.20$ , and  $13.20 \leq s_z^* \leq 16.40$ ) are remarkably similar. In order to correlate the microscopic structure of the confined film with features of  $f(s_z)$ , it is convenient to label these portions as “decrease,” “increase,” and “shoulder” zones and to introduce the density–alignment distribution defined by [78,101]

$$\eta(z, u_z^2; s_z) := \frac{\tilde{f}(z, u_z^2; s_z)}{\tilde{f}_{\text{iso}}(u_z^2)} \quad (98)$$

where  $\tilde{f}(z, u_z^2; s_z) dz du_z^2$  is the probability of finding a film molecule at position  $z$  with orientation  $u_z$ , which is the cosine of the angle  $\theta$  between the microscopic director  $\hat{\mathbf{u}}$  and the  $z$  axis. The argument  $u_z^2$  of the probability density  $\tilde{f}(z, u_z^2; s_z)$  reflects the nonpolarity of Gay–Berne molecules (i.e., the equivalence of  $\hat{\mathbf{u}}$  and  $-\hat{\mathbf{u}}$ ). By definition,  $u_z^2 = 1$  if  $\hat{\mathbf{u}}$  is orthogonal to the plane of a wall and  $u_z^2 = 0$  if  $\hat{\mathbf{u}}$  is parallel with that plane. In Eq. (98),  $\tilde{f}_{\text{iso}}(u_z^2)$

is the probability density of finding a Gay-Berne molecule with a particular orientation ( $\propto u_z^2$ ) in the homogeneous, isotropic phase [78]. Clearly,  $\eta(z, u_z^2; s_z) = 0$  in regions inaccessible to film molecules (e.g., sufficiently close to a wall);  $\eta(z, u_z^2; s_z) = 1$  where the film is homogeneous and isotropic, and  $\eta(z, u_z^2; s_z) \neq 1$  elsewhere.

Figs. 8 and 9 illustrate the change of spatial and orientational order with increasing wall separation. The figures show “snapshots” (see Fig. 8) of film configurations as well as corresponding density–alignment distributions (see Fig. 9) for certain characteristic wall separations in the three zones (see Table 1). The “snapshots” exhibit typical configurations of film molecules, whereas the density–alignment distributions reflect the microscopic structure of the confined film on the basis of proper ensemble averages. For simplicity, the discussion is restricted to the first decrease, increase, and shoulder zones and the interested reader is referred to Ref. 102 for a comprehensive discussion of structural changes occurring in the confined film over the entire range of substrate separations plotted in Fig. 7.

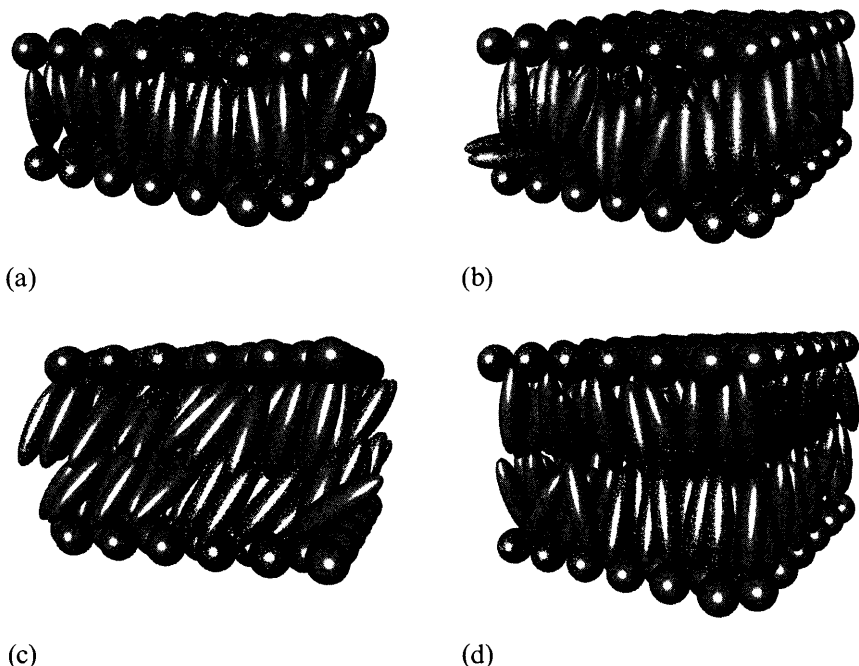


**FIG. 8** “Snapshots” of configurations of “nematic” Gay-Berne films with walls at various separations in the first “increase”, “decrease”, and “shoulder” zone of  $T_{zz}$  (see Table 1). (a)  $s_z^* = 4.6$ ; (b)  $s_z^* = 5.4$ ; (c)  $s_z^* = 6.3$ ; (d)  $s_z^* = 7.5$  (from Ref. 102).

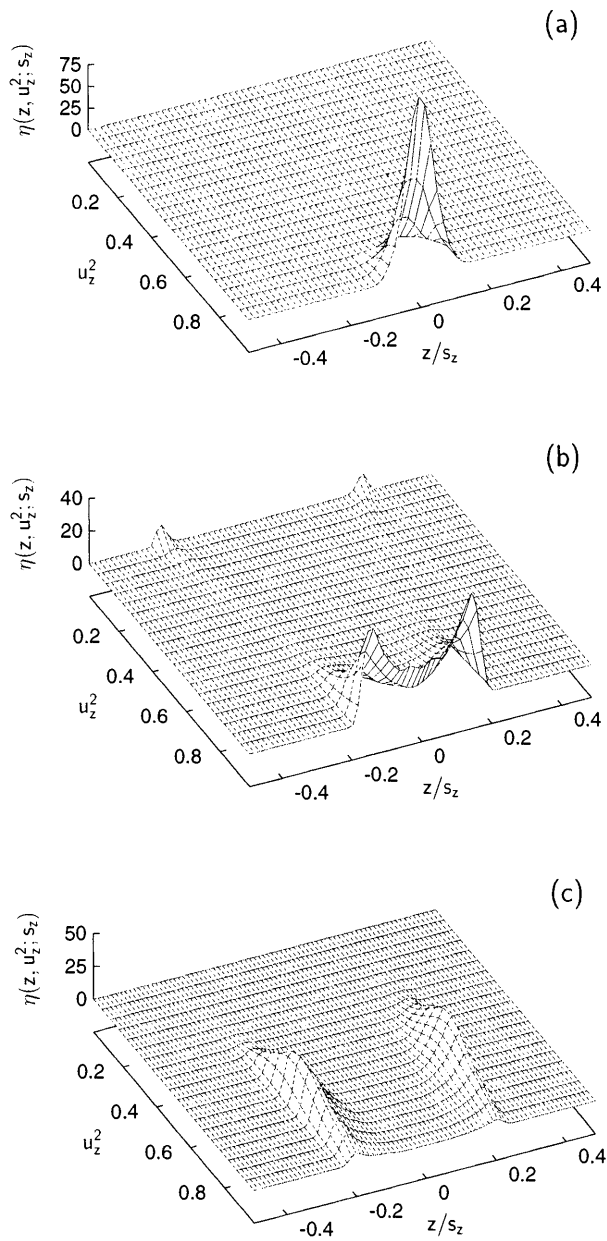


**FIG. 9** Density-alignment distributions  $\eta(z, u_z^2; s_z)$  corresponding to “snapshots” shown in Fig. 8 (from Ref. 102).



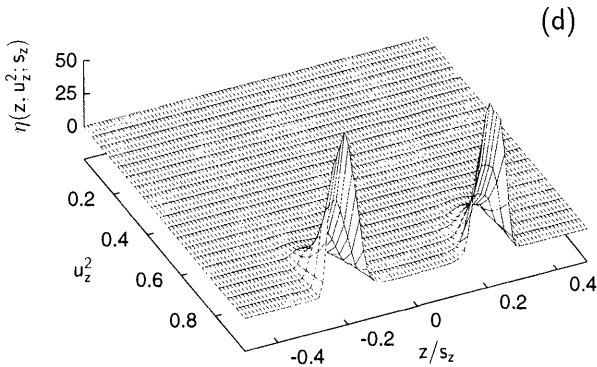


FIG. 9 Continued.

**TABLE 1** Decrease, Increase, and Shoulder Zones in the Plot of  $-T_{zz}(s_z)$  Shown in Fig. 7

Zone	Range <sup>a</sup>
Decrease	$s_z^* \leq 11.40$
Decrease	$6.80 \leq s_z^* \leq 8.20$
Decrease	$10.00 \leq s_z^* \leq 11.40$
Decrease	$13.10 \leq s_z^* \leq 14.50$
Increase	$4.90 \leq s_z^* \leq 5.80$
Increase	$8.20 \leq s_z^* \leq 8.80$
Increase	$11.40 \leq s_z^* \leq 12.00$
Increase	$14.50 \leq s_z^* \leq 15.50$
Shoulder	$5.80 \leq s_z^* \leq 6.80$
Shoulder	$8.80 \leq s_z^* \leq 10.00$
Shoulder	$12.00 \leq s_z^* \leq 13.10$
Shoulder	$15.50 \leq s_z^* \leq 16.50$

<sup>a</sup> Source: Ref. 102.

In this first decrease zone ( $4.0 \leq s_z^* \leq 4.9$ ) the film consists of a homeotropic monolayer [see Fig. 8(a)]. In the corresponding plot of the density–alignment distribution [see Fig. 9(a)] this is reflected by a rather tall and narrow peak around  $u_z^2 = 1.0$ . The centers of mass of film molecules are located halfway between the substrate surfaces so that the peak in  $\eta(z, u_z^2; s_z)$  is centered on  $z = 0$ . In the adjacent increase zone ( $4.9 \leq s_z^* < 5.8$ ) substrate separations are too large to accommodate a homeotropic monolayer

conveniently, but too small for a fully developed homeotropic bilayer film [see Fig. 8(b)]. Therefore molecules contact either wall with a more diffuse, but still preferentially homeotropic, orientation. This, however, leaves limited space which can accommodate a few additional molecules that lie parallel with the walls [see Fig. 8(b)]. Consequently, a plot of the corresponding density–alignment distribution [see Fig. 9(b)] exhibits two unresolved peaks corresponding to homeotropically oriented molecules in contact with either wall, and two much smaller peaks. The latter appear at larger values of  $|z|/s_z$  (i.e., closer to a wall) at  $u_z^2 = 0.0$  and reflect the small number of molecules with a parallel orientation. As the wall separation increases beyond  $s_z^* \simeq 5.8$  (first shoulder zone, see Table 1), the structure of the film changes dramatically [see Fig. 8(c)]. In this range of wall separations the film comprises two well-defined strata in which molecules appear to be tilted. A plot of the associated density–alignment distribution shows two broad peaks centered on  $u_z^2 \approx 0.5$  [see Fig. 9(c)]. They correspond to two individual strata which are symmetrically distributed with respect to the plane  $z = 0$ , as is expected because of the symmetry of the film–wall potential with respect to that plane. If  $s_z$  increases further in the shoulder zone, molecules in the bilayer film gradually change their orientation from tilted to homeotropic and a smectic, homeotropically anchored bilayer film eventually forms [see Figs. 8(d), 9(d)]. In a similar fashion, variations in the film’s microscopic structure can be correlated with  $T_{zz}$  in decrease, increase, and shoulder zones for larger  $s_z$  [102].

How would these structural features manifest themselves in the corresponding pseudo-experimental solvation-force curve  $F(h)/R$ ? The plot of  $F(h)/R$  in Fig. 7 shows that it is again a damped oscillatory, but less regular, function of  $h$  compared with its counterpart for the confined “simple” fluid (see Fig. 5). For example, maxima are much broader than in the case of a “simple” fluid. The widths of the peaks in  $F(h)/R$  are again related to the large diameter of the Gay–Berne molecules. This observation seems to accord with experimental data (see Fig. 4(a) in [107]), as far as “nematic” films of 8CB between homeotropically anchoring walls are concerned. However, it is very difficult to obtain a reliable estimate of the peak width from the experimental curve [107]. It is, furthermore, interesting to note that the slope of  $F(h)/R$  in the experimentally inaccessible regions (where  $d[F(h)/R]/dh > 0$ ) is substantially larger than in the accessible regions (where  $d[F(h)/R]/dh < 0$ ), which seems to be in agreement with the plot in Fig. 4(a) of [107]. In addition, the height of maxima of  $F(h)/R$  in Fig. 7 exceeds the depth of minima considerably, which can also be seen in the data plotted in Fig. 4(a) of [107].

Based on Figs. 7–9, another interesting observation can be made concerning orientational effects in the confined film. As shown above on the

basis of density–alignment distributions, reorientation of film molecules is reflected in shoulder regions of  $f(s_z)$ . Provided a suitable decomposition of the experimental  $F(h)/R$  can be found [see Eq. (23)], reorientation of film molecules should be visible as similar shoulders in the local stress  $f(h)$  because these appear over ranges of  $h$  that are accessible experimentally (i.e.,  $d[F(h)/R]/dh < 0$ , see Fig. 7). However, such a decomposition requires data of sufficiently high precision and resolution. Additional elastic contributions to the solvation force from a confinement-induced distortion of the director field are negligible [113].

## B. The Transverse Structure of Confined Fluids

Although stratification, according to the plot in Fig. 10, occurs continuously as  $s_z$  increases, it is accompanied by a curious structural reorganization in transverse directions (i.e., parallel to the planar substrate). A suitable measure of transverse structure is the pair correlation function defined in Eq. (62). However, for simplicity we are concerned only with the in-plane pair correlation function defined as [see Eq. (62)]

$$g^{[2]}(z_1, \rho_{12}, z_{12} = 0) = \frac{\langle N(z_1, \rho_{12}) \rangle}{2\pi\Delta\rho_{12}\Delta z_{12}\bar{\rho}^{[1]}(z_1)} \quad (99)$$

where  $\langle N(z_1, \rho_{12}) \rangle$  is the average number of atoms in a cylindrical annulus of

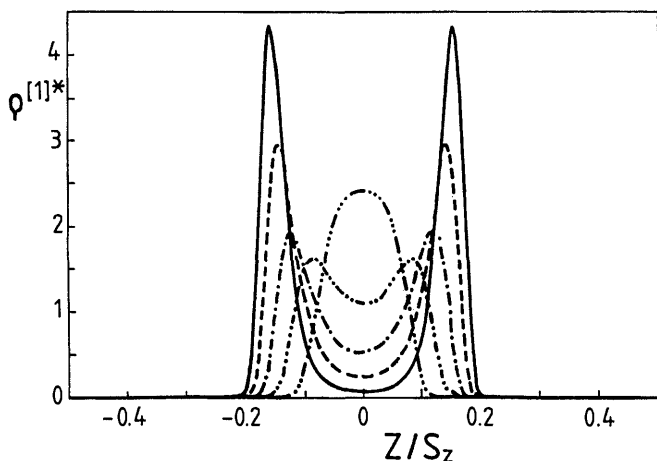


**FIG. 10** The local density  $\rho^{[1]}(z; s_z)$  as a function of position  $z/s_z$  between lower ( $z/s_z = +0.5$ ) and upper ( $z/s_z = -0.5$ ) substrates. (— · — · —)  $s_z^* = 2.20$ ; (— · — · —)  $s_z^* = 2.55$ ; (— — —)  $s_z^* = 2.65$ ; (—)  $s_z^* = 2.75$  (from Ref. 114).

radius  $\rho_{12}$ , width  $\Delta\rho_{12}$ , and height  $\Delta z_{12}$  centered on a reference molecule 1. The value of  $\Delta z_{12}$  is taken as the distance between adjacent minima of  $\rho^{[1]}(z_1)$  bracketing the peak centered on  $z_1$  (see Fig. 10). Hence,  $\bar{\rho}^{[1]}(z_1)$  is the *average* density of a stratum centered at  $z_1$ . Correlating the dependence of the in-plane pair correlation function on  $s_z$  with the transverse isothermal compressibility  $\kappa_{\parallel}$  permits additional insight into stratification. From Eq. (11)

$$-\left(\frac{\partial^2 \Omega}{\partial \mu^2}\right)_{T,A,R,s_z} = \left(\frac{\partial N}{\partial \mu}\right)_{T,A,R,s_z} = \beta^{-1} \left(\frac{\partial^2 \ln \Xi}{\partial \mu^2}\right)_{T,A,R,s_z} = \beta[\langle N^2 \rangle - \langle N \rangle^2] \quad (131)$$

which permits one to derive  $\kappa_{\parallel} = \beta s_z A[\langle N^2 \rangle / \langle N \rangle^2 - 1]$  as a molecular expression in terms of density fluctuations in the confined fluid via Eq. (42) [55,114].

Fig. 11(a) displays plots of the in-plane pair correlation function for  $s_z^* = 2.1$  and 3.0 well outside the regime where  $\kappa_{\parallel}$  exhibits its first maximum (see Fig. 12). The plots indicate that the transverse structures of one- and two-layer fluids (see Fig. 10) are essentially identical and typical of dense Lennard-Jones fluids. However, the transverse structure of a two-layer fluid is significantly affected as the peak of  $\kappa_{\parallel}$  is approached, as can be seen in Fig. 11(b) where  $g^{[2]}(z_1, \rho_{12})$  is plotted for  $s_z^* = 2.55$  and 2.75, which points

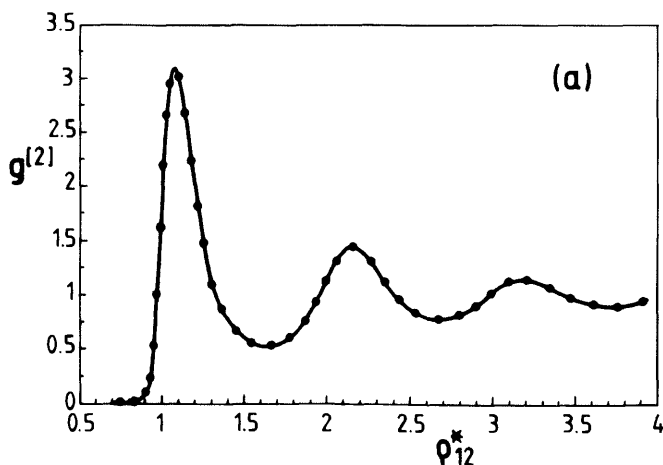


**FIG. 11** The in-plane pair correlation function  $g^{[2]}(z_1, \rho_{12})$  as a function of intermolecular separation  $\rho_{12}$  for various substrate separations. (a)  $s_z^* = 2.10$  (—),  $s_z^* = 3.00$  (•); (b)  $s_z^* = 2.55$  (---),  $s_z^* = 2.75$  (—); (c)  $s_z^* = 2.625$  (---),  $s_z^* = 2.65$  (— · —),  $s_z^* = 2.675$  (—) (from Ref. 114).

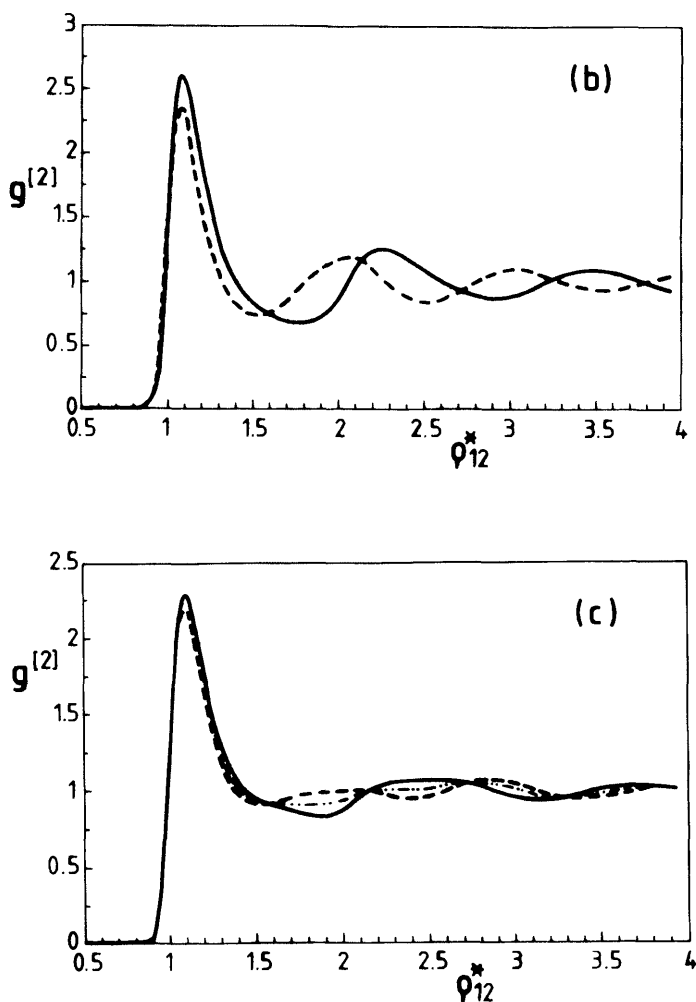
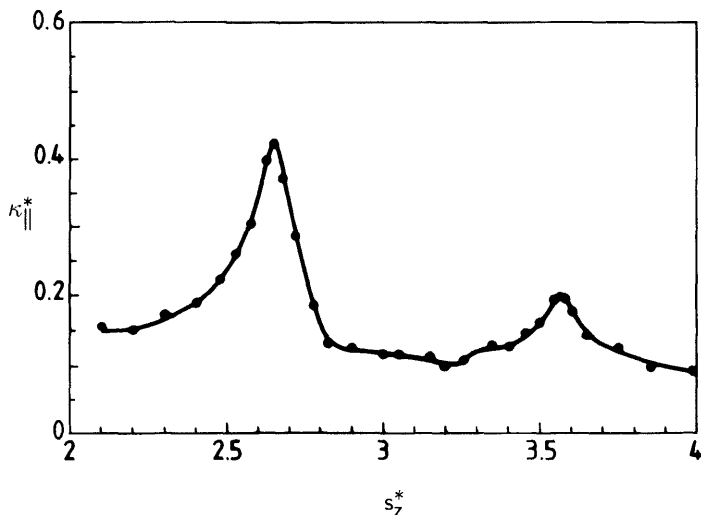


FIG. 11 Continued.

are located symmetrically around the maximum in  $\kappa_{\parallel}$  at approximately  $s_z^* = 2.65$  (see Fig. 12). In general, the peaks of  $g^{[2]}(z_1, \rho_{12})$  reflect an arrangement of fluid molecules in cylindrical shells around a given reference molecule. The height of the first peak in  $g^{[2]}(z_1, \rho_{12})$  corresponding to the first shell of (nearest) neighbors is smaller at  $s_z^* = 2.55$  than at  $s_z^* = 2.75$ . Thus, at  $s_z^* = 2.55$  (on the average) fewer molecules form the immediate neighborhood of a reference molecule compared with  $s_z^* = 2.75$ .



**FIG. 12** The transverse isothermal compressibility  $\kappa_{||}$  as a function of substrate separation  $s_z$  (from Ref. 114).

From Figs. 11(a) and (b), it is also evident that the height of the first peak diminishes as the maximum in  $\kappa_{||}$  at  $s_z^* = 2.65$  is approached from either above or below. At the same time higher-order peaks in  $g^{[2]}(z_1, \rho_{12})$  are shifted consistently to *smaller* values of  $\rho_{12}$  as  $s_z^* = 2.65$  is approached from *below* and to larger  $\rho_{12}$  as  $s_z^* = 2.65$  is approached from *above*. This general trend persists as the peak of  $\kappa_{||}$  is approached more closely, which is clear from the plots in Figs. 11(b) and 11(c). However, the peaks are generally much less pronounced in Fig. 11(c), reflecting an overall loss of structure as  $s_z^* \rightarrow 2.65$ . This is particularly evident if one compares the curves at  $s_z^* = 2.625$  and  $2.675$  with the one at  $s_z^* = 2.65$ , where  $\kappa_{||}$  assumes its maximum. Here the film appears to be least structured. The latter is plausible because density fluctuations are expected to be greatest for least ordered phases.

That the first near-neighbor peak in  $g^{[2]}(z_1, \rho_{12})$  is higher for  $s_z^* = 2.675$  than for  $s_z^* = 2.625$  indicates that the structural transformation at  $s_z^* = 2.65$  carries the fluid from a less to a more ordered state (increasing  $s_z$ ). That is, molecules become more tightly packed in the transverse dimensions. The height of the first peak in  $g^{[2]}(z_1, \rho_{12})$  is directly proportional to the mean number of nearest neighbors, which should be larger the more tightly packed the molecules are. In addition, the apparent outward shift in the higher-order peaks in  $g^{[2]}(z_1, \rho_{12})$  for  $s_z^* = 2.675$  relative to  $s_z^* = 2.625$

supports this notion, as one can readily verify for quasi-two-dimensional arrays (e.g., coins arranged in close-packed configuration on a table top).

The order-disorder transformation is not unique to two-layer fluids, which is readily concluded from the second maximum of  $\kappa_{\parallel}$  in the vicinity of  $s_z^* \approx 3.55$  where the fluid consists of three strata. However, it turns out that only the innermost, middle stratum undergoes the same kind of structural reorganization just explained for the two-layer fluid; the two contact strata (i.e., the strata closest to the substrate) do not participate in the transformation. The intensity of the second maximum in  $\kappa_{\parallel}$  is therefore reduced by roughly 2/3 compared with the first one, as one would expect.

### C. Nonplanar Substrates

Unless substrates have been treated with great care they are typically rough so that an adjacent fluid is exposed to a geometrically disordered wall. The effect of such disorder on wetting phenomena has been studied experimentally [115–118] and theoretically [119–122] by coarse-grained approaches which average laterally over the local height variation of the substrate. An understanding of the *local* microscopic structure of fluids filling the grooves and covering the tips of such disordered substrates is still in its infancy (see also this volume, chapter by Patrykiewicz, Borówko).

This dearth of information is aggravated by the fact that in the meantime it became possible to prepare substrates which exhibit well-defined geometric structures with lateral periodicity in one direction. X-ray scattering provides spatially resolved density distributions of fluids in contact with such substrates [123]. First steps in understanding wetting of single wedges have been made but they focus on the shape of the meniscus forming inside the grooves [124]. Therefore, these studies do not address packing effects occurring in a fluid when its confining walls start to interfere upon approaching the center of a wedge or when they form a tip. Such effects are important in the context of microfluidity where one follows the spreading of liquids in artificial grooves [125–127]. At the surfaces of certain materials grooves may even form spontaneously. One may encounter situations in which planar terraces of molecularly large areas are separated by steps of a height of several atomic layers. Such structures can be quite regular, even in natural materials. For instance, minerals of the palygorskite and sepiolite group consist of stacks of alternating tetrahedral and octahedral silicate sheets [128]. Structure and diffusion of “simple” fluids in grooves of this particular geometry were recently investigated by computer simulation methods [129].

To illustrate the effects of nonplanarity of the substrate on fluid structure, a hard-sphere fluid exposed to a periodic array of wedges (see Fig. 13) is

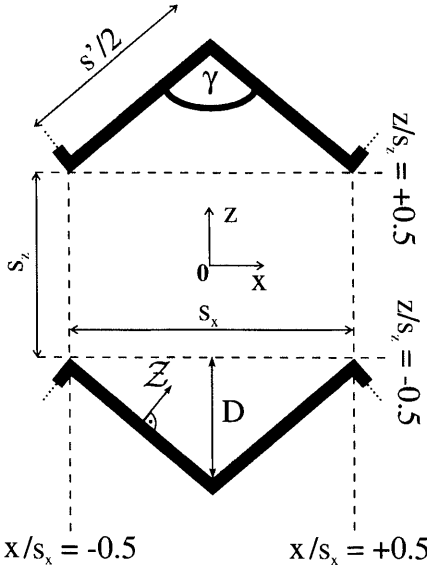


**FIG. 13** Side view of the model system consisting of two opposite hard wedges of side length  $s'$  and dihedral angle  $\gamma$  in the  $(x, z)$  plane. The origin  $0$  of the coordinate system is at the center, halfway in between the wedges. The corner of the wedge is located at  $x/s_x = 0$  and the two tips at  $x/s_x = \pm 0.5$  are separated by a distance  $s_z$  along the  $z$  axis of the coordinate system. Also shown is a point at a distance  $Z$  in a direction normal to a wedge wall. The system is periodically extended in the  $x$  direction by a unit length  $s_x$ . The depth of a wedge is denoted by  $D$  (from Ref. [130]).

analyzed through [130]

$$\rho^{[1]}(x, z; \gamma) := \frac{\langle N(x, z; \gamma) \rangle}{s' \delta x \delta z} = \frac{\langle N(x, z; \gamma) \rangle}{s_x \delta x \delta z} \sin \frac{\gamma}{2} \quad (101)$$

which depends implicitly on the dihedral angle  $\gamma$  (see Fig. 13). However, it is more convenient to express the effects of substrate corrugation in terms of the deviation of the local density

$$\Delta \rho(x, \Delta z; \gamma) := \rho^{[1]}(x, \Delta z; \gamma) - \rho^{[1]}(x, Z; \gamma = \pi) \quad (102)$$

in a wedge of dihedral angle  $\gamma$  from the corresponding one at a planar wall at the same distance  $Z$  (see Fig. 13) from that wall. This is shown in Fig. 14 for four selected dihedral angles  $\gamma$ . For  $\gamma = 8\pi/9$  the substrate is almost planar so that  $\Delta \rho$  vanishes nearly everywhere except in the close vicinity of corner ( $|x|/s_x \ll 1$ ) and tips ( $|x|/s_x \simeq 0.5$ ) of the wedge [see Fig. 14(a)].



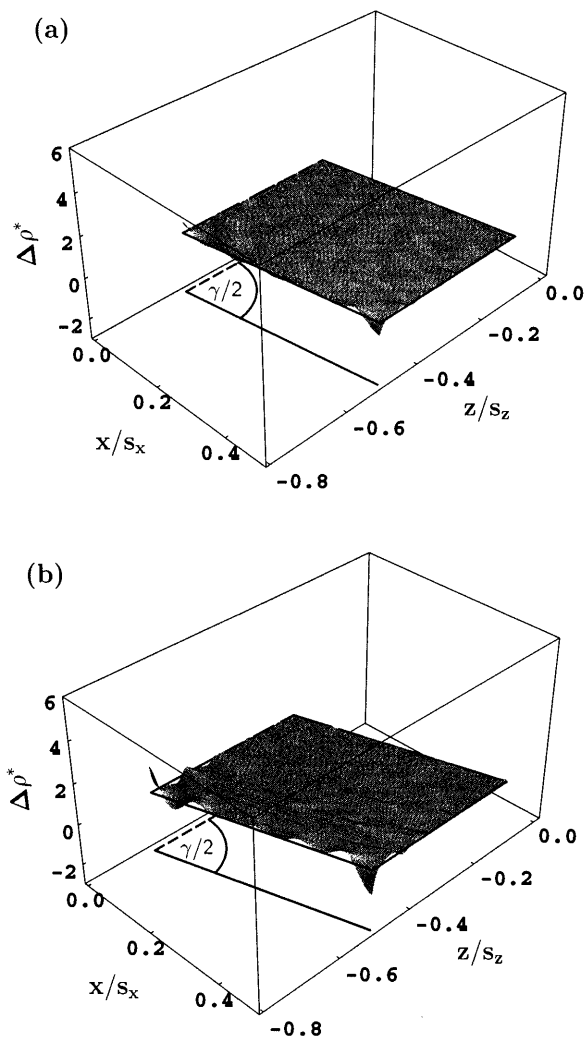


**FIG. 14** The deviation  $\Delta\rho^*$  of the local density in a wedge of dihedral angle  $\gamma = 8\pi/9$  (a),  $\gamma = 7\pi/9$  (b),  $\gamma = 2\pi/3$  (c), and  $\gamma = \pi/2$  (d) from the corresponding local density near a planar hard wall [see Eq. (102)]. The solid line on the bottom of the box indicates the line of fluid-wall contact,  $-z_{\text{wall}}(x, \gamma)(s_x/2 - x) \cot(\gamma/2) + s_z/2 - \sigma/\sin(\gamma/2)$ ,  $|x| \leq s_x/2$ , and the dashed line represents the bisector of the dihedral angle. Because of the symmetry of the system, data are shown only for one quadrant  $0.0 \leq x/s_x \leq 0.5$ ,  $-z_{\text{wall}}(x, \gamma) \leq z/s_z \leq 0.0$ , for which the plane  $\Delta\rho = 0$  is also indicated. In all cases  $s'^* = 10.0$ ,  $s_z^* = 12.0$  (see Fig. 13) (from Ref. 130).

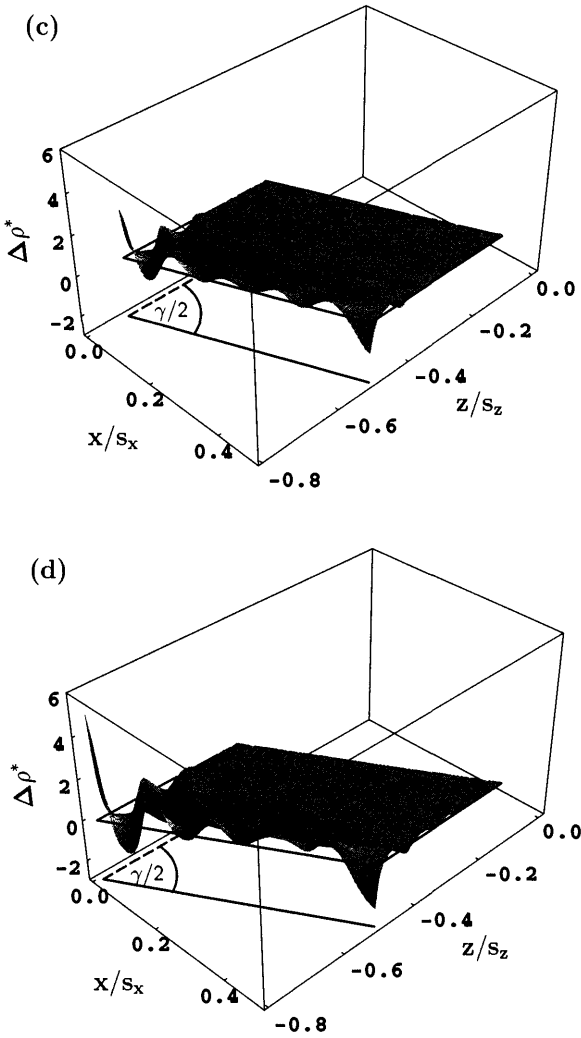


**FIG. 14** Continued.

Inspection of Fig. 14(a) reveals that  $\Delta\rho > 0$  in the corner while  $\Delta\rho < 0$  at the tip. The positive deviation indicates that the two walls forming the wedge squeeze the hard spheres into the corner; this effect is more pronounced for smaller values of  $\gamma$ . Around a tip, on the other hand, the hard spheres are spatially less constrained so that the fluid is more disordered, as in the corresponding planar case, so that  $\Delta\rho < 0$ .

Fig. 14(b) demonstrates the onset of a modulation of  $\Delta\rho(x, z; \gamma)$  along the line of fluid–wall contact which extends slightly into fluid regions further removed from the wall. At planar walls lateral density oscillations occur only at high bulk densities on account of surface-induced freezing [131]. Because of its corrugation the present substrate facilitates lateral packing effects at values of  $\mu$  corresponding to considerably lower densities. These lateral oscillations decay upon moving away from the corner of the wedge towards its tip. In the vicinity of the tip the amplitude of the oscillations in  $\Delta\rho(x, z; \gamma)$  increases again. Thus at  $\gamma = 7\pi/9$  and for the present system size  $s_x^* = 9.397$  both structural elements (i.e., corner and tip) give rise to localized lateral ordering without strong interference. Therefore, this case resembles closely the behavior of a fluid in a single wedge or at a single tip. For smaller dihedral angles [see Figs. 14(c), 14(d)] packing effects induced by corner and tip merge so that the oscillations in  $\Delta\rho(x, z; \gamma)$  at fluid–wall contact persist from corner to tip and can no longer be attributed unambiguously to one or the other as in Fig. 14(b). For smaller dihedral angles the lateral extension of packing effects increases together with their amplitude. Both effects lead to more pronounced positive deviations  $\Delta\rho(x, z; \gamma)$  (i.e., “squeezing”) in the corner region. Increasingly negative deviations  $\Delta\rho(x, z; \gamma)$  in the tip regime, on the other hand, reflect the more disordered character of the fluid as the tip sharpens with decreasing  $\gamma$ . That the effect of “squeezing” in the corner is stronger than the impact of the tip can be inferred from Fig. 14(d), where oscillations in  $\Delta\rho(x, z; \gamma)$  along the line  $x/s_x = 0$  extend further into the fluid than along lines  $|x|/s_x = 0.5$ . Along the former line  $\Delta\rho(x, z; \gamma)$  exhibits three distinct maxima, whereas there are two at most along the latter. These findings agree quantitatively with a recent study by Henderson et al. [132].

## V. PHASE TRANSITIONS

### A. Shear-induced Phase Transitions in Confined Fluids

#### 1. Shear Stress and Shear Modulus

If confined phases are exposed to a shear strain, their unique structure, analyzed in the previous section, permits them to sustain a remarkable stress. This is a consequence of mere confinement and is not necessarily coupled to the presence of any solid-like structures of the confined phase [133]. The effect of an exposure to shear stress(es) can be investigated experimentally with the SFA (see Sec. II A 1). A key quantity determined (in principle) experimentally is the shear stress  $T_{zx}$ . By using arguments similar to the ones for  $T_{zz}$  (see Sec. IV A 1), virial and force expressions for  $T_{zx}$  can

be derived easily [75,133,134]. In the present context the latter is more transparent and can be written as

$$AT_{zx}(\alpha_x \ell_x) = \left( \frac{\partial \Phi}{\partial(\alpha_x \ell)} \right)_{T, \mu, A, R, T_{zz}, \alpha_y, \ell_y} =: \left( \frac{\partial \Phi}{\partial(\alpha_x \ell)} \right)_{\dots} = \langle F_x^{[2]} \rangle = -\langle F_x^{[1]} \rangle \quad (103)$$

from Eqs. (1), (9), (11), (52), and (53). Another interesting quantity is the shear modulus

$$Ac_{44} := \left( \frac{\partial^2 \Phi}{\partial(\alpha_x \ell)^2} \right)_{\dots} = -\frac{\beta}{A} \underbrace{[\langle F_x^{[2]} \rangle^2 - \langle F_x^{[2]} \rangle^2]}_{>0} + \frac{1}{A} \underbrace{\left\langle \frac{\partial^2 U_{FW}^{[2]}}{\partial(\alpha_x \ell)^2} \right\rangle}_{<0} \cong 0 \quad (104)$$

in Voigt's notation (see [135], p. 14 in [136]), where the positive contribution turns out to exceed the negative one in magnitude up to the yield point (i.e., the shear strain  $\alpha_x \ell_x$  for which  $T_{zx}$  is maximum). Noting, however, that in the actual SFA experiment strains rather than stresses are controlled, we define  $\hat{\Phi} := \Phi - T_{zx} A \alpha_x \ell_x$  and obtain

$$\hat{\Phi} = -\beta^{-1} \ln \mathcal{Y} = \sum_N \exp(\beta \mu N) \sum_{s_z} \exp(T_{zz} A s_z) \sum_{\alpha_x \ell_x} \exp(T_{zx} A \alpha_x \ell_x) \mathcal{Q}_{\text{class}} \quad (105)$$

by a procedure parallel to the one detailed in Sec. II C where, however, an additional constraint of fixed total substrate registration  $\widehat{\alpha_x \ell_x}$  of the super-system has to be imposed in addition to Eqs. (43). From Eq. (105) and the exact differential of  $\hat{\Phi}$  it follows that [134]

$$\begin{aligned} \langle \alpha_x \ell(T_{zx}) \rangle &= \left( \frac{\partial \hat{\Phi}}{\partial T_{zx}} \right)_{T, \mu, A, R, T_{zz}, \alpha_y, \ell_y}, \\ Ac_{44} &= \left( \frac{\partial^2 \Phi}{\partial(\alpha_x \ell)^2} \right)_{T, \mu, A, R, T_{zz}, \alpha_y, \ell_y} = A \left( \frac{\partial(\alpha_x \ell)}{\partial T_{zx}} \right)^{-1}_{\dots} \\ &= \frac{\beta}{\underbrace{\langle (\alpha_x \ell - \langle \alpha_x \ell \rangle)^2 \rangle}_{\geq 0}} = -A^2 \left( \frac{\partial^2 \hat{\Phi}}{\partial(T_{zx})^2} \right)^{-1}_{\dots} \geq 0 \end{aligned} \quad (106)$$

where the expression for  $c_{44}$  differs from the one in Eq. (104) in that  $c_{44}$  is positive semidefinite here because registry fluctuations cannot be negative.

## 2. Stick–Slip Transitions from an Equilibrium Perspective

Theoretically, many attempts have been made in recent years to elucidate details of the behavior of confined fluids under shear. The approaches can generally be grouped into two different categories which may be labelled “dynamical” [137–143] and “quasistatic” [58,66,133,144–147]. In the dynamical approaches a stationary nonequilibrium state is created either by applying an external driving force [137] or by explicitly moving a substrate [138,140–143] in nonequilibrium molecular dynamics (NEMD) simulations in order to mimic dynamical aspects of a corresponding SFA experiment directly on a molecular scale. However, the relationship between NEMD simulations [138,140–143] and SFA experiments remains highly questionable for a number of reasons. First, in order to describe the motion of the substrate on a physical time scale, an equation of motion needs to be solved which inevitably involves the substrate mass. However, there are no physical criteria on which the choice of a specific value for this mass could be based. Second, even though the substrate is a macroscopic object in the SFA experiment, its mass cannot be too much larger than the mass of a film molecule in the NEMD simulations because otherwise the wall would remain at rest on the time scale on which film molecules move. In fact, the ratio of the mass of a single film molecule to that of the entire wall is sometimes as small as  $1/8$  [142,143], so that one can expect relaxation phenomena in the film to depend sensibly (and therefore unphysically from an experimental perspective) on this arbitrarily selected wall mass [58]. Third, the speed at which the walls are slid in the SFA experiment is typically of the order of  $10^{-9}$ – $10^{-7}$  Å ps<sup>-1</sup> [21], so that under realistic conditions the walls remain practically stationary on a typical length and time scale of molecular relaxation processes. To avoid these problems, and in view of the characteristic low shear rates in the actual SFA experiments, we employ a “quasistatic” or reversible approach in which the thermodynamic state of the film passes through a succession of equilibrium states (see Sec. 3.3 in [136]), each being distinguished by a different (average) lateral alignment of the walls [58,66,69,144–146]. Equilibrium properties of the film can be computed within the framework of Monte Carlo simulations carried out in the ensembles introduced in Sec. V B 1, which are designed to capture key characteristics of a corresponding SFA experiment to a maximum degree.

Two situations are considered which differ in the number of constraints imposed. In the first one the shear strain in  $x$  and  $y$  directions is fixed, infinitesimal, reversible transformations are governed by the thermodynamic potential  $\Phi$  [see Eq. (9)], and  $\mathcal{X}$  is the relevant partition function [see Eq. (52)]. Here the shear stress is computed as a function of the registry

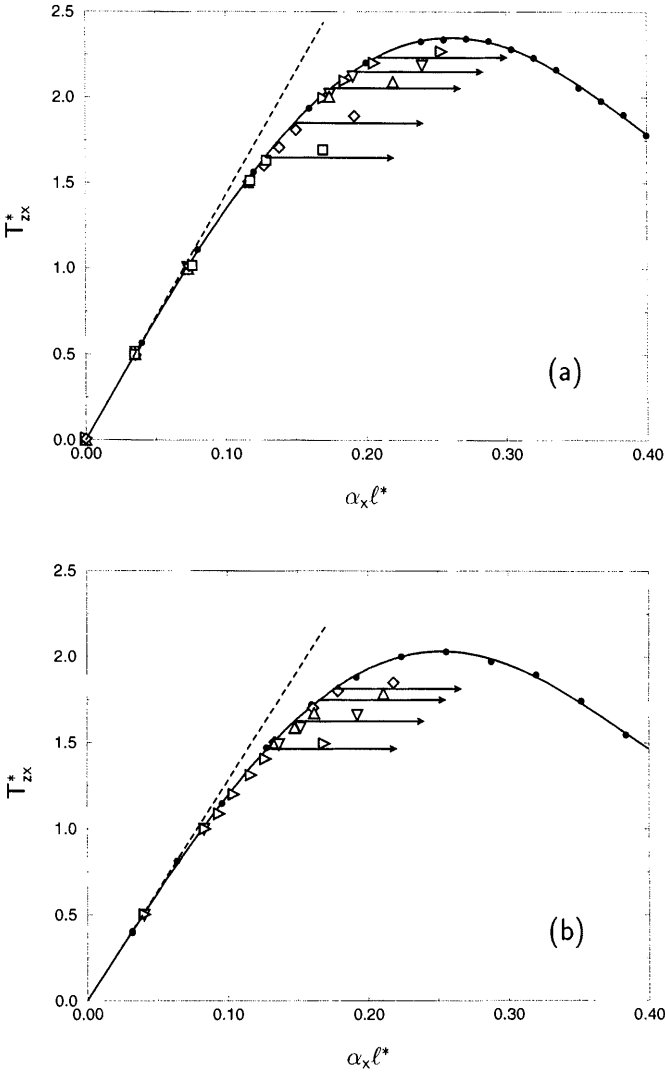


**FIG. 15** The shear stress  $T_{zx}$  as a function of the shear strain  $\alpha_x \ell_x$  for  $T^* = 1.00$ ,  $\mu^* = -11.00$ . (a):  $T_{zz}^* = -1.00$ ; ( $\bullet$ ): isostrain ensemble, open symbols represent iso-stress results for various areas  $A^* = 63.880$  ( $\square$ ), 91.987 ( $\diamond$ ), 163.533 ( $\triangle$ ), 255.520 ( $\nabla$ ), and 574.921 ( $\triangleright$ ). The full curve is a fit to the grand isostrain-ensemble data intended to guide the eye. The dashed line corresponds to the Hookean limit (see text). The horizontal arrows indicate the shear stress at the rupture points (see text). (b): as (a), but for  $T_{zz}^* = -0.50$  (from Ref. 134);  $A^* = 63.880$  ( $\triangleright$ ), 91.9876 ( $\nabla$ ), 163.533 ( $\triangle$ ), 255.520 ( $\diamond$ ).

via Eq. (103). In the second case, the registry is permitted to vary during the course of the simulation, subject to a fixed shear stress. This permits one to compute the average registry as a function of the shear stress via the first Eq. (106). Since the registry may vary in this isostress ensemble it has one additional degree of freedom compared with the previous isostrain ensemble.

For a monolayer film, the stress–strain curve from Eqs. (103) and (106) is plotted in Fig. 15. For small shear strains (or stress) the stress–strain curve is linear (Hookean limit). At larger strains the stress–strain curve is increasingly nonlinear, eventually reaching a maximum stress at the yield point defined by  $T_{zx}^{yd} := dT_{zx}/d(\alpha_x \ell_x) = 0$ , or equivalently by  $c_{44}^{yd}(\alpha_x \ell_x) = 0$ . The stress  $T_{zx} =: AS_c$ , where  $S_c$  is the (experimentally accessible) static friction force [138]. By plotting  $T_{zx}/T_{zx}^{yd}$  versus  $\alpha_x/\alpha_x^{yd}$  shear–stress curves for various “loads”  $T_{zx}$  can be mapped onto a universal master curve irrespective of the number of strata [148]. Thus, for stresses (or strains) lower than those at the yield point the substrate “sticks” to the confined film while it can “slip” across the surface of the film otherwise so that the yield point separates the sticking from the slipping regime. By comparison with Eq. (106) it is also clear that at the yield point  $|\alpha_x \ell_x - \langle \alpha_x^{yd} \ell_x \rangle| \rightarrow \infty$ . Since there is no reason to suspect that  $\langle \alpha_x \ell_x \rangle$  exhibits any anomalies up to and, in the thermodynamic limit, at the yield point,  $\langle \alpha_x^{yd} \ell_x \rangle$  is a finite quantity. This situation is akin to the one encountered in liquid–gas equilibria where, at the critical point, the density remains finite while density fluctuations diverge. In this sense, the yield point may be viewed as a shear-critical point with the registry  $\alpha_x \ell_x$  as the analogue of the density. This notion is supported by the fact that in a finite system a pronounced system-size effect is observed, as one would expect for a critical phenomenon. The plots in Fig. 15 show that the transition from stick to slip conditions occurs prior to the yield point in a finite system. The location of these so-called *rupture* points depends on the area of the film–substrate interface. In the thermodynamic limit ( $A \rightarrow \infty$ ) rupture and yield points coincide (see Fig. 5 in [134]).

### 3. Thermodynamic Stability of Sheared Confined Phases

If a confined fluid is thermodynamically open to a bulk reservoir, its exposure to a shear strain generally gives rise to an apparent multiplicity of microstates all compatible with a unique macrostate of the fluid. To illustrate the associated problem, consider the normal stress  $T_{zz}$  which can be computed for various substrate separations in grand canonical ensemble Monte Carlo simulations. A typical curve, plotted in Fig. 16, shows the oscillatory decay discussed in Sec. IV A 2. Suppose that instead

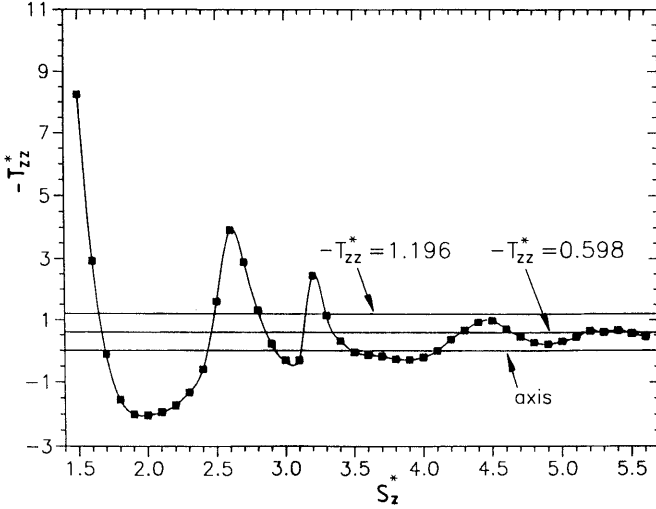


**FIG. 16** Negative normal stress  $T_{zz}$  as a function of substrate separation  $s_z$  from grand canonical ensemble Monte Carlo simulations at  $T^* = 1.00$ ,  $\mu^* = -11.0$ , and  $\alpha_x \ell_x = 0.0$  (■) ( $P_{\text{bulk}} = 0.486$ ); the solid line represents a cubic spline fit to the discrete data to guide the eye. Also shown are three isobars  $-T_{zz}^* = 0.000, 0.598$ , and  $1.196$ , indicated by horizontal lines. Intersections between the isobars and the curve  $T_{zz}(s_z)$  correspond to stable and metastable phases of the confined fluid (see text) (from Ref. 66).

of computing  $T_{zz}$  from Eqs. (93), (94), or (97) in the grand canonical ensemble one would prefer to fix it and compute  $\langle s_z \rangle = f(T_{zz})$  in an isostress ensemble. An inspection of Fig. 16 immediately shows that this causes a multiplicity of phases  $\langle s_z \rangle_i$ ,  $i = 1, \dots, m$  to be compatible with any set  $\{T, \mu, A, R, T_{zz}, \alpha_x \ell_x, \alpha_y \ell_y\}$  identified from the plot as the intersection of the curve  $T_{zz}(s_z)$  with the isobar  $T_{zz} = \text{const}$ . However, from an equilibrium perspective the apparent multiplicity of states must be regarded as virtual in general. Except for points of phase coexistence only one phase can be thermodynamically stable; the others must be “unstable” or metastable at best. The globally stable phase is the one having the lowest value of  $\Phi$ . However, from the discussion in Sec. II B it follows that  $\Phi$  cannot be computed in general from a mechanical expression [like, for example, Eq. (27)]. Fortunately, a stability analysis of phases does not really require the absolute value of a thermodynamic potential but rather its difference from that of a(n arbitrary) reference state. Thus, instead of  $\Phi$  itself,  $\Delta\Phi := \Phi_i - \Phi_{\text{ref}}$  is sought, where  $\Phi_i$  refers to  $\langle s_z \rangle_i$  and  $\Phi_{\text{ref}}$  to the reference



state. From

$$\Delta\Phi_1 = \Delta\Omega - T_{zz}A\Delta s_z = A \int_{s_z^i}^{s_z^{\text{ref}}} T_{zz}(s_z) ds_z, \quad \text{fixed } T, \mu, A, R, \alpha_x \ell_x, \alpha_y \ell_y$$

$$\Delta\Phi_2 = A \int_0^{\alpha_x \ell_x} d(\alpha_x \ell_x)' T_{zx}[(\alpha_x \ell_x)'], \quad \text{fixed } T, \mu, A, R, T_{zz}, \alpha_y \ell_y \quad (107)$$

$\Delta\Phi := \Delta\Phi_1 + \Delta\Phi_2$  is accessible by numerically integrating the curve plotted in Fig. 16 between  $s_z^i$  for state  $i$  and  $s_z^{\text{ref}}$  and performing a similar integration of  $T_{zx}$  [66].

Taking as the reference system an unsheared monolayer ( $\alpha_x = 0$ ), the thermodynamic integration procedure in Eqs. (107) permits one to construct the plot shown in Fig. 17. For  $\alpha_x = 0$ ,  $\Delta\Phi = 0$  vanishes for the monolayer as expected. As  $\alpha_x$  increases,  $\Delta\Phi$  rises, indicating that the sheared monolayer is increasingly less stable. A bilayer film, on the other hand, becomes increasingly stable as  $\alpha_x \rightarrow 0.5$ , eventually intersecting the monolayer curve at  $\alpha_x^{\text{ID}}$ . As  $\alpha_x$  increases from 0.0 up to  $\alpha_x^{\text{ID}}$  the monolayer is the thermodynamically stable phase because its  $\Delta\Phi$  is smallest; for  $\alpha_x > \alpha_x^{\text{ID}}$  the bilayer

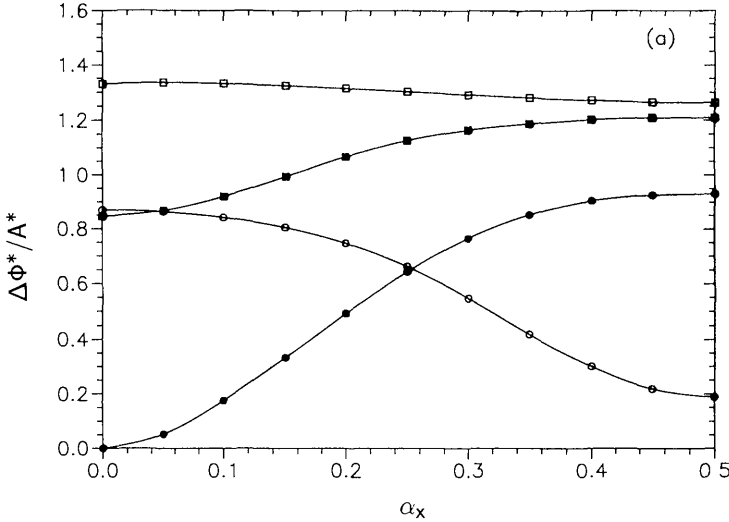


**FIG. 17** (a) The change in the thermodynamic potential  $A^{-1}\Delta\Phi$  as a function of the shear strain  $\propto \alpha_x$  at  $T^* = 1.0$ ,  $\mu^* = -11.0$ ,  $T_{zz}^* = -0.598$ ; (●) one-layer, (○) two-layer, (■) three-layer, (□) four-layer phase. (b) Average number of molecules accommodated by the thermodynamically stable phase as a function of shear strain  $\propto \alpha_x$ ; symbols as in (a) (from Ref. 66).

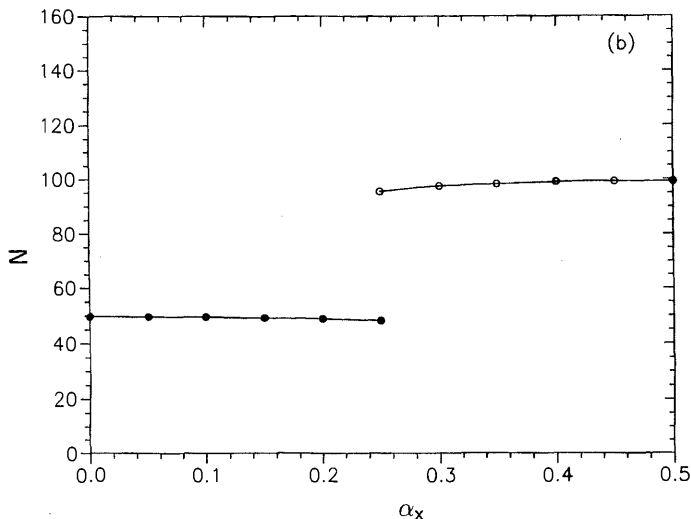


FIG. 17 Continued.

film is globally stable. The stability analysis also enables one to plot the average number of molecules  $\langle N \rangle$  as a function of the shear strain (see Fig. 17) which changes discontinuously at  $\alpha_x^{\text{ID}}$  in a first-order phase transition. Thus, at  $\alpha_x^{\text{ID}}$  imbibition or drainage of matter is observed as a result of the discontinuous variation of  $\Delta\Phi$  with  $\alpha_x$ . The location of  $\alpha_x^{\text{ID}}$  depends on the precise thermodynamic conditions [66].

## B. Liquid-Gas Equilibria in Confined Systems

### 1. The Thommes-Findenegg Experiment

Besides shear-induced phase transitions, liquid-gas equilibria in confined phases have been extensively studied in recent years, both experimentally [149–155] and theoretically [156–163]. For example, using a volumetric technique, Thommes et al. [149,150] have measured the excess coverage  $\Gamma$  of  $\text{SF}_6$  in controlled pore glasses (CPG) as a function of  $T$  along subcritical isochoric paths in bulk  $\text{SF}_6$ . The experimental apparatus, fully described in Ref. 149, consists of a reference cell filled with pure  $\text{SF}_6$  and a sorption cell containing the adsorbent in thermodynamic equilibrium with bulk  $\text{SF}_6$  gas at a given initial temperature  $T_i$  of the fluid in both cells. The pressure  $P$  in the reference cell and the pressure difference  $\Delta P$  between sorption and reference cell are measured. The density of (pure)  $\text{SF}_6$  at  $T_i$  is calculated from  $P$  via an equation of state.

At the beginning of an experimental scan the reference-cell volume is adjusted such that  $\Delta P(T_i) = 0$ , that is, the thermodynamic state of  $\text{SF}_6$  is the same in both cells. The temperature is then lowered from  $T_i$  to a new temperature  $T_{i+1} = T_i - \Delta T$ , at which  $\Delta P(T_{i+1}) \neq 0$  because more  $\text{SF}_6$  is adsorbed. The volume of the sorption cell is then adjusted to reestablish the original condition  $\Delta P(T_{i+1}) = 0$ . The change in the excess coverage is given by  $\Delta \Gamma \propto \rho \Delta V$ , where  $\Delta V$  is the change in the volume of the sorption cell between  $T_i$  and  $T_{i+1}$ . Measurements are repeated by lowering the temperature in a stepwise fashion until the bulk coexistence temperature  $T_{ob}$  of  $\text{SF}_6$  for the given isochore is reached and the gas in the reference cell begins to condense. By means of a high-pressure microbalance technique [164,165] the absolute value of  $\Gamma(T_i)$  is determined in an independent experiment so that  $\Gamma(T)$  can be calculated from  $\Delta \Gamma$  for each temperature in the range  $T_i \geq T \geq T_{ob}$ .

From a theoretical perspective these experiments are particularly appealing for two reasons. First, CPG is characterized by a very narrow pore-size distribution. As pointed out in Ref. 149, 80% of all pores have a diameter within 5% of the average diameter of the (approximately) cylindrical pores. Disregarding connections between individual pores, the phase behavior of the adsorbate should therefore closely resemble that in a single pore. Second, the CPG employed by Thommes et al. [149,150] is mesoporous, as reflected by the nominal average pore radii of 24 nm (CPG-240) and 35 nm (GCP-350). Since these values are large compared with the range of fluid-substrate intermolecular forces, the inhomogeneous region of the pore fluid near the substrate surfaces is much smaller than the homogeneous inner region. Hence the shape of the pores should not matter greatly.

## 2. Mean-field Theory of Adsorption in Mesoporous Media

Theoretically, several aspects of the Thommes-Findenegg experiment can be analyzed at the mean-field level [157]. A key quantity of a mean-field theory of confined fluids is the (Helmholtz) free energy, given by

$$\mathcal{F} = -\beta^{-1} \ln \frac{Z_N(\beta; A, s_z)}{N! \Lambda^{3N}} \quad (108)$$

If the configurational energy is split into a contribution from a(n unperturbed) reference system  $U^{(0)}$  and a perturbation  $U^{(1)}$  the free energy can be split accordingly for sufficiently high temperatures, that is

$$\mathcal{F} \simeq \mathcal{F}^{(0)} + \mathcal{F}^{(1)} = -\beta^{-1} \ln \frac{Z_N^{(0)}}{N! \Lambda^{3N}} + \langle U^{(1)} \rangle_0 \quad (109)$$

where the angular brackets signify an ensemble average over the unperturbed probability distribution  $Z_N^{(0)-1} \exp[-\beta U^{(0)}(\mathbf{r}^N)]$  and  $Z_N^{(0)}$  is the

configuration integral for the reference system. Henceforth, the reference system is taken to be a hard-sphere fluid between planar hard walls, and the perturbation is related to attractive parts  $u_{ff}^{att}(r_{12})$  and  $u_{fs}^{att}(z_1)$  of the fluid–fluid and fluid–substrate potential, respectively. The perturbational contribution to  $\mathcal{F}$  can then be written as

$$\langle U^{(1)} \rangle_0 = \int d\mathbf{r}_1 \rho_0^{[1]}(\mathbf{r}_1) u_{fs}^{att}(z_1) + \frac{1}{2} \int_V d\mathbf{r}_1 \int_V d\mathbf{r}_2 \rho_0^{[2]}(\mathbf{r}_1, \mathbf{r}_2) u_{ff}^{att}(r_{12}) \quad (110)$$

where  $\rho_0^{[1]}(\mathbf{r}_1)$  and  $\rho_0^{[2]}(\mathbf{r}_1, \mathbf{r}_2)$  are, respectively, the local density and the pair distribution function in the reference system, which are related to one another through the pair correlation function  $g(\mathbf{r}_1, \mathbf{r}_2)$  [see Eq. (62)]. At mean-field level all intermolecular correlations are ignored, that is

$$g(\mathbf{r}_1, \mathbf{r}_2) = \begin{cases} 0, & r_{12} < \sigma \\ 1, & r_{12} \geq \sigma \end{cases} \quad (111)$$

where  $\sigma$  is the diameter of a hard sphere (fluid molecule or substrate atom) in the reference system. Moreover, neglecting fluid–substrate correlations, the fluid is taken to be homogeneous; that is, the local density is approximated by

$$\rho_0^{[1]}(\mathbf{r}_1) = \rho_0^{[1]}(\mathbf{r}_2) = \rho_p \quad (112)$$

Because of the hard-sphere reference system and because of Eqs. (111) and (112),  $Z_N^{(0)}$  and Eq. (110) can be evaluated in closed form [157]. One obtains [see Eq. (109)]

$$\mathcal{F} = -\beta^{-1} \left\{ N \ln \left[ \frac{1 - b\rho_p}{\rho_p \Lambda^3} \right] + N \right\} + N\Psi(\xi) - a_p(\xi)N\rho_p \quad (113)$$

In Eq. (113),  $b := 2\pi\sigma^3/3$  is (half) the volume excluded to one hard-sphere molecule by another

$$\Psi(\xi) = \Psi_0 \frac{1}{\xi - 2} \left[ \frac{1}{(\xi - 1)^2} - 1 \right], \quad \xi > 2 \quad (114)$$

where  $\Psi_0$  is a measure of strength of the fluid–substrate attraction,

$$a_p(\xi) = a_b \left[ 1 - \frac{3}{4(\xi - 2)} + \frac{1}{8(\xi - 2)^3} \right] \leq a_b \quad (115)$$

is the contribution of attractive fluid–fluid interactions to the free energy ( $a_b = 8\pi\epsilon_{ff}\sigma^3/3$ ), and  $\xi := s_z/\sigma$  is a reduced substrate separation. Subscripts  $p$  and  $b$  refer to pore and bulk phase, respectively. From

Eqs. (10), (11), and (113)

$$-\frac{\rho_p^2}{N} \left( \frac{\partial \mathcal{F}}{\partial \rho_p} \right)_{T, N, s_z} = T_{\parallel} = -\frac{\rho_p}{\beta(1 - b\rho_p)} + a_p(\xi)\rho_p^2 \quad (116)$$

which matches the (bulk) van der Waals equation of state except for the parameter  $a_p(\xi)$  which depends on the substrate separation [157].

Theoretically, the Thommes–Findenegg experiment [149] can be represented by

$$\mu_b(T, \rho_b) - \mu_p(T, \rho_p) \stackrel{!}{=} 0, \quad \rho_b = \text{const}, \quad T \rightarrow T_{0b}^+ \quad (117)$$

where  $T_{0b}$  is the bulk liquid–gas coexistence temperature. From  $\mu := (\partial \mathcal{F} / \partial N)_{T, A, s_z}$  and Eqs. (113) and (117) one gets

$$0 \stackrel{!}{=} \ln \frac{\rho_p(1 - \rho_b b)}{\rho_b(1 - \rho_p b)} + \frac{(\rho_p - \rho_b)b}{(1 - \rho_p b)(1 - \rho_b b)} + \beta \Psi(\xi) - 2\beta[a_p(\xi)\rho_p - a_b\rho_b] \quad (118)$$

which can only be solved numerically for  $\rho_p$  in terms of  $\rho_b$  and  $T$  as detailed in Ref. 157.

For subcritical densities and the thermodynamically stable pore phase (see Ref. 157) the excess coverage

$$\Gamma(T, \rho_b) = (s_z - 2\sigma_{fw})(\rho_p - \rho_b) \quad (119)$$

is calculated from the solution of Eq. (118), which is the primary experimental quantity [149,150]. If the fluid–substrate interaction is sufficiently attractive,  $\Gamma(T, \rho_b) > 0$  for all  $T$  and  $\rho_b/\rho_{cb} \leq 1$  ( $\rho_{cb} = 1/3b$  is the bulk critical density). Plots in Fig. 18 show that under these conditions  $\Gamma(T, \rho_b)$  may exhibit a discontinuity at some temperature  $T_{0p}(\rho_b)$ . This discontinuity corresponds to pore condensation [156], which is also observed experimentally over a similar density range  $\rho_b/\rho_{cb}$  and reduced temperatures  $[T - T_{0b}(\rho_b)]/T_{0b}(\rho_b)$  (see Fig. 5 of Ref. 149). It is, however, noted that since the measurement is ineluctably performed on a collection of pores having a distribution of sizes, true discontinuities in  $\Gamma(T, \rho_b)$  are not observed. The analog of condensation in the bulk, pore condensation, occurs at temperatures  $T > T_{0b}$  because of the attractive fluid–substrate forces [158,156]. The plots in Fig. 18 also show that pore condensation does not take place at sufficiently high densities  $\rho_b/\rho_{cb}$  if  $T_{0b}(\rho_b)$  exceeds the pore critical temperature  $T_{cp}(\xi) = 8a_p(\xi)/27b \leq T_{cb}$ . For example, the curve for  $\rho_b/\rho_{cb} = 0.78$  is continuous. If  $T_{0b}(\rho_b) = T_{cp}(\xi)$ ,  $\Gamma(T, \rho_b)$  is continuous and finite for all  $T$ , but  $(\partial \Gamma(T, \rho_b) / \partial T)_{\rho_b} = \infty$  (see Fig. 1 in Ref. 149).

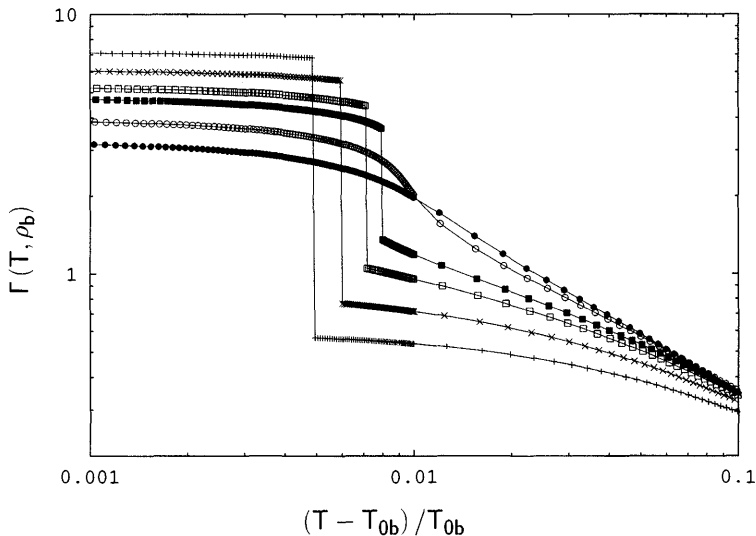


**FIG. 18** Excess coverage  $\Gamma(T, \rho_b)$  as function of temperature  $T$  for fluid confined by attractive substrate for  $s_z = 50$  and bulk isochores  $\rho_b/\rho_{cb} = 0.545$  (+),  $\rho_b/\rho_{cb} = 0.595$  (x),  $\rho_b/\rho_{cb} = 0.645$  ( $\square$ ),  $\rho_b/\rho_{cb} = 0.675$  ( $\blacksquare$ ),  $\rho_b/\rho_{cb} = 0.730$  ( $\circ$ ), and  $\rho_b/\rho_{cb} = 0.780$  ( $\bullet$ ). Solid lines are intended to guide the eye (from Ref. 157).

### 3. Chemically Heterogeneous Substrate Materials

If the substrate is composed of more than one chemical species the phase behavior of confined fluids is altered remarkably (this volume, chapter by Patrykiewicz, Borówko). For substrates consisting of alternating strips of weakly ( $\epsilon_{fw} < \epsilon_{ff}$ , width  $d_w$ ) and strongly adsorbing materials ( $\epsilon_{fs} > \epsilon_{ff}$ , width  $d_s$ ) (see Fig. 19), this was recently demonstrated in a sequence of papers in which the phase behavior of a “simple” fluid confined between such substrates was investigated in GCEMC simulations [77,79,166]. In these simulations the thermodynamic state was fixed corresponding to a Lennard–Jones gas of an average number density  $\rho_b^* \simeq 0.036$  [167]. To illustrate the peculiar phase behavior it is instructive to turn to the local density as the simplest quantitative measure of fluid structure in an inhomogeneous system. It is again a function of both  $x$  and  $z$  (see Sec. IV C) because of the symmetry of the chemically striped substrate (see Fig. 19).

In Fig. 20  $\rho(x, z)$  is plotted for three selected values of  $s_z$  and  $s_x^* = 12.0$ . For  $s_z^* = 7.2$  a stratified “liquid” bridges the gap between the strongly attractive portions of the opposite substrates [i.e., for  $|x^*| \leq 2.0$ , see Fig. 20(a)]. Because of the decay of the fluid–substrate interaction potential, stratification in the liquid bridge diminishes as  $z$  increases along lines of

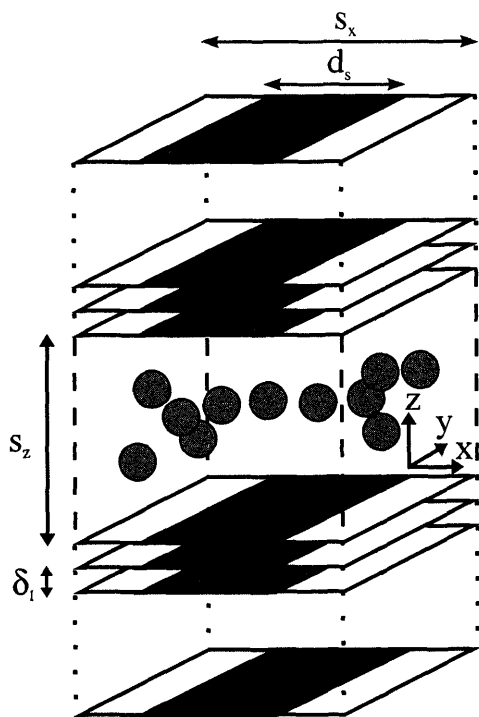


**FIG. 19** Scheme of a simple fluid confined by a chemically heterogeneous model pore. Fluid molecules (grey spheres) are spherically symmetric. Each substrate consists of a sequence of crystallographic planes separated by a distance  $\delta_i$  along the  $z$  axis. The surface planes of the two opposite substrates are separated by a distance  $s_z$ . Periodic boundary conditions are imposed in the  $x$  and  $y$  directions (see text) (from Ref. 77).

constant  $x$ . Stratification is absent over the weakly attractive portion of the substrate. Here an inhomogeneous gas-like phase exists, as indicated by the low value of  $\rho(x, z)$  and its weak dependence on  $x$  and  $z$  for  $|x^*| \gtrsim 4.0$ . For larger  $s_z^* = 7.5$  [see Fig. 20(b)], the structure of the fluid changes significantly. Over the strongly attractive portion of the substrate the fluid remains stratified. However, the gas-like phase has given way to an inhomogeneous liquid-like phase over the weakly attractive portion of the substrate. Consequently, the liquid–gas interface visible in Fig. 20(a) has disappeared in Fig. 20(b). Since the weak portions of the substrate are essentially repulsive,  $\rho(x, z)$  decreases for  $|x^*| \gtrsim 4.0$  from the center of the fluid ( $z = 0$ ) towards the substrate ( $|z| \rightarrow s_z/2$ ). If the distance between the substrates

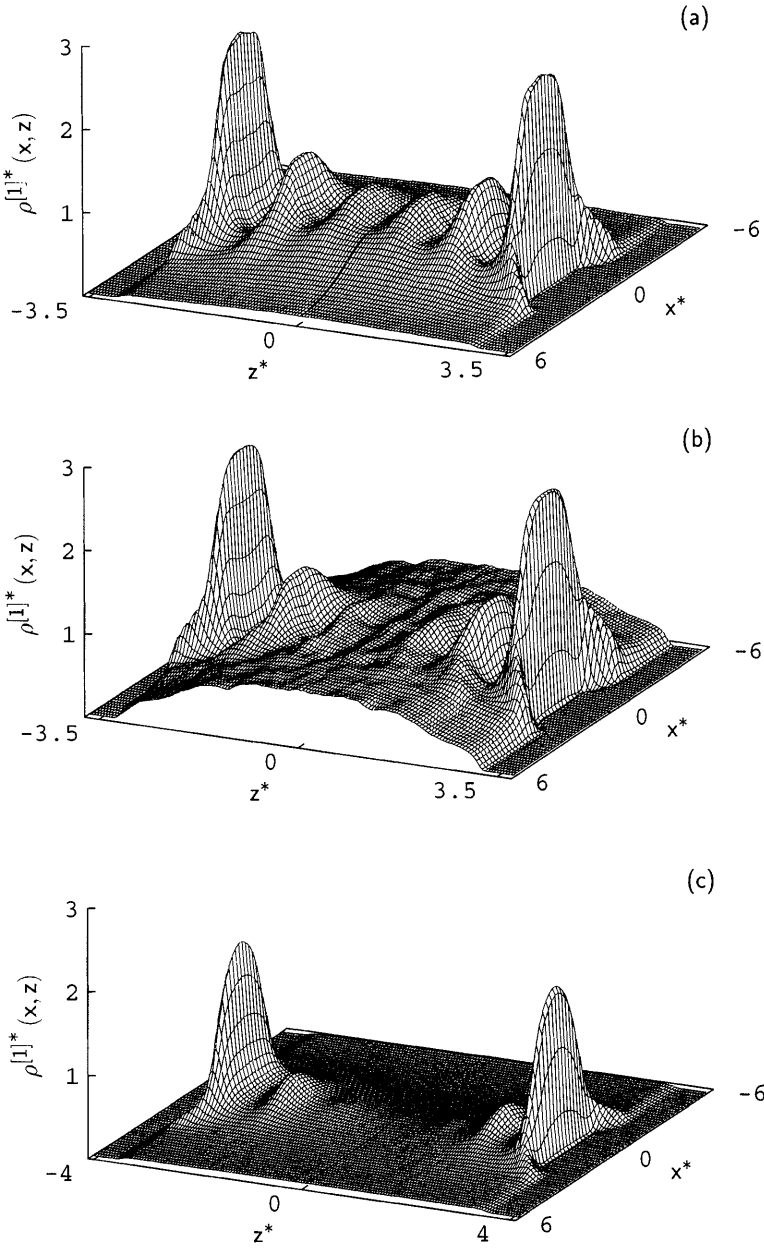


**FIG. 20** Local density  $\rho^{[1]}(x, z)$  as a function of position in the  $x$ - $z$  plane for  $s_x^* = 12.0$ . (a)  $s_z^* = 7.2$ , (b)  $s_z^* = 7.5$ , (c)  $s_z^* = 8.2$ .



is increased even further another significant structural change occurs in the fluid. It is illustrated by the plot of  $\rho(x, z)$  for  $s_z^* = 8.2$  in Fig. 20(c), where the fluid bridge has disappeared and only two strata of fluid molecules “cling” to the strongly attractive portion of the substrate. For example, for  $|z^*| \lesssim 3$  and  $x = 0$  the density is gas-like and decreases monotonically towards the center of the fluid at  $z = 0$ . The height of the two maxima of  $\rho(x, z)$  appears to be substantially reduced compared with the plots in Figs. 20(a) and 20(b). Thus, by increasing  $s_z$ , the liquid-like phase [see Fig. 20(b)] eventually evaporates leaving behind two inhomogeneous fluid columns (because of the translational invariance of the system in the  $y$  direction, see Fig. 19) that are stabilized by the strongly attractive portions of the opposite substrates. These columns are surrounded by a gas-like phase of low density as revealed by the plot in Fig. 20(c).

To illustrate the complexity of the phase behavior in a more compact way it is instructive to employ a mean-field lattice-gas model. The relative simplicity of the grand potential

$$\Omega[\rho(\mathbf{r})] = \mathcal{F}[\rho(\mathbf{r})] + \sum_{\mathbf{r}} [\Phi(\mathbf{r}; s_x, s_z) - \mu] \rho(\mathbf{r}) \quad (120)$$

permits one to determine the entire coexistence curve at the expense of only a fraction of the computer time required by the more complex model studied in the parallel GCEMC simulations [166,168,169]. Following earlier work [168–170], it suffices to employ the mean-field free-energy functional

$$\begin{aligned} \mathcal{F}[\rho(\mathbf{r})] = \sum_{\mathbf{r}} \Big\{ & k_B T [\rho(\mathbf{r}) \ln \rho(\mathbf{r}) + [1 - \rho(\mathbf{r})] \ln [1 - \rho(\mathbf{r})]] \\ & - \frac{\epsilon_{ff}}{2} \sum_{\mathbf{r}'}' \rho(\mathbf{r}) \rho(\mathbf{r}') \Big\} \end{aligned} \quad (121)$$

where  $\epsilon_{ff}$  determines the strength of the interaction between a molecule at site  $\mathbf{r}$  and its six nearest neighbors on a simple-cubic lattice. The interaction between a lattice-gas molecule and the chemically corrugated substrate is represented by  $\Phi(\mathbf{r}; s_x, s_z)$ . By analogy with the model depicted in Fig. 19 the substrate consists of alternating weakly and strongly attractive strips (see Fig. 21). A plot of the numerically determined coexistence curve (see Ref. 166 for details of the numerical procedure) for the bulk lattice gas (for which  $\Phi(\mathbf{r}; s_x, s_z) \equiv 0$ ) in Fig. 22(a) shows that  $T_{cb}^* = 3/2$  and  $\rho_{cb}^* = 1/2$ , as expected analytically [171]. Furthermore, as  $T \rightarrow T_{cb}^-$  the shape of the coexistence curve  $\Delta \rho_{\text{coex}}^g := \rho_{\text{coex}}^l - \rho_{\text{coex}}^g \propto (T_{cb} - T)^\beta$ , where  $\rho_{\text{coex}}^l$  and  $\rho_{\text{coex}}^g$  are the densities of coexisting bulk liquid and gas phases, respectively, and the critical exponent  $\beta = 1/2$  as it must for a mean-field theory [171]. Turning now to a mean-field lattice gas confined by chemically

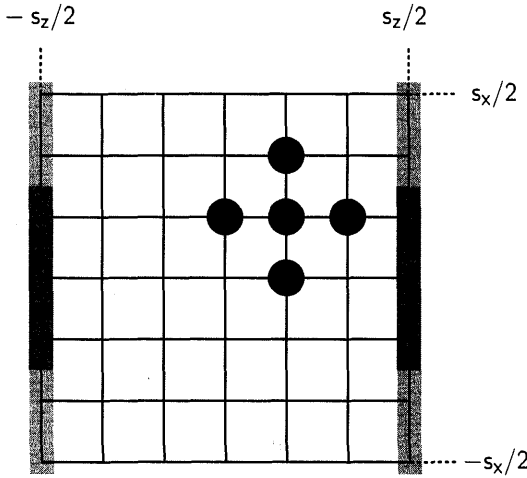


**FIG. 21** Scheme of the lattice-gas model of a fluid confined between chemically corrugated substrates in the  $x$ - $z$  plane. The coordinate system is centered at the point  $(0, 0)$  halfway between the substrates located at  $\pm s_z/2$ . Each module (black circle) interacts with its nearest neighbors. The two remaining nearest neighbors on the simple-cubic lattice located at lattice sites in the  $y$  direction perpendicular to the paper plane are not shown. Sites at which a lattice-gas molecule is subject to the substrate interaction  $\Phi(\mathbf{r}; s_x, s_z) = -\epsilon_{fs}$  are shaded in dark grey (strongly attractive substrate portions, width  $d_s$ ) whereas sites at which  $\Phi(\mathbf{r}; s_x, s_z) = -\epsilon_{fw}$  (weakly attractive substrate portions, width  $d_w$ ) are shaded in lighter grey. In the  $x$  direction periodic boundary conditions are applied (see text).

heterogeneous substrates, one realizes from the work of Röcken and Tarazona [168] that the phase diagram may exhibit a triple point at which (inhomogeneous) gas- and liquid-like phases coexist with liquid bridges. One also expects two critical points at which gas-like phases and liquid bridges and liquid bridges and liquid-like phases become indistinguishable. This situation is depicted in Figs. 22(a) and 22(b). Because, in Fig. 22(a),  $d_s^* = d_w^* = 8$  (in units of  $\ell$ ) and because  $\epsilon_{fs}^* = 0.8$  and  $\epsilon_{fw}^* = 0.2$  (in units of  $\epsilon_{ff}$ ), both critical temperatures are the same but significantly lower than  $T_{cb}$ . Compared with the bulk critical density  $\rho_{cb} = 1/2$ , the gas-bridge critical densities are shifted to lower ( $\rho_{cp}^{gb*} \approx 0.395$ ) and higher values ( $\rho_{cp}^{bl*} \approx 0.605$ ), respectively. With respect to  $\rho_{cb}$  this shift is symmetric because of the present choice of  $d_s$ ,  $d_w$ ,  $\epsilon_{fw}$ , and  $\epsilon_{fs}$  [see Fig. 22(a)] [168]. As expected, a triple point is observed at  $\rho_{tr}^* = 1/2$  and  $T_{tr}^* \approx 1.055$  below the critical temperatures  $T_{cp}^{gb*} = T_{cp}^{bl*} \approx 1.410$ . For different substrate parameters less symmetric curves obtain as the plot in Fig. 22(b) shows. Similar effects have been

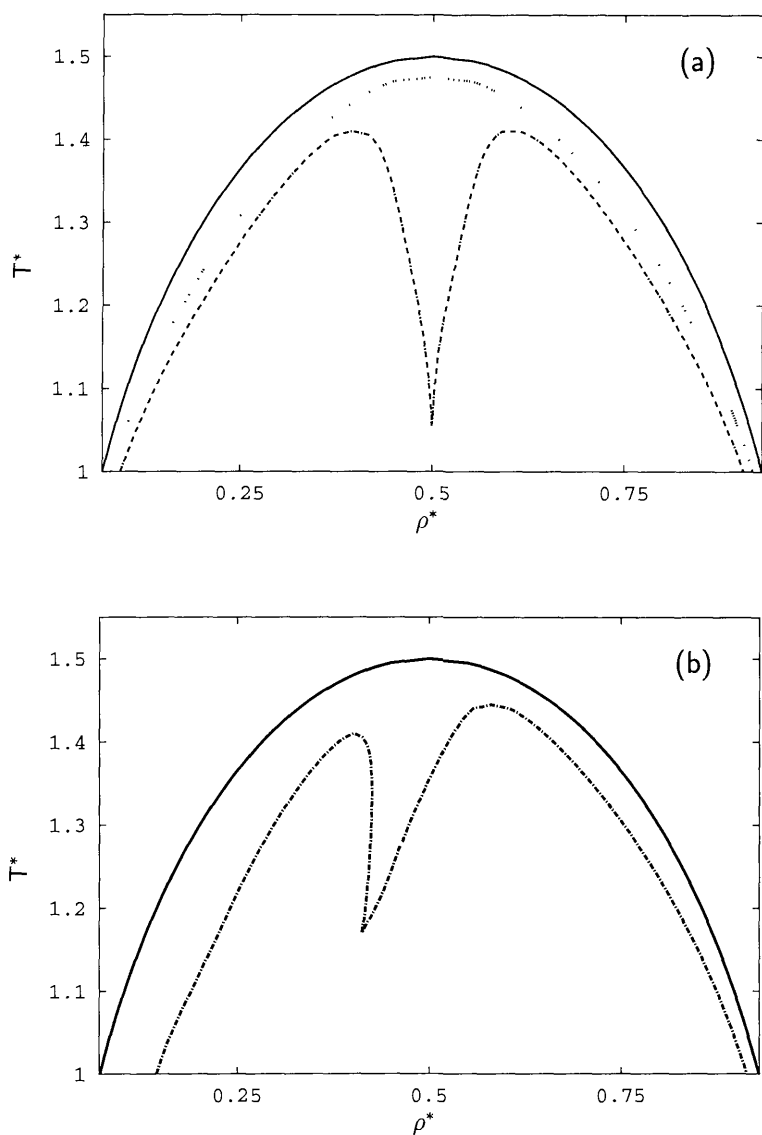


**FIG. 22** Coexistence curves for the lattice-gas model. (a) bulk (—); chemically corrugated substrate ( $n_v = 16$ ,  $c_r = 8/16$ ,  $\epsilon_{fs} = 0.8$ ,  $\epsilon_{fw} = 0.2$ )  $n_z = 15$  (- - -),  $n_z = 7$  (- · -). (b) Chemically corrugated substrate characterized by  $n_\lambda = 18$ ,  $n_z = 9$ ,  $c_r = 6/18$ ,  $\epsilon_{fs} = 1.4$ ,  $\epsilon_{fw} = 0.3$  (- · -); for comparison the bulk coexistence curve (—) is also shown. Chemical corrugation is cast quantitatively in terms of  $c_i := d_s/n_\lambda$ .

observed earlier by Röcken and Tarazona [168] who employed a different model substrate. For a lessened degree of confinement (i.e., as  $s_z$  increases) the chemical heterogeneity of the substrate becomes increasingly insignificant. This can be seen in Fig. 22(a) where the coexistence curve for an  $s_x/\ell \times s_z/\ell := n_x \times n_z = 16 \times 15$  lattice exhibits no triple point and only a single critical point  $T_{cp}^* \approx 1.475$  and  $\rho_{cp}^* = 1/2$  which is, however, still lower than  $T_{cb}^* = 3/2$  on account of the prevailing confinement effect.

The interaction of a simple fluid with a single chemically heterogeneous substrate has also been studied. Koch et al. consider a semiinfinite planar substrate with a sharp junction between weakly and strongly attractive portions and investigate the influence of this junction on the density profile of the fluid in front of the substrate [172–174]. Lenz and Lipowsky, on the other hand, are concerned with formation and morphology of micrometer droplets [175].

## ACKNOWLEDGMENTS

I dedicate this manuscript to my senior colleague and mentor, Professor Siegfried Hess, whose advice, support, and many expressions of personal sympathy have been of vital importance to my scientific work over the past years. Without him nothing would have been accomplished.

## REFERENCES

1. T. A. Core, W. K. Tsang, S. J. Sherman. Fabrication technology for an integrated surface-machined sensor. *Solid State Technol* 36:39–44, 1993.
2. J. B. Knight, A. Vishwanath, J. P. Brody, R. H. Austin. Hydrodynamic focussing on a silicon chip: mixing nanoliters in microseconds. *Phys Rev Lett* 80:3863–3866, 1998.
3. D. W. L. Tolfree. Microfabrication using synchrotron radiation. *Rep Prog Phys* 61:313–351, 1998.
4. B. Bhushan, J. N. Israelachvili, U. Landman. Nanotribology: friction, wear and lubrication at the atomic scale. *Nature (London)* 374:607–616, 1995.
5. B. Bhushan, ed. *Handbook of Micro-/Nanotribology*. New York: CRC Press, 1995.
6. J. Van Alsten, S. Granick. Molecular tribometry of ultrathin liquid films. *Phys Rev Lett* 61:2570–2573, 1988.
7. F. Burmeister, C. Schläfle, B. Keilhofer, C. Bechinger, J. Boneberg, P. Leiderer. From mesoscopic to nanoscopic surface structures: lithography with colloid monolayers. *Adv Mater* 10:495–497, 1998.
8. P. Bönsch, D. Wüllner, T. Schrimpf, A. Schlachletzki, R. Lacmann. Ultra-smooth V-grooves in InP by two-step chemical etching. *J Electrochem Soc* 145:1273–1276, 1998.

9. A. Kumar, G. M. Whitesides. Features of gold having micrometer to centimeter dimensions can be formed through a combination with an elastomeric stamp and an alkanethiol "ink" followed by chemical etching. *Appl Phys Lett* 63:2002–2004, 1993.
10. J. Drelich, J. D. Miller, A. Kumar, G. M. Whitesides. Wetting characteristics of drops at heterogeneous surfaces. *Colloids and Surfaces A* 93:1–13, 1994.
11. J. L. Wilbur, A. Kumar, E. Kim, G. M. Whitesides. Microfabrication by microcontact printing of self-assembled monolayers. *Adv Mater* 6:600–604, 1994.
12. R. J. Jackman, J. L. Wilbur, G. M. Whitesides. Fabrication of submicrometer features on curved substrates by microcontact printing. *Science* 269:664–666, 1995.
13. G. Binnig, C. F. Quate, C. Gerber. Atomic force microscope. *Phys Rev Lett* 56:930–933, 1986.
14. C. M. Mate, G. M. McClelland, R. Erlandsson, S. Chiang. Atomic-scale friction of a tungsten tip on a graphite surface. *Phys Rev Lett* 59:1942–1945, 1987.
15. R. Erlandsson, G. Hadzioannou, C. M. Mate, G. M. McClelland, S. Chiang. Atomic scale friction between the muscovite mica cleavage plane and a tungsten tip. *J Chem Phys* 89:5190–5193, 1989.
16. E. Meyer. Atomic force microscopy. *Prog Surf Sci* 41:3–49, 1992.
17. M. B. Salmeron. Use of the atomic force microscope to study mechanical properties of lubricant layers. *MRS Bull* 18:20–25, 1993.
18. D. Tabor, R. H. S. Winterton. The direct measurement of normal and retarded van der Waals forces. *Proc Roy Soc London, Ser A* 312:435–450, 1969.
19. J. N. Israelachvili, D. Tabor. The measurement of van der Waals dispersion forces in the range 1.5 to 130 nm. *Proc Roy Soc London, Ser A* 331:19–38, 1973.
20. J. N. Israelachvili, P. M. McGuiggan. Forces between surfaces in liquids. *Science* 241:795–800, 1989.
21. S. Granick. Motions and relaxations of confined liquids. *Science* 253:1374–1379, 1991.
22. G. Reiter, A. L. Demirel, J. Peanasky, L. L. Cai, S. Granick. Stick to slip transition and adhesion of lubricated surfaces in moving contact. *J Chem Phys* 101:2606–2615, 1994.
23. B. J. Alder, T. E. Wainwright. Studies in molecular dynamics. I. General method. *J Chem Phys* 31:459–466, 1959.
24. J. Lyklema. *Fundamentals of Interface and Colloid Science, Vol. I, Fundamentals*. London: Academic, 1991.
25. M. P. Allen, D. J. Tildesley. *Computer Simulation of Liquids*. Oxford: Clarendon, 1987.
26. M. Schoen. *Computer Simulation of Condensed Phases in Complex Geometries*. Heidelberg: Springer-Verlag, 1993.
27. J. N. Israelachvili. *Intermolecular and Surface Forces*. 2nd ed. London: Academic, 1992.

28. A. Tonck, J. M. Georges, J. L. Loubet. Measurements of intermolecular forces and the rheology of dodecane between alumina surfaces. *J Colloid Interface Sci* 126:150–163, 1988.
29. B. Derjaguin. Theorie über die Reibung und Adhäsion, IV. Theorie des Anhaftens kleiner Teilchen. *Kolloid-Z* 69:155, 1934.
30. M. L. Gee, P. M. McGuiggan, J. N. Israelachvili, A. M. Homola. Liquid to solidlike transitions of molecularly thin films under shear. *J Chem Phys* 93:1895–1906, 1990.
31. J. N. Israelachvili, P. M. McGuiggan, A. M. Homola. Dynamic properties of molecularly thin liquid films. *Science* 240:189–191, 1988.
32. J. Israelachvili, P. McGuiggan, M. Gee, A. Homola, M. Robbins, P. Thompson. Liquid dynamics in molecularly thin films. *J Phys: Condens Matter* 2:SA89–98, 1990.
33. M. Schoen, D. J. Diestler, J. H. Cushman. Fluids in micropores. I. Structure of a simple classical fluid in a slit-pore. *J Chem Phys* 87:5464–5476, 1987.
34. S. Asakura, F. Oosawa. On the interaction between bodies immersed in a solution of macromolecules. *J Chem Phys* 22:1255–1256, 1954.
35. W. B. Russell, D. A. Saville, W. R. Schowalter. *Colloidal Dispersions*. Cambridge: Cambridge University Press, 1989.
36. P. Attard, G. N. Patey. Hypernetted-chain closure with bridge diagrams. Asymmetric hard sphere mixtures. *J Chem Phys* 92:4970–4982, 1990.
37. P. Attard. Spherically inhomogeneous fluids. II. Hard-sphere solute in a hard-sphere solvent. *J Chem Phys* 91:3083–3089, 1989.
38. P. Attard, D. R. Bérard, C. P. Ursenbach, G. N. Patey. Interaction free energy between planar walls in dense fluids: an Ornstein–Zernike approach for hard-sphere, Lennard–Jones, and dipolar systems. *Phys Rev A* 44:8224–8234, 1991.
39. P. Attard, D. Wei, G. N. Patey, G. M. Torrie. The interaction between macroparticles in molecular fluids. *J Chem Phys* 93:7360–7368, 1990.
40. T. Biben, J.-P. Hansen. Phase separation of asymmetric binary hard-sphere fluids. *Phys Rev Lett* 66:2215–2218, 1991.
41. T. Biben, J. P. Hansen. Spinodal instability of suspensions of large spheres in a fluid of small spheres. *J Phys: Condens Matter* 3:F65–72, 1991.
42. B. Götzelmann, S. Dietrich. Density profiles and pair correlation functions of hard spheres in narrow slits. *Phys Rev E* 55:2993–3005, 1997.
43. B. Götzelmann, R. Evans, S. Dietrich. Depletion forces in fluids. *Phys Rev E* 57:6785–6800, 1998.
44. Y. Mao, M. E. Cates, H. Lekkerkerker. Depletion force in colloidal systems. *Physica A* 222:10–24, 1995.
45. M. Dijkstra, D. Frenkel. Evidence for entropy-driven demixing in hard-core fluids. *Phys Rev Lett* 72:298–300, 1994.
46. R. Dickman, P. Attard, V. Simonian. Entropic forces in binary hard sphere mixtures. *J Chem Phys* 107:205–213, 1997.
47. T. Biben, P. Bladon, D. Frenkel. Depletion effects in binary hard-sphere fluids. *J Phys: Condens Matter* 8:10799–10821, 1996.

48. M. Schoen, T. Gruhn, D. J. Diestler. Solvation forces in thin films between macroscopically curved substrates. *J Chem Phys* 109:301–311, 1998.
49. H. T. Davis. *Statistical Mechanics of Phases, Interfaces, and Thin Films*. New York: Wiley-VCH, 1996.
50. P. Attard, J. L. Parker. Oscillatory solvation forces: A comparison of theory and experiment. *J Phys Chem* 96:5086–5093, 1992.
51. J. Klein, E. Kumacheva. Simple liquids confined to molecularly thin layers. I. Confinement-induced liquid-to-solid phase transitions. *J Chem Phys* 108:6996–7009, 1998.
52. T. L. Hill. *Thermodynamics of Small Systems*. Minneola: Dover, 1994.
53. T. L. Hill. *Statistical Mechanics*. Minneola: Dover, 1987.
54. D. J. Diestler, M. Schoen, J. E. Curry, J. H. Cushman. Thermodynamics of a fluid confined to a slit pore with structured walls. *J Chem Phys* 100:9140–9146, 1994.
55. M. Schoen. On the uniqueness of stratification-induced structural transformations in confined films. *Ber Bunsenges Phys Chem* 100:1355–1362, 1996.
56. E. Schrödinger. *Statistical Thermodynamics*. New York: Dover, 1989.
57. D. A. McQuarrie. *Statistical Mechanics*. New York: Harper & Row, 1976.
58. P. Bordarier. Les forces de surface des systèmes nanolubrifiés. Simulations et théorie. PhD dissertation, Université de Paris-Sud, Paris, France, 1997.
59. P. Bordarier, B. Rousseau, A. Fuchs. Rheology of model confined ultrathin fluid films. I. Statistical mechanics of surface forces apparatus experiments. *J Chem Phys* 106:7295–7302, 1997.
60. K. Binder, D. W. Heermann. *Monte Carlo Simulation in Statistical Physics*. Heidelberg: Springer-Verlag, 1988, p. 1.
61. R. Haberlandt, S. Fritzsche, G. Peinel, K. Heinzinger. *Molekularodynamik*. Wiesbaden:Vieweg, 1995.
62. W. G. Hoover. *Molecular Dynamics*. Heidelberg: Springer-Verlag, 1986.
63. S. Hess. Constraints in molecular dynamics, nonequilibrium processes in fluids via computer simulations. In: K. H. Hoffmann, M. Schreiber, eds. *Computational Physics*. Heidelberg: Springer-Verlag, 1996, pp. 268–293.
64. D. P. Landau, M. Krech. Spin dynamics simulations of ferro- and antiferromagnetic model systems: comparison with theory and experiment. *J Phys: Condens Matter* 11:R175–R213, 1999.
65. D. J. Evans, G. P. Morriss. *Statistical Mechanics of Nonequilibrium Liquids*. London: Academic, 1990.
66. M. Schoen, D. J. Diestler, J. H. Cushman. Fluids in micropores. IV. The behavior of molecularly thin confined films in the grand isostress ensemble. *J Chem Phys* 100:7707–7717, 1994.
67. N. Metropolis, A. W. Rosenbluth, M. N. Rosenbluth, A. H. Teller, E. Teller. Equation of state calculations by fast computing machines. *J Chem Phys* 21:1087–1092, 1953.
68. W. W. Wood. Monte Carlo studies. In: H.N.V Temperley, G. S. Rushbrooke, J. S. Rowlinson, eds. *Physics of Simple Liquids*. Amsterdam: North Holland, 1968, pp. 116–230.

69. M. Schoen. Taylor-expansion Monte Carlo simulations of classical fluids in the canonical and grand canonical ensembles. *J Comput Phys* 118:159–171, 1995.
70. S. Blenk, W. Muschik. Orientational balances for nematic liquid crystals. *J Non-Equilib Thermodyn* 16:67–87, 1991.
71. S. Blenk, H. Ehrentraut, W. Muschik. Statistical foundation of macroscopic balances for liquid crystals in alignment tensor formulation. *Physica A* 174:119–138, 1991.
72. P. G. de Gennes, J. Prost. *The Physics of Liquid Crystals*. 2nd ed. Oxford: Clarendon, 1993, Chap. 1.3.1.
73. R. F. Cracknell, D. Nicholson, N. G. Parsonage, H. Evans. Rotational insertion bias: a novel method for simulating dense phases of structured particles, with particular application to water. *Mol Phys* 71:931–943, 1990.
74. R. Eppenga, D. Frenkel. Monte Carlo study of the isotropic and nematic phases of infinitely thin hard platelets. *Mol Phys* 52:1303–1334, 1984.
75. M. Schoen. Rheology and local structure of thin films confined between thermally corrugated walls. *Physica A* 240:328–339, 1997.
76. G. Arfken. *Mathematical Methods for Physicists*. London: Academic, 1985, p. 478.
77. M. Schoen, D. J. Diestler. Ultrathin fluid films confined to a chemically heterogeneous slit-shaped nanopore. *Phys Rev E* 56:4427–4440, 1997.
78. T. Gruhn, M. Schoen. Microscopic structure of molecularly thin confined liquid-crystal films. *Phys Rev E* 55:2861–2875, 1997.
79. M. Schoen, D. J. Diestler. Liquid-vapor phase equilibria in a chemically heterogeneous slit-nanopore. *Chem Phys Lett* 270:339–344, 1997.
80. I. K. Snook, W. van Megen. Solvation forces in simple dense fluids. *J Chem Phys* 72:2907–2913, 1980.
81. J. J. Magda, M. Tirrell, H. T. Davis. Molecular dynamics of narrow, liquid-filled pores. *J Chem Phys* 83:1888–1901, 1985.
82. P. Bordarier, B. Rousseau, A. H. Fuchs. Solvation forces and confinement-induced phase transitions of model ultrathin films. *Mol Simul* 17:199–215, 1996.
83. S. Toxvaerd. The structure and thermodynamics of a solid–fluid interface. *J Chem Phys* 74:1998–2005, 1981.
84. J. E. Lane, T. H. Spurling. Monte Carlo simulation of the effects of adsorption on interparticle forces. *Aust J Chem* 33:231–239, 1980.
85. A. Luzar, D. Bratko, L. Blum. Monte Carlo simulation of hydrophobic interaction. *J Chem Phys* 86:2955–2959, 1987.
86. R. Kjellander, S. Sarman. A study of anisotropic pair distribution theories for Lennard–Jones fluids in narrow slits. II. Pair correlations and solvation forces. *Mol Phys* 74:665–688, 1991.
87. D. Henderson, M. Lozada-Cassou. A simple theory for the force between spheres immersed in a fluid. *J Colloid Interface Sci* 114:180–183, 1986.
88. M. Lozada-Cassou, E. Diaz-Herrera. Three-point extension for hypernetted chain and other integral equation theories: numerical results. *J Chem Phys* 92:1194–1210, 1990.



89. S. Sarman. The influence of the fluid-wall interaction potential on the structure of a simple fluid in a narrow slit. *J Chem Phys* 92:4447–4455, 1990.
90. B. Götzelmann. Hartkugelflüssigkeiten in begrenzten Geometrien. PhD dissertation, Bergische Universität Wuppertal, Wuppertal, Germany, 1998.
91. I. K. Snook, D. Henderson. Monte Carlo study of a hard-sphere fluid near a hard wall. *J Chem Phys* 68:2134–2139, 1978.
92. V. Y. Antonchenko, V. V. Ilyin, N. N. Makovsky, A. N. Pavlov, V. P. Sokhan. On the nature of disjoining pressure oscillations in fluid films. *Mol Phys* 52:345–355, 1984.
93. R. Evans, J. R. Henderson, D. C. Hoyle, A. O. Parry, Z. A. Sabeur. Asymptotic decay of liquid structure: oscillatory liquid–vapour density profiles and the Fisher–Widom line. *Mol Phys* 80:755–775, 1993.
94. T. K. Vanderlick, H. T. Davis, J. K. Percus. The statistical mechanics of hard rod mixtures. *J Chem Phys* 91:7136–7145, 1989.
95. Z. Tang, L. E. Scriven, H. T. Davis. Size selectivity in adsorptions of poly-disperse hard-rod fluids in micropores. *J Chem Phys* 97:5732–5737, 1992.
96. H. T. Davis. Density distribution functions of confined Tonks–Takahashi fluids. *J Chem Phys* 93:4339–4344, 1990.
97. P. A. Monson. The properties of inhomogeneous square-well mixtures in one dimension. *Mol Phys* 70:401–423, 1990.
98. M. Iwamatsu. A molecular theory of solvation force oscillations in nonpolar liquids. *J Colloid Interface Sci* 204:374–388, 1998.
99. M. Krech. *The Casimir Effect in Critical Systems*. Singapore: World Scientific, 1994, Chap. 3.
100. J. G. Gay, B. J. Berne. Modification of the overlap potential to mimick a linear site–site potential. *J Chem Phys* 74:3316–3319, 1981.
101. T. Gruhn, M. Schoen. A grand canonical ensemble Monte Carlo study of confined planar and homeotropically anchored Gay–Berne films. *Mol Phys* 93: 681–692, 1998.
102. T. Gruhn, M. Schoen. Substrate-induced order in confined nematic liquid-crystal films. *J Chem Phys* 108:9124–9136, 1998.
103. M. K. Chalam, K. E. Gubbins, E. de Miguel, L. F. Rull. A molecular simulation of a liquid-crystal model: bulk and confined fluid. *Mol Sim* 7:357–385, 1991.
104. R. G. Horn, J. N. Israelachvili, E. Perez. Forces due to structure in a thin liquid crystal film. *J Physique* 42:39–52, 1981.
105. S. H. J. Idziak, C. R. Safinya, R. S. Hill, M. Ruths, H. E. Warriner, K. E. Kraiser, K. S. Liang, J. N. Israelachvili. The X-ray surface forces apparatus: structure of a thin smectic liquid crystal under confinement. *Science* 264:1915–1918, 1994.
106. S. H. J. Idziak, I. Koltover, J. N. Israelachvili, C. R. Safinya. Structure in a confined smectic liquid crystal with competing surface and sample elasticities. *Phys Rev Lett* 76:1477–1480, 1996.
107. M. Ruths, S. Steinberg, J. N. Israelachvili. Effects of confinement and shear on the properties of thin films of thermotropic liquid crystal. *Langmuir* 12, 6637–6650, 1996.

108. P. Kékicheff, H. K. Christenson. Forces measured in a swollen smectic lyotropic lamellar mesophase confined between solid surfaces. *Phys Rev Lett* 63:2823–2826, 1989.
109. P. Kékicheff, P. Richetti, H. K. Christenson. Structure and elastic properties of lamellar mesophases from direct force measurements. *Langmuir* 7:1874–1879, 1991.
110. P. Richetti, P. Kékicheff, P. Barois. Measurement of the layer compressibility modulus of a lamellar mesophase with a surface forces apparatus. *J Phys II* 5:1129–1154, 1995.
111. B. Bahadur, ed. *Liquid Crystals, Applications and Uses, Vol. 1*. Singapore: World Scientific, 1990.
112. J. Cognard. Lubrication with liquid crystals. In: G. Biresaw, ed. *Tribology and the Liquid-Crystalline State*. Washington, DC: American Chemical Society, 1990, pp. 1–47.
113. T. Gruhn. Substrate-induced order in molecularly thin confined liquid-crystalline films. PhD dissertation, Technische Universität Berlin, Berlin, Germany, 1998.
114. M. Schoen, D. J. Diestler, J. H. Cushman. Stratification-induced order–disorder phase transitions in molecular confined films. *J Chem Phys* 101:6865–6872, 1994.
115. D. Beaglehole. Finite thickness variation of the spreading coefficient in wetting phenomena. *J Phys Chem* 93:5900–5902, 1989.
116. S. Garoff, E. B. Sirota, S. K. Sinha, H. B. Stanley. The effects of substrate roughness on ultrathin water films. *J Chem Phys* 90:7505–7515, 1989.
117. I. M. Tidswell, T. A. Rabedeau, P. S. Pershan, S. D. Kosowsky. Complete wetting of a rough surface: an X-ray study. *Phys Rev Lett* 66:2108–2111, 1991.
118. P. S. Pershan. X-ray studies of the thickness and roughness of thin adsorbed fluid layers. *Ber Bunsenges Phys Chem* 98:372–375, 1994.
119. D. Andelman, J.-F. Joanny, M. O. Robbins. Complete wetting on rough surfaces: statics. *Europhys Lett* 7:731–736, 1988.
120. M. O. Robbins, D. Andelman, J.-F. Joanny. Thin liquid films on rough or heterogeneous solids. *Phys Rev A* 43:4344–4354, 1991.
121. J. L. Harden, D. Andelman. Thermal fluctuations of thin wetting films on disordered solids. *Langmuir* 8:2547–2551, 1992.
122. R. R. Netz, D. Andelman. Roughness-induced wetting. *Phys Rev E* 55:687–700, 1997.
123. P. Müller-Buschbaum, M. Tolan, W. Press, F. Brinkop, J. P. Kotthaus. Wetting of laterally structured surfaces. *Ber Bunsenges Phys Chem* 98:413–414, 1994.
124. M. Napiórkowski, W. Koch, S. Dietrich. Wedge wetting by van der Waals fluids. *Phys Rev A* 45:5760–5770, 1992.
125. J. A. Mann Jr, L. Romero, R. R. Rye, F. G. Yost. Flow of simple liquids down narrow V grooves. *Phys Rev E* 52:3967–3972, 1995.
126. R. R. Rye, F. G. Yost, J. A. Mann. Wetting kinetics in surface capillary grooves. *Langmuir* 12:4625–4627, 1996.

127. R. R. Rye, F. G. Yost, J. A. Mann. The flow of liquids in surface grooves. *Langmuir* 12:555–565, 1996.
128. B. F. Jones, E. Galan. *Reviews in Mineralogy, Vol. 19: Hydrous Phyllosilicates*. Chelsea: Bookcrafters, 1988.
129. J. E. Curry, F. Zhang, J. H. Cushman, M. Schoen, D. J. Diestler. Transiently coexisting nanophases in ultrathin films confined between corrugated walls. *J Chem Phys* 101:10824–10832, 1994.
130. M. Schoen, S. Dietrich. Structure of a hard-sphere fluid in hard wedges. *Phys Rev E* 56:499–510, 1997.
131. D. J. Courtemanche, F. van Swol. Wetting state of a crystal-fluid system of hard spheres. *Phys Rev Lett* 69:2078–2081, 1992.
132. D. Henderson, S. Sokolowski, D. Wasan. Structure of a hard-sphere fluid near a rough surface: a density-functional approach. *Phys Rev E* 57:5539–5543, 1998.
133. M. Schoen, S. Hess, D. J. Diestler. Rheological properties of confined thin films. *Phys Rev E* 2:2587–2602, 1995.
134. P. Bordarier, M. Schoen, A. H. Fuchs. Stick-slip transitions in confined films from an equilibrium perspective. *Phys Rev E* 57:1621–1635, 1998.
135. H. B. Callen. *Thermodynamics*. New York: Wiley, 1960.
136. J. H. Weiner. *Statistical Mechanics of Elasticity*. New York: Wiley, 1983.
137. B. N. J. Persson. Theory of friction and boundary lubrication. *Phys Rev B* 48:18140–18158, 1993.
138. P. A. Thompson, M. O. Robbins. Origin of stick-slip motion in boundary lubrication. *Science* 250:792–794, 1990.
139. P. A. Thompson, M. O. Robbins. Shear flow near solids: epitaxial order and flow boundary conditions. *Phys Rev A* 41:6830–6837, 1990.
140. M. Lupkowski, F. van Swol. Ultrathin films under shear. *J Chem Phys* 95:1995–1998, 1991.
141. P. A. Thompson, G. S. Grest, M. O. Robbins. Phase transitions and universal dynamics in confined films. *Phys Rev Lett* 68:3448–3451, 1992.
142. M. G. Rozman, M. Urbakh, J. Klafter. Stick-slip motion and force fluctuations in a driven two-wave potential. *Phys Rev Lett* 77:683–686, 1996.
143. M. G. Rozman, M. Urbakh, J. Klafter. Origin of stick-slip motion in a driven two-wave potential. *Phys Rev E* 54:6485–6494, 1996.
144. M. Schoen, C. L. Rhykerd Jr, D. J. Diestler, J. H. Cushman. Shear forces in molecularly thin films. *Science* 245:1223–1225, 1989.
145. M. Schoen, D. J. Diestler, J. H. Cushman. Shear melting of confined monolayer films. *Phys Rev B* 47:5603–5613, 1993.
146. D. J. Diestler, M. Schoen, J. H. Cushman. On the thermodynamic stability of confined films under shear. *Science* 262:545–547, 1993.
147. M. Schoen. Computer simulations of the rheological behavior of confined films. *Mol Simul* 17:369–419, 1996.
148. P. Bordarier, B. Rousseau, A. H. Fuchs. A model for the static friction behavior of nanolubricated contacts. *Thin Solid Films* 330:21–26, 1998.

149. M. Thommes, G. H. Findenegg. Pore condensation and critical-point shift of a fluid in controlled-pore glass. *Langmuir* 10:4270–4277, 1994.
150. M. Thommes, G. H. Findenegg, M. Schoen. Critical depletion of a pure fluid in controlled-pore glass. Experimental results and grand canonical ensemble Monte Carlo simulation. *Langmuir* 11:2137–2142, 1995.
151. G. V. Burgess, D. H. Everett, S. Nutall. Adsorption hysteresis in porous materials. *Pure Appl Chem* 61:1845–1852, 1989.
152. A. de Keizer, T. Michalski, G. H. Findenegg. Fluids in pores: experimental and computer simulation studies of multilayer adsorption, pore condensation and critical point shifts. *Pure Appl Chem* 63:1495–1502, 1991.
153. W. D. Machin. Temperature of hysteresis and the pore size distributions of two mesoporous adsorbents. *Langmuir* 10:1235–1240, 1994.
154. A. P. Y. Wong, S. B. Kim, W. I. Goldburg, M. H. W. Chan. Phase separation, density fluctuations, and critical dynamics of  $N_2$  in aerogel. *Phys Rev Lett* 70:954–957, 1993.
155. A. P. Y. Wong, M. H. W. Chan. Liquid–vapor critical point of  $^4\text{He}$  in aerogel. *Phys Rev Lett* 65:2567–2570, 1990.
156. R. Evans. Microscopic theories of simple fluids and their interfaces. In: J. Charvolin, J. F. Joanny, J. Zinn-Justin, eds. *Liquids at Interfaces*. Amsterdam: North-Holland, 1990, pp. 4–98.
157. M. Schoen, D. J. Diestler. Analytical treatment of a simple fluid adsorbed in a slit-pore. *J Chem Phys* 109:5596–5605, 1998.
158. R. Evans. Fluids adsorbed in narrow pores: phase equilibria and structure. *J Phys: Condens Matter* 2:8989–9007, 1990.
159. H. Nakanishi, M. E. Fisher. Critical point shift in films. *J Chem Phys* 78:3279–3293, 1983.
160. M. E. Fisher, H. J. Nakanishi. Scaling theory for the criticality of fluids between plates. *J Chem Phys* 75:5857–5863, 1981.
161. R. Evans, U. Marini Bettolo Marconi, P. Tarazona. Capillary condensation and adsorption in cylindrical and slit-like pores. *J Chem Soc Faraday Trans 2* 82:1763–1787, 1986.
162. P. Tarazona, U. Marini Bettolo Marconi, R. Evans. Phase equilibria of fluid interfaces and confined fluids. Non-local versus local density functionals. *Mol. Phys* 60:573–595, 1987.
163. Y. K. Tovbin, E. V. Votyakov. Adsorption in pores with heterogeneous surfaces. *Langmuir* 9:2652–2660, 1993.
164. T. Michalski. Physisorptionsuntersuchungen von Fluiden in mesoporösen  $\text{SiO}_2$ -Materialien: Mehrschichtadsorption, Porenkondensation, Hystereseverhalten und porenkritischer Punkt. PhD dissertation, Ruhr-Universität Bochum, Bochum, Germany, 1995.
165. S. Groß. Untersuchungen zur Porenkondensation und zum Zustandsverhalten reiner Fluide in mesoporösen  $\text{SiO}_2$ -Materialien. PhD dissertation, Technische Universität Berlin, Berlin, 1997.
166. H. Bock, M. Schoen. Phase behavior of a simple fluid confined between chemically corrugated substrates. *Phys Rev E* 59:4122–4136, 1999.

167. V. P. Gregory, J. C. Schug. NPT Monte Carlo calculation of isotherms for the Lennard-Jones fluid. *Mol Phys* 82:677–688, 1994.
168. P. Röcken, P. Tarazona. Capillary condensation in structured pores. *J Chem Phys* 105:2034–2043, 1996.
169. P. Röcken, A. Somoza, P. Tarazona, G. H. Findenegg. Two-stage capillary condensation in pores with structured walls: a non-local density functional study. *J Chem Phys* 108:8689–8697, 1998.
170. P. Röcken. Capillary condensation of simple fluids in chemically structured slit-pores: from statistical-mechanical calculations to a thermodynamic theory. PhD dissertation, Technische Universität Berlin, Berlin, 1998.
171. R. J. Baxter. *Exactly Solved Models in Statistical Physics*. London: Academic, 1991.
172. W. Koch. Benetzung heterogener Substrate. PhD dissertation, Bergische Universität Wuppertal, Wuppertal, 1993.
173. W. Koch, S. Dietrich, M. Napiórkowski. Morphology and line tension of liquid films adsorbed on chemically structured substrates. *Phys Rev E* 51:3300–3317, 1995.
174. S. Dietrich. Fluids in contact with structured substrates. In: C. Caccamo ed. *Proceedings of the NATO-ASI "New approaches to old and new problems in liquid state theory—inhomogeneities and phase separation in simple, complex, and quantum fluids."* Dordrecht: Kluwer, 1999.
175. P. Lenz, R. Lipowsky. Morphological transitions of wetting layers on structured substrates. *Phys Rev Lett* 80:1920–1923, 1998.

# 2

## Quantum Effects in Adsorption at Surfaces

**PETER NIELABA** Department of Physics, University of Konstanz,  
Konstanz, Germany

I. Introduction	78
II. Experimental Situation	78
A. Phase transitions in adsorbed layers	78
B. Quantum effects	80
C. Examples (He, H <sub>2</sub> , D <sub>2</sub> , N <sub>2</sub> , CO on graphite)	81
III. Models and Surface Potentials	82
A. Methods for computing potentials	82
B. Example (graphite)	83
IV. Monte Carlo Simulations	84
A. Finite size scaling at phase transitions	84
B. Phase Diagrams of 2D systems with repulsive interactions	85
C. Model alloys with elastic interaction	88
D. Path integral Monte Carlo	91
V. Path Integral Monte Carlo—Analysis of Quantum Effects in Adsorbed layers	97
A. Phase transitions in quantum 2D fluids	98
B. Phase transitions in layers of H <sub>2</sub> and D <sub>2</sub> on graphite	107
C. Orientational phase transitions in adsorbed monolayers	110
VI. Conclusions	123
References	123

## I. INTRODUCTION

In modern materials science topics of high interest are surface structures on small (nanometer-length) scales and phase transitions in adsorbed surface layers. Many interesting effects appear at low temperatures, where quantum effects are important, which have to be taken into account in theoretical analyses. In this review a progress report is given on the “state of the art” of (quantum) simulations of adsorbed molecular layers.

Phase transitions in two-dimensional layers often have very interesting and surprising features. The phase diagram of the multicomponent Widom–Rowlinson model with purely repulsive interactions contains a nontrivial phase where only one of the sublattices is preferentially occupied. Fluids and molecules adsorbed on substrate surfaces often have phase transitions at low temperatures where quantum effects have to be considered. Examples are molecular layers of  $H_2$ ,  $D_2$ ,  $N_2$  and CO molecules on graphite substrates. We review the path integral Monte Carlo (PIMC) approach to such phenomena, clarify certain experimentally observed “anomalies” in  $H_2$  and  $D_2$  layers, and give predictions for the order of the  $N_2$  “herringbone” transition. Dynamical quantum phenomena in fluids are analyzed via PIMC as well. Comparisons with the results of approximate analytical theories demonstrate the importance of the PIMC approach to phase transitions where quantum effects play a role.

The computation of quantum many-body effects requires additional effort compared to classical cases. This holds in particular if strong collective phenomena such as phase transitions are considered. The path integral approach to critical phenomena allows the computation of collective phenomena at constant temperature—a condition which is preferred experimentally. Due to the link of path integrals to the partition function in statistical physics, methods from the latter—such as Monte Carlo simulation techniques—can be used for efficient computation of quantum effects.

In Sec. II we briefly review the experimental situation in surface adsorption phenomena with particular emphasis on quantum effects. In Section III models for the computation of interaction potentials and examples are considered. In Section IV we summarize the basic formulae for path integral Monte Carlo and finite size scaling for critical phenomena. In Section V we consider in detail examples for phase transitions and quantum effects in adsorbed layers. In Section VI we summarize.

## II. EXPERIMENTAL SITUATION

### A. Phase Transitions in Adsorbed Layers

Specific heat measurements [1] of  $^4\text{He}$  layers on  $\text{Fe}_2\text{O}_3$  have shown the dependency of the onset of superfluidity on the width of the film thickness.

Further studies [2,3] showed that the first layers may be regarded as solid layers. The influence of the substrate potential on the stability of these layers has been identified and analyzed in additional studies [4]. About 1970, exfoliated graphite became available as substrate material with good surface properties which made it possible to determine different two-dimensional phases, in particular that of adsorbed Kr on graphite [5] and of adsorbed  $^4\text{He}$  and  $^3\text{He}$  layers [6,7]. Two different phases were found, the  $\sqrt{3} \times \sqrt{3}$ -phase at a coverage where every third place is occupied and which is *commensurate* with the graphite substrate (see Fig. 1), and an (*incommensurate*) phase at higher coverages. The theoretical analysis of the phase transition between these phases by lattice gas models [8–12] revealed that the commensurate–incommensurate transition in He on graphite belongs to the three-state Potts universality class.

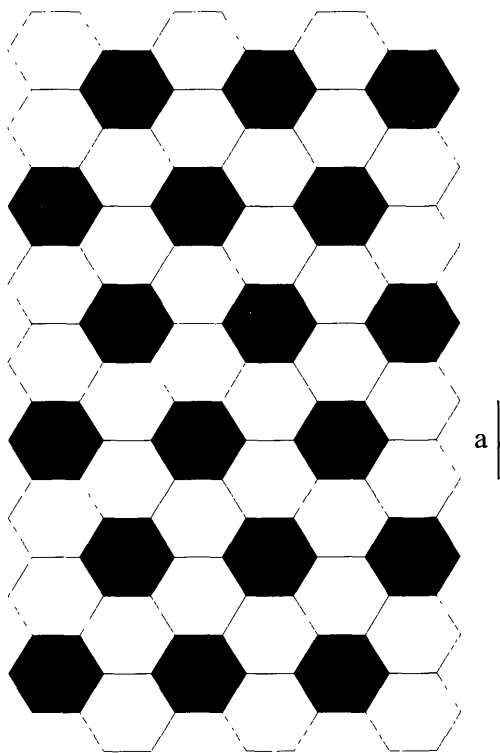


**FIG. 1** Schematic picture of the graphite surface (C atoms occupy the corners, periodic boundary conditions apply in  $x$  and  $y$  directions); the adsorption sites in the  $\sqrt{3} \times \sqrt{3}$  structure are shaded.



In the last decade two-dimensional (2D) layers at surfaces have become an interesting field of research [13–27]. Many experimental studies of molecular adsorption have been done on metals [28–40], graphite [41–46], and other substrates [47–58]. The adsorbate particles experience intermolecular forces as well as forces due to the surface. The structure of the adsorbate is determined by the interplay of these forces as well as by the coverage (density of the adsorbate) and the temperature and pressure of the system. In consequence a variety of superstructures on the surfaces have been found experimentally [47–58], a typical example being the  $\sqrt{3} \times \sqrt{3}$ - structure of adsorbates on a graphite structure (see Fig. 1).

In this review we consider several systems in detail, ranging from idealized models for adsorbates with purely repulsive interactions to the adsorption of spherical particles (noble gases) and/or (nearly) ellipsoidal molecules ( $\text{N}_2$ ,  $\text{CO}$ ). Of particular interest are the stable phases in monolayers and the phase transitions between these phases when the coverage and temperature in the system are varied. Most of the phase transitions in these systems occur at fairly low temperatures, and for many aspects of the behavior quantum effects need to be considered. For several other theoretical studies of adsorbed layer phenomena see Refs. 59–89.

## B. Quantum Effects

Many interesting quantum effects appear at low temperatures due to the effect of quantum statistics. Very interesting PIMC studies of such effects have been done for structural phase transitions in adsorbed  $^4\text{He}$  and  $^3\text{He}$  layers [90–91] and for the superfluidity of  $\text{H}_2$  layers [92]. For studies of related systems and additional information see Sec. IVD 2.

Of the variety of quantum effects which are present at low temperatures we focus here mainly on *delocalization* effects due to the position–momentum uncertainty principle. Compared to purely classical systems, the quantum delocalization introduces fluctuations in addition to the thermal fluctuations. This may result in a decrease of phase transition temperatures as compared to a purely classical system under otherwise unchanged conditions. The ground state order may decrease as well. From the experimental point of view it is rather difficult to extract the amount of “quantumness” of the system. The delocalization can become so pronounced that certain phases are stable in contrast to the case in classical systems. We analyze these effects in Sec. V, in particular the phase transitions in adsorbed  $\text{N}_2$ ,  $\text{H}_2$  and  $\text{D}_2$  layers.

### C. Examples (He, H<sub>2</sub>, D<sub>2</sub>, N<sub>2</sub>, CO on Graphite)

For many years, adsorbed layers of N<sub>2</sub> on graphite have served constantly as a prototype example to study phase transitions in two dimensions. The phase diagram [93], includes, below 50 K, a registered phase having a commensurate  $(\sqrt{3} \times \sqrt{3})R30^\circ$  structure. The orientations of the molecular axes undergo in this phase an *orientational* phase transition quite independent from coverage (below a coverage of 1.2) at around 27 K to the “2-in” herringbone phase, keeping the translationally ordered  $\sqrt{3}$  structure of the molecular centers of mass; for an overview of the experimental and theoretical literature see Refs. 94–96. Stimulated by a controversial discussion on the order of the transition (for an overview see Ref. 94), the herringbone phase transition of N<sub>2</sub> in the  $(\sqrt{3} \times \sqrt{3})R30^\circ$  commensurate phase on graphite has been investigated [94] by large-scale Monte Carlo simulations using the anisotropic planar-rotor model. We discuss these and related studies in Sec. V. For related studies on CO layers adsorbed on graphite see Refs. 97, 98; for investigations on the random field induced rounding of the Ising-type transition in physisorbed (CO)<sub>1-x</sub>(N<sub>2</sub>)<sub>x</sub> mixtures see Refs. 99–103.

Nielsen et al. [104] studied H<sub>2</sub> and D<sub>2</sub> layers adsorbed on graphite by neutron diffraction techniques. Wiechert et al. [105–109] showed that the adsorbates of molecular hydrogen isotopes, H<sub>2</sub>, HD and D<sub>2</sub>, are model systems for the study of phases and phase transitions in two-dimensional condensed quantum systems. Besides the commensurate and incommensurate phases, which have been found in He films as well, reentrant fluid phases and phases with large supercells are present in the phase diagram. The layer growth has been analyzed as well. At low temperatures and coverages below the  $\sqrt{3} \times \sqrt{3}$ -monolayer coverage  $\rho_{\sqrt{3}}$  Freimuth and Wiechert [107] found phase coexistence of a gas phase with a  $\sqrt{3} \times \sqrt{3}$ -ordered phase. The coexistence region ends in a tricritical point at a temperature  $T_{\text{tri}}$ , with  $T_{\text{tri}}(\text{H}_2) < T_{\text{tri}}(\text{D}_2)$ . Above  $T_{\text{tri}}$  the phase transition from the ordered to the disordered phase is of second order and the transition temperature  $T_c$  increases with the coverage. An “anomalous” effect was found at a full  $\sqrt{3} \times \sqrt{3}$ -monolayer coverage  $\rho = \rho_{\sqrt{3}}$ : the critical temperature for the disordering transition  $T_c(\text{D}_2)$  for the D<sub>2</sub> system is smaller than for the H<sub>2</sub> system, with  $T_c(\text{H}_2) - T_c(\text{D}_2) \approx 2.5$  K. Usually one would expect a lower transition temperature for the system with the lighter particles. In order to analyze the observed “anomaly”, PIMC simulations for both systems have been done [15,16,110]; we come back to these in Sec. V.

Phase diagrams of adsorbed He particles show interesting features which have many similarities to the phase diagrams of adsorbed hydrogen systems.

For the PIMC study of quantum statistics effects in He systems and additional references see Refs. 90, 91.

### III. MODELS AND SURFACE POTENTIALS

#### A. Methods for Computing Potentials

The computation of equilibrium structures and phases of the system with several thousand atoms and all its electrons is still a problem which is far beyond tractability by present-day computers. Thus good approximative schemes or parameterizations of interaction potentials are important.

In 1985 Car and Parrinello invented a method [111–113] in which molecular dynamics (MD) methods are combined with first-principles computations such that the interatomic forces due to the electronic degrees of freedom are computed by density functional theory [114–116] and the statistical properties by the MD method. This method and related *ab initio* simulations have been successfully applied to carbon [117], silicon [118–120], copper [121], surface reconstruction [122–128], atomic clusters [129–133], molecular crystals [134], the epitaxial growth of metals [135–140], and many other systems; for a review see Ref. 113.

Despite the successes of this method in describing surface and bulk phenomena, in many problems involving the thermodynamics of large systems and/or phase transitions the computation or parameterization of interaction potentials is desirable. Due to the small ratio of the electron and proton masses (about 1/1800), in many condensed matter phenomena the electron can follow the motion of the atomic nuclei instantaneously (Born–Oppenheimer approximation). The resulting effective potentials between the atoms consist of short-range repulsive (overlap) interactions and more or less strong attractive Van der Waals interactions due to electronic correlation effects. The interaction may consist of a pair interaction, as for many atomic liquids, and of  $N$ -body interactions ( $N > 2$ ), as in the case of silicon, where three body terms in the interaction potential [141] turn out to be important for structural stability. In many cases the parameters of the interaction potentials are obtained by fitting certain system properties to experimental data. It would of course be convenient to adjust reliable interaction potentials microscopically, for example by fitting the free parameters to results obtained by the Car–Parrinello method or a related method. In many cases, however, the choice of the Lennard–Jones pair interaction is sufficiently good to describe the system properties; for an overview over other potentials see Ref. 142.

The simplest choice for the interaction potentials between the particles (at distance  $r$ ) is the assumption of Lennard–Jones pair potentials,

$$V(r) = 4\epsilon \left( \left( \frac{\sigma}{r} \right)^{12} - \left( \frac{\sigma}{r} \right)^6 \right) \quad (1)$$

In the examples discussed in the sections below the interaction parameters are given by:  $\epsilon_{\text{Ar–Ar}} = 121 k_B \text{K}$ ,  $\sigma_{\text{Ar–Ar}} = 3.40 \text{ \AA}$ ,  $\epsilon_{\text{N–N}} = 37.3 k_B \text{K}$ ,  $\sigma_{\text{N–N}} = 3.31 \text{ \AA}$ , the radius of the  $\text{N}_2$  molecule is  $0.545 \text{ \AA}$ . In the PIMC simulations interactions up to the fourth neighbor shell were taken into account, the next neighbor shells (5–20) have been treated in a static lattice approximation, the rest in a continuum static approximation.

In some studies of pure  $\text{N}_2$  solids more realistic potentials have been used by considering electrostatic interaction in addition. The electrostatic interaction sites are positive charges of  $q_1 = q_2 = 0.373e$  at distances  $\pm 1.044 \text{ \AA}$  away from the molecular center-of-mass on the molecular symmetry axis and negative charges  $q_3 = q_4 = -0.373e$  at distances  $\pm 0.874 \text{ \AA}$  respectively [143–145].

## B. Example (Graphite)

A parameterization of many different surface potentials, ranging from (100) surfaces of FCC crystals to graphite surfaces, has been given by Steele [146–148]. Since most of the systems discussed below are adsorbed layers on graphite surfaces, we consider the graphite substrate in detail. The interaction potential  $V_{\text{surf}}$  between an adsorbate particle at the position  $\mathbf{r} = (x, y, z)$  and all other substrate particles consists of two contributions,

$$V_{\text{surf}}(x, y, z) = E_0(z) + E_1(z)f_1(x, y) \quad (2)$$

$E_0(z)$  is a laterally averaged contribution, which has only a  $z$  dependence ( $z$  is the distance from the surface).  $E_1(z)f_1(x, y)$  depends on the position parallel to the surface,

$$f_1(x, y) = -2 \left\{ \cos \frac{2\pi}{a} \left( x + \frac{y}{\sqrt{3}} \right) + \cos \frac{2\pi}{a} \left( x - \frac{y}{\sqrt{3}} \right) + \cos \frac{4\pi}{a} \left( \frac{y}{\sqrt{3}} \right) \right\} \quad (3)$$

$$E_1(z) = \frac{2\pi\epsilon_{\text{PS}}\sigma_{\text{PS}}^6}{a_s} \left\{ \frac{\sigma_{\text{PS}}^6}{30} \left( \frac{g_1}{2z} \right)^5 K_5(g_1 z) - 2 \left( \frac{g_1}{2z} \right)^2 K_2(g_1 z) \right\} \quad (4)$$

where  $g_1 = 4\pi/a\sqrt{3}$ ,  $a_s = 5.24 \text{ \AA}$ ,  $\epsilon_{\text{PS}}$  is the interaction energy of a particle with the surface and  $\sigma_{\text{PS}}$  is the diameter in the particle–surface interaction,  $K_n$  is the modified Bessel function of kind  $n$ , and  $a = 2.456 \text{ \AA}$  is the graphite lattice constant.

## IV. MONTE CARLO SIMULATIONS

The computer simulation of models for condensed matter systems has become an important investigative tool in both fundamental and engineering research [149–153]; for reviews on MC studies of surface phenomena see Refs. 154, 155. For the realistic modeling of real materials at low temperatures it is essential to take quantum degrees of freedom into account. Although much progress has been achieved on this topic [156–166], computer simulation of quantum systems still lags behind the development in the field of classical systems. This holds particularly for the determination of dynamical information, which was not possible until recently [167–176].

### A. Finite Size Scaling at Phase Transitions

A fingerprint of a continuous phase transition is the divergence of the correlation length  $\xi$  at the critical temperature  $T_c$ , with  $\xi \propto |t|^{-\nu}$  for  $t := 1 - T/T_c$ ,  $|t| \ll 1$ . Under these conditions, on the reduced distance from the phase transition  $t \geq 0$ , the order parameter  $\Phi$  in the infinitely large system depends on  $t$  as  $\Phi \propto |t|^\beta$ , where  $\nu$  and  $\beta$  denote here the usual critical exponents. In finite systems [177,178] of linear dimension  $L$  the order parameter is given by the expression [179]

$$\langle \Phi \rangle_L = L^{-\beta/\nu} \tilde{\Phi}(L/\xi) \quad (5)$$

where  $\tilde{\Phi}$  is the scaling function that is associated to  $\Phi$ . The order parameter distribution function  $P_L(\Phi)$  in the finite system is thus a function of the scaling variables  $L^{\beta/\nu} \Phi$  and  $L/\xi$ ,

$$P_L(\Phi) = L^{\beta/\nu} \tilde{P}(L^{\beta/\nu} \Phi, L/\xi) \quad (6)$$

and the  $k$ th moment of the order parameter distribution function is given by

$$\langle \Phi^k \rangle_L = L^{\beta/\nu} \int d\Phi \Phi^k \tilde{P}(L^{\beta/\nu} \Phi, L/\xi) = L^{-\beta k/\nu} \tilde{\Phi}_k(L/\xi) \quad (7)$$

where the symbols  $\langle \rangle_L$  denote canonical averages with systems of linear dimension  $L$ .

#### 1. Cumulant Analysis

A very useful quantity for the determination of a critical point which is directly based on order parameter moments is the fourth-order cumulant [179–181]  $U_L^{(4)}$  or the second-order cumulant [182,183]  $U_L^{(2)}$ ,

defined as

$$U_L^{(4)} = 1 - \frac{\langle \Phi^4 \rangle_L}{3 \langle \Phi^2 \rangle_L^2} \quad (8)$$

$$U_L^{(2)} = 1 - \frac{\langle \Phi^2 \rangle_L}{3 \langle \Phi \rangle_L^2} \quad (9)$$

where one can see that the explicit dependence on system size drops out if the  $k$ th moments  $\propto L^{-\beta k/\nu}$  are re-expressed with the aid of Eq. (7) in terms of their scaling functions. We compile here only the main features and usage of these quantities, and refer for further details to the literature [179–181].

In the case of second-order transitions, the cumulants adopt a non-trivial universal value  $U^*$  (for given shape, boundary condition and algorithm) at the critical point, irrespective of system sizes  $\{L\}$  in the scaling limit. Thus, plotting  $U_L^{(4)}(T)$  or  $U_L^{(2)}(T)$  for different linear dimensions as a function of temperature yields an intersection point  $U(T_c) =: U^*$  which gives an accurate estimate of the critical temperature in the *infinite* system for a temperature-driven second-order transition. Below and above the transition, the cumulants flow to trivial limiting values depending on the definition of the order parameter; the larger the system, the faster the convergence. Instead of the temperature, other parameterizations of approaching a critical point can also be chosen. More recently, it was worked out that the concept of order parameter cumulant crossings is also useful in analyzing first-order phase transitions [184]. In this case, one can observe an *effective* crossing point at a non-universal value  $U^*$  at the phase transition. The approach of both the transition point and the value of  $U$  at the transition to the infinite system limit is quite fast: the correction depends, roughly speaking, on the inverse volume of the system [184]. Thus, for practical numerical purposes the order parameter cumulant can be taken as acquiring an intersection point at a first-order transition in a way similar to that occurring at a second-order transition.

## B. Phase Diagrams of 2D Systems with Repulsive Interactions

In this section we study a system with purely repulsive interactions which demonstrates the importance of entropy effects on the stability of phases when the effect of the corrugation potential due to the structured surface is completely neglected. The phase diagrams are determined by finite size scaling methods, in particular the methods of Sec. IV A.

### 1. Multicomponent Widom–Rowlinson Models

In 1970 Widom and Rowlinson (WR) introduced an ingeniously simple model for the study of phase transitions in fluids [185]. It consists of two species of particles,  $A$  and  $B$ , in which the only interaction is a hard core between particles of unlike species; i.e., the pair potential  $v_{\alpha\beta}(r)$  is infinite if  $\alpha \neq \beta$  and  $r < R_{AB}$ , and is zero otherwise. WR assumed an  $A$ – $B$  demixing phase transition to occur in dimensions  $D \geq 2$  when the fugacity  $z_A = z_B = z$  is large. Proofs of the existence of the demixing transition are given in the literature [186–188].

The lattice version of the multicomponent WR model—hard core exclusion between particles of different species on nearest neighbor sites of a simple hypercubic lattice in  $D$  dimensions is much easier to handle rigorously. A rather surprising result was found by Runnels and Lebowitz [189]. They proved that when the number of components  $M$  is larger than some minimum  $M_0$  then the transition from the gas phase at small values of  $z$  to the demixed phase at large values of  $z$  does not take place directly. Rather there is, at intermediate values of  $z$ ,  $z_c < z < z_d$ , an ordered phase (“crystal phase”) in which one of the sublattices (even or odd) is preferentially occupied. The origin of spontaneous symmetry breaking, leading to the ordered phase, is purely entropic. For  $z$  fixed,  $M$  large enough it “pays” for the system to occupy just one sublattice without any constraint; there being no interaction between particles on the same sublattice, each site can be occupied independently by a particle of any species; i.e., there are  $M$  independent choices at each site. This more than compensates for the “loss” of fugacity occasioned by keeping the other sublattice essentially empty.

A natural question is just how big does  $M_0$  have to be to see this ordered phase for  $M \geq M_0$ . It was shown in Ref 189 that  $M_0 < 27^6$ , a very large upper bound. A direct computation on the Bethe lattice (see Fig. 2) with  $q$  neighbors [190,191] gives  $M_0 = [q/(q-2)]^2$ , which would suggest  $M_0 \approx 4$  for the square lattice. By transfer matrix methods and by Pirogov–Sinai theory asymptotically ( $M \gg 1$ ) exact formulas were derived [190,191] for the transition lines between the gas and the crystal phase ( $M_c \approx 3.7962/z$ ) and between the crystal and the demixed phase ( $M_d = z + 2 - 1/z + \dots$ ), respectively (see Fig. 2). Monte Carlo simulations [190,191] were done to evaluate  $M_0$  numerically on a square lattice. By taking histograms of the crystal structure order parameter we were able to locate the transition fugacity for a given  $M$  by finite size scaling techniques [177–181]; i.e., by looking for intersection points of the fourth-order cumulant [179–181] (see Sec. IV A) as a function of the fugacity. For  $M \geq 7$  we find such intersection points indicating the presence of a gas to crystal phase transition, the transition points are shown in Fig. 2. For  $M \leq 6$  we were not able to find

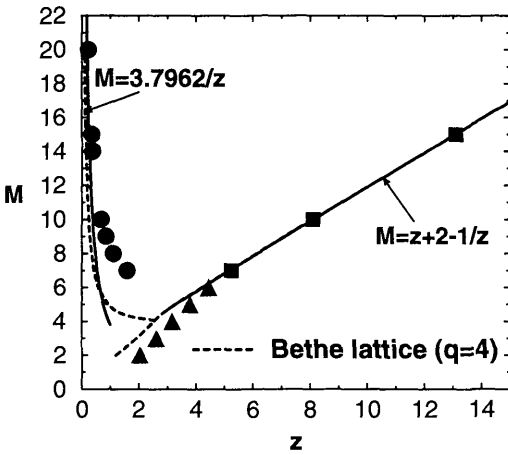


**FIG. 2** Phase diagram in the  $M$ - $z$  plane for a square lattice (MC) and for a Bethe lattice ( $q = 4$ ). Dashed lines: Exact results for the Bethe lattice for the transition lines from the gas phase to the crystal phase, from the gas to the demixed phase and from the crystal to the demixed phase; full lines: asymptotic expansions. Symbols for MC: transition points from the gas phase to the crystal phase (circles), from the gas to the demixed phase (triangles) and from the crystal to the demixed phase (squares). (Reprinted with permission from Ref. 190, Fig. 7. © 1995, American Physical Society.)

cumulant intersection points indicating the nonexistence of this transition; for details of these transitions and information the demixing transition see Refs. 190, 191.

## 2. Phase Transitions in Non-additive Symmetric Hard Disc Fluids

Another example of phase transitions in two-dimensional systems with purely repulsive interaction is a system of hard discs (of diameter  $d$ ) with  $N_A$  particles of type  $A$  and  $N_B$  particles of type  $B$  in volume  $V$  and interaction potential  $U$  ( $U(r_{12}) = \infty$  for  $r_{12} < d_{s_1 s_1}$  and zero otherwise,  $r_{12}$  is the distance of two particles,  $s_1, s_2 \in \{A, B\}$  are their species and  $d_{AA} = d_{BB} = d$ ,  $d_{AB} = d + \Delta/2$ ). The total number of particles  $N = N_A + N_B$  and the total volume  $V$  is fixed and thus the average density  $\rho^* = \rho * d^2 = Nd^2/V$ . Due to the additional repulsion between  $A$  and  $B$  type particles one can expect a phase separation into an  $A$ -rich and a  $B$ -rich fluid phase for large values of  $\Delta > \Delta_c$ . In a Gibbs ensemble Monte Carlo (GEMC) [192] simulation a system is simulated in two boxes with periodic boundary conditions, particles can be exchanged between the boxes and the volume of both boxes can



vary but the sum of both volumes is constant. The Monte Carlo moves are such that both boxes have the same chemical potential and pressure, so that in the case of phase coexistence the interfacial energy can be minimized by putting the two phases separately into the two boxes. Since for hard discs the phase separation is driven by entropy only a small interfacial free energy is expected in the case of phase coexistence. In order to locate the critical values  $\Delta_c$  as a function of  $\rho^*$ , GEMC [192] simulation techniques have been combined [193,194] with block analysis finite-size scaling techniques [179–181]. The GEMC results [193,194] were obtained with  $N = 512$  particles and about  $10^6$  MC steps, where each of the steps consisted of 400 attempted moves, 20 particle exchange and 2 volume change attempts. Cell occupancy lists were successfully used to speed up the procedure, the overall computing time for which was about 4300 CPU hours on RISC 6000/250 workstations. A first approximation for the critical line can be computed, in analogy to a study in three dimensions [195], by convex envelope arguments for the free energy, resulting in the compact expression

$$\rho_c^*(\Delta_c) = (4/\pi)(1 - \sqrt{\Delta/(d + \Delta)}) \quad (10)$$

Critical points were obtained by inspection of histograms  $P_L(N_A - N_B)$  of the number difference on different length scales  $L$  and analysis by the fourth-order cumulant (see Sec. IV A) obtained by subdivision of the simulation boxes of sizes  $V_1$  and  $V_2$  ( $V_1 + V_2 = V$ ) into smaller subsystems of size  $L \times L$ . For  $\Delta < \Delta_c$  the distributions are all singly peaked, for larger  $\Delta$  a single-peak structure of  $P_L(N_A - N_B)$  results for large  $L$  and a double-peak structure for small  $L$ . An analysis of these histograms with the cumulants  $U_L = 1 - \langle (N_A - N_B)^4 \rangle_L / 3 \langle (N_A - N_B)^2 \rangle_L^2$  allows a determination of critical points, due to the cumulants'  $L$ -invariance at the critical point. The GEMC results for points on the critical line are:  $(\rho_c^*, \Delta_c/d) = (0.6, 0.562 \pm 0.04)$ ,  $(0.55, 0.66 \pm 0.01)$ ,  $(0.5, 0.789 \pm 0.01)$ ,  $(0.499 \pm 0.01, 0.85)$ ,  $(0.5 \pm 0.02, 0.9)$ ,  $(0.508 \pm 0.03, 0.95)$ ,  $(0.46 \pm 0.02, 1)$ . Similarly to Eq. (10),  $\rho_c$  is a decreasing function of  $\Delta_c$ ; however, at a given density the GEMC results for  $\Delta_c$  are about 20% larger than the predictions of Eq. (10).

### C. Model Alloys with Elastic Interaction

Precipitate microstructures are important for the strength and hardness of many alloys [196–210]. A number of experimental [211–228] and theoretical [220,229–247] investigations have shown that the development of precipitate morphologies is influenced by elastic interactions (EI) resulting from a lattice misfit between matrix and precipitates and from an externally applied elastic strain.

Thus, in nickel-base superalloys [221–226] cuboidal precipitates develop as a result of EI [220]. These cuboids may join into large plates either spontaneously in the coarsening process or, more impressively, as a result of an externally applied uniaxial stress. These processes are reasonably well described by models where anisotropic elastic strains are incorporated into the kinetics of a phase separating system [202,231,232,235,245–249]. Such models include continuum approaches as well as atomistic computer simulations. In particular, an Ising-type model has been developed [241–244] which predicts the growth of plate-like domains oriented perpendicular to the elastically soft directions, in agreement with experiment. The model fails, however, to reproduce some of the microstructural details [220], like narrow channels of disordered phase effectively cutting the plates into a succession of cuboids.

It has been suggested [235] that these channels correspond to wetted anti-phase boundaries (APBs) between variants of atomically ordered precipitates. Such a proposal is very difficult to check experimentally since variants of an ordered phase can be distinguished in electron microscopy only by measuring large specimen areas using atomic resolution, which is generally not possible. Similarly, the Ising model mentioned above did not include the possibility of different atomically ordered domains and cannot therefore give an answer to this question. On the other hand, it is well known that the precipitation of ordered domains inside a random matrix is strongly influenced by the ordering tendency [221–226]. Simulations of Ising models (not including EI) in which the ordered domains were of two types gave a precipitate morphology strongly dependent on the volume fraction of the disordered domain [210]. This can be interpreted as being due to the fact that the disordered phase has always a tendency to wet the surface of the ordered domains [210].

Following the work of Refs. 210, 241–244, 250, 251, we generalized [252] the model of Ref 210 by including EI resulting from a different size of the two types of atoms. We then studied [252], via MC simulations, the coarsening of anti-ferromagnetically (AFM) ordered domains in two dimensions under the influence of elastic misfit interactions with and without externally applied uniaxial stress. The EI led to the development of a platelet morphology consisting of two types of ordered domains (differing by a phase) and a disordered domain. Characteristic lengths associated with these domains follow a law of the type  $R = a + bt^{1/3}$ . We observed the presence of narrow channels subdividing the ordered plates (or strips) into subdomains. Such channels are typically observed in nickel-base superalloys where the precipitates are ordered. It was commonly found that neighboring subdomains are ordered on a different sublattice, which means that the narrow channels are, in fact, wetted APBs. This is in good agreement with Khachaturyan's

ideas [235]. We believe that the APBs are responsible for the morphology with 30% ordered phase in the disordered matrix being quite different from that with 30% disordered phase. (Such an effect was also found earlier in this AFM model with no EI but is absent in ferromagnetic (FM) systems.) In fact, the main difference in the kinetics and morphologies between the present AFM model and the previously studied FM ones appears to be due to the presence of the APB. Since these APBs disappear only when two of

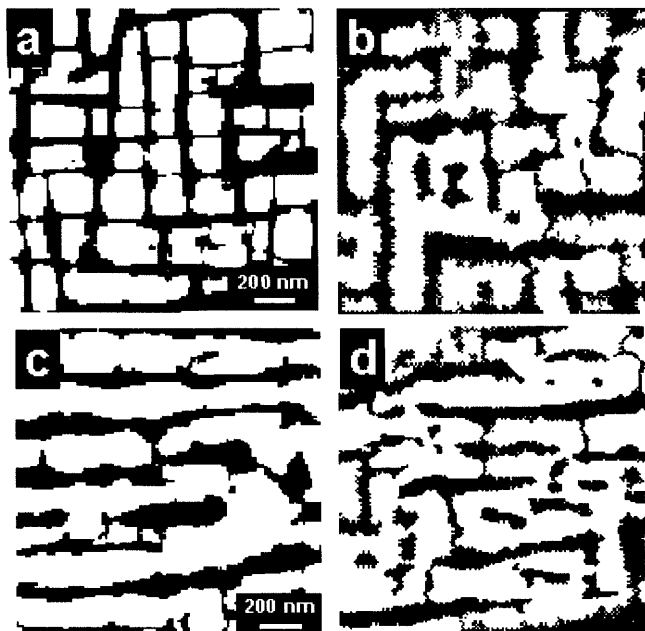


**FIG. 3** (a) Transmission electron microscopic image of Ni–Al–Mo alloy with Mo composition chosen such as to make the lattice spacing in the precipitates (gamma-prime phase) smaller than in the disordered matrix (misfit  $-0.5\%$ ). Treatment: 5 h at 1253 K (orientation 001). One observes cube-like precipitates aligned along the elastically soft directions  $[010]$  and  $[100]$ . (b) MC configurations after 100 000 MCs for  $c = 0.35$ ; the disordered phase is shown black, whereas both variants of the ordered phase are shown in white. (c) Transmission electron microscopic image of the same Ni–Al–Mo alloy as in (a). Same thermal treatment as in (a) but now with an external compressive load of 130 MPa applied to it along the vertical  $[010]$  direction. (d) MC configurations due to rafting with uniaxial external tensile stress in the  $x$  direction ( $\zeta = 0.1$ ) after 100 000 MCs with a random solution as a starting configuration for  $c = 0.35$ ; the disordered phase is shown black, whereas both variants of the ordered phase are shown in white. (Reprinted with permission from Ref. 252, Fig. 8. © 1999, Plenum Publishing Corporation.)

them meet and annihilate, it is very difficult for neighbouring subdomains to join up into a single domain. Hence, the growth kinetics is hindered by the presence of the APBs and thus the average domain size was found to decrease monotonically with the amount of ordered phase (varying from 30% to 70%). The wide channels between neighbouring strips, also found in the FM case, are probably due to an effective repulsion of the strips due to the EI. This means that neighboring ordered strips are not necessarily on different sublattices. The growth in thickness is, therefore, unrelated to APBs. The effect of uniaxial external stress is to cause “rafting” of the domains. The APBs cause the strips to be segmented. Finally, we mention the great similarity between the morphologies obtained from our simulations and those obtained from experiment (despite the great difference in scales) once the distinction between the differently ordered subdomains (not distinguished in the experiments) is removed from the simulation output; see Fig. 3. This compares our data with transmission electron micrographs of Ni–Al–Mo alloys annealed with and without external stress.

## D. Path Integral Monte Carlo

### 1. Path Integrals and Simulation Method

The partition function at temperature  $T = \beta^{-1}/k_B$  of the system with Hamiltonian  $H$  in an ensemble with constant number of particles  $N$  and constant volume  $V$  is given by

$$Z(N, V, T) = \text{tr} \exp[-\beta H] = \sum_n \langle n | \exp[-\beta H] | n \rangle \quad (11)$$

where the states  $|n\rangle$  form a complete and orthonormal basis set. The trace in the partition function usually cannot be evaluated without introducing approximations, particularly if quantum-mechanical effects play an important role. We emphasize the quantum Monte Carlo treatment in the following, since classical MC is rather well known and straightforward [149–151, 153] and furthermore is a simple special case of the general formalism outlined below. In the position representation the computation of potential energy is easily performed, and thus a factorization of the Boltzmann factor into terms containing the potential energy and the kinetic energy is useful. Due to the non-commutativity of the kinetic and potential energy such a factorization in general involves an error which is proportional to the commutator of both operators; however, if the Trotter product formula is applied [156–166, 253–258].

$$\exp[-\beta H] = \lim_{P \rightarrow \infty} (\exp[-\beta V/P] \exp[-\beta T/P])^P \quad (12)$$

the coefficient of the error decreases to zero as  $P \rightarrow \infty$ .

Let us consider systems which consist of a mixture of spherical atoms and rigid rotators, i.e., linear  $N_2$  molecules and spherical Ar atoms. We denote the position (in  $D$  dimensions) and momentum of the (point) particles  $i$  with mass  $m$  (modeling an Ar atom) by  $\mathbf{r}_i$  and  $\mathbf{p}_i$  and the center-of-mass position and momentum of the linear molecule  $I$  with mass  $M$  and moment of inertia  $\mathcal{I}$  (modeling the  $N_2$  molecule) by  $\mathbf{R}_I$  and  $\mathbf{P}_I$ , the normalized director of the linear molecule by  $\mathbf{n}_I$ , and the angular momentum by  $\mathbf{L}_I$ .

The Hamiltonian  $H$  consists of kinetic energy due to the translational and rotational degrees of freedom and the potential energy contributions due to the coupling between the particles,

$$H = T_{\text{trans}}(\{\mathbf{p}\}, \{\mathbf{P}\}) + T_{\text{rot}}(\{\mathbf{L}\}) + V_{\text{pp}}(\{\mathbf{r}\}) + V_{\text{pr}}(\{\mathbf{r}\}, \{\mathbf{R}\}, \{\mathbf{n}\}) + V_{\text{rr}}(\{\mathbf{R}\}, \{\mathbf{n}\}) \quad (13)$$

where the contributions to  $H$  are given by

$$T_{\text{trans}}(\{\mathbf{p}\}, \{\mathbf{P}\}) = \sum_i \frac{\mathbf{p}_i^2}{2m} + \sum_I \frac{\mathbf{P}_I^2}{2M} \quad (14)$$

$$T_{\text{rot}} = \sum_I \frac{\mathbf{L}_I^2}{2\mathcal{I}} \quad (15)$$

$$V_{\text{pp}}(\{\mathbf{r}\}) = \sum_{i < j} V_{\text{pp}}(|\mathbf{r}_i - \mathbf{r}_j|) \quad (16)$$

$$V_{\text{pr}}(\{\mathbf{r}\}, \{\mathbf{R}\}, \{\mathbf{n}\}) = \sum_{i,I} V_{\text{pr}}(\mathbf{r}_i, \mathbf{R}_I, \mathbf{n}_I) \quad (17)$$

$$V_{\text{rr}}(\{\mathbf{R}\}, \{\mathbf{n}\}) = \sum_{I < J} V_{\text{rr}}(\mathbf{R}_I, \mathbf{n}_I, \mathbf{R}_J, \mathbf{n}_J) \quad (18)$$

In the following discussion we ignore quantum-statistical effects due to exchange of indistinguishable particles. If particles with rotational degrees of freedom are considered, one choice for  $|n\rangle$  is the tensor product of the position eigenstates  $|\mathbf{r}, \mathbf{R}\rangle$  with the free rotator eigenstates  $|\{\mathbf{Y}_{lm}(\Omega)\}\rangle$  where  $\{\mathbf{Y}_{lm}(\Omega)\}$  are the spherical harmonics at spatial angle  $\Omega$ . In position representation the application of the Trotter product formula to the partition function results in an expression for  $T_{\text{trans}}$  which suggests the interpretation of this energy as an energy of chains with harmonically connected beads, where the spring constant for a particle with mass  $m$  is given by

$mP/\hbar^2\beta^2$ . Here the partition function  $Z_P$  at fixed  $P$  for a system with  $N_p$  point particles and  $N_r$  rotators is given by:

$$\begin{aligned}
 Z_P = & \left( \frac{mP}{2\pi\hbar^2\beta} \right)^{dN_p/2} \left( \frac{MP}{2\pi\hbar^2\beta} \right)^{dN_r/2} \int d\{\mathbf{r}\} \int d\{\mathbf{R}\} \\
 & \times \prod_{s=1}^P \left( \exp \left[ -\frac{\beta}{P} \left( V_{pp}(\{\mathbf{r}\}^{(s)}) \right) \right] \right) \\
 & \times \sum_{\{l,m\}} \left\langle \{\mathbf{Y}_{lm}\}^{(s)} \middle| \exp \left[ -\frac{\beta}{P} \left( \frac{\sum_I \mathbf{L}_I^2}{2I} + V_{pr}(\{\mathbf{r}, \mathbf{R}, \mathbf{n}\}) + V_{rr}(\{\mathbf{R}, \mathbf{n}\}) \right) \right] \right. \\
 & \times \left. |\{\mathbf{Y}_{lm}\}^{(s+1)}\rangle \right\rangle \\
 & \times \exp \left[ -\frac{P}{2\hbar^2\beta} \left( \sum_i^{N_p} m[\mathbf{r}_i^{(s)} - \mathbf{r}_i^{(s+1)}]^2 + \sum_I^{N_r} M[\mathbf{R}_I^{(s)} - \mathbf{R}_I^{(s+1)}]^2 \right) \right]
 \end{aligned} \tag{19}$$

The partition function  $Z$  is given in the large- $P$  limit,  $Z = \lim_{P \rightarrow \infty} Z_P$ , and expectation values of an observable are given as averages of corresponding estimators with the canonical measure in Eq. (19). The variables  $\{\mathbf{r}\}^{(s)}$  and  $\{\mathbf{R}\}^{(s)}$  can be used as classical variables and classical Monte Carlo simulation techniques can be applied for the computation of averages. Note that if we formally put  $P = 1$  in Eq. (19) we recover classical statistical mechanics, of course.

The “\*” in Eq. (19) reflects that the trace is cyclic; e.g.,  $\mathbf{r}^{(P+1)} = \mathbf{r}^{(0)}$ . The integrations  $\langle \{\mathbf{Y}_{lm}\}^{(s)} | \bullet | \{\mathbf{Y}_{lm}\}^{(s+1)} \rangle$  have to be done over  $\Omega$ , representing the fact that the quantum rotator is not pointing in one “classical” direction but rather is delocalized over the unit sphere. A convenient scheme for 3-dimensional rotors [259] has recently been used for the analysis of molecular  $N_2$  solids [260]; Sec. IV D 3. If rotors only are present ( $N_p = 0$ ), the partition function can be written as

$$Z(N_r, V, T) = \lim_{P \rightarrow \infty} \prod_{s=1}^P \int d\{\mathbf{R}^{(s)}\} \int d\{\mathbf{n}^{(s)}\} \exp[-\beta(\hat{T}_{\text{trans}} + \hat{T}_{\text{rot}} + \hat{V}_{\text{rr}})/P] \tag{20}$$

where  $\mathbf{n}^{(s)}$  is the molecular director at imaginary time slice  $s$ . The

contributions in  $Z$  are given by:

$$\begin{aligned}\hat{T}_{\text{trans}} &= \hat{T}_{\text{trans}}(\{\mathbf{R}^{(s)}, \mathbf{R}^{(s+1)}\}) \\ &= \sum_{I=1}^{N_r} \frac{MP^2}{2\hbar^2\beta^2} (\mathbf{R}_I^{(s)} - \mathbf{R}_I^{(s+1)})^2 - \frac{3N_r P^2}{2\beta} \ln \frac{MP}{2\pi\hbar^2\beta}\end{aligned}\quad (21)$$

$$\begin{aligned}\hat{T}_{\text{rot}} &= \hat{T}_{\text{rot}}(\{\mathbf{n}^{(s)}, \mathbf{n}^{(s+1)}\}) \\ &= \sum_{I=1}^{N_r} \sum_{L=0}^{\infty} \left[ BL(L+1) + \frac{P}{\beta} \ln \frac{2L+1}{4\pi} P_L(\mathbf{n}_I^{(s)} \cdot \mathbf{n}_I^{(s+1)}) \right]\end{aligned}\quad (22)$$

$$\hat{V}_{\text{rr}} = \hat{V}_{\text{rr}}(\{\mathbf{R}^{(s)}, \mathbf{n}^{(s)}\}) \quad (23)$$

where  $P_L$  denotes the Legendre polynomial. For  $N_2$  rotators, the mass  $M$  and the rotational constant  $B$  are equal to  $M = 28.02$  u and  $B = 2.88$  K, respectively.

Thermal averages in the ensemble with constant pressure  $p$  are given via the corresponding partition function  $\Delta_{NpT} = \int_0^\infty dV \exp[-\beta pV] Z(N, V, T)$ .

Other quantum simulations involve simulations with effective Hamiltonians [261–263] or the simulation of ground state wave properties by Green's function Monte Carlo or diffusion Monte Carlo; for reviews and further references on these methods see Refs. 162, 264–268.

## 2. Quantum Statistics

An additional complication in the PIMC simulations arises when Bose or Fermi statistics is included in the formalism. The trace in the partition function allows for paths which may end at a particle index which is different from the starting index. In this way larger, closed paths may build up which eventually spread over the entire system. All such possible paths corresponding to the exchange of indistinguishable particles have to be taken into account in the partition function. For bosons these contributions are summed up; for fermions the number of permutations of particle indices involved decides whether the contribution is added (even) or subtracted (odd) in the partition function.

Permutations of this type have to be considered in PIMC simulations if a full account of the quantum statistics is intended in the study and required by the physical effect under consideration, which means that additional permutation moves have to be done in the simulation. In this way quantum statistics has been included in a few PIMC simulations, in particular for the study of superfluidity in He [287] and in adsorbed  $\text{H}_2$  layers [92], for the Bose–Einstein condensation of hard spheres [269], and for the analysis of

structures in adsorbed He layers [90,91]. For additional studies and information see Refs. 270–297.

### 3. Examples

As examples of the successful application of the PIMC method outlined in Sec. IV D 1, we focus here on studies of crystal properties where either Ar, Ne atoms or  $N_2$  molecules occupy sites on an fcc lattice.

The special case where only rotators are present,  $N_p = 0$ , is of particular interest for the analysis of molecular crystals and will be studied below. Here we note that in the other limit, where only spherical particles are present,  $N_r = 0$ , and where only symmetrical box elongations are considered with boxes of side length  $S$ , the corresponding measure in the partition function  $\propto \exp[-\beta E_P(S, \{\mathbf{r}\})]$ , involving the random variable  $S$ , can be simplified considerably, resulting in the effective Hamiltonian

$$E_P(S, \{\mathbf{r}_0\}) = -k_B T [d(N_p P + 1) - 1] \ln(S) + p V_0 S^d \\ + \frac{1}{P} \sum_{s=1}^P \left( V_{pp}(\{\mathbf{S}\mathbf{r}_0\}^{(s)}) + \frac{m P^2 S^2}{2\hbar^2 \beta^2} \sum_i^{N_p} [\mathbf{r}_{0_i}^{(s)} - \mathbf{r}_{0_i}^{(s+1)}]^2 \right) \quad (24)$$

Here  $\mathbf{r}_0$  are coordinates in a reference volume  $V_0$  and  $\mathbf{r} = \mathbf{S}\mathbf{r}_0$ . With this formalism the kinetic and potential energy of Ar crystals has been computed [288] as well as lattice constants, thermal expansion coefficients, and isotope effects in other Lennard–Jones solids. In Fig. 4 we show the kinetic and potential energy of an Ar crystal in the canonical ensemble versus temperature for different values of  $P$ ; we note that in the classical limit ( $P = 1$ ) the low temperature specific heat does not decrease to zero; however, with increasing  $P$  values the quantum limit is approached. In Fig. 5 the isotope effect on the lattice constant (at  $p = 0$ ) in a Lennard–Jones system with parameters suitable for Ne atoms is presented, and a comparison with experimental data is made. Please note that in a classical system no isotope effect can be observed,  $\chi = 0$ , and the deviations between simulations and experiments are mainly caused by non-optimized potential parameters.

Next we consider a molecular crystal composed of  $N_2$  molecules, ( $N_p = 0$ ). Molecular  $N_2$  solids at low temperatures and low pressures are in the  $\alpha$  structure (Pa3). Using PIMC simulations we studied the low temperature properties of  $N_2$  solids [260] ( $B = 2.88$  K,  $N_r = 500$ ). In Fig. 6 the temperature dependence of the molar volume is shown for our simulational as well as for experimental [289] data. We note that the classical simulations (corresponding to  $P = 1$ ) lead to a nonzero slope of the volume at very low temperatures, which is in sharp contrast to the experimental behavior [289].



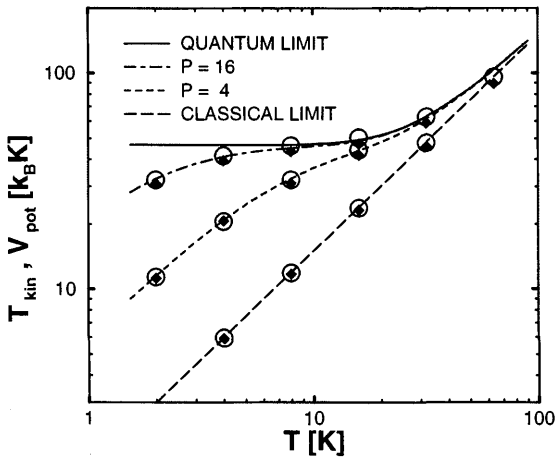


**FIG. 4** Kinetic and potential energy of  $^{40}\text{Ar}$  as a function of temperature, for different Trotter dimensions  $P=1$  (classical), 4, 16, and in the quantum limit ( $P \rightarrow \infty$ ) in the harmonic approximation (lines) and simulated results (symbols). Circles correspond to kinetic energy ( $T_{\text{kin}}$ ), diamonds to potential energy ( $V_{\text{pot}}$ ). The system size is  $N=256$ , error bars are much smaller than symbol sizes. (Reprinted with permission from Ref. 288, Fig. 4. © 1995, American Physical Society.)

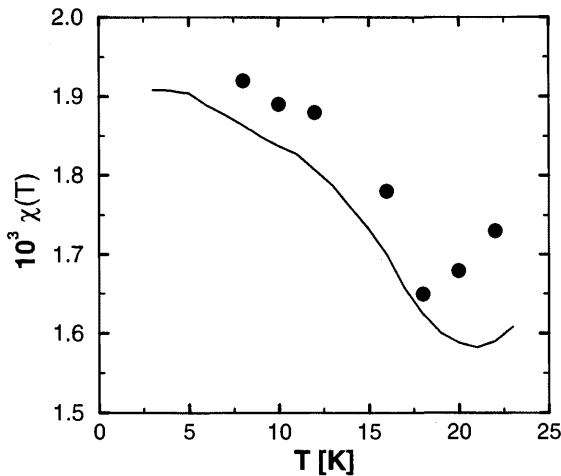


**FIG. 5** Relative difference  $\chi$  of the lattice constants of  $^{20}\text{Ne}$  and  $^{22}\text{Ne}$  as a function of temperature. Lines are experimental values [346], symbols are PIMC results, the error bars of the  $10^3 \chi(T)$  data values are about  $\pm 0.03$ . (Reprinted with permission from Ref. 288, Fig. 8. © 1995, American Physical Society.)

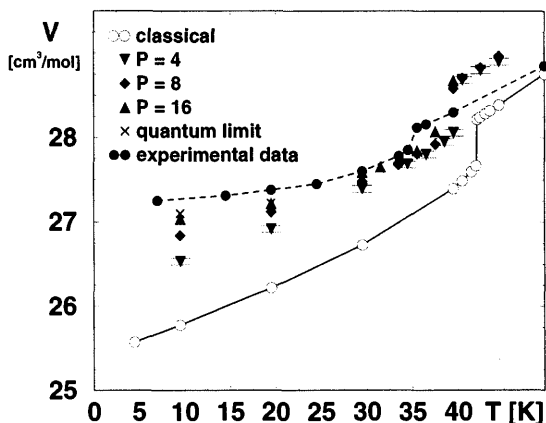


**FIG. 6** Equilibrium volume of  $N_2$  solids versus temperature at zero pressure. Experiments [289] and PIMC results [260]; lines are for visual help. (Reprinted with permission from Ref. 260, Fig. 1 © 1998, American Physical Society.)

With increasing values of  $P$  the molar volume is in progressively better agreement with the experimental values. Upon heating a phase transition takes place from the  $\alpha$  phase to an orientationally disordered fcc phase at the transition temperature  $T_1$ , where we find a jump in the molar volume (Fig. 6), the molecular energy, and in the order parameter. The transition temperature of our previous classical Monte Carlo study [290,291] is  $T_1 = 42.5(\pm 0.3)$  K, with increasing  $P$ ,  $T_1$  is shifted to smaller values, and in the quantum limit we obtain  $T_1^{qm} = 38(\pm 0.5)$  K, which represents a reduction of about 11% with respect to the classical value.

We also note that similar PIMC studies for Si crystals and crystalline silicates have been carried out recently [292].

## V. PATH INTEGRAL MONTE CARLO — ANALYSIS OF QUANTUM EFFECTS IN ADSORBED LAYERS

In this section we review several studies of phase transitions in adsorbed layers. Phase transitions in adsorbed (2D) fluids and in adsorbed layers of molecules are studied with a combination of path integral Monte Carlo, Gibbs ensemble Monte Carlo (GEMC), and finite size scaling techniques. Phase diagrams of fluids with internal quantum states are analyzed. Adsorbed layers of  $H_2$  molecules at a full monolayer coverage in the  $\sqrt{3} \times \sqrt{3}$  structure have a higher transition temperature to the disordered phase compared to the system with the heavier  $D_2$  molecules; this effect is

analyzed by PIMC. Linear  $N_2$  molecules adsorbed on graphite show a transition from a high-temperature phase to a low-temperature phase with *herringbone* ordering of the orientational degrees of freedom; the order of the transition and quantum effects are discussed.

## A. Phase Transitions in Quantum 2D Fluids

Phase transitions in adsorbed layers often take place at low temperatures where quantum effects are important. A method suitable for the study of phase transitions in such systems is PIMC (see Sec. IV D). Next we study the gas-liquid transition of a model fluid with internal quantum states. The model [193,293–300] is intended to mimic an adsorbate in the limit of strong binding and small corrugation. No attempt is made to model any real adsorbate realistically. Despite the crudeness of the model, it has been shown by various previous investigations [193,297–300] that it captures the essential features also observed in real adsorbates. For example, the quite complex phase diagram of the model is in qualitative agreement with that of real substances. The Hamiltonian is given by

$$H = \sum_{i=1}^N \frac{\mathbf{p}_i^2}{2m} - \frac{\omega_0}{2} \sum_{i=1}^N \sigma_i^x + \sum_{i<j} U(r_{ij}) - \sum_{i<j} J(r_{ij}) \sigma_i^z \sigma_j^z \quad (25)$$

where  $m$  is the particle mass,  $\mathbf{p}_i$  is the momentum of particle  $i$ ,  $r_{ij}$  is the distance between particles  $i$  and  $j$ ,  $\sigma^x$  and  $\sigma^z$  are the Pauli spin-1/2 matrices,  $U$  is a hard-disc potential for particles with diameter  $d$ , and  $J(r) = J$  for  $d < r < 1.5d$  and zero elsewhere. For motivation and literature background for these types of model see Refs. 296,297; for recent reviews on fluids with classical internal states see Refs. 301,302. In the adiabatic approximation (large  $M$ ), one assumes a separation of time scales for the translational degrees of freedom and the internal quantum states. An application of the Trotter formula results in an expression [193,296,297] for the partition function  $Z = \lim_{P \rightarrow \infty} Z_P$  at temperature  $T^* = (\beta J)^{-1}$  involving an effective classical Hamiltonian  $H_{\text{eff}} \approx \sum_{i=1}^N \sum_{s=1}^P (K_P S_{i,s} S_{i,s+1} + (1/P) \sum_{i \neq j=1}^N J(r_{ij}) S_{i,s} S_{j,s})$ ; the quantum chains have periodic boundary conditions with respect to  $P$ ,  $K_P = \ln[\coth(\beta\omega_0/2P)]/2\beta$  and  $S_{i,p} = \pm 1$ . The phase diagram of this fluid (see Fig. 7) was studied by a combination of PIMC and GEMC [193,300] and finite size scaling techniques [297]. Good agreement with density functional theory results [298] was found for the freezing densities (see Sec. V A 1). In the high temperature regime, as the density is increased a second-order transition from a paramagnetic (PM) to a ferromagnetic (FM) *fluid* phase takes place; the magnetization is measured in the  $z$  direction,  $m_i = \langle \sum_{s=1}^P S_{i,s} \rangle / P$ . The tricritical point at the end of the critical line can be

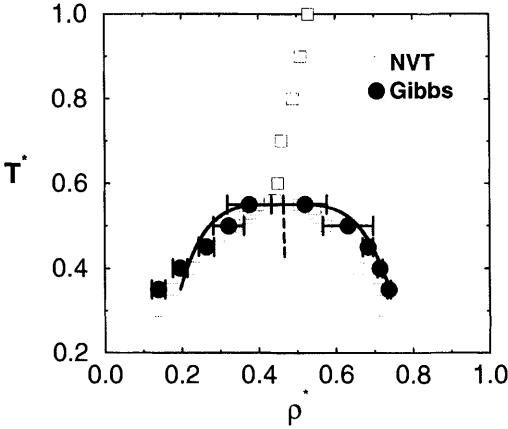


**FIG. 7** Phase diagram ( $\omega_0/J = 4$ ,  $J = 1$ ,  $N = 200$ ,  $P/\beta J \approx 40$ ). Circles: GEMC results [193,300] for coexistence densities; squares: NVT results [297] (squares above  $T_{\text{tri}}^*$  mark the PM–FM transition in the fluid phase). Line: data fit to the scaling behavior  $(\rho_l - \rho_g) = B(T_c - T)^{1/4}$ ; dashed line: “rectilinear diameter data”  $((\rho_g + \rho_l)/2 = a + bT)$ . (Reprinted with permission from Ref. 300, Fig. 4. © 1995, American Physical Society.)

located at  $(T_{\text{tri}}^*, \rho_{\text{tri}}^*) = (0.57 \pm 0.02, 0.45 \pm 0.01)$  (for a study on tricritical universality of the model in the limit  $\omega_0 = 0$  see Ref. 303). Below  $T_{\text{tri}}^*$  a PM *gas* phase coexists with a FM *liquid* phase, and at very low temperatures a PM *gas* phase is in coexistence with a *square*-lattice FM *solid* phase. The mean field (MF) theory [296,297] provides a qualitatively correct phase diagram but it underestimates the fluctuations and in principle contains only the  $D = 3$  tricritical exponents. The exponent describing the merging of the phase boundaries in the tricritical point is distinctly smaller than the MF value (unity), resulting in a much flatter shape of the coexistence region, and thus the tricritical temperature is different by a factor of two as compared to PIMC!

For other studies on related classical models see Refs. 302,304,305.

## 1. Density Functional Theory

Freezing transitions have been examined in recent years by density functional methods [306–313]. Here we review the results [298] of a modification of the Ramakrishnan–Yussouff theory to the model fluid with Hamiltonian (Eq. (25)); a related study of phase transitions in a system of hard discs in two dimensions with Ising internal states which couple anti-ferromagnetically to their neighbors is shown in Ref. 304. First, a combined

classical– quantum free energy functional of the time-averaged number density  $\rho(\mathbf{r})$  and the magnetization density  $m(\mathbf{r})$  is introduced for the Helmholtz free energy per unit volume. The magnetic interaction arising from the presence of the internal quantum states is incorporated in the sense of a mean field treatment [296] of the attractive interaction in addition to the classical hard disc contribution to the free energy. The magnetization density  $m(\mathbf{r})$ , for the ferromagnetic solid that is considered here, is proportional to the number density; i.e.,  $m(\mathbf{r}) = m_0\rho(\mathbf{r})$ . In the mean-field model, the magnetic field on one particle due to the interaction with all other particles is approximated by the average molecular field,  $\xi_m(\mathbf{r}) = \int d\mathbf{r}' m(\mathbf{r} - \mathbf{r}')J(\mathbf{r}')$ . As a result the (many body) Hamiltonian (Eq. (25)) effectively reduces to a one-body Hamiltonian, which can be straightforwardly diagonalized. The free energy functional in this approximation is given by

$$\beta f([\rho]) = \beta f_{\text{cl}}([\rho]) + \frac{\beta}{2} \int \frac{d\mathbf{r}}{V} m(\mathbf{r}) \xi_m(\mathbf{r}) - \int \frac{d\mathbf{r}}{V} \rho(\mathbf{r}) \ln[2 \cosh\{\beta(\xi_m^2(\mathbf{r}) + \omega_0^2/4)^{1/2}\}] \quad (26)$$

The integrals are over the full two-dimensional “volume”  $V$ . For the classical contribution to the free energy  $\beta f_{\text{cl}}([\rho])$  the Ramakrishnan–Yussouff functional has been used in the form recently introduced by Ebner *et al.* [314] which is known to reproduce accurately the phase diagram of the Lennard–Jones system in three dimensions. In the classical part of the free energy functional, as an input the Ornstein–Zernike direct correlation function for the hard disc fluid is required. For the DFT calculations reported, the accurate and convenient analytic form due to Rosenfeld [315] has been used for this quantity.

The free energy functional (Eq. (26)) needs to be minimized with respect to choices of (non-uniform) densities  $\rho(\mathbf{r})$  to obtain the Helmholtz free energies of the solid phases. Motivated by the simulation results, in addition to the usual triangular lattice the square lattice solid has also been studied. In order to obtain the free energies of the solids, the one-body density  $\rho(\mathbf{r})$  at position  $\mathbf{r}$  is approximated by a set of non-overlapping Gaussians of width  $\alpha/a^2$  centered on lattice sites  $\mathbf{R}$  in a lattice of lattice parameter  $a$ ,  $\rho(\mathbf{r}) = (\rho_0 A_n \alpha / a^2 \pi) \sum_{\mathbf{R}} \exp[-\alpha(\mathbf{r} - \mathbf{R})^2 / a^2]$ , where  $\rho_0$  is the average density of the solid and  $A_n$  denotes the area of the unit cell. This ansatz for the density now reduces the free energy functional to a *function* of the variables  $m_0$  and  $\alpha$ . The global minimum of this function in the space of  $\alpha$  and  $m_0$  for a choice of  $\{\mathbf{R}\}$  gives the Helmholtz free energy of the chosen lattice. Knowing the Helmholtz free energy in the fluid phase from the mean field

analysis of the same system for the homogeneous case carried out by de Smedt et al. [296], it is straightforward to obtain the  $T^*-\rho^*$  phase diagram by performing double tangent constructions to obtain coexistence densities.

The phase diagram of Hamiltonian (Eq. (25)) has the following features ( $\omega_0 = 4$  and  $J_0 = 1$  where chosen, as in the simulation). In the high temperature limit, the system is paramagnetic for all densities and the (temperature independent) hard disc freezing transition can be found. The estimates for the freezing density ( $\rho_l^* = 0.847$ ) and the fractional density change during freezing ( $\eta = 0.066$ ) are close to the estimates for the same quantities in computer simulations ( $\rho_l^* = 0.878$ ,  $\eta = 0.0499$ ) and previous theoretical studies ( $\rho_l^* = 0.858$ ,  $\eta = 0.0723$ ) of the two-dimensional hard disc system, both known from the literature [298]. As the temperature is reduced below  $T^* = 5.9$ , the system undergoes a second-order transition from a paramagnetic fluid phase at low densities to a ferromagnetic fluid at high densities and a first-order transition from a ferromagnetic fluid to a ferromagnetic triangular solid. As expected, the freezing density decreases with decreasing temperature due to the greater stability of the solid phase arising from the magnetic interaction. The DFT prediction for the location of the fluid–solid transition was confirmed by an analysis of the bond orientation order parameter of Monte Carlo data [299]. Also, the average magnetization of the solid  $m_0$  is observed to be higher than that of the fluid. At temperatures below the tricritical point  $T_{\text{TCP}}^* = 1.25$ , one gets a first-order transition from a paramagnetic gas to a ferromagnetic fluid in addition to the liquid–solid transition. The liquid phase is stable only for temperatures above a first triple temperature  $T_{\text{TP}_1}^* = 0.55$ , whereas for temperatures below  $T_{\text{TP}_1}^*$  and above  $T_{\text{TP}_2}^* = 0.07$ , a paramagnetic gas is in coexistence with a ferromagnetic triangular solid. The square lattice solid, observed in the Monte Carlo simulations [297] at  $T^* = 0.16 \pm 0.01$ , starts appearing at temperatures below  $T^* = 0.09$ , and for a range of temperatures  $T_{\text{TP}_2}^* < T^* < 0.09$  there exists a re-entrant transition with the triangular solid appearing for low and high densities separated by a narrow region of square solid stability centered around  $\rho^* = 1.0$ . Upon lowering temperatures below the paramagnetic gas – ferromagnetic square solid–ferromagnetic triangular solid triple point ( $T_{\text{TP}_2}^*$ ), a gas phase is in coexistence with a square solid, followed by a square solid–triangular solid structural transition at higher densities.

The topology of the phase diagram is in agreement with Monte Carlo results; a thermodynamically stable *square lattice solid* is predicted successfully, a surprising finding in the simulation [297]. Because of second nearest neighbor contributions in the square lattice structure, resulting from the particular choice of the magnetic interaction  $J(\mathbf{r})$ , the square lattice has a lower magnetic energy. The hard disc contribution, however, strongly disfavors the square lattice structure in two dimensions.

## 2. Quantum Dynamics

A successful method to obtain dynamical information from computer simulations of quantum systems has recently been proposed by Gubernatis and coworkers [167–169]. It uses concepts from probability theory and Bayesian logic to solve the analytic continuation problem in order to obtain real-time dynamical information from imaginary-time computer simulation data. The method has become known under the name *maximum entropy* (MaxEnt), and has a wide range of applications in other fields apart from physics. Here we review some of the main ideas of this method and an application [175] to the model fluid described in the previous section.

Path integral Monte Carlo simulations were performed [175] for the system with Hamiltonian (Eq. (25)) for  $\omega^* = \omega_0/J = 4$  (where  $J = 1$ ) with  $N = 256$  particles and a Trotter dimension  $P = 64$  chosen to achieve good computer performance. It turned out that only data with noise of less than 0.1% led to statistically reliable results, which were only possible to obtain with about  $10^7$  MC steps. The whole study took approximately 5000 CPU hours on a CRAY YMP.

In the paramagnetic region of the phase diagram the dynamics of the internal degrees of freedom is quite different from the dynamics in the ferromagnetic region since in the latter the “classical spins” along the Trotter direction are pointing mainly in the same direction (high “tunneling” frequency) whereas in the paramagnetic region fluctuations of the spin values along the Trotter direction are frequent (low “tunneling” frequency). The dynamics near the continuous phase transition is of particular interest since at this point the correlation length diverges and the magnetic ordering differs in spatial regions of different sizes. This results in a mixing of the dynamics of low density paramagnetic areas with the dynamics of high density ferromagnetic areas, and thus the full dynamics should contain contributions from many “tunneling” frequency ranges (see below). In order to study the quantum dynamics of our adsorbate in the different regions of the phase diagram in detail with the methods mentioned above, we focused on a particular choice of the temperature,  $T^* = 1$ . The imaginary-time correlation functions  $\mathcal{G}(\tau) = \langle \sigma^z(\tau) \sigma^z(0) \rangle$  of the  $\sigma^z$ -spins are given by

$$\mathcal{G}(\tau) = \frac{1}{N} \sum_{i=1}^N \langle e^{\tau H} \sigma_i^z e^{-\tau H} \sigma_i^z \rangle \quad (27)$$

with  $0 \leq \tau \leq \beta$ . The numerical values  $G(\tau)$  at imaginary time  $\tau = s\beta/P$  ( $s = 1, 2, \dots, P$ ) are obtained from

$$G(s\beta/P) = \frac{1}{NP} \left\langle \sum_{i=1}^N \sum_{l=1}^P S_{i,l} S_{i,l+s} \right\rangle. \quad (28)$$

The first term of a virial expansion [296] of the correlation function is

$$\mathcal{G}(\tau) = \frac{\cosh[\omega_0(\tau - \beta/2)]}{\cosh[\omega_0\beta/2]} \quad (29)$$

It represents the correlations of non-interacting particles.

In mean field approximation we obtain for the imaginary-time correlation functions [296]

$$\mathcal{G}(\tau) = J_0^2 m^2 / (\Omega/2)^2 + (\omega_0/\Omega)^2 \frac{\cosh[\Omega(\tau - \beta/2)]}{\cosh[\Omega\beta/2]} \quad (30)$$

where  $J_0 = \rho \int d^2r J(r)g(r)$  is determined by the classical correlation function  $g(r)$ , which was computed iteratively in Percus–Yevick approximation in two spatial dimensions.  $\Omega/2 = [(J_0 m)^2 + (\omega_0/2)^2]^{1/2}$ , and the magnetization  $m$  is the solution of the equation

$$m(h) = \frac{J_0 m(h) + h}{\Omega(h)/2} \tanh[\beta\Omega(h)/2] \quad (31)$$

for  $h \rightarrow 0$ . From Eq. (30) we see that for  $m \neq 0$  the mean field correlation function contains a time-independent constant  $J_0^2 m^2 / (\Omega/2)^2$ , which leads to a peak at  $\omega = 0$  in the spectral density (see below).

The PIMC data obtained for the imaginary-time correlations are shown in Fig. 8 for different densities at  $T^* = 1$ . The relative errors of the data are of the order  $10^{-4}$ , which is necessary for the maximum entropy method to work when there is little previous knowledge, as in the present case. At low densities the average particle distances are large and, since the particle interaction is restricted to a “square well” region ( $d < r < 1.5d$ , see Eq. (25)), the probability for particle interactions is small. Thus the particles occupy mainly  $\sigma^x$  eigenstates, resulting in a small correlation of the  $\sigma^z$  spins and a small value of  $G(\beta/2)$ . In the limit of zero density the dynamics is given purely by the tunneling of the spins with frequency  $\omega_0$  which can be described by the zeroth-order term in the virial expansion [296] (see Eq. (29)), which is shown in Fig. 8 for comparison. At higher densities the probability for interaction increases and the particles “hybridize” by leaving their  $\sigma^x$  ground states and occupying more and more  $\sigma^z$  eigenstates, and thus the value of  $G(\beta/2)$  increases. This effect finally even leads to a continuous phase transition [297–299] from a paramagnetic to a ferromagnetic phase at about  $\rho_c^* \approx 0.53$ . In mean field approximation [296] the critical density is at  $\rho_{c, MF}^* = 0.4$ , and from Eq. (30) we see that for all  $\rho^* < \rho_{c, MF}^*$  the resulting correlation functions agree with the lowest-order virial expansion result, since the mean field value for  $m$  is zero. Thus the MF correlation functions increasingly deviate from the PIMC data with increasing density. Only for  $\rho^* > \rho_{c, MF}^*$  is there reasonably good agreement.



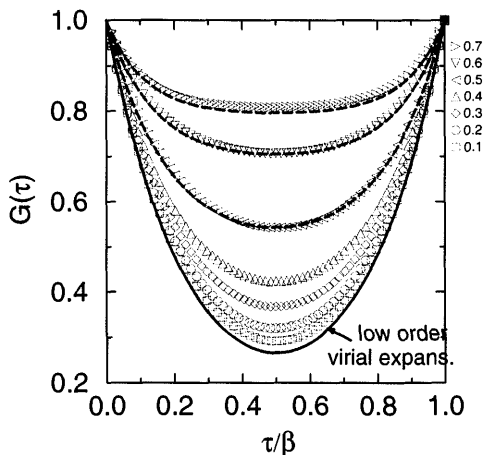


**FIG. 8** PIMC results (symbols) of the  $\sigma^z$  imaginary-time correlations  $G(\tau)$  versus imaginary time for densities  $\rho^* = 0.1, 0.2, \dots, 0.7$  from bottom to top; the temperature is  $T^* = 1$ . The full line shows the results for  $G(\tau)$  according to the lowest-order virial expansion; the dashed lines give the MF values of  $G(\tau)$  for the densities  $\rho^* = 0.7, 0.6$ , and  $0.5$  from top to bottom. (Reprinted with permission from Ref. 175, Fig. 1. © 1996, American Physical Society.)

In the inset of Fig. 9 we show the mean field frequency  $\Omega^* = \Omega/J$  as a function of density for  $T^* = 1$ . At this temperature the system undergoes a phase transition from a paramagnetic to a ferromagnetic fluid at a density whose mean field value is  $\rho_{c, MF}^* = 0.4$ . For densities below this value we obtain  $\Omega = \omega_0$ , which agrees with the frequency value of the low-order virial expansion (see Eq. (34)). For  $\rho > \rho_{c, MF}$ ,  $\Omega$  increases with the density due to increase of the magnetization.

Besides the deviation mentioned above, the main problem with the dynamical information from the MF approximation is that it contains only one positive frequency and so the resulting real-time correlations cannot be damped or describe localizations “on one side of the double well” due to interference effects, as one expects for real materials. Thus we expect that the frequency distribution is not singly peaked but has a broad distribution, perhaps with several maxima instead of a single peak at an average mean field frequency. In order to study the shape of the frequency distribution we analyze the imaginary-time correlations in more detail.

We briefly repeat now the essential parts of the *maximum entropy* method; for details we refer to the literature [167–169]. We seek to obtain information on the dynamics of the internal degree of freedom of the model from PIMC simulations. The solution of this problem is not

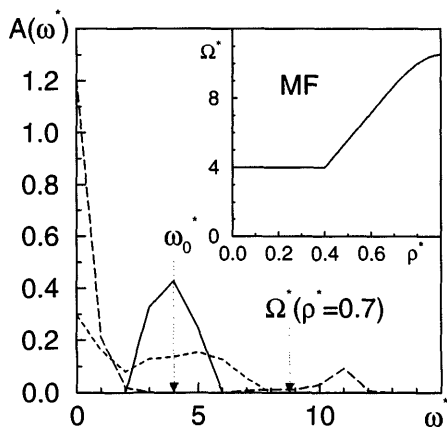


**FIG. 9**  $A(\omega)$  via MaxEnt for the densities  $\rho^* = 0.1$  (full line),  $\rho^* = 0.45$  (dashed line),  $\rho^* = 0.7$  (long dashed line); the temperature is  $T^* = 1$ ; in all cases a flat default model in the maximum entropy procedure was used. The vertical lines refer to the results of the mean field approximation for  $\Omega^* = \Omega/J = \omega_0^*$  for  $\rho^* = 0.1$  and  $\Omega^*(\rho^* = 0.7)$ . Inset: Mean field frequency  $\Omega^* = \Omega/J$  versus density at temperature  $T^* = 1$ . (Reprinted with permission from Ref. 175, Fig. 2. © 1996, American Physical Society.)

straightforward, since PIMC simulations yield dynamical correlation functions in imaginary time whereas of course, are real time data are physically relevant, especially regarding comparison with experimental results. Fortunately there is an integral relation

$$\mathcal{G}(\tau) = \int_{-\infty}^{+\infty} d\omega \frac{e^{-\tau\omega} A(\omega)}{1 \pm e^{-\beta\omega}} \quad (32)$$

that connects correlations  $\mathcal{G}(\tau)$  in imaginary time  $\tau$  with real frequency spectral densities  $A(\omega)$ . If this relation could be inverted, and if  $A$  could be determined from the numerical estimate  $G(\tau)$  for  $\mathcal{G}(\tau)$ , one would have the desired dynamical information.

The double sign in Eq. (32) usually refers to Fermi (+) and Bose (−) statistics respectively. In our system we neglect the statistics and study the  $\sigma^z$  “self correlations.” We consider the symmetrized correlation functions [316] resulting in the “+” sign in Eq. (32) and  $A(\omega) = A(-\omega)$ .

Since the numerical estimate  $G(\tau)$  is necessarily incomplete and inaccurate the inversion is not possible without any ambiguity. Gubernatis and coworkers now suggested resolving the ambiguity by choosing the most probable  $A$  consistent with the data  $G$ ; i.e., they chose the  $A$  that maximizes the conditional probability  $P[A|G]$ . This is justified since  $A$  has the

properties of a probability distribution function:  $A(\omega) \geq 0$ ,  $\int d\omega A(\omega) < \infty$ ,  $A(\omega)$  is bounded.

The *a posteriori* probability  $P[A|G]$  for having the spectral density  $A(\omega)$ , given the simulation data  $G$ , is

$$P[A|G] \propto e^Q \quad (33)$$

with  $Q = \alpha S - \chi^2/2$ .  $S$  has the meaning of an entropy and is of the form

$$S = - \int d\omega \left( A(\omega) \ln \left[ \frac{A(\omega)}{M(\omega)} \right] - A(\omega) + M(\omega) \right) \quad (34)$$

$M(\omega)$  is the *default model*, by which additional knowledge about system properties can be incorporated. Minimum additional knowledge is equivalent to  $M(\omega) = \text{const.}$  Without data,  $S$  is maximized by  $A(\omega) = M(\omega)$ .  $\chi^2$  measures the deviation of the time correlation function  $\mathcal{G}$  computed from a proposed  $A$  via Eq. (32) from the PIMC value  $G$  at the point  $\tau_k$  in imaginary time,

$$\chi^2 = \sum_s [G(\tau_s) - \mathcal{G}(\tau_s)]^2 / \sigma_s^2 \quad (35)$$

$\sigma_s$  is the standard deviation of the simulation data for  $G(\tau_s)$  at  $\tau_s$ . The problem of maximizing  $P[A|G]$  can be solved by maximizing  $Q$  w.r.t.  $A(\omega)$ , which is solved iteratively for given PIMC data for  $G$ .

In Fig. 9 we show  $A(\omega)$  for the densities  $\rho^* = 0.1, 0.45$  and  $0.7$ . Due to results of virial expansions we expect that at low densities the behavior is dominated by the dynamics of the isolated particles, resulting in a peak in  $A(\omega)$  at the tunneling frequency  $\omega_0$ . With increasing density due to increasing probability of particle interactions we expect a broadening of the spectral density around  $\omega_0$ . These expectations have indeed been obtained by MaxEnt. In the case of high densities, where the system is in the ferromagnetic phase we obtain a double peak structure for  $A(\omega)$  with a sharp peak at  $\omega = 0$  and a broadened peak at a higher frequency. The center of this peak is shifted to higher frequencies with increasing density. This behavior is plausible according to the mean field results which predict a peak at  $\omega = 0$  and a second peak at the frequency  $\Omega$ . The values of  $\Omega$  are close to the center of mass of the broadened high frequency peaks; see Fig. 9 for results at the density  $\rho^* = 0.7$ .

For densities close to the phase transition density we obtain a broad frequency distribution (see Fig. 9). This shows that due to the diverging correlation length particles interact in spatial areas of different sizes, densities and magnetizations, resulting in a spectral density being given approximately as a superposition of the functions corresponding to the ferromagnetic and paramagnetic cases. In this region of the phase diagram

the results of the mean field study are not reliable since critical fluctuations are not treated properly in this approximation.

In order to analyze the quantum dynamics of a two-dimensional fluid undergoing a phase transition, it turns out to be essential to go beyond MF approximation and to apply methods such as those presented here.

## B. Phase Transitions in Layers of $H_2$ and $D_2$ on Graphite

In an interesting study [107] Freimuth and Wiechert studied the phase diagrams of  $H_2$  and  $D_2$  molecules adsorbed on graphite. At low temperatures and coverages below the  $\sqrt{3} \times \sqrt{3}$  monolayer coverage  $\rho_{\sqrt{3}}$  they found phase coexistence of a gas phase with a  $\sqrt{3} \times \sqrt{3}$ -ordered phase. The coexistence region ends in a tricritical point at a temperature  $T_{\text{tri}}$ , with  $T_{\text{tri}}(H_2) < T_{\text{tri}}(D_2)$ . Above  $T_{\text{tri}}$  the phase transition from the ordered to the disordered phase is of second order and the transition temperature  $T_c$  increases with the coverage. An “anomalous” effect was found at a full  $\sqrt{3} \times \sqrt{3}$  monolayer coverage  $\rho = \rho_{\sqrt{3}}$ : the critical temperature for the disordering transition  $T_c(D_2)$  for the  $D_2$  system is smaller than for the  $H_2$  system, with  $T_c(H_2) - T_c(D_2) \approx 2.5$  K. Usually one would expect a lower transition temperature for the system with the lighter particles. In order to analyze the observed “anomaly” we performed PIMC simulations for both systems [15,16,110]. We approximate all  $N$  molecules as spherical particles interacting with a Lennard–Jones potential, and since the energy difference from the rotational ground state to the first excited state is in the order of 100 K we assume that the particles occupy only the rotational ground state at the temperatures considered ( $T < 20$  K).

The Hamiltonian of this system contains the kinetic energy  $T_{\text{kin}}$ , the pair interaction of the Lennard–Jones form,  $V_{\text{pp}}(\{\mathbf{r}\}) = V_{\text{LJ}}(\{\mathbf{r}\})$  ( $\sigma = 2.96$ ,  $\varepsilon = 36.7$  K [317]), and the interaction potential [146–148,318]  $V_{\text{surf}}$  between an adsorbate particle at the position  $\mathbf{r} = (x, y, z)$  and all other substrate particles,  $V_{\text{surf}}(x, y, z) = E_0(z) + E_1(z)f_1(x, y)$  (see Sec. III B); the interaction parameters are  $\varepsilon_{\text{HC}} = 32.05$  K,  $\sigma_{\text{HC}} = 3.18$  [146–148,318]. The model is defined on a 2D lattice with side length  $S$ , the simulations are done at a coverage  $\rho_{\sqrt{3}}$ . After using the Trotter product formula the partition function with Trotter dimension  $P$  is  $(\mathbf{r}_j^{(P+1)} = \mathbf{r}_j^{(1)})$ :

$$Z = \lim_{P \rightarrow \infty} \left( \frac{mP}{2\pi\hbar^2\beta} \right)^{NP} \prod_{j=1}^N \prod_{s=1}^P \int_{-\infty}^{\infty} d\mathbf{r}_j^{(s)} \exp \left[ -\beta \sum_{i < j}^N \sum_{s=1}^P \frac{1}{P} V_{\text{LJ}}(\mathbf{r}_j^{(s)}, \mathbf{r}_i^{(s)}) \right] \\ \times \exp \left[ -\beta \sum_{j=1}^N \sum_{s=1}^P \left\{ \frac{mP}{2\hbar^2\beta^2} [\mathbf{r}_j^{(s)} - \mathbf{r}_j^{(s+1)}]^2 + \frac{1}{P} V_{\text{surf}}(\mathbf{r}_j^{(s)}) \right\} \right] \quad (36)$$

The phase transition temperature  $T_c$  was determined with finite size scaling methods, in particular through determining the cumulant intersection points (see Sec. IV A) of the commensurate phase order parameter distribution. In the quantum study the ordered  $\sqrt{3} \times \sqrt{3}$  phase is found in contrast to the classical case. In Fig. 10 the cumulants for different subsystem sizes are shown for  $H_2$  and  $D_2$ , at a coverage  $\bar{\rho} = \rho\sqrt{3}$ ; clearly the transition temperature for  $D_2$ , which is found by the cumulant intersection point, is smaller than in the  $H_2$  system, the temperature difference between the two critical temperatures is about 3 K, in rough agreement with the experimental findings. At a given temperature the average “extent” (diameter) of the quantum chains in the case of  $H_2$  molecules is bigger compared to the  $D_2$  molecules, in agreement with the de Broglie wavelengths of the particles. Thus the delocalization of  $H_2$  molecules is more pronounced than for  $D_2$  molecules due to the larger de Broglie wavelength of  $H_2$  molecules. As a result the effective repulsion of two  $H_2$  particles is stronger and so the average distance between two  $H_2$  particles is larger, favoring the ordered structure. This may explain why the system with the lighter particles has a higher transition temperature to the disordered phase. A question, which cannot be answered by experimental techniques, is how the behavior of the system changes when the mass of the particles increases beyond the value of the  $D_2$  particles, approaching the classical limit. In the PIMC we can study [16] the system properties by modifying the mass and keeping the other interaction parameters fixed. For adsorbed particles with a mass  $m = 1.5m_{H_2}$  we find at high temperatures ( $T > 11.5$  K) a density distribution peaked around the average density. At low temperatures ( $T < 11.5$  K) we obtain a doubly peaked density distribution with a peak at the low density gas phase and one peak at the monolayer density ( $\rho = \rho\sqrt{3}$ ). This shows that for masses in the range of the  $H_2$  and  $D_2$  molecules at low temperatures there is a phase coexistence between the gas phase and the  $\sqrt{3} \times \sqrt{3}$  structure. For particles with a mass  $m = 10m_{H_2}$  we find at low temperatures ( $T < 16$  K) a doubly peaked density distribution with a peak at the low density gas phase and one peak at a fluid density which is much higher than the monolayer density ( $\rho > \rho\sqrt{3}$ ). For large particle masses ( $m > 2.5m_{H_2}$ ) the quantum delocalization is not very pronounced at low temperatures [16] and so the repulsive interaction between the particles in the surface potential due to their effective “size” is reduced and smaller distances compared to the  $H_2$  system are frequent, resulting in a destabilization of the  $\sqrt{3} \times \sqrt{3}$  structure and stabilization of a liquid phase instead. The results for the gas–liquid coexistence region for large masses are in good agreement with the critical point estimates for the (classical) two-dimensional Lennard–Jones fluid [319–321] ( $T_c = 17.25$  K,  $\rho_c \approx 0.627\rho\sqrt{3}$ ).

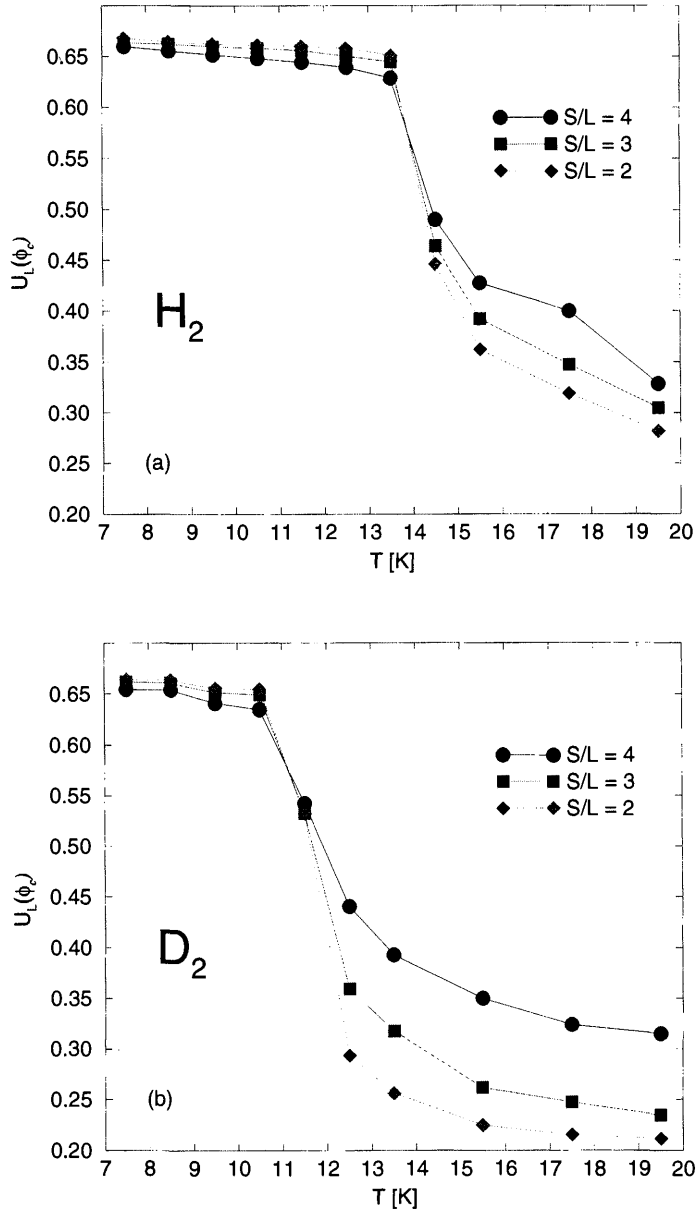


**FIG. 10** Cumulants of the  $\sqrt{3} \times \sqrt{3}$  structure order parameter  $\phi_c$  for  $H_2$  (a) and  $D_2$  (b) adsorbed on graphite ( $S = 18a$ ,  $N = 108$ ,  $P = 25$ ). Points: PIMC results for different subsystem sizes  $L$ ; lines are for visual help. (Reprinted with permission from Ref. 16, Fig. 1. © 1997, Springer-Verlag.)

## C. Orientational Phase Transitions in Adsorbed Monolayers

### 1. The Order of the Herringbone Transition of N<sub>2</sub> on Graphite

Linear N<sub>2</sub> molecules adsorbed on graphite show a transition from a high-temperature phase with orientational disorder to a low-temperature phase with *herringbone* ordering of the orientational degrees of freedom (see Sec. II C and Fig. 11).

In interesting studies [322] of the order of the N<sub>2</sub> herringbone transition on graphite, the APR Hamiltonian [155]

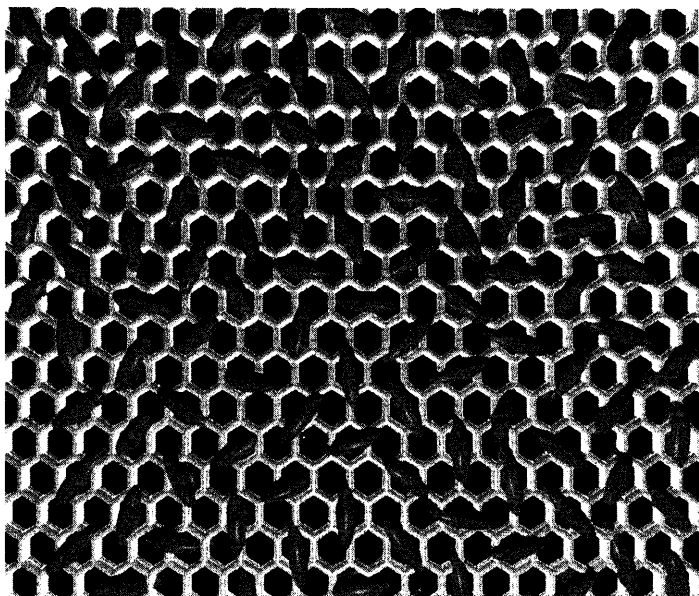
$$H = K(N_2) \sum_{\langle i, j \rangle}^N \cos[2\varphi_i + 2\varphi_j - 4\phi_{i,j}] \quad (37)$$

is used to model the quadrupolar interactions between the  $N = L^2$  molecules;  $\varphi_j$  is the angle  $\varphi(\mathbf{R}_j)$  of the  $j$ th rotator whose center of mass is pinned at site  $\mathbf{R}_j$  of a triangular lattice representing the  $(\sqrt{3} \times \sqrt{3})R30^\circ$  structure. All angles are measured relative to one symmetry axis of this lattice and only nearest neighbor interactions  $\langle i, j \rangle$  are taken into account.  $\phi_{i,j}$  measures the angle between neighboring sites  $\mathbf{R}_i$  and  $\mathbf{R}_j$ , i.e.,  $\phi_{i,j} \in \{0, \pi/3, 2\pi/3, \pi, 4\pi/3, 5\pi/3\}$ . The coupling constant  $K(N_2) = 33 \text{ K}$  is obtained [322,155] from the electrostatic quadrupole moment of N<sub>2</sub> and the  $\sqrt{3}$ -lattice constant is  $a = 4.26 \text{ \AA}$ . We stress that for this system the triangular lattice structure is essential in order to produce a nontrivial ordered phase. On a simple square lattice the quadrupolar interaction would just favor unfrustrated perpendicular nearest-neighbor orientations of the characteristic T shape.

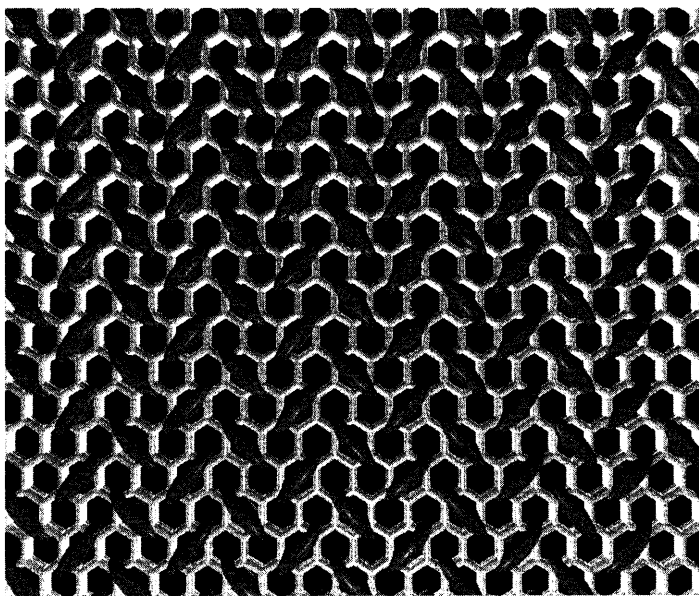
The correlation functions are defined as

$$\Gamma_\alpha(l) = \left\langle \frac{1}{N} \sum_{i=1}^N \cos[2\varphi(\mathbf{R}_i) + 2\varphi(\mathbf{R}_i + l\mathbf{a}_\alpha)] \right\rangle \quad (38)$$

along the three symmetry axes, where  $\{\mathbf{a}_\alpha\}$  denotes lattice vectors ( $|\mathbf{a}_\alpha| = a$ ) along these axes and  $l$  runs over the neighbors along these directions. Although it is known that the decay of  $\Gamma_\alpha(l)$  for large distances  $l$  should be exponential,  $\Gamma_\alpha(l) \propto \exp[-l/\xi]$ , an estimation of  $\xi$  from simulations is difficult. For small  $l$  there may be strong systematic corrections to this law, whereas for large  $l$  there are not only severe statistical problems but also systematic corrections due to the periodic boundary conditions, i.e.,  $\Gamma_\alpha(l) = \Gamma_\alpha(L - l)$ . Also, lattice structure effects such as an even-odd oscillation of  $\Gamma_\alpha(l)$  present a difficulty. Thus  $\xi$  often depends on the range of  $l$  used in a fit to the exponential decay law. These problems are avoided by the procedure



(a)



(b)

**FIG. 11** Schematic configurations of  $N_2$  molecules on a graphite substrate ( $\rho = \rho_{\sqrt{3}}$ ) for temperatures above the herringbone transition temperature (a) and below it (b).



[323] defining  $\xi_l$  via

$$\delta_m \ln \Gamma_\alpha(l) := \ln \left[ \frac{\Gamma_\alpha(l) - \Gamma_\alpha(\infty)}{\Gamma_\alpha(l+m) - \Gamma_\alpha(\infty)} \right] = \frac{m}{\xi_l} \quad (39)$$

where  $\Gamma_\alpha(\infty) := \Gamma_\alpha(L/2 \gg l \gg \xi)$  denotes the constant asymptotic value of (38) which vanishes in the disordered phase;  $m = 2$  takes care of the fact that  $\Gamma_\alpha(l)$  oscillates with period two (see Ref. 324). The advantage of this approach is that no (possibly uncontrolled) fitting is involved, and especially that the range where  $\xi_l$  approximates the true  $\xi$  can be assessed by inspection. If a plot of  $\delta_m \ln \Gamma_\alpha(l)$  versus  $l$  yields a *plateau* for a certain window of distances  $l$ , then  $\xi$  may safely be extracted from such a plateau value; i.e., the linear dimension of the system and the quality of the data (equilibration, statistics) are sufficient. The simulations were carried out [94] with a standard Metropolis MC algorithm which is highly vectorized via a three sublattice checkerboard decomposition using fully tabulated potentials. The linear dimensions were  $L = 60, 90, 120$  and  $180$ , the statistical effort went up to 1 500 000 MC sweeps over the lattice.

From the plateau,  $2/\xi$  is obtained directly and  $\xi^{-1}$  is plotted in Fig. 12 as a function of temperature. The behavior of  $\xi^{-1}$  demonstrates that the correlation length increases upon approaching  $T_0$  but without showing even an onset of a divergence upon coming close to  $T_0$ ; it should be noted that  $\xi$  is measured as close as only 2% (0.3%) off  $T_0$ , and that roughly one decade in reduced temperature is covered both from above and from below. The temperature dependence of the data suggests extrapolating  $\xi^{-1}$  linearly which yields a *finite*  $\xi_+ \approx 23$  ( $\xi_- \approx 12$ ) upon approaching  $T_0$  from above (below). Thus, judging from the behavior of  $\xi$ , one can conclude that the herringbone transition of the APR model is a weak first-order transition. For comparison the  $\xi^{-1}(T)$  data have been fitted to the power law (including the known critical exponent [325] and amplitude ratio [326]) expected for the  $q = 3$  Potts model in 2D. But, as can clearly be seen from Fig. 12, especially near  $T_0$ , the critical fit is not at all satisfactory.

## 2. Quantum Effects on the Orientational Phase Transition

Now the problem being addressed is to *quantify* the effect of *quantum fluctuation* on the orientational ordering in this molecular system.

The quantum generalization of the APR Hamiltonian results after supplementing this classical Hamiltonian with a non-commuting angular momentum part  $[L_j, \varphi_i] = -i\hbar\delta_{j,i}$  which introduces quantum dispersion and thus qualitatively new effects due to additional fluctuations and tunneling.

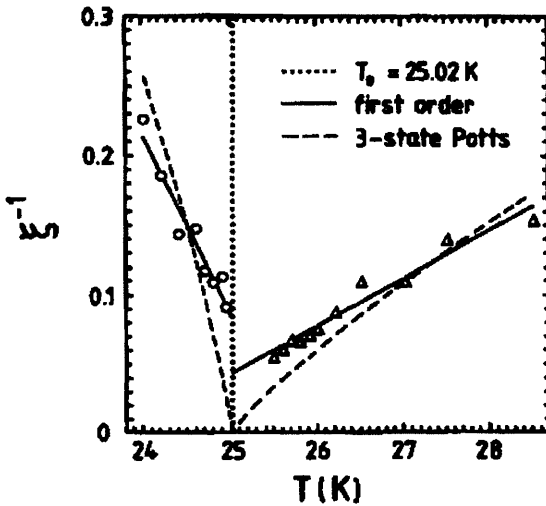


**FIG. 12** Inverse effective correlation length  $\xi^{-1}$  in units of the lattice constant  $a = 4.26 \text{ \AA}$  as a function of temperature; the extrapolated transition temperature  $T_0 = 25.02 \pm 0.08 \text{ K}$ , as obtained independently from energy cumulants, is marked by a dotted line. Full lines correspond to a fit assuming a simple linear dependence  $\xi = \xi_{\pm} + C_{\pm}|1 - T/T_0|$  expected near  $T_0$  for a first-order transition, whereas dashed lines assume the critical behavior of the 3-state 2D Potts class,  $\xi = \xi_0^{\pm}|1 - T/T_0|^{-\nu}$ , with [325]  $\nu = 5/6$  and [326]  $\xi_0^+/\xi_0^- = 4.1$ . (Reprinted with permission from Ref. 94, Fig. 2. © 1993, Elsevier Science.)

Correspondingly, the quantum APR Hamiltonian reads

$$H = \sum_{j=1}^N \frac{L_j^2}{2\mathcal{I}} + \sum_{\langle j,i \rangle}^N V(\varphi_j, \varphi_i) \quad (40)$$

$$= -\Theta \sum_{j=1}^N \frac{\partial^2}{\partial \varphi_j^2} + K \sum_{\langle j,i \rangle}^N \cos(2\varphi_j + 2\varphi_i - 4\phi_{j,i}) \quad (41)$$

The moment of inertia  $\mathcal{I}$  determines the rotational constant  $\Theta = \hbar^2/2\mathcal{I}$ , which is the parameter that controls the strength of quantum effects. The other parameter of the model, which is the quadrupolar coupling constant  $K$ , can be conveniently taken as the energy and temperature scale. We can thus reduce all quantities related to energies by  $K$ , and define, e.g., the dimensionless temperature  $T^* = k_B T/K$ , energy  $E^* = E/K$ , and rotational constant  $\Theta^* = \Theta/K$ .

The properties of the Hamiltonian (41) have been studied by means of PIMC simulations [327,328]. We stress here that for rotational motion in

two dimensions new features, connected with the restricted integration space, show up in the formalism [253–258,329]. This latter aspect and our implementation of these specialties in a PIMC scheme are discussed in detail in Refs. 95,96, and here we present only the essential features. A very efficient PIMC scheme [330], especially tailored to simulate rotational motion, is used to study a many-body system [95,96]. This allows us to investigate a *highly realistic* adsorbate composed of as many as  $N = 900$  quantum  $N_2$  rotators and Trotter dimensions up to  $P = 500$ .

In general, the partition function of a Hamiltonian of type (40) is given by

$$\begin{aligned}
 Z = & \lim_{P \rightarrow \infty} \left( \frac{\mathcal{I}P}{2\pi\hbar^2\beta} \right)^{NP/2} \prod_{j=1}^N \left\{ \sum_{n_j=-\infty}^{\infty} \int_0^{2\pi} d\varphi_j^{(1)} \prod_{s=2}^P \left[ \int_{-\infty}^{\infty} d\varphi_j^{(s)} \right] \right\} \\
 & \times \exp \left[ -\beta \sum_{s=1}^P \left[ \sum_{j=1}^N \frac{\mathcal{I}P}{2\hbar^2\beta^2} [\varphi_j^{(s)} - \varphi_j^{(s+1)} + 2n_j\pi\delta_{s,P}]^2 \right. \right. \\
 & \left. \left. + \sum_{\langle j,i \rangle} \frac{1}{P} V(\varphi_j^{(s)}, \varphi_i^{(s)}) \right] \right] \quad (42)
 \end{aligned}$$

where  $V(\varphi_j^{(s)}, \varphi_i^{(s)})$  denotes the pair potential evaluated separately for the configuration at each imaginary-time slice  $s = 1, \dots, P$ . Each quantum mechanical rotational degree of freedom is represented in this path integral representation by  $P$  classical rotators which form closed loops and interact via harmonic type interactions; the configuration  $\{\varphi_j^{(1)}, \varphi_j^{(2)}, \dots, \varphi_j^{(P)}\}$  is a realization of a Trotter path, and the path integral results from the proper integration and summation over all possible paths. However, contrary to path integrals for translational degrees of freedom, these loops need not be closed using periodic boundary conditions, but only modulo  $2\pi$ ; note that the classical angles  $\varphi_j^{(s)}$  of Eq. (42) are not confined to  $[0, 2\pi)$  but are allowed on the whole interval  $[-\infty, \infty]$ . The resulting mismatch  $n_j$  is called the “winding number representation” of the  $j$ th path [253–258,329] and the formulation (42) is the “winding number representation” of the partition function. Only the Boltzmann-weighted summation over all possible winding numbers, in addition to the integration over all paths having a certain winding number, yields the correct quantum partition function in the Trotter limit  $P \rightarrow \infty$ ; see Refs. 95,96 for a full discussion of that issue. Thus we have to include in the algorithm, in addition to local and global moves of the angular degrees of freedom  $\{\varphi_j^{(s)}\}$ , attempts to change the winding numbers  $\{n_j\}$  of the individual rotators. Our algorithm was tested [95,96,330] against exact (single-particle) results and a close agreement was observed. In a previous study [327] it turned out that the use of a

finite Trotter number of  $P = 500$  at a temperature of  $T^* = 0.03$  and a progressive linear decrease of  $P$  were increasing temperature were sufficient to be within the large  $P$  limit as required in (42). We note that other methods have been suggested for the path integral simulation of rotational degrees of freedom in two-dimensional [331] and three-dimensional space, [259,332–337], respectively.

The energies can be obtained from the primitive estimators [159–166] which proved to be sufficient in the present case [95,96]. The kinetic energy  $E_{\text{kin}}$  and the potential energy  $E_{\text{pot}}$  per particle are given by

$$E_{\text{kin}} = \frac{Pk_{\text{B}}T}{2} - \left\langle \frac{1}{N} \sum_{j=1}^N \sum_{s=1}^P \frac{\mathcal{I}P}{2\hbar^2\beta^2} [\varphi_j^{(s)} - \varphi_j^{(s+1)} + 2n_j\pi\delta_{s,P}]^2 \right\rangle \quad (43)$$

$$E_{\text{pot}} = \left\langle \frac{1}{P} \sum_{s=1}^P \frac{1}{N} \sum_{\langle j,i \rangle} V(\varphi_j^{(s)}, \varphi_i^{(s)}) \right\rangle \quad (44)$$

and the total energy  $E_{\text{tot}}$  is given by the sum of  $E_{\text{kin}}$  and  $E_{\text{pot}}$ . The estimator for the long range order parameter component  $\Phi_\alpha$  is given by the expression

$$\Phi_\alpha = \frac{1}{NP} \sum_{j=1}^N \sum_{s=1}^P \sin(2\varphi_j^{(s)} - 2\eta_\alpha) \exp[i\mathbf{Q}_\alpha \mathbf{R}_j], \quad (45)$$

with  $\mathbf{Q}_1 = \pi(0, 2/\sqrt{3})$ ,  $\mathbf{Q}_2 = \pi(-1, -1/\sqrt{3})$ ,  $\mathbf{Q}_3 = \pi(1, -1/\sqrt{3})$ , and  $\eta_1 = 0$ ,  $\eta_2 = 2\pi/3$ ,  $\eta_3 = 4\pi/3$ . The total long-range order parameter is defined as the length [94–96,338]

$$\Phi = \left\langle \left[ \sum_{\alpha=1}^3 \Phi_\alpha^2 \right]^{1/2} \right\rangle \quad (46)$$

of the three-component vector order parameter (45).

A quantity which measures the quantum delocalization of the rotational degrees of freedom can be defined by the expression [95,96]

$$R_\varphi = \left\langle \frac{1}{N} \sum_{j=1}^N \frac{1}{P} \sum_{s=1}^P \left[ \varphi_j^{(s)} - \frac{1}{P} \sum_{k=1}^P \varphi_j^{(k)} \right]^2 \right\rangle^{1/2} \quad (47)$$

This average spread is, by its definition, zero for a classical system and is thus a measure of the pure quantum contribution to the librations or rotations of the individual rotators.

A realistic modeling of  $\text{N}_2$  monolayers on graphite was done in Refs. 95,96. Concerning the  $\text{N}_2$ – $\text{N}_2$  interactions in Hamiltonian (40) and Eq. (42), the  $X1$  model [146–148,318], consisting of site–site Lennard–Jones and quadrupole interactions, was shown to yield a realistic representation;

the rotational constant  $\Theta_{N_2}$  was 2.9 K. Steele's Fourier representation [146–148] is used to model the  $N_2$ -graphite interactions; the molecular axes stay *in* the graphite plane.

The central quantity is the order parameter as a function of temperature (see Fig. 13). The phase transition temperature  $T_0$  of the classical system can be located around 38 K. At high temperatures, the quantum curve of the order parameter merges with the classical curve, whereas it starts to deviate below  $T_0$ . Qualitatively, quantum fluctuations lower the ordering and thus the quantum order parameter is always smaller than its classical counterpart. The inclusion of quantum effects results in a nearly 10% lowering of  $T_0$  (see Fig. 13).

Furthermore, one can infer *quantitatively* from the data in Fig. 13 that the quantum system cannot reach the maximum herringbone ordering even at extremely low temperatures: the quantum librations depress the saturation value by 10%. In Fig. 13, the order parameter and total energy as obtained from the full quantum simulation are compared with standard *approximate theories* valid for low and high temperatures. One can clearly see how the quasiclassical Feynman–Hibbs curve matches the “exact” quantum data above 30 K. However, just below the phase transition, this second-order approximation in the quantum fluctuations fails and yields *uncontrolled* estimates: just below the point of failure it gives classical values for the order parameter and the herringbone ordering even *vanishes* below

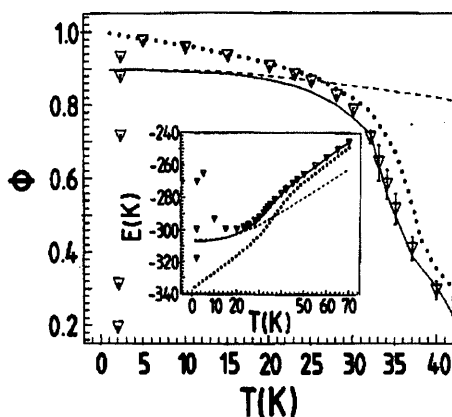


**FIG. 13** Herringbone order parameter and total energy for  $N_2$  (X1 model with Steele's corrugation). Quantum simulation, full line; classical simulation, dotted line; quasiharmonic theory, dashed line; Feynman–Hibbs simulation, triangles. The lines are linear connections of the data. (Reprinted with permission from Ref. 95, Fig. 4. © 1993, American Physical Society.)

5 K. On the other hand, the quasiharmonic theory comes from the other end of the temperature axis and yields very accurate data below 5 K.

An average zero-point libration amplitude of  $14^\circ$  can be extracted from the data, which compares favorably with the  $18^\circ$  from quasiharmonic lattice dynamics [339] for  $X1-N_2$  at 0 K in three dimensions. Since the validity of such approximations is very difficult to estimate *a priori*, exact full quantum *reference* simulations, as presented here, are clearly required to control such approximation schemes. This becomes clear when one considers the shift in  $T_0$  as obtained from the second-order Feynman–Hibbs simulation: it breaks down essentially at the same temperature at which the transition occurs and a breakdown at a slightly higher temperature would give wrong results. In addition, one does not know where to match the regimes where different approximations are still valid. The PIMC simulations, however, yield exact results over the *whole* temperature range from the classical to the quantum regime.

### 3. Mean-field Theory

Here we review the properties of the model in the mean field theory [328] of the system with the quantum APR Hamiltonian (41). This consists of considering a single quantum rotator in the mean field of its six nearest neighbors and finding a self-consistent condition for the order parameter. Solving the latter condition, the phase boundary and also the order of the transition can be obtained. The mean-field approximation is similar in spirit to that used in Refs. 340,341 for the case of 3D rotators.

We assume that the order parameter component  $\Phi_1$  becomes non-zero in the ordered phase,  $\Phi_1 = \pm \langle \sin 2\varphi \rangle \neq 0$  while  $\Phi_2 = \Phi_3 = 0$ . After writing each interaction term  $K \cos(2\varphi + 2\varphi' - 4\phi_{ij})$  as a product of trigonometric functions depending separately on the angular variables  $\varphi$  of the single rotator and  $\varphi'$  of its nearest neighbors, we can average over the variables  $\varphi'$  and sum over the six nearest neighbors. The resulting total mean-field potential acting on the single rotator is given by

$$H_{\text{pot}}^{\text{MF}} = -4K\Phi_1 \sin 2\varphi \quad (48)$$

Adding the kinetic energy and changing the variables to  $q = -2K\Phi_1/\Theta$  and  $\theta = \varphi - \pi/4$  (this angle  $\theta$  differs from the rotational constant  $\Theta$ , of course), we get the corresponding one-particle Schrödinger equation

$$\frac{d^2\Psi}{d\theta^2} + \left( \frac{E}{\Theta} - 2q \cos 2\theta \right) \Psi = 0 \quad (49)$$

which is the well-known Mathieu's equation [342].

In order to find the self-consistent condition, we have to determine the order parameter

$$\Phi_1 = \langle \cos 2\theta \rangle = \frac{\sum_i \langle \Psi_i | \cos 2\theta | \Psi_i \rangle e^{-\beta E_i}}{\sum_i e^{-\beta E_i}} = \frac{1}{2} \frac{\partial f_0}{\partial q} \quad (50)$$

as a function of the parameter  $q$ . In the last equation we have used the free energy per site, defined as  $f_0 = -(1/\beta) \ln \sum_i e^{-\beta E_i}$ . Solving Eq. (50) simultaneously with the condition  $q = -2K\Phi_1/\Theta$ , we find the equilibrium value of the order parameter for given values of inverse temperature  $\beta$  and model parameters  $K, \Theta$ . Expansions of  $\Phi_1(q)$  and  $f_0$  are given by the expansions of the eigenvalues of the Mathieu equation, which can be found in [342]. The result for the phase boundary  $K_c$  (up to 6th order in  $B_m = \exp[-m^2\Theta_c/T_c]$ ) is given by

$$K_c = \frac{420\Theta_c Z_6}{\left[ 420 + 210B_1 \left( \frac{4\Theta_c}{T_c} + 1 \right) - 280B_2 - 105B_3 - 56B_4 - 35B_5 - 24B_6 \right]} \quad (51)$$

where  $Z_6 = \sum_{m=-6}^6 B_m$ .

In the high-temperature, classical limit this agrees with the finding in Ref. 343. In order to map the phase diagram in the  $\Theta^*-T^*$  plane, we have to set  $K_c = 1$  in (51) and solve for  $T_c^*$  as a function of  $\Theta_c^*$ . This can be done numerically and the resulting phase diagram is shown in Fig. 14.

We see that at zero temperature there is a quantum phase transition at the value of  $\Theta_c^{*MF} = 1$ . The most interesting feature of the phase diagram is that there is a region of rotational constants ranging from 1 to roughly 1.25 for which the system is ordered at intermediate temperatures but disordered in the ground state (reentrance). The intuitive explanation of this phenomenon is the following. At low temperatures, the individual rotors are mostly in their totally rotationally symmetric ground state, which does not possess quadrupolar moment and therefore cannot induce ordering via the quadrupolar term. At intermediate temperatures, the excited states with non-zero quadrupolar moment become populated and induce ordering which persists to larger values of the rotational constant. According to the mean field theory, reentrance takes place for a fairly broad range of rotational constants  $1 < \Theta^* < 1.25$ . This corresponds to a decrease of the critical rotational constant by roughly 20% from its maximum value of about 1.25 to the value of 1 at the ground state transition, and represents a well pronounced feature. Concerning the validity of this mean-field result, it is

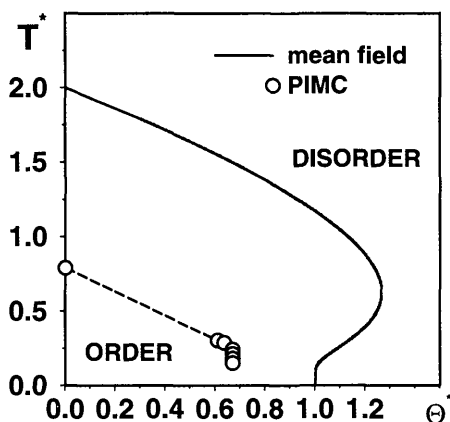


**FIG. 14** Phase diagram of the quantum APR model in the  $\Theta^*-T^*$  plane. The solid curve shows the line of continuous phase transitions from an ordered phase at low temperatures and small rotational constants to a disordered phase according to the mean-field approximation. The symbols show the transitions found by the finite-size scaling analysis of the path integral Monte Carlo data. The dashed line connecting these data is for visual help only. (Reprinted with permission from Ref. 328, Fig. 2. © 1997, American Physical Society.)

known that the mean-field approximation sometimes tends to overemphasize or even create reentrant behavior, as pointed out in Ref. 344. On the other hand, reentrant behavior has been experimentally observed in solid HD under compression [345]. This three-dimensional system, however, although consisting of diatomic molecules interacting via approximate quadrupolar interactions, differs fundamentally from our model in spatial dimensionality and structure of the lattice as well as in the dimensionality of the order parameter. In order to settle the question of reentrance in the 2D quantum APR model, the results of numerical simulations and analysis techniques are discussed in the next section.

#### 4. The PIMC Phase Diagram

To start the review of the PIMC results [328], we note that the detailed study of the quantum APR model (Eq. (41)) was partly motivated by the strong changes in shape of the orientational order parameter  $\Phi$  as a function of temperature as the rotational constant was increasing from its classical value  $\Theta^* = 0$  (see Fig. 3 in Ref. 327). For small enough  $\Theta^*$  it was found that the order parameter decays monotonically with increasing temperature, similarly to the classical case. This is qualitatively different for larger  $\Theta^*$ , where  $\Phi(T^*)$  becomes a non-monotonic function of temperature.



PIMC results for the kinetic and potential energies for  $\Theta^* = 0.6109$  and  $\Theta^* = 0.6982$  have been analyzed. In both cases the potential energy first decreases with temperature until maximum order is achieved, whereas the kinetic energy increases strongly in this region. For larger temperatures both  $E_{\text{pot}}$  and  $E_{\text{kin}}$  increase with temperature. Thus, when the temperature is increased from zero the rotators occupy higher rotational states which allow for more pronounced orientational ordering than that in the ground state. In these ordered states the attractive quadrupolar interaction is larger, resulting in a lower potential energy, and the kinetic energy increases strongly with rising temperature due to enhanced localization of the rotators along some direction. This scenario continues with rising temperature until maximum order is achieved. Further increase of temperature results in an increase of  $E_{\text{pot}}$  due to thermal disorder, making the quadrupolar interaction less important compared to the thermal energy. This can finally lead to a phase transition from the low temperature orientationally ordered phase to a high temperature disordered phase, provided the rotational constant does not exceed a certain value. At very low temperatures the slope of the total energy as a function of temperature, i.e., the specific heat, approaches zero, as expected for quantum systems. We did not find a strong size dependency of  $E_{\text{tot}}(T^*)$ , and thus the specific heat behavior also does not seem to depend on the system size.

Similar to the total energy, the average spread  $R_\varphi$ , which is a measure of the quantum mechanical delocalization of the rotators, is not dependent on system size, as shown in Fig. 15. As can be seen from its definition (47), this quantity is a single particle property that is, by construction, not particularly sensitive to collective effects. The spread approaches its classical limit, i.e., zero, for high temperatures, the approach being slower for larger  $\Theta^*$ . In the limit of low temperatures, it reaches a ground state value that is larger than  $90^\circ$  for the rotational constant  $\Theta^* = 0.6982$ , which means that an individual rotator is no longer confined to perform librational motion around a preferred orientation but is instead strongly delocalized. On the other hand, the order parameter is vanishingly small at low temperatures and decreases even more with increasing system size for this value of  $\Theta^*$ . The behavior of the average spread is thus a clear demonstration that it is the quantum tunneling which induces the disordering of the ground state for sufficiently large rotational constants.

In order to finally address the question whether our system has a re-entrant phase transition, as predicted by the mean-field study the low temperature region was analyzed by the cumulant intersection finite-size scaling method described in Sec. IV A. For the rotational constant  $\Theta^* = 0.6109$  an intersection point was found for both  $U_L^{(4)}$  and  $U_L^{(2)}$  at about  $T^* \approx 0.303$ . For the larger rotational constant  $\Theta^* = 0.6364$ , the intersections of the

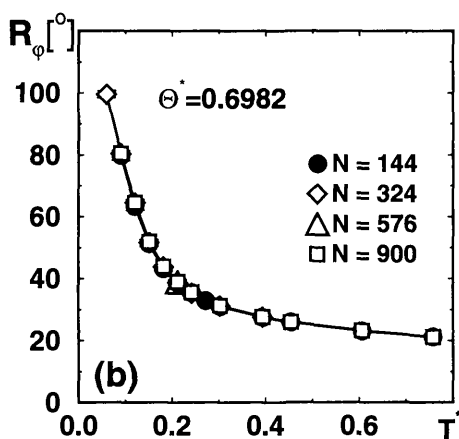
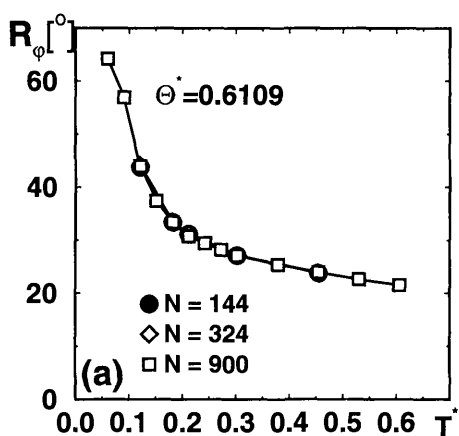


**FIG. 15** Average spread  $R_\phi$  in degrees as a function of temperature. The values of the rotational constants are: (a)  $\Theta^* = 0.6109$ , (b)  $\Theta^* = 0.6982$ . Symbols indicate different system sizes; lines are for visual help only. (Reprinted with permission from Ref. 328, Fig. 5. © 1997, American Physical Society.)

fourth- and second-order cumulants occur, again both at the same value within the error bars. These crossings arise because the cumulants for larger systems approach their limiting values faster than those for smaller systems. For  $\Theta^* = 0.6666$  the cumulants on the different length scales at low temperatures have values which cannot be distinguished within the error bars. The large value of  $U^* \approx 0.65$  that was found for the classical APR model [94,338] causes here the problem that, within our numerical accuracy

we cannot identify an intersection point but rather obtain a whole temperature region that is characterized by pronounced fluctuations. For larger  $\Theta^*$  constants the behavior of the two cumulants can again be distinguished fairly well. However, contrary to what we found for  $\Theta^* \leq 0.6364$ , the larger system has now the smaller cumulant throughout the whole temperature range. This signals the presence of the orientationally disordered phase for  $\Theta^* = 0.6982$  that extends from the ground state up to high temperatures. From this behavior of the cumulants we conclude that there is no evidence for the reentrance transition but rather a pronounced increase of short-range order at intermediate temperatures in the neighborhood of the phase boundary line. The latter has, at low temperatures, a roughly vertical (i.e.,  $\Theta^*$ -independent) slope, rather than the characteristic shape suggested by the mean-field result in Fig. 14.

In order to reinforce such conclusion for this part of the phase boundary we also studied the cumulants as functions of the rotational constant at constant temperature in the range  $T^* \leq 0.2424$ . The fourth-order cumulant plots show that the intersection occurs in this low temperature range at a value of about  $\Theta^* \approx 0.667 \pm 0.015$ , which stays constant within the numerical noise; the second-order cumulants  $U_L^{(2)}$  show the same behavior. Note that a systematic increase followed by a decrease of this quantity is expected as a function of temperature if reentrance does occur. We can furthermore infer that the non-trivial value  $U^*$  of the cumulants at crossing is also in this low temperature regime with pronounced tunneling and quantum effects, within the numerical accuracy identical to the value  $U^* \approx 0.65$  found for the classical APR phase transition [94,338]. We are thus lead to conclude that the APR transition temperature decreases slowly from its classical limit value of  $T^* \approx 0.76$  at  $\Theta^* = 0$  down to about  $T^* \approx 0.24$  at  $\Theta^* \approx 0.67$ , where it suddenly drops dramatically. This numerically obtained non-reentrant phase diagram is included in Fig. 14. The PIMC simulation results clearly exclude the existence of a strongly pronounced reentrant feature in the phase diagram. Of course, we cannot exclude the possible existence of a narrow reentrance region falling within the error bars of the present data. However, in any case these error bars are much smaller than the 20% decrease of the critical rotational constant predicted by the mean field theory. The latter approximation is successful in predicting the phenomenon of enhanced ordering at intermediate temperatures, but the deficiency is that it exaggerates the range of order and incorrectly predicts it to become long-ranged. As can be seen from Fig. 14, the mean-field theory apparently treats the quantum fluctuations (the limit  $T^* \rightarrow 0$ ) better than the thermal fluctuations (the limit  $\Theta^* \rightarrow 0$ ), since the transition point of the quantum induced transition is overestimated only by a factor of about 1.5, whereas the purely classical transition is out by a factor of more than 2.

## VI. CONCLUSIONS

Phase transitions in two-dimensional (adsorbed) layers have been reviewed. For the multicomponent Widom–Rowlinson model the minimum number of components was found that is necessary to stabilize the non-trivial “crystal phase.” The effect of elastic interaction on the structures of an alloy during the process of spinodal decomposition is analyzed and results in configurations similar to those found in experiments. Fluids and molecules adsorbed on substrate surfaces often have phase transitions at low temperatures where quantum effects have to be considered. Examples are layers of  $H_2$ ,  $D_2$ ,  $N_2$ , and CO molecules on graphite substrates. We review the PIMC approach to such phenomena, clarify certain experimentally observed “anomalies” in  $H_2$  and  $D_2$  layers and give predictions for the order of the  $N_2$  “herringbone” transition. Dynamical quantum phenomena in fluids are also analyzed via PIMC. Comparisons with the results of approximate analytical theories demonstrate the importance of the PIMC approach to phase transitions, where quantum effects play a role.

## ACKNOWLEDGMENTS

Discussions and cooperation with K. Binder, P. Fratzl, W. Helbing, M. O. Ihm, M. Kreer, J. L. Lebowitz, D. Löding, R. Martonak, D. Marx, A. Mazel, M. Müser, O. Opitz, V. Pereyra, M. Presber, M. Reuhl, C. Rickwardt, L. Samaj, F. Schmid, F. Schneider, S. Sengupta, H. Wiechert, N. Wilding and support from the DFG (Heisenberg Fellowship) are gratefully acknowledged as well as the granting of computer time on the Cray-T90 and the Cray-T3E (HLRZ Jülich, HLRS Stuttgart and RHRK Kaiserslautern).

## REFERENCES

1. H. P. R Frederikse. *Physica* 15:860, 1949.
2. M. F. M. Osborne. *Phys Rev* 76:296, 1949.
3. W. Band. *Phys Rev* 76:441, 1949.
4. G. A. Stewart, J. G. Dash. *Phys Rev Lett* 26:918, 1970.
5. A. Thomy, X. Duval. *J Chim Phys* 66:1966, 1969.
6. M. Bretz, J. G. Dash. *Phys Rev Lett* 26:963, 1971.
7. M. Bretz, J. G. Dash, D. C. Hickernell, E. O. McLean, O. E. Vilches. *Phys Rev A* 8:1589, 1973.
8. S. Ostlund, A. N. Berker. *Phys Rev Lett* 42:843, 1979; *Phys Rev B* 21:5410, 1980.
9. M. Schick. *Progr Surf Sci* 11:245, 1981.
10. S. Alexander. *Phys Lett A* 54:353, 1975.

11. F. Y. Wu. *Rev Mod Phys* 54:235, 1982.
12. R. J. Baxter. *Exactly Solved Models in Statistical Mechanics*. London: Academic, 1982.
13. S. K. Sinha, ed. *Ordering in Two Dimensions*. Amsterdam: North-Holland, 1980.
14. C. Domb, J. L. Lebowitz, eds. *Phase Transitions and Critical Phenomena, Vol. 11*. London: Academic, 1987.
15. M. Kreer, P. Nielaba. In: K. Binder, G. Ciccotti, eds. *Monte Carlo and Molecular Dynamics of Condensed Matter Systems*. Bologna: SIF, 1996, p. 501.
16. M. Kreer, P. Nielaba. In: D. P. Landau, K. K. Mon, H. B. Schüttler, eds. *Computer Simulation Studies in Condensed Matter Physics IX*. Berlin: Springer, 1997, p. 111.
17. D. Marx, H. Wiechert. *Adv Chem Phys* 95:213, 1996.
18. H. Taub, G. Torzo, H. J. Lauter, S. C. Fain Jr, eds. *Phase Transitions in Surface Films 2*. New York: Plenum, 1991.
19. A. F. G. Wyatt, H. J. Lauter, eds. *Excitations in 2-D and 3-D Quantum Fluids*. New York: Plenum, 1991.
20. J. G. Dash. *Films on Solid Surfaces*. New York: Academic Press, 1974.
21. J. G. Dash. *Phys Rep C* 38:177, 1978.
22. K. J. Strandburg, ed. *Bond Orientational Order in Condensed Matter Systems*. New York: Springer, 1992.
23. K. J. Strandburg. *Rev Mod Phys* 60:161, 1988; 61:747, 1989.
24. C. J. Wright, C. M. Sayers. *Rep Prog Phys* 46:773, 1983.
25. R. K. Thomas. *Prog Solid State Chem* 14:1, 1982.
26. J. G. Dash, J. Ruvalds, eds. *Phase Transitions in Surface Films*. New York: Plenum, 1980.
27. N. D. Shrimpton, M. W. Cole, W. A. Steele, M. H. W. Chan. In: G. Benedek, ed. *Surface Properties of Layered Structures*. Dordrecht: Kluwer Academic, 1992, p. 219.
28. E. Bauer, T. Engel. *Surf Sci* 71:695, 1978.
29. E. Bauer, H. Poppa. *Surf Sci* 88:31, 1979; 127, 243, 1983.
30. E. Bauer, H. Poppa, Y. Viswanath. *Surf Sci* 58:58, 1976.
31. J. P. Biberian, M. Huber. *Surf Sci* 55:259, 1976.
32. M. A. Chesters, J. Pritchard. *Surf Sci* 28:460, 1971.
33. M. A. Chesters, M. Hussain, J. Pritchard. *Surf Sci* 35:161, 1973.
34. J. M. Dickey, H. H. Farrell, M. Strongin. *Surf Sci* 23:448, 1970.
35. A. Glachant, M. Jaubert, M. Bienfait, G. Boato. *Surf Sci* 115:219, 1981.
36. A. Glachant, M. Bienfait, M. Jaubert. *Surf Sci Lett* 148:L665, 1984.
37. J. Küppers, F. Nitchke, K. Wandelt, G. Ertl. *Surf Sci* 87:295, 1979.
38. E. R. Moog, M. B. Webb. *Surf Sci* 148:338, 1984.
39. P. W. Palmberg. *Surf Sci* 25:598, 1971.
40. H. Pfnür, D. Menzel. *Surf Sci* 148:411, 1984.
41. T. T. Chung, J. G. Dash. *Surf Sci* 66:559, 1977.
42. R. Marx, E. F. Wassermann. *Surf Sci* 117:267, 1982.
43. J. Regnier, A. Thomy, X. Duval. *J Coll Interf Sci* 70:105, 1979.

44. J. Suzanne, M. Bienfait. *J Phys (Paris)* 38:93, 1977.
45. J. A. Venables, J. L. Sequin, J. Suzanne, M. Bienfait. *Surf Sci* 145:345, 1984.
46. P. Vora, S. K. Sinha, R. K. Crawford. *Phys Rev Lett* 43:704, 1979.
47. J. P. Coulomb, T. S. Sullivan, O. E. Vilches. *Phys Rev B* 30:4753, 1984.
48. A. Enault, Y. Larher. *Surf Sci* 62:233, 1977.
49. J. Heidberg, E. Kampshoff, R. Kühnemuth, O. Schönekas. *Surf Sci* 269/270:120, 1992.
50. J. Heidberg, E. Kampshoff, R. Kühnemuth, M. Suhren, H. Weiss. *Surf Sci* 269/270:128, 1992.
51. J. L. Jourdan, J. P. McTague, J. B. Hastings, L. Pasell. *Surf Sci Lett* 150:L82, 1985.
52. M. Matecki, A. Thomy, X. Duval. *J Chem Phys* 71:1484, 1974.
53. K. Morishige, S. Kittaka, T. Morimoto. *Surf Sci* 148:401, 1984.
54. Y. Nardon, Y. Larher. *Surf Sci* 42:299, 1974.
55. D. Scarano, A. Zecchina. *J Chem Soc Faraday Trans I* 82:3611, 1986.
56. D. Schmickler, J. P. Toennies, R. Vollmer, H. Weiss. *J Chem Phys* 95:9412, 1991.
57. M. Sidoumon, T. Angot, J. Suzanne. *Surf Sci* 272:347, 1992.
58. A. Thomy, X. Duval, J. Regnier. *Surf Sci Rep* 1:1, 1981.
59. A. Patrykiewicz. *Thin Solid Films* 81:89, 1981; 88:359, 1982.
60. A. Patrykiewicz, S. Sokolowski, T. Zientarski, K. Binder. *J Chem Phys* 102:8221, 1995.
61. M. Borowko, W. Rzyso. *J Colloid Interf Sci* 182:268, 1995.
62. F. F. Abraham. *Phys Rev Lett* 44:463, 1980.
63. F. F. Abraham. *Phys Rep* 80:339, 1981.
64. F. F. Abraham. *Phys Rev B* 29:2606, 1984.
65. F. F. Abraham. *Adv Phys* 35:1, 1986.
66. A. N. Berker, S. Ostlund, F. A. Putnam. *Phys Rev B* 17:3650, 1978.
67. L. W. Bruch. *Surf Sci* 150:503, 1985.
68. L. W. Bruch, J. M. Phillips. *Surf Sci* 91:1, 1980.
69. L. W. Bruch, J. A. Venables. *Surf Sci* 148:167, 1984.
70. S. Calisti, J. Suzanne, J. A. Venables. *Surf Sci* 115:455, 1982.
71. J. Villain, M. B. Gordon. *Surf Sci* 125:1, 1983.
72. D. K. Fairbent, F. W. Saam, L. M. Sander. *Phys Rev B* 26:179, 1982.
73. J. M. Gottlieb, L. W. Bruch. *Phys Rev B* 44:5759, 1991.
74. P. A. Heiney, P. W. Stephans, R. J. Birgeneau, P. M. Horn, D. E. Moncton. *Phys Rev B* 28:6416, 1983.
75. P. A. Heiney, P. W. Stephans, R. J. Birgeneau, P. M. Horn, D. E. Moncton. *Phys Rev B* 28:6416, 1983.
76. J. M. Houldrik, D. P. Landau. *Phys Rev B* 44:8962, 1991.
77. H.-Y. Kim, M. W. Cole. *Surf Sci* 194:257, 1988.
78. H.-Y. Kim, W. A. Steele. *Phys Rev B* 45:6226, 1992.
79. S. W. Koch, F. F. Abraham. *Phys Rev B* 27:2964, 1983.
80. K. J. Niskanen. *Phys Rev B* 33:1830, 1986.
81. A. D. Novaco, J. P. McTague. *Phys Rev Lett* 38:1286, 1977.

82. A. D. McLachlan. *Mol Phys* 7:381, 1964.
83. J. P. McTague, A. D. Novaco. *Phys Rev B* 19:5299, 1979.
84. J. P. McTague, J. Als-Nielsen, J. Bohr, M. Nielsen. *Phys Rev B* 25:7765, 1982.
85. D. E. Taylor, E. D. Williams, R. L. Park, N. C. Bartelt, T. L. Einstein. *Phys Rev B* 32:4653, 1985.
86. E. Vives, P.-A. Lindgard. *Surf Sci* 284:L449, 1993.
87. E. Vives, P.-A. Lindgard. *Phys Rev B* 44:1318, 1991.
88. E. Vives, P.-A. Lindgard. *Phys Rev B* 47:7431, 1991.
89. Q. M. Zhang, H. K. Kim, M. H. W. Chan. *Phys Rev B* 33:5149, 1986.
90. F. F. Abraham, J. Q. Broughton. *Phys Rev Lett* 59:64, 1987.
91. F. F. Abraham, J. Q. Broughton, P. W. Leung, V. Elser. *Europhys Lett* 12:107, 1990.
92. M. C. Gordillo, D. M. Ceperley. *Phys Rev Lett* 79:3010, 1997.
93. M. H. W. Chan, A. D. Migone, K. D. Miner, Z. R. Li. *Phys Rev B* 30:2681, 1984.
94. O. Opitz, D. Marx, S. Sengupta, P. Nielaba, K. Binder. *Surf Sci* 297:L122, 1993.
95. D. Marx, O. Opitz, P. Nielaba, K. Binder. *Phys Rev Lett* 70:2908, 1993.
96. D. Marx, S. Sengupta, P. Nielaba. *J Chem Phys* 99:6031, 1993.
97. D. Marx, S. Sengupta, P. Nielaba, K. Binder. *Phys Rev Lett* 72:262, 1994.
98. D. Marx, S. Sengupta, P. Nielaba, K. Binder. *Surf Sci* 321:195, 1994.
99. V. Pereyra, P. Nielaba, K. Binder. *J Phys: Condensed Matter* 5:6631, 1993.
100. H. Wiechert, St-A. Arlt. *Phys Rev Lett* 71:2090, 1993.
101. Y. Imry, S. K. Ma. *Phys Rev Lett* 35:1399, 1975.
102. K. Binder. *Z Phys B* 50:343, 1983.
103. S. Fishman, A. Aharony. *J Phys C: Solid State Phys* 12:L729, 1979.
104. M. Nielsen, J. P. McTague, W. Ellenson. *J Phys Suppl* 47:582, 1977.
105. J. Cui, S. C. Fain, H. Freimuth, H. Wiechert, H. P. Schildberg, H. J. Lauter. *Phys Rev Lett* 60:1848, 1988.
106. H. Wiechert. *Physica B* 169:144, 1991.
107. H. Freimuth, H. Wiechert. *Surf Sci* 178:716, 1986.
108. H. Freimuth, H. Wiechert, H. P. Schildberg, H. J. Lauter. *Phys Rev B* 42:587, 1990.
109. H. Wiechert, K. D. Kortmann. *J Low Temp Phys* 111:561, 1998.
110. M. Kree. PhD thesis, Mainz, Germany, 1996.
111. R. Car, M. Parrinello. *Phys Rev Lett* 55:2471, 1985.
112. G. Pastore, E. Smargiassi, F. Buda. *Phys Rev A* 44:6334, 1991.
113. G. Galli, A. Pasquarello. In: M. P. Allen, D. J. Tildesley, eds. *Computer Simulation in Chemical Physics*. Dordrecht: NATO-ASI series 397, Kluwer Academic, 1993, p. 261.
114. P. Hohenberg, W. Kohn. *Phys Rev B* 136:864, 1964.
115. W. Kohn, P. Vashishta. In: S. Lundqvist, N. H. March, eds. *Theory of the Inhomogeneous Electron Gas*. New York: Plenum, 1983, p. 79.
116. W. Kohn, L. J. Sham. *Phys Rev A* 140:1133, 1965.

117. G. Galli, R. M. Martin, R. Car, M. Parrinello. *Phys Rev Lett* 62:555, 1989; *Phys Rev Lett* 63:988, 1989; *Phys Rev B* 42:7470, 1990; *Science* 250:1547, 1990.
118. F. Buda, G. Chiarotti, R. Car, M. Parrinello. *Phys Rev B* 44:5908, 1991.
119. R. Car, M. Parrinello. *Phys Rev Lett* 60:204 1988.
120. I. Stich, R. Car, M. Parrinello. *Phys Rev Lett* 63:2240, 1989; *Phys Rev B* 44:11092, 1991.
121. A. Pasquarello, K. Laasonen, R. Car, C. Lee, D. Vanderbilt. *Phys Rev Lett* 69:1982, 1992.
122. F. Ancilotto, W. Andreoni, A. Selloni, R. Car, M. Parrinello. *Phys Rev Lett* 65:3148, 1990.
123. F. Ancilotto, A. Selloni, W. Andreoni, S. Baroni, R. Car, M. Parrinello. *Phys Rev B* 43:8930, 1991.
124. F. Ancilotto, A. Selloni, E. Tosatti. *Phys Rev B* 43:5180, 1991; *Phys Rev B* 43:14726, 1991.
125. F. Ancilotto, A. Selloni. *Phys Rev Lett* 68:2640, 1991.
126. S. Iarlorigi, G. Galli, F. Gygi, M. Parrinello, E. Tosatti. *Phys Rev Lett* 69:2947, 1992.
127. I. Moullet, W. Andreoni, M. Parrinello. *Phys Rev B* 46:1842, 1992.
128. N. Takeuchi, A. Selloni, E. Tosatti. *Phys Rev Lett* 69:648, 1991.
129. D. Hohl, R. O. Jones, R. Car, M. Parrinello. *Chem Phys Lett* 139:540, 1987; *J Chem Phys* 89:6823, 1988.
130. P. Ballone, W. Andreoni, R. Car, M. Parrinello. *Europhys Lett* 8:73, 1989; *Phys Rev Lett* 60:271, 1988.
131. U. Roethlisberger, W. Andreoni. *J Chem Phys* 94:8129, 1991.
132. B. Fueston, W. Andreoni, E. Clementi, M. Parrinello. *Phys Rev B* 44:4056, 1991.
133. W. Andreoni, F. Gygi, M. Parrinello. *Chem Phys Lett* 189:241, 1992.
134. M. E. Tuckerman, T. von Rosenvinge, M. L. Klein. *Mater Res Soc Symp Proc* 408:477, 1996.
135. P. Ruggerone, C. Ratsch, M. Scheffler. In: D. A. King, D. P. Woodruff, eds. *Growth and Properties of Ultrathin Epitaxial Layers*. Amsterdam: Elsevier, 1997.
136. B. Hammer, M. Scheffler, K. W. Jacobsen, J. K. Norskov. *Phys Rev Lett* 73:1400, 1994.
137. B. Hammer, M. Scheffler. *Phys Rev Lett* 74:3487, 1995.
138. B. D. Yu, M. Scheffler. *Phys Rev Lett* 77:1095, 1996.
139. R. Stumpf, M. Scheffler. *Comp Phys Commun* 79:447, 1994.
140. M. Bockstedte, A. Kley, J. Neugebauer, M. Scheffler. *Comp Phys Commun* 107:187, 1997.
141. F. H. Stillinger, T. A. Weber. *Phys Rev B* 31:5262, 1985.
142. M. Sprik. In: M. P. Allen, D. J. Tildesley, eds. *Computer Simulation in Chemical Physics*. Dordrecht: NATO-ASI series 397, Kluwer Academic, 1993, p. 211.



143. R. D. Etters, V. Chandrasekharan, E. Uzan, K. Kobashi. *Phys Rev B* 33:8615, 1986.
144. J. Belak, R. Le Sar, R. D. Etters. *J Chem Phys* 89:1625, 1988.
145. B. Kuchta, K. Rohleder, R. D. Etters, J. Belak. *J Chem Phys* 102:3349, 1995.
146. W. A. Steele. *Surf Sci* 36:317, 1973.
147. W. A. Steele. *The Interaction of Gases with Solid Surfaces*. London: Pergamon, 1974.
148. W. A. Steele. *J Phys Chem* 82:817, 1978.
149. K. Binder, ed., *Applications of the Monte Carlo Method in Statistical Physics*. Berlin: Springer, 1984.
150. M. P. Allen, D. J. Tidesley. *Computer Simulation of Liquids*. Oxford: Clarendon, 1987.
151. K. Binder, D. W. Heermann. *Monte Carlo Simulation in Statistical Physics. Springer Series in Solid State Sciences, Vol. 80*. Berlin: Springer, 1988.
152. D. Stauffer, ed. *Annual Reviews of Computational Physics I-IV*. Singapore: World Scientific, 1994-96.
153. K. Binder, G. Ciccotti, eds. *Monte Carlo and Molecular Dynamics of Condensed Matter Systems*. Bologna: Societa Italiana di Fisica, 1996.
154. K. Binder, D. P. Landau. *Adv Chem Phys* 76:91, 1989.
155. O. G. Mouritsen. *Computer Studies of Phase Transitions and Critical Phenomena*. Berlin: Springer, 1984.
156. J. A. Barker. *J Chem Phys* 70:2914, 1979.
157. K. S. Schweizer, R. M. Stratt, D. Chandler, P. G. Wolynes. *J Chem Phys* 75:1347, 1981.
158. D. Chandler, P. G. Wolynes. *J Chem Phys* 74:4078, 1981.
159. B. J. Berne, D. Thirumalai. *Annu Rev Phys Chem* 37:401, 1986.
160. M. Suzuki, ed. *Quantum Monte Carlo Methods. Springer Series in Solid State Sciences. Vol. 74*. New York: Springer, 1987.
161. J. D. Doll, J. E. Gubernatis, eds. *Quantum Simulation of Condensed Matter Phenomena*. Singapore: World Scientific, 1990.
162. K. E. Schmidt, D. M. Ceperley. In: K. Binder, ed. *The Monte Carlo Method in Condensed Matter Physics. Topics in Applied Physics, Vol. 71*. Berlin, Heidelberg: Springer, 1992.
163. M. J. Gillan. In: C. R. A. Catlow, S. C. Parker, M. P. Allen, eds. *Computer Modeling of Fluids, Polymers and Solids*. Dordrecht: Kluwer, 1990.
164. D. Chandler. In: J. P. Hansen, D. Levesque, J. Zinn-Justin, eds. *Liquids, Freezing and Glass Transition*. Amsterdam: Elsevier, 1991.
165. D. M. Ceperley. *Rev Mod Phys* 67:279, 1995.
166. P. Nielaba. In: D. Stauffer, ed. *Annual Reviews of Computational Physics V*. Singapore: World Scientific, 1997.
167. J. E. Gubernatis, M. Jarrell, R. N. Silver, D. S. Sivia. *Phys Rev B* 44:6011, 1991.
168. R. N. Silver, D. S. Sivia, J. E. Gubernatis. *Phys Rev B* 41:2380, 1990.
169. M. Jarrell, J. E. Gubernatis. *Phys Rep* 269:133, 1996.
170. E. Gallicchio, B. Berne. *J Chem Phys* 101:9909, 1994.

171. C. H. Mak, D. Chandler. *Phys Rev A* 41:5709, 1990.
172. V. S. Filinov, Y. V. Medvedev, V. L. Kamskyi. *Mol Phys* 85:711, 1995.
173. V. S. Filinov, Y. E. Lozovik, A. M. Oparin. *Physica Scripta* 58:297, 1998; 58:304, 1998.
174. V. S. Filinov. *Mol Phys* 88: 1517, 1996; 88:1529, 1996.
175. F. Schneider, P. Nielaba. *Phys Rev E* 54:5826, 1996.
176. P. Nielaba, J. L. Lebowitz, H. Spohn, J. L. Valles. *J Stat Phys* 55:745, 1989.
177. V. Privman, ed. *Finite Size Scaling and Numerical Simulation*. Singapore: World Scientific, 1990.
178. M. N. Barber. In: C. Domb, J. L. Lebowitz, eds. *Phase Transitions and Critical Phenomena* 8. London: Academic, 1983.
179. K. Binder. *Ferroelectrics* 73:43, 1987.
180. K. Binder. *Z Phys B* 43:119, 1981.
181. K. Binder. *Phys Rev Lett* 47:693, 1981.
182. H. P. Deutsch. *J Stat Phys* 67:1039, 1992.
183. H. P. Deutsch, K. Binder. *Macromolecules* 25:6214, 1992.
184. K. Vollmayr, J. D. Reger, M. Scheucher, K. Binder. *Z Phys B* 91:113, 1993.
185. B. Widom, J. S. Rowlinson. *J Chem Phys* 52:1670, 1970.
186. D. Ruelle. *Phys Rev Lett* 27: 1040, 1971.
187. J. L. Lebowitz, E. H. Lieb. *Phys Lett A* 39:98, 1972.
188. J. Bricmont, K. Kuroda, J. L. Lebowitz. *Z Wahrscheinlichkeitstheor Verw Geb* 67:121, 1984.
189. L. K. Runnels, J. L. Lebowitz. *J Math Phys* 15:1712, 1974.
190. J. L. Lebowitz, A. Mazel, P. Nielaba, L. Šamaj. *Phys Rev E* 52:5985, 1995.
191. P. Nielaba, J. L. Lebowitz. *Physica A* 244:278, 1997.
192. A. Z. Panagiotopoulos. *Mol Phys* 61:813, 1987; *Mol Simul* 9:1, 1992.
193. F. Schneider, M. O. Ihm, P. Nielaba. In: D. P. Landau, K. K. Mon, H. B. Schüttler, eds. *Computer Simulation Studies in Condensed Matter Physics VII*. Berlin: Springer, 1994, p. 188.
194. M. O. Ihm, F. Schneider, P. Nielaba. *Progr Colloids and Polymer Science* 104:166, 1997.
195. T. W. Melnyk, B. L. Sawford. *Mol Phys* 29:891, 1975.
196. J. W. Cahn. *Acta Metall* 9:795, 1961; 10:179, 1962.
197. A. B. Bortz, M. H. Kalos, J. L. Lebowitz, M. H. Zendejas. *Phys Rev B* 10:535, 1974.
198. J. Marro, A. B. Bortz, M. H. Kalos, J. L. Lebowitz. *Phys Rev B* 12:2000, 1975.
199. J. D. Gunton, M. San Miguel, P. S. Sahni. In: C. Domb, J. L. Lebowitz, eds. *Phase Transitions and Critical Phenomena, Vol. 8*, New York: Academic Press, 1983.
200. K. Binder. In: P. Haasen, ed. *Materials Science and Technology, Vol. 5*. Weinheim: VCH, 1991, Chap. 7.
201. R. Wagner, R. Kampmann. In: P. Haasen, ed. *Phase Transformations in Materials, Vol. 5*. Weinheim: VCH, 1991, Chap. 4.
202. A. G. Khachaturyan. *Theory of Structural Transformations in Solids*. New York: Wiley, 1983.

203. J. Marro, J. L. Lebowitz, M. H. Kalos. *Phys Rev Lett* 43:282, 1979.
204. J. L. Lebowitz, J. Marro, M. H. Kalos. *Acta Metall* 30:297, 1982.
205. P. Fratzl, J. L. Lebowitz, J. Marro, M. H. Kalos. *Acta Metall* 31:1849, 1983.
206. I. M. Lifshitz, V. V. Slyozov. *J Phys Chem Solids* 19:35, 1961.
207. C. Wagner. *Z Elektrochem* 65:581, 1961.
208. P. Fratzl, J. L. Lebowitz, O. Penrose, J. Amar. *Phys Rev B* 44:4794, 1991.
209. P. Fratzl, J. L. Lebowitz. *Acta Metall* 37:3245, 1989.
210. V. I. Goretsveig, P. Fratzl, J. L. Lebowitz. *Phys Rev* 55:2912, 1997.
211. J. K. Tien, S. M. Copley. *Metall Trans* 2:215, 1971.
212. For a recent short review see, e.g., S. Socrate, D. M. Parks. *Acta Metall Mater* 41:2185, 1993.
213. Linear elastic models for rafting are reviewed in: J. C. Chang, S. M. Allen. *J Mater Res* 6:1843, 1991.
214. T. Miyazaki, K. Nakamura, H. Mori. *J Mater Sci* 14:1827, 1979.
215. M. V. Nathal, R. A. MacKay, R. V. Miner. *Metall Trans A* 20:133, 1989.
216. M. Feller-Kniepmeier, T. Link. *Metall Trans A* 20:1233, 1989.
217. C. Carry, J. L. Strudel. *Acta Metall* 25:767, 1977; 26:859, 1978.
218. T. M. Pollock, A. S. Argon. *Acta Metall Mater* 42:1859, 1994.
219. J. Y. Buffiere, M. Ignat. *Acta Metall Mater* 43:1791, 1995.
220. O. Paris, M. Fährmann, E. Fährmann, T. M. Pollock, P. Fratzl. *Acta Mater* 45:1085, 1997.
221. T. Miyazaki, M. Doi, T. Kozaki. *Solid State Phen* 3:158, 1988.
222. T. Miyazaki, M. Doi. *Mater Sci Eng A* 110:175, 1989.
223. A. Maheshwari, A. J. Ardell. *Phys Rev Lett* 70:2305, 1993.
224. O. Paris, M. Fährmann, P. Fratzl. *Phys Rev Lett* 75:3458, 1995.
225. A. D. Sequeira, H. A. Calderon, G. Kostorz, J. A. Pedersen. *Acta Metall Mater* 43:3427, 1995; 43:3441, 1995.
226. M. Fährmann, P. Fratzl, O. Paris, E. Fährmann, W. C. Johnson. *Acta Metall Mater* 43:1007, 1995.
227. P. Fratzl, F. Langmayr, G. Vogl, W. Miekeley. *Acta Metall Mater* 39:753, 1991.
228. F. Langmayr, P. Fratzl, G. Vogl, W. Miekeley. *Phys Rev B* 49:11759, 1994.
229. J. D. Eshelby. *Prog Solid Mech* 2:89, 1961.
230. A. J. Ardell, R. B. Nicholson, J. D. Eshelby. *Acta Metall* 14:1295, 1966.
231. A. Onuki, H. Nishimori. *Phys Rev B* 43:13649, 1991.
232. H. Nishimori, A. Onuki. *Phys Rev B* 42:980, 1990.
233. Y. Wang, L. Q. Chen, A. G. Khachaturyan. *Acta Metall Mater* 41:279, 1993.
234. Y. Wang, A. G. Khachaturyan. *Acta Metall Mater* 43:1837, 1995.
235. Y. Wang, A. G. Khachaturyan. *Scripta Metall Mater* 31:1425, 1994.
236. W. C. Johnson. *Acta Metall* 32:465, 1984.
237. T. A. Abinandanan, W. C. Johnson. *Acta Metall Mater* 41:17, 1993.
238. P. W. Voorhees, G. B. McFadden, W. C. Johnson. *Acta Metall Mater* 40:2979, 1992.
239. K. Kawasaki, Y. Enomoto. *Physica A* 150:463, 1988.

- 240. Y. Enomoto, K. Kawasaki. *Acta Metall* 37:1399, 1989.
- 241. P. Fratzl, O. Penrose. *Acta Metall Mater* 43:2921, 1995.
- 242. P. Fratzl, O. Penrose. *Acta Mater* 44:3227, 1996.
- 243. C. L. Laberge, P. Fratzl, J. L. Lebowitz. *Phys Rev Lett* 75:4448, 1995.
- 244. C. L. Laberge, P. Fratzl, J. L. Lebowitz. *Acta Mater* 45:3949, 1997.
- 245. W. A. Soffa, D. E. Laughlin. *Acta Metall* 37:3019, 1989.
- 246. A. Pineau. *Acta Metall* 24:559, 1976.
- 247. W. C. Johnson, M. B. Birkenpas, D. E. Laughlin. *Acta Metall* 36:3149, 1988.
- 248. C. Sagui, A. M. Somoza, R. C. Desai. *Phys Rev E* 50:4865, 1994.
- 249. J. Gayda, D. J. Srolovitz. *Acta Metall* 37:641, 1989.
- 250. A. G. Khachaturyan. *Soviet Phys Crystallogr* 10:256, 1965.
- 251. H. E. Cook, D. DeFontaine. *Acta Metall* 17:915, 1969.
- 252. P. Nielaba, P. Fratzl, J. L. Lebowitz. *J Stat Phys* 95:23, 1999.
- 253. R. P. Feynman, A. R. Hibbs. *Quantum Mechanics and Path Integrals*. New York: McGraw-Hill, 1965.
- 254. R. P. Feynman. *Statistical Mechanics*. Reading, MA: Addison-Wesley, 1972.
- 255. H. F. Trotter. *Proc Am Math Soc* 10:545, 1959.
- 256. M. Suzuki. *Prog Theor Phys* 46:1337, 1971; *Commun Math Phys* 51:183, 1976.
- 257. L. S. Schulman. *Techniques and Applications of Path Integration*. New York: Wiley, 1981.
- 258. H. Kleinert. *Path Integrals in Quantum Mechanics, Statistics and Polymer Physics*. Singapore: World Scientific, 1990.
- 259. M. H. Müser. *Mol Simul* 17:131, 1996.
- 260. M. Presber, D. Löding, R. Martonak, P. Nielaba. *Phys Rev B* 58:11937, 1998.
- 261. R. Giachetti, V. Tognetti. *Phys Rev Lett* 55:912, 1985; *Phys Rev B* 33:7647, 1986.
- 262. R. Feynman, H. Kleinert. *Phys Rev A* 34:5080, 1986.
- 263. A. Cuccoli, R. Giachetti, V. Tognetti, R. Vaia, P. Verruchi. *J Phys: Condensed Matter* 7:7891, 1995.
- 264. M. H. Kalos, M. A. Lee, P. A. Whitlock, G. V. Chester. *Phys Rev B* 24:115, 1981.
- 265. M. H. Kalos, D. Levesque, L. Verlet. *Phys Rev A* 9:2178, 1974.
- 266. B. J. Alder, D. M. Ceperley, E. L. Pollock. *Acc Chem Res* 18:268, 1985.
- 267. D. M. Ceperley, B. J. Alder. *Science* 231:555, 1986.
- 268. D. M. Ceperley, M. H. Kalos. In: K. Binder, ed. *Monte Carlo Methods in Statistical Physics*. Heidelberg: Springer, 1979, p. 145.
- 269. P. Grüter, D. Ceperley, F. Laloë. *Phys Rev Lett* 79:3549, 1997.
- 270. E. L. Pollock, K. J. Runge. *Phys Rev B* 46:3535, 1992.
- 271. E. L. Pollock, D. M. Ceperley. *Phys Rev B* 36:8343, 1987.
- 272. J. Cao, B. J. Berne. *J Chem Phys* 97:2382, 1992.
- 273. K. J. Runge, G. V. Chester. *Phys Rev B* 38:135, 1988.
- 274. R. P. Feynman. *Phys Rev* 90:1116, 1953; 91:1291, 1953; 94:262, 1954.
- 275. S. Giorgini, L. Pitaevskii, S. Stringari. *Phys Rev A* 54:R4633, 1996.

- 276. W. Krauth. *Phys Rev Lett* 77:3695, 1996.
- 277. R. H. Torii, H. J. Maris, G. M. Seidel. *Phys Rev B* 41:7161, 1990.
- 278. J. DeKinder, A. Bouwen, D. Schoemaker. *Phys Rev B* 52:15872, 1995.
- 279. D. F. Brewer, J. C. N. Rajendra, A. L. Thomson. *J Low Temp Phys* 101:317, 1995.
- 280. M. Schindler, A. Dertinger, Y. Kondo, F. Pobell. *Phys Rev B* 53:11451, 1996.
- 281. P. E. Sokol, R. T. Azuah, M. R. Gibbs, S. M. Bennington. *J Low Temp Phys* 103:23, 1996.
- 282. O. E. Vilches. *J Low Temp Phys* 89:267, 1992.
- 283. H. Wiechert. In: A. G. F. Wyatt, H. J. Lauter, eds. *Excitations in Two-Dimensional and Three-Dimensional Quantum Fluids*. New York: Plenum Press, 1991.
- 284. F. C. Lui, Y. M. Lui, O. E. Vilches. *Phys Rev B* 51:2848, 1995.
- 285. I. F. Silvera, V. V. Goldman. *J Chem Phys* 69:4209, 1978.
- 286. M. Wagner, D. M. Ceperley. *J Low Temp Phys* 89:581, 1992; 102:275, 1996.
- 287. D. M. Ceperley, E. L. Pollock. *Phys Rev Lett* 56:351, 1986; *Can J Phys* 65:1416, 1987; *Phys Rev B* 39:2084, 1989.
- 288. M. H. Müser, P. Nielaba, K. Binder. *Phys Rev B* 51:2723, 1995.
- 289. H. Klee, K. Knorr. *Phys Rev B* 42:3152, 1990; 43:8658, 1991.
- 290. D. Löding, M. H. Müser, P. Nielaba. *Z Phys B* 102:505, 1997.
- 291. M. H. Müser, D. Löding, P. Nielaba, K. Binder. *Ferroelectrics* 208:293, 1998.
- 292. Chr. Rickwardt. PhD thesis, Mainz, Germany 1998; Chr. Rickwardt, P. Nielaba, K. Binder (preprint); Chr. Rickwardt, P. Nielaba (in preparation).
- 293. R. M. Stratt. *J Chem Phys* 80:5764, 1984.
- 294. S. G. Desjardins, R. M. Stratt. *J Chem Phys* 81:6232, 1984.
- 295. P. Ballone, P. de Smedt, J. L. Lebowitz, J. Talbot, E. Waisman. *Phys Rev A* 35:942, 1987.
- 296. P. de Smedt, P. Nielaba, J. L. Lebowitz, J. Talbot, L. Dooms. *Phys Rev A* 38:1381, 1988.
- 297. D. Marx, P. Nielaba, K. Binder. *Phys Rev Lett* 67:3124, 1991; *Phys Rev B* 47:7788, 1993.
- 298. S. Sengupta, D. Marx, P. Nielaba. *Europhys Lett* 20:383, 1992.
- 299. A. C. Mitus, D. Marx, S. Sengupta, P. Nielaba, A. Z. Patashinskii, H. Hahn. *J Phys Condensed Matter* 5:8509, 1993.
- 300. F. Schneider, D. Marx, P. Nielaba. *Phys Rev E* 51:5162, 1995.
- 301. M. J. P. Nijmeijer, J. J. Weis. In: D. Stauffer, ed. *Annual Reviews of Computational Physics IV*. Singapore: World Scientific, 1996, p. 1.
- 302. N. B. Wilding. In: D. Stauffer, ed. *Annual Reviews of Computational Physics IV*. Singapore: World Scientific, 1996, p.37.
- 303. N. B. Wilding, P. Nielaba. *Phys Rev E* 53:926, 1996.
- 304. P. Nielaba, S. Sengupta. *Phys Rev E* 55:3754, 1997.
- 305. N. B. Wilding, F. Schmid, P. Nielaba. *Phys Rev E* 58:2201, 1998.
- 306. T. V. Ramakrishnan, M. Yussouff. *Phys Rev B* 19:2775, 1979.
- 307. A. D. J. Haymet, D. J. Oxtoby. *J Chem Phys* 74:2559, 1981.

- 308. M. Baus. *J Phys: Condensed Matter* 2:2111, 1990; *J Stat Phys* 48:1129, 1987; *J Condens Matter* 1:3131, 1989.
- 309. A. D. J. Haymet. *Prog Solid State Chem* 17:1, 1986.
- 310. D. W. Oxtoby. In: J. P. Hansen, D. Levesque, J. Zinn-Justin, eds. *Liquids, Freezing and the Glass Transition—Les Houches Session LI*. Amsterdam: North-Holland, 1991.
- 311. Y. Singh. *Phys Rep* 207:351, 1991.
- 312. A. R. Denton, N. W. Ashcroft. *Phys Rev A*, 39:4701, 1989.
- 313. T. V. Ramakrishnan. *Phys Rev Lett* 48:541, 1982.
- 314. C. Ebner, H. R. Krishnamurthy, R. Pandit. *Phys Rev A* 43:4355, 1990.
- 315. Y. Rosenfeld. *Phys Rev A* 42:5983, 1990.
- 316. R. Kubo, M. Toda, N. Hashitsume. *Statistical Physics II*. Berlin: Springer, 1985.
- 317. X. Z. Ni, L. W. Bruch. *Phys Rev B* 33:4584, 1986.
- 318. C. S. Murthy, K. Singer, M. L. Klein, I. R. McDonald. *Mol Phys* 41:1387, 1980.
- 319. M. Rovere, D. W. Heermann, K. Binder. *Europhys Lett* 6:585, 1988.
- 320. M. Rovere, D. W. Heermann, K. Binder. *J Phys: Condensed Matter* 2:7009, 1990.
- 321. M. Rovere, P. Nielaba, K. Binder. *Z Phys B* 90:215, 1993.
- 322. O. G. Mouritsen, A. J. Berlinsky. *Phys Rev Lett* 48:181, 1982.
- 323. W. Selke. *Physica A* 177:460, 1991.
- 324. S. Sengupta, O. Opitz, D. Marx, P. Nielaba. *Europhys Lett* 24:13, 1993.
- 325. F. Y. Wu. *Rev Mod Phys* 54:235, 1982.
- 326. V. Privman, P. C. Hohenberg, A. Aharony. In: C. Domb, J. L. Lebowitz, eds. *Phase Transitions and Critical Phenomena, Vol. 14*. London: Academic, 1991.
- 327. D. Marx, P. Nielaba. *J Chem Phys* 102:4538, 1995.
- 328. R. Martoňák, D. Marx, P. Nielaba. *Phys Rev E* 55:2184, 1997.
- 329. W. K. Burton, A. H. De Borde. *Nuovo Cim* 2:197, 1955.
- 330. D. Marx, P. Nielaba. *Phys Rev A* 45:8968, 1992.
- 331. J. Cao. *Phys Rev E* 49:882, 1994.
- 332. P. Nielaba, K. Binder. *Europhys Lett* 13:327, 1990.
- 333. W. Helbing, P. Nielaba, K. Binder. *Phys Rev B* 44:4200, 1991.
- 334. M. H. Müser, W. Helbing, P. Nielaba, K. Binder. *Phys Rev E* 49:3956, 1994.
- 335. M. H. Müser, B. J. Berne. *Phys Rev Lett* 77:2638, 1996.
- 336. D. Marx. *Mol Simul* 12:33, 1994.
- 337. K. J. Runge, M. P. Surh, C. Mailhot, E. L. Pollock. *Phys Rev Lett* 69:3527, 1992.
- 338. D. Marx, S. Sengupta, O. Opitz, P. Nielaba, K. Binder. *Mol Phys* 83:31, 1994.
- 339. S. E. Roosevelt, L. W. Bruch. *Phys Rev B* 41:12236, 1990.
- 340. Yu. A. Freiman, V. V. Sumarokov, A. P. Brodyanskii, A. Jezowski. *J Phys: Condens Matter* 3:3855, 1991.
- 341. A. P. Brodyanskii, V. V. Sumarokov, Yu. A. Freiman, A. Jezowski. *Low Temp Phys* 19:368, 1993.

- 342. M. Abramowitz, I. A. Stegun, eds. *Handbook of Mathematical Functions*. New York: Dover, 1965.
- 343. E. Chacón, P. Tarazona. *Phys Rev B* 39:7111, 1989.
- 344. R. M. Stratt. *Phys Rev Lett* 55:1443, 1985; *J Chem Phys* 84:2315, 1986.
- 345. F. Moshary, N. H. Chen, I. F. Silvera. *Phys Rev Lett* 71:3814, 1993.
- 346. D. N. Batchelder, D. L. Losee, R. O. Simmons. *Phys Rev* 173:873, 1968.

# 3

## Integral Equations in the Theory of Simple Fluids

**DOUGLAS HENDERSON** Department of Chemistry and Biochemistry,  
Brigham Young University, Provo, Utah

**STEFAN SOKOŁOWSKI and MALGORZATA BORÓWKO** Department  
for the Modelling of Physico-Chemical Processes,  
Maria Curie-Skłodowska University, Lublin, Poland

I. Introduction	135
II. Distribution Functions	138
III. Integral Equations	139
IV. Geometrically Based Integral Equation Hierarchy for Hard Sphere Systems	151
V. The Structure of Infinitely Polydisperse Fluids	154
VI. Inhomogeneous Fluids	158
VII. Bridge Functions for Homogeneous Fluids	161
VIII. Summary	162
References	163

### I. INTRODUCTION

In this book, the theory of gases and liquids and its application to surface and interfacial problems is considered. In this chapter, theories based on integral equations are reviewed. Since these theories were developed originally for bulk fluids, we will consider this case first and indicate the extension of the theories to interfaces.

As has been known since the experiments of Andrews [1,2], one can pass continuously from the gas state to the liquid state and back by increasing the



temperature above the critical temperature (if required) and changing the density until it is above or below the critical density and then lowering the temperature. Thus, it is possible to pass from gas to liquid and back without any apparent change.

Therefore, one might ask what is meant by the terms liquid and gas. We all know what is the characteristic of a liquid. It has a free surface. However, as soon as we compress the liquid, there is no free surface and the distinction between a gas and liquid is lost. The most logical terminology would be to reserve the terms liquid and vapor for the two coexisting phases and call all other states fluid. A more common terminology is to call the fluid a liquid if its density exceeds the critical density and a gas if its density is lower. Generally speaking, in this chapter we will use the term fluid to describe both the gas and liquid phases and not make any distinction.

The theory of liquids is based on statistical mechanics [2–5]. A fundamental result in statistical mechanics is that the probability of a state having an energy  $E_i$  is given by

$$p(E_i) = \frac{e^{-\beta E_i}}{\sum_i e^{-\beta E_i}}, \quad (1)$$

where  $\beta = 1/kT$ ,  $T$  being the temperature and  $k$  being the Boltzmann constant. The sum in the denominator of Eq. (1) is called the partition function. With the exception of helium, and to a lesser extent hydrogen and neon, quantum mechanics is not necessary to describe fluids. This means that the sum in Eq. (1) becomes an integral. Further, the kinetic energy contribution to the partition is separable and can be integrated to give a purely multiplicative term. Thus, a simplified version of Eq. (1),

$$p(U) = \frac{e^{-\beta U}}{\int e^{-\beta U} d\mathbf{r}_1 \cdots d\mathbf{r}_N} \quad (2)$$

is all that is needed. In Eq. (2),  $N$  being the number of molecules in the system,  $U = U(\mathbf{r}_1, \dots, \mathbf{r}_N)$  is the potential energy of the fluid, and  $\mathbf{r}_i$  is the position of the center of mass of molecule  $i$ . If the molecules are non-spherical then the orientation as well as the position of a molecule must be specified. However, in this chapter we will confine our discussion to spherical molecules with central forces.

To make further progress,  $U$  must be specified. It is usual to assume *pairwise additivity*

$$U(\mathbf{r}_1, \dots, \mathbf{r}_N) = \sum_{i < j} u(r_{ij}) \quad (3)$$

where  $r_{ij} = |\mathbf{r}_i - \mathbf{r}_j|$  and  $u(r_{ij})$  is the interaction between molecules  $i$  and  $j$ . In making this assumption, we achieve a great simplification at the price of a small error. There are many pair potentials. A few of interest will now be listed. First, there is the hard sphere potential

$$u(r) = \begin{cases} \infty & r < d \\ 0 & r > d \end{cases} \quad (4)$$

where  $d$  is the hard sphere diameter. Another useful pair potential is the square well potential

$$u(r) = \begin{cases} \infty & r < \sigma \\ -\epsilon & \sigma < r < \lambda\sigma \\ 0, & r > \lambda\sigma \end{cases} \quad (5)$$

where  $\sigma$  is the hard core diameter that is a measure of the size of the molecules,  $\epsilon$  and  $\lambda$  are measures of strength and range of the interaction. The value  $\lambda = 1.5$  is commonly used and is appropriate for the inert gases. The square well potential is more realistic than the hard sphere potential because both repulsive and attractive terms are considered. However, an even more realistic potential would have the attractive term go to zero gradually. Such a potential is the Yukawa potential

$$u(r) = \begin{cases} \infty & r < \sigma \\ \epsilon\sigma \exp \left\{ -\frac{\lambda}{\sigma} (r - \sigma) \right\} / r & r > \sigma \end{cases} \quad (6)$$

In the Yukawa potential,  $\lambda$  is an inverse range parameter. The value  $\lambda = 1.8$  is appropriate for the inert gases. Each of the above potentials has a hard core. Real molecules are hard but not infinitely so. A slightly softer core is more desirable. The Lennard-Jones potential

$$u(r) = \epsilon \left\{ \left( \frac{\sigma}{r} \right)^{12} - \left( \frac{\sigma}{r} \right)^6 \right\}, \quad (7)$$

has this property. Of course, there are many possible potentials for spherical molecules: triangular wells, potentials with an exponential character, and others. The above potentials suffice for our needs. However, before leaving this subject, we mention the Coulomb interaction. This is a central potential and is appropriate for charged fluids, such as electrolytes and plasmas, which are a field in themselves and lie outside the scope of this chapter.

## II. DISTRIBUTION FUNCTIONS

The probability given by Eq. (2) is a function of an enormous number of variables. We can neither compute nor display such a function. The most with which we can deal are functions of the coordinates of one, two, three, or, at the outside, four molecules. It takes six variables to specify the positions of four molecules. Therefore, it is helpful to integrate over the positions of most of the molecules. The  $h$  molecule distribution function is given by

$$g(\mathbf{r}_1, \dots, \mathbf{r}_h) = \frac{(N-h)!}{N!} \frac{\int \exp(-\beta U) d\mathbf{r}_{h+1} \dots d\mathbf{r}_N}{\int \exp(-\beta U) d\mathbf{r}_1 \dots d\mathbf{r}_N} \quad (8)$$

This function is the probability of finding molecules  $1, \dots, h$  at positions  $\mathbf{r}_1, \dots, \mathbf{r}_h$  normalized so that  $g(\mathbf{r}_1, \dots, \mathbf{r}_h) = 1$  when all the molecules are far from each other.

The definition of the distribution function given above is valid in the canonical ensemble. This means that  $N$  is finite. Of course,  $N$  will, in general, be very large. Hence,  $g(\mathbf{r}_1, \dots, \mathbf{r}_h)$  approaches 1 when all the molecules are far apart but there is a term of order  $1/N$  that sometimes must be considered. This problem can be avoided by using the grand canonical ensemble. We will not pursue this point here but do wish to point it out.

The case  $h = 2$  is of greatest interest. Since the force is central, it is not necessary to use  $\mathbf{r}_1$  and  $\mathbf{r}_2$  as variables. The single variable  $r_{12}$  is sufficient since the position of the center of mass is irrelevant. Thus, we have the *radial distribution function* (RDF),  $g(r_{12})$ .

Since we have assumed pairwise additivity, the thermodynamic properties can be obtained from the RDF. For example, the energy is given by

$$E = \frac{3}{2} NkT + \frac{1}{2} N\rho \int u(r)g(r)dr \quad (9)$$

and the pressure is given by

$$\frac{pV}{NkT} = 1 - \frac{\rho}{6kT} \int r \frac{du(r)}{dr} g(r)dr \quad (10)$$

In Eqs. (9) and (10),  $\rho = N/V$ , where  $V$  is the volume of the fluid. Equation (10) can be simplified if the core is hard, using the fact that  $du(r)/dr$  is related to the delta function,  $\delta(r - \sigma)$ . Thus,

$$\frac{pV}{NkT} = 1 + \frac{2\pi}{3} \rho\sigma^3 g(\sigma) - \frac{\rho}{6kT} \int_{r>\sigma} r \frac{du(r)}{dr} g(r)dr \quad (11)$$

In the particular case of hard spheres,  $d = \sigma$  and the integral in Eq. (11) does not appear. Hence,

$$\frac{pV}{NkT} = 1 + \frac{2\pi}{3} \rho d^3 g(d) \quad (12)$$

The RDF in Eqs. (11) and (12) is discontinuous for a hard core. It must vanish if  $r < d$ , since the molecules cannot overlap. Strictly speaking,  $g(d)$  [or  $g(\sigma)$ ], which is called the *contact value*, is the limiting value of  $g(r)$  as  $r \rightarrow d$  from values of  $r > d$ .

There is another relation between  $g(r)$  and thermodynamics. In contrast to Eqs. (9) and (10), that are almost self evident, this relation is subtle and is related to the term of order  $1/N$  that has been mentioned; its derivation requires care. Here, we will content ourselves to quoting the result,

$$kT \frac{\partial \rho}{\partial p} = 1 + \rho \int h(r) dr, \quad (13)$$

where  $h(r) = g(r) - 1$  is called the *total correlation function*.

In the absence of any approximations, Eqs. (9), (10), and (13) must yield the same thermodynamic functions. However, if approximate expressions for the RDF are used, these various equations may yield different thermodynamic functions.

The RDF can be measured [3–5] by X-ray and neutron scattering. We shall discuss how it may be calculated.

### III. INTEGRAL EQUATIONS

Differentiation of Eq. (8) with respect to the position of a molecule gives a hierarchy of integro-differential equations, each of which relates a distribution function to the next higher order distribution function. Specifically,

$$\nabla_1 \ln g(\mathbf{r}_1, \dots, \mathbf{r}_j) = -\beta \sum_{i=1}^{j-1} \nabla_1 u(r_{ij}) - \beta \rho \int \nabla_j u(r_{(j-1)j}) \frac{g(\mathbf{r}_1, \dots, \mathbf{r}_{j+1})}{g(\mathbf{r}_1, \dots, \mathbf{r}_j)} d\mathbf{r}_j \quad (14)$$

This hierarchy is called the *Born–Green–Yvon* (BGY) hierarchy [6,7]. Again the specific case  $j = 2$  is of most interest,

$$\nabla_1 \ln g(\mathbf{r}_1, \mathbf{r}_2) = -\beta \nabla_1 u(r_{12}) - \beta \rho \int \nabla_3 u(r_{12}) \frac{g(\mathbf{r}_1, \mathbf{r}_2, \mathbf{r}_3)}{g(\mathbf{r}_1, \mathbf{r}_2)} d\mathbf{r}_3 \quad (15)$$

To make any progress, a relation between the pair and triplet function must be specified. Unfortunately, no accurate relation exists. Kirkwood [8,9]

has proposed the superposition approximation

$$g(r_{12}, r_{13}, r_{23}) = g(r_{12})g(r_{13})g(r_{23}) \quad (16)$$

Using this approximation, the derivative in Eq. (15) can be integrated and an integral equation results. The equation of state for hard spheres, obtained from the BGY equation, is plotted in Fig. 1. Regrettably, the results are not very satisfactory. This is because the superposition approximation is reasonable only at low densities. The BGY results have one virtue. The BGY compressibility results tend to  $(\partial p / \partial \rho)_T = 0$ , indicative of the freezing transition found, by simulation, in the hard sphere fluid. No simple improvement of the superposition approximation is available. Lee et al. [10,11] have obtained good results by using an approximation, similar to Eq. (16), for the four-body distribution to calculate the three-body distribution function and, from this, the RDF. The results for the RDF are quite good. However, the method has not been pursued. At the time, computers were slower and memory was expensive. Presumably, the calculations were assumed to be impractical. Today, with bigger and faster computers, a return to this method may be of value.

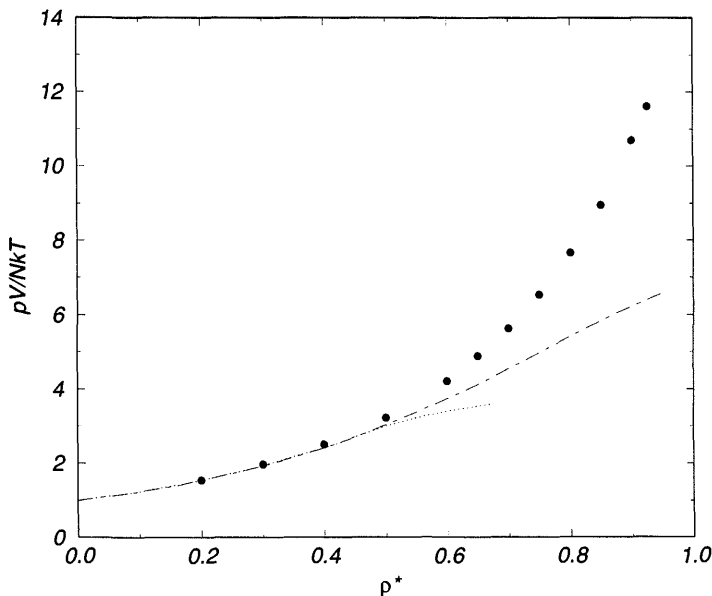


**FIG. 1** The equation of state for hard spheres, obtained from the BGY equation. The dot-dashed and dotted curves give the pressure and compressibility results, respectively. The points give the computer simulation results. The quantity  $\rho^* = Nd^3/V$ .

Most integral equations are based on the *Ornstein–Zernike* (OZ) equation [3–5]. The idea behind the OZ equation is to divide the total correlation function  $h(r_{12})$  into a *direct correlation function* (DCF)  $c(r_{12})$  that describes the fact that molecules 1 and 2 can be directly correlated, and an indirect correlation function  $\gamma(r_{12})$ , that describes the correlation of molecule 1 with the other molecules that are also correlated with molecule 2. At low densities, when only direct correlations are possible,  $\gamma(r) = 0$ . At higher densities, where only triplet correlations are possible, we can write

$$\gamma(r_{12}) = \rho \int c(r_{13})c(r_{23})d\mathbf{r}_3 \quad (17)$$

Including 3, 4, 5, ... correlations, we expect

$$\gamma(r_{12}) = \rho \int c(r_{13})c(r_{23})d\mathbf{r}_3 + \rho^2 \int c(r_{13})c(r_{34})c(r_{24})d\mathbf{r}_3d\mathbf{r}_4 + \cdots \quad (18)$$

The integrals in Eqs. (17) and (18) are called convolution integrals. In Fourier space they are products of the Fourier transforms of  $c(r)$ . Thus, Eq. (18) is a geometric series in Fourier space, which can be summed. Performing this summation and returning to direct space, we have the OZ equation

$$\gamma(r_{12}) \equiv h(r_{12}) - c(r_{12}) = \rho \int h(r_{13})c(r_{23})d\mathbf{r}_3 \quad (19)$$

As long as  $h(r)$  and  $c(r)$  are related by the OZ equation, the results of

$$\beta \left( \frac{\partial p}{\partial \rho} \right)_T = 1 - \rho \int c(r)d\mathbf{r} \quad (20)$$

are exactly the same as those from Eq. (13). The OZ equation is exact. It is the definition of  $c(r)$ . An additional relation, called a *closure*, is needed in order to obtain values for  $h(r)$ , or  $g(r)$ , and  $c(r)$ . One such closure is the *hypernetted chain* (HNC) approximation [3–5,12]

$$\gamma(r) = \ln y(r) = \beta u(r) + \ln g(r) \quad (21)$$

where

$$y(r) = \exp[\beta u(r)]g(r) \quad (22)$$

The function  $y(r)$  is called the *cavity function* or *background function*. If  $u(r)$  is discontinuous,  $g(r)$  is discontinuous for the same values of  $r$ . However,  $y(r)$  is continuous. Eq. (12) is more correctly written as

$$\frac{pV}{NkT} = 1 + \frac{2\pi}{3} \rho d^3 y(d) \quad (23)$$

It is difficult to give a reference for the HNC closure because so many different authors developed this approximation at about the same time. A full set of references can be found in the review of Barker and Henderson [4,5].

Consistency between the thermodynamic functions that are obtained from Eqs. (9), (10), and (13) is often used as the criterion for the accuracy of a theory. In this regard it is worth pointing out that, in the HNC approximation, the thermodynamic functions that are obtained from Eqs. (9) and (10) are identical. Thus, a partial degree of consistency is achieved.

The equation of state, obtained from the HNC equation, is displayed in Fig. 2(a). The results are an improvement over the BGY results but are not very satisfactory.

Linearizing Eq. (21) yields the *Percus-Yevick* (PY) [13] closure

$$\gamma(r) = y(r) - 1 \quad (24)$$

$$c(r) = \{\exp[-\beta u(r)] - 1\}y(r) \quad (25)$$

The PY closure is less sophisticated than the HNC closure. Generally, the HNC closure is better. However, as we shall see, the PY closure is better for hard spheres. With the help of Eqs. (24) and (25) the OZ relation becomes

$$y(r_{12}) + 1 = \rho \int \{y(r_{13})[f(r_{12}) + 1] - 1\}y(r_{23})f(r_{13})d\mathbf{r}_3 \quad (26)$$

where  $f(r) = \exp[-\beta u(r)] - 1$  is the Mayer function. The last equation, commonly known as the PY equation for the cavity function, can be also developed from the BGY equation [14]. Namely, using the definition of the cavity function (22), the superposition approximation (15), and the approximation (24), the first equation of the BGY hierarchy, Eq. (14), can be written as follows

$$\nabla_1 \ln y(r_{12}) = -\rho \nabla_1 \int f(r_{13})y(r_{13})h(r_{23})d\mathbf{r}_3 - \rho \int f(r_{13})\nabla_1 y(r_{13})h(r_{23})d\mathbf{r}_3 \quad (27)$$

If the cavity function does not change fast in the region of interest, then the derivative  $\nabla_1 y(r_{13})$  is small and thus the integral involved may be neglected. In this approximation on integrating Eq. (27), we obtain the integral equation

$$\ln y(r_{12}) = \rho \int f(r_{13})y(r_{13})h(r_{23})d\mathbf{r}_3 + C \quad (28)$$

where  $C$  is the integration constant. It is set to zero since the cavity function  $y(r)$  tends to unity as  $r \rightarrow \infty$  and the integral also vanishes as either  $r_{13}$  or  $r_{23}$

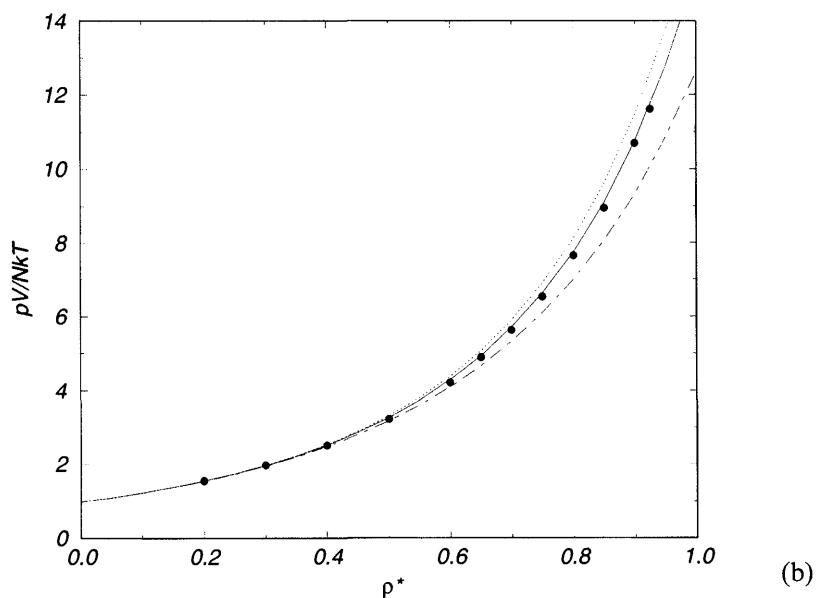
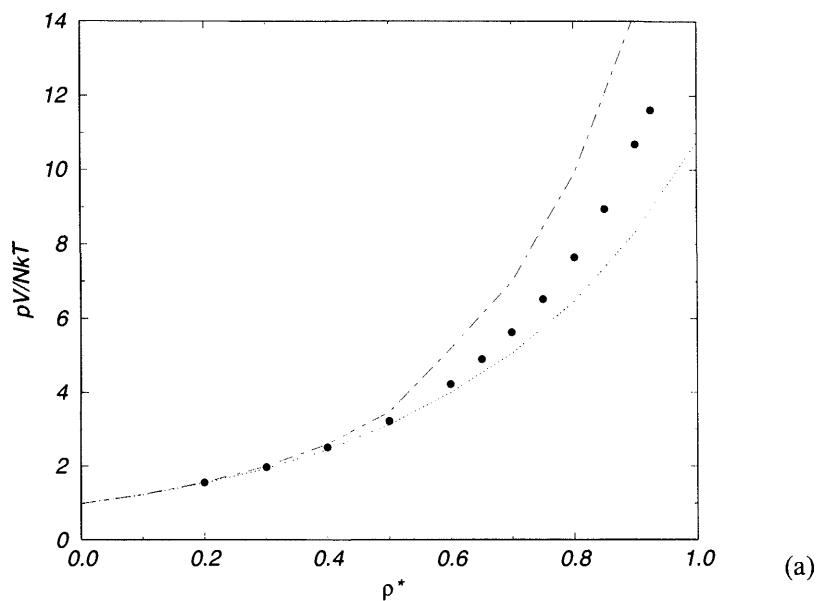


**FIG. 2** The equation of state for hard spheres, obtained from the HNC equation (part a) and the PY equation (part b). The dot-dashed and dotted curves and the circles have the same meaning as in Fig. 1. The solid curves give the results of the CS equation.



tends to infinity in the limit. If the left-hand side of Eq. (28) is linearized, then the PY integral equation (25) follows. This argument can be recast so that the HNC equation follows.

For hard spheres, the PY approximation yields an analytic solution [15–17]. The result for the direct correlation function is

$$c(r) = \begin{cases} a + b\left(\frac{r}{d}\right) + c\left(\frac{r}{d}\right)^3 & r < d \\ 0 & r > d \end{cases} \quad (29)$$

where

$$a = -\frac{(1 + 2\eta)^2}{(1 - \eta)^4} \quad (30)$$

$$b = 6\eta \frac{(1 + \eta/2)^2}{(1 - \eta)^4} \quad (31)$$

and

$$c = \frac{\eta}{2} a \quad (32)$$

where  $\eta = (\pi/6)\rho d^3$ . The equation of state can be obtained from this result. From Eq. (23)

$$\left(\frac{pV}{NkT}\right)_p = \frac{1 + \eta + \eta^2 - 3\eta^3}{(1 - \eta)^3} \quad (33)$$

and from Eq. (20)

$$\left(\frac{pV}{NkT}\right)_c = \frac{1 + \eta + \eta^2}{(1 - \eta)^3}. \quad (34)$$

As is seen in Fig. 2(b), the results of Eqs. (33) and (34) are in fair agreement with computer simulation results. Carnahan and Starling (CS) [18] have made the observation that the result

$$\frac{pV}{NkT} = \frac{1 + \eta + \eta^2 - \eta^3}{(1 - \eta)^3} \quad (35)$$

that is obtained by a linear combination of Eqs. (28) and (29) is a good fit of computer simulation results for hard spheres, as is seen in Fig. 2(b).

In Fig. 3, the PY  $g(r)$  and  $y(r)$  are compared with computer simulation results and with a fit [19–21] of the computer simulation results. The agreement is quite good except that the PY result is too small at contact. This

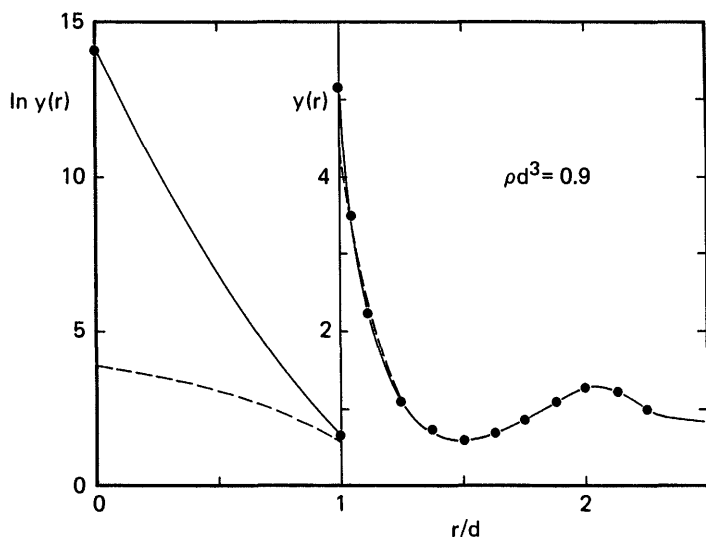


**FIG. 3** The functions  $g(r)$  and  $y(r)$  for a hard sphere fluid. The broken curve gives PY results and the solid curve gives the results of a fit of the simulation data. The circle gives the simulation results. The point at  $r = 0$  gives the result obtained from Eq. (36), using the CS equation of state.

problem at contact is the beginning of a severe failure of the PY result for hard spheres in the region  $0 < r < d$ . For example, there is an exact result for  $y(0)$  for hard spheres

$$y(0) = \frac{\exp[\beta\mu]}{\lambda^3 \rho} \quad (36)$$

where  $\lambda$  is the thermal de Broglie wavelength and  $\mu$  is the chemical potential that can be obtained by integrating Eq. (35). As is seen from Fig. 2(b) and Eqs. (25) and (29), the PY result for  $y(0)$  is not even of the correct order of magnitude.

Although Eqs. (33), (34), and especially (35), are useful they have a problem. They all predict that the hard sphere system is a fluid until  $\eta = 1$ . This is beyond close packing and quite impossible. In fact, hard spheres undergo a first order phase transition to a solid phase at around  $\rho d^3 \sim 0.9$ . This has been established by simulations [3–5]. To a point, the BGY approximation has the advantage here. As is seen in Fig. 1, the BGY equation does predict that  $(\partial p / \partial \rho)_T = 0$  at high densities. However, the location of the transition is quite wrong. Another problem with the PY theory is that it can lead to negative values of  $g(r)$ . This is a result of the linearization of  $y(r) - 1$  that

is inherent in the PY approximation. Lebowitz [22] has obtained an analytical solution of the PY approximation for hard sphere mixtures.

An even better closure, for hard spheres at least, is the Verlet [23] closure, as modified by Henderson et al. [24],

$$\gamma(r) = \ln y(r) - \frac{1}{2} \frac{\gamma^2(r)}{1 + \alpha\gamma(r)} \quad (37)$$

Verlet used  $\alpha = 0.8$ ; the modification of Henderson et al. is to use a state-dependent  $\alpha$ . For hard spheres

$$\alpha = \frac{17}{120\eta} + 0.5150 - 0.2210\eta \quad (38)$$

or

$$\alpha = \frac{17}{120\eta} e^{-2\eta} + 0.8 - 0.45\eta \quad (39)$$

The two forms are almost identical.

The  $g(r)$  that results from the modified Verlet (MV) closure is very close to the simulation results in Figs. 2 and 3. The MV results for  $g(d)$ , or equivalently,  $y(d)$ , are plotted in Fig. 4(a). The resulting equation of state is similar to the CS expression. An even more demanding test is an examination of the MV results for  $y(r)$  for  $r < d$ . As is seen in Fig. 4(b), the MV results for  $y(0)$  are quite good [25], and are better than the PY and HNC results. Some results have also indicated that the MV closure gives quite accurate results for a mixture of hard spheres [26].

The Duh–Haymet–Henderson (DHH) closure [27–29] is similar to the MV closure but has  $\alpha$  as a functional of a function that is closely related to  $\gamma(r)$ . This closure has been successful for LJ fluids and their mixtures, even in the case of non-additive mixtures [29]. A comparison of the  $g_{ij}(r)$  for a non-additive mixture, obtained with the DHH closure, is made with simulations in Fig. 5.

Since the results for thermodynamics from the Yukawa potential, with  $\lambda = 1.8$ , are similar to the results of the LJ potential, it is quite possible that the DHH closure may be applicable to the Yukawa potential. With  $\lambda = 1.5$ , the thermodynamics of the square well fluid are also similar. Here, too, the DHH closure may be useful. However, the DHH closure has not been applied to either of these potentials.

Another linearization of the HNC closure leads to the mean spherical approximation (MSA). For a fluid with a hard core, the MSA is

$$h(r) = -1, r < \sigma \quad (40)$$

$$c(r) = -\beta u(r), r > \sigma \quad (41)$$

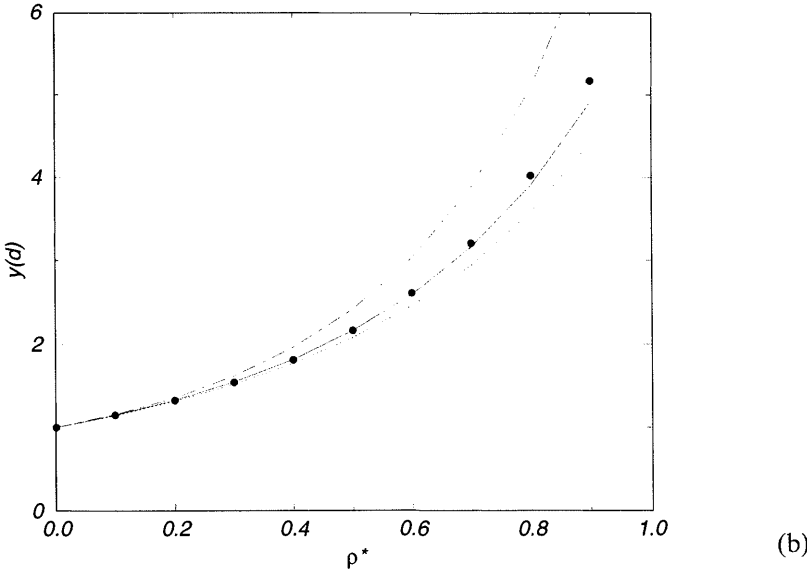
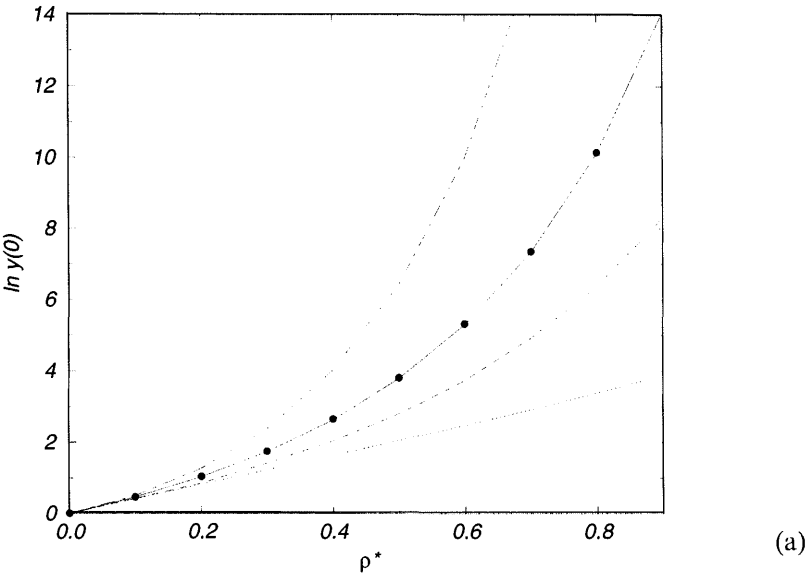


**FIG. 4** Values for  $y(0)$  (a) and  $y(d) = g(d)$  (b) for hard spheres. The solid circles give the results obtained from the CS equation. The solid, broken, dot-dash, and dotted curves give the MV, MS, HNC, and PY results, respectively. In (b), the MS and MV results are nearly identical.

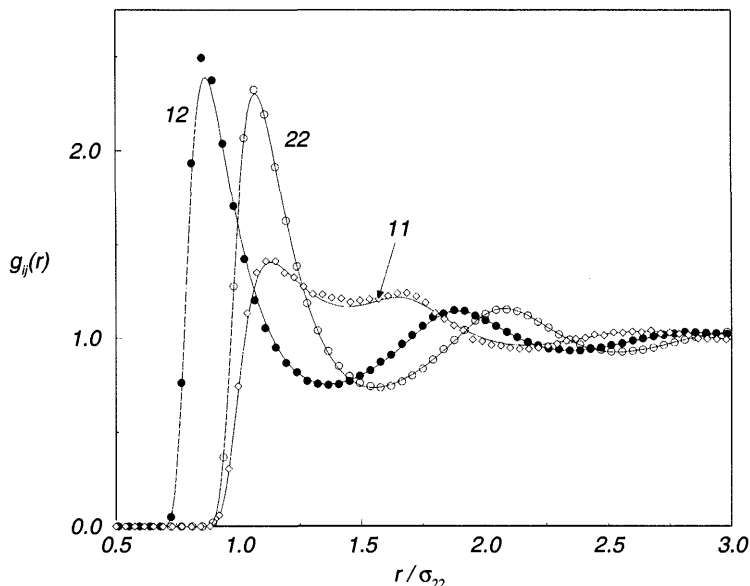


**FIG. 5** Radial distribution functions,  $g_{ij}(r)$  for a non-additive mixture of Lennard-Jones molecules with  $\sigma_{11} = \sigma_{22}$  and  $\sigma_{12} = 0.8\sigma_{11}$  and  $\epsilon_{11} = \epsilon_{12} = \epsilon_{22}$  at  $kT/\epsilon_{11} = 1.5$  and  $\rho_1\sigma_{11}^3 + \rho_2\sigma_{22}^3$ . The fraction of molecules of species 1 is 0.0625.

Eq. (40) is a statement of the fact that molecules cannot penetrate into each other. Eq. (41) is the approximation. It is correct when  $r$  is large. The approximation consists in assuming that Eq. (41) is valid for all  $r > \sigma$ .

Coupling Eqs. (40) and (41) with the OZ equation gives an integral equation, which can be solved numerically. Perhaps the main reason for the interest in the MSA equation is that it can be solved analytically for several important fluids. For example, the PY approximation for the hard sphere fluid can be regarded as a special case of the MSA for a fluid with an infinitely hard core and no attractive interactions. Another case is the Yukawa fluid [30–37], whose potential is given by Eq. (6). Other fluids that yield analytic solutions are ionic fluids [38–41], where the ions interact with the Coulomb potential and the solvent molecules interact with a dipole–dipole interaction [42], and mixtures of fluids with these charged and dipolar potentials [43–47]. The MSA is very useful at higher densities, as long as the interactions are not too strong, but is less useful at low densities. Because of the linearization it can lead to negative values of  $g(r)$ .

The Yukawa potential is of interest in another connection. According to the Derjaguin–Landau–Verwey–Overbeek (DLVO) theory, colloidal

particles interact with a Yukawa potential where the Debye screening parameter  $\kappa$  for charged systems takes the place of  $\lambda$ . Colloidal systems will be treated in detail elsewhere in this volume.

One should perhaps mention some other closures that are discussed in the literature. One possibility is to combine the PY approximation for the hard core part of the potential and then use the HNC approximation to compute the corrections due to the attractive forces. Such an approach is called the reference hypernetted chain or RHNC approximation [48,49]. Recently, some new closures for a mixture of hard spheres have been proposed. These include one by Rogers and Young [50] (RY) and the Martynov-Sarkisov [51] (MS) closure as modified by Ballone, Pastore, Galli and Gazzillo [52] (BPGG). The RY and MS/BPGG closure relations take the forms

$$g(r) = \exp[-\beta u(r)] \left\{ 1 + \frac{\exp[m(r)\gamma(r)] - 1}{m(r)} \right\} \quad (42)$$

where the function  $m(r) = 1 - \exp(-\zeta r)$  varies between 0 and 1, and

$$g(r) = \exp[-\beta u(r)] \exp\{[1 + s\gamma(r)]^{1/s} - 1\} \quad (43)$$

The MS closure results from  $s = 2$ . The HNC closure results from  $s = 1$ . In the latter two expressions, additional adjustable parameters occur, namely  $\zeta$  for the RY closure and  $s$  for the BPGG version of the MS approximation. However, even when adjustable, these parameters cannot be chosen at will, as they should be chosen such that they eliminate the so-called thermodynamic inconsistency that plagues many approximate integral equations. We recall that a manifestation of this inconsistency is that there is a difference between the pressure as computed from the virial equation (10) and as computed from the compressibility equation (20). Note that these equations have been applied to a very asymmetric mixture of hard spheres [53,54]. Some results of the MS closure are plotted in Fig. 4. The MS result for  $y(d) = g(d)$  is about the same as the MV result. However, the MS result for  $y(0)$  is rather poor. Using a value between 1 and 2 improves  $y(0)$  but makes  $y(d)$  worse. Overall, we believe the MS/BPGG is less satisfactory than the MV closure.

Integral equation approaches with improved self-consistency were reviewed recently by Caccamo [55]. Unfortunately, in the case of almost all approaches, their accuracy begins to decrease as one leaves the liquid state region located slightly above the triple point in temperature and follows the liquid-gas coexistence curve in the density-temperature plane up to the critical region. In particular, the shape of the coexistence curve and location

of the critical point are not reproduced accurately; nor are related critical parameters. However, in the cases in which there are substantial discrepancies between several paths available for obtaining thermodynamics from  $g(r)$ , often the most reliable and accurate coexistence behavior is obtained from evaluating the thermodynamics through the excess internal energy (see Eq. (9)).

Quite recently, Pini et al. [56] have reported a new, thermodynamically self-consistent approximation to the OZ relation for a fluid of spherical particles for a pair potential given by a hard-core repulsion and a Yukawa attractive tail (Eq. (6)). The closure to the OZ equation they have proposed has the form

$$\begin{cases} g(r) = 0 & r < \sigma \\ c(r) = K \exp[-\lambda(r - \sigma)/\sigma]/r + c_{\text{hs}}(r) & r > \sigma \end{cases} \quad (44)$$

where  $c_{\text{hs}}(r) = K_1 \exp[-\lambda_1(r - \sigma)/\sigma]/r$  for  $r > \sigma$  is the direct correlation function of the hard sphere fluid. The coefficients  $K_1$  and  $\lambda_1$  are functions of the thermodynamic state of the system. They can be determined by requiring, as in the Verlet-Weis [19–21] parameterization, that both compressibility and virial routes give the CS equation of state. The parameter  $K_1$  fixes the condition

$$\frac{\partial}{\partial \beta} \left[ 1 - \rho \int c(r) d\mathbf{r} \right] = \rho \frac{\partial^2}{\partial \rho^2} \left[ \rho^2 \int u(r) g(r) d\mathbf{r} \right] \quad (45)$$

The last equation comes from the condition that both the compressibility and the energy route lead to the same value of the Helmholtz free energy.

The calculations that have been carried out [56] indicate that the approximations discussed above lead to very good thermodynamic functions overall and a remarkably accurate critical point and coexistence curve. The critical density and temperature predicted by the theory agree with the simulation results to about 0.6%. Of course, dealing with the Yukawa potential allows certain analytical simplifications in implementing this approach. However, a similar approach can be applied to other similar potentials that consist of a hard core with an attractive tail. It should also be pointed out that the idea of using the requirement of self-consistency to yield a closed theory is pertinent not only to the realm of simple fluids, but also has proved to be a powerful tool in the study of a system of spins with continuous symmetry [57,58] and of a site-diluted or random-field Ising model [59,60].

#### IV. GEOMETRICALLY-BASED INTEGRAL EQUATION HIERARCHY FOR HARD SPHERE SYSTEMS

Alternative integral equations for the cavity functions of hard spheres can be derived [61,62] using geometrical and physical arguments. Theories and results for hard sphere systems based on geometric approaches include the scaled particle theory [63,64], and related theories [65,66], and approaches based on zero-separation theorems [67,68]. These geometric theories have been reviewed by Stell [69].

Although the geometric approaches have produced a number of exact results, they apparently have not been absorbed into mainstream approaches. One reason may be the fact that, apart from success in predicting thermodynamic properties (for example, the scaled particle theory yields the same results as the PY equation for hard spheres), it has not been clear how to improve these theories in a systematic manner. Moreover, until recently, these theories have had only moderate success in predicting hard-sphere structural properties. However, quite recently Labík et al. [61] have proposed a new hierarchy of integral equations for the  $h$  particle distribution functions of the hard-sphere system. This hierarchy may be closed using a clearly defined sequence of approximations, the most accurate of which can make predictions for the hard-sphere equation of state that are as accurate as those resulting from the most sophisticated first principles theories. Because, in our opinion, the theory of Labík et al. seems to be one of the most promising approaches that have been developed recently, we have included its detailed description here. To our knowledge, this approach has not been reviewed previously.

The theory of Labík et al. [61,62,70] can be derived by combining the BGY equations with some geometrical considerations. We rewrite Eq. (14) in terms of the generalized cavity functions  $Y(\mathbf{r}_1, \dots, \mathbf{r}_n)$ ,

$$\rho(\mathbf{r}_1, \dots, \mathbf{r}_n) = y(\mathbf{r}_1, \dots, \mathbf{r}_n) \exp \left[ -\beta \sum_{i=1}^{n-1} \sum_{j=i+1}^n u(r_{ij}) \right] \quad (46)$$

and

$$Y(\mathbf{r}_1, \dots, \mathbf{r}_n) = y(\mathbf{r}_1, \dots, \mathbf{r}_n) / y(\mathbf{r}_1, \dots, \mathbf{r}_{n-1}) \quad (47)$$

We obtain

$$\begin{aligned} \nabla_j \ln y(\mathbf{r}_1, \dots, \mathbf{r}_j) = & -\beta \rho \int \nabla_2 u(r_{(n-1)n}) Y(\mathbf{r}_1, \dots, \mathbf{r}_n + 1) \\ & \times \sum_{i=1}^n \exp[-\beta u(r_{i(n+1)})] d\mathbf{r}_{n+1} \end{aligned} \quad (48)$$



In the general case the  $j$ th sphere can be characterized by the vector  $\mathbf{r}_j = (\Omega_j, \mathbf{R}_j) \equiv (\theta_j, \phi_j, \mathbf{r}_{(j-1)j})$ , where  $R_j = |\mathbf{R}_j| = r_{(j-1)j}$  is the distance between the spheres  $j-1$  and  $j$ ,  $\cos \theta_j = (\mathbf{r}_{j-1} \mathbf{r}_j) / (r_{j-1} r_j)$ , and  $\phi_j$  is an azimuthal angle. Using such a coordinate system, Eq. (48) becomes

$$\frac{\mathbf{R}_n}{R_n} \frac{d \ln y(\mathbf{R}_1, \dots, \mathbf{R}_{n-1}, \Omega_n, R_n)}{dR_n} = -\beta \rho \int \sum_{i=1}^{n-1} \exp[-\beta u(r_{i(n+1)})] \frac{\mathbf{R}_{n+1}}{R_{n+1}} \frac{du(R_{n(n+1)})}{dR_{n+1}} y(\mathbf{R}_1, \dots, \mathbf{R}_n, \Omega_{n+1}, R_{n+1}) d\mathbf{R}_{n+1} \quad (49)$$

For hard spheres of diameter  $d = 1$ , the derivative in the integrand of Eq. (49) becomes the delta function. We get

$$\frac{d \ln y(\mathbf{R}_1, \dots, \mathbf{R}_{n-1}, \Omega_n, R_n)}{dR_n} = -\rho \int_{-1}^{+1} d \cos \theta_{n+1} \int_0^{2\pi} d\phi_{n+1} \times \sum_{i=1}^{n-1} \exp[-\beta u(r_{i(n+1)})] \cos \theta_{n+1} y(\mathbf{R}_1, \dots, \mathbf{R}_n, \Omega_{n+1}, 1) \quad (50)$$

Integrating from 0 to  $R_n$  gives

$$\ln y(\mathbf{R}_1, \dots, \mathbf{R}_{n-1}, \Omega_n, R_n) = \ln y(\mathbf{R}_1, \dots, \mathbf{R}_{n-1}, \Omega_n, 0) - \rho \int_0^{R_n} dR_n \int_{-1}^{+1} d \cos \theta_{n+1} \int_0^{2\pi} d\phi_{n+1} \sum_{i=1}^{n-1} \exp[-\beta u(r_{i(n+1)})] \cos \theta_{n+1} y(\mathbf{R}_1, \dots, \mathbf{R}_n, \Omega_{n+1}, 1) \quad (51)$$

Finally, using the zero-separation theorem, when particles  $n-1$  and  $n$  coincide we have

$$\ln y(\mathbf{R}_1, \dots, \mathbf{R}_{n-1}, \Omega_n, 0) = \ln y(\mathbf{R}_1, \dots, \mathbf{R}_{n-1}, \Omega_n, R_{n-1}) + \beta \mu \quad (52)$$

When the last equation is used in conjunction with Eq. (51), we obtain the final equation for the pair cavity function

$$\beta \mu = \ln y(r_{12}) + 2\pi \rho \int_0^{r_{12}} dR_2 \int_{-1}^{+1} d \cos \theta_3 \exp[-\beta u(r_{13})] y(\mathbf{R}_2, \theta_3, 1) \quad (53)$$

The hard-sphere excess chemical potential  $\mu$  that appears on the left-hand side of the hierarchy is related to the compressibility factor  $Z = pV/\rho kT$ ,

$$\beta \mu = \int_0^\eta \frac{Z-1}{\eta'} d\eta' + Z - 1 \quad (54)$$

where  $\eta$  is the packing fraction defined above (Eq. (29)). The compressibility factor is related to the two-particle background function at contact, cf. Eq. (23). Thus, from Eq. (54) we get

$$\beta\mu = 4 \int_0^\eta y(d) d\eta' + 4\eta y(d) \quad (55)$$

Eq. (55) assumes the form

$$4 \int_0^\eta y(d) d\eta' + 4\eta y(d) = \ln Y(r_{12}) + 2\pi\rho \int_0^{r_{12}} dR_2 \int_{-1}^{+1} d\cos\theta_3 \\ \times \exp[-\beta u(r_{13})] y(R_2, \theta_3, 1) \quad (56)$$

To close the last equation, an approximation for  $y(\mathbf{R}_2, \theta_3, 1)$  (or for  $y(\mathbf{R}_2, \theta_3, 1)$ , cf. Eq. (47)) is required. Labík et al. [61,62] proposed a systematic way for the construction of several closures that are increasingly sophisticated. In particular, the second-order closure invoked by them is

$$y(R_2, \theta_3, 1) = y(R_2)y(1) \exp \left\{ 2\pi\rho \int_0^1 dR_3 \int_1^1 d\cos\theta_4 \exp[-\beta u(r_{24})] \right. \\ \times \cos\theta_4 \left[ 1 + \frac{\pi\rho}{6} V^{(3)}(R_3, \theta_4, 1) - \frac{1}{2\pi} \int_0^{2\pi} d\phi_4 \exp[-\beta u(r_{14})] \right. \\ \left. \left. \times \left( 1 + \frac{\pi\rho}{6} V^{(4)}(R_2, \theta_3, R_3, \theta_4, \phi_4, 1) \right) \right] \right\} \quad (57)$$

where  $V^{(i)}$  is the volume excluded to other spheres by  $i$  (eventually fused!) hard spheres in a given geometrical configuration. The evaluation of these volumes can be performed conveniently using the algorithm of Lustig [71].

It is interesting to compare [61,62] the first ten hard-sphere virial coefficients in the expansion of the equation of state resulting from the theory quoted above with Monte Carlo data. The theory reproduces the exact values of the second through fifth virial coefficients. The sixth coefficient resulting from the theory is  $B_6 = 38.33$ , whereas its exact value (obtained from Monte Carlo integration) is  $B_6^{\text{MC}} = 39.74 \pm 0.06$ . The seventh through tenth virial coefficients are:  $B_7 = 49.4$  ( $B_7^{\text{MC}} = 53.5 \pm 0.3$ ),  $B_8 = 64.9$  ( $B_8^{\text{MC}} = 70.8 \pm 1.6$ ),  $B_9 = 88$  ( $B_9^{\text{MC}} = 93$ ), and ( $B_{10} = 118$   $B_{10}^{\text{MC}} = 122$ ). The agreement is very good; accordingly, it is not surprising that the equation of state (up to the packing fraction  $\eta = 0.5$ ) resulting from this theory reproduces the Monte Carlo data more accurately than the CS equation.

A comparison of the predictions for the cavity pair correlation function of some first-principles theories with computer simulation results [72] at a fairly high density has been presented by Stell (see Fig. 2 in Ref. 69). The

results of the above theory are seen to be much better than those of many other theories and, in fact, are indistinguishable from those of computer simulations on the scale of the graph. The results of the MV theory are nearly the same as the results of the Labík et al. theory.

Geometrically based theories, especially that of Labík et al., are remarkably accurate and are no more difficult to implement computationally than other theories that involve the correlations of order higher than  $h = 2$ . Their only disadvantage is that they are limited to the case of hard spheres. If a generalization to other systems could be found, this would be an important advance.

## V. THE STRUCTURE OF INFINITELY POLYDISPERSE FLUIDS

Several colloidal systems, that are of practical importance, contain spherically symmetric particles the size of which changes continuously. Polydisperse fluid mixtures can be described by a continuous probability density of one or more particle attributes, such as particle size. Thus, they may be viewed as containing an infinite number of components. It has been several decades since the introduction of polydispersity as a model for molecular mixtures [73], but only recently has it received widespread attention [74–82]. Initially, work was concentrated on “nearly monodisperse” mixtures and the polydispersity was accounted for by the construction of perturbation expansions with a pure, monodisperse, component as the reference fluid [77,80]. Subsequently, Kofke and Glandt [79] have obtained the equation of state using a theory based on the distinction of particular species in a polydisperse mixture, not by their intermolecular potentials but by a specific form of the distribution of their chemical potentials. Quite recently, Lado [81,82] has generalized the usual OZ equation to the case of a polydisperse mixture. Recently, the latter theory has been also extended to the case of polydisperse quenched–annealed mixtures [83,84]. As this approach has not been reviewed previously, we shall consider it in some detail.

In order to develop integral equations for the correlation functions, we consider the system composed of  $N$  polydisperse spheres. The average density of particles with diameter  $\sigma_i$  is given by

$$\rho(\sigma_i) = \rho F(\sigma_i) \quad (58)$$

where  $\rho = N/V$ ,  $V$  is the volume of the system and  $F(\sigma)$  is the fixed distribution of the particle diameters, normalized to unity

$$\int F(\sigma) d\sigma = 1 \quad (59)$$

The polydisperse fluid structure is characterized by the total,  $h(r, \sigma_i, \sigma_j)$ , and the direct,  $c(r, \sigma_i, \sigma_j)$ , correlation function, both being functions of the particle diameters. These functions are related via the OZ equation (17), which is rewritten in the form

$$\begin{aligned} \gamma(r_{12}, \sigma_i, \sigma_j) &\equiv h(r_{12}, \sigma_i, \sigma_j) - c(r_{12}, \sigma_i, \sigma_j) \\ &= \rho \int d\mathbf{r}_3 \int d\sigma F(\sigma) h(r_{13}, \sigma_i, \sigma) c(r_{32}, \sigma, \sigma_j) \end{aligned} \quad (60)$$

In comparison with the ordinary OZ equation, there is an additional integration with respect to the particle size. To proceed further, this integration can be removed by applying the method proposed by Lado [81,82]. Thus, we expand the  $\sigma$ -dependent functions in orthogonal polynomials  $P_j(\sigma)$ ,  $j = 0, 1, 2, \dots$ , defined such that

$$\int d\sigma F(\sigma) P_i(\sigma) P_j(\sigma) = \delta_{ij} \quad (61)$$

where  $\delta_{ij}$  is the Kronecker delta. Any function  $\theta(x, \sigma_i, \sigma_j)$  can be thus represented by

$$\theta(x, \sigma_i, \sigma_j) = \sum_{kl} \theta_{kl}(x) P_k(\sigma_i) P_l(\sigma_j) \quad (62)$$

The coefficients entering the last equation are given by

$$\theta_{kl}(x) = \int d\sigma_i d\sigma_j F(\sigma_i) F(\sigma_j) \theta(x, \sigma_i, \sigma_j) P_k(\sigma_i) P_l(\sigma_j) \quad (63)$$

The orthonormality of the functions  $P_i(\sigma_i)$  allows us to rewrite Eq. (59) in the following form

$$\tilde{\gamma}_{nm}(t) = \rho \sum_l [\tilde{c}_{nl}(t) + \tilde{\gamma}_{nl}(t)] \tilde{c}_{lm}(t) \quad (64)$$

where  $\tilde{\gamma}_{nm}(t)$  and  $\tilde{c}_{nm}(t)$  stand for the Fourier transforms of the coefficients  $\gamma_{nm}(r)$  and  $c_{nm}(r)$ .

The generalized pair distribution function

$$g(r, \sigma_1, \sigma_2) = \exp[-\beta u(r, \sigma_1, \sigma_2) + \gamma(r, \sigma_1, \sigma_2) + b(r, \sigma_1, \sigma_2)] \quad (65)$$

is finally constructed from the self-consistent solution of the OZ plus the closure equations for the coefficients  $\gamma_{nm}(r)$ . The thermodynamic quantities, directly computable from the pair distribution function, are the internal energy

$$E = \frac{3}{2} NkT + \frac{1}{2} \rho \int d\mathbf{r} d\sigma_1 d\sigma_2 F(\sigma_1) F(\sigma_2) g(r, \sigma_1, \sigma_2) u(r, \sigma_1, \sigma_2) \quad (66)$$

and the pressure

$$\frac{\beta p}{\rho} = 1 - \frac{1}{6}\rho \int d\mathbf{r} d\sigma_1 d\sigma_2 F(\sigma_1)F(\sigma_2)g(r, \sigma_1, \sigma_2) \frac{d\beta u(r, \sigma_1, \sigma_2)}{dr} \quad (67)$$

In addition, the isothermal compressibility

$$\begin{aligned} \beta \frac{\partial p}{\partial \rho} &= 1 - \rho \int d\mathbf{r} d\sigma_1 d\sigma_2 F(\sigma_1)F(\sigma_2)c(r, \sigma_1, \sigma_2) \\ &= 1 - \rho \tilde{c}_{00}(0) \end{aligned} \quad (68)$$

is obtained from the direct correlation function.

The pair correlation functions can be expressed directly in terms of the computed coefficients from Eq. (61); in particular, the number–number pair distribution function  $g_{NN}(r)$  and the number–number structure factor  $S_{NN}(k)$ . Thus,

$$g_{NN}(r) = \int d\sigma_1 d\sigma_2 F(\sigma_1)F(\sigma_2)g(r, \sigma_1, \sigma_2) = g_{00}(r) \quad (69)$$

and

$$\begin{aligned} S_{NN}(k) &= \int d\sigma_1 d\sigma_2 [F(\sigma_1)\delta(\sigma_1 - \sigma_2) + \rho F(\sigma_1)F(\sigma_2)\tilde{h}(k, \sigma_1, \sigma_2)] \\ &= 1 + \rho \tilde{h}_{00}(k) \end{aligned} \quad (70)$$

Obviously, the theory outlined above can be applied to two- and three-dimensional systems. In the case of a two-dimensional system the Fourier transforms of the two-particle function coefficients are carried out by using an algorithm, developed by Lado [85], that preserves orthogonality. A monolayer of adsorbed colloidal particles, having a continuous distribution of diameters, has been investigated by Lado. Specific calculations have been carried out for the system with the Schulz distribution [86]

$$F(\sigma) = \left( \frac{\alpha + 1}{\bar{\sigma}} \right)^{\alpha+1} \frac{\sigma^\alpha e^{-(\alpha+1)\sigma/\bar{\sigma}}}{\Gamma(\alpha + 1)} \quad (71)$$

where  $\Gamma(x)$  is the gamma function. The relative standard deviation of this distribution is

$$s_\sigma = \frac{1}{\sqrt{\alpha + 1}} \quad (72)$$

The orthonormal polynomials satisfying Eq. (61) for the distribution (71) are

$$P_j(\sigma) = \left[ \frac{j!}{\Gamma(\alpha+1)\Gamma(j+\alpha+1)} \right]^{1/2} L_j^{(\alpha)} \left[ (\alpha+1) \frac{\sigma}{\bar{\sigma}} \right] \quad (73)$$

where  $L_j^{(\alpha)}(t)$  are the associated Laguerre polynomials.

The calculations of Lado [82] have been performed for the repulsive DLVO potential

$$\beta u(r, \sigma_1, \sigma_2) = \begin{cases} \infty & r < 0.5(\sigma_1 + \sigma_2) \\ A(\sigma_1)A(\sigma_2) \exp(-\kappa r)/r & r > 0.5(\sigma_1 + \sigma_2) \end{cases} \quad (74)$$

where

$$A(\sigma) = \frac{Z(\sigma)L_B^{1/2} \exp(\kappa\sigma/2)}{1 + \kappa\sigma/2} \quad (75)$$

$\kappa$  is the inverse Debye-Hückel screening length,  $L_B$  is Bjerrum length,  $Z(\sigma) = Z(\bar{\sigma})(\sigma/\bar{\sigma})^2$ , and  $Z(\bar{\sigma})$  is the number of elementary charges on a particle of mean diameter  $\bar{\sigma}$ . Following Crocker and Gier [87], Lado used  $\bar{\sigma} = 650$  nm,  $L_B = 0.715$  nm,  $\kappa\bar{\sigma} = 4$ , and  $Z(\bar{\sigma}) = 1990$ . Under these conditions, the electrostatic repulsion keeps the spheres from touching, so, in practice, only polydispersity in charge is relevant.

The OZ equation was solved using the closure of Rogers and Young [50], Eq. (42), which for the multicomponent system takes the form

$$g(r, \sigma_1, \sigma_2) = \exp[-\beta u(r, \sigma_1, \sigma_2)] \left\{ 1 + \frac{\exp[m(r)\gamma(r, \sigma_1, \sigma_2)] - 1}{m(r)} \right\} \quad (76)$$

This closure mixes, via the function

$$m(r) = 1 - \exp(-\xi r) \quad (77)$$

the PY and hypernetted chain closures. As we have already noted, the parameter  $\xi$  in the last equation is chosen to enforce consistency between the compressibility calculated and the virial equation of state.

Numerical results for the some model polydisperse systems have been reported in Refs. 81–83. It has been shown that the effect of increasing polydispersity on the number–number distribution function is that the structure decreases with increasing polydispersity. This pattern is common for the behavior of two- and three-dimensional polydisperse fluids [81] and also for three-dimensional quenched–annealed systems [83].

It would be interesting, but non-trivial, to study polydisperse systems by means of a simulation, both for distributions that allow large spheres and for distributions that prevent the existence of large spheres. The conceptual

problem is that in the grand canonical ensemble we need a distribution in both size and chemical potential. Interesting questions for future study are phase separation in such systems and their behavior in the presence of a membrane.

## VI. INHOMOGENEOUS FLUIDS

The discussion so far has related to homogenous fluids where the density is the same everywhere in the fluid. In the presence of a surface, the density  $\rho(r)$  is a function of position and the fluid is inhomogeneous.

Integral equations have been developed for inhomogeneous fluids. One such integral equation is that of Henderson, Abraham and Barker (HAB) [88] who assumed the OZ equation for a mixture and regarded the surface as a giant particle. For planar geometry they obtained

$$h(z) = c(z) + 2\pi\rho \int_{-\infty}^{\infty} h(z')C(|z - z'|)dz' \quad (78)$$

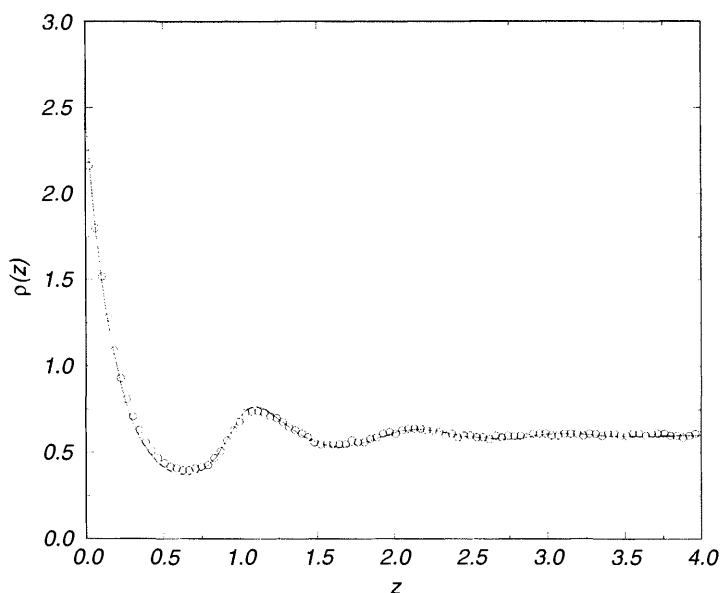


**FIG. 6** Density profile of a hard sphere fluid near a hard wall. The bulk density is  $\rho d^3 = 0.6$ . The curve gives the results of the IOZ equation with the PY closure and the circles give the simulation results. The results obtained using the HAB equation together with the MV closure are very close to the solid curve whereas the results obtained from the HAB equation with the HNC and PY closures are too large and too small, respectively.

where  $\mathcal{C}(x)$  is a function obtained by integrating the DCF of the fluid far from the surface

$$\mathcal{C}(x) = \int_x^\infty c(r) r dr \quad (79)$$

One reason the HAB approach is so useful is that once  $\mathcal{C}(x)$  has been determined, only one integration is required. Since the HAB equation is a version of the OZ equation, a closure is needed.

The HAB equation has been applied to hard spheres near a wall using the PY closure [88] and the HNC and MV closures. As is seen in Figs. 6 and 7, the results obtained from the HAB equation with the HNC and PY closures are not very satisfactory. However, if the MV closure is used, the results are quite good. In addition, the HAB equation has been applied to charged particles near a charged hard wall using the HNC closure [89–95]. The

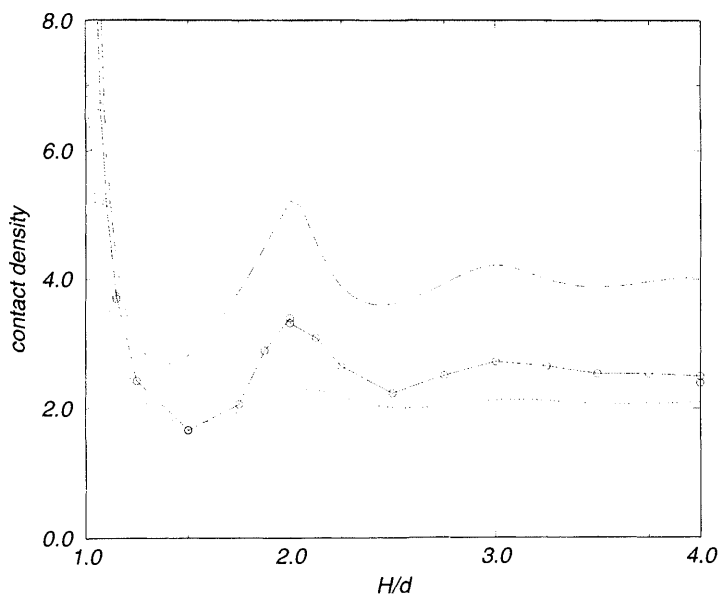


**FIG. 7** Values of the density profile at contact for hard spheres in a slit of width  $H$  as a function of  $H$ . The density of the hard sphere fluid that is in equilibrium with the fluid in the slit is  $\rho d^3 = 0.6$ . The solid curve gives the IOZ equation results obtained using the PY closure. The broken and dotted curves give the results of the HAB equation obtained using the HNC and PY closures, respectively. The results obtained from the HAB equation with the MV closure are very similar to the solid curve. The circles give the simulation results.



HAB equation with the MSA closure gives analytic results for charged particles near a charged hard wall [96] and for a mixture of dipolar and charged hard spheres near a charged hard wall [97,98]. These applications yield good results as long as the wall charge is not too large [97,98].

Recently, the HAB approach plus the MV closure has been applied both to hard spheres near a single hard wall [24,25] and in a slit formed by two hard walls. Some results [99] for the latter system are compared with simulation results in Fig. 7. The results obtained from the HAB equation with the HNC and PY closures are not very satisfactory. However, if the MV closure is used, the results are quite good. There have been a few applications of the HAB equation to inhomogeneous fluids with attractive interactions. The results have not been very good. The fault lies with the closure used and not Eq. (78). A better closure is needed. Perhaps the DHH closure [27,28] would yield good results, but it has never been tried.

A more sophisticated approach, but one that is more demanding of computational resources, is based on the *inhomogeneous* OZ (IOZ) equation

$$h(r_1, r_2) = c(r_1, r_2) + \int \rho(r_3) h(r_1, r_3) c(r_2, r_3) d\mathbf{r}_3 \quad (80)$$

Again, a closure is needed. Even with a closure, the system of equations is not complete. A relation between the singlet function  $\rho(r)$  and the pair functions is needed. For this purpose the first equation of the BGY hierarchy may be used. Alternatively, one can apply the *Lovett-Mou-Buff-Wertheim* equation [100,101]

$$\nabla \rho(\mathbf{r}_1) = -\beta \rho(\mathbf{r}_1) \nabla v(\mathbf{r}_1) + \int c(\mathbf{r}_1, \mathbf{r}_2) \nabla \rho(\mathbf{r}_2) d\mathbf{r}_2 \quad (81)$$

where  $v(\mathbf{r})$  is the external potential. This potential can be considered as due to a surface or a selected particle in the system that is regarded as the source of the inhomogeneity. In the latter case  $v(\mathbf{r})$  is just the pair potential.

Sokołowski [102,103] and Plischke and Henderson [104,105] have applied the IOZ equation, with the PY and HNC closures, to hard spheres near a hard wall. Using the HNC and MSA closures, Plischke and Henderson [106–108] have studied charged hard spheres near a charged planar hard wall. The results are very good. In contrast to the results obtained from the OZ equation, the IOZ yields results for  $\rho(r)$  that are nearly independent of the closure. As might be expected, the results for the pair functions are closure dependent and show similar problems to those seen for the RDF with the OZ and similar closures.

Henderson et al. [109] have applied the IOZ equation with the PY closure to hard spheres in a slit formed by hard parallel walls. Some of these results are displayed in Fig. 7. The agreement with the simulation results is good.

## VII. BRIDGE FUNCTIONS FOR HOMOGENEOUS FLUIDS

For homogeneous fluids, it is desirable to have a systematic method of going beyond the closures that have been discussed above. Equation (21) can be generalized

$$\gamma(r) = \ln y(r) - B(r) \quad (82)$$

where  $B(r)$  is called the *bridge function*. The bridge function is simply what is missing from the HNC approximation.

About all that is known of the bridge function is that at low densities

$$B(r_{12}) = \frac{1}{2}\rho^2 \int f(r_{13})f(r_{23})f(r_{14})f(r_{24})f(r_{34})dr_3dr_4 + \cdots \quad (83)$$

where  $f(r) = \exp[-\beta u(r)] - 1$ . The bridge function gets its name from the fact that the integral in the last equation is like a bridge when written in diagrammatic notation.

The various closures that have been discussed can be written in terms of the bridge function. For example, the HNC closure is

$$B(r) = 0 \quad (84)$$

The PY closure is

$$B(r) = \ln y(r) - y(r) + 1 \quad (85)$$

and the MV closure is

$$B(r) = -\frac{1}{2}\rho^2 \frac{\gamma^2(r)}{1 + \alpha\gamma(r)} \quad (86)$$

The expression for  $B(r)$  in the DHH is somewhat similar to Eq. (86).

Note that, except for the DHH closure, all of the closures discussed above lead to a bridge function that is always negative or zero. In the case of the DHH closure, there can be a small positive region. It is interesting to note that recent unpublished work indicates that the bridge function may be positive near the critical point.

It is desirable to have a systematic procedure for going beyond these approximations. Attard [110] has suggested using Eq. (80) for this purpose. In an application to a homogeneous fluid, we use Eq. (80) but regard the source of the inhomogeneity as one of the molecules. When Eq. (80) is used in this manner, we shall call it the OZ2 equation.

Attard has obtained OZ2 results for hard spheres. Henderson and Sokołowski have obtained results for hard spheres [111], an LJ fluid [112], and a mixture of LJ fluids [113]. The results are very good. The values of  $y(r)$  obtained from the OZ2 equation with the PY closure are very similar to the

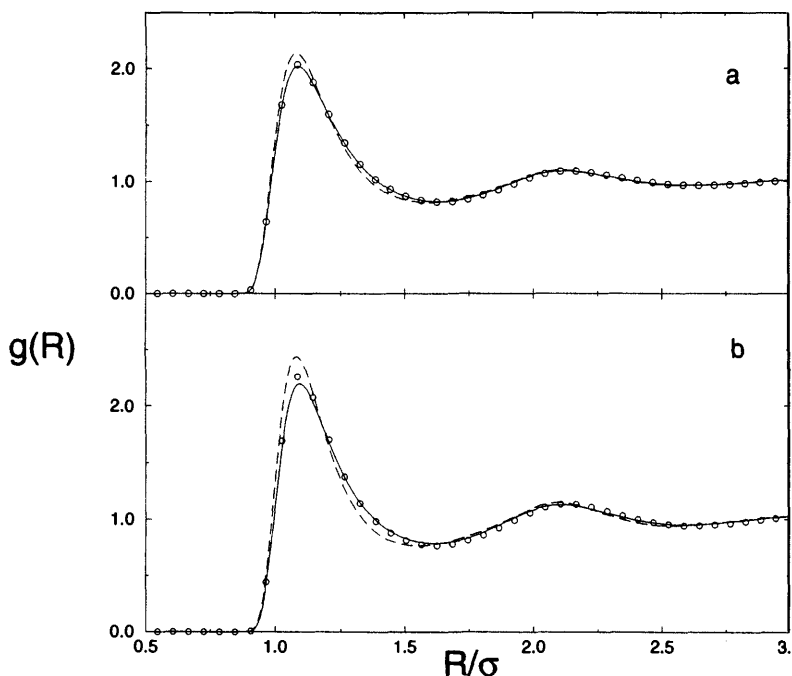


**FIG. 8** Radial distribution of an LJ fluid as a function of  $r$  for  $T^* = 1.5$  and  $\rho^* = 0.60$  (a) and for  $T^* = 1.1$  and  $\rho^* = 0.65$  (b). The solid and broken curves give the IOZ and OZ results, respectively. The PY closure was used in obtaining both the IOZ and OZ results. The circles give the simulation results (from Ref. 112).

solid curves plotted in Fig. 3 (cf. Fig. 2 in Ref. 69). The OZ2 results obtained with the HNC closure are somewhat less satisfactory but are an improvement over the usual HNC results obtained with the OZ equation. Some results for  $g(r)$ , obtained from the OZ2 equation using the PY closure, are plotted in Fig. 8. The agreement with simulation results is very good. The results of the usual PY equation, based on the usual OZ equation, are less satisfactory.

## VIII. SUMMARY

Integral equations provide a satisfactory formalism for the study of homogeneous and inhomogeneous fluids. If the usual OZ equation is used, the best results are obtained from semiempirical closures such as the MV and DHH closures. However, this empirical element can be avoided by using integral equations that involve higher-order distribution functions, but at the cost of some computational complexity.

## ACKNOWLEDGMENTS

This work has been supported in part by the National Science Foundation (Grants CHE-9601971 and CHE-9813729), the donors of the Petroleum Research Fund, administered by the American Chemical Society (Grant No. ACS-PRF 31573-AC9), and a NATO Collaborative Research Grant (Grant HTECH.CRG972915).

## REFERENCES

1. T. Andrews. *Phil Trans Roy Soc Lond* 159:575, 1869.
2. T. Andrews. *Phil Trans Roy Soc Lond* 169:421, 1876.
3. J. P. Hansen, I. R. McDonald. *Theory of Simple Liquids*. 2nd ed. London: Academic Press, 1986.
4. J. A. Barker, D. Henderson. *Ann Rev Phys Chem* 23:439, 1972.
5. J. A. Barker, D. Henderson. *Ann Rev Mod Phys* 48:587, 1976.
6. M. Born, M. S. Green. *A General Kinetic Theory of Liquids*. Cambridge: Cambridge University Press, 1949.
7. J. Yvon. *La Théorie Statistique des Fluides et l'Equation d'Etat, Actualités Scientifiques et Industrielles*. Paris: Hermann, 1935, p. 203.
8. J. G. Kirkwood. *J Chem Phys* 3:300, 1935.
9. J. G. Kirkwood. *J Chem Phys* 7:911, 1939.
10. Y. T. Lee, F. H. Ree, T. Ree. *J Chem Phys* 48:3506, 1968.
11. F. H. Ree, Y. T. Lee, T. Ree. *J Chem Phys* 55:234, 1971.
12. D. Henderson. In: D. Henderson, ed. *Fundamentals of Inhomogeneous Fluids*. New York: Marcel Dekker, 1992.
13. J. K. Percus, G. J. Yevick. *Phys Rev* 110:1, 1958.
14. J. Stecki. Private communication.
15. M. S. Wertheim. *Phys Rev Lett* 10:321, 1963.
16. M. S. Wertheim. *J Math Phys* 5:643, 1964.
17. E. Thiele. *J Chem Phys* 39:474, 1963.
18. N. F. Carnahan, K. E. Starling. *J Chem Phys* 51:635, 1969.
19. L. Verlet, J. J. Weis. *Mol Phys* 24:1013, 1972.
20. L. Verlet, J. J. Weis. *Mol Phys* 28:665, 1974.
21. L. Verlet, J. J. Weis. *Phys Rev A* 5:939, 1972.
22. J. L. Lebowitz. *Phys Rev A* 133:895, 1964.
23. L. Verlet. *Mol Phys* 41:183, 1980.
24. D. Henderson, K. Y. Chan, L. Degreve. *J Chem Phys* 101:6975, 1994.
25. M. Beard, D. Henderson. *Mol Phys* 92:1083, 1997.
26. D. Henderson, A. Malijevsky, S. Labik, K. Y. Chan. *Mol Phys* 87:6875, 1994.
27. D. M. Duh, A. D. J. Haymet. *J Chem Phys* 97:7716, 1992.
28. D. M. Duh, A. D. J. Haymet. *J Chem Phys* 102:2625, 1995.
29. D. M. Duh, D. Henderson. *J Chem Phys* 104:6742, 1996.
30. E. Waisman. *Mol Phys* 25:45, 1973.
31. J. S. Höye, G. Stell. *Mol Phys* 16:399, 1977.

32. J. S. Höye, G. Stell. *J Stat Phys* 16:399, 1977.
33. L. Blum, J. S. Höye, G. Stell. *J Stat Phys* 19:317, 1978.
34. M. Ginoza. *J Phys Soc Japan* 54:2783, 1985.
35. M. Ginoza. *J Phys Soc Japan* 55:95, 1985.
36. M. Ginoza. *J Phys Soc Japan* 56:5, 1987.
37. D. Henderson, L. Blum, J. P. Noworyta. *J Chem Phys* 102:4973, 1995.
38. E. Waisman, J. Lebowitz. *J Chem Phys* 52:430, 1970.
39. E. Waisman, J. Lebowitz. *J Chem Phys* 56:3086, 1972.
40. E. Waisman, J. Lebowitz. *J Chem Phys* 56:3093, 1972.
41. L. Blum. *Theor Chem Adv Perspectives* 5:1, 1980.
42. M. S. Wertheim. *J Chem Phys* 55:4291, 1971.
43. M. S. Wertheim. *J Chem Phys* 55:1556, 1971.
44. L. Blum. *Chem Phys Lett* 26:200, 1974.
45. L. Blum. *J Chem Phys* 61:2129, 1974.
46. L. Blum. *J Stat Phys* 18:451, 1978.
47. S. A. Adelman, J. M. Deutch. *J Chem Phys* 60:3935, 1974.
48. F. Lado. *Phys Rev A* 135:1013, 1964.
49. F. Lado. *Mol Phys* 31:1117, 1976.
50. F. J. Rogers, D. A. Young. *Phys Rev A* 46:7652, 1992.
51. G. A. Martynov, G. N. Sarkisov. *Mol Phys* 48:1495, 1983.
52. P. Ballone, G. Pastore, G. Galli, D. Gazzillo. *Mol Phys* 59:275, 1986.
53. T. Biben, J. P. Hansen. *Europhys Lett* 12:347, 1990.
54. T. Biben, P. Bladon, D. Frenkel. *J Phys Condensed Matter* 8:10799, 1996.
55. C. Caccamo. *Phys Rept* 274:1, 1996.
56. D. Pini, G. Stell, N. B. Wilding. *Mol Phys* 95:483, 1998.
57. J. S. Höye, G. Stell. *Physica A* 244:176, 1997.
58. J. S. Höye, G. Stell. *Physica A* 247:497, 1997.
59. E. Kierlik, M. L. Rosinberg, G. Trajus. *J Stat Phys* 89:215, 1997.
60. E. Kierlik, M. L. Rosinberg, G. Trajus, P. A. Monson. *J Phys Condensed Matter* 8:9621, 1998.
61. S. Labík, A. Malijevský, W. R. Smith. *Mol Phys* 83:983, 1994.
62. S. Labík, A. Malijevský, W. R. Smith. *Mol Phys* 83:1223, 1994.
63. H. Reiss, H. L. Frisch, J. L. Lebowitz. *J Chem Phys* 31:369, 1959.
64. H. Reiss, P. Schaff. *J Chem Phys* 91:2514, 1989.
65. J. A. Ballance, R. J. Speedy. *Mol Phys* 54:1035, 1984.
66. R. J. Speedy, H. Reiss. *Mol Phys* 72:999, 1990.
67. E. Meeron, A. J. F. Siegert. *J Chem Phys* 48:3139, 1968.
68. S. Labík, A. Malijevský, I. Nezbeda. *Mol Phys* 60:1107, 1987.
69. G. Stell. In: B. D. Hughes, B. W. Ninham, eds. *The Wonderful World of Stochastics*. Berlin: Springer, 1985.
70. W. R. Smith, S. Labík, A. Malijevský, J. Sedlbauer. *Mol Phys* 83:1223, 1994.
71. R. Lustig. *Mol Phys* 59:195, 1986.
72. S. Labík, A. Malijevský. *Mol Phys* 53:381, 1984.
73. R. Aris, G. R. Gavalas. *Phil Trans Roy Soc Lond A* 260:351, 1966.
74. J. J. Salacuse, G. Stell. *J Chem Phys* 77:3715, 1982.

75. K. A. Johnson, D. A. Jonah, M. J. Kincaid, G. Morrison. *J Chem Phys* 82:5178, 1985.
76. P. McRae, A. D. J. Haymet. *J Chem Phys* 88:1114, 1988.
77. J. G. Briano, E. D. Glandt. *J Chem Phys* 80:3336, 1984.
78. D. A. Kofke, E. D. Glandt. *J Chem Phys* 87:4881, 1987.
79. D. A. Kofke, E. D. Glandt. *J Chem Phys* 90:439, 1989.
80. J. M. Kincaid, R. A. McDonald, G. Morrison. *J Chem Phys* 97:5425, 1987.
81. F. Lado. *Phys Rev E* 54:4411, 1996.
82. F. Lado. *J Chem Phys* 108:6441, 1998.
83. J. Ilnytskij, A. Patrykiewicz, O. Pizio, S. Sokołowski. *J Phys Chem B* 103:868, 1999.
84. B. D'Aguzzo, R. Klein, J. M. Méndez Alcaraz, G. Nägele. In: L. Garrido, ed. *Complex Fluids*. Berlin: Springer, 1993.
85. F. Lado. *J Chem Phys* 49:3092, 1968.
86. G. V. Schulz. *Z Phys Chem Abt A* 43:25, 1939.
87. J. C. Crocker, D. G. Gier. *Phys Rev Lett* 73:352, 1994.
88. D. Henderson, F. F. Abraham, J. A. Barker. *Mol Phys* 31:1291, 1976.
89. D. Henderson, L. Blum, W. R. Smith. *Chem Phys Lett*. 63:381. 1971.
90. D. Henderson, L. Blum. *J Electroanal Chem* 111:217, 1980.
91. S. L. Carnie, D. Y. C. Chan, D. J. Mitchell, B. W. Ninham. *J Chem Phys* 74:1472, 1981.
92. S. L. Carnie. *Mol Phys* 54:509, 1985.
93. M. Lozada-Cassou, R. Saavedra-Barrera, D. Henderson. *J Chem Phys* 77:5150, 1982.
94. M. Lozada-Cassou, D. Henderson. *J Phys Chem* 87:2821, 1983.
95. J. Barojas, D. Henderson, M. Lozada-Cassou. *J Phys Chem* 87:4583, 1983.
96. L. Blum. *J Phys Chem* 81:136, 1977.
97. S. L. Carnie, D. Y. C. Chan. *J Chem Phys* 73:2949, 1980.
98. L. Blum, D. Henderson. *J Chem Phys* 74:1902, 1981.
99. D. Henderson, S. Sokołowski, D. T. Wasan. *J Phys Chem B* 102:3009, 1998.
100. R. Lovett, C. Y. Mou, F. P. Buff. *J Chem Phys* 65:570, 1976.
101. M. Wertheim. *J Chem Phys* 65:2377, 1976.
102. S. Sokołowski. *J Chem Phys* 73:3507, 1980.
103. S. Sokołowski. *Mol Phys* 49:481, 1983.
104. M. Plischke, D. Henderson. *J Phys Chem* 88:6544, 1984.
105. M. Plischke, D. Henderson. *Proc Roy Soc A Lond* 404:323, 1986.
106. M. Plischke, D. Henderson. *J Chem Phys* 88:2712, 1988.
107. M. Plischke, D. Henderson. *J Chem Phys* 90:5738, 1989.
108. M. Plischke, D. Henderson. *Electrochim Acta* 34:1863, 1989.
109. D. Henderson, S. Sokołowski, D. T. Wasan. *J Stat Phys* 89:233, 1997.
110. P. Attard. *J Chem Phys* 91:3072, 1989.
111. D. Henderson, S. Sokołowski. *J Chem Phys* 103:7541, 1995.
112. D. Henderson, S. Sokołowski. *J Chem Phys* 104:2971, 1996.
113. D. Henderson, S. Sokołowski. *Mol Phys* 90:85, 1997.

# 4

## Nonuniform Associating Fluids

**MALGORZATA BORÓWKO and STEFAN SOKOŁOWSKI** Department for the Modelling of Physico-Chemical Processes, Maria Curie-Skłodowska University, Lublin, Poland

**OREST PIZIO** Instituto de Química de la Universidad Nacional Autónoma de México, Coyoacán, México

I.	Introduction	168
II.	Nonuniform Fluids with Spherically Symmetric Associative Potentials	171
A.	Basic relations of the theory of inhomogeneous fluids	171
B.	Application of the singlet-level and pair-level theories for fluids with spherically symmetric associative interactions in contact with surfaces	178
III.	Nonuniform Associating Fluids with Directional Forces	192
A.	The bulk model for association with directional bonding	193
B.	The multidensity Ornstein–Zernike integral equations	194
C.	Elements of thermodynamic perturbation theory	196
D.	Pair theory of nonuniform associating fluids	200
E.	Singlet level theory for fluids with directional bonding	204
IV.	Density Functional Approaches in the Theory of Inhomogeneous Associating Fluids	211
A.	The theory of Segura, Chapman, and Shukla	211
B.	A modified Meister–Kroll theory	214
C.	Associating hard spheres at a hard wall	216
D.	Association effects on wettability of solid surfaces	219
E.	Association effects on capillary condensation	222
V.	Computer Simulation of Inhomogeneous Associating Fluids	228
A.	A Monte Carlo study of wetting of associating fluids	229

B. Chemical potential of inhomogeneous associating fluids from osmotic Monte Carlo simulation	233
VI. Concluding Remarks	237
References	238

## I. INTRODUCTION

This chapter is concerned with the theory of inhomogeneous associating fluids. Much previous effort has been focused on simple (nonassociating) fluids under confinement and a large amount of results for the structure, thermodynamics and phase behavior of these systems has been accumulated in the literature during the past few decades; see, e.g., [1–3]. Computer simulation methods, integral equations and density functional techniques provide powerful tools to investigate inhomogeneous fluids.

Our focus in the present study is, however, on *inhomogeneous associating fluids*. There is no need to recall that the properties of fluids in thin films and at surfaces differ in many respects from the homogeneous phase (bulk) properties. On the other hand, molecular association has a significant effect on the properties of fluids, due to the formation of molecular clusters. Theoretical investigation of *inhomogeneous associating* fluids, involving a combined difficulty due both to inhomogeneity and to association effects, therefore represents a challenge in chemical physics. However, the subject of this research is not entirely academic.

Several areas of chemistry and of chemical engineering require good knowledge of the properties of inhomogeneous associating fluids. Phenomena of adsorption and chemisorption, of heterogeneous catalysis on crystalline and noncrystalline materials, of corrosion and many others, imply that chemical association at interfaces occurs or may occur. The formation of molecular clusters due to strong finite-range forces is considered, in statistical mechanics of equilibrium fluids, as a chemical reaction with corresponding equilibrium constants. Therefore, we use both terms: inhomogeneous associating, and chemically reacting, fluids, in what follows.

Phenomena taking place in inhomogeneous associating fluids (IAFs) are much richer than those occurring in their bulk counterparts. However, the theory of IAFs intrinsically requires methods to describe successfully the bulk, homogeneous associating systems. These latter systems have become the subject of intense research during the last two decades. Pioneering efforts of Andersen, Chandler and Pratt, Høye and Olaussen [4–7] in the formulation of the theory of association in bulk systems have been reconsidered by



Wertheim and have permitted him to formulate a very successful approach for the description of association [8–11].

The theory of Wertheim is based on activity expansions for the correlation functions and the grand thermodynamic potential, in contrast to the density expansion techniques common in the theory of nonassociating fluids. Successful treatment of the steric constraints due to the short-ranged, strong attractive, saturable forces has permitted Wertheim to resume the series for the grand potential and the correlation function in terms of densities of the unbonded and bonded particles. The correlation functions then satisfy a multidensity integral equation of the Ornstein–Zernike (OZ) form. The usual particle–particle pair correlation function can be written as a linear combination of the “partial” correlation functions that represent sums of a certain class of diagrams corresponding to correlations of unbonded and bonded species. The theory of Wertheim has been used extensively by different groups to study nonionic and ionic associating (dimerizing, polymerizing, and network-forming) fluids. However, most important is that the theory permits successful description of the effects of association into thermodynamic properties of the systems in question. As a result, not only can an integral equation methodology be used to investigate thermodynamics, but also a density functional technique can be extended to associating fluids. This issue is crucial for inhomogeneous associating fluids that represent our main focus.

The bulk associating fluids have been intensively studied using computer simulation [12–20]. In many cases simulation has been performed to verify theoretical predictions. The studies of Chapman and Zhang [17,18], in particular, have been concerned with a comparison of the results of a traditional Metropolis Monte Carlo simulation for dimerization of methanol with the prior predictions of the theory of Wertheim. It appeared, however, that in several applications the traditional Monte Carlo method does not provide reasonable statistical averages. At high degrees of association bonded configurations represent a small part of the configuration space. In the traditional method, the configurational space is randomly sampled, thus the small spatial volume of bonded configurations may be difficult to sample adequately in the framework of the common algorithm. In order to overcome this difficulty, Busch et al. [19] have proposed the association-biased Monte Carlo method. The canonical ensemble algorithm biases sampling to the regions of configuration space where the association or dissociation of particles is likely to occur. This is an efficient simulation technique for associating fluids in a wide range of densities. Unfortunately, the application of the method to nonuniform associating fluids requires a great deal of numerical effort.

The theory of inhomogeneous associating fluids evidently has benefited from the developments available for bulk associating models. The theory of

IAFs has been initiated only very recently. The first methodological steps undertaken in the consideration of IAFs have actually been borrowed from the theory of inhomogeneous nonassociating fluids. The works from the laboratory of Holovko [21–23] have focused on obtaining analytical solutions for the *associative extension* of the Henderson–Abraham–Barker (HAB) equation for the density profile of particles in contact with an impermeable hard wall [24]. Simultaneously, Henderson, in collaboration with Pizio and Sokołowski, has applied the bulk solutions for dimerizing hard spheres of Cummings and Stell [25–27] to investigate the behavior of associating fluids under several confinement conditions [28–33]. More sophisticated, second-order integral equations for the density profiles of particles in the theory of IAFs have been applied first in [34,35]. Theoretical work on IAFs has been developed simultaneously with computer simulation [36,37]. Only very recently, methodological tools for investigating IAFs have been extended by the application of density functional techniques [38–45]. We discuss all the aforementioned theories to a greater extent in the body of our chapter.

It is worth mentioning, however, that only the simplest models of inhomogeneous associating fluids which give insight into a restricted set of interfacial phenomena have been studied so far. Nevertheless, a successful description of adsorption phenomena can be reached, even within the framework of quite simple theoretical procedures. Much room remains for further studies of more complex phenomena with more sophisticated theoretical and computational algorithms. In the present chapter, we restrict ourselves only to associating fluids in contact with solid surfaces and in pores of well-defined geometry. More sophisticated types of confinement are not discussed. Moreover, the effects of association between species at a liquid–gas or liquid–liquid interface, as well as adsorption in random microporous materials (see, e.g., chapter 6 by O. Pizio), are not considered. Also, due to space limitations of this chapter, we have restricted our attention to fluids without long-range electrostatic interactions between species as well as between them and confining surfaces. Research into charged inhomogeneous associating fluids is of much interest for several applications but is in its very initial stage so far.

The present chapter is organized as follows. We focus first on a simple model of a nonuniform associating fluid with spherically symmetric associative forces between species. This model serves us to demonstrate the application of so-called first-order (singlet) and second-order (pair) integral equations for the density profile. Some examples of the solution of these equations for associating fluids in contact with structureless and crystalline solid surfaces are presented. Then we discuss one version of the density functional theory for a model of associating hard spheres. All aforementioned issues are discussed in Sec. II.

Sec. III is concerned with the description of models with directional associative forces, introduced by Wertheim. Singlet and pair theories for these models are presented. However, the main part of this section describes the density functional methodology and shows its application in the studies of adsorption of associating fluids on partially permeable walls. In addition, the application of the density functional method in investigations of wettability of associating fluids on solid surfaces and of capillary condensation in slit-like pores is presented.

Finally, in Sec. IV, two examples of the application of the Monte Carlo simulation to investigate the structure and thermodynamic properties of adlayers of an associating fluid are given. The results of simulations are compared with those from theoretical approaches. In conclusion, we discuss some methodological perspectives in the discussed area of research.

## II. NONUNIFORM FLUIDS WITH SPHERICALLY SYMMETRIC ASSOCIATIVE POTENTIALS

### A. Basic Relations of the Theory of Inhomogeneous Fluids

Let us consider an  $N$ -component fluid in a volume  $V$ , at temperature  $T$ , and at chemical potentials  $\{\mu\} = \{\mu_1, \mu_2, \dots, \mu_N\}$ . The fluid is in contact with an impermeable solid surface. We assume that the fluid particles interact between themselves via the pair potential denoted by  $u_{\alpha\beta}(r)$ , and interact with the confining surface via the potential  $v_\alpha$  ( $\alpha, \beta = 1, 2, \dots, N$ ). The potential  $v_\alpha(\mathbf{r})$  contains a hard-wall term to ensure that the solid surface is impermeable. For the sake of convenience, the hard-wall term is assumed to extend into the bulk of the solid [46,47], such that the Boltzmann factor  $g_\alpha(\mathbf{r})$ , and the local density  $\rho_\alpha(\mathbf{r})$  are cutoff at a certain distance  $z = z_\Omega$ ,

$$g_\alpha(\mathbf{r}) = \begin{cases} \exp[-v_\alpha(\mathbf{r})/k_B T] & z > z_\Omega \\ 0 & z < z_\Omega \end{cases} \quad (1)$$

The equilibrium theory of *homogeneous* fluids may be constructed by using the hierarchy of the direct correlation functions [48]. This approach has been of much utility for the development of the theory of *inhomogeneous* simple fluids. The hierarchy of the direct correlation functions is defined by the following relation

$$c_{\alpha\beta,\dots,N}(\mathbf{r}_1, \mathbf{r}_2, \dots, \mathbf{r}_N) = - \frac{\delta^N F^{\text{ex}}}{\delta \rho_\alpha(\mathbf{r}_1) \dots \delta \rho_N(\mathbf{r}_N)} \quad (2)$$

which is equivalent to the hierarchy of the functional derivatives of the grand thermodynamic potential  $\Omega$  with respect to the conjugated external

fields,  $\mu_\alpha - v_\alpha(\mathbf{r})$  [49]. Common notation has been used in Eq. (2):  $F^{\text{ex}}$  is the excess, over ideal, free energy,  $c_{\alpha\beta,\dots,N}(\mathbf{r}_1, \mathbf{r}_2, \dots, \mathbf{r}_N)$  is the  $N$ th order direct correlation function. The first member of the hierarchy given by Eq. (2), for the system at equilibrium, yields

$$c_\alpha(\mathbf{r}) = \ln \rho_\alpha(\mathbf{r}) - \mu_\alpha/k_B T + v_\alpha(\mathbf{r})/k_B T \quad (3)$$

where  $c_\alpha(\mathbf{r})$  is the one-particle direct correlation function. Clearly,  $c_\alpha(\mathbf{r})$  approaches zero (for interparticle potentials of finite range) if all the densities  $\rho(\mathbf{r})$  are equal to zero. One can perform straightforwardly a functional expansion of  $c_\alpha(\mathbf{r})$  with respect to a *uniform* equilibrium mixture considered at densities of species  $\rho_1(\mathbf{r}_0), \rho_2(\mathbf{r}_0), \dots, \rho_N(\mathbf{r}_0)$

$$\begin{aligned} c_\alpha(\mathbf{r}_1) = & c_\alpha^0 + \sum_\beta \int d\mathbf{r}_2 \left( \frac{\delta c_\alpha(\mathbf{r}_1)}{\delta \rho_\beta(\mathbf{r}_2)} \right)_{\{\rho(\mathbf{r}_0)\}} [\rho_\beta(\mathbf{r}_2) - \rho_\beta(\mathbf{r}_0)] \\ & + \frac{1}{2} \sum_{\beta,\gamma} \int d\mathbf{r}_2 d\mathbf{r}_3 \left( \frac{\delta c_\alpha(\mathbf{r}_1)}{\delta \rho_\beta(\mathbf{r}_2) \delta \rho_\gamma(\mathbf{r}_3)} \right)_{\{\rho(\mathbf{r}_0)\}} \\ & \times [\rho_\beta(\mathbf{r}_2) - \rho_\beta(\mathbf{r}_0)] [\rho_\gamma(\mathbf{r}_3) - \rho_\gamma(\mathbf{r}_0)]. \end{aligned} \quad (4)$$

This expansion can be rewritten in another form, by taking into account Eq. (3). Namely, we obtain

$$\begin{aligned} \ln \rho_\alpha(\mathbf{r}_1) + v_\alpha(\mathbf{r}_1)/k_B T = & \ln \rho_\alpha(\mathbf{r}_0) + v_\alpha(\mathbf{r}_0)/k_B T \\ & + \sum_\beta \int d\mathbf{r}_2 c_{\alpha,\beta}^0(|\mathbf{r}_1 - \mathbf{r}_2|) [\rho_\beta(\mathbf{r}_2) - \rho_\beta(\mathbf{r}_0)] \\ & + \frac{1}{2} \sum_{\beta,\gamma} \int d\mathbf{r}_2 d\mathbf{r}_3 c_{\alpha,\beta,\gamma}^0(\mathbf{r}_1, \mathbf{r}_2, \mathbf{r}_3) [\rho_\beta(\mathbf{r}_2) - \rho_\beta(\mathbf{r}_0)] \\ & \times [\rho_\gamma(\mathbf{r}_3) - \rho_\gamma(\mathbf{r}_0)] + \dots \end{aligned} \quad (5)$$

where the superscript 0 denotes that the direct correlation functions are for a uniform fluid at a set of densities  $\{\rho_1(\mathbf{r}_0), \rho_2(\mathbf{r}_0), \dots, \rho_N(\mathbf{r}_0)\}$ .

Eq. (5) is useful when analyzing different approximations in the theory of inhomogeneous fluids. In particular, if all the terms involving third- and higher-order correlations in the right-hand side of Eq. (5) are neglected, and if  $\rho_1(\mathbf{r}_0), \rho_2(\mathbf{r}_0), \dots, \rho_N(\mathbf{r}_0)$  are chosen as the densities of species for a uniform system at temperature  $T$  and the chemical potentials  $\{\mu\}$ , the singlet hypernetted chain equation (HNC1) [50] results

$$\ln t_\alpha(\mathbf{r}_1) = \sum_\beta \rho_\beta \int c_{\alpha\beta}^0(r_{12}) [t_\beta(\mathbf{r}_2) g_\beta(\mathbf{r}_2) - 1] d\mathbf{r}_2 \quad (6)$$

where the one-particle cavity or background function,  $t_\alpha(\mathbf{r})$ , is defined by  $\rho_\alpha t_\alpha(\mathbf{r})g_\alpha(\mathbf{r}) = \rho_\alpha(\mathbf{r})$ . If the two-particle correlation functions  $c_{\alpha\beta}(r)$  are known, the HNC1 equation can be solved numerically to yield the local densities of an inhomogeneous fluid mixture. One of the possible forms of the singlet Percus–Yevick equation (PY1) is obtained by linearization of Eq. (6)

$$t_\alpha(\mathbf{r}_1) = 1 + \sum_\beta \rho_\beta \int c_{\alpha\beta}^0(r_{12})[t_\beta(\mathbf{r}_2)g_\beta(\mathbf{r}_2) - 1]d\mathbf{r}_2 \quad (7)$$

We need, however, some means to calculate the direct correlation functions  $c_{\alpha\beta}(\mathbf{r}_1, \mathbf{r}_2)$  of a nonuniform fluid. In order to make further progress, the Taylor series representation for  $c_{\alpha\beta}(\mathbf{r}_1, \mathbf{r}_2)$  can be made

$$\begin{aligned} c_{\alpha\beta}(\mathbf{r}_1, \mathbf{r}_2) &= c_{\alpha\beta}^0(r_{12}) + \sum_\gamma \int d\mathbf{r}_3 c_{\alpha\beta\gamma}^0(\mathbf{r}_1, \mathbf{r}_2, \mathbf{r}_3)[\rho_\gamma(\mathbf{r}_3) - \rho_\gamma] \\ &\quad + \frac{1}{2} \sum_{\gamma,\delta} \int d\mathbf{r}_3 d\mathbf{r}_4 c_{\alpha\beta\gamma\delta}^0(\mathbf{r}_1, \mathbf{r}_2, \mathbf{r}_3, \mathbf{r}_4)[\rho_\gamma(\mathbf{r}_3) - \rho_\gamma] \\ &\quad \times [\rho_\delta(\mathbf{r}_3) - \rho_\delta] + \dots \end{aligned} \quad (8)$$

Eq. (8) now can be used in conjunction with Eq. (5) to obtain another relation for  $\rho_\alpha(\mathbf{r})$  [46,47]. Differentiating Eq. (5) with respect to  $\rho_\beta(\mathbf{r})$ , and making use of the Baxter relations [51],

$$\begin{aligned} \frac{\partial c_{\alpha\beta}^0(\mathbf{r}_1, \mathbf{r}_2)}{\partial \rho_\gamma} &= \int c_{\alpha\beta\gamma}^0(\mathbf{r}_1, \mathbf{r}_2, \mathbf{r}_3)d\mathbf{r}_3 \\ \frac{\partial c_{\alpha\beta\gamma}^0(\mathbf{r}_1, \mathbf{r}_2, \mathbf{r}_3)}{\partial \rho_\delta} &= \int c_{\alpha\beta\gamma\delta}^0(\mathbf{r}_1, \mathbf{r}_2, \mathbf{r}_3, \mathbf{r}_4)d\mathbf{r}_4, \quad \text{etc.}, \end{aligned} \quad (9)$$

after some rearrangement of terms, we obtain [46,47]

$$\frac{\partial t_\alpha(\mathbf{r}_1)}{\partial \rho_\beta} = - \int c_{\alpha\beta}^0(r)d\mathbf{r} + \sum_\gamma \int c_{\alpha\gamma}^0(\mathbf{r}_1, \mathbf{r}_2) \frac{\partial \rho_\gamma(\mathbf{r}_2)}{\partial \rho_\beta} d\mathbf{r}_2 \quad (10)$$

Finally, we relate the gradient of the local density  $\nabla_1 \rho_\alpha(\mathbf{r}_1)$  to the pair correlation functions. For this purpose we take the gradient of the expansion (5)

$$\begin{aligned} \nabla_1 [\ln \rho_\alpha(\mathbf{r}_1) + v_\alpha(\mathbf{r}_1)/k_B T] &= \sum_\beta \int \nabla_1 c_{\alpha\beta}^0(\mathbf{r}_1, \mathbf{r}_2)[\rho_\beta(\mathbf{r}_2) - \rho_\beta]d\mathbf{r}_2 \\ &\quad + \frac{1}{2} \int \nabla_1 c_{\alpha\beta\gamma}^0(\mathbf{r}_1, \mathbf{r}_2, \mathbf{r}_3)[\rho_\beta(\mathbf{r}_2) - \rho_\beta][\rho_\gamma(\mathbf{r}_3) - \rho_\gamma]d\mathbf{r}_2 d\mathbf{r}_3 \end{aligned} \quad (11)$$

The correlation functions  $\{c\}$  are totally symmetric, e.g.,  $c_{\alpha\beta}(\mathbf{r}_1, \mathbf{r}_2) = c_{\beta\alpha}(\mathbf{r}_2, \mathbf{r}_1)$ , etc. Moreover, all the  $\{c^0\}$  functions are translational invariant; they depend only on the  $\mathbf{r}_{ij} = |\mathbf{r}_i - \mathbf{r}_j|$  coordinates. Thus

$$\begin{aligned} \int \nabla_1 c_{\alpha\beta}^0(r_{12})[\rho_\beta(\mathbf{r}_2) - \rho_\beta]d\mathbf{r}_2 &= - \int \nabla_2 c_{\alpha\beta}^0(r_{12})[\rho_\beta(\mathbf{r}_2) - \rho_\beta]d\mathbf{r}_2 \\ &= \int c_{\alpha\beta}^0(r_{12})\nabla_2 \rho_\beta(\mathbf{r}_2)d\mathbf{r}_2 \end{aligned} \quad (12)$$

and similarly

$$\begin{aligned} \int \nabla_1 c_{\alpha\alpha\alpha}(\mathbf{r}_1, \mathbf{r}_2, \mathbf{r}_3)[\rho_\alpha(\mathbf{r}_2) - \rho_\alpha][\rho_\alpha(\mathbf{r}_3) - \rho_\alpha]d\mathbf{r}_2 d\mathbf{r}_3 \\ = 2 \int c_{\alpha\alpha\alpha}^0(\mathbf{r}_1, \mathbf{r}_2, \mathbf{r}_3)[\rho_\alpha(\mathbf{r}_3) - \rho_\alpha]\nabla_2 \rho_\alpha(\mathbf{r}_2)d\mathbf{r}_2 d\mathbf{r}_3, \quad \text{etc.} \end{aligned} \quad (13)$$

Substituting (12) and (13) into (11), and making use of the expansion (8), we obtain

$$\nabla_1 \ln t_\alpha(\mathbf{r}_1) - \sum_\beta \int d\mathbf{r}_2 c_{\alpha\beta}(\mathbf{r}_1, \mathbf{r}_2) \nabla_2 \rho_\beta(\mathbf{r}_2) = 0 \quad (14)$$

The left-hand side is the convolution of  $\nabla_1 \rho_\alpha(\mathbf{r}_1)$  with the familiar expression  $\sum_\beta [\delta_{\alpha\beta} \delta(\mathbf{r}_1 - \mathbf{r}_2) / \rho_\alpha(\mathbf{r}_1) - c_{\alpha\beta}(\mathbf{r}_1, \mathbf{r}_2)]$ , which has a matrix inverse given by the Ornstein-Zernike relations [49]

$$h_{\alpha\beta}(\mathbf{r}_1, \mathbf{r}_2) = c_{\alpha\beta}(\mathbf{r}_1, \mathbf{r}_2) + \sum_\gamma \int d\mathbf{r}_3 \rho_\gamma(\mathbf{r}_3) c_{\alpha\gamma}(\mathbf{r}_1, \mathbf{r}_3) h_{\gamma\beta}(\mathbf{r}_3, \mathbf{r}_2) \quad (15)$$

where  $h_{\alpha\beta}(\mathbf{r}_1, \mathbf{r}_2)$  is the two-particle total correlation function. This can be used to transform Eq. (14) into

$$\nabla_1 \ln t_\alpha(\mathbf{r}_1) = - \sum_\beta \int [\nabla_2 v_\beta(\mathbf{r}_2) / k_B T] \rho_\beta(\mathbf{r}_2) h_{\alpha\beta}(\mathbf{r}_1, \mathbf{r}_2) d\mathbf{r}_2 \quad (16)$$

In the case of a single-component fluid, both equations (14) and (16) reduce to the relations obtained by Wertheim [52], by Lovett et al. [53], and by Sullivan and Stell [54].

In any relation given above, the knowledge of the total or direct pair correlation functions yields an equation for the density profile. The domain of integration in Eqs. (14)–(16) must include all the points where  $\rho_\alpha(\mathbf{r}) \neq 0$ . In the case of a completely impermeable surface,  $\rho_\alpha(\mathbf{r}) = 0$  inside the wall

located at  $z = z_\Omega$ . Thus, Eq. (14) can be integrated by parts to give

$$\nabla_1 \ln t_\alpha(\mathbf{r}_1) + \sum_\beta \int d\mathbf{r}_2 \rho_\beta(\mathbf{r}_2) \nabla_2 c_{\alpha\beta}(\mathbf{r}_1, \mathbf{r}_2) = 0 \quad (17)$$

The integral in Eq. (17) is confined to the points in the interior of the volume  $V$ , and there are no additional surface contributions. One can note that the approximation

$$c_{\alpha\beta}(\mathbf{r}_1, \mathbf{r}_2) = c_{\alpha\beta}^0(r_{12}) \quad (18)$$

in Eq. (17) leads to the singlet hypernetted chain approximation (6). Eq. (17) is really equivalent to Eq. (6); both methods of derivation involve neglect of the contributions of the bulk direct correlations in terms of  $c_{\alpha\beta\gamma}$ ,  $c_{\alpha\beta\gamma\delta}$ , and of higher-order direct correlation functions.

A set of equations (15)–(17) represents the background of the so-called second-order or pair theory. If these equations are supplemented by an approximate relation between direct and pair correlation functions the problem becomes complete. Its numerical solution provides not only the density profile but also the pair correlation functions for a nonuniform fluid [55–58]. In the majority of previous studies of inhomogeneous simple fluids, the inhomogeneous Percus–Yevick approximation (PY2) has been used. It reads

$$c_{\alpha\beta}(\mathbf{r}_1, \mathbf{r}_2) = [g_{\alpha\beta}(\mathbf{r}_1, \mathbf{r}_2) - c_{\alpha\beta}(\mathbf{r}_1, \mathbf{r}_2)] f_{\alpha\beta}(\mathbf{r}_1, \mathbf{r}_2) \quad (19)$$

where  $f_{\alpha\beta}(\mathbf{r}_1, \mathbf{r}_2)$  is the Mayer function. On the other hand, the inhomogeneous hypernetted chain equation (HNC2)

$$c_{\alpha\beta}(\mathbf{r}_1, \mathbf{r}_2) = [f_{\alpha\beta}(\mathbf{r}_1, \mathbf{r}_2) + 1] \exp[h_{\alpha\beta}(\mathbf{r}_1, \mathbf{r}_2) - c_{\alpha\beta}(\mathbf{r}_1, \mathbf{r}_2)] - 1 - [h_{\alpha\beta}(\mathbf{r}_1, \mathbf{r}_2) - c_{\alpha\beta}(\mathbf{r}_1, \mathbf{r}_2)] \quad (20)$$

can also be used.

Obviously, the implementation of the second-order equations is a completely numerical procedure [55–58]. It is a complicated numerical task even for simple fluids. However, the accuracy of the results depends on the closures applied.

Now, we would like to comment on some general features of the solutions of integral equations for the local density. We use superscripts  $H$  and  $P$  to abbreviate the solutions of the HNC1 and PY1 equations (6) and (7), respectively. By considering the limiting behavior of the cavity functions “inside the solid” one obtains

$$\lim_{z \rightarrow -\infty} \ln t_\alpha^H(\mathbf{r}) = \lim_{z \rightarrow -\infty} t_\alpha^P(\mathbf{r}) - 1 = - \sum_\beta \rho_\beta \int c_{\alpha\beta}^0(r) d\mathbf{r} = \frac{\partial p / k_B T}{\partial \rho_\alpha} \quad (21)$$

whereas the exact cavity function must satisfy

$$\lim_{z \rightarrow -\infty} \frac{\partial \ln t_\alpha(\mathbf{r})}{\partial \rho_\beta} = \frac{1}{\rho_\alpha} \delta_{\alpha\beta} - \frac{\partial \mu_\alpha / k_B T}{\partial \rho_\beta} \quad (22)$$

In the case of a one-component system we have

$$\lim_{z \rightarrow -\infty} \ln t(\mathbf{r}) = \Delta \mu_{ex} / k_B T \quad (23)$$

where  $\Delta \mu_{ex}$  is the excess (above the ideal gas) chemical potential of a one-component fluid.

Some useful exact relations can be obtained for specific fluid-wall interactions. With this aim, we now consider a one-dimensional external potential,  $v_\alpha(z)$ . First, let us introduce the abbreviation  $\tilde{\phi}(z_1, z_2, k)$ , for the Fourier-Bessel transform of a function  $\phi(z_1, z_2, R_{12})$ , where  $R_{12}^2 + (z_1 - z_2)^2 = r_{12}^2$ ,

$$\tilde{\phi}(z_1, z_2, k) = 2\pi \int_0^\infty J_0(R_{12}k) \phi(z_1, z_2, R_{12}) R_{12} dR_{12} \quad (24)$$

$J_0$  denotes the Bessel function of the first kind and  $\phi$  stands for  $c_{\alpha\beta}^0$  and  $h_{\alpha\beta}$ . With this notation, Eqs. (10), (14), and (16) can be rewritten as follows

$$\frac{\partial \ln t_\alpha(z_1)}{\partial \rho_\beta} = -4\pi \int_0^\infty r^2 c_{\alpha\beta}^0(r) dr + \sum_\gamma \int_{z_\Omega}^\infty \frac{\partial \rho_\gamma(z_2)}{\partial \rho_\beta} \tilde{c}_{\alpha\beta}(z_1, z_2, 0) dz_2 \quad (25)$$

$$\frac{\partial \ln t_\alpha(z_1)}{\partial z_1} + \sum_\beta \int_{z_\Omega}^\infty \frac{\partial \rho_\beta(z_2)}{\partial z_2} \tilde{c}_{\alpha\beta}(z_1, z_2, 0) dz_2 = 0 \quad (26)$$

and

$$\frac{\partial \ln t_\alpha(z_1)}{\partial z_1} + \sum_\beta \int_{z_\Omega}^\infty \frac{\partial v_\beta(z_2)}{\partial z_2} \rho_\beta(z_2) \tilde{h}_{\alpha\beta}(z_1, z_2, 0) dz_2 = 0 \quad (27)$$

In the case of a hard wall located at  $z_\Omega = 0$ , the latter equation yields

$$\rho'_\alpha(z_1) = \rho_\alpha(z_1) \sum_\beta \rho_\beta(0^+) \tilde{h}_{\alpha\beta}(z_1, 0, 0) \quad (28)$$

This expression requires a knowledge of only the correlation functions  $h_{\alpha\beta}$  between two molecules, one of which is located on the wall. Also, we can prove that in the case of a hard wall the following sum rule is valid [46,47]

$$\sum_\beta \rho_\beta(0^+) = p / k_B T \quad (29)$$

The singlet equations, PY1 and HNC1, can alternatively be derived [24,50] by considering a homogeneous mixture of  $N + 1$  components



containing a giant molecule  $G$ , whose diameter  $D_G$  and density  $\rho_G$  satisfy the following conditions

$$D_G \rightarrow \infty, \quad \rho_G \rightarrow 0, \quad \rho_G D_G^3 \rightarrow 0 \quad (30)$$

The giant particle- $\alpha$  particle total correlation function,  $h_{G\alpha}$ , which is equivalent to  $t_\alpha g_\alpha - 1$ , is given by

$$\begin{aligned} h_{G\alpha}(|\mathbf{r}_G - \mathbf{r}_1|) &\equiv t_\alpha(|\mathbf{r}_G - \mathbf{r}_1|)g_\alpha(|\mathbf{r}_G - \mathbf{r}_1|) - 1 \\ &= c_{G\alpha}(|\mathbf{r}_G - \mathbf{r}_1|) + \sum_\beta \rho_\beta \int d\mathbf{r}_2 c_{G\beta}(|\mathbf{r}_G - \mathbf{r}_2|)h_{\alpha\beta}^0(|\mathbf{r}_1 - \mathbf{r}_2|) \\ &\equiv \sum_\beta \rho_\beta \int d\mathbf{r}_2 h_{G\beta}(|\mathbf{r}_G - \mathbf{r}_2|)c_{\alpha\beta}^0(|\mathbf{r}_1 - \mathbf{r}_2|) \end{aligned} \quad (31)$$

where the superscript 0 corresponds to the correlation functions of the uniform fluid. In the case of a one-dimensional external potential we then obtain the most widely used form of Eq. (31) [24]

$$h_{G\alpha}(z) \equiv t_\alpha(z)g_\alpha(z) - 1 = c_{G\alpha}(z) + \sum_\beta \rho_\beta \int_{-\infty}^{\infty} dz_2 h_{G\beta}(t) C_{\alpha\beta}^0(|z - t|) \quad (32)$$

where

$$C_{\alpha\beta}^0(x) = 2\pi \int_x^\infty dr r c_{\alpha\beta}^0(r) \quad (33)$$

The approach described above introduces the concept of a giant particle (wall)- $\alpha$  particle direct correlation function. As far as the relation between  $h_{G\alpha}$  and  $c_{G\alpha}$  is not specified, Eq. (32) is exact. However, in contrast to Eq. (14), (32) contains the direct correlation function for a *uniform* fluid. The general relation between  $h_{G\alpha}$  and  $c_{G\alpha}$  involves the *bridge wall- $\alpha$  particle function*,  $B_{G\alpha}(r)$

$$\begin{aligned} h_{G\alpha}(r) &= [t_{G\alpha}(r) + 1] \exp[-u_{G\alpha}(r)/k_B T] \\ c_{G\alpha}(r) &= [t_{G\alpha}(r) + 1] \exp[-u_{G\alpha}(r)/k_B T] - \ln t_\alpha(r) + B_{G\alpha}(r) \end{aligned} \quad (34)$$

If  $B_{G\alpha}$  is set to zero, Eqs. (34) and (32) reduce to the singlet HNC1 equation (6). We would like to stress, however, that although two described approaches may lead to an identical final equation for the density profile, the approximations involved in their derivation are different. According to the former method of derivation, the HNC1 equation is obtained by neglecting the third-order and higher-order direct correlation functions of the bulk fluid, whereas the latter approach (Eq. (32)) requires neglecting the wall- $\alpha$  particle bridge functions  $B_{G\alpha}(r)$  to arrive at HNC1. This means that the

introduction of an appropriate approximation for the bridge function may lead to as accurate a singlet equation for the density profile as from the second-order equations [59,60]. There is evidence that the bridge function does not depend strongly on intermolecular potential [61]. Therefore, if the bridge function can be parametrized accurately for some fluid, such as a hard-sphere fluid, the resulting  $B_{G\alpha}$  can then be used in several applications. We proceed now with the extension and application of equations constituting the essence of the singlet-level and pair-level theories for inhomogeneous simple fluids to fluids with associative forces.

## **B. Application of the Singlet-level and Pair-level Theories for Fluids with Spherically Symmetric Associative Interactions in Contact with Surfaces**

The extension and application of the approaches discussed above rely to a great extent on the models for bulk fluids. Therefore, in this section we first describe a model of hard spheres with spherically symmetric associative forces. Next, we proceed with the description of theoretical approaches for inhomogeneous associating spheres. Some results following from the application of the computational algorithms are presented. We discuss first the singlet level theory for associating hard spheres in contact with a hard wall and with a crystalline surface. A more sophisticated pair-level theory is considered next. Finally, we discuss an attempt to employ the density functional approach for hard spheres with spherically symmetric associative forces.

### **1. The Bulk Model of Overlapping Hard Spheres**

As we have mentioned earlier, the models of associating fluids differ in respect of the symmetry of associative interactions. The models with highly directional bonding interactions will be discussed in Sec. III. Here, our focus is on the model with spherically symmetric associative interactions between species. We would like to mention first that this class of models in the region of high densities of particular interest in liquid state theory is successfully described with quite simple closure approximations that complete the common Ornstein–Zernike integral equation. The application of a more sophisticated Wertheim’s type Ornstein–Zernike equation is also possible and will be discussed below.

Our interest is in the model of hard spheres with spherically symmetric associative interactions. This has been proposed and well studied by Cummings and Stell [25–27]. The model represents a two-component mixture of hard sphere species,  $\alpha$  and  $\beta$ , with equal diameters,  $\sigma_\alpha = \sigma_\beta = \sigma = 1$ . The model is considered at the condition of equimolarity,  $\rho_\alpha = \rho_\beta = \rho/2$ .

The interaction between particles belonging to the same species is a hard sphere interaction

$$u_{\alpha\alpha}(r) = u_{\beta\beta}(r) = \begin{cases} \infty & r < \sigma \\ 0 & r > \sigma \end{cases} \quad (35)$$

whereas the particles of the unlike species interact via the following potential:

$$u_{\alpha\beta}(r) = \begin{cases} \infty & r < L - w/2 \\ -\varepsilon^{\text{as}} & L - w/2 < r < L + w/2 \\ D & L + w/2 < r < \sigma \\ 0 & r > \sigma \end{cases} \quad (36)$$

The height of the square mound,  $D$ , in the course of calculations is chosen to satisfy the condition,  $\exp(-D/k_B T) \approx 0$ , in order to prevent overlap of spheres at distances between  $L + w/2$  and  $\sigma$ . The bonding distance is denoted by  $L$  and  $w$  is the width of the attractive square well. The dimerization of species is permitted only if the bonding length is chosen such that  $L + w/2 < \sigma/2$ . On the other hand, chain-like structures of the type  $\dots\alpha\beta\alpha\beta\dots$  etc. can be formed if the bonding length is chosen in the interval  $\sigma/2 < L + w/2 < \sqrt{3}\sigma/2$ . Moreover, for larger values of the bonding length vulcanization of species, i.e., the formation of chain-like and branched structures with a high coordination number, may be expected; see, e.g., Refs. 25–27.

The structure of the bulk associating fluid in the framework of the model in question can be determined by solving the common Ornstein–Zernike (OZ) equation

$$h_{\alpha\beta}(r_{12}) = c_{\alpha\beta}(r_{12}) + \sum_{\gamma=\alpha\beta} \rho_{\gamma} \int d\mathbf{r}_3 h_{\alpha\gamma}(r_{13}) c_{\gamma\beta}(r_{23}) \quad (37)$$

with appropriate closures. In the above  $h_{\alpha\beta}(r)$  and  $c_{\alpha\beta}(r)$  are the total and direct correlation functions of the bulk fluid. The simplest procedure is to complement the OZ equation by the Percus–Yevick closure and solve the problem either analytically [25–27] or numerically [28,31,32]. The PY closure reads

$$c_{\alpha\beta}(r) = f_{\alpha\beta}(r)[1 + h_{\alpha\beta}(r) - c_{\alpha\beta}(r)] \quad (38)$$

However, it is known that the direct correlation functions have an exact long-range asymptotic form, arising due to intramolecular correlations in clusters formed via the association mechanism. This asymptotics is not included in the Percus–Yevick approximation. Other common liquid state approximations also do not provide correct asymptotic behavior of  $c_{\alpha\beta}(r)$ .

The inaccuracy seems not to prohibit study of the structural properties of associating fluids, at least at low values of the association energy. However, what is most important is that this difficulty results in the violation of the mass action law, see Refs. 62–64 for detailed discussion. To overcome the problem, one can apply thermodynamical correspondence between a dimerizing fluid and a mixture of free monomers of density  $\rho_{\alpha 0} = \rho_{\beta 0} = \rho_0/2$  and dimer species [12]. The equation of state of the corresponding mixture [65,66] can then be used to determine the degree of association,  $\Lambda = 2\rho_{\alpha\beta}/\rho_0$  ( $\rho_{\alpha\beta}$  is the density of dimers in the system), and fit it to the association energy at a given density.

Once the degree of association is known, the structure of the bulk dimerizing fluid can be determined by implementation of the adequate closures, such as, for example, the extended mean spherical approximation (EMSA) [12,67]. It reads

$$h_{\alpha\beta}(r) = -1 + (1 - \delta_{\alpha\beta}) \frac{\Lambda}{4\pi L^2 \sqrt{\rho_{\alpha}\rho_{\beta}}} \delta(r - L), \quad r < 1$$

$$c_{\alpha\beta}(r) = (-1)^{\delta_{\alpha\beta}} \frac{3[\Lambda(1 - \delta_{\alpha\beta}) + \delta_{\alpha\beta}]}{4\pi L^2 \sqrt{\rho_{\alpha}\rho_{\beta}} r} \exp[-\kappa r], \quad r > 1 \quad (39)$$

where  $\delta(x)$  is the Dirac function and  $\kappa$  describes the decay of correlations

$$\kappa = \frac{[3(1 - \Lambda^2)]^{1/2}}{\Lambda L} \quad (40)$$

The EMSA requires the degree of dimerization  $\Lambda$  as an input parameter. This is quite disappointing. However, it eliminates the deficiency of the Percus–Yevick approximation, Eq. (38). The EMSA represents a simplified version, to obtain an analytic solution, of a more sophisticated site–site extended mean spherical approximation (SSEMSA) [67–69]. The results of the aforementioned closures can be used as an input for subsequent calculations of the structure of nonuniform associating fluids.

## 2. Associating Fluid Near a Structureless Surface

Let us begin our discussion from the model of Cummings and Stell for heterogeneous dimerization  $\alpha + \beta \rightleftharpoons \alpha\beta$  described in some detail above. In the case of singlet-level equations, HNC1 or PY1, the direct correlation function of the bulk fluid  $c_{\alpha\beta}^0(r)$  represents the only input necessary to obtain the density profiles from the HNC1 and PY1 equations; see Eqs. (6) and (7) in Sec. II A. It is worth noting that the transformation of a square-well, short-range attraction, see Eq. (36), into a  $\delta$ -type associative interaction, see Eq. (39), is unnecessary unless one seeks an analytic solution. The  $\delta$ -type term must be treated analytically while solving the HNC1

and PY1 equations. In the case of a square-well interaction, the equations of the singlet-level theory can be solved numerically without difficulty. The application of the square-well associative interaction and a numerical solution of the integral equations seem preferable, because only the numerical methods can be applied for realistic interactions between fluid species and confining surfaces.

For simplicity, let us consider first the case of a fluid in contact with a hard wall. This is the simplest model involving the geometrical constraints of the solid surface

$$v_{\alpha}(z) = \begin{cases} \infty & z \leq 0 \\ 0 & z > 0 \end{cases} \quad (41)$$

The behavior of associating fluid near the hard wall was extensively studied in the framework of the theory discussed above. The model of Cummings and Stell was applied to relatively dense fluids at a high degree of dimerization [33,36]. Fig. 1 presents the density profiles calculated within the framework of the combined PY1/EMSA theory (i.e., the density profiles were evaluated from the PY1 equation, whereas the bulk direct correlation functions follow from the EMSA equation) and HNC1/EMSA approximations [33]. The calculations were performed for  $L = 0.42\sigma$ ,  $w = 0.1\sigma$  and for a

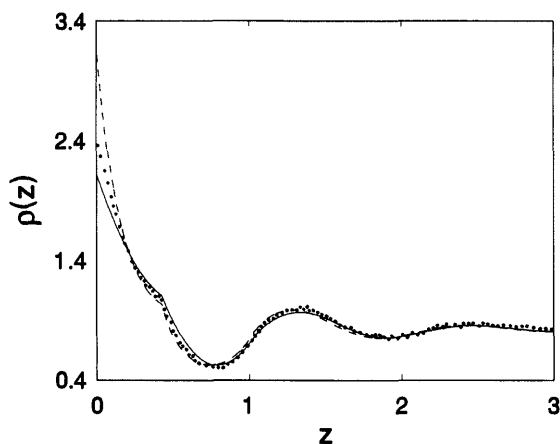


**FIG. 1** Total local density  $\rho(z)$  for bulk density  $\rho = 0.821$  and  $\varepsilon^{\text{as}}/k_B T = 4.25$ . The solid line is for PY1 theory, the dashed line is for HNC1 approximation and the points denote the Monte Carlo simulation results. (Reprinted from: S. Sokółowski, D. Henderson, A. Trokhymchuk, O. Pizio. Density profiles of associating fluid near a hard wall: PY/EMSA and HNC/EMSA singlet theory, *Physica A*, 220, 22–32. © (1995), with permission from Elsevier Science.)

quite high association energy ( $\varepsilon^{\text{as}}/k_B T = 4.25$ ). Fig. 1 indicates that the first-order equations provide an adequate description of the density profiles except in the vicinity of the wall. This is not surprising at all, because the contact values of the density profiles are insufficiently accurately predicted by the PY1 and HNC1 theories. The oscillating behavior of the profiles for high bulk fluid densities reflects the tendency for the formation of a multi-layer structure near a hard wall. However, the cusp on the density profiles, at  $z \approx L$ , serves as a manifestation of the presence of dimers in the adlayer. We can also see that the HNC1/EMSA approximation overestimates, whereas the PY1/EMSA underestimates, the contact value of the local density. In general, the PY1/EMSA approximation seems to be preferable. The contact value of the local density at a hard wall is lower for an associating fluid than for a hard sphere fluid. For the states of incomplete association and moderate fluid density, the monomers adsorb on the wall rather than dimers. However, for a highly dimerized fluid, such as that presented in Fig. 1, the adlayer is mostly composed of dimers which prefer to lie parallel to the wall. This follows from the position of the cusp of the density profiles. Obviously, one cannot discuss the pair correlations in more detail with only the density profiles available from the singlet level theory. However, useful information about the orientational distribution of dimers can be obtained from computer simulation data [33,36].

The singlet-level theories have also been applied to more sophisticated models of the fluid–solid interactions. In particular, the structure of associating fluids near partially permeable surfaces has been studied in Ref. 70. On the other hand, extensive studies of adsorption of associating fluids in a slit-like [71–74] and in spherical pores [75], as well as on the surface of spherical colloidal particles [29], have been undertaken. We proceed with the application of the theory to more sophisticated impermeable surfaces, such as those of crystalline solids.

### 3. Associating Fluid in Contact with a Crystalline Solid

The singlet-level theory has also been used to describe the structure of associating fluids near crystalline surfaces [30,31,76,77]. The surface consists explicitly of atoms which are arranged on a lattice of a given symmetry. The fluid atom–surface atom potential can also involve an associative term, i.e., the chemical-type bonding of the adsorbate particles with the surface may be included into the model. However, we restrict ourselves to the case of a nonassociative crystalline surface first.

We would like to follow the method developed previously to study the adsorption of simple fluids on crystalline surfaces [78–81]. The potential of interaction of a fluid particle with the surface is obtained by summing up the

interaction with all the atoms forming the solid body [80,81]

$$v_{\alpha}(\mathbf{r}) = \sum_i v_{i\alpha}(|\mathbf{r}_i - \mathbf{r}|) \quad (42)$$

where  $\mathbf{r}_i$  denotes the position of the  $i$ -th atom of the solid.

The potential  $v_{\alpha}(\mathbf{r})$  is a periodic function in the surface plane,  $v_{\alpha}(\mathbf{r}) = v_{\alpha}(\mathbf{r} + \mathbf{l})$ ;  $\mathbf{l} = l_1 \mathbf{a}_1 + l_2 \mathbf{a}_2$  is the lattice vector,  $l_1$  and  $l_2$  are integers, and  $\mathbf{a}_1$  and  $\mathbf{a}_2$  are the unit lattice vectors. The potential  $v_{\alpha}(\mathbf{r})$ , the local density,  $\rho_{\alpha}(\mathbf{r})$ , the Boltzmann factor,  $g_{\alpha}(\mathbf{r}) = \exp[-v_{\alpha}(\mathbf{r})/k_B T]$ , as well as the one-particle background correlation function  $t_{\alpha}(\mathbf{r})$ , can be expanded into two-dimensional Fourier series [78–81]

$$\psi_{\alpha}(\mathbf{r}) = \sum_{\mathbf{q}} \psi_{\alpha\mathbf{q}}(z) \exp[-i\mathbf{R}\mathbf{q}] \quad (43)$$

where  $\psi$  stands for  $v$ ,  $t$ ,  $g$ , or  $\rho$ , as appropriate;  $\mathbf{R} = (x, y)$  and  $\mathbf{q} = 2\pi(q_1 \mathbf{b}_1 + q_2 \mathbf{b}_2)$ , with  $\mathbf{b}_1$  and  $\mathbf{b}_2$  being two-dimensional reciprocal lattice vectors. The expansion coefficients  $\psi_{\alpha\mathbf{q}}$  are defined as

$$\psi_{\alpha\mathbf{q}}(z) = \frac{1}{a_s} \int d\mathbf{R} \exp[i\mathbf{R}\mathbf{q}] \psi_{\alpha}(\mathbf{r}) \quad (44)$$

where  $a_s$  is the area of the unit lattice cell. Due to the symmetry properties of the lattice, the expansion coefficients  $\psi_{\alpha\mathbf{q}}$  depend only on the magnitude of the vector  $\mathbf{q}$ . It means that Eq. (43) can be rewritten in the form

$$\psi_{\alpha q}(z) = \sum_{l \geq 0} \psi_{\alpha l} \phi_l(x, y) \quad (45)$$

The functions  $\psi_{\alpha l}$  are obtained from

$$\phi_l(x, y) = \sum_{\mathbf{q}} \exp[i\mathbf{q}\mathbf{R}] \quad (46)$$

where the summation runs over all reciprocal vectors of a given length  $q$ ; these functions can be found in Ref. 81 for some simple lattices.

Using the two-dimensional Fourier–Bessel transform, the PY1 equation (7) becomes (cf. Refs. 30,31)

$$\begin{aligned} t_{\alpha\mathbf{q}}(z_1) = & \sum_{\mathbf{q}_1 + \mathbf{q}_2 = \mathbf{q}} \sum_{\gamma = \alpha, \beta} \rho_{\gamma} \int dz_2 t_{\gamma\mathbf{q}_1}(z_2) g_{\gamma\mathbf{q}_2}(z_2) c_{\alpha\gamma}^0(|z_1 - z_2|, q) \\ & + (a_{\alpha} + 1) \delta_{0\mathbf{q}} \end{aligned} \quad (47)$$

where  $q = |\mathbf{q}|$ ,

$$a_\alpha = -2\pi \sum_{\gamma=\alpha,\beta} \rho_\gamma \int dr r^2 c_{\alpha\gamma}^0(r) \quad (48)$$

and where

$$c_{\alpha\gamma}^0(|z_1 - z_2|, |q|) = 2\pi \sum_{\gamma=\alpha,\beta} \rho_\gamma \int dR R c_{\alpha\gamma}^0(\sqrt{|z_1 - z_2|^2 + R^2}) J_0(qR) \quad (49)$$

The function  $J_0(x)$  denotes the Bessel function of the first kind.

In the case of the HNC1 equation (6), we obtain

$$T_{\alpha\mathbf{q}}(z_1) = \sum_{\mathbf{q}_1 + \mathbf{q}_2 = \mathbf{q}} \sum_{\gamma=\alpha,\beta} \rho_\gamma \int dz_2 t_{\gamma\mathbf{q}_1}(z_2) g_{\gamma\mathbf{q}_2}(z_2) c_{\alpha\gamma}^0(|z_1 - z_2|, \mathbf{q}) + a_\alpha \delta_{0\mathbf{q}} \quad (50)$$

where  $T_{\alpha\mathbf{q}}$  is the two-dimensional Fourier–Bessel expansion coefficient of  $\ln t_\alpha(\mathbf{r})$ .

The density profiles are presented for the model of Cummings and Stell [25–27]. The fluid is in contact with the (100) plane of the face-centered cubic lattice, the bulk fluid particles and the solid atoms are assumed of the same size,  $\mathbf{a}_1 = \mathbf{a}_2 = \sigma$ , and the bonding distance is chosen as appropriate for dimerization,  $L = 0.5$ . Also, the interactions of both species with the surface are assumed identical. The strength of associative forces is characterized by means of the equilibrium constant of dimerization reaction at infinite dilution ( $K_0 \sim \exp(\varepsilon^{\text{as}}/k_B T)$ ) [25]. The calculations have been done by using PY1 approximation and the results are shown in Fig. 2. The inset in Fig. 2(a) shows the unit lattice cell with three characteristic positions. The symbol  $s$  denotes the adsorbing site (the adsorbing potential over this site is the highest);  $sp$  denotes the saddle point and  $a$  abbreviates the atomic position. The effect of dimerization leads to a decrease in the height of the first maximum of the density profile over the adsorbing site position. The dimers prefer to adsorb over this position compared with the saddle point ( $sp$ ) and atom ( $a$ ) positions. At higher bulk fluid densities the dimers assume orientation perpendicular to the surface, which is manifested by the existence of a double first maximum over the  $s$  position.

A more sophisticated model, which permits associative adsorption on the crystalline lattices, has been introduced in Refs. 82, 83. The model assumes that the atoms forming the crystal lattice interact with fluid particles not only via the van der Waals potential but also via associative forces. The associative adsorption is characterized by a high degree of localization of the adsorbed particles as a consequence of a strong bonding between the bulk



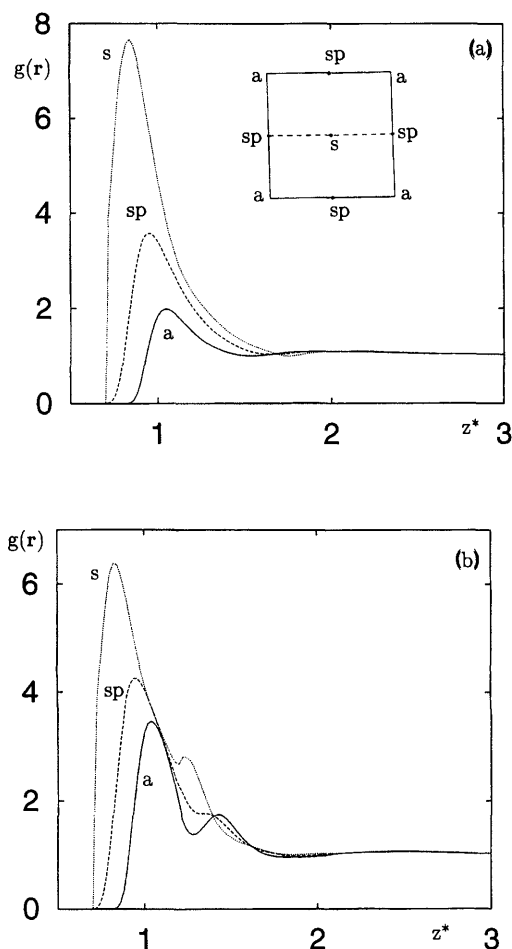


**FIG. 2** Normalized density profiles  $g(z)$  as a function of the distance from the surface obtained for  $\varepsilon/k_B T = 0.25$ ,  $\rho = 0.191$ ,  $L = 0.5$  and for  $K_0 = 0.131$ , weak dimerization (a) and for  $K_0 = 13.1$ , high dimerization (b). The labels  $s$ ,  $sp$  and  $a$  denote ( $s$ ), ( $sp$ ) and ( $a$ ) positions, respectively. The inset in part (a) shows the surface lattice cell and the location of the ( $s$ ), ( $sp$ ) and ( $a$ ) positions (from Ref. 31.)

species and the surface atoms. It has been shown that for a dimerizing fluid,  $\alpha + \beta \rightleftharpoons \alpha\beta$ , in which the surface association,  $\alpha + S \rightleftharpoons \alpha S$  ( $S$  denotes surface atoms), may occur, one can generate the formation of different surface complexes consisting of the fluid species and surface atoms. A highly localized adsorption and the formation of surface complexes results in an

adlayer structure which is very different from that obtained for nonassociative adsorption.

#### 4. Second-Order Integral Equations for Associating Fluids

As mentioned above in Sec. II A, the second-order theory consists of simultaneous evaluation of the one-particle (density profile) and two-particle distribution functions. Consequently, the theory yields a much more detailed description of the interfacial phenomena. In the case of confined simple fluids, the PY2 and HNC2 approaches are able to describe surface phase transitions, such as wetting and layering transitions, in particular; see, e.g., Ref. 84.

Again, we consider the model of an associating fluid by Cummings and Stell [25–27]. The fluid is studied in contact with a hard wall;  $v_\alpha(z)$  is given by Eq. (41). In this case Eq. (16) becomes [85,86]

$$\frac{d \ln t_\alpha(z_1)}{dz_1} = \sum_\beta \rho_\beta(0^+) \int_0^\infty R_{12} dR_{12} h_{\alpha\beta}(z_1, 0, R_{12}) \quad (51)$$

A numerical algorithm for the solution of the system of Eqs. (15), (19) and (51) consists of the expansion of the two-particle functions into a Fourier–Bessel series. We omit all the details of the numerical method; they can be found in Refs. 55–58, 85, 86. In Fig. 3 we show a comparison of the total

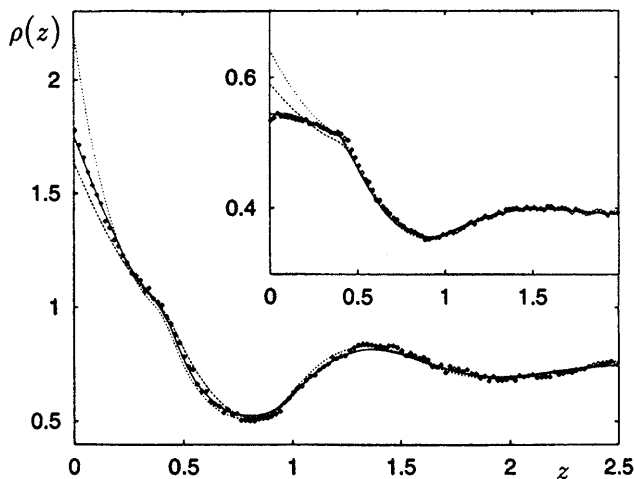


**FIG. 3** A comparison of the Monte Carlo (points), PY2 (solid lines), HNC1 (short dashed lines), and PY1 (long dashed lines) density profiles. The model parameters used in calculations are:  $\varepsilon^{\text{as}}/k_B T = 4.245$ ,  $L = 0.42\sigma$ ,  $w = 0.1\sigma$ . The bulk density is  $\rho = 0.728$  (the main part of the figure) and  $0.391$  (the inset). (From Ref. 85.)

density profile,  $\rho(z) = \rho_\alpha(z) + \rho_\beta(z)$  (both species are indistinguishable), calculated for the bulk fluid density  $\rho = 0.728$  by solving the PY2 equation and both singlet approximations, PY1 and HNC1, with Monte Carlo simulation [85]. Inspection of the curves presented in Fig. 3 indicates that the PY2 theory predicts the structure in the nearest vicinity of the wall significantly better than the singlet theory; at larger distances from the wall the results of the singlet theory coincide with the results of the PY2 approximation. Fig. 4 contains some examples of the two-particle distribution functions  $g_{\alpha\beta}(\mathbf{r}_1, \mathbf{r}_2) = h_{\alpha\beta}(\mathbf{r}_1, \mathbf{r}_2) + 1$  [85]. For all the curves the particles are equidistant from the wall, i.e.,  $z_1 = z_2$ . The lowest curves are for the particles lying on the wall. The dependence of the distribution functions on the particles' position is rather weak; this reflects the fact that the density profiles are smoother for associating fluids than for hard spheres.

We should mention here one of the important limitations of the singlet level theory, regardless of the closure applied. This approach may not be used when the interaction potential between a pair of fluid molecules depends on their location with respect to the surface. Several experiments and theoretical studies have pointed out the importance of surface-mediated [1,87] three-body forces between fluid particles for fluid properties at a solid surface. It is known that the depth of the van der Waals potential is significantly lower for a pair of particles located in the first adsorbed layer. In

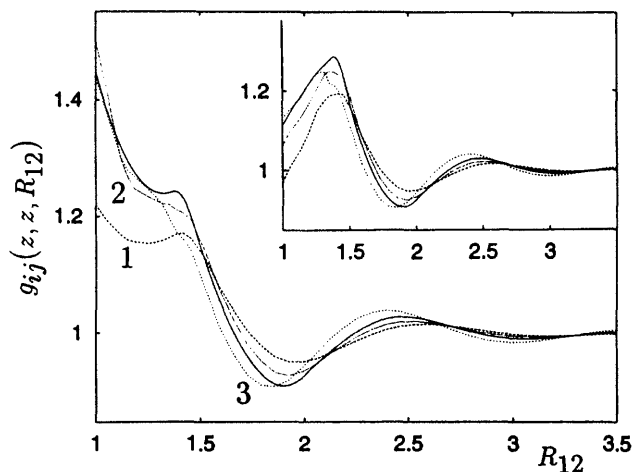


**FIG. 4** Pair distribution functions  $g_{\alpha\alpha}(z, z, R_{12})$  (the main part of the figure) and  $g_{\alpha\beta}(z, z, R_{12})$  (the inset). The solid lines denote the bulk function, the labels 1, 2 and 3 refer to  $z = 0$ ,  $z = 0.8\sigma$  and  $z = 1.2\sigma$ , respectively. The bulk density is  $\rho = 0.728$ . The meaning of the curves in the inset is the same as in the main figure. (From Ref. 85.)

the case of chemically reacting fluids, the surface can play a much more important role and can change the ability of particular species to react [88,89].

Let us thus consider a model in which the association energy depth changes when two reacting particles are approaching the surface; see Refs. 86,90. If in the vicinity of the surface the binding energy is lower than it is far from the surface, the probability of the chemical reaction to occur in the surface zone decreases. Similarly to the previous case, we consider an equimolar mixture of associating hard spheres of equal diameters. The interaction between the species  $\alpha$  and  $\beta$  is assumed in the form

$$u_{\alpha\beta}(\mathbf{r}_1, \mathbf{r}_2) = \begin{cases} \infty & |\mathbf{r}_1 - \mathbf{r}_2| < L - w/2 \\ -\varepsilon^{as}\omega(z_1, z_2) & L - w/2 < |\mathbf{r}_1 - \mathbf{r}_2| < L + w/2 \\ \infty & L + w/2 < |\mathbf{r}_1 - \mathbf{r}_2| < 1 \\ 0 & |\mathbf{r}_1 - \mathbf{r}_2| > 1 \end{cases} \quad (52)$$

where  $\varepsilon$  is the parameter characterizing the strength of the associative interaction,  $w$  and  $L$  have the same meaning as in Eq. (36). The function  $\omega(z_1, z_2)$  has the property that, for  $z_1, z_2 \rightarrow \infty$ ,  $\omega(z_1, z_2) \rightarrow 1$ ; i.e., far away from the surface, the associative energy becomes constant and attains its bulk value. We use a very simple model, assuming that (cf. Ref. 87)

$$\omega(z_1, z_2) = 1 - \epsilon_{gs}/(z_c + \Delta_{gs})^3 \quad (53)$$

where  $z_c = (z_1 + z_2)/2$  is the position of the center of mass of two particles. Obviously, this is a crude model, but it ensures that in the vicinity of the surface the binding energy is reduced.

The interaction of a fluid particle with the adsorbing wall is given by a hard wall potential, Eq. (41). In Fig. 5 we show a comparison of theoretical (resulting from the PY2 approximation) and simulation results. Part (a) of the figure is for systems without third-order interactions,  $\epsilon_{gs} = 0$ . Part (b) is for  $\epsilon_{gs}/k_B T = 10$ . The remaining parameters are:  $\Delta_{gs} = \sigma$ ,  $L = 0.45\sigma$ ,  $w = 0.1\sigma$  and  $\varepsilon^{as}/k_B T = 1$ . We stress some general features shown in Fig. 5. All the curves presented exhibit cusps at a distance from the surface equal to the average bond length. These cusps become weaker when the third-order forces are turned on. Despite the limitations of the PY closure, the agreement between the simulated and theoretical data is very good. Only in the nearest vicinity of the wall is a slight difference observed. It is obvious that, when the third-order energy vanishes, the height of the first local density peak and the contact value of the density profile increase. However, taking into account the fact that the "chemical interaction" essentially decreases, the observed changes in the density profiles are relatively weak.

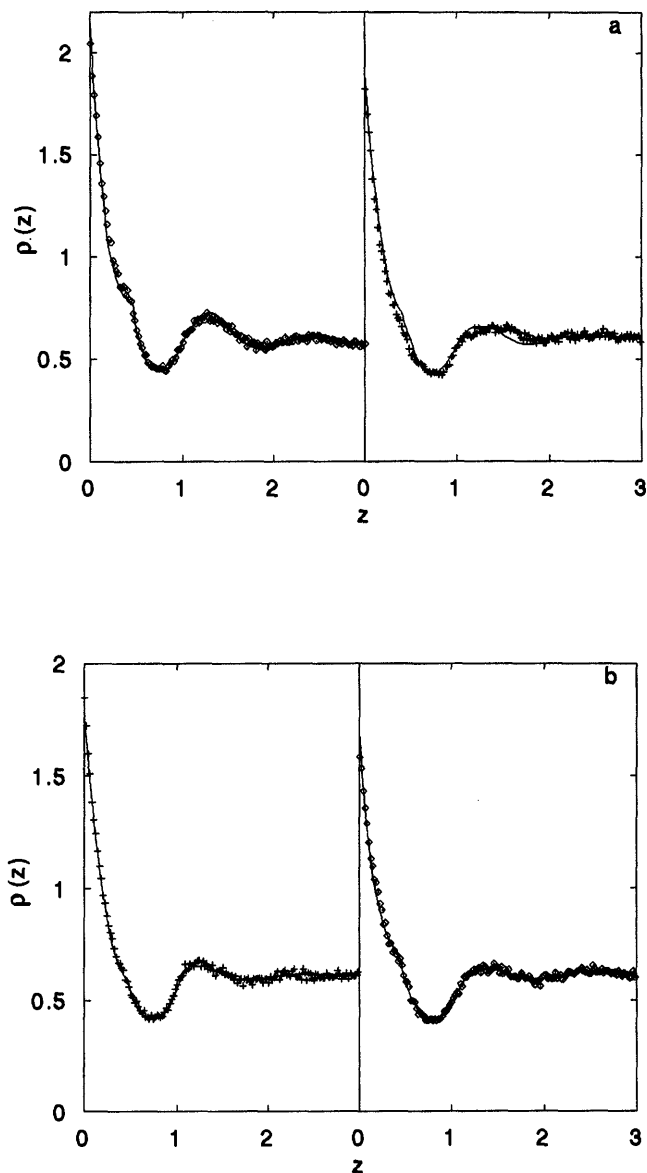


**FIG. 5** Density profiles from the PY2 theory (lines) and computer simulations (points) for the system without (a) and with (b) third-body forces. The association energy  $\epsilon^{\text{as}}/k_B T = 1$  for all profiles except for the right panel in (b), where  $\epsilon^{\text{as}}/k_B T = 4$ . The bulk density is 0.605 (left panel, part (a)), 0.586 (right panel, part (a)), 0.621 (left panel, part (b)) and 0.618 (right panel, part (b)). (From Ref. 86.)

Far from the surface, the theory reduces to the PY theory for the bulk pair correlation functions. As we have noted above, the PY theory for bulk pair correlation functions does not provide an adequate description of the thermodynamic properties of the bulk fluid. To eliminate this deficiency, a more sophisticated approximation, e.g., the SSEMSA, should be used.

### 5. Local Density from a Density Functional Approach

It is known that singlet-level approaches, i.e., the PY1 or HNC1 equations, are not able to account for surface phase transitions such as wetting or layering transitions [49]. The second-order theories allow us to describe surface transitions, but their solution requires remarkable numerical work. As a result, in the case of simple fluids, the interpretation of wetting phenomena has relied mainly on the density functional theories. The theories have several versions, each of which provides a recipe for calculating the properties of inhomogeneous fluids (see Ref. 49 for a review). The commonly used approaches are based on the perturbational division of the interparticle potential and on the mean-field type approximation for the contribution to the free energy functional arising from the attractive part of the interparticle forces. An alternative density functional approach, based on the use of the Ornstein–Zernike equation for the wall–particle correlations and on a nonlocal density functional closure for the direct wall–particle correlation function, has been proposed by Blum, Zhou and Stell [91,92].

To illustrate this theory, we consider a one-component fluid with the interaction between the same species given by Eq. (36). Obviously, the model differs from that described in Sec. (II B1). In particular, the geometrical constraints, which determine the type of association products in the case of a two-component model, are no longer valid. If we restrict ourselves to the case  $L < \sigma/2$ , only dimers and  $n$ -mers built up of rigid, regular polygons are possible.

The density functional approach of Refs. 91, 92 introduces a correction to the wall–particle direct correlation function resulting from the HNC1 approximation (see Eqs. (32)–(34)). A correction to Eq. (34) reads (we drop the species label because the model is one-component)

$$c_G(r) = c_G^H(r) - \mu_{ex}(\bar{\rho})/k_B T + \mu_{ex}(\rho)/k_B T + \rho \tilde{h}_G(r) \frac{\partial \mu_{ex}}{\partial \rho} + \sum_{i=1}^{\infty} S_i^H \quad (54)$$

The definition of the  $S_i^H$  terms can be found in Refs. 91, 92. The excess chemical potential, computed from the direct correlation function of the

bulk fluid, is

$$\frac{\partial \mu_{ex}(\rho')}{\partial \rho'} = - \int d\mathbf{r} c(r) \quad (55)$$

The density  $\tilde{\rho}$  in Eq. (54) is the average density, and  $\tilde{h}_G(r) = \tilde{\rho}(r)/\rho - 1$ . According to the theory of Zhou and Stell [91], the averaged density is calculated from the relation

$$\tilde{\rho}(r_1) = \int d\mathbf{r}_2 \rho(r_2) W(|\mathbf{r}_1 - \mathbf{r}_2|) \quad (56)$$

where  $W$  is a weight function. One of the possible approximations is

$$W(r) = f(r) / \int d\mathbf{r} f(r) \quad (57)$$

where  $f(r)$  is the Mayer function. This choice is suitable for a repulsive interaction, but not for a fluid with attractive forces, such as a chemically associating fluid or even a Lennard–Jones (12–6) fluid, because it can generate negative averaged densities. Therefore, it has been assumed that  $f(r)$  is just the Mayer function for a hard sphere interaction, i.e.,  $f(r) = -1$  for  $r < \sigma$  and  $f(r) = 0$  otherwise. Evidently, other choices can improve the final results. One can intend to introduce self-consistency into the scheme by using a weight function, such that the thermodynamics of the system matches the chemical potential input in a homogeneous system.

When all  $S_I^H$  terms in Eq. (54) are neglected, Eqs. (32)–(34) form a closed set, which can be solved. This kind of approximation has been called by Zhou and Stell “the hydrostatic hypernetted chain approximation” (HHNC1) [91]; a procedure for the numerical solution of the HHNC1 equations can be found in Ref. 45.

A comparison of the predictions of the HNC1 and HHNC1 theories with Monte Carlo simulations is given in Fig. 6. The calculations have been performed for the model with  $L = 0.45\sigma$ ,  $w = 0.1\sigma$ ,  $\varepsilon/k_B T = 2.522$  [45]. The bulk direct correlation function has been obtained from EMSA theory. Inspection of the curves given in Fig. 6 indicates that the HHNC1 approximation leads to a more accurate description of the associating fluid structure than the HNC1 approximation. In general, we can state that the application of this type of theory for associating fluids is encouraging. Similar theoretical treatments can be eventually used in further studies of wettability of solid surfaces by chemically associating fluids. No such calculations have been carried out so far. An alternative density functional theory for associating fluids is presented in the following section.

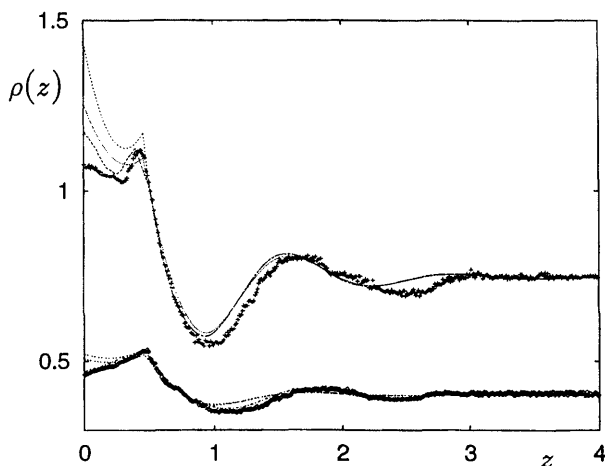


**FIG. 6** A comparison of the Monte Carlo (points), HHNC1, HNC1, and PY1 density profiles. The results are for bulk density 0.403 (lower group of curves) and 0.741 (upper group of curves). The curves at  $z = 0$ , are, from the bottom, from HHNC1 and HNC1 approximations. (Reprinted from: A. Trokhymchuk, D. Henderson, S. Sokolowski. Local density of overlapping spheres near a hard wall: A density functional approach. *Physics Letters A* 209, 317–320. © 1995, with permission from Elsevier Science.)

### III. NONUNIFORM ASSOCIATING FLUIDS WITH DIRECTIONAL FORCES

The chemical bonds between molecules are highly directional in many liquids. Water is one of the good examples of this class of liquids [93]. The formation of directional bonds can be generated in the statistical mechanics of fluids by the introduction of short-range, orientation-dependent, attractive forces into the Hamiltonian. Different types of molecular clusters can be formed (dimers, trimers, chains, fragments of a network of bonds, or an entire network), dependent on the nature of these short-range forces and mechanism of their saturation. The theory developed by Wertheim [8–11] provides effective tools to investigate thermodynamics and structural properties of this class of fluid systems. In fact, careful examination of the mechanism of saturation of the orientation-dependent forces had permitted Wertheim to formulate his theory. Extension of the theory of Wertheim to seemingly simpler models with spherically symmetric association, due to the efforts of Kalyuzhnyi and Stell [94], appeared later than the original theory.

According to Wertheim, association of species is generated by a strong, square-well attraction between the sites either on the surface or embedded



into the core of each molecule. A molecule can possess one, two, or more sites. The essential feature of the approach is that a set of additional density parameters ("densities") appears in the theory in addition to the overall density of a fluid. The density parameters characterize the bonding states of molecules and are mutually related via a statistical-mechanical analogue of the mass action law. The multidensity formalism provided efficient resumption of the cluster expansions for the grand canonical potential and for the distribution functions.

The theory of Wertheim for bulk associating fluids has been extensively used during the last decade. In particular, Ghonasgi and Chapman [95,96] have studied tangent polymer chains, whereas the flexible chains of fused monomers have been investigated in Refs. 97, 98. A special, interesting case of ring-like polymers has been considered in Ref. 99. The structural properties of several models for bulk associating fluids in the framework of the theory have been studied; see e.g., Refs. 100–105. Theoretical results have been supplemented and tested with respect to Monte Carlo computer simulation data both for thermodynamics and structural properties [13–19,106–111]. Chapman et al. have generalized Wertheim's approach to binary mixtures [15,112]. For better understanding of the reader, and in part due to space limitations of the chapter, we restrict ourselves to simple models of the bulk association via directional bonding and put emphasis on the treatment of the inhomogeneous association effects. Two basic elements of the bulk theory, namely the multidensity Ornstein–Zernike equation and thermodynamic perturbation theory for associating fluids, will be considered for this purpose.

### A. The Bulk Model for Association with Directional Bonding

A simple model for interactions between particles in an associating bulk fluid consists of a particle–particle potential and the interactions between sites belonging to different molecules. Supposing that each molecule has  $M$  sites, the potential of interaction between molecules 1 and 2 is [14]

$$u(12) = u^{\text{non}}(12) + u^{\text{as}}(12) = u^{\text{non}}(12) + \sum_{\alpha} \sum_{\beta} u_{\alpha\beta}^{\text{as}}(12)(\mathbf{r}_{\alpha\beta}) \quad (58)$$

where the symbols 1 and 2 denote the Cartesian and orientational coordinates of the corresponding particles and

$$\mathbf{r}_{\alpha\beta} = \mathbf{r}_2 - \mathbf{r}_1 + \mathbf{d}_{\beta}(\omega_2) - \mathbf{d}_{\alpha}(\omega_1) \quad (59)$$

is the vector connecting the site  $\alpha$  on molecule 1 with the site  $\beta$  on molecule 2. Here  $\mathbf{r}_i$  is the vector describing the position of the center of molecule  $i$ ,  $\omega_i$

is its orientation and  $\mathbf{d}_\gamma(\omega_i)$  is the vector from the molecular center to the site  $\gamma$ . Part of the potential,  $u^{\text{non}}(12)$ , corresponds to the nonassociative (not necessarily spherical) forces.

The usual model of square-wall associative potential takes the form

$$u_{\alpha\beta}^{\text{as}}(\mathbf{r}_{\alpha\beta}) = \begin{cases} -\varepsilon_{\alpha\beta}^{\text{as}} & |\mathbf{r}_{\alpha\beta}| < a \\ 0 & \text{otherwise} \end{cases} \quad (60)$$

A bond is formed if two sites are within the distance  $a$ . One can restrict bonding to dimer formation by requiring that  $(\sigma - 2d) < a < (\sqrt{\sigma^2 - \sqrt{3}\sigma d} - d)$ .

In the case of computer simulations of fluids with directional associative forces a less intuitive but computationally more convenient potential model has been used [14,16,106]. According to that model the attraction sites  $\alpha$  and  $\beta$  on two different particles form a bond if the centers of reacting particles are within a given cut-off radius  $a$  and if the orientations of two spheres are constrained as follows:  $|\theta_1| < \theta_{c1}$  and  $|\pi - \theta_2| < \theta_{c2}$ . The interaction potential is

$$u_{\alpha\beta}^{\text{as}}(12) = \begin{cases} -\varepsilon_{\alpha\beta}^{\text{as}}, & d < |\mathbf{r}_{12}| < a, |\theta_1| < \theta_{c1}, |\pi - \theta_2| < \theta_{c2} \\ 0, & \text{otherwise} \end{cases} \quad (61)$$

The constraints of the potential, Eq. (61), are fast to calculate in computer simulation [14]. Moreover, in the extensions of the theory to mixtures of different sized molecules [13,15,16], the calculations are significantly simpler.

If the associative site (a square-well, or defined by setting limits of appropriate angles) is embedded into a hard core of the molecule, there must be a “hole” in the infinite repulsive part of the nonassociative potential,  $u^{\text{non}}$ , to make the bond formation possible, i.e.

$$u^{\text{non}}(12) = \begin{cases} \tilde{u}^{\text{non}}(12), & \text{if } u^{\text{as}}(12) = 0 \\ 0, & \text{otherwise} \end{cases} \quad (62)$$

Alternatively, one can assume the nonassociative potential is equal to a value  $D$ , such that  $\exp(-D/k_B T) \approx 0$  in the region where  $u^{\text{as}}(12) \neq 0$ , and then redefine the associative potential by setting it equal to  $u^{\text{as}}(12) - D$ .

## B. The Multidensity Ornstein–Zernike Integral Equations

To discuss briefly the reformulation of the Ornstein–Zernike equation it is most convenient to consider the case of one associating site per molecule,  $M = 1$ . A more general derivation can be found, for example, in Ref. 104. The most important ingredient for the following derivation is the associative “Mayer function.” It characterizes the bonding effects and is

defined as [8–11]

$$f_M^{\text{as}}(r_{12}) = \int d\omega_1 \int d\omega_2 \exp[-\beta u^{\text{non}}(r_{12})] \tilde{f}_M^{\text{as}}(12) \quad (63)$$

where

$$\tilde{f}_M^{\text{as}}(12) = \exp[-u^{\text{as}}(12)/k_B T] - 1 \quad (64)$$

If all the associating sites are identical, or for the model with  $M = 1$ , the subscript index for the site can be dropped. For the potential model (60) the above definition of the Mayer function yields [14]

$$f_M^{\text{as}}(r_{12}) = \begin{cases} [\exp(\varepsilon^{\text{as}}/k_B T) - 1](2a - 2d + r_{12})(a + 2d - r_{12})^2/24d^2 r_{12} & r_{12} < a + 2d \\ 0 & r_{12} > a + 2d \end{cases} \quad (65)$$

whereas for the potential (61) we get [14]

$$f_M^{\text{as}}(r_{12}) = \begin{cases} [\exp(\varepsilon^{\text{as}}/k_B T) - 1](1 - \cos \theta_{c1})(1 - \cos \theta_{c2})/4 & r < a \\ 0 & r > a \end{cases} \quad (66)$$

One can see that, for the model given by Eq. (61),  $f_M^{\text{as}}(r_{12})$  is independent of the distance between the centers of the molecules. This simplicity of the model allows extension to mixtures without difficulty [13,15,16].

According to Wertheim [8–11], the fluid density at a point 1 of the bulk associating fluid is split into two terms, namely the density of unbonded species,  $\rho_0(1)$ , and the density of (singly) bonded species,  $\rho_1(1)$ , such that the total density is  $\rho(1) = \rho_0(1) + \rho_1(1)$ . We set the matrix of densities for a dimerizing fluid

$$[\rho_{ij}] = \begin{bmatrix} \rho(1) & \rho_0(1) \\ \rho_0(1) & 0 \end{bmatrix} \quad (67)$$

To describe the pair correlations, Wertheim [8–11] has introduced “partial” pair correlation functions  $h_{ij}(r)$ . They are defined by an appropriate classification of the graphs in the cluster expansion of  $h(12)$  into four sets. Note that none of the functions  $h_{ij}$  has the meaning of the correlation functions between the bonded and/or unbonded sites; the physical meaning corresponding to the total correlation function possesses only their linear combination

$$h(12) = h_{00}(12) + [\rho_0(1)/\rho(1)]h_{01}(12) + [\rho_0(2)/\rho(2)]h_{10}(12) + [\rho_0(1)\rho_0(2)/\rho(1)\rho(2)]h_{11}(12) \quad (68)$$

There is no other means but to define, if necessary, the total *direct* correlation function via the common Ornstein–Zernike equation

$$h(12) - c(12) = \int c(13)\rho(3)h(13)d(3). \quad (69)$$

However, the partials  $h_{ij}$ , and the “partials” of the direct correlation function  $c_{ij}$ , the latter defined as the subsets of graphs in  $h_{ij}$  without bridge points, are related via a Wertheim-type multidensity Ornstein–Zernike equation

$$h_{ij}(12) - c_{ij}(12) = \sum_k \sum_l \int d(3)c_{ik}(13)\rho_{kl}(3)h_{lj}(32) \quad (70)$$

where the matrix  $[\rho_{ij}]$  is given by Eq. (67). Moreover, the partial densities are related to the total fluid density via the self-consistency relation, which represents an analogue of the mass action law

$$\rho(1) = \rho_0(1) + \rho_0(1) \int d(2)\rho_0(2)[h_{00}(12) + 1]\tilde{f}_M^{\text{as}}(12) \quad (71)$$

In order to obtain a closed set of equations, the Ornstein–Zernike-like equation (70) must be supplemented by a closure approximation. The associative generalization of the Percus–Yevick closure reads [9,10]

$$c_{ij}(12) = \{\exp[-u^{\text{non}}(r)/k_B T] - 1\}\{\delta_{i0}\delta_{j0} + h_{ij}(12) - c_{ij}^0(12)\} \\ + \delta_{i1}\delta_{j1}f_M^{\text{as}}(r)\{1 + h_{ij}(12) - c_{ij}(12)\} \quad (72)$$

More sophisticated closures, such as the associative HNC or the associative mean spherical approximation, can also be used for specific systems in which the nonassociative interaction contains attraction, for example.

## C. Elements of Thermodynamic Perturbation Theory

We consider first the case of entirely repulsive nonassociative potential,  $u^{\text{non}}(12)$ . In a straightforward perturbational treatment, one chooses a system of molecules at the same density and temperature as the real one, but interacting only with  $u^{\text{non}}(12)$  as a reference system. As has been shown by Wertheim [11] and subsequently by several authors [13–17,95–99], the difference of free energies between the system with dimerization and the reference system is

$$(F - F^{\text{non}})/k_B T = \int d(1)\rho(1)[\ln \chi(1) - \frac{1}{2}\chi(1) + \frac{1}{2}] \quad (73)$$

where

$$\chi(1) = \rho_0(1)/\rho(1) \quad (74)$$

is the fraction of monomers. The self-consistency relation (71) becomes

$$\rho(1) = \rho_0(1) + \rho_0(1) \int d(2)[h^{\text{non}}(12) + 1]f_M^{\text{as}}(12)\rho_0(2) \quad (75)$$

For a one-component system with  $M$  directional attractive sites per molecule, the generalization of Eq. (73) is

$$\begin{aligned} (F - F^{\text{non}})/k_B T &= \sum_{\alpha=1,M} \int d(1)\rho(1)[\ln \chi_\alpha(1) - \frac{1}{2}\chi_\alpha(1) + \frac{1}{2}] \\ &= N \sum_{\alpha=1,M} \rho[\ln \chi_\alpha - \frac{1}{2}\chi_\alpha] + \frac{M}{2} \end{aligned} \quad (76)$$

where  $\chi_\alpha(1)$  is the fraction of molecules *not* bonded at a site  $\alpha$  and the last line of Eq. (76) applies to a uniform associating fluid. The individual  $\chi_\alpha$ 's are obtained via the mass-action equation

$$\chi_\alpha = \frac{1}{1 + \sum_{\beta=1,M} \rho \chi_\beta \Delta_{\alpha\beta}} \quad (77)$$

where  $\Delta_{\alpha\beta}$  is defined by

$$\Delta_{\alpha\beta} = \frac{1}{V} \int d(1)d(2)g^{\text{non}}(12)f_{M,\alpha\beta}^{\text{as}}(12) \quad (78)$$

with  $f_{M,\alpha\beta}^{\text{as}}(12)$  given by Eq. (64) and  $g^{\text{non}}(12) = h^{\text{non}}(12) + 1$ . In the limit of zero density the latter equation becomes

$$\Delta_{\alpha\beta}^0 = \frac{1}{V} \int d(1)d(2) \exp[u^{\text{non}}(12)/k_B T] f_{M,\alpha\beta}^{\text{as}}(12) \quad (79)$$

The parameter  $\Delta_{\alpha\beta}^0$  is an analog of the equilibrium association constant. The value of  $\Delta_{\alpha\beta}^0$  itself, rather than the potential  $u_{\alpha\beta}^{\text{as}}$ , is used to characterize the strength of the associative forces.

Let us consider the case of associating hard spheres. The properties of the associating fluid can be calculated if one knows the pair distribution function of the reference hard sphere fluid. Once this function is available, Eq. (79) can be integrated to give  $\Delta_{\alpha\beta}$ . In general, for associating sites of different kinds, the solution of Eq. (77) for  $\chi_\alpha$  requires application of a numerical procedure. However, in the particular case of molecules with identical associative sites, an analytical expression can be written for  $\chi_\alpha$ . The change in the Helmholtz free energy due to association is obtained by

using Eq. (76). All other thermodynamic properties may be straightforwardly determined by differentiating the Helmholtz free energy.

Now, let us consider a model in which the association site is located at a distance slightly larger than the hard-core diameter  $\sigma$ . The excess free energy for a hard sphere fluid is given by the Carnahan–Starling equation [113]

$$F^{\text{non}}/k_B T \equiv F^{\text{HS}}/k_B T = N \frac{4\eta - 3\eta^2}{(1 - \eta)^2} \quad (80)$$

where  $\eta = \pi\sigma^3\rho/6$  and  $N$  is the number of particles. It has often been assumed that  $r^2[h^{\text{non}}(r) + 1]$  is constant and equal to the value of the radial distribution function at contact, i.e.,  $\sigma^2 g^{\text{non}}(\sigma) = \sigma^2 g^{\text{HS}}(\sigma)$ , where  $g^{\text{HS}}(r)$  denotes the hard sphere pair distribution function. The value of  $\Delta_{\alpha\beta}$  is then given by

$$\Delta_{\alpha\beta} = 4\pi g^{\text{HS}}(\sigma) K_{\alpha\beta} [\exp(-\varepsilon_{\alpha\beta}^{\text{as}}/k_B T) - 1] \quad (81)$$

where  $K_{\alpha\beta}$  measures the volume available to sites  $\alpha$  and  $\beta$  on molecules 1 and 2

$$K_{\alpha\beta} = \Delta_{\alpha\beta}^0 / [\exp(-\varepsilon_{\alpha\beta}^{\text{as}}/k_B T) - 1] \quad (82)$$

On the other hand, for the potential model given by Eq. (60),  $K_{\alpha\beta}$  is [14]

$$K_{\alpha\beta} = \sigma^2 \{ \ln[(a + 2d)/\sigma] (6a^3 + 18ad - 24d) \\ + (a + 2d - \sigma)(22d^2 - 5ad - 7d\sigma - 8a^2 + a\sigma + \sigma^2) / (72d^2) \} \quad (83)$$

whereas the potential, Eq. (61), yields [14]

$$K_{\alpha\beta} = \sigma^2 \frac{[1 - \cos(\theta_{c1})][1 - \cos\theta_{c2}]}{4} (a - \sigma) \quad (84)$$

The expression (81) for  $\Delta_{\alpha\beta}$  is expected to be accurate at moderate densities, since in this region of density  $r^2 g^{\text{HS}}(r)$  is constant over the range of the potential. For lower densities this approximation underestimates, whereas for high densities it overestimates the exact value.

In the case of an associating fluid with the repulsive–attractive reference system potential, the attractive van der Waals forces between molecules may also be considered in a perturbational manner [114]. The Helmholtz free energy can be written as a sum of three terms

$$F = F^{\text{non}} + F^{\text{ass}}, \quad F^{\text{non}} = F^{\text{HS}} + F^{\text{att}} \quad (85)$$

where  $F^{\text{att}}$  is the contribution to the free energy resulting from the dispersion forces. If the dispersion forces are considered in a mean-field

approximation, then [14]

$$F^{\text{att}} = -N\rho\varepsilon_{\text{MF}} \quad (86)$$

where  $\varepsilon_{\text{MF}}$  is the measure of the strength of the mean-field attraction.

Obviously, the mean-field treatment of the attractive van der Waals interaction results in neglect of the influence of the interparticle correlations on  $F^{\text{att}}$ , as well as the influence of attractive forces on association effects (cf. the definition of  $\Delta_{\alpha\beta}$ , Eq. (78)). To obtain a more adequate approximation, Johnson and Gubbins (see, e.g., [114]), have developed an accurate equation of state for associating Lennard-Jones fluids, or more precisely for the following nonassociative potential

$$u^{\text{non}}(r) \equiv u^{\text{LJ}}(r) = \begin{cases} 4\varepsilon^{\text{LJ}}[(\sigma/r)^{12} - (\sigma/r)^6] & r < r_{\text{cut}} \\ 0 & r > r_{\text{cut}} \end{cases} \quad (87)$$

where  $r_{\text{cut}}$  is the cut-off distance. Their method uses  $F^{\text{non}}$ , which follows from the modified Nicolas equation of state of Lennard-Jones fluids [115,116]. The associative contribution to the free energy is nevertheless calculated by using Eqs. (73) and (76), but the integrals  $\Delta_{\alpha\beta}$  are evaluated from (78) with the following approximation for,  $g^{\text{non}}(r)$

$$g^{\text{non}}(r) = [1 - f_{\text{mix}}(\rho)]g^{\text{HS}}(r) + f_{\text{mix}}(\rho)g^{\text{LD}}(r) \quad (88)$$

where  $g^{\text{LD}}$  is the low-density limit of the radial distribution function for a Lennard-Jones fluid

$$g^{\text{LD}}(r) \approx \exp[-u^{\text{LJ}}(r)/k_B T] \quad (89)$$

and  $g^{\text{HS}}(r)$  is the hard sphere radial distribution function. The mixing function  $f_{\text{mix}}(\rho)$  is chosen as

$$f_{\text{mix}}(\rho) = \begin{cases} \exp[-(\rho\sigma^3 - \bar{a})^2/\rho\sigma^3] & \rho\sigma^3 < \bar{a} \\ 1 & \rho\sigma^3 > \bar{a} \end{cases} \quad (90)$$

where  $\bar{a}$  is an empirical parameter. It has been found that the choice of  $\bar{a} = 0.5$  works well for several systems [114]. The hard-sphere function  $g^{\text{HS}}(r)$  is given by

$$g^{\text{non}}(r) \approx \exp[-u^{\text{WCA}}(r)/k_B T]y^{\text{HS}}(r) \quad (91)$$

where  $y^{\text{HS}}(r)$  is the cavity correlation function of a fluid of hard spheres with the diameter optimized according to the Weeks-Chandler-Andersen scheme

[117] and  $u^{\text{WCA}}(r)$  is the repulsive part of the Lennard–Jones potential

$$u^{\text{WCA}}(r) = \begin{cases} u^{\text{LJ}}(r) + \varepsilon^{\text{LJ}} & r < 2^{1/6}\sigma \\ 0 & r > 2^{1/6}\sigma \end{cases} \quad (92)$$

The phase diagrams for associating fluids evaluated by using the Johnson and Gubbins approach [114] are in good agreement with computer simulation.

There are some deficiencies of the first-order perturbation theory discussed above. First, the graphs involving the formation of ring-like bonded structures have been neglected and only tree-like structures have been included. Thus, the approach may be inadequate for a fluid permitting the formation of ring-like structures. Next, thermodynamic properties predicted by the theory are independent of the angles between the vectors from the center of a molecule to various attractive sites. Wertheim had extended the thermodynamic perturbation theory to the second order [11] to include the formation of ring-like structures and the case in which bonding at one site blocks bonding at another site. The thermodynamic equations derived in this way are dependent on the bond angles. However, although the second-order theory shows better agreement with simulation data, the differences between the first-order and the second-order theories are small. Since the first-order theory is easier to apply than the second-order theory, the expressions derived at the level of the first-order will be used for the development of the density functional method.

## D. Pair Theory of Nonuniform Associating Fluids

The multidensity Ornstein–Zernike equation (70) and the self-consistency relation (71) actually describe a nonuniform system. To solve these equations numerically for inhomogeneous fluids one needs only an appropriate generalization of the Lowett–Mou–Buff–Wertheim equation (14). Such a generalization, employing the concept of the partial correlation function  $h_{ij}(12)$ , has been considered in Refs. 34,35.

For simplicity, we restrict ourselves to a one-component dimerizing fluid,  $\alpha + \alpha \rightleftharpoons \alpha_2$ , and define the one-particle cavity functions  $t_i$ ,  $i = 0, 1$ , for bonded and unbonded species as follows

$$\begin{aligned} \rho_0(1) &= t_0(1) \exp[-v(1)/k_B T] \\ \rho_1(1) &= t_1(1) \exp[-v(1)/k_B T] \end{aligned} \quad (93)$$



where  $v(1)$  is the external potential field. It can be proved that the Lovett–Mou–Buff–Wertheim equation (14) takes the form [35]

$$\nabla_1 \ln t_0(1) = \int d(2) \{ \nabla_2 [\rho_0(2) + \rho_1(2)] \} c_{00}(12) \quad (94)$$

and

$$\nabla_1 \left[ \frac{t_1(1)}{t_0(1)} \right] = \int d(2) \{ \nabla_2 [\rho_0(2) + \rho_1(2)] \} c_{01}(12) \quad (95)$$

These two equations represent the associative analogue of Eq. (14) for the partial one-particle cavity function. It is convenient to use equivalent equations containing the inhomogeneous total pair correlation functions. Similarly to the theory of inhomogeneous nonassociating fluids, this equivalence is established by using the multidensity Ornstein–Zernike equation (68). Eq. (14) then reduces to [35]

$$\nabla_1 \ln t_0(1) = \int d2 \{ h_{00}(12) \rho(2) \nabla_2 [-v(2)/k_B T] - h_{10}(12) \rho_0(2) \nabla_2 \ln t_0(2) \} \quad (96)$$

and

$$\nabla_1 \left[ \frac{t_1(1)}{t_0(1)} \right] = \int d2 \{ h_{01}(12) \rho(2) \nabla_2 [-v(2)/k_B T] - h_{11}(12) \rho_0(2) \nabla_2 \ln t_0(2) \} \quad (97)$$

The theory, consisting of Eqs. (68) and (94) and (95) (or (96) and (97)), must be supplemented by a closure relation, e.g., the associative Percus–Yevick approximation, Eq. (72). Far from the surface, the density profiles  $\rho_0(1)$  and  $\rho_1(1)$  and the two-particle partial correlation functions tend to their bulk counterparts for associating fluid. The technique of the solution of this set is essentially the same as for the system of equations of the pair theory discussed in Sec. II.

Now we turn our attention to the results obtained from the pair theory for the system of associating Lennard–Jones fluid in contact with a hard wall. The nonassociative part of the interparticle potential is given by Eq. (87), whereas the associative interaction is given by Eq. (60), with  $d = 0.45$  and  $a = 0.1$ . The diameter of fluid particles  $\sigma$  is taken as the unit of length.

To begin with, we recall that, for nonassociating fluids at  $T^* = kT_B/\epsilon^{LJ} = 1.35$ , Plischke and Henderson [58] have observed a depletion of the fluid density at a hard wall, starting from the bulk fluid density  $\rho = 0.4$  up to  $\rho = 0.65$ . For higher bulk fluid densities the contact values of the reduced density profile,  $\rho(z)/\rho$ , become greater than unity and the profiles

behave similarly to the density profiles of a hard sphere fluid near a hard wall [55–57].

A dimerizing Lennard–Jones fluid has been studied for the bulk density  $\rho = 0.75$ , and at temperature  $T^* = 1.35$ , for different values of the association energy, namely  $\varepsilon^{\text{as}}/k_B T = 2, 6, 10$ , and  $11.5$  [118]. The results for  $\varepsilon^{\text{as}}/k_B T = 2$  are very close to the case of the nonassociating Lennard–Jones fluid near a hard wall and therefore are omitted. The above choice of the density and temperature provides stable thermodynamic states for all systems under study.

The density profiles are shown in Fig. 7(a). Fig. 7(b), however, illustrates the dependence of the degree of dimerization,  $\chi(z) = \rho_1(z)/\rho(z)$ , on the distance from the wall. It can be seen that, at a sufficiently low degree of dimerization ( $\varepsilon^{\text{as}}/k_B T = 6$ ), the profile exhibits oscillations quite similar to those for a Lennard–Jones fluid and for a hard sphere fluid near a hard wall. For a high degree of dimerization, i.e., for  $\varepsilon^{\text{as}}/k_B T = 10$  and  $11.5$ , we observe a substantial decrease of the contact value of the profile in a wide layer adjacent to a hard wall. In the case of the highest association energy,  $\varepsilon^{\text{as}}/k_B T = 11.5$ , the density profile increases almost smoothly from a low contact density and reaches its “bulk” value at  $z \approx 3.5$ . It is of interest to mention that the profile of undimerized particles, which is shown in the inset for this figure, does exhibit oscillations. However, the influence of dimerized particles is overwhelming. From Fig. 7(b) one can see that the degree of dimerization for high values of association energy,  $\varepsilon^{\text{as}}/k_B T = 10$  and  $11.5$ , saturates at  $z \approx 3.5$ , i.e., at distances where the fluid density reaches its bulk value. Close to the wall, the degree of dimerization is substantially lower.

It is of interest to consider the pair structure in terms of the inhomogeneous pair distribution functions obtained from the second-order (pair) theory. In Fig. 8 we present the results for the intramolecular and intermolecular parts of three functions, namely the function  $g_{\text{bulk}}(r_{12})$  which follows from the inhomogeneous pair distribution function  $g(z_1, z_2, R_{12})$  for  $z_1, z_2 \rightarrow \infty$ ;  $g_{\parallel} \equiv g(z_1 = 0, z_2 = 0, R_{12})$  and  $g_{\perp} \equiv g(z_1 = 0, z_2, R_{12} = 0)$ . The calculations have been carried out for  $\varepsilon^{\text{as}}/k_B T = 10$ . It can be seen that the first maxima of the intermolecular parts of the function  $g_{\text{bulk}}(r_{12})$  and  $g_{\parallel}$  are almost the same. However, the way in which these functions decay is very different. The lateral correlations in the surface plane, described by  $g_{\parallel}$ , decay much faster than those exhibited by  $g_{\text{bulk}}(r_{12})$ . Furthermore, the highest first maximum is observed for  $g_{\perp}$ . For larger interparticle separations the shape of  $g_{\text{bulk}}(r_{12})$  and  $g_{\perp}$  is almost similar. The function  $g_{\parallel}$  becomes long-ranged, describing the correlations of dimers in the surface plane. The intramolecular peaks of these functions, multiplied by the corresponding local densities, provide information about the number of dimers.

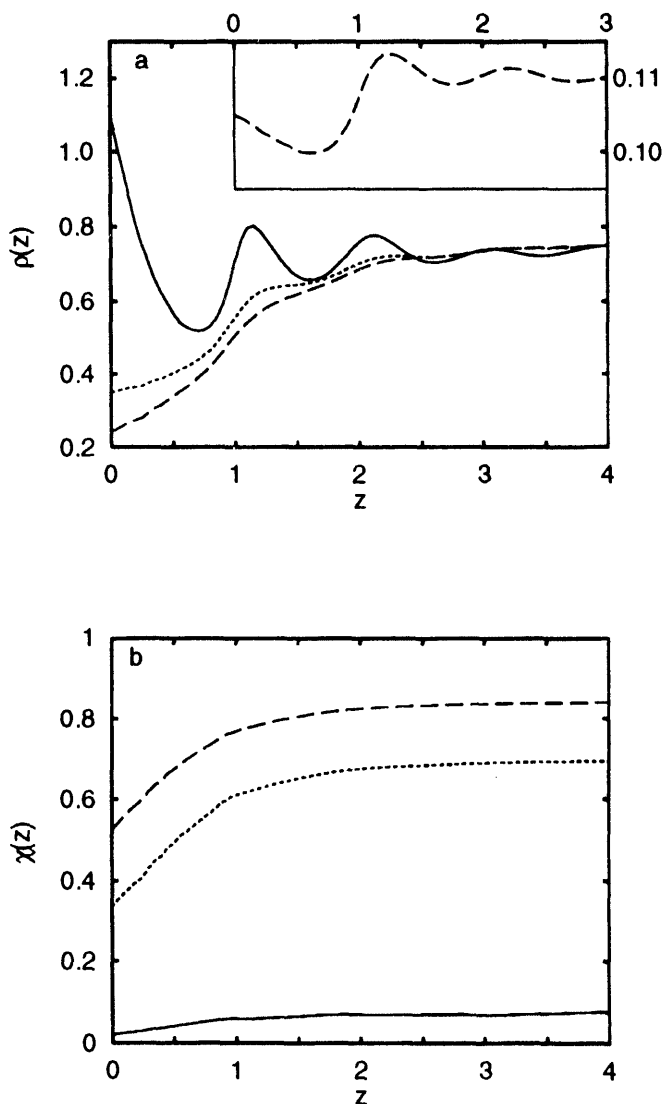


**FIG. 7** Density profiles  $\rho(z)$  of dimerizing LJ spheres near a hard wall, at density  $\rho = 0.75$  and at  $T^* = 1.35$  (a). The association energy,  $\epsilon^{as}/k_B T$ , is 6 (solid line), 10 (short-dashed line), and 11.5 (long-dashed line). The results follow from the second-order theory. In the inset the density profile of the undimerized species,  $\rho_0(z)$ , for  $\epsilon^{as}/k_B T = 11.5$  is presented. In (b) the curves for  $\chi(z) = \rho_1(z)/\rho(z)$  are given for the states shown in (a). The nomenclature of the lines in (b) is similar to that in (a). (From Ref. 118.)

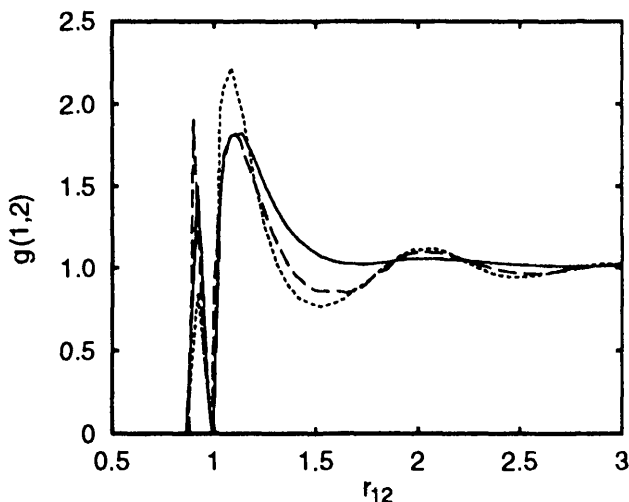


**FIG. 8** Inhomogeneous pair distribution functions for the bulk fluid  $g_{\text{bulk}}(r_{12})$  (dashed line),  $g(z_1 = 0, z_2 = 0, R_{12}) \equiv g_{\parallel}$  (solid line) and  $g(z_1 = 0, z_2 = 0, R_{12} = 0) \equiv g_{\perp}$  (dotted line). The value of the association energy is  $\varepsilon^{\text{as}}/k_B T = 10$ , bulk density is  $\rho = 0.75$  and the temperature  $T^* = 1.35$ . (From Ref. 118.)

The main conclusion which can be drawn from the results presented above is that dimerization of particles in a Lennard–Jones fluid leads to a stronger depletion of the profiles close to the wall, compared to a nonassociating fluid. On the basis of the calculations performed so far, it is difficult to conclude whether the second-order theory provides a correct description of the drying transition. An unequivocal solution of this problem would require massive calculations, including computer simulations. Also, it would be necessary to obtain an accurate equation of state for the bulk fluid. These problems are the subject of our studies at present.

## E. Singlet Level Theory for Fluids with Directional Bonding

### 1. Structureless Surfaces

As we have noted in Sec. II, one of the methods leading to the so-called singlet equations for the density profiles, originally initiated for simple fluids in Ref. 24, starts from considering a mixture of fluid particles and another species of hard spheres at density  $\rho_G$  and diameter  $D_G$ , taking next the limit  $\rho_G \rightarrow 0$ ,  $D_G \rightarrow \infty$ .

As in Sec. II, we consider a mixture composed of a dimerizing one-component fluid and a giant hard sphere [21,119]. We begin with the multi-density Ornstein–Zernike equation for the mixture

$$h_{ij,\eta\delta}(r_{12}) = c_{ij,\eta\delta}(r_{12}) + \sum_{lm=(0,1)} \sum_{\gamma=\alpha,G} \int d\mathbf{r}_3 c_{il,\eta\gamma}(r_{13}) \rho_{lm,\gamma} h_{mj,\gamma\delta}(r_{23}) \quad (98)$$

where the Greek symbols denote species. The matrix  $[\rho_{ij}]$  is a generalization of the matrix given by Eq. (67) and reads

$$[\rho_{ij}] = \begin{bmatrix} \rho_{0,\alpha} + \rho_{1,\alpha} & \rho_{0,\alpha} & 0 & 0 \\ \rho_{0,\alpha} & 0 & 0 & 0 \\ 0 & 0 & 0 & \rho_G \\ 0 & 0 & 0 & \rho_G \end{bmatrix} \quad (99)$$

The self-consistency relation between densities (cf. Eq. (75)) takes the form

$$\rho_\alpha = \rho_{0,\alpha} + \rho_{1,\alpha} + [\rho_{0,\alpha}]^2 \int d\mathbf{r} [1 + h_{00,\alpha\alpha}(r)] f_M^{\text{as}}(r) \quad (100)$$

After taking the limit  $\rho_G \rightarrow 0$ ,  $D_G \rightarrow \infty$ , we obtain equations which describe the pair correlations of interest

$$h_{ij,\alpha\alpha}(r_{12}) - c_{ij,\alpha\alpha}(r_{12}) + \sum_{lm} \int d\mathbf{r}_3 c_{il,\alpha\alpha}(r_{13}) \rho_{lm,\alpha} h_{mj,\alpha\alpha}(r_{23}) \quad (101)$$

$$h_{0j,G\alpha}(r_{12}) - c_{0j,G\alpha}(r_{12}) + \sum_{lm} \int d\mathbf{r}_3 c_{0l,G\alpha}(r_{13}) \rho_{lm,\alpha} h_{mj,G\alpha}(r_{23}) \quad (102)$$

$$h_{i0,\alpha G}(r_{12}) - c_{i0,\alpha G}(r_{12}) + \sum_{lm} \int d\mathbf{r}_3 c_{il,\alpha G}(r_{13}) \rho_{lm,\alpha} h_{m0,\alpha G}(r_{23}) \quad (103)$$

and

$$h_{00,GG}(r_{12}) - c_{00,GG}(r_{12}) + \sum_{lm} \int d\mathbf{r}_3 c_{0l,G\alpha}(r_{13}) \rho_{lm,\alpha} h_{m0,\alpha G}(r_{23}) \quad (104)$$

Eq. (101) is the multidensity Ornstein–Zernike equation for the bulk, one-component dimerizing fluid. Eqs. (102) and (103) are the associative analog of the singlet equation (31). The last equation of the set, Eq. (104), describes the correlations between two giant particles and may be important for theories of colloid dispersions. The partial correlation functions yield three

total correlation functions

$$h_{\alpha\alpha}(r) = h_{00,\alpha}(r) + (\rho_{0,\alpha}/\rho_\alpha)[h_{01,\alpha\alpha}(r) + h_{10,\alpha\alpha}(r)] + (\rho_{0,\alpha}/\rho_\alpha)^2 h_{11,\alpha\alpha}(r) \quad (105)$$

$$h_{\alpha G} = h_{00,G\alpha}(r) + (\rho_{0,\alpha}/\rho_\alpha) h_{01,G\alpha}(r) \quad (106)$$

and

$$h_{GG}(r) = h_{00,GG}(r) \quad (107)$$

Eqs. (102) and (103) are equivalent and give the distribution of  $\alpha$  particles “around” the wall. Thus, the local density of a fluid in contact with a flat wall is

$$\rho(z) \equiv \rho_\alpha(z) = \rho_\alpha[h_{\alpha G}(z) + 1] \quad (108)$$

Obviously, Eqs. (101–103) are exact. However, their solution requires closures. The associative Percus–Yevick closure to Eq. (101) has been given by Eq. (72); the associative Percus–Yevick closure to Eq. (103) reads

$$h_{j0,\alpha G}(r) - \delta_{j0} = \{\delta_{j0} + h_{j0,\alpha G}(r) - c_{j0,\alpha G}(r)\} \exp[-v(r)/k_B T] \quad (109)$$

where we use the symbol  $v(r)$  to abbreviate the wall–fluid potential  $u_{\alpha G}(r)$ .

An analytic solution of the singlet equations (102) (or (103)) and (101) can be obtained for a particular model for a fluid interacting via sticky associative potential [21]

$$f_M^{\text{as}}(r) = b\delta(r - \sigma) \quad (110)$$

in contact with a hard wall at  $z = 0$ . The solution has been given in the form of the Laplace transform of the partial correlation function. We do not present these results here, referring the reader to the original work [21]. Also, it has been shown that the contact value of the local density of a sticky fluid is

$$\rho(z=0)/\rho = \frac{1+2\eta}{(1-\eta)^2} - \frac{1-\chi_s}{2(1-\eta)} \quad (111)$$

where  $\chi_s$  is the fraction of undimerized particles resulting from this singlet theory

$$\chi_s = \frac{\sqrt{1+24\sigma^2\pi b\eta g(\eta)} - 1}{12\sigma^2\pi b\eta g(\eta)} \quad (112)$$

and

$$g(\eta) = \frac{4}{\pi\sigma^3} \frac{1+0.5\eta}{(1-\eta)^2} \quad (113)$$

For  $\chi_s = 1$ , Eq. (111) reduces to that for hard spheres [24].

The surface excess isotherm is given by [21]

$$\Gamma = \frac{1}{\pi\sigma^2} \frac{9\eta^2 + 1.5\eta(4\eta - 1)(1 - \chi_s)}{1 + 2\eta + 1.5\eta(1 - \chi_s)} \quad (114)$$

In the limit of zero association,  $\chi_s \rightarrow 0$ , the latter equation reduces to the adsorption isotherm of hard spheres, evaluated within the singlet Percus–Yevick approximation, whereas for  $\chi_s \rightarrow 1$  (i.e., in the limit of complete association) one obtains the adsorption isotherm of tangent dimers

$$\Gamma = \frac{1}{\pi\sigma^2} \frac{15\eta^2 - 1.5\eta}{1 + \frac{7}{2}\eta} \quad (115)$$

The singlet multidensity Ornstein–Zernike approach for the density profile described in this section has also been applied to study the role of association effects in the ionic liquid at an electrified interface [22].

## 2. Crystalline Surfaces

We apply the singlet theory for the density profile by using Eqs. (101) and (103) to describe the behavior of associating fluids close to a crystalline surface [120–122]. First, we solve the multidensity OZ equation with the Percus–Yevick closure for the bulk partial correlation functions, and next calculate the total correlation function via Eq. (68) and the direct correlation function from Eq. (69). The bulk total direct correlation function is used next as an input to the singlet Percus–Yevick or singlet hypernetted chain equation, (6) or (7), to obtain the density profiles. The same approach can be used to study adsorption on crystalline surfaces as well as in pores with walls of crystalline symmetry.

Following Ref. 122, we consider the adsorption of associating hard spheres, Eq. (60), with  $d = 0.45$ ,  $a = 0.09$  in a slit-like pore with crystalline walls. A weakly associated fluid and a highly associated fluid have been studied. The weakly associated fluid was characterized by the coefficient  $\Delta^0$  (cf. Eq. (79)) equal to 1, whereas in the case of the highly associated fluid  $\Delta^0 = 100$ .

The fluid–pore potential has been chosen as a sum of interactions of the fluid with two commensurate parallel crystalline pore walls. The potential of interaction between fluid particles and the pore walls is given by

$$v(\mathbf{r}_i) = v^{\text{HW}}(z_i) + \sum_j [v^{\text{LJ}}(r_{ij}) + v^{\text{as}}(r_{ij})] \quad (116)$$

where  $r_{ij}$  is the distance between the particle and the site  $j$  of the square crystal lattice (100) plane. The first term of the potential (116) is the

confining potential

$$v^{\text{HW}}(z) = \begin{cases} 0 & 0 < z < H \\ \infty & \text{otherwise} \end{cases} \quad (117)$$

where  $H$  denotes the pore width. The two remaining terms in Eq. (116) are

$$v^{\text{LJ}}(r) = \begin{cases} \infty & r < L_s - 0.5w \\ D_s & L_s - 0.5w < r < L_s + 0.5w \\ 4\varepsilon_s^{\text{LJ}}[(\sigma_s/r)^{12} - (\sigma_s/r)^6] & r > L_s + 0.5w \end{cases} \quad (118)$$

and

$$v^{\text{as}}(r) = \begin{cases} 0 & 0 < L < L_s - 0.5w \\ -\varepsilon_s^{\text{as}} - D_s & L_s - 0.5w < r < L_s + 0.5w \\ 0 & r > L_s + 0.5w \end{cases} \quad (119)$$

In the above,  $\varepsilon_s^{\text{as}}$  is the energy of chemical binding of a fluid particle with the solid atom. In the calculations performed it was assumed that  $\sigma_s = \sigma = 1$  and the square mound  $D_s$  satisfies the condition  $\exp[-D_s/k_B T] \approx 0$ . The bonding length of a fluid particle with the solid atom is  $L_s$  and  $w$  is the width of the attractive square well ( $w$  was set to 0.1 in the calculations).

The associative part of the adsorbing potential, Eq. (116), generates a highly localized adsorption which corresponds to the onefold, to the twofold bridging site, and to the fourfold hollow site adsorption dependence of the length  $L_s$ . Note that in the absence of the associative part, Eq. (119), and in the limit  $\varepsilon_s^{\text{LJ}} \rightarrow 0$  the pore walls reduce to an array of hard spheres.

Comparing Figs. 9(a) and 9(b), it can be seen that stronger bonding with the pore walls results in a lower density in the region of the first maxima for the density profiles over three positions:  $s$ ,  $sp$  and  $a$  (cf. Sec. II B 3). This effect is clearly apparent for low and high degrees of dimerization of the bulk fluid. For a weakly dimerized fluid, a rather small influence of the shape of the density profiles in the center of the pore, due to bonding, is observed. When the fluid is highly dimerized, bonding influences the profiles over the one-fold ( $a$ ) and two-fold ( $sp$ ) positions. Specifically, the density over the  $a$  position increases and consequently the difference in the density over  $s$  and  $a$  positions becomes larger at  $\approx 1.4$ . It is difficult to argue whether the effect of bonding can lead to a preference for in-plane orientations of dimers. However, the tendency for an increase of the fraction of dimers oriented perpendicularly and tilted with respect to the pore walls follows from the peculiar decaying shape of the first maxima of the density profiles.

The  $a$ - $s$ - $a$  and  $sp$ - $s$ - $sp$  cuts of the density profiles (Figs. 9(c) and 9(d)) clearly demonstrate that for a highly dimerized fluid the nonassociatively adsorbed dimers have a tendency to orient perpendicularly or slightly tilted



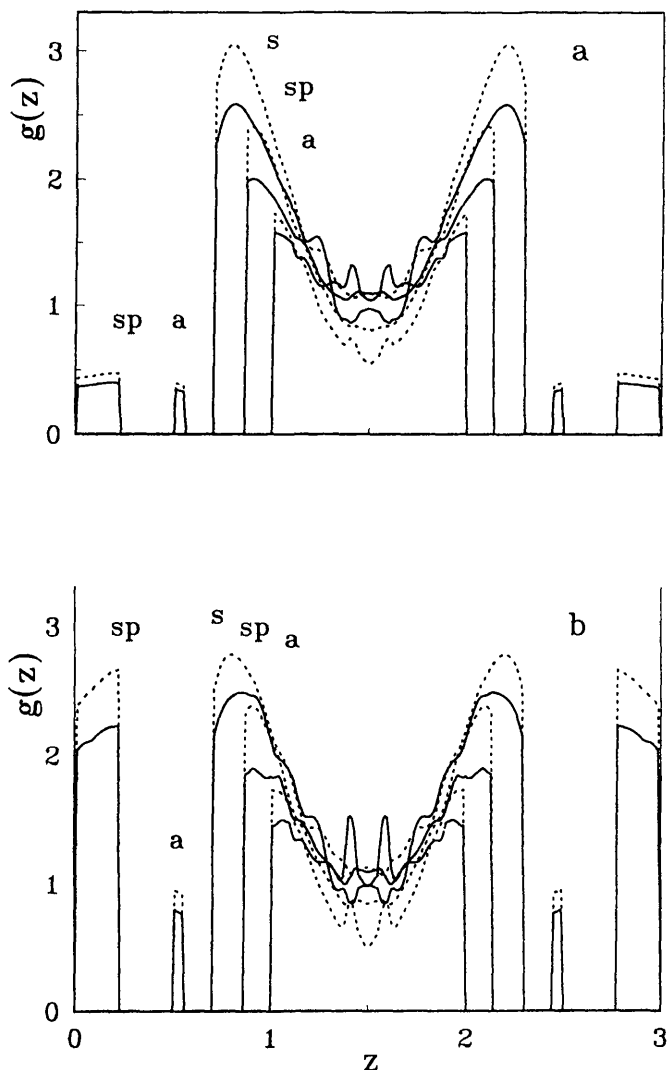


**FIG. 9** Normalized density profiles  $\rho(z)/\rho$  as a function of  $z$  in the pore of width  $H = 3$  with attractive walls obtained for  $L = 0.9$ ,  $\rho = 0.4$ ,  $\Delta^0 = 100$  (solid lines) and  $\Delta^0 = 1$  (dotted lines), and for  $L_s = 0.525$ ,  $\epsilon^{as}/k_B T = 0.1$ ,  $\epsilon_s/k_B T = 0.25$  (a) and for  $\epsilon^{as}/k_B T = 1$  (b). The intraparticle peaks are scaled by the factor 0.1. The labels  $s$ ,  $sp$ , and  $a$  denote the profiles over the adsorbing site, saddle point and atom position, respectively. The  $(a)-(s)-(a)$  and  $(sp)-(s)-(sp)$  cuts of the density profile, (c) and (d) (respectively), are for  $L_s = 0.525$ ,  $\epsilon^{as}/k_B T = 1$ ,  $\epsilon_s/k_B T = 0.25$  and  $\Delta^0 = 100$ . (From Ref. 122.)

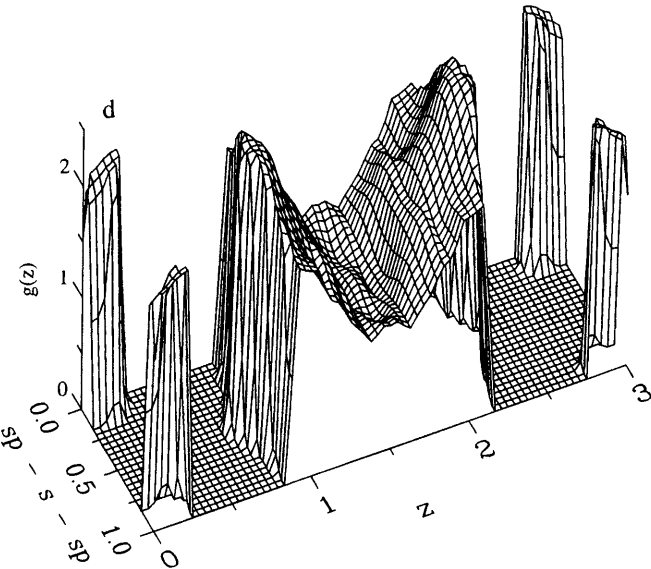
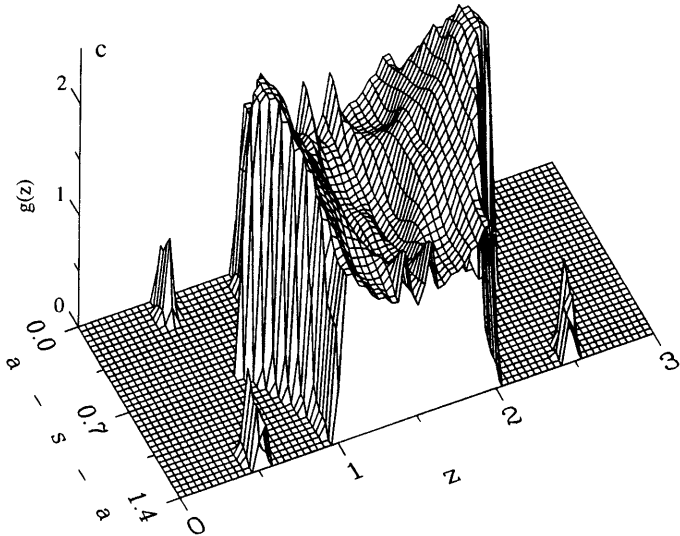


FIG. 9 Continued.

with respect to the normal to the pore wall. Associative adsorption results in a variety of tilted configurations; some of the dimers associatively adsorbed in the one-fold position  $a$  can tend to the tilted or even perpendicular orientation with respect to the pore wall. This is in line with the Monte Carlo simulations [123,124] revealing that molecules grafted to wall association sites prefer an orientation perpendicular to the wall.

The problem of adsorption of associating fluids on crystalline surfaces has also been studied by Borówko et al. by using the density functional approach [43].

#### **IV. DENSITY FUNCTIONAL APPROACHES IN THE THEORY OF INHOMOGENEOUS ASSOCIATING FLUIDS**

The first density-type approach for associating inhomogeneous fluids with directional associative forces was proposed by Kierlik and Rosinberg [125–127]. Their theory was developed to describe fluid consisting of completely associated non-overlapping hard spheres (i.e., tangent chains) and was based on Kierlik–Rosinberg [128] and Rosenfeld [129,130] weighted free energy density functional for a hard-sphere mixture and on the Wertheim theory of association. This density functional theory self-consistently determines the density profiles at a hard wall. However, the contact densities disagree with the bulk pressures unless adjustable parameters are used. Moreover, for high fluid densities and long associated chains, the singlet integral equation theory of Holovko and Vakarin [21] was shown to give better results than the theory of Kierlik and Rosinberg. The theory which we would like to present below has been developed for the case of associative sites located at or outside the molecular core. The theory can then involve a hard sphere reference system.

##### **A. The Theory of Segura, Chapman, and Shukla**

Recently, Segura, Chapman, and co-workers [38,39] have presented a successful version of the density functional theory describing adsorption of an associating fluid on a hard wall. In their approach the clusters and chains form in a way dependent on association energy. The tests performed for the theory have shown reasonably good agreement with Monte Carlo simulation data. However, as Segura et al. [38] have noted, the theory gives insufficiently accurate results when passing from adsorption to desorption. The Segura–Chapman–Shukla approach has been based on the Evans–Tarazona theory for the reference hard-sphere system [49,131–136]. The reference hard-sphere system can be described by using alternative density

functional formulations, e.g., the theory of Kierlik–Rosinberg [137], of Meister–Kroll–Groot [138,139] or of Curtin and Ashcroft [140]. This is particularly important for multicomponent systems, because the extension of the Evans–Tarazona approach for mixtures encounters difficulties [141,142].

We begin with the definition of the grand potential  $\Omega$  as a functional of the number density of a fluid [49],  $\rho(\mathbf{r})$

$$\Omega = F + \int \rho(\mathbf{r})[v(z) - \mu]d\mathbf{r} \quad (120)$$

where  $\mu$  is the configurational chemical potential, and the configurational Helmholtz free energy  $F$  is split into a sum of an ideal and the excess parts

$$F = F^{\text{id}} + F^{\text{ex}} \quad (121)$$

where

$$F^{\text{id}}/k_B T = \int \rho(\mathbf{r})[\ln \rho(\mathbf{r}) - 1]d\mathbf{r} \quad (122)$$

The excess free energy is divided into terms representing the contributions due to repulsive and attractive nonassociative forces acting between molecules, as well as into a contribution arising from association [38,39]

$$F^{\text{ex}} = F^{\text{rep}} + F^{\text{att}} + F^{\text{as}} \quad (123)$$

The first step towards the development of appropriate expressions is the decomposition of the nonassociative pair potential into repulsive and attractive terms. In this work we apply the Weeks–Chandler–Andersen separation of interactions [117], according to which the attractive part of the Lennard–Jones potential is defined by

$$u^{\text{att}}(r) = u^{\text{WCA}}(r) \quad (124)$$

where  $u^{\text{WCA}}(r)$  is given by Eq. (92).

The repulsive forces,  $u^{\text{rep}}(r) = u^{\text{LJ}}(r) - u^{\text{WCA}}(r)$ , are next approximated by a hard sphere potential with an effective hard sphere diameter  $d_{\text{HS}}$ . There are several possible routes to obtain  $d_{\text{HS}}$ , such as that of Barker–Henderson, for example; see Ref. 143. However, usually in the case of nonuniform systems this parameter is simply set to be equal to the Lennard–Jones diameter  $\sigma$ .

The contribution  $F^{\text{rep}}$  is computed in a nonlocal manner by employing the concept of smoothed density [49],  $\tilde{\rho}(\mathbf{r})$ , i.e., the density obtained by averaging the local density with a weight function  $W(r)$

$$\tilde{\rho}(\mathbf{r}) = \int d\mathbf{r}' \rho(\mathbf{r}') W[|\mathbf{r} - \mathbf{r}'|, \tilde{\rho}(\mathbf{r})] \quad (125)$$

According to Evans and Tarazona [133–135], the weight function  $W(r)$  is given as a power series

$$W(r; \rho) = W_0(r) + W_1(r)\rho + W_2(r)\rho^2 \quad (126)$$

and the coefficients  $W_0(r)$ ,  $W_1(r)$  and  $W_2(r)$  in this expression can be found in Ref. 135. The equation defining  $F^{\text{rep}}$  takes the form

$$F_{\text{rep}}^{\text{ex}} = \int d\mathbf{r} \rho(\mathbf{r}) f^{\text{rep}}(\tilde{\rho}(\mathbf{r})) \quad (127)$$

where  $f^{\text{rep}}$  is modelled by the free energy density of a hard sphere fluid with diameter  $d_{\text{HS}}$ , and is usually evaluated from the Carnahan–Starling equation of state [113]

$$f^{\text{rep}}(\tilde{\rho}) = F^{\text{HS}}/N, \quad (128)$$

where  $F^{\text{HS}}$  is calculated from Eq. (80) at a density equal to the averaged density  $\tilde{\rho}$ . The nonassociative attractive forces are treated in a mean field approximation

$$F^{\text{att}} = \int d\mathbf{r} f^{\text{att}}(\mathbf{r}) \rho(\mathbf{r}) \quad (129)$$

where

$$f^{\text{att}} = \frac{1}{2} \int d\mathbf{r}' \rho(\mathbf{r}') u^{\text{att}}(|\mathbf{r} - \mathbf{r}'|) \quad (130)$$

Finally, the associative term is computed by using generalizing thermodynamic perturbation theory. One then obtains [38]

$$F^{\text{as}} = \int d\mathbf{r} \rho(\mathbf{r}) f^{\text{as}}(\tilde{\rho}(\mathbf{r})) \quad (131)$$

where, for a particular model of a one-component fluid with  $M$  associating sites per particle, each of which can form a bond with  $M'$  sites of another particle, we have

$$f^{\text{as}}(\tilde{\rho})/k_B T = \sum_{\alpha=1, M} [\ln \chi_{\alpha}(\tilde{\rho}) - \chi_{\alpha}(\tilde{\rho})/2 + 0.5] \quad (132)$$

We would like to recall that  $\chi_{\alpha}(\tilde{\rho})$  is the fraction of molecules not bonded at an associative site; now it is a function of the averaged density  $\tilde{\rho}(\mathbf{r})$ . A generalization of the perturbational theory allows us to define  $\chi_{\alpha}(\tilde{\rho})$  similar to the case of bulk associating fluids. Namely

$$\chi_{\alpha}(\tilde{\rho}) = \frac{1}{1 + \sum_{\beta=1, M'} \tilde{\rho} \chi_{\beta}(\tilde{\rho}) \Delta_{\alpha\beta}(\tilde{\rho})} \quad (133)$$

where  $\Delta(\tilde{\rho})$  is given by the relation analogous to Eq. (78); i.e.,  $\Delta(\tilde{\rho})$  is approximated by

$$\Delta_{\alpha\beta}(\tilde{\rho}) \approx \int d\mathbf{r} g^{\text{non}}(r; \tilde{\rho}) f_{\alpha\beta}^{\text{as}}(r) \quad (134)$$

where  $g^{\text{non}}(r; \tilde{\rho})$  is the pair distribution function of the system interacting via the potential  $u^{\text{rep}}(r)$ , but evaluated at density  $\tilde{\rho}$  and  $f_{\alpha\beta}^{\text{as}}$  is the analog of  $f_M^{\text{as}}$  (Eq. (63)) for sites  $\alpha$  and  $\beta$ . This function is approximated by Eq. (91) in which the Percus–Yevick hard-sphere cavity function,  $y_{\text{HS}}(r; \tilde{\rho})$  at density  $\tilde{\rho}$  is used. Although the Percus–Yevick cavity function is not accurate for hard spheres, it has been shown that the application of this approximation for bulk fluids yields more accurate results than the exact cavity function from computer simulation [17].

The equilibrium density profile is obtained by minimizing the grand potential,  $\delta\Omega/\delta\rho(z) = 0$ . Hence we obtain

$$\begin{aligned} -k_B T \ln[\rho(z)/\rho_b] &= v(z) + f^{\text{rep}}[\tilde{\rho}(z)] - f^{\text{rep}}(\rho_b) \\ &+ f^{\text{as}}[\tilde{\rho}(z)] - f^{\text{as}}(\rho_b) + \int d\mathbf{r}' u^{\text{att}}(|\mathbf{r}' - \mathbf{r}|) [\rho(z) - \rho_b] \\ &+ \int \frac{\delta\tilde{\rho}(z')}{\delta\rho(z)} (f^{\text{rep}}[\tilde{\rho}(z')] + f^{\text{as}}[\tilde{\rho}(z')])' \rho(z') d\mathbf{r}' - \rho_b [f^{\text{rep}'}(\rho_b) + f^{\text{as}'}(\rho_b)] \end{aligned} \quad (135)$$

where the prime denotes the free energy derivative with respect to density, and  $\rho_b$  is the bulk (reference) density corresponding to the chemical potential  $\mu$ . In the case of a fluid in contact with a single wall,  $\rho_b = \lim_{z \rightarrow \infty} \rho(z)$ . The functional derivative  $\delta\tilde{\rho}(z')/\delta\rho(z)$  is calculated by differentiating Eq. (125), cf. Ref. 133.

## B. A Modified Meister–Kroll Theory

The theory presented above has been based on the Evans–Tarazona density functional approach. Therefore its generalization to multicomponent systems is not instantaneous. However, a modified Meister–Kroll theory, introduced by Rickayzen et al. [143,144], does not suffer from the above-mentioned drawback and provides an accurate description of nonuniform simple (nonassociating) fluids.

According to this approach, the hard-sphere free energy functional is given by

$$F^{\text{rep}} = \int \rho(\mathbf{r}) f^{\text{rep},c}[\tilde{\rho}(\mathbf{r})] d\mathbf{r} - kT \int d\mathbf{r} \int d\mathbf{r}' G[|\mathbf{r} - \mathbf{r}'|; \tilde{\rho}(\mathbf{r}')] [\rho(\mathbf{r}') - \tilde{\rho}(\mathbf{r}')] \quad (136)$$

where

$$G(r, \bar{\rho}) = \int_0^1 x c(r; x \bar{\rho}) dx \quad (137)$$

and  $c(r; \bar{\rho})$  is the direct correlation function for a homogeneous fluid of hard spheres with bulk density  $\bar{\rho}$ . To provide consistency with the approximation used for the direct correlation function,  $f^{\text{rep},c}$  must be chosen to satisfy the compressibility equation. If the Percus–Yevick approximation is used, one obtains

$$f^{\text{rep},c}(\bar{\rho})/k_B T = -\ln(1 - \tilde{\eta}) + \frac{3\tilde{\eta}}{1 - \tilde{\eta}} + \frac{3}{2} \left( \frac{\tilde{\eta}}{1 - \tilde{\eta}} \right)^2 \quad (138)$$

The prescription proposed in the original Meister–Kroll–Groot [138,139] theory for hard spheres requires the determination of the local density and the averaged density as two independent variational variables by minimizing the grand potential with respect to these variables. The modification introduced by Rickayzen et al. [143,144] arises from another definition of the average density

$$\bar{\rho}(\mathbf{r}) = \int d\mathbf{r}' W_g(|\mathbf{r} - \mathbf{r}'|) \rho(\mathbf{r}') \quad (139)$$

where

$$W_g(|\mathbf{r} - \mathbf{r}'|) = (2\pi\lambda^2)^{3/2} \exp[-\lambda^2|\mathbf{r} - \mathbf{r}'|^2/2] \quad (140)$$

is the Gaussian weight function,  $\lambda = 1/\sigma$ , and from a new definition of the coupling function  $G$ . Its Fourier transform reads [143,144]

$$\begin{aligned} \hat{G}(k, \bar{\rho}) &= 0.5\{\hat{c}(k; \bar{\rho}) + \hat{w}^2(k)[\hat{c}(0; \bar{\rho}) - 2\hat{G}(0; \bar{\rho})]\} \\ &\quad - \frac{1}{2} \int_0^{\bar{\rho}} d\zeta \left( \frac{\zeta}{\bar{\rho}} \right)^{1/\hat{w}(k)} \{\hat{c}'(k; \zeta) + \hat{w}^2(k)[\hat{c}'(0; \zeta) - 2\hat{G}(0; \zeta)]\} \end{aligned} \quad (141)$$

where the prime denotes differentiation with respect to density. The zero-component Fourier transform is obtained from the compressibility equation

$$k_B T \frac{\partial f^{\text{rep},c}(\bar{\rho})}{\partial \bar{\rho}} = \hat{G}(0; \bar{\rho}) \quad (142)$$

According to these modifications, the grand potential of hard spheres is the function only of the true density  $\rho(\mathbf{r})$ . Similarly to the theory described in the previous subsection, the associative contribution to the free energy

assumes the form given by Eq. (132). Consequently, the local density equation reads

$$\begin{aligned}
 & -k_B T \ln \rho(\mathbf{r}) = v(\mathbf{r}) + f^{\text{rep},c}[\tilde{\rho}(\mathbf{r})] - f^{\text{rep},c}(\rho_b) + f^{\text{as}}[\tilde{\rho}(\mathbf{r})] - f^{\text{as}}(\rho_b) \\
 & + \rho_b f^{\text{rep},c'}(\tilde{\rho}) + \rho_b f^{\text{as}'}(\tilde{\rho}) - \int d\mathbf{r}' \{ G[|\mathbf{r} - \mathbf{r}'|; \tilde{\rho}(\mathbf{r})][\rho(\mathbf{r}') - \tilde{\rho}(\mathbf{r})] \\
 & + G[|\mathbf{r} - \mathbf{r}'|; \tilde{\rho}(\mathbf{r}')] \rho(\mathbf{r}') \} - \int d\mathbf{r}' w_g(|\mathbf{r} - \mathbf{r}'|) \rho(\mathbf{r}') \\
 & \times \left\{ \int G[|\mathbf{r}' - \mathbf{r}''|; \tilde{\rho}(\mathbf{r}')][\rho(\mathbf{r}'') - \tilde{\rho}(\mathbf{r}')] d\mathbf{r}'' + f_{\text{ex}}^{\text{as}'}[\tilde{\rho}(\mathbf{r}')] \right\} \\
 & + \int d\mathbf{r}' u^{\text{att}}(|\mathbf{r}' - \mathbf{r}|) [\rho(z) - \rho_b]
 \end{aligned} \tag{143}$$

The latter relation is the final equation for the density profile, resulting from the modified Meister–Kroll–Groot theory if applied to associating fluids [145].

### C. Associating Hard Spheres at a Hard Wall

Let us consider a one-component system of hard spheres of unit diameter  $\sigma = 1$  with angular-dependent associative potential. The nonassociative potential is thus given by Eq. (35), whereas the associative forces are described by Eq. (61) with  $d = \sigma = 1$ ,  $a = 1.05$ , and  $\theta_c = 27^\circ$ .

As an illustration, we discuss a particular model of associative interactions with only one binding site per particle. The adsorbing surface, for simplicity, is a hard wall located at  $z = 0$ .

Fig. 10(a) presents a comparison of computer simulation data with the predictions of both density functional theories presented above [144]. The computations have been carried out for  $\varepsilon^{\text{as}}/k_B T = 7$  and for a bulk fluid density equal to  $\rho_b = 0.2098$ . One can see that the contact profiles,  $\rho(z = 0)$ , obtained by different methods are quite similar and approximately equal to 0.5. We realize that the surface effects extend over a wide region, despite the very simple and purely repulsive character of the particle–wall potential. However, the theory of Segura et al. [38,39] underestimates slightly the range of the surface zone. On the other hand, the modified Meister–Kroll–Groot theory [145] leads to a more correct picture.

In Fig. 10(b) one can see the density profiles calculated for the system with  $\varepsilon^{\text{as}}/k_B T = 5$  and at a high bulk density,  $\rho_b = 0.9038$ . The relevant computer simulation data can be found in Fig. 5(c) of Ref. 38. It is evident that the theory of Segura et al. slightly underestimates the multilayer structure of the film. The results of the modified Meister–Kroll–Groot theory [145] are more consistent with the Monte Carlo data (not shown in our



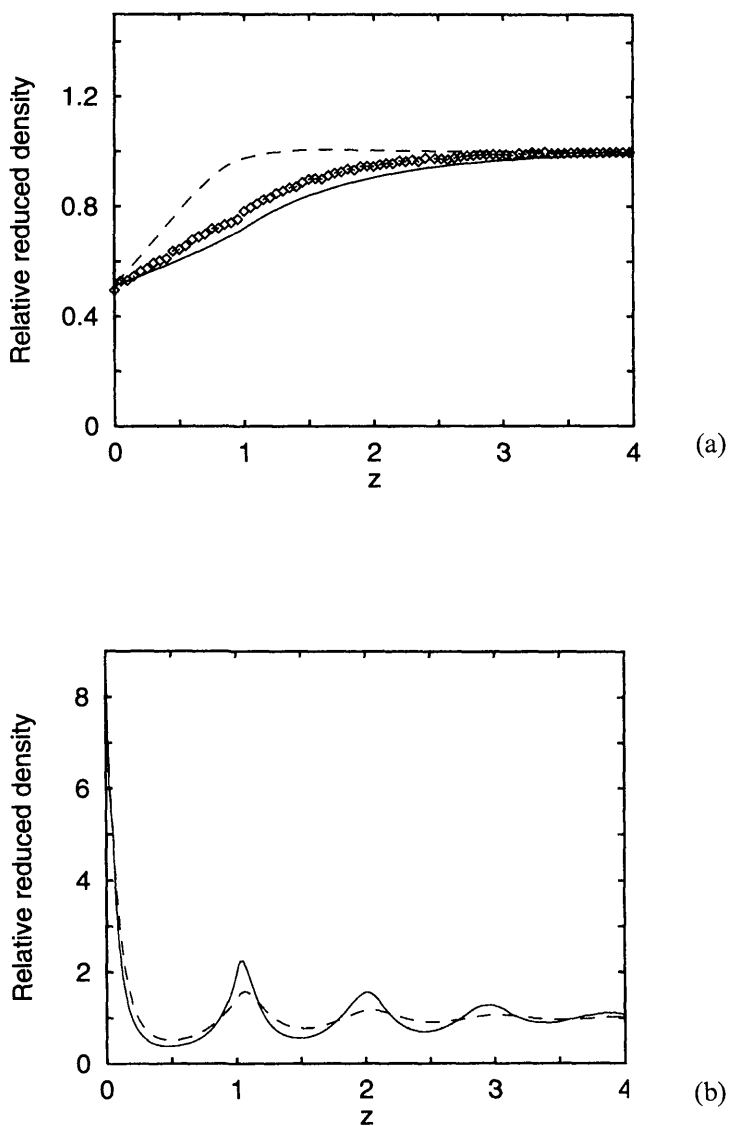


**FIG. 10** Normalized density profiles  $\rho(z)/\rho_b$  for the associating fluid at a hard wall. The association energy is  $\varepsilon^{\text{as}}/k_B T = 7$  and the bulk density is  $\rho = 0.2098$  (a),  $\varepsilon^{\text{as}}/k_B T = 5$  and the bulk density equals 0.9038 (b). The solid and dashed lines denote the results of the modified Meister-Kroll theory and the theory of Segura et al., respectively. The Monte Carlo data in (a) are marked as points. (From Ref. 145.)

Fig. 10(b)). One of the reasons for the differences between both theories is a different form of a hard sphere part of the free energy functional. Segura et al. have used the expression resulting from the Carnahan–Starling equation of state, whereas the Meister–Kroll–Groot approach requires the application of the PY compressibility equation of state, which produces higher oscillations.

Both versions of the functional theory allow an estimation of the fraction of unbonded particles in the system [14] (see Sec. III C). Fig. 11 shows some examples of the dependence of the monomer fraction upon the distance from the surface. For one of the systems the results of a Monte Carlo simulation are also presented. It can be seen that the differences between the two versions of the density functional theory become more pronounced when the association energy increases. Also, a long-range behavior of the fraction of unbonded species profile is slightly better reproduced by the Meister–Kroll–Groot theory [145]. All the presented profiles exhibit a sort of kink at the distance from the surface corresponding to the bonding distance. The origin of this effect has been discussed already by Segura et al. [38].

The calculations performed in Refs. 38,39,145 for hard associating spheres near a hard wall have indicated that the theory described above works reasonably well. Discrepancies between the theory and simulations have

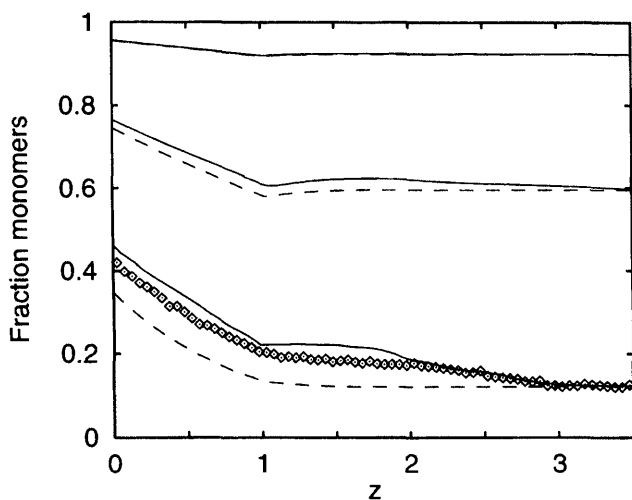


**FIG. 11** Dependence of the fraction of monomers on the distance from the hard wall for the associating fluid. The curves, from top to bottom, are for  $\epsilon^{as*} = \epsilon^{as}/k_B T$  equal to: 3 ( $\rho_b = 0.2$ ), 5 ( $\rho_b = 0.2$ ) and 7 ( $\rho_b = 2098$ ). The meaning of the symbols is the same as in Fig. 10. (From Ref. 145.)

occurred at high association energies and low bulk fluid densities  $\rho_b$ , where a crossover from desorption to adsorption takes place.

## D. Association Effects on Wettability of Solid Surfaces

In the case of bulk systems it has been established that the increase of the association energy results in a gradual increase of the critical temperature and slight widening of the coexistence region. Plots of such phase diagrams for several systems can be found in Refs. 13–17, 114. On the other hand, the effects of association on adsorption have received less attention. In particular, to our best knowledge, the prewetting transition [49] in such systems has been studied only in Refs. 40, 41. Namely, in Ref. 41, results from the density functional theory concerning the influence of association on wettability of solid surfaces have been reported. We discuss here some of the results obtained in Ref. 40.

The calculations have been carried out for a one-component, Lennard–Jones associating fluid with one associating site. The nonassociative van der Waals potential is thus given by Eq. (87) with  $r_{\text{cut}} = 2.5\sigma$ , whereas the associative forces are described by means of Eq. (60), with  $d = 0.5\sigma$  and  $a = 0.1\sigma$ . The fluid is in contact with an attracting wall. The fluid–wall potential is given by the Lennard–Jones (9–3) function

$$v(z) = \varepsilon_s \frac{3\sqrt{3}}{2} \left[ \left( \frac{z_0}{z} \right)^9 - \left( \frac{z_0}{z} \right)^3 \right] \quad (144)$$

Since the prewetting transition may occur only for weakly attractive surfaces [146], we must choose an appropriate value for the parameter  $\varepsilon_s$ . This value has been set as follows:  $\varepsilon_s^* = 3\sqrt{3}/2\varepsilon_s/\varepsilon^{\text{LJ}} = 6$ . This corresponds to a relative strength of the fluid–fluid and fluid–surface potential minima close to that for Ar in contact with solid carbon dioxide [147]. The second parameter in Eq. (144),  $z_0$ , was set to  $0.8\sigma$ .

To elucidate the role of association effects, three values of the ratio  $\varepsilon^{\text{as}*} = \varepsilon^{\text{as}}/\varepsilon^{\text{LJ}}$  have been considered, namely  $\varepsilon^{\text{as}*} = 0, 7$ , and  $10$ . The calculations have been performed at several reduced temperatures,  $T^* = k_B T/\varepsilon^{\text{LJ}}$ .

In order to demonstrate that the systems in question exhibit nonzero wetting temperature, we have displayed the results of calculations for one of the systems (with  $\varepsilon^{\text{as}*} = 7$  at  $T^* = 0.7$ ). Fig. 12 testifies that only a thin (monolayer) film develops even at densities extremely close to the bulk coexistence density ( $\rho_b(T^* = 0.7) = 0.001\,664$ ). In Fig. 13(a) we show the density profiles obtained at temperature  $0.9$  evaluated for  $\varepsilon^{\text{as}*} = 7$ . Part (b) of this figure presents the fraction of nonassociated particles,  $\chi(z)$ . We

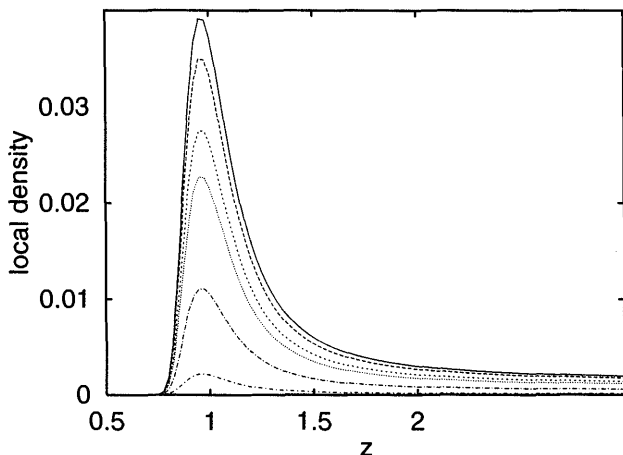


**FIG. 12** Density profiles at  $T^* = 0.7$  and association energy  $\varepsilon^{as*} = 7$ . The curves, from top to bottom, correspond to  $\rho_b = 0.001662, 0.0015, 0.0012, 0.001, 0.0005$  and  $0.0001$ . (Reprinted with permission from J Phys Chem B 103:4466 © 1999, American Chemical Society.)

observe the coexistence of two films: a thin film and a thick one in some interval of the bulk density. The transition point is evaluated from the condition of a minimum for the grand potential  $\Omega$ ; the stable film corresponds to the minimum of  $\Omega$ .

We observe that association leads to pronounced differences in the behavior of the system. In particular, we find that for the thick film the increase of the association energy leads to the increase of the height of the first local density peak. In contrast, the height of the local density maximum decreases at the region of small adsorption (below the prewetting transition). One can say that for increasing association energy the film structure becomes more ordered and its layered structure is more visible.

There are two characteristic temperatures: the wetting temperature,  $T_w^*$  and the surface critical temperature  $T_{sc}^*$ . Below the wetting temperature, the adsorption remains finite up to a density equal to the bulk coexistence density. In the case of the existence of the first-order prewetting, there is a jump discontinuity in the adsorption isotherms at temperatures between  $T_w^*$  and  $T_{sc}^*$ . The first-order prewetting transition terminates at the surface critical temperature; above this temperature the thick film development is continuous. The surface phase diagrams have been evaluated for different values of the association energy [40]. These calculations indicate that the main effect of association is the shift of the wetting temperature towards higher values.

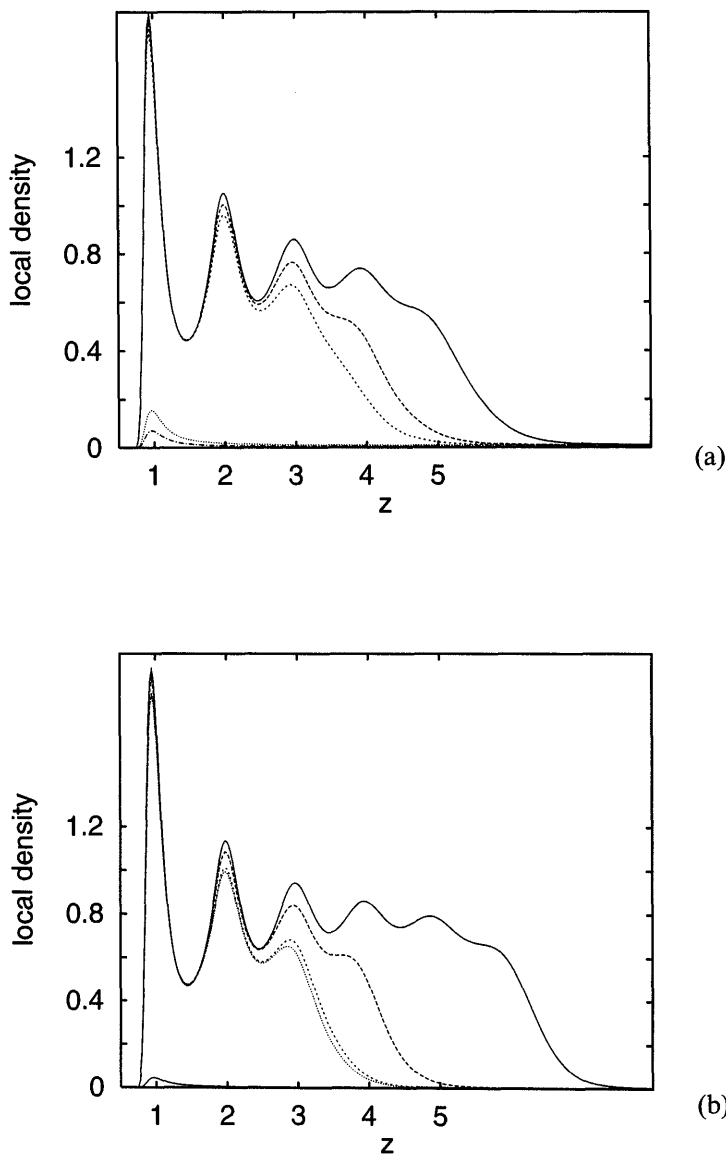


**FIG. 13** Density profile for the thermodynamically stable states at  $T^* = 0.9$  and association energy  $\epsilon^{as*} = 7$  (a) and  $\epsilon^{as*} = 10$  (b). The curves from top to bottom in (a) correspond to  $\rho_b = 0.01, 0.0097, 0.0096, 0.0095$ , and  $0.005$ . The curves from top to bottom in part (b) correspond to  $\rho_b = 0.00325, 0.0031, 0.00302, 0.00301$ , and  $0.003$ . (Reprinted with permission from J Phys Chem B 103:4466 © 1999, American Chemical Society.)

The reduced wetting and the surface critical temperatures evaluated from the density functional calculations are  $T_w^* = 0.66$ ,  $T_{sc}^* = 1.09$  for  $\varepsilon^{as*} = 0$  (i.e., for nonassociating fluid);  $T_w^* = 0.71$ ,  $T_{sc}^* = 1.12$  for  $\varepsilon^{as*} = 7$  and  $T_w^* = 0.85$  and  $T_{sc}^* = 1.19$  for  $\varepsilon^{as*} = 10$ . In general, changes in the wetting temperature are considerably larger than changes in the surface critical temperature. This effect is due to stronger effects of association in the surface layer than in the bulk fluid. The interaction between a pair of dimers is stronger than between a pair of monomers. The wetting behavior at the fluid–solid interface is determined by the relative strength of the fluid–fluid and fluid–solid interactions. When the fluid–fluid interaction energy increases with respect to the fluid–solid energy, the wetting temperature also increases. To a first approximation, we can say that the interaction of completely dimerized fluid with the wall is maximally two times greater than the interaction between a monomer with the wall. On the other hand, the interaction between a pair of dimers is more than two times greater than the interaction between two monomer particles. Therefore, the effective ratio of the fluid–fluid and fluid–wall interactions increases as the association strength grows. This explains why dimerization more strongly influences the wetting temperature rather than the surface critical temperature.

## E. Association Effects on Capillary Condensation

The density functional approach has also been used to study capillary condensation in slit-like pores [148,149]. As in the previous section, a simple model of the Lennard–Jones associating fluid with a single associative site is considered. All the parameters of the interparticle potentials are chosen the same as in the previous section. Our attention has been focused on the influence of association on capillary condensation and the evaluation of the phase diagram [42].

The fluid is confined to a slit-like pore of width  $H$ . Each of the pore walls is the source of the Lennard–Jones (9–3) potential and the total adsorbing potential, thus

$$v_{\text{por}}(z) = v(z) + v(H - z) \quad (145)$$

where  $v(z)$  is given by Eq. (144). The parameters of this potential are different from those used in Sec. IV D; namely, we set  $z_0 = 0.6$  and  $\varepsilon_s^* = 10$ .

We now proceed with the study of the phase behavior of associating fluids in pores. To elucidate the effects of changes of the association energy, again we have considered  $\varepsilon^{as*} = 0, 7$ , and 10. The pore width was fixed and set to  $H = 6\sigma$ . Figs. 14(a) and 14(b) show some examples of the

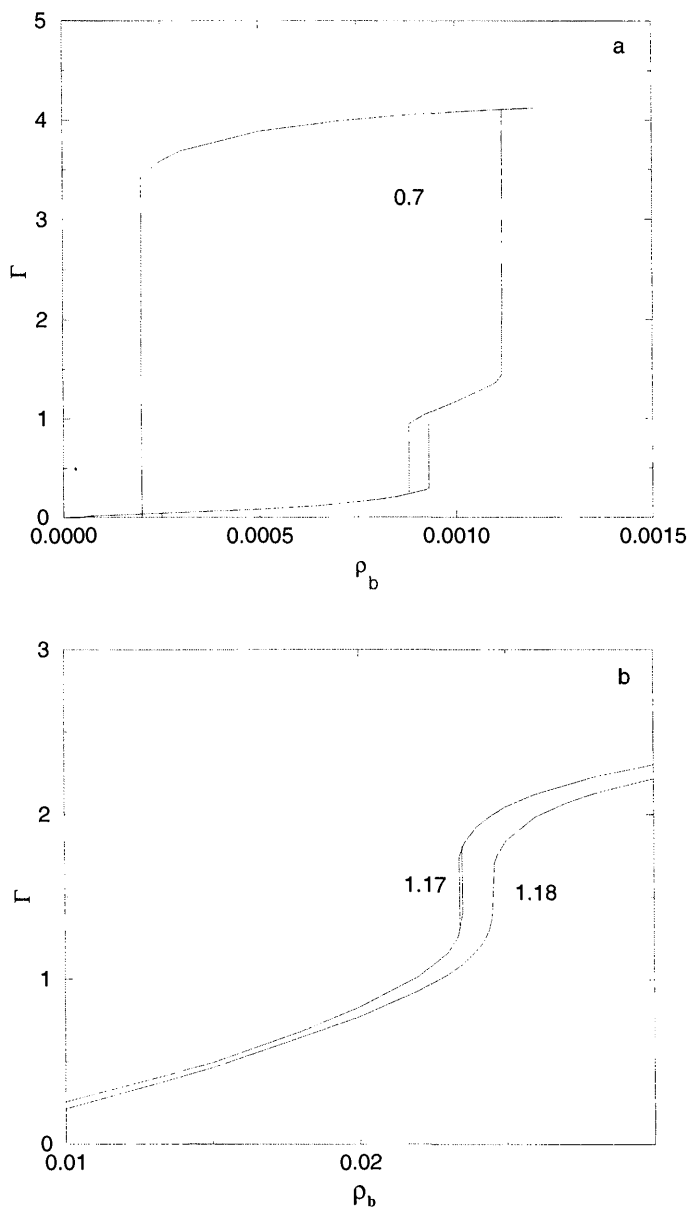


**FIG. 14** Adsorption isotherms, (a) and (b), and density profiles, (c) and (d), for nonassociating fluid in pore with  $H = 6$ . The isotherm in (a) is at  $T^* = 0.7$ ; in (b),  $T^* = 1.17$  and  $1.18$ . Density profiles in (c) are at  $T^* = 0.7$  and for (from bottom to top)  $\rho_h = 0.0009$ ,  $0.00091$ , and  $0.001$ . (From Ref. 42.)

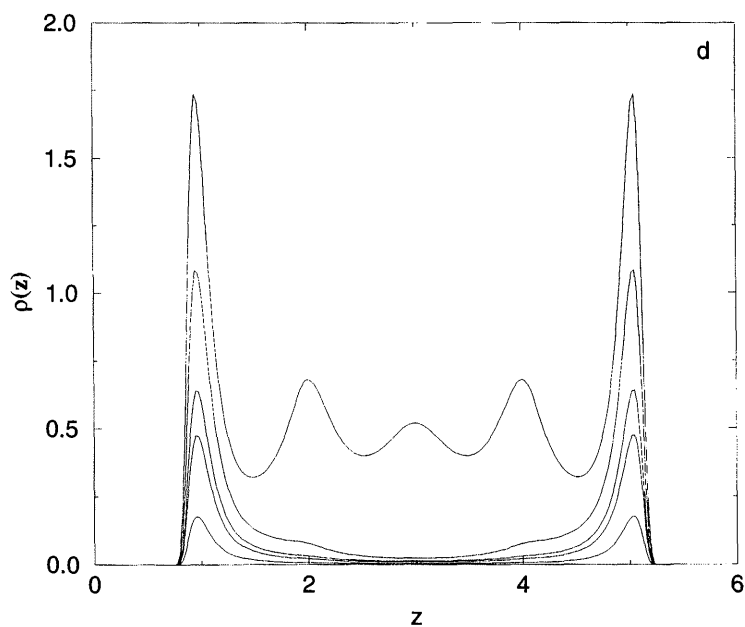
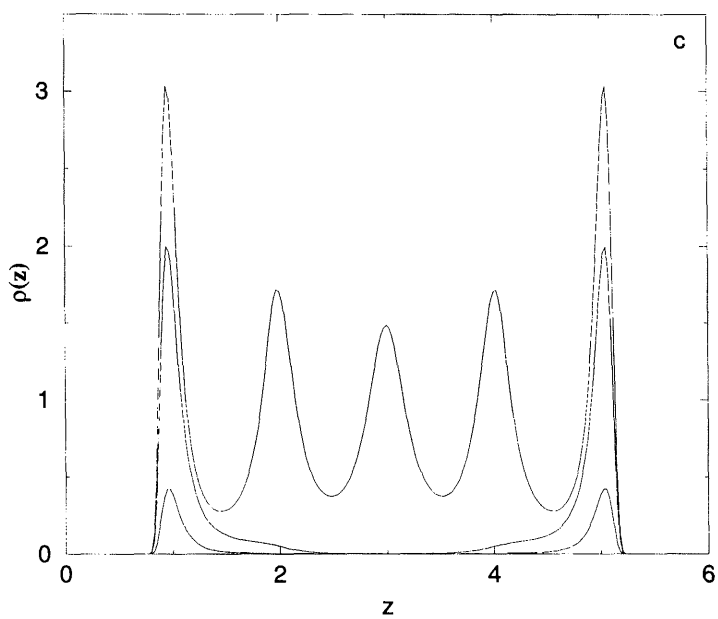


FIG. 14 Continued.



adsorption isotherms  $\Gamma$

$$\Gamma = \int dz [\rho(z) - \rho_b] \quad (146)$$

at  $T^* = 0.7$  (part (a)) and at  $T^* = 1.17$  and  $1.18$  (part (b)), calculated for nonassociating fluid,  $\epsilon^{as*} = 0$ . The latter temperature is higher than the capillary condensation critical temperature for this system, which equals  $1.176$ . At  $T^* = 1.17$  only a very narrow hysteresis loop is observed, indicating that this temperature is very close to the critical temperature. The transition between a “liquid-like” and a “gas-like” adsorbate is at  $\rho_b = 0.0234$ . However, at  $T^* = 0.7$  the hysteresis is more pronounced. Moreover, the adsorption branch exhibits an additional loop, reflecting the layering transition within the first layer adjacent to the pore walls. In fact, inspecting the behavior of the density profiles, Fig. 14(c), we realize that this loop is associated with a rapid filling of the first layer. The lowest local density profile is at the bulk density just before completion of the first layer; the subsequent profile corresponds to the filled first layer. The profile at the highest bulk density is for a liquid-like adsorbate inside the entire pore. The bulk fluid density at which the layering transition occurs is  $\rho_b = 0.000905$  and is higher than the bulk density corresponding to the equilibrium condensation point,  $\rho_b = 0.00059$ .

Our calculations have revealed that for nonassociating fluid the transition within the first layer occurs for  $T^* < 0.74$ . This temperature is close to the critical temperature of the layering transition for the first layer. We must stress, however, that we have not performed any calculations for  $T^* < 0.67$ ; therefore, we are not able to estimate the lower temperature limit for this transition. The strength of the adsorbing potential used in our model calculations is about 2.4 times weaker than the strength of the adsorbing field of the graphite surface. The layering transition occurs if the adsorbate wets the pore wall, and terminates at its own critical point. Thus, it occurs within a finite interval of temperatures.

In Fig. 15 we show similar results, but for  $\epsilon^{as*} = 10$ . Part (a) displays some examples of the adsorption isotherms at three temperatures. The highest temperature,  $T^* = 1.27$ , is the critical temperature for this system. At any  $T^* > 0.7$  the layering transition is not observed, always the condensation in the pore is via an instantaneous filling of the entire pore. Part (b) shows the density profiles at  $T^* = 1$ . The transition from gas to liquid occurs at  $\rho_b = 0.00415$ . Before the capillary condensation point, only a thin film adjacent to a pore wall is formed. The capillary condensation is now competing with wetting.

Fig. 15(c) shows changes of the ratio of unbounded particles in the system. The state conditions of the fluid are the same as in Fig. 15(b).

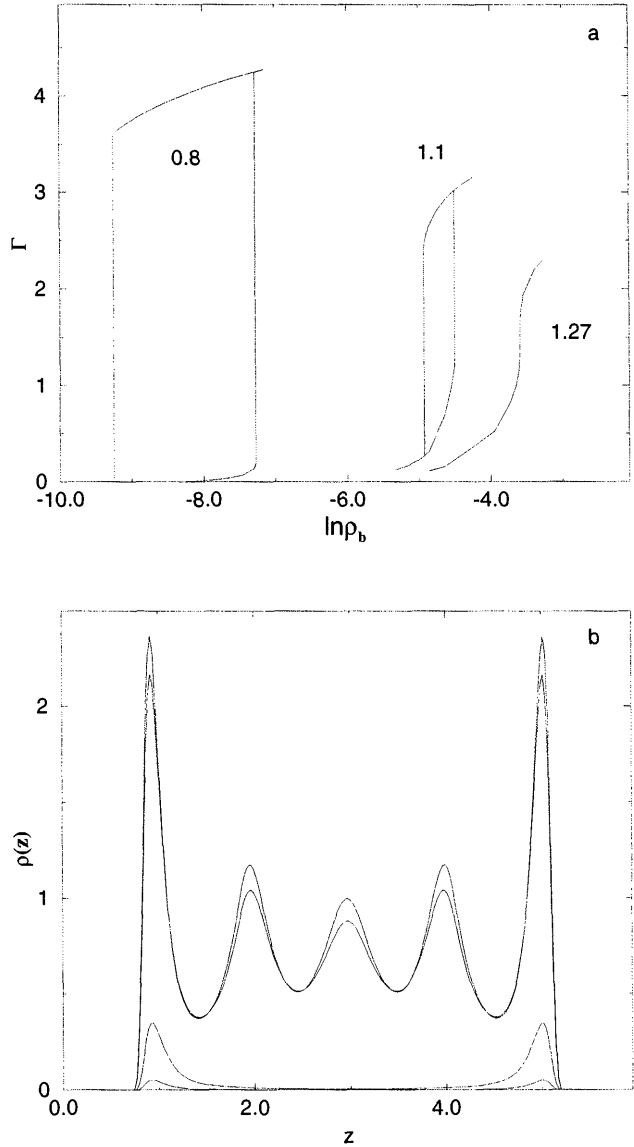


**FIG. 15** Adsorption isotherms (a), density profiles (b), and the ratio of unbounded particles,  $\chi(z)$  (c) for the associating fluid with  $\epsilon^{as*} = 10$ . The isotherms in (a) are for  $T^* = 0.8, 1.1$ , and  $1.27$ ; the last temperature is the critical temperature for this system. Density profiles (b) and ratios  $\chi(z)$  (c) are at  $T^* = 1$  and for (from bottom to top in (b) and from top to bottom in (c))  $\rho_b = 0.001, 0.00401$  (two coexisting functions), and  $0.006$ . (From Ref. 42.)

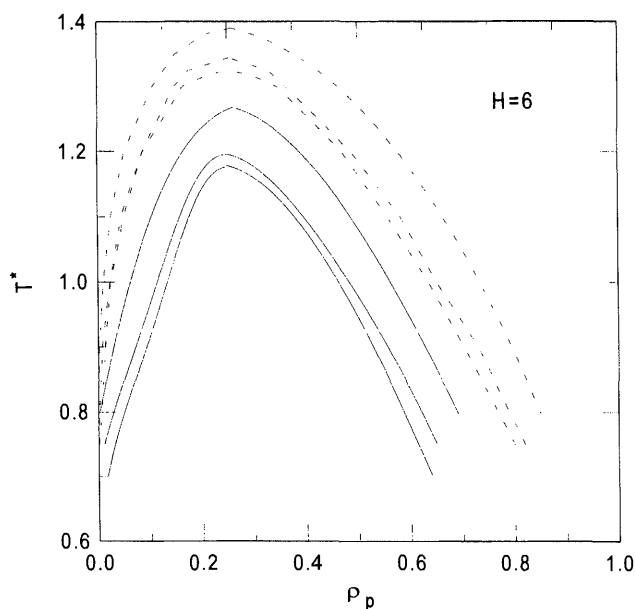
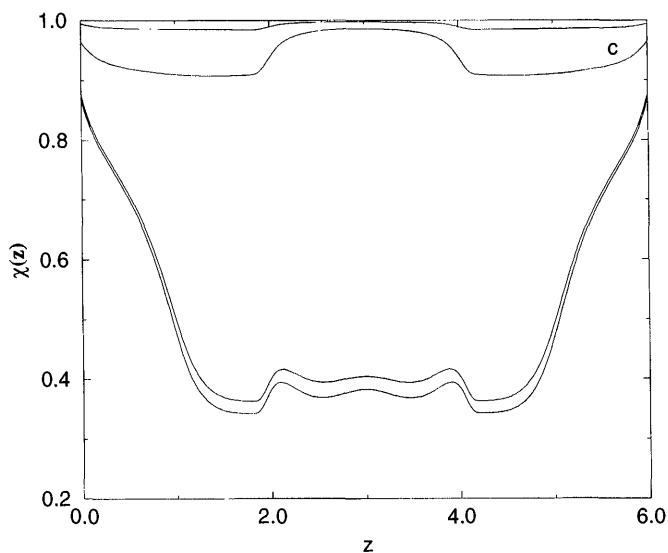


**FIG. 16** Phase diagrams for nonassociating and associating systems. The dashed lines denote the bulk coexistence while the solid lines denote the location of the capillary condensation. The solid and dashed lines are, from the bottom, for  $\varepsilon^{AS*} = 0, 7$ , and 10. (From Ref. 42.)

For a gas-like adsorbed phase  $\chi(z)$  is close to 1 in the entire pore, whereas for a liquid-like phase  $\chi(z)$  exhibits a layered structure. The oscillations in  $\chi(z)$  follow changes in the local density, though they are much less pronounced. Inside the pore,  $\chi(z)$  is close to 0.4. Obviously, when the bulk density increases, the ratio  $\chi(z)$  inside the pore decreases.

Fig. 16 presents a comparison of the phase diagrams for confined (solid lines) and bulk fluids (dashed lines). The average density in the pore  $\rho_p$  is defined as

$$\rho_p = \int_0^H \rho(z) dz / H \quad (147)$$

For a confined system the critical temperature is lower than for the bulk system. However, the value of  $\rho_b$  at the critical point is nearly the same in all cases, such that confinement causes only a slight increase of the value of the critical density. The density functional theory has also been applied to study the adsorption of associating hard spheres on crystalline surfaces [43]. However, this research is in its initial stage at present.

## V. COMPUTER SIMULATION OF INHOMOGENEOUS ASSOCIATING FLUIDS

The subject of previous sections has been to review and discuss some theoretical approaches and computer algorithms used to describe nonuniform associating fluids. However, many studies have been carried out by using computer simulation techniques. Computer simulation provides a powerful tool enabling a detailed study of the inner structure and thermodynamic properties of chemically associating fluids. In particular, it may be used to determine several structural properties such as, for example, the angular distributions of complexes formed due to association, that are not accessible from classical integral equation theories.

In this section of our work we present examples of the application of computer simulation methods to study chemically associating fluids. In the first case we consider the adsorption and surface phase transitions by means of a constant pressure Monte Carlo simulation. The second example is focused on the problem of chemical potential evaluation.

The application of lattice models in computer modeling of chemical reactions at solid surfaces is beyond the scope of the present chapter; the reader is referred to Chapter 8 by E. Albano for a detailed discussion of this area of research.

One can treat the association or, more generally, the reaction step in the same fashion as the usual canonical ensemble Monte Carlo displacement step by defining appropriate chemical or associative components of the pair potential. Methods suitable for treating central and orientational associative components of the pair potential, including smart biased sampling, have been developed in Ref. 19. However, the extension of the smart biased sampling method [19] to nonuniform associating fluids is not straightforward and leads to a complicated and time-consuming numerical algorithm. To find a compromise between simplicity of the algorithm, its convergence and speed of program, we have proposed some modifications of the classical displacement scheme. These modifications result in addition of the moves (translational and rotational) of the entire associates formed in the system [150,151]. We have found these modifications efficient not only in simulating nonuniform fluids with directional bonds, but also in other applications such as, for example, simulation of monolayers of associating fluids [152].

Another method of simulating chemical reactions is to separate the reaction and particle displacement steps. This kind of algorithm has been considered in Refs. 90, 153–156. In particular, Smith and Triska [153] have initiated a new route to simulate chemical equilibria in bulk systems. Their method, being in fact a generalization of the Gibbs ensemble Monte Carlo technique [157], has also been used to study chemical reactions at solid surfaces [90]. However, due to space limitations of the chapter, we have decided not to present these results.

### **A. A Monte Carlo Study of Wetting of Associating Fluids**

In the case of simple fluids, the wetting behavior of fluid–solid interfaces has been discussed in detail [49,158]. The most interesting issue is the determination of state conditions at which the adsorbed film undergoes a surface wetting transition. In the case of the first-order wetting transition the pre-wetting line lies very close to the bulk gas–liquid coexistence line, which makes simulational studies difficult. The most convenient simulational technique applied to study the wetting behavior is the method of isobaric-isothermal ensemble, introduced by Finn and Monson [159,160]. The wetting of nonassociating fluids has been also studied using molecular dynamics simulations [161].

We report here some results for a simple model of a one-component fluid interacting via a slightly modified Lennard–Jones potential, with angular-dependent associative forces. The model is considered in contact with the adsorbing surface. The principal aim of the simulation is to investigate the

influence of chemical dimerization on the wettability of a structureless wall. The nonassociative interparticle potential  $\tilde{u}^{\text{non}}(r)$  is given by

$$\tilde{u}^{\text{non}}(r) = \begin{cases} 4\varepsilon^{\text{LJ}} \left[ \left( \frac{\sigma}{r} \right)^{12} - \left( \frac{\sigma}{r} \right)^6 \right], & \sigma < r < r_{\text{cut}} \\ \infty & 0 < r < \sigma \\ 0 & r > r_{\text{cut}} \end{cases} \quad (147)$$

with the cut-off distance  $r_{\text{cut}} = 3.39\sigma$ . The associative interactions are described by means of Eq. (60), with  $d = 0.45\sigma$  and  $a = 0.1\sigma$ .

The fluid is adsorbed by a structureless surface, interacting via the Lennard–Jones (9-3) potential, Eq. (144). To make contact with the simulations of Finn and Monson [159], we set  $\varepsilon_s/\varepsilon^{\text{LJ}} = 9.24$  and  $z_0/\sigma = 0.562$ . Note that, for  $\varepsilon^{\text{as}} = 0$ , the potential given above does not reduce to the Lennard–Jones (12–6) function, because the soft Lennard–Jones repulsive branch is replaced by a hard-sphere potential, located at  $r = \sigma$ . The results for the nonassociating Lennard–Jones fluid can be found in Ref. 159.

All the simulation runs have been carried out at reduced temperature  $T^* = k_B T / \varepsilon^{\text{LJ}} = 1.002$ . Two values of the association energy have been studied,  $\varepsilon^{\text{as}*}/T^* = 3$  and 10. These systems have been abbreviated to A3 and A10, respectively. The Monte Carlo method in the isobaric-isothermal ensemble has been based on the algorithm given by Finn and Monson [159] with, however, the particle movement scheme described in Ref. 150. All the details of the numerical calculations have been given in Ref. 41. During the simulation runs, the density profiles of all particles,  $\rho(z)$ , of the center of mass of dimers,  $\rho_1(z)$ , and the orientational density of dimers,  $\rho_d(z, \theta)$ , where  $\theta$  is the tilting angle, measured with respect to the normal to the surface, have been evaluated. The adsorption isotherms of particles and dimers have been obtained by integrating the corresponding local densities.

The gas branch densities along coexistence, evaluated for the bulk systems A3 and A10, are:  $\rho_{\text{gas}} = 0.046 \pm 0.001$  and  $\rho_{\text{gas}} = 0.0237 \pm 0.005$ , respectively. The system A3 is weakly associated; however, in the system A10 the gas phase remains weakly associated. On the other hand, association in the liquid phase is significant and greater than 80% [41].

Fig. 17 shows the adsorption isotherms of all (undimerized and dimerized) particles. Except for a very fast increase of adsorption connected with filling of the first adlayer, the adsorption isotherm for the system A3 is quite smooth. The step at  $p/k_B T \approx 0.28$  corresponds to building up of the multilayer structure. The most significant change in the shape of the adsorption isotherm for the system A10, in comparison with the system A3, is the presence of a jump discontinuity at  $p/k_B T = 0.0099$ . Inspection of the density profiles attributes this jump to the prewetting transition in the

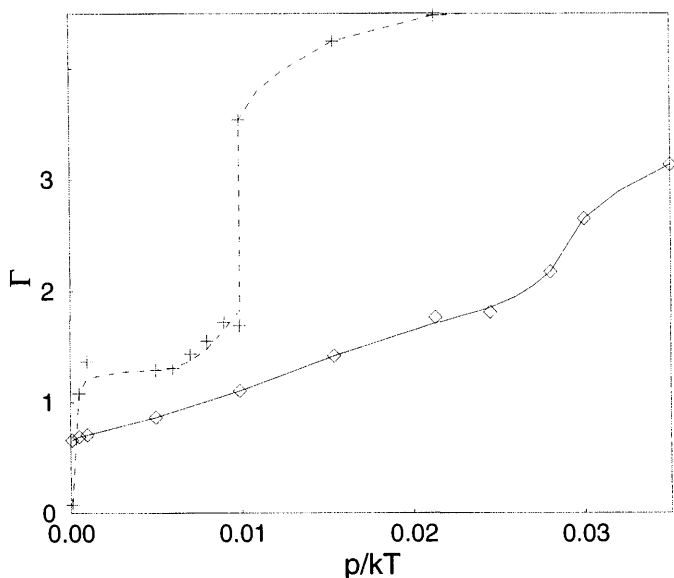


**FIG. 17** Adsorption isotherms for the system *A3* (solid line) and *A10* (dashed line). (From Ref. 41.)

system: there are *two* coexisting profiles at  $p\sigma^3/k_B T = 0.009\,91$  (cf. Fig. 18). Thus, an increase of the association energy qualitatively changes the behavior of the system. Also it is of interest that the adsorption isotherm for the system *A10* is significantly higher than the adsorption isotherm for the system *A3*. The associative interaction leads to the effect of “sucking” the particles towards the adsorbed layer.

The fine structure of the density profiles of centers of dimers is much richer than the distribution of all particles, cf. Fig. 18(b). The first and second (adjacent to the wall) peaks divide into two; the difference in the position of these two “subpeaks” is  $\approx 0.45\sigma$  for the first adlayer, i.e., it is almost equal to half of the bonding distance. In the second adlayer this difference is slightly higher. We can attribute the first “subpeak” to the in-plane dimers parallel to the adsorbing surface, whereas the second one is attributed to dimers oriented along the normal to the surface. The center-of-mass density profiles indicate that the orientational ordering vanishes at large separation from the adsorbing surface.

Fig. 19 shows an example of the orientational density profile evaluated for the system *A10*. Most of the particles of the first adlayer assume two limiting configurations: parallel to the surface and vertical to the surface. The second adlayer exhibits also well pronounced orientational ordering;

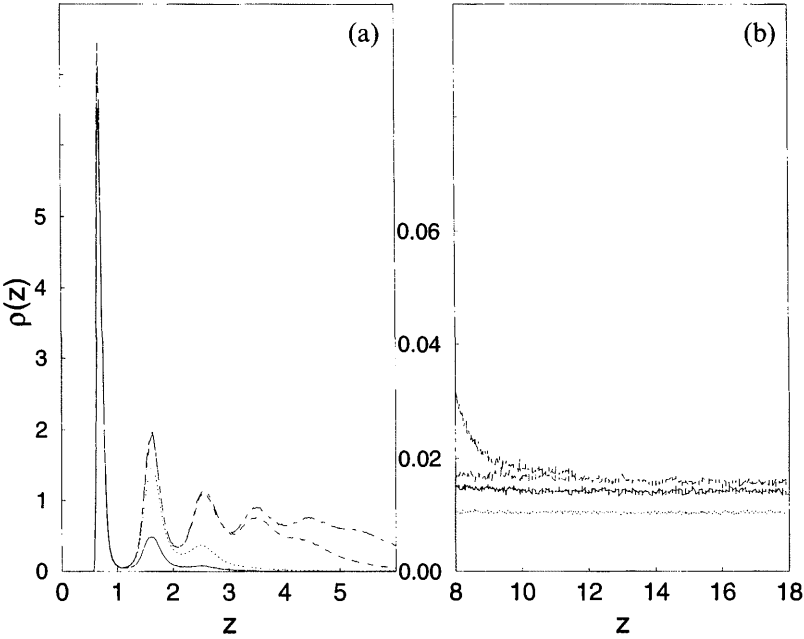


**FIG. 18** Density profiles  $\rho(z)$  (a) and center of mass density profiles of the dimers (b) for the system *A10*. The lines in the order from the bottom have been evaluated at  $p/k_B T = 0.0005, 0.00991, 0.00991$ , and  $0.0245$ . At  $p/k_B T = 0.0991$  we have two profiles, corresponding to two coexisting phases. (From Ref. 41.)

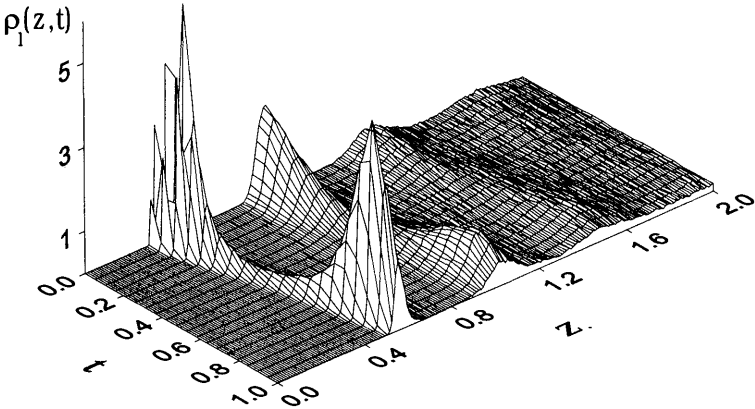


**FIG. 19** Orientational density profiles for the system *A10* at  $p/k_B T = 0.03$ . The orientation is characterized by  $t = \cos \theta$ , where  $\theta$  is the tilting angle, measured with respect to the normal to the surface. (From Ref. 41.)



residual orientational effects are also seen within the third layer. However, no orientational effects are present in the higher adlayers. The investigations have indicated that the prewetting jump of the adsorption does not change orientation of the first and second layer dimers.

The results provide new insight into the behavior of associating fluids near a solid surface. The most interesting finding is the observation of the prewetting transition due to associative forces. The prewetting transition does not lead to significant changes of the preferable orientations of adsorbed dimers. Of course, the molecules located in higher layers are considerably less ordered, but they remain preferentially oriented in the same manner in the first, in the second, as well as in the third layer.

## **B. Chemical Potential of Inhomogeneous Associating Fluids from Osmotic Monte Carlo Simulation**

Computer simulation of the chemical potential of model fluids is of considerable interest, due to its role in phase and chemical reaction equilibria [162]. Several methods of evaluating chemical potentials have been discussed in the literature (see, e.g., Refs. 163–169). The chemical potential can be evaluated by performing several simulational runs and then integrating the Gibbs–Helmholtz equation. Such a method, however, is rather inconvenient because it requires much CPU time. Therefore, any technique that uses only a single simulational run would be preferable. Up to date, the most popular methods have been based on the insertion of some “test” particles into the fluid [163], to probe the interaction energy between them and the surrounding fluid molecules. In the case of classical fluids, the main limitation of this approach is its failure at high densities where the probability of particle insertion decreases rapidly. In the case of a mixture of associating particles with a “chemical component” of the pair potential located inside the core of the reacting species, one cannot expect the usual test particle method to be successful. Therefore, a development of an appropriate simulational technique for chemical potential determination is highly desirable.

Recently, Rowley et al. [170,171] have introduced a new method for the determination of the chemical potential from molecular dynamics simulation. This method uses a semipermeable membrane and the simulation relies on the establishment of osmotic equilibrium across the membrane. Recently, a similar technique has been used to calculate the chemical potentials of associating fluids from the canonical ensemble Monte Carlo simulation [172,173]. Briefly, chemical association has been allowed in some selected parts of the system. Because of the “sucking” of the particles into these parts of the simulation box, the density in other parts of the box falls. As long as

chemical equilibrium is attained, the chemical potential should be kept constant through the system, and therefore one can measure it in less dense parts of the system. This method has been tested for the systems of overlapping hard spheres [172] and Lennard–Jones particles [173].

The model of associating hard spheres has been described in Sec. II B. The system has consisted of two equally sized species  $\alpha$  and  $\beta$  interacting according to the potentials (35) and (36) with  $L = 0.45\sigma$  and  $w = 0.1\sigma$ . The concentrations of both components are equal. The fluid is closed in a simulational non-cubic box with standard periodic boundary conditions. The box is elongated in the  $z$  direction and is divided into four regions, called I, II, III, and IV (see Ref. 172). Each of the regions is separated by semi-permeable membranes. The membranes delimiting region II are permeable to the particles of species  $\beta$ , whereas the membranes delimiting region IV are permeable to the particles  $\alpha$ . The dimers can be formed only in parts I and III; no dimer can cross any membrane. Thus, part II of the box contains only particles of species  $\beta$  and part IV only particles of species  $\alpha$ .

The chemical potential of particles belonging to species  $\alpha$  and  $\beta$  is measured by using the classical test particle method (as proposed by Fischer and Heinbuch [166]) in parts II and IV of the system; i.e., we calculate the average value of  $\langle e \rangle = \langle \exp[-U/kT] \rangle$ , where  $U$  denotes the potential energy of the inserted particles.

Each of the membranes acts like a hard wall for dimer molecules. Consequently, in parts I and III we observe accumulation of dimer particles at the membrane. The presence of this layer can prohibit translation of particles through the membrane. Moreover, in parts II and IV of the box, at the membranes, we observe a depletion of the local density. This phenomenon can artificially enhance diffusion in the system. In order to avoid the problem, a double translation step has been applied. In one step the maximum displacement allows a particle to “jump” through the surface layer; in the second step the maximum translation is small, to keep the total acceptance ratio as desired.

The results for the chemical potential determination are collected in Table 1 [172]. The nonreactive parts of the system contain a single-component hard-sphere fluid and the excess chemical potential is evaluated by using the test particle method. Evidently, the quantity  $\Delta\mu_\alpha^{\text{MC}}$  should agree well with the value from the Carnahan–Starling equation of state [113]

$$\mu_{\text{ex}}^{\text{CS}}/kT = \eta \frac{8 - 9\eta + 3\eta^2}{(1 - \eta)^3} \quad (148)$$

for the average hard-sphere density  $\rho_\alpha$ , in the middle of part II of the box.

TABLE 1 Results of the MC Simulations<sup>a</sup>

$\varepsilon/kT$	$N$	$\langle\rho_{\text{dim}}\rangle$	$\langle\rho_a\rangle$	$\langle\rho_b\rangle$	$\langle e\rangle$	$\mu_{\text{ex}}^{\text{MC}}/kT$	$\mu_{\text{ex}}^{\text{CS}}/kT$
5	800	0.1537	0.1133	0.1133	0.5875	0.5319	0.5328
	1200	0.2464	0.1875	0.1879	0.3839	0.9574	0.9587
	1600	0.3305	0.2844	0.2846	0.1967	1.6261	1.6264
	2000	0.4180	0.3599	0.3590	0.1059	2.2448	2.2517
	2400	0.4782	0.5185	0.5217	0.0164	4.4110	4.4104
1	1600	0.1417	0.4087	0.4089	0.0648	2.7364	2.7399
0.01	800	0.0117	0.2109	0.2116	0.3327	1.1005	1.1092

<sup>a</sup> Abbreviations:  $N$  is the total number of particles;  $\rho_{\text{dim}}$  is the average density of dimers in each of the parts I and III;  $\rho_a$  is the average density of monomers in each of the parts II and IV;  $\rho$  is the average density at the middle of parts II and IV; this value has been used to calculate the excess chemical potential from Eq. (148). All remaining symbols are explained in the text.

Similar calculations have been carried out for an equimolar binary mixture of associating Lennard–Jones particles with spherically symmetric associative potential [173]. The interaction between similar species is given by Eq. (87), whereas the interaction between different species is chosen in the form

$$u_{\alpha\beta} = \begin{cases} -\varepsilon^{\text{as}} & (L - w/2) < r < (L + w/2) \\ u^{\text{LJ}}(r) & \text{otherwise} \end{cases} \tag{149}$$

where  $u^{\text{LJ}}(r)$  is given by Eq. (87). The values  $L = 0.45\sigma$  and  $w = 0.1\sigma$  have been used.

To test the results of the chemical potential evaluation, the grand canonical ensemble Monte Carlo simulation of the bulk associating fluid has also been performed. The algorithm of this simulation was identical to that described in Ref. 172. All the calculations have been performed for states far from the liquid–gas coexistence curve [173].

Fig. 20 shows the density profiles in the reactive and nonreactive parts of the system. The number density in the reactive part is very high (a one-component density at the center of this part is 0.596, so the number density of two components is twice as high). However, the density in the nonreactive part is much lower and equal to 0.404. The application of the test particle methods is therefore easy. There is a well-established density plateau in the nonreactive part; consequently, the determination of the bulk density in this part is straightforward and accurate.

In the case of a Lennard–Jones fluid, the knowledge of the bulk density in the nonreactive part is all that is needed to calculate the chemical potential. Actually, one can use the equation of state of Nicolas et al. [115] (or the

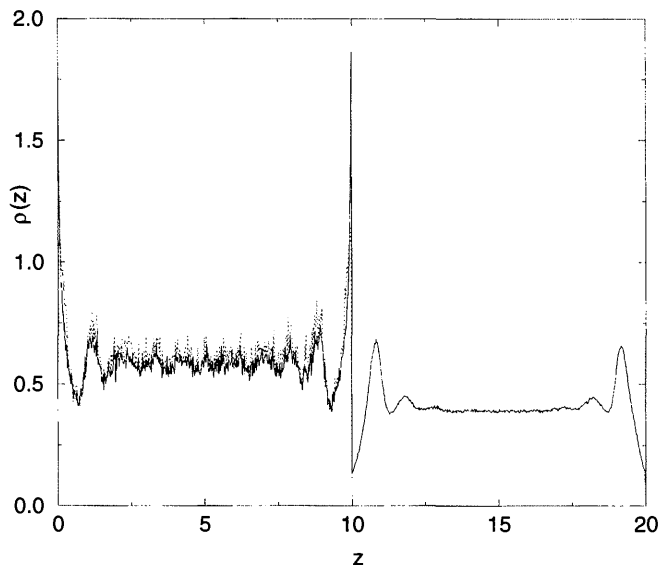


**FIG. 20** Density profiles of particles of one component  $\alpha$  or  $\beta$  (solid lines) and the density profile of the center of mass of the dimers (dashed line). The results are for  $T^* = 2$ ,  $\epsilon^{as*} = 5$ , and the total number of particles equal to 3200. The volume of each part of the simulational cell was  $1000\sigma^3$ . (From Ref. 172.)

modified Nicolas' equation of state [116]) to calculate the chemical potential. In the case of more complicated nonassociative potentials, the test particle method can be used.

Fig. 21 presents a comparison of the dependence of the fluid density  $\rho_\alpha$  on the chemical potential  $\mu_\alpha$  from the grand canonical ensemble simulation of the bulk system and with the results of the proposed osmotic Monte Carlo simulations. The agreement between the results from both ensembles is sufficiently good, although the osmotic method slightly overestimates the chemical potential in comparison with the grand canonical Monte Carlo data. The observed discrepancy between both sets of data is due to the confinement effect of the membranes; it should vanish in the thermodynamic limit. Indeed, when the simulations are performed in a longer box,  $ZL = 80$ , a better agreement between both sets of results is seen.

However, one should emphasize that the proposed model of the interactions does not exclude a possibility of the formation of higher-order associates. On average, the concentration of trimers and higher-order mers is about 8% in the case of systems presented in Fig. 20. Thus, the presence of associates larger than dimers does not prevent the applicability of the

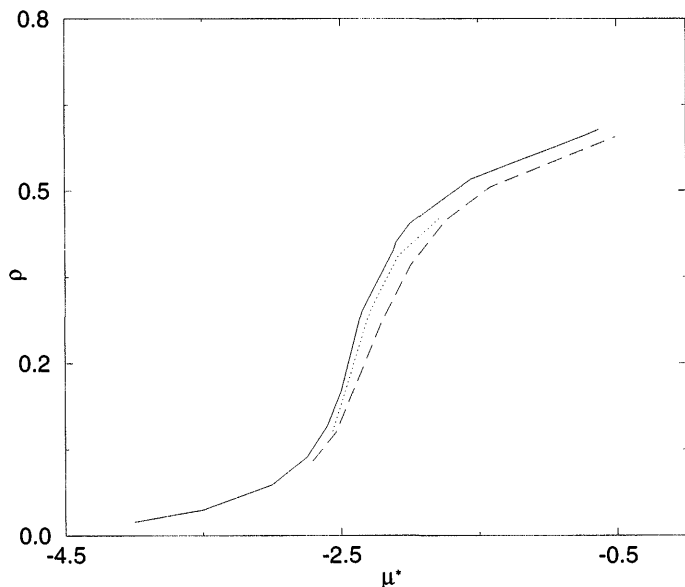


**FIG. 21** Dependence of the average density  $\rho_\alpha$  on the configurational chemical potential. The solid line denotes the grand canonical Monte Carlo data, the long dashed line corresponds to the osmotic Monte Carlo results for  $ZL = 40$ , and the dotted line for  $ZL = 80$ . (From Ref. 172.)

method. One of the interesting applications of the approach seems to be the determination of the chemical potential for polymerizing systems.

To conclude, the introduction of species-selective membranes into the simulation box results in the osmotic equilibrium between a part of the system containing the products of association and a part in which only a one-component Lennard-Jones fluid is present. The density of the fluid in the “nonreactive” part of the system is lower than in the “reactive” part, at osmotic equilibrium. This makes the calculations of the chemical potential efficient. The quality of the results is similar to those from the grand canonical Monte Carlo simulation. The method is neither restricted to dimerization nor to spherically symmetric associative interactions. Even in the presence of higher-order complexes in large amounts, the proposed approach remains successful.

## VI. CONCLUDING REMARKS

In this chapter we have reviewed several theories describing the behavior of nonuniform associating fluids. What new developments can be expected? In

the case of bulk systems, modern integral equation approaches are very accurate. It is thus likely that integral equation theories based on the inhomogeneous Ornstein–Zernike equation and some sophisticated closure approximations made of the pair level will prove more accurate for the calculation of the one- and two-particle distribution function of nonuniform associating fluid. On the other hand, these theories require a lot of computational effort and do not yield the free energy (or the grand potential) directly. This makes their application to the calculation of phase equilibria problematic. In contrast, methods based on the variational principle of the grand potential should continue to have the edge as regards the thermodynamic properties.

The density functional calculations should be complemented by computer simulations, especially in the context of investigation of various surface phase transitions. The determination of global phase diagram via simulation is a daunting task. However, the density functional results can point to what types of transitions may occur and where they are eventually located. Thus, there is no doubt that the development of density functional approaches will continue. First of all, the density functional approximations will find wider applications to describe the adsorption of associating fluids on crystalline and even on energetically and/or geometrically heterogeneous surfaces. Techniques proposed for simple associating fluids should next be extended to more complex fluids. We hope that the process of development of new theories of nonuniform associating fluids will lead to significant progress, guaranteeing that the subject remains ebullient.

## ACKNOWLEDGMENTS

M.B. and S.S. thank KBN for financial support under Grant No. 3T09A-062-10.

O.P. acknowledges support of the Ministry of Science and Technology (CONACyT) of Mexico (Grant No. 25301-E) and the National University of Mexico (project IN111597). O.P. is also grateful to Silicon Graphics Inc.—Cray Research of Mexico for partial financial support and generous allocation of computer time.

## REFERENCES

1. D. Nicholson, N. D. Parsonage. *Computer Simulation and the Statistical Thermodynamics of Adsorption*. New York: Academic Press, 1983.
2. D. Henderson, ed. *Fundamentals of Inhomogeneous Fluids*. New York: Marcel Dekker, 1992.

3. M. Schoen. *Computer Simulation of Condensed Phases in Complex Geometries: Lecture Notes in Physics*. Heidelberg: Springer-Verlag, 1993.
4. H. C. Andersen. *J Chem Phys* 59:4714, 1973.
5. D. Chandler, L. R. Pratt. *J Chem Phys* 65:2925, 1976.
6. D. Chandler, L. R. Pratt. *J Chem Phys* 66:147, 1977.
7. J. S. Høye, K. Olaussen. *Physica A* 104:435, 1980.
8. M. S. Wertheim. *J Stat Phys* 35:19; 35:35, 1984.
9. M. S. Wertheim. *J Stat Phys* 42:459; 42:477, 1986.
10. M. S. Wertheim. *J Chem Phys* 85:2929, 1986.
11. M. S. Wertheim. *J Chem Phys* 87:7323, 1987.
12. Yu. V. Kalyuzhnyi, G. Stell, M. L. Llano-Restrepo, W. G. Chapman, M. F. Holovko. *J Chem Phys* 101:7939, 1994.
13. C. G. Joslin, C. G. Gray, W. G. Chapman, K. E. Gubbins. *Mol Phys* 62:843, 1987.
14. G. Jackson, W. G. Chapman, K. E. Gubbins. *Mol Phys* 65:1, 1988.
15. W. G. Chapman, K. E. Gubbins, C. G. Joslin, C. G. Gray. *Fluid Phase Equilibria* 29:337, 1986.
16. W. G. Chapman, G. Jackson, K. E. Gubbins. *Mol Phys* 65:1057, 1988.
17. W. G. Chapman. *J Chem Phys* 93:4299, 1990.
18. C. Zhang, D. L. Freeman, J. D. Doll. *J Chem Phys* 91:2489, 1989.
19. N. A. Busch, M. S. Wertheim, Y. C. Chiew, M. L. Yarmush. *J Chem Phys* 101:3147, 1994.
20. E. Lomba, J. L. Lopez-Martin, M. Holovko. *J Chem Phys* 108:10175, 1998.
21. M. F. Holovko, E. V. Vakarín. *Mol Phys* 84:1057, 1995.
22. M. F. Holovko, E. V. Vakarín. *Mol Phys* 87:123, 1996.
23. M. F. Holovko, E. V. Vakarín. *Mol Phys* 87:1375, 1996.
24. D. Henderson, F. Abraham, J. A. Barker. *Mol Phys* 31:1291, 1976.
25. P. T. Cummings, G. Stell. *Mol Phys* 51:253, 1984.
26. P. T. Cummings, G. Stell. *Mol Phys* 55:33, 1985.
27. P. T. Cummings, G. Stell. *Mol Phys* 60:1315, 1987.
28. O. Pizio, D. Henderson, S. Sokołowski. *J Phys Chem* 99:2408, 1995.
29. O. Pizio, D. Henderson, S. Sokołowski. *J Coll Interface Sci.* 173:254, 1995.
30. O. Pizio, D. Henderson, S. Sokołowski. *Mol Phys* 85:407, 1995.
31. D. Henderson, S. Sokołowski, O. Pizio. *J Chem Phys* 102:9048, 1995.
32. D. Henderson, O. Pizio, S. Sokołowski. *Langmuir* 13:1162, 1997.
33. S. Sokołowski, D. Henderson, A. Trokhymchuk, O. Pizio. *Physica A* 220:24, 1995.
34. A. Trokhymchuk, O. Pizio, D. Henderson, S. Sokołowski. *Chem Phys Lett* 262:33, 1996.
35. D. Henderson, O. Pizio, S. Sokołowski, A. Trokhymchuk. *Physica A* 244:147, 1997.
36. A. Trokhymchuk, D. Henderson, S. Sokołowski. *Can J Phys* 74:65, 1996.
37. Yu. V. Kalyuzhnyi, G. Stell. *Chem Phys Lett* 240:157, 1995.
38. C. J. Segura, W. G. Chapman, K. P. Shukla. *Mol Phys* 90:759, 1997.

39. C. J. Segura, E. V. Vakarin, W. G. Chapman, M. F. Holovko. *J Chem Phys* 108:4837, 1998.
40. A. Patrykiewicz, S. Sokołowski. *J Phys Chem B* 103:4466, 1999.
41. M. Borówko, A. Patrykiewicz, S. Sokołowski, R. Zagórski. *J Chem Soc Faraday Trans* 94:771, 1998.
42. K. Stępiak, A. Patrykiewicz, Z. Sokołowska, S. Sokołowski. *J Colloid Interface Sci* 214:91, 1999.
43. M. Borówko, S. Sokołowski, R. Zagórski, O. Pizio. *Mol Phys* 96:855, 1999.
44. A. Huerta, S. Sokołowski, O. Pizio. *J Chem Phys* (in press).
45. A. Trokhymchuk, D. Henderson, S. Sokołowski. *Phys Lett A* 209:317, 1995.
46. S. Sokołowski. *Mol Phys* 41:859, 1980.
47. S. Sokołowski. *Mol Phys* 44:557, 1981.
48. J. K. Percus. In: H. L. Frisch and J. L. Lebowitz, eds. *The Equilibrium Theory of Classical Fluids*. New York: Benjamin, 1964.
49. R. Evans. In: D. Henderson, ed. *Fundamentals of Inhomogeneous Fluids*. New York: Marcel Dekker, 1992.
50. D. Henderson. Integral equation theories for inhomogeneous fluids. In: D. Henderson, ed. *Fundamentals of Inhomogeneous Fluids*. New York: Marcel Dekker, 1992.
51. R. J. Baxter. *J Chem Phys* 49:2770, 1968.
52. M. S. Wertheim. *J Chem Phys* 65:2377, 1976.
53. R. Lovett, C. Y. Mou, F. P. Buff. *J Chem Phys* 65:570, 1976.
54. D. E. Sullivan, G. Stell. *J Chem Phys* 67:2567, 1977.
55. S. Sokołowski. *J Chem Phys* 73:3507, 1980.
56. S. Sokołowski. *Mol Phys* 49:1481, 1983.
57. D. Henderson, M. Plischke. *Proc R Soc London A* 400:163, 1985; 404:323, 1986; 410:409, 1987.
58. M. Plischke, D. Henderson. *J Chem Phys* 84:2846, 1986.
59. D. Henderson, K. Y. Chan, L. Degreve. *J Chem Phys* 101:6875, 1994.
60. D. Henderson, S. Sokołowski, D. Wasan. *J Phys Chem* 102:3009, 1998.
61. Y. Rosenfeld, N. W. Ashcroft. *Phys Rev A* 20:1208, 1979.
62. Y. Zhou, G. Stell. *J Chem Phys* 102:8089, 1995.
63. G. Stell, Y. Zhou. *J Chem Phys* 91, 3618:1989.
64. Y. Zhou, G. Stell. *J Chem Phys* 96:1504; 96:1507, 1992.
65. J. A. Balance, R. J. Speedy. *Mol Phys* 54:1035, 1985.
66. T. Boublik. *Mol Phys* 59:371; 59:775, 1986.
67. G. Stell. *Cond Matter Phys Lviv: Acad Sci of Ukraine*, 2:4, 1993.
68. G. Stell, Y. Zhou. *J Chem Phys* 91:4861; 91:4869, 1989.
69. Y. Zhou, H. L. Fredman, G. Stell. *J Chem Phys* 91:4879; 91:4885, 1989.
70. D. Henderson, A. Trokhymchuk, O. Pizio. *Chem Phys Lett* 245:615, 1995.
71. A. Jamnik, D. Bratko. *Phys Rev E* 50:1151, 1994.
72. A. Jamnik, D. Bratko. *Chem Phys Lett* 203:465, 1993.
73. A. Trokhymchuk, O. Pizio, S. Sokołowski, D. Henderson. *Mol Phys* 86:55, 1995.
74. A. Trokhymchuk, O. Pizio, S. Sokołowski. *J Coll Interface Sci* 178:436, 1966.



75. A. Trokhymchuk, D. Henderson, S. Sokolowski. *J Phys Chem* 99:17509, 1995.
76. D. Henderson, O. Pizio, S. Sokolowski. *Czech J Phys* 46:67, 1996.
77. D. Henderson, O. Pizio, S. Sokolowski, A. Trokhymchuk. *Cond Matter Phys Lviv: Acad Sci Ukraine*, 7:71, 1996.
78. S. Sokolowski. *J Chem Soc Faraday Trans II* 78:243, 1982.
79. S. Sokolowski. *J Coll Interface Sci* 88:129, 1982.
80. W. A. Steele. *The Interaction of Gases with Solid Surfaces*. Oxford: Pergamon Press, 973.
81. W. A. Steele. *Surface Sci* 36:317, 1973.
82. O. Pizio, S. Sokolowski. *Phys Rev E* 53:820, 1996.
83. A. Trokhymchuk, O. Pizio, D. Henderson, S. Sokolowski. *J Phys Chem* 100:5941, 1996.
84. E. Bruno, C. Cacamo, P. Tarazona. *Phys Rev A* 35:1210, 1987.
85. D. Henderson, S. Sokolowski, A. Trokhymchuk. *J Chem Phys* 103:4693, 1995.
86. D. Henderson, S. Sokolowski, R. Zagórski, A. Trokhymchuk. *Mol Phys* 91:761, 1997.
87. O. Sinanoglu, K. S. Pitzer. *J Chem Phys* 32:1279, 1960.
88. Adsorption at solid surfaces. In: D. A. King, D. P. Woodruff, eds. *The Chemical Physics of Solid Surfaces and Heterogeneous Catalysis*, Vol. 2. Amsterdam: Elsevier, 1983.
89. Fundamental studies of heterogeneous catalysis. In: D. A. King, D. P. Woodruff, eds. *The Chemical Physics of Solid Surfaces and Heterogeneous Catalysis*, Vol. 4. Elsevier, 1985.
90. M. Borówko, A. Patrykiewicz, S. Sokolowski, R. Zagórski, O. Pizio. *Czech J Phys* 48:371, 1998.
91. Y. Zhou, G. Stell. *J Chem Phys* 92:5533; 92:5544, 1990.
92. L. Blum, G. Stell. *J Stat Phys* 15:439, 1976.
93. F. Franks, ed. *Water, a Comprehensive Treatise*. Vols. 1–7. New York: Plenum, 1972–1977.
94. Yu. V. Kalyuzhnyi, G. Stell. *Mol Phys* 78:1247, 1993.
95. D. Ghonasgi, W. G. Chapman. *J Chem Phys* 100:6633, 1994.
96. D. Ghonasgi, W. G. Chapman. *J Chem Phys* 102:2585, 1995.
97. Y. Zhou, C. K. Hall, G. Stell. *J Chem Phys* 103:2688, 1995.
98. S. Phan, E. Kierlik, M. L. Rosinberg. *J Chem Phys* 101:7997, 1994.
99. R. P. Sear, G. Jackson. *Mol Phys* 81:801, 1994.
100. Y. C. Chiew. *Mol Phys* 73:359, 1991.
101. K. S. Schweizer, J. G. Curro. *J Chem Phys* 89:3342; 89:3350, 1988.
102. J. Chang, S. Sandler. *J Chem Phys* 102:437, 1995.
103. J. Chang, S. Sandler. *J Chem Phys* 103:3196, 1995.
104. E. Vakarin, Yu. Duda, M. F. Holovko. *Mol Phys* 90:611, 1997.
105. Yu. V. Kalyuzhnyi, M. F. Holovko. *Mol Phys* 80:1165, 1993.
106. Yu. V. Kalyuzhnyi, P. T. Cummings. *Mol Phys* 87:249, 1996.
107. A. Yethiraj, C. K. Hall, K. G. Honell. *J Chem Phys* 93:4453, 1990.
108. A. Yethiraj. *Mol Phys* 82:957, 1994.
109. A. Yethiraj. *J Chem Phys* 102:6874, 1995.

110. A. Yethiraj, J. G. Curro, J. J. Rajasekaran. *J Chem Phys* 103:2229, 1995.
111. J. Kolafa, I. Nezbeda. *Mol Phys* 61:161, 1987.
112. W. G. Chapman, K. E. Gubbins, C. G. Joslin, C. G. Gray. *Pure Appl Chem* 59:53, 1987.
113. N. F. Carnahan, K. E. Starling. *J Chem Phys* 51:635, 1969.
114. J. K. Johnson, K. E. Gubbins. *Mol Phys* 77:1033, 1992.
115. J. J. Nicolas, K. E. Gubbins, W. B. Street, D. J. Tildesley. *Mol Phys* 37:1429, 1979.
116. J. K. Johnson, J. A. Zollweg, K. E. Gubbins. *Mol Phys* 78:591, 1993.
117. J. D. Weeks, D. Chandler, H. C. Andersen. *J Chem Phys* 54:5237, 1971.
118. D. Henderson, O. Pizio, A. Trokhymchuk, S. Sokołowski. *Czech J Phys* 48:925, 1998.
119. Yu. V. Kalyuzhnyi, O. Pizio, S. Sokołowski. *Chem Phys Lett* 242:297, 1995.
120. D. Henderson, A. Kovalenko, O. Pizio, S. Sokołowski. *Physica A* 231:254, 1996.
121. A. Trokhymchuk, O. Pizio, S. Sokołowski. *J Coll Interfaces Sc.* 178:436, 1996.
122. A. Kovalenko, O. Pizio, D. Henderson, S. Sokołowski. *J Coll Interface Sci* 182:407, 1996.
123. L. F. Vega, E. A. Müller, L. F. Rull, K. E. Gubbins. *Mol Simul* 15:141 1995.
124. E. A. Müller, L. F. Vega, K. E. Gubbins, L. F. Rull. *Mol Phys* 85:9, 1995.
125. E. Kierlik, M. L. Rosinberg. *J Chem Phys* 97:9222, 1992.
126. E. Kierlik, M. L. Rosinberg. *J Chem Phys* 99:3950, 1993.
127. E. Kierlik, M. L. Rosinberg. *J Chem Phys* 100:1716, 1994.
128. E. Kierlik, M. L. Rosinberg. *Phys Rev A* 42:3382, 1990.
129. Y. Rosenfeld. *Phys Rev Lett* 63:980, 1989.
130. Y. Rosenfeld. *J Chem Phys* 89:4272, 1988.
131. P. Tarazona, R. Evans. *Mol Phys* 48:799, 1983.
132. P. Tarazona, R. Evans. *Mol Phys* 52:847, 1984.
133. P. Tarazona. *Phys Rev A* 31:2672, 1985.
134. P. Tarazona. *Phys Rev A* 32:3148, 1985.
135. P. Tarazona, U. M. B. Marconi, R. Evans. *Mol Phys* 60:573, 1987.
136. E. Chacon, A. M. Somoza, P. Tarazona. *J Chem Phys* 109:2371, 1998.
137. E. Kierlik, Y. Fan, P. A. Monson, M. L. Rosinberg. *J Chem Phys* 102:3712, 1995.
138. T. Meister, D. Kroll. *Phys Rev A* 31:4055, 1985.
139. R. D. Groot. *Mol Phys* 60:45, 1987.
140. W. A. Curtin, N. W. Ashcroft. *Phys Rev A* 32:2909, 1985.
141. G. S. Heffelfinger, Z. Tan, K. E. Gubbins, U. M. B. Marconi, F. van Swol. *Mol Simul* 2:393, 1989.
142. Z. Tan, U. M. B. Marconi, F. van Swol, K. E. Gubbins. *J Chem Phys* 90:3704, 1989.
143. M. Calleja, G. Rickayzen. *Mol Phys* 79:809, 1993.
144. P. Marsh, G. Rickayzen, M. Calleja. *Mol Phys* 84:799, 1995.
145. A. Patrykiewicz, S. Sokołowski, D. Henderson. *Mol Phys* 95:211, 1988.
146. R. Pandit, M. Schick, M. Wortis. *Phys Rev B* 26:5112, 1982.

147. C. Ebner, W. F. Saam. *Phys Rev Lett* 38:1486, 1977.
148. R. Evans. *J Phys Condens Matter* 2:8989, 1990.
149. S. Sokołowski, J. Fischer. *J Chem Soc Faraday Trans* 89:789, 1993.
150. S. Sokołowski, A. Trokhymchuk. *Phys Lett A* 236:557, 1997.
151. D. Henderson, A. Huerta, O. Pizio, A. Trokhymchuk. *Mol Phys* 90:571, 1997.
152. N. Batina, A. Huerta, O. Pizio, S. Sokołowski, A. Trokhymchuk. *J Electroanal Chem* 450:213, 1998.
153. W. R. Smith, B. Triska. *J Chem Phys* 100:3019, 1994.
154. D. M. Pfund, L. L. Lee, H. D. Cochran. *J Chem Phys* 94:3114; 94:3207, 1991.
155. D. A. Kofke, E. D. Glandt. *Mol Phys* 64:1105, 1988.
156. R. D. Groot. *J Chem Phys* 97:3537, 1992.
157. A. Z. Panagiotopoulos. *Mol Simul* 9:1, 1992.
158. S. Dietrich. In: C. Domb, J. L. Lebowitzin, eds. *Phase Transitions and Critical Phenomena. Vol. 12* London: Academic Press, 12, 1988, p 1.
159. J. E. Finn, P. A. Monson. *Mol Phys* 65:1345, 1988.
160. J. E. Finn, P. A. Monson. *Phys Rev A* 39:6402, 1989.
161. S. Sokołowski, J. Fischer. *Phys Rev A* 41:6866, 1990.
162. M. P. Allen, D. J. Tildesley. *Computer Simulation of Liquids*. Oxford: Clarendon Press, 1986.
163. B. Widom. *J Chem Phys* 39:2808, 1963.
164. S. Labik, W. R. Smith. *Mol Simul* 12:23, 1994.
165. S. Labik, V. Jirásek, A. Malihevsky, W. R. Smith. *Mol Phys* 94:385, 1998.
166. J. Fischer, U. Heinbuch. *Mol Simul* 1:109, 1987.
167. S. Romano, K. Singer. *Mol Phys* 37:1765, 1979.
168. J. G. Powles. *Mol Phys* 41:715, 1980.
169. G. M. Torrie, J. P. Valleau. *J Comput Phys* 23:187, 1977.
170. R. L. Rowley, M. W. Schuck, J. C. Perry. *Mol Phys* 86:125, 1995.
171. R. L. Rowley, T. D. Shupe, M. W. Schuck. *Mol Phys* 82:841, 1994.
172. P. Bryk, A. Patrykiewicz, O. Pizio, S. Sokołowski. *Mol Phys* 90:483, 1997.
173. P. Bryk, A. Patrykiewicz, O. Pizio, S. Sokołowski. *Mol Phys* 92:949, 1997.

# 5

## Computer Simulations and Theory of Adsorption on Energetically and Geometrically Heterogeneous Surfaces

**ANDRZEJ PATRYKIEJEW and MAŁGORZATA BORÓWKO**

Department for the Modelling of Physico-Chemical Processes,  
Maria Curie-Skłodowska University, Lublin, Poland

I. Introduction	245
II. Basic Concepts and Models of Surface Heterogeneity	250
III. Surface Heterogeneity and Phase Transitions in Monolayer Films	261
IV. Multilayer Adsorption and Wetting Phenomena	276
References	286

### I. INTRODUCTION

The first notions about the importance of surface heterogeneity effects in adsorption processes go back to the time when Langmuir [1] proposed his famous model of localized adsorption on so-called homogeneous, or uniform, surfaces. The concept of heterogeneous surface arose naturally from the appreciation of the fact that real surfaces are never free of various defects, irregularities in the geometrical structure, chemical impurities, etc. It is now commonly accepted that surface heterogeneity is to be considered as an important intrinsic property of adsorption systems that very often leads to qualitative changes in the behavior of adsorbed films relative to the properties such films would have when formed on uniform surfaces.

Theoretical studies aiming at the incorporation of heterogeneity effects into the formalism describing adsorption phenomena gained a new impetus

in the early 1950s, after Sips [2,3] had proposed the so-called “integral equation of adsorption isotherm,” which can be written as

$$\Theta(p, T) = \int_{\varepsilon_{\min}}^{\varepsilon_{\max}} \chi(\varepsilon) \theta_l(p, T, \varepsilon) d\varepsilon \quad (1)$$

In the above equation, the overall adsorption isotherm,  $\Theta(p, T)$ , which is a function of bulk gas pressure  $p$  and temperature  $T$ , is considered to be a superposition, or rather a weighted average, of adsorption taking place on the surface elements characterized by a given value of the adsorption energy  $\varepsilon$ . This “local adsorption” is represented by the function  $\theta(p, T, \varepsilon)$  while the weighting function  $\chi(\varepsilon)$  is nothing but the probability distribution function for finding the adsorption energy  $\varepsilon$  in the system. In adsorption literature [4] the function  $\chi(\varepsilon)$  is customarily called the *adsorption energy distribution function* (AEDF). The range of integration in Eq. (1) is somewhat ambiguous, for it is rather difficult to determine *a priori* the minimal and maximal values of the adsorption energy for a system under study. In the majority of theoretical applications [5,6] it is assumed that  $\varepsilon_{\min} = 0$  and  $\varepsilon_{\max} = \infty$ , with a hope that physically inaccessible values of  $\varepsilon$  have only negligible influence on the final results. It should also be noted that several methods devoted to AEDF evaluation rest upon the analytical solution of the above integral equation, and, in such cases, the assumption of the integration limits of 0 and  $\infty$  simplifies the problem [6,7].

The above-quoted integral equation has been widely used over the last 50 years and to give a detailed account of all its divergent applications would require a whole book. The interested reader is advised to consult several already available review articles [8–10] as well as a number of excellent monographs [4–6,11,12]. Here we only mention some directions of research that use the integral equation approach and will shortly point some of its advantages as well as limitations and drawbacks it suffers from.

One important direction of study has been to use empirical adsorption data, together with the preassumed model for local adsorption, and attempt to extract information about the form of  $\chi(\varepsilon)$  [13,14]. The choice of the model for local adsorption, which is an important input here, has been customarily treated quite casually, assuming that it has rather limited influence on the form and properties of the evaluated EADFs. Usually, one of so many existing equations developed for adsorption on uniform surfaces is used as the local adsorption isotherm. The most often used forms of  $\theta(p, T, \varepsilon)$  are the Langmuir [6] and the Fowler–Guggenheim [15] equations for localized adsorption. Ross and Olivier [4] extensively used the equation for mobile adsorption, which results from the two-dimensional version of the van der Waals theory of fluids. The most radical solution has been

proposed by Cerofolini [16,17], who decided to replace the local adsorption isotherm by a simple step function, such that to any given value of the adsorption energy corresponds the value of the gas pressure at which all parts of the surface characterized by a given value of adsorption energy are instantaneously covered by the adsorbate. This so-called "condensation approximation" has also found numerous applications [6,18].

Several numerical procedures for EADF evaluation have also been proposed. Morrison and Ross [19] developed the so-called CAEDMON (Computed Adsorption Energy Distribution in the Monolayer) method. Adamson and Ling [20] proposed an iterative approximation that needs no *a priori* assumptions. Later, House and Jaycock [21] improved that method and proposed the so-called HILDA (Heterogeneity Investigation at Loughborough by a Distribution Analysis) algorithm. Stanley et al. [22,23] presented two regularization methods as well as the method of expectation maximalization.

Another school has also developed and attempted to understand the functional dependence of adsorption on heterogeneous surfaces on the vapor pressure and temperature. Various empirical or semiempirical equations were proposed [24–26] and used later to represent experimental data and to evaluate EADF by inverting Eq. (1), which belongs to the class of linear Fredholm integrals of the first kind [27].

Here one should also mention important contributions reporting applications of calorimetric methods to the experimental evaluation of  $\chi(\varepsilon)$  [28–31].

An interesting method of a direct evaluation of the EADF from adsorption isotherm data was proposed by Dash and Puff [32]. Instead of using low coverage parts of the isotherm [28,33] they suggested working within the two-phase region of the film, in which a dilute (two-dimensional) gas phase coexists with a dense (two-dimensional liquid) condensed phase. On the homogeneous surface, the presence of such a region, associated with the first-order phase transition, is manifested by a vertical step at the adsorption isotherm at a certain value of the gas pressure. The values of the surface coverage at both sides of the step give the densities of coexisting phases, as implied by the well known condition of thermodynamic equilibrium. In the case of a heterogeneous surface, the condensed phase is preferentially located over more attractive parts of the surface, and hence any changes in the surface coverage (resulting from the changes of the bulk gas pressure) shift the interface between the dilute and dense phases towards less attractive parts of the adsorbing surface. This in turn leads to changes of the film chemical potential. In consequence the adsorption isotherm exhibits finite and coverage dependent slope within the two-phase region. The distribution of adsorption energies can be obtained directly from the changes of that

slope. Possible applications of that method are limited to very weakly heterogeneous solids with, however, the sites of the same energy grouped into rather compact domains. In the case of a highly heterogeneous surface the idea of equilibrium between two surface phases and the existence of any well defined interface between such phases is not very appealing. The process of adsorbate nucleation on the surface is severely perturbed by the surface heterogeneity and may not allow for the appearance of the usual equilibrium between dilute and dense phases.

The basic assumption underlying Eq. (1), namely the principle of superposition, is incidentally also one of its basic weaknesses. It is fully satisfied only in the case of lack of interactions (other than area or site exclusion) in the film, or when the heterogeneous surface can be considered as composed of a number of macroscopically large uniform domains, i.e., for the so-called "patchwise model" of heterogeneity [5]. (We shall come back to this model later, in the next section.) In real systems one should not expect that the superposition principle will be satisfied. Fortunately, the main stream of interest has concentrated on the development of portable methods enabling quantitative and fast characterization of strongly heterogeneous surfaces, where the effects of heterogeneity dominate over molecular interaction effects so that errors due to the assumption of superposition approximation are not very important. Many technologically important adsorption processes take place on various natural and synthesized materials which exhibit very high heterogeneity of both chemical and geometrical nature. It is enough to mention here large-scale separations on porous materials, gas purification processes, etc.

It is true, however, that the conventional integral approach, with the built-in superposition principle, is not the best tool for treating the effects due to weakly heterogeneous surfaces on such processes as the two-dimensional condensation and other phase transitions, so often observed in adsorbed films [34–38]. The point is that any form of disorder in the system affects primarily correlations between the particles and hinders the development of long-wavelength fluctuations, which are essential for various phase transitions [37,39]. In such cases, the results obtained within the general framework of Eq. (1) need to be treated very cautiously. Another important shortcoming of the integral approach is the usual mean-field character of the local adsorption isotherms. In consequence, the final results are also of the mean field type. Mean-field theory, even in the case of uniform systems, is a very bad guide when one wishes to study phase transitions. Often the ordering temperature is vastly overestimated by a factor of two or more, and it also happens that even the topology of phase diagrams is predicted incorrectly [39]. In systems with intrinsic disorder mean-field theory notoriously predicts the first-order character of truly continuous transitions [40,41].

The above remarks might lead one to the conclusion that the integral approach is unable to provide really important results or to give any true insight into adsorption on heterogeneous surfaces, but, of course, this is not the case. Numerous important results, also concerning surface topography of heterogeneous surfaces, can be found in the literature [42–48]. Some of them will also be presented and discussed in the following sections of this chapter.

A new opportunity, which creates good prospects to overcome many of the above-mentioned problems, has appeared owing to the introduction of computer simulation methods [49–52] which are now recognized as very powerful tools. Based directly on a truly microscopic model of the system, computer simulations can, in principle at least, provide an exact (though numerical only) solution of the model. The only necessary input for computer simulation calculations are the potentials representing all forms of interaction in the system. In the case of adsorption phenomena the surface of any preassumed structure and properties can be created and fed into the computer. Then, one proceeds very much the same as in a real laboratory, but usually gets much richer output than that available from real experiments. The rules of the game are very precisely determined by statistical mechanics and thermodynamics [51], as has already been shown in one of the earlier chapters of this volume.

Using either the Monte Carlo or the molecular dynamics method, one can “measure” various thermodynamic quantities under predetermined conditions. Thus, it is possible to perform measurements of adsorption isotherms, adsorption isobars and isosters, to calculate various heats of adsorption and the heat capacity, isothermal compressibility of the adsorbed layer, spreading pressure, to evaluate the local density profiles, radial distribution functions, structure factors and so on. One of the most attractive features of computer simulation methods is that they allow one to define various quantities which provide very precise information about the inner structure of the system and which are inaccessible in conventional experiments. It is even possible to observe, as in a movie, how the system evolves in time, changes its inner structure, and what happens with every single particle. By making changes in the assumed model and/or changing the parameters of interaction potentials it is easy to track all the effects such changes have on the properties of investigated systems. In the particular case of adsorption on heterogeneous surfaces, it is possible to observe how the spatial distribution of heterogeneities changes the form of adsorption isotherm and all other thermodynamic properties. The output of the simulation calculations can then be compared with experimental data as well as with the predictions of various theoretical approaches. In this way the results of experiments may be better interpreted and theoretical models verified.



This chapter attempts to present some selected problems of adsorption on nonuniform surfaces with a stress on the results obtained just with the help of computer simulation methods. First, however, in Sec. II we briefly summarize basic models of surface heterogeneity and various methods used to generate heterogeneous surfaces for computer simulation studies. In the same section we tackle the problem of correlations between geometrical and energetical heterogeneities. In Sec. III we concentrate the discussion on monolayer adsorption. In particular, we consider the effects of surface heterogeneity on phase transitions and ordering phenomena in adsorbed layers. More complex systems involving multilayer films and wetting phenomena on energetically and geometrically nonuniform surfaces are considered in the final Sec. IV.

## **II. BASIC CONCEPTS AND MODELS OF SURFACE HETEROGENEITY**

The first theoretical model of heterogeneous surface has been introduced already by Langmuir [1], who assumed that the surface of a heterogeneous adsorbent can be viewed as composed of a certain number of uniform regions (patches). Each homogeneous patch is characterized by its own energy of adsorption, and adsorption processes which occur on different patches are completely uncorrelated. This model was then widely used in theoretical studies [5,6,53–56]. In the case of Langmuirian adsorption, which assumes that the only effect of interaction between the adsorbed particles is the site exclusion, no additional conditions are required for the patchwise model to be used. The situation looks considerably different when one tries to take into account mutual attractive interaction between the adsorbed species [6]. The presence of boundaries between patches of different adsorption energy may introduce important effects, due to modifications of the density distribution in the vicinity of such boundaries [57,58]. To avoid the difficulties arising from such effects and still be able to work within a general framework of the superposition approximation, it is postulated that the patches are macroscopically large [5,6], so that boundary effects can be neglected. The above assumption allows one to use Eq. (1) without any modification, though one immediately recognizes that such a model vastly oversimplifies the real situation. Even for various graphitized carbons [34,59] and single crystals [60–62], considered to be characterized by a highly homogeneous surface, the coherence length is seldom larger than about 1000 Å. Real heterogeneous surfaces do not exhibit such large uniform domains and hence the size, as well as the boundary effects, is quite important. Fortunately, such effects are rather subtle and can be neglected in the

case of a strongly heterogeneous surface and when one is primarily interested in the global characterization of such a system via the determination of  $\chi(\varepsilon)$ . In the next section we shall consider the effects due to finite patch size and boundaries between different patches on adsorption phenomena in a more detailed fashion.

A completely different concept of the surface heterogeneity arises from the assumption that sites of different energies are completely randomly distributed over the surface [5,6]. This is the so-called *random model* of heterogeneous surface. Here, again, application of Eq. (1) causes same problems and requires additional assumptions. One immediately notes that the superposition approximation is fulfilled only for noninteracting films. Only in this case are the probabilities of adsorption determined entirely by the energies of adsorption assigned to different sites. In the case of an interacting system the molecule adsorbed on a highly attractive site modifies strongly the potential field in its neighborhood, so that the probabilities of adsorption on neighboring sites are determined not only by the values of the adsorption energy associated to them but also by the mutual interaction between the adsorbed particles. A simple way to take into account the effects of lateral interactions is to assume that the force field due to mutual interactions between the adsorbed molecules is unperturbed by local heterogeneities and can be expressed within the general framework of the mean-field theory, in the same way as for the uniform system [6]. We shall return to this problem later in the following section.

Both extreme models of surface heterogeneity presented above can be readily used in computer simulation studies. Application of the patchwise model is amazingly simple, if one recalls that adsorption on each patch occurs independently of adsorption on any other patch and that boundary effects are neglected in this model. For simplicity let us assume here the so-called "two-dimensional model" of adsorption, which is based on the assumption that the adsorbed layer forms an individual thermodynamic phase, being in thermal equilibrium with the bulk uniform gas. In such a case, adsorption on a uniform surface (a single patch) can be represented as

$$p = K(\varepsilon, T) \cdot f(\theta, T) \quad (2)$$

where  $K(\varepsilon, T)$  is the familiar Henry law constant [11], which carries all the dependence on  $\varepsilon$ , while the function  $f(\theta, T)$  depends only on the surface coverage and, in the general case, on the temperature. Assume now that we wish to perform a Monte Carlo simulation aiming at the evaluation of an adsorption isotherm for the heterogeneous surface with a given adsorption energy distribution function  $\chi(\varepsilon)$  and then confront the result with experimental data. The natural choice of the simulation method in this case seems to be the Monte Carlo method in the grand canonical ensemble, in which the

control thermodynamic variables are the chemical potential  $\mu$ , the temperature  $T$ , and the system volume or rather its area  $A$  when one considers practically two-dimensional monolayer systems. First, we note that the chemical potential of the adsorbed phase can be represented by the following equation

$$\mu_{\text{ad}} = kT \ln \tilde{K}(\varepsilon, T) + kT \ln f(\theta, T) \quad (3)$$

where again all the dependence upon  $\varepsilon$  is located in the first, coverage-independent term. Making the usual assumption that the bulk gas is ideal, we have

$$\mu_{\text{g}} = \mu_{\text{g}}^0 + kT \ln p \quad (4)$$

where  $\mu_{\text{g}}^0$  is the standard chemical potential of the gas. From the above equations (2–4) we immediately find that

$$K(\varepsilon, T) = \tilde{K}(\varepsilon, T) \exp[-\mu_{\text{g}}^0/kT] \quad (5)$$

On the other hand, the dependence of the Henry constant upon  $\varepsilon$  can be represented as [63]

$$\tilde{K}(\varepsilon, T) = K_0(T) \exp[-\varepsilon/kT] \quad (6)$$

Of course, in a more rigorous treatment [11] it should be taken into account that the normal vibrational modes of every adsorbed particle depend upon  $\varepsilon$ , and such a dependence is buried in the preexponential factor  $K_0(T)$ . We shall ignore this question here (an interested reader is advised to consult Ref. 11). A direct implication of Eq. (3) is that in order to calculate the adsorption isotherm for a patchwise heterogeneous surface one needs to calculate *only one* adsorption isotherm for a homogeneous surface, but taken over a sufficiently wide region of the chemical potential. Note that Eqs. (3) and (6) imply that if we use the shifted chemical potential  $\mu' = \mu + \varepsilon$ , then the right-hand side of Eq. (3) becomes independent of  $\varepsilon$ . If our experimental adsorption isotherm spans a certain pressure region, i.e., a certain region of the chemical potential  $\mu$ , between  $\mu_1$  and  $\mu_2$ , and we assume that the adsorption energies belong to a certain interval  $[\varepsilon_{\text{min}}, \varepsilon_{\text{max}}]$ , then the simulated adsorption isotherm must be recorded over the shifted chemical potential ranging between  $\mu_1 + \varepsilon_{\text{min}}$  and  $\mu_2 + \varepsilon_{\text{max}}$ . Now, if we want to evaluate the overall adsorption isotherm, Eq. (1), for the preassumed form of  $\chi(\varepsilon)$ , we can use an appropriately shifted isotherm obtained for a homogeneous surface and weight it with the chosen EADF. Of course, the adsorption isotherm obtained from computer simulation is given only in a finite set of points and one needs to find the continuous approximation to it. That, however, is

no serious problem and can be readily solved using well known standard approximation procedures [64].

In a very similar fashion we can treat the problem of adsorption within the framework of the "three-dimensional model" of adsorption [42].

Application of computer simulations to study adsorption on randomly heterogeneous surfaces is not that simple, and requires some more computational effort. First of all we have to realize that creation of a truly random surface characterized by the *a priori* given energy distribution function is, strictly speaking, impossible. We can only consider a finite system, which is bound to exhibit some deviations of the distribution of adsorption energies from the truly random case and may also show some remnants of correlations between different values of energy. That problem can be overcome with the help of an appropriate averaging method [65,66]. Here we present a simple case of a lattice system, which allows us to understand the principle of the method as well as to tackle some technical problems. Then we consider the more difficult problem of generating random surfaces suitable for work in the continuous space.

In the case of a lattice model the procedure to generate a pseudo-random distribution of adsorption energies over sites, with the preassumed form of the EADF, can be summarized in just a few steps:

1. Define the lattice of the size  $L_x \times L_y$ . (Here we note that the lattice symmetry is quite arbitrary.)
2. Choose the required form of EADF and specify the lower and upper limits of  $\varepsilon$ .
3. Choose a site on the lattice. That can be done either in a systematic or a random way, but the latter method requires more computing time.
4. Draw the value of the adsorption energy, from the specified interval, according to the assumed form of  $\chi(\varepsilon)$  and assign this value to the chosen site. (The procedures to generate random sequences of numbers according to a given probability distribution can be found in many textbooks on probability theory [67] and computer simulation methods [52].)
5. Go back to point 3, until all sites have been visited.

Once the surface has been generated we can perform any sort of simulation calculation we wish.

The problems with computer generation of random surfaces are mostly connected with small sizes of systems we can use. Each such a small system has somewhat different realization of the spatial distribution of heterogeneities. Only at the thermodynamic limit of a truly macroscopic system does the self-averaging of extensive thermodynamic quantities occur. It means that, when using small systems, it is necessary to generate several (often of

the order of  $10^2$ – $10^3$ ) replicas of the system, using the same EADF, but characterized by different spatial distribution of adsorption energies, and repeat the calculation for all of them. The final result is obtained by averaging over all samples. This method is very often used to study systems with random disorder and whenever self-averaging does not occur due to the finite size effects [68–70].

It is fairly easy to imagine that the above-presented random and patchwise topographies can be treated as some limiting cases of a more general topography which assumes partial correlation between probabilities of finding sites of given energies at a certain distance. The idea of partially correlated distribution of adsorption energies has already been suggested by Roy and Halsey [71], and later exploited by Zgrablich and his coworkers [43,44,45,72–75]. They have considered a heterogeneous surface of a given EADF and assumed that the correlation between different energies,  $\varepsilon_i$  and  $\varepsilon_j$ , is described by a pair density distribution function  $\tilde{\chi}(\varepsilon_i, \varepsilon_j)$ . In the case of a completely random surface, the pair distribution function is given by

$$\tilde{\chi}(\varepsilon_i, \varepsilon_j) = \chi(\varepsilon_i)\chi(\varepsilon_j) \quad i \neq j \quad (7)$$

In the opposite extreme case of a patchwise surface

$$\tilde{\chi}(\varepsilon_i, \varepsilon_j) = \begin{cases} \chi(\varepsilon_i) & i = j \\ 0 & \text{otherwise} \end{cases} \quad (8)$$

In the case of intermediate topography, they assume that there is a certain characteristic (for a given surface) length,  $r_{\text{cor}}$ , which defines the size of small domains characterized by the same value of adsorption energy, and write the pair density distribution as

$$\tilde{\chi}(\varepsilon_i, \varepsilon_j) = \alpha(r_{\text{cor}})\chi(\varepsilon_i)\chi(\varepsilon_j) \quad i \neq j \quad (9)$$

and

$$\tilde{\chi}(\varepsilon_i, \varepsilon_i) = \chi(\varepsilon_i) - \sum_{j \neq i} \alpha(r_{\text{cor}})\chi(\varepsilon_i)\chi(\varepsilon_j) \quad (10)$$

where  $\alpha(r_{\text{cor}})$  is a factor related to the correlations of different energy values. Now  $\alpha(r_{\text{cor}}) = 1$  corresponds to the random topography and  $\alpha(r_{\text{cor}}) = 0$  to the patchwise topography. The procedure for assigning  $k$  different values of energy to sites belonging to a square lattice of the specified size  $L$ , with the preassumed form of the single-site distribution function  $\chi(\varepsilon)$  and for a given characteristic length,  $r_{\text{cor}}$ , has been described in Ref. 44. Here we recall its basic steps. First we note that the distribution function  $\chi(\varepsilon)$  is discrete, i.e., for the chosen  $k$  values of the adsorption energy  $\{\varepsilon_1, \varepsilon_2, \dots, \varepsilon_k\}$  the values of  $\chi(\varepsilon_i)$  for  $i = 1, 2, \dots, k$  are specified. Then one chooses a site at random and if the site has not been already assigned any value of energy, a random

number  $\zeta$  from the interval  $[0, 1]$  is generated and used to specify the energy to be assigned to the chosen site. This is done by using the following condition

$$\sum_{i=1}^{l-1} \chi(\varepsilon_i) < \zeta \leq \sum_{i=1}^l \chi(\varepsilon_i) \quad (11)$$

and the chosen energy is equal to  $\varepsilon_l$ . Next, the sites within the circle of the characteristic length  $r_{\text{cor}}$ , around the chosen site are considered, and the predominant energy within the circle is assigned to all the sites encompassed by the circle. After all the sites in the system have been assigned the values of energy, the relaxation procedure is applied using the above equations (9) and (10).

The models of heterogeneous surfaces presented above are all based on the idealized regular lattice model. In a real situation, heterogeneities may originate from the impurities built into the surfacial layer of the solid, from various geometric defects (dislocations, natural surface roughness, different crystal planes exposed, etc.) of an otherwise periodic lattice, or be the intrinsic property of the material, as happens in the case of amorphous solids [76–78]. The approaches that have been recently used to construct such random lattices are based on perturbing on an initially perfect lattice, by a random displacement of all vertices [79], or on a random packing of hard spheres as is proposed in the Bernal model of amorphous solids [80–84]. Benegas et al. [79] have created a random lattice by perturbing the positions of the constituting atoms, of an initially perfect square lattice, by stochastic vectors taken randomly from the Gaussian distribution of the specified mean and dispersion. Thus obtained, the random lattice has then been used to simulate adsorption isotherms, in the general framework of a lattice gas model of particles interacting via the pairwise additive forces characterized by the (12,6) Lennard–Jones potential

$$u(r) = 4\varepsilon \left[ \left( \frac{\sigma}{r} \right)^{12} - \left( \frac{\sigma}{r} \right)^6 \right] \quad (12)$$

In their model they retained only the first- and second-nearest neighbor interactions, so that the Hamiltonian assumed the following form

$$\mathcal{H} = \sum_{lm} n_l n_j u(r_{ij}) + \sum_{2nm} n_l n_j u(r_{ij}) + \sum_i \varepsilon_i n_i \quad (13)$$

where the values of the adsorption energy at a given site  $\varepsilon_i$  have not been exactly those corresponding to the disordered lattice used in simulation but assigned randomly from the Gaussian distribution of predetermined mean and dispersion. Due to the randomness of the lattice, the interactions  $u(r_{ij})$

also are randomly distributed and such a model can be mapped onto the random Ising model subjected to an, also random, external field [41,85–88]. We shall briefly discuss some results obtained for that model in the next section.

A certain shortcoming of the approach used by Benegas et al. [79] is that they have specified the adsorption energy distribution function somehow independently of the geometrical structure of their random lattice. One can readily devise a simple model that allows one to calculate the energies over all adsorption sites. For example, one can assume that the energy of adsorption over each lattice cell is given by the minimum of the summed interactions between the incoming gas molecule and all the atoms constituting a given cell. The cells differ in shape and size, as well as in the number of constituting atoms, so that such calculations may look a little troublesome but in practice are very simple indeed and pay off well, since the subsequent “computer adsorption experiments” are performed on a precisely defined system.

Good examples of such calculations are brought by the work of Bakaev and Steele [81–83], who have studied adsorption of simple gases on model amorphous oxides surfaces. Here we discuss briefly the model used in Ref. 81. The heterogeneous surface has been obtained by a random packing of 1000 hard balls using the algorithm described by Bonissent and Mutaftschiev [89]. This model has been previously applied to study adsorption on heterogeneous surfaces by Bakaev [90] and by Bakaev and Voit [91]. The balls formed the simulation cell of about five layers thickness and size in  $x$  and  $y$  directions equal to  $14.000 \times 13.856$  (in units of the oxygen ion, of the diameter 0.28 nm). The surface has then been divided into a  $20 \times 20$  rectangular mesh, and each element of the surface has been considered as a single adsorption site. Then a “probe ball” of about the size of the helium atom (0.29 nm) has been put over the center of each site and its distance from the surface  $z$  has been assigned to a given site. Fig. 1 shows the examples of cross-sections of the surface obtained in the above-described way. The Monte Carlo simulations have been carried out for argon adsorption in the region of submonolayer coverages using the grand canonical ensemble method (which allowed them to obtain well-equilibrated states, not so easily accessible in the canonical simulations for such systems as used by Bakaev and Steele—a detailed discussion of this technical problem can be found in Ref. 81) and followed by the conventional canonical ensemble simulation.

The low-coverage parts of the adsorption isotherms evaluated at different temperatures have shown a remarkable feature of linear dependence between the adsorption and the logarithm of gas pressure. This sort of behavior corresponds to the well-known Temkin equation of adsorption

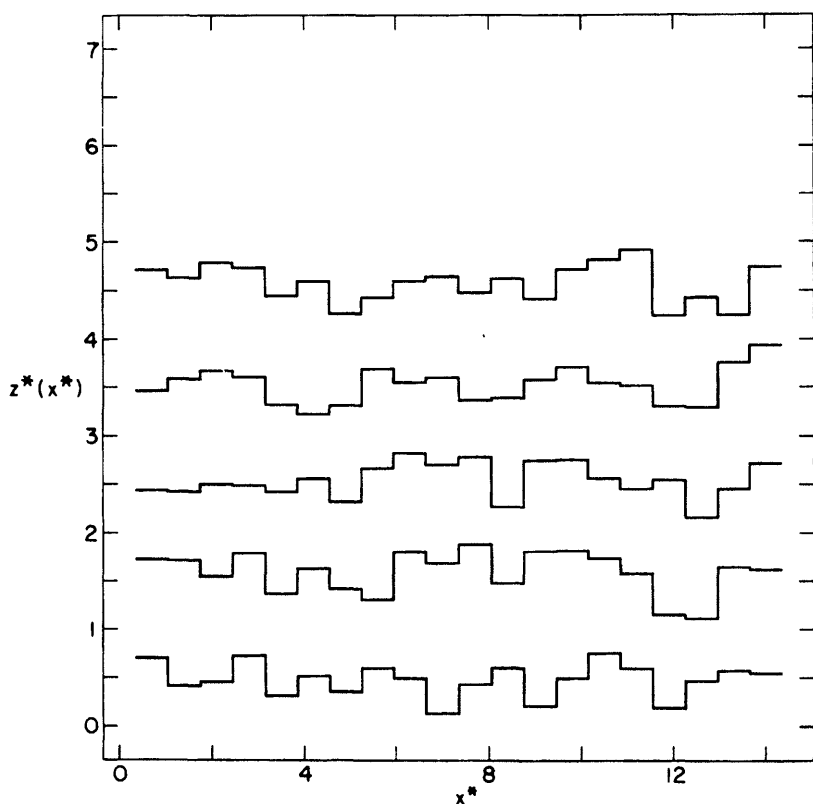


**FIG. 1** Profiles of the heterogeneous surface generated by the procedure of Bakaev and Steele [81]. Each profile (except the upper one) is shifted downward with respect to the previous one by the unit of length. (Reprinted with permission from: *Langmuir* 8:148–154, August 1992. © 1992, American Chemical Society.)

isotherm (see Ref. 5, p. 53). The evaluated distributions of the gas–solid and gas–gas interaction energies for different concentrations of the adsorbate at the surface have also shown interesting properties. In particular, it has been clearly demonstrated that the increase of the surface coverage changes the obtained energy distribution functions. In the case of the gas–solid interaction energy distribution function, which can be considered as a measure of EADF, a gradual widening with a shift towards lower energy values was observed (see Fig. 2(a)). This results from the fact that, for higher surface coverages, the adsorbed atoms are more likely to adsorb on weakly attractive sites. This process should not, and does not, influence the contributions



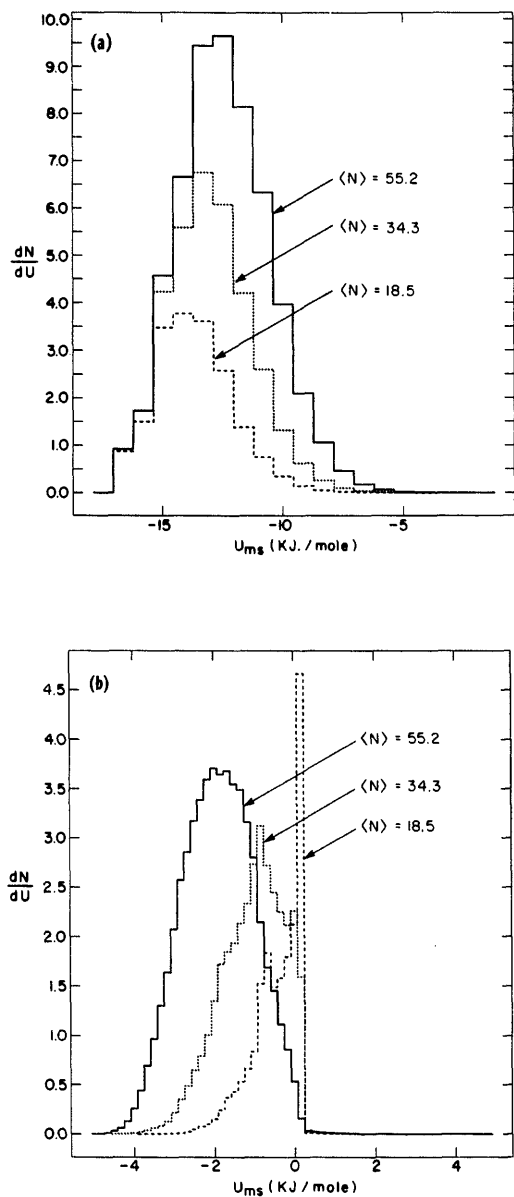


**FIG. 2** Distribution of the adsorption energy (a) and of the adsorbate-adsorbate interaction energy (b) for the adsorbed Ar atoms obtained from computer simulations at  $T = 90$  K. (Reprinted with permission from: Langmuir 8:148-154, August 1992. © 1992, American Chemical Society.)

due to strongly adsorbing sites. The distribution functions for the gas–gas interaction energy have shown in a very explicit way that the use of Langmuir-like models neglecting mutual interaction between the adsorbed particles is adequate only at very low coverages, and that the increase of the surface coverage to about one-third of the monolayer capacity introduces quite large effects due to admolecule–admolecule interactions (Fig. 2(b)).

While discussing those last-mentioned models of heterogeneous surfaces we have tackled a very important and general issue of correlations between the geometrical irregularities present in the system and the resulting energetical heterogeneity. In this context we should mention here other works in which the surface heterogeneity has been considered as having originated from geometrical effects. The simplest model introducing some small heterogeneity effects is that of the stepped substrate [92–94], of the surface consisting of terraces characterized by a finite width ( $L_x$ ) and assumed to be macroscopically long ( $L_y \rightarrow \infty$ ) (see Fig. 3). In practice, the limit of infinite terrace length can not be met in computer simulation studies and one usually imposes periodic boundary conditions to mimic the macroscopic situation [52]. The heterogeneity effects arise from the fact that the potential field felt by the adsorbed molecule is different at both terrace edges and in the terrace interior [95,96]. Such models have been used to describe adsorption on stepped vicinal planes of metal crystals [97–99]. The results obtained for the models of stepped surfaces are very interesting, in particular in relation to general problems of phase transitions in systems with restricted geometry and wetting phenomena. Some of the results that seem pertinent to the scope of the present review will be discussed in the following section.

A very interesting model of geometry-induced surface heterogeneity has been proposed by Bakaev [100] and devised in order to describe adsorption on nongraphitized carbons. The basic idea of that so-called “rumpled graphite basal plane” model has arisen from experimental observations [101–103] which suggested that the nongraphitized carbons, though clearly

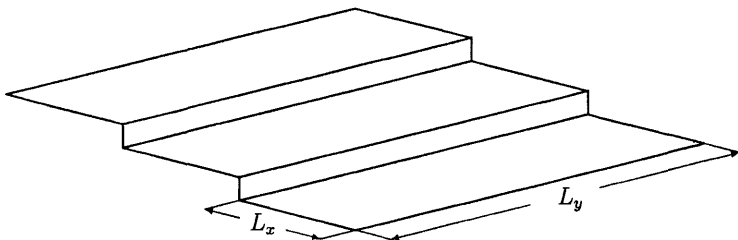


**FIG. 3** Model stepped surface used in computer simulation studies.

exhibiting the presence of domains corresponding to the graphite basal plane, also show broad adsorption energy distribution functions. These two features cannot be well described by the vastly popular so-called "paracrystalline" model [104]. In particular, broad EADF is rather characteristic of the previously mentioned amorphous surface model. Electron microscopy [101] does not allow one to assume that the surface of nongraphitized carbon is amorphous. On the contrary, it is the interior of the sample that exhibits irregular structure, while the surface appears much more ordered. The rumpled graphite basal plane model assumes that the surface is not a rigid ("flat") basal graphite plane, but exhibits distortions and looks like that shown in Fig. 4. In order to generate such a structure, for later use in the computer simulation study, Bakaev has applied the molecular dynamics simulation method [105]. The interested reader will find a detailed description of the algorithm and the potential functions in Ref. 100. From the results of simulation of the adsorption on the rumpled graphite basal plane surface it clearly follows that the model quite well describes the main features of X-ray and neutron scattering patterns of nongraphitized carbons as well as their adsorption behavior.

At this point we should also recall another application of the already mentioned Bernal model of amorphous surface. Namely, Cascarini de Torre and Bottani [106] have used it to generate a mesoporous amorphous carbonaceous surface, with the help of computer simulation and for further application to the computer simulation study of adsorption. They have added a new component to the usual Bernal model by introducing the possibility of the deletion of atoms, or rather groups of atoms, from the surface according to some rules. Depending on the particular choice of those rules, surfaces of different porosity and structure can be obtained. In particular, they have shown examples of mono- as well as polydispersed porous surfaces

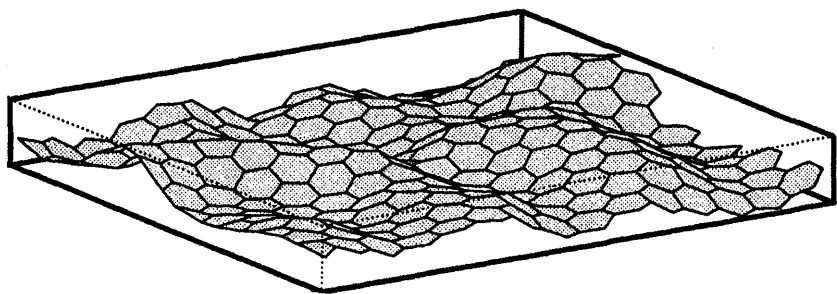


**FIG. 4** Distorted graphite surface generated according to the rumpled graphite model. (From Ref. 100.)

characterized by different uniformity of walls. All the above-presented models of amorphous surface are of great importance for theoretical studies directed towards development of reliable methods allowing for the estimation of  $\chi(\varepsilon)$ , in particular in all such cases in which random distribution of adsorption energies can be expected. Strong heterogeneity effects in such systems allow for the application of relatively simple methods based on the mean-field approximations and developed for adsorption on uniform surfaces [5,6]. One can also check the validity of various theoretical concepts by a direct comparison of the predictions stemming from them with the results obtained from the computer simulations.

### III. SURFACE HETEROGENEITY AND PHASE TRANSITIONS IN MONOLAYER FILMS

A direct link between the surface heterogeneity of real surfaces and possible phase transitions in adsorbed layers is supplied by the great difficulties in experimental observation of the characteristic for the phase transition behavior of thermodynamic quantities in adsorption experiments. The first nonquestionable direct experimental evidence of the existence of phase equilibria in adsorbed layers was provided by Thomy and Duval [107–109], who measured adsorption isotherms of simple gases (krypton, xenon, methane) on exfoliated graphite. Unlike other carboneous adsorbents, exfoliated graphite is characterized by very high uniformity of its surface, consisting of large domains of nearly perfect graphite basal plane [110]. Thomy and Duval demonstrated that the phase behavior of, essentially two-dimensional, adsorbed monolayers resembles, to some extent, what we know from everyday observation of three-dimensional bulk matter. Thus, the adsorbed layers have been found to exhibit the existence of two-dimensional counterparts of gas, liquid and solid phases. The evaluated phase diagrams of such films have appeared to be qualitatively quite similar to, say, the bulk water phase diagram. In particular, it was found that the two-dimensional gas–liquid coexistence ends at the corresponding two-dimensional critical point, that there is a triple point at which the two-dimensional gas, liquid and solid phases coexist and that the melting line exhibits only a slight temperature dependence, which is a signature of low compressibility of the two-dimensional solid phase. However, further studies [34,111–116] have demonstrated that such a picture vastly oversimplifies the real situation and that phase behavior of adsorbed films is much richer. Many of the observed phenomena do not have simple bulk counterparts, e.g., the commensurate–

incommensurate transition [117–119], various surface order–disorder transitions [37,120,121], etc.

From the time when Thomy and Duval presented the results of their early experiments (late 1960s) the field has grown enormously. Hundreds of papers and several monographs have been published and many conferences have been held to present new results of experimental and theoretical studies and to exchange ideas as well as to stimulate further developments. A vast majority of all that activity has been directed towards the understanding of the fundamental problems of phase transitions on uniform surfaces, whereas problems of the surface heterogeneity effects have been much less intensively studied [11,57,122–126].

In this section we begin the discussion with some basic thermodynamic considerations which, as we hope, will show clearly why the effects of surface heterogeneity make the study of surface phase transitions so difficult. Then we shall concentrate mainly on the results of the recent computer simulation studies of phase transitions in model systems exhibiting various forms of disorder.

To begin with, let us consider an adsorption system, i.e., the film formed on the surface of the total area  $A$  and held at the temperature  $T$ . For the sake of simplicity, we also assume that the film is only one atomic layer thick. The discussion of multilayer films on heterogeneous surfaces is presented in the next section of this chapter.

The chemical potential of the film on the uniform surface can be written as [32]

$$\mu_a(\varepsilon, \phi, T) = -\varepsilon + \mu_a^*(\phi, T) \quad (14)$$

where  $\mu_a^*(\phi, T)$  is just the two-dimensional equation of state with  $\phi$  being the spreading pressure. The film is in thermal equilibrium with the bulk gas of chemical potential  $\mu_g(p, T)$ , and of course we have

$$\mu_g(p, T) = \mu_a(\varepsilon, \phi, T) \quad (15)$$

Now, assume that the adsorbed layer is not a homogeneous phase but exhibits two-phase coexistence between the low density phase (1) and the high density phase (2) and that these two phases contain  $N_1$  and  $N_2$  molecules, respectively, and occupy the areas  $A_1$  and  $A_2$ . Of course, the total area of the sample is  $A = A_1 + A_2$  and the total number of adsorbed particles is equal to  $N = N_1 + N_2$ . When these two phases are separated by the first-order transition, then the spreading pressure as well as the chemical potentials of both phases are the same and equal to  $\phi_{eq}$  and  $\mu_{a,eq}$ , respectively. Of course, the chemical potential of the bulk gas must also be the same as the chemical potential of the adsorbed film ( $\mu_g = \mu_{a,eq}$ ), so that the bulk pressure is fixed, as long as the system remains within the two-phase

coexistence region. The values of  $\phi_{eq}$  and  $\mu_{eq}$  are also constant all along the coexistence line and independent of  $N$ . Thus, the presence of such equilibrium corresponds to a discontinuity (vertical step) at the adsorption isotherm (Fig. 5). The constancy of the equilibrium gas pressure causes that the isosteric heat of adsorption

$$q_{st} = kT^2 \left( \frac{\partial \ln p}{\partial T} \right)_N \quad (16)$$

is also constant within the two-phase region.

Then the heat capacity of the film has the form [32]

$$C_A = c_1(T)N_1 + c_2(T)N_2 + T \left[ \left( \frac{\partial S_1}{\partial N_1} \right)_{T,A_1} - \left( \frac{\partial S_2}{\partial N_2} \right)_{T,A_2} \right] \left( \frac{\partial N_1}{\partial T} \right)_{N,A} \\ + T \left[ \left( \frac{\partial S_1}{\partial A_1} \right)_{T,N_1} - \left( \frac{\partial S_2}{\partial A_2} \right)_{T,N_2} \right] \left( \frac{\partial A_1}{\partial T} \right)_{N,A} \quad (17)$$

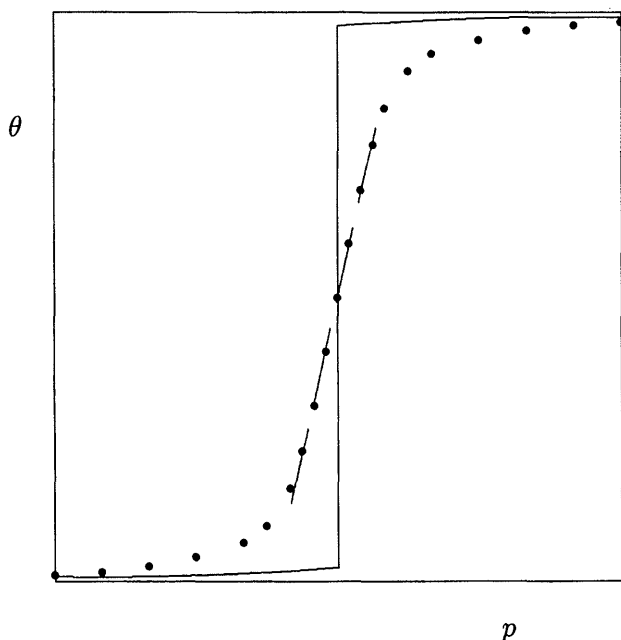


**FIG. 5** Schematic representation of adsorption isotherms in the region of the first-order phase transition on a homogeneous (solid line) and heterogeneous (filled circles) surface.

where  $c_1$  and  $c_2$  are the specific heats of both phases and the next two terms constitute the so-called conversion term, in which  $S_i$  denotes the entropy of the  $i$ th phase. At the first-order transition, which occurs at a certain temperature  $T_{tr}(\theta)$  (here  $\theta$  is the density of the adsorbed film, equal to  $N/A$ ), the presence of the conversion term leads to the appearance of a finite discontinuity at  $C_A$  at the temperature  $T_{tr}(\theta)$ , and this discontinuity is equal to [32]

$$C_{A,-} - C_{A,+} = \frac{T_{tr}(\theta)}{\kappa_+} \left( \theta \frac{dT_{tr}(\theta)}{d\theta} \right)^2 \quad (18)$$

where the lower index  $-(+)$  means that the transition temperature is approached from below (above), and  $\kappa$  is the film compressibility

$$\kappa = \frac{1}{\theta} \left( \frac{\partial \theta}{\partial \phi} \right)_T$$

Of course,  $\kappa$  can be readily related [32] to the slope of the adsorption isotherm.

In the case of a heterogeneous surface, the chemical potential of the film is no longer constant along the coexistence line but changes with  $\theta$  (see Fig. 5). This is so because the interface between the dilute and the dense phases changes its position as the film density increases and encounters surface regions characterized by different values of  $\varepsilon$ . At the same time the value of  $\phi_{eq}$  must be unchanged in the two-phase region. Changes in  $\varepsilon$  in Eq. (14), with the second term unchanged, lead to changes of the equilibrium chemical potential of the bulk gas and hence to changes of the bulk gas pressure. Thus the adsorption isotherm no longer exhibits discontinuity, but only a finite slope which is a function of  $\theta$  (at constant temperature). A good example of an experimental system which clearly shows the heterogeneity effects on two-dimensional condensation is krypton adsorbed on MgO [61]. Fig. 6 presents a series of adsorption isotherms measured at the same temperature of 77.3 K but on different samples of magnesium oxide. The estimated critical temperature for this system is equal to about 87 K [127], so that the adsorption isotherms should exhibit very pronounced discontinuities if the adsorbent were homogeneous. Here we observe that none of the adsorption isotherms shows a truly discontinuous portion, though the adsorption isotherm labeled d, is nearly vertical over a wide coverage range, pointing to the presence of the two-phase coexistence region.

From the above argument and Eq. (16) we instantaneously find that the isosteric heat of adsorption cannot be constant within the two-phase region but must also show changes with the surface coverage. In the case of heat capacity we also observe important effects due to the surface heterogeneity.

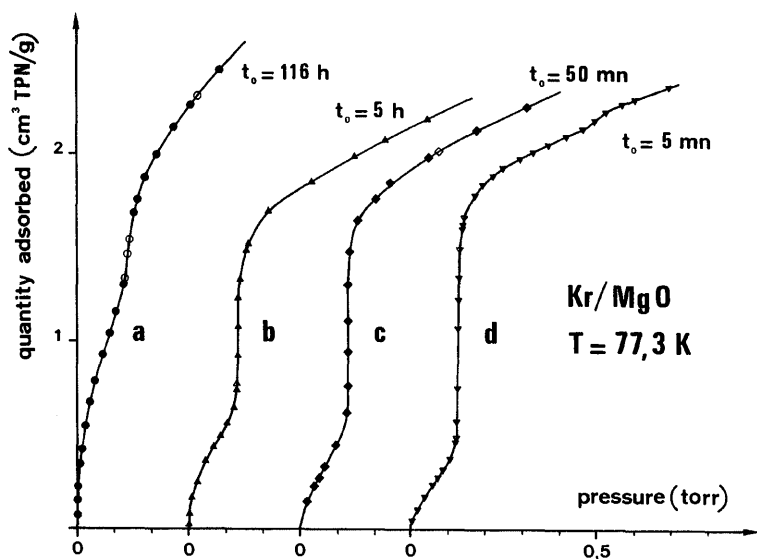


**FIG. 6** Examples of adsorption isotherms for the Ar/MgO system measured on different samples of MgO crystals. (From Ref. 61.)

The discontinuity disappears, since the boundary line is very sensitive to the local density variations, so that it is not only the function of the average film density, specified by  $\theta$ , but it also changes when the local density exhibits deviations from the average density of a given phase, (1) or (2), due to changes in the surface field. Thus, there will be a rounding of the transition region over a certain range of temperatures around  $T_{tr}(\theta)$ . Explicit calculations, performed by Ecke et al. [128] for model systems, have very clearly confirmed the above discussion. The same conclusion has been reached by Gelband and Doniach [129], who applied the renormalization group method [130] to the random-field Ising model.

One should note that the above argument about the heterogeneity effects on the first-order phase transition holds only for sufficiently weak heterogeneity. For highly heterogeneous surfaces the inhomogeneity of the surface field also induces high variations of lateral fields and these combined effects lead to severe perturbations in the local densities in the film, which may produce qualitative changes in the film behavior. In particular, there will be nothing like a two-phase coexistence as the adsorbate nucleation may be driven by the presence of strongly attracting local centres and not by mutual interactions that are responsible for homogeneous nucleation. In such cases the adsorption isotherms change their shape and become more like the



adsorption isotherm obtained from the Langmuir equation. This has been very explicitly shown by Benegas et al. [79].

At this point a series of questions can be asked: How to distinguish weakly and strongly heterogeneous surfaces? How to define the "measure of heterogeneity" with respect to its effects on surface phase transitions? Is the cross-over between these two regimes abrupt or does the change between the weak and the strong heterogeneity regimes occur gradually?

In the light of the above questions, it is tempting to refer to the results emerging from numerous theoretical and computer simulation studies [40,41,85–88,129–131] of the random field Ising model, and we shall do so, but only after completing the present discussion.

In addition to purely energetical heterogeneity one should also take into account some basic aspects of possible heterogeneities resulting from geometrical effects. The simplest and yet experimentally quite important geometric effects are due to the finite size of crystallites. Experimental measurements have clearly demonstrated that the size of typical crystallites may be quite small (of the order of 50–100 Å [116,132] and quite large (of the order of  $10^3$  Å [61]).

From the finite-size scaling theory of the first-order phase transitions [133–135] it follows that under isothermal conditions, i.e., for the pressure driven transition, at  $T < T_c$ , where  $T_c$  is the corresponding critical temperature, the finite size of the crystallite causes a rounding of the singularities in the behavior of the isothermal compressibility and the heat capacity. In particular, the discontinuities are replaced by finite rounded peaks, and the heights of their corresponding maxima,  $\kappa_{\max}$  and  $C_{A,\max}$  both scale with the crystallite size as  $L^2$  (in the case of a two-dimensional system, while in the general case of a  $d$ -dimensional system as  $L^d$ ) [135]. Besides, the boundary of the two-phase region formed on finite crystallites, and characterized by the interfacial line tension  $\gamma_l$ , has length proportional to  $L$ . This introduces an additional term [136,137]

$$\Delta\mu_a = 2\gamma_l[L(\theta_2 - \theta_1)]^{-1} \quad (20)$$

to Eq. (14) and hence shifts the location of the transition point. Now, if the system exhibits a certain distribution of the crystallite sizes, represented by the appropriate distribution function  $C(L)$ , defined as [32]

$$C(L) = \left( \frac{\partial \ln N}{\partial L} \right)_{T,A} \quad (21)$$

where  $N$  is the number of atoms enclosed in all domains of diameter equal to  $L$  or greater, the transition point is met at different values of the bulk gas

pressure for each type of crystallite, and similarly, as in the case of energetical heterogeneity, the adsorption isotherm should exhibit a finite slope.

Now, assume that we are getting closer to the critical point of our transition, i.e., to the point of the second-order transition. In the case of a uniform system the critical region can be described by the divergent correlation length of statistical fluctuations [138]

$$\xi \propto t^{-\nu} \quad (22)$$

where  $t = |(T - T_c)/T_c|$ . Similarly, the isothermal compressibility and the heat capacity diverge to infinity as

$$\kappa \propto t^{-\gamma} \quad (23)$$

and

$$C_A \propto t^{-\alpha} \quad (24)$$

Moreover, the order parameter, which in the case of the gas-liquid transition is defined as the difference between the densities of both coexisting phases,  $\Delta\theta = \theta_2 - \theta_1$ , approaches zero when the temperature goes to  $T_c$  (from below, since above  $T_c$  the above order parameter is always equal to zero) as

$$\Delta\theta \propto t^\beta \quad (25)$$

In the above,  $\nu$ ,  $\gamma$ ,  $\alpha$  and  $\beta$  are the familiar critical exponents [138].

The question we ask here is whether the surface heterogeneity, either energetical or geometrical, changes the properties of the critical region and whether the transition retains its second-order character.

In the case of purely geometrical heterogeneity, i.e., when the size of uniform surface domains (patches) is limited by the finite size of crystallites and/or the presence of steps a general answer to our question can be deduced from the finite size scaling theory of critical phenomena [133]. For instance, when the transition in the macroscopic system occurs at the temperature  $T_c(\infty)$ , then in the finite system of the linear dimension  $L$ , the same transition appears at the shifted temperature  $T_c(L)$  and is also smeared over a certain range of temperature. In particular, the usual critical divergences of the heat capacity and compressibility (compare Eqs. (23) and (24)) are replaced by finite peaks. The shift in the critical temperature can be related to the system size through the following relation

$$T_c(L) - T_c(\infty) \simeq L^{-\lambda} \quad (26)$$

where the maximum values of both the heat capacity  $C_{\max}(L)$  and the compressibility  $\kappa_{\max}(L)$ , also scale with  $L$ , so that the following relationships are satisfied:

$$\kappa_{\max}(L) \simeq L^{\gamma_s} \quad \text{and} \quad C_{\max}(L) \simeq L^{\alpha_s} \quad (27)$$

where  $\gamma_s$  and  $\alpha_s$  are the exponents describing the size dependence of the compressibility and the heat capacity, respectively, at the critical region [139]. One can also introduce a quantitative measure of the smearing of the critical region as the width of the compressibility peak at half of the peak height, and define the appropriate "rounding exponent" such that

$$\Delta T(L) \simeq L^{-\Theta} \quad (28)$$

All the above scaling relations have one common origin in the behavior of the correlation length of statistical fluctuations,  $\xi$ , in a finite system [140,141]. Namely, the most specific feature of the second-order transition is the divergence of  $\xi$  at the transition point, as is described by Eq. (22). In the finite system, the development of long-wavelength fluctuations is suppressed by the system size limitation;  $\xi$  can be, at the most, of the same order as  $L$ . Taking this into account, we find from Eqs. (22) and (26) that

$$T_c(L) - T_c(\infty) \sim L^{-1/\nu} \quad (29)$$

so that  $\lambda = 1/\nu$ , and  $\nu$  is the correlation length critical exponent of the macroscopic system. Similarly, it can be shown that  $\gamma_s = \gamma/\nu$ ,  $\alpha_s = \alpha/\nu$ , and  $\Theta = 1/\nu$ .

Similarly to the previously considered case of the first-order transitions, the above picture applies to a specific situation in which the sample exhibits just one type of crystallites, all of the same size, and where we neglect the effects of energetical heterogeneity that are bound to be present at the crystallite boundaries. In real samples one expects to find a distribution of the crystallite sizes, and hence more complex behavior.

Another special case of weak heterogeneity is found in the systems with stepped surfaces [97,142–145], shown schematically in Fig. 3. Assuming that each terrace has the lattice structure of the exposed crystal plane, the potential field experienced by the adsorbate atom changes periodically across the terrace but exhibits nonuniformities close to the terrace edges [146,147]. Thus, we have here another example of geometrically induced energetical heterogeneity. Adsorption on stepped surfaces has been studied experimentally [95,97,148] as well as with the help of both Monte Carlo [92–94,98,99,149–152] and molecular dynamics [153,154] computer simulation methods.

All those studies have been performed rather to study the scaling relations for various phase transitions occurring in systems of restricted

geometry than to consider adsorption phenomena on nonuniform surfaces. More realistic situations have been considered by Merikoski et al. [98]. They have applied the transfer matrix method to obtain thermodynamic information on adsorption on stepped substrates characterized by substrate steps of infinite length and small widths, not greater than 10 lattice sites. The results of Merikoski *et al.* have clearly demonstrated that even a very weak potential field acting along the step edges considerably changes the behavior of adsorbed films, which show properties characteristic of one-dimensional systems. In particular, the adsorption isotherms exhibit a finite slope even at very low temperatures, indicating clearly that the adsorbate condensation does not occur via the first-order transition, as in two-dimensional systems, but is a continuous process.

The effects due to the finite size of crystallites (in both lateral directions) and the resulting effects due to boundary fields have been studied by Patrykiewicz [57], with help of Monte Carlo simulation. A solid surface has been modeled as a collection of finite, two-dimensional, homogeneous regions and each region has been assumed to be a square lattice of the size  $L \times L$  (measured in lattice constants). Patches of different size contribute to the total surface with different weights described by a certain *size distribution function*  $C(L)$ . Following the basic assumption of the patchwise model of surface heterogeneity [6], the patches have been assumed to be independent one of another.

The behavior of an adsorbate on a single patch of size  $L$  has been represented by the familiar two-dimensional lattice gas model Hamiltonian with the added term resulting from the presence of a boundary field:

$$\mathcal{H}_L = -\frac{1}{2} u_{NN} \sum_{\langle i,j \rangle} n_i n_j - (V - \mu) \sum_i n_i - V_b \sum_{i \in \Omega(L)} n_i \quad (30)$$

In the above,  $u_{NN}$  is the nearest neighbor interaction energy,  $V$  is the adsorption energy and  $V_b$  is the boundary field acting on the particles located at the patch boundary  $\Omega_L$ .

In the case of a single patch, the size dependence of the system follows directly from the finite size scaling theory [133]. In particular, the critical point temperature scales with the system size as predicted by the equation

$$T_c(L) - T_c(\infty) \propto L^{-1} \quad (31)$$

which follows from the general relation (29) for the exponent  $\nu = 1$ . The above equation is satisfied independently of the magnitude of the boundary field  $V_b$ , as Fig. 7 demonstrates. Despite apparent independence of  $V_b$  of the critical temperature phase diagrams obtained for systems with different  $V_b$  are different and show pronounced effects of asymmetry of phase boundaries

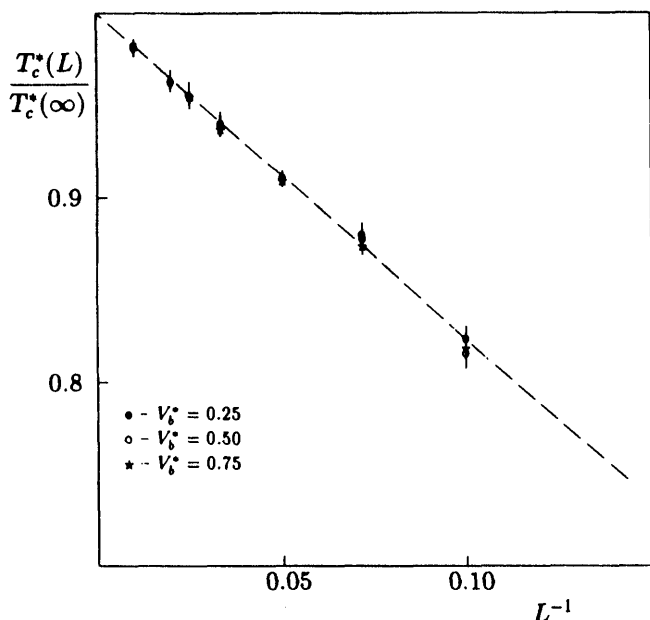


**FIG. 7** Changes of critical temperature with system size for different values of the boundary potential. (Reprinted with permission from: *Langmuir* 9:2562–2568, October 1993. © 1993, American Chemical Society.)

(see Fig. 8). The magnitude of the boundary field influences also the chemical potential at which the condensation in the adsorbed film takes place.

Here, we should note that the phase transitions observed in computer simulation result from the limited “time of observation” and large effects due to metastability. In the finite system, the free energy is always a regular function of its parameters and does not show any true singularities [37,133]. In particular, the correlation length does not diverge on the approach to the critical point, but stays always finite. Thus, we do not observe a true critical region, but only a pseudocritical behavior. Strictly speaking, in the finite systems considered here no true phase transition can appear. One should remember, however, that real experiments also suffer from similar effects, apart from the limited precision and accuracy. Therefore, the results of computer simulation studies may be closer to the experimental results than to the rigorous results of statistical mechanics.

In the systems characterized by more complex surface structure, consisting of patches of different size and different magnitude of the boundary field, the properties of adsorption isotherms have been found to depend on the

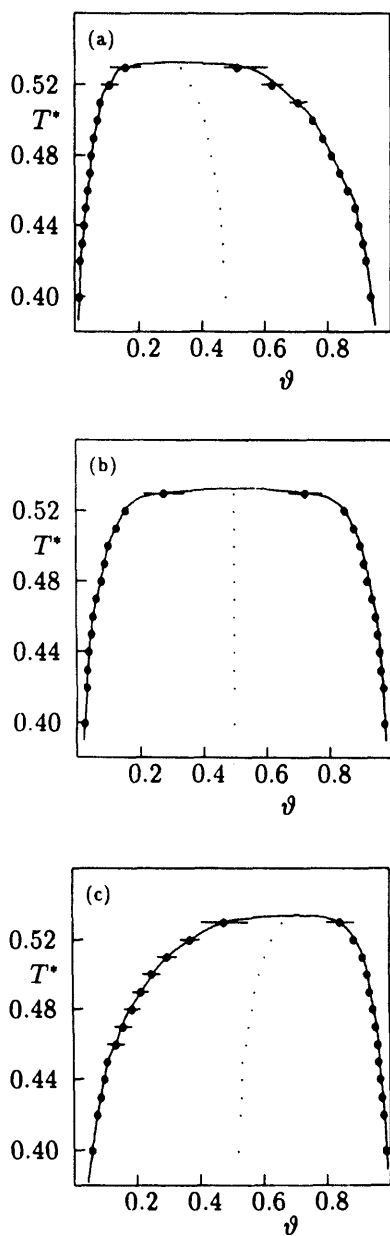


**FIG. 8** Phase diagrams for monolayer films on surfaces with boundary potential ( $V_b/u_{NN}$ ) equal to 0.25 (a), 0.50 (b), and 0.75 (c). (Reprinted with permission from: Langmuir 9:2562–2568, October 1993. © 1993, American Chemical Society.)

form of the patch size distribution function as well as on the magnitudes of the boundary fields. In particular, it has been demonstrated that the first-order character of adsorbate condensation is not observed and the adsorption isotherm shows a finite slope even at quite low temperatures.

The Monte Carlo simulation method has also been used by Patrykiewicz [125] to study phase transitions in adsorbed monolayers formed on a single heterogeneous surface with only two different values of adsorption energy. Sites of the same energy have been grouped into finite clusters of a given size and arranged in a regular, checkerboard, way over the surface.

Assuming that the interaction between the adsorbed particles is confined to the first nearest neighbors, the Hamiltonian of the model reads

$$\mathcal{H} = -\frac{1}{2} u_{NN} \sum_{\langle i,j \rangle} n_i n_j - \sum_{k=1}^2 V_k \sum_i n_i - \mu \sum_i n_i \quad (32)$$

The main controlling parameters of that model are the size of homogeneous clusters  $M$ , and the difference between the adsorption energies  $\Delta V = V_1 - V_2$ .

Already from the ground state analysis of the model it follows that for a given size of homogeneous domains  $M$  there exists a certain limiting value of  $\Delta V_0$

$$\Delta V_0 \propto \frac{1}{M} \quad (33)$$

delimiting the regions in which the adsorbed film shows qualitatively different behavior. For  $\Delta V$  lower than  $\Delta V_0$  the condensation in the adsorbed layer appears to be qualitatively the same as in a purely homogeneous system. Thus, one finds the first-order transition at sufficiently low temperatures and only the location of the critical point changes with  $\Delta V$  and  $M$ . For small values of the ratio  $\Delta V/\Delta V_0$  the critical temperature changes with  $\delta V$  as

$$\frac{T_c(0) - T_c(\Delta V)}{T_c(0)} \propto \left( \frac{\Delta V}{\Delta V_0} \right)^2 \quad (34)$$

independently of the size of the homogeneous domains. Application of the scaling theory [140] has confirmed that the observed transition belongs to the universality class of the two-dimensional Ising model.

On the other hand, whenever  $\Delta V$  exceeds the value of  $\Delta V_0$  the formation of a dense monolayer film appears to be the continuous process. It has been demonstrated that the observed crossover between those two regimes is due to the changes in the mechanism of the adsorbate nucleation, as determined by the calculation of the nucleated cluster size distribution functions. For

small differences in the adsorption energies the cluster size distribution function resembles that for a homogeneous system, while for large values of  $\Delta V$  ( $> \Delta V_0$ ) the cluster size distribution function indicates that the first stages of condensation are associated with the preferential occupation of strongly adsorbing sites. Then the nucleation spreads gradually towards less favorable regions of the surface.

From Eq. (33) it follows that, in the case of very large homogeneous domains, even very small heterogeneity effects should completely destroy any phase transition connected with the adsorbate condensation. This result is quite consistent with the theoretical predictions stemming from the random field Ising model [40,41].

The situation looks slightly different in the case of a simple model that assumes that there are only two types of randomly distributed sites [124]. When the contribution due to one type of site is sufficiently low, then the qualitative behavior of the adsorbed film is quite similar to that observed in adsorption on homogeneous surfaces. The effects of surface heterogeneity lead only to the lowering of the critical point of the adsorbate condensation and to the rounding of the low (high) density part of the adsorption isotherm when the impurity sites assume higher (lower) adsorption energy than the remaining part of the surface. In particular, the critical temperature appears to decrease linearly with the concentration of the impurities. Fig. 9 presents the changes of the critical point as a function of the impurity concentration obtained from the Monte Carlo simulation and from a simple mean field theory [124]. As expected, the results obtained from computer simulations predict much stronger heterogeneity effects than the mean-field theory. This is so because the mean-field theory neglects the effects of statistical fluctuations, which increase the entropy and hence lower the critical temperature.

Concluding this section, we shall briefly discuss the problem of surface heterogeneity effects on the commensurate-incommensurate (C-IC) transition in monolayer films [155–158]. In fact we do not know much about the changes in the behavior of incommensurate phases on weakly nonuniform surfaces. In particular, as far as we know no computer simulation studies of such effects have yet been reported. The only theoretical papers relevant to the present discussion are those published in the early 1980s by Villain [159,160] and we shall briefly discuss his argument. In Ref. 159 he considered the behavior of the hexagonal incommensurate phase close to the C-IC transition at zero temperature. The treatment is based on the theory of C-IC transition developed by Bak et al. [157] and uses the domain wall formalism, which is commonly accepted to be adequate for describing incommensurate phases in graphite and many other crystal surfaces. According to the domain wall theory [157], the incommensurate phase near the C-IC transi-



tion can be treated as a collection of practically fully commensurate domains separated by a network of walls. Only within those walls are the particles packed differently from in the domains. In the case of rare gas monolayers on graphite, there are three different, but fully equivalent, sublattices of adsorption sites and in the commensurate phase only one type of site is covered, which results simply from the system geometry. In the incommensurate phase, the domains with A, B and C occupied sublattices are present and the separating walls form a honeycomb lattice at zero temperature. The energy of such a system of walls can be represented as a sum of three contributions

$$E = \mu L + 2n_l \Lambda + C' L \exp[-\omega l \sqrt{3}] \quad (35)$$

where  $\mu$  is the chemical potential of the film,  $L$  is the total wall length in the monolayer,  $\Lambda$  and  $C'$  are constants assumed to be independent of  $\mu$ ,  $2n_l$  is

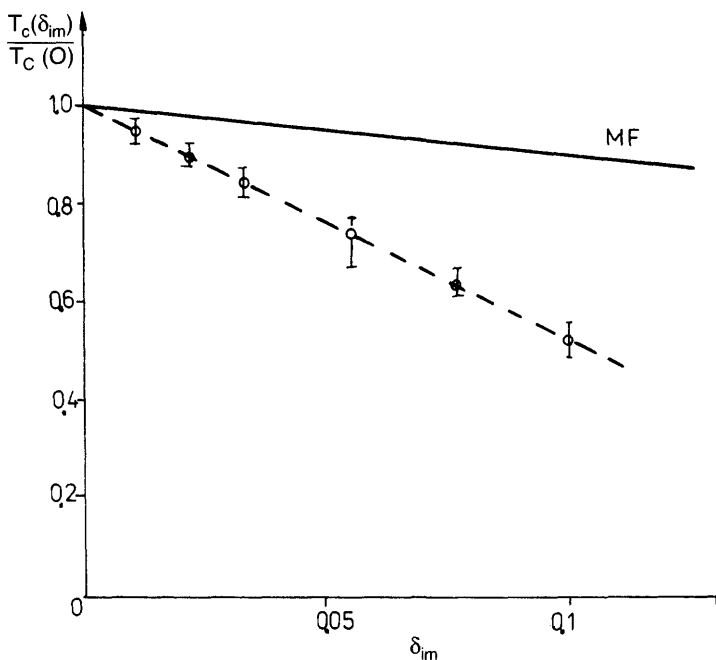


**FIG. 9** Changes of the monolayer film critical temperature with the concentration of impurities obtained from the Monte Carlo simulations (open circles) and resulting from the mean field theory (solid line). (Reprinted from: A. Patrykiewicz. Monte Carlo studies of adsorption. II: Localized monolayers on randomly heterogeneous surfaces. *Thin Solid Films*, 208:189–196, with permission from Elsevier Science.)

the number of wall intersections,  $\omega$  is a constant and  $l\sqrt{3}$  is the distance between the walls [161–164]. The above expression applies to the ideal network of domain walls at  $T = 0$ . Now, in the presence of surface defects, such as impurities, small terraces, etc., the above ideal structure of domain walls is perturbed. Defects create a sort of local random field which may favour occupation of one type of site (A, B, or C) and distort the structure of domain walls in order to achieve the most stable state. At  $T = 0$  this means the state of lower energy. The energy gain due to the distortion of the domain wall network structure can be represented as

$$\Delta E = -w_d A \sqrt{n_l/A} \quad (36)$$

where  $A$  is the total area of the surface and the parameter  $w_d$  is associated with the presence and type of defect. For an obvious reason,  $w_d$  must be greater than zero. Next, taking into account that by changing all sides of any hexagon of the honeycomb lattice the total wall length  $L$  and the number  $n_l$  remain unchanged, the final structure has energy equal to

$$E = \mu L - w_d A \sqrt{n_l/A} + 2n_l \Lambda + L[C_x \exp[-\omega l_x] + C_y \exp[-\omega l_y] + C_z \exp[-\omega l_z]] \quad (37)$$

where  $l_x$ ,  $l_y$ , and  $l_z$  are the lengths of differently oriented walls and the parameters  $C_x$ ,  $C_y$  and  $C_z$  are functions of  $l_x/l_z$  and  $l_y/l_z$ .

Considering the changes of  $E$  upon  $\mu$  for different values of the parameters, Villain has concluded that imperfections in the surface structure may have a very strong influence on the behavior of incommensurate phases and on the C–IC transition. The usual lowering of symmetry during the C–IC transition does not occur here and the nature of the C–IC transition may be quite different from that on the surface free of defects.

In the next paper [160], Villain discussed the model in which the local impurities are to some extent treated in the same fashion as in the random field Ising model, and concluded, in agreement with earlier predictions for RFIM [165], that the commensurate, ordered phase is always unstable, so that the C–IC transition is destroyed by impurities as well. The argument of Villain, though presented only for the special case of  $T = 0$ , suggests that at finite temperatures the effects of impurities should be even stronger, due to the presence of strong statistical fluctuations in two-dimensional systems which further destabilize the commensurate phase.

Of course, the above discussion applies only to systems exhibiting domain wall structure, i.e., to weakly inhomogeneous phases formed on surfaces with low corrugation of the gas–solid potential and characterized by the presence of more than one type of equivalent sublattices. When this is not the case, i.e., when the dense incommensurate phase can be considered to be

a floating solid, than the situation may look quite different. Since the compressibility of such a dense phase is rather small, its structure and stability should not be much affected by weak heterogeneity effects [32].

Experimental studies of heterogeneity effects on the C-IC transition seem to be very difficult. In particular, a unique interpretation of the phenomena observed in experiment as resulting from heterogeneity effects is presently impossible. Also, computer simulation calculations that aim at the study of such effects would require extremely large systems. We note that even in the case of a uniform system the observation of the development of the domain walls network requires a simulation containing well over 100 000 particles [166]. To detect and measure the effects of weak surface heterogeneity would require still larger systems and averaging over different realizations of disorder in the system. Calculations of that sort are presently impossible, due to outrageous cost and computing time required. Besides, the output of such calculations would still be quite uncertain.

#### **IV. MULTILAYER ADSORPTION AND WETTING PHENOMENA**

The presence of weak heterogeneities at the adsorbing surface has, of course, the strongest influence on the behavior of monolayer films. From the discussion of the previous section it clearly follows that even very weak heterogeneity effects may qualitatively change the behavior of adsorbed monolayers. The adsorbed particles located in the close vicinity of the surface can feel even very small local perturbations to the surface potential arising from the presence of heterogeneities. In physical adsorption we can assume that the interactions in the system, whether the adsorbate-adsorbate interaction or the interaction of the adsorbate with the adsorbent, are dominated by the van der Waals forces [11]. Adopting this picture, we know that, in general, the potential describing the admolecule-substrate interaction decays with the distance from the surface,  $z$ , as  $z^{-3}$  [11,42], so that it acts even at quite large distances from the surface. On the other hand, the potential representing the interaction between individual molecules decays with their mutual distance,  $r$ , as  $r^{-6}$ . So the influence of any local heterogeneity, e.g., the impurity atom built into the crystal lattice, small crack or step, produces the perturbation to the surface potential that also decays with the distance from the surface as  $z^{-6}$ . Here we can also mention that the periodic variations of the surface potential generated over an ideal crystal decay even more rapidly with  $z$ , as  $\exp[-qz]$  [167], where  $q$  is the length of the reciprocal surface lattice vector. Thus, a direct influence of such local heterogeneities on the particles located in the second and further

adsorbed layers is expected to be very small, if not entirely negligible. In real systems the situation looks considerably different since any local perturbations of the surface potential lead to the development of nonuniformities in the density distribution in the first layer, and these effects can be easily transmitted to subsequent layers. In this section we attempt to demonstrate that such transmission of heterogeneity effects does occur and leads to quite important effects. We concentrate the discussion on three main topics. The first problem which we shall consider here involves the effects of weak heterogeneity on the formation of multilayer films at low temperatures. We will be primarily interested in layering transitions and the effects of surface heterogeneity on their location and sharpness. Then we consider the effects of weak heterogeneity on wetting phenomena. The above two problems are closely related to each other, as will be shown shortly. Finally we will discuss the problem of wetting phenomena on strongly heterogeneous surfaces.

To present briefly the different possible scenarios for the growth of multilayer films on a homogeneous surface, it is very convenient to use a simple lattice gas model language [168]. Assuming that the surface is a two-dimensional square lattice of sites and that also the entire space above the surface is divided into small elements, forming a cubic lattice such that each of the cells can be occupied by one adsorbate particle at the most, the Hamiltonian of the system can be written as [168,169]

$$\mathcal{H} = \frac{1}{2} u \sum_{\langle i,j \rangle} n_i n_j + \sum_i V(i) n_i - \mu \sum_i n_i \quad (38)$$

In the above we have assumed that the interaction between the adsorbate particles is short-ranged and confined to the first nearest neighbors,  $u$  being the energy of that interaction,  $V(i)$  representing the surface potential acting on the  $i$ th site,  $\mu$  the chemical potential and  $n_i = 0$  (1) when the  $i$ th site is empty (occupied). In the case of a homogeneous surface the potential  $V(i)$  depends only on the distance from the surface, i.e., on the number of layer,  $l$ , and can be represented as [169]

$$V(l) = V_0/l^3 \quad (39)$$

where  $V_0$  is the energy of adsorption for the adsorbate particles located in the first layer adjacent to the surface.

It has been demonstrated in a very elegant way by Pandit *et al.* [168] that mechanism of multilayer film formation depends crucially on the ratio  $V_0/u$ . When this ratio is sufficiently high, i.e., when the surface is highly attractive towards the adsorbate, the film grows in a layer-by-layer mode. At low temperatures this corresponds to the presence of a series of layering

transitions which terminate at the corresponding critical points  $T_c(l)$ . From the mean-field theory it follows that

$$\lim_{l \rightarrow \infty} T_c(l) = T_c^{3D} \quad (40)$$

where  $T_c^{3D}$  is the critical temperature of the uniform bulk gas, while the exact result is [170]

$$\lim_{l \rightarrow \infty} T_c(l) = T_R \quad (41)$$

where  $T_R$  is the roughening temperature, which in general is much lower than  $T_c^{3D}$  and only slightly exceeds  $T_c(1) \approx 0.5674u/k$  [170] ( $k$  is the Boltzmann constant). In the above situation the adsorbate wets the surface at any temperature down to  $T = 0$ .

When the ratio  $V_0/u$  becomes lower than the value for which

$$\frac{V_0}{u} < \left[ \sum_{l=1}^{\infty} l^{-3} \right]^{-1} \quad (42)$$

the adsorbate does not wet the surface at  $T = 0$ , but may still exhibit complete wetting at temperatures which exceed the wetting temperature  $T_W$ . Thus, below  $T_W$  the film thickness remains finite up to the bulk condensation point, while for  $T > T_W$  we observe again the formation of macroscopically thick adsorbed film as the chemical potential approaches its bulk coexistence value. That change of the film behavior at  $T_W$  marks the so-called *wetting transition* which can be either the first-order transition or the continuous transition (critical wetting), depending on the value of  $V_0/u$  and on the range of molecular interactions in the system [171]. When the wetting transition is first order it is often preceded by the *prewetting transition* between the thin and thick film. The prewetting transition occurs at a chemical potential below the bulk coexistence value. As the temperature increases, the prewetting transition terminates at the corresponding critical point. Due to the finite extent of thin and thick films on both sides of the prewetting transition, it belongs to the universality class of the two-dimensional Ising model.

Here we consider the problem of changes in the picture presented above when the adsorbing surface is not homogeneous but exhibits various heterogeneities of energetical as well as geometrical nature. Let us begin with the assumption that the adsorption energy is not constant but assumes different values for different adsorption sites. We can assume that the AEDF is such that

$$V_{0,i} = V_0 + \delta V_{0,i} \quad (43)$$

with  $\delta V_{0,i}$  being a random variable of zero mean. This last assumption allows us to consider all shifts in the location of any phase transitions in the system as resulting entirely from the perturbations due to heterogeneity effects.

The mean field treatment of such a model has been presented by Forgacs *et al.* [172]. They have considered the particular problem of the effects of surface heterogeneity on the order of wetting transition. Using the replica trick and assuming a Gaussian distribution of  $\delta V_0$  with the variance  $\Delta$  ( $\Delta/kT \ll 1$ ), they found that the prewetting transition critical point is a function of  $\Delta$  and

$$T_c(\Delta) = T_c(0) \left[ 1 - \left( \frac{\Delta}{kT_c(0)} \right)^2 \right] \quad (44)$$

Thus, an increase in the distribution width ( $\Delta$ ) leads to a decrease in the critical temperature of the prewetting point. Besides, under the simplifying assumption that the heterogeneity effects are directly felt only by the particles from the first layer, they found that the wetting transition, which is first order in a pure system, becomes continuous in the presence of randomly distributed heterogeneities. This, of course, occurs only when the heterogeneity becomes strong enough. Infinitesimal heterogeneity does not change the character of the wetting transition, according to the mean-field predictions at least.

Monte Carlo studies of layering transitions on heterogeneous surfaces have been carried out by Gac *et al.* [173]. The results reported in Ref. 173 have been obtained for three different models of heterogeneous surface. The first model assumed that the surface is composed of only two types of (strong and weak) adsorption site. The second model assumed the discrete Gaussian distribution of adsorption energies, while the third model corresponded to, also discrete, uniform distribution of adsorption energies. In all cases the adsorbate-substrate interaction potential has been assumed to be given by the potential (39) with different values of the parameter  $V_0$  for each type of adsorption site.

In the case of the first model, and when both types of site are strong enough to lead to the sequence of layering transitions  $0 \rightarrow 1 \rightarrow 2 \rightarrow 3 \dots$ , the main effect of surface heterogeneity was found to be a gradual decrease of the critical temperature for each layering transition. Of course, the greatest changes are observed in the first layer, adjacent to the solid surface, while the changes of the critical point in the second and subsequent layers are much smaller. This results directly from the assumed form of the adsorbate-substrate potential, which decays quite rapidly with distance from the solid surface.

In the case of Gaussian and uniform distributions of the adsorption energy, the smearing of the phase transition region in the first as well as higher layers was observed. Thus, instead of vertical jumps, the adsorption isotherms exhibited only finite slope even at quite low temperatures. This result is consistent with the predictions of Dash and Puff [32].

The problem of wetting phenomena on both energetically and geometrically heterogeneous surfaces has recently been a subject of quite intensive theoretical [174–186], experimental [187–194] and computer simulation [195,196] studies. The first theoretical work devoted to the question of surface heterogeneity effects on the shape of the interface between a thick adsorbed layer of liquid and the bulk gas was published as early as 1976 by Cole and Vittoratos [186]. In fact, they did not consider wetting phenomena, as the very idea of wetting transition came up a year later [197,198]. Those authors have discussed the density profiles of the film adsorbed on a heterogeneous surface. They considered a very simple model of dual surface, composed of two differently adsorbing parts. The free energy functional of the system assumed the following simple form

$$F(\{l(x)\}) = F_0(T) + \int_{-L_x}^{+L_x} f(x, \{l(x)\}) dx \quad (45)$$

where  $F_0(T)$  is the bulk liquid free energy and  $f(x, \{l(x)\})$  is the free energy density of the adsorbed layer at the point  $x$ , over which the film thickness is  $l(x)$ . The expression for  $f(x, \{l(x)\})$  was approximated as

$$f(x, \{l(x)\}) dx = \sigma_{gl} \left[ \sqrt{1 - [\nabla l(x)]^2} - 1 \right] + \rho \int_0^{l(x)} V(x, l') dl' \quad (46)$$

where  $\sigma_{gl}$  is the gas–liquid surface tension,  $\rho$  is the film number density and  $V(x, l)$  is the surface potential. Minimizing the free energy difference  $\Delta F = F - F_0$  with respect to  $l(x)$  for the specified form of  $V(x, l)$  they obtained a quite simple equation for the equilibrium shape of the density profile  $l(x)$ . Numerical calculations showed that the film thickness on different portions of the surface is different and that the transition region between uniform parts of the density profile depends on the difference in the surface potentials representing each type of surface as well as on the average film thickness. In particular, they demonstrated that the size of the transition region grows with the film thickness and becomes narrow and sharp for a very thin film consisting of just a couple of layers. Similar geometrical models of the surface have been recently considered by Napiórkowski et al. [183] and by Koch et al. [199], who used the density functional theory and explicitly included long-range interactions between

the fluid particles as well as between the fluid and the substrate. The grand canonical functional of the free energy assumes the form

$$\Omega[\{\rho(r)\}; T, \mu] = \int dr f_h(\rho(r), T) + \int dr [V(r) - \mu] \rho(r) + \frac{1}{2} \int dr \int dr' \rho(r) \rho(r') \tilde{w}(|r - r'|) \quad (47)$$

where the first term is the free energy of the hard sphere reference fluid of the density  $\rho$ ,  $\rho(r)$  is the local density at the point  $r = (x, y, z)$ ,  $\mu$  is the fluid chemical potential, and  $\tilde{w}(|r - r'|)$  is the attractive part of the potential representing the interaction between fluid particles. Both  $V(r)$  and  $\tilde{w}(r)$  have been assumed to be long-range potentials. As the distance from the surface ( $z$ ) becomes large the potential  $V(r)$  decays as  $z^{-3}$  while the potential  $\tilde{w}(r)$  decays as  $1/r^6$  for large  $r$ . In the model assumed here the fluid-substrate potential depends only on  $x$  and  $z$ , so does the local density and we can write  $\rho(x, z)$  instead of  $\rho(r)$ .

In the limit of infinite system size in the  $y$  direction, the free energy functional can be represented as a sum of bulk ( $\Omega_b$ ), surface ( $\Omega_s^{\parallel}$  and  $\Omega_s^{\perp}$ ), and line ( $\Omega_l$ ) contributions as

$$\begin{aligned} \lim_{L_y \rightarrow \infty} \Omega[\{\rho(x, z)\}; T, \mu] / L_y &= L_x L_z \Omega_b(\rho_b, T, \mu) \\ &+ L_x \Omega_s^{\parallel}[\{\rho_A(z)\}, \{\rho_B(z)\}; T, \mu, \rho_l, \rho_g] \\ &+ L_z \Omega_s^{\perp}(\rho_g, T, \mu) + \Omega_l[\{\rho(x, z)\}, T, \mu, \rho_l, \rho_g] \end{aligned} \quad (48)$$

The bulk contribution, as well as the surface contribution  $\Omega_s^{\perp*}$ , depends only on the bulk gas density  $\rho_g$ . Then the surface contribution  $\Omega_s^{\parallel}$  depends only on the asymptotic density profiles  $\rho_A(z)$  and  $\rho_B(z)$  corresponding to adsorbed layers formed over semi-infinite uniform surfaces  $A$  and  $B$ , i.e., when  $x \rightarrow \pm\infty$ . The line contribution  $\Omega_l$  can also be decomposed into an artificial term, resulting from the lateral cutoff, and a "physical" term as

$$\Omega_l[\{\rho(x, z)\}, T, \mu] = \Omega_{l, \text{art}}[\{\rho_A(z)\}, \{\rho_B(z)\}, T, \mu] + \Omega_{l, \text{phys}}[\{\rho(x, z)\}, T, \mu] \quad (49)$$

\*This is the artificial contribution resulting only from the presence of lateral cutoff at  $x = \pm L_x/2$ .



Thus, the only term that determines the full density profile  $\rho(x, z)$  is the physical part of the line contribution, and the condition for the equilibrium density profile  $\bar{\rho}(x, z)$  reads

$$\left. \frac{\delta \Omega}{\delta \rho} \right|_{\rho=\bar{\rho}(x,z)} \equiv \left. \frac{\delta \Omega_{l,\text{phys}}}{\delta \rho} \right|_{\rho=\bar{\rho}(x,z)} = 0 \quad (50)$$

When applied to the grand canonical free energy functional (47) the above condition leads to the following integral equation

$$\mu - \mu_h(\bar{\rho}(x, z), T) = V(x, z) + \int_{-\infty}^{\infty} dx' \int_0^{\infty} dz' \bar{w}(|x - x'|, |z - z'|) \bar{\rho}(x', z') \quad (51)$$

where

$$\mu_h(\rho(x, z), T) = \frac{\partial f_h(\rho(x, z), T)}{\partial \rho} \quad (52)$$

and

$$\bar{w}(x, z) = \int_{-\infty}^{\infty} dy \tilde{w}(\sqrt{x^2 + y^2 + z^2}) \quad (53)$$

Having solved Eq. (51), which is subject to the boundary conditions  $\rho(x \rightarrow -\infty, z) = \bar{\rho}_A(z)$  and  $\rho(x \rightarrow \infty, z) = \bar{\rho}_B(z)$ , one obtains  $\bar{\rho}(x, z)$ .

Numerical solution of Eq. (51) was carried out for a nonlocal effective Hamiltonian as well as for the approximated local Hamiltonian obtained by applying a gradient expansion. It was demonstrated that the nonlocal effective Hamiltonian represents quite well the lateral variation of the film density distribution. The results obtained showed also that the film behavior on the inhomogeneous substrate depends crucially on the temperature regime. Note that the film exhibits different wetting temperatures on both parts of the surface. For chemical potential below the bulk coexistence value the film thickness on both parts of the surface tends to appropriate asymptotic values at  $x \pm \infty$  and obeys the power law  $x^{-3}$ . Such a behavior of the film thickness is a consequence of van der Waals tails. The above result is valid when both parts of the surface exhibit either continuous (critical) or first-order wetting.

When the temperature lies in between the wetting temperatures of both substrates, then one substrate is wet and the film thickness on that part diverges when the distance from the boundary between different substrates increases. This divergence is found to be represented by a power law  $x^{1/2}$  for

the first-order wetting and  $x^{2/5}$  for the critical wetting. In the close vicinity of the wetting transition the interface profile broadens and exhibits specific scaling behavior

$$\bar{l}(x) = \bar{l}_B f(x/\xi_\perp) \quad (54)$$

where the normal correlation length  $\xi_{\text{bot}}$  scales as  $\bar{l}_B^2$  and the scaling function shows the following asymptotic behavior

$$f(\infty) = 1 \text{ and } f(x/\xi_\perp \rightarrow 0) \simeq \left(\frac{x}{\xi_\perp}\right)^{1/2} \quad (55)$$

Similar systems of dual surfaces were studied by Monte Carlo simulation for lattice systems [196]. The model assumed that there exists a narrow strip of weakly adsorbing sites surrounded by strongly adsorbing sites. It has been demonstrated that surface nonuniformity plays an important role in the first stages of film growth and the density distribution shows spatial nonuniformities which depend on the width and the energy of the weakly and strongly adsorbing parts of the surface. One of the interesting results emerging from the performed calculations is the observation of two regimes of film growth. In the case of small difference in adsorption energies on both types of site and when the width of the weakly adsorbing strip is narrower than a certain limiting value  $L_{\text{lim}}$ , the film spreads over the entire surface and shows only small lateral changes. In the case of large differences between adsorption energies and when the width of the weakly adsorbing strip is large enough, a drop of liquid-like film forms only over the strongly adsorbing sites, while the weakly adsorbing surface remains nearly empty. The transition between these regimes is quite sharp. In this second situation, and when the temperature exceeds the wetting temperature of the strongly adsorbing surface, the film thickness is found to diverge when the chemical potential approaches the bulk coexistence, and the transition between the drop-like and uniform regimes is found to be a first-order transition.

The more general problem of surface heterogeneity effects on wetting phenomena was considered by Borgs et al. [200], Netz and Andelman [185], Swain and Parry [201], and by Giugliarelli and Stella [202]. Borgs et al. [200] addressed the problem of wetting on a rough surface using the Ising model formalism. They derived the expression for the difference between the gas-wall ( $f_{\text{gw}}$ ) and the fluid-wall ( $f_{\text{fw}}$ ) free energies in terms of the roughness parameter

$$r = \frac{A}{A_0} \quad (56)$$

where  $A$  and  $A_0$  are the areas of the rough and the corresponding flat surfaces. Their analysis showed that at sufficiently low temperatures the following relation is satisfied

$$\Delta f(r) = f_{\text{gw}} - f_{\text{lw}} \geq rf(1) \quad (57)$$

The above inequality implies that the surface roughness enhances wetting whenever  $\Delta f(1) > 0$  and is quite consistent with the experimentally determined Wenzel law [203]

$$f_{\text{gl}} \cos \theta_r \simeq r \Delta f(1) \quad (58)$$

where  $f_{\text{gl}}$  is the gas–liquid interface free energy and  $\theta_r$  is the contact angle of a drop deposited on a rough surface.

The same general result was obtained by Netz and Andelman [185], who presented a very elegant phenomenological argument. Apart from the necessary condition for roughness-induced wetting, given by Eq. (57), they also derived explicit expression for the sufficient condition for roughness induced wetting when the surface has sinusoidal undulations along one direction with the amplitude low enough for the harmonic approximation to apply. Here we discuss briefly some basic points of the theory used by Netz and Andelman [185] as it shows in a simple way how the problem can be attacked.

First, we recall the expression for the free energy of a liquid layer of finite thickness  $l$  formed on a flat surface

$$F_0(l) = \gamma_{\text{lw}} + \gamma_{\text{lg}} + \Delta\mu l + y_0(l) \quad (59)$$

where  $\gamma_{\text{lw}}$  and  $\gamma_{\text{lg}}$  are the liquid–wall and the liquid–gas interfacial tensions,  $\Delta\mu$  is the chemical potential difference between the liquid and gas phases, while  $y_0(l)$  is the contribution due to interaction between the two flat interfaces (liquid–wall and liquid–gas), which are at a distance  $l$  one from another, and depends on the form of the interaction potentials operating in the system.

For  $l$  approaching zero,  $y_0(l)$  is a constant known as the spreading coefficient, defined as  $s = \gamma_{\text{gw}} - \gamma_{\text{lw}} - \gamma_{\text{lg}}$ . In the limit of  $l \rightarrow \infty$  the two interfaces become decoupled and hence  $y_0(l)$  is expected to vanish.

In the case of a rough surface, the expression for the free energy of a liquid layer, per unit projected area, can be represented as

$$F(x, y, [\zeta_{\text{liq}}]) = \sqrt{1 + [\Delta\zeta_{\text{w}}(x, y)]^2} \gamma_{\text{lw}} + \sqrt{1 + [\Delta\zeta_{\text{liq}}(x, y)]^2} \gamma_{\text{lg}} + \Delta\mu[\zeta_{\text{liq}}(x, y)] - \zeta_{\text{w}}(x, y) + y(x, y, [\zeta_{\text{liq}}]) \quad (60)$$

where  $\zeta_{\text{liq}}(x, y)$  and  $\zeta_{\text{w}}(x, y)$  represent local variations of the liquid layer and the substrate interfaces. After averaging over the in-plane coordinates  $x$  and  $y$ , the effective free energy is given by

$$F_{\text{eff}}(l, [\zeta_{\text{liq}}]) = \alpha_{\text{w}}\gamma_{\text{lw}} + \alpha_{\text{liq}}(l, [\zeta_{\text{liq}}])\gamma_{\text{lg}} + \gamma_{\text{eff}}(l, [\zeta_{\text{liq}}]) + \Delta\mu l \quad (61)$$

where

$$l = \langle \zeta_{\text{liq}}(x, y) - \zeta_{\text{w}}(x, y) \rangle_{x,y} \quad (62)$$

and

$$\gamma_{\text{eff}}(l, [\zeta_{\text{liq}}]) = \langle \gamma(x, y, [\zeta_{\text{liq}}]) \rangle_{x,y} \quad (63)$$

The parameters  $\alpha_{\text{w}}$  and  $\alpha_{\text{liq}}(l, [\zeta_{\text{liq}}])$  are defined as the averages of the first two terms entering Eq. (60).

Within the mean-field approximation one can minimize the free energy (64) with respect to a fixed profile  $\zeta_{\text{liq}}^*$  and this leads to the minimized free energy  $F^*(l)$ . Next, one can define the free energy difference

$$\Delta F(l, [\zeta_{\text{liq}}]) = F_{\text{eff}}(l, [\zeta_{\text{liq}}]) - F^*(\infty) \quad (64)$$

which, for  $\Delta\mu = 0$ , is equal to

$$\Delta F(l, [\zeta_{\text{liq}}]) = \gamma_{\text{lg}} \{ \alpha_{\text{liq}}(l, [\zeta_{\text{liq}}]) - 1 \} + \gamma_{\text{eff}}(l, [\zeta_{\text{liq}}]) \quad (65)$$

Now, minimizing  $\Delta F(l, [\zeta_{\text{liq}}])$  with respect to  $\zeta_{\text{liq}}$  leads to the following limiting values of  $\Delta F^*(l)$

$$\Delta F^*(l) = \begin{cases} \alpha_{\text{s}}(\gamma_{\text{gw}} - \gamma_{\text{lw}}) - \gamma_{\text{lg}} & l \rightarrow 0 \\ 0 & l \rightarrow \infty \end{cases} \quad (66)$$

The necessary condition for wetting is that  $\Delta F^*(l) > 0$  for any value of  $l < \infty$ .

When the flat substrate is not wet ( $s < 0$ ), the wetting of a rough surface requires that the spreading coefficient

$$s = (\alpha_{\text{w}} - 1)\gamma_{\text{lg}} + \alpha_{\text{w}}s \quad (67)$$

is larger than zero. This requirement leads to the following inequality

$$\gamma_{\text{gw}} - \gamma_{\text{lw}} < \gamma_{\text{lg}} < \alpha_{\text{w}}(\gamma_{\text{gw}} - \gamma_{\text{lw}}) \quad (68)$$

For the rough surface,  $\alpha_{\text{w}} \geq 0$  and one obtains that  $\gamma_{\text{lg}} > -s$  must hold. Eq. (71) leads also to the following lower bound for the surface ratio  $\alpha_{\text{w}}$ :

$$\alpha_{\text{w}} > \frac{1}{1 + s/\gamma_{\text{lg}}} \quad (69)$$

The above equations (68) and (69) do not guarantee wetting of a rough substrate and express only the fact that the interfacial free energy of a thick

liquid layer ( $l \rightarrow \infty$ ) is lower than the free energy of a film with vanishing thickness ( $l \rightarrow 0$ ). It is possible that the free energy  $\Delta F^*(l)$  exhibits a local minimum for a finite film thickness.

It is an extremely difficult task to establish generally valid sufficient conditions for roughness-induced wetting. This is a direct consequence of the loss of translational invariance in such systems. A vast majority of the hitherto performed calculations [185,201] have been based on a simplified model of a rough substrate which assumes periodic variation of the substrate surface location.

Netz and Andelman [185] derived the sufficient condition for roughness-induced wetting using the harmonic approximation to the model with sinusoidal variation of the substrate surface position. They determined the lower bound for  $y_0(l)$  which delimits the nonwetting and wetting regimes. Thus, wetting occurs whenever  $y_0(l)$  exceeds this lower bound  $y_{0,\text{low}}(l)$ . It should be noted that  $y_{0,\text{low}}(l)$  depends on the amplitude of the surface corrugation as well as on the assumed models for the interactions operating in the system.

Parry et al. [204] also studied wetting transition at a periodic rough wall using a Landau square gradient theory and concluded that the surface roughness may change the order of the wetting transition. In particular, the critical wetting transition occurring at a flat surface becomes a first-order transition when the root mean square amplitude of the corrugation is higher than a certain tricritical value.

Wetting phenomena on irregularly rough surfaces have not been studied so far. It seems quite reasonable to use computer simulation methods for this purpose. Of course, such computer simulation would be very expensive as the finite size of the simulation cells would require appropriate averaging over different spatial distributions of surface inhomogeneities. Nevertheless, with modern fast computers and using multispin coding techniques such calculations can be efficiently carried out for lattice gas systems.

## ACKNOWLEDGMENTS

Authors thank the KBN (Poland) for partial financial support under the Grant No. 3TO9A 08216.

## REFERENCES

1. I. Langmuir. *J Amer Chem Soc* 40:1361–1370, 1918.
2. R. Sips. *J Chem Phys* 16:490–495, 1949.
3. R. Sips. *J Chem Phys* 18:1024–1026, 1950.
4. S. Ross, J. P. Olivier. *On Physical Adsorption*. New York: Interscience, 1964.

5. M. Jaroniec, R. Madey. *Physical Adsorption on Heterogeneous Surfaces*. Amsterdam: Elsevier, 1988.
6. W. Rudziński, D. H. Everett. *Adsorption of Gases on Heterogeneous Surfaces*. New York: Academic Press, 1992.
7. W. Rudziński, M. Jaroniec. *Surface Sci* 42:552–564, 1974.
8. M. Jaroniec, P. Bräuer. *Surface Sci Rep* 6:65–118, 1986.
9. M. Jaroniec, A. Patrykiewicz, M. Borówko. In: D. A. Cadenhead, J. F. Danielli, eds, *Progress in Surface and Membrane Science, Vol 14*. New York: Academic Press, 1981, pp 1–68.
10. M. Jaroniec. *Adv Coll Interface Sci* 18:149–225, 1983.
11. J. G. Dash. *Films on Solid Surfaces*. New York: Academic Press, 1975.
12. W. Rudziński, G. Zgrablich, eds. Equilibria dynamics of gas adsorption on heterogeneous solid surfaces. In: *Studies in Surface Science and Catalysis, Vol 104*. Amsterdam: Elsevier, 1997.
13. W. Rudziński, J. Jagiełło. *J Low Temp Phys* 45:1–19, 1981.
14. W. A. House, M. J. Jaycock. *J Coll Interface Sci* 59:252–265, 1977.
15. D. J. Jackson, B. W. Davis. *J Coll Interface Sci* 47:499–514, 1974.
16. G. F. Cerofolini. *Surface Sci* 24:391–403, 1971.
17. G. F. Cerofolini. *Surface Sci* 47:469–476, 1975.
18. C. C. Hsu, W. Rudziński, B. W. Wojciechowski. *Phys Lett A* 54:365–369, 1975.
19. I. D. Morrison, S. Ross. *Surface Sci* 39:21–36, 1973.
20. A. W. Adamson, I. Ling. *Adv Chem Ser* 33:51–61, 1961.
21. W. A. House, M. J. Jaycock. *J Coll Polymer Sci* 256:52–61, 1978.
22. B. J. Stanley, S. E. Bialkowski, D. B. Marshall. *Anal Chem* 65:259–267, 1993.
23. B. J. Stanley, G. Guiochon. *J Phys Chem* 97:8098–8104, 1993.
24. M. M. Dubinin, L. V. Radushkevich. *C R (Dokl) Acad Sci USSR* 55:327–333, 1947.
25. H. Freundlich. *Trans Faraday Soc* 28:195–201, 1932.
26. A. Patrykiewicz, M. Jaroniec, A. Dabrowski. J. Toth. *Croat Chem Acta* 53:9–23, 1980.
27. S. W. Provencher. *Comput Phys Commun* 27:213–228, 1982.
28. L. E. Drain, J. A. Morrison. *Trans Faraday Soc* 48:316–326, 1952.
29. L. E. Drain, J. A. Morrison. *Trans Faraday Soc* 48:840–847, 1952.
30. D. W. Princehouse. *J Low Temp Phys* 8:287–303, 1972.
31. S. Cerný, M. Smutek, F. Buzek. *J Catal* 38:245–256, 1975.
32. J. G. Dash, R. D. Puff. *Phys Rev B* 24:295–309, 1981.
33. R. L. Elgin, D. L. Goodstein. *Phys Rev A* 9:2657–2675, 1974.
34. A. Thomy, X. Duval, R. Regnier. *Surf Sci Rep* 1:1–38, 1981.
35. A. Patrykiewicz, M. Jaroniec. *Adv Coll Interface Sci* 20:273–339, 1984.
36. K. J. Strandburg. *Rev Mod Phys* 60:161–207, 1988.
37. K. Binder. In: F. R. de Boer, D. G. Pettifor, eds. *Cohesion and Structure of Surfaces*. Amsterdam: Elsevier, 1995, pp. 121–283.
38. K. Binder, D. P. Landau. *Adv Chem Phys* 76:91–152, 1989.
39. K. Binder, W. Kinzel, D. P. Landau. *Surface Sci* 117:232–244, 1982.

40. Y. Imry, S. K. Ma. *Phys Rev Lett* 35:1399–1401, 1975.
41. I. Morgernstern, K. Binder, R. M. Hornreich. *Phys Rev B* 23:287–297, 1981.
42. W. A. Steele. *The Interaction of Gases with Solid Surfaces*. New York: Pergamon, 1974.
43. P. Ripa, G. Zgrablich. *J Phys Chem* 79:2118–2122, 1975.
44. A. J. Ramirez-Pastor, M. S. Nazzaro, J. L. Ricardo, G. Zgrablich. *Surface Sci* 341:249–261, 1995.
45. J. L. Ricardo, M. A. Chade, V. D. Pereyra, G. Zgrablich. *Langmuir* 8:1518–1531, 1995.
46. W. Rudziński, L. Łajtar, A. Patrykiewicz. *Surface Sci* 67:195–204, 1977.
47. W. Rudziński, J. Jagiello, Y. Grillet. *J Coll Interface Sci* 87:478–491, 1982.
48. W. Rudziński, J. Baszyńska. *Z Phys Chem Leipzig* 262:533–550, 1981.
49. K. Binder, ed. *Monte Carlo Methods in Statistical Physics*. Berlin: Springer, 1986.
50. D. Nicholson, N. G. Parsonage. *Computer Simulations and Statistical Mechanics of Adsorption*. London: Academic Press, 1982.
51. K. Binder, ed. *Applications of Monte Carlo Methods in Statistical Physics*. Berlin: Springer, 1984.
52. M. P. Allan, D. J. Tildesley. *Computer Simulation of Liquids*. Oxford: Oxford University Press, 1987.
53. A. W. Adamson, I. Ling, L. Dormant, M. Orem. *J Coll Interface Sci* 21:445–457, 1966.
54. L. B. Harris. *Surface Sci* 10:129–145, 1968.
55. L. B. Harris. *Surface Sci* 13:377–392, 1969.
56. W. Rudziński, J. Narkiewicz, A. Patrykiewicz. *Z Phys Chem* 260:1097–1112, 1979.
57. A. Patrykiewicz. *Langmuir* 9:2562–2568, 1993.
58. M. E. Fisher, A. N. Berker. *Phys Rev B* 26:2507–2513, 1982.
59. U. Bardi, A. Glachant, M. Bienfait. *Surf Sci* 97:137–157, 1980.
60. J. P. Coulomb, O. E. Vilches. *J Phys (Paris)* 45:1381–1389, 1984.
61. J. P. Coulomb. In: H. Taub, G. Torzo, H. J. Lauter, S. C. Fain Jr, eds. *Phase Transitions in Surface Films, Vol. 2*. New York: Plenum Press, 1991, pp. 113–134.
62. K. Christmann. *Introduction to Surface Physical Chemistry*. Darmstadt: Steinkopff Verlag, 1991.
63. A. Clark. *The Theory of Adsorption and Catalysis*. New York: Academic Press, 1972.
64. W. H. Press, B. P. Flannery, S. A. Teukolsky, W. T. Vetterling. *Numerical Recipes in C*. Cambridge: Cambridge University Press, 1988.
65. H. Rieger, A. P. Young. *J Phys* 26:5279–5284, 1993.
66. A. Patrykiewicz, K. Binder. *Surf Sci* 273:413–426, 1992.
67. N. G. Van Kampen. *Stochastic Processes in Physics and Chemistry*. Amsterdam: North-Holland, 1981.
68. A. Patrykiewicz. *Pol J Chem* 68:1405–1426, 1994.
69. J. Cortés, E. Valencia, P. Araya. *J Chem Phys* 100:7672–7676, 1994.

70. A. Milchev, K. Binder, D. W. Heermann. *Z Phys B* 63:521–535, 1986.
71. N. N. Roy, G. D. Halsey. *J Low Temp Phys* 4:231–237, 1971.
72. J. L. Riccardo, V. Pereyra, J. L. Rezzano, D. A. Rodriguez Saa, G. Zgrablich. *Surf Sci* 204:289–297, 1988.
73. J. L. Riccardo, V. Pereyra, G. Zgrablich, F. Rojas, V. Mayagoitia, I. Kornhauser. *Langmuir* 9:2730–2736, 1993.
74. V. Mayagoitia, F. Rojas, V. D. Pereyra, G. Zgrablich. *Surf Sci* 221:394–408, 1989.
75. V. Mayagoitia, F. Rojas, J. L. Riccardo, V. D. Pereyra, G. Zgrablich. *Phys Rev B* 41:7150–7155, 1990.
76. A. M. Baro, G. Binnig, H. Rohrer, Ch. Gerber, E. Stoll, A. Bartoff, F. Salvan. *Phys Rev Lett* 52:1304–1307, 1984.
77. G. Binnig, H. Fuchs, E. Stoll. *Surf Sci* 169:L295–L300, 1986.
78. R. Zallen. *The Physics of Amorphous Solids*. New York: Interscience, 1983.
79. E. I. Benegas, V. D. Pereyra, G. Zgrablich. *Surf Sci* 187:L647–L653, 1987.
80. J. D. Bernal. *Proc Roy Soc London A* 284:299–308, 1964.
81. V. A. Bakaev, W. A. Steele. *Langmuir* 8:148–154, 1992.
82. V. A. Bakaev, W. A. Steele. *Langmuir* 8:1379–1384, 1992.
83. V. A. Bakaev, W. A. Steele. *J Chem Phys* 98:9922–9932, 1993.
84. M. J. Bojan, A. V. Vernov, W. A. Steele. *Langmuir* 8:901–908, 1992.
85. S. E. Edwards, P. W. Anderson. *J Phys F* 5:965–974, 1975.
86. T. Schneider, E. Pytte. *Phys Rev B* 15:1519–1522, 1977.
87. W. Kinzel. *Phys Rev B* 27:5819–5820, 1983.
88. D. P. Belanger, A. P. Young. *J Magn & Magn Mater* 100:272–291, 1991.
89. A. Bonissent, B. Mutaftschiev. *Philos Mag* 35:65–72, 1977.
90. V. A. Bakaev. *Surf Sci* 198:571–592, 1988.
91. V. A. Bakaev, A. V. Voit. *Izv Akad Nauk SSSR, Ser Khim* 2007, 1990.
92. E. V. Albano, K. Binder, D. W. Heermann, W. Paul. *Z Phys B* 77:445–460, 1989.
93. E. V. Albano, K. Binder, D. W. Heermann, W. Paul. *Surf Sci* 223:151–178, 1989.
94. E. V. Albano, K. Binder, D. W. Heermann, W. Paul. *J Chem Phys* 91:3700–3706, 1989.
95. K. Christmann, G. Ertl. *Surf Sci* 60:365–384, 1976.
96. R. Miranda, S. Daiser, K. Wandelt, G. Ertl. *Surf Sci* 131:61–91, 1983.
97. R. Miranda, E. V. Albano, S. Daiser, K. Wandelt, G. Ertl. *J Chem Phys* 80:2931–2938, 1984.
98. J. Merikoski, J. Timonen, K. Kaski. *Phys Rev B* 50:7925–7931, 1994.
99. J. Merikoski, S. C. Ying. *Surf Sci* 381:L623–L627, 1997.
100. V. Bakaev. *J Chem Phys* 102:1398–1404, 1995.
101. W. M. Hess, Ch. R. Herd. In: J. B. Donnet, R. C. Bansal, M. J. Wang, eds. *Carbon Black*, 2nd ed. New York: Marcel Dekker, 1993.
102. J. B. Donnet, E. Custadéro. In: J. B. Donnet, R. C. Bansal, M. J. Wang, eds. *Carbon Black*, 2nd ed. New York: Marcel Dekker, 1993.



103. M. J. Wang, S. Wolff. In: J. B. Donnet, R. C. Bansal, M. J. Wang, eds. *Carbon Black*, 2nd ed. New York: Marcel Dekker, 1993.
104. S. Ergun. *Carbon* 6:141, 1968.
105. D. C. Rapaport. *The Art of the Molecular Dynamics Simulation*. Cambridge: Cambridge University Press, 1995.
106. L. E. Cascarini de Torre, E. J. Bottani. *Langmuir* 13:3499–3507, 1997.
107. A. Thomy, X. Duval. *J Chim Phys (Paris)* 66:1966–1973, 1969.
108. A. Thomy, X. Duval. *J Chim Phys (Paris)* 67:286–290, 1970.
109. A. Thomy, X. Duval. *J Chim Phys (Paris)* 67:1101–1110, 1970.
110. A. Thomy, X. Duval. *Surf Sci* 299/300:415–425, 1994.
111. M. Nielsen, J. P. McTague, L. Passell. In: J. G. Dash, J. Ruvalds, eds. *Phase Transitions in Surface Films*. New York: Plenum Press, 1980.
112. T. T. Chung, J. G. Dash. *Surf Sci* 66:559–580, 1977.
113. J. Regnier, A. Thomy, X. Duval. *J Coll Interface Sci* 70:105–111, 1979.
114. J. A. Veanbles, J. L. Seguin, J. Suzanne, M. Bienfait. *Surf Sci* 145:345–363, 1984.
115. R. Marx, E. F. Wassermann. *Surf Sci* 117:267–276, 1982.
116. A. Marx. *Phys Rep* 125:1–67, 1985.
117. M. Schick. *Progr Surf Sci* 11:254, 1981.
118. M. Grunze, P. H. Kleban, W. N. Unertl, F. S. Rhys. *Phys Rev Lett* 51:582–585, 1983.
119. A. Patrykiewicz, S. Sokołowski, T. Zientarski, K. Binder. *Surf Sci* 421:308–319, 1999.
120. R. J. Behm, K. Christmann, G. Ertl. *Surf Sci* 99:320–340, 1980.
121. R. Imbihl, R. J. Behm, K. Christmann, G. Ertl, T. Matsushima. *Surf Sci* 117:257–266, 1982.
122. O. P. Mahajan, P. L. Walker Jr. *J Coll Interface Sci* 31:79–84, 1969.
123. D. J. Callaway, M. Schick. *Phys Rev B* 23:3494–3503, 1981.
124. A. Patrykiewicz. *Thin Solid Films* 208:189–196, 1992.
125. A. Patrykiewicz. *Thin Solid Films* 223:39–50, 1993.
126. N. M. Svrakić. *J Phys A* 18:L891–L894, 1985.
127. J. P. Coulomb, T. S. Sullivan, O. E. Vilches. *Phys Rev B* 30:4753–4760, 1985.
128. R. E. Ecke, J. G. Dash, R. D. Puff. *Phys Rev B* 26:1288–1297, 1982.
129. P. Gelband, S. Doniach. *Phys Rev B* 31:4361–4368, 1985.
130. U. Glaus. *Phys Rev B* 34:3203–3211, 1986.
131. A. P. Young. In: K. Binder, G. Cicotti, eds. *Monte Carlo and Molecular Dynamics of Condensed Matter Systems*. Bologne: Italian Physical Society, 1996, pp. 285–307.
132. R. J. Birgeneau, E. M. Hammonds, P. Heiney, P. W. Stephans, P. M. Horn. In: S. K. Sinha, ed. *Ordering in Two Dimensions*, Amsterdam: North-Holland, 1980.
133. V. Privman. In: V. Privman, ed. *Finite Size Scaling and Numerical Simulation of Statistical Systems*. Singapore: World Scientific, 1990, pp. 1–98.
134. K. Binder. *Phys Rev Lett* 47: 693–696, 1981.

135. D. P. Landau. In: V. Privman, ed. *Finite Size Scaling and Numerical Simulation of Statistical Systems*. Singapore: World Scientific, 1990, pp. 223–260.
136. L. Landau, E. M. Lifschitz. *Statistical Physics, 3rd ed.* New York: Pergamon Press, 1980, Part I.
137. U. Bardi, A. Glachant, M. Bienfait. *Surf Sci* 97:137–157, 1980.
138. H. E. Stanley. *Introduction to Critical Phenomena and Phase Transitions*. London: Pergamon Press, 1976.
139. K. Binder. In: V. Privman, ed. *Finite Size Scaling and Numerical Simulation of Statistical Systems*. Singapore: World Scientific, 1990, pp. 173–221.
140. M. E. Fisher, In: M. S. Green, ed. *Critical Phenomena*. New York: Academic Press, 1971, p. 1.
141. M. E. Fisher, M. N. Barber. *Phys Rev Lett* 28:1516–1519, 1972.
142. G. Paccioni. *Surf Sci* 281:207–219, 1993.
143. X. D. Xiao, X. D. Zhu, W. Daum, Y. R. Shen. *Phys Rev B* 46:9732–9743, 1992.
144. R. C. Nelson, T. L. Einstein, S. V. Khare, P. T. Rous. *Surf Sci* 295:462–484, 1993.
145. R. Nada, A. C. Hess, C. Pisani. *Surf Sci* 336:353–361, 1995.
146. A. Natori, R. W. Godby. *Phys Rev B* 47:15816–15822, 1993.
147. S. Briquez, A. Marmier, C. Girardet. *Langmuir* 12:3969–3975, 1993.
148. Th. Michely, G. Comsa. *Surf Sci* 256:217–226, 1991.
149. C. D. Pownall, P. A. Mulheren. *Phys Rev B* 57:R9463–R9466, 1998.
150. J. Merikoski, S. C. Ying. *Phys Rev B* 56:2166–2174, 1997.
151. E. V. Albano, D. W. Heermann, K. Binder, W. Paul. *J Stat Phys* 61:161–178, 1990.
152. E. V. Albano, D. W. Heermann, K. Binder, W. Paul. *Physica A* 183:130–147, 1992.
153. M. Boyan, W. A. Steele. *Surface Sci* 199:L395–L399, 1988.
154. M. Boyan, W. A. Steele. *Langmuir* 9:2569–2575, 1993.
155. M. D. Chinn, S. C. Fain Jr. *Phys Rev Lett* 39:146–149, 1977.
156. M. Nielson, J. P. McTague, W. Ellenson. *J Phys (Paris)* 38:C4–10, 1977.
157. P. Bak, D. Mukamel, J. Villain, K. Wentowska. *Phys Rev B* 19:1610–1613, 1979.
158. J. A. Venables, P. S. Scabes-Rechkiman. *Surf Sci* 71:27–41, 1978.
159. J. Villain. *J Phys Lett (Paris)* 41:L267–L270, 1980.
160. J. Villain. *J Phys Lett (Paris)* 43:L551–L558, 1982.
161. W. L. McMillan. *Phys Rev B* 14:1496–1502, 1976.
162. P. Bak, V. Emery. *Phys Rev Lett* 36:978–981, 1976.
163. M. Luban, D. Mukamel, S. Shtrikman. *Phys Rev A* 10:360–367, 1976.
164. J. Villain. *Phys Rev Lett* 41:36–39, 1978.
165. Y. Imry, S. K. Ma. *Phys Rev Lett* 35:1399–1402, 1975.
166. F. F. Abraham, W. E. Rudge, D. J. Auerbach, S. W. Koch. *Phys Rev Lett* 52:445–448, 1984.
167. W. A. Steele. *Surf Sci* 36:317–332, 1973.
168. R. Pandit, M. Schick, M. Wortis. *Phys Rev B* 26:5112–5138, 1982.

169. A. Patrykiewicz, D. P. Landau, K. Binder. *Surf Sci* 238:317–327, 1990.
170. K. Binder, D. P. Landau. *Surf Sci* 108:503–525, 1981.
171. S. Dietrich, M. Schick. *Phys Rev B* 33:4952–4968, 1986.
172. G. Forgacs, H. Orland, M. Schick. *Phys Rev B* 32:4683–4686, 1985.
173. W. Gac, M. Kruk, A. Patrykiewicz, S. Sokołowski. *Langmuir* 12:159–169, 1996.
174. Y. Pomeau, J. Vannimenus. *J Coll Interface Sci* 104:477–488, 1985.
175. D. Andelman, J. F. Joanny, M. O. Robbins. *Europhys Lett* 7:731–736, 1988.
176. W. Li, M. Kardar. *Phys Rev B* 42:6546–6554, 1990.
177. M. O. Robbins, D. Andelman, J. F. Joanny. *Phys Rev A* 43:4344–4354, 1991.
178. J. L. Harden, D. Andelman. *Langmuir* 8:2547–2551, 1992.
179. P. Pfeiffer, Y. J. Wu, M. W. Cole, J. Krim. *Phys Rev Lett* 62:1997–2000, 1987.
180. M. Kardar, J. O. Indekeu. *Europhys Lett* 12:161–164, 1990.
181. M. Napiórkowski, W. Koch, S. Dietrich. *Phys Rev A* 45:5760–5771, 1992.
182. A. Korociński, M. Napiórkowski. *Mol Phys* 84:171–184, 1995.
183. M. Napiórkowski, W. Koch, S. Dietrich. *Ber Bunsenges Phys Chem* 98:411–412, 1994.
184. V. E. Smorodin. *Langmuir* 10:2250–2256, 1994.
185. R. R. Netz, D. Andelman. *Phys Rev E* 55:687–700, 1997.
186. M. W. Cole, E. Vittoratos. *J Low Temp Phys* 22:223–230, 1976.
187. D. Beaglehole. *J Phys Chem* 93:5900–5902, 1989.
188. S. Garoff, E. B. Sirota, S. K. Sinha, H. B. Stanley. *J Chem Phys* 90:7505–7515, 1989.
189. I. M. Tidswell, T. A. Rabedeau, P. S. Pershan, S. D. Kosowsky. *Phys Rev Lett* 66:2108–2111, 1991.
190. P. S. Pershan. *Ber Bunsenges Phys Chem* 98:372–375, 1994.
191. P. Müller-Buschbaum, M. Tolan, W. Press, F. Brinkop, J. P. Kotthaus. *Ber Bunsenges Phys Chem* 98:413–414, 1994.
192. J. Drelich, J. D. Miller. *J Coll Interface Sci* 164:252–259, 1994.
193. J. Drelich, J. D. Miller. *Colloids and Surfaces* 69:35–43, 1992.
194. D. Beaglehole, P. Wilson. *J Phys Chem* 98:8096–8100, 1994.
195. W. Gac, A. Patrykiewicz, S. Sokołowski. *Surf Sci* 318:413–420, 1994.
196. G. Chmiel, A. Patrykiewicz, W. Rżysko, S. Sokołowski. *Phys Rev B* 48:14454–14462, 1993.
197. J. W. Cahn. *J Chem Phys* 66:3367, 1977.
198. C. Ebner, W. F. Saam. *Phys Rev Lett* 38:1486–1489, 1977.
199. W. Koch, S. Dietrich, M. Napiórkowski. *Phys Rev E* 51:3300–3317, 1995.
200. C. Borgs, J. De Coninck, R. Kotecký, M. Zinque. *Phys Rev Lett* 74:2292–2294, 1995.
201. P. S. Swain, A. O. Parry. *J Phys C* 30:4597–4605, 1997.
202. G. Giugliarelli, A. L. Stella. *Physica A* 239:467–476, 1997.
203. A. W. Adamson. *Physical Chemistry of Surfaces*. New York: Wiley-Interscience, 1990.
204. A. O. Parry, P. S. Swain, J. A. Fox. *J Phys Condens: Matter* 8:L659–L663, 1996.

# 6

## Adsorption in Random Porous Media

**OREST PIZIO** Instituto de Química de la Universidad Nacional Autónoma de México, Coyoacán, México

I. Introduction	293
II. Theoretical Background	297
III. Applications of the ROZ Theory for Homogeneous, Partly Quenched Systems with Short-range Interactions	305
IV. Elements of the Theory of Partly Quenched Inhomogeneous Fluids	330
V. The ROZ Theory for Ionic Partly Quenched Systems	337
VI. Concluding Remarks	341
References	343

### I. INTRODUCTION

Very recently, the scientific interests of several leading theoretical laboratories have turned to studies of quenched-annealed fluids. To the best of our knowledge, there has not been a comprehensive review of the theoretical studies of quenched-annealed fluid systems. Our intention in this chapter is to fill, at least partially, an existing vacuum. Evidently, it is impossible to discuss the state of the art in this rapidly developing area in every detail in a single paper with restricted dimensions. We will omit, for example, the discussion of the fundamentals of the replica method for lattice systems, referring the reader to a monograph [1].

The structure of the chapter is as follows. First, we start with a brief introduction of the important theoretical developments and relevant interesting experimental observations. In Sec. 2 we present fundamental relations of the liquid-state replica methodology. These include the definitions of the partition function and averaged grand thermodynamic potential, the fluctuations in the system and the correlation functions. In the second part of

this section the replica Ornstein–Zernike equations and relevant closure approximations are discussed. Finally, a derivation of thermodynamic properties of partly quenched systems is given.

In Sec. 3 our presentation is focused on the most important results obtained by different authors in the framework of the replica Ornstein–Zernike (ROZ) integral equations and by simulations of simple fluids in microporous matrices. For illustrative purposes, we discuss some original results obtained recently in our laboratory. Those allow us to show the application of the ROZ equations to the structure and thermodynamics of fluids adsorbed in disordered porous media. In particular, we present a solution of the ROZ equations for a hard sphere mixture that is highly asymmetric by size, adsorbed in a matrix of hard spheres. This example is relevant in describing the structure of colloidal dispersions in a disordered microporous medium. On the other hand, we present some of the results for the adsorption of a hard sphere fluid in a disordered medium of spherical permeable membranes. The theory developed for the description of this model agrees well with computer simulation data. Finally, in this section we demonstrate the applications of the ROZ theory and present simulation data for adsorption of a hard sphere fluid in a matrix of short chain molecules. This example serves to show the relevance of the theory of Wertheim to chemical association for a set of problems focused on adsorption of fluids and mixtures in disordered microporous matrices prepared by polymerization of species.

Sec. 4 is concerned with the development of the theory of inhomogeneous partly quenched systems. The theory involves the inhomogeneous, or second-order, replica OZ equations and the Born–Green–Yvon equation for the density profile of adsorbed fluid in disordered media. Some computer simulation results are also given.

The aforementioned developments deal with fluids either without long-range or with weakly long-range interactions. However, the problem of adsorption of fluids interacting via long-range forces and, in particular, of charged fluids adsorbed in charged disordered matrices is of much interest for basic and applied research. Therefore, we proceed in Sec. 5 with the theory of quenched-annealed charged systems. Peculiarities of the screening of Coulomb interactions in adsorbed charged fluids restricted to charged obstacles are shown explicitly. Some results of the partly quenched model of charged hard spheres are also discussed.

Concluding remarks include a summarizing discussion and an outline of possible future studies of partly quenched systems that are, in our opinion, of interest.

We would like, however, to start with a clear description of the subject of our work. We are interested in quenched-annealed, or partly quenched,

systems, i.e., those in which some degrees of freedom are quenched (fixed) whereas the others are allowed to equilibrate in the presence of a subsystem of quenched variables. The ensemble averages corresponding to the expectation values of physical quantities represent double averages. Thermal averaging must be performed with the quenched variables kept fixed, and then averaging over a spectrum of values of the quenched degrees of freedom must be done.

Continuum systems with quenched disorder include porous and sintered porous materials, gels (silica gels and polymer organic gels, for example), amorphous substances, porous glasses such as Vycor, engineering composites, etc. Vycor glass has a porosity of about 30% and consists of interconnecting pores of radius  $\approx 30 \text{ \AA}$ . In contrast to this dense structure, gels may be thought of as a network of interconnecting strands and are characterized by very high porosities, in the range of 90–98%. Therefore, the behavior of adsorbed fluids in these two types of material may differ significantly [2].

Experimental studies of fluids and mixtures in microporous disordered media have discovered their uncommon structural, thermodynamic, and dynamic properties [3–11]. It was shown, in particular, that the liquid–vapour transition and liquid–liquid separation are quite different in annealed and partly quenched systems [3–8]. A remarkable narrowing of the liquid–vapour coexistence curve, in comparison with that for the bulk, has been observed for  $^4\text{He}$  in aerogel. Besides, a phase separation in a mixture at a temperature sufficiently below the critical temperature of the bulk mixture has been observed. Specific structures of solid phases formed upon cooling of rare gases and water in porous glasses have been the subject of recently performed diffraction experiments [10,11]. Static and dynamic aspects of the behavior of colloidal dispersions in quasibidimensional porous media also have been studied and are worth mentioning [12–14]. At present there exists a considerable literature concerning theory and experiments on liquid crystalline phases in disordered porous media. However, these systems do not fit exactly with the principal objectives of our study and therefore will be excluded from our consideration. All the works cited above require undoubtedly more attention, and may be discussed in much more detail in a separate publication. However, our focus in this review is on theoretical developments rather than experimental advances.

Theoretical investigations of quenched-annealed systems have been initiated with success by Madden and Glandt [15,16]; these authors have presented exact Mayer cluster expansions of correlation functions for the case when the matrix subsystem is generated by quenching from an equilibrium distribution, as well as for the case of arbitrary distribution of obstacles. However, their integral equations for the correlation functions

appeared to be only approximate; this has been demonstrated explicitly by Given and Stell [17,18]. By performing a detailed analysis of the cluster series of Madden and Glandt, Given and Stell have derived a correct set of equations and called them the replica Ornstein–Zernike equations [17–19]. The closure relations have been proposed for the ROZ equations and tested against computer simulation data [20,21].

However, thermodynamic properties of quenched-annealed systems are much more difficult to obtain, both from the theory and from simulations. This problem has been addressed in Refs. 22–27, but still lacks a complete solution. The majority of the aforementioned studies, in their practical realization, have been restricted to adsorbed fluids with only repulsive interparticle forces. The question of liquid–vapor transition has remained out of the question. Recently, a mean-field theory has been applied to fluids with square-well attraction [24]. On the other hand, Kierlik et al. [27] have used optimized cluster expansions to investigate the phase diagram of Lennard–Jones fluids adsorbed in a hard sphere disordered matrix. In spite of profound theoretical analysis of the critical behavior of a fluid in a disordered porous matrix by Pitard et al. [28], much room remains for improvement of the theory to explain, in particular, a specific shape of liquid–vapor coexistence curve and liquid–liquid equilibria. Liquid–vapor and liquid–liquid equilibria have also been investigated by using grand canonical and restricted Gibbs ensemble Monte Carlo simulations for sufficiently simple models (see Refs. 29 and 30, respectively), such that the theoretical constructions must pass through severe tests. Actually, the application of Gibbs ensemble methodology, as well as of isobaric ensemble, encounters very serious difficulties for models other than that studied in Ref. 30. In that work, volume changes of the simulational box have been unnecessary due to a special symmetry of the model for a fluid mixture.

There have been other promising lines along which the theory of quenched-annealed systems has progressed recently. One of them, worth discussing in more detail, is the adsorption of fluids in inhomogeneous, i.e. geometrically restricted, quenched media [31,32]. In this area one encounters severe methodological and technical difficulties. At the moment, a set of results has been obtained at the level of a hard sphere type model adsorbed in slit-like pores with quenched distribution of hard sphere obstacles [33]. However, the problem of phase transitions has remained out of the question so far.

Our final focus in this review is on charged quenched-annealed fluid systems. Very recently Bratko, Chakraborty and Chandler have addressed this problem [34–36]. A set of grand canonical computer simulation results for infinitely diluted electrolyte adsorbed in an electroneutral matrix of ions has been presented and an attempt to describe them at the level of

Debye-Hückel type theory has been undertaken [35]. On the other hand, we have consistently considered the problem using the ROZ equations for point ions and then for non-point charged particles [37,38]. The former case has been solved by us to renormalize the ROZ equations in view of long-range Coulomb interactions. However, interesting observations concerning the screened potentials of point ions in an environment of fixed point charge distribution have been obtained. The systems discussed above have one common feature; namely, a configuration of matrix species is assumed to correspond to a fixed distribution of the Cartesian coordinates of particles. We are not aware of studies in which degrees of freedom other than co-ordinates are held fixed.

The theory of quenched-annealed fluids is a rapidly developing area. In this chapter we have attempted to present some of the issues already solved and to discuss only some of the problems that need further study. Undoubtedly there remains much room for theoretical developments. On the other hand, accumulation of the theoretical and simulation results is required for further progress. Of particular importance are the data for thermodynamics and phase transitions in partly quenched, even quite simple systems. The studies of the models with more sophisticated interactions and model complex fluids, closer to the systems of experimental focus and of practical interest, are of much interest and seem likely to be developed in future.

## II. THEORETICAL BACKGROUND

Let us consider a simple model of a quenched-annealed system which consists of particles belonging to two species: species 0 is quenched (matrix) and species 1 is annealed, i.e., the particles are allowed to equilibrate between themselves in the presence of 0 particles. We assume that the subsystem composed of 0 particles has been a usual fluid before quenching. One can characterize it either by the density  $\rho^0$  or by the value of the chemical potential  $\mu^0$ . The interparticle interaction  $u_{00}(r)$  does not need to be specified for the moment. It is just assumed that the fluid with interaction  $u_{00}(r)$  has reached an equilibrium at certain temperature  $T_0$ , and then the fluid has been quenched at this temperature without structural relaxation. Thus, the distribution of species 0 is any one from a set of equilibrium configurations corresponding to canonical or grand canonical ensemble. We denote the interactions between annealed particles by  $u_{11}(r)$ , and the "cross" fluid-matrix interactions by  $u_{10}(r)$ .

We introduce the notation **0** and **1** for the vector of coordinates of the quenched and annealed particles, respectively. For the sake of



methodologically clear presentation, we restrict ourselves to the canonical ensemble for the moment. The Helmholtz free energy of the partly quenched system in question is given by [15–18,22]

$$-\beta A_{PQ} = \langle \ln Z_1 \rangle_0 = Z_0^{-1} \int d\mathbf{0} \exp(-\beta_0 H_{00}) \ln Z_1 \quad (1)$$

where  $\beta_0 = 1/kT_0$ ,

$$\left. \begin{aligned} Z_1 &= \int d\mathbf{1} \exp[-\beta(H_{10} + H_{11})] \\ Z_0 &= \int d\mathbf{0} \exp(-\beta_0 H_{00}) \end{aligned} \right\} \quad (2)$$

are usual expressions for the partition sums,  $H_{ij}$  are the Hamiltonians consisting of relevant pairwise interactions. It is important to mention that the temperature of observation of the annealed fluid  $T$  ( $\beta = 1/kT$ ) does not necessarily coincide with the temperature  $T_0$  at which the matrix has been quenched.

The logarithm of the partition sum of the annealed species under the sign of integration in Eq. (1) makes the analytical treatment difficult. Therefore, the replica method, see, e.g., Ref. 1, is used, or, in other words the following identity is exploited

$$\ln Z = \lim_{s \rightarrow 0} (Z^s - 1)/s \equiv \left. \frac{d}{ds} \right|_{s \rightarrow 0} Z^s \quad (3)$$

where the limit  $\lim_{s \rightarrow 0} (d/ds)$  in Eq. (3) has been denoted as  $(d/ds)|_{s \rightarrow 0}$ ; similar notation will be used below for the sake of brevity. The free energy of the system given by Eq. (1) can then be written in the “replicated” form

$$\begin{aligned} -\beta A_{PQ} &= Z_0^{-1} \left. \frac{d}{ds} \right|_{s \rightarrow 0} \int d\mathbf{0} \exp(-\beta_0 H_{00}) (d\mathbf{1}) \\ &\quad \times \exp \left\{ -\beta \sum_{1 \leq s} (H_{10}^{(m)} + H_{11}^{(m)}) \right\} \end{aligned} \quad (4)$$

where the variables describing species 1 appear in  $s$  copies or *replicas* according to the representation of the logarithm in the form of Eq. (3). Our notation  $(d\mathbf{1})$  indicates that integration is performed over  $s$  sets of variables for annealed particle coordinates. The form provided by Eq. (4) is much more convenient to apply because it represents a limit,  $s \rightarrow 0$ , of the partition sum for a *replicated* system. This replicated system is an *equilibrium* system with

the following Hamiltonian

$$\mathcal{H} = \sum_{i < j} u_{00}(ij) + \sum_{1 \leq m \leq s} \sum_{i < j} u_{10}^m(ij) + \sum_{1 \leq m \leq s} \sum_{1 \leq n \leq s} \sum_{i < j} u_{11}^{mn}(ij) \quad (5)$$

Here the superscripts serve as replica indices; they attribute the coordinates of particles to a given replica but do not alter interactions in the system

$$\left. \begin{aligned} u_{10}^m(ij) &\equiv u_{10}(ij) \\ u_{11}^{mn}(ij) &\equiv \delta_{mn} u_{11}(ij) \end{aligned} \right\} \quad (6)$$

where  $\delta_{mn}$  is the Kronecker symbol. However, the particles belonging to different replicas do not interact. As a result of the procedure presented above, the quenched-annealed system has been “converted” into an equilibrium system with nonadditive interactions with the partition sum  $Z_{\text{rep}}$ . It is worth mentioning that the  $s \rightarrow 0$  limit of the partition function of the replicated system yields  $Z_0$ . Therefore, Eq. (4) can be rewritten in the form

$$-\beta A_{PQ} = \left. \frac{d}{ds} \right|_{s \rightarrow 0} \ln Z_{\text{rep}} = \left. \frac{d}{ds} \right|_{s \rightarrow 0} (-\beta A_{\text{rep}}(s)) \quad (7)$$

which establishes the relation between the free energy of the original partly quenched system and its replicated counterpart [22]. Usually, one does not need to bother with the fluctuations in the number of matrix particles. The experiment is performed to investigate adsorption of a fluid in a matrix (of average density  $\rho^0$ ), i.e., in contact with a reservoir that fixes the chemical potential [22].

However, if one focuses on the adsorption of a fluid in heterogeneous matrices [32,33] and/or on the fluctuations in an adsorbed fluid, it is inevitable to perform developments similar to those above in the grand canonical ensemble. Moreover, this derivation is of importance for the formulation of the virial route to thermodynamics of partially quenched systems. For this purpose, we include only some basic relations of this approach.

By definition, an observable property of a partly quenched system,  $f_{PQ}$ , in the grand canonical ensemble is obtained as

$$f_{PQ} = \langle f(0) \rangle_0 = (1/\Xi_0) \sum_{0 \leq N_0 \leq \infty} (1/N_0!) z_0^{N_0} \int d\mathbf{0} f(N_0, 0) \exp(-\beta_0 H_{00}) \quad (8)$$

where the angular brackets  $\langle \dots \rangle_0$  denote an average over the quenched degrees of freedom, i.e., over the coordinates of matrix species;  $N_0$ ,  $z_0$  and

$H_{00}$  are the average number, the activity of the matrix particles, and the Hamiltonian of the matrix system, respectively. The grand potential of this system is

$$\Xi_0 = \sum_{0 \leq N_0 \leq \infty} (1/N_0!) z_0^{N_0} \int d\mathbf{0} \exp(-\beta_0 H_{00}) \quad (9)$$

According to Eq. (8) the pressure in terms of the grand canonical potential per unit volume is

$$\beta V P^{PQ} \equiv \beta V \langle P(0) \rangle_0 = \langle \ln \Xi_1(0) \rangle_0 \quad (10)$$

Using then the replica representation, one can easily obtain

$$\beta V P^{PQ} = \left. \frac{d}{ds} \right|_{s \rightarrow 0} \ln \Xi^{\text{rep}} = \left. \frac{d}{ds} \right|_{s \rightarrow 0} \beta V P^{\text{rep}} \quad (11)$$

In spite of its simplicity and the visual similarity of this equation to Eq. (7), we would like to note that Eq. (11) leads to a nontrivial thermodynamics of a partially quenched system in terms of correlation functions, see, e.g., Ref. 25 for detailed discussion. Evidently, the principal route for  $P^{PQ}$  and to the virial theorem is to exploit the thermodynamics of the replicated system. However, special care must be taken then, because the  $V$  and  $s$  derivatives do not commute. Moreover, the presence of two different temperatures,  $\beta_0$  and  $\beta$ , requires attention in taking temperature derivatives, setting those temperatures equal, if appropriate, only at the end of the calculations.

To define the correlation functions of partly quenched systems requires one to consider fluctuations. There are two types of fluctuations: thermal fluctuations for a given configuration of matrix species, and fluctuations induced by disorder. We characterize the average over disorder of thermal fluctuations by the variance

$$\sigma_{\text{therm}}^2 = \langle \langle N_1(\mathbf{q}^{N_0})^2 \rangle_{\text{th}} \rangle_{\text{d}} - \langle \langle N_1(\mathbf{q}^{N_0}) \rangle_{\text{th}} \rangle_{\text{d}}^2 \quad (12)$$

and the fluctuations of the thermal average induced by disorder by

$$\sigma_{\text{disord}}^2 = \langle \langle N_1(\mathbf{q}^{N_0})^2 \rangle_{\text{th}} \rangle_{\text{d}} - \langle \langle N_1(\mathbf{q}^{N_0}) \rangle_{\text{th}} \rangle_{\text{d}}^2 \quad (13)$$

where  $\langle \dots \rangle_{\text{th}}$  and  $\langle \dots \rangle_{\text{d}}$  denote thermal and disorder averaging, respectively. It is expected, that the average density of fluid particles in a matrix,  $N_1(\mathbf{q}^{N_0})/V$ , is a self-averaging quantity, i.e.  $\sigma_{\text{disord}}/N_1 \rightarrow 0$  in the thermodynamic limit.

In close relation to the fluctuations, one may introduce the correlation functions. The pair density distribution function for fluid particles  $\rho^{11}(\mathbf{r}_1, \mathbf{r}_2)$  is defined as the average over all realizations of the matrix structure of the

function  $\rho^{11}(\mathbf{r}_1, \mathbf{r}_2; \mathbf{q}^{N_0})$ . One can then define the pair correlation function in the usual manner

$$\rho^1(\mathbf{r}_1)\rho^1(\mathbf{r}_2)h^{11}(\mathbf{r}_1, \mathbf{r}_2) = \rho^{11}(\mathbf{r}_1, \mathbf{r}_2) - \rho^1(\mathbf{r}_1)\rho^1(\mathbf{r}_2) \quad (14)$$

in terms of averaged pair distribution function and the density profiles. The matrix is statistically homogeneous, therefore the fluid density is constant throughout the matrix,  $\rho^1(\mathbf{r}) = \rho^1$ , where  $\rho^1 = N_1/V = \langle\langle N_1(\mathbf{q}^{N_0}) \rangle\rangle_{\text{th}}/V$ . The pair correlation function then depends only on the distance between particles, i.e.,  $h^{11}(\mathbf{r}_1, \mathbf{r}_2) = (h|\mathbf{r}_{12}|)$ .

On the other hand, the *connected* pair distribution function for a given matrix configuration  $\rho^{11,c}(\mathbf{r}_1, \mathbf{r}_2; \mathbf{q}^{N_0})$

$$\rho^{11,c}(\mathbf{r}_1, \mathbf{r}_2; \mathbf{q}^{N_0}) = \rho^{11}(\mathbf{r}_1, \mathbf{r}_2; \mathbf{q}^{N_0}) - \rho^1(\mathbf{r}_1; \mathbf{q}^{N_0})\rho^1(\mathbf{r}_2; \mathbf{q}^{N_0}) \quad (15)$$

generates two additional correlation functions (called the connected and blocking correlation functions)

$$\begin{aligned} \langle \rho^1 \rangle^2 h^{11,c}(\mathbf{r}_1, \mathbf{r}_2) &= \langle \rho^{11,c}(\mathbf{r}_1, \mathbf{r}_2; \mathbf{q}^{N_0}) \rangle_{\text{d}} \\ &= \rho^{11}(\mathbf{r}_1, \mathbf{r}_2) - \langle \rho^1(\mathbf{r}_1; \mathbf{q}^{N_0}) \rho^1(\mathbf{r}_2; \mathbf{q}^{N_0}) \rangle_{\text{d}}, \end{aligned} \quad (16)$$

and

$$\langle \rho^1 \rangle^2 h^{11,b}(\mathbf{r}_1, \mathbf{r}_2) = \langle \rho^1(\mathbf{r}_1; \mathbf{q}^{N_0}) \rho^1(\mathbf{r}_2; \mathbf{q}^{N_0}) \rangle_{\text{d}} - \langle \rho^1 \rangle^2 \quad (17)$$

such that  $h^{11}(r_{12}) = h^{11,c}(r_{12}) + h^{11,b}(r_{12})$ . The isothermal compressibility of adsorbed fluid,  $\chi_1$ , has been shown in Ref. 22 to be related to the averaged thermal average as follows

$$\rho_1 k T \chi_1 = \sigma_{\text{therm}}^2 / N_1 \quad (18)$$

The one-particle density  $\rho^1(\mathbf{r}_1; \mathbf{q}^{N_0})$  and the pair density  $\rho^{11}(\mathbf{r}_1, \mathbf{r}_2; \mathbf{q}^{N_0})$  are normalized in the grand canonical ensemble, as usual

$$\begin{aligned} \int d\mathbf{r}_1 \rho^1(\mathbf{r}_1; \mathbf{q}^{N_0}) &= \langle N_1(\mathbf{q}^{N_0}) \rangle_{\text{th}} \\ \int d\mathbf{r}_1 d\mathbf{r}_2 \rho^{11}(\mathbf{r}_1, \mathbf{r}_2; \mathbf{q}^{N_0}) &= \langle N_1(\mathbf{q}^{N_0})^2 \rangle_{\text{th}} - \langle N_1(\mathbf{q}^{N_0}) \rangle_{\text{th}}^2 \end{aligned} \quad (19)$$

Then, performing a disorder average in Eq. (19), and using Eq. (18) we can obtain the following two relations for the connected and blocking correlation functions

$$\left. \begin{aligned} \rho^1 k T \chi_1 &= \sigma_{\text{therm}}^2 / N_1 = 1 + \rho^1 \int d\mathbf{r}_{12} h^{11,c}(r_{12}) \\ \rho^1 \int d\mathbf{r}_{12} h^{11,b}(r_{12}) &= \sigma_{\text{disord}}^2 / N_1 \end{aligned} \right\} \quad (20)$$

The former of these two relations is the compressibility equation for the fluid in the matrix.

We proceed with cluster series which yield the integral equations. Evidently the correlation functions presented above can be defined by their diagrammatic expansions. In particular, the blocking correlation function  $h^{11,b}(r_{12})$  is the subset of graphs of  $h^{11}(r_{12})$ , such that all paths between the fluid root points 1 and 2 pass through at least one matrix  $\rho^0$ -field point. The direct correlation function  $c^{11}$  is the sum of all graphs in  $h^{11}$  with no nodal points. The cluster expansions for the correlation functions were first obtained and analyzed in detail by Madden and Glandt [15,16]. However, the exact equations for the correlation functions, which have been called the replica Ornstein–Zernike (ROZ) equations, have been derived by Given and Stell [17–19]. These equations, for a one-component fluid in a one-component matrix, have the following form

$$h^{00} - c^{00} = \rho^0 c^{00} \otimes h^{00} \quad (21)$$

for the matrix–matrix correlations,

$$h^{10} - c^{10} = \rho^0 c^{10} \otimes h^{00} + \rho^1 c^{11,c} \otimes h^{10} \quad (22)$$

for the fluid–matrix correlations, and finally two equations for the fluid–fluid correlations

$$\left. \begin{aligned} h^{11} - c^{11} &= \rho^0 c^{10} \otimes h^{01} + \rho^1 c^{11,c} \otimes h^{11} + \rho^1 c^{11,b} \otimes h^{11,c} \\ h^{11,c} - c^{11,c} &= \rho^1 c^{11,c} \otimes h^{11,c} \end{aligned} \right\} \quad (23)$$

In all the equations above we have omitted the dependencies on  $r$ ; the symbol  $\otimes$  denotes convolution in  $r$ -space. The symmetry of the correlation functions implies that  $h^{10} = h^{01}$ ,  $c^{10} = c^{01}$ . Similarly to the total pair correlation function  $h^{11}$ , the direct correlation function of fluid particles  $c^{11}$  has also been presented as a sum of the connected and blocking terms,  $c^{11} = c^{11,c} + c^{11,b}$ . It is important to mention that the equation for the matrix structure decouples from the equations for the fluid–matrix and fluid–fluid structure. This occurs because neither fluid–matrix nor fluid–fluid correlations influence the matrix structure.

To solve the replica OZ equations, they must be completed by closure relations. Several closures have been tested against computer simulations for various models of fluids adsorbed in disordered porous media. In particular, common Percus–Yevick (PY) and hypernetted chain approximations have been applied [20]. Eq. (21) for the matrix correlations can be solved using any approximation. However, it has been shown by Given and Stell [17–19] that the PY closure for the fluid–fluid correlations simplifies the ROZ equation, the blocking effects of the matrix structure are neglected in this

approximation, i.e.,  $c^{11,b}(r) = 0$ . Therefore, the PY approximation may yield (and really this happens for partly quenched models with hard core repulsion between species [23,39]) sufficiently accurate results due to mutual cancellation of inaccuracies in the description of fluid–matrix and fluid–fluid correlations. Lomba et al. [20] have discussed replica extensions for the reference PY and reference HNC closures, but have tested only the reference PY one, for a simple model of adsorbed fluid in a hard sphere disordered matrix. Meroni et al. [21] have demonstrated that the inclusion of the contribution of bridge diagrams in the parametrized form improves the accuracy of the common HNC closure. However, these authors, in their evaluation of the bridge diagrams term, have used a set of effective diameters which is difficult to justify in the limit  $s \rightarrow 0$  for the number of replicas. Adequacy of closures in more detail for a particular class of models must be studied, however, by using computer simulation data.

Finally, in this part of the work we would like to discuss to some extent practical tools to obtain thermodynamic properties of adsorbed fluids. We have mentioned above that the compressibility equation is the only simple recipe, for the moment, to obtain the thermodynamics of partly quenched simple fluids. The reason is that the virial equation is difficult to implement; it has not been tested for partly quenched systems. Nevertheless, for the sake of completeness, we present the virial equation in the form [22,25]

$$\begin{aligned} \beta P^1 - \rho^0 [\partial(\beta P^1)/\partial \rho^0]_{\mu^1} = \rho^1 + \frac{2\pi}{3} (\rho^0)^2 \sigma_0^3 \lim_{s \rightarrow 0} [dg_{\text{rep}}^{00}(\sigma_0; s)/ds] \\ + \frac{2\pi}{3} (\rho^1)^2 \sigma_1^3 g^{11}(\sigma_1) + \frac{4\pi}{3} \rho^0 \rho^1 \sigma_{01}^3 g^{01}(\sigma_{01}) \quad (24) \end{aligned}$$

where  $\sigma_{01} = 0.5(\sigma_0 + \sigma_1)$ ,  $\sigma_{ii} = \sigma_i$ , and  $g^{ij}(\sigma_{ij})$  are the contact values of the corresponding distribution functions. The subscript “rep” corresponds to the replicated system with  $s$  replicas. We must note that the second term in the left-hand side and the first term in the right-hand side of this equation do not have transparent interpretation. If one neglects the contribution of the order  $\rho^0(\rho^1)^2$  in both of these terms, then [22]

$$\left. \begin{aligned} \lim_{s \rightarrow 0} [dg_{\text{rep}}^{00}(\sigma_0; s)/ds] &= g_{\text{rep}}^{00}(r; s) [W_{\text{rep}}^{00}(r; s = 1) - W_{\text{rep}}^{00}(r; s = 0)] \\ W_{\text{rep}}^{00}(r; s) &= \ln g_{\text{rep}}^{00}(r; s) + \beta U_{00}(r) \\ -[\partial(\beta P^1)/\partial \rho^0]_{\mu^1} &= \beta \mu_{\text{rep}}^0(s = 1) - \beta \mu_{\text{rep}}^0(s = 0) \end{aligned} \right\} \quad (25)$$

where  $W_{\text{rep}}^{00}(r; s)$  is the excess potential of mean force for the replicated system. To use this virial equation, one needs to consider equilibrium ensembles made of either matrix particles or a mixture of matrix and fluid particles, in addition to terms involving the pair distribution functions.

The equilibrium between the bulk fluid and fluid adsorbed in disordered porous media must be discussed at fixed chemical potential. Evaluation of the chemical potential for adsorbed fluid is a key issue for the adsorption isotherms, in studying the phase diagram of adsorbed fluid, and for performing comparisons of the structure of a fluid in media of different microporosity. At present, one of the popular tools to obtain the chemical potentials is an approach proposed by Ford and Glandt [23]. From the detailed analysis of the cluster expansions, these authors have concluded that the derivative of the excess chemical potential with respect to the fluid density equals the connected part of the fluid–fluid direct correlation function (dcf). Then, it follows that the chemical potential of a fluid adsorbed in a disordered matrix,  $\mu^1(\rho^1, \rho^0)$ , is

$$\beta\mu^1(\rho^0, \rho^1) = \beta\mu_{\text{id}}^1(\rho^1) + \beta\mu_{\text{ex}}^1(\rho^0, \rho^1) \quad (26)$$

where the ideal gas contribution is chosen as  $\beta\mu_{\text{id}}^1(\rho^1) = \ln(\rho^1 \sigma_1^3)$ , and the excess term  $\beta\mu_{\text{ex}}^1(\rho^0, \rho^1)$  is taken in the form

$$\beta\mu_{\text{ex}}^1(\rho^0, \rho^1) = \beta\mu_{\text{ex}}^1(\rho^0, \rho^1 = 0) - \int_0^{\rho^1} d\rho' \int d\mathbf{R} c^{11,c}(R, \rho') \quad (27)$$

The second term in Eq. (27) follows from the linear “charging” scheme applied to the functional relation between the chemical potential and adsorbed fluid density. The first term in the excess chemical potential,  $\beta\mu_{\text{id}}^1(\rho^0, \rho^1 = 0)$ , is the excess chemical potential of a fluid component at infinite dilution in the mixture composed of matrix and fluid particles. The second term comes straightforwardly from the ROZ equation. It is an integral along a density path (to a desired density) of the Fourier-transformed connected part of the fluid–fluid dcf (at  $k = 0$ ). For hard sphere models, the first term of the excess chemical potential,  $\beta^1\mu_{\text{ex}}(\rho^0, \rho^1 = 0)$ , may be approximated using the theoretical Mansoori–Carnahan–Starling–Leland equation of state for a mixture of hard spheres [40]. One can easily obtain the free energy of this mixture by integrating the equation of state. Then the chemical potential follows straightforwardly.

However, we also need to discuss how the attractive interactions between species can be included in the theory of partly quenched systems. These interactions comprise an intrinsic feature of realistic models for partially quenched fluid systems. In particular, the model for adsorption of methane in xerosilica gel of Kaminsky and Monson [41] is characterized by very strong attraction between matrix obstacles and fluid species. Besides, the fluid particles attract each other via the Lennard–Jones potential. Both types of attraction (the fluid–matrix and fluid–fluid) must be included to gain profound insight into the phase transitions in partly quenched media. The approach of Ford and Glandt to obtain the chemical potential utilizing

the direct correlation function becomes impractical for this purpose. It is well known that the HNC closure possesses a discontinuity line along which convergent solutions of integral equations cannot be obtained. This line is close to the liquid-vapor coexistence but cannot be attributed to the coexistence curve. The PY closure also possesses its own discontinuity line. Therefore one cannot perform integration by density in Eq. (27) along a path which can be of interest in the study of instabilities and phase transitions. The discontinuity lines, corresponding either to HNC or to PY closures for partly quenched systems, follow from the failure of convergence of the numerical algorithm of the solution of relevant integral equations for some thermodynamic states and do not have any other significance.

We now proceed with a brief description of the most important results obtained for some simple models, and with some original applications of the ROZ equations.

### **III. APPLICATIONS OF THE ROZ THEORY FOR HOMOGENEOUS, PARTLY QUENCHED SYSTEMS WITH SHORT-RANGE INTERACTIONS**

We begin our discussion in this section by recalling that a one-component model of hard spheres adsorbed in a matrix of hard spheres (disordered matrix) has been well studied. In particular, Lomba et al. [20] have shown, by comparison with simulation data, that the PY closure represents an adequate tool to describe the structure of a hard sphere adsorbate in the case when matrix and fluid hard spheres are of equal diameter. Similar conclusions have been obtained in the case of adsorption into a random matrix, i.e., one of freely overlapping spheres [20]. On the other hand, the HNC closure has been shown to perform less satisfactorily. Meroni et al. [21] have performed extensive computer simulations of hard sphere models in a hard sphere adsorbent for several sets of diameter ratio and have concluded that the HNC approximation, supplemented by a parametrized form of the bridge diagrams contribution, performs sufficiently well; this approximation works better than the PY closure. The most nonsymmetric model of hard spheres, in which the matrix species diameter is seven times larger than the diameter of adsorbed hard spheres, has been considered by Vega et al. [39] in the framework of the PY approximation. A set of theoretical and simulation results for adsorption isotherms of a hard sphere fluid in a hard sphere disordered matrix has been presented in Refs. 20,21,23,39. It follows that both PY and HNC closures provide qualitatively correct isotherms. The inaccuracies of the HNC approach at high values of the chemical potential seem to be slightly larger than those of the PY theory [23].



Adsorption of hard sphere fluid mixtures in disordered hard sphere matrices has not been studied profoundly and the accuracy of the ROZ-type theory in the description of the structure and thermodynamics of simple mixtures is difficult to discuss. Adsorption of mixtures consisting of argon with ethane and methane in a matrix mimicking silica xerogel has been simulated by Kaminsky and Monson [42,43] in the framework of the Lennard-Jones model. A comparison with experimentally measured properties has also been performed. However, we are not aware of similar studies for simpler hard sphere mixtures, but the work from our laboratory has focused on a two-dimensional partly quenched model of hard discs [44]. That makes it impossible to judge the accuracy of theoretical approaches even for simple binary mixtures in disordered microporous media.

Let us proceed to a brief description of the treatment of attractive forces. The simplest tools to include the attractive interactions between species have been proposed by Ford and Glandt [24]. They have considered the mean field approximation (MFA) for the model in which fluid particles possess hard cores and, in addition, attract each other and with matrix species via a finite ranged square-well potential [24]. For this model, Eqs. (26) and (27) have been used to obtain the chemical potential of a reference system only, i.e., of a hard sphere fluid adsorbed in a hard sphere matrix. Due to the mean field approximation for the contribution of attractive forces, the isotherms obtained,  $\beta\mu^1(\rho^1)$ , permit one to obtain the liquid-vapor coexistence curve if the Maxwell construction is used. It follows that the critical temperature of adsorbed fluid decreases, and that the coexistence envelope shrinks, with increasing matrix density, i.e., with decreasing microporosity of the adsorbent. This behavior is in qualitative agreement with trends observed in experimental studies; however, the magnitude of effects obtained in simple MFA theory is essentially overestimated. Moreover, this theoretical approach does not permit one to gain insight into the influence of fluid-fluid and fluid-matrix attraction separately on the coexistence of phases. A simplified consideration of attractive forces also does not yield the peculiar shape of the liquid-vapor coexistence line observed in computer simulation [29].

Motivated by a puzzling shape of the coexistence line, Kierlik et al. [27] have investigated the model with Lennard-Jones attractive forces between fluid particles as well as matrix particles and have shown that the mean spherical approximation (MSA) for the ROZ equations provides a qualitatively similar behavior to the MFA for adsorption isotherms. It has been shown, however, that the optimized random phase (ORPA) approximation (the MSA represents a particular case of this theory), if supplemented by the contribution of the second and third virial coefficients, yields a peculiar coexistence curve. It exhibits much more similarity to trends observed in

computer experiments [29]. A comparison of the theory and simulations has not been performed so far, due to differences of the model involved in theory and in simulation. Nevertheless, these results evidence the necessity to apply nonlinear-type theoretical approaches rather than linearized versions such as the MFA or MSA. Many unsolved issues remain if one decides to apply the ORPA plus virial coefficients theory. Such an application may elicit much criticism. This approach seems promising, however, at present, for developing an adequate thermodynamic description of partly quenched fluid systems with not too strong attractive forces. To finalize discussion of the role of attractive forces, we would like to mention that very recently a liquid–vapor coexistence curve has been obtained at the MSA level for a model mixture with fluid–fluid Yukawa forces (similar to a primitive model of an electrolyte solution with screened interparticle interactions) in a matrix of hard spheres [45]. It has been shown that, in close similarity to one-component adsorbed fluids, the critical temperature of the mixture decreases and the coexistence envelope shrinks with increasing matrix density. However, in addition, trends of behavior of the coexistence and of critical temperature on the extent of forces have been studied.

At present, there is no satisfactory theory to describe liquid–liquid equilibria for fluid mixtures in microporous media, which reflects to some extent the difficulties in describing this type of equilibria for bulk systems. A simulation study of Gordon and Glandt [30] of a Lennard–Jones mixture adsorbed in disordered matrices remains a challenge for theoreticians. We have performed very recently a similar study of a simpler fluid–fluid equilibrium of the symmetric model of nonadditive hard spheres and hard discs in a hard core matrix by using restricted Gibbs ensemble simulations [46]. Similarly to the results obtained by Gordon and Glandt [30], the coexistence shifts to higher densities and shrinks with decreasing microporosity of the adsorbent. However, we have been unable to develop a theoretical description of these results so far.

Let us proceed now with some original results from our laboratory [47] that illustrate possibilities of the application of the ROZ theory for partly quenched fluid systems.

First, we would like to consider a simple hard sphere model in a hard sphere matrix, similar to the one studied in Refs. 20, 21, 39. However, our focus is on a *very asymmetric hard sphere mixture* adsorbed in a disordered matrix. Moreover, having assumed a large asymmetry of diameters of the components and a very large difference in the concentration of components, here we restrict ourselves to the description of the structural properties of the model. Our interest in this model is due, in part, to experimental findings concerning the potential of the mean force acting between colloids in a colloidal dispersion in the presence of a matrix of obstacles [12–14].

We introduce, for the sake of convenience, species indices “ $s$ ” and “ $c$ ” for the components of the fluid mixture mimicking solvent species and colloids, and species index “ $m$ ” for the matrix component. The matrix and both fluid species are at densities  $\rho_m\sigma_m^3$ ,  $\rho_c\sigma_c^3$ , and  $\rho_s\sigma_s^3$ , respectively. The diameter of matrix and fluid species is denoted by  $\sigma_m$ ,  $\sigma_c$ , and  $\sigma_s$ , respectively. We choose the diameter of solvent particles as a length unit,  $\sigma_s = 1$ . The diameter of matrix species is chosen similar to a simplified model of silica xerogel [39],  $\sigma_m = 7.055$ . On the other hand, as in previous theoretical works on bulk colloidal dispersions, see e.g., Ref. 48 and references therein, we choose the diameter of large fluid particles mimicking colloids,  $\sigma_c = 5$ . As usual for these dispersions, the concentration of large particles,  $c$ , must be taken much smaller than that of the solvent. For all the cases in question we assume  $\rho_c\sigma_c^3 = 1.25 \times 10^{-3}$ . The model for interparticle interactions is

$$U_{ij}(r) = \begin{cases} \infty, & r < 0.5(\sigma_i + \sigma_j) \\ 0, & r > 0.5(\sigma_i + \sigma_j) \end{cases} \quad (28)$$

where  $i, j$ , take values  $m, c$ , and  $s$ .

The matrix distribution is assumed to correspond to an equilibrium distribution of spheres. The structure of the matrix follows from the common OZ equation coinciding with Eq. (21)

$$h_{mm} - c_{mm} = \rho_m c_{mm} \otimes h_{mm} \quad (29)$$

complemented by the PY closure

$$c_{mm}(r) = \{\exp[-\beta U_{mm}(r)] - 1\}\{1 + h_{mm}(r) - c_{mm}(r)\} \quad (30)$$

The ROZ equations are similar to Eqs. (22) and (23). However, we will apply PY closures for the description of both fluid–matrix and fluid–fluid interactions and therefore the ROZ equations reduce to the Madden–Glandt [15,16] form

$$h_{im} - c_{im} = \sum_{j=c,s} c_{ij} \otimes \rho_j h_{jm} + c_{im} \otimes \rho_m h_{mm} \quad (31)$$

$$h_{ij} - c_{ij} = \sum_{l=c,s} c_{il} \otimes \rho_l h_{lj} + c_{im} \otimes \rho_m h_{mj} \quad (32)$$

These equations are complemented by the PY closure

$$\left. \begin{aligned} c_{im}(r) &= \{\exp[-\beta U_{im}(r)] - 1\}\{1 + h_{im}(r) - c_{im}(r)\} \\ c_{ij}(r) &= \{\exp[-\beta U_{ij}(r)] - 1\}\{1 + h_{ij}(r) - c_{ij}(r)\} \end{aligned} \right\} \quad (33)$$

and the blocking terms of the direct correlation functions,  $c_{ij}^{bl}(r)$ , have been assumed to vanish from the very beginning,  $c_{ij}^{bl}(r) = 0$ . Our main focus is on the potential of the mean force (PMF) acting between large spheres in the

presence of smaller solvent spheres. Both species are considered inside the matrix medium. The PMF is defined in the standard manner

$$-\beta W_{cc}(r) = \ln[1 + h_{cc}(r)] \quad (34)$$

The evolution of the potential of the mean force with solvent density in the matrix at negligible concentration,  $\rho_m \sigma_m^3 = 10^{-7}$ , is shown in Fig. 1(a). Similar dependence of the PMF on the solvent density, however, in the matrix at density  $\rho_m \sigma_m^3 = 0.386$  is shown in Fig. 1(b). Finally, in Fig. 1(c) we present the evolution of the PMF on matrix density at a fixed value of the density of colloidal particles and of solvent species.

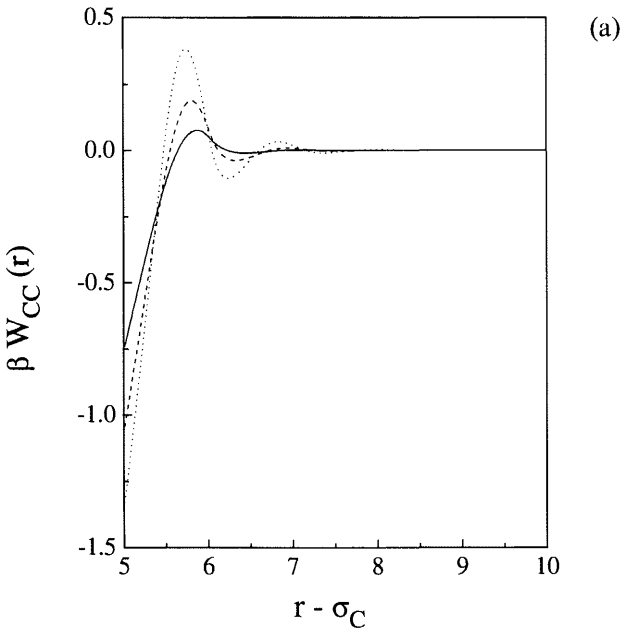


**FIG. 1** The mean force potential acting between colloidal species,  $\beta W_{cc}(r)$ , in adsorbed colloidal dispersion. In parts (a) and (b) the matrix density is taken as negligibly small,  $\rho_m \sigma_m^3 = 10^{-7}$  and  $\rho_m \sigma_m^3 = 0.193$ , respectively. In both parts, the evolution of the mean force potential with solvent density is shown;  $\rho_s = 0.2, 0.3$  and  $0.4$  (solid, dashed, and dotted lines, respectively). In part (c) the evolution of the PMF on matrix density is presented. The solvent density is held constant,  $\rho_s = 0.3$ ; the matrix density is  $\rho_m \sigma_m^3 = 0.193, 0.386$ , and  $0.772$  (dotted, dashed, and solid lines, respectively). The diameter of the matrix species is  $\sigma_m = 7.055$ . The density of colloids is  $\rho_c \sigma_c^3 = 10^{-6}$ , with  $\sigma_c = 5$ , in all the cases in question.

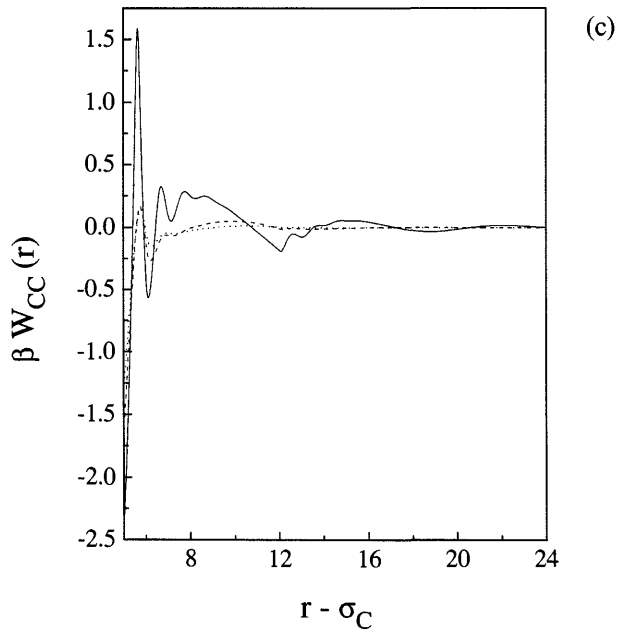
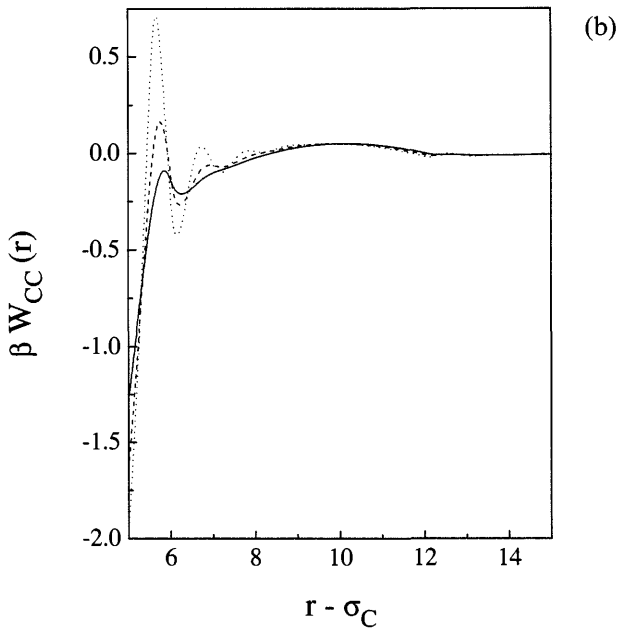


FIG. 1 Continued.

As in previous theoretical studies of the bulk dispersions of hard spheres we observe in Fig. 1(a) that the PMF exhibits oscillations that develop with increasing solvent density. The phase of the oscillations shifts to smaller intercolloidal separations with augmenting solvent density. Depletion-type attraction is observed close to the contact of two colloids. The structural barrier in the PMF for solvent-separated colloids, at the solvent densities in question, is not at  $\sigma_s/2$  but at a larger distance between colloids. These general trends are well known in the theory of colloidal systems and do not require additional comments.

However, as follows from the results presented in Fig. 1(b), the behavior of the PMF for the case of adsorbed dispersion in the matrix at  $\rho_m \sigma_m^3 = 0.386$  contains interesting features in addition to those shown in Fig. 1(a). We observe that the PMF is modulated by the presence of solvent species and in addition is modulated by the presence of matrix particles. The structural repulsive barrier appears, due to matrix particles. An additional weak attractive minimum exists at separations corresponding to matrix-separated colloids. It is interesting that the effects of solvent modulation of the PMF in the adsorbed dispersion are seen for matrix separated colloids. The matrix particles are larger than colloids; adsorption of solvent species on the surface of a matrix particle is stronger than on the surface of a colloid. Therefore, the solvent modulating effects of the PMF result from colloids separated by a matrix particle covered by a single layer of solvent species.

The effects of confinement due to matrix species on the PMF between colloids is very well seen in Fig. 1(c). At a small matrix density, only the solvent effects contribute to the formation of the PMF. At a higher matrix density, the solvent preserves its role in modulating the PMF; however, there appears another scale. The PMF also becomes modulated by matrix species; additional repulsive maxima and attractive minima develop, reflecting configurations of colloids separated by one or two matrix particles or by a matrix particle covered by the solvent layer. It seems very difficult to simulate models of this sort. However, previous experience accumulated in the studies of bulk dispersions and validity of the PY closure results gives us confidence that the results presented are at least qualitatively correct.

Let us proceed with the second interesting example concerning application of the ROZ equations. We would like first to mention that simple fluids confined to slits with permeable membranes have been studied by both computer simulations and theory, see, e.g., Refs. 49–52. The simplest way is to visualize a permeable membrane as a barrier of finite height and width. To our best knowledge, no studies of a system containing multiple barriers of a more sophisticated geometry than the slit-like have been undertaken so

far. In this example of the application of the theory of partly quenched fluids, we would like to consider a microporous medium consisting of rigidly fixed spherical obstacles in a disordered configuration. A space between obstacles may formally be thought of as a system of interconnecting pores permitting adsorption of a fluid. However, we assume that the surface of each of the obstacles is permeable to fluid species, such that fluid particles are adsorbed not only into the space between obstacles but also into their interior. I do not want to use words such as, for example, encapsulation or bilayer permeable membranes; just the model in question represents a partly quenched system consisting of a disordered set of permeable simple membranes of spherical shape in which a fluid may adsorb. The model permits us to implement theoretical developments quite easily and, besides, perform computer simulation.

Imagine a system of matrix hard spheres of diameter  $\sigma_m = 5\sigma_f$  (the diameter of fluid species is taken as a length unit,  $\sigma_f = 1$ ). The fluid to be adsorbed is a hard sphere fluid. The essence of our modeling is in the fluid-matrix potential. It is chosen in the following form [53]

$$U_{fm}(r) = 4\varepsilon_{fm} \frac{\{U_0 - (U_0 + \varepsilon_{fm})[(\sigma_m/2 - r)/w]^6\}}{\{4\varepsilon_{fm} + (U_0 + \varepsilon_{fm})[(\sigma_m/2 - r)/w]^{12}\}} \quad (35)$$

where  $\varepsilon_{fm}$  is the depth of the attractive part of the potential,  $U_0$  is the height of the barrier,  $w$  is the halfwidth of the barrier. The potential is centered at  $\sigma_m/2$ . For small values of  $\varepsilon_{fm}$ , the potential is almost entirely repulsive. For large values of  $\varepsilon_{fm}$ , one obtains attraction between fluid particles and both surfaces of the membrane barrier exposed to the interior of each matrix cavity and to the external porous space. We choose two values of the halfwidth of the barrier to study:  $w = 0.5$  and  $w = 1$ . The center of the fluid-matrix barrier, according to Eq. (35), is located at  $\sigma_m/2$ . The barrier is considered at a height,  $\beta U_0 = 1.25$ .

To begin with, we describe a computer simulation procedure in detail. It is necessary first to generate a multiple set of membranes. We assume that the configuration of an array of matrix particles (obstacles) corresponds to an equilibrium configuration of hard spheres. Therefore, we consider a system of hard spheres at dimensionless density  $\rho_m^* = \rho_m \sigma_m^3$ . A system of hard spheres has been generated and equilibrated by using common canonical Monte Carlo simulation in the NVT ensemble. After equilibration, i.e., in the productive part of the simulation run during which the pair distribution function of matrix spheres can be calculated if necessary, we pick up a set of "independent" matrix configurations distanced from each other by at least  $10^3$  Monte Carlo steps. Next, a grand canonical Monte Carlo simulation (GCMC) has been performed for fluid species. The fluid particles are hard

spheres of diameter  $\sigma_f$ . However, the GCMC simulation experiment for adsorption is performed in a given, rigidly fixed matrix configuration under the assumption that the fluid–matrix interaction potential,  $U_{fm}(r)$ , permits partitioning of fluid species into the matrix interior. We attempt to create (and annihilate) the fluid species in the entire simulation box, i.e., in the space between fixed matrix particles, in their interior, and in the permeable region of the fluid–matrix interface.

The GCMC part of the simulations has been performed in a commonly used manner. One attempts to displace fluid particles, to create and annihilate them in the entire box, keeping the overall acceptance ratio around 30%. The type of Monte Carlo move (displacement, creation, annihilation) has been chosen randomly. In the majority of runs equilibration has been reached after at most  $10^4$  Monte Carlo steps; the productive part of a run, during which the averages have been collected, involved approximately  $10^5$  steps. The input parameters for the GCMC run are the chemical potential of fluid species,  $\mu_f/kT \equiv \beta\mu_f$ , the configuration of matrix species and their density, and the parameters of the fluid–matrix potential,  $\beta\epsilon_{fm}$ ,  $\beta U_0$ , and  $w$ . The output of simulations will be given in terms of the adsorbed fluid density  $\rho_f = \rho_f(\beta\mu_f)$  and in terms of the fluid–matrix,  $g_{fm}(r)$ , and fluid–fluid,  $g_{ff}(r)$ , pair distribution functions. All the quantities obtained in a simulation run for a given matrix configuration have been saved. We have performed three independent GCMC simulations (for matrix configurations following from the NVT run) and, as a final step, averaged the results.

However, before proceeding with the description of simulation data, we would like to comment the theoretical background. Similarly to the previous example, in order to obtain the pair correlation function of matrix spheres we solve the common Ornstein–Zernike equation complemented by the PY closure. Next, we would like to consider the adsorption of a hard sphere fluid in a microporous environment provided by a disordered matrix of permeable species. The fluid to be adsorbed is considered at density  $\rho_f^* = \rho_f\sigma_f^3$ . The equilibrium between an adsorbed fluid and its bulk counterpart (i.e., in the absence of the matrix) occurs at constant chemical potential. However, in the theoretical procedure we need to choose the value for the fluid density first, and calculate the chemical potential afterwards. The ROZ equations, (22) and (23), are applied to describe the fluid–matrix and fluid–fluid correlations. These correlations are considered by using the PY closure, such that the ROZ equations take the Madden–Glandt form as in the previous example. The structural properties in terms of the pair correlation functions (the fluid–matrix function is of special interest for models with permeability) cannot represent the only issue to investigate. Moreover, to perform comparisons of the structure under different conditions we need to calculate the adsorption isotherms  $\rho_f(\beta\mu_f)$ . The chemical potential of a



fluid adsorbed in a matrix is calculated according to Eqs. (26) and (27). The term describing the chemical potential of adsorbed fluid species at infinite dilution in a matrix,  $\beta\mu_{\text{ex}}^f(\rho_f = 0, \rho_m)$ , corresponds to the second virial coefficient of the fluid–matrix interaction

$$\beta\mu_{\text{ex}}^f(\rho_f = 0, \rho_m) = \rho_m \sigma_f^3 \int d\mathbf{r} \{ \exp[-\beta U_{fm}(r)] - 1 \} \quad (36)$$

The second term in Eq. (27) has been obtained by using  $c_{ff}(r)$  from the solution of the ROZ equations.

Let us proceed with the description of the results from theory and simulation. First, consider the case of a narrow barrier,  $w = 0.5$ , and discuss the pair distribution functions (pdfs) of fluid species with respect to a matrix particle,  $g_{fm}(r)$ . This pdf has been a main focus of previous statistical mechanical investigations of simple fluids in contact with an individual permeable barrier via integral equations and density functional methodology [49–52].

The ROZ equations, for the model in question, have been solved by using the PY approximation at a given matrix and several fluid densities. These densities follow from the GCMC simulations at a chosen value of the chemical potential for fluid species. The fluid–matrix distribution function,  $g_{fm}(r)$ , is shown in Fig. 2. In addition, in Fig. 2(a), we have shown the Boltzmann factor of the fluid–matrix interaction,  $\exp[-\beta U_{fm}(r)]$ , to demonstrate that even at a low fluid density the distribution function inside the barrier exhibits differences from the interaction potential. We observe that, for a narrow barrier, the ROZ–PY theory is very successful in describing the fluid–matrix correlations. Over a wide range of adsorbed fluid density, the theoretical results and simulation data almost coincide for the entire interval of distances. Stronger oscillations of the fluid density in the interior of matrix obstacles, in comparison to the exterior, are promoted by the spherical confinement. Layering effects are strong close to the internal surface of a matrix particle; trends for layering extend up to the center of a matrix particle with increasing adsorbed fluid density. In contrast, close to the external surface the correlations decay rapidly. Stronger trends for layering yield lower fluid density occur in the center of a matrix particle at a chosen value of the diameter for matrix species. The “contact” values, i.e., the values of the  $g_{fm}(r)$  at distances that correspond to vanishing repulsion at both sides of the permeable barrier, are different (despite symmetry of the fluid–matrix potential); a higher value of the pdf is observed close to the internal surface of the barrier.

In Fig. 3, we present the theoretical curves and simulation data for  $g_{fm}(r)$  in the model, similar to the one studied in Fig. 2, but for a twice wider permeable surface of matrix species, i.e.,  $w = 1$ . In general, the agreement of

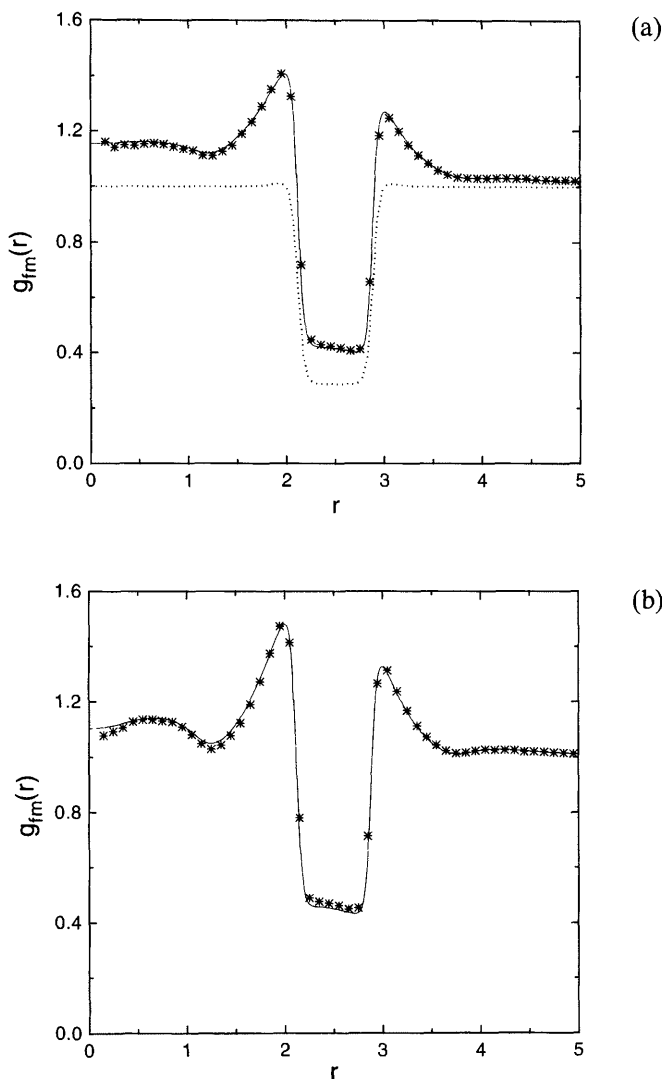


**FIG. 2** Fluid-matrix pair distribution functions  $g_{fm}(r)$  for adsorbed fluid at a chemical potential  $\beta\mu_f = -1, 0$ , and  $2$ , in parts (a), (b), and (c), respectively. The matrix is at density  $\rho_m\sigma_m^3 = 0.6$  and with  $\sigma_m = 5$ . The parameters of the barrier are  $\beta U_0 = 1.25$ ,  $\beta\epsilon_{fm} = 10^{-2}$ , and  $w = 0.5$ . The adsorbed densities are  $0.142$ ,  $0.226$ , and  $0.396$ , in parts (a), (b), and (c), respectively. In (a), the Boltzmann factor of the fluid-matrix interaction is shown by the dotted line, for the reader's convenience. The solid lines here, and in all the following figures, correspond to the ROZ-PY theory, whereas the symbols denote GCMC data.

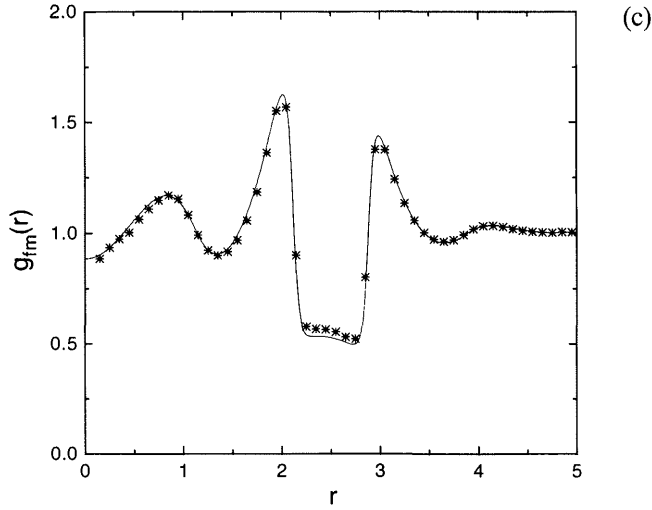


**FIG. 2** Continued.

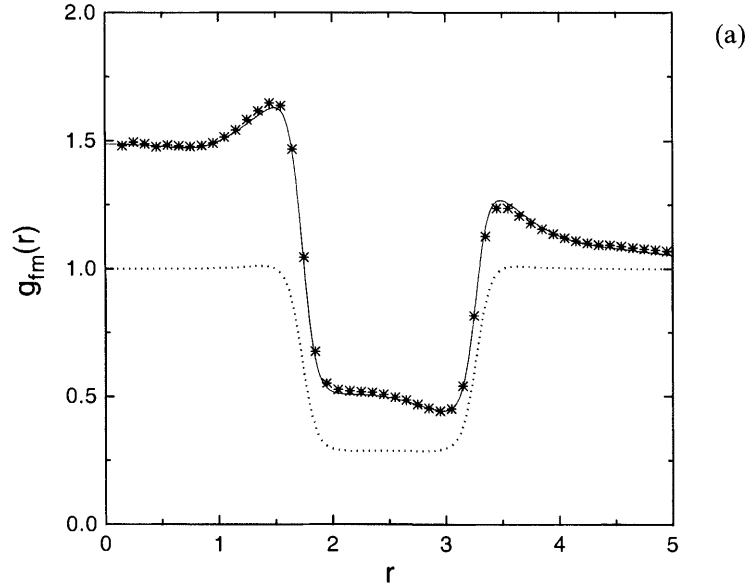
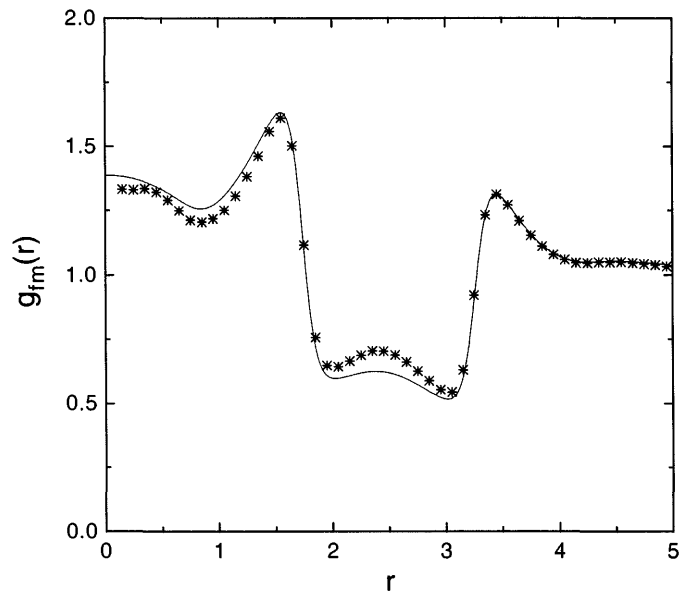


**FIG. 3** The same as in Fig. 2, but for a wider barrier,  $w = 1.0$ . In part (a), the Boltzmann factor of the fluid–matrix interaction is also shown by the dotted line. The chemical potentials are  $\beta\mu_f = -2, 0$ , and  $1$ , and adsorbed densities are  $0.06, 0.195$  and  $0.281$ , in parts (a), (b), and (c), respectively.

(b)



(c)

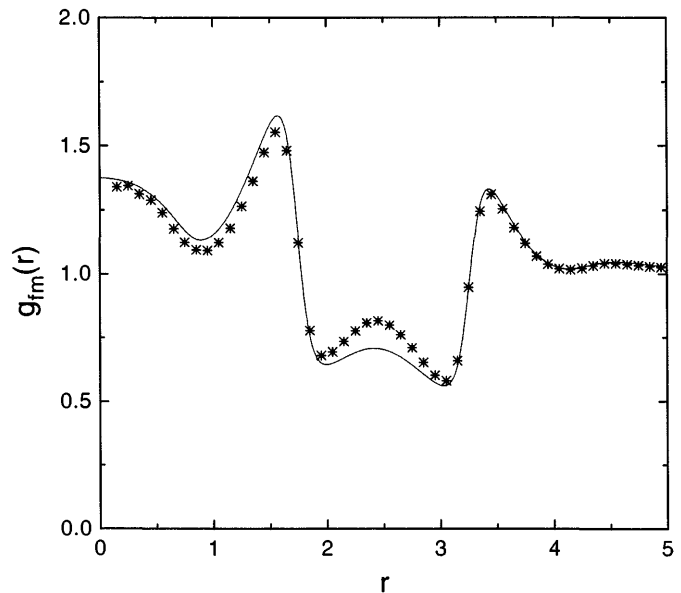
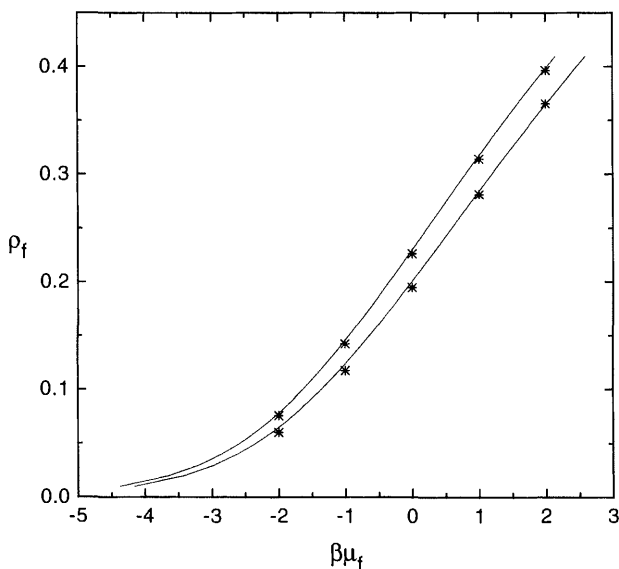


FIG. 3 Continued.

the theory and simulations is good. Only at a high adsorbed fluid density does one observe inaccuracy of the theoretical predictions. In particular, the theory overestimates values of  $g_{fm}(r)$  inside spherical confinement and underestimates the value of a maximum of the fluid density in the center of a permeable barrier. The  $g_{fm}(r)$  at the external surface of matrix species is nevertheless described very well. It is worth mentioning that the ratio of the diameter of matrix particles w.r.t. the diameter of fluid particles, as well as the parameter of the width of the barrier, is of importance. Dependent on these factors, one can observe augmenting density in the center of the permeable core or lower density, in comparison with the fluid density outside matrix species, cf. Fig. 2(c) and 3(c).

Finally, let us discuss the adsorption isotherms. The chemical potential is more difficult to evaluate adequately from integral equations than the structural properties. It appears, however, that the ROZ-PY theory reflects trends observed in simulation perfectly well. The results for the adsorption isotherms for a hard sphere fluid in permeable multiple membranes, following from the ROZ-PY theory and simulations for a matrix at  $\rho_m^* = 0.6$ , are shown in Fig. 4. The agreement between the theoretical results and compu-



**FIG. 4** Adsorption isotherms for a fluid in a matrix with permeable surface,  $\beta U_0 = 1.25$ ,  $\beta \varepsilon_{fm} = 10^{-2}$ , and  $w = 0.5$  (upper line and symbols), and  $w = 1.0$  (lower line and symbols). In both cases,  $\rho_m \sigma_m^3 = 0.6$  and  $\sigma_m = 5$ .

ter simulation data is almost perfect. The adsorbed density increases with increasing chemical potential, as expected. Lower adsorbed density, at a given value of the chemical potential, has been observed in the case of a wider barrier, or in other words for a larger excluded volume due to membranes. The ROZ-PY approximation properly takes into account the effects of the "excluded volume" due to permeable cores, as well as the effects of smoothness of the fluid-matrix repulsive forces. A wider repertoire of closures for the ROZ equations may be required, and a larger set of the GCMC simulation data would be necessary, in order to extend our study for the case of attractive fluid-matrix interactions. The ROZ-PY approach is, however, adequate for models with repulsive interactions. The model under consideration is very simple. However, it permits several interesting extensions. Sophistication of the fluid-matrix interaction may put the system in question closer to the modeling of less idealized, (see, e.g., Refs. 54,55) and seemingly more realistic multimembrane media. Evidently, the adsorption of a fluid mixture into a disordered matrix of species permeable for one component and impermeable for another component would be of interest for the study of osmotic phenomena in microporous media.

A final, simple example to illustrate the application of the ROZ-type theory concerns adsorption of a hard sphere fluid in a matrix of short chain molecules. In general, complex fluids in complex matrices have been investigated less frequently [56–58] than simple fluids in simple matrices, in spite of much interest of the former for basic research and applications. In this part of our study our main goal is to investigate a hard sphere fluid in a disordered matrix of chain molecules [59]. Branched and crosslinked polymers represent basic elements of organic and inorganic gels. These types of structure, however, are too complicated to begin a systematic theoretical and simulation study of the behavior of fluids in microporous disordered media. Therefore, our interest is focused on matrices made of flexible chain molecules.

We consider a fluid of flexible chain molecules made of tangent hard sphere monomers. Each chain consists of  $m$  monomers of diameter  $\sigma_0$ ; the distance between centers of adjacent monomers in a chain is fixed and equals  $\sigma_0$ . However, the angle formed by any three consecutive monomers in a chain is not fixed. The only restriction is that monomers belonging to a given chain do not overlap each other. Let us describe first a computer simulation procedure.

A set of flexible chains is considered in the canonical  $NVT$  ensemble. The density of chains,  $\rho_{\text{ch}} = N_{\text{ch}}/V$  ( $N_{\text{ch}}$  is a chosen number of chains), is the parameter of simulation. The system of flexible chains in question has been equilibrated, then during the productive part of the simulation run the pair

distribution function of monomers,  $g_{mm}(r)$ , belonging either to a given chain or to two different chains, has been evaluated. Stability of the  $g_{mm}(r)$ , as well as the value of acceptance ratio around 30%, serves as a criterion that the values for statistical averages are adequate. A Monte Carlo step consists of attempts to displace all the chains in a simulation box and of a combination of slithering snake movements for each chain. Several algorithms have been used for simulations of chain molecules, see, e.g., Refs. 60–63. In this study, one end of a chain has been chosen at random and designated the “head.” A new monomer is attempted to be attached to the head. The monomer at the other end of the chain is removed if the attachment attempt is successful. Next, we proceed in a similar manner with other monomers in a chosen chain. In all the *NVT* runs we have performed  $10^4$  MC steps for equilibration of a chain fluid and  $10^5$  MC steps for the collection of ensemble averages. The accuracy of the pair distribution functions of a chain fluid with molecules each containing 4, 8, and 16 monomers has been verified by a comparison with the simulation data of Chang and Sandler [61].

A few configurations (usually not more than three) picked up from the productive part of the *NVT* run have been chosen as configurations for matrix species. These fixed configurations are used in the following independent GCMC runs for fluid hard sphere adsorption. The only requirement implied at the *NVT* step is that the configurations of matrix chains are statistically “independent” with respect to each other. We have chosen matrix configurations such that they are distanced by not less than  $10^3$  Monte Carlo steps in the *NVT* runs. The input data for the GCMC simulations of adsorption of a fluid in a matrix media are the chemical potential, the volume of the simulation box used in the *NVT* ensemble simulation of chains, and the configurations of matrix species. The results of independent GCMC runs for each matrix configuration have been averaged at the end of the procedure. We have observed that, for the model in question, the results for adsorbed density are weakly dependent on the number of matrix configurations used for averaging.

In the GCMC simulations we are considering a fluid of hard spheres with diameter  $\sigma_1$  such that it equals the diameter of monomers belonging to chains, i.e.,  $\sigma_1 = \sigma_0$ . The density of a hard sphere fluid in the presence of a rigidly fixed matrix “adjusts” to a chosen value of the chemical potential species, and at the end of the simulation run attains a stable value  $\rho_f$ . The bulk value of fluid density,  $\rho_f^{\text{bulk}}$ , has been evaluated by using the chemical potential according to the Carnahan–Starling equation of state for hard spheres. Then the partitioning coefficient for fluid species in a matrix,  $K = \rho_f / \rho_f^{\text{bulk}}$ , can be calculated. It characterizes adsorption dependent on the chemical potential.

At present, one of the most successful theories for the description of flexible chain molecules is the chemical association theory of Wertheim [64–66]. A chain molecule in this approach is thought of as a result of the site–site association of monomers each possessing two attractive sites. To avoid unnecessary repetition (we refer the reader to Ref. 67 for a more detailed presentation), we would like to mention that the Ornstein–Zernike-like integral equation is solved for the model of associating monomers in the Percus–Yevick approximation complemented by the ideal chain approximation discussed in detail by Chang and Sandler [61]. Dependent on the monomer density and the energy of association, chain molecules with an average number of beads,  $M$ , are formed. By comparison with computer simulation data for flexible chains with a fixed number of beads,  $m$ , it has been shown in Ref. 61 that the theory provides a very accurate description of the pair distribution function,  $g_{mm}(r)$ , over a wide range of particle density (except in the very low density region) and up to  $M = m = 16$ . We are exactly interested in this range of parameters.

As in our previous notations, the species superscript “0” is for the matrix component and the species superscript “1” denotes the fluid component. The fluid–matrix interaction is chosen between a fluid particle and a monomer belonging to a chain by using the model of additive hard spheres. The fluid–matrix and fluid–fluid interactions are

$$U^{10}(r) = U^{11}(r) = \begin{cases} \infty, & r < \sigma \\ 0, & r > \sigma \end{cases} \quad (37)$$

where  $\sigma = \sigma_1 = \sigma_0$ . Without loss of generality let us choose it as the length unit,  $\sigma = 1$ . The ROZ equations necessary to apply to the model are exactly the equations (22) and (23) with  $\rho^0 = N_{\text{ch}}M/V$  corresponding to the number of monomer beads in the entire matrix of chains. For the sake of technical convenience, let us introduce the notation  $\gamma = h - c$ . In this part of our work, the hypernetted chain approximation (HNC) and the Percus–Yevick (PY) approximations are involved. The HNC closures for the fluid–matrix and fluid–fluid correlation functions are

$$c^{10}(r) = \exp[-\beta U^{10}(r)] \exp[\gamma^{00}(r)] - 1 - \gamma^{10}(r) \quad (38)$$

and

$$c^{11}(r) = \exp[-\beta U^{11}(r)] \exp[\gamma^{11}(r)] - 1 - \gamma^{11}(r) \quad (39)$$

However, in the case of the ROZ equations, in addition to these closures, we also must use the closure for the blocking part of the direct correlation function. The HNC closure for this function reads

$$c^{11(2)}(r) = \exp[\gamma^{11(2)}(r)] - 1 - \gamma^{11(2)}(r) \quad (40)$$



Eqs. (22) and (23), together with closures (38)–(40), represent a complete ROZ–HNC problem for the numerical solution. The Percus–Yevick closure is given similarly to Eq. (33); however, in addition, the blocking term in the fluid–fluid direct correlations is neglected,  $c^{11(2)}(r) = 0$ .

The adsorption isotherms have been obtained according to the procedure of Ford and Glandt for a hard sphere fluid in a hard sphere matrix [23]. Let us denote the packing fraction of matrix species by  $\eta_m$  ( $\eta_m = \pi N_{\text{ch}} M \sigma^3 / 6$ ). The chemical potential,  $\beta\mu_1(\rho^1, \rho^{\text{ch}}; M) \equiv \beta\mu_1(\rho^1, \eta_m; M)$ , is given as

$$\beta\mu_1(\rho^1, \eta_m) = \ln(\rho_1 \sigma_1^3) - \beta\mu_1(\rho^1 = 0, \eta_m) - \int_0^{\rho^1} d\rho' \int d\mathbf{r} c^{11(1)}(r, \rho'; \eta_m), \quad (41)$$

where  $c^{11(1)}(r, \rho^1; \eta_m)$  is the connected part of the direct correlation function between hard sphere particles in a matrix of chains; the term

$$\beta\mu_1(\rho^1 = 0, \eta_m) = (3\eta_m^3 - 9\eta_m^2 + 8\eta_m)/(1 - \eta_m)^3 - \frac{(M - 1)}{M} \eta_m(5 - 2\eta_m)/(1 - \eta_m)(2 - \eta_m) \quad (42)$$

corresponds to an infinite dilution of fluid particles in a matrix of chains (this term has been approximated by using the expression for a mixture of hard spheres and chains [68]). The accuracy of the adsorption isotherms has been evaluated by comparison with our simulation data.

We would like to discuss consistently the results obtained in the theory and simulations for a hard sphere fluid adsorbed in a matrix of chains with four, eight, and sixteen monomer beads ( $m = M = 4; 8; 16$ ).

Our estimates for the partitioning coefficients of hard spheres in matrices of chain molecules are collected and given in Table 1. In qualitative similarity to the adsorption isotherms, the partitioning coefficient  $K$  decreases with increasing matrix packing fraction, i.e., with decreasing microporosity. However, the values of the partitioning coefficient are very close in the cases  $m = 4$  and  $m = 8$ , at a fixed value of the matrix packing fraction. In matrices with a higher packing fraction,  $\eta_m = 0.126$  and  $0.25$ , we observe that the partitioning coefficient increases with increasing chemical potential in the region of  $\beta\mu_1$  investigated.

Let us describe the results for the case of a matrix made of chains with four beads, i.e.,  $m = M = 4$ . We observe that both the PY and the HNC approximation quite accurately describe the adsorption isotherms in matrices of different microporosity (Fig. 5). However, a discrepancy between the HNC results and simulation data increases with increasing chemical potential, especially at higher matrix densities. The structural

**TABLE 1** The Partitioning Coefficient,  $K$ , for Hard Spheres in a Matrix of Chains with  $m$  Monomers at Packing Fraction  $\eta_m$

$\eta_m$	$\beta\mu_1$	$m = 4$		$m = 8$		$m = 16$	
		$\rho_1^{\text{MC}}$	$K$	$\rho_1^{\text{MC}}$	$K$	$\rho_1^{\text{MC}}$	$K$
0.052	0	0.189	0.792	0.200	0.800	0.201	—
0.052	1.5	0.313	0.824	0.315	0.829	0.313	—
0.052	2.5	0.382	0.830	0.384	0.835	0.383	—
0.126	0	0.130	0.520	0.131	0.524	0.134	0.000
0.126	1.5	0.220	0.580	0.222	0.584	0.223	0.000
0.126	2.5	0.280	0.609	0.281	0.611	0.282	0.000
0.250	0	0.036	0.144	0.025	0.100	0.026	0.000
0.250	1.5	0.077	0.203	0.060	0.158	0.079	0.000
0.250	2.5	0.110	0.239	0.089	0.193	0.112	0.000

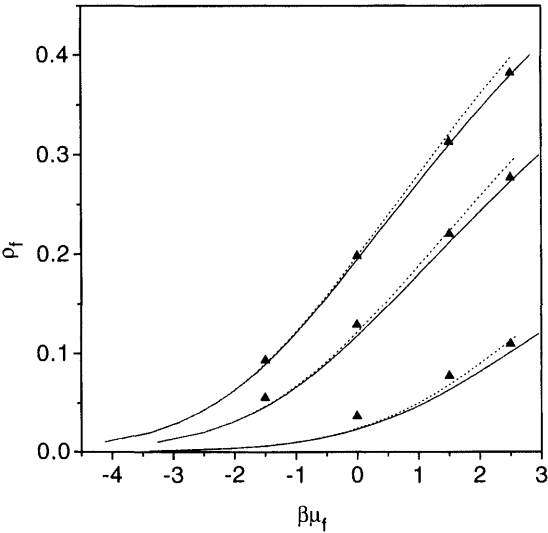


**FIG. 5** Adsorption isotherms for a hard sphere fluid from the ROZ–PY and ROZ–HNC theory (solid and dashed lines, respectively) and GCMC simulations (symbols). Three pairs of curves from top to bottom correspond to matrix packing fraction  $\eta_m = 0.052, 0.126$ , and  $0.25$ , respectively. The matrix in simulations has been made of four beads ( $m = M = 4$ ).

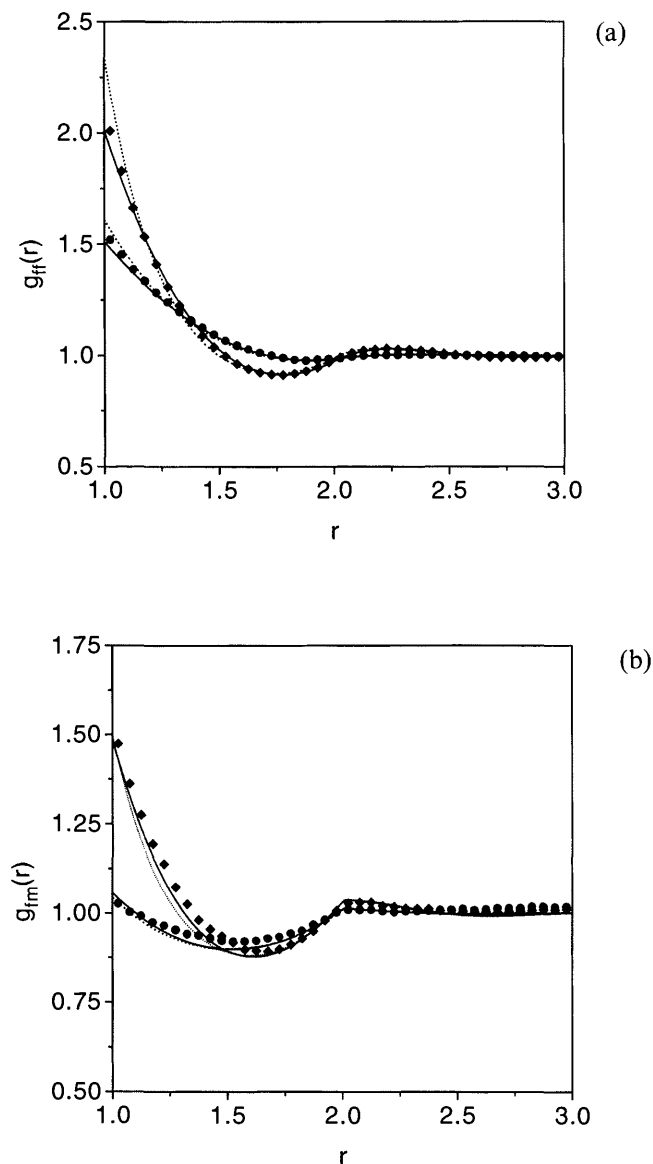


**FIG. 6** The fluid–fluid (a) and fluid–matrix monomer (b) pair distribution functions for the matrix made of chains with four beads ( $m = M = 4$ ) at packing fraction  $\eta_m = 0.052$ . The nomenclature of lines and symbols is similar to that of Fig. 5; however, the upper group of results with square symbols is for  $\beta\mu_f = 2.5$  and the lower group of results with circles is for  $\beta\mu_f = 0$ .

properties, following from the PY approximation, agree very well with simulation data for a highly microporous matrix ( $\eta_m = 0.052$ ); see Fig. 6. At a lower matrix porosity ( $\eta_m = 0.126$ ) theoretical predictions for  $g_{10}(r)$  remain successful, whereas the function  $g_{11}(r)$  is reproduced less accurately (Fig. 7). We observe, however, that the fluid–fluid correlations are stronger

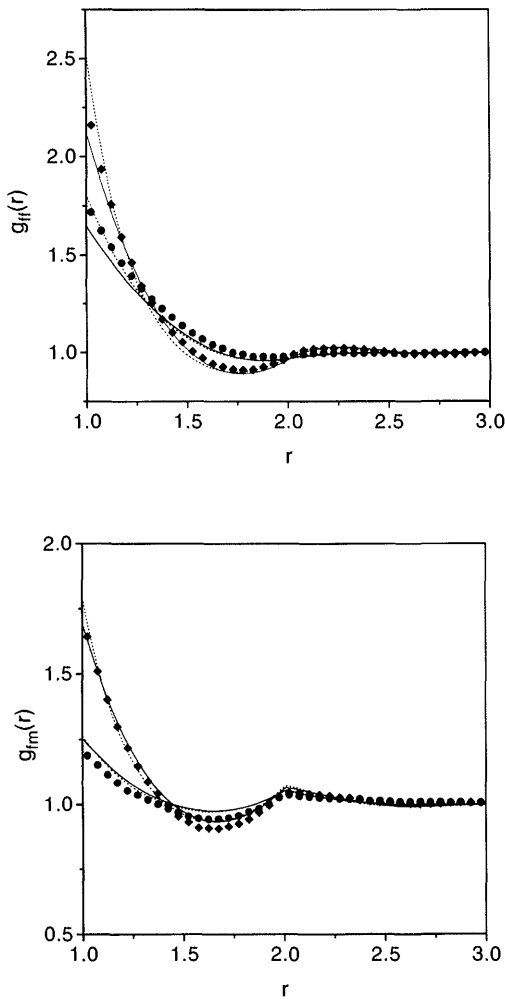


**FIG. 7** The same as in Fig. 6, for the matrix made of chains with four beads ( $m = M = 4$ ) at packing fraction 0.126. The nomenclature of lines and symbols and their location are similar to those of Fig. 6.

than the fluid–matrix correlations for the values of the chemical potential in question. These trends are well described by the closures involved in our study.

Theoretical results of similar quality have been obtained for thermodynamics and the structure of adsorbed fluid in matrices with  $m = M = 8$ , see Figs. 8 and 9, respectively. However, at a high matrix density ( $\eta_m = 0.273$ ) we observe that the fluid structure, in spite of qualitatively similar behavior to simulations, is described inaccurately (Fig. 10(a)). On the other hand, the fluid–matrix correlations from the theory agree better with simulations in the case  $m = M = 8$  (Fig. 10(b)). Very similar conclusions have been obtained in the case of matrices made of 16 hard sphere beads. As an example, we present the distribution functions from the theory and simulation in Fig. 11. It is worth mentioning that the fluid density obtained via GCMC simulations has been used as an input for all theoretical calculations.

We conclude, from the results given above, that both the ROZ–PY and ROZ–HNC theories are sufficiently successful for the description of the pair distribution functions of fluid particles in different disordered matrices. It seems that at a low adsorbed density the PY closure is preferable, whereas

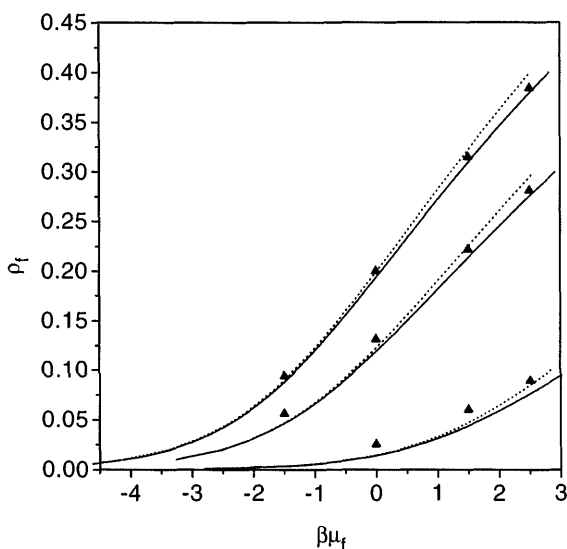


**FIG. 8** The same as in Fig. 5, but for the matrix made of chains with eight beads ( $m = M = 8$ ). Three pairs of curves from top to bottom correspond to matrix packing fraction  $\eta_m = 0.052$ ,  $0.126$  and  $0.273$ , respectively.

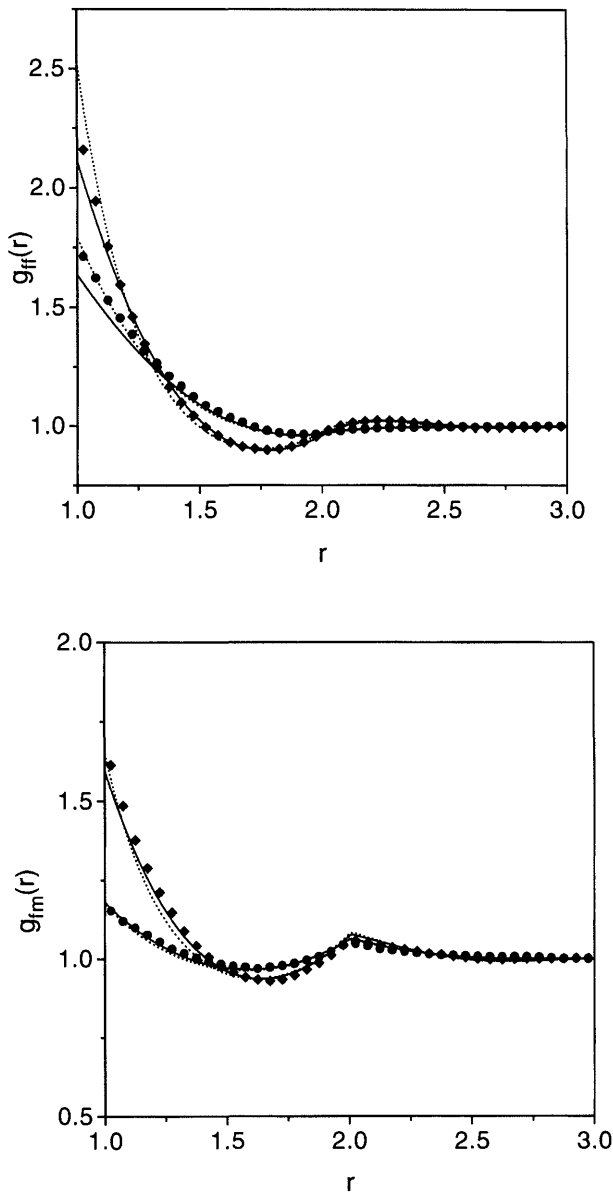


**FIG. 9** The same as in Fig. 6, but for the matrix model  $m = M = 8$ , at packing fraction 0.126. The nomenclature of lines and symbols and their location are similar to those of Fig. 6. The upper group of results is for  $\beta\mu_f = 2.5$  and the lower group of results is for  $\beta\mu_f = 0$ .

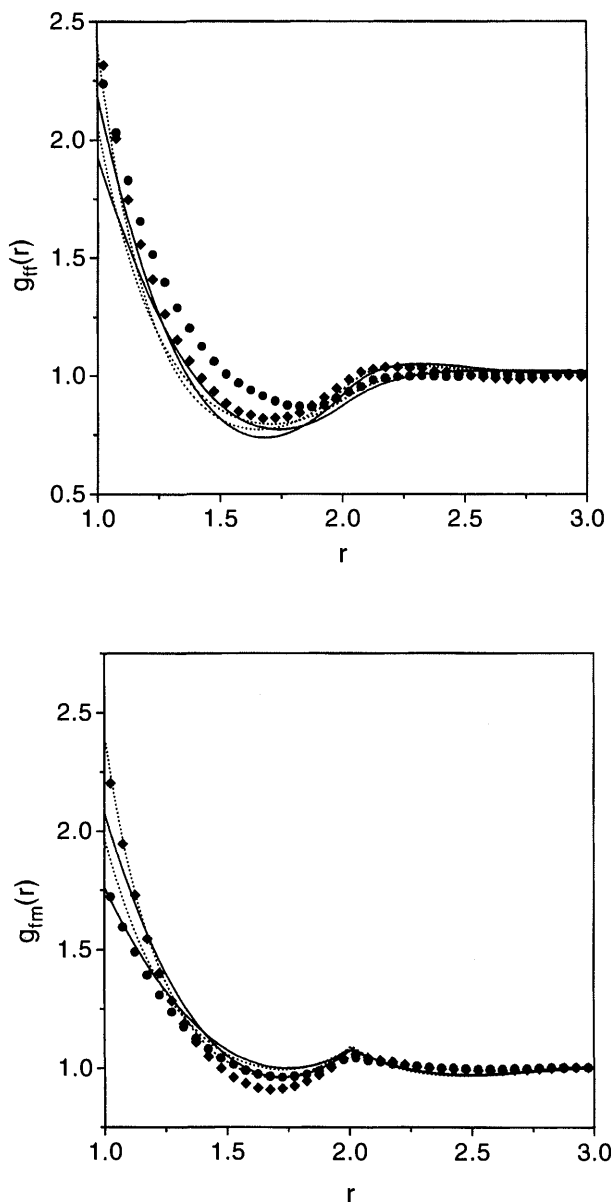


**FIG. 10** The same as in Fig. 6, but for the matrix model  $m = M = 8$ , at packing fraction 0.273. The nomenclature of lines and symbols is similar to that of Fig. 6. Squares and circles are for  $\beta\mu_f = 2.5$  and for  $\beta\mu_f = 0$ , respectively. Similarly upper and lower lines at contact are for a higher and lower value of the chemical potential.

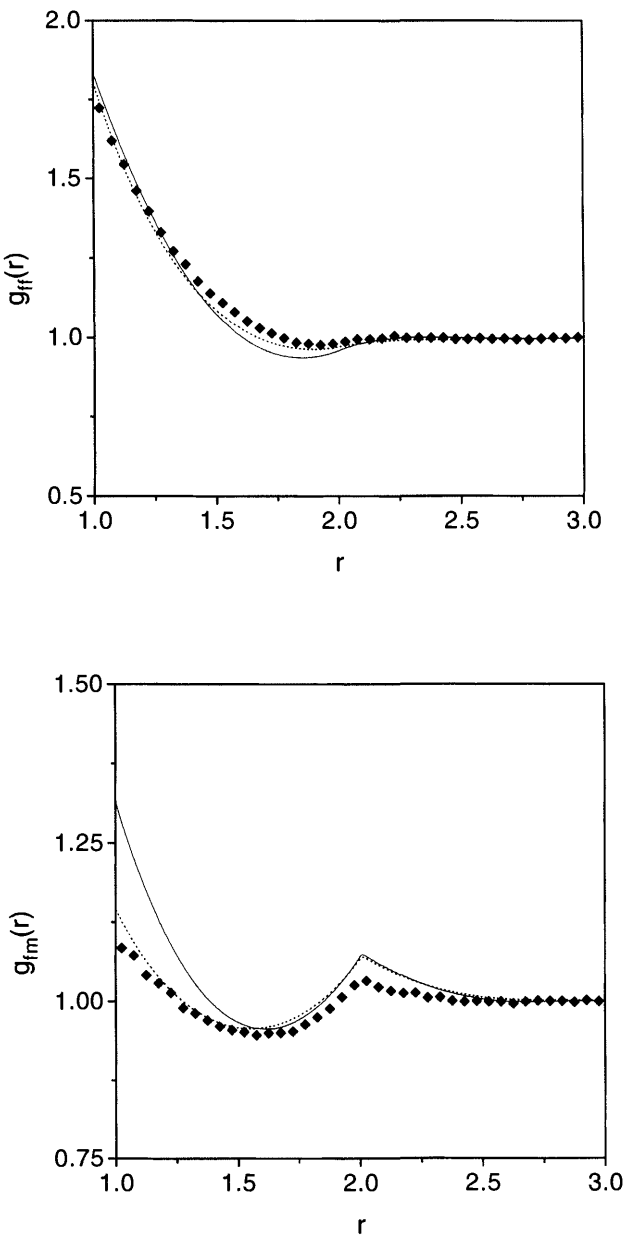


**FIG. 11** The same as in Fig. 6, but for the matrix model  $m = M = 16$ , at packing fraction 0.126. The chemical potential of fluid species is zero,  $\beta\mu_1 = 0$ . The nomenclature of lines and symbols is similar to that of Fig. 6.



the HNC works slightly better for high adsorbed densities. Our expectation is that a combined closure (in the spirit of Rogers–Young or Verlet) combining two approximations, such as the PY and the HNC, may yield quite accurate structure properties and adsorption isotherms. The HNC closure with the bridge functions contribution (see, e.g., Ref. 21) may be successful as well. However, this closure is too involved to apply to the model in question. We have shown that the adsorption is predominantly determined by the matrix packing fraction effects; at fixed  $\eta_m$  the fluid density in the matrix is almost equal for the cases  $m = 4$  and 8. The theory correctly shows prevailing fluid–fluid correlations compared with the fluid–matrix correlations, in close agreement with the predictions of computer simulations.

The model in question may serve as a benchmark, or as a reference system, for several extensions. In particular, the adsorption of simple fluids in cross-linked and branched-chain molecules may be studied as the next logical step. Adsorption of a two-component fluid mixture in a matrix of chain molecules made of two types of monomer with different fluid–matrix affinity may exhibit interesting features.

#### **IV. ELEMENTS OF THE THEORY OF PARTLY QUENCHED INHOMOGENEOUS FLUIDS**

To the best of our knowledge, there was only one attempt to consider inhomogeneous fluids adsorbed in disordered porous media [31] before our recent studies [32,33]. Inhomogeneous replica Ornstein–Zernike equations, complemented by either the Born–Green–Yvon (BGY) or the Lovett–Mou–Buff–Wertheim (LMBW) equation for density profiles, have been proposed to study adsorption of a fluid near a plane boundary of a disordered matrix, which has been assumed uniform in a half-space [31]. However, the theory has not been complemented by any numerical solution. Our main goal is to consider a simple model for adsorption of a simple fluid in confined porous media and to solve it. In this section we follow our previously reported work [32,33].

First we are looking for the adsorption of a fluid consisting of particles of species  $m$ , in a slit-like pore of width  $H$ . The pore walls are chosen normal to the  $z$  axis and the pore is centered at  $z = 0$ . Adsorption of the fluid  $m$ , i.e., the matrix, occurs at equilibrium with its bulk counterpart at the chemical potential  $\mu_m$ . The matrix fluid is then characterized by the density profile,  $\rho_m(z)$  and by the inhomogeneous pair correlation function  $h_{mm}(1, 2)$ . The structure of that fluid is considered

quenched at a state determined by  $\mu_m$ , thus a confined porous medium is formed.

Now, we would like to investigate adsorption of another fluid of species  $f$  in the pore filled by the matrix. The fluid  $f$  outside the pore has the chemical potential  $\mu_f$ ; at equilibrium the adsorbed fluid  $f$  reaches the density distribution  $\rho_f(z)$ . The pair distribution of  $f$  particles is characterized by the inhomogeneous correlation function  $h_{ff}(1, 2)$ . The matrix and fluid species are denoted by 0 and 1. We assume the simplest form of the interactions between particles and between particles and pore walls, choosing both species as hard spheres of unit diameter

$$U_{ij}(r) = \begin{cases} \infty, & r < 1 \\ 0, & r > 1 \end{cases}; \quad U(z) = \begin{cases} \infty, & z > 0.5|H - 1| \\ 0, & \text{otherwise} \end{cases} \quad (43)$$

where  $i, j$  are species indices. The evaluation of the matrix structure is irrelevant to the procedure below; it is obtained using the second order Ornstein-Zernike (OZ2) equation

$$h_{00}(1, 2) - c_{00}(1, 2) = \int d^3\rho_0(z_3) c_{00}(1, 3) h_{00}(3, 2) \quad (44)$$

supplemented by the LMBW equation for the density profile (DP)

$$\frac{\partial \ln \rho_1(z_1)}{\partial z_1} + \frac{\partial \beta U(z_1)}{\partial z_1} = \int d^2 c_{00}(1, 2) \frac{\partial \rho_0(z_2)}{\partial z_2} \quad (45)$$

and the second-order Percus-Yevick (PY2) closure

$$y_{00}(1, 2) = 1 + h_{00}(1, 2) - c_{00}(1, 2) \quad (46)$$

where  $y_{00}(1, 2)$  is the inhomogeneous cavity distribution function. The solution of the problem comprising Eqs. (44)–(46) yields  $\rho_0(z)$  and  $h_{00}(1, 2)$ , such that the one-particle cavity distribution function  $y_0(z) = \rho_0(z) \exp[\beta U(z)]$  outside the pore tends to its limiting value, determined by the configurational chemical potential  $y_0(z \rightarrow \pm\infty) = \exp(\beta\mu_0)$ . The inhomogeneous ROZ (IROZ) equations represent the essence of the procedure. They are [31,32]

$$\left. \begin{aligned}
 h_{10}(1,2) - c_{10}(1,2) &= \int d^3\rho_0(z_3) c_{10}(1,3) h_{00}(3,2) \\
 &\quad + \int d^3\rho_1(z_3) c_{c,11}(1,3) h_{10}(3,2) \\
 h_{01}(1,2) - c_{01}(1,2) &= \int d^3\rho_0(z_3) c_{00}(1,3) h_{01}(3,2) \\
 &\quad + \int d^3\rho_1(z_3) c_{01}(1,3) h_{c,11}(3,2) \\
 h_{11}(1,2) - c_{11}(1,2) &= \int d^3\rho_0(z_3) c_{10}(1,3) h_{01}(3,2) \\
 &\quad + \int d^3\rho_1(z_3) c_{c,11}(1,3) h_{11}(3,2) \\
 &\quad + \int d^3\rho_1(z_3) c_{b,11}(1,3) h_{c,11}(3,2), \\
 h_{c,11}(1,2) - c_{c,11}(1,2) &= \int d^3\rho_1(z_3) c_{c,11}(1,3) h_{c,11}(3,2)
 \end{aligned} \right\} \quad (47)$$

The fluid–fluid pair ( $h$ ) and direct ( $c$ ) correlation functions consist of the blocking and connected part,  $\varphi_{11}(1,2) = \varphi_{b,11}(1,2) + \varphi_{c,11}(1,2)$ , where  $\varphi$  stands for  $h$  and  $c$ , as appropriate. Similarly to [31], the BGY equation is used to relate the DPs with the pair functions

$$\frac{\partial \ln \rho_1(z_1)}{\partial z_1} + \beta \frac{\partial w(z_1)}{\partial z_1} = -\beta \int d^2\rho_1(z_2) g_{11}(1,2) \frac{\partial U_{11}(12)}{\partial z_2} \quad (48)$$

where  $g_{11}(1,2) = 1 + h_{11}(1,2)$ , and the effective one-body potential satisfies the relation

$$\frac{\partial w(z_1)}{\partial z_1} = \frac{\partial U(z_1)}{\partial z_1} + \int d^2\rho_0(z_2) g_{10}(1,2) \frac{\partial U_{10}(12)}{\partial z_2} \quad (49)$$

and where  $g_{10}(1,2) = 1 + h_{10}(1,2)$ .

Finally, the closure relations for the inhomogeneous pair functions must be chosen. The PY approximation for the fluid–fluid direct correlation function presumes that its blocking part vanishes. This implies that  $c_{b,11}(i,j) = 0$ , and

$$y_{ij}(1,2) = 1 + h_{ij}(1,2) - c_{ij}(1,2) \quad (50)$$

for  $(i,j) = (1,0)$  and  $(1,1)$ . On the other hand, the inhomogeneous or second-order hypernetted chain (HNC2) approximation reads

$$c_{b,11}(i,j) = \exp \{h_{b,11}(i,j) - c_{b,11}(i,j)\} - 1 - \{h_{b,11}(i,j) - c_{b,11}(i,j)\} \quad (51)$$

for the blocking term of the fluid–fluid function, and

$$y_{ij}(1,2) = \exp \{h_{ij}(1,2) - c_{ij}(1,2)\} \quad (52)$$

for  $(i,j) = (1,0)$  and  $(1,1)$ .

In the numerical solution the matrix structure is evaluated from Eqs. (44)–(46). Then Eqs. (47)–(49) with corresponding closure approximations are solved. Details of the solution have been presented in Refs. 32 and 33. Briefly, the numerical algorithm uses an expansion of the two-particle functions into a Fourier–Bessel series. The three-fold integrations are then reduced to sums of one-dimensional integrations. In the case of hard-sphere potentials, the BGY equation contains the delta function due to the derivative of the pair interactions. Therefore, the integrals in Eqs. (48) and (49) are onefold and contain the “contact” values of the functions  $g_{ij}(z_1, z_2, \sqrt{R^2 + z_{12}^2} = 1)$  for  $(i,j) = (1,0)$  and  $(1,1)$ ; these values have been evaluated by interpolation. As is often the case, the convergence of the numerical scheme is more difficult for the HNC2 closure than for the PY2 closure.

In order to test the theory, we have performed grand canonical ensemble Monte Carlo (GCMC) simulations. A rectangular simulation cell of dimensions  $XL \times YL \times H$  with periodic boundary conditions in the plane parallel to the pore walls has been used. The simulations consist of two steps. First, the grand canonical ensemble technique is used to fill the pore with the hard sphere matrix. After equilibration, a configuration of matrix particles, where the number of particles corresponds to the average number of particles at the given chemical potential, is selected and the second step of the simulations is started. During this step, we perform grand canonical ensemble simulations of the fluid in a pore filled with the matrix species.

The simulations are repeated several times, starting from different matrix configurations. We have found that about 10 replicas of the matrix usually assure good statistics for the determination of the local fluid density. However, the evaluation of the nonuniform pair distribution functions requires much longer runs; at least 100 matrix replicas are needed to calculate the pair correlation functions for particles parallel to the pore walls. However, even as many as 500 replicas do not ensure the convergence of the simulation results for perpendicular configurations.

We present some of the results obtained for equal sized hard-sphere fluid and hard-sphere matrix in Figs. 12 and 13. In these figures we show the

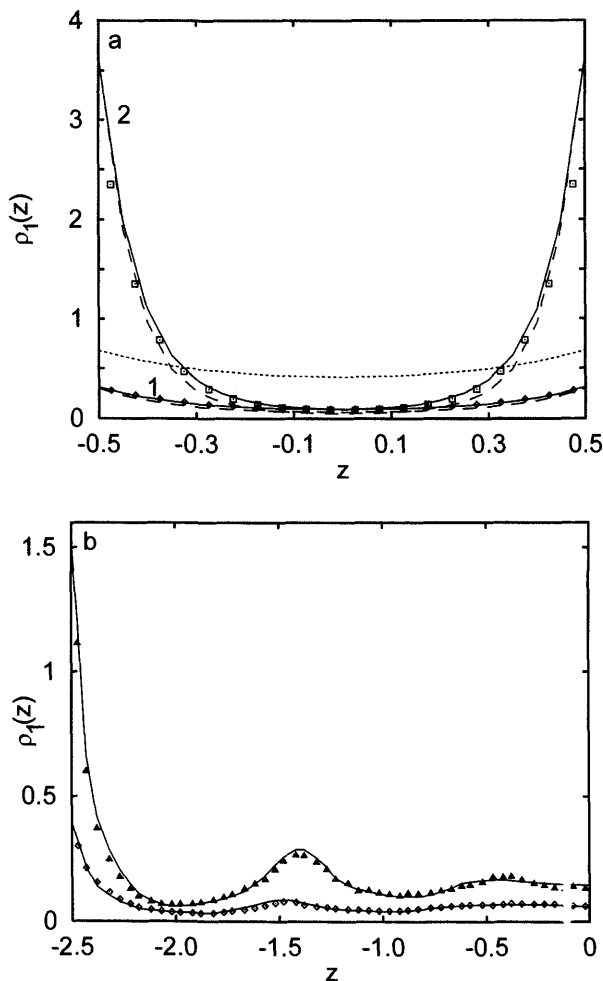


**FIG. 12** (a) A comparison of the simulated (GCMC) and theoretical (ROZ2 + BGY + HNC2 and PY2 approximations) density profiles  $\rho_1(z)$  of an adsorbed fluid and in a disordered inhomogeneous matrix in a slit-like pore of width  $H=2$ . The chemical potential of the matrix particles is  $\beta\mu_0=0.935$ . The curves labeled 1 and 2 are for the chemical potential of fluid species  $\beta\mu_1=0.935$  and 5.8346, respectively. The PY2, HNC2, and Monte Carlo results are given by the solid and dashed lines, and the symbols, respectively. The dotted line corresponds to the density profile of fixed obstacles,  $\rho_0(z)$ . (b) HNC2 and GCMC results for the density profiles for the case of a wide pore,  $H=6$ . The chemical potential of the matrix species is  $\beta\mu_0=4.8147$ ; the chemical potential of the fluid species is  $\beta\mu_1=3.1136$  (lower curve and symbols) and  $\beta\mu_1=7.0026$  (upper curve and symbols).

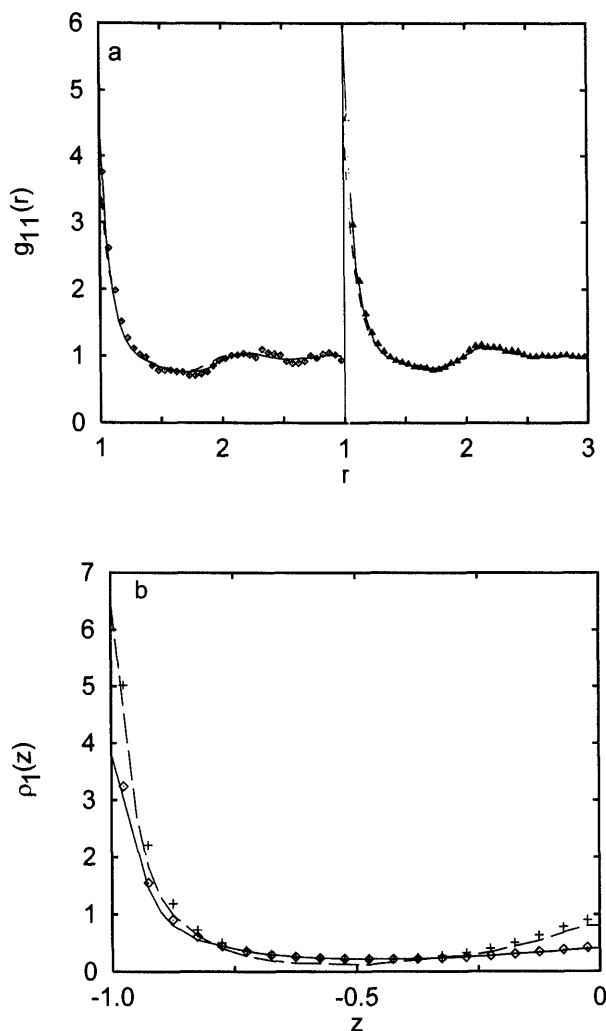


**FIG. 13** (a) A comparison of the fluid–fluid inhomogeneous pair distribution functions  $g_{11}(1,2)$  obtained using the HNC2 and PY2 approximations in the ROZ2 + BGY equations, with GCMC results. The functions  $g_{11}^{\parallel,w}$  (left panel) and  $g_{11}^{\parallel,c}$  (right panel) are for the fluid particles in a parallel configuration in the plane of closest approach to the pore walls and in the pore center. The HNC2 and PY2 results are given by the solid and dashed lines, respectively. The GCMC results are given as symbols. The fluid and matrix particles are of equal size. The chemical potentials of matrix and fluid species are  $\beta\mu_0 = 3.1136$  and  $\beta\mu_1 = 8.3530$  ( $\rho_0^3\sigma_0^3 = 0.75$ ). The pore width is  $H = 3$ . (b) The same as in (a), but for the fluid–matrix inhomogeneous pair distribution function.

density profiles and pair distribution functions of a fluid adsorbed in a pore filled with quenched matrix. Fig. 12 shows the density profiles obtained for  $\beta\mu_0 = 0.935$  (corresponding to the bulk fluid density  $\rho_0\sigma_0^3 = 0.25$  when the Carnahan–Starling equation of state is used) and  $H = 2$  (part (a)) and for  $\beta\mu_0 = 4.8147$  (corresponding to the bulk density equal to  $\rho_0\sigma_0^3 = 0.5$ ) and  $H = 6$  (part (b)).

Let us first analyze the results for  $H = 2$ . At  $\beta\mu_0 = 0.935$  the matrix density distribution  $\rho_0(z)$  in the entire pore is almost uniform. Consequently, the distribution of empty space throughout the pore is almost homogeneous. When the chemical potential of the fluid species,  $\mu_1$ , increases, the density of fluid close to the pore walls increases substantially, whereas in the pore center  $\rho_1(z)$  remains almost independent of  $\mu_1$ . Both theories, HNC2 and PY2, yield similar results for the density profiles and both agree well with the GCMC data. However, some discrepancies between the theory and simulations are observed close to the walls in a narrow pore. The absence of a large difference between the PY2 and HNC2 theories indicates that blocking effects due to the presence of the matrix are not essential.

We also have studied fluid distribution in the pore  $H = 6$  (Fig. 12(b)) at  $\beta\mu_0 = 4.8147$  and at two values of  $\beta\mu_1$ , namely at 3.1136 ( $\rho_1\sigma_1^3 = 0.4$ ) and at 7.0026 ( $\rho_0\sigma_0^3 = 0.7$ ; Fig. 12(b)). In this pore, we observe layering of the adsorbed fluid at high values of the chemical potential  $\beta\mu_1$ . The maxima of the density profile  $\rho_1(z)$  occur at distances that correspond to the diameter of fluid particles. With an increase of the fluid chemical potential, pore filling takes place primarily at pore walls, but second-order maxima on the density profile  $\rho_1(z)$  are also observed. The theory reproduces the computer simulation results quite well.

Let us now show the results obtained for inhomogeneous pair correlation functions. In Figs. 13(a) and 13(b) we present the projections of the pair correlation functions for particles parallel to the pore walls in the plane of the closest approach to the walls,  $g_{ij}^{\parallel,w}$ , and in the pore center,  $g_{ij}^{\parallel,c}$ , for pore width  $H = 3$ . We observe that parallel correlations between the fluid particles are stronger in the pore center than at the pore walls. In contrast, the fluid–matrix parallel correlations are slightly stronger in the plane of closest approach, due to the higher value of the matrix density at the walls. The theoretical approximations (HNC2 and PY2) agree well with the simulation data. The HNC2 approximation yields slightly higher contact values for the pair correlation functions at the contact than does the PY2 approximation.

The theory presented in this section is based on the grand canonical ensemble formulation, which is perfectly well-suited for the description of confined systems. Undoubtedly, in the case of attractive–repulsive interparticle forces unexpected structural and thermodynamic behavior in partly

quenched confined systems may be observed. However, this problem has not been addressed so far.

## V. THE ROZ THEORY FOR IONIC PARTLY QUENCHED SYSTEMS

It is of special interest for many applications to consider adsorption of fluids in matrices in the framework of models which include electrostatic forces. These systems are relevant, for example, to colloidal chemistry. On the other hand, electrodes made of specially treated carbon particles and impregnated by electrolyte solutions are very promising devices for practical applications. Only a few attempts have been undertaken to solve models with electrostatic forces, those have been restricted, moreover, to ionic fluids with Coulomb interactions. We would like to mention in advance that it is clear, at present, how to obtain the structural properties of ionic fluids adsorbed in disordered charged matrices. Other systems with higher-order multipole interactions have not been studied so far. Thermodynamics of these systems, and, in particular, peculiarities of phase transitions, is the issue which is practically unsolved, in spite of its great importance. This part of our chapter is based on recent works from our laboratory [37,38].

It is well known that it is difficult to solve numerically integral equations for models with Coulomb interaction [69,70]. One needs to develop a re-normalization scheme for the long-range terms of ion-ion correlations. Here we must do that for ROZ equations.

We consider a partly quenched mixture consisting of two ionic fluids of point-like particles. Each of the fluids contains a neutral combination of positively and negatively charged ions. One of the fluids describes a quenched charged system. It is equilibrated at temperature  $T_0$  in a medium with dielectric constant  $\varepsilon_0$ . The quenched and fluid components are denoted by superscripts 0 and 1, respectively. An ionic fluid adsorbed in this quenched matrix is investigated at temperature  $T_1$  in a medium with dielectric constant  $\varepsilon_1$ . Depending on the conditions of matrix preparation and on the conditions of observation, the parameter  $\varepsilon_1 T_1$  can be either smaller than  $\varepsilon_0 T_0$ , equal to, or larger than  $\varepsilon_0 T_0$ .

The charges of matrix ions are  $ez_+^0 = |ez_-^0| = ez^0$ ; and the density of the matrix subsystem is  $\rho^0$  ( $\rho_+^0 = \rho_-^0 = \rho^0/2$ ). We define the functions  $\Phi_{ij}^{mm}(r)$  describing the interactions between particles. In particular, the interactions between matrix ions are given as

$$\Phi_{ij}^{00}(r) = -U_{ij}^{00}(r)/\varepsilon_0 k T_0 = -e^2 z_i^0 z_j^0 / \varepsilon_0 k T_0 r \quad (53)$$

where  $i$  and  $j$  take values  $+$  and  $-$ .



The electrolyte solution is modelled as a two-component, electroneutral system of point ions with charges  $ez_+^1 = |ez_-^1| = ez^1$ . The density of the fluid is  $\rho^1$  ( $\rho_+^1 = \rho_-^1 = \rho^1/2$ ). The fluid–fluid and fluid–matrix Coulomb interactions are

$$\Phi_{ij}^{11}(r) = -U_{ij}^{11}(r)/\varepsilon_1 kT_1 = -e^2 z_i^1 z_j^1 / \varepsilon_1 kT_1 r \quad (54)$$

and

$$\Phi_{ij}^{10}(r) = -U_{ij}^{10}(r)/\varepsilon_1 kT_1 = -e^2 z_i^1 z_j^0 / \varepsilon_1 kT_1 r \quad (55)$$

In addition, it is convenient to define the Bjerrum length parameter  $L_b = e^2(z^1)^2/\varepsilon_r \varepsilon_1 kT_1$  (where  $\varepsilon_r$  is the universal dielectric constant) and the so-called quenching parameter, defined as  $Q = \varepsilon_0 T_0 / \varepsilon_1 T_1$ .

The correlation functions of the partly quenched system satisfy a set of replica Ornstein–Zernike equations (21)–(23). Each of them is a  $2 \times 2$  matrix equation for the model in question. As in previous studies of ionic systems (see, e.g., Refs. 69, 70), we denote the long-range terms of the pair correlation functions in ROZ equations by  $q_{ij}$ . Here we apply a linearized theory and assume that the long-range terms of the direct correlation functions are equal to the Coulomb potentials  $\Phi_{ij}$ , which are given by Eqs. (53)–(55). This assumption represents the mean spherical approximation for the model in question. Most importantly,  $\Phi_{ij}^{12}(r) = 0$ ; as mentioned before, the particles from different replicas do not interact. However,  $q_{ij}^{12}(r) \neq 0$ ; these functions describe screening effects of the ion–ion interactions between ions from different replicas mediated by the presence of charged obstacles, i.e., via the matrix. The functions  $q_{ij}^{12}(r)$  need to be obtained to apply them for proper renormalization of the ROZ equations for systems made of non-point ions.

The equation determining the matrix structure is

$$\mathbf{q}^{00} - \mathbf{\Phi}^{00} = \rho^0 \mathbf{\Phi}^{00} \otimes \mathbf{q}^{00} \quad (56)$$

where  $\rho^0$  is a  $2 \times 2$  diagonal matrix with diagonal elements  $\rho_+^0 = \rho_-^0 = \rho_0/2$ . We next perform the calculations using the ROZ equations for the fluid–matrix and fluid–fluid correlations. By restricting the analysis to the symmetric case, i.e., to 1–1 electrolytes adsorbed in 1–1 charged matrix, we can simplify the problem, taking advantage of the symmetry of the correlation functions. The equations for  $\mathbf{q}^{10}$ ,  $\mathbf{q}^{11}$  and  $\mathbf{q}^{12}$  read

$$\left. \begin{aligned} \mathbf{q}^{10} - \mathbf{\Phi}^{10} &= \rho^0 \mathbf{\Phi}^{10} \otimes \mathbf{q}^{00} + \rho^1 \mathbf{\Phi}^{11} \otimes \mathbf{q}^{10} \\ \mathbf{q}^{11} - \mathbf{\Phi}^{11} &= \rho^0 \mathbf{\Phi}^{10} \otimes \mathbf{q}^{10} + \rho^1 \mathbf{\Phi}^{11} \otimes \mathbf{q}^{11} \\ \mathbf{q}^{12} &= \rho^0 \mathbf{\Phi}^{10} \otimes \mathbf{q}^{10} + \rho^1 \mathbf{\Phi}^{11} \otimes \mathbf{q}^{12} \end{aligned} \right\} \quad (57)$$

The matrix  $\rho^1$  is a  $2 \times 2$  diagonal matrix with diagonal elements  $\rho_+^1 = \rho_-^1 = \rho_1/2$ . Eqs. (56) and (57) can be readily solved to obtain Fourier transforms of the screened potentials.

The expressions for the screened potentials in Cartesian space are then obtained straightforwardly

$$\left. \begin{aligned} \begin{pmatrix} q_{++}^{00}(r) & q_{+-}^{00}(r) \\ q_{+-}^{00}(r) & q_{--}^{00}(r) \end{pmatrix} &= L_b/Q \begin{pmatrix} -1 & 1 \\ 1 & -1 \end{pmatrix} \exp(-\kappa_0 r)/r \\ \begin{pmatrix} q_{++}^{10}(r) & q_{+-}^{10}(r) \\ q_{+-}^{10}(r) & q_{--}^{10}(r) \end{pmatrix} &= \frac{1}{Q} [\kappa_1^2/(\kappa_0^2 - \kappa_1^2)] L_b \left( \frac{\rho^0}{\rho^1} \right) \begin{pmatrix} -1 & 1 \\ 1 & -1 \end{pmatrix} \\ &\times \left[ \exp(-\kappa_0 r)/r - \left( \frac{\kappa_1^2}{\kappa_0^2} \right) \exp(-\kappa_1 r)/r \right] \end{aligned} \right\} \quad (58)$$

for the interactions between matrix ions and for the interactions between fluid and matrix ions, respectively. Here  $\kappa_0 = (4\pi\rho^0 L_b/Q)^{1/2}$  and  $\kappa_1 = (4\pi\rho^1 L_b)^{1/2}$  are the reciprocal Debye-Hückel radii of screening for the matrix and fluid ionic subsystem, respectively. For the correlations between fluid ions we have

$$\begin{pmatrix} q_{++}^{11}(r) & q_{+-}^{11}(r) \\ q_{+-}^{11}(r) & q_{--}^{11}(r) \end{pmatrix} = L_b \begin{pmatrix} -1 & 1 \\ 1 & -1 \end{pmatrix} \exp(-\kappa_1 r)/r + \begin{pmatrix} q_{++}^{12}(r) & q_{+-}^{12}(r) \\ q_{+-}^{12}(r) & q_{--}^{12}(r) \end{pmatrix} \quad (59)$$

where the blocking contributions are the following

$$\begin{pmatrix} q_{++}^{12}(r) & q_{+-}^{12}(r) \\ q_{+-}^{12}(r) & q_{--}^{12}(r) \end{pmatrix} = L_b Q [\kappa_0^4/(\kappa_0^2 - \kappa_1^2)^2] \{ \exp(-\kappa_0 r)/r \\ - [\exp(-\kappa_1 r)/r] [1 - (1 - \kappa_1^2/\kappa_0^2) \kappa_1 r/2] \} \begin{pmatrix} -1 & 1 \\ 1 & -1 \end{pmatrix} \quad (60)$$

It is evident that, under certain conditions, an unusual shape of  $q_{ij}^{11}(r)$  functions may be expected. This is a result of the blocking term contribution. Some rearrangement of terms is necessary for the case where  $\kappa_1 = \kappa_0$ , but no peculiar behavior is observed under these conditions. It is worth emphasizing that our result for  $q_{ij}^{11}(r)$  generalizes the expression obtained by Bratko and Chakraborty for infinite dilution of fluid particles [35]. The  $q_{ij}^{11}(r)$  functions coincide with their result for  $\rho^1 \rightarrow 0$ .

Let us discuss some of the results obtained so far. We present the screened potentials of Coulomb interaction between point ions in the

quenched matrix of point-like ions in Fig. 14. We also give the blocking contributions into the screened potentials in this figure. In Fig. 14 we show the results which demonstrate the effect of quenching parameter on the screening of interactions between fluid ions. Here two values of quenching parameter have been examined,  $Q = 0.7$  and  $Q = 1.7$  at a matrix concentration  $c^0 = 1M$  and at fluid concentration  $c^1 = 0.75 \times 10^{-2}M$ . It follows from the results presented that at small interparticle distances the blocking effect is larger for  $Q = 1.7$  than for  $Q = 0.7$ . Prequenching conditions provide that at

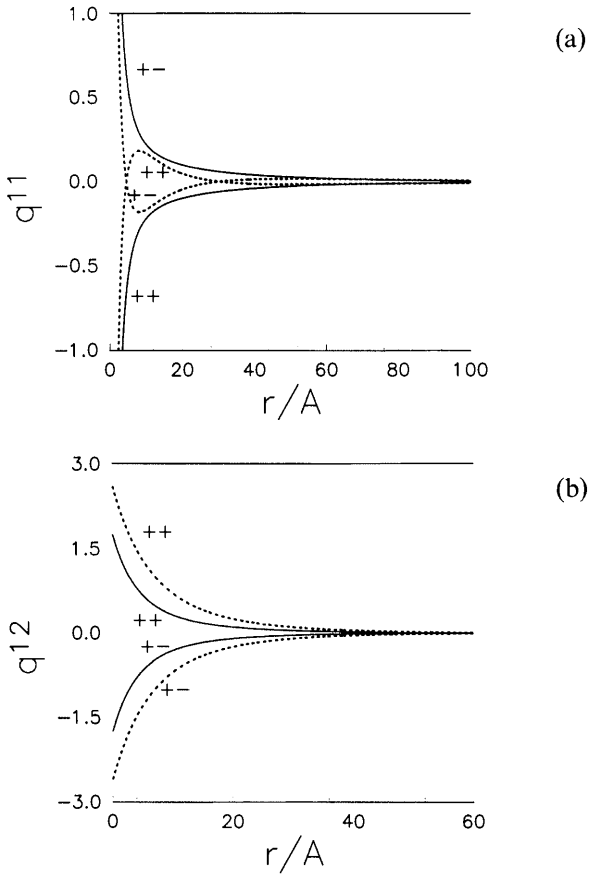


**FIG. 14** Screened potentials of fluid ion-ion interactions,  $q^{11}_{+-}(r)$  and  $q^{11}_{++}(r)$  (a) and blocking parts of the screened potentials,  $q^{12}_{+-}(r)$  and  $q^{12}_{++}(r)$  (b) at different values of the quenching parameter. The solid and dashed lines correspond to  $Q = 0.7$  and  $Q = 1.7$ , respectively.

$Q = 1.7$  we observe two points of crossing of the screened potentials and no crossing points can be seen at  $Q = 0.7$ . These results qualitatively coincide with computer simulation data [35]. With the screened potentials available, it is straightforward to solve the problem of renormalization of the ROZ equations for any system of non-point ions. A symmetric system of charged hard spheres adsorbed in an electroneutral symmetric matrix of charged hard spheres has been investigated in very detail in our recent publication [38]. It is worth mentioning that not only have the structural properties been studied. In addition, the internal energy and the chemical potentials of adsorbed ions have been obtained in the mean spherical approximation according to the expressions used by Kierlik et al. [27]. It is of much interest along this line, to investigate adsorbed electrolytes in the framework of an unrestricted model of charged hard spheres with asymmetry of diameters and charges.

## VI. CONCLUDING REMARKS

In conclusion, we have presented fundamental relations and reviewed some recent developments in the theory of quenched-annealed or partly quenched fluid systems. Theoretical developments presented in this study are focused on the problem of adsorption of fluids and mixtures in a rigidly fixed system of interconnecting micropores. In contrast to previous studies of fluids confined in pores of idealized geometry, such as slit-like, cylindrical, or spherical, a microporous media considered in this work results from, for example, quenching of a system of particles. These can be either spherical or non-spherical in shape. Moreover, a disordered rigidly fixed matrix can be prepared of from chains or polymerizing monomers that may form branched and network-like structures. Most important, is that the matrix provides a disordered medium of interconnecting space for adsorption of a fluid. A highly non-trivial structure can be formed by considering a system of freely overlapping spherical particles, so-called random matrix [17–20]. Adsorption of fluids and mixtures into a system of interconnecting pores has many specific features that are not observed for an individual pore.

Our main focus in this chapter has been on the applications of the replica Ornstein–Zernike equations designed by Given and Stell [17–19] for quenched-annealed systems. This theory has been shown to yield interesting results for adsorption of a hard sphere fluid mimicking colloidal suspension, for a system of multiple permeable membranes and for a hard sphere fluid in a matrix of chain molecules. Much room remains to explore even simple quenched-annealed models either in the framework of theoretical approaches or by computer simulation.

We have discussed only one extension of the theory available at present. Namely, recently developed inhomogeneous ROZ equations have been considered and solved for a simple model. Due to space restrictions of this chapter, the extension of the ROZ theory for chemically associating fluids yielding the associative ROZ equations has not been considered [71–73]. This line of studies has been initiated in our laboratory recently, leading to many interesting results. In particular, we have investigated the structure of several models of associating fluids and also developed tools for the description of thermodynamical properties of these systems [74–78]. However, the associative interactions on their own do not yield phase transitions, unless one considers models with many associating sites per particle. Besides, we have not commented on advances in the theory of complex molecules permitting formation of mesophases in microporous media. This is an interesting line of research both for theoreticians and experimentalists.

Nevertheless, previous developments and some of our results prove that the structural properties of several systems with short-range repulsive forces are straightforwardly and sufficiently accurately given by ROZ integral equations. Thermodynamic properties are much more difficult to describe. Reliable tools exist to obtain thermodynamics at high temperatures or for states far from phase transitions. Of particular importance, and far from being solved, are the issues related to phase transitions in partly quenched systems, even for simple models with attractive interactions. It seems that the results obtained by Kierlik et al. [27], may serve as a helpful reference in this direction.

More sophisticated models, especially with those long-range electrostatic forces await their turn to be studied. Phase transitions in Coulombic systems confined to disordered media are one of the challenges for the theory. Charged colloids adsorbed in charged media represent one more interesting subject. On the other hand, important applications may be expected from the relevant developments for dipolar and ion-dipole fluids confined to disordered microporous media. Other degrees of freedom rather than the coordinates of particles may be considered rigidly fixed in systems with multipole moments.

One can expect further progress, not only along the line of studies involving integral equations. Computer simulations have already shown their ability to perform with success in this area of research. In this respect, it is worth mentioning that lattice Monte Carlo simulations may contribute much to studies of thermodynamics of quenched-annealed systems. This methodology can, in particular, clarify the role of cooperativity effects in network-forming fluids adsorbed in microporous media. The bulk counterparts of these fluids possess intriguing coexistence curves [79,80]. There

remains much room for applications of molecular dynamics and Brownian dynamics simulations for partly quenched systems in question, in particular for studying mixing-demixing behavior of fluid mixtures.

From the theoretical point of view, a density functional type theory for systems confined to microporous media is lacking. This seems to be one of the reasons why the problem of crystallization of fluids in disordered media has not been solved so far. Further work in future is needed, however, to solve this and relevant problems. Our expectation is that a combined application of theoretical methods and simulation would provide faster progress in studies of fluids and mixtures in microporous media. At present, the models studied in theory and simulations are quite far from the systems of experimental focus. Hopefully, favorable changes will occur in future.

## ACKNOWLEDGMENTS

This project has been supported in part by Silicon Graphics Inc.-Cray Research of Mexico under its University Research and Development grant, by DGAPA of the UNAM under research grant IN111597, and by CONACyT of Mexico under Grant 25301-E. The majority of the results presented here have followed from our fruitful, long-term collaboration with Stefan Sokolowski. I am grateful to Prof. V. Renugopalakrishnan for his attention, his critical and careful reading of the manuscript. Also it is my pleasure to acknowledge helpful discussions during preparation of this manuscript with my students and collaborators A. Huerta, B. Hribar, B. Millan Malo, L. Ibarra Bracamontes, G. Anguiano Orozco, G. Fuentes, and M. Franco.

## REFERENCES

1. M. Mezard, G. Parisi, M. A. Virasoro. *Spin Glass Theory, Beyond*. Singapore: World Scientific. 1987.
2. B. J. Friskén, A. J. Liu, D. S. Cannell. *Mater Res Soc Bull* May:19–26, 1994.
3. B. J. Friskén, D. S. Cannell. *Phys Rev Lett* 69:632–635, 1992.
4. A. P. Y. Wong, M. H. W. Chan. *Phys Rev Lett* 65:2567–2570, 1990.
5. M. C. Goh, W. I. Goldberg, C. M. Knobler. *Phys Rev Lett* 58:1008–1011, 1987.
6. S. B. Dierker, P. Wiltzius. *Phys Rev Lett* 66:1185–1188, 1991.
7. S. B. Dierker, P. Wiltzius. *Phys Rev Lett* 58:1865–1868, 1987.
8. B. J. Friskén, F. Ferri, D. S. Cannell. *Phys Rev E* 51:5922–5943, 1995.
9. A. Golov, J. V. Porto, J. M. Parpia. *Phys Rev Lett* 80:4486–1489, 1998.
10. D. W. Brown, P. E. Sokol, S. N. Ehrlich. *Phys Rev Lett* 81:1019–1022, 1998.
11. M.-C. Bellisent-Funel, J. Lal, L. Bosio. *J Chem Phys* 98:4246–4252, 1993.
12. H. Acuna-Campa, M. D. Carbajal-Tinoco, J. L. Arauz-Lara, M. Medina-Noyola. *Phys Rev Lett* 80:5802–5805, 1995.

13. G. Viramontes-Gamboa, J. L. Arauz-Lara,, M. Medina-Noyola. *Phys Rev E* 52:4035–4044, 1995.
14. G. Cruz de Leon, J. M. Saucedo-Solorio, J. L. Arauz-Lara. *Phys Rev Lett* 81:1122–1125, 1998.
15. W. G. Madden, E. D. Glandt. *J Stat Phys* 51:537–558, 1988.
16. W. G. Madden. *J Chem Phys* 96:5422–5432, 1988.
17. J. A. Given, G. Stell. *Physica A* 209:495, 1994.
18. J. A. Given, G. Stell. XVI International Workshop on Condensed Matter Theories, San Juan, Puerto Rico, 1992 (New York: Plenum, 1993), pp. 395–410.
19. J. A. Given, G. Stell. *J Chem Phys* 97:4573–4574, 1992.
20. E. Lomba, J. A. Given, G. Stell, J. J. Weis, D. Levesque. *Phys Rev E* 48:233–244, 1993.
21. A. Meroni, D. Levesque, J. J. Weis. *J Chem Phys* 105:1101–1112, 1996.
22. M. L. Rosinberg, G. Tarjus, G. Stell. *J Chem Phys* 100:5172–5177, 1994.
23. D. M. Ford, E. D. Glandt. *J Chem Phys* 100:2391–2393, 1994.
24. D. M. Ford, E. D. Glandt. *Phys Rev E* 50:1280, 1994.
25. J. A. Given. *J Chem Phys* 102:2934–2945, 1995.
26. E. Kierlik, M. L. Rosinberg, G. Tarjus, P. A. Monson. *J Chem Phys* 103:4256, 1995.
27. E. Kierlik, M. L. Rosinberg, G. Tarjus, P. A. Monson. *J Chem Phys* 106:264–279, 1997.
28. E. Pitard, M. L. Rosinberg, G. Stell, G. Tarjus. *Phys Rev Lett* 74:4361–4364, 1995.
29. S. Page, P. A. Monson. *Phys Rev E* 54:R29–R32, 1996.
30. P. A. Gordon, E. D. Glandt. *J Chem Phys* 105:4257–4264, 1996.
31. W. Dong, E. Kierlik, M. L. Rosinberg. *Phys Rev E* 50:4750–4753, 1994.
32. O. Pizio, S. Sokolowski. *Phys Rev E* 56:R63–R66, 1997.
33. A. Kovalenko, S. Sokolowski, D. Henderson, O. Pizio. *Phys Rev E* 57:1824–1831, 1998.
34. D. Bratko, A. K. Chakraborty. *Phys Rev E* 51:5805, 1995.
35. D. Bratko, A. K. Chakraborty. *J Chem Phys* 104:7700, 1996.
36. A. K. Chakraborty, D. Bratko, D. Chandler. *J Chem Phys* 100:1528, 1994.
37. B. Hribar, O. Pizio, A. Trokhymchuk, V. Vlachy. *J Chem Phys* 107:6335–6341, 1997.
38. B. Hribar, O. Pizio, A. Trokhymchuk, V. Vlachy. *J Chem Phys* 109:2480–2491, 1998.
39. C. Vega, R. D. Kaminsky, P. A. Monson. *J Chem Phys* 99:3003, 1993.
40. G. A. Mansoori, N. F. Carnahan, K. E. Starling, T. W. Leland. *J Chem Phys* 54:1523, 1971.
41. R. D. Kaminsky, P. A. Monson. *J Chem Phys* 95:2936–2948, 1996.
42. R. D. Kaminsky, P. A. Monson. *Chem Eng Sci* 49:2967, 1994.
43. R. D. Kaminsky, P. A. Monson. *Langmuir* 10:530, 1994.
44. Yu. Duda, D. Henderson, O. Pizio, D. T. Wasan. *Molec. Phys.* 94:341, 1998.
45. A. Trokhymchuk, G. Anguiano Orozco, O. Pizio, V. Vlachy. *J Coll Interface Sci* 207:379, 1998.

46. G. Fuentes, A. Huerta, O. Pizio. Unpublished, 1998.
47. G. Anguiano Orozco, O. Pizio, A. D. Nikolov, D. T. Wasan. Unpublished, 1998.
48. X. L. Chu, A. D. Nikolov, D. T. Wasan. *J Chem Phys* 103:6653–6661, 1995.
49. J. G. Powles, M. Pogoda. *Molec Phys* 78:757, 1993.
50. J. G. Powles, S. E. Baker, W. A. B. Evans. *J Chem Phys* 101:4098, 1994.
51. P. Marsh, G. Rickayzen, M. Calleja. *Molec Phys* 84:799, 1995.
52. N. Margaritis, G. Rickayzen. *Molec Phys* 90:189, 1997.
53. L. Ibarra Bracamontes, O. Pizio, S. Sokołowski. *Molec Phys* 96:1341, 1999.
54. M. A. Wilson, A. Pohorille. *J Am Chem Soc* 116:1490, 1994.
55. A. Pohorille, M. A. Wilson. *J Chem Phys* 104:3760, 1996.
56. D. M. Ford, A. P. Thompson, E. D. Glandt. *J Chem Phys* 103:1099, 1995.
57. P. Padilla, C. Vega. *J Chem Phys* 106:1997, 1997.
58. P. Padilla, O. Pizio, A. Trokhymchuk, C. Vega. *J Phys Chem* 102:3012–3017, 1998.
59. B. Millan Malo, O. Pizio, A. Trokhymchuk, Y. Duda. *J Coll Interface Sci* 211:387, 1999.
60. S. Sunderrajan, C. K. Hall, B. Freeman. *Molec Phys* 92:109, 1997.
61. J. Chang, S. I. Sandler. *J Chem Phys* 102:437, 1995.
62. J. I. Siepmann, D. Frenkel. *Molec Phys* 75:59, 1992.
63. C. Bender, M. Lax. *J Chem Phys* 79:2423, 1983.
64. M. S. Wertheim. *J Stat Phys* 35:19, 35, 1984.
65. M. S. Wertheim. *J Stat Phys* 42:459, 477, 1986.
66. M. S. Wertheim. *J Chem Phys* 87:7323, 1987.
67. O. Pizio, A. Trokhymchuk, D. Henderson, S. Labik. *J Coll Interface Sci* 191:86, 1997.
68. J. Chang, S. I. Sandler. *J Chem Phys* 103:3196, 1995.
69. T. Ichije, A. D. J. Haymet. *J Chem Phys* 93:8954, 1990.
70. V. Vlachy, T. Ichije, A. D. J. Haymet. *J Am Chem Soc* 113:1077, 1991.
71. D. Henderson, A. Patrykiewicz, O. Pizio, S. Sokołowski. *Physica A* 233:67, 1995.
72. A. Trokhymchuk, O. Pizio, M. Holovko, S. Sokołowski. *J Phys Chem* 100:17004, 1996.
73. A. Trokhymchuk, O. Pizio, M. Holovko, S. Sokołowski. *J Chem Phys* 106:200, 1997.
74. G. Anguiano Orozco, O. Pizio, S. Sokołowski, A. Trokhymchuk. *Molec Phys* 91:625, 1997.
75. A. Kovalenko, O. Pizio. *J Chem Phys* 108:8651, 1998.
76. O. Pizio, V. Renugopalakrishnan, A. Trokhymchuk. *J Coll Interface Sci* 211:367, 1999.
77. O. Pizio, Yu. Duda, S. Sokołowski, A. Trokhymchuk. *J Molec Liq* 76:183, 1998.
78. A. Huerta, Y. Duda, O. Pizio, D. Wasan. *Molec Phys* 96:795, 1999.
79. C. J. Roberts, P. G. Debenedetti. *J Chem Phys* 105:658, 1996.
80. C. J. Roberts, A. Z. Panagiotopoulos, P. G. Debenedetti. *Phys Rev Lett* 77:4386–4389, 1996.



# 7

## Water and Solutions at Interfaces: Computer Simulations on the Molecular Level

**ECKHARD SPOHR** Department of Theoretical Chemistry, University of  
Ulm, Ulm, Germany

I.	Introduction	348
II.	Computer Simulation Methods	349
III.	Models	352
	A. Geometries and long-range interactions	352
	B. Interaction potentials	353
IV.	Water Near Nonpolar Surfaces	355
	A. The free water surface	355
	B. Water near smooth nonpolar walls	356
	C. Interfaces between two immiscible liquids	358
V.	Electrochemical interfaces	358
	A. The water/metal interface	359
	B. The interface between metal and electrolyte solution	365
	C. Reactions at the electrochemical interface	368
VI.	Electrolyte Solutions in Cylindrical Pores	369
	A. Model pores	369
	B. Water in Vycor glass	373
VII.	Interfaces between Water and Inorganic Materials	376
	A. The ice/water interface	376
	B. Water on ionic salt surfaces	376
	C. Water on oxide surfaces	377
	D. Water/clay systems	377

VIII. Water/Membrane interfaces	378
IX. Summary and Outlook	378
References	379

## I. INTRODUCTION

Over the last three decades, computer simulations on the molecular level have grown into the third fundamental discipline of liquid state research besides experiment and analytic theory. The study of water and aqueous solutions has especially benefitted from this molecular simulation method, largely because of the complexity of the intermolecular interactions, which give rise to hydrogen bonds and which are not easily described by the analytic methods of statistical mechanics. Since simulation methods can, at least in principle, be easily adapted from bulk systems to systems with interfaces, they have been used extensively to study aqueous/nonaqueous interfaces, which are ubiquitous in nature and which determine the properties of many materials. Among the systems studied are the free water surface, water and aqueous solutions near nonpolar hydrophobic and polar hydrophilic surfaces, interfaces between two immiscible liquids, the electrochemical double layer of an aqueous solution and a metal electrode, water near oxides, salts, clays, polymers and biological membranes, and confined electrolyte solutions in porous systems. In what follows I want to briefly summarize the key findings of such studies and relate them to hydrogen bonding and ionic solvation. Specific examples are drawn mostly from my own work.

Various levels of modeling can be applied to the study of liquids and interfaces. They may be classified by the degree of atomic and molecular detail in the description of the microscopic interactions. What I mean here by the term "computer simulation on the molecular level" is the realistic description of both the solvent, water, and the solutes, ions, as an assembly of charged or uncharged atoms, which interact through a Born-Oppenheimer potential energy surface (PES). The PES can be either precalculated and used in parametrized form as input for the simulation as in classical molecular dynamics (MD) and Monte Carlo (MC) simulations, or it can be calculated during the course of the simulation as in so-called *ab initio* molecular dynamics methods. I do not wish to discuss here those simulations which have been performed without explicit description of solvent molecules (like the so-called primitive model of electrolytes, in which the solvent enters only through its dielectric constant), or those in which the

solvent is described in a simplified manner by hard or soft spheres with embedded point dipoles. While much has been learned from these models regarding nonpolar and polar liquids, they are in general not able to account for the phenomenon of hydrogen bonding in an adequate way, although more elaborate models, which include quadrupole and octupole interactions, appear to do so [1].

In the following the term "aqueous interface" has the meaning of an interface either between two phases, one of which is liquid pure water or a (usually ionic) aqueous solution, or of films of water with varying thickness on various substrates. The second phase can be either a solid or liquid phase; it is described either in molecular detail or as an external potential function, which generates a phase boundary and which acts on solvent and solute species in the aqueous phase. In this chapter, I want to confine myself to extended planar or cylindrical interfaces of rather homogeneous composition. These will not include aqueous systems of biological interest, like dissolved proteins in water, models for cell membranes, or ion carrier channels such as Gramicidin A and others. The surface of these molecules is very non-uniform, and distinguishing between solutes and interfaces becomes a matter of length scale.

## II. COMPUTER SIMULATION METHODS

In addition to various analytic or semi-analytic methods, which are based on the theory of the liquid state and which are not the subject of this chapter, almost the entire toolbox of molecular computer simulation methods has been applied to the theoretical study of aqueous interfaces. They have usually been adapted and modified from schemes developed in a different context.

By far the most common methods of studying aqueous interfaces by simulations are the Metropolis Monte Carlo (MC) technique and the classical molecular dynamics (MD) techniques. They will not be described here in detail, because several excellent textbooks and proceedings volumes (e.g., [2–8]) on the subject are available. In brief, the stochastic MC technique generates microscopic configurations of the system in the canonical (NVT) ensemble; the deterministic MD method solves Newton's equations of motion and generates a time-correlated sequence of configurations in the microcanonical (NVE) ensemble. Structural and thermodynamic properties are accessible by both methods; the MD method provides additional information about the microscopic dynamics of the system.

In most publications on simulations of the aqueous interface the discussion emphasizes the structure of the interface. The inhomogeneity and

anisotropy of the interfacial region is often characterized by means of so-called density and polarization profiles and various orientational distributions. These structural properties are, to a certain extent, the analogs to the pair correlation functions (PCFs) between atoms or molecules [9], which play a fundamental role in the theoretical and experimental description of the bulk state of liquids. The importance of density and polarization profiles in structural characterization derives from the fact that these properties can, quite readily, be compared to predictions from analytic theory and, in some special cases, also to experimental results. Typical studies also analyze details about pair correlations, hydrogen bonding or hydration properties.

Among the dynamical properties the ones most frequently studied are the lateral diffusion coefficient for water motion parallel to the interface, re-orientational motion near the interface, and the residence time of water molecules near the interface. Occasionally the single particle dynamics is further analyzed on the basis of the spectral densities of motion. Benjamin studied the dynamics of ion transfer across liquid/liquid interfaces and calculated the parameters of a kinetic model for these processes [10]. Reaction rate constants for electron transfer reactions were also derived for electron transfer reactions [11–19]. More recently, systematic studies were performed concerning water and ion transport through cylindrical pores [20–24] and water mobility in disordered polymers [25,26].

Simulations of aqueous interfaces are performed with two goals in mind. The first goal is the modeling of experimental situations with as realistic microscopic interactions as possible and the exploration of the consequences of various aspects of the interactions between water molecules and solutes on the one side and the atoms or molecules in the second phase on the other side of the interface. The second goal is the simulation of systems that can be treated both by simulation methods and by analytic theory. Since water is a complex liquid which forms a hydrogen bond network, analytic theories involve a large number of approximations and are generally more difficult to apply to water than to simple liquids. Therefore, the role of simulation as an “experimental” verification of the theory is even more important than in other branches of liquid state theory. On the other hand, computer simulations of interfaces in general and specifically of interfaces involving water and other polar liquids suffer, more than simulations of bulk liquids, from the finiteness of the “observation time” or, in other words, the possibly incomplete sampling of relevant configurations in the phase space of the system. Available computer resources limit, at present, the duration of typical simulations to between a few hundred picoseconds and a few nanoseconds with system sizes of a few hundred to a few thousand water molecules, although substantially larger systems or longer times have occasionally been achieved. Sometimes, such simulations are not long enough to sample phase

space adequately, and comparisons with the results of analytic theory are very helpful in order to detect such a situation. The so-called ergodicity problem is aggravated by the substantial computational expense demanded by the long-range nature of the electrostatic interactions, which dominate the properties of the aqueous interface and which mandate adequate lattice summation techniques. It has been realized recently that simulations without such lattice summation techniques can lead to unphysical results [27–29].

Simulations of the electrochemical interface between an aqueous electrolyte solution and a metal electrode usually need to be performed at low solute concentration in order to facilitate comparison with experiments. In such a situation, the calculation of density distributions is not possible by direct simulation methods. On the one hand, the low concentration can be achieved only by simulating a large number of solvent molecules and thus a very large system. On the other hand, there is only one or at most a few solute particles present in the simulation cell. Consequently, excessively large simulation times, for a large system, would be needed in order to adequately average over the sampled positions of the solute particles. As an alternative, constrained dynamics and umbrella sampling techniques have been used to calculate the potential of mean force of adsorption,  $W(z)$ , for various ions and neutral species (e.g., [13,15,30–38]) in the vicinity of nonpolar, polar and metallic surfaces.  $W(z)$  is related to the density profile of the species through  $W(z) = -kT \ln[\rho(z)/\rho_{\text{bulk}}]$ , where  $k$ ,  $T$ ,  $\rho_{\text{bulk}}$ , and  $\rho$  denote Boltzmann's constant, the absolute temperature, the bulk density and the local density at position  $z$ , respectively. The potential of mean force contains valuable information about the activation properties of ion transfer reactions near interfaces, which are one fundamental input for reaction rate theories [10,39].

Such free energy calculations consist not only of one but of a series of simulations in which a solute particle is confined, either rigidly to a specified position (constrained dynamics) or within a certain range of positions specified by a so-called umbrella potential (umbrella sampling). In the constrained dynamics calculations, the potential of mean force or the Landau free energy is obtained by integrating the simulation averaged force, the “mean force”, from a reference state (usually chosen as the solute at a position far away from the interface and characteristic for the solute in the bulk phase) to the position  $z$  close to the interface. In the umbrella sampling scheme, relative positional probabilities are obtained for the different regions which, after accounting for the effect of the confining umbrella potential, can be transformed into a continuous density profile, provided the various regions overlap.

The umbrella sampling and constrained dynamics techniques are sufficiently general to investigate the free energy profile not only as a function of

simple spatial coordinates (like the distance of the solute from the interface) but also of more complex degrees of freedom like orientational coordinates or collective coordinates. In one recent study [40], free energy barriers for reorientation of the molecular ion  $\text{H}_3\text{O}^+$  have been computed by umbrella sampling in a study of the Grotthuss mechanism of the electrochemical proton transfer reaction. Outer sphere electron transfer reactions near interfaces have been studied by several groups of authors [11–19]. According to Marcus's theory (see, e.g., [41]), the reaction coordinate, along which this process proceeds, is a collective solvent coordinate, namely the electrostatic potential produced by the solvent (and other solutes) at the position of the solute particle undergoing electron transfer. The free energy as a function of the reaction coordinate has been calculated for various situations using the umbrella sampling method.

Grand canonical simulations, in which the chemical potential of water is controlled and, therefore, the particle number is allowed to fluctuate, have only rarely been used. The basic reason is the difficulty, and thus the inefficiency, in performing the necessary particle insertions at high density. Using grand canonical simulation techniques, Ulberg and Gubbins [42] studied the water condensation in graphite pores, Patey and coworkers [43] the water/mercury interface, and Karaborni *et al.* [44] the swelling of clays. Since many phase equilibrium problems can be tackled only by grand canonical simulation methods, there is a big need for future developments in this field.

### III. MODELS

#### A. Geometries and Long-range Interactions

Computer simulations of bulk liquids are usually performed by employing periodic boundary conditions in all three directions of space, in order to eliminate artificial surface effects due to the small number of molecules. Most simulations of interfaces employ parallel planar interfaces. In such simulations, periodic boundary conditions in three dimensions can still be used. The two phases of interest occupy different parts of the simulation cell and two equivalent interfaces are formed. The simulation cell consists of an infinite stack of alternating phases. Care needs to be taken that the two phases are thick enough to allow the neglect of interaction between an interface and its images. An alternative is to use periodic boundary conditions in two dimensions only. The first approach allows the use of readily available programs for three-dimensional lattice sums if, for typical systems, the distance between equivalent interfaces is at least equal to three to five times the width of the cell parallel to the interfaces. The second approach prevents possible interactions between interfaces and their periodic images,

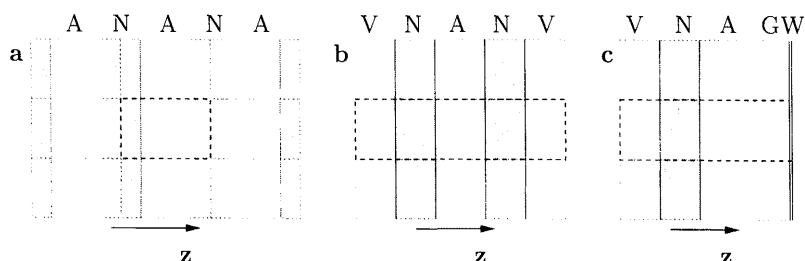
but requires the use of a computationally more expensive two-dimensional lattice summation method [29].

Fig. 1 illustrates possible setups that have been used in various studies. Scheme (a) allows the simulation of two equivalent interfaces between aqueous and non-aqueous phases. Scheme (b) simulates two equivalent aqueous/non-aqueous and two equivalent non-aqueous/vacuum interfaces and can be used to avoid the interactions between the aqueous phase and its images. Scheme (c), usually used when the non-aqueous phase is solid, simulates simultaneously an aqueous/non-aqueous, a solid/vacuum and an aqueous/gas interface. In addition, a confining wall at large distances from the aqueous/gas interface may be employed to prevent the loss of molecules from the simulation cell.

Simulations of water in synthetic and biological membranes are often performed by modeling the pore as an approximately cylindrical tube of infinite length (thus employing periodic boundary conditions in one direction only). Such a system contains one (curved) interface between the aqueous phase and the pore surface. If the entrance region of the channel is important, or if the pore is to be simulated in equilibrium with a bulk-like phase, a scheme like the one in Fig. 2 can be used. In such a system there are two planar interfaces (with a hole representing the channel entrance) in addition to the curved interface of interest. Periodic boundary conditions can be applied again in all three directions of space.

## B. Interaction Potentials

The interactions between water and aqueous solutions and another phase have been modeled in various ways. The most simple models consist of an aqueous system in contact with a hard or soft wall described by



**FIG. 1** Geometries for simulations of aqueous/non-aqueous interfaces. A, N, G, V, and W denote aqueous phase, non-aqueous phase, gas phase, vacuum, and confining wall, respectively. The basic simulation box is indicated by thick dashes.

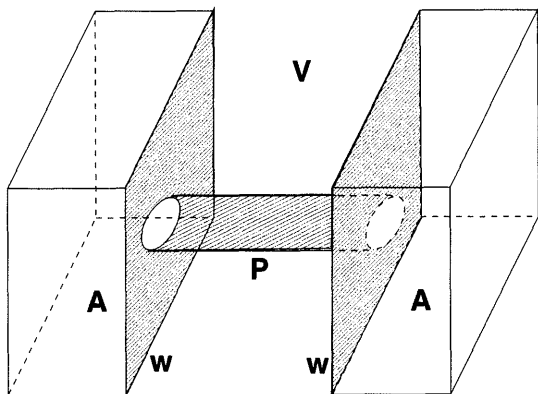


**FIG. 2** Geometry for a simulation of a cylindrical pore in contact with a bulk-like aqueous phase. A, V, P, and W denote the aqueous phase, the excluded volume, the pore wall, and the confining walls, respectively.

one-dimensional repulsive or weakly attractive potential functions. The free surface of a film of water or aqueous solution has also been simulated (see, e.g., [45] and references therein). More realistic models contain an atomic representation of such a wall or an atomic or molecular representation of the entire non-aqueous phase. The latter approach is, of course, mandatory in simulations of all realistic systems. The interaction potentials for the atomic representation have either been chosen empirically, by employing standard force fields from molecular mechanics, or by parametrizing *ab initio* or semiempirical quantum chemical calculations [46–50]. In addition to models based on quantum chemical calculations, the electronic properties of the metal near aqueous/metallic interfaces have been modeled by employing image charges as in continuum electrostatics (e.g., [51–55]), by the jellium model [56], and by more sophisticated methods based on Gaussian or plane-wave representations of the charge distribution [57–59].

Simulations of liquid and solid water have always been (and still are) the traditional testing ground for methods and models. Consequently, an overwhelming number of models for water–water and water–ion interactions have been developed which cannot be discussed here in any detail. By and large, these models can be classified into rigid models, flexible models, and polarizable models. In order to describe hydrogen bonding between molecules in an adequate way, most water models consist of a rigid or flexible framework of three (or more) point charges, which is augmented by Lennard–Jones type or exponential energy terms describing short-range repulsion and dispersion. The most simple description of a water molecule



is thus a (12-6) Lennard-Jones center on the oxygen atom and three embedded point charges at the positions of the oxygen and hydrogen sites. In this class fall the so-called simple point charge models, of which one of the most successful is the SPC/E model [60] by Berendsen and co-workers. Polarizable models employ various schemes of fluctuating charges or point polarizabilities. All types of models have been applied to interfacial simulations. Rigid models, however, have been favored, because they can be simulated with a rather long integration time step in MD or a large maximum displacement in MC. Since statistical convergence and ergodicity is an important issue in interfacial simulations, rigid models allow the longest simulation times at fixed computational expense. In a similar fashion, ions are modeled as point charges embedded in a Lennard-Jones or Born-Mayer-Huggins-type potential.

The number of models and combinations thereof that have been used in interfacial simulations is too large to review here. The reader is referred to the quoted original studies or recent reviews [51,61-67] for details.

## IV. WATER NEAR NONPOLAR SURFACES

### A. The Free Water Surface

The simulated free surface of liquid water is relatively stable for several nanoseconds [68-72] because of the strong hydrogen bonds formed by liquid water. The density decrease near the interface is smooth; it is possible to describe it by a hyperbolic tangent function [70]. The width of the interface, measured by the distance between the positions where the density equals 90% and 10% of the bulk density, is about 5 Å at room temperature [70,71]. The left side of Fig. 3 shows a typical density profile of the free interface for the TIP4P water model [73].

The orientational distribution (Fig. 3, right) in the immediate vicinity of the interface shows a clear preference for configurations in which the molecular dipoles are aligned parallel to the surface plane. The observed alignment is driven by the tendency of the molecules in liquid water to maximize the number of hydrogen bonds. Water molecules being aligned almost parallel to the surface plane can participate easily in three hydrogen bonds, whereas molecules aligned perpendicularly to the surface plane are only able to form two hydrogen bonds with molecules in the liquid. Other possible arrangements with high hydrogen bond connectivity are less favorable since they would give rise to a significant surface dipole with repulsive long-range interactions within the interface.

The density of simple ions near the water/vapor interface in simulated films of water is reduced relative to the bulk density [74-76]. The depletion

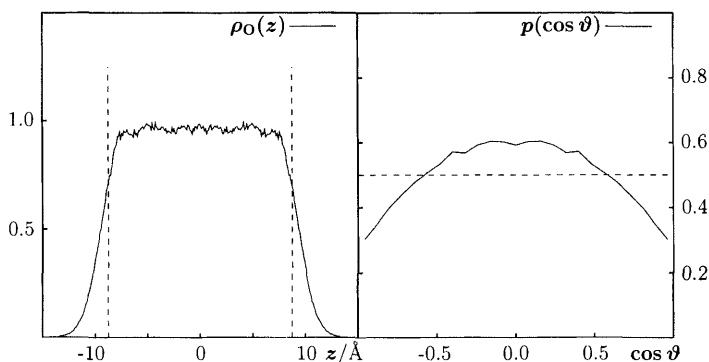


**FIG. 3** Left: density profile,  $\rho(z)$ , from a 500 ps simulation of a thin film consisting of 200 TIP4P water molecules at room temperature. Right: orientational distribution,  $p(\cos \vartheta)$ , with  $\vartheta$  the angle between the molecular dipole moment  $\mu$  and the surface normal  $\hat{z}$ . The vertical lines in the left plot indicate the boundary  $z$ -ranges,  $|z| > 8.3$  Å, which contribute to  $p(\cos \vartheta)$  plotted on the right. (From Ref. 245.)

near the interface is a consequence of the reduced number of water molecules available to fully hydrate the ions. In other studies, the behavior of surface-active substances near the water/vapor interface has been simulated [77–80]. In agreement with experimental evidence, phenol molecules, for instance, are found to be arranged in such a way that the OH group is fully immersed in water, with orientations similar to the ones found for water OH groups near the interface.

## B. Water Near Smooth Nonpolar Walls

Very similar to the properties of the free surface are the properties of water near smooth walls, which interact only weakly with water molecules. Many different models have been used, such as hard walls [81–83], exponentially repulsive walls [84–86], and Lennard–Jones potentials of various powers [81,87–96].

The principal effect of the presence of a smooth wall, compared to a free surface, is the occurrence of a maximum in the density near the interface due to packing effects. The height of the first maximum in the density profile and the existence of additional maxima depend on the strength of the surface–water interactions. The thermodynamic state of the liquid in a slit pore, which has usually not been controlled in the simulations, also plays a role. If the two surfaces are too close to each other, the liquid responds by producing pronounced density oscillations.

The orientational structure of water near smooth nonpolar surfaces is similar to that of the free surface (see also Fig. 3). The number of hydrogen bonds decreases only in the immediate vicinity of the wall, but less strongly than the coordination number. Rossky and coworkers [89,97] showed that the orientational structure is due to the tendency to maximize the number of hydrogen bonds under the geometrical constraint of the interface. In addition to hydrogen bond maximization, the long-range repulsion between parallel dipoles drives the system to reduce the interfacial polarization and thus produces the predominance of parallel dipolar configurations near the interface.

When the interaction of water with a solid phase exceeds thermal energies, density oscillations develop. With increasing strength of interaction, up to four more or less pronounced layers form. The heights of the first and second maxima increase with increasing adsorption energy [98]. Fig. 4 shows the dependence of the density profile and, in the inset, the dependence of the peak heights from the adsorption energy. For adsorption energies above about 30 or 40 kJ mol<sup>-1</sup>, even substantial increases of adsorption energy lead to only minor increases in peak height and, thus, to only minor increases in correlation between the molecule positions and the surface. Typical adsorption energies of water on transition metal surfaces are in this range or above (see below). It should be noted that a density maximum of, say, 5 does *not* imply a fivefold increase in water density near the

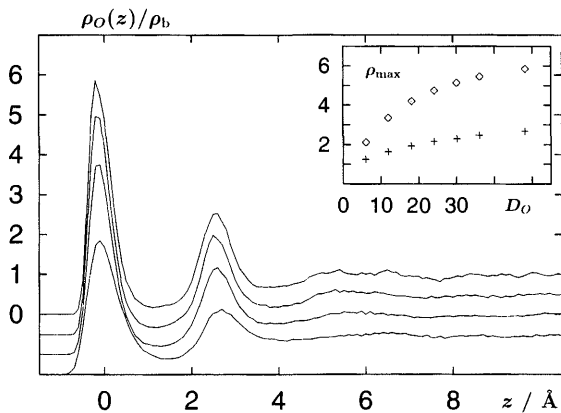


**FIG. 4** Normalized oxygen density profile perpendicular to the surface from simulations of pure water with adsorption energies of 12, 24, 36, and 48 kJ/mol (from bottom to top). The lower curves are shifted downwards by 0.5, 1.0, and 1.5 units. The inset shows the height of the first (diamonds) and second peak (crosses) as a function of adsorption energy. Water interacts with the surface through a Morse potential. (From Ref. 98.)

interface, but only shows a large correlation between water locations and the location of the surface plane. Such well-pronounced density maxima are observed only on ideally smooth surfaces. Near a surface with defects, or near a liquid/liquid interface such as the water/mercury interface, the reduction or absence of lateral correlations between equivalent adsorption sites leads to a decrease of the maximum in the density profile and an accompanying broadening of the peaks.

### C. Interfaces Between Two Immiscible Liquids

Computer simulation studies of the neat interface between water and benzene [99], cyclohexane [100],  $\text{CCl}_4$  [101,102],  $\text{CH}_3\text{Cl}$  [103], 1,2-dichloroethane [104], decane [105],  $\text{N,N}'$ -diethyl-*p*-nitroaniline [106], and possibly others have been performed. In addition, much simulation work has been done on conformational equilibria [78,79], electron [103,107], ion [108–110], and molecule transfer [102] across liquid/liquid interfaces consisting of water and an organic solvent. This work has recently been reviewed by Benjamin [64,111]. Chang and Dang studied the water/ $\text{CCl}_4$  interface in order to investigate the influence of polarizable models on the interface properties [101,102]. Close to the interface, they observed a reduction of the induced dipole moment of water and an increase in that of  $\text{CCl}_4$ , due to the strong electric fields produced by the water phase. Much of the interest in interfaces between two immiscible electrolyte solutions derives from the fact that they can be regarded as models for biological and artificial membranes, which are also actively studied by computer simulation methods. New experimental techniques, foremost the sum frequency generation and other spectroscopic methods, provide a wealth of data on microscopic structure and dynamics that need to be interpreted on the molecular level [112–119]. Hydrogen bonding and orientational polarization of water near the nonpolar liquid/water interface are determined by the same driving forces as near the nonpolar solid/water interface. For other aspects of these interesting interfaces, consult the excellent reviews by Benjamin.

## V. ELECTROCHEMICAL INTERFACES

The behavior of simple and molecular ions at the electrolyte/electrode interface is at the core of many electrochemical processes. The complexity of the interactions demands the introduction of simplifying assumptions. In the classical double layer models due to Helmholtz [120], Gouy and Chapman [121,122], and Stern [123], and in most analytic studies, the molecular nature of the solvent has been neglected altogether, or it has been described in a very approximate way, e.g. as a simple dipolar fluid. Computer simulations

can overcome this restriction and describe the solvent in a more realistic fashion. They are thus able to paint a detailed picture of the microscopic structure near a metal electrode. Models of the interface range from simple image charge models [83] through jellium models [56] to complex potential energy functions derived from quantum chemical calculations of clusters of metal atoms interacting with water molecules [49,124]. These studies have been reviewed recently [63,67,125,126]. Only some key results are discussed below, and the interested reader should consult the reviews and the references therein for further information.

## A. The Water/Metal Interface

Structure and dynamics of water on Pt(100) [46,47,127–129], Pt(111) [62,129,130], and the rigid [131] and liquid [132,133] mercury surface have been investigated. This subject has also been reviewed recently [134]. As an example, I want to briefly discuss the results on the water/mercury interface.

Fig. 5 shows data from a simulation of TIP4P water that is confined on both sides by a rhombohedral mercury crystal with (111) surface structure. Bosio *et al.* [135] deduce from their X-ray studies that a solid  $\alpha$ -mercury lattice with a larger lattice constant in the  $z$  direction may be used as a good structural model for liquid mercury. Thus, the mercury phase was modeled as a rigid crystal in order to simplify the simulations. The surface of such a crystal shows rather low corrugation.

Fig. 5(a) contains the oxygen and hydrogen density profiles; it demonstrates clearly the major differences between the water structure next to a metal surface and near a free or nonpolar surface (compare to Fig. 3). Due to the significant adsorption energy of water on transition metal surfaces (typically of the order of 20–50 kJ mol<sup>-1</sup>; see, e.g., [136]), strong density oscillations are observed next to the metal. Between three and four water layers have also been identified in most simulations near uncharged metal surfaces, depending on the model and on statistical accuracy. Beyond about 10–12 Å from the surface the density is typically constant and equal to the bulk value. In strong unscreened electric fields several authors [137–140] report a phase transition towards a ferroelectric crystalline state in their simulations. However, it should be kept in mind that these systems, because of the absence of ionic screening, are rather unphysical in nature.

The charge density profile,  $\rho_c(z)$ , and the dipole density profile,  $\rho_\mu(z)$ , can be calculated from the atomic density profiles and the orientational distributions. Figs. 5(b) and 5(c) show the dipole and charge density, respectively, for water near the mercury surface. For both the first and the second water layers, a quadrupolar charge profile with alternating regions of positive, negative, and again positive charge density is observed. The form of the

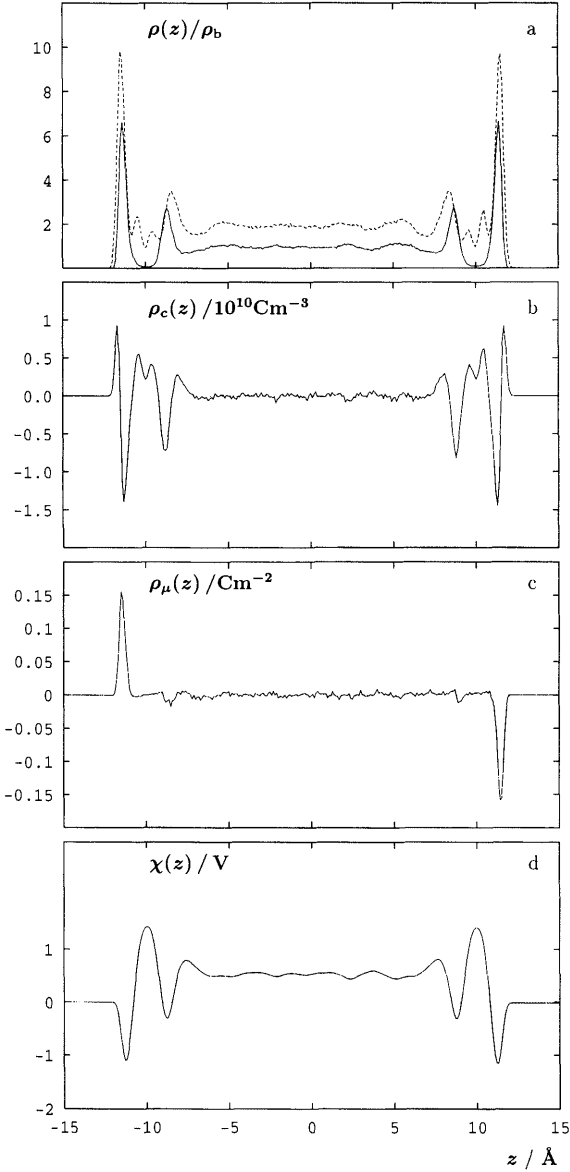


**FIG. 5** (a) Oxygen (full) and hydrogen (dashed) density profiles. (b) Charge density  $\rho_c$ . (c) Dipole density  $\rho_\mu$ . (d) Water contribution to the surface potential  $\chi$  calculated from the charge density  $\rho_c$  by means of Eq. (1). All data are taken from a 150 ps simulation of 252 water molecules between two mercury phases with (111) surface structure using Ewald summation in two dimensions for the long-range interactions.

charge profiles originates from the fact that the centers of mass (or the oxygen atom) of the water molecules are mostly well localized while the hydrogen density distribution is broadened due to librational motions and due to the hydrogen bonding between layers. Beyond the second layers the charge density approaches zero within the limits of statistical uncertainty.

The dipole density profile  $\rho_\mu(z)$  indicates ordered dipoles in the adsorbate layer. The orientation is largely due to the anisotropy of the water-metal interaction potential, which favors configurations in which the oxygen atom is closer to the surface. Most quantum chemical calculations of water near metal surfaces to date predict a significant preference of "oxygen-down" configurations over "hydrogen-down" ones at zero electric field (e.g., [48,124,141–145]). The dipole orientation in the second layer is only weakly anisotropic (see also Fig. 7).

Solving the one-dimensional Poisson equation with the charge density profile  $\rho_c(z)$ , the electrostatic potential drop near the interface can be calculated according to

$$\chi(z) = -\frac{1}{\epsilon_0} \int_{-\infty}^z \rho_c(z')(z - z') dz' \quad (1)$$

with  $\epsilon_0$  the permittivity of the vacuum (Fig. 5(d)). It has been demonstrated in Refs. 27,29 that the use of the Ewald summation is crucial to obtain the field-free bulk region of constant electrostatic potential in the center of the lamina. In the case of the rigid mercury/water interface, the potential drop across the interface is 0.55 V. Inclusion of molecular polarizability into the water model and the flexibility of the mercury surface lead to a reduction of this value by about 0.2 V. The experimental number cannot be determined unambiguously but is most likely around 0.2–0.3 V [146].

Lateral density fluctuations are mostly confined to the adsorbed water layer. The lateral density distributions are conveniently characterized by scatter plots of oxygen coordinates in the surface plane. Fig. 6 shows such scatter plots of water molecules in the first (left) and second layer (right) near the Hg(111) surface. Here, a dot is plotted at the oxygen atom position at intervals of 0.1 ps. In the first layer, the oxygen distribution clearly shows the structure of the substrate lattice. In the second layer, the distribution is almost isotropic. In the first layer, the oxygen motion is predominantly oscillatory rather than diffusive. The self-diffusion coefficient in the adsorbate layer is strongly reduced compared to the second or third layer [127]. The data in Fig. 6 are qualitatively similar to those obtained in the group of Berkowitz and coworkers [62,128–130]. These authors compared the structure near Pt(100) and Pt(111) in detail and also noted that the motion of water in the first layer is oscillatory about equilibrium positions and thus characteristic of a solid phase, while the motion in the second layer has more

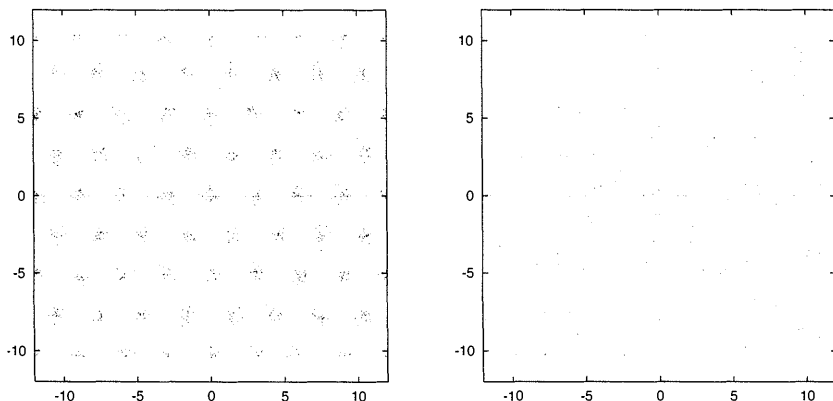


**FIG. 6** Lateral density distribution of oxygen atoms in the first (left) and second layer (right) on Hg(111). A symbol is plotted at time intervals of 0.1 ps.

liquid-like character. Since the surface corrugation on the Pt surface is larger than on the mercury atoms, the localization of water molecules and the concomitant reduction of the self-diffusion coefficient are more pronounced than on the mercury surface.

The major difference of the water structure between the liquid/solid and the liquid/liquid interface is due to the roughness of the liquid mercury surface. The features of the water density profiles at the liquid/liquid interface are washed out considerably relative to those at the liquid/solid interface [131,132]. The differences between the liquid/solid and the liquid/liquid interface can be accounted for almost quantitatively by convoluting the water density profile from the liquid/solid simulation with the width of the surface layer of the mercury density distribution from the liquid/liquid simulation [66].

The orientational structure of water near a metal surface has obvious consequences for the electrostatic potential across an interface, since any orientational anisotropy creates an electric field that interacts with the metal electrons. Hydrogen bonds are formed mainly within the adsorbate layer but also between the adsorbate and the second layer. Fig. 3 already shows quite clearly that the requirements of hydrogen bond maximization and minimization of interfacial dipoles lead to preferentially planar orientations. On the metal surface, this behavior is modified because of the anisotropy of the water/metal interactions which favors adsorption with the oxygen end towards the metal phase.

The left side of Fig. 7 shows the orientational distribution of the molecular dipole moment relative to the surface normal in various distance



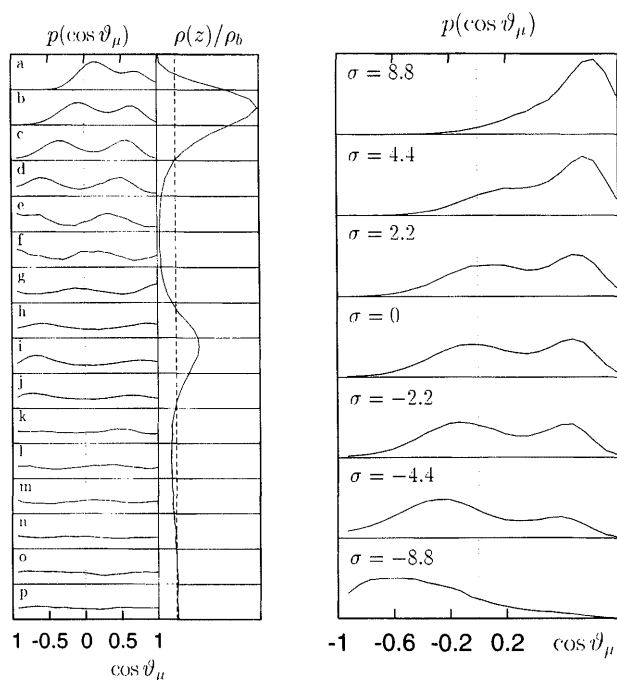


**FIG. 7** Left: orientational distribution of the molecular dipole moment on uncharged Hg(111).  $\cos \vartheta_\mu$  is the cosine of the angle between the water dipole vector and the surface normal that points into the water phase. Panels a to p on the left are sampled from the distance intervals which are indicated by the cuts through the density profile  $\rho(z)/\rho_b$  on the right. Right: Orientational distributions of adsorbed water molecules for various homogeneous surface charge densities,  $\sigma$ , which are given in units of  $\mu\text{C cm}^{-2}$  on the graphs. Data are from simulations of 700 TIP4P water molecules between Hg(111) surfaces.

ranges from the Hg(111) surface. Additionally, the oxygen density profile is plotted. The baselines between distribution functions cut through the density profile. The distribution function in each panel on the left side is for the subset of molecules that are located in the distance range between these lines on the right side. Over the first peak in the density profiles (panels a to d) there are almost no molecules whose dipole moment is perpendicular to the surface, as would be expected for an isolated molecule on the basis of the water-metal interaction potential. Within the adsorbate layer, there is a transition from the preference for orientations in which the dipoles point more or less into the solution (a and b) to one where a substantial fraction of the dipoles point more or less towards the surface (c and d). The orienta-

tional anisotropy ranges as far into the liquid phase as the density inhomogeneities do (roughly up to panel *m*), with increasingly less pronounced features. Slightly beyond the second maximum in the density profile the orientational distribution is isotropic, as has to be the case for a bulk-like liquid. Thus, as in the case of nonpolar surfaces, the orientational distribution is governed by water–water interactions. All orientational distributions are rather wide and liquid-like, although the fact that the orientational preference changes within the adsorbate layer is sometimes attributed to ice-like structural elements near the interface (see Ref. 134 for a more detailed discussion).

An external electric field changes the orientational distribution and consequently the orientational polarization of the water molecules in the interfacial region. The effect of homogeneous [93,94,137,138,147,148] and inhomogeneous [83] electric fields on the orientational distribution near smooth model surfaces has been investigated using lattice models [148] and distributed point charge models for water. Heinzinger and coworkers [149,150] and later Xia and Berkowitz [139] investigated the changes on the more realistic Pt(100) surface. Because of the absence of free ions in these simulations of pure water, the electric field is screened only by the water dipoles themselves; consequently a net electric field and a concomitant polarization persist through the lamina. At large field strengths, this has been observed to lead to a field-induced phase transition to a crystalline water phase [137–139].

The right part of Fig. 7 shows the orientational distribution of the dipole moment vectors in the adsorbed water layer for various surface charge densities  $\sigma$  (corresponding to homogeneous electric fields,  $E$ , according to  $\sigma = E \cdot \epsilon_0$ ). In the field-free case, a wide bimodal orientational distribution is observed. The overall preference of “oxygen down” bonding is manifest in the larger probability to find positive values of  $\cos\vartheta$  (corresponding to angles smaller than  $90^\circ$  between dipole vector and the surface normal that points into the liquid phase) than to find negative ones. For positive surface charges the average dipole moment (the first moment of the distribution) shifts with increasing surface charge density towards larger absolute values and the distribution becomes increasingly narrower. For low negative surface charge densities, the dipole orientational distribution becomes more symmetric around the parallel orientation. At larger negative surface charge densities, the orientational distribution changes in such a way that the hydrogen atoms point preferentially to the surface. The effect of field-induced crystallization was observed at much higher surface charges [139].

The surface X-ray experiments by Toney et al. [151] give experimental evidence for voltage-dependent ordering of water on a silver electrode. They observed a shift of the silver–oxygen distance with applied potential.

However, they also predict a strong increase in local water density near the surface, whereas MD data (see above) suggest only an increase in correlation but not in overall packing density.

## B. The Interface Between Metal and Electrolyte Solution

Several simulation studies of the potential of mean force of a single ion near a metal surface have been performed, with image charge models and quantum chemical models of the metal [34–38,152–157]. With the image charge models, only the larger halide ions are contact adsorbed, whereas small ions like  $\text{Li}^+$  and  $\text{F}^-$  are not contact adsorbed,  $\text{Cl}^-$  being a borderline case. Calculations on the basis of quantum chemical potentials [49,131] show contact adsorption for almost all ions, although a detailed analysis of the local structures around these ions reveals characteristic differences between large and small ions. Further work needs to be done to obtain more quantitative potential energy surfaces. Contrary to metallic interfaces, the free water surface is depleted of ions in the interfacial region [74–76] (see above).

The first simulation studies of full double layers with molecular models of ions and solvent were performed by Philpott and coworkers [51,54,158] for the NaCl solution, using the fast multipole method for the calculation of Coulomb interactions. The authors studied the screening of a negative surface charge by free ions in several highly concentrated NaCl solutions. A combination of (9–3) LJ potential and image charges was used to describe the metal surface.

More recently, Spohr [55,159] investigated 2.2 molal NaCl and CsF solutions in the vicinity of a corrugated surface as a function of surface charge density. Water films consisting of 400 water molecules solvate 32 ions in the vicinity of the metal surface, with image charges and a full 2D Ewald treatment for the Coulomb interactions. As in the studies by Philpott et al., the solution is not necessarily electroneutral; the total charge in the solution is balanced by the image charges which give rise to a surface charge density  $\sigma$  equal to the excess image charge divided by the area of the interface.

Fig. 8 shows the ion density profiles near the metal surface for three surface charges. Beyond  $z = 15 \text{ \AA}$  all ion density profiles are identical, within the limits of statistical error. The oxygen density profile does not change much with surface charge and is repeated here only to provide a geometric reference for the ion positions. Together with the ion densities the running integrals,  $n$ , of the densities, defined as

$$n(z) = L_x L_y \int_0^z \rho(z') dz', \quad (2)$$

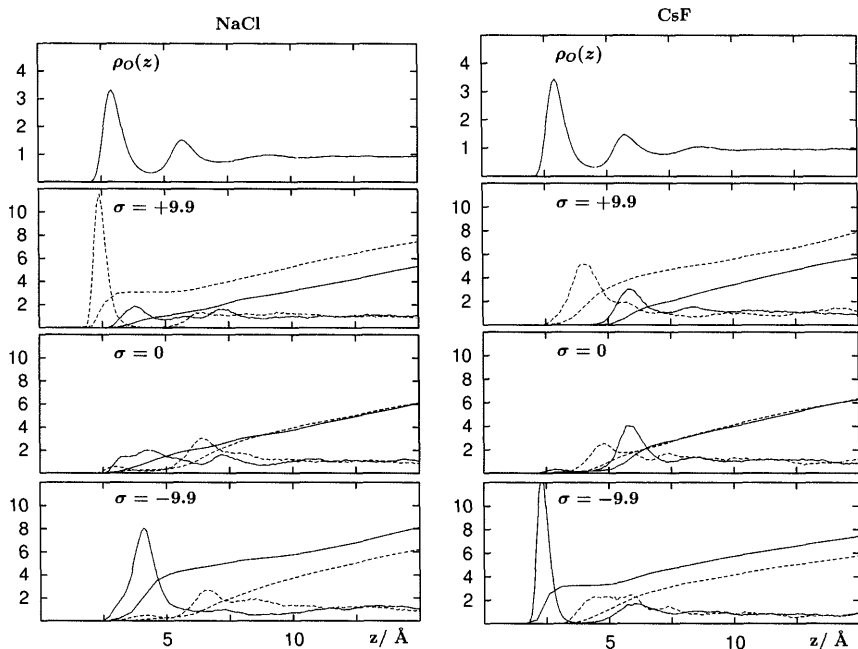


**FIG. 8** Density profiles  $\rho(z)$  and running integrals  $n(z)$  of the ion densities for cations (full lines) and anions (dashed lines) at three different surface charge densities in units of  $\mu\text{C cm}^{-2}$  as indicated. Left: NaCl solutions; right: CsF solutions.

are plotted for cations (full lines) and anions (dashed lines).  $L_x = L_y = 18 \text{ \AA}$  are the box dimensions parallel to the interface and  $\rho$  is the particle number density.

Fig. 8 (left) shows the ion density distributions of  $\text{Na}^+$  and  $\text{Cl}^-$  in the vicinity of the metal electrode. Near the uncharged electrode there are no pronounced adsorption maxima. The density of  $\text{Na}^+$  (full line) is slightly increased in the range around  $z = 4.3 \text{ \AA}$  between the first and second density maximum of water. The  $\text{Cl}^-$  density (dashed line) is significantly reduced up to about  $z = 5 \text{ \AA}$ . There is no contact adsorption of  $\text{Na}^+$ , since no cations are found for  $z < 2.8 \text{ \AA}$ , while water molecules can be found up to  $z = 2 \text{ \AA}$ .  $\text{Cl}^-$  ions, on the other hand, can be found (with low probability) at distances below  $2.3 \text{ \AA}$ .

At positive surface charge density, the  $\text{Cl}^-$  density exhibits a large maximum at a very short distance from the electrode. The position of this maximum is closer to the electrode than that of the first water layer, thus giving a clear indication of contact adsorption of this anion. The  $\text{Na}^+$

density near the electrode is slightly reduced due to the repulsion between the positively charged cations and the positively charged surface. The position of the first maximum of the  $\text{Na}^+$  density profile is not shifted very much.

At negative surface charge density, the  $\text{Na}^+$  density exhibits a large maximum at around  $z = 4 \text{ \AA}$ . This position is very similar to the one at vanishing and positive surface charge densities. Obviously, with the models used in this study,  $\text{Na}^+$  does not contact-adsorb. The  $\text{Cl}^-$  density profile at  $\sigma = -9.9 \mu\text{C cm}^{-2}$  is similar to the one at  $\sigma = 0$ .

The monotonically increasing curves of the running integrals give the number of ions whose distance from the electrode is smaller than  $z$ . The position at which the difference between the anion and cation running integral becomes 0 (for the uncharged surface) or  $\pm 2$  (for the charged surfaces) corresponds roughly to the thickness of the diffuse part of the double layer. This thickness is less than  $10 \text{ \AA}$  in all cases.

Fig. 8 (right) shows the corresponding density profiles for the CsF solutions. At zero surface charge, there is very little contact adsorption of  $\text{Cs}^+$  and no contact adsorption of  $\text{F}^-$ . The preferred position of the  $\text{Cs}^+$  ions is in the second water layer, while  $\text{F}^-$  ions prefer the region between two water layers, similar to  $\text{Na}^+$ . At positive surface charge densities, the amount of  $\text{F}^-$  in the interlayer region increases, but no contact adsorption is observed. No  $\text{Cs}^+$  cations are found in the first layer. At the negative surface charge density,  $\text{Cs}^+$  forms a contact-adsorbed layer, similar to  $\text{Cl}^-$  at the positive surface charge. The thickness of the diffuse layer is also in the range of  $10 \text{ \AA}$ , judging from the behavior of the running integral of the ion density.

No contact adsorption occurs in the simulations on uncharged electrodes. The small ions  $\text{Na}^+$  and  $\text{F}^-$  do not adsorb directly on the electrode surface at moderate negative and positive surface charge densities, respectively. These ions form rather rigid hydration shells consisting of 6 or 7 water molecules and favor the interlayer region between the first and second water layer, where they can form stable hydration shells. However, the large ions  $\text{Cs}^+$  and  $\text{Cl}^-$  exhibit contact adsorption when their interaction with the surface charge density becomes attractive.

From the ion density profiles it is obvious that the surface charge is screened within less than  $10 \text{ \AA}$ . Thus, the thickness of the diffuse layer is of the same order of magnitude as the one derived from the Debye length ( $r_D = 2.1 \text{ \AA}$  at  $2.2 \text{ mol/liter}$ ), in spite of the invalidity of the Gouy-Chapman theory at these high concentrations. Similar estimates have been made by Philpott and coworkers [51] for NaCl solutions near positively charged electrode surfaces. The results clearly show the correlation between the strength of the hydration forces and the preferred

positions of the various ions relative to charged and uncharged electrode surfaces.

### C. Reactions at the Electrochemical Interface

Outer sphere electron transfer (e.g., [11–19,107,160–162]), ion transfer [10,109,163,164] and proton transfer [165] are among the reactions near electrodes and the liquid/liquid interface which have been studied by computer simulation. Much of this work has been reviewed recently [64,111,125,126] and will not be repeated here. All studies involve the calculation of a free energy profile as a function of a spatial or a collective solvent coordinate.

As an example, the temperature dependence of ion transfer reactions is considered here. In an ion transfer reaction the transfer of the ion from the solution to the surface of the electrode is one elementary step. In many cases the rate-determining step of such a reaction is the adsorption of the ion on the electrode, which involves the penetration of a barrier formed by the adsorbed solvent. The height of the barrier is associated with the strength of hydrogen bonding and ion hydration; there is experimental evidence that this barrier is temperature dependent [166–168], while the often-used description by the phenomenological Butler–Volmer law implicitly assumes a temperature-independent barrier. We have therefore calculated the solvent free energy barrier for the adsorption of  $\text{I}^-$  on Pt(100). Fig. 9 shows the contribution by the solvent to the local free energy of an iodide ion at three different temperatures. Each curve has been calculated through constrained dynamics from several simulations in which the ion is kept at a fixed distance

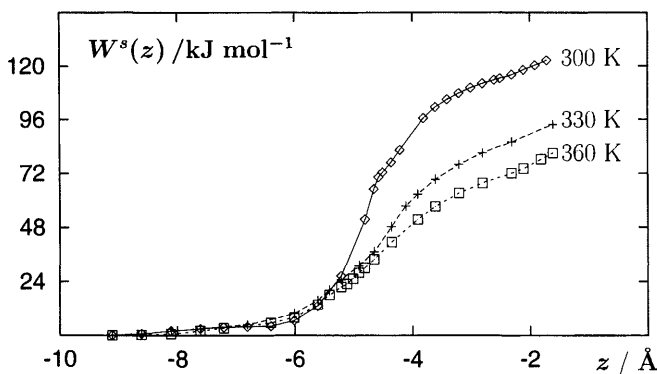


**FIG. 9** Solvent contribution  $W^s$  to the free energy of adsorption of  $\text{I}^-$  on Pt(100) at different temperatures as indicated. (From Ref. 164.)

from the surface. The effect of the solvent is to produce a monotonic barrier for ion adsorption, which is due to the work of hole formation near the surface. The barrier is indeed not constant but decreases from about  $120 \text{ kJ mol}^{-1}$  at room temperature to about  $80 \text{ kJ mol}^{-1}$  at 360 K. A closer analysis reveals that an increasing number of hydrogen bonds break when the temperature increases, which facilitates the penetration of the ion.

## VI. ELECTROLYTE SOLUTIONS IN CYLINDRICAL PORES

Ion transport in narrow cell membrane structures such as the Gramicidine A channel has been investigated by MD in several research groups (e.g., [169–172]). The pores of most ion-carrying channel proteins allow only single-file motion of ions and water molecules. Synthetic materials with pore diameters in the range of 1–100 nm, such as nonpolar and polar functionalized polymer membranes (e.g., [173]) and porous inorganic glasses (e.g., Vycor), are interesting because of their technological applications as molecular sieves and in heterogeneous catalysis. In the following I want to discuss briefly the results of two studies, which show the relationship between the relative strength of hydrogen bonding, ion hydration, and interactions between ions and polar surface group to the material properties.

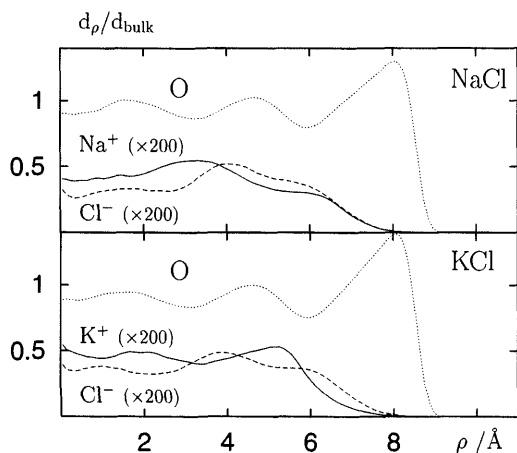
### A. Model Pores

We have studied, by MD, pure water [22] and electrolyte solutions [23] in cylindrical model pores with pore diameters ranging from 0.8 to more than 4 nm. In the nonpolar model pores the surface is a smooth cylinder, which interacts only weakly with water molecules and ions by a Lennard–Jones potential; the polar pore surface contains additional point charges, which model the polar groups in functionalized polymer membranes.

Very narrow pores with diameters less than about 1 nm show interesting non-equilibrium properties over times of a few nanoseconds. Water forms solid-like, helical structures, in which the self diffusion coefficient is reduced by several orders of magnitude. Lynden-Bell and Rasaiah [20] observed a drastic reduction of mobility only in pores with a single-file arrangement of water molecules. In pores with diameter larger than about 2 nm a constant density region develops in the pore center with properties similar to bulk water. In non-polar pores, the self-diffusion coefficient (SDC) along the pore axis of molecules close to the surface is larger than the SDC of molecules in the center of the pore. The increased diffusion coefficient is a consequence of the reduced number of hydrogen bonds near the pore surface. In all investigated cases with pore diameters between 1.3 and 4 nm the total diffusion

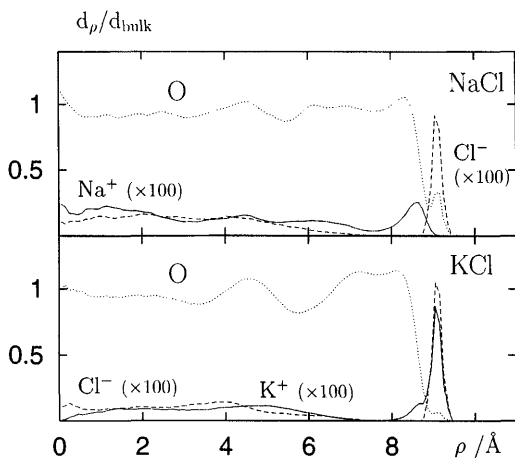
coefficient (averaged over all water molecules) along the pore axis is increased substantially relative to bulk liquid water; dipolar relaxation times are also shorter than in the bulk liquid. Contrary to our results, Sansom et al. [21] observed, in non-polar pores, an overall reduction of mobility for all pores with diameter less than 2.4 nm. The difference between our and their results may be due to differences in the interaction models, the occupancy (the amount of water in the pore), and the way the SDC is calculated (see [22] for discussion). The introduction of surface charges changes the transport properties and reorientational dynamics of the water molecules in the pore. The SDC in the polar pores decreases with increasing proximity of the water molecule to the pore surface. The total diffusion coefficient is reduced in comparison with the bulk liquid, and dipolar relaxation times are larger than in the bulk.

Fig. 10 shows the radial particle densities,  $d\rho/d_{\text{bulk}}$ , as a function of the coordinate  $\rho$  perpendicular to the pore axis for electrolyte solutions in non-polar pores, Fig. 11 the corresponding data for electrolyte solutions in functionalized pores with immobile point charges on the cylinder surface. All ion density profiles in the nonpolar pores show a clear preference for the interior of the pore. The ions avoid the pore surface, a consequence of the tendency to form complete hydration shells. The ionic distribution is analogous to the one of electrolytes near planar nonpolar surfaces or near the liquid/gas interface (*vide supra*).



**FIG. 10** Cation (full), anion (dashed), and oxygen (dotted) radial density distributions in nonpolar pores. Top: NaCl solution; bottom: KCl solution.





**FIG. 11** Cation (full), anion (dashed), and oxygen (dotted) radial density distributions in polar pores with embedded surface charges. Top: NaCl solution; bottom: KCl solution.

The ionic distribution in the polar functionalized pores is completely changed due to the interactions of the ions with the stationary charges on the pore surface (Fig. 11). In all cases, the center of the distribution moves to larger values of  $\rho$ . Both the  $\text{K}^+$  and  $\text{Cl}^-$  densities exhibit significant peaks at values of  $\rho = 9.1 \text{ \AA}$ , which are obviously due to contact ion pairs of  $\text{K}^+$  with the negative surface charges (representing sulfonate groups) and of  $\text{Cl}^-$  with the positive surface charges (modeling ammonium groups).  $\text{Na}^+$ , on the other hand, exhibits only a small density maximum at  $\rho = 8.6 \text{ \AA}$ , which is the consequence of the formation of solvent-separated ion pairs with the negative surface charges.

Fig. 12 shows the atom density profiles as a function of the coordinate  $z$  along the pore axis. Oxygen atom positions correlate with positive and negative surface charges as a result of direct hydration and through hydrogen bonds, respectively. In a similar manner the maxima of the  $\text{K}^+$  and  $\text{Cl}^-$  density distributions correlate with the locations of the surface charges. The corresponding maxima in the  $\text{Na}^+$  density distributions are significantly less pronounced, in agreement with the absence of contact pairs between  $\text{Na}^+$  and negative surface charges. When comparing the hydrogen density profiles in the NaCl and in the KCl solutions, it is evident that the maxima due to the formation of hydrogen bonds with the negative surface charges are still present for the NaCl case but are almost completely absent for the KCl solution. Obviously,  $\text{K}^+$  ions displace the hydrogen bonding water molecules.

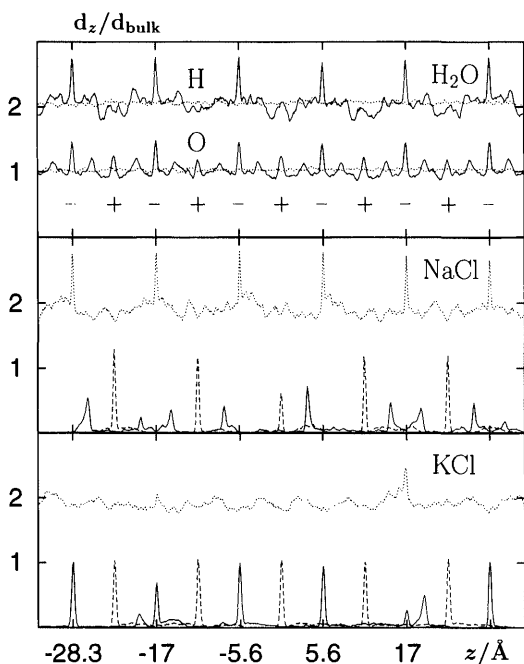


**FIG. 12** Normalized density profiles,  $d_z/d_{\text{bulk}}$ , along the pore axis. Top: oxygen and hydrogen density profiles from the simulation of pure water in the polar functionalized pore (full line) and in the nonpolar pore (dotted). The location of positive and negative charges is indicated by symbols. Center:  $\text{Na}^+$  (full),  $\text{Cl}^-$  (dashed), and hydrogen (dotted) density profiles from the simulation of a NaCl solution in the polar functionalized pore. Bottom:  $\text{K}^+$  (full),  $\text{Cl}^-$  (dashed), and hydrogen (dotted) density profiles from the simulation of a KCl solution in the polar functionalized pore.

In the polar pores, the diffusion coefficient of all ions is strongly reduced relative to the bulk values. No counterion dependence is observed for the SDC of  $\text{Cl}^-$ . A more detailed analysis shows that the ion SDC depends on the ion's relative position in the pore [174]. In the case of the  $\text{K}^+$  ion, this dependence is particularly strong.  $\text{K}^+$  ions forming contact pairs with the surface charges are almost completely immobilized on the time scale of the simulations. The few remaining ions in the center of the pore are almost unaffected by the (screened) surface charges. The fact that most of the  $\text{K}^+$  ions form contact pairs substantially reduces the average value of the normalized  $\text{K}^+$  SDC to 0.2. The behavior of  $\text{Cl}^-$  is similar to that of  $\text{K}^+$ . The SDC of sodium ions, which

are less likely to form contact ion pairs, is reduced less strongly than that of  $K^+$  or  $Cl^-$ . The simulations suggest an explanation for the observed ion selectivity (sodium transport is enhanced relative to potassium transport) and concentration dependence of ion mobility (transport is enhanced at higher concentration) in such polymer membranes. Weakly solvated ions form stronger bonds with polar surface groups, which last for a longer time, thus favoring the transport of smaller ions. Furthermore, ion mobility along the channel varies with the distance of an ion from the pore surface. Thus, the overall ion mobility increases at higher concentration, because the effect of polar surface groups is screened through the formation of stable ion pairs.

## B. Water in Vycor Glass

Recently, many experiments have been performed on the structure and dynamics of liquids in porous glasses [175–190]. These studies are difficult to interpret because of the inhomogeneity of the sample. Simulations of water in a cylindrical cavity inside a block of hydrophilic Vycor glass have recently been performed [24,191,192] to facilitate the analysis of experimental results. Water molecules interact with Vycor atoms, using an empirical potential model which consists of (12–6) Lennard–Jones and Coulomb interactions. All atoms in the Vycor block are immobile. For details see Ref. 191. We have simulated samples at room temperature, which are filled with water to between 19 and 96 percent of the maximum possible amount. Because of the hydrophilicity of the glass, water molecules cover the surface already in nearly empty pores; no molecules are found in the pore center in this case, although the density distribution is rather wide. When the amount of water increases, the center of the pore fills. Only in the case of 96 percent filling, a continuous aqueous phase without a cavity in the center of the pore is observed.

We have analyzed the number of neighbors and the number of hydrogen bonds in which a molecule engages as a function of the radial coordinate  $\rho$ . Two water molecules are termed neighbors if the oxygen–oxygen distance is smaller than 3.35 Å. They are termed hydrogen bonded if, in addition, the angle between an intramolecular O–H vector and the intermolecular O–O vector is smaller than 20°. Fig. 13 depicts the number of water–water hydrogen bonds (full lines), the number of water–Vycor hydrogen bonds (long dashes) and the total number of bonds. At the larger water concentrations, the number of hydrogen bonds in the center is roughly constant, whereas the number of bonds for low hydration decreases near the center (just like the number of neighbors and the particle density). The fact that the number of hydrogen

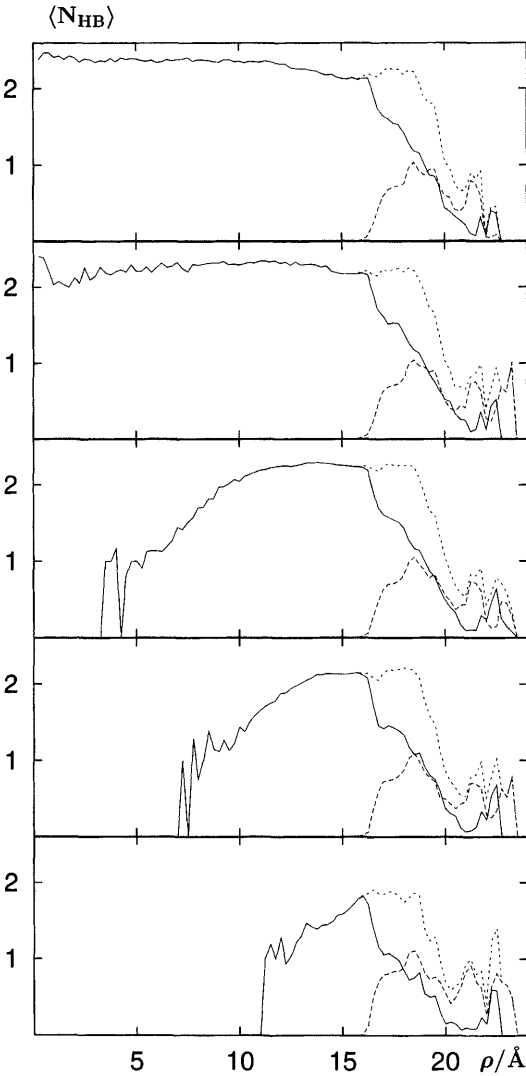


**FIG. 13** Average number of hydrogen bonds (for definition see text) as a function of  $\rho$  in five simulations at different levels of hydration in a Vycor pore. Full lines show the number of water–water bonds, long-dashed lines show the number of bonds between water molecules and Vycor, and short-dashed lines denote the sum of the two. From top to bottom, the frames correspond to a water content of about 96, 74, 55, 37, and 19% of the maximum possible (corresponding to 2600, 2000, 1500, 1000, and 500 water molecules in a cylindrical cavity of about 4 nm diameter and 7.13 nm length). (From Ref. 24.)

bonds between water and Vycor balances the loss of water–water hydrogen bonds near the pore surface demonstrates, to a large extent, the hydrophilic nature of the Vycor glass.

Fig. 14 shows mobility profiles across two pores with a filling of 74 and 96 percent. The figure displays the mean-square displacement after 10 ps as a function of the  $\rho$  coordinate of the water molecule at initial time. The mobility is highest in the center of the pore and lowest near the pore surface. When the pore is almost completely filled (full line), the mobility is more or less constant in the range  $0 < \rho < 10 \text{ \AA}$  and then decreases monotonically. Beyond about  $\rho = 18 \text{ \AA}$  the mean square displacement is very small and the adsorbed water molecules in this range do not contribute substantially to the total transport coefficient along the pore axis. If the pore is not completely filled and if there is an “empty” region in the center (symbols), the mean-square displacement is not constant in the inner region of the cylinder. The mobility keeps increasing towards the pore center, which is due to the fact that water molecules near a free surface are more mobile than in the interior of the liquid phase, since they are bonded to the liquid by a smaller than average number of hydrogen bonds (see Fig. 13). The behavior near the Vycor surface at lower water concentration is unchanged from that at the highest concentration. The total SDC decreases with decreasing level of hydration. Neutron scattering experiments, which probe only the total water dynamics, show a similar trend of mobility with the level of hydration [188].

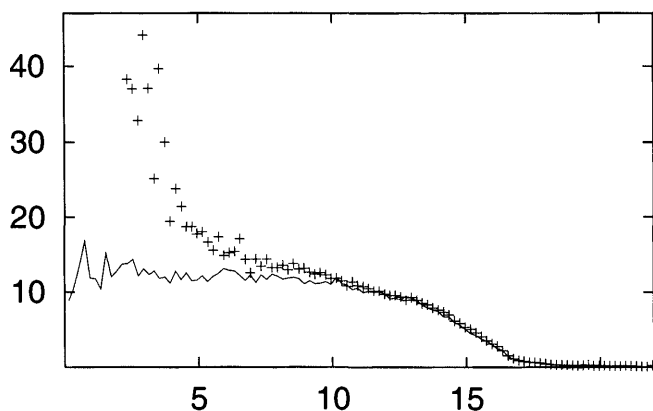


**FIG. 14** Mean square displacement  $\langle \Delta r^2 \rangle_{10}$  after 10 ps as a function of the initial distance  $\rho$  of a water molecule from the pore axis for the two runs with 96% (full line) and 74% filling. (Taken with permission from Ref. 24.)

## VII. INTERFACES BETWEEN WATER AND INORGANIC MATERIALS

Interfaces between water and a variety of different inorganic solids have been investigated by simulation methods. In the following, a brief review of key references and findings is given. The list of references is not necessarily complete and the interested reader should consult the work cited and references therein in order to find out more about the subject.

### A. The Ice/Water Interface

The molecular structure and dynamics of the ice/water interface are of interest, for example, in understanding phenomena like frost heaving, freezing (and the inhibition of freezing) in biological systems, and the growth mechanisms of ice crystals. In a series of simulations, Haymet and co-workers (see Refs. 193–196) studied the density variation, the orientational order and the layer-dependence of the mobility of water molecules. The ice/water basal interface is found to be a relatively broad interface of about 15 Å width (compared to about 5 Å for the free water surface). The authors observed a continuous change of the self-diffusion coefficient from liquid-like to solid-like values over this interval. The results have been extensively reviewed by Laird and Haymet [197].

More recently, simulation studies focused on surface melting [198] and on the molecular-scale growth kinetics and its anisotropy at ice-water interfaces [199–204]. Essmann and Geiger [202] compared the simulated structure of vapor-deposited amorphous ice with neutron scattering data and found that the simulated structure is between the structures of high and low density amorphous ice. Nada and Furukawa [204] observed different growth mechanisms for different surfaces, namely layer-by-layer growth kinetics for the basal face and what the authors call a collected-molecule process for the prismatic system.

### B. Water on Ionic Salt Surfaces

The properties of water near ionic salt surfaces are of interest not only for the understanding of the mechanism of dissolution processes but also for the understanding of the  $\text{NO}_x$  chemistry in the atmosphere next to oceans [205]. Experiments in UHV [205–208] indicate that the water-covered NaCl surface is quite stable at low temperatures. An early simulation study by Anastasiou et al. [209] focused on the arrangements and orientations of water molecules in contact with a rigid NaCl crystal. Ohtaki and coworkers investigated the dissolution of very small cubic crystals of NaF, KF, CsF, LiCl, NaCl, and KCl [210] and the nucleation [211] of NaCl and CsF in a

series of rather short molecular dynamics simulations. Over the time span of their simulations, the authors observed anion dissolution only from the CsF, LiCl and NaCl crystals and no cation dissolution. Recently, Shinto et al. [212] studied the water/NaCl surface; NaCl(001) and NaCl(011) surfaces were stable on the time scale of 10 ps. The shortness of these simulation studies certainly does not allow a final conclusion concerning the stability of the model NaCl surface. The dissolution of ionic crystals is, however, interesting both from a thermodynamic and from a kinetic viewpoint and certainly warrants more extensive work.

### C. Water on Oxide Surfaces

Oxide surfaces play an important role in heterogeneous catalysis both as catalysts and catalyst supports. In addition to their role as catalysts, oxides are key components in many subsurface minerals. As such, they influence the chemical reactivity and the transport of water and dissolved substances in soil. The water/MgO interface, especially, has been studied extensively by quantum chemistry and computer simulation. McCarthy and coworkers [213] studied the structure and dynamics at the water/MgO interface by means of classical MC and MD simulations and calculated, among other properties, the desorption rate and the orientational structure of water on this surface. Lynden-Bell and coworkers [214] conclude in their MD study that the interactions of water with the oxide surface are mainly governed by electrostatic interactions and not by hydrogen bonding; they observe several regular overlayer structures that have been known from experiments in ultra-high vacuum. Both studies agree on the fact that water molecules align with their dipole mostly parallel to the surface, in order to minimize interfacial polarization.

*Ab initio* molecular dynamics has been used to study water adsorption and dissociation on MgO [215,216] and on TiO<sub>2</sub> [217]. Water is weakly physisorbed on the perfect MgO (001) surface, but dissociates readily on the stepped surface. Dissociative adsorption is observed at fivefold-coordinated Ti sites on the TiO<sub>2</sub> (110) surface.

### D. Water/Clay Systems

The adsorption of water on various clay surfaces and the swelling behavior of clays, especially montmorillonite, has been studied by several groups of authors. Delville [218–221] compared the adsorption of water from the gas phase onto the surface of sodium–montmorillonite, kaolinite, and potassium–mica clays. Using grand canonical Monte Carlo (GCMC) calculations, he demonstrated how the surface properties of the clays, e.g., wetting and solvent organization, depend on the electric charge and chemi-

cal composition of the minerals. Skipper and coworkers [223–229] investigated, by standard MD and MC techniques, the interfacial structure of water in one-, two-, and three-layer hydrates. Specifically, they studied the cation dependence in lithium, sodium, and potassium montmorillonite [223,224,229]. They observed that, because of its lower hydration energy, potassium ions screen the mutual repulsion between the negatively charged clay surfaces more effectively than  $\text{Li}^+$  and  $\text{Na}^+$  ions, thus providing qualitative insight into the role of  $\text{K}^+$  as swelling inhibitor. Note how the same property of the potassium ion, namely its relatively weak hydration, was found to be related to the selectivity of ion transport in functionalized polymer membranes (*vide supra*).

In the studies by Skipper et al. the number of water layers (and thus molecules) was fixed on the basis of experimental evidence; consequently, the stable states or degrees of swelling were presumed. Quite differently, Karaborni et al. [44] determined, by means of a combination of GCMC and MD, the number of water molecules directly from a series of simulations in which the distance between montmorillonite planes was varied systematically. They observed that swelling proceeded from the dry state through the formation of one, three, and then five layers of water. This is very different from the usually believed hydration sequence from one layer to two, then to three layers, and so on, which has been intrinsically assumed by Skipper and coworkers. The authors conclude that the complex swelling behavior accounts for many of the experimental facts. This work demonstrates impressively the power of the grand canonical simulation method.

## VIII. WATER/MEMBRANE INTERFACES

Biological membranes in contact with water or aqueous solutions have been modeled by many groups using a wide range of models derived from molecular mechanics force fields. For the sake of brevity, here only a few subjects are mentioned: general aspects of the structure of the interface [230–236], the ordering of water and its relationship to the hydration force [237,238], the transport of small molecules [239,240], simulations of anesthetic molecules [241], antibiotic activity [242], peptide signal sequences [243], membrane fluidity [244], and many more were investigated. This list is far from being complete.

## IX. SUMMARY AND OUTLOOK

Many vastly different interfacial systems with one aqueous phase have been studied by computer simulations with detailed molecular representation of



the solvent and ionic and molecular solutes. The common features of molecular models of the interface, which have been used in computer simulations, are the explicit consideration of solvent properties through the inclusion of hydrogen bonding and ionic hydration. The above discussion shows that many properties of interfaces can be understood on the basis of the relative strength of hydrogen bonding and ionic hydration relative to the interaction of solvent and solute with the second phase.

Most simulations have been performed in the microcanonical, canonical, or NPT ensemble with a fixed number of molecules. These systems typically require an iterative adjustment process until one part of the system exhibits the required properties, like, eg., the bulk density of water under ambient conditions. Systems which are equilibrated carefully in such a fashion yield valuable insight into the physical and, in some cases, chemical properties of the materials under study. However, the specification of volume or pressure is at variance with the usual experimental conditions where control over the composition of the interfacial region is usually exerted through the chemical potential, i.e., the interfacial system is in thermodynamic and chemical equilibrium with an extended bulk phase. Such systems are best simulated in the grand canonical ensemble where particle numbers are allowed to fluctuate. Only a few simulations of aqueous interfaces have been performed to date in this ensemble, but this technique will undoubtedly become more important in the future. Particularly the amount of solvent and/or solute in random disordered or in ordered porous media can hardly be estimated by a judicious equilibration procedure. Chemical potential control is mandatory for the simulation of these systems. We will certainly see many applications in the near future.

## REFERENCES

1. L. Blum, F. Vericat, D. Bratko. *J Chem Phys* 102:1461, 1995.
2. K. Binder, ed. *Applications of the Monte Carlo Method in Statistical Physics*. (Berlin: Springer-Verlag, 1984).
3. K. Binder, ed. *Monte Carlo Methods in Statistical Physics, 2nd ed.* Berlin: Springer-Verlag, 1986.
4. K. Binder, ed. *The Monte Carlo Method in Condensed Matter Physics*, Vol. 71 of *Topics in Applied Physics*. Berlin: Springer-Verlag, 1992.
5. M. P. Allen, D. J. Tildesley, *Computer Simulations of Liquids*. New York: Oxford University Press, 1987.
6. R. Haberlandt, S. Fritzsche, G. Peinel, K. Heinzinger. *Molekulardynamik. Grundlagen und Anwendungen*. Braunschweig, Wiesbaden: Vieweg, 1995.
7. B. Smit, D. Frenkel, *Understanding Molecular Simulations. From Algorithms to Applications*. San Diego: Academic Press, 1996.

8. A. R. Leach, *Molecular Modeling. Principles and Applications*. Singapore: Longman, 1996.
9. D. Henderson, F. F. Abraham, J. A. Barker. *Mol Phys* 31:1291, 1976.
10. I. Benjamin. *J Chem Phys* 96:577, 1992.
11. D. A. Rose, I. Benjamin. *J Chem Phys* 100:3545, 1994.
12. X. Xia, M. L. Berkowitz. *Chem Phys Lett* 227:561, 1994.
13. J. B. Straus, G. A. Voth. *J Phys Chem* 97:7388, 1993.
14. J. B. Straus, A. Calhoun, G. A. Voth. *J Chem Phys* 102:529, 1995.
15. B. B. Smith, J. W. Halley. *J Chem Phys* 101:10915, 1994.
16. D. A. Rose, I. Benjamin. *Chem Phys Lett* 234:209, 1995.
17. B. B. Smith, J. W. Halley, A. J. Nozik. *Chem. Phys.* 205:245, 1996.
18. A. Calhoun, G. A. Voth. *J Phys Chem* 100:10746, 1996.
19. Y. G. Boroda, A. Calhoun, G. A. Voth. *J Chem Phys* 107:8940, 1997.
20. R. M. Lynden-Bell, J. C. Rasaiah. *J Chem Phys* 105:9266, 1996.
21. M. S. P. Sansom, I. D. Kerr, J. Breed, R. Sankararamakrishnan. *Biophys J* 70:693, 1996.
22. C. Hartnig, W. Witschel, E. Spohr. *J Phys Chem B* 107:1241, 1998.
23. C. Hartnig, W. Witschel, E. Spohr. *Ber Bunsenges Phys Chem* 102:1689, 1998.
24. E. Spohr, C. Hartnig, P. Gallo, M. Rovere. *J Mol Liq* 80:165, 1999.
25. F. Müller-Plathe. *J Chem Phys* 108:8252, 1998.
26. F. Müller-Plathe. *J Membrane Sci* 141:147, 1998.
27. S. E. Feller, R. W. Pastor, A. Rojnuckarin, S. Bogusz, B. R. Brooks. *J Phys Chem* 100:17011, 1996.
28. J. C. Shelley, G. N. Patey. *Mol Phys* 88:385, 1996.
29. E. Spohr. *J Chem Phys* 107:6342, 1997.
30. A. Wallqvist, B. J. Berne. *Chem Phys Lett* 45:26, 1988.
31. A. Wallqvist, D. G. Covell. *J Phys Chem* 99:5705, 1995.
32. A. Wallqvist, B. J. Berne. *J Phys Chem* 99:2885, 1995.
33. N. T. Skipper. *Chem Phys Lett* 207:424, 1993.
34. D. A. Rose, I. Benjamin. *J Chem Phys* 95:6956, 1991.
35. D. A. Rose, I. Benjamin. *J Chem Phys* 98:2283, 1993.
36. L. Perera, M. L. Berkowitz. *J Phys Chem* 97:13803, 1993.
37. E. Spohr. *Chem Phys Lett* 207:214, 1993.
38. E. Spohr. *Acta Chem Scand* 49:189, 1995.
39. W. Schmickler. *Chem Phys Lett* 237:152, 1995.
40. O. Pecina, W. Schmickler. *J Electroanal Chem* 431:47, 1997.
41. R. A. Marcus. *Rev Mod Phys* 65:599, 1993.
42. D. E. Ulberg, K. E. Gubbins. *Mol Simulation* 13:205, 1994.
43. J. C. Shelley, G. N. Patey, D. R. Bérard, G. M. Torrie. *J Chem Phys* 107:2122, 1997.
44. S. Karaborni, B. Smit, W. Heidug, J. Urai, E. van Oort. *Science* 271:1102, 1996.
45. E. Spohr, K. Heinzinger. *Electrochim Acta* 33:1211, 1988.
46. E. Spohr, K. Heinzinger. *Ber Bunsenges Phys Chem* 92:1358, 1988.
47. E. Spohr. *J Phys Chem* 93:6171, 1989.

48. R. R. Nazmutdinov, M. Probst, K. Heinzinger. *J Electroanal Chem* 369:227, 1994.
49. J. Seitz-Beywl, M. Poxleitner, M. M. Probst, K. Heinzinger. *Int J Quant Chem* 42:1141, 1992.
50. G. Tóth, E. Spohr, K. Heinzinger. *Chem Phys* 200:347, 1995.
51. M. R. Philpott, J. N. Glosli. Molecular dynamics simulation of interfacial electrochemical processes: electric double layer screening. In: G. Jerkiewicz, M. P. Soriaga, K. Uosaki, A. Wieckowski, eds. *Solid-Liquid Electrochemical Interfaces*, Vol. 656 of *ACS Symposium Series*. Washington: ACS, 1997, Chap. 2, pp. 13–30.
52. J. N. Glosli, M. R. Philpott. *Electrochim Acta* 41:2145, 1996.
53. M. R. Philpott, J. N. Glosli. *J Electroanal Chem* 409:65, 1996.
54. M. R. Philpott, J. N. Glosli. *J Electrochem Soc* 142:L25, 1995.
55. E. Spohr. *J Electroanal Chem* 450:327, 1998.
56. W. Schmickler, E. Leiva. *Mol Phys* 86:737, 1995.
57. J. I. Siepmann, M. Sprik. *Surf Sci Lett* 279:L185, 1992.
58. J. I. Siepmann, M. Sprik. *J Chem Phys* 102:511, 1995.
59. D. L. Price, J. W. Halley. *J Chem Phys* 102:6603, 1995.
60. H. J. C. Berendsen, J. R. Grigera, T. P. Straatsma. *J Phys Chem* 91:6269, 1987.
61. K. Heinzinger. Molecular dynamics of water at interfaces. In: J. Lipkowski, P. N. Ross, eds. *Structure of Electrified Interfaces, Frontiers of Electrochemistry*. New York: VCH: 1993, Chap 7, p. 239.
62. M. L. Berkowitz, L. Perera. In: H. L. Sella, J. T. Golab, eds. *Theoretical and Computational Approaches to Interface Phenomena*. New York: Plenum Press, 1994.
63. E. Spohr. *Computer Modeling of Aqueous/Metallic Interfaces*. Ulm: Habilitationsschrift, 1995.
64. I. Benjamin. *Chem Rev* 96:1449, 1996.
65. E. Spohr, G. Tóth, K. Heinzinger. *Electrochim Acta* 41:2131, 1996.
66. E. Spohr. Computer simulation of the structure and dynamics of water near metal surfaces. In: G. Jerkiewicz, M. P. Soriaga, K. Uosaki, A. Wieckowski, eds. *Solid-Liquid Electrochemical Interfaces*, Vol. 656 of *ACS Symposium Series*. Washington: ACS, 1997, Chap. 3, pp. 31–44.
67. P. A. Bopp, A. Kohlmeier, E. Spohr. *Electrochim Acta* 43:2911, 1998.
68. K. A. Motakabbir, M. L. Berkowitz. *Chem Phys Lett* 176:61, 1991.
69. M. A. Wilson, A. Pohorille, L. R. Pratt. *J Phys Chem* 91:4873, 1987.
70. M. Matsumoto, Y. Kataoka. *J Chem Phys* 88:3232, 1988.
71. G. C. Lie, S. Grigoras, L. X. Dang, D. Y. Yang, A. D. Mclean. *J Chem Phys* 99:3933, 1993.
72. M. A. Wilson, A. Pohorille, L. R. Pratt. *J Chem Phys* 99:3281, 1988.
73. W. L. Jorgensen, J. Chandrasekhar, J. D. Madura, R. W. Impey, M. L. Klein. *J Chem Phys* 79:926, 1983.
74. M. A. Wilson, A. Pohorille, L. R. Pratt. *Chem Phys* 129:209, 1989.
75. I. Benjamin. *J Chem Phys* 95:3698, 1991.

76. M. A. Wilson, A. Pohorille. *J Chem Phys* 95:6005, 1991.
77. A. Pohorille, I. Benjamin. *J Chem Phys* 94:5599, 1991.
78. I. Benjamin, A. Pohorille. *J Chem Phys* 98:236, 1993.
79. A. Pohorille, I. Benjamin. *J Phys Chem* 97:2665, 1993.
80. V. P. Sokhan, D. J. Tildesley. *Faraday Discuss* 104:193, 1996.
81. B. Joensuu. *Chem Phys Lett* 82:520, 1981.
82. J. P. Valteau, A. A. Gardner. *J Chem Phys* 86:4162, 1987.
83. A. A. Gardner, J. P. Valteau. *J Chem Phys* 86:4171, 1987.
84. M. Marchesi. *Chem Phys Lett* 97:224, 1983.
85. R. M. Townsend, J. Gryko, S. A. Rice. *J Chem Phys* 82:4391, 1985.
86. R. M. Townsend, S. A. Rice. *J Chem Phys* 94:2207, 1991.
87. N. I. Christou, J. S. Whitehouse, D. Nicholson, N. G. Parsonage. *Faraday Symp Chem Soc* 16:139, 1981.
88. R. Sonnenschein, K. Heinzinger. *Chem Phys Lett* 102:550, 1983.
89. C. Y. Lee, J. A. McCammon, P. J. Rossky. *J Chem Phys* 80:4448, 1984.
90. N. I. Christou, J. S. Whitehouse, D. Nicholson, N. G. Parsonage. *Mol Phys* 55:397, 1985.
91. G. Aloisi, R. Guidelli, R. A. Jackson, S. M. Clark, P. Barnes. *J Electroanal Chem Interfacial Electrochem* 206:131, 1986.
92. N. G. Parsonage, D. Nicholson. *J Chem Soc Faraday Trans II* 83:663, 1987.
93. J. Hautman, J. W. Halley, Y.-J. Rhee. *J Chem Phys* 91:467, 1989.
94. S. B. Zhu, G. W. Robinson. *J Chem Phys* 94:1403, 1991.
95. A. Wallqvist. *Chem Phys Lett* 165:437, 1990.
96. E. Spohr. *J Chem Phys* 106:388, 1997.
97. S. H. Lee, P. J. Rossky. *J Chem Phys* 100:3334, 1994.
98. E. Spohr. *J Mol Liquids* 64:91, 1995.
99. P. Linse. *J Chem Phys* 86:4177, 1987.
100. I. L. Carpenter, W. J. Hehre. *J Phys Chem* 94:531, 1990.
101. T.-M. Chang, L. X. Dang. *J Chem Phys* 104:6772, 1996.
102. T.-M. Chang, L. X. Dang. *Chem Phys Lett* 263:39, 1996.
103. D. A. Rose, I. Benjamin. *J Phys Chem* 96:9561, 1992.
104. I. Benjamin. *J Chem Phys* 97:1432, 1992.
105. A. R. V. Buuren, S. J. Marrink, H. J. C. Berendsen. *J Phys Chem* 97:9206, 1993.
106. D. Michael, I. Benjamin. *J Phys Chem B* 102:5145, 1998.
107. I. Benjamin. *J Phys Chem* 95:6675, 1991.
108. K. J. Schweighofer, I. Benjamin. *Chem Phys Lett* 202:379, 1993.
109. I. Benjamin. *Science* 261:1558, 1993.
110. K. J. Schweighofer, I. Benjamin. *J Electroanal Chem* 391:1, 1995.
111. I. Benjamin. *Ann Rev Phys Chem* 48:407, 1997.
112. R. Dryfe, Z. Ding, R. Wellington, P. Brevet, A. M. Kuznetsov, H. H. Girault. *J Phys Chem A* 101:2519, 1997.
113. A. Tamburello, P. Hebert, P. Brevet, H. Girault. *J Electroanal Chem* 409:123, 1996.
114. Z. Ding, R. Wellington, P. Brevet, H. Girault. *J Phys Chem* 100:10658, 1996.

115. H. Girault. *J Electroanal Chem* 388:93, 1995.
116. H. Wang, E. Borguet, K. Eisenthal. *J Phys Chem A* 101:713, 1997.
117. K. Eisenthal. *J Phys Chem* 100:12997, 1996.
118. K. Eisenthal. *Chem Rev* 96:1343, 1996.
119. X. Shi, E. Borguet, A. Tarnovsky, K. Eisenthal. *Chem Phys* 205:167, 1996.
120. H. L. F. von Helmholtz. *Ann Physik* 89:211, 1853.
121. G. Gouy. *J Phys* 9:457, 1910.
122. D. L. Chapman. *Phil Mag* 25:475, 1913.
123. O. Stern. *Z Electrochem* 30:508, 1924.
124. S. Holloway, K. H. Bennemann. *Surf Sci* 101:327, 1980.
125. I. Benjamin. *Modern Aspects of Electrochemistry* 31:115, 1997.
126. E. Spohr. In: D. M. Kolb and R. Alkire, eds. *Advances in Electrochemical Science and Technology*, Vol. 6. VCH Weinheim: Wiley-VCH, pp. 1-75.
127. E. Spohr. *Chem Phys* 141:87, 1990.
128. K. Foster, K. Raghavan, M. Berkowitz. *Chem Phys Lett* 162:32, 1989.
129. K. Raghavan, K. Foster, M. Berkowitz. *Chem Phys Lett* 177:426, 1991.
130. K. Raghavan, K. Foster, K. Motakabbir, M. Berkowitz. *J Chem Phys* 94:2110, 1991.
131. J. Böcker, R. R. Nazmutdinov, E. Spohr, K. Heinzinger. *Surf Sci* 335:372, 1995.
132. J. Böcker, E. Spohr, K. Heinzinger. *Z Naturforsch* 50a:611, 1995.
133. J. Böcker, Z. N. Gurskii, K. Heinzinger. *J Phys Chem* 100:14969, 1996.
134. M. L. Berkowitz, I.-C. Yeh, E. Spohr. Structure of water at the water/metal interface. Molecular dynamics computer simulations. In: A. Wieckowski, ed. *Interfacial Electrochemistry*. New York: Marcel Dekker, 1999, (in press).
135. L. Bosio, R. Cortes, C. Segaud. *J Chem Phys* 71:3595, 1979.
136. P. A. Thiel, T. E. Madey. *Surf Sci Reports* 7:211, 1987.
137. A. M. Brodsky, M. Watanabe, W. P. Reinhardt. *Electrochim Acta* 36:1695, 1991.
138. M. Watanabe, A. M. Brodsky, W. P. Reinhardt. *J Chem Phys* 95:4593, 1991.
139. X. Xia, M. L. Berkowitz. *Phys Rev Lett* 74:3193, 1995.
140. K. J. Schweighofer, X. Xia, M. L. Berkowitz. *Langmuir* 12:3747, 1996.
141. M. W. Ribarsky, W. D. Luedtke, U. Landman. *Phys Rev B* 32:1430, 1985.
142. A. Ignaczak, J. A. N. F. Gomes. *J Electroanal Chem* 420:209, 1997.
143. H. Sellers, P. V. Sudhakar. *J Chem Phys* 97:6644, 1992.
144. H. Yang, J. L. Whitten. *Surf Sci* 223:131, 1989.
145. M. Rosi, C. W. Bauschlicher Jr. *J Chem Phys* 90:7264, 1989.
146. S. Trasatti. Personal communication.
147. G. Aloisi, M. L. Foresti, R. Guidelli, P. Barnes. *J Chem Phys* 91:5592, 1989.
148. G. Aloisi, R. Guidelli. *J Chem Phys* 95:3679, 1991.
149. G. Nagy, K. Heinzinger. *J Electroanal Chem* 296:549, 1990.
150. G. Nagy, K. Heinzinger, E. Spohr. *Faraday Discuss* 94:307, 1992.
151. M. F. Toney, J. N. Howard, J. Richter, G. L. Borges, J. G. Gordon, O. R. Melroy, D. G. Wiesler, D. Yee, L. B. Sorensen. *Nature* 368:444, 1994.
152. J. N. Glosli, M. R. Philpott. *J Chem Phys* 96:6962, 1992.

153. J. N. Glosli, M. R. Philpott. In: J. W. Halley and L. Blum, eds. *Microscopic Models of Electrode–Electrolyte Interfaces*. Pennington: Electrochemical Society Inc., 1993, No. 93-5, pp. 90–103.
154. J. N. Glosli, M. R. Philpott. *J Chem Phys* 98:9995, 1993.
155. J. Seitz-Beywl, M. Poxleitner, K. Heinzinger. *Z Naturforsch* 46a:876, 1991.
156. B. Eck, E. Spohr. *Electrochim Acta* 42:2779, 1997.
157. G. Tóth, K. Heinzinger. *Chem Phys Lett* 245:48, 1995.
158. M. R. Philpott, J. N. Glosli, S. B. Zhu. *Surf Sci* 335:422, 1995.
159. E. Spohr. *Electrochim Acta* 44:1697, 1999.
160. J. W. Halley, S. Pratt, B. Johnson. *J Electroanal Chem Interfacial Electrochem* 150:355, 1983.
161. B. B. Smith, J. T. Hynes. *J Chem Phys* 99:6517, 1993.
162. B. B. Smith, A. J. Nozik. *J Phys Chem* 101B:2459, 1997.
163. O. Pecina, W. Schmickler, E. Spohr. *J Electroanal Chem* 394:29, 1995.
164. O. Pecina, W. Schmickler, E. Spohr. *J Electroanal Chem* 405:239, 1995.
165. O. Pecina, W. Schmickler. *J Electroanal Chem* 431:47, 1997.
166. B. E. Conway. In: B. E. Conway, R. E. White, J. O. Bockris, eds. *Modern Aspects of Electrochemistry*, Vol. 16. New York: Plenum Press, 1985.
167. U. Frese, W. Schmickler. *Ber Bunsenges Phys Chem* 92:1413, 1988.
168. U. Frese, U. Stimming. *J Electroanal Chem* 198:409, 1986.
169. K. S. Kim, H. L. Nguyen, P. K. Swaminathan, E. Clementi. *J Phys Chem* 89:2870, 1985.
170. M. Schlenkrich, P. Bopp, A. Skerra, J. Brickmann. In: A. Pullman, J. Jortner, B. Pullman, eds. *Through Membranes: Carriers and Channels and Pumps*, Dordrecht: Kluwer Academic Publishers, 1988, pp. 219–235.
171. M. Poxleitner, J. Seitz-Beywl, K. Heinzinger. *Z Naturforsch C* 48:654, 1993.
172. B. Roux, M. Karplus. *J Am Chem Soc* 113:3250, 1993.
173. H. Gankema, M. A. Hempenius, M. Möller. *Rec Trav Chim Pays-Bas* 113:241, 1994.
174. C. Hartnig. Computer simulation von Elektrolytlösungen in hydrophoben und hydrophilen Poren. Ph.D. Thesis. Universität Ulm, 1999.
175. M. R. Pereira, J. Yarwood. *J Chem Soc Faraday Trans* 92:2731, 1996.
176. R. Kimmich, S. Stapf, A. I. Maklakov, V. D. Skirda, E. V. Khozina. *Mag Res Imag* 14:793, 1996.
177. P. Levitz, G. Ehret, S. K. Sinha, J. M. Drake. *J Chem Phys* 95:6151, 1991.
178. A. C. Mitropoulos, J. M. Haynes, R. M. Richardson, N. K. Kanellopoulos. *Phys Rev B* 52:10035, 1995.
179. A. Mitropoulos, P. Makri, N. Kanellopoulos, U. Keiderling, A. Wiedenmann. *J Coll Interface Sci* 193:137, 1997.
180. A. B. Shelekhin, S. Pien, Y. H. Ma. *J Membrane Sci* 103:39, 1995.
181. Y. Guo, K. H. Langley, F. E. Karasz. *Phys Rev B* 50:3400, 1994.
182. J. H. Page, J. Liu, B. Abeles, H. W. Deckman, D. A. Weitz. *Phys Rev Lett* 71:1216, 1993.
183. Y. Hirama, T. Takahashi, M. Hino, T. Sato. *J Colloid Interface Sci* 184:349, 1996.

184. M. Agamalian, J. M. Drake, S. K. Sinha, J. D. Axe. *Phys Rev E* 55:3021, 1997.
185. M. C. Bellissent-Funel, J. Lal, L. Bosio. *J Chem Phys* 98:4246, 1993.
186. M. C. Bellissent-Funel, K. F. Bradley, H. Chen, J. Lal, J. Teixeira. *Physica A* 201:277, 1993.
187. J. Teixeira, J. M. Zanotti, M. C. Bellissent-Funel, S. H. Chen. *Physica B* 234–236:370, 1997.
188. M. C. Bellissent-Funel, S. H. Chen, J. M. Zanotti. *Phys Rev E* 51:4558, 1995.
189. F. Bruni, M. A. Ricci, A. K. Soper. *J Chem Phys* 109:1478, 1998.
190. A. K. Soper, F. Bruni, M. A. Ricci. *J Chem Phys* 109:1486, 1998.
191. M. Rovere, M. A. Ricci, D. Vellati, F. Bruni. *J Chem Phys* 108:9859, 1998.
192. C. Hartnig, W. Witschel, E. Spohr, P. Gallo, M. A. Ricci, M. Rovere. *J Mol Liq* (In press, 1999).
193. O. A. Karim, A. D. J. Haymet. *Chem Phys Lett* 138:531, 1987.
194. O. A. Karim, A. D. J. Haymet. *J Chem Phys* 89:6889, 1988.
195. O. A. Karim, P. A. Kay, A. D. J. Haymet. *J Chem Phys* 92:4634, 1990.
196. J. A. Hayward, A. D. J. Haymet. Personal communication, 1998.
197. B. B. Laird, A. D. J. Haymet. *Chem Rev* 92:1819, 1992.
198. G.-J. Kroes. *Surf Sci* 275:365, 1992.
199. I. M. Svishchev, P. G. Kusalik. *Phys Rev Lett* 73:975, 1994.
200. I. M. Svishchev, P. G. Kusalik. *Phys Rev B* 53:R8815, 1996.
201. I. M. Svishchev, P. G. Kusalik. *J Am Chem Soc* 118:649, 1996.
202. U. Essmann, A. Geiger. *J Chem Phys* 103:4678, 1995.
203. L. A. Báez, P. Clancy. *J Chem Phys* 103:9744, 1995.
204. H. Nada, Y. Furukawa. *J Phys Chem B* 101:6163, 1997.
205. H. C. Allen, J. M. Laux, R. Vogt, B. J. Finalyson-Pitts, J. C. Hemminger. *J Phys Chem* 100:6371, 1996.
206. Q. Dai, J. Hu, M. Salmeron. *J Phys Chem* 101B:1994, 1997.
207. L. Xu, H. Bluhm, M. Salmeron. *Surface Science* 407:251, 1998.
208. M. Luna, F. Rieutord, N. A. Melman, Q. Dai, M. Salmeron. *J Phys Chem A* 102:6793, 1998.
209. N. Anastasiou, D. Fincham, K. Singer. *J Chem Soc Faraday Trans II* 79:1639, 1983.
210. H. Ohtaki, N. Fukushima. *Pure & Appl Chem* 12:1743, 1991.
211. N. Fukushima, Y. Tamura, H. Ohtaki. *Z Naturforsch* 46a:193, 1991.
212. H. Shinto, T. Sakakibara, K. Higashitani. *J Phys Chem B* 102:1974, 1998.
213. M. I. McCarthy, G. K. Schenter, C. A. Scamehorn, J. B. Nicholas. *J Phys Chem* 100:16989, 1996.
214. A. Marmier, P. N. M. Hoang, S. Picaud, C. Giradet, R. M. Lynden-Bell. *J Chem Phys* 109:3245, 1998.
215. W. Langel, M. Parrinello. *Phys Rev Lett* 73:504, 1994.
216. W. Langel, M. Parrinello. *J Chem Phys* 103:3240, 1995.
217. P. J. D. Lindan, N. M. Harrison, J. M. Holender, M. J. Gillan. *Chem Phys Lett* 261:246, 1996.
218. A. Delville. *J Phys Chem* 97:9703, 1993.

219. A. Delville. *J Phys Chem* 99:2033, 1995.
220. A. Delville. *Langmuir* 7:547, 1991.
221. A. Delville. *Langmuir* 8:1796, 1991.
222. G. Nagy, G. Denuault. *J Electroanal Chem* 437:37, 1997.
223. F.-R. C. Chang, N. T. Skipper, G. Sposito. *Langmuir* 13:2074, 1997.
224. E. S. Boek, P. V. Coveney, N. T. Skipper. *J Am Chem Soc* 117:12608, 1995.
225. G. D. Williams, N. T. Skipper, M. V. Smalley, A. K. Soper. *Faraday Discuss* 104:295, 1996.
226. A. V. C. de Siqueira, N. T. Skipper, P. V. Coveney, E. S. Boek. *Mol Phys* 92:1, 1997.
227. C. H. Bridgeman, N. T. Skipper. *J Phys Condensed Matter* 9:4081, 1997.
228. F.-R. C. Chang, N. T. Skipper, G. Sposito. *Langmuir* 14:1201, 1998.
229. F.-R. C. Chang, N. T. Skipper, G. Sposito. *Langmuir* 11:2734, 1995.
230. J. J. López Cascales, J. Garcia de la Torre, S. J. Marrink, H. J. C. Berendsen. *J Chem Phys* 104:2713, 1996.
231. M. Pasenkiewicz-Gierula, Y. Takaoka, H. Miyagawa, K. Kitamura, A. Kusumi. *J Phys Chem A* 101:3677, 1997.
232. F. Zhou, K. Schulten. *J Phys Chem* 99:2194, 1995.
233. K. Raghavan, M. R. Reddy, M. L. Berkowitz. *Langmuir* 8:233, 1992.
234. M. L. Berkowitz, K. Raghavan. *Langmuir* 7:1042, 1991.
235. M. Schlenkrich, K. Nicklas, J. Brickmann, P. Bopp. *Ber Bunsenges Phys Chem* 94:133, 1990.
236. W. Shinoda, M. Shimizu, S. Okazaki. *J Phys Chem B* 102:6647, 1998.
237. S.-J. Marrink, M. Berkowitz, H. J. C. Berendsen. *Langmuir* 9:3122, 1993.
238. L. Perera, U. Essmann, M. L. Berkowitz. *Langmuir* 12:2625, 1996.
239. R. M. Sok, H. J. C. Berendsen, W. V. van Gunsteren. *J Chem Phys* 96:4699, 1992.
240. S. J. Marrink, H. J. C. Berendsen. *J Phys Chem* 100:16729, 1996.
241. J. J. López Cascales, J. G. Hernández Cifre, J. García de la Torre. *J Phys Chem B* 102:625, 1998.
242. T. R. Forester, W. Smith, J. H. R. Clarke. *J Chem Soc Faraday Trans* 93:613, 1997.
243. E. P. G. Arêas, P. G. Pascutti, S. Schreier, K. C. Mundim, P. M. Bisch. *J Phys Chem* 99:14885, 1995.
244. R. M. Venable, Y. Zhang, B. J. Hardy, W. Pastor. *Science* 262:223, 1993.
245. A. Kohlmeyer, C. Hartnig, E. Spohr. *J Mol Liq* 78:233, 1998.



# 8

## Surface Chemical Reactions

**EZEQUIEL VICENTE ALBANO** Instituto de Investigaciones  
Fisicoquímicas Teóricas y Aplicadas, Universidad Nacional de La Plata,  
La Plata, Argentina

I. Introduction	387
II. Elementary Steps in Surface Chemical Reaction Processes	388
III. Modeling and Simulation of Surface Chemical Reactions	390
IV. Outlook of Relevant Simulation Results for some Specific Reaction Models	391
A. The catalytic oxidation of CO	391
B. The catalyzed reaction $\text{CO} + \text{NO}$	415
C. The catalytic oxidation of $\text{H}_2$	419
D. Brief overview of other surface reaction processes	421
V. Conclusions and Outlook of Some Directions for Further Studies	429
References	431

### I. INTRODUCTION

During the second half of this century the study of surface and interface phenomena has steadily gained considerable interest. Information technology, heterogeneous catalysis, metallurgy, material science, microelectronics, corrosion, energy conversion, ecology and environmental sciences, etc., are some fields or disciplines whose rapid growth is mostly based on recent progress in the study of the physical chemistry properties of surfaces and interfaces. Within this context the understanding of surface chemical reactions is a challenge for researchers worldwide which is motivated by

both technical applications and scientific interest. Examples of the former are: the large-scale fabrication of chemicals via heterogeneously catalyzed reactions; the treatment of automotive exhaust causing environmental pollution; coating, corrosion, and passivation of surfaces; synthesis and refinement of hydrocarbons; etc. Furthermore, scientific interest in the study of these processes is due to the emergence of a rich and complex variety of physical-chemistry phenomena including, e.g., chaotic behavior, bistability, critical phenomena and irreversible phase transitions, propagation and interference of chemical waves of adsorbed reactants, oscillatory behavior of some reactions, etc.

Recent development of experimental techniques such as scanning tunneling microscopy (STM), low energy electron diffraction (LEED), high resolution electron energy loss spectroscopy (HREELS), ultraviolet photoelectric spectroscopy (UPS), photoelectron emission microscopy (PEEM), etc. [1,2], to name a few, allows the scientists to gather detailed physical and chemical information about surfaces, adsorbates, and reaction products. Perhaps the most dramatic example of this progress is the recent STM-based measurement of reaction rate parameters at microscopic level for the catalytic oxidation of CO [3]. Remarkably, these parameters agree very well with those previously obtained by means of macroscopic measurements.

Also, surface reaction systems are certainly a challenging scientific field for the development and application of analytical methods and theories, including recent advances in the area of non-linear dynamics.

Complementing these very well established approaches for the study of any scientific field, namely experiments and analytical theory, very recently, computer simulations have become a powerful tool for the study of a great variety of processes occurring in nature in general [4–6], as well as surface chemical reactions in particular [7]. Within this context, the aim of this chapter is not only to offer a critical overview of recent progress in the area of computer simulations of surface reaction processes, but also to provide an outlook of promising trends in most of the treated topics.

## **II. ELEMENTARY STEPS IN SURFACE CHEMICAL REACTION PROCESSES**

In most cases surface reactions proceed according to well-established elementary steps, as schematized in Fig. 1. The first one comprises trapping, sticking, and adsorption. Gaseous reactants atoms and/or molecules are trapped by the potential well of the surface. This rather weak interaction is commonly considered as a physisorbed precursor state. Subsequently, species are promoted to the chemisorbed state, that is, a much stronger

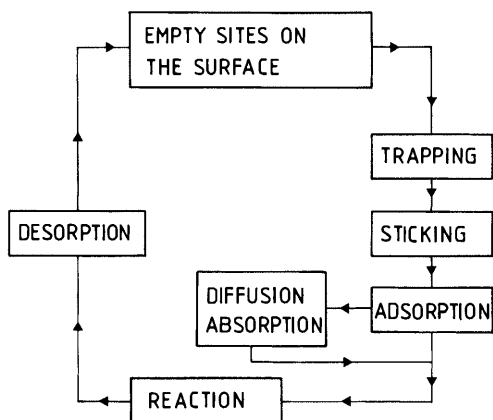


**FIG. 1** Schematic description of the relevant steps involved in a surface catalyzed reaction within the reactive regime. The cycle starts with the empty sites of the surface (top) and is followed by interactions between reactants and the surface (right branch). Such interaction finally leads to the reaction (bottom) and desorption of the products (left branch), a process which generates new empty sites (top).

interaction potential. Particularly important, from the catalytic point of view, is that molecules frequently undergo dissociation; e.g.  $N_2$ ,  $O_2$ ,  $H_2$ , etc.; a process which places on the surface highly reactive atomic species. Sticking and adsorption are processes dependent on surface structure (both geometric and electronic). In some cases chemisorption of small atoms and molecules may induce the reconstruction of the surface. This effect, coupled with structure-dependent sticking coefficients, may lead to the occurrence of collective phenomena such as oscillations.

After adsorption, species may diffuse on the surface or, eventually, become absorbed in the bulk. Due to collisions between adsorbed species of different kinds the actual reaction step can occur. Of course, this step requires that some energetic and spatial constraints have to be fulfilled. The result of the reaction step is the formation of a product molecule. This product can be either an intermediate of the reaction or its final output.

The final step of the whole reaction process is the desorption of the products. This step is essential not only for the practical purpose of collecting and storing the desired output, but also for the regeneration of the catalytic active sites of the surface. Most reactions have at least one rate-limiting step, which frequently makes the reaction prohibitively slow for practical purposes when, e.g., it is intended for homogeneous (gas or fluid) media. The role of a good solid-state catalyst is to obtain an acceptable

output rate of the products. Reactions occurring in this way are commonly known as heterogeneously catalyzed.

A detailed discussion of all steps involved in surface chemical reactions is beyond the scope of this chapter. For further information, the reader is addressed to available review articles, e.g., Ref. 1.

### **III. MODELING AND SIMULATIONS OF SURFACE CHEMICAL REACTIONS**

Why do we perform modeling and simulations (MS)? Of course, there is no an unique answer to this question. From the point of view of industrial chemical reaction engineering, the common goal is to minimize energy and raw material consumption and to optimize the yield of the reaction. Another aim, less obvious but very important, is to ensure safe reactor operation. So, extensive MS are relatively cheap procedures which frequently give valuable hints contributing to a profitable optimization of the process. From the academic point of view, surface chemical reaction systems are certainly one of the more challenging scientific fields. The understanding of these systems requires a multidisciplinary approach involving many branches of chemistry, physics, mathematics, and materials science, such as, e.g., thermodynamics, quantum mechanics, reaction, collision, and transition state theories, statistical mechanics, theory of nonlinear dynamic processes, crystallography, etc.

According to the aim of the present chapter, let us focus our attention on the academic-theoretical approach. It should be mentioned that in the study of surface reaction processes one frequently has to deal with fairly complex systems. Since the handling of such systems imposes severe problems, the standard procedure is to rationalize their study. The academic approach starts from simplified systems and a reduced number of plausible assumptions, and the goal is to achieve a general solution. The knowledge and understanding of these solutions allows us to undertake specific topics and more complex problems.

Several methods have been employed to study chemical reactions theoretically. Mean-field modeling using ordinary differential equations (ODE) is a widely used method [8]. Further extensions of the ODE framework to include diffusional terms are very useful and, e.g., have allowed one to describe spatio-temporal patterns in diffusion-reaction systems [9]. However, these methods are essentially limited because they always consider average environments of reactants and adsorption sites, ignoring stochastic fluctuations and correlations that naturally emerge in actual systems; e.g., very recently by means of in situ STM measurements it has been demon-

strated that, during the catalytic oxidation of CO, reactants tend to form islands and the reaction actually occurs at the periphery of islands formed by different species [3]. These limitations can be overcome by means of Monte Carlo (MC) simulations, where local environments are explicitly considered since they follow from the computational implementation of the previously stated microscopic mechanisms. Such mechanisms are the “rules” of the computer algorithm. Of course, the operation of the rules may lead to the development of correlations, while stochastic fluctuations are inherent to the method. The MC simulation method often faces the limitations imposed by the size of the lattices used to mimic the catalyst surface. In some particular cases, e.g., when studying second-order phase transitions, this shortcoming can be overcome by appealing to the well-established finite-size-scaling theory [10]. Also, very often one can develop extrapolation methods which give reliable results for the thermodynamic limit, i.e., infinite lattices. Another limitation arises when the diffusion rate of the adsorbed species is very large. In this case most of the computational time has to be devoted to the diffusion process while the quantity of interest, namely the number of reaction events, becomes negligible. This drawback may be overcome by implementing a mixed treatment: mean-field description of the diffusion and MC simulation of the reaction [11]. This approach may become an interesting and powerful tool in the near future. Also, MC simulations of dynamic and kinetic processes are often hindered by the fact that the Monte Carlo time, usually measured in Monte Carlo time steps, is only roughly proportional to the actual time. So, direct comparison with experiments becomes difficult. However, very recently a more sophisticated implementation of the MC method has been envisioned: namely, the dynamic Monte Carlo (DMC) approach which incorporates the actual time dependence of the processes, allowing direct comparison with experiments [12–15]. Further developments and applications of the DMC method are a promising field of research.

Within this context, the following sections are devoted to the description of the state of the art in the modeling and simulation of surface chemical reactions of simple systems using Monte Carlo techniques.

## **IV. OUTLOOK OF RELEVANT SIMULATION RESULTS FOR SOME SPECIFIC REACTION MODELS**

### **A. The Catalytic Oxidation of CO**

#### **1. A Lattice Gas Model and the Phase Diagram**

The surface reaction  $2\text{CO} + \text{O}_2 \rightarrow 2\text{CO}_2$  is likely the most studied reaction system [16,17]. This fact is due to both its practical importance and its rich

and complex behavior. It is well known that the reaction proceeds according to the Langmuir–Hinshelwood mechanism, i.e., with both reactants adsorbed on the catalyst's surface:



where S is an empty site on the surface, while (a) and (g) refer to the adsorbed and gas phases, respectively.

The lattice gas version of this reaction, as proposed by Ziff, Gulari and Barshad (ZGB) [18], has renewed the interest in the study of irreversible phase transitions (IPTs) in surface reaction systems. The ZGB model, also known as the monomer–dimer model, adopts the following generalized notation: A is CO, B<sub>2</sub> is O<sub>2</sub> and AB is CO<sub>2</sub>. The CO molecule is treated as a monomer because it takes a single site of the adsorbing surface (see Eq. (1)). The ZGB model uses a square lattice to represent the catalytic surface. The Monte Carlo algorithm for the simulation of the model is as follows: (i) A or B<sub>2</sub> molecules are selected randomly with relative probabilities  $Y_A$  and  $Y_B$ , respectively. These probabilities are the relative impingement rates of both species, which are proportional to their partial pressures in the gas phase in contact with the catalyst. Due to the normalization,  $Y_A + Y_B = 1$ , the model has a single parameter, i.e.,  $Y_A$ . If the selected species is A, one surface site is selected at random, and if that site is vacant, A is adsorbed on it [Eq. (1)]. Otherwise, if that site is occupied, the trial ends and a new molecule is selected. If the selected species is B<sub>2</sub>, a pair of nearest neighbor sites is selected at random and the molecule is adsorbed on them only if they are both vacant [Eq. (2)]. (ii) After each adsorption event, the nearest neighbors of the added molecule are examined in order to account for the reaction given by Eq. (3). If more than one [B(a), A(a)] pair is identified, a single one is selected at random and removed from the surface.

The model is intrinsically irreversible. It is assumed that both dissociation of the dimer and reaction between a pair of adjacent species of different type are instantaneous. The ZGB model basically retains the adsorption–desorption selectivity rules of the Langmuir–Hinshelwood mechanism, it has no energy parameters, and the only independent parameter is  $Y_A$ . Obviously, these crude assumptions imply that, for example, diffusion of adsorbed species is neglected, desorption of the reactants is not considered, lateral interactions are ignored, adsorbate-induced reconstructions of the surface are not considered, etc. Efforts to overcome these shortcomings will be briefly discussed below.

Interest in the ZGB model arises due to its rich and complex irreversible critical behavior. In fact, in two dimensions and for the asymptotic regime ( $t \rightarrow \infty$ ), the system reaches a stationary state whose nature solely depends on the parameter  $Y_A$ . For  $Y_A \leq Y_{1A} \cong 0.3874$  ( $Y_A \geq Y_{2A} \cong 0.5250$ ) the surface becomes irreversibly poisoned by B (A) species, while for  $Y_{1A} < Y_A < Y_{2A}$  a steady state with sustained production of AB is observed. Fig. 2 shows plots of the rate of AB production ( $R_{AB}$ ) and the surface coverage with A ( $\theta_A$ ) and B ( $\theta_B$ ) species versus  $Y_A$ . So, just at  $Y_{1A}$  and  $Y_{2A}$  the ZGB model exhibits IPTs between the reactive regime and poisoned states, which are of second and first order, respectively. Experimental evidence of a first-order "transition-like" behavior has been reported for the catalytic oxidation of carbon monoxide on Pt(210) and Pt(111) [19], as shown, e.g., in Fig. 3.

The second-order IPT is fairly well understood. In fact, it has been conjectured that this kind of transition, characterized by an scalar order parameter, given in this example by the concentration of the minority species

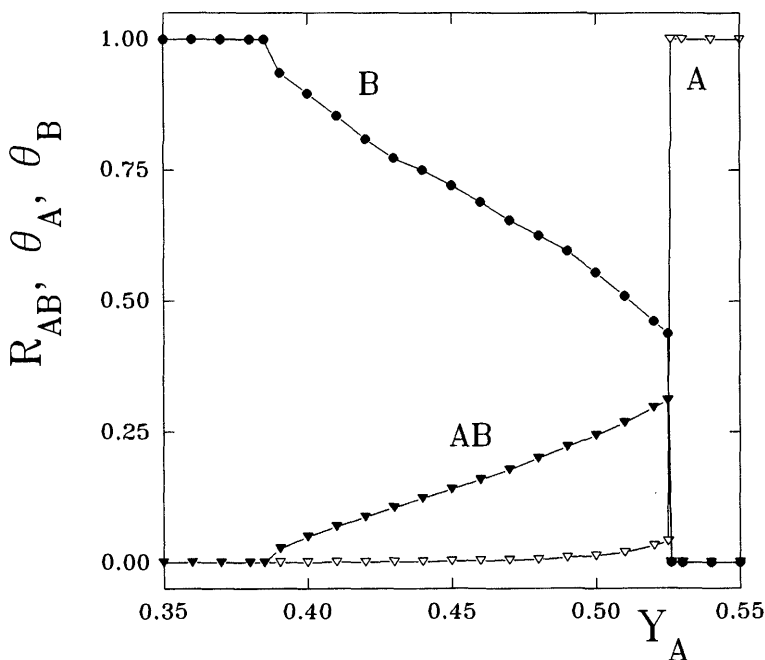


**FIG. 2** Phase diagram of the ZGB model showing the dependence of the rate of AB production ( $R_{AB}$ ) and the surface coverages with A and B species ( $\theta_A$  and  $\theta_B$ , respectively) with the adsorption probability of A species given by  $Y_A$ .

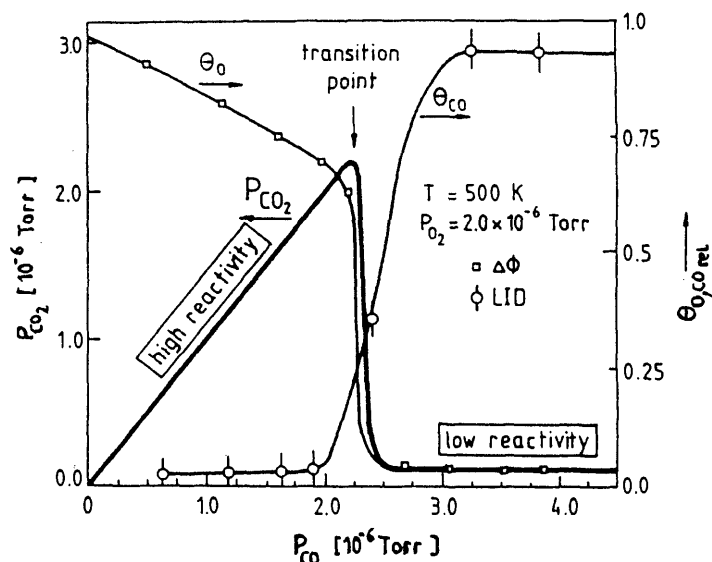


**FIG. 3** Plot of the rate of reaction ( $P_{\text{CO}_2}$ ) on Pt(210) as a function of CO pressure ( $P_{\text{CO}}$ ) recorded for  $T = 500 \text{ K}$  and  $\text{O}_2$  pressure  $P_{\text{O}_2} = 2.0 \times 10^{-6}$ . Relative coverages of CO and oxygen ( $\theta/\theta_{\text{max}}$ ) were determined using laser-induced desorption (LID) and adsorbate induced work function changes ( $\Delta\phi$ ) measurements during the reaction. In the high reactive region, nearly every CO impinging on the surface adsorbs and reacts. (From Ref. 2.)

( $\theta_A$ ), may generically belong to the universality class of directed percolation (DP) or, equivalently, Reggeon field theory [20]. In fact, an intriguing feature of continuous, reversible and irreversible transitions is the existence of universal behavior near the critical point, characterized by a set of critical exponents. These exponents are universal since they are independent of the microscopic details of the model. The basic idea behind universality is that the correlation length diverges when approaching criticality and consequently becomes the only relevant scale of length, provided that the interactions between the species is short ranged. However, the determination of the order parameter critical exponent  $\beta$  is rather difficult due to large fluctuations which can cause poisoning in finite systems even above the critical point. Meakin and Scalapino [21] found that near  $Y_{\text{IA}}$  the steady-state coverages with the reactants scale as:

$$1 - \theta_B \propto (Y_A - Y_{\text{IA}})^{\beta_0} \quad (4)$$

$$\theta_A \propto (Y_A - Y_{\text{IA}})^{\beta_{\text{CO}}} \quad (5)$$



with  $\beta_O \approx 0.61$  and  $\beta_{CO} \approx 0.69$ . Due to errors in the numerical simulation, Meakin and Scalapino [21] argue that their results may indicate that  $\beta_O = \beta_{CO}$ . Fluctuations close to criticality can be avoided by using the “damage spreading” method, as suggested in Refs. 22,23, which effectively suppress the fluctuations of the stochastic system and yield  $\beta = 0.578 \pm 0.010$  [22] in agreement with the known exponent  $\beta \approx 0.58$  of DP in  $(2 + 1)$  dimensions [20]. However, the unambiguous placement of the second-order IPT of the ZGB model within the DP universality class is due to the application of “epidemic studies” [24,25] which yield very precise dynamic critical exponents in excellent agreement with similar studies on DP clusters. Second-order IPTs belonging to the universality class of DP are found quite often in the simulation of reaction systems [26,27] and also in a great variety of other models, e.g. forest fire [28], the contact process [29], branching annihilating walkers [30], etc. However, due to the lack of experimental evidence on such kinds of transition I would like to restrict myself to the above brief discussion. Further details can be found elsewhere [20,24–29].

As can be observed in the phase diagram of the ZGB model (Fig. 2), when  $Y_A$  increases from  $Y_{1A}$  towards  $Y_{2A}$  the catalytic activity increases. However, when  $Y_{1A}$  is reached, due to the fact that large clusters of A-species suddenly grow up and cover every lattice site, an abrupt transition occurs. This IPT exhibits discontinuity of the coverages and activity, implying that it is of first order, in qualitative agreement with experiments (Fig. 3). Therefore, just at  $Y_A = Y_{2A}$ , the two adsorbed phases (a B-rich phase and a solid A-phase) coexist [18]. Fig. 4 shows a qualitative phase diagram close to a first order IPT where the relevant characteristics are indicated. Notice that the existence of metastable phases is essential for the propagation of chemical waves, as discussed below. The actual critical behavior can be obtained using the constant-coverage ensemble introduced by Ziff and Brosilow [31]. This method prevents undesired effects due to long-lived metastable states. In a constant A-coverage ensemble ( $\theta_A$  constant), the coverage of A is to be kept as close as possible to a desired value. This ensemble is achieved by carrying out an A adsorption trial whenever the instantaneous coverage of A is less than the desired value, and a  $B_2$  adsorption trial otherwise. The rest of the procedure remains the same as in the original ZGB algorithm. The average or effective value of the adsorption rate corresponding to a given fixed value of  $\theta_A$ ,  $\bar{Y}_A$ , is the fraction of A adsorption trials to the total A and  $B_2$  trials. Using this technique, the upper spinodal point is found close to  $Y_{US} \approx 0.527$  while a precise determination of the critical point is also possible given  $Y_{2A} = 0.52560 \pm 0.00001$  [31].

Another approach, useful for the study of the first-order IPT, is to perform an “epidemic analysis” [32–34]. Starting from a (small) empty hole on

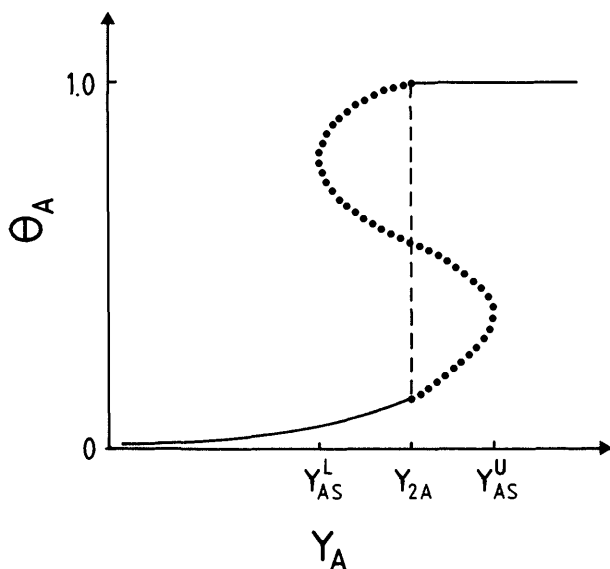


**FIG. 4** Qualitative phase diagram close to a first-order irreversible phase transition. The solid line shows the dependence of the coverage of A species ( $\theta_A$ ) on the partial pressure ( $Y_A$ ). Just at the critical point  $Y_{2A}$  one has a discontinuity in  $\theta_A$  (dashed line) which indicates coexistence between a reactive state with no large A clusters and an A rich phase (likely a large A cluster). The dotted line shows a metastability loop where  $Y_{AS}^U$  and  $Y_{AS}^L$  are the upper and lower spinodal points, respectively. Between  $Y_{2A}$  and  $Y_{AS}^U$  the reactive state is unstable and is displaced by the A rich phase. In contrast, between  $Y_{AS}^L$  and  $Y_{2A}$  the reactive state displaces the A rich phase.

an otherwise A-poisoned lattice, i.e., an initial condition very close to the inactive phase, the evolution of the system is followed as a function of time. The measured quantities are: (i) the survival probability  $P(t)$ , that is, the probability that the lattice was not poisoned with A-species after time  $t$ ; and (ii) the average number of empty sites  $N(t)$ . It is expected that such quantities would exhibit power law behavior, namely

$$P(t) \propto t^{-\delta} \quad (6)$$

and

$$N(t) \propto t^{\eta} \quad (7)$$

Evans and Miesch [32–34] have reported the following figures for the dynamic exponents:  $\delta = 3.70 \pm 0.2$  and  $\eta = -2.4 \pm 0.2$ . These values are

quite different from the conventional epidemic analysis of the directed percolation second-order IPT, namely  $\delta = 0.452 \pm 0.008$  and  $\eta = 0.224 \pm 0.010$  [20,24,25]. The large positive  $\delta$  value reveals a greatly reduced epidemic survivability and the change of sign and increase of magnitude of  $\eta$  has particular significance for the kinetics. In fact, most of the small empty holes initially present are quickly A-poisoned. However, for longer times, a few surviving epidemics grow with constant velocity, eventually spreading the reactive state across the entire lattice [32,33]. Further epidemic studies of first-order IPTs reveal that the dynamic critical exponents depend sensitively on the details of the model, such as the rate of reaction, the adsorption mechanism [35], etc. For first-order IPTs, this behavior can be understood because, due to the lack of a diverging correlation length, there is no relevant length scale (unlike for second-order IPTs), and consequently all microscopic details of the model become important. In spite of this progress, extensive simulations are still necessary in order to check that the observed power-law dependence reflects the actual behavior of the system. In fact, the obtained exponents may merely be “effective exponents” describing the crossover to asymptotic behavior.

The cluster structure of the reactants within the reactive regime was investigated by Kolb and Boudeville [36]. When  $Y_A$  increases from the second-order towards the first-order transition point, the domains of A species gradually increase from small isolated clusters to large compact structures with possibly fractally rough interfaces. On the other hand, B species form a compact structure close to  $Y_{1A}$ . With increasing  $Y_A$  the clusters become more ramified and the largest B cluster spans the whole lattice (percolates) for  $Y_A^p \approx 0.51$ . Above the percolation threshold,  $Y_A > Y_A^p$ , no percolating B clusters are found [36]. At the critical percolation threshold one has  $\theta_B \approx 0.52$ , indicating that particles are correlated. In fact, the adsorption–reaction mechanism leads to the operation of an “effective” attractive interaction, since for random non-correlated structures the threshold would be close to  $\theta_B \approx 0.59275$  [37].

The ZGB lattice gas model is an oversimplified approach to the actual processes involved in the catalytic oxidation of CO. Consequently several attempts have been made in order to give a more realistic description. Some of them are the following: (i) The inclusion of A desorption [19,38–40] causes the first order IPT to become reversible and slightly rounded, in qualitative agreement with experiments (Fig. 3). (ii) The influence of lateral interactions between reactants adsorbed on the catalyst surface have been considered by various authors, e.g., [38,41,42]. (iii) Studies on the influence of the fractal nature of the catalyst surface were motivated by the fact that most catalysts are constituted by small fractal (metallic) clusters dispersed on a fractal support. The fractal surfaces have been modeled by means of

random fractals, such as percolating clusters (see, e.g., [43–45]), diffusion limited aggregates [46], and also deterministic fractals, such as Sierpinsky carpets (see, e.g., [47,48]), etc. [49,50]. (iv) The influence of different kind's of adsorption mechanism, such as hot dimer adsorption [35], local versus random adsorption [51,52], etc., has been investigated. (v) The influence of surface diffusion has also been addressed, using different approaches [38,53–55]. Particularly interesting is the hybrid lattice–gas mean-field treatment developed by Evans and coworkers [11] for the study of surface reactions with coexisting immobile and highly mobile reactants. (vi) Considering the Eley–Rideal mechanism [56–57] as an additional step of the set of equations (1–3), namely including the following path



poisoning of the surface by complete occupation by B-species is no longer possible. Finally, the influence of adsorbate induced reconstructions of the catalyst surface in the rate of reaction will be discussed in detail in IV A 3.

## 2. Propagation of Reaction Fronts

The propagation of concentration fronts, involving the interface between reactants, in heterogeneous reaction processes operating far from equilibrium, has recently been very well documented in various experimental systems (see [16,17,58,59] and references therein). The observed spatio-temporal patterns include trigger waves, rotating spirals, and turbulence. The propagation of a reaction front requires the displacement of an unstable phase by a stable one (see, e.g., Fig. 4 for an explanation of the underlying mechanism) and the formation of an interface where most reaction events take place. It should be noticed that the study of interfaces is one of the most active areas in physics and physical chemistry (for a review see, e.g., [60]). In particular, the structure of a non-equilibrium interface and the dynamic of its roughening are issues of considerable interest.

On the basis of general scaling arguments it can be shown that the stochastic evolution of a driven interface along a strip of width  $L$  is characterized by long wavelength fluctuations ( $w(L, t)$ ) which have the following time and finite-size behavior [60]

$$w(L, t) \propto L^\alpha F(t/L^z) \quad (9)$$

where  $F(x) \propto x^\beta$  for  $x \ll 1$  and  $F(x) \rightarrow 1$  for  $x \gg 1$ , with  $z = \alpha/\beta$  where  $\alpha$  and  $\beta$  are the roughness and growth exponents, respectively. Thus, for an infinite system ( $L \rightarrow \infty$ ), one has  $w(t) \propto t^\beta$ , as  $t \rightarrow \infty$ . Notice that  $w$  is also known as the interface width. The dynamic of an interface between two phases, one of which is growing into the other, is believed to be correctly described by the Kardar–Parisi–Zhang (KPZ) framework [60,61]. For a

surface reaction lattice gas model, an interface exists between two reactant species. So, for a stochastic reactive interface propagation one may expect the exponents to assume KPZ values, namely  $\beta = 1/3$ ,  $\alpha = 1/2$ , and  $z = 3/2$ . However, the characteristics of the interface may depend on the specific reaction system. In some cases it may undergo large fluctuations during the reaction and its perimeter may look quite rough (fractal like); occasionally the interface is essentially flat. Under these circumstances the Monte Carlo simulation technique has become a powerful tool for the study of reaction interfaces.

Monte Carlo simulations due to Moller *et al.* [62] have demonstrated that a monomer-dimer model, which aims to describe the catalytic oxidation of carbon monoxide and includes reactant-assisted surface reconstruction, can support the propagation of trigger waves even if surface diffusion is not explicitly considered. However, after this early work, most simulations have been performed within the framework of the ZGB model. In order to investigate the properties of the interface between the reactive regime and the A-poisoned state Brosilow *et al.* [63] have simulated the ZGB model on the square lattice in a rectangular geometry of  $L \times M$  sites. The leftmost column of  $M$  sites was initially occupied by B atoms, the rightmost  $L/2$  columns were initially occupied by A species, and the remaining sites were initially vacant. In order to prevent A-poisoning, whenever a B species was removed (through reaction) from the leftmost column of the lattice, it was immediately replaced by another B species. Running simulations for ( $Y_A \geq Y_{2A}$ ), the imposed geometry causes the occurrence of an interface between the reactive state and an A-poisoned state. The width of the reactive phase ( $\xi$ ) is found to scale with  $Y_A$  as  $\xi = k(Y_A - Y_{2A})^{-\nu}$ , with  $\nu \cong 0.40$  and  $k \cong 0.74$  [63].

Another possibility is to study the behavior of the interface for  $Y_A$  below the A-poisoning transition  $Y_{2A}$ . Within this regime one expects that the reactive state will displace the A-poisoned one (see, e.g., Fig. 4), resulting in a propagation velocity ( $V_p$ ) normal to the interface. Studying this case, Evans and Ray [64] have proposed that  $V_p$  must vanish as  $Y_A \rightarrow Y_{2A}$ , where both states become equistable, so one has

$$V_p \propto (Y_A - Y_{2A})^{-\gamma} \quad (10)$$

with  $\gamma > 0$ . The limit of high diffusibility of the reactants can be well described by mean-field reaction-diffusion equations which give  $\gamma = 1$ . It is interesting to note that if diffusion is restricted or even suppressed, simulation results give values of  $\gamma$  very close to unity, suggesting that the exponent is independent of the surface diffusibility of the reactants [64]. In this case the propagation of the reaction interface has also been described in terms of the KPZ framework and scaling arguments [64]. From Monte

Carlo simulations at the first-order critical point it is reported that  $\beta \simeq 0.3$ , i.e., a figure close to the KPZ value ( $\beta = 1/3$ ). However, it is expected that the operation of a weak stabilizing effect may play an important role in the reaction system. This effect can be described by introducing correction terms of higher order to the KPZ equation [64].

Recently, Goodman *et al.* [65] have studied the propagation of concentration waves in the ZGB surface reaction model. It is found that the model supports trigger waves within the bistable regime of the process, i.e., close to the first-order irreversible phase transition, as already discussed in relation to Fig. 4. Within that regime one has the coexistence of a stable state with a metastable one. At the boundary between the two, the stable state will displace the metastable one and the boundary will move, so this process leads to the propagation of concentration fronts (trigger waves). Goodman *et al.* [65] have found that the velocity of A fronts depends on the diffusion rate of A species  $D$  (B-diffusion is neglected) and the sticking probability of A monomers ( $Y_A$ ). The velocity of the front vanishes when approaching the poisoning transition at  $Y_{2A}(D)$  (note that the critical point now depends on  $D$ ), according to Eq. (10) with  $\gamma \simeq 1$ , in agreement with the results of Evans and Ray [64].

As suggested by the experimental work of Haas *et al.* [58], the propagation of reaction fronts on narrow channels has also been simulated [66] using the ZGB model on the square lattice with rectangular geometry of sides  $L \times M$  ( $L \ll M$ ). Thus  $L$  is the width of the channel and  $M$  its length. Free boundary conditions are taken along the channel while the opposite ends are assumed to be in contact with A and B sources, respectively. If A or B species are removed from the ends of the channels (i.e. the "sources"), due to the reaction process, they are immediately replaced. The propagation of the B concentration profiles is studied starting with a sample fully covered by A, except for the first and second columns which are covered by B (the B source) and left empty. The propagation of A profiles is followed using a similar procedure. Under these conditions one always has two competing interfaces along the channel. Fig. 5 shows a set of snapshot configurations, taken at different times and obtained using channels of size  $L = 20$  and  $M = 100$ , corresponding to the propagation of the reactive phase (left side of the snapshots) into an otherwise fully A poisoned phase (right side of the snapshots). Quantitative analysis of the concentration profiles of the reactants allows the evaluation of the interface propagation velocity and the interface width, respectively [66]. It is found that the front propagation velocity depends on  $Y_A$  and the channel width  $L$ , as is shown, e.g., in Fig. 6. This figure also shows that the displacement of A- and B-poisoned channels by the reactive regime stops at certain ( $L$ -dependent) critical values  $Y_A^{c2}(L)$  and  $Y_A^{c1}(L)$ , respectively. Also, it is found that close to  $Y_A^{c2}$  when the

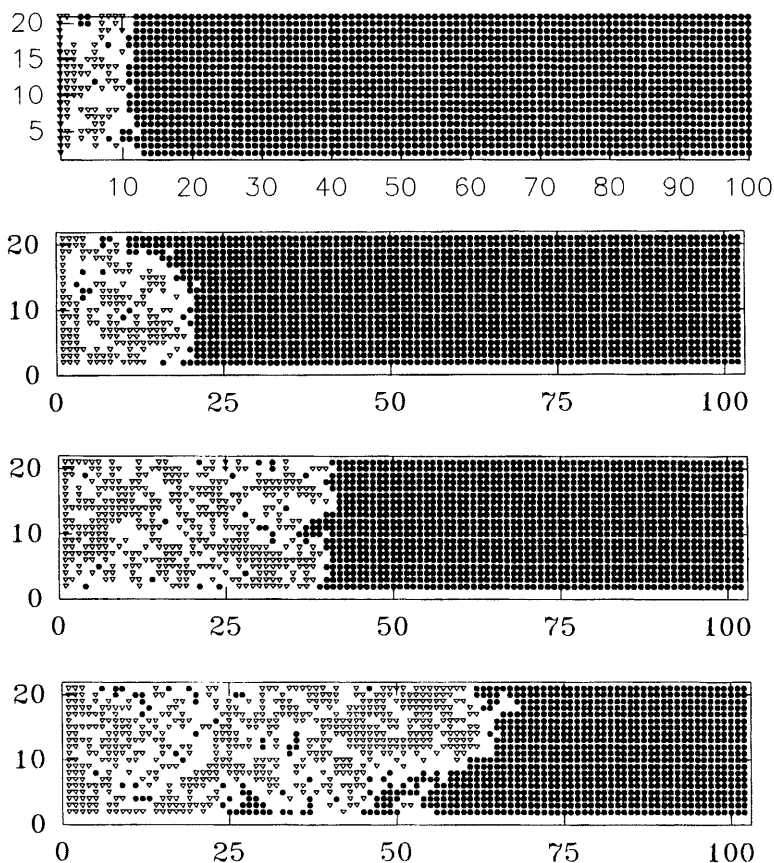


**FIG. 5** Typical snapshot configurations obtained during the displacement of the A poisoned phase (right-hand side of the figures) by the reactive phase (left-hand side of the figures). Results obtained with channels of size  $L = 20$  and  $M = 100$  and taking  $Y_A = 0.515$ . The snapshots are plotted for different times (measured in Monte Carlo steps (MCS)), from top to bottom:  $t = 25$  MCS,  $t = 100$  MCS,  $t = 400$  MCS and  $t = 900$  MCS, respectively.

propagation of the B profile ceases the speed of the A profile undergoes a sharp increment. This behavior can be correlated with the first order irreversible phase transition between the stationary reactive regime and the A poisoned state [66], which is observed in the ZGB model at  $Y_{2A}$  (see Fig. 1).

It is well known that lattice gas modeling of surface reactions, in contrast to traditional mean-field treatments, provides a realistic description of the fluctuations and correlations resulting from the adsorption and reaction

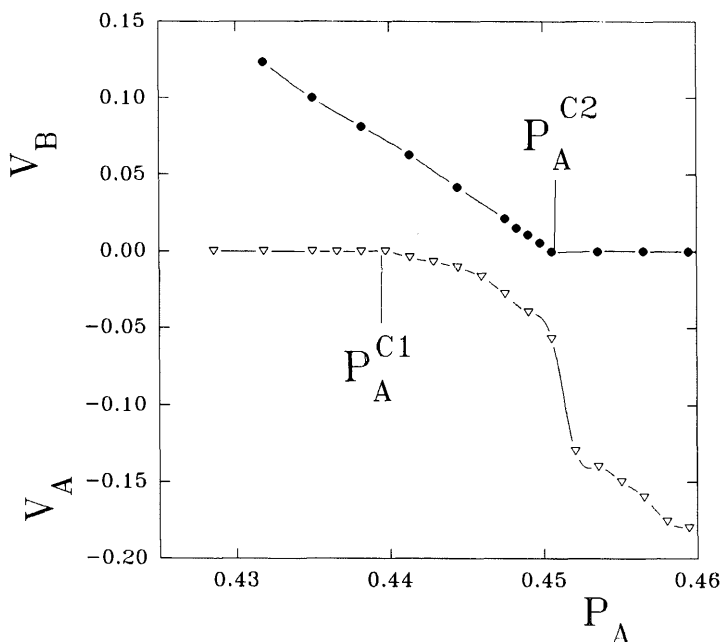


**FIG. 6** Plots of the propagation velocity of B and A profiles versus  $Y_A$  for channels of width  $L = 3$ . The lines show the critical probabilities at which propagation stops.

processes. In a deterministic process described by a set of reaction-diffusion equations, the interface between coexisting phases may have a fixed width [65]. Such width should be of the order of the size of the region near the propagating front. In contrast, in the lattice-gas description, shot noise in the pressure of the incoming reactants and statistical fluctuations are extra sources of broadening which lead to wandering of the front [65]. Fig. 7 shows the dependence of the reaction interface width (see Eq. (9)) as a function of time obtained for channels of fixed width and at various pressures, when the A poisoned phase is displaced by the reactive phase. Two different regimes can clearly be observed. For low A pressures, well inside the reactive state, the fluctuations diverge and the poisoned state will ultimately be completely displaced. For high enough A pressures, well inside the A poisoned state, the fluctuations saturate, i.e., the reactive state cannot displace the stable poisoned state and the interface remains bounded. The crossover between these two regimes is observed just at the critical pressure  $Y_A^{c2}(L)$  where log-log plots of  $w_L^2$  versus  $t$  give straight line behavior. So, on



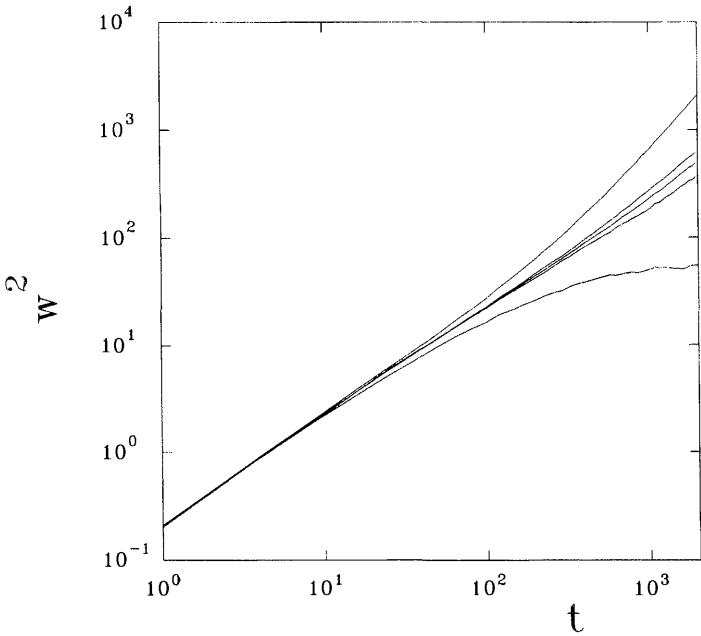


**FIG. 7** Log-log plots of the interface width ( $w^2$ ) versus the Monte Carlo time  $t$ , measured at different adsorption probabilities using channels of width  $L = 30$ . Data were obtained during the displacement of an A-poisoned phase by the reactive regime. From top to bottom the probabilities  $Y_A$  are: 0.5192, 0.5202, 0.5211, 0.5215, and 0.5238.

the basis of general dynamic scaling arguments, similar to those used to describe the interface fluctuations upon thin film growth (see Eq. (9)) [60], it can be expected that the stochastic evolution of a driven interface along a strip of width  $L$  may be characterized by long wavelength fluctuations ( $w_L^2(t, \Delta Y_A)$ ) which have the following time- and pressure-dependence [66]:

$$w_L^2(t, \Delta Y_A) \propto t^{\beta^*} F[t(\Delta Y_A)^\gamma] \tag{11}$$

where  $\Delta Y_A = Y_A - Y_A^{c2}(L)$ , with  $F(x) = \text{constant}$  for  $x \rightarrow 0$  (i.e.,  $\Delta Y_A \rightarrow 0$ ) and  $F(x) \rightarrow x^{-\beta^*}$  for  $x \rightarrow \infty$  (i.e.,  $\Delta Y_A > 0$  and  $t \rightarrow \infty$ ). Thus, just at the critical pressure the time-divergency of the fluctuations is given by  $w_L^2(t) \propto t^{\beta^*}$  as  $t \rightarrow \infty$ , whereas, off criticality, the fluctuations may diverge according to  $w_L^2(\Delta Y_A) \propto \Delta Y_A^{-\delta}$ , with  $\delta = -\gamma\beta^*$ . Notice that  $\beta = \beta^*/2$ , where  $\beta$  has been defined in Eq. (9). It has been reported [66] that for narrow channels  $\beta^*$  depends on  $L$ , but increasing the channel width one has  $\beta^* \rightarrow 1$

for  $L \rightarrow \infty$ ; that is,  $\beta \rightarrow 1/2$ ; pointing out that the noise should dominate over the nonlinear and surface tension terms in the KPZ equation [66]. It is also found that  $\delta$  is sensitively dependent on the channel width  $L$ , with  $\delta \rightarrow 3/2$  for  $L \rightarrow \infty$  [66].

All the described results [64–66] pointed out that the standard dynamic scaling formalism developed for the description of rough interfaces [60] is suitable for the rationalization of the interface behavior in reactive systems far from equilibrium such as the ZGB model. However, much work remains to be done in order to clarify the role of high surface mobility of A species in the behavior of the reaction interfaces.

### 3. Simulation of Oscillatory Behavior

So far, none of the simulations of the ZGB model discussed above attempt to describe one of the most fascinating and well documented [2,16,16] behaviors of the catalytic oxidation of CO on some crystallographic planes of Pt, namely the occurrence of oscillations. After the early simulation work of Moller et al. [62], very recently numerous lattice-gas models have been studied. There are various mechanisms that might be invoked in order to explain the oscillations observed experimentally [15,62,67–74]. A simple approach is to introduce an inert species capable of blocking surface sites. Also, oscillations can be due to adsorbate-induced surface reconstructions of the surface. So, let us discuss both approaches in detail.

In order to study the influence of site blocking by an inert species (say X) [68] one has to add to the reaction steps given by Eqs. (1–3) the desorption of A species, namely



as well as the adsorption-desorption processes for the site blocking X-species:



Neglecting CO desorption, as in the standard ZGB model, the CO-poisoned state is irreversible since there is no possibility of removing CO from the surface. So, CO desorption has to be considered in order to avoid the fully CO-poisoned state. The adsorption and desorption of X then drives the system from a state with high concentration of adsorbed CO to the reactive state and back. This process can be understood with the aid of Fig. 8. At low X coverage only the reactive state is stable. Increasing X coverage causes site blocking and consequently the adsorption of both CO and O<sub>2</sub> is reduced.

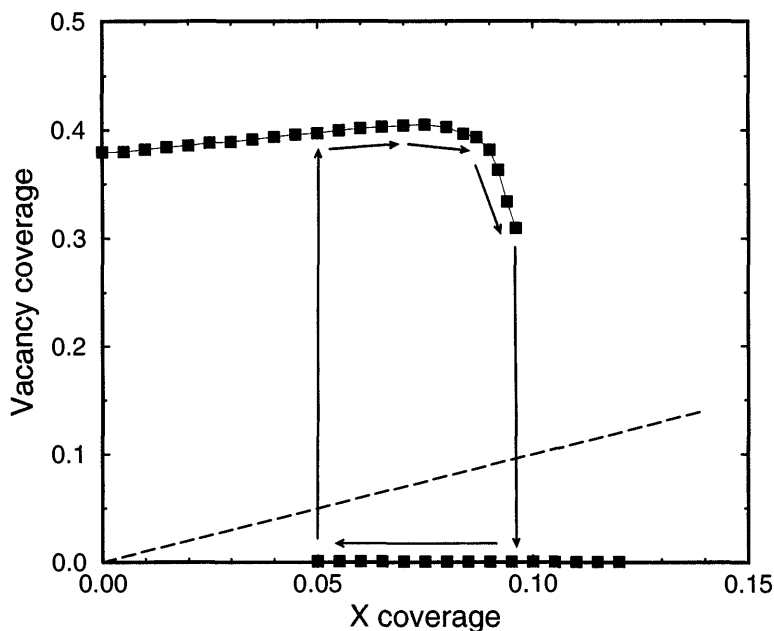


**FIG. 8** Plot of the fraction of vacant sites as a function of the coverage of inert species (X) during CO oxidation. The squares are determined using Monte Carlo simulations with a fixed X coverage using a grid of  $256 \times 256$  sites. The arrows depict how the system evolves. The production of  $\text{CO}_2$  is proportional to the number of vacant sites. (From Ref. 68.)

This effect is stronger for  $\text{O}_2$  because it needs two adjacent sites for dissociative adsorption. Increasing the coverage with X species thus destabilizes the reactive state, and drives the system to the high CO coverage regime. Then, decreasing X coverage will show a transition back to the reactive regime. If both transitions are discontinuous and takes place at different values of X coverage one has a hysteresis loop, i.e., an interval of the X coverage where there is bistability as shown in Fig. 8 [68]. If the adsorption and desorption of the inert species is slow with respect to the other reactions, one has a quasi-steady state for CO oxidation, and the system is always on the bistable regime. When it is in the upper part of Fig. 8 there are many vacancies and few X. So, X will adsorb and the system will move along the upper curve to the right, but it will become unstable, dropping to the lower curve. Here there are many vacancies and many X. Consequently, X will desorb and the system will move to the left, until it becomes unstable again and moves to the upper curve. This trajectory is

shown in Fig. 8 [68]. Under these operating conditions the system displays oscillatory behavior, as shown in Fig. 9. Within this regime the system spends most of its time in the high CO concentration state, but eventually moves to the reactive regime originating the oscillations.

Recently, Vigil and Willmore [67] have reported mean field and lattice gas studies of the oscillatory dynamics of a variant of the ZGB model. In this example oscillations are also introduced, allowing the reversible adsorption of inert species. Furthermore, Sander and Ghaisas [69] have very recently reported simulations for the oxidation of CO on Pt in the presence of two forms of oxygen, namely chemisorbed atomic O and oxidized metal surface. These species, which are expected to be present for reaction under atmospheric pressure, are relevant for the onset of oscillatory behavior [69].

It is well known that the catalytic oxidation of CO on certain Pt surfaces exhibits oscillatory behavior, within a restricted range of pressures and temperatures, which are coupled with adsorbate-induced surface phase transitions [16,17]. In fact, in their clean states the reconstructed surfaces of some crystallographic planes, e.g. Pt(100) and Pt(110), are

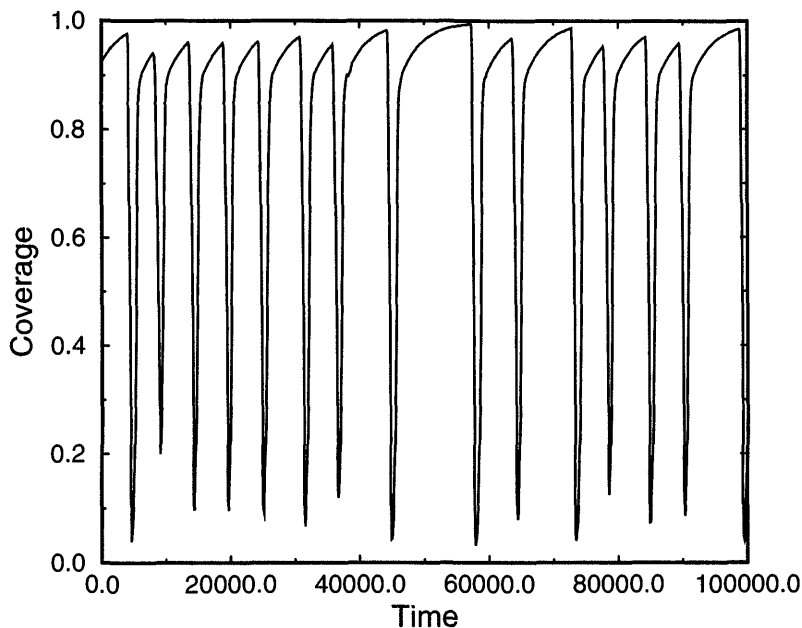


**FIG. 9** The coverage of CO as a function of time as obtained from Monte Carlo simulations with a  $256 \times 256$  grid and for the model with site blocking by inert X species. (From Ref. 68.)

thermodynamically stable. However, the reconstruction can be lifted by adsorbed species such as CO, NO, O<sub>2</sub>, etc. So, the atoms of the topmost layer move back into their  $1 \times 1$  positions. The adsorbate-induced transition (AIT) between the reconstructed and the  $1 \times 1$  phases is reversible and therefore can be driven by critical adsorbate coverages. For a detailed discussion on the nature of the transition see Refs. 16,17. The observed variations in catalytic activity occur because, due to the change in surface geometry which takes place as a consequence of the AITs, the adsorption properties of the surface also change. On some Pt surfaces the O<sub>2</sub> sticking coefficient ( $S_{O_2}$ ) is highly structure dependent and, since the oscillations occur when oxygen adsorption is rate limiting, the catalytic activity is thus periodically modulated by the AITs. Oxygen adsorption experiments on Pt(100) show that  $S_{O_2} \cong 0.1$  on the  $1 \times 1$  phase while a drastic decrease of about 2–3 orders of magnitude is observed for the reconstructed phase. On Pt(110) a variation of  $S_{O_2}$  is also observed, but it is smaller. A single oscillatory cycle can be described as follows [16,17]:

CO coverage	high	low
Surface structure	$1 \times 1$	reconstructed
O <sub>2</sub> adsorption	$S_{O_2}$ large	$S_{O_2}$ small
Catalytic activity	high	low

Starting with a CO-covered  $1 \times 1$  surface one has a high  $S_{O_2}$  value. This leads to a high reaction rate, causing the CO-coverage ( $\theta_{CO}$ ) to decrease. Below a certain critical value,  $\theta_{1CO}$ , the surface relaxes into the reconstructed phase. Now  $S_{O_2}$  is small and the reaction rate also decreases, causing the growth of  $\theta_{CO}$ . Above another critical value,  $\theta_{2CO}$ , an AIT of the surface takes place and the catalyst recovers the initial  $1 \times 1$  structure again.

In order to simulate the ZGB model with adsorbate-induced surface phase transitions a square lattice of side  $L$  has been used to represent the catalytic surface. Let us first describe a model which assumes the global reconstruction of the surface [70]. Let  $\theta_{1A}$  and  $\theta_{2A}$  be the critical coverages at which the reversible phase transitions of the surface take place, and  $S_{1B_2}$  and  $S_{2B_2}$  the corresponding sticking probabilities of  $B_2$  species. The Monte Carlo algorithm for the simulation is almost the same as for the standard ZGB model, but adsorption of  $B_2$  species proceeds according to (Eq. (2) but with probabilities  $S_{1B_2}$  or  $S_{2B_2}$ , depending on the structure of the surface. Also, notice that the structure of the whole surface is updated after each event, comparing  $\theta_A$  with the critical coverages  $\theta_{1A}$  and  $\theta_{2A}$ . A model with

local reconstructions of the surface has been studied [71,72]. Here, the lattice of size  $L \times L$  is the result of the addition of small patches of size  $L_p \times L_p$ , such as  $L = nL_p$ , where  $n$  is an integer with  $n \gg 1$ . Each atom of a dimer can adsorb on adjacent patches and also neighboring A and B species adsorbed on different patches are allowed to react. In this way correlations may develop through the whole sample via neighboring patches. The reconstruction rules described above are now applied to the individual patches, considering the local coverages. It should be mentioned that recent STM measurements suggest that reconstruction of the Pt(100) surface at microscopic (local scale) can be driven by 4–5 CO molecules [75]. In the case of the local reconstruction model, the diffusion of A species at a rate  $K_{Di}$  has also been considered.

Fig. 10 shows the phase diagram of the ZGB model with global reconstructions. For the standard ZGB model a narrow reactive regime within the range  $Y_{1A} < Y_A < Y_{2A}$  is observed, as discussed above in the description of

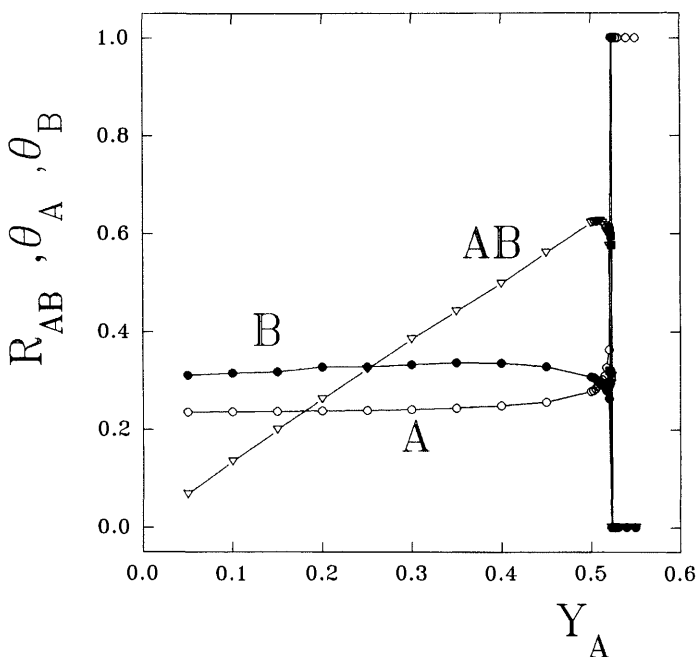


**FIG. 10** Phase diagram of the ZGB model with adsorbate induced global reconstructions of the surface. The plots show the dependence of the rate of AB production ( $R_{AB}$ ) and the surface coverages with A and B species ( $\theta_A$  and  $\theta_B$ , respectively) with the adsorption probability of A species given by  $Y_A$ .

Fig. 2. For the case of global reconstruction of the surface, the phase diagram retains a discontinuous IPT of first order at the critical point  $Y_{Ac} \cong 0.5235 \pm 0.0005$ , i.e., a value very close to but slightly smaller than that of the standard ZGB model given by  $Y_{2A} \cong 0.52560 \pm 0.00001$  [31]. Also, the second-order IPT of the standard ZGB model is no longer observed, in qualitative agreement with experiment, e.g., Fig. 3.

Fig. 11(a) shows the temporal dependence of the reactant' s coverages measured at  $Y_A = 0.50$  for the ZGB model with global surface reconstruction. A self-sustained oscillatory behavior is clearly observed. Increments in the coverage of A species are in phase with drops in B coverage, and *vice versa*. Oscillations exhibit a well defined periodicity. When approaching the critical threshold oscillations become non-periodic, that is, oscillations of short period may be followed by long-lived oscillations. It seems that the occurrence of oscillations of different period does not follow any regular behavior. This observation may suggest stochastic or chaotic behavior; however, a more precise characterization of the process deserves careful study. At criticality (Fig. 11(b)), non-periodic oscillations eventually evolve into the poisoned regime and the reaction stops.

Considering local reconstructions of the surface and taking patches of different size, one also observes the occurrence of IPTs between the reactive regime and the poisoned state with A species [71,72]. However, these transitions are less abrupt and become slightly rounded. This effect is due to the cooperative contribution of many individual patches which may not necessarily be in the same surface structural state and consequently their coverages and rates of AB production may be different. Also the location of the IPT is quite sensitive to the size of the patches; i.e., one has  $Y_{Ac} \cong 0.3485 \pm 0.0005$  and  $Y_{Ac} \cong 0.5035 \pm 0.0005$  for  $L_p = 3$  and  $L_p = 8$ , respectively [71,72]. It is also observed that the oscillatory behavior, already observed assuming global reconstructions, remains in finite samples with local reconstructions, but a careful analysis is necessary. Simulations are started far from the stationary state, with all patches having the same surface structure. During the stochastic evolution of the reaction system different patches may adopt different structures and when arriving at the stationary state, the homogeneous surface structure of the initial configuration may no longer remain. Patches with different structures have different physical properties because the adsorption probability of  $B_2$  species is structure sensitive. Therefore, the reaction proceeds at distinct rates on the various patches, causing the rounding of the peaks in plots of  $R_{AB}$  versus  $Y_A$  and the occurrence of irregular oscillations (see, e.g., Fig. 12). Fig. 13 is a snapshot obtained within the reactive regime for  $L_p = 3$  which shows the formation of small islands of A and B species on different patches. Thus reaction events take place mostly at the borders of neighboring islands of

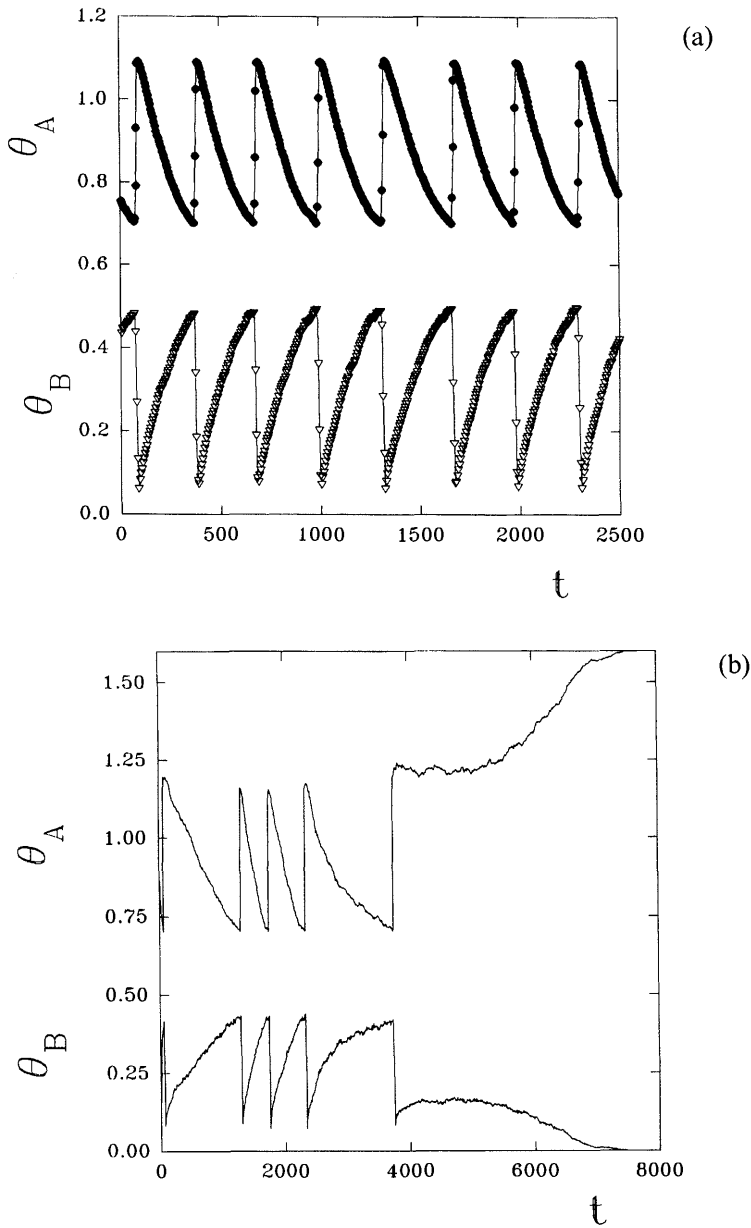


**FIG. 11** Plots of  $\theta_A$  and  $\theta_B$  versus time. Note that  $\theta_B$  values were shifted up by adding 0.5 for the sake of clarity. (a) Data taken for  $Y_A = 0.500$ , i.e., rather away from criticality. (b) Data taken at criticality.



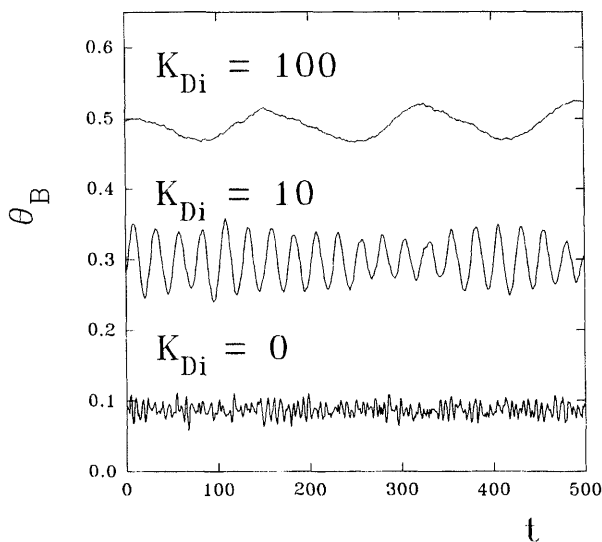


**FIG. 12** Plots of  $\theta_B$  versus time for the ZGB model with local reconstructions using lattices and patches of side  $L = 528$  and  $L_p = 8$ , respectively. Plots for  $K_{Di} = 10$  and  $K_{Di} = 100$  were shifted up by 0.20 and 0.40 for the sake of clarity, respectively.

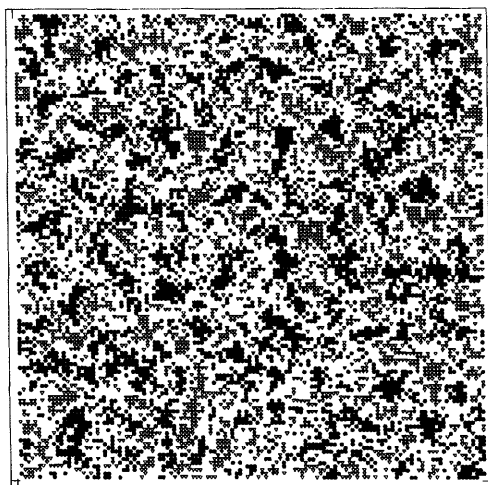


**FIG. 13** Snapshot configuration of the catalyst surface obtained for the ZGB model with local reconstructions using lattices and patches of side  $L = 129$  and  $L_p = 3$ , respectively, and taking  $Y_A = 0.331$  and  $K_{Di} = 0$ .  $\nabla$ , B species;  $\bullet$ , A species. Empty sites are left white. Notice the formation of clusters of both species surrounded by empty sites.

different species and consequently the reaction rate becomes proportional to the perimeter of the islands. A key open question is whether the system will display oscillations at all in the thermodynamic limit ( $L \rightarrow \infty$ ) and for very long measurement times. Finite size analysis of the dependence of the amplitude of the oscillations on the system size indicates that, for the whole reactive regime and local reconstructions, oscillations are restricted to finite samples [72]. An essential feature in the observation of oscillations on the global scale in the thermodynamic limit is the occurrence of correlations among all patches. So there should be at least one mechanism operating at local scale capable of spreading out the information throughout the sample. In principle one may identify two such mechanisms: dimer adsorption and reaction events at neighboring patches. Nevertheless, since finite size analysis shows that oscillations vanish in the thermodynamic limit, the correlations constructed by the operation of such mechanisms do not diverge at all and are restricted to short distances [72]. Observing Fig. 12, it follows that, considering the diffusion of A species, e.g., for  $K_{Di} = 10$ , the pattern becomes clearly oscillatory, but both the amplitude and the period of the oscillation remain irregular. However, taking  $K_{Di} = 100$ , due to the high surface mobility of A species the oscillatory behavior is quite regular, as in the case of global reconstruction (Fig. 11), suggesting the cooperative behavior of the patches at global scale. Thus it is expected that oscillations will remain in the thermodynamic limit only when the large diffusion rate of A species provides the mechanism to build up long-range correlations. Simulations aimed at understanding this conjecture will be welcomed.

A different approach to the simulation of oscillations, namely the HS model, has very recently been proposed by Gelten et al. [15]. Here the grid consists of unit cells with two kind of site, "H" and "S", which indicate the surface phase, hexagonal and  $(1 \times 1)$ , respectively. A site of the  $(1 \times 1)$  phase has four neighbors whereas a site of the hexagonal type has only three neighbors. A species adsorbs and desorbs from both phases whereas  $B_2$  can only dissociatively adsorb on neighboring unit cells of the  $(1 \times 1)$  type. Reaction events (Eq. (3)) occur between different species in adjacent sites. Plausible rules for reversible phase transformation between H and S phases are also stated (for more details see Ref. 15). The model is simulated by applying the dynamic Monte Carlo approach, so that parameters such as the rates of desorption, diffusion, etc., are taken from experimental data. The model exhibits self-sustained oscillations within temperature and pressure ranges compatible with experimental observations, as shown in Fig. 14 [15]. The sharp peak in the power spectra of the oscillations indicates that they are almost "monochromatic". However, an interesting finding is that the amplitude of the oscillations depends on the grid size, as, e.g., in the ZGB model with local reconstruction of the surface [72]. It is also interesting

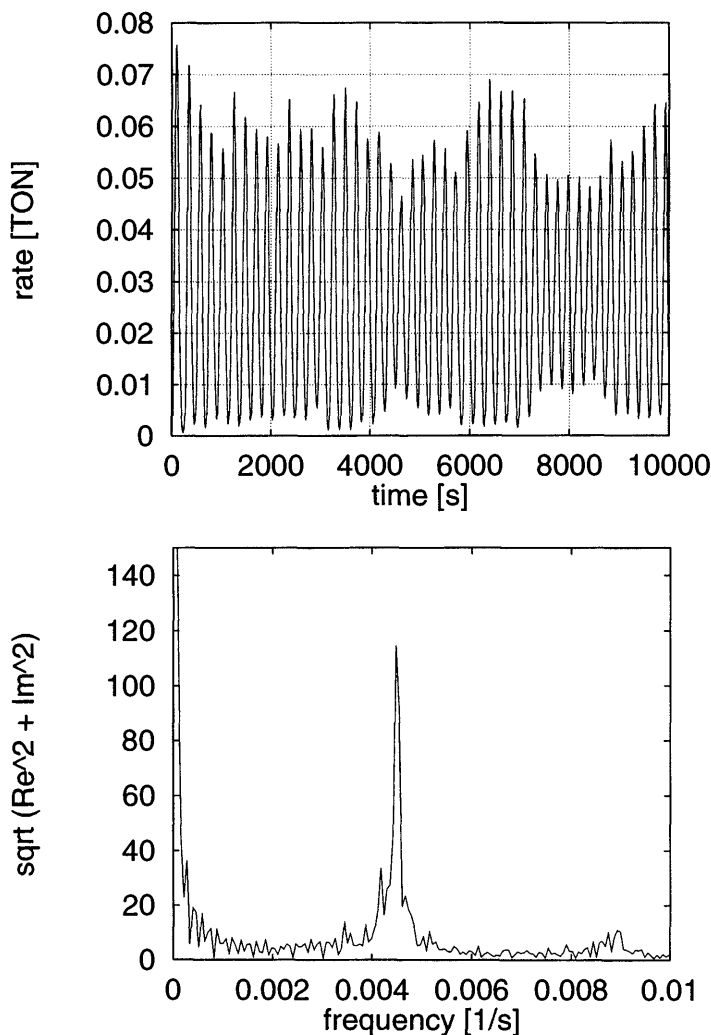


**FIG. 14** Example of simulated oscillations in the rate of  $\text{CO}_2$  production (left) and its power spectrum averaged over 10 simulation runs. (From Ref. 15.)

to mention that, neglecting surface diffusion of the reactants (particularly of  $\text{CO}$ , i.e. the monomer A species), oscillations vanish in the thermodynamic limit. In fact, the observed oscillations are due to the averaged superposition of a certain number of independent oscillators, each having a random phase shift but all having the same period. Thus the averaged amplitude shows

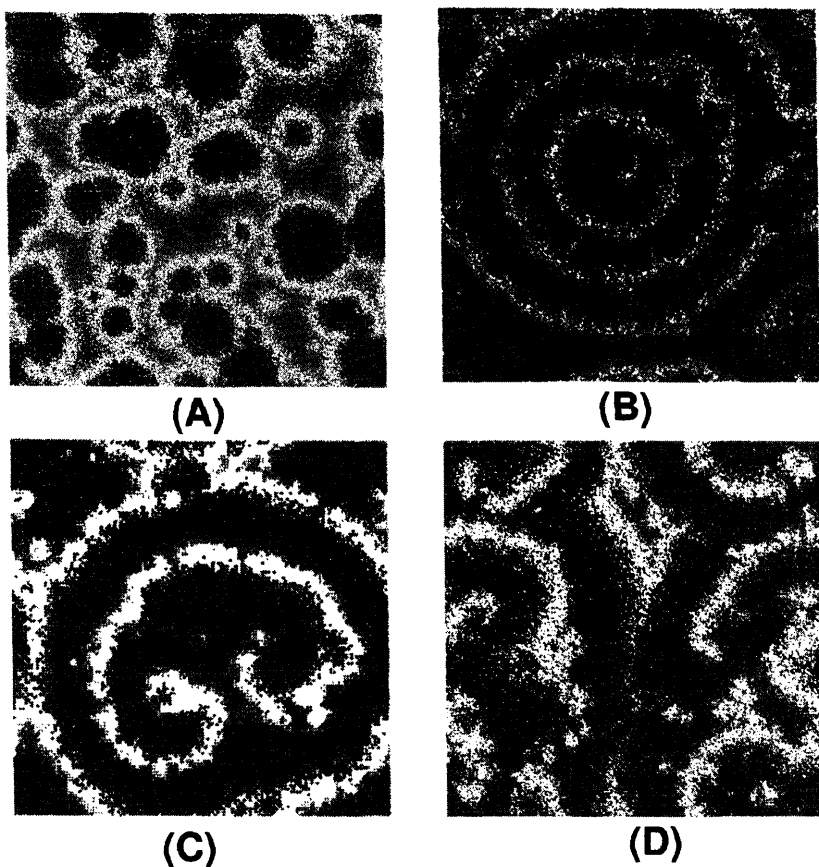


**FIG. 15** Series of snapshot configurations obtained using lattices of side  $L = 1024$  during the stationary regime of the HS model. (A) Cellular structures, (B) target patterns, (C) double spirals and (D) turbulence. (From Ref. 15.)

destructive interference. Introducing surface diffusion, one provides a mechanism for the synchronization of the oscillations which prevents the random phase shift from resulting in non-vanishing oscillations for  $L \rightarrow \infty$ .

The HS model exhibits a rich variety of spatio-temporal patterns. During the oscillatory behavior, if the simulation starts with an empty grid in the hexagonal phase the only possible event is CO adsorption. Consequently, when a certain CO coverage is reached, the surface starts to convert into the  $1 \times 1$  phase. Oxygen cannot adsorb yet, due to the lack of empty sites.

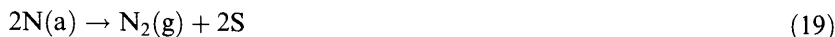
However, once a pair of neighboring CO molecules desorbs, oxygen can adsorb on this spot. Hereafter, oxygen reacts with neighboring CO molecules and the number of vacant sites increases. These sites will preferentially be occupied by oxygen again, starting new reactions and vacating additional sites. In this way reaction fronts start to propagate. Subsequently, fronts grow and collide and extinguish one another. Behind the front there is not much CO adsorption and the  $1 \times 1 \rightarrow \text{hex}$  transformation starts to develop. Oxygen adsorption is not possible in the hex phase, so the surface slowly transforms back and the cycle starts again. As pointed out by Gelten et al. [15], cellular structures very similar to those observed during the oscillatory regime have been observed experimentally upon CO oxidation on the Pt(110) surface [76]. Fig. 15 shows the types of pattern observed when the parameters of the reaction are changed and the system is driven into a (non-oscillatory) stationary state. These patterns include : cellular structures (Fig. 15(a)), target patterns (Fig. 15(b)), double spirals (Fig. 15(c)), and turbulence (Fig. 15(d)) [15], in qualitative agreement with spatio-temporal patterns observed in actual experiments.

A lattice gas model with adsorbate-induced surface reconstructions has also very recently been proposed by Kusovkov et al. [73]. This model also exhibits a rich oscillatory behavior.

## B. The Catalyzed Reaction CO + NO

### 1. Lattice Gas Models and Critical Behavior

The catalytic reaction of NO and CO on single crystal substrates, under ultra-high vacuum conditions, has been extensively studied. Neglecting  $\text{N}_2\text{O}$  formation and CO desorption, the Langmuir–Hinshelwood mechanism of the  $\text{NO} + \text{CO}$  reaction can be described by the following sequence of steps [16,17]:



where S is an empty site on the surface, while (a) and (g) refer to the adsorbed and gas phases, respectively. This reaction can also be thought of as an alternative dimer–monomer model, as early proposed by Yaldram and Khan [77]; namely  $\text{AB} + \text{C} \rightarrow (1/2)\text{A}_2 + \text{CB}$ , where the dimer AB is

NO, the monomer C is CO, and the products are  $A_2 \equiv N_2$  and  $CB \equiv CO_2$ . The adsorption probability of C species ( $Y_C$ ) is the parameter of the model. The slow rate-determining step in this sequence is the dissociation of NO which requires a neighboring site to proceed. Since product formation liberates more vacant sites than those necessary for the dissociation of NO, an autocatalytic production of vacant sites takes place.

Early simulations due to Yaldram and Khan [77] (performed skipping the pre-adsorption of molecular NO) showed that, in contrast to the already discussed dimer–monomer ZGB model for the catalytic oxidation of CO, the present lattice gas model has no reactive state on the square lattice: in the long-time regime of the reaction the surface always becomes poisoned by mixed adlayers. A proof of this finding was later given by Brosilow and Ziff [77]. Furthermore, Khan et al. [79] have systematically investigated the influence of surface diffusion of the reactants in the behavior of the reaction. It is found that diffusion of the main reactants, namely  $AB \equiv NO$  and  $C \equiv CO$ , cannot establish a reactive stationary state. However, diffusion of  $A \equiv N$  species causes the occurrence of a reaction window whose width  $\Delta$  depends on the diffusion probability of A ( $D_A$ ) according to  $\Delta \simeq 0.1 D_A^{1/3}$  [79]. These results point out the intriguing difference between both types of monomer–dimer process, i.e. the CO–NO and CO–O<sub>2</sub> reactions.

A reactive reaction window, with self-sustained production of CB species, can be obtained by increasing the coordination number of the grid, e.g., by using hexagonal lattices. Taking the dissociation rate of AB as unity ( $r_{AB} = 1$ ), it is found that the model exhibits a second order IPT, close to  $Y_{1C} \simeq 0.185$ , between the stationary regime and a poisoned surface consisting of a mixed adlayer with B species ( $\theta_B \simeq 0.83$ ) and A species ( $\theta_A \simeq 0.17$ ). Further increment of  $Y_C$  causes the reactive state to suddenly stop close to  $Y_{2C} \simeq 0.338$ , where a first-order IPT takes place. For  $Y_C > Y_{2C}$  the poisoned state is a binary compound of C and A species with coverages close to  $\theta_C \simeq 0.88$  and  $\theta_A \simeq 0.12$ , respectively. Using the constant-coverage ensemble, Brosilow and Ziff [78] have shown that the upper spinodal point of the first-order IPT lies close to  $Y_{sC} \simeq 0.3552$ , while an improved estimate of the location of the transition close to  $Y_{2C} \simeq 0.35140$  is also reported.

As discussed above, by changing the geometry of the lattice, it is possible to change the intrinsic nature of the stochastic process. On the other hand, Meng et al. [80] have shown that by adding a new reaction channel, namely



in order to decrease the possibility of poisoning, one may enhance the reactivity of the system and consequently also modify the nature of the poisoning transition. In fact, for simulations on the square lattice, the addi-

tion of the side reaction channel causes the opening of a reaction window with a continuous IPT close to  $Y_{1C} \simeq 0.262$  and a first-order IPT close to  $Y_{2C} \simeq 0.501$ . This behavior is reminiscent of the dimer-monomer ZGB model for the catalytic oxidation of CO, discussed in Sec. IV A.

Assuming that the dissociation of AB is preceded by molecular adsorption in a single site, as described by the set of equations (15–19), as well as considering desorption of both AB and C species, Meng et al. [81] have shown that the system also exhibits a reactive state and IPTs. Fig. 16 shows the dependence of the rate of CO<sub>2</sub> production ( $R_{\text{CO}_2}$ ) on the normalized CO pressure ( $P_{\text{CO}}$ ), taking a fixed desorption probability of NO given by  $d_{\text{NO}} = 0.50$  and changing the desorption probability of CO such that  $d_{\text{CO}} \rightarrow 0$ . For  $0 \leq P_{\text{CO}} \leq 0.50$ ,  $R_{\text{CO}_2}$  is largely insensitive to the value of  $d_{\text{CO}}$ . However, for  $P_{\text{CO}} > 0.50$  the behavior of  $R_{\text{CO}_2}$  depends sensitively on  $d_{\text{CO}}$ : for  $d_{\text{CO}} < 0.04$  the rate of production shows an almost discontinuous

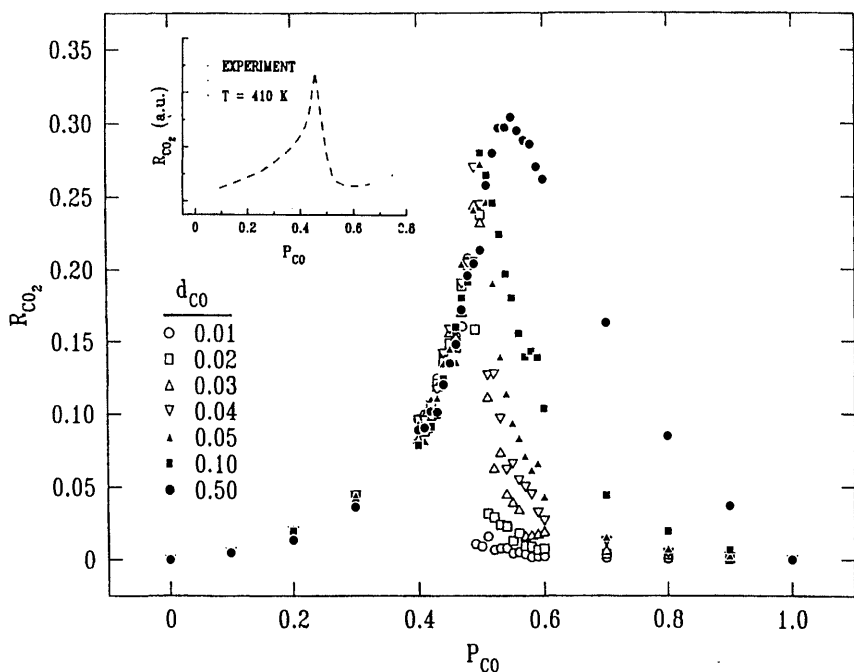


**FIG. 16** Variation of the steady-state rate of production,  $R_{\text{CO}_2}$ , with  $P_{\text{CO}}$  in the NO + CO lattice gas model with NO desorption (rate  $d_{\text{NO}} = 0.5$ ), and CO desorption at various rates (shown). The inset shows the reaction rate measured experimentally at 410 K. (From Ref. 81.)

drop and thereafter it decreases continuously to zero. For  $d_{\text{CO}} > 0.04$  the discontinuity disappears and  $R_{\text{CO}_2}$  decreases smoothly with  $P_{\text{CO}}$ , depending sensitively on  $d_{\text{CO}}$ . Thus, for  $d_{\text{NO}} = 0.50$ ,  $d_{\text{CO}} \simeq 0.044$ , and  $P_{\text{CO}} \simeq 0.50$ , one has a critical point [81]. A similar behavior has been reported for the ZGB dimer-monomer model  $\text{CO} + \text{O}_2$  with CO desorption where the drop of  $R_{\text{CO}_2}$  takes place close to  $d_{\text{CO}} \simeq 0.05$  [39,40]. The insert of Fig. 16 shows the dependence of  $R_{\text{CO}_2}$  on  $P_{\text{CO}}$ , measured experimentally at 410 K on Pt(100) surfaces. This finding is in qualitative agreement with the lattice gas model, suggesting that, close to this temperature, the actual system might be near a critical point for  $P_{\text{CO}} \simeq P_{\text{NO}}$  [81].

## 2. Propagation of Reaction Fronts

Very recently Tammaro et al. [82] have studied the reactive removal of unstable mixed  $\text{CO} + \text{NO}$  adlayers, using a lattice gas model. Due to the presence of pre-adsorbed species, the steps considered for the simulation are those given by Eqs. (16), (18) and (19), respectively. Furthermore, in order to account for the diffusion of the reactants, the hopping of all species (except for O atoms whose mobility is negligible) is considered. An interesting contribution of this manuscript, which may also be generalized to other systems involving mixed species, is the development of an elaborate treatment for the chemical diffusion of mixed adlayers reflecting the interference of the adsorbed species on the surface due to co-adsorption. Simulations are started with the surface fully covered by an  $(\text{AB} + \text{C})$  adlayer, which constitutes an unstable steady state, e.g., in the sense that vacation of a single site may produce the dissociation of AB and its reaction with C and the subsequent creation of more vacancies, triggering an autocatalytic reaction. Subsequently, a very small number of adspecies is desorbed and the reactive removal of the mixed adlayer is followed. Due to the high mobility of most adsorbed species, initially an exponential increase in the number of highly dispersed vacancies is observed. Thereafter, a transition to a reaction front propagation regime of the adlayer removal is observed. At this stage a chemical wave develops that propagates into the  $(\text{AB} + \text{C})$  covered (unstable) part of the surface. Fig. 17 shows the steady-state concentration profiles across the propagating reaction front for various initial concentrations of the mixed adlayer. One can observe a significant build-up of O(a) in the wake of the reaction front when  $\theta_{\text{NO}} > 1/2$  and of CO(a) when  $\theta_{\text{NO}} < 1/2$ , as expected on the basis of stoichiometric considerations. The building up of non-reactive species in the wake of the chemical wave does not affect its velocity, which is almost constant, because it is controlled by the highly reactive portion of the front. Also, the long tail of N(a) behind the wave is due to its low reaction rate constant [82].



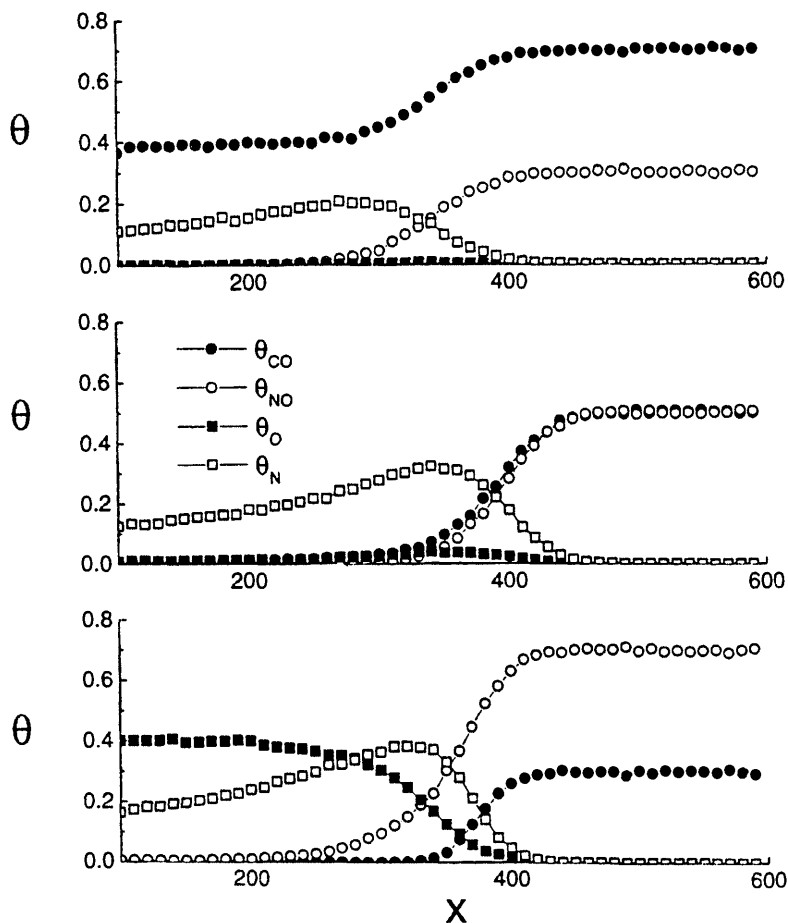


**FIG. 17** Concentration profiles (in monolayers) measured in a  $60 \times 200$  site lattice, showing the propagation of a reaction front. The  $\text{NO} + \text{CO}$  covered region is at the right and the front is roughly close to  $X \simeq 400$ . The initial coverages of NO are, from top to bottom,  $\theta_{\text{CO}} = 0.3, 0.5$ , and  $0.7$ , respectively. (From Ref. 82.)

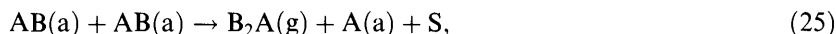
### C. The Catalytic Oxidation of $\text{H}_2$

A dimer-dimer (DD) surface reaction scheme of the type  $(1/2)\text{A}_2 + \text{B}_2 \rightarrow \text{B}_2\text{A}$  has been proposed in order to mimic the catalytic oxidation of hydrogen:  $\text{A}_2$  is  $\text{O}_2$ ,  $\text{B}_2$  is  $\text{H}_2$ ,  $\text{AB}$  is  $\text{OH}$  and  $\text{B}_2\text{A}$  is  $\text{H}_2\text{O}$ . The model reaction proceeds according to the Langmuir-Hinshelwood

mechanism [83–86]:



and



where  $S$  is an empty site on the surface, while  $(a)$  and  $(g)$  refer to the adsorbed and gas phases, respectively.

The proposed mechanism for the DD process is not intended to represent that of any actual catalytic reaction, but to simulate a generic bimolecular reaction. Monte Carlo simulations of the reaction mechanism described by Eqs. (21)–(25) have shown the existence of IPTs exhibiting a rich variety of critical behavior.

The DD model can be briefly described as follows. The catalytic surface is assumed to be homogeneous. Surface sites can be empty or occupied by adsorbed  $A$ ,  $B$ , and  $AB$ -species with average coverage  $\theta_A$ ,  $\theta_B$ , and  $\theta_{AB}$ , respectively. The gas phase in contact with the catalyst surface is assumed to be kept at constant pressure and composition of  $A_2$  and  $B_2$  dimers. Let  $Y_{B_2}$  be the mole fraction of  $B_2$  in the gas phase, so the striking molecule could be a  $B_2$  ( $A_2$ ) with probability  $Y_{B_2}$  and  $(1 - Y_{B_2})$ , respectively. Both  $A_2$  and  $B_2$  dimers dissociate upon adsorption (Eqs. (21–22)) occupying two neighboring surface sites. The reaction between adsorbed  $A$  and  $B$  species gives an  $AB$  intermediate and leaves an empty site on the catalyst surface (Eq. (23)). This mechanism is suggested by the actual catalytic reaction because it is known that hydroxyl groups are bonded to the surface through the oxygen atom ( $A$  is  $O$ ) with the hydrogen ( $B$  is  $H$ ) pointing away or slightly tilted. Also the reaction between  $AB$  species (Eq. (25)) is relevant at lower temperatures in the actual catalytic process. For more details on the Monte Carlo algorithm see [83–86].

Eight variants of the DD reaction mechanism, described by Eqs. (21–25) have been simulated. The simplest approach is to neglect  $B_2$  desorption in Eq. (22) and the reaction between  $AB$  species (Eq. (25)). For this case, an IPT is observed at the critical point  $Y_{1B_2} = 2/3$ . Thus this variant of the model has a zero-width reaction window and the trivial critical point is given by the stoichiometry of the reaction. For  $Y_{B_2} < Y_{1B_2}$  the surface becomes poisoned by a binary compound of  $(A + AB)$  species and the lattice cannot be completely covered because of the dimer adsorption requirement of a

pair of neighboring empty sites. In fact, for this poisoned state it is found that  $\theta_A + \theta_{AB} \approx 0.90$ , which is very close to the occupancy probability of the random dimer filling problem in two dimensions given by  $\theta \approx 0.907$ . Considering  $B_2$  desorption and the addition of the reaction between AB species, the phase diagram exhibits a finite-width reaction window, as in the case of the ZGB model, but now both IPTs are of second order. Another interesting result is that the second-order transition in the low  $Y_2$  regime, which is observed close to  $Y_{1B_2} \approx 0.454$ , occurs between the reactive regime and a non-unique poisoned state in the sense that there are infinite different configurations which can lead to the poisoned state. This is in contrast to the ZGB model where the poisoned state is unique with the surface fully covered by one reactant. The remaining variants of the DD model also exhibit interesting critical behavior with second-order IPTs between reactive regimes and non-unique poisoned states [85].

Recently a cellular automata version of the DD model has been studied [87]. The reported results are in qualitative agreement with Monte Carlo simulations [83,84]. Also, mean-field results [87] are in agreement with those early obtained in [85]. Very recently, simulations of the kinetic behavior of the DD model have been reported [88].

## D. Brief Overview of Other Surface Reaction Processes

### 1. Monomer–Monomer Processes

The monomer–monomer (MM) model, for the reaction  $A + B \rightarrow AB$ , assumes the following Langmuir–Hinshelwood reaction schema:



where S is an empty site on the surface, while (a) and (g) refer to the adsorbed and gas phases, respectively. The Monte Carlo algorithm is similar to those of the ZGB and DD models, but since now both species are monomers, adsorption attempts on empty sites are always successful. The impingement rate of A and B-species is  $Y_A$  and  $Y_B$ , respectively. Thus  $Y_A$  is the single parameter of the model (for more details see [18,21,57]).

The phase diagram of the MM model is quite simple: for  $Y_A < Y_{1A} = 1/2$  ( $Y_A > Y_{1A}$ ) the catalyst becomes poisoned by A (B) species, respectively. Thus one has a first-order IPT where  $Y_{1A} = 1/2$  is a trivial critical point given by the stoichiometry of the reaction. In contrast to the ZGB model,

the reaction window now has zero width. It becomes clear that the dimer deposition mechanism, which requires two adjacent sites for adsorption, causes the occurrence of a finite-width reaction window in the ZGB model.

The cluster properties of the reactants in the MM model at criticality have been studied by Ziff and Fichthorn [89]. Evidence is given that the cluster size distribution is a hyperbolic function which decays with exponent  $\tau = 2.05 \pm 0.02$  and that the fractal dimension ( $D_F$ ) of the clusters is  $D_F = 1.90 \pm 0.03$ . This figure is similar to that of random percolation clusters in two dimensions [37]. However, clusters of the reactants appear to be more solid and with fewer holes (at least on the small-scale length of the simulations,  $L = 1024$  sites).

An epidemic analysis of the MM model reveals that the number of empty sites (and the rate of AB production) decays according to Eq. (7) with  $\eta = -0.055 \pm 0.015$  [21,34,57]. This small figure may also be compatible with a logarithmic decay [34,57]. Also, the survival probability of a blob of A species embedded in a B sea (separated by a wall of empty sites) decreases in time with exponent  $\delta = 0.80 \pm 0.20$  (see Eq. (6)), reminiscent of critical behavior of the ZGB model at the first-order IPT [34].

The MM model with one species desorption (say B) has also been studied [90]. Due to desorption, the B-poisoned state is no longer observed and the system undergoes a second-order IPT between a reactive regime and an A-poisoned state. The behavior of the MM model with one species desorption is similar to another variant of the MM model which incorporates the Eley-Rideal mechanism [57].

In order to study the influence of surface disorder in the MM reaction, Frachenbourg et al. [91] have considered a substratum which has two types of randomly distributed sites with different adsorption rates. It is found that such a kind of disorder can sustain a reactive steady state, in contrast to the standard MM process on homogeneous surfaces.

Another interesting version of the MM model considers a variable excluded-volume interaction between same species particles [92]. In the absence of interactions the system is mapped on the standard MM model which has a first-order IPT between A- and B-saturated phases. On increasing the strength of the interaction the first-order transition line, observed for weak interactions, terminates at a tricritical point where two second-order transitions meet. These transitions, which separate the A-saturated, reactive, and B-saturated phases, belong to the same universality class as directed percolation, as follows from the value of critical exponents calculated by means of time-dependent Monte Carlo simulations and series expansions [92].

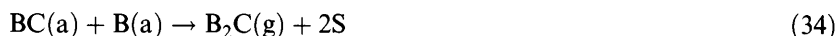
The properties of the interface between an A-rich and a B-rich patch in the MM model have also been studied [93]. The geometry used is the same as

in the studies of the front propagation in the ZGB model described in Sec. IV 1 2 (see, e.g., Fig. 5). Fluctuations in the particle density resulting from the formation of clusters in the reactive zone play a significant role in the interfacial roughening. Overhangs, holes, fingers, and clusters are observed. It is found that the interface roughness scales as  $w \sim t^\beta$  (see, e.g., Eq. (9)), with  $\beta = 1/2$  [93] as in the case of the interface width of the reaction fronts of the ZGB model on narrow channels [66]. For further details on the properties of the A–B interface of various MM models, see, e.g., [93–95].

## 2. Multi-component Reaction Processes

Recently the simulation of reaction processes involving more than two reactants has received growing attention. One example of these processes is a multiple-reaction surface reaction model based upon both the ZGB and the DD models [96–98]. This ZGB–DD model may apply to the oxidation of CO in the presence of H<sub>2</sub> traces as well as to the oxidation of hydrogen in the presence of CO traces. Interest in this model is due to various reasons. For example, the oxidation of hydrogen and carbon monoxide plays a dominant part in the understanding of the process of hydrocarbon oxidation. In fact, the oxy-hydrogen reaction mechanism contains the chain-branching steps producing O, H, and OH radicals which attack the hydrocarbon species. Also, CO is the primary product of hydrocarbon oxidation and it is converted to carbon dioxide in a subsequent slow secondary reaction. Furthermore, the ZGB–DD model exhibits interesting irreversible critical behavior with non-unique multi-component poisoned states [96–98].

The reaction scheme of the ZGB–DD model is based upon the Langmuir–Hinshelwood mechanism. Thus, it is assumed that the reaction occurs according to the following steps:



where S is an empty site on the surface, while (a) and (g) refer to the adsorbed and gas phases, respectively. Notice that Eqs (29), (30), and (32) correspond to the ZGB model and Eqs. (30), (31), (33), and (34) correspond to the DD model. The gas phase in contact with the catalyst surface is assumed to be kept at constant pressure and composition of A, B<sub>2</sub>, and

$C_2$  molecules. Thus the respective rate of arrival and subsequent sticking coefficient are  $Y_A$ ,  $Y_B$ , and  $Y_C$ , which are normalized so that  $Y_A + Y_B + Y_C = 1$ , and consequently the model has two parameters, namely  $Y_A$  and  $Y_C$ .

For  $Y_C = 0$  the MR model is mapped onto the DM model (see, e.g., Fig. 2). The presence of a very small amount of  $C_2$  species in the gas phase causes a drastic shift of the first-order IPT with respect to its position in the ZGB phase diagram [96]. Fig. 18 shows the complete phase diagram

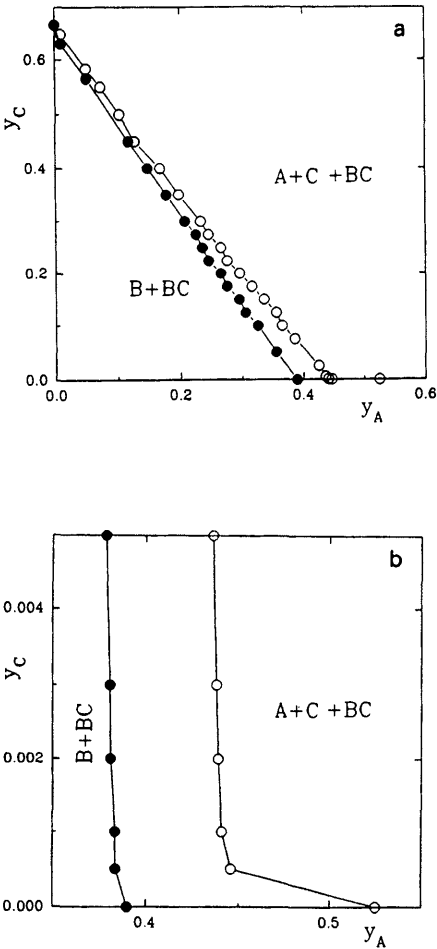
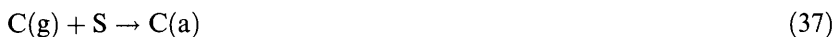


**FIG. 18** (a) Plot of the critical points  $Y_C$  versus  $Y_A$  for the ZGB-DD model: (●) second-order IPTs; (○) first-order IPTs. (b) Detailed view of (a) in the limit  $Y_C \rightarrow 0$ .

of the ZGB-DD model. Two non-unique poisoned states with  $B + BC$  and  $A + B + BC$  species and a stationary regime with sustained reaction are observed. IPTs are of second and first order. So far, except for the case of the DD model, in all previously discussed second-order IPTs one has transitions between the reactive state and a poisoned inactive state where the surface is covered by one species. In contrast the ZGB-DD model exhibits second order IPT's from the active state to a *non-unique* poisoned state where the surface of the catalyst is covered by a mixture of  $A + BC$  species. A Monte Carlo spreading analysis strongly suggests that these IPTs belong to the same universality class as directed percolation and allow us to further extend the conjecture of Grinstein et al [10] to this kind of complex system [98].

Another multiple-reaction irreversible surface reaction process is the dimer-monomer-monomer (DMM) model as proposed in Ref. 99. This model is suitable for investigating, on the one hand, the influence caused by dimer traces in the MM model, and on the other hand the effect of monomer traces in the ZGB model. In fact, the DMM model assumes the following reaction steps:



where Eqs. (35), (37) and (39) correspond to the MM model, while Eqs. (35), (36) and (38) and (36), (37) and (40) are those of the ZGB model. The sticking coefficients of the species are  $Y_A$ ,  $Y_B$  and  $Y_C$ , respectively. In this case  $Y_A$  and  $Y_C$  are taken as parameters of the DMM model. For  $Y_C = 0$  the DMM model is mapped onto the ZGB model, so the phase diagram is given by Fig. 2. It is found that the introduction of traces of dimers in the MM model causes the occurrence of a finite-width reaction window, as shown in Fig. 19 for  $Y_B = 0.10$ . In this case two first-order IPTs are observed. A careful scanning of the model's parameters gives the diagram shown in Fig. 20. The horizontal and vertical axes correspond to the ZGB model, while the diagonal one represents the MM model. The diagram shows that the DMM exhibits three different poisoned states, with A, B, and C species, respectively. IPTs between the reactive regime and A- and C-poisoned states are of first order. The dynamical critical exponents along the

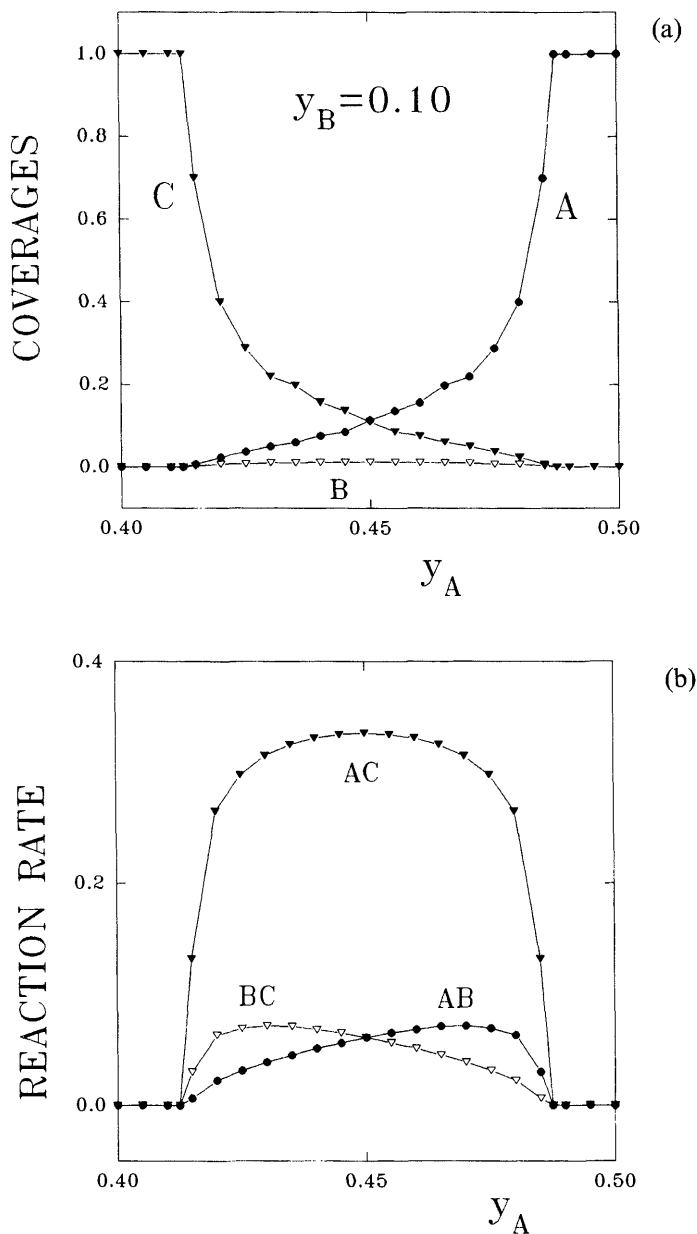


**FIG. 19** Simulation results of the DMM model showing: (a) plots of the reactants coverages  $\theta_A$ ,  $\theta_B$  and  $\theta_C$  and (b) the reaction rates  $R_{AB}$ ,  $R_{BC}$ , and  $R_{AC}$  versus  $Y_A$ , obtained keeping  $Y_B = 0.10$ .



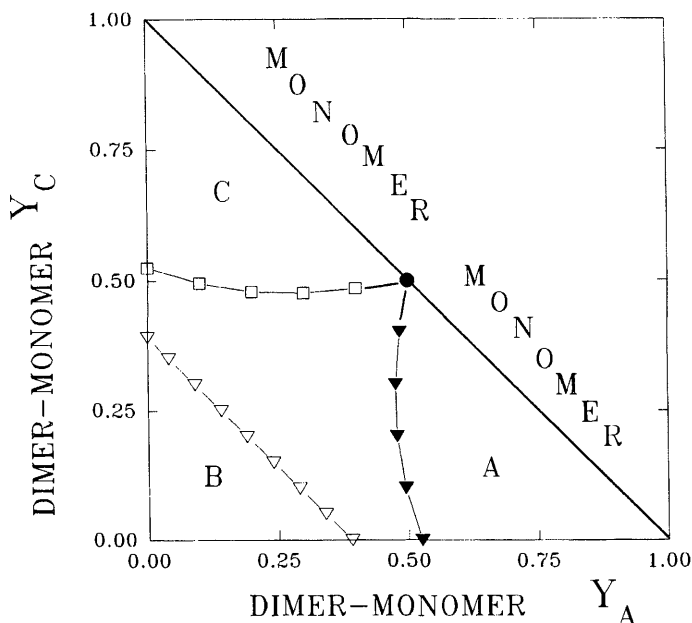


**FIG. 20** Plot of the critical points  $Y_C$  versus  $Y_A$  for the DMM model. Second order IPTs (▽) and first-order IPTs (□ and ▼). (●) shows the location of the IPT of the MM model.

first-order critical lines cross over from the values characteristic of the ZGB model to those of the MM model. On the contrary, transitions into the B-poisoned state are of second order and belong to the universality class of directed percolation.

### 3. Single-component Reaction Processes

The study of the behavior of reactions involving a single species has attracted theoretical interest. In fact, the models are quite simple and often exhibit IPT. In contrast to standard reversible transitions, IPTs are also observed in one-dimensional systems. The study of models in 1D is very attractive because, in some cases, one can obtain exact analytical results [100–104]. There are many single-component non-equilibrium stochastic lattice reaction processes of *interacting particle systems* [100,101]. The common feature of these stochastic models is that particles are created autocatalytically and annihilated spontaneously (eventually particle diffusion is also considered). Furthermore, since there is no spontaneous creation of particles, the zero-particle

state or vacuum plays the same role as the poisoned surface in a catalyst and is known as the *absorbing* state. These simple models have been studied extensively in order to contribute to the understanding of the universality classes of nonequilibrium critical behavior. Among the most studied systems one could mention the contact process (CP) [29,100,105], the A-model [105], the N3-model [105], the BK-model [26,106], branching annihilating walkers [30], etc. Using epidemic studies and finite-size scaling analysis of the Monte Carlo data, in all cases it has been found that irreversible second-order transitions between the active and the absorbing state belong to the same universality class as directed percolation, in full agreement with the conjecture of Grinstein et al. [10]. These findings are not surprising since the absorbing state is unique. Recently, Jensen and Dickman [27] have proposed a single-component reaction process, i.e., the dimer reaction (DR) model, which has infinitely many absorbing states. By means of both an epidemic analysis of the time-dependent behavior and a finite-size scaling study of the stationary regime it was found that the DR model also belongs to the same universality class as directed percolation. This finding allows us to extend the conjecture of Grinstein et al. [10] to single-component systems with non-unique absorbing states.

So far, in all these examples of surface reaction models, long-range correlations between the reactants are developed as a consequence of the microscopic mechanisms governing the evolution of the systems. In particular, close to second-order IPT the correlation length diverges and universal behavior is observed. In most cases the “potential energy” of interaction between particles is simply ignored, while in other examples only short-range interactions are considered [42,107]. Therefore, our understanding of IPTs in systems with long-range interactions is restricted to some scarce analytical results [101]. The lack of computer simulations in this field is probably due to the huge effort required to obtain accurate critical exponents. Recently it has been demonstrated, in the field of reversible phase transitions, that random exchange via Lévy flights can effectively generate long range interactions [108,109]. The Lévy flight is a random walk in which the step length ( $l$ ) is a random variable with a probability distribution given by

$$P(l) \propto l^{-d-\sigma} \quad (41)$$

where  $d$  is the spatial dimension and the parameter  $\sigma$  is the dimension of the random walk for  $0 < \sigma < 1$ . It should be noted that within that range of  $\sigma$  the walker exhibits superdiffusive behavior, while for  $\sigma = 1$  one recovers ordinary diffusion. So, in Ising-like models, the random Lévy exchange of

spins generates an effective interaction potential decaying with distance  $r$  as a power law of the form [108,109]

$$V(r) \propto r^{-d-\sigma} \quad (42)$$

Recently two models, aiming to contribute to the understanding of both irreversible reaction processes with anomalous diffusion and IPTs in the presence of long-range exchanges/interactions, have been proposed and studied by means of computer simulations. One model is the contact process [29,100,105] with Lévy exchanges (CPLF) [110] and the other is the branching annihilating walker model [30] where the walkers undergo Lévy exchanges (BALW) [111]. Both models exhibit IPTs between an active stationary state and a vacuum state. Within the range of Lévy exponents ( $\sigma > 1$ ) which corresponds to standard diffusion the obtained critical exponents reveal that the models belong to the universality class of directed percolation. This finding is in agreement with well-established concepts of universal behavior: since exchanges are restricted to finite distances, the diverging correlation length remains as the only relevant length scale. However, for smaller  $\sigma$  values, when superdiffusive behavior is observed, the exchanges are no longer restricted to finite distances and additional long-range correlations can effectively be established. So, in these cases, one observes departure from the standard directed percolation behavior and the critical exponents depend on  $\sigma$ ; in other words, they can be tuned to varying  $\sigma$ . A comparison of the critical exponents obtained for both models, namely the CPLF and BALF reactions, strongly suggests the existence of a new universality class of directed percolation, i.e., all second order irreversible phase transitions in processes involving Lévy exchanges/flights may have the same critical exponents depending only on  $\sigma$  and the dimensionality [110,111]. However, simulations do not allow us to confirm whether the Lévy exchange mechanism can effectively simulate a long-range interactive potential, as in the case of reversible phase transitions. It is expected that the study of this open question will certainly stimulate further work due to its relevance in the study of far-from-equilibrium irreversible processes.

## V. CONCLUSIONS AND OUTLOOK OF SOME DIRECTIONS FOR FURTHER STUDIES

The study of surface chemical reaction processes using computer simulation techniques is quite an active field of research. Within this context the Monte Carlo method emerges as a powerful tool which contributes to the

understanding of the complex behavior of many systems. The input of the Monte Carlo algorithm is a relatively small number of relevant microscopic mechanisms and the desired output is a reliable description of the macroscopic behavior of the reaction. This procedure is in contrast to the standard experimental approach where, on the basis of measurements of the macroscopic behavior, one has to speculate on the underlying microscopic mechanisms. Therefore, the combination of simulations and experimental techniques provides the stimulating feedback necessary for the achievement of a better understanding of the studied reaction. The recent implementation of *in situ* STM measurements of surface chemical reactions has allowed us to establish the agreement between reaction parameters derived macroscopically microscopically. More experiments of this type are still necessary for various reaction systems. However, this preliminary finding further reinforces the validity of the Monte Carlo approach for the study of surface reactions.

Due to the lack of a general theory, Monte Carlo simulations have greatly contributed to the understanding of IPTs in surface reaction systems. Second order IPTs are very well understood and, in most cases, they can unambiguously be placed in the universality class of directed percolation or, equivalently, Reggeon field theory. However, the fact that this kind of transition has never been observed experimentally is rather discouraging. Metastability and phase coexistence at first-order IPTs provides the mechanism for the propagation of chemical waves, a matter of active research where considerable progress has been achieved but where further work is still necessary in order to study models with high diffusion rates of the reactants. The continuous outcome of experimental data in this field is quite stimulating.

Very recently, considerable effort has been devoted to the simulation of the oscillatory behavior which has been observed experimentally in various surface reactions. So far, the most studied reaction is the catalytic oxidation of carbon monoxide, where it is well known that oscillations are coupled to reversible reconstructions of the surface via structure-sensitive sticking coefficients of the reactants. A careful evaluation of the simulation results is necessary in order to ensure that oscillations remain in the thermodynamic limit. The roles of surface diffusion of the reactants versus direct adsorption from the gas phase, at the onset of self-organization and synchronized behavior, is a topic which merits further investigation.

Due to the interesting technological applications, challenging phenomena, and continuous output of experimental information, it is expected that the study of surface chemical reactions will continue to attract increasing activity in the future.

## ACKNOWLEDGMENTS

This work is financially supported by the CONICET, the ANPCyT (Argentina) and the National University of La Plata. The author is deeply indebted to many colleagues for useful discussions and the submission of reprints/preprints and figures. He also acknowledges the kind hospitality of Prof. K. Binder during his stay in Mainz, where most of this chapter was written.

## REFERENCES

1. K. Christmann. *Introduction to Surface Physical Chemistry*. Darmstadt: Steinkopff-Verlag, 1991, pp. 1–274.
2. J. H. Block, M. Ehsasi, V. Gorodetskii. Dynamic studies of surface reactions with microscopic techniques. *Prog Surf Sci* 42:143–168, 1993.
3. J. Wintterlin, S. Volkening, T. V. W. Janssens, T. Zambelli, G. Ertl. Atomic and macroscopic reaction rates of a surface-catalyzed reaction. *Science* 278:1931–1933, 1997.
4. K. Binder. Introduction. In: K. Binder, ed. *The Monte Carlo Method in Condensed Matter Physics*. Vol. 71. Berlin: Springer-Verlag, 1992, pp. 1–22.
5. K. Binder, ed. *Applications of the Monte Carlo method in Statistical Physics*, 2nd ed. Berlin: Springer-Verlag, 1984, pp. 1–341.
6. K. Binder, D. Heermann. *Monte Carlo Simulations in Statistical Physics*, *Springer Series in Solid State Sciences*, Vol. 80. Berlin: Springer-Verlag, 1992, pp. 1–129.
7. E. Albano. The Monte Carlo simulation method: A powerful tool for the study of reaction processes. *H Chem Rev* 3:389–418, 1996.
8. V. P. Zhdanov, B. Kasemo. Kinetic phase transitions in simple reactions on solid surfaces. *Surf Sci Rep* 20:111–189, 1994.
9. D. Walgraef. *Spatio-Temporal Pattern Formation*. New York: Springer Verlag, 1997, pp. 1–301.
10. G. Grinstein, Z.-W. Lai, D. A. Browne. Critical phenomena in a non-equilibrium model of heterogeneous catalysis. *Phys Rev A* 40:4820–4823, 1989.
11. M. Tammaro, M. Sabella, J. W. Evans. Hybrid treatment of spatio-temporal behavior in surface reactions with coexisting immobile and highly mobile reactants. *J Chem Phys* 103:10277–10285, 1995.
12. K. A. Fichthorn, W. H. Weinberg. Theoretical foundations of dynamical Monte Carlo simulations. *J Chem Phys* 95:1090–1096, 1991.
13. B. Meng, W. H. Weinberg. Monte Carlo simulation of temperature programmed desorption spectra. *J Chem Phys* 100:5280–1589, 1994.
14. A. P. J. Jansen. Monte Carlo simulation of chemical reactions on a surface with time-dependent reaction-rate constants. *Comp Phys Commun* 86:1–12, 1995.
15. R. J. Gelten et al. Monte Carlo simulation of a surface reaction model showing spatio-temporal pattern formations and oscillations. *J Chem Phys* 108:5921–5934, 1998.

16. R. Imbhil. Oscillatory reactions on single crystal surfaces. *Prog Surf Sci* 44:185–343, 1993.
17. R. Imbhil, G. Ertl. Oscillatory kinetics in heterogeneous catalysis. *Chem Rev* 95:697–733, 1995.
18. R. M. Ziff, E. Gulari, Y. Barshad. Kinetic phase transitions in an irreversible surface-reaction model. *Phys Rev Lett* 56:2553–2556, 1986.
19. M. Ehsasi et al. Steady and nonsteady rates of reaction in a heterogeneously catalyzed reaction: Oxidation of CO on platinum, experiments and simulations. *J Chem Phys* 91:4949–4956, 1989.
20. P. Grassberger, A. De La Torre. *Ann Phys (New York)* 122:373–396, 1979; P. Grassberger. *J Phys A (Math & Gen)* 22:3673–3679, 1989.
21. P. Meakin, D. J. Scalapino. Simple models for heterogeneous catalysis: Phase transitions-like behavior in nonequilibrium systems. *J Chem Phys* 87:731–741, 1987.
22. E. V. Albano. Determination of the order-parameter critical exponent of an irreversible dimer–monomer surface reaction model. *Phys Rev E* 49:1738–1739, 1994.
23. E. V. Albano. Damage spreading in the Ziff Gulari Barshad model. *Phys Rev E* 50:1129–1134, 1994.
24. I. Jensen, H. C. Fogedby, R. Dickman. Critical exponents for an irreversible surface reaction model. *Phys Rev A* 41:3411–3414, 1990.
25. C. A. Voigt, R. M. Ziff. Epidemic analysis of the second-order transition in the Ziff Gulari Barshad surface-reaction model. *Phys Rev. E* 56:R6241–R6244, 1997.
26. T. Aukrust, D. A. Browne, I. Webman. Critical behavior of an autocatalytic reaction model. *Phys Rev A* 41:5294–5301, 1990.
27. I. Jensen, R. Dickman. Nonequilibrium phase transitions in systems with infinitely many absorbing states. *Phys Rev E* 48:1710–1725, 1993.
28. E. V. Albano. Critical behaviour of a forest fire model with immune trees. *J Phys A (Math & Gen)* 27:L881–L886, 1994.
29. I. Jensen. Critical behavior of the three dimensional contact process. *Phys Rev A* 45:R563–R566, 1992.
30. H. Takayasu, N. Inui, A. Y. Tretyakov. Extinction, survival, and dynamic phase transition of branching annihilating random walk. *Phys Rev Lett* 68:3060–3063, 1992.
31. R. M. Zif, B. J. Brosilow. Investigation of the first-order phase transition in the A–B<sub>2</sub> reaction model using a constant-coverage kinetic ensemble. *Phys Rev A* 46:4630–4633, 1992.
32. J. W. Evans, M. S. Miesch. Catalytic reaction kinetics near a first-order poisoning transition. *Surf Sci* 245:401–410, 1991.
33. J. W. Evans, M. S. Miesch. Characterizing kinetics near a first-order catalytic poisoning transition. *Phys Rev Lett* 66:833–836, 1991.
34. J. W. Evans. Kinetic phase transitions in catalytic reaction models. *Langmuir* 7:2514–2519, 1991.

35. V. D. Pereyra, E. V. Albano. On the influence of the hot-dimer adsorption mechanism in the critical behavior of the ZGB model. *J Phys A (Math & Gen)* 27:7763–7770, 1994.
36. M. Kolb, Y. Boudeville. Kinetic model for heterogeneous catalysis: Cluster and percolation properties. *J Chem Phys* 92:3935–3945, 1990.
37. A. Bunde, S. Havlin. *Fractals and Disordered Systems*. Berlin: Springer-Verlag, 1991, pp. 1–350.
38. H. P. Kaukonen, R. M. Nieminen. Computer simulations studies of the catalytic oxidation of carbon monoxide on platinum metals. *J Chem Phys* 91:4380–4386, 1989.
39. B. J. Brosilow, R. M. Ziff. Effects of A desorption on the first-order transition in the A–B<sub>2</sub> reaction model. *Phys Rev A* 46:4534–4538, 1992.
40. E. V. Albano. Monte Carlo simulation of a bimolecular reaction of the type  $A + (1/2) B_2 \rightarrow AB$ . The influence of A-desorption on kinetic phase transitions. *Appl Phys A* 55:226–230, 1992.
41. J. J. Luque, F. Jiménez-Morales, M. C. Lemos. Monte Carlo simulation of a surface reaction model with local interaction. *J Chem Phys* 96:8535–8538, 1992.
42. J. Satulovsky, E. V. Albano. The influence of lateral interactions on the critical behavior of a dimer–monomer surface reaction model. *J Chem Phys* 97:9440–9446, 1992.
43. E. V. Albano. Finite-size effects in kinetic phase transitions of a model reaction on a fractal surface: Scaling approach and Monte Carlo investigation. *Phys Rev B* 42:R10818–R10821, 1990.
44. E. V. Albano. Monte Carlo simulation of the oxidation of carbon monoxide on fractal surfaces. *Surf Sci* 235:351–359, 1990.
45. A. Casties, J. Mai, W. von Niessen. A Monte Carlo study of the CO oxidation on probabilistic fractals. *J Chem Phys* 99:3082–3091, 1993.
46. J. Mai, A. Casties, W. von Niessen. A Monte Carlo simulation of the catalytic oxidation of CO on DLA clusters. *Chem Phys Lett* 211:197–202, 1993.
47. J. Mai, A. Casties, W. von Niessen. A model for the catalytic oxidation of CO on fractal lattices. *Chem Phys Lett* 196:358–362, 1992.
48. E. V. Albano. Irreversible phase transitions in the dimer–monomer surface reaction process on fractal media. *Phys Lett A* 168:55–58, 1992.
49. I. Jensen. Non-equilibrium critical behavior on fractal lattices. *J Phys A (Math & Gen)* 24:L1111–L1117, 1991.
50. E. V. Albano. Critical behavior of the irreversible phase transitions of a dimer–monomer process on fractal media. *J Phys A (Math & Gen)* 27:431–436, 1994.
51. M. Tammaro, J. W. Evans. Monomer–dimer surface reaction models: Influence of the dimer adsorption mechanism. *Phys Rev E* 52:2310–2317, 1995.
52. J. Cortés, E. Valencia. Effect of the coordination of the superficial site in the ZGB model for the CO–CO<sub>2</sub> reaction. *Surf Sci* 371:L243–L247, 1997.

53. I. Jensen, H. C. Fogedby. Kinetic phase transitions in a surface-reaction model with diffusion : Computer simulations and mean-field theory. *Phys Rev A* 42:1969–1975, 1990.
54. J. Mai, W. von Niessen. The  $\text{CO} + \text{O}_2$  reaction on metal surfaces. Simulation and mean-field theory: The influence of diffusion. *J Chem Phys* 93:3685–3692, 1990.
55. J. W. Evans. ZGB surface reaction model with high diffusion rates. *J Chem Phys* 98:2463–2465, 1993.
56. J. Mai, W. von Niessen. The influence of physisorption and the Eley–Rideal mechanism on the surface reaction:  $\text{CO} + \text{O}_2$ . *Chem Phys* 156:63–69, 1991.
57. P. Meakin. Simple models for heterogeneous catalysis with a poisoning transition. *J Chem Phys* 93:2903–2910, 1990.
58. G. Haas, M. Bar, I. G. Kevrekides, P. B. Rasmussen, H. H. Petermund, G. Ertl. Observation of front bifurcations in controlled geometries: from one to two dimensions. *Phys Rev Lett* 75:3560–3563, 1995.
59. S. Jabubith, H. H. Rotermund, W. Engel, A. von Oertzen, G. Ertl. Spatio-temporal concentration patterns in a surface reaction: Propagation of standing waves, rotating spirals and turbulence. *Phys Rev Lett* 65:3013–3016, 1990.
60. A. L. Barabási, H. E. Stanley. *Fractal Concepts in Surface Growth*. Cambridge: Cambridge University Press, 1995, pp. 1–366.
61. M. Kardar, G. Parisi, Y. C. Zhang. Dynamic scaling of growing interfaces. *Phys Rev Lett* 56:889, 1986.
62. P. Moller, K. Wetzl, M. Eiswirth, G. Ertl. Kinetic oscillations in the catalytic CO oxidation: Computer simulations. *J Chem Phys* 85:5328–5334, 1986.
63. B. J. Brosilow, E. Gulari, R. Ziff. Boundary effects in a surface reaction model for CO oxidation. *J Chem Phys* 99:1–5, 1993.
64. J. W. Evans, T. R. Ray. Interface propagation and nucleation phenomena for discontinuous poisoning transitions in surface reaction models. *Phys Rev E* 50:4302–4314, 1994.
65. R. H. Goodman, D. S. Graff, L. M. Sander, P. Leroux-Hugon, E. Clément. Trigger waves in a model for catalysis. *Phys Rev E* 52:5904–5909, 1995.
66. E. Albano. Displacement of inactive phases by the reactive regime in a lattice gas model for a dimer–monomer irreversible surface reaction. *Phys Rev E* 55:7144–7152, 1997.
67. R. D. Vigil, F. T. Willmore. Oscillatory dynamics in a heterogeneous surface reaction: Breakdown of the mean-field approximation. *Phys Rev E* 54:1225–1231, 1996.
68. A. P. J. Jansen, R. M. Nieminen. A Monte Carlo study of CO oxidation with oscillations induced by site blocking. *J Chem Phys* 106:2038–2044, 1997.
69. L. M. Sander, S. V. Ghaisas. Monte Carlo simulations of oscillations in the oxidation of CO on Pt at atmospheric pressure. *Surf Sci* 391:125–33, 1997.
70. E. V. Albano. A dimer–monomer catalyzed reaction process with surface reconstruction coupled to reactant coverages. *Langmuir* 13:4013–4017, 1997.
71. E. V. Albano. Critical and oscillatory behaviour of a dimer–monomer catalyzed reaction process. *Phys Rev E* 57:6840–6843, 1998.



72. E. V. Albano. On the influence of reactant's induced surface transformations in the behavior of a heterogeneously catalyzed dimer-monomer reaction model. *J Chem Phys* 109:7498–7505, 1998.
73. V. N. Kusovkov, O. Kortluke, W. von Niessen. Kinetic oscillations in the catalytic CO oxidation on Pt single crystal surfaces: Theory and simulation. *J Chem Phys* 108:5571–5580, 1998.
74. K. Fichthorn, E. Gulari, R. Ziff. Self-sustained oscillations in a heterogeneous catalytic reaction: A Monte Carlo simulation. *Chem Eng Sci* 44:1403–1411, 1989.
75. A. Hopkinson, J. M. Bradley, X.-C. Guo, D. A. King. Nonlinear island growth dynamics in adsorbate-induced restructuring of quasihexagonal reconstructed Pt(100) by CO. *Phys Rev Lett* 71:1597–1600, 1993.
76. K. C. Rose, D. Battogtokh, A. Mikhailov, R. Imbihl, W. Engel, A. M. Bradshaw. *Phys Rev Lett* 76:3582–3585, 1996.
77. K. Yaldrum, M. A. Khan. NO–CO reaction on square and hexagonal surfaces : A Monte Carlo simulation. *J Catal* 131:369–377, 1991; 136:279–280, 1992.
78. B. J. Brosilow, R. M. Ziff. Comment on NO–CO reaction on square and hexagonal surfaces : A Monte Carlo simulation. *J Catal* 136:275–278, 1992.
79. M. A. Khan, K. Yaldrum, G. K. Khalil, K. M. Khan. NO–CO surface reaction on a square lattice. *Phys Rev E* 50:2156–2160, 1994.
80. B. Meng, W. H. Weinberg, J. W. Evans. Transitions in the kinetics and steady states of irreversible  $A + BC$  surface reaction models. *Phys Rev E* 48:3577–3588, 1993.
81. B. Meng, W. H. Weinberg, J. W. Evans. Lattice gas model mimicking the  $NO + CO$  reaction on Pt(100). *J Chem Phys* 101:3234–3242, 1994.
82. M. Tammaro, J. W. Evans. Reactive removal of unstable mixed NO + CO adlayers: Chemical diffusion and reaction front propagation. *J Chem Phys* 108:7795–7806, 1998.
83. E. V. Albano. Irreversible saturation transitions in dimer–dimer reaction models of heterogeneous catalysis. *J Phys A (Math & Gen)* 25:2557–2568, 1992; Corrigendum. *J Phys A (Math & Gen)* 26:3667, 1993.
84. E. V. Albano. The critical behavior of dimer–dimer surface reaction models. Monte Carlo and finite-size scaling investigation. *J Stat Phys* 69:643–666, 1992.
85. A. Maltz, E. V. Albano. Kinetic phase transitions in dimer-dimer surface reaction models studied by means of mean-field and Monte Carlo methods. *Surf Sci* 277:414–428, 1992.
86. K. Yaldrum, K. M. Khan, N. Ahmed, M. A. Khan. A comment on “Irreversible saturation transitions in dimer–dimer reaction models of heterogeneous catalysis”. *J Phys A (Math & Gen)* 26:2663–2665, 1993.
87. P. Hui-Yun, W. H. Jun, Z. Z. Sen. Dimer–dimer surface reaction of Albano's type: a cellular automata approach. *J Phys A (Math & Gen)* 28:4279–4283, 1995.
88. K. M. Khan, K. Yaldrum, A. Ahmad. Kinetics of a dimer–dimer irreversible catalytic surface reaction. *J Chem Phys* (in press).

89. R. M. Ziff, K. Fichthorn. Fractal clustering on a catalyst surface. *Phys Rev B* 34:2038–2040, 1986.
90. E. V. Albano. Critical exponents for the irreversible surface reaction  $A + B \rightarrow AB$  with B desorption on homogeneous and fractal media. *Phys Rev Lett* 69:656–659, 1992.
91. L. Frachenbourg, P. L. Krapivsky, S. Redner. Heterogeneous catalysis on a disordered surface. *Phys Rev Lett* 75:2891–2894, 1995.
92. J. Zhuo, S. Redner, H. Park. Critical behavior of an interacting surface reaction model. *J Phys A (Math & Gen)* 26:4197–4213, 1993.
93. H. C. Kang, W. H. Weinberg. Roughening of chemical reacting interfaces. *Phys Rev E* 47:1604–1609, 1993.
94. H. C. Kang, W. H. Weinberg. Structure of a Langmuir Hinshelwood reaction interface. *Phys Rev E* 48:3464–3469, 1993.
95. H. C. Kang, W. H. Weinberg. Interface roughening and kinetics of poisoning in a surface reaction. *J Chem Phys* 100:1630–1633, 1994.
96. E. V. Albano. Critical behavior of an irreversible multiple reaction process. *Surf Sci* 306:240–246, 1994.
97. E. V. Albano. On the universality classes of the discontinuous irreversible phase transitions of a multicomponent reaction system. *J Phys A (Math & Gen)* 27:3751–3758, 1994.
98. E. V. Albano. Irreversible phase transitions into non-unique absorbing states in a multicomponent reaction system. *Physica A* 214:426–434, 1995.
99. E. V. Albano. Irreversible phase transitions in a dimer–monomer–monomer reaction model. *J Phys A* 29:3317–3327, 1996.
100. T. M. Liggett. *Interacting Particle Systems*. New York: Springer-Verlag, 1983, pp. 1–486.
101. N. Konno. *Phase transitions of interacting particle systems*. Singapore: World Scientific, 1994, pp. 1–228.
102. E. Clément, P. Leroux-Hugon, L. M. Sander. Exact results for a chemical reaction model. *Phys Rev Lett* 67:1661–1664, 1991.
103. E. Clément, P. Leroux-Hugon, L. M. Sander. Analytical solution of an irreversible surface reaction model. *J Stat Phys* 65:925–939, 1991.
104. C. Flamet, E. Clément, P. Leroux-Hugon, L. M. Sander. Exact dynamics of a bistable chemical reaction model. *J Phys A (Math & Gen)* 25:L1317–L1322, 1992.
105. R. Dickman, I. Jensen. Time-dependent perturbation theory for nonequilibrium lattice models. *Phys Rev Lett* 67:2391–2394, 1991.
106. D. A. Browne, P. Kleban. Equilibrium statistical mechanics for kinetic phase transitions. *Phys Rev A* 40:1615–1626, 1989.
107. M. H. Kim, H. Park. Critical behavior of an interacting monomer–dimer model. *Phys Rev Lett* 73:2579–2582, 1994.
108. B. Bergersen, Z. Rácz. Dynamical generation of long-range interactions: Random Lévy flights in the kinetic Ising and spherical models. *Phys Rev Lett* 67:3047–3050, 1991.

109. H. J. Xu, B. Bergersen, Z. Rácz. Long-range interactions generated by random Lévy flights: Spin-flip and spin exchange kinetic Ising models. *Phys Rev E* 47:1520–1524, 1993.
110. E. V. Albano. Irreversible phase transitions in contact processes with Lévy exchanges and long-range interactions. *Phys Rev E* 54:3436–3441, 1996.
111. E. V. Albano. Branching annihilating Lévy flights: Irreversible phase transitions with long-range exchanges. *Europhys Lett* 34:97–102, 1996.

# 9

## Theoretical Approaches to the Kinetics of Adsorption, Desorption, and Reactions at Surfaces

**H. J. KREUZER and STEPHEN H. PAYNE** Department of Physics,  
Dalhousie University, Halifax, Nova Scotia, Canada

I. Introduction	439
II. Desorption Under Quasi-equilibrium Conditions	441
A. Lattice gas models	443
B. The chemical potential	444
C. Transfer matrix method	446
D. Examples	453
III. Kinetic Lattice Gas Models	462
A. Nondissociative adsorption	463
B. Adsorption and desorption via precursors	470
C. Adsorption and desorption with surface reconstruction	472
IV. Concluding Remarks	476
References	477

### I. INTRODUCTION

Kinetic theories of adsorption, desorption, surface diffusion, and surface reactions can be grouped into three categories. (i) At the macroscopic level one proceeds to write down kinetic equations for macroscopic variables, in particular rate equations for the (local) coverage or for partial coverages. This can be done in a heuristic manner, much akin to procedures in gas-phase kinetics or, in a rigorous approach, using the framework of nonequilibrium thermodynamics. Such an approach can be used as long as

the adsorbate remains in local equilibrium. (ii) If it cannot be guaranteed that the adsorbate remains in local equilibrium during its time evolution, then a set of macroscopic variables is not sufficient and an approach based on nonequilibrium statistical mechanics involving time-dependent distribution functions must be invoked. The kinetic lattice gas model is an example of such a theory. It is derived from a Markovian master equation, but is not totally microscopic in that it is based on a phenomenological Hamiltonian and on postulated transition probabilities, albeit subject to the principle of detailed balance. For the kinetics in chemisorbed systems, this is as far as theory has progressed. (iii) Lastly, we realize that a proper theory of the time evolution of adsorption and desorption must start from a microscopic Hamiltonian of the coupled gas–solid system. A master equation must then be derived from first principles, with the benefit that transition probabilities are calculated explicitly involving microscopic parameters only. So far this program has been only completed for phonon-mediated physisorption kinetics, as reviewed in a monograph by Kreuzer and Gortel [1].

In this review we put less emphasis on the physics and chemistry of surface processes, for which we refer the reader to recent reviews of adsorption–desorption kinetics which are contained in two books [2,3] with chapters by the present authors where further references to earlier work can be found. These articles also discuss relevant experimental techniques employed in the study of surface kinetics and appropriate methods of data analysis. Here we give details of how to set up models under basically two different kinetic conditions, namely (i) when the adsorbate remains in quasi-equilibrium during the relevant processes, in which case nonequilibrium thermodynamics provides the needed framework, and (ii) when surface nonequilibrium effects become important and nonequilibrium statistical mechanics becomes the appropriate vehicle. For both approaches we will restrict ourselves to systems for which appropriate lattice gas models can be set up. Further associated theoretical reviews are by Lombardo and Bell [4] with emphasis on Monte Carlo simulations, by Brivio and Grimley [5] on dynamics, and by Persson [6] on the lattice gas model.

This review is structured as follows. In the next section we present the theory for adsorbates that remain in quasi-equilibrium throughout the desorption process, in which case a few macroscopic variables, namely the partial coverages  $\theta_r$ , and their rate equations are needed. We introduce the lattice gas model and discuss results ranging from non-interacting adsorbates to systems with multiple interactions, treated essentially exactly with the transfer matrix method, in Sec. II. Examples of the accuracy possible in the modeling of experimental data using this theory, from our own work, are presented for such diverse systems as multilayers of alkali metals on metals, competitive desorption of tellurium from tungsten, and dissociative

adsorption of hydrogen on rhodium. In Sec. III we proceed to the mesoscopic level by outlining recent advances in the theory of the kinetic lattice gas model, such as precursor-mediated adsorption and desorption and the kinetics of adsorption and desorption in the presence of surface reconstruction.

A theory of surface processes must provide a consistent description and explanation of the available experimental data on a particular adsorbate system. For adsorption it is the coverage and temperature dependence of the sticking coefficient. For desorption it is the desorption rate of the various desorbing species, again as a function of coverage and temperature. This may either be the isothermal desorption rate or the rate of temperature-programmed desorption (TPD). In the latter experimental setup the adsorbate is prepared for different initial coverages at low temperature and the substrate is then heated to give a (preferably linear) rise in temperature during which the desorption products are detected. With time-resolved EELS and IR spectroscopies some species remaining at the surface can also be monitored, with which the partial coverages of the theory must agree. In addition, LEED can be used to record, via the scattering intensities, the time evolution of local correlations in the adsorbate, which thus must also be provided by the theory. Lastly, because any kinetic theory yields via its time-independent solution the equilibrium properties of the adsorbate, these must be consistent with the measured equilibrium properties of the system such as adsorption isotherms and isobars, the heat of adsorption and the differential entropy, and correlation functions, all as a function of coverage and temperature. Only when a large set of kinetic data and all equilibrium data are explained satisfactorily within the same theory, can one claim to have a realistic model of the system. What has been done successfully for a number of systems is to postulate a lattice gas Hamiltonian with appropriate binding sites and lateral interactions and fit the predictions of the theory to all the available equilibrium and kinetic data. This will yield a set of interaction parameters whose uniqueness becomes more reliable the more data are fitted. The associated theory and techniques are those presented below.

## II. DESORPTION UNDER QUASI-EQUILIBRIUM CONDITIONS

We consider desorption from an adsorbate where surface diffusion is so fast (on the time scale of desorption) that the adsorbate is maintained in equilibrium throughout the desorption process. That is to say that, at the remaining coverage  $\theta(t)$  at temperature  $T(t)$ , all correlation functions attain

their equilibrium values. Thus the adsorbate can be characterized by its chemical potential,  $\mu(\theta(t), T(t))$ . For example, if we were to look at desorption of an adsorbate that shows coexistence of a dense and a dilute two-dimensional phase in a certain range of coverage and temperature, then the assumption of quasi-equilibrium implies that at the remaining coverage,  $\theta(t)$ , the distribution of particles among the two phases is identical to that in equilibrium at this coverage. In such situations a purely macroscopic description of the desorption process in terms of a few macroscopic variables, the partial coverages,  $\theta_r(t)$ , for the various species on the surface is sufficient.

To derive an explicit expression of the rate of desorption we restrict ourselves to nondissociative adsorption, listing references to other systems—such as multicomponent and multilayer adsorbates with and without precursors—for which such a treatment has been given, later. We look at a situation where the gas phase pressure of a molecular species,  $P$ , is different from its value,  $\bar{P}$ , which maintains an adsorbate at coverage  $\theta$ . There is then an excess flux to re-establish equilibrium between gas phase and adsorbate so that we can write [7–10]

$$d\theta/dt = S(\theta, T)(P - \bar{P}) \frac{a_s \lambda_{th}}{h} \quad (1)$$

where

$$\lambda_{th} = h/(2\pi mk_B T)^{1/2} \quad (2)$$

is the thermal wavelength. Next we express the equilibrium pressure in terms of the gas phase chemical potential,  $\mu_g$ ,

$$\bar{P} = \frac{k_B T}{\lambda_{th}^3} Z_{int} \exp(\mu_g/k_B T) \quad (3)$$

Here  $Z_{int}$  is the intramolecular partition function accounting for rotations and vibrations. However, in equilibrium, the chemical potential in the gas phase is equal to that in the adsorbate,  $\mu_a$ , so that we can write the desorption rate in (1) as

$$R_d = S(\theta, T) \frac{a_s^2}{\lambda_{th}} \frac{k_B T}{h} Z_{int} \exp(\mu_a/k_B T) \quad (4)$$

This is our principal result for the rate of desorption from an adsorbate that remains in quasi-equilibrium throughout desorption. Noteworthy is the clear separation into a dynamic factor, the sticking coefficient  $S(\theta, T)$ , and a thermodynamic factor involving single-particle partition functions and the chemical potential of the adsorbate. The sticking coefficient is a measure of the efficiency of energy transfer in adsorption. Since energy supply from the

substrate is required for desorption, the sticking coefficient, albeit usually at a higher temperature, must appear in the desorption rate by the detailed balance argument. The sticking coefficient cannot be obtained from thermodynamic arguments but must be calculated from a microscopic or mesoscopic theory or be postulated in a phenomenological approach, based on experimental evidence for a particular system or on some simple arguments.

For dissociative adsorption, i.e., for systems in which the gas phase is predominantly molecules which dissociate into fragments  $A$  and  $B$  on the surface (not necessarily atoms), the desorption rate is given by

$$R_d(A + B \rightarrow AB) = S_{\text{dis}}(\theta_A, \theta_B, T) \frac{a_s^2}{\lambda_{\text{th}}} \frac{k_B T}{h} Z_{\text{int}}^{(A)} Z_{\text{int}}^{(B)} \times \exp((\mu_A + \mu_B)/k_B T) \quad (5)$$

where  $S_{\text{dis}}(\theta_A, \theta_B, T)$  is the dissociative sticking coefficient at the indicated partial coverages and at the desorption temperature.

In a recent paper [11] this approach has been generalized to deal with reactions at surfaces, notably dissociation of molecules. A lattice gas model is employed for homonuclear molecules with both atoms and molecules present on the surface, also accounting for lateral interactions between all species. In a series of model calculations equilibrium properties, such as heats of adsorption, are discussed, and the role of dissociation disequilibrium on the time evolution of an adsorbate during temperature-programmed desorption is examined. This approach is adaptable to more complicated systems, provided the individual species remain in local equilibrium, allowing of course for dissociation and reaction disequilibria.

## A. Lattice Gas Models

Most microscopic theories of adsorption and desorption are based on the lattice gas model. One assumes that the surface of a solid can be divided into two-dimensional cells, labelled  $i$ , for which one introduces microscopic variables  $n_i = 1$  or  $0$ , depending on whether cell  $i$  is occupied by an adsorbed gas particle or not. (The connection with magnetic systems is made by a transformation to spin variables  $\sigma_i = 2n_i - 1$ .) In its simplest form a lattice gas model is restricted to the submonolayer regime and to gas-solid systems in which the surface structure and the adsorption sites do not change as a function of coverage. To introduce the dynamics of the system one writes down a model Hamiltonian which, for the simplest system of a one-component adsorbate with one adsorption site per unit cell, is

$$H = E_s \sum_i n_i + V_{1n} \sum_{\langle ij \rangle} n_i n_j + V_{2n} \sum_{\langle ij' \rangle} n_i n_{j'} + \cdots \quad (6)$$



Here  $E_s$  is a single particle energy and  $V_{1n}$  and  $V_{2n}$  are the two-particle interactions between nearest neighbors  $\langle ij \rangle$  and next nearest neighbors  $\langle ij' \rangle$ , respectively. Interactions between farther neighbours and many-particle interactions can be easily added. As long as the number of particles in the adsorbate does not change, which is the case for systems in equilibrium, or for diffusion studies, the first term in Eq. (6) is constant and can be dropped from further consideration. However, if we want to study adsorption-desorption kinetics, the number of particles in the adsorbate changes as a function of time and a proper identification of  $E_s$  is mandatory. Arguing that the lattice gas Hamiltonian should give the same Helmholtz free energy as a microscopic Hamiltonian (for non-interacting particles), one can show that the proper identification is given by

$$E_s = -V_0 - k_B T \ln(q_3 q_{\text{int}}) \quad (7)$$

where  $V_0$  is the (positive) binding energy of an isolated particle on the surface. Moreover,

$$q_3 = q_z q_{xy} \quad (8)$$

is the vibrational partition function of an adsorbed particle with

$$q_z = \exp(h\nu_z/2k_B T) / [\exp(h\nu_z/k_B T) - 1] \quad (9)$$

its component for the motion perpendicular to the surface. Likewise,  $q_{xy}$  is the partition function for the motion parallel to the surface. We have also made adjustment for the fact that the internal partition function for rotations and vibrations of an adsorbed molecule might be changed from its free gas phase value  $Z_{\text{int}}$  to  $q_{\text{int}}$ , if some of the internal degrees of freedom get frozen out or frustrated.

## B. The Chemical Potential

Eqs. (1,4,5) show that to determine the equilibrium properties of an adsorbate and also the adsorption-desorption and dissociation kinetics under quasi-equilibrium conditions we need to calculate the chemical potential as a function of coverage and temperature. We illustrate this by considering a single-component adsorbate. The case of dissociative equilibrium with both atoms and molecules present on the surface has recently been given elsewhere [11].

We start with a non-interacting molecular adsorbate for which the chemical potential is given by

$$\mu_a(\theta, T) = -V_0 + k_B T [\ln(\theta/(1-\theta)) - \ln(q_3 q_{\text{int}})] \quad (10)$$

Inserted in Eq. (3), this gives the Langmuir isotherm

$$\bar{P} = \frac{k_B T}{\lambda_{th}^3} Z_{int} \exp(\mu_a/k_B T) = \frac{k_B T}{\lambda_{th}^3} \frac{Z_{int}}{q_3 q_{int}} \exp(-V_0/k_B T) \frac{\theta}{1-\theta} \quad (11)$$

from which we get the isosteric heat of adsorption

$$Q_{iso}(\theta, T) = k_B T \left. \frac{\partial \ln \bar{P}}{\partial T} \right|_{\theta} = V_0 + \frac{5}{2} k_B T - k_B T^2 \frac{d}{dT} \ln(q_3 q_{int}/Z_{int}) \quad (12)$$

and the differential entropy

$$\Delta s(\theta, T) = \bar{s} - s_G = -k_B \ln(\bar{P}/P_0) - Q_{iso}/T$$

where

$$\bar{s} = \left. \frac{\partial S}{\partial n} \right|_{T, P, A}$$

is the differential entropy of the adsorbate and  $s_G$  that of the gas phase.  $P_0$  is the pressure of the reference state.

Similarly, we get the rate of desorption

$$R_d = S(\theta, T) \frac{\theta}{1-\theta} \frac{a_s}{\lambda_{th}^2} \frac{k_B T}{h} \frac{Z_{int}}{q_3 q_{int}} \exp(-V_0/k_B T) \quad (13)$$

Note that if sticking is controlled by site-exclusion only, i.e., if  $S(\theta, T) = S_0(T)(1-\theta)$ , this rate is that of a first-order reaction at low coverage. This simple picture breaks down when either the sticking coefficient depends differently on the coverage, as it does for instance for precursor-mediated adsorption, or when lateral interactions become important. It then does not make much physical sense to talk about the order of the desorption process.

To gain some qualitative insight into the effect of lateral interactions it is useful to employ simple analytical approximations in the calculation of the chemical potential, of which the quasichemical approximation is the best suited. We split the chemical potential into a non-interacting part, Eq. (10), and a term due to lateral interactions,  $\mu_a = \mu_a^{(ni)} + \mu_a^{(lat)}$ , and get for the latter, for  $c$  nearest neighbor interactions only,

$$\mu_a^{(lat)}(\theta, T) = cV_{ln} + \frac{1}{2} c k_B T \ln \left[ \frac{\alpha - 1 + 2\theta}{\alpha + 1 - 2\theta} \frac{1-\theta}{\theta} \right] \quad (14)$$

where

$$\alpha^2 = 1 - 4\theta(1-\theta)[1 - \exp(-V_{ln}/k_B T)] \quad (15)$$

This adds to the isosteric heat, which now reads

$$Q_{\text{iso}}(\theta, T) = Q_{\text{iso}}(0, T) + \frac{1}{2} c V_{1n} [(1 - \alpha - 2\theta)/\alpha] \quad (16)$$

For a large repulsive interaction,  $V_{1n}/k_B T \gg 1$ , for example,  $Q_{\text{iso}}$  exhibits two distinct and essentially constant values for  $\theta \leq 1/2$  because, for  $\theta < 1/2$ , adsorbed particles are essentially isolated from each other by the mutual repulsion on nearest neighbor sites, whereas, for  $\theta > 1/2$ , those particles that have  $c$  neighbors have their binding energy reduced by  $cV_{1n}$ . The consequence of this energetics on desorption is that, in temperature-programmed desorption, one observes one desorption peak for initial coverages  $\theta_0 < 1/2$ , essentially that of a non-interacting adsorbate, and, for initial coverages  $\theta_0 > 1/2$ , an additional peak at lower temperature for desorption out of a local environment of  $c$  neighbors.

Such analytic approximations based on clusters of particles quickly become mathematically intractable with variation in cluster size, geometry, and range of interactions [12,13].

### C. Transfer Matrix Method

With the availability of computers, the transfer matrix method [14] emerged as an alternative and powerful technique for the study of cooperative phenomena of adsorbates resulting from interactions [15–17]. Quantities are calculated exactly on a semi-infinite lattice. Coupled with finite-size scaling towards the infinite lattice, the technique has proved popular for the determination of phase diagrams and critical-point properties of adsorbates [18–23] and magnetic spin systems [24–26], and further references therein. Application to other aspects of adsorbates, e.g., the calculation of desorption rates and heats of adsorption, has been more recent [27–30]. Sufficient accuracy can usually be obtained for the latter without scaling and essentially exact results are possible. In the following, we summarize the elementary but important aspects of the method to emphasize the ease of application. Further details can be found in the above references.

To introduce the transfer matrix method we repeat some well-known facts for a 1-D lattice gas of  $N_s$  sites with nearest neighbor interactions  $V_{1n}$  [31]. Its grand canonical partition function is given by

$$\Xi(T, N_s, \mu) = \sum_{\mathbf{n}} \exp[-(H(\mathbf{n}) - \mu N(\mathbf{n}))/k_B T] \quad (17)$$

$$N(\mathbf{n}) = \sum_{i=1}^{N_s} n_i \quad (18)$$

where  $\mathbf{n} = (n_1, n_2, \dots, n_{N_s}, n_{N_s+1} = n_1)$  specifies one of the  $2^{N_s}$  microstates of the (two-state) adsorbate, with cyclic boundary conditions imposed. Substituting the Hamiltonian (6) we can rewrite  $\Xi$  as a sum over products

$$\begin{aligned}\Xi &= \sum_{\mathbf{n}} \prod_{i=1}^{N_s} T(n_i, n_{i+1}) \\ &= \sum_{\mathbf{n}} T(n_1, n_2) T(n_2, n_3) \dots T(n_{N_s}, n_1)\end{aligned}\quad (19)$$

$$T(n_i, n_{i+1}) = \exp \left[ \frac{\varepsilon}{2} (n_i + n_{i+1}) - v n_i n_{i+1} \right] \quad (20)$$

with  $\varepsilon = (\mu - E_s)/k_B T$  and  $v = V_{1n}/k_B T$ . If the factors  $T(n_i, n_{i+1})$  are regarded as the elements of a  $2 \times 2$  matrix in the basis  $\{|0\rangle, |1\rangle\}$  for each site  $i$  ( $z = \exp(\varepsilon)$ ;  $y = \exp(-v)$ )

$$\mathbf{T} = \begin{bmatrix} T(0,0) & T(0,1) \\ T(1,0) & T(1,1) \end{bmatrix} = \begin{bmatrix} 1 & z^{1/2} \\ z^{1/2} & zy \end{bmatrix} \quad (21)$$

then the summation over states in (19) is equivalent to matrix multiplication, e.g.

$$\sum_{n_2=0,1} T(n_1, n_2) T(n_2, n_3) = T^2(n_1, n_3) \quad (22)$$

where  $T^2(n_1, n_3)$  is an element of the matrix  $\mathbf{T}^2$ . Summing over all intermediate states gives

$$\begin{aligned}\Xi &= \sum_{n_1=0,1} T^{N_s}(n_1, n_1) = \text{Tr}[\mathbf{T}^{N_s}] \\ &= \lambda_1^{N_s} + \lambda_2^{N_s}\end{aligned}\quad (23)$$

where  $\lambda_{1,2}$  are the eigenvalues of the transfer matrix  $\mathbf{T}$ . With  $\lambda_2 < \lambda_1$  the second term becomes insignificant for "large"  $N_s$  so that all thermodynamic information about the system is contained in the largest eigenvalue of the transfer matrix.

One obtains the coverage as ( $\beta = 1/k_B T$ )

$$\begin{aligned}\theta(T, \mu) &= \frac{\langle N \rangle}{N_s} = \frac{1}{N_s} \frac{\partial \ln \Xi}{\partial (\beta \mu)} \bigg|_{T, N_s} \\ &= \frac{\partial \ln(\lambda_1)}{\partial (\beta \mu)} \bigg|_{T, N_s}\end{aligned}\quad (24)$$

To avoid numerical differentiation (which is inherently unstable) one uses the fact that an eigenvalue can be expressed as  $\lambda_1 = \mathbf{v}_1^L \mathbf{T} \mathbf{v}_1^R$  where  $\mathbf{v}_1^{L,R}$  are the corresponding normalized left and right eigenvectors. Differentiation of the eigenvalue with respect to any parameter is then equivalent to the differentiation of the transfer matrix, and one finds

$$\theta(T, \mu) = \frac{z}{\lambda_1} \mathbf{v}_1^L \frac{\partial \mathbf{T}}{\partial z} \bigg|_{T, N_s} \mathbf{v}_1^R \quad (25)$$

$$= \sum_{k=1,2} p_k v_{1k}^2 \quad (26)$$

where  $\mathbf{v}_1^L = (\mathbf{v}_1^R)^T = \mathbf{v}_1 = (v_{11}, v_{12})$  in the basis in which the first and second components are the empty ( $p_1 = 0$ ) and occupied ( $p_2 = 1$ ) sites, respectively. Thus the problem of finding the coverage as a function of temperature and chemical potential is reduced to the determination of the (largest) eigenvalue and corresponding eigenvector of a matrix of Boltzmann factors. Other information can be readily extracted in the same way; for instance, the (average) nearest-neighbor correlation function is given by

$$\begin{aligned} \langle n_i n_{i+1} \rangle &= \frac{1}{N_s \Xi} \sum_{\mathbf{n}} \sum_{i=1}^{N_s} n_i n_{i+1} \exp[-(H(\mathbf{n}) - \mu N(\mathbf{n}))/k_B T] \\ &= -\frac{1}{N_s} \frac{\partial \ln \Xi}{\partial (\beta V_{1n})} \bigg|_{T, N_s} = \frac{y}{\lambda_1} \mathbf{v}_1^L \frac{\partial \mathbf{T}}{\partial y} \bigg|_{T, N_s} \mathbf{v}_1^R \end{aligned} \quad (27)$$

The transfer matrix method extends rather straightforwardly to more than one dimension, systems with multiple interactions, more than one adsorption site per unit cell, and more than one species, by enlarging the basis in which the transfer matrix is defined.

As a simple extension we discuss a two-layer adsorbate with ontop stacking in one dimension with a Hamiltonian

$$\begin{aligned} H &= E_s^{(1)} \sum_i n_i^{(1)} + E_s^{(2)} \sum_i n_i^{(1)} n_i^{(2)} + V_{11} \sum_{\langle ij \rangle} n_i^{(1)} n_j^{(1)} \\ &+ V_{12} \sum_{\langle ij \rangle} n_i^{(1)} n_j^{(2)} + V_{22} \sum_{\langle ij \rangle} n_i^{(2)} n_j^{(2)} \end{aligned} \quad (28)$$

where the superscripts refer to the first and second layer,  $V_{11}$  and  $V_{22}$  are first-neighbor interactions within each layer, and  $V_{12}$  is a second-neighbor interaction between layers. For this 3-state adsorbate the basis at a site is

given by  $\{|n_i^{(1)}, n_i^{(2)}\rangle = |00\rangle, |10\rangle, |11\rangle\}$ , resulting in the transfer matrix

$$\begin{bmatrix} 1 & z_1^{1/2} & z_1^{1/2} z_2^{1/2} \\ z_1^{1/2} & z_1 y_1 & z_1 y_1 z_2^{1/2} y_{12} \\ z_1^{1/2} z_2^{1/2} & z_1 y_1 z_2^{1/2} y_{12} & z_1 y_1 z_2 y_2 y_{12}^2 \end{bmatrix} \quad (29)$$

This matrix must be diagonalized to obtain the largest eigenvalue and its eigenvector, which allows the partial coverages and the correlation functions to be obtained. This is trivial for no interactions ( $y_1 = y_2 = y_{12} = 1$ ) and gives

$$\theta_1 = \frac{1}{N_s} \sum_i n_i^{(1)} = \frac{z_1(1 + z_2)}{1 + z_1(1 + z_2)} \quad (30)$$

$$\theta_2 = \frac{1}{N_s} \sum_i n_i^{(2)} = \frac{z_1 z_2}{1 + z_1(1 + z_2)} \quad (31)$$

For the extension to two dimensions we consider a square lattice with nearest-neighbor interactions on a strip with  $N_s$  sites in one direction and  $M$  sites in the second so that, with cyclic boundary conditions in the second dimension as well, we get a toroidal lattice with of  $2^{N_s+M}$  microstates. The occupation numbers  $n_i$  at site  $i$  in the 1-D case now become a set  $\mathbf{n}_i = (n_{i1}, n_{i2}, \dots, n_{iM})$  of occupation numbers of  $M$  sites along the second dimension, and the transfer matrix elements are generalized to

$$T(\mathbf{n}_i, \mathbf{n}_{i+1}) = \exp \left[ \frac{1}{2} (\varepsilon(\mathbf{n}_i) + \varepsilon(\mathbf{n}_{i+1})) - \mathbf{v}(\mathbf{n}_i, \mathbf{n}_{i+1}) \right] \quad (32)$$

$$\varepsilon(\mathbf{n}_i) = \varepsilon \sum_{j=1}^M n_{ij} - v \sum_{j=1}^M n_{ij} n_{i,j+1} \quad (33)$$

$$\mathbf{v}(\mathbf{n}_i, \mathbf{n}_{i+1}) = v \sum_{j=1}^M n_{ij} n_{i+1,j} \quad (34)$$

Thus  $\varepsilon(\mathbf{n}_i)$  is the energy of the row of  $M$  sites and  $\mathbf{v}(\mathbf{n}_i, \mathbf{n}_{i+1})$  is the interaction energy of two adjacent rows. The partition function is then given in terms of the  $2^M$  eigenvalues of this matrix as

$$\Xi(T, N_s, M, \mu) = \sum_{j=1}^{2^M} \lambda_j^{N_s} \quad (35)$$

For large  $N_s$  this sum is again dominated by the first eigenvalue,  $\lambda_1$ , which will now depend on  $M$ . For practical calculations  $M$  is restricted by computer memory. However, the symmetry of the Hamiltonian allows a block

diagonalization of the transfer matrix, and it can be shown that  $\lambda_1$  occurs in its totally symmetric subblock,  $\mathbf{T}_s$  [16]. This significantly reduces the size of the matrix to be handled. This reduced matrix  $\mathbf{T}_s$  is constructed by [15–17]

- (i) Identifying equivalence classes, labeled  $\alpha$ , of  $\mathbf{n}_i$  states which can be transformed into each other by rotations and/or reflections among the  $M$  sites in one row (ring).
- (ii) Constructing the matrix elements

$$(\mathbf{T}_s)_{\alpha\beta} = \sum_{\mathbf{n}_{i+1} \in \beta} T(\mathbf{n}_i \in \alpha, \mathbf{n}_{i+1}) \quad (36)$$

Here  $\mathbf{n}_i$  is any one member of the equivalence class  $\alpha$  and the sum is over all the members of  $\beta$ , i.e., over columns of Boltzmann factors in  $\mathbf{T}$ .

As an example, for  $M = 4$ , we list the six equivalence classes of the four sites in terms of their occupation numbers:

	1	2	3	4	5	6
$\alpha$	(0000)	(0001) (0010) (0100) (1000)	(0011) (0110) (1100) (1001)	(0101) (1010)	(0111) (1110) (1101) (1011)	(1111)
$p_\alpha$	0	1	2	2	3	4
$d_\alpha$	1	4	4	2	4	1
$m_\alpha$	0	1	3	5	7	15

We have also given the number of particles,  $p_\alpha$ , and the degeneracy,  $d_\alpha$ , associated with each equivalence class and the base-10 equivalent,  $m_\alpha$ , of the binary number associated with state  $\alpha$ . Because  $m_\alpha$  uniquely determines the occupancies in  $\alpha$  a mere (cyclic) bitshifting generates all equivalent states. This results in a reduced transfer matrix  $\mathbf{T}_s$  of the form

$$\begin{bmatrix} 1 & 4z^{1/2} & 4zy & 2z & 4z^{3/2}y^2 & z^2y^4 \\ z^{1/2} & z(3+y) & z^{3/2}y(3+y) & z^{3/2}(1+y) & z^2y^2(3+y) & z^{5/2}y^5 \\ 2y & 2z^{3/2}y^2(1+y) & z^2y^2(1+y)^2 & 2z^2y^2 & 2z^{5/2}y^4(1+y) & z^3y^7 \\ z & 2z^{3/2}(1+y) & 4z^2y^2 & z^2(1+y^2) & 2z^{5/2}y^3(1+y) & z^3y^6 \\ z^{3/2}y^2 & z^2y^2(1+3y) & 2z^{5/2}y^4(1+y) & z^{5/2}y^3(1+y) & z^3y^6(1+3y) & z^{7/2}y^9 \\ z^2y^4 & 4z^{5/2}y^5 & 4z^3y^7 & 2z^3y^6 & 4z^{7/2}y^9 & z^4y^{12} \end{bmatrix} \quad (37)$$

Terms in this matrix have the form  $z^{(p_\alpha+p_\beta)/2}y^{c_{\alpha\beta}}$ , where  $c_{\alpha\beta}$  is the total number of nearest-neighbor pairs within and between states  $\alpha$  and  $\beta$ . The

determination of the latter is a straightforward procedure in binary operations. For example, to get the number of nearest-neighbor bonds in state  $\alpha$  one performs a cyclic bitshift by one lattice site, followed by a binary AND of the two states, and counts the number of bits. Because the coverage and the correlation functions are obtained as derivatives of  $T_s$  with respect to  $z$  or  $y$ , this simply brings down the powers of  $z$  and  $y$ ; i.e., the terms in the derivative matrix become simple multiples of those in  $T_s$  itself. In terms of its eigenvectors the coverage can be written as

$$\theta = \frac{1}{M} \sum_{\alpha} p_{\alpha} v_{1\alpha}^L v_{1\alpha}^R \quad (38)$$

If  $T$  is symmetric then  $v_{1\alpha}^L = d_{\alpha} v_{1\alpha}^R$  and only one eigenvector calculation is required. Multi-site and longer-ranged correlators are obtained by appropriate bond counting, without the explicit introduction of the corresponding interactions into the Hamiltonian, however.

Because the eigenvalue  $\lambda_1$  depends on the strip width  $M$ , the latter must be chosen large enough to render the observables of interest independent of this choice. In addition, the strip geometry and width must be commensurate with possible ordered structures. For a square lattice we can account for all nearest and next-nearest neighbor interactions by considering the states of two adjacent rows, provided  $M$  is a multiple of 2. For example, for the numbered sites shown in Fig. 1(a), sites 1 and 4 are neighbors in the construction of  $T$  as are sites 5 and 8. For  $V_{1n} > 0$  the proper minimum energy configuration at half a monolayer, corresponding to a  $c(2 \times 2)$  structure, has  $n_1 = n_3 = n_6 = n_8 = 1$  and  $n_2 = n_4 = n_5 = n_7 = 0$ , or vice versa. If one chose

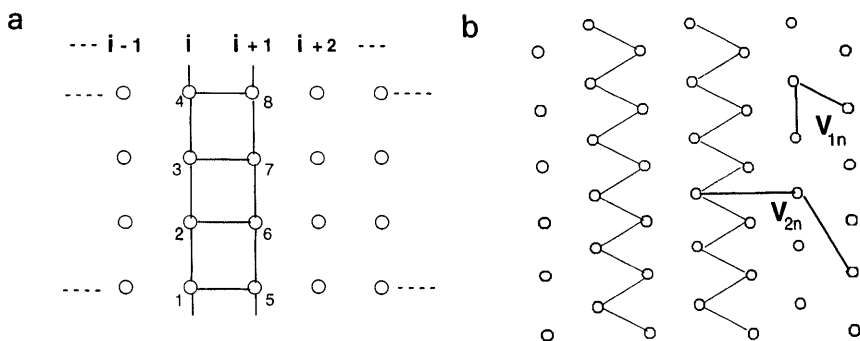


**FIG. 1** (a) Schematic of a semi-infinite square lattice of width four sites, nearest neighbor interactions indicated. (b) The 24 sites involved in the construction of the transfer matrix for nearest and next-nearest neighbor interactions on a hexagonal lattice for  $M = 6$ .



$M = 3$  one would average over configurations which have periodicity 2 in either direction. For attractive interactions this is of no concern. However, if third-neighbor interactions are to be included, the elementary unit for which the equivalence class states are constructed must now consist of two adjacent rows of  $M$  sites each. The original (2-row) transfer matrix is no longer symmetric and has dimension  $2^{2M}$  where now, in addition,  $M$  must be a multiple of 4 for  $V_{3n} > 0$ . As an example, for first and second neighbor interactions on a hexagonal lattice with the strip geometry, as shown in Fig. 1(b), the reduced 2-row transfer matrix  $\mathbf{T}_s$  has dimension 700 for  $M = 6$ .

To determine the largest eigenvalue and eigenvector the power method [32] is most efficient. However, in the presence of interactions it is frequently the case that a second and third eigenvalue approach the first in magnitude, which requires the extension of the method to guarantee the accuracy of the solution. In particular, the onset of degeneracy of the two largest eigenvalues signals the approach to a phase boundary, for which the correlation length, given by the ratio of the two largest eigenvalues,  $\xi_M^{-1} \sim \ln(\lambda_1/|\lambda_2|)$ , diverges.

As almost all quantities of interest are required as a function of coverage and temperature, an inversion of  $\theta(T, \mu, M)$  to  $\mu(T, \theta, M)$  is required. The computationally accurate method of doing this is to find the zero of  $\theta(T, \mu, M) - \theta_i$  as a function of  $\mu$  on a prescribed coverage mesh  $\{\theta_i\}$  with an efficient routine. This requires an initial estimate of a range of  $\mu$  (i.e., extrapolation from the last mesh point), starting at low coverage where  $\mu(T, \theta)$  is known analytically. The coverage mesh can be nonuniform but must be dense enough to ensure continuation in regions where  $\mu$  varies rapidly with  $\theta$ . Any further calculation, for example of desorption spectra where both  $T$  and  $\theta$  vary, is most efficiently done by interpolating a set of such isotherms.

Transfer matrix calculations of the adsorbate chemical potential have been done for up to four sites (ontop, bridge, hollow, etc.) or four states per unit cell, and for 2-, 3-, and 4-body interactions up to fifth neighbor on primitive lattices. Here the various states can correspond to quite different physical systems. Thus a 3-state, 1-site system may be a two-component adsorbate, e.g., atoms and their diatomic molecules on the surface, for which the occupations on a site are no particles, an atom, or a molecule. On the other hand, the three states could correspond to a molecular species with two bond orientations, perpendicular and tilted, with respect to the surface. An  $n$ -state system could also be an  $(n - 1)$  layer system with ontop stacking. The construction of the transfer matrices and associated numerical procedures are essentially the same for these systems, and such calculations are done routinely [33]. If there are two or more non-reacting (but interacting) species on the surface then the partial coverages depend on the chemical potentials specified for each species.

## D. Examples

To illustrate the power of the transfer matrix approach and, at the same time, the effect of the dimension  $M$ , we calculate the heat of adsorption for a simple adsorbate on a square lattice with nearest neighbor repulsion [29]. In Fig. 2(a) we show  $Q_{\text{iso}}(\theta, T)$  for a set of reduced temperatures,  $T/V_{1n}$ , obtained (a) in the (analytical) quasichemical approximation, Eq. (16), (b) from the  $M = 4$  transfer matrix, Eq. (37), and (c) for  $M = 8$ , for which the results are essentially exact. The drop at half coverage has been discussed earlier. The significant new features emerging from the semi-infinite ( $M \times \infty$ ) lattice are (i) the sharpening of the plateaus at lowest  $T$ , and (ii) the appearance of local maxima and minima around half coverage, most pronounced for temperatures less than the ordering temperature of the  $c(2 \times 2)$  structure at  $T_c/V_{1n} \simeq 0.57$ . This latter feature has been experimentally observed and quantitatively explained for CO on (hexagonal) Ru(0001) [30]. It cannot be reproduced in any finite cluster calculations because they treat the statistics of lattices of such small size that they miss much of the variation of entropy that occurs upon ordering. The correlators and comparison TPD spectra, corresponding to the panels in Fig. 2, can be found elsewhere [29].

As an example of a multilayer system we reproduce, in Fig. 3, experimental TPD spectra of Cs/Ru(0001) [34,35] and theoretical spectra [36] calculated from Eq. (4) with  $\mu(\theta, T)$  calculated by the transfer matrix method with  $M = 6$  on a hexagonal lattice. In the lattice gas Hamiltonian we have short-ranged repulsions in the first layer to reproduce the  $(\sqrt{3} \times \sqrt{3})$  and  $p(2 \times 2)$  structures in addition to a long-ranged mean field repulsion. Second and third layers have attractive interactions to account for condensation in layer-by-layer growth. The calculations not only successfully account for the gross features of the TPD spectra but also explain a subtle feature of delayed desorption between third and second layers. As well, the lattice gas parameters obtained by this fit reproduce the bulk sublimation energy of cesium in the third layer.

As an example of a system with a complex desorption mechanism and considerable complexity in its adsorbate structure we look at Te/W(100) [37]. The adsorbate has atoms on both bridge and hollow sites on a square lattice, and shows a variety of ordered structures at  $\theta = 1/3, 1/2, 2/3$ , and  $1ML$ . The interesting feature in desorption is the competition between a direct atomic (as Te) and an associative molecular channel (as  $\text{Te}_2$ ). The rate of the latter has a form similar to Eq. (5). Fig. 4 shows the experimental spectra [38]. The minimum set of interactions amongst hollow and bridge sites necessary to explain the orderings is shown in Fig. 5. Implicit in the model is a hardcore exclusion of the four neighboring bridge (hollow) sites of each hollow (bridge) site. The transfer matrix was constructed for all the

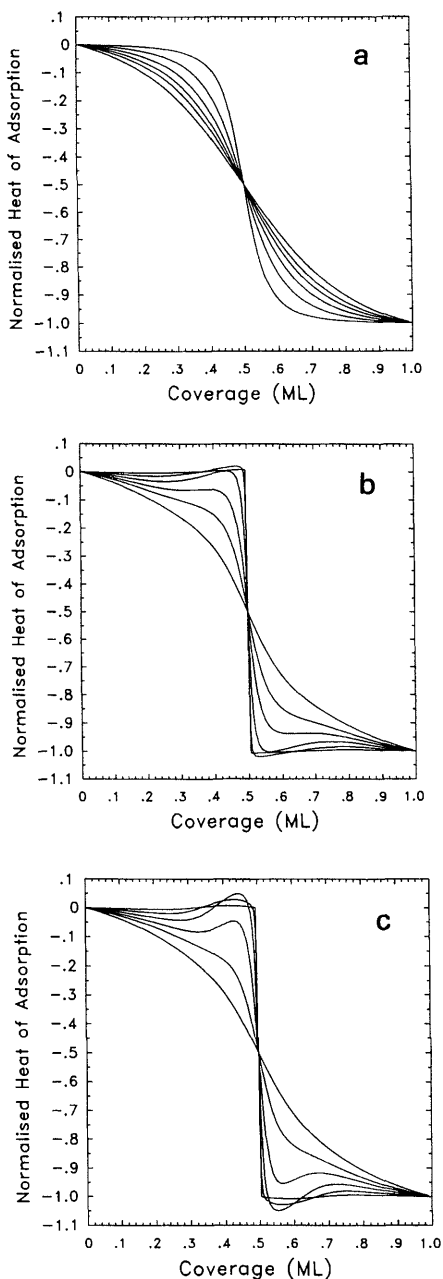


**FIG. 2** Normalized isosteric heat,  $(Q_{\text{iso}}(\theta, T) - Q_{\text{iso}}(0, T))/4V_{ln}$ , as a function of coverage for first neighbor repulsion on a square lattice, for temperatures (top to bottom at  $0.2 \text{ ML}$ )  $k_B T / V_{ln} = 0.25, 0.35, 0.45, 0.55, 0.65, 0.85$ . (a) Quasichemical approximation, see Eq. (16); (b) transfer matrix result for  $M = 4$ ; and (c) for  $M = 8$ .

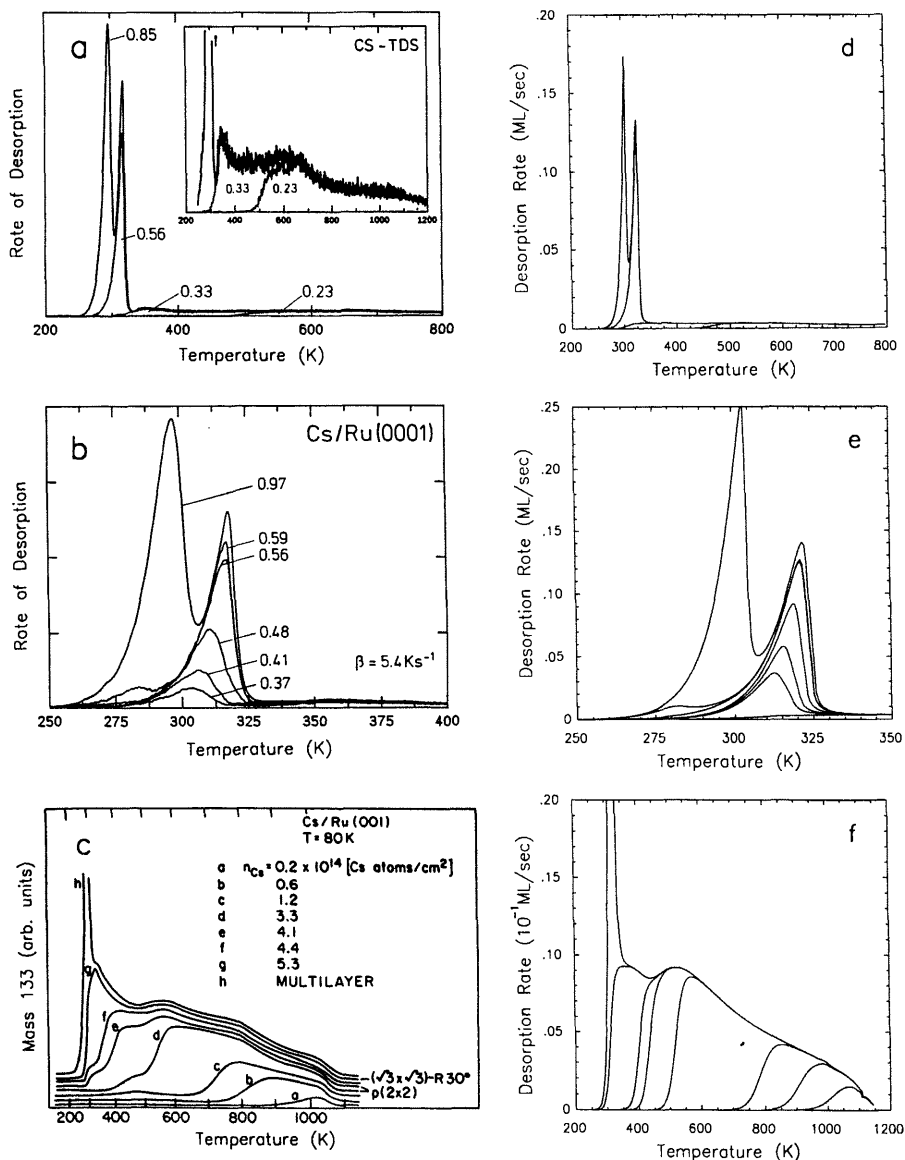


**FIG. 3** (a) TPD data of the first three layers of Cs on Ru(001) obtained with a heating rate of  $5.4 \text{ K s}^{-1}$ . (b) TPD for second and third layers with  $5.4 \text{ K s}^{-1}$  [35]. (c) TPD for first layer with  $15 \text{ K s}^{-1}$  [34]. The theoretical fit to these data is with the following parameters, cf. Eq. (28):  $V_0^{(1)} = 3.1 \text{ eV}$ ,  $V_0^{(2)} = 2.67 \text{ eV}$ ,  $V_0^{(3)} = 2.59 \text{ eV}$ ,  $V_{11} = V_{12} = 0.172 \text{ eV}$ , (second neighbor)  $V'_{11} = 0.02 \text{ eV}$ ,  $V_{22} = V_{33} = 0.05 \text{ eV}$ ,  $V'_{22} = -0.05 \text{ eV}$ ,  $V'_{33} = -0.06 \text{ eV}$ ,  $\nu_z = 1.8 \times 10^{12} \text{ s}^{-1}$ ,  $\nu_x = \nu_y = 3 \times 10^{11} \text{ s}^{-1}$ . Initial coverages in the lattice gas  $\theta_0 = 1.0, 0.66, 0.33, 0.23$  for (d),  $1.14, 0.69, 0.66, 0.56, 0.48, 0.43$  for (e), and  $0.4, 0.33, 0.27, 0.25, 0.20, 0.074, 0.037, 0.012$  for (f). (From Ref. 36.)

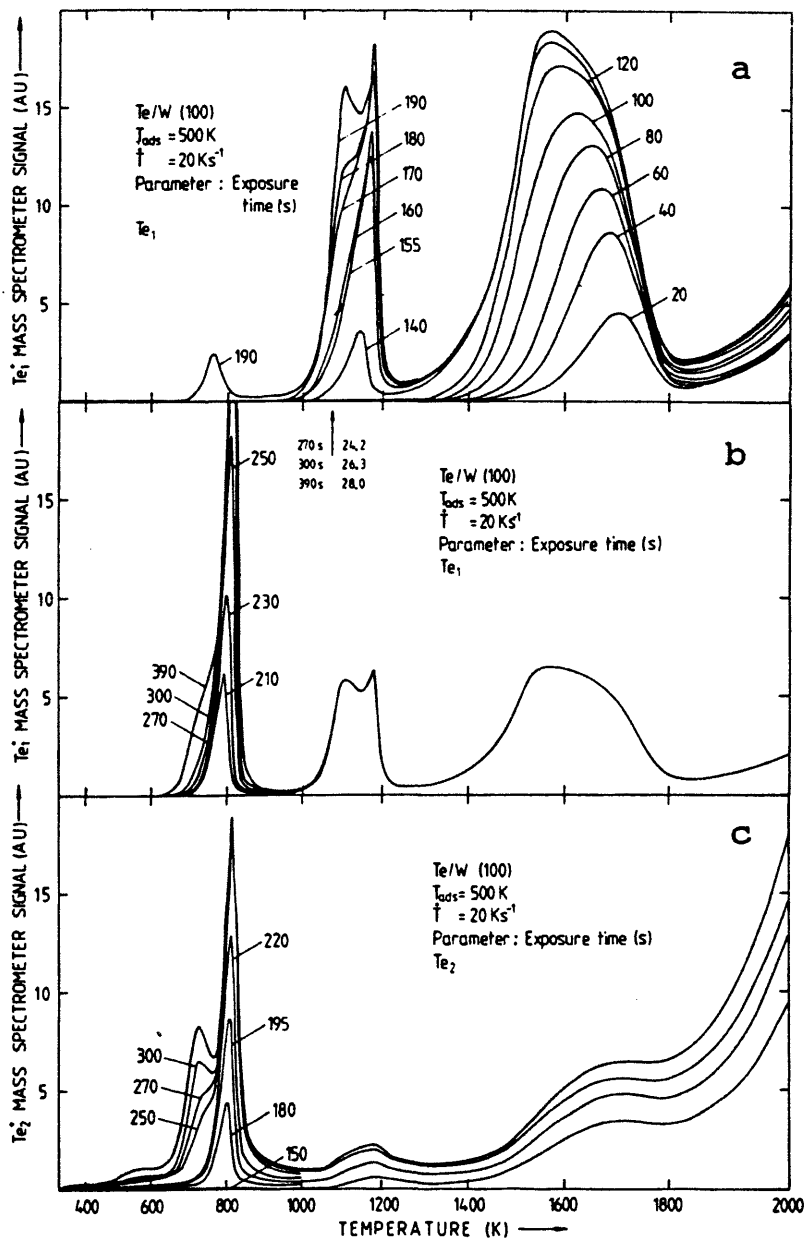


**FIG. 4** TPD spectra for Te adsorbed on W(100) at 500 K, and desorbing as  $\text{Te}_1$  (a,b) and  $\text{Te}_2$  (c). Mass spectrometer/electrometer ranges vary as  $1 \times 10^{-8}$  (a),  $3 \times 10^{-8}$  (b),  $3 \times 10^{-9}$  (c). Heating rate  $20 \text{ K s}^{-1}$ . Coverage parameter is exposure (s) with 1 ML corresponding to 300 s approximately. Signals above 1800 K (a), 900 K (c) are spurious. (Reprinted from Ref. 38 with permission from Elsevier Science.)

possible occupations of two adjacent strips of hollow and bridge sites, each containing six hollow sites, which accommodate structures of period 2 and 3. One such strip is shown in Fig. 5. Although hardcore exclusion eliminates many of the site occupations occurring in two neighboring strips, the matrix  $T_s$  has dimension 700. In Fig. 6 the results of the lattice gas calculations of the TPD spectra of the atomic and molecular components are shown in panels (a) and (b). Note that once the atomic desorption spectra are fitted, the desorption temperature of the molecular spectra is essentially fixed. The magnitude of molecular desorption is solely determined by the dissociative sticking coefficient for adsorption! As a further example of the information that can be extracted from transfer matrix calculations we show, in panels (c) and (d) of Fig. 6, some isothermal partial coverages and desorption rates for the hollow and bridge sites, demonstrating the transfer of particles between these sites.

Our last example of the utility of the transfer matrix approach concerns the thermodynamics and desorption kinetics of H/Rh(311) obtained from

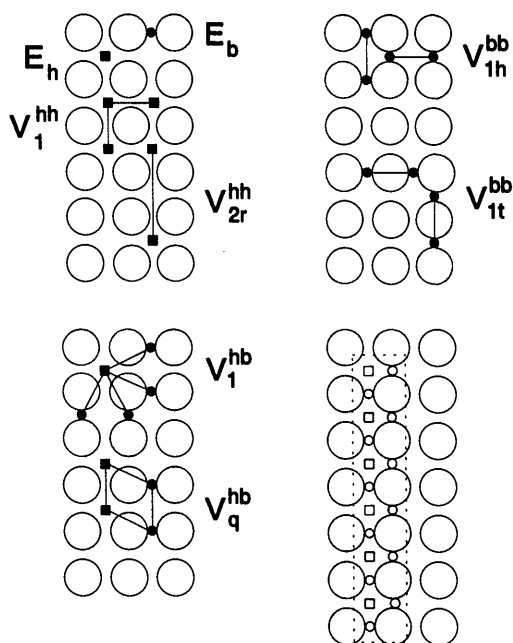


**FIG. 5** Schematic of site parameters and interactions employed for the hollow-bridge site model of Te on W(100). Also depicted are the six hollow sites (squares) and adjacent bridge sites (small open circles) allowed in one strip in the construction of the transfer matrix. (Reprinted from Ref. 37 with permission from Elsevier Science.)

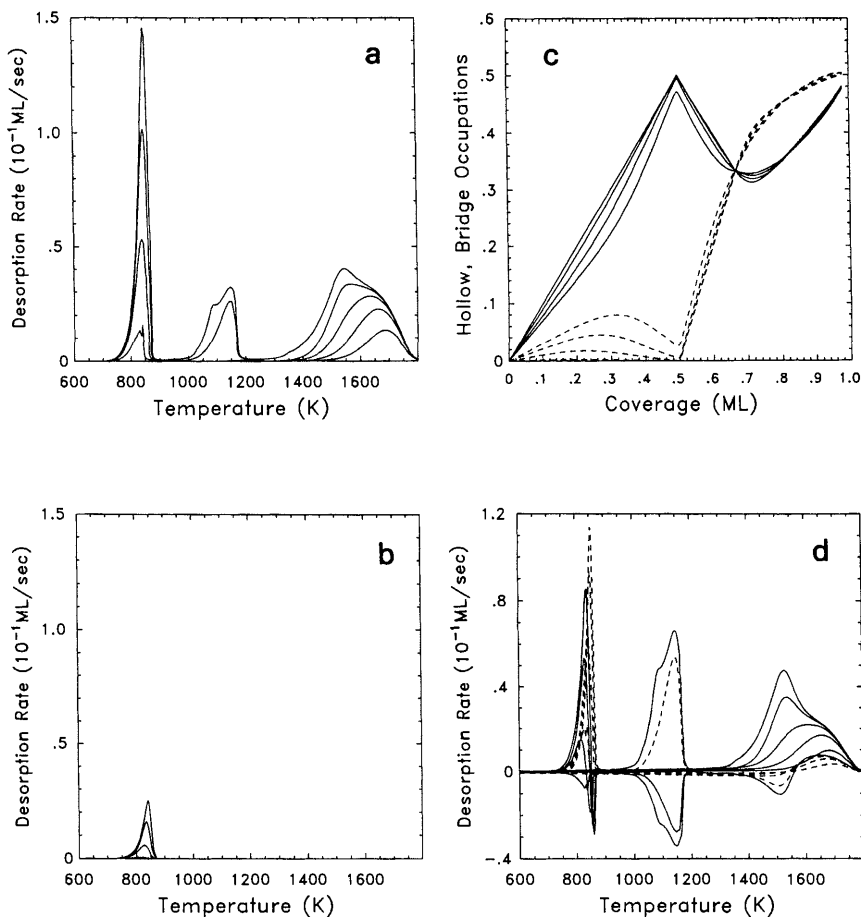


**FIG. 6** (a) Atomic desorption rates calculated with the two-site lattice gas model of Te/W(100). Adatom binding energies  $V_{0h} = 5.09$  eV,  $V_{0b} = 4.81$  eV,  $\nu_x = \nu_y = \nu_z = 5 \times 10^{12} \text{ s}^{-1}$ , (for both sites); adatom interactions,  $V_{1h}^{(hh)} = 0.69$  eV,  $V_{2r}^{(hh)} = 0.026$  eV,  $V_{1h}^{(bb)} = 0.30$  eV,  $V_{1t}^{(bb)} = 0.69$  eV,  $V_{1h}^{(hb)} = 0.26$  eV,  $V_q^{(hb)} = -0.043$  eV,  $m = 127$  amu;  $\text{Te}_2$  dissociation energy  $D_0 = 2.38$  eV,  $T_{\text{vib}} = 356$  K,  $T_{\text{rot}} = 0.06$  K; atomic and dissociative sticking  $S_a = 1$ ,  $S_{\text{dis}} = 0.005$ , heating rate  $20 \text{ K s}^{-1}$ , adsorption site area  $a_s = 8 \text{ \AA}^2$ . Initial coverages 0.1, 0.2, ..., 0.9, 1.0 ML. (b) Molecular rate. (c) Isothermal coverages of hollow and bridge sites (solid and dashed lines, respectively) as a function of total coverage for temperatures spanning the desorption range (top to bottom at 0.3 ML for solid lines),  $T = 600 \text{ K}$ , 1000 K, 1400 K, 1800 K. (d) Desorption rates from these sites for the initial coverages of (a). (Reprinted from Ref. 37 with permission from Elsevier Science.)

an anisotropic lattice gas model [39] with three- and fourfold coordinated adsorption sites, first neighbor attraction along the closed-packed  $[01\bar{1}]$  direction, and first and second neighbor and trio repulsions in the  $[1\bar{1}\bar{2}]$  direction to account for  $(1 \times n)$  structures at coverages  $\theta = 1/4, 1/3, 1/2$ , and  $2/3$ , shown in Fig. 7. The experimental TPD data and the theoretical fit are overlaid in Fig. 8(a). LEED intensities were also measured during desorption. Because they are proportional to the square of density-density

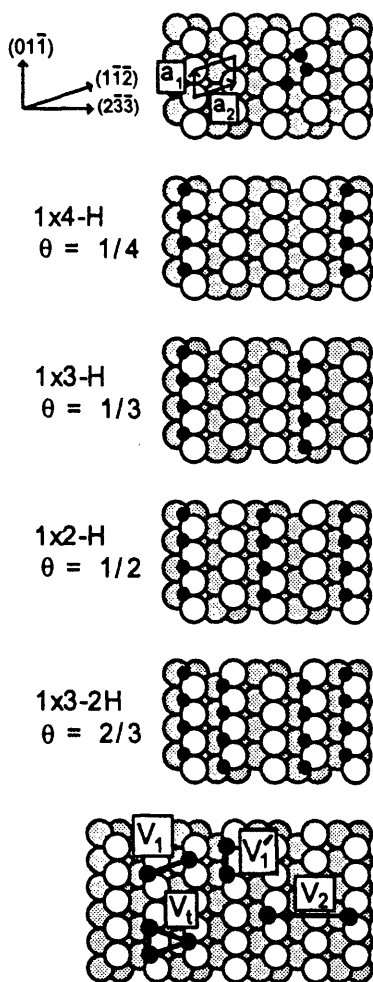


**FIG. 7** Ordered structures of hydrogen on Rh(311) and model interactions. (Reprinted from Ref. 39 with permission from Elsevier Science.)



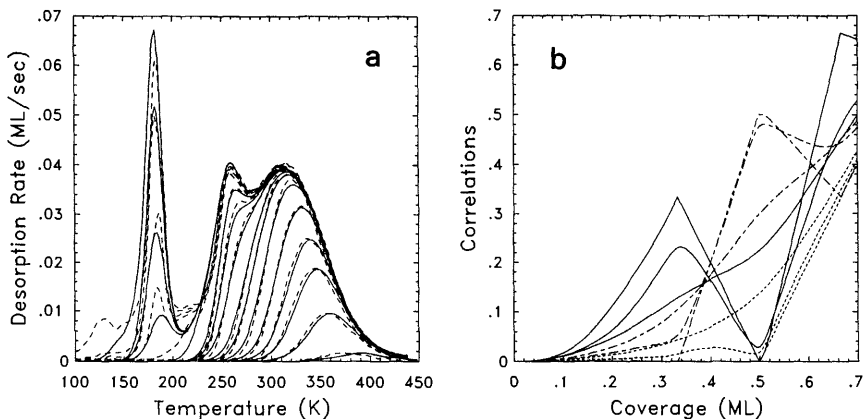


**FIG. 8** (a) Model TPD spectra (solid lines) and experimental data (dashed lines) for H on Rh(311) for initial coverages in the range 0.01 to 0.68 ML. Heating rate 10 K/s. Surface energy parameters:  $V_0 = 2.647$  eV,  $V'_{1n} = -0.029$  eV,  $V_{1n} = 0.035$  eV,  $V_{2n} = 0.022$  eV,  $V_{\text{trio}} = 0.011$  eV; vibrational frequencies  $2 \times 10^{13} \text{ s}^{-1}$ ,  $1.3 \times 10^{13} \text{ s}^{-1}$ ,  $5 \times 10^{10} \text{ s}^{-1}$ ; site area  $a_s = 12 \text{ \AA}^2$ ; dissociation energy  $D_0 = 4.478$  eV;  $T_{\text{vib}} = 6332$  K,  $T_{\text{rot}} = 87.6$  K. (b) Isothermal correlators as a function of coverage, for temperatures 350, 220, 100 K (with sharpest features at lowest temperature):  $C_1$  dotted line,  $C_2$  long-short dashed,  $C_3$  solid. (Reprinted from Ref. 39 with permission from Elsevier Science.)

correlations and the latter can be calculated from the transfer matrix, simultaneously with the chemical potential, one can further elucidate the structures and show their influence on TPD. The 2-site correlators of interest are

$$C_k = \langle n_{rc} n_{r,c+k} \rangle \quad (39)$$

which for  $k = 1, 2, 3$  give the probabilities of finding first, second, and third neighbor sites occupied in the  $[1\bar{1}\bar{2}]$  direction. For a completely disordered adsorbate these correlators have the value  $\theta^2$ . At sufficiently low temperature they attain the values  $(C_1, C_2, C_3) = (0, 0, 1/3)$ ,  $(0, 1/2, 0)$ , and  $(1/3, 1/3, 2/3)$  at  $\theta = 1/3$ ,  $1/2$ , and  $2/3$  for the  $1 \times 3$ -H,  $1 \times 2$ -H and  $1 \times 3$ -2H structures of Fig. 7, respectively. Fig. 8(b) shows their coverage dependence for temperatures over the desorption range. Segments of linear dependence on coverage at the lowest temperature show rises and falls which are characteristic of the changes of order taking place.

In Fig. 9 we show the evolution of the experimental (left panels) and calculated (right panels) LEED intensities during desorption for initial coverages  $1/3$ ,  $1/2$ , and  $2/3$  ML but for a smaller heating rate ( $1 \text{ K s}^{-1}$ ) than in Fig. 8(a). Also shown are the corresponding experimental and

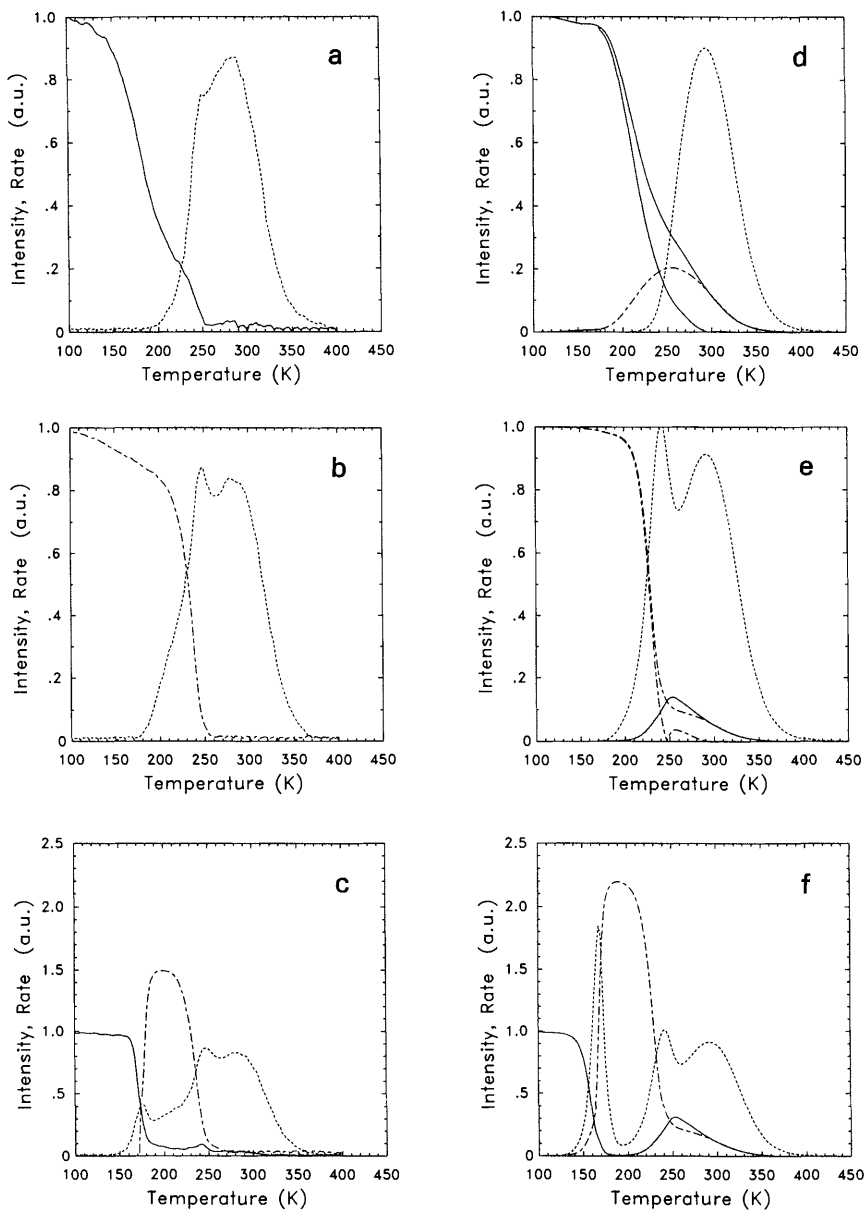


**FIG. 9** (a–c) Experimental LEED intensities for  $(1 \times 3)$  (solid line) and  $(1 \times 2)$  (long-short dashed) structures and corresponding TPD rates (dotted lines) as a function of desorption temperature for approximate initial coverages  $1/3$ ,  $1/2$ ,  $2/3$  ML. Arbitrary units. (d–f) Theoretical LEED intensities, calculated with Eq. (40), and theoretical TPD rates for these initial coverages. Heating rate 1 K/s. (Reprinted from Ref. 39 with permission from Elsevier Science.)

calculated TPD spectra for this heating rate (dotted lines). The intensities are calculated from

$$I(\mathbf{k}, T) = I_0 \sum_{i,j=1}^M \langle n_i n_j \rangle \exp(i\mathbf{k} \cdot (\mathbf{r}_i - \mathbf{r}_j)) \quad (40)$$

in terms of two-particle correlators. Because of the attraction in the  $[01\bar{1}]$  direction the correlators do not depend crucially on the interparticle spacings in this direction. Ordering is therefore mainly reflected in the variation of the correlators in the  $[1\bar{1}\bar{2}]$  direction and, consequently, we can simplify the calculation and use the 2-site correlators calculated in the finite strip direction of the transfer matrix. We have  $|i - j| < 12$  in our calculations.

For initial coverage  $1/3$  we show in panel (d) of Fig. 9 the intensity of the third-order spot ( $|\mathbf{k}| = 1/3(2\pi/|a_2|)$ ) (upper solid line) and that of the half-order spot (long-short dashed line) as a function of desorption temperature. The rise of the half-order intensity reflects the disordering as the coverage diminishes below  $1/3$  ML in desorption. This intensity also builds up for other wave vectors in the same temperature range, approaching the same value in the high temperature edge where total disordering has occurred. Experimentally this is seen as a smearing of the LEED intensities along the line of the third-order spots. This background has already been subtracted for the experimental spot intensity in panel (a). We mimic this procedure by subtracting the half-order intensity (the largest background contribution) from the third-order intensity to obtain the lower solid line in panel (d). A similar subtraction has been done in panel (e). The agreement with the experimental curves is very good in all cases, considering that the subtraction procedures are not identical.

Additional applications of the transfer matrix method to adsorption and desorption kinetics deal with other molecules on low index metal surfaces [40–46], multilayers [47–49], multi-site stepped surfaces [50], and co-adsorbates [51–55]. A similar approach has been used to study electrochemical systems.

### III. KINETIC LATTICE GAS MODELS

If it cannot be guaranteed that the adsorbate remains in local equilibrium during its time evolution, then a set of macroscopic variables is not sufficient and an approach based on nonequilibrium statistical mechanics involving time-dependent distribution functions must be invoked. The kinetic lattice gas model is an example of such a theory [56]. It is derived from a Markovian master equation, but is not totally microscopic in that it is based on a phenomenological Hamiltonian. We demonstrate this approach

with three examples: (i) an adsorbate with nondissociative adsorption; (ii) precursor-mediated adsorption and desorption, and (iii) a system in which adsorption and desorption are accompanied by surface reconstruction. Our basic assumption is that the kinetic phenomena of adsorption, desorption, and surface diffusion can be described as Markov processes with the occupation numbers in the Hamiltonian (6) as stochastic variables.

### A. Nondissociative Adsorption

We introduce a function  $P(\mathbf{n}, t)$  which gives the probability that the state  $\mathbf{n} = (n_1, n_2, \dots, n_{N_s})$  is realized at time  $t$ , where  $N_s$  is now the total number of adsorption sites on the surface. It satisfies a master equation

$$\frac{dP(\mathbf{n}, t)}{dt} = \sum_{\mathbf{n}'} [W(\mathbf{n}, \mathbf{n}')P(\mathbf{n}', t) - W(\mathbf{n}', \mathbf{n})P(\mathbf{n}, t)] \quad (41)$$

where  $W(\mathbf{n}', \mathbf{n})$  are the transition probabilities per unit time that the system changes from a state  $\mathbf{n}$  to  $\mathbf{n}'$ . They are not completely arbitrary but must satisfy detailed balance

$$\begin{aligned} W(\mathbf{n}', \mathbf{n}) \exp \left[ -\beta \left( H(\mathbf{n}) - \mu \sum_{i(\mathbf{n})} n_i \right) \right] \\ = W(\mathbf{n}, \mathbf{n}') \exp \left[ -\beta \left( H(\mathbf{n}') - \mu \sum_{i(\mathbf{n}')} n'_i \right) \right] \end{aligned} \quad (42)$$

To specify these transition probabilities we make the further assumption that the residence time of a particle in a given adsorption site is much longer than the time of an individual transition to or from that state, either in exchange with the gas phase in adsorption and desorption or for hopping across the surface in diffusion. In such situations there will be only one individual transition at any instant of time and the transition probabilities can be summed, one at a time, over all possible processes (adsorption, desorption, diffusion) and over all adsorption sites on the surface. To implement this we first write

$$W(\mathbf{n}', \mathbf{n}) = W_{\text{ad-des}}(\mathbf{n}', \mathbf{n}) + W_{\text{diff}}(\mathbf{n}', \mathbf{n}) \quad (43)$$

as a sum of adsorption-desorption and diffusion terms. For the former we

then write the most general power series in the occupation numbers [57]

$$\begin{aligned}
 W_{\text{ad-des}}(\mathbf{n}', \mathbf{n}) = w_0 \sum_l \left[ (1 - n_l) \left( 1 + A_1 \sum_{l'} n_{l'} + A_2 \sum_{l'l''} n_{l'} n_{l''} + \cdots \right) \right. \\
 \left. + D_0 n_l \left( 1 + D_1 \sum_{l'} n_{l'} + D_2 \sum_{l'l''} n_{l'} n_{l''} + \cdots \right) \right] \\
 \times \delta(n'_l, 1 - n_l) \prod_{l' \neq l} \delta(n'_l, n_l)
 \end{aligned} \quad (44)$$

Here the sums over  $l', l''$  run over the neighbors of  $l$ . The highest term is a product of  $(c + 1)$  factors with  $c$  the coordination number of the lattice.

Detailed balance imposes a set of restrictions on the coefficients  $A_n, D_n$ . For example, if there is only one adparticle present, say in site  $i$ , so that  $n_i = 1$  and all other  $n_j = 0, j \neq i$ , then Eq. (42) gives

$$w_0 D_0 \exp[-E_s/k_B T] = w_0 \quad (45)$$

so that

$$D_0 = e^{\beta(E_s - \mu)} \quad (46)$$

Note that  $w_0$  cannot be fixed by detailed balance, the reason being that it contains the information about the energy exchange with the solid which is not contained in the static lattice gas Hamiltonian. However, by comparison with the phenomenological rate equation (1) we can identify it as

$$w_0 = S_0 \frac{P \lambda_{\text{th}} a_s}{h} \quad (47)$$

To get the other coefficients we next specify that two particles are adsorbed on neighboring sites,  $n_i = n_{i+a} = 1$  with all other sites empty, and get

$$1 + A_1 = (1 + D_1) e^{-\beta V_{1n}} \quad (48)$$

From situations where three and four neighboring sites are occupied we get, respectively,

$$1 + 2A_1 + A_2 = (1 + 2D_1 + D_2) e^{-2\beta V_{1n}} \quad (49)$$

$$1 + 3A_1 + 3A_2 + A_3 = (1 + 3D_1 + 3D_2 + D_3) e^{-3\beta V_{1n}} \quad (50)$$

and so on, for a total of  $c$  constraints (and nearest neighbor interactions only). If longer-ranged interactions are included, this introduces further coefficients and half as many further constraints.

The fact that detailed balance provides only half the number of constraints to fix the unknown coefficients in the transition probabilities is not really surprising considering that, if it would fix them all, then the static (lattice gas) Hamiltonian would dictate the kind of kinetics possible in the system. Again, this cannot be so because this Hamiltonian does not include the energy exchange dynamics between adsorbate and substrate. As a result, any functional relation between the  $A$  and  $D$  coefficients in (44) must be postulated *ad hoc* (or calculated from a microscopic Hamiltonian that accounts for coupling of the adsorbate to the lattice or electronic degrees of freedom of the substrate). Several scenarios have been discussed in the literature [57].

The simplest choice is to set all  $A_i = 0$  in (44). Physically this means that an adsorbing particle will not experience any interactions with its prospective neighbors, and sticking is solely controlled by the availability of sites. Thus the sticking coefficient becomes (for  $A_i = 0$ )

$$S(\theta, T) = S_0(T)(1 - \theta) \quad (51)$$

The sticking coefficient at zero coverage,  $S_0(T)$ , contains the dynamic information about the energy transfer from the adsorbing particle to the solid which gives rise to its temperature dependence, for instance, an exponential Boltzmann factor for activated adsorption.

The desorption kinetics are thus specified by

$$D_r = [e^{\beta V_{1n}} - 1]^r \quad (52)$$

for  $r = 1, \dots, c$ . Because  $(e^\alpha - 1)n = e^{n\alpha} - 1$  for  $n = 0, 1$  we can rewrite (44) as

$$W_{\text{ad-des}}(\mathbf{n}', \mathbf{n}) = w_0 \sum_l \left[ (1 - n_l) + D_0 n_l \exp \left( \beta V_{1n} \sum_j n_l n_j \right) \right] \\ \times \delta(n'_l, 1 - n_l) \prod_{l' \neq l} \delta(n'_{l'}, n_{l'}) \quad (53)$$

implying that the local environment enters the desorption rate via a Boltzmann factor. This kind of kinetics has been termed Langmuir kinetics: It contains simple desorption kinetics and trivial adsorption due to site exclusion only. This interconnection between adsorption and desorption is dictated by the principle of detailed balance: If an adsorption system with nondissociative adsorption does not show the linear decrease of sticking as a function of coverage, then its desorption kinetics is most likely also not controlled by (52); if direct sticking and desorption are still maintained then Langmuir kinetics must be abandoned. (Precursors, i.e., nondirect

adsorption and desorption, can also alter the kinetics and this will be discussed below.)

Insisting on the Langmuir kinetics is overly restrictive because in most systems sticking is not controlled by site exclusion only. Because the energy transfer in the adsorption process takes place within angstroms of the surface, the adsorbing particle actually experiences the interaction with particles already adsorbed on neighboring sites in more or less the same way as desorbing particles do, i.e., a lateral repulsion (attraction) will aid (hinder) desorption. Thus, making the effect of lateral interactions symmetric for adsorption and desorption, one would set  $A_r = -D_r$ ; we have called this the interaction kinetics. More generally, one can assume a linear relationship (although this is dictated only by arguments of simplicity) and find

$$A_r = \gamma D_r \quad (54)$$

$$D_r = \frac{\exp(r\beta V_{1n}) - 1}{1 - \gamma \exp(r\beta V_{1n})} - \binom{r}{1} D_1 - \binom{r}{2} D_2 - \cdots - \binom{r}{r-1} D_{r-1} \quad (55)$$

This completes the adsorption-desorption kinetics.

Turning next to diffusion, we consider hopping from a site  $l$  to its neighbors  $l+a$  and write

$$\begin{aligned} W_{\text{diff}}(\mathbf{n}', \mathbf{n}) = w_{\text{diff}} \sum_{l,a} \left[ n_l (1 - n_{l+a}) \left( 1 + B_1 \sum_{l'} n_{l'} + B_2 \sum_{l'l''} n_{l'} n_{l''} + \cdots \right) \right. \\ \left. \times \left( 1 + \tilde{B}_1 \sum_{l'} n_{l'} + \tilde{B}_2 \sum_{l'l''} n_{l'} n_{l''} + \cdots \right) \right] \\ \times \delta(n'_l, 1 - n_l) \delta(n'_{l+a}, 1 - n_{l+a}) \prod_{l' \neq l, l+a} \delta(n'_l, n_l) \end{aligned} \quad (56)$$

The individual hopping rate (per unit time) is given by  $w_{\text{diff}}$  which most likely contains a Boltzmann factor to account for an activation barrier to diffusion. The sums over  $l'$  and  $l''$  run over the neighbors of  $l$  (with the exception of  $l+a$ ) and  $l+a$  (with the exception of  $l$ ), respectively. The terms with the coefficients  $B_i$  account for the fact that hopping will be enhanced (hindered) if the particle in its initial state experiences a repulsive (attractive) interaction with some neighbors. Likewise, via the terms with  $\tilde{B}_i$ , hopping will be reduced (enhanced) if the particle tries to jump into a site that is surrounded by occupied sites with which the particle will interact repulsively (attractively). Detailed balance again imposes conditions on these coefficients similar to those in Eqs. (49,50) for adsorption and desorption.

To study the time evolution of the adsorbate we define the coverage

$$\theta(t) = \langle \bullet \rangle = N_s^{-1} \sum_i \sum_{\mathbf{n}} n_i P(\mathbf{n}, t) \quad (57)$$

and get its equation of motion by multiplying the master equation, Eq. (41), with  $n_i$  and summing over all sites and states. This will introduce on its right-hand side  $n$ -site correlation functions which will be site independent if it can be assured that the adsorbate remains homogeneous throughout its time evolution. For a square lattice, as an example, we find

$$\begin{aligned} \frac{d\theta}{dt} = S(\theta, T) \frac{P\lambda_{th}a_s}{h} - r_{des} & \left[ \langle \bullet \rangle + 4D_1 \langle \bullet \bullet \rangle \right. \\ & + D_2 \left( 4 \left\langle \begin{array}{c} \bullet \\ \bullet \end{array} \right\rangle + 2 \langle \bullet \quad \bullet \quad \bullet \rangle \right) \\ & \left. + 4D_3 \left\langle \begin{array}{c} \bullet \\ \bullet \end{array} \right\rangle + D_4 \left\langle \begin{array}{c} \bullet \\ \bullet \end{array} \right\rangle \right] \quad (58) \end{aligned}$$

where we have introduced a symbolic notation

$$\begin{aligned} \langle \circ \rangle &= 1 - \langle \bullet \rangle \\ \langle \circ \bullet \rangle &= N_s^{-1} \sum_{\mathbf{n}} (1 - n_i) n_{i+a} P(\mathbf{n}, t) \\ \left\langle \begin{array}{c} \bullet \\ \bullet \end{array} \right\rangle &= N_s^{-1} \sum_{\mathbf{n}} (1 - n_i) n_{i+a} n_{i+a'} P(\mathbf{n}, t) \end{aligned} \quad (59)$$

The sticking coefficient in Eq. (58) is given explicitly by

$$\begin{aligned} S(\theta, T) = S_0(T) & \left[ \langle \circ \rangle + 4A_1 \langle \circ \bullet \rangle + A_2 \left( 4 \left\langle \begin{array}{c} \bullet \\ \circ \end{array} \right\rangle + 2 \langle \bullet \quad \circ \quad \bullet \rangle \right) \right. \\ & \left. + 4A_3 \left\langle \begin{array}{c} \bullet \\ \circ \end{array} \right\rangle + A_4 \left\langle \begin{array}{c} \bullet \\ \circ \end{array} \right\rangle \right] \quad (60) \end{aligned}$$

In addition to the temperature dependence of  $S_0(T)$  is that of the correlation functions, which also determine the coverage dependence.

The correlators (59) are subject to similar equations of motion involving yet higher correlators, the whole hierarchy being equivalent to the original



master equation. For instance, for the 2-particle correlator we have

$$\begin{aligned} \frac{d\langle \bullet\bullet \rangle}{dt} = 2S_0(T) \frac{P\lambda_{th}a_s}{h} & \left[ (1 + A_1)\langle \circ\bullet \rangle + (A_1 + A_2)\left(\langle \bullet \circ \bullet \rangle + 2\left\langle \begin{smallmatrix} \bullet \\ \circ \end{smallmatrix} \bullet \right\rangle\right) \right. \\ & + 3(A_2 + A_3)\left\langle \begin{smallmatrix} \bullet \\ \bullet \end{smallmatrix} \circ \bullet \right\rangle + (A_3 + A_4)\left\langle \begin{smallmatrix} \bullet \\ \bullet \end{smallmatrix} \circ \begin{smallmatrix} \bullet \\ \bullet \end{smallmatrix} \right\rangle \Big] \\ & - 2r_{des} \left[ (1 + D_1)\langle \bullet\bullet \rangle + (D_1 + D_2)\left(\langle \bullet\bullet\bullet \rangle + 2\left\langle \begin{smallmatrix} \bullet \\ \bullet \end{smallmatrix} \bullet \right\rangle\right) \right. \\ & + 3(D_2 + D_3)\left\langle \begin{smallmatrix} \bullet \\ \bullet \end{smallmatrix} \bullet \bullet \right\rangle + (D_3 + D_4)\left\langle \begin{smallmatrix} \bullet \\ \bullet \end{smallmatrix} \bullet \begin{smallmatrix} \bullet \\ \bullet \end{smallmatrix} \right\rangle \Big] \quad (61) \end{aligned}$$

To describe an arbitrary nonequilibrium evolution of the adsorbate we need the whole hierarchy, or at least a suitably truncated subset. We can close the hierarchy at the level of 2-site correlators by a factorization of higher correlators with 1-site overlap [58,59]

$$\langle \bullet \bullet \bullet \rangle = \left\langle \begin{smallmatrix} \bullet \\ \bullet \end{smallmatrix} \bullet \right\rangle = \langle \bullet\bullet \rangle^2 / \langle \bullet \rangle \quad (62)$$

$$\left\langle \begin{smallmatrix} \bullet \\ \bullet \end{smallmatrix} \bullet \bullet \right\rangle = \langle \bullet\bullet \rangle^3 / \langle \bullet \rangle^2 \quad (63)$$

$$\left\langle \begin{smallmatrix} \bullet \\ \bullet \end{smallmatrix} \circ \bullet \right\rangle = \langle \bullet\circ \rangle^3 / \langle \circ \rangle^2 \quad (64)$$

This is the simplest closure and corresponds, for the equilibrium solution, to the quasi-chemical approximation (14). If higher accuracy is required one must keep larger correlators and factor with larger overlap. As an example with 2-site overlap, one writes

$$\left\langle \begin{smallmatrix} \bullet \\ \bullet \end{smallmatrix} \bullet \bullet \right\rangle = \left\langle \begin{smallmatrix} \bullet \\ \bullet \end{smallmatrix} \bullet \right\rangle^2 / \langle \bullet\bullet \rangle \quad (65)$$

which results in three coupled nonlinear equations of motion for  $\langle \bullet \rangle$ ,  $\langle \bullet\bullet \rangle$ , and  $\left\langle \begin{smallmatrix} \bullet \\ \bullet \end{smallmatrix} \bullet \right\rangle$ .

In one dimension the truncation of the equations of motion has been worked out in detail [59]. This has allowed an accurate examination of the role of diffusion in desorption, and implications for the Arrhenius analysis in nonequilibrium situations. The largest deviations from the desorption kinetics of a mobile adsorbate obviously occur for an immobile adsorbate

where surface diffusion is negligible throughout the temperature range of desorption.

We next explore the implications of assuming that surface diffusion is much faster than desorption so that, during desorption, the structure of the adsorbate rearranges itself appropriately for equilibrium at the instantaneous coverage and temperature. As a result, all correlators also assume their equilibrium values and are thus only functions of (instantaneous) coverage and temperature. In such a system the adsorbate is thus in local or quasi-equilibrium on the surface, although during desorption there is no overall equilibrium with the 3-dimensional gas phase above the adsorbate. Because, for a system in quasi-equilibrium, the correlators are known (equilibrium) functions of coverage and temperature, we need only one macroscopic equation to describe the time evolution. This equation has a remarkable structure. First, we note that the equilibrium solution,  $d\theta/dt = 0$ , in Eq. (58) gives for the chemical potential

$$e^{\beta\mu} = \frac{\bar{P}}{k_B T Z_{\text{int}}} \lambda_{\text{th}}^3 = \frac{e^{-\beta V_0}}{q_3 q_{\text{int}}} \frac{\langle \bullet \rangle + 4D_1 \langle \bullet\bullet \rangle_0 + \dots}{\langle \circ \rangle + 4A_1 \langle \circ\bullet \rangle_0 + \dots} \quad (66)$$

where all correlators attain their equilibrium values, indicated by the subscript zero, and should be calculated from the (canonical or grand canonical) partition function, or equivalently from the right-hand sides of their (coupled) equations of motion.

With the help of Eq. (66) we can now rewrite the equation of motion for the coverage (58) for a system maintained in quasi-equilibrium by fast surface diffusion as

$$\frac{d\theta}{dt} = S(\theta, T) \frac{a_s \lambda_{\text{th}}}{h} P - S(\theta, T) \frac{a_s}{\lambda_{\text{th}}^2} \frac{k_B T Z_{\text{int}}}{h} e^{\beta\mu(\theta, T)} \quad (67)$$

where the sticking coefficient is given, as a function of coverage and temperature, by (60). This is precisely the phenomenological rate equation presented in (1) with, however, the sticking coefficient specified explicitly, and is valid for any system. To reiterate: the desorption rate in Eq. (67) consists now of two factors: (i) the equilibrium fugacity of the adsorbate,  $\exp(\beta\mu)$ , controlling the adsorbate energetics and structure, and (ii) the sticking coefficient controlling the gas-substrate energy transfer in adsorption and desorption. Such factorizations, or similar ones, must always be possible for processes that proceed through a sequence of local equilibrium states because they are completely described by equations of motion for the relevant thermodynamic variables, and the factorization ensures that the equilibrium state is independent of the kinetics. An application of this

approach has been presented for oxygen adsorption and desorption from silver [46]

## B. Adsorption and Desorption via Precursors

To further demonstrate the power of the kinetic lattice gas approach we review briefly the work on precursor-mediated adsorption and desorption [60,61]. We consider an adsorbate in which, in addition to the most strongly bound chemisorbed (or physisorbed) adsorbed state, the adparticles can also be found in intrinsic or extrinsic precursor states. One introduces three sets of occupation numbers,  $n_i = 0$  or 1,  $m_i = 0$  or 1, and  $l_i = 0$  or 1, depending on whether the final adsorbed (chemisorbed) state, the intrinsic precursor state (above an empty adsorbed state), or the extrinsic precursor state (above an occupied adsorbed state) is empty or occupied. The static properties of this lattice gas are controlled by a Hamiltonian

$$H = E_s^{(c)} \sum_i n_i + E_s^{(i)} \sum_i m_i + E_s^{(e)} \sum_i l_i + V_{ln}^{(c)} \sum_{i,a} n_i n_{i+a} + V_{ln}^{(i)} \sum_{i,a} m_i n_{i+a} + V_{ln}^{(e)} \sum_{i,a} n_i l_i n_{i+a} + \dots \quad (68)$$

The single particle free energies are given by

$$E_s^{(r)} = -V_R - k_B T \ln(q_3^{(r)} q_{\text{int}}^{(r)}) \quad (69)$$

( $r = c, i, e$ ) in terms of their respective binding energies and partition functions. Furthermore,  $V_{ln}^{(c)}$  is the lateral interaction between two particles in the adsorbed state in nearest neighbor sites, and  $V_{ln}^{(i)}$  and  $V_{ln}^{(e)}$  are the interactions between a particle in the intrinsic or extrinsic precursor state in cell  $i$  and a particle in the adsorbed state in a neighboring site. Longer ranged interactions can easily be added, as is done elsewhere [61]. To describe the time evolution of the adsorbate we use a kinetic lattice gas model recently developed to study the effect of lateral interactions on sticking. For the coverages of the three states we get kinetic equations

$$\begin{aligned} \frac{d\langle n \rangle}{dt} = & S_C^0(T) (1 - \langle n \rangle) \tilde{S}_C \frac{a_s \lambda_{\text{th}}}{h} P - r_C \tilde{f}_C \langle n \rangle \\ & + w_{\text{CI}} [\tilde{f}_{\text{CI}} \langle m \rangle - (a_C/a_I) \tilde{f}_{\text{IC}} \langle n \rangle] \\ & + z w_{\text{CE}} [\tilde{f}_{\text{CE}} (1 - \langle n \rangle) \langle l \rangle - (a_C/a_E) \tilde{f}_{\text{EC}} \langle n \rangle^2] \end{aligned} \quad (70)$$

$$\begin{aligned} \frac{d\langle m \rangle}{dt} = & S_I^0(T) \tilde{S}_I (1 - \langle n \rangle) \frac{a_s \lambda_{th}}{h} P - r_I \tilde{f}_I \langle m \rangle \\ & - w_{CI} [\tilde{f}_{CI} \langle m \rangle - (a_C/a_I) \tilde{f}_{IC} \langle n \rangle] + w_{II} + w_{IE} \end{aligned} \quad (71)$$

$$\begin{aligned} \frac{d\langle l \rangle}{dt} = & S_E^0(T) \theta \tilde{S}_E \frac{a_s \lambda_{th}}{h} P - r_E \tilde{f}_E \langle l \rangle + w_{EE} - w_{IE} \\ & - z w_{CE} [\tilde{f}_{CE} (1 - \langle n \rangle) \langle l \rangle - (a_C/a_E) \tilde{f}_{EC}^2 \langle n \rangle^2] \end{aligned} \quad (72)$$

The constants  $r_C$ ,  $w_{IC}$ , etc. are specified in terms of microscopic parameters and the functions  $\tilde{f}_C$ ,  $\tilde{f}_I$ ,  $\tilde{f}_{IC}$ , etc. account for the various lateral interactions between the particles in the adsorbed and precursor states. We have factored out an explicit dependence on the coverages so that in the absence of any lateral interactions these functions are all equal to one.

To get the equilibrium conditions for the adsorbate we use Eq. (2) with  $P = \bar{P}$ , and get for the chemical potential of the adsorbate as a function of coverage and temperature

$$\exp(\mu_C/k_B T) = \frac{h \lambda_{th}^2}{k_B T Z_{int} a_s} \frac{a_C \tilde{f}_C}{\tilde{S}_C} \frac{\langle n \rangle}{1 - \theta} \quad (73)$$

$$\exp(\mu_I/k_B T) = \frac{h \lambda_{th}^2}{k_B T Z_{int} a_s} \frac{r_I \tilde{f}_I}{S_I^0(T) (1 - \theta) \tilde{S}_I} \langle m \rangle \quad (74)$$

$$\exp(\mu_E/k_B T) = \frac{h \lambda_{th}^2}{k_B T Z_{int} a_s} \frac{r_E \tilde{f}_E}{S_E^0(T) \theta \tilde{S}_E} \langle l \rangle \quad (75)$$

$$\tilde{f}_{CI} \langle m \rangle = (a_C/a_I) \tilde{f}_{IC} \langle n \rangle \quad (76)$$

$$\tilde{f}_{CE} \langle l \rangle = (a_C/a_E) \tilde{f}_{EC} \langle n \rangle \quad (77)$$

where  $\mu_C = \mu_I = \mu_E$ .

To get the equilibrium sticking coefficient we assume that at an ambient pressure  $P_0$  the adsorbate is in equilibrium at a temperature  $T$  with partial coverages  $n_0$ ,  $m_0$ , and  $l_0$ . We then increase the pressure slightly to  $P = P_0 + \Delta P$  and linearize the rate equations in the increase in the precursor coverages  $\Delta m = \langle m \rangle - m_0$  and  $\Delta l = \langle l \rangle - l_0$ . If adsorption into and desorption from the precursors is much faster than transitions from the precursors into the adsorbed state, we can ignore terms proportional to  $\Delta n = \langle n \rangle - \theta$  on the right-hand side of Eqs. (70–72) and also assume that the precursors will be in a steady state. It has been shown that the sticking

coefficient is then given by [61]

$$S(\theta, T) = S_C(\theta, T) + S_I(\theta, T) \frac{w_{CI}\tilde{f}_{CI}X_1 + zw_{CE}\tilde{f}'_{CE}Y_1(1-\theta)}{X_1X_2 - Y_1Y_2} \\ + S_E(\theta, T) \frac{w_{CI}\tilde{f}_{CI}Y_2 + zw_{CE}\tilde{f}'_{CE}X_2(1-\theta)}{X_1X_2 - Y_1Y_2} \quad (78)$$

If we suppress the exchange of particles between the intrinsic and extrinsic precursors,  $w_{IE} = 0$ , we get

$$S(\theta, T) = S_C(\theta, T) + S_I(\theta, T) \frac{w_{CI}\tilde{f}_{CI}}{r_I\tilde{f}_I + w_{CI}\tilde{f}_{CI}} \\ + S_E(\theta, T) \frac{zw_{CE}\tilde{f}'_{CE}(1-\theta)}{r_E\tilde{f}_E + zw_{CE}\tilde{f}'_{CE}(1-\theta)} \quad (79)$$

$$= S_C(\theta, T) + S_{\text{intr}}(\theta, T) + S_{\text{extr}}(\theta, T) \quad (80)$$

Only under this condition are the three adsorption channels independent of each other. This is the standard scenario always used in interpreting data. However, this is only one because if, on the other hand, the exchange between the two precursors is the fastest process on the surface we get

$$S(\theta, T) = S_C(\theta, T) + (S_I(\theta, T) + S_E(\theta, T)) \\ \times \frac{[w_{CI}\tilde{f}_{CI}a_E + zw_{CE}\tilde{f}'_{CE}a_I\theta](1-\theta)}{(r_I\tilde{f}_I + w_{CI}\tilde{f}_{CI})a_I\theta + [r_E\tilde{f}_E + zw_{CE}\tilde{f}'_{CE}(1-\theta)]a_E(1-\theta)} \quad (81)$$

and the two precursor channels of adsorption are maximally coupled, and straightforward interpretation is at a loss.

Along similar lines, one can study the desorption kinetics in the presence of precursors.

### C. Adsorption and Desorption with Surface Reconstruction

In this section we review a generalization of the kinetic lattice gas model when surface reconstruction takes place upon adsorption and desorption.

In the standard lattice gas model of adsorption we assume that the surface of the solid remains inert, providing adsorption sites. This implies that the state of the surface before adsorption and after desorption is the same. This is not the case if the surface reconstructs or lifts the reconstruction upon adsorption. Such a situation we want to describe. We introduce occupation numbers for the surface  $s_i = 0$  or 1, depending on whether the surface

is unreconstructed or reconstructed in cell  $i$ . We assume that in reconstruction the contribution of the solid surface to the total energy is

$$H_s = E_s \sum_i s_i + V_{1s} \sum_{i,a} s_i s_{i+a} + V_{2s} \sum_{i,b} s_i s_{i+b} \quad (82)$$

Here  $E_s$  is the energy gain or loss when a site reconstructs. The lateral interaction energies  $V_{1s}$  and  $V_{2s}$  between nearest (a) and next nearest (b) (and further) neighbors are most likely attractive to favor the growth of domains that are either reconstructed or unreconstructed. If  $V_{2s}$  were repulsive then a  $c(2 \times 2)$  pattern of alternately reconstructed and unreconstructed cells would be favored. A gas phase particle can adsorb either on the unreconstructed ( $u_i = 0$  or 1) or the reconstructed surface ( $r_i = 0$  or 1) subject to the constraints

$$u_i r_i = u_i s_i = r_i (1 - s_i) = 0 \quad (83)$$

The particle contributions to the total energy are then given by

$$\begin{aligned} H_a = E_u \sum_i u_i (1 - s_i) + (E_s + E_r) \sum_i r_i s_i \\ + V_{uu} \sum_i u_i u_{i+a} + V_{rr} \sum_i r_i r_{i+a} + V_{ru} \sum_i r_i u_{i+a} \end{aligned} \quad (84)$$

with single particle energies

$$E_u = -V_u - k_B T \ln(q_3^{(u)} q_{\text{int}}^{(u)}) \quad (85)$$

$$E_r = -V_r - k_B T \ln(q_3^{(r)} q_{\text{int}}^{(r)}) \quad (86)$$

The lateral interactions in the adsorbate can enhance or diminish the interaction energy in the surface. If the adsorption sites at the boundary between reconstructed and unreconstructed areas of surface are further distinguished from those inside these patches, we can introduce more interactions such as

$$H_{as} = V_{us} \sum_{i,a} u_i (1 - s_i) s_{i+a} (1 - r_{i+a}) + V_{rs} \sum_{i,a} r_i s_i s_{i+a} (1 - r_{i+a}) \quad (87)$$

If, as an example,  $E_u < V_{us} < E_r$  then, at least in the absence of lateral interactions, adsorption will be first on the unreconstructed surface, then at the boundary between unreconstructed and reconstructed regions, and lastly on the reconstructed surface. We do not need terms like  $u_i (1 - s_i) (1 - s_{i+a})$  because they can be subsumed in the first terms of Eqs. (84) and (87).

To set up the kinetics, we introduce a function  $P(\mathbf{u}, \mathbf{r}, \mathbf{s}; t)$  which gives the probability that a given microscopic configuration

$$(\mathbf{u}, \mathbf{r}, \mathbf{s}) = (u_1, u_2, \dots, u_{N_s}, r_1, r_2, \dots, r_{N_s}, s_1, s_2, \dots, s_{N_s}) \quad (88)$$

is realized at time  $t$ , where  $N_s$  is the fixed total number of adsorption sites on the surface. If all relevant processes, like adsorption, desorption, diffusion, etc. are Markovian, the probability function satisfies a master equation

$$\begin{aligned} dP(\mathbf{u}, \mathbf{r}, \mathbf{s}; t)/dt = \sum_{\mathbf{u}', \mathbf{r}', \mathbf{s}'} [W(\mathbf{u}, \mathbf{r}, \mathbf{s}; \mathbf{u}', \mathbf{r}', \mathbf{s}')P(\mathbf{u}', \mathbf{r}', \mathbf{s}'; t) \\ - W(\mathbf{u}', \mathbf{r}', \mathbf{s}'; \mathbf{u}, \mathbf{r}, \mathbf{s})P(\mathbf{u}, \mathbf{r}, \mathbf{s}; t)] \end{aligned} \quad (89)$$

where  $W(\mathbf{u}'\mathbf{r}'\mathbf{s}'; \mathbf{u}, \mathbf{r}, \mathbf{s})$  is, again, the transition probability that the microstate  $(\mathbf{u}, \mathbf{r}, \mathbf{s})$  changes into  $(\mathbf{u}', \mathbf{r}', \mathbf{s}')$  per unit time. Again, an expansion in the occupation numbers determines its structure, which, for the situation where lateral interactions are not important, reads

$$\begin{aligned} W(\mathbf{u}', \mathbf{r}', \mathbf{s}'; \mathbf{u}, \mathbf{r}, \mathbf{s}) = w_r \sum_i [1 - r_i + C_r r_i] s_i (1 - u_i) \delta(r'_i, 1 - r_i) \\ + w_u \sum_i [1 - u_i + C_u u_i] (1 - s_i) (1 - r_i) \delta(u'_i, 1 - u_i) \\ + w_s \sum_i [1 - s_i + C_s s_i] (1 - r_i) (1 - u_i) \delta(s'_i, 1 - s_i) \\ + w_{sr} \sum_i [(1 - s_i) (1 - r_i) + C_{sr} s_i r_i] (1 - u_i) \\ \times \delta(s'_i, 1 - s_i) \delta(r'_i, 1 - r_i) \\ + w_{su} \sum_i [s_i (1 - u_i) + C_{su} (1 - s_i) u_i] (1 - r_i) \\ \times \delta(s'_i, 1 - s_i) \delta(u'_i, 1 - u_i) \\ + w_{ur} \sum_i [s_i r_i (1 - u_i) + C_{ur} (1 - s_i) (1 - r_i) u_i] \\ \times \delta(s'_i, 1 - s_i) \delta(r'_i, 1 - r_i) \delta(u'_i, 1 - u_i) \end{aligned} \quad (90)$$

The terms proportional to  $w_r$  and  $w_u$  describe adsorption on, and desorption from, the reconstructed and unreconstructed surfaces, respectively, without a simultaneous change in the surface structure. The term with  $w_s$  accounts for the spontaneous reconstruction and the spontaneous lifting of the reconstruction in the absence of an adsorbate. The expressions with  $w_{sr}$  and  $w_{su}$  give the rates of adsorption and desorption with concurrent reconstruction or lifting of the reconstruction. Finally, the terms proportional to

$w_{ur}$  describe the process of reconstruction in the presence of an adsorbate. From detailed balance we find

$$C_r = e^{(E_r - \mu_r)/k_B T} \quad (91)$$

$$C_u = e^{(E_u - \mu_u)/k_B T} \quad (92)$$

$$C_s = e^{(E_s/k_B T)} \quad (93)$$

$$C_{sr} = e^{(E_r - \mu_r + E_s)/k_B T} = C_s C_r \quad (94)$$

$$C_{su} = e^{(E_u - \mu_u - E_s)/k_B T} = C_u / C_s \quad (95)$$

$$C_{ur} = e^{(E_u - \mu_u - E_s - E_r + \mu_r)/k_B T} = C_u / (C_s C_r) \quad (96)$$

We can include surface diffusion by adding to (90), neglecting again the effects of lateral interactions,

$$\begin{aligned} W_{\text{diff}} = \sum_{i,a} [ & J_{r \rightarrow r} r_i s_i (1 - r_{i+a}) s_{i+a} \delta(r'_i, 1 - r_i) \delta(r'_{i+a}, 1 - r_{i+a}) \\ & + J_{u \rightarrow u} u_i (1 - s_i) (1 - u_{i+a}) (1 - s_{i+a}) \delta(u'_i, 1 - u_i) \delta(u'_{i+a}, 1 - u_{i+a}) \\ & + J_{r \rightarrow u} r_i s_i (1 - u_{i+a}) (1 - s_{i+a}) \delta(r'_i, 1 - r_i) \delta(u'_{i+a}, 1 - u_{i+a}) \\ & J_{u \rightarrow r} u_i (1 - s_i) (1 - r_{i+a}) s_{i+a} \delta(u'_i, 1 - u_i) \delta(r'_{i+a}, 1 - r_{i+a}) ] \quad (97) \end{aligned}$$

Detailed balance demands that

$$J_{u \rightarrow r} = J_{r \rightarrow u} \exp[(E_u - E_r)/k_B T] \quad (98)$$

For an adsorbate which is homogeneous within the patches of reconstructed and unreconstructed surface only the diffusional exchange of mass between these two types contributes to the time evolution. The equations of motion read

$$\begin{aligned} \frac{d\theta_r}{dt} = & w_r(\theta_s - \theta_r) - w_r C_r \theta_r \\ & + w_{sr}(1 - \theta_s - \theta_u - C_{sr} \theta_r) - w_{ur}(\theta_r - C_{ur} \theta_u) \\ & - J_{r \rightarrow u} \theta_r (1 - \theta_s - \theta_u) + J_{u \rightarrow r} \theta_u (\theta_s - \theta_r) \quad (99) \end{aligned}$$

$$\begin{aligned} \frac{d\theta_u}{dt} = & w_u(1 - \theta_u - \theta_s) - w_u C_u \theta_u \\ & + w_{su}(\theta_s - \theta_r - C_{su} \theta_u) + w_{ur}(\theta_r - C_{ur} \theta_u) \\ & + J_{r \rightarrow u} \theta_r (1 - \theta_s - \theta_u) - J_{u \rightarrow r} \theta_u (\theta_s - \theta_r) \quad (100) \end{aligned}$$



$$\begin{aligned} \frac{d\theta_s}{dt} = & w_s(1 - \theta_s - \theta_u - C_s(\theta_s - \theta_r)) + w_{sr}(1 - \theta_s - \theta_u - C_{sr}\theta_r) \\ & - w_{su}(\theta_s - \theta_r - C_{su}\theta_u) - w_{ur}(\theta_r - C_{ur}\theta_u) \end{aligned} \quad (101)$$

The first terms in (99) and (100) say that adsorption can take place either on the remaining sites of the reconstructed surface or on those surface sites that are neither reconstructed nor occupied. The first term in (101) allows for reconstruction from the unreconstructed area,  $1 - \theta_s$ , but also says that this reconstruction may be hindered or helped if there is an adsorbate on the unreconstructed surface. A similar interpretation holds for the last term in (101) describing the lifting of the reconstruction. For the adsorption coefficients  $w_r$ ,  $w_s$ , etc., one writes expressions analogous to (47).

As an application, we list the sticking coefficient on an equilibrium adsorbate at coverage  $\theta$

$$S(\theta, T) = (1 - \theta) \left[ \frac{1}{C_s + 1} (S_r + S_{su}) + \frac{C_s}{C_s + 1} (S_u + S_{sr}) \right] \quad (102)$$

It shows that sticking is proportional to the availability of empty sites (because there are no lateral interactions in the adsorbate), and the sticking probabilities,  $S_r$  and  $S_u$ , are weighted by the fraction of the adsorbate-free surface that is reconstructed or not. This can obviously introduce a substantial temperature dependence in the sticking coefficient.

#### IV. CONCLUDING REMARKS

In this review article we have tried to show that an analytical approach to the thermodynamics and the kinetics of adsorbates is not restricted to simple systems but can deal with rather complicated situations in a systematic approach, such as multi-site and multi-component systems with or without precursor-mediated adsorption and surface reconstruction, including multi-layers/subsurface species. This approach automatically ensures that such fundamental principles as detailed balance are implemented properly.

For the equilibrium properties and for the kinetics under quasi-equilibrium conditions for the adsorbate, the transfer matrix technique is a convenient and accurate method to obtain not only the chemical potentials, as a function of coverage and temperature, but all other thermodynamic information, e.g., multiparticle correlators. We emphasize the economy of the computational effort required for the application of the technique. In particular, because it is based on an analytic method it does not suffer from the limitations of time and accuracy inherent in statistical methods such as Monte Carlo simulations. The task of variation of Hamiltonian parameters in the process of fitting a set of experimental data (thermodynamic and

kinetic) is both fast and systematic. To date, the most accurate modeling of desorption and thermodynamic data has been obtained by this method.

For adsorbates out of local equilibrium, an analytic approach to the kinetic lattice gas model is a powerful theoretical tool by which, in addition to numerical results, explicit formulas can be obtained to elucidate the underlying physics. This allows one to extract simplified pictures of and approximations to complicated processes, as shown above with precursor-mediated adsorption as an example. This task of theory is increasingly overlooked with the trend to using cheaper computer power for numerical simulations. Unfortunately, many of the simulations of adsorbate kinetics are based on unnecessarily oversimplified assumptions (for example, constant sticking coefficients, constant prefactors etc.) which rarely are spelled out because the physics has been introduced in terms of a set of computational instructions rather than formulating the theory rigorously, e.g., based on a master equation.

Ultimately, the coverage and temperature dependence of the kinetic and equilibrium properties of an adsorbate are the result of interactions of the adsorbed species with the substrate and with each other. In the ideal scenario one would start the theoretical development with quantum mechanical calculations of the potential energy surfaces for the coupled adsorbate-substrate system. If the system can be approximately described by a lattice gas model one then has all the necessary information to specify the interaction parameters in the corresponding lattice gas Hamiltonian. All equilibrium and kinetic properties then follow from a good theory. This scenario has so far only been attempted for one system, namely oxygen on Ru(001), using density functional theory for the energy calculations [62]. This approach—density functional calculations, lattice gas modeling and kinetic theory—provides the necessary link between the fundamental interactions of the adsorbate and the macroscopic theories of equilibrium and kinetics. It is parameter-free and thus should lead to a deeper understanding of surface physics and chemistry.

## REFERENCES

1. H. J. Kreuzer, Z. W. Gortel. *Physisorption Kinetics*. Berlin: Springer-Verlag, 1986.
2. M. N. R. Ashfold, C. T. Rettner, eds. *Dynamics of Gas-Surface Collisions*. Cambridge: Royal Society of Chemistry, 1991.
3. W. Rudszinski, W. A. Steele, G. Zgrablich, eds. *Equilibrium and Dynamics of Gas Adsorption on Heterogeneous Solid Surfaces*. Amsterdam: Elsevier, 1997.
4. S. J. Lombardo, A. T. Bell. *Sur Sci Rep* 13:1–72, 1991.
5. G. P. Brivio, T. B. Grimley. *Surf Sci Rep* 17:1–84, 1993.

6. B. N. J. Persson. *Surf Sci Rep* 15:1-135, 1992.
7. W. Brenig. In: M. Grunze, H. J. Kreuzer, eds. *Kinetics of Interface Reactions*. Berlin: Springer-Verlag, 1987, pp. 19-36.
8. H. J. Kreuzer, S. H. Payne. *Surf Sci* 198:235-262, 1988.
9. H. J. Kreuzer, S. H. Payne. *Surf Sci* 200:L433-L440, 1988.
10. S. H. Payne, H. J. Kreuzer. *Surf Sci* 205:153-176, 1988.
11. S. H. Payne, A. Drozdowski, H. J. Kreuzer, D. Menzel. *J Chem Phys* 110:6982-6999, 1999.
12. J. M. Honig. In: E. Alison Flood, ed. *The Gas-Solid Interface*. New York: Marcel Dekker, 1966-1967, Vol. 1, pp. 371-412.
13. D. M. Burley. In: C. Domb, M. S. Green, eds. *Phase Transitions and Critical Phenomena*. New York: Academic Press, 1972, Vol. 2, pp. 325-374.
14. C. Domb. *Adv Phys* 9:149-361, 1960.
15. L. K. Runnels, L. L. Combs. *J Chem Phys* 55:2482-2492, 1966.
16. F. H. Ree, D. A. Chesnut. *J Chem Phys* 45:3983-4003, 1966.
17. L. K. Runnels. In: C. Domb, M. S. Green, eds. *Phase Transitions and Critical Phenomena*. New York: Academic Press, 1972, Vol. 2, pp. 305-328.
18. W. Kinzel, M. Schick. *Phys Rev B* 24:324-328, 1981.
19. W. Kinzel, W. Selke, K. Binder. *Surf Sci* 121:13-31, 1982.
20. P. A. Rikvold, W. Kinzel, J. D. Gunton, K. Kaski. *Phys Rev B* 28:2686-2892, 1983.
21. P. A. Rikvold, K. Kaski, J. D. Gunton, M. C. Yalabik. *Phys Rev B* 29:6285-6294, 1984.
22. N. C. Bartelt, T. L. Einstein. *Phys Rev B* 30:5339-5341, 1984.
23. N. C. Bartelt, T. L. Einstein, L. D. Roelofs. *Phys Rev B* 34:1616-1623, 1986.
24. K. Kinzel, M. Schick. *Phys Rev B* 23:3435-3441, 1981.
25. N. H. Fuchs, S. Gartenhaus. *Phys Rev B* 31:7261-7273, 1985.
26. N. H. Fuchs. *Phys Rev B* 41:2173-3183, 1990.
27. A. V. Myshlyavtsev, V. P. Zhdanov. *Chem Phys Lett* 162:43-46, 1989.
28. A. V. Myshlyavtsev, J. L. Sales, G. Zgrablich, V. P. Zhdanov. *J Stat Phys* 58:1029-1039, 1990.
29. S. H. Payne, H. J. Kreuzer, L. D. Roelofs. *Surf Sci Lett* 259:781-786, 1991.
30. S. H. Payne, Zhang Jun, H. J. Kreuzer. *Surf Sci* 264:185-196, 1992.
31. C. J. Thompson. *Mathematical Statistical Mechanics*. Princeton, NJ: Princeton University Press, 1979.
32. J. H. Wilkinson. *The Algebraic Eigenvalue Problem*. 2nd. ed. Oxford: Clarendon Press, 1988.
33. Transfer matrix calculations can be done routinely, for instance, with the ASTEK program package for the analysis and simulation of thermal equilibrium and kinetics of gases adsorbed on solid surfaces, written by H. J. Kreuzer and S. H. Payne (available from Helix Science Applications, 618 Ketch Harbour Road, Portuguese Cove, N.S., B3V 1K1, Canada).
34. J. Hrbek. *Surf Sci* 164:139-148, 1985.
35. H. Over, H. Bludau, M. Stottke-Klein, G. Ertl, W. Moritz, C. T. Campbell. *Phys Rev B* 45:8638-8649, 1992.

36. S. H. Payne, H. A. MacKay, H. J. Kreuzer, M. Gierer, H. Bludau, H. Over, G. Ertl. *Phys Rev B* 54: 5073–5080, 1996.
37. S. H. Payne, Zhang Jun, H. J. Kreuzer. *Surf Sci* 396:369–387, 1998.
38. C. Park, H. M. Kramer, E. Bauer. *Surf Sci* 116:456–466, 1982.
39. W. Frie, L. Hammer, K. Heinz, S. H. Payne, H. J. Kreuzer. *Surf Sci* 421:279–295, 1999.
40. S. H. Payne, H. J. Kreuzer, K. A. Peterlinz, T. J. Curtiss, C. Uebing, S. J. Sibener. *Surf Sci* 272:102–110, 1992.
41. H. J. Kreuzer, Zhang Jun, S. H. Payne, W. Nichtl-Pecher, L. Hammer, K. Müller. *Surf Sci* 303:1–15, 1994.
42. D. C. Skelton, D. H. Wei, S. D. Kevan. *Surf Sci* 320:77–84, 1994.
43. D. H. Wei, D. C. Skelton, S. D. Kevan. *Surf Sci* 326:167–176, 1995.
44. D. H. Wei, D. C. Skelton, S. D. Kevan. *Surf Sci* 381:49–64, 1997.
45. H. J. Kreuzer, S. H. Payne, M. Grunze, C. Wöll. *Z Phys Chemie* 202:273–296, 1997.
46. F. Buatier de Mongeot, M. Rocca, A. Cupolillo, U. Valbusa, H. J. Kreuzer, S. H. Payne. *J Chem Phys* 106:711–718, 1997.
47. S. H. Payne, H. J. Kreuzer. *Surf Sci* 338:261–278, 1995.
48. S. H. Payne, H. J. Kreuzer, A. Pavlovskaya, E. Bauer. *Surf Sci* 345:L1–L10, 1996.
49. W. Widdra, P. Trischberger, W. Friess, D. Menzel, S. H. Payne, H. J. Kreuzer. *Phys Rev B* 57:4111–4126, 1998.
50. S. H. Payne, H. J. Kreuzer. *Surf Sci* 399:135–159, 1998.
51. P. A. Rikvold, J. B. Collins, G. D. Hansen, J. D. Gunton. *Surf Sci* 203:500–524, 1988.
52. J. B. Collins, P. Sacramento, P. A. Rikvold, J. D. Gunton. *Surf Sci* 221:277–298, 1989.
53. P. A. Rikvold, M. R. Deakin. *Surf Sci* 249:180–193, 1991.
54. D. C. Skelton, D. H. Wei, S. D. Kevan. *Surf Sci Lett.* 355:319–324, 1996.
55. H. J. Kreuzer, S. H. Payne, P. Jakob, D. Menzel. *Surf Sci* 424:36–54, 1999.
56. For a review and the history of the kinetic lattice (or Ising) model, see K. Kawasaki. In: C. Domb, M. S. Green, eds. *Phase Transitions and Critical Phenomena*. New York: Academic Press, 1972, Vol. 2, p. 443–501.
57. H. J. Kreuzer, Zhang Jun. *Appl Phys A* 51:183–195, 1990.
58. A. Wierzbicki, H. J. Kreuzer. *Surf Sci* 257:417–426, 1991.
59. S. H. Payne, A. Wierzbicki, H. J. Kreuzer. *Surf Sci* 291:242–260, 1993.
60. H. J. Kreuzer. *Surf Sci* 238:305–316, 1990.
61. H. J. Kreuzer. *J Chem Phys* 104:9593–9612, 1996.
62. C. Stampfl, H. J. Kreuzer, S. H. Payne, H. Pfnür, M. Scheffler. *Phys Rev Lett* (in press).

# 10

## Computer Simulations of Dense Polymers

**KURT KREMER and FLORIAN MÜLLER-PLATHE** Max-Planck-Institut für Polymerforschung, Mainz, Germany

I. Introduction	481
II. Which Model, and When?	482
III. Molecular Dynamics Simulation on the Atomistic Level	485
A. Methods	485
B. Applications of atomistic simulations	488
IV. Mesoscopic Monte Carlo (MC) and Molecular Dynamics (MD)	493
A. Polymer melts and networks	493
B. Polymer glasses	499
V. Conclusions	505
References	506

### I. INTRODUCTION

Due to the complexity of macromolecular materials computer simulations become increasingly important in polymer science or, better, in what is now called “soft matter physics.” There are several reviews available which deal with a great variety of problems and techniques [1–7]. It is the purpose of the present introduction to give a very brief overview of the different approaches, mainly for dense systems, and a few applications. To do so we will confine ourselves to techniques describing polymers on a “molecular” level. By molecular level we mean both the microscopic and the mesoscopic level of description. In the case of the microscopic description (all)

chemical details are taken into account, while on the mesoscopic level the polymer chains are reduced to essential properties like connectivity and excluded volume. While the latter is sufficient to determine universal properties like scaling of the chain radius of gyration or the diffusion constant as a function of contour length  $L$  [6], the former is needed in order to get a better feeling for the “prefactors” which determine the amplitude of physical quantities, e.g.  $c_\infty$  in Flory’s notation.

It is the interplay of universal and material-specific properties which causes the interesting macroscopic behavior of macromolecular materials. This introduction will not consider scales beyond the universal or scaling regime, such as finite element methods. First we will give a short discussion on which method can be used under which circumstances. Then a short account on microscopic methods will follow. The fourth section will contain some typical coarse-grained or mesoscopic simulations, followed by some short general conclusions.

## II. WHICH MODEL, AND WHEN?

At a first glance, it is tempting to perform a full-scale MD (molecular dynamics) simulation, which includes all the chemical detail of the system under consideration. Starting from a detailed force field  $U(\vec{R})$ , Newton’s equations of motion

$$m \frac{d^2 \vec{R}}{dt^2} = -\nabla U(\vec{R}) \quad (1)$$

are solved on a computer. ( $U(\vec{R})$  is the potential energy function of the system,  $\vec{R}$  an atom’s position and  $m$  its mass.) A valid question, however, is to what extent can this be done *and* where is this necessary or even useful? Such simulations are certainly not possible in general. There are by far too many different polymers which can be synthesized or are provided by nature. One would thus be restricted to a small number of model monomers. However, even then it is not trivial to properly determine the often very complicated inter- and intra-chain interactions. In particular the complicated inter-chain or polymer–solvent interactions are only poorly understood so far. Even if one were able to overcome all these difficulties, the situation would still not be resolved satisfactorily [4,6]. In order to illustrate this, typical time scales for polymeric melts are given in Fig. 1.

The difficulties arise from the enormous variation in time and length scales. They range from microscopic oscillation periods of the order

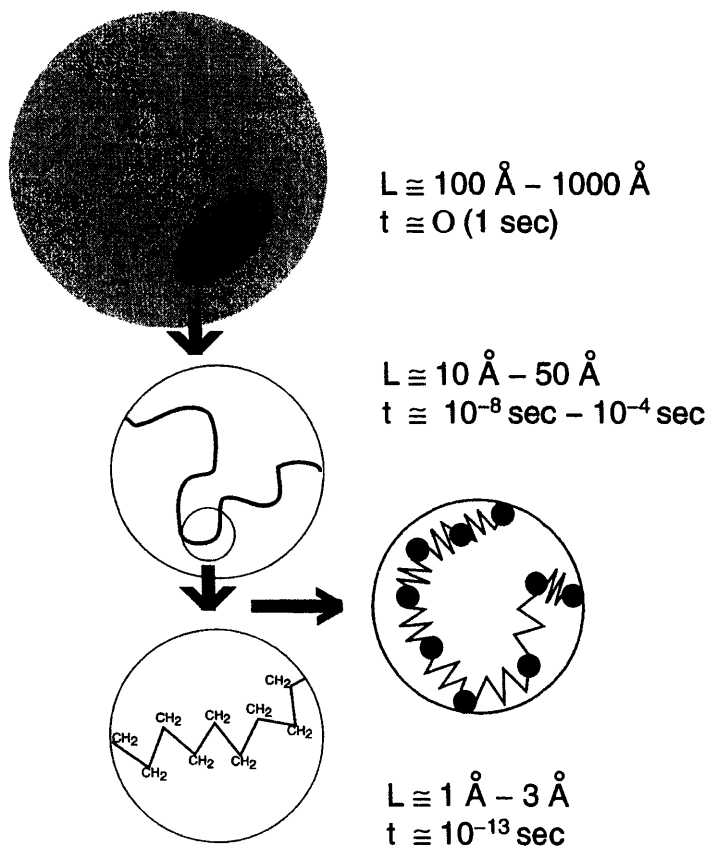


**FIG. 1** A sketch of the different time and length scales in polymer problems. Starting from the top, one can only observe a marked chain in a melt or dense solution of otherwise identical chains as a very pale shadow. The typical extension of the shadow is given by the diameter of the overall coil, as indicated. The characteristic time for this picture to change can vary dramatically, depending on chain length and temperature, starting at about  $10^{-4}$  s for short chains and “high temperatures” with essentially no upper limit. Looking more closely, more of the chain structure is revealed. This is the universal coil regime. Times and lengths for this regime are indicated. Again, the variation of time is very large, especially as a function of temperature. Typical times, as present in typical experiments, are indicated. Only if one again looks much more closely can the chemical details of the polymers be identified. There the behavior is governed by the local chemical details of the species under consideration. The lower time boundary is given by the highest frequency, which usually is from the C–C bond oscillations. Typical coarse-grained simulations are situated somewhere between the coil and the microscopic regime.

of  $10^{-13}$  s, requiring MD integration time steps of at most  $10^{-14}$  s, to macroscopic times ( $10^{-6}$ – $10^{-3}$  s) for the overall diffusion of a chain, which is needed to relax the system. Of course, near the glass transition or near critical points, e.g., critical points of a mixture of two different polymers, the upper time limit can shift upwards arbitrarily. It is easy to show that a full-scale MD simulation with all chemical details, for a reasonable system size, takes a prohibitively long time even for the coming generations of computers. To convey a feeling for the time needed, let us look at the following first estimate. The fastest MD programs, using only simplest models and potentials, roughly give about 300 000 particle moves per second on a Cray YMP processor. First, we assume the same speed for the more complicated atomistically detailed interactions, which is certainly not very realistic. Now, for example, let us take PDMS (poly dimethyl siloxane) and count each atom or superatom, giving 4 particles per monomer. This is certainly at the low end of complexity compared to typical systems. Taking a small melt sample, typically corresponding to a cubic box of roughly 80 Å length, of 100 chains of 50 monomers results in 20 000 particles. We thus get of the order of 15 time steps per second. Typical relaxation times of such a system are around  $10^{-4}$  s, giving  $O(10^{10})$  s or 3000 years of CPU time [9]. It should be kept in mind that, though fairly large for microscopic simulations, this is still an extremely small system of very limited experimental relevance for many macroscopic properties. Though, meanwhile, significant progress has been made on both the hardware and software sides [10], the general line of argument remains unchanged. The chains are not yet entangled and the model is simplified. It is thus easy to imagine the requirements for more complicated systems. Thus, before starting a simulation, one should ask carefully to what extent one really needs the chemical details of the chains. This estimate also clearly shows that simulations, which reproduce the slow physical dynamics of the system should be avoided whenever possible. It is thus not useful at all to simulate a single isolated chain by, e.g., an MD simulation or a Monte Carlo (MC) technique which follows the Rouse model. For dense systems, however, in many cases there is no way out.

In addition, Fig. 1 illustrates that for many studies chemical details are not needed and, due to the overwhelming amount of information generated, might even obscure the results. If one is interested in general aspects of the glass transition of amorphous polymers, it is sufficient to study highly simplified systems in the scaling regime. If, however, one is looking for local conformations of specific chemical groups, the consideration of the detailed structure is obviously required. These simulations, even on modern supercomputers, only run up to a few nanoseconds at most. In the following, three characteristic examples of simulations



in the condensed phase are given: MD simulations with all chemical details using atomistic force fields, then MC or MD of melts in the scaling or universal regime and finally an example of a simple coarse-grained model for polymer glasses. For more technical details, see [1–6].

### III. MOLECULAR DYNAMICS SIMULATION ON THE ATOMISTIC LEVEL

#### A. Methods

The conceptionally simplest and most straightforward way to study computationally the motion of individual atoms or molecules is the molecular dynamics (MD) method [5,6,11–14].

Starting from a potential function  $U(\vec{R})$  or force field, the forces are calculated and then Newton's equation of motion is integrated for each atom (Eq. 1).

Eq. (1) would correspond to a constant energy, constant volume, or micro-canonical simulation scheme. There are various approaches to extend this to a canonical (constant temperature), or other thermodynamic ensembles. (A discussion of these approaches is beyond the scope of the present review.) However, in order to perform such a simulation there are several difficulties to overcome. First, the interactions have to be determined properly, which means that one needs a potential function which describes the system correctly. Second, one needs good initial conditions for the velocities and the positions of the individual particles since, as shown in Sec. II, simulations on this detailed level can only cover a fairly short period of time. Moreover, the overall conformation of the system should be in equilibrium.

The potential energy function  $U(\vec{R})$  describes the Born–Oppenheimer surface for the atomic motion. It would be desirable to obtain the surface quantum-chemically, i.e., by solving the electronic Schrödinger equation of the system for every atom configuration. Using *ab initio* or semi-empirical quantum-chemical methods, this has recently become possible for systems of a few atoms for simulations of a few hundred time steps. Using local density methods and plane-wave basis sets, larger systems have been treated for longer times [15]. However, for treating a polymeric system, one needs several thousands of atoms and several millions of time steps based on these short integration time steps. If one uses analytical representations which contain certain simplifications of the potential surface resulting in the so-called force fields, the typical form of a force field

is given by

$$\begin{aligned}
 U(\vec{R}) = & \sum_{\text{bonds}} \frac{k_d}{2} (d - d_0)^2 + \sum_{\substack{\text{bond} \\ \text{angles}}} \frac{k_\phi}{2} (\phi - \phi_0)^2 \\
 & + \sum_{\substack{\text{improper} \\ \text{dihedrals}}} \frac{k_\Theta}{2} (\Theta - \Theta_0)^2 \\
 & + \sum_{\substack{\text{dihedral} \\ \text{angles}}} \frac{k_\tau}{2} [1 - \cos(n\tau - \tau_0)] \\
 & + \sum_{\substack{\text{nonbonded} \\ \text{pairs } ij}} \left\{ 4\varepsilon_{ij} \left[ \left( \frac{\sigma_{ij}}{r_{ij}} \right)^{12} - \left( \frac{\sigma_{ij}}{r_{ij}} \right)^6 \right] + \frac{1}{4\pi\varepsilon\varepsilon_0} \frac{q_i q_j}{r_{ij}} \right\} \quad (2)
 \end{aligned}$$

where  $d$ ,  $\phi$ ,  $\theta$ , and  $\tau$  are actual values for bond length, bond angle, improper (harmonic) dihedral and dihedral angles,  $d_0$ ,  $\phi_0$ ,  $\Theta_0$ , and  $\tau_0$  are the equilibrium values and  $k_d$ ,  $k_\phi$ ,  $k_\Theta$ , and  $k_\tau$  the associated force constants,  $n$  is the periodicity of the torsional potential,  $r_{ij}$  is the distance between the two nonbonded atoms  $i$  and  $j$ ,  $\varepsilon_{ij}$  and  $\sigma_{ij}$  are the well depth and contact radius of the Lennard–Jones potential between these atoms,  $q_i$  and  $q_j$  are the charges on  $i$  and  $j$ ,  $\varepsilon_0$  is the vacuum permittivity ( $8.854\,18 \times 10^{-12} \text{ C}^2 \text{ J}^{-1} \text{ m}^{-1}$ ) and  $\varepsilon$  is the effective dielectric constant of the medium. The Lennard–Jones parameters for pairs of unlike atoms are often derived by mixing rules, e.g., the Lorentz–Berthelot mixing rules

$$\varepsilon_{ij} = \sqrt{\varepsilon_{ii}\varepsilon_{jj}}, \quad \sigma_{ij} = (\sigma_{ii} + \sigma_{jj})/2$$

Non-bonded interactions are usually excluded between atoms which are already interacting by a bond or bond angle term (first and second neighbors) and are often modified for the end atoms of dihedral angles (third neighbors).

Note also that different analytical forms are used for some of the terms (angles harmonic in  $\cos \phi$  rather than  $\phi$ , cosine expansions for dihedrals,  $r^{-9}$  or  $\exp(-Ar_{ij})$  instead of  $r^{-12}$  repulsions, etc.). Some force fields also have cross-terms between different degrees of freedom. Additional terms may be present for out-of-plane bendings, hydrogen bonds, etc.

It is important to mention that for most applications the special form of the force field is not as important as the actual values of the parameters. These parameters are determined in a number of ways, mainly by comparison with experiments, e.g., vibrational spectroscopy. Torsional potentials, which are crucial for polymer configurations and dynamics of polymers, can

be determined by *ab initio* or density-functional calculations on fragments, as is done e.g., for poly(ethylene oxide) [16–18].

The non-bonded interaction energy, the van-der-Waals and electrostatic part of the interaction Hamiltonian are best determined by parametrizing a molecular liquid that contains the same chemical groups as the polymers against the experimentally measured thermodynamical and dynamical data, e.g., enthalpy of vaporization, diffusion coefficient, or viscosity. The parameters can then be transferred to polymers, as was done in our case, for instance in polystyrene (from benzene) [19] or poly(vinyl alcohol) (from ethanol) [20,21].

From this discussion, the limitations of the force field should have become clear. There is no such thing as a universal force field which describes every system in every condition. The force field is a function with few adjustable parameters and can, therefore, not be expected to reproduce all properties of all chemical species under all circumstances. This means, for example, that an OH group in an aliphatic alcohol will have to be treated differently from a phenolic OH or from the OH of a carboxylic acid group. Similarly, the density and temperature window of a force field is often limited [22].

Since it is impossible to equilibrate the conformations of the system, it is especially important to start with an appropriately equilibrated sample. That means that for every atom its initial position and velocity have to be specified in the proper way. The velocities are usually picked randomly from a Maxwell–Boltzmann distribution at the desired temperature. This is the trivial part. The highly non-trivial part is to start out with a statistically correct polymer conformation. In the typical time of our simulations (a few nanoseconds) the polymer undergoes only local rearrangements, thus, not altering its global conformation. This is in contrast to faster relaxing systems such as liquids which can be started off in almost any conformation. Hence, by some means, amorphous polymer structures have to be generated that are low in energy and have the correct distribution of torsional angles, the correct distribution of free volume, and so on. It should be noted, however, that to date no completely satisfactory scheme exists. For a variety of different approaches, see [2–7].

Since these microscopic simulations typically can only treat short times and small samples, it is important to avoid surface effects. It is common to employ periodic boundary conditions. A special trick often used for these kinds of simulation is, instead of simulating a melt of many chains, to simulate one very long chain which falls back again and again into the box. In this way, the effect of the chain ends, which introduces artificially high free volume can be reduced. However, one should keep in mind that this chain interacts with its own periodic images. It is known that this may

introduce certain artefacts into the conformation statistics. Especially in systems under shear, this leads to artificial modification of the results.

In addition to the MD method, a wealth of Monte Carlo methods is used also at the atomistic level [6]. They use essentially the same models, force fields, for polymers. Their main advantage, however, is that by introduction of clever moves one can beat the slow physical dynamics of the systems and can run through phase space much faster than by MD. These methods are still in their infancy, but will certainly become more important.

## **B. Applications of Atomistic Simulations**

The complexity of the molecular description makes atomistic simulations relatively costly in terms of computer time. In addition, one has to take great care in order to optimize the programs with respect to the hardware they are being run on. These problems, together with the apparent ease of use of some packages, especially commercial ones, have led to a number of computational studies appearing in the literature in which simulations were too short to deliver meaningful results. The estimates of Sec. II give a feeling of the power and the limitations of atomistically detailed molecular dynamics simulations.

It is therefore clear that atomistic MD is limited to events which are local (a few nm) and fast (a few ns). Events which are rare but do not take long are accessible via special techniques [6]. This has manifested itself in the sort of polymer problems which have been addressed by atomistic simulations. Many of them are, however, of practical interest. The failure characteristics of polymeric materials change with time [23]. This is due not only to long-time physical processes such as creep, flow, case-II diffusion, etc. Often also the environment has a significant effect on polymer stability. Deterioration of performance can be caused by chemical, physical, or biological processes and their combinations. Examples of physical effects are radiation damage, plasticization due to solvent (particularly water) uptake, and so on. Chemical degradation includes oxidation, radical reactions, and solvolysis. Many of the degradation/deterioration mechanisms mentioned above involve the local mobility of polymer segments and, in particular, of small molecules in and around the polymer. The small molecules can be gases, for instance Oxygen,  $O_2$ , radicals ( $Cl$ ,  $OH$ ,  $CH_n$ ) or solvents (plasticization, swelling, solvolysis). One of the keys to controlling the lifetime of polymers, therefore, is the mobility of these small species. Processes involving small molecules as well as polymers often have characteristic time scales well suited to MD simulations. To illustrate this, we will discuss three examples: the permeation of bulk polymers by small molecules, which means that we have a few small molecules in a matrix of bulk polymers; the swelling of such

a matrix by many small molecules; and finally the behavior of a chain in a solvent.

### 1. Permeation of Bulk Polymers by Small Molecules

The field of gas diffusion in polymers is probably one of the mature areas in atomistic simulations, as two reviews [24,25] illustrate. Mostly, standard gases (He, H<sub>2</sub>, N<sub>2</sub>, O<sub>2</sub>, CH<sub>4</sub>, Ar, etc.) in standard amorphous polymers (PE, PDMS, PP, PIB) have been studied. If a bulk polymer contains trace amounts of small molecules, like gas molecules, its structure and dynamics can be expected to be essentially unperturbed. Therefore, the polymer will undergo only local structural fluctuations. These are essentially vibrations of the atoms around their equilibrium positions. However, these fluctuations are sufficient to allow small molecules to diffuse through the polymer. The diffusion coefficients of gas molecules in some polymers are high enough for the molecules to travel a meaningful distance during a simulation. For example, a diffusion coefficient  $D$  of O<sub>2</sub> in LDPE is of the order of  $10^{-6}$  cm<sup>2</sup>/s. This gives rise to a displacement of about 2.4 nm in a 10 ns simulation. From such a displacement it is possible to estimate the diffusion coefficient in a statistically meaningful manner. Currently, the lower limit for determining diffusion coefficients by atomistic MD simulations is about  $10^{-7}$  to about  $10^{-8}$  cm<sup>2</sup>/s. Thus, at present, predictive calculations of polymers which are designed to provide high barriers are still impossible. However, typical materials for gas separation membranes can be studied, since a high transmembrane flux is important in addition to selectivity.

In addition to the quantitative calculation of diffusion coefficients of gases in polymers, the most important contribution of MD was the elucidation of the hopping mechanism by which the gas molecules migrate through the polymer. Typically, the polymer matrix does not contain connected paths of free volume which would allow the free diffusion of the gas molecules. Thus, the local mobility of the polymer is important for the hopping mechanism of the gas molecules. All calculations have found that this mechanism is brought about by the opening and closing of transient channels of free volume connecting cavities in the polymer. The gas molecules take advantage of these channels for diffusion. The restriction of available pathways for diffusion leads to anomalous non-Einstein diffusion at short length and time scales, which is evident from the power laws found for the penetrants' mean-square displacements (Fig. 2). This is similar to anomalous diffusion found in other disordered systems.

### 2. Solvent Swelling of Polymers

Swollen polymers fall, in a sense, between the case of a few small polymers in a polymer matrix and a polymer chain in a solvent. The amount of

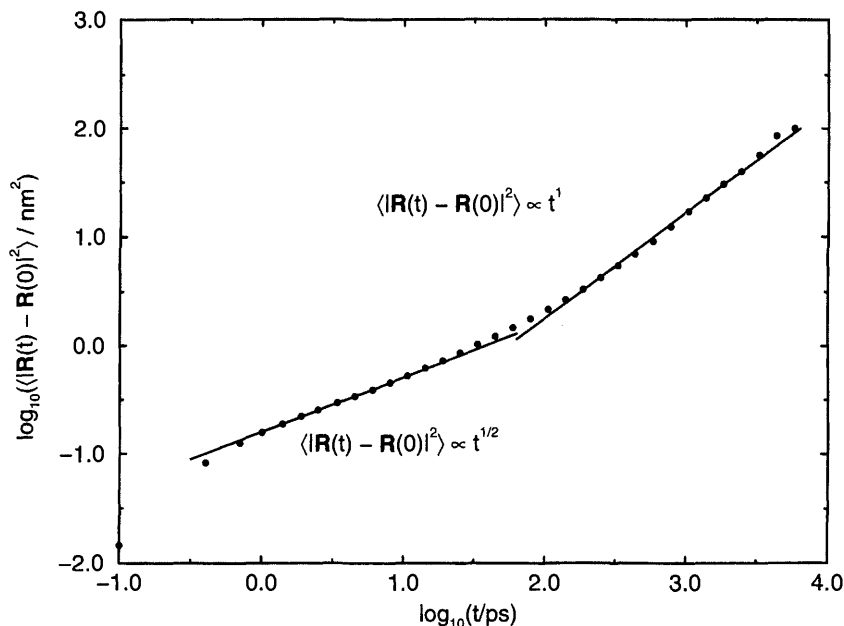


**FIG. 2** Mean-square displacement (MSD) of helium atoms dissolved in polyisobutylene. There is a regime of anomalous diffusion ( $\text{MSD} \propto t^{1/2}$ ) followed by a crossover at 100 ps to normal (Einstein) diffusion ( $\text{MSD} \propto t$ ) [24].

solvent and polymer are of comparable size. However, this area is the least developed among atomistically modeled small-molecule/polymer systems, and only recently have a few studies emerged [19,26–30]. This is in spite of the enormous technical importance of solvent-swollen systems. Solvent uptake followed by swelling is often the first step to deterioration of a polymeric material [23]. The swollen polymer normally lacks some of the mechanical strength of the dry polymer. In addition, swelling can sometimes change the barrier properties drastically, so that degrading components like oxygen can enter the polymer. Also, swelling inducing a glass-to-melt transition can lead to enormous inhomogeneous stress distributions in the system, causing mechanical failure of the polymeric material. This example of case-II diffusion causes many technical difficulties. However, controlled decomposition of the polymer can also be a design goal, like the degradation by hydrolysis of poly(glycolide)-co-poly(lactide) implants for drug release. Besides polymer lifetime considerations, solvent swelling of the polymer is a prerequisite for applications like pervaporation membranes and superabsorbers.

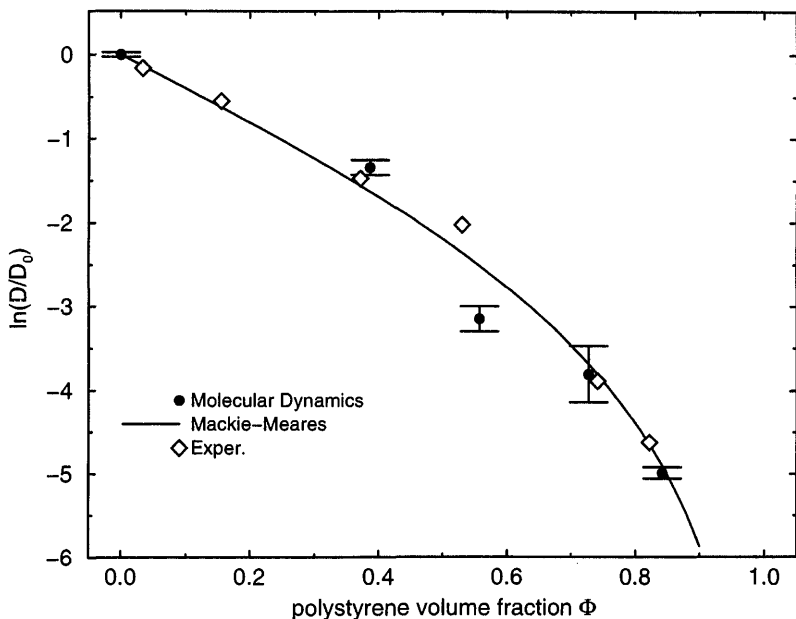


**FIG. 3** Diffusion coefficient of benzene molecules in benzene–polystyrene mixtures normalized by the diffusion coefficient of neat benzene: molecular dynamics results, NMR measurements and prediction by the Mackie–Meares model [26].

Mixed benzene–polystyrene systems have been simulated up to a PS content of 84 wt.% [19,26]. These studies were mainly targeted at the solvent structure and dynamics around the polymer and the translational and rotational diffusion of the solvent molecules. The simulations show that a styrene monomer exchanges benzene molecules of its first solvation shell as quickly as does a benzene molecule in bulk solvent. This is an indication that the notion of a solvent-decorated polymer with solvent molecules being divided into mobile bulk solvent molecules and molecules firmly attached to the polymer is inappropriate in this case. The change of the diffusion coefficient with polymer concentration can be well reproduced, even though it changes by two orders of magnitude between 0 and 84 wt.% PS (Fig. 3). Somewhat unexpected was the result that the polymer has a large influence on the reorientational anisotropy of benzene. One can define two different reorientational correlation times  $\tau_{\parallel}$  and  $\tau_{\perp}$  for the parallel (“frisbee”) and perpendicular (“tumbling”) modes of the molecular reorientation of benzene molecules.  $\tau_{\parallel}$  is much less affected by the presence of polymer than  $\tau_{\perp}$  (Fig. 4). The reason is that the increased viscosity hinders the perpendicular

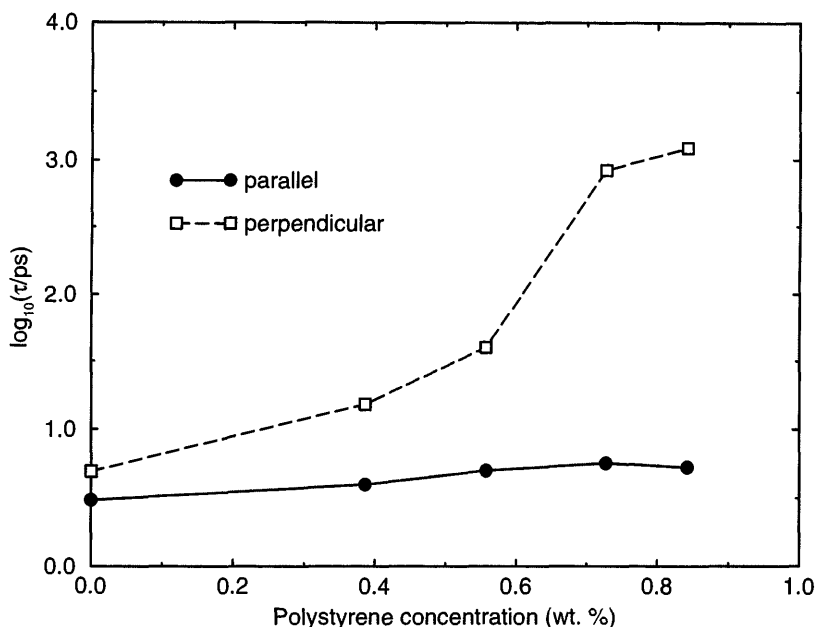


**FIG. 4** Dependence of molecular reorientation times of benzene on the concentration of polystyrene;  $\tau_{\parallel}$  denotes the parallel (“frisbee”) mode,  $\tau_{\perp}$  the perpendicular (“tumbling”) mode [26].

reorientation effectively, whereas the small extra free volume needed for a parallel rotation is still available even at large polymer concentrations. More recently, it was shown that these qualitative features of solvent motion are independent of the chemistry of the polymer–solvent system. They were also found for the very polar hydrogels of water and poly(vinyl alcohol) [27–30].

### 3. Polymers in Solution

Finally, we want to describe two examples of those isolated polymer chains in a sea of solvent molecules. Polymer chains relax considerably faster in a low-molecular-weight solvent than in melts or glasses. Yet it is still almost impossible to study the conformational relaxation of a polymer chain in solvent using atomistic simulations. However, in many cases it is not the polymer dynamics that is of interest but the structure and dynamics of the solvent around the chain. Often, the first and maybe second solvation shells dominate the solvation. Two recent examples of aqueous and non-aqueous polymer solutions should illustrate this: poly(ethylene oxide) (PEO) [31]



and poly(vinyl alcohol) (PVA) [21]. In both cases, hydrogen bonding is the clue to solvation. This is evident from comparison of the structures of a PEO 15-mer in water and in benzene [31]. The conformation is helical in water and a random coil in benzene. The reason for the observed helicity is that water molecules form hydrogen bonds simultaneously with two different ether oxygens of the PEO, thereby linking two different monomers along the backbone of the chain. These are not consecutive monomers, but there is one monomer between them. In benzene, this specific interaction is absent and the polymer adopts its random-coil conformation.

The simulations of a 15-mer of PVA in water, ethanol, and a water-ethanol mixture provide the explanation why PVA is miscible with water but not with organic solvents, even if they are polar and hydrogen-bonding like ethanol. In aqueous solution, every OH group in PVA has on average 1.1 hydrogen bonds to solvent molecules, whereas in ethanol it has only 0.6. Hence, the contribution of hydrogen bonds to the enthalpy of mixing is larger in water than in ethanol. The reason for the higher number of hydrogen bonds is the smaller size of the water molecules, which allows some of the OH groups to be approached by two water molecules. This effect becomes very visible in the system of PVA in a 1 : 1 mixture of water and ethanol where the two solvents compete for the polymer. One finds a fourfold enhancement of water density in the immediate vicinity of the PVA compared to the density in the bulk mixed solvent (Fig. 5).

From this short discussion, it is clear that atomistically detailed molecular dynamics or Monte Carlo simulations can provide a wealth of information on systems on a local molecular atomistic level. They can, in particular, address problems where small changes in chemical composition have a drastic effect. Since chemical detail is avoided in mesoscopic models, these can often capture such effects only indirectly.

#### **IV. MESOSCOPIC MONTE CARLO (MC) AND MOLECULAR DYNAMICS (MD)**

##### **A. Polymer Melts and Networks**

To understand the global mechanical and statistical properties of polymeric systems as well as studying the conformational relaxation of melts and amorphous systems, it is important to go beyond the atomistic level. One of the central questions of the physics of polymer melts and networks throughout the last 20 years or so dealt with the role of chain topology for melt dynamics and the elastic modulus of polymer networks. The fact that the different polymer strands cannot cut through each other in the

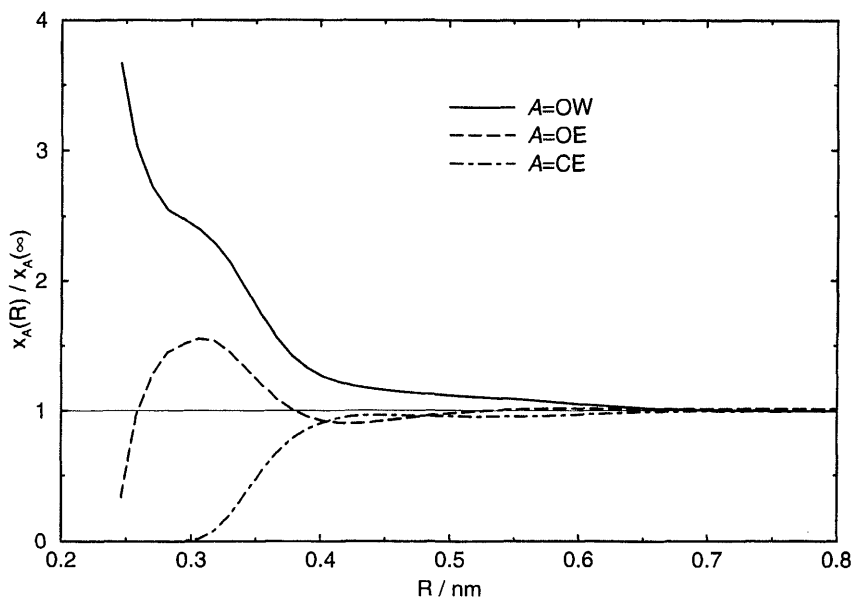


**FIG. 5** Local concentration profiles around a hydroxyl group in poly(vinyl alcohol) of heavy atoms in a (1:1) water/ethanol mixture; A = OW: water oxygen, A = OE: ethanol oxygen, A = CE: ethanol carbon. The local atomic fractions are defined as  $x_A(R) = n_A(R) / \sum_B n_B(R)$ , where  $n_A(R)$  is the average number of atoms of type A within a radius  $R$  of the hydroxyl group. The local atomic fraction is normalized by  $x_A(\infty)$ , the atomic fraction of A in the bulk [21].

course of thermal motion leads to severe topological constraints on the diffusion of individual chains and, in a similar way, on the conformational relaxation of network strands. For short-chain melts, the dynamics is well described by the Rouse model [32]. This model describes the Langevin dynamics of a single random walk chain (no excluded volume) coupled to a heat bath. The friction of the individual beads and the heat bath, of temperature  $T$ , are coupled by the fluctuation-dissipation theorem. Thus, the complicated interactions of the chain under consideration with all the other chains in its immediate surrounding are reduced to background friction and thermal activation [33]. Although this model is a most drastic simplification it describes the dynamics of short chain melts extremely well, giving the viscosity  $\eta \propto N$ ,  $N$  being the number of beads, and  $D \propto 1/N$  for the self-diffusion of the chain. Even the hierarchy of power laws for the mean-square displacements of individual monomers is given properly. In spite of this remarkable success, the deeper reasons are not understood at all [34].

Once the chains become larger and larger, the dynamics of the melt slows down dramatically, due to the topological constraints imposed by the chains on each other. For the chain diffusion one observes a transition

$$D \propto \begin{cases} 1/N & N < N_e \\ 1/N^2 & N \gg N_e \end{cases}$$

and for the viscosity, respectively

$$\eta \propto \begin{cases} N & N < N_e \\ N^{3.4} & N \gg N_e \end{cases}$$

with a rather extended crossover regime.  $N_e$  is the so-called entanglement molecular weight or chain length, which is the same on this coarse-grained level. It is, in principle, accepted now that this behavior can be understood qualitatively by the so-called reptation model [32,35]. Many details are still unclear, and a precise quantitative description is still missing.

Since this behavior is universal, it is obvious that the simplest simulation models which contain the essential aspects of polymers are sufficient to study these phenomena. Two typical examples of such models are the bond fluctuation Monte Carlo model and the simple bead-spring model employed in molecular dynamics simulations. Both models are illustrated in Fig. 6.

In the case of the bond fluctuation model [36,37], the polymer is confined to a simple cubic lattice. Each monomer occupies a unit cube of the system and the bond length between the monomers can fluctuate. On the other

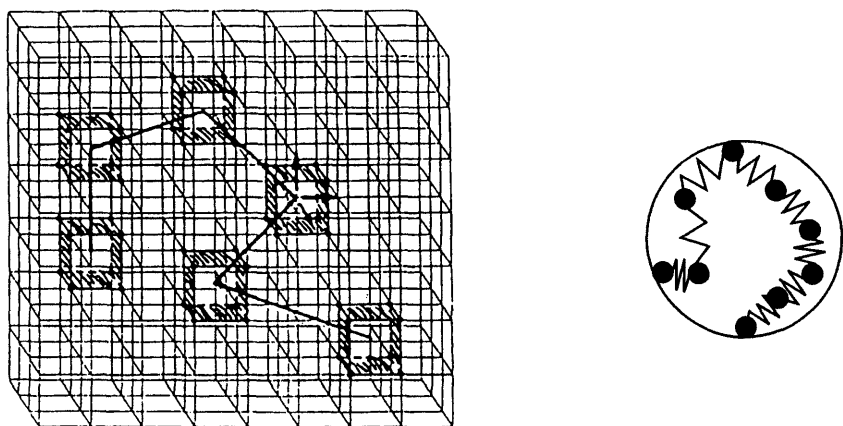


**FIG. 6** Illustration of the bond fluctuation Monte Carlo model and the standard bead-spring chain (see, e.g. [4]).

hand, in the simple bead-spring model the individual monomers are connected by anharmonic springs. The excluded volume is introduced by a simple repulsive Lennard-Jones potential which is cut off at the minimum [38]. In both cases, the excluded volume either due to the constraints of the lattice or due to the Lennard-Jones potential, is set up in such a way that during the simulation the polymers never cut through each other. While in the case of the bond fluctuation models this is completely impossible, in the case of the bead-spring polymers it is forbidden by a prohibitive Boltzmann factor. In both cases, the simulation progresses by local motions of the monomers. This is important to mention, especially for Monte Carlo simulations. Any dynamical Monte Carlo simulation, which can be used to investigate polymer dynamics, has to consist of local moves in order to simulate properly the local stochastic excitations by the background. Faster algorithms like the slithering snake algorithm, where the whole chain is moved by one lattice constantly forward and backward, or generalizations of this approach are very well suited to equilibrate a polymer melt. However, they cannot be used to study dynamical properties. Thus, both classes of models contain the two essential features needed to study polymer melts: connectivity of the polymers and non-crossability of the polymer strands. In both cases this is achieved by the excluded volume. If universality holds, both models should reproduce the behavior of polymer melts. If the chains become longer we should observe a crossover, e.g., in the diffusion constant from  $D \propto 1/N$  to  $D \propto 1/N^2$ . One could even view these two model systems as two artificial species. Thus, it should be possible by a suitable normalization to plot diffusion constant data from simulations as well as experiments into one curve without any additional adjustable parameter.

Fig. 7 gives an example of such a comparison between a number of different polymer simulations and an experiment. The data contain a variety of Monte Carlo simulations employing different models, molecular dynamics simulations, as well as experimental results for polyethylene. Within the error bars this universal analysis of the diffusion constant is independent of the "chemical species," be they simple computer models or real chemical materials. Thus, on this level, the simplified models are the most suitable models for investigating polymer materials. (For polymers with side branches or more complicated monomers, the situation is not that clear cut.) It also shows that the so-called entanglement length  $N_e$  or entanglement molecular mass  $M_e$  is the universal scaling variable which allows one to compare different polymeric melts in order to interpret their viscoelastic behavior.

If this is true, this should hold not only for polymer melts but, in the limit of long chains, also for polymer networks. In the simplest case the elastic properties of polymer networks are entirely governed by the entropic

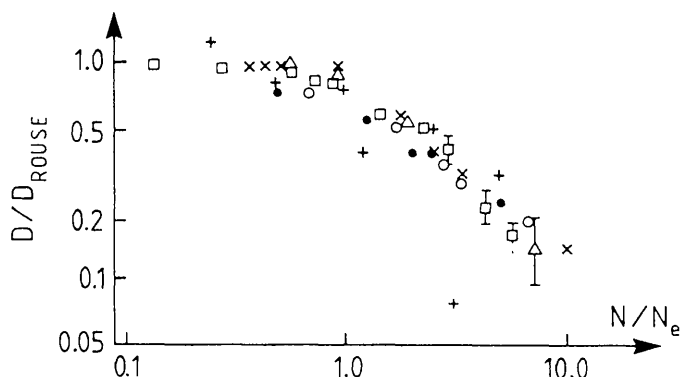


**FIG. 7**  $D(N)/D_{\text{Rouse}}(N)$  vs  $N/N_e$  or  $M/M_e$  respectively.  $D_{\text{Rouse}}$  is the short chain diffusion constant, as given by the Rouse model and measured for short chain melts.  $N_e$  and  $M_e$ , respectively, are the entanglement length and molecular weight. Data from MD and MC simulations as well as experiments on PE. (As with the simulations, uncorrected data for  $D$  are taken. Using experimental data of  $D$ , which have been treated by the usual time-temperature scaling procedure, shifts the curve but does not alter the scaling behavior.) [8,33].

elasticity of the individual strands. Classically, there are two limiting analytical models which describe the rubber elastic behavior [39]: the phantom network model where only the connectivity is considered and chains and crosslinks can freely move through each other, and the affine deformation model where the crosslinks are fixed in space and their positions distort affinely under deformation of the sample. Neither of these two models takes the non-crossability of the chains into account. Since in both models the elastic modulus is proportional to the density of polymer strands, one expects a vanishing elastic modulus  $G^0(N_s) \propto 1/N_s$  for network strand length  $N_s \rightarrow \infty$ . On the other hand, from the viscoelastic behavior of polymer melts one would expect that, for strand length going to infinity, similar effects to those in polymer melts should occur, resulting in a finite elastic modulus for infinite chain length. Again, this can be tested by polymer simulations, since this is the only situation where one has detailed control over the network properties: one knows precisely the distribution of strand lengths, the distribution of crosslinks, connectivity, etc. If one plots  $G^0(N_s)$  versus  $1/N_s$  the classical models expect linearity with an intercept at 0. On the other hand, from the so-called rubber plateau behavior of polymeric melts one would expect crossing of these curves toward a finite value  $O(1/N_e)$  for  $N_s \rightarrow \infty$ . Again, if the entanglement length is the characteristic length which governs the behavior and makes different models or different

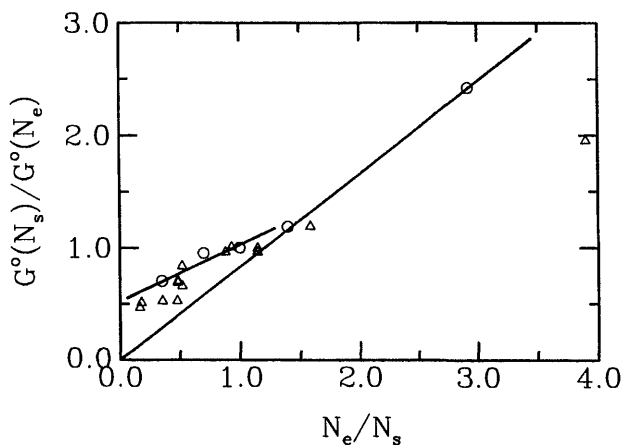


**FIG. 8** Normalized plot of the modulus compared to PDMS networks [40].

systems comparable, it should be possible to compare simulation data to experimental data in a suitably normalized way without any adjustable parameter.

Fig. 8 gives an example of a comparison between simulation data from a molecular dynamics simulation and experiments of an end-linked PDMS network [40]. There we plot the elastic modulus of a polymeric network divided by the elastic modulus of a polymeric network where the strand length between consecutive crosslinks is just the entanglement length  $N_s = N_e$  versus the reciprocal normalized chain length. Normalized chain length means  $N_s/N_e$ . Here the modulus is determined from an approximate Rouse mode analysis of the network chains. More elaborate procedures do not alter the curve (for details of more recent methods see [41]). Again, the agreement between simulation and experiment is striking.

Since, in contrast to experiment, the simulation knows in detail what the connectivity looks like, how long the strands are, and how the network loops are distributed, one can attribute this behavior to the non-crossability of the chains. Actually, one can even go further by allowing the chains to cross each other but still keep the excluded volume. Such a technical trick, which is only possible in simulations, allows one to isolate the effect of entanglement and non-crossability in such a case. As one would expect, if one allows chains to cross through each other one recovers the so-called phantom network result.

These are just two simple examples which display the power of simulation employing coarse-grained or highly simplified models. Since these simulations are extremely time consuming even at this level, results of such quality

would never be achieved with a simulation containing detailed chemical information. However, one of the challenges of the future will be to connect methods which contain all chemical details, as described in Sec. III, and simulation on a coarse-grained level in a way that one can directly make predictions about the macroscopic physical behavior of a specific polymer material [7].

## B. Polymer Glasses

Just as many small-molecule materials, polymers also form glasses [4]. Actually, most polymeric materials of everyday use are made of polymer glasses, polystyrene (PS) cups or compact discs made of polycarbonates, for instance. In many respects polymer glasses are very similar to small-molecule glasses, and there is nothing special about them. However, on the other hand, the special aspects of polymer materials allow specific studies beyond characteristic studies on small-molecule glasses.

By a variation of chemistry and/or chain length the different time regimes can be shifted. From a simulation point of view we are again faced by the decision what kind of information we want to get out of the simulation. If one wants to look at very local properties, depending on the local chemistry of the individual monomers, there is no way around a simulation with all chemical details. However, one should keep in mind that by such a technique it is impossible to equilibrate the system near the glass transition temperature.

On the other hand, polymeric materials show universal aspects of glass transition behavior, just like other materials. For instance, the classical Vogel–Fulcher behavior

$$\eta = \eta_{\infty} \exp \left\{ \frac{A}{T - T_0} \right\}$$

is also observed by polymers and frequently used to characterize systems. At the Vogel–Fulcher temperature  $T_0$  the viscosity apparently diverges, which is of course never reached in experiment, as  $T_0$  is about  $80^\circ$  below the glass transition temperature  $T_G$ .  $A$  is the generalized activation energy.  $T_G$  is often defined to be the point where the viscosity reaches the value of  $10^{13}$  poise. Even with the simplest models it is impossible to investigate viscosities comparable to this. However, by employing simple models one can try to analyze the slowing down of melt dynamics as a function of temperature, approaching the glass transition regime. In order to devise the simplest model able to describe this behavior, which is able to allow a detailed investigation into the transition regime, one can go back to simulation of spin glasses or related models. The crucial point for glass-forming materials

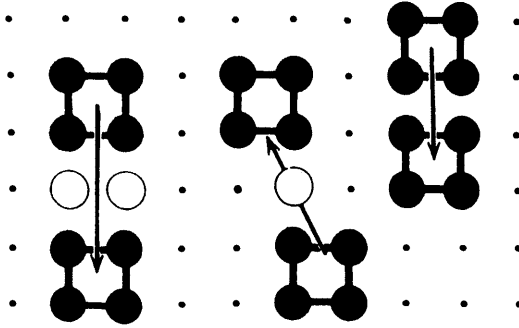


**FIG. 9** Typical ground states for a simple glass forming bond fluctuation model [42,47].

is competition between different states, absence of crystallization, and especially frustration [42]. Frustration means that a system cannot reach the ground state for all degrees of freedom simultaneously. From spin glasses it is known that frustration is a key ingredient for transition into a glassy state. A very simple, and in the course of the simulations very successful, attempt is made to include this concept within the bond fluctuation simulations. Fig. 9 gives a very simple example of how, in two dimensions, preferred bond orientations can lead to frustrations. Adopting the bond fluctuation model, as explained in Sec. IV A, one can introduce a bond energy  $H(\vec{b})$  which is given by [4]

$$H(\vec{b}) = \varepsilon(l(\vec{b}) - \sqrt{10})^2$$

or

$$H(\vec{b}) = \begin{cases} \varepsilon & \text{else} \\ 0 & \vec{b} \in \{[\pm 3, 0, 0]\} \end{cases} \quad (3)$$

Eq. 3 gives two examples of energy functions which either block one site (in the first case) or two sites (in the second case) in the ground state of each bond. If one runs the simulation at high density the situation occurs where it is impossible for all bonds to reach the ground state. This is called frustration.

The first Hamiltonian was used in the early simulations on two-dimensional glass-forming lattice polymers [42]; the second one is now most frequently used in two and three dimensions [4]. Just to illustrate the effect of such an energy function, which is given by the bond length, Fig. 10 shows two different states of a two-dimensional polymer melt and, in part,



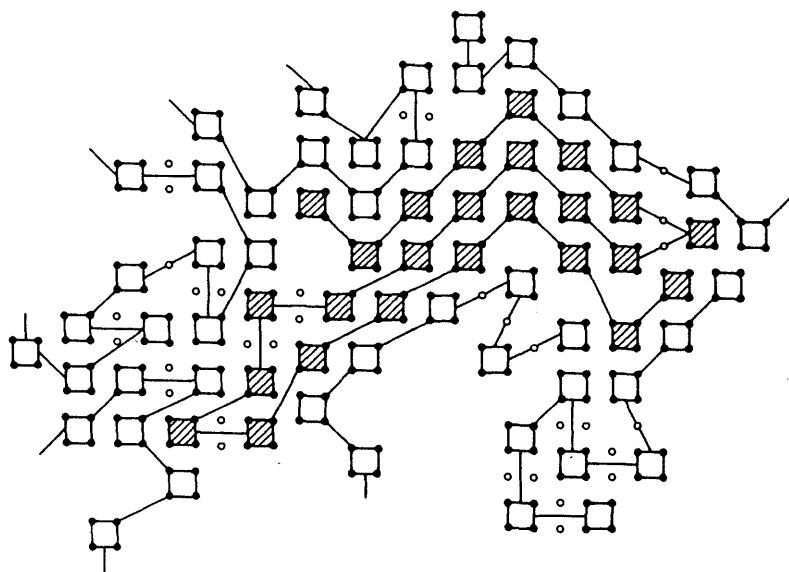
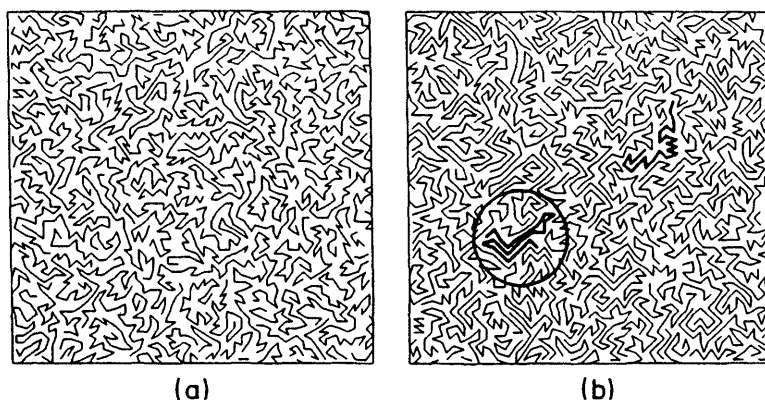


**FIG. 10** Typical conformation of a 2D polymer melt at two different temperatures:  $T = 1.0$  (a) and  $T = 0.1$  (b) for  $N = 25$  and density 0.8. The lower part gives a magnification of the encircled region of the low temperature conformation [42].

the blow-up of a special region. In a very similar way one can construct continuous-space models allowing the same investigation.

For the simulation of Fig. 10 the first form of the interaction Hamiltonian of Eq. 3 was used. Only very few bonds reach the ground state and the system is almost frozen. What is also obvious is that this

Hamiltonian does not give rise to any crystalline order in the system. By employing models like this, the quench-rate and chain-length dependence of the glass transition temperature, as well as time-temperature superposition, similar to experiments [23], were investigated in detail.

The advantage of the simulations compared to the experiments is that the correspondence between the tracer diffusion coefficient and the internal states of the chains can be investigated without additional assumptions. In order to perform a more complete analysis of the data one has to look at the quench-rate and chain-length dependence of the glass transition temperature for a given density [43]. A detailed discussion of these effects is far beyond the scope of this review. Here we just want to discuss a characteristic quantity which one can analyze in this context.

Fig. 11 shows the increase of the bond length as a function of decreasing temperature. This is from a three-dimensional simulation of chains of length  $N = 10$  at a volume fraction of  $\rho = 0.53$ . The interaction Hamiltonian is the second one from Eq. 3. The quantities are given for different quench rates. As one can clearly see from Fig. 11, with increasing quench rate the maximum bond length decays. The ground-state bond length in this case would be  $l^2 = 9$ . Note that a volume fraction of  $\rho = 0.53$  is still low enough to allow a ground state for every bond in the system. Thus, this function can be

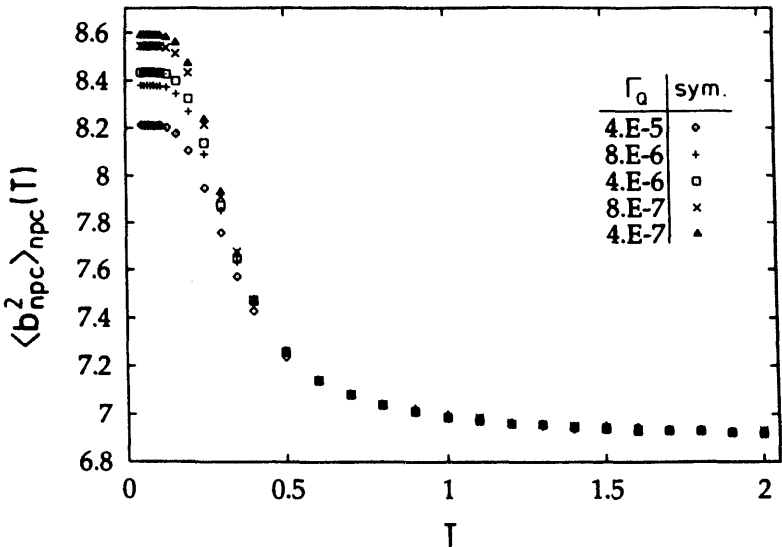


**FIG. 11** Plot of squared bond length vs  $T$  for five cooling rates, glass-forming bond fluctuation Monte Carlo simulations [47].

interpreted as departure out of equilibrium as a function of the quench rate. In a similar way, the radius of gyration of the system can be analyzed as well as structural relaxations such as the structure function  $S(\vec{q})$  of a whole system or of single chains.

Since quench rates in simulations typically are artificially high, this leads to a special problem for comparison with experiment as well as to the question whether there is a more general way to determine the glass transition temperature from the structure of the system. The experimental definition of viscosity is certainly not applicable to simulations.

In this context it turned out to be useful to investigate data in terms of the difference between the "external" and "internal" temperature of the system [43,44]. The external temperature is the temperature given from outside and used in the Metropolis sampling for the acceptance of moves of the monomers. The internal temperature, in contrast to the external temperature, is given by the occupation number of the states of a free bond in equilibrium.

The internal temperature  $T_i$  is then defined as

$$T_i = \epsilon / \ln \frac{g_\epsilon \mathcal{N}(0)}{g_0 \mathcal{N}(\epsilon)} \quad (4)$$

where  $\mathcal{N}(0)$  and  $\mathcal{N}(\epsilon)$  are the number of bonds in the ground and in the excited state respectively;  $g_0$  and  $g_\epsilon$  give the degeneracy of the states. Thus  $T_i$  defines the deviation from equilibrium in the course of the simulation.

For high temperatures one would naively expect that  $T/T_i$  is near to 1, and then for lower temperatures slowly starts to deviate from equilibrium, meaning that this ratio should decay. However, as Fig. 12 shows, for high temperatures this ratio is significantly smaller than 1, increasing with decreasing temperature and then breaking down to approach 0. The deviation at high temperatures comes from the fact that the simple definition of Eq. 4 takes into account only uncorrelated intra-chain effects. However, when one simulates a melt of chains the degeneracy of the states is significantly different, due to the constraints on a given monomer induced by all the other monomers. If one corrects for this, one actually finds that for high temperatures this ratio is very near to 1 and slowly decays as a function of temperature until it starts to break down around the glass transition temperature. However, the general scaling picture as shown in Fig. 12 does not change significantly up to a shift. Since all the data for the different cooling rates more or less coincide and define a characteristic temperature where the curve changes its behavior, this figure suggests that there might be a possibility of defining a universal glass transition temperature for the cooling rate going to 0. This procedure actually allows one to compare the cooling rate dependent glass transition temperature with the asymptotic freezing temperature of a system. Certainly, there has to be much more research in this

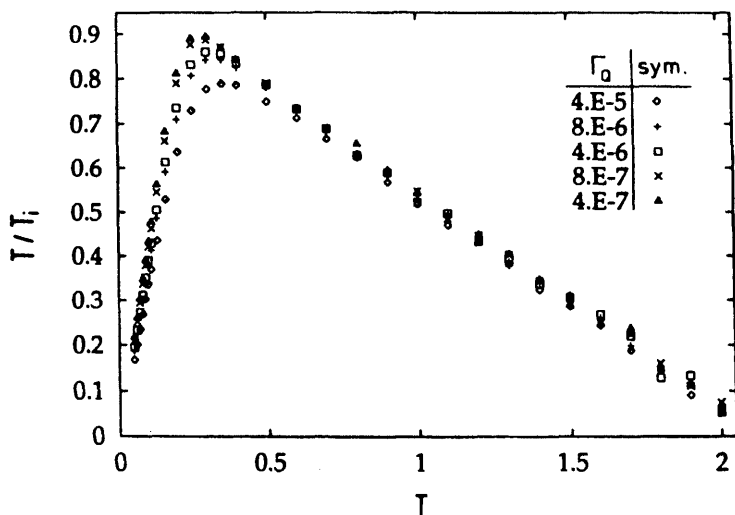


**FIG. 12** Plot of  $T/T_i$  vs  $T$  for five different cooling rates [43].

direction to determine whether the glass transition is a real phase transition, or whether it is just freezing of a liquid as it departs out of equilibrium.

Another important characteristic aspect of systems near the glass transition is the time-temperature superposition principle [23,34,45,46]. This simply means that suitably scaled data should all fall on one common curve independent of temperature, chain length, and time. Such generalized functions which are, for example, known as generalized spin autocorrelation functions from spin glasses can also be defined from computer simulation of polymers. Typical quantities for instance are the autocorrelation function of the end-to-end distance  $\vec{R}_{EE}$  or radius of gyration  $R_G$  of a polymer chain in a suitably normalized manner:

$$\Phi_{R_{EE}}(t) = \frac{\langle \vec{R}_{EE}(t) \vec{R}_{EE}(0) \rangle}{\langle R_{EE}^2 \rangle} \quad (5)$$

averaged for each chain separately.

Fig. 13 shows this autocorrelation function where the time is scaled by mean square displacement of the center of mass of the chains normalized to  $\langle R_{EE}^2 \rangle$ . All these curves follow one common function. It also shows that for these melts (note that the chains are very short!) the interpretation of a chain dynamics within the Rouse model is perfectly suitable, since the time is just given within the Rouse scaling and then normalized by the typical extension of the chains [47].

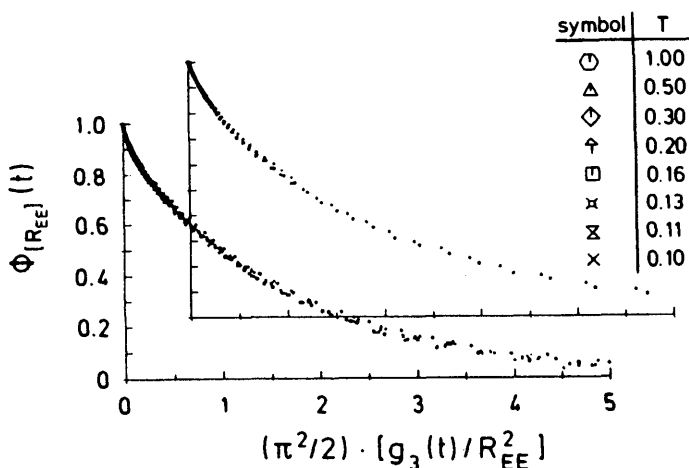


**FIG. 13** Scaling plot of the auto-correlation function  $\Phi(R_{EE}(t))$  for different temperatures for a bond fluctuation MC simulation [47].

Experimentally, these functions are usually determined only indirectly via the scattering functions of the whole system or the scattering functions of marked chains (see, e.g., [34]). This is one of the advantages of computer simulations over to experiments. However, in order to make significant statements for experimental systems it is always very important to directly compare computer simulations with experimental investigations as well as analytic theories.

## V. CONCLUSIONS

This short overview can only give an impression of what can be done with modern molecular simulations. We have tried to present the strength as well as the limitations of the various approaches. Many aspects had to be omitted or treated in a cursory way. For other techniques as well as other application areas (morphology of mixtures, interfaces, polymers in solution) the reader is referred to a number of books and reviews [2–7]. It should have become clear, though, that both atomistic and mesoscopic approaches have their place in polymer science and that they are complementary to analytical theory as well as to experiment. In the future, especially systematic attempts to connect simulations on different scales should lead to significant progress [7]. This would enable the prediction of macroscopic properties, such as those governing the performance of polymers, from the chemical structure of the polymer. However, a rigorous

connection of length scales is still one of the challenges of polymer theory for the years to come.

## ACKNOWLEDGMENT

The authors benefitted from discussions and a fruitful collaboration with the groups of K. Binder, G. S. Grest, W. F. van Gunsteren, and U. W. Suter.

## REFERENCES

1. D. Frenkel, B. Smit. *Understanding Molecular Simulation: From Basic Algorithms to Applications*. San Diego, CA: Academic Press, 1996.
2. L. Monnerie, U. W. Suter, eds. *Atomistic Modeling of Physical Properties. Advances in Polymer Science No. 116*. Berlin: Springer, 1994.
3. E. A. Colbourn, ed. *Complex Simulation of Polymers*, London: Longman Group, 1994.
4. K. Binder, ed. *Monte Carlo and Molecular Dynamic Simulations in Polymer Science*, New York: Oxford University Press, 1995.
5. R. J. Roe, ed. *Computer Simulation of Polymers*. Englewood Cliffs, NJ: Prentice Hall, 1991.
6. K. Binder, G. Ciccotti, eds. *Monte Carlo and Molecular Dynamics of Condensed Matter Systems, Como Conference Proceeding*. Bologna: Società Italiana di Fisica, 1996.
7. J. Baschnagel, K. Binder, P. Doruker, A. A. Gusev, O. Hahn, K. Kremer, W. L. Mattice, F. Müller-Plathe, M. Murat, W. Paul, S. Santos, U. W. Suter, V. Tries. *Adv Poly Sci* (in press).
8. G. S. Grest, B. Dünweg, K. Kremer. *Comp Phys Comm* 55:269, 1989.
9. K. Kremer, G. S. Grest. *J Chem Phys*. 92:5057, 1990.
10. M. Pütz, A. Kolb. *Comp Phys Comm* 113:145, 1998.
11. M. P. Allen, D. J. Tildesley. *Computer Simulations of Liquids*. London: Oxford University Press, 1989.
12. W. F. van Gunsteren, H. J. C. Berendsen. *Angew Chem Int Ed Engl* 29:992, 1990.
13. C. R. A. Catlow, S. C. Parker, M. P. Allen. *Computer Simulation of Fluids, Polymers and Solids*. Dordrecht: Kluwer, 1990.
14. W. F. van Gunsteren, P. K. Weiner, A. J. Wilkinson. *Computer Simulation of Biomolecular Systems, Vol. 2*. Leiden: ESCOM, 1993.
15. R. Car, M. Parrinello. *Phys Rev Lett* 55:2471, 1985.
16. F. Müller-Plathe, W. F. van Gunsteren. *Macromolecules* 27:6040, 1994.
17. H. Liu, F. Müller-Plathe, W. F. van Gunsteren. *J Chem Phys* 103:4745, 1995.
18. F. Müller-Plathe, H. Liu, W. F. van Gunsteren. *Comput Polym Sci* 5:89, 1995.
19. F. Müller-Plathe. *Macromolecules* 29:4782, 1996.
20. F. Müller-Plathe. *Mol Sim* 18:133, 1996.
21. F. Müller-Plathe, W. F. van Gunsteren. *Polymer* 38:2259, 1997.

22. C. D. Berweger, W. F. van Gunsteren, F. Müller-Plathe. *Chem Phys Lett* 232:429, 1995.
23. W. Brostow, R. D. Corneliussen. *Failure of Plastics*. München: Hanser, 1993.
24. F. Müller-Plathe. *Acta Polym* 45:259, 1994.
25. A. A. Gusev, F. Müller-Plathe, U. W. Suter, W. F. van Gunsteren. In: L. Monnerie, U. W. Suter, eds. *Atomistic Modeling of Physical Properties, Advances in Polymer Science No. 116*. Berlin: Springer: 1994, pp. 207–248.
26. F. Müller-Plathe. *Chem Phys Lett* 252:419, 1996.
27. F. Müller-Plathe. *J Membr Sci* 141:147, 1998.
28. F. Müller-Plathe. *J Chem Phys* 108:8252, 1998.
29. F. Müller-Plathe. *Macromolecules* 31:6721, 1998.
30. F. Müller-Plathe. *Ber Bunsen-Ges Phys Chem* 102:1679, 1998.
31. K. Tasaki. *J Am Chem Soc* 118:8459, 1996.
32. M. Doi, S. F. Edward. *The Theory of Polymer Dynamics*. Oxford: Clarendon Press, 1986.
33. B. Dünweg, G. S. Grest, K. Kremer. In: S. G. Whittington, ed. *Proceedings of Numerical Methods for Polymeric Systems*. New York: Springer, 1997.
34. B. Ewen, D. Richter. In: K. Dusek, ed. *Advances in Polymer Science No. 134*, Berlin: Springer, 1997, pp. 3–129.
35. P. G. de Gennes. *J Chem Phys* 55:572, 1971.
36. H. P. Wittmann, K. Kremer. *Comp Phys Comm* 61:309, 1990.
37. H. P. Wittmann, K. Kremer. *Comp Phys Comm* 71:343, 1992.
38. G. S. Grest, K. Kremer. *Phys Rev A* 33:3628, 1986.
39. H. E. Mark, B. Erman, eds. *Elastomeric Polymer Networks*, Englewood Cliffs, NJ: Prentice Hall, 1992.
40. E. R. Duering, K. Kremer, G. S. Grest. *J Chem Phys* 101:8169, 1994.
41. R. Everaers. *Eur Phys J* 4:341, 1998.
42. H. P. Wittmann, K. Kremer, K. Binder. *J Chem Phys* 96:6291, 1992.
43. J. Baschnagel, K. Binder, H. P. Wittmann. *J Phys C* 5:1597, 1993.
44. J. Baschnagel, R. Dickmann. *J Chem Phys* 101:3326, 1994.
45. J. Jäcke, *Rep Progr Phys* 49:171, 1986.
46. K. Binder, A. P. Young. *Rev Mod Phys* 58:801, 1986.
47. H. P. Wittmann, K. Kremer, K. Binder. *Macrom Theory Simul* 1:275, 1992.

# 11

## Computer Simulations of Living Polymers and Giant Micelles

**ANDREY MILCHEV** Institute for Physical Chemistry,  
Bulgarian Academy of Sciences, Sofia, Bulgaria

I. Introduction and Overview	510
II. Models and Methods	511
A. Static models	512
B. Dynamic models	515
III. Scaling Predictions for EP	520
A. MFA treatment	520
B. Beyond MFA: Correlation effects	521
IV. Simulational Results—Static Properties	522
A. Molecular weight distribution	522
B. Conformational properties	526
C. Equilibrium polymerization as a phase transition	529
D. Living polymers in constrained geometries	532
V. Simulational Results—Dynamic Properties	537
A. Kinetics of relaxation to equilibrium	537
B. Transport properties in giant micelles	544
VI. Conclusions and Outlook	547
References	549



## I. INTRODUCTION AND OVERVIEW

Systems in which polymerization is believed to take place under conditions of chemical equilibrium between the polymers and their respective monomers are termed "living polymers" (LP). These polymers, as well as some surfactant molecules which spontaneously assemble in solutions into "wormlike" micelles, can be considered as long linear-chain macromolecules that can break and recombine reversibly and so are in dynamic equilibrium with respect to their molecular weight distribution (MWD). In contrast to giant wormlike micelles (GM), however, LP grow only from the active sites and do not break in the middle of the polymer chain. LP chains do not combine together, and ends of a given chain do not combine to make a ring. Thus, despite wide ranging similarity in the properties of LP and GM, they comprise quite different systems and this distinction is necessary to bear in mind in order to understand some differences in their behavior. Probably a more appropriate generic name for both LP and GM would be the term *equilibrium polymers* (EP), emphasizing the state of chemical equilibrium—we shall use the term EP throughout this article.

A number of examples have been studied in recent years, including liquid sulfur [1–3,8] and selenium [4], poly( $\alpha$ -methylstyrene) [5–7], polymer-like micelles [9,11], and protein filaments [12]. Besides their importance for applications, EP pose a number of basic questions concerning phase transformations, conformational and relaxational properties, dynamics, etc. which distinguish them from conventional "dead" polymers in which the reaction of polymerization has been terminated. EP motivate intensive research activity in this field at present.

The reversible aggregation of monomers into linear polymers exhibits critical phenomena which can be described by the  $n \rightarrow 0$  limit of the  $n$ -vector model of magnetism [13,14]. Unlike mean field models, the  $n$ -vector model allows for fluctuations of the order parameter, the dimension  $n$  of which depends on the nature of the polymer system. (For linear chains  $n \rightarrow 0$ , whereas for ring polymers  $n = 1$ .) In order to study equilibrium polymers in solutions, one should model the system using the *dilute*  $n \rightarrow 0$  magnet model [14]; however, a theoretical solution presently exists only within the mean field approximation (MFA), where it corresponds to the Flory theory of polymer solutions [16].

The equilibrium form of the MWD of EP has also been subject to controversy and discussions [15,33,34]. Also, the relaxation of the MWD after a temperature quench, or sudden change of the density of the system, is non-trivial and proceeds very differently in LP and GM.

Eventually one should emphasize that in GM stress relaxation proceeds through a unique mechanism [11], very different from what is well established

in polymer melts, for instance, and this finding has initiated a lot of scientific interest recently.

Due to experimental difficulties [7,11], EP are not easy to study in laboratory conditions and their properties still pose a number of questions. While phase diagrams of LP can be reasonably described by the MFA [5], the experimental evidence concerning microscopic properties such as, e.g., the extent of growth in micelles is controversial [17]. Some light scattering, NMR, and sedimentation experiments [19] suggest that micelles in solutions grow considerably with decreasing temperature and rising density, whereas other neutron scattering measurements [20] and transient fluorescent experiments [18] have been interpreted in terms of much smaller growth with temperature and density. So far we are not aware of any direct measurements of the MWD in such systems.

Given the shortcomings of an approximate analytical treatment (MFA) and the difficulties with laboratory measurements, it is conceivable that numerical experiments, being exact within the framework of the respective model and able to account explicitly for various factors which influence experiments, might help much in understanding the thermodynamic behavior and the properties, both static and dynamic, of living polymers. It should be emphasized that, in their latest versions, computer algorithms are capable of reproducing average chain lengths comparable to those measured in laboratory experiments, so that a meaningful comparison of simulational and measured data can be performed.

In the next section we describe the basic models that have been used in simulations so far and summarize the Monte Carlo and molecular dynamics techniques that are used. Some principal results from the scaling analysis of EP are given in Sec. 3, and in Sec. 4 we focus on simulational results concerning various aspects of static properties: the MWD of EP, the conformational properties of the chain molecules, and their behavior in constrained geometries. The fifth section concentrates on the specific properties of relaxation towards equilibrium in GM and LP as well as on the first numerical simulations of transport properties in such systems. The final section then concludes with summary and outlook on open problems.

## II. MODELS AND METHODS

Generally, the models used for simulation of living polymers can be divided roughly into two classes, focused on static or dynamic properties of the LP or GM. The "static" models are mainly designed to study equilibrium conformational properties of the polymer chains, critical behavior at the polymerization transition, and molecular weight distribution

[21,25–27,29,55]. For dynamical studies of diffusion, conformational and transport behavior under shear stress, or kinetics of relaxation, one resorts to “dynamic” models [54,58,65] in which the topological connectivity of the chains is maintained during the simulation.

## A. Static Models

One of the main objectives of such models is to overcome the extremely slow dynamics of polymer chains by creating configurations, each of them assembled at random, according to a Metropolis criterion for creation or breaking of existing energy bonds while no extra movement of the monomers on the lattice is considered. Thus one can map the problem of GM onto a generalized Potts model [25,27,28], sometimes referred to as that of independent monomer states [21–24], whereby each new configuration is derived from the preceding one by creation or annihilation of monomers on the sites of a lattice (subject to some chemical potential  $\mu$ ) and the filled lattice sites are connected into chains in compliance with standard energy considerations. One considers a regular cubic lattice of size  $\mathcal{L}^d$  in  $d = 2$  [25,27] or in  $d = 3$  [28] dimensions with periodic boundary conditions. (If interaction with impenetrable walls is to be studied, in one direction the boundary conditions are then chosen as free.) Each lattice site may be either empty or occupied by a *bifunctional* monomer with two strong (covalent) “dangling” bonds, pointing along separate lattice directions. These monomers fuse when dangling bonds of nearest-neighbor monomers point toward one another, releasing an energy  $J > 0$  and forming the backbone of self-avoiding polymer chains (no crossing at vertices is allowed). Right-angle bends, ensuring the semiflexibility of such chains, are assigned an additional energy  $\sigma > 0$  in order to include the inequivalence between rotational isomeric states (e.g. *trans* and *gauche*) which is found in real polymers. The third energetic parameter,  $W$ , accounting for the weak (van der Waals) *interchain* interactions, may be introduced as being responsible for the phase separation of the system into dense and sparse phases when temperature,  $T$  and/or chemical potential  $\mu$  are changed.  $W$  is thus the work for creation of empty lattice sites (holes) in the system. Such vacancies may represent also solvent molecules. On a cubic lattice in three dimensions ( $d = 3$ ) one then defines  $q = 16$  possible states ( $q = 7$  in  $d = 2$ ),  $S_i$ , of a monomer  $i$  (three straight “stiff” junctions,  $S_i = 2, 3, 4$ , twelve bends,  $S_i = 5, \dots, 16$ , and a hole  $S_1$ )—cf. Table 1. The Hamiltonian for the model can be written as

$$H = \sum_{i < j} \mathcal{J}_{ij} S_i S_j - \sum_i (\mu + e_i) S_i \quad (1)$$

**TABLE 1** The 16 Independent Monomer States.

1	2	3	4	5	6	7	8
9	10	11	12	13	14	15	16

where  $|S_i| = 1$  for  $S_i = 2, 3, \dots, 16$ , and  $|S_1| = 0$  (a hole). It is important to note that the interaction constant depends on the relative position of the nearest-neighbor monomer states,  $\mathcal{J}_{ij} \neq \mathcal{J}_{ji}$ . Thus, for example,  $\mathcal{J}_{27} = -J$  whereas  $\mathcal{J}_{72} = -W$  (see Table 1). The local energies  $e_i = \sigma$  for the bends and  $e_i = 0$  for the *trans* segments. An additional energy  $\epsilon$  may be ascribed to segments which are in contact with the adsorbing wall.

The ground states of this lattice model depend on the relative strengths of the three characteristic parameters  $J$ ,  $W$ , and  $\sigma$ . Long chains at low temperature are energetically favored only if  $J/W > 1$  (in reality the ratio  $J/W$  of covalent to van der Waals bond energies varies roughly from 10 to 100). It is also clear that for  $\sigma > 0$  the chains will lose flexibility with decreasing temperature and at  $T = 0$  the system will consist of parallel long stiff rods.

In the simulation one computes an orientational order parameter,  $\Psi$

$$\Psi = \begin{cases} |c_1 - c_2| & \text{for } d = 2 \\ \sqrt{[(c_1 - c_2)^2 + (c_1 - c_8)^2 + (c_2 - c_8)^2]/2} & \text{for } d = 3 \end{cases} \quad (2)$$

where  $c_1$ ,  $c_2$ , and  $c_8$  are the fraction of *trans*-bonds pointing in the  $x$ ,  $y$ , and  $z$  directions. Usually one computes the order parameter susceptibility  $\chi$ , the cumulant  $U = 1 - \langle \Psi^4 \rangle / [3 \langle \Psi^2 \rangle^2]$ , as well as a number of thermodynamic quantities such as internal energy  $E$ , total concentration of monomers  $\phi$ , specific heat  $C = (\mathcal{L}^3/k_B T^2)(\langle E^2 \rangle - \langle E \rangle^2)$ , compressibility  $\kappa = (\mathcal{L}^3/k_B T)(\langle \phi^2 \rangle - \langle \phi \rangle^2)$ , and the average flexibility of the chains  $f = (1 - c_1 - c_2 - c_8)/(1 - c_0)$ , which is given by the ratio of the number of bends over the total number of monomers ( $c_0$  is the concentration of vacancies in the lattice).

The simulation starts usually from an initial configuration with lattice sites assigned "spin" values between 1 and 16 at random, although at lower

temperature ordered configurations of parallel stiff rods may save equilibration time when  $W \neq 0$ . In the course of a sweep through the lattice each "spin" is updated, depending on a Boltzmann factor according to a Metropolis rule [53]. Periodically a cluster counting algorithm is applied in order to gather statistics on the molecular weight distribution (MWD), center of mass distribution and density profile at hard walls. Cluster counting may be carried out either by the standard Hoshen–Koppelman summation method [30], or by a faster technique [28] using the fact that an inner monomer of a chain may be linked to only two neighbors and exploiting the topological connectivity of the chain. In this latter method a randomly chosen monomer is tested for a (right) neighbor. If there is such, the neighbor is tested in turn for a new neighbor until one of the chain ends is reached. Then, starting from the initial monomer, the other fraction of the chain is traced, and all sites belonging to this chain are declared "empty" until the end of the scan through the lattice. Since in this model polymer chains may, in principle, form rings, in addition to the MWD and the average chain length  $\langle L \rangle$  the average number of rings is calculated.

Another efficient simulation technique for studying reversible polymerizing systems such as LP, used by Livne [26], is based on stepwise elongation and contraction of polymer chains in a grand canonical ensemble of chain lengths. This procedure is governed by a fugacity  $\lambda$  for adding or deleting a chain-end link, and the number of chains is controlled by another fugacity  $\eta$  for chain ends. Since only chain ends are involved in this process, chains cannot break in the middle or aggregate with other chains, and no rings are formed. The method is thus suitable for describing systems like poly- $\alpha$ -methylstyrene [5–7], liquid sulfur [8], and certain dyes [9]. Some of these systems [5] require an initiator so, in the method, only one of the chain ends is considered active. The partition function is given by

$$\Xi = \sum_{p=1}^{\infty} \sum_{l=1}^{\infty} \eta^p \lambda^l U_{pl} \quad (3)$$

where  $U_{pl}$  is the number of ways to arrange  $p$  different chains of a total number of  $l$  links on a lattice of  $N_0$  sites ( $N_0$ , which is the volume of the system, is kept fixed).

The concentration of links,  $\Phi_l = l/N_0$ , and that of polymers,  $N_p = p/N_0$ , follow from standard relations between concentrations and activities

$$\Phi_l = \frac{1}{N_0} \frac{\partial \ln \Xi}{\partial \ln \lambda}, \quad \Phi_p = \frac{1}{N_0} \frac{\partial \ln \Xi}{\partial \ln \eta} \quad (4)$$

and the average polymer length is  $\langle L \rangle = \Phi_l / \Phi_p$ .

At each Monte Carlo step (MCS), either a dimer is formed from two adjacent monomers or a monomer is added or deleted from the chain end. The transition probabilities are

$$P_d = \frac{n_d \eta}{n_d \eta + n_e} \quad (5)$$

$$P(N \rightarrow N + 1) = \frac{z\lambda}{1 + z\lambda} \frac{n_e}{(n_d \eta + n_e)},$$

$$P(N \rightarrow N - 1) = \frac{1}{1 + z\lambda} \frac{n_e}{(n_d \eta + n_e)} \quad (6)$$

where  $P_d$  is the probability to form a dimer,  $n_d$  is the number of empty sites in the lattice,  $n_e$  is the number of chain ends, and  $z$  is the coordination number of the lattice. A random number is chosen between zero and one and is compared to the transition probabilities of Eqs. (5,6), where three possibilities can occur: (1) if the random number is less than  $P_d$ , a random site is chosen from the list  $n_d$ , and a new dimer, which starts a new chain, is located; (2) if the random number is larger than  $P_d$  but less than the sum  $P_d + P(N \rightarrow N + 1)$ , one chain end is chosen from the list  $n_e$  and in a direction, selected at random, a new link is added to the chain, provided the new site has been originally empty; otherwise the move is rejected; (3) since the probabilities (5,6) are normalized to one, the last possibility is to remove a link from one of the chains, selected at random from the list  $n_e$ ; if the chain consists of a single link, the chain is discarded from the lattice. One should note that this model, like the previous one, is ergodic. Uncorrelated configurations are separated by roughly  $\langle L \rangle^2$  MCS from each other.

## B. Dynamic Models

These models are designed to reproduce the random movement of flexible polymer chains in a solvent or melt in a more or less realistic way. Simulation results which reproduce in simple cases the so-called Rouse [49] or Zimm [50] dynamics, depending on whether hydrodynamic interactions in the system are neglected or not, appear appropriate for studying diffusion, relaxation, and transport properties in general. In all dynamic models the monomers perform small displacements per unit time while the connectivity of the chains is preserved during the simulation.

The bond fluctuation model (BFM) [51] has proved to be a very efficient computational method for Monte Carlo simulations of linear polymers during the last decade. This is a coarse-grained model of polymer chains, in which an "effective monomer" consists of an elementary cube whose eight sites on a hypothetical cubic lattice are blocked for further occupation (see



of the lattice spacing and the symbol  $P$  stands for all permutations and sign combinations of the Cartesian coordinates  $(l_x, l_y, l_z)$ . Monomer–monomer interactions can extend over a certain range in the lattice and the flexibility of the chains may be accounted for by ascribing some additional energy to certain bond angles. The algorithm displays Rouse behavior for all spatial dimensions and combines typical advantages of the lattice MC methods with those of the continuous Brownian dynamics algorithm. The adequacy of the BFM algorithm to describe static and dynamic behavior of polymers has been proven in a number of sensitive investigations [52] on conventional polymer systems.

The BFM has been modified so as to describe GM [58] by allowing for scission and recombination of the bonds, according to the following scheme:

- A monomer is chosen at random and allowed to perform a move according to the BFM algorithm.
- If the monomer happens to be at the end of a chain, an attempt is made to create a bond with another monomer that might be present on any one of the 108 neighboring sites which are also chosen at random. If a single monomer or a polymer end is found, a new bond is created and the length of the chain is increased by one.
- Another monomer is chosen at random and, if the bond to the right of it exists, it is attempted to break it according to the standard Metropolis rule [53].

With the total number of monomers and the volume of the system fixed, a number of statistical averages can be sampled in the course of canonical ensemble averaging, like the mean squared end-to-end distance  $\langle R_e^2 \rangle$ , gyration radius  $\langle R_g^2 \rangle$ , bond length  $\langle l^2 \rangle$ , and mean chain length  $\langle L \rangle$ .

A major problem in such an algorithm turns out to be data organization. Since chains constantly break and recombine, neither the identity of the chains or their number, nor the sequence of particular monomers within a given chain, persist for more than an MCS. Thus comparatively small lattices of size  $30 \times 30 \times 30$  for densities  $\phi \leq 0.4$ , containing less than a total of 1300 monomers while requiring about 60 Mbytes of operational memory, have been sampled [58–62, 64] in the first applications of this method. Finite size effects, therefore, become important for systems of that size since, in order to ensure good statistics for the different chain lengths, the mean chain length has always been kept smaller than 10% of the total number of monomers. It is clear that this condition restricts the choice of lower temperatures where  $\langle L \rangle \rightarrow \infty$ .

Recently this model was largely improved by a novel and more efficient organization of data [65,66] (Fig. 2), so that the total number of particles



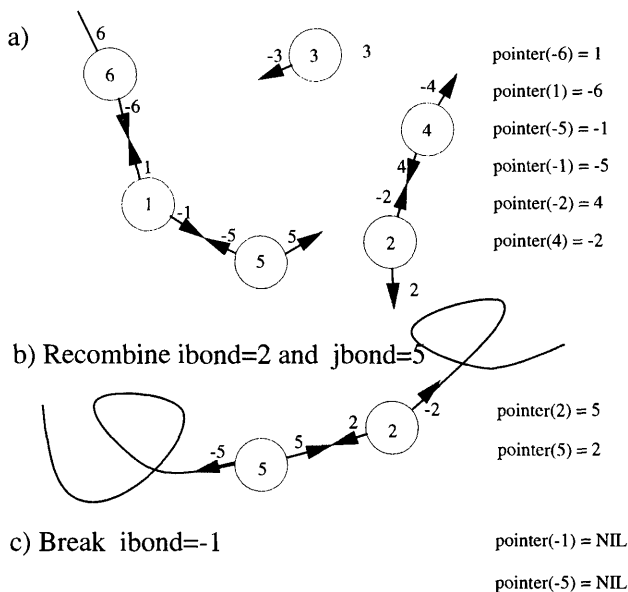


**FIG. 2** Sketch of algorithm [65]: (a) Each monomer has two (saturated or unsaturated) bonds. Chains consist of coupled bonds, each pointing to a counterpart:  $jbond = pointer(ibond) \Leftrightarrow ipoint = pointer(jpoint)$ . The pointers of all end-bonds point to 0. (b) Recombination of two initially unsaturated bonds  $ibond = 2$  and  $jbond = 5$  connects the respective monomers  $imon = 2$  and  $jmon = 5$ . Note that only two pointers have to be changed and that the remaining chains (bold lines) behind both monomers are not involved. (c) Breaking a saturated bond  $ibond$  requires resetting the pointers of the two coupled bonds  $ibond$  and  $jbond = pointer(ibond)$  to 0.

during the simulation has been increased by two orders of magnitude. Instead of chains, the data organization has been based on the two saturated or unsaturated *bonds* of each monomer [66]. Using the assumption that no branching of chains is allowed, the two bonds of each monomer  $imon$  are called  $ibond = imon$  and  $ibond = -imon$ . No specific meaning (or direction) is attached to the sign: this is merely a convenience for identifying the monomer from the bond list using  $imon = |ibond|$ . Pointers are taken to couple independently of sign (Fig. 2). The bonds are coupled by means of a pointer list in a completely transitive fashion [ $jbond = pointer(ibond) \Leftrightarrow ibond = pointer(jbond)$ ] so as to make recombination and scission as fast as possible; only two simple vector operations are required for breaking bonds or recombination as shown in Fig. 2. Note that this would be impossible in any algorithm involving only one bond per

monomer; the latter requires implicit sequential order of the segments in the chains, forcing sorting operations of the order of the mean chain length for every recombination. Unsaturated bonds at chain ends point to NIL (nowhere). Only these bonds may recombine. With this algorithm no explicit distinction between end-monomers, free monomers or middle monomers is required.

The data structure organization described above has been implemented in the BFM as well as in a very efficient off-lattice Monte Carlo algorithm, discussed in detail in the next chapter, which was modified to handle EP and used to study shear rate effects on GM [57].

Molecular dynamics, in contrast to MC simulations, is a typical model in which hydrodynamic effects are incorporated in the behavior of polymer solutions and may be properly accounted for. In the so-called non-equilibrium molecular dynamics method [54], Newton's equations of a (classical) many-particle problem are iteratively solved whereby quantities of both macroscopic and microscopic interest are expressed in terms of the configurational quantities such as the space coordinates or velocities of all particles. In addition, shear flow may be imposed by the homogeneous shear flow algorithm of Evans [56].

In the case of micellar solutions, studied in this work, the monomers interact via two-body potentials. The non-bonded particles interact via the repulsive part of a Lennard-Jones potential

$$U_{\text{LJ}} = \begin{cases} 4\epsilon[r^{-12} - r^{-6} + \frac{1}{4}] & \text{for } r \leq r_{\text{cut}} \\ 0 & \text{for } r \geq r_{\text{cut}} \end{cases} \quad (7)$$

where distance  $r$  is measured in units of the monomer radius.

Nearest neighbors along a chain interact by means of a FENE (finitely extendible nonlinear elastic) potential

$$U_{\text{FENE}} = \begin{cases} -\frac{kR_0^2}{2} \ln[1 - (r/R_0)^2] & \text{for } r \leq \min(R_0, R_C) \\ -\frac{kR_0^2}{2} \ln[1 - (r/R_C)^2] & \text{for } r \geq R_C \end{cases} \quad (8)$$

where  $R_0$  is the maximum bond length and  $R_C$  is some cut-off radius. This truncated FENE potential provides the scission energy, so that a bond is likely to break because of thermal fluctuations if it is stretched. In this work a total of 8400 beads has been simulated in order to study flow effects on the MWD and  $\langle L \rangle$ .

### III. SCALING PREDICTIONS FOR EP

#### A. MFA Treatment

As pointed out by Flory [16], the principle of equal reactivity, according to which the opportunity for reaction (fusion or scission) is independent of the size of the participating polymers, implies an exponential decay of the number of polymers of size  $l$  as a function of  $l$ . Indeed, at the level of mean-field approximation in the absence of closed rings, one can write the free energy for a system of linear chains [11] as

$$\frac{F}{k_B T} = \sum_l C(l, T) b^d \left\{ \ln[C(l, T) b^d] + \frac{J}{k_B T} + \mu l \right\} \quad (9)$$

where the MWD for chain length  $l$  is denoted by  $C(l, T)$ ,  $k_B$  stands for the Boltzmann constant,  $b^d$  is the volume of a single monomer in  $d$  dimensions, and the chemical potential  $\mu$  is a Lagrange multiplier. Without loss of generality one may set to zero in Eq. (9) the part of the free energy linear in chain length. The density of the system  $\phi$  is then

$$\phi = \sum_l l C(l, T) \quad (10)$$

Minimization of Eq. (9) with respect to  $C(l, T)$ , subject to the condition (10), yields

$$C(l, T) = \frac{1}{\langle L \rangle} \exp \left( -\frac{l}{\langle L \rangle} \right) \quad (11)$$

$$\langle L \rangle = \sqrt{\frac{\phi}{e}} \exp \left( \frac{J}{2k_B T} \right) \quad (12)$$

This result should be valid for sufficiently high density  $\phi$  where correlations, brought about by the mutual avoidance of the chains, are negligible. Due to the recombination–scission process a polydisperse solution of living polymers should absorb or release energy as the temperature is varied. This is reflected by the specific heat  $c_v$ , which can be readily obtained from Eq. (9) as a derivative of the internal energy  $U$

$$U = J \sum_l C(l, T) = J \langle L \rangle \exp \left( -\left( \frac{J}{k_B T} - 1 \right) \right) \quad (13)$$

For  $c_v$  (per monomer) one has

$$c_v = \frac{1}{\sqrt{\phi e}} \frac{\exp \left[ -\frac{J}{2k_B T} \right]}{2k_B T^2} J^2 \quad (14)$$

which has a maximum at  $k_B T_c = J/4$ .

## B. Beyond MFA: Correlation Effects

One can easily extend the above analysis to dilute and semi-dilute solutions of EP [65,66] if one recalls [67] from ordinary polymers that the correlation length  $\xi$  for a chain of length  $l$  in the dilute limit is given by the size  $R$  of the chain:  $\xi \propto l^\nu$ . When chains become so long that they start to overlap at  $l \approx l^* \propto \phi^{-1/(\nu d-1)}$ , the correlation length of the chain decreases and reflects the (chain length independent) "blob"-size  $\xi$ : thus  $\xi \propto l^{*\nu}$ . The introduction of these correlations into the minimization procedure is fairly straightforward. The MFA approach remains valid [31] as long as the basic "monomer" is replaced by a coarse-grained blob of monomers, of size  $\xi$ . Accordingly, for the free energy one may write

$$\frac{F}{k_B T} = \sum_l C(l, T) \xi^d \left\{ \ln[C(l, T) \xi^d] - \ln \left( \frac{\xi}{b} \right)^{d+\theta} + \frac{J}{k_B T} + \mu l \right\} \quad (15)$$

In Eq. (15) the second term reflects the *gain in entropy* when a chain breaks so that the two new ends can explore a volume  $\xi^d$ . Entropy is increased because the excluded volume repulsion on scales less than  $\xi$  is reduced by breaking the chain; this effect is accounted for by the additional exponent  $\theta = (\gamma - 1)/\nu$  where  $\gamma > 1$  is a standard critical exponent, the value of  $\gamma$  being larger in 2 dimensions than in 3 dimensions:  $\gamma_{2d} = 43/32 \simeq 1.34$ ,  $\gamma_{3d} \simeq 1.17$ . In MFA  $\gamma = 1$ ,  $\theta = 0$ , and Eq. (15) simplifies to Eq. (9), where correlations, brought about by mutual avoidance of chains, i.e., excluded volume, are ignored.

In the dilute regime Eq. (15) can be rewritten as  $F/(k_B T) = \sum_l C(l, T) b^d \{ \ln[C(l, T) b^d] + (\gamma - 1) \ln l + J/(k_B T) + \mu l \}$ , so that the relation with the well known partition function of self-avoiding random walks [67] (with an effective coordination number  $\tilde{z}$ ),  $Q_l \propto \tilde{z}^l l^{\gamma-1}$ , is evident. Hence, Eq. (15) covers the entire concentration range.

Minimization of Eq. (15) at fixed  $\phi$  yields the MWD [66]

$$p(x) dx = \begin{cases} \exp(-x) dx & (\langle L \rangle \gg l^*), \end{cases} \quad (16a)$$

$$p(x) dx = \begin{cases} \frac{\gamma^\gamma}{\Gamma(\gamma)} x^{\gamma-1} \exp(-\gamma x) dx & (\langle L \rangle \ll l^*) \end{cases} \quad (16b)$$

where we use the normalized probability distribution  $p(x) = (\langle L \rangle / \phi) C(l, T)$ , so that  $\sum_x p(x) = 1$ , and the reduced (dimensionless) chain length  $x = l / \langle L \rangle$ . Using again the conservation law, one obtains a mean chain length

$$\langle L \rangle = l^* (\phi / \phi^*)^\alpha \propto \phi^\alpha \exp(\delta E) \quad (17)$$

with exponents  $\alpha_d = \delta_d = 1/(1 + \gamma) \approx 0.46$  in the dilute and  $\alpha_s = 1/2(1 + (\gamma - 1)/(\nu d - 1)) \approx 0.6$ ,  $\delta_d = 1/2$  in the semi-dilute regime. Note that for self-consistency one requires  $\langle L \rangle_d = \langle L \rangle_s$  at  $\phi = \phi^*$ , which imposes that the crossover density obeys  $\phi^* \propto \exp(-J/k_B T/\varphi)$  and the crossover chain length  $l^* \propto \exp(J/k_B T/\rho)$ . Here the exponents are  $\varphi = (\alpha_s - \alpha_d)/(\delta_s - \delta_d) \approx 3.8$  and  $\rho = (\nu d - 1)\varphi \approx 2.93$ .

Evidently, both the form of the MWD and the critical exponents, governing the variation of essential properties of the EP system with independent parameters such as density  $\phi$  or strength of interaction  $J/k_B T$ , should differ and reflect the particular regime in which the system is kept at equilibrium. It is therefore to be expected that computer experiments in different concentration or temperature regimes could verify these scaling predictions, provided one is able to vary  $\phi$  or  $\langle L \rangle$  of the system within a sufficiently large interval so that an unambiguous scaling relationship can be established.

Eventually one can also estimate the change in specific heat when correlations are accounted for. Specific heat  $c_v$  offers a possibility of experimental calorimetric measurement of the typical scission energy  $J$ . Eq. (13), along with (16), yields  $c_v \propto (\delta/\phi^\alpha)[J/(k_B T)]^2 \exp[-\delta/(k_B T)]$ . Thus  $c_v$  attains its maximum now at  $J_{\max}/(k_B T) = 2/\delta$  which shifts slightly to higher values at lower densities (from 4 above  $l^*$  to 4.4 below).

## IV. SIMULATIONAL RESULTS—STATIC PROPERTIES

### A. Molecular Weight Distribution

Unfortunately, we do not deal at present with MWDs obtained directly from a real experiment, so numerical evidence appears to be the only source of data which can be compared to theoretical predictions.

As a rule, simulational studies of EP [21–28,54,58,59] produce compelling evidence of an exponential MWD in agreement with the MFA predictions. Even if formation of rings is allowed for [21,25,28], the MWD,  $C(l, T)$ , retains its exponential form with respect to chain length  $l$ , although at small  $l$  and low temperature, where entropic effects are unimportant, the presence of rings is observed to change the form qualitatively (Fig. 3). The oscillations at small  $l$  and low  $T$ , however, showing higher concentration of small chains with *even* numbers of segments, are an artifact of the cubic lattice and vanish in off-lattice simulations.

The scaling analysis, mentioned in Sec. III B, predicts that one should observe a different kind of distribution in the dilute regime for chains which are smaller than the blob size [32] and thus behave essentially as isolated chains. These chains, which are fully swollen and may slip through the network made up from the chains of average size  $\langle L \rangle$  without being seriously

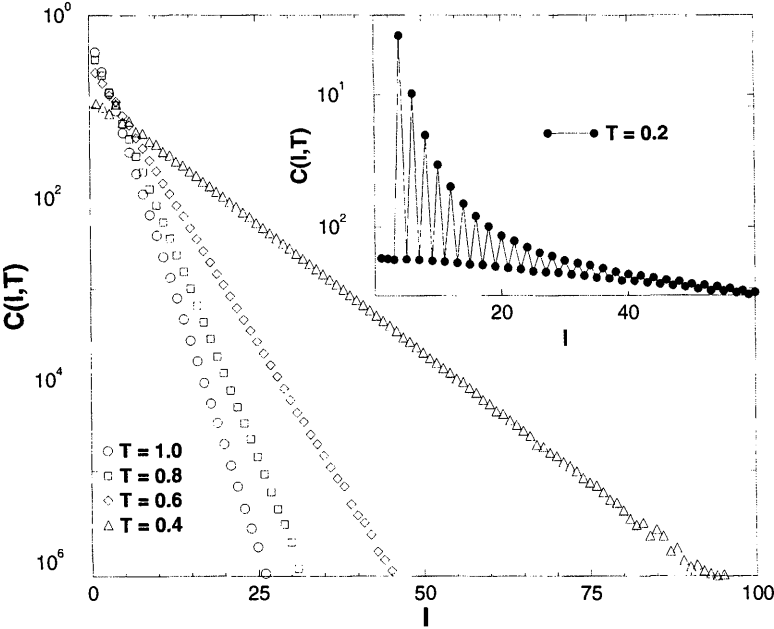


**FIG. 3** Probability distributions of chain lengths at four temperatures (given as parameter) [28]. In the inset, oscillations of the MWD due to the formation of rings are shown for  $T = 0.2$ .

perturbed by the inter-chain interaction, are subject to a *power-law* distribution [33]

$$C(l, T) \propto l^{\gamma-1} \tag{18}$$

where  $\gamma > 1$  is the critical exponent of the magnetic  $n \rightarrow 0$  vector model. The scaling analysis, cf. Eq. (16), takes this fact into account.

Since the power  $\gamma$  is easier to detect in two than in three dimensions, the first MC study [62] sampled a two-dimensional MWD in a range of temperatures (that is, of  $\langle L \rangle$ ), so that a change in the degree of interpenetration should trigger a crossover from dilute to semi-dilute regime at some density  $\phi^*$ . Evidently, indeed, from Fig. 4, the MWD follows the form of Eq. (16). At  $\phi^*$  one observes a power  $\gamma_{\text{eff}} \approx 1.300 \pm 0.005$  which comes closely to the expected one. Above  $\phi^*$  one finds  $\gamma_{\text{eff}} \rightarrow 1$ , and the distribution (11) becomes relevant.

Recently, with an improved version of the algorithm [65], this effect has been found in the more difficult case of 3d too (Fig. 5), where the normalized

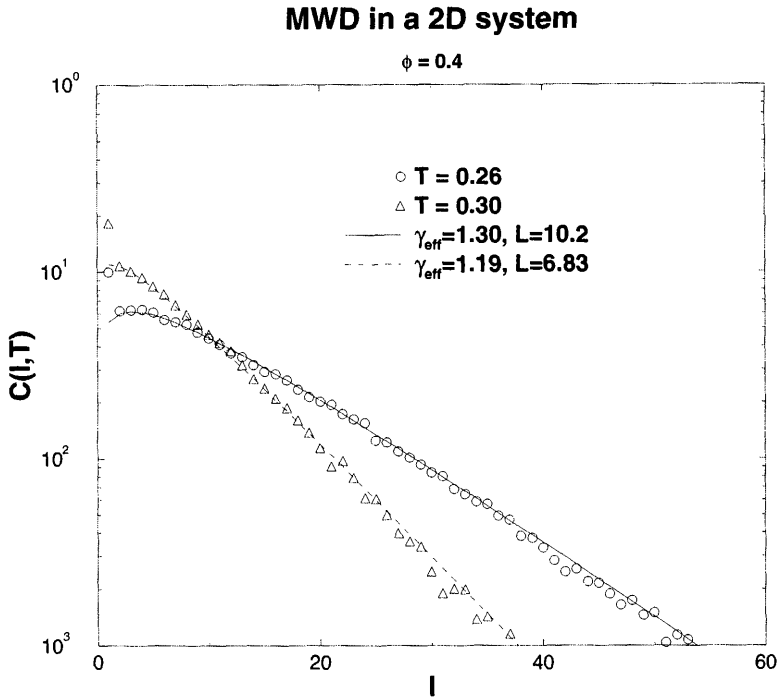


**FIG. 4** Semi-log plot [62] of the MWD at  $T = 0.26$  and  $T = 0.30$ . Full lines represent a fit with Eq. (4) and parameters given in the legend. The total monomer density in the system is  $\phi = 0.4$ .

MWDs  $p(x)$  are plotted against reduced size  $x = l/\langle L \rangle$  of the chains for a number of densities  $\phi$  and are seen to collapse nicely on a single “master” curve, Fig. 5(a). The exponential decay, expected from Eq. (16) at high densities, is clearly observed in contrast to the indicated  $\exp(-\gamma x)$  behavior. This finding is in agreement with the simulations in  $2d$  [62], but it contradicts the predictions of Gujrati [15] according to whom the Shulz distribution, Eq. (16b), holds independently of the overlap.

While at high densities we observe perfect exponential scaling of  $p(x)$ , at lower dilute densities (with sufficiently long chains!) one observes results consistent with Eq. (16b). The insert in Fig. 5 shows that the MWD at dilute densities agrees with the additional power-law dependence  $p(x) \propto x^{\gamma-1}$  in the limit of small  $x$ , confirming the theoretical predictions [33,34].

One should point out too that no evidence for an MWD with a *negative* power  $s$  of  $l/\langle L \rangle$ , i.e.,  $C(l) \propto (l/\langle L \rangle)^{-2s} \exp[-l/\langle L \rangle]$ , as speculated in some theoretical treatments [35], has so far been observed in computational

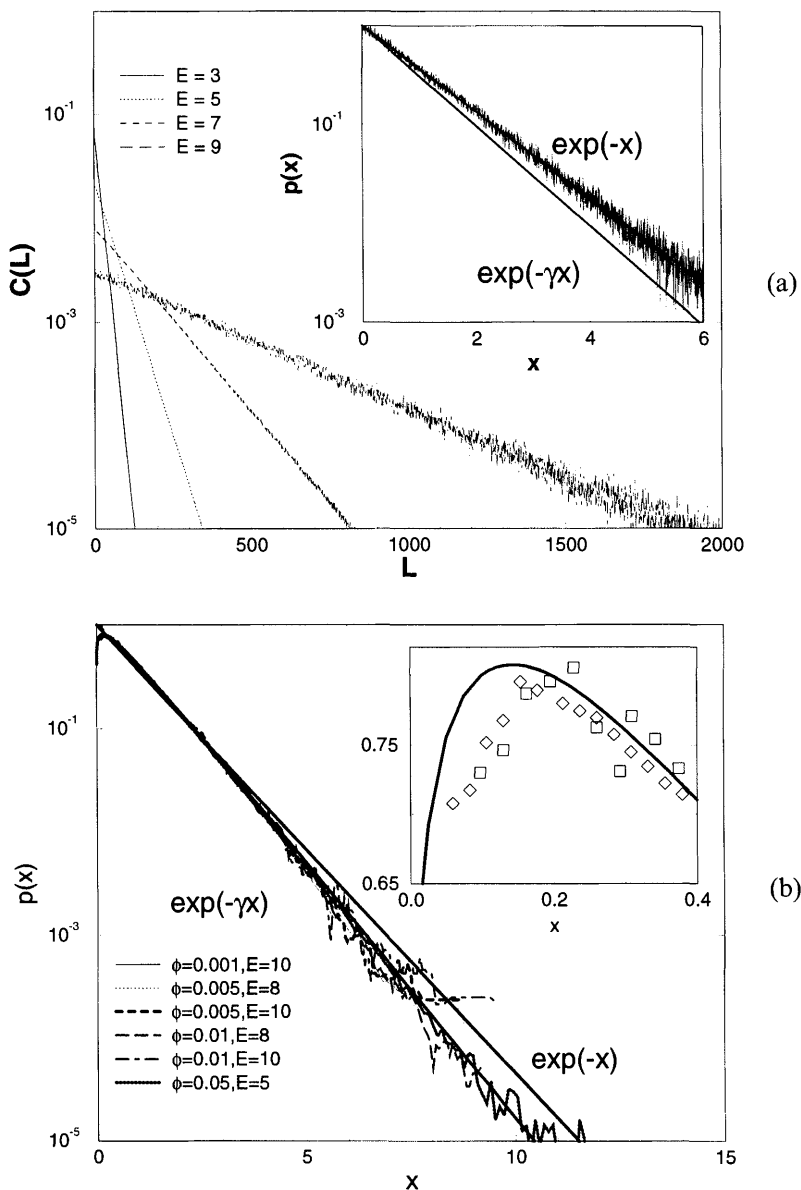


**FIG. 5** MC results for MWD of GM on a 3d lattice [65] for reduced chain length  $x = l/\langle L \rangle$  and different densities  $\phi$ : (a)  $C(L)$  at high (melt) density  $\phi = 0.5$  and  $E = J/k_B T$  as indicated in the figure. The insert shows data collapse of the normalized distribution  $p(x) \propto \exp(-x)$ . (b) Dilute limit confirming  $p(x) \propto \exp(-\gamma x)$ . Insert: MWD for small  $x$  for two densities  $\phi = 0.005$  (squares) and  $\phi = 0.01$  (diamonds), both at  $E = 10$  in the dilute regime. Straight lines compare the predictions of Eq. (16).



experiments. The latter has been assumed [35,36] in order to interpret unusual diffusive behavior in GM as a manifestation of *enhanced* diffusion. In a porous medium, however, where GM move among solid obstacles, a change of the MWD into  $C(l) \propto (l/\langle L \rangle)^{-2s} \exp[-l/\langle L \rangle]$  has recently been observed in a 2d MC study [37].

Finally, one should note some interesting results about the influence of shear stress on the MWD [54,57]. The form of  $C(l)$  at different shear rates appears to be qualitatively preserved, although with growing shear rate  $\langle L \rangle$  it is found to decrease, which is interpreted as being due to shear-induced stretching of the bonds.

## B. Conformational Properties

Most computer simulations of LP or GM so far have been focused on measuring thermodynamic and conformational properties in equilibrium [21,22,25–28,55,58] whereby comparison of measurements to MFA and scaling results has played a prominent role. Most of these simulations have been carried out at rather large density  $\phi$  of the system [21,22,25,27,28,58] where MFA is expected to work well, and indeed its predictions have been largely confirmed by all computer experiments. At lower densities, however, where deviations from the simple MFA behavior are expected, simulations demonstrate clearly such deviations. Thus some important theoretical predictions have been tested only very recently [26,65,66].

An important quantity which has been frequently studied is the mean chain length,  $\langle L \rangle$ , and the variation of  $\langle L \rangle$  with the energy  $J$ , following Eq. (12), has been neatly confirmed [58,65] for dense solutions (melts), whereas at small density the deviations from Eq. (12) are significant. This is demonstrated in Fig. 6, where the slopes  $L_s$  and  $L_d$  nicely confirm the expected behavior from Eq. (17) in the dilute and semi-dilute regimes\*. The predicted exponents  $\delta_d \approx 0.46 \pm 0.01$  and  $\delta_s \approx 0.50 \pm 0.005$  can be recovered with high precision. Also, the variation of  $\langle L \rangle$  at the threshold  $\phi^*$ , denoted by  $L^*$ , shows a slope equal to  $\rho^{-1}$ .

The growth exponents  $\alpha$  are most readily confirmed by plotting directly the “number of blobs”  $\langle L \rangle/l^*$  against reduced density  $\phi/\phi^*$ . The data collapse onto a single master curve, seen in Fig. 7, which is indeed remarkable and a central result of the simulation [65,66]. The two indicated slopes match exactly the predicted exponents  $\alpha_d \approx 0.46$ ,  $\alpha_s \approx 0.60$  (note that in the dilute limit finite size effects are visible for low  $E = J/k_B T$  since chains

---

\*Note that the measured mean chain lengths of up to  $\langle L \rangle \approx 5100$  are comparable with those of some experimental systems of EP.

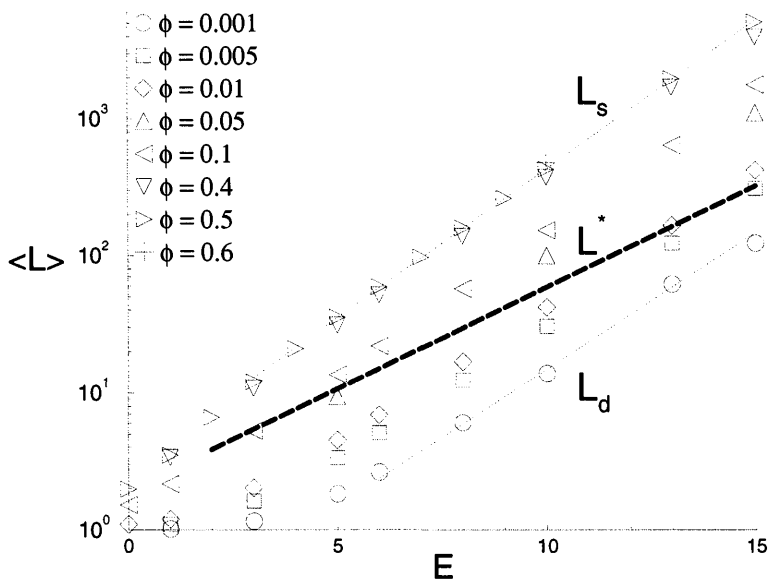


**FIG. 6** Dependence of  $\langle L \rangle$  on bond energy  $J$  for various concentration regimes [65]. The dashed line represents measurements at  $\phi^*$ .

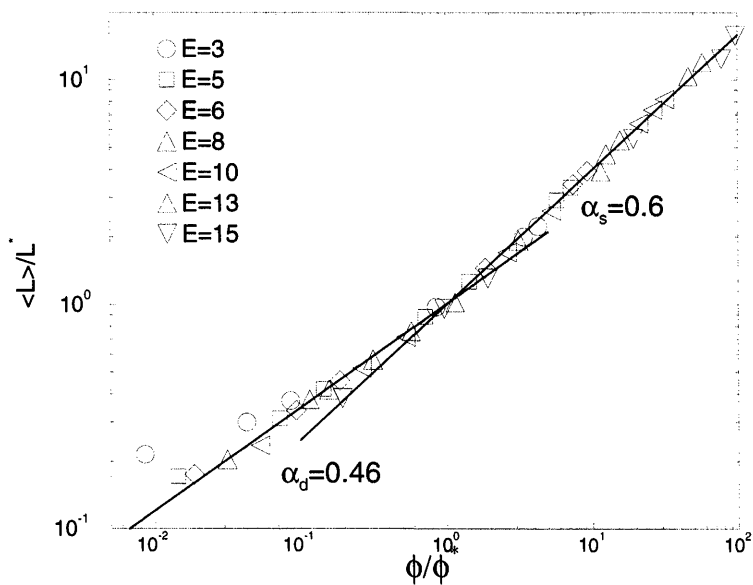


**FIG. 7** Proof of the scaling result,  $\langle L \rangle \propto \phi^{0.6}$ , in the asymptotic limit of sufficiently long chains [65].

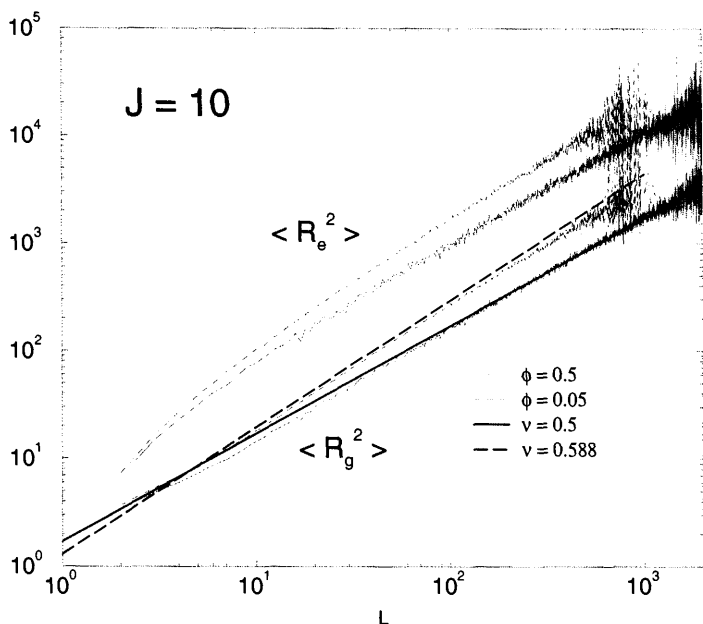


**FIG. 8** Variation of  $\langle R_e^2 \rangle$  and  $\langle R_g^2 \rangle$  with chain length  $l$  at  $J/k_B T = 10$  in dilute,  $\phi = 0.05$ , and dense,  $\phi = 0.5$ , solutions of living polymers [65]. Thick dashed and full lines denote the measured exponents  $\nu$ .

become extremely short,  $\langle L \rangle \approx 5$ ). This finding is at variance with an MD simulation [54] where a much stronger growth with density was observed in a system containing only 8400 monomers with  $\langle L \rangle \approx 210$ . One may thus conclude from Fig. (7) that the expected scaling regime is reached for sufficiently long micellar polymers, which also explains discrepancies with some laboratory observations [75] of  $\langle L \rangle \propto \phi^{0.25-0.4}$  in which  $\langle L \rangle \approx 1000-2000 \text{ \AA}$  while their persistent length is  $\approx 150 \text{ \AA}$ .

It is instructive to consider the scaling of the average end-to-end distance  $R_e^2$  and gyration radius  $R_g^2$  of living polymers as a function of chain length  $l$ . These quantities can be computed directly along with the MWD by counting routines and in Fig. 8 one can readily see that for a dilute system ( $\phi = 0.05$ ) of swollen chains the measured Flory exponent  $\nu = 0.588$ , while in a dense system ( $\phi = 0.5$ ) the screening of excluded volume interactions leads to  $\nu = 0.5$ , as should be expected for Gaussian chains. The *asymptotic* nature of the scaling laws,  $R_e^2 \approx R_g^2 \propto l^{2\nu}$ , is also clearly seen from Fig. 8 to hold for  $l \geq 10$ .

In order to get a better notion of the scaling relationship between gyration radius and average chain length for different density regimes, it is convenient

to introduce a scaling variable  $y$  as

$$y = \frac{\langle L \rangle^2}{r^2} \quad (19)$$

where  $r = (\langle L \rangle / \phi)^{1/d}$  can be considered as some mean interchain distance and directly measured. Using the crossover concentration,  $\phi^* = \langle L \rangle / \langle R_g^2 \rangle^{3/2} = \langle L \rangle^{1-3\nu}$ , in the semi-dilute regime, one has for  $y$  an expression in terms of relative concentration,  $y^{3/2} = \langle L \rangle^{3\nu} / r^3 = \phi / \phi^*$ . The concentrational dependence of  $\langle R_g^2 \rangle$  on  $\phi$  may then be conveniently expressed by a scaling function  $\mathcal{G}(y)$

$$\frac{\langle R_g(\phi)^2 \rangle}{\langle R_g(\phi = 0)^2 \rangle} = \mathcal{G}(y) = y^\eta \propto [\langle L \rangle^{2\nu-2/3} \phi^{2/3}]^\eta \quad (20)$$

For  $y \ll 1$   $\mathcal{G}(y) \rightarrow 1$ , whereas for  $y \geq 1$   $\langle R_g^2 \rangle \propto \langle L \rangle$  and therefore  $\mathcal{G}(y) \propto \langle L \rangle^{1-2\nu}$ . This can be fulfilled only if, in Eq. (20), one has  $\eta = (1 - 2\nu) / (2\nu - 2/3) \approx -0.346$ . And indeed, in Fig. (9) the scaling function

$$\mathcal{G}(y) \propto \begin{cases} y^{-0.346} & y \geq 1 \\ 1 & y \ll 1 \end{cases}$$

can be clearly seen and the location of the crossover density at  $y \approx 1$  determined [65]. It is remarkable that in their scaling behavior GM are nearly indistinguishable from conventional “dead” polymers (Fig. 9)—the two universal functions are virtually identical, within numerical accuracy.

### C. Equilibrium Polymerization as a Phase Transition

It has been suggested by Wheeler et al. [2] that the polymerization–depolymerization transition in LP can be treated as a continuous or second-order phase transition in systems with an initiator triggering the equilibrium polymerization. Thus a formal analogy between polymers and magnetic systems [13], based on the remarkable observation that the properties of a self-avoiding walk can be mapped onto the  $n \rightarrow 0$  limit of an  $n$ -component field theory, has provided a number of accurate predictions [14] about the critical properties of systems which undergo the transition of equilibrium polymerization. A number of laboratory experiments have provided qualitative confirmation of these theoretical predictions [5,6]. An extensive computer simulational study, covering the whole range of concentrations from dilute, through semi-dilute and up to dense systems (polymer melts), carried out by Livne [26], has shown that the MC simulational results for LP agree very well with those of the  $n$ -vector model.

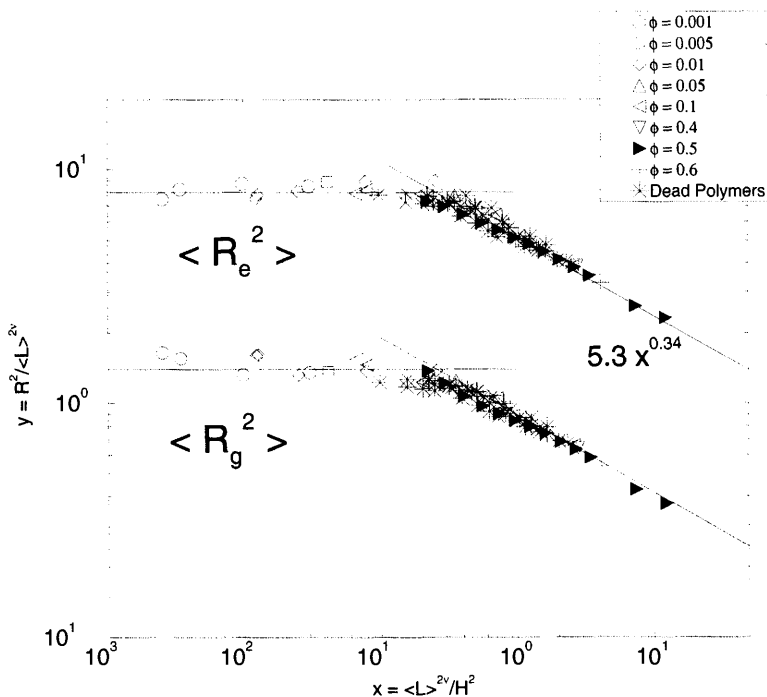


**FIG. 9** Collapse of various density data on a scaling function of  $\langle R_g(\phi)^2 \rangle / \langle R_g(\phi=0)^2 \rangle = \mathcal{G}(y)$ . The crossover from dilute to dense regime at  $y \approx 0.3$  is clearly seen [65].

The partition function,  $\Xi$ , Eq. (3), can be solved only approximately, e.g., in the MFA. However, from the magnetic analog one can obtain scaling relations for the concentration of links  $\Phi_l$  and polymer chains  $\Phi_p$ , cf. Eq. (4)

$$\Phi_l = \epsilon^{d\nu-1} f_l(x), \quad \Phi_p = \epsilon^{d\nu} f_p(x) \quad (21)$$

where the scaling functions  $f_l$  and  $f_p$  depend on  $x = M\epsilon^\beta$ ,  $\epsilon = |(T - T_c)/T_c|$  ( $M$  is the magnetization), and  $\nu$  and  $\beta$  are the standard critical exponents. One can exploit the analogy between  $T_c$  and  $\lambda_c$  so that the critical value for reversible polymerization is obtained [26] for  $\lambda_c \equiv 1/z$ , where  $z$  is the effective coordination number of the lattice. In the dilute regime,  $\lambda < \lambda_c$ , which is analogous to the high-temperature expansion of the magnetic system, one obtains  $\Phi_l = \epsilon^{-\gamma-1}\eta$ ,  $\Phi_p = \epsilon^{-\gamma}\eta$ , and  $\langle L \rangle \propto \epsilon^{-1}$ , with  $\gamma$  the free energy critical exponent. In the crossover from dilute to semi-dilute regime where the chains just start to touch each other,  $\lambda = \lambda_c$  ( $\epsilon = 0$ ). In this regime  $f_l(x) \propto x^{d\nu-1/\beta}$ ,  $f_p(x) \propto x^{d\nu/\beta}$ , so that  $\Phi_l \propto \eta^{d\nu-1/2(\gamma+\beta)}$ ,

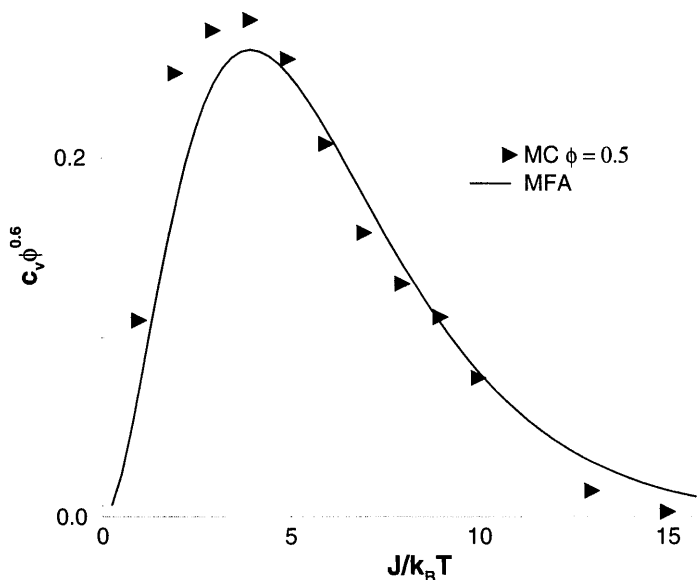


**FIG. 10** Specific heat at the polymerization transition vs  $J/k_B T$  from MC results [65] and according to Eq. (14).

$\Phi_p \propto \eta^{d\nu-1/2(\gamma+\beta)}$ , and  $\langle L \rangle \propto \eta^{1/2(\gamma+\beta)}$ . The measurements of the slopes of  $\Phi_1$  and  $\Phi_p$  with  $\eta$  yield results which agree very well with the known exponents of the  $n$ -vector model:  $\beta(2d) = 0.078$ ,  $\gamma(2d) = 1.3437$ ,  $\beta(3d) = 0.30$ ,  $\gamma(3d) = 1.162$ . The values for the Flory exponent are recovered as  $\nu(2d) = 0.75 \pm 0.01$  and  $\nu(3d) = 0.59 \pm 0.02$ .

In systems without initiator, like wormlike micelles, the degree of polymerization changes gradually with temperature (without divergence of  $\langle L \rangle$ ). However, one should observe a maximum in the specific heat of the system, which according to the MFA treatment [58] (Eq. (14)), should occur at  $J/k_B T = 4$ . Results from MC simulations [65] are compared in Fig. 10 with the MFA prediction, Eq. (14), and found to be in good agreement.

In another study Milchev and Landau [27] investigated in detail the transition from a disordered state of a polydisperse polymer melt to an ordered (liquid crystalline) state, which occurs in systems of GM when the chains are considered as semiflexible. It turns out that in two dimensions this order-disorder transition is a continuous second-order transformation whereas in  $3d$  the simulational results show a discontinuous first-order transformation. Comprehensive finite-size analysis [27] has established

that the second-order transition is characterized by critical exponents in the Ising class of universality. In  $3d$  the phase transition is weakly first order with almost no detectable hysteresis. In both two and three dimensions the critical temperature of the transition is found to rise steeply with the energy  $\sigma$ , responsible for the degree of flexibility of the chains.

Ending this section, we should like to point out the relevance of this order-disorder transition in self-assembling polymers for the studies of the nature of vitrification phenomena. Since glasses most easily form in complex associated liquids and polymers, the interplay of semiflexibility, self-avoidance (i.e., free volume) and the energy cost for breaking chains makes this model a good testing ground for theories of the glass transition. Attempts in the past [38] to interpret vitrification, traditionally believed to be of kinetic origin, as a second-order phase transition of purely thermodynamic nature, have caused much attention. This important but rather controversial interpretation has been challenged both theoretically [39] and by means of computer experiments [40,41].

## D. Living Polymers in Constrained Geometries

### 1. Adsorption

There has been much interest in the behavior of polymers in constrained geometries (polymers at surfaces or interfaces [42,43]), polymers confined in thin films [43,44] or in bilayer membranes and micelles [45,46]. This interest is due to applications in technology (lubrication, corrosion-protective coatings, adhesives, etc.) and biology (proteins confined between cell membranes, etc.), but it also reveals challenging theoretical problems from the point of view of statistical mechanics. Since polymer chains are generally imagined as random coils, the proximity of a solid surface, near which such coils would decrease their conformational freedom, leads to a decrease of the entropy of these chains. The extent of entropy decrease and the energy gain from contact interactions with the adsorbing surface would then determine the nature of adhesion of the polymer with the substrate.

A MC study of adsorption of living polymers [28] at hard walls has been carried out in a grand canonical ensemble for semiflexible  $\sigma \neq 0$  polymer chains and adsorbing interaction  $e < 0$  at the walls of a box of size  $\mathcal{L}$ . A number of thermodynamic quantities, such as internal energy (per lattice site)  $U$ , bulk density  $\phi$ , surface coverage (the fraction of the wall that is directly covered with segments)  $\theta$ , specific heat  $C = (\mathcal{L}^3/[k_B T^2])(\langle U^2 \rangle - \langle U \rangle^2)$ , bulk isothermal compressibility  $\kappa_T = (\mathcal{L}^3/[k_B T])(\langle \phi^2 \rangle - \langle \phi \rangle^2)$ , surface compressibility  $k_T^s$ , and adsorption isotherms have provided a lot of information on adsorption. In Fig. 11

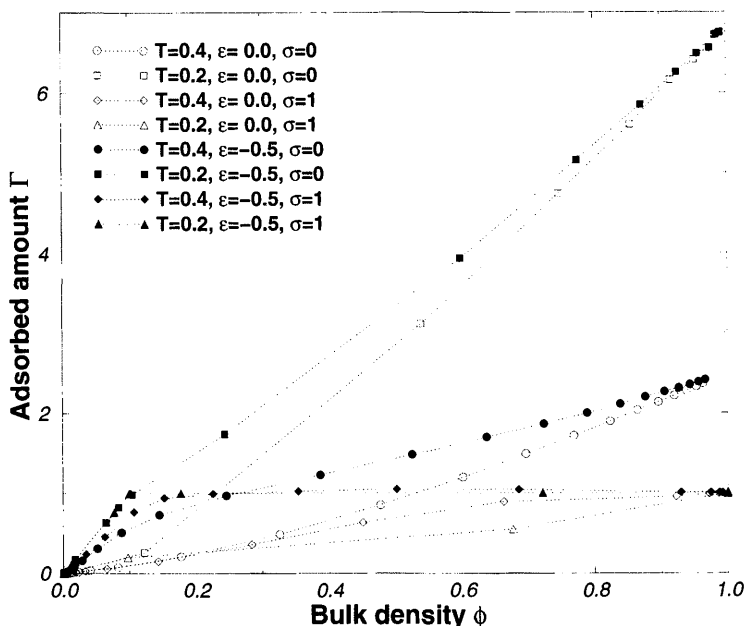


**FIG. 11** Adsorbed amount as a function of bulk concentration for a non-interacting (empty symbols) and adsorbing (full symbols) wall. Diamonds and triangles correspond to a system with semi-rigid chains, circles and squares for flexible chains [28].

we show the variation of the adsorbed amount  $\Gamma$  with changing bulk density  $\phi$

$$\Gamma = \sum_l c_l^s l / \mathcal{L}^2 \quad (22)$$

where  $c_l^s$  is the number of chains of length  $l$  which are in contact with the wall, as the bulk density,  $\phi$ , changes. As expected,  $\Gamma$  exceeds the surface coverage,  $\theta \leq 1$ , for completely flexible chains only and increases rapidly with increasing average chain length  $\langle L \rangle$  as temperature is lowered. From this data one finds that  $\Gamma$  is roughly proportional to  $\langle L \rangle$ . For semi-flexible chains, however,  $\Gamma$  never exceeds unity. Evidently the segments adsorbed on the substrate rearrange themselves into an array of stiff parallel rods, thus screening the adsorbing potential from other segments in the bulk and effectively converting the surface into a non-interacting wall.



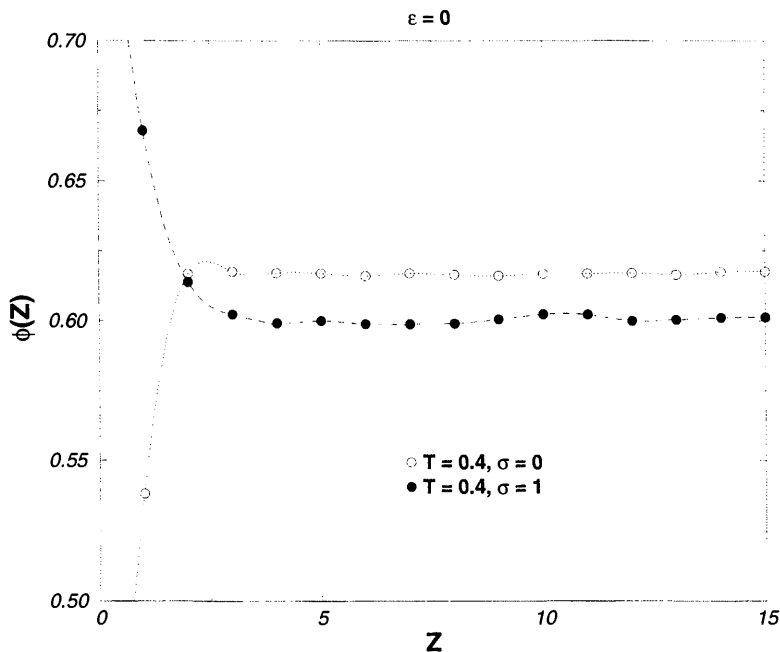


**FIG. 12** Segment density profile as function of the distance from the wall  $Z$  for flexible (empty symbols) and semi-rigid (full symbols) living polymer chains at  $T = 0.4$  [28]. The fractional occupancy of lattice sites by polymer segments is shown for the layers in the left half of the box. Dashed lines are guides for the eyes.

The effect of a non-interactive solid surface on a system of self-assembling chains is shown in Fig. 12. For completely flexible chains one observes a depletion of polymer segments at the surface, which is a purely entropic effect due to restrictions imposed by the solid surface on chain conformations. On the other hand, for semi-rigid chains the fractional occupancy of the layers immediately at the wall is increased, although  $e = 0$ . The solid wall acts as an ordering field on the shorter chains as well as on rod-like fractions of long semi-rigid chains. The analysis of the center-of-mass distribution for different chain lengths within the box, Fig. 13, shows that the surfaces are occupied predominantly by larger chains (larger than  $\langle L \rangle$ ) whereas shorter chains and single monomers are pushed away from the surface into the bulk. Evidently, this is just the opposite of what happens to a system of absolutely flexible chains. Thus the results of the calculations show that entropic effects cause a rearrangement of the species with different length into an “onion shell” structure and should be accounted for if the

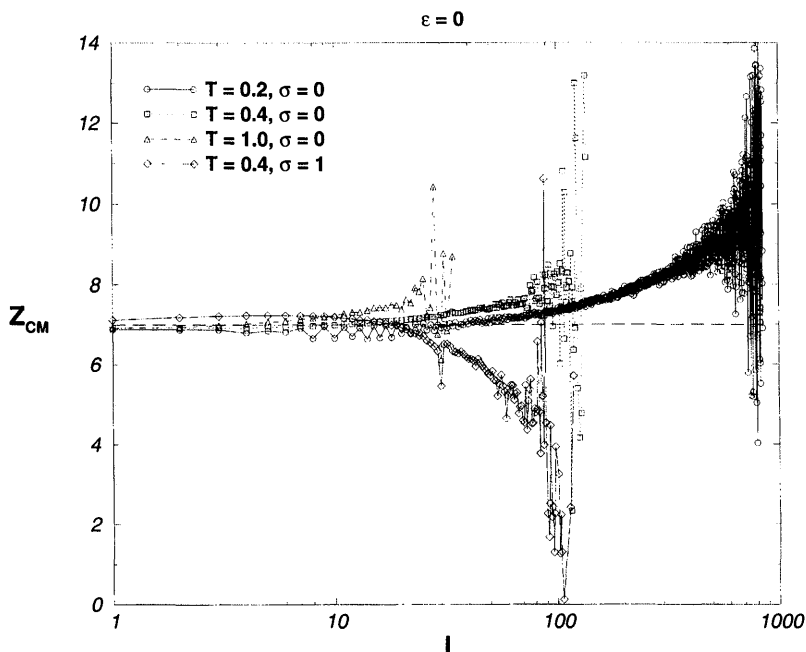


**FIG. 13** Average center-of-mass position of flexible chains  $Z_{CM}$  of length  $l$  with respect to the nearest solid surfaces for different  $l$ . Diamonds denote a system of semi-rigid chains in which the opposite effect is observed [28].

surface tension of such a polydisperse system is to be determined, bearing in mind that surface tension is different for polymers with different molecular weight.

## 2. Dependence of $\langle L \rangle$ on the Width $\mathcal{D}$ of a Narrow Slit

The changes in the average chain length of a solution of semi-flexible self-assembling chains confined between two hard repulsive walls as the width of the slit  $\mathcal{D}$  is varied, have been studied [61] using two different Monte Carlo models for fast equilibration of the system, that of a “slithering snake” and of the “independent monomer states.” A polydisperse system of chain molecules in conditions of equilibrium polymerization, confined in a gap which is either closed (with fixed total density) or open and in contact with an external reservoir, has been considered.

It appears that the mean chain length  $\langle L \rangle$  in a state of equilibrium polymerization depends essentially on the geometry constraints for sufficiently small  $\mathcal{D}$ . In contrast to recent theoretical predictions [47], which treat the

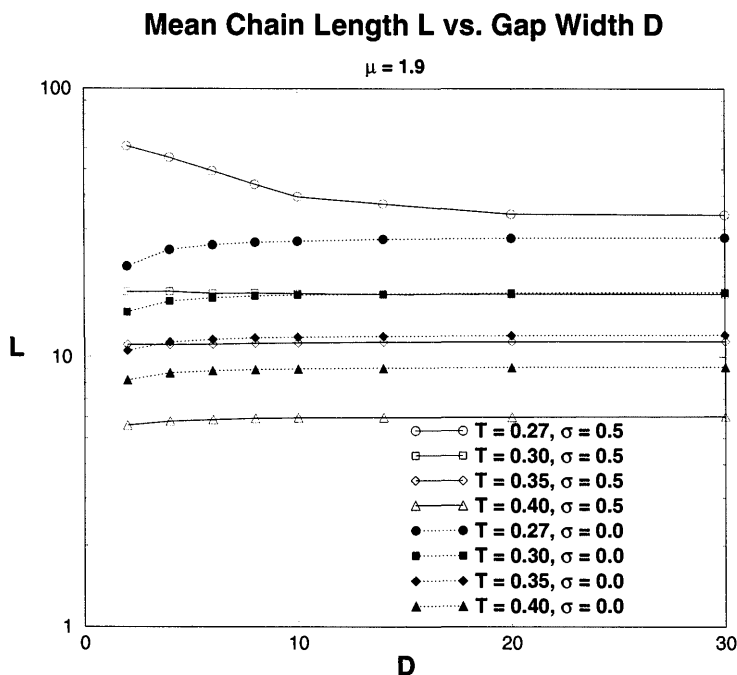


**FIG. 14** Semi-log plot of mean chain length  $L$  vs. width of the open slit  $D$  at various temperatures in  $3d$ . Full symbols denote flexible chains and empty symbols semi-rigid chains with activation energy  $\sigma = 0.5$  [61].

chains as “random walks” without excluded-volume interactions, it was found from the simulations that in the case of an *open* slit the mean length  $\langle L(D) \rangle$  decreases with  $D \rightarrow 0$  for flexible chains whereas it *grows* if the chains are sufficiently stiff (Fig. 14).

On the other hand, as the width of a *closed* three-dimensional gap  $D$  is decreased,  $\langle L(D) \rangle$  gradually decreases for absolutely flexible chains whereas for semi-rigid chains it goes through a minimum at  $D = 2$  monomer diameters and then grows again for  $D \rightarrow 0$  (Fig. 15).

In two dimensions, in a closed strip the average chain length  $\langle L(D) \rangle$  for *both* flexible and rigid macromolecules goes through a sharp minimum and then grows steeply, in compliance with a predicted divergence [47] for semi-rigid polymers as  $D \rightarrow 0$ .

Eventually, one should also note that even in the case of “dead” polymers one has also observed a variation of the gyration radius  $\langle R_g^2 \rangle$  with  $D$ , which goes through a minimum as  $D \rightarrow 0$  [48] although the contour length of the chains  $L$  does not change. Thus computer simulations, being capable of

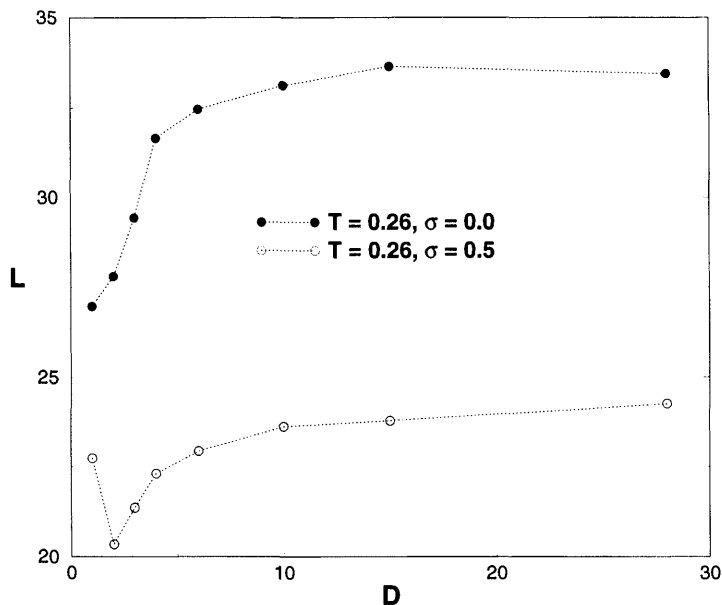


**FIG. 15** Mean chain length  $L$  vs. strip thickness  $D$  for semi-rigid (open symbols) and flexible (full symbols) polymer chains [61].

measuring *both*  $\langle R_g^2 \rangle$  and  $L$ , help to distinguish between rather different reasons for the same observation.

## V. SIMULATIONAL RESULTS—DYNAMIC PROPERTIES

### A. Kinetics of Relaxation to Equilibrium

#### 1. Wormlike Micelles

Under a sudden change in one of the thermodynamic variables (most commonly, of the temperature) the MWD, Eq. (11), relaxes to a new equilibrium exponential distribution,  $C(l, T)$ , characterized by a new average length  $\langle L \rangle$ . This is in general a complicated, nonlinear decay which can be monitored, e.g., by light scattering which probes the average length of the polymer size distribution. Recently [68,69] a theoretical description of living polymer kinetics was suggested under the assumption that a chain can change mass only either by breaking into two new shorter chains or by recombination with another to form a longer chain. This scission–fusion scheme leads to an integro-differential equation for the time evolution of the

MWD  $C(t, L)$ :

$$\begin{aligned} \dot{C}(t, L) = & -k_s LC(t, L) + 2k_s \int_L^\infty C(t, l) dl \\ & + k_r/2 \int_0^L C(t, l) C(t, L-l) dl - k_r C(t, L) \int_0^\infty C(t, l) dl \end{aligned} \quad (23)$$

where  $k_s$  and  $k_r$  are respectively the scission and recombination rate constants. The principle of detailed balance requires that these rate constants are not independent, a stationary solution of Eq. (23) exists only under the condition  $\phi(k_r/2k_s) = L_0^2$ . If an instantaneous perturbation (a step-change in the thermodynamic conditions) is imposed on the system, the rate constants acquire new equilibrium values which obey  $\phi(k_r/2k_s) = L_\infty^2$ , where  $L_\infty$  is the new mean length after equilibrium has been established again. It turns out that one may solve Eq. (23) exactly whereby the complete nonlinear response of the size distribution of GM to an instantaneous jump in the thermodynamic parameters is given by the nonlinear eigenfunction of Eq. (23),  $C(t, L) = \phi f^2(t) \exp[-Lf(t)]$ , with a (time-dependent) eigenvalue  $f(t)$  which for the case of a temperature-jump with the initial condition  $f(t=0) = 1/L_0$  is

$$\begin{aligned} f(t) & \equiv \langle L(t) \rangle^{-1} \\ & = \left\{ \begin{array}{ll} L_\infty^{-1} \tanh \left[ \frac{t+t_0}{2\tau} \right], & t_0 = 2\tau \tanh^{-1}[L_\infty/L_0] \quad \text{if } L_0 > L_\infty \\ L_\infty^{-1} \coth \left[ \frac{t+t_0}{2\tau} \right], & t_0 = 2\tau \coth^{-1}[L_\infty/L_0] \quad \text{if } L_0 < L_\infty \end{array} \right\} \end{aligned} \quad (24)$$

The relaxation time  $\tau$  of the mean length,  $\tau^{-1} = 2kL_\infty$ , gives a measure of the microscopic breaking rate  $k_s$ . In Fig. 16 the relaxation of the average length  $\langle L \rangle$  with time after a quench from initial temperature  $T_0 = 1.0$  to a series of lower temperatures (those shown on the plot are  $T_\infty = 0.35, 0.37$ , and  $0.40$ ) is compared to the analytical result, Eq. (24). Despite some statistical fluctuations at late times after the quench it is evident from Fig. 16 that predictions (Eq. (24)) and measurements practically coincide. In the inset is also shown the reverse  $T$ -jump from  $T_0 = 0.35$  to  $T_\infty = 1.00$ . Clearly, the relaxation in this case is much ( $\approx 20$  times) faster and is also well reproduced by the non-exponential law, Eq. (24). In the absence of laboratory investigations so far, this appears the only unambiguous confirmation for the nonlinear relaxation of GM after a  $T$ -quench.

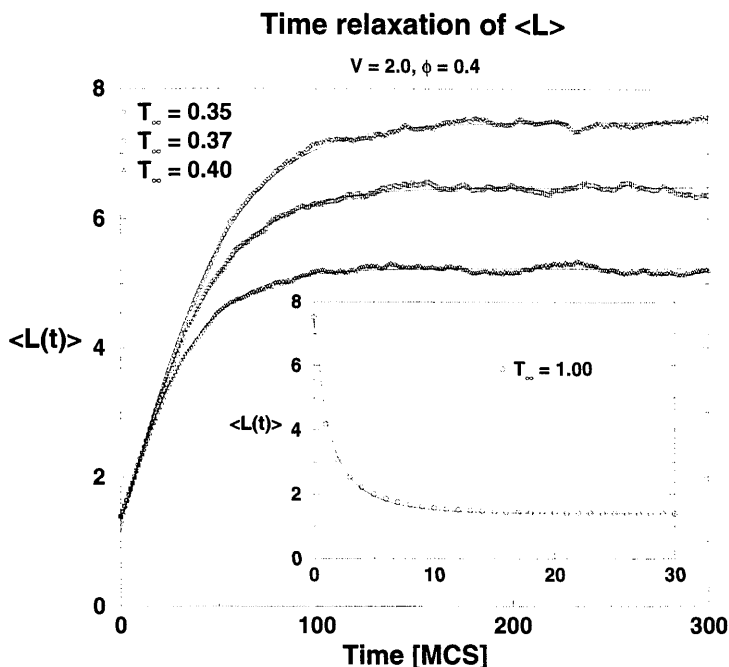


**FIG. 16** Time evolution of the average length for a living polymer system [59] after a quench from an initial  $T_0 = 1.0$  to three final temperatures:  $T_\infty = 0.35$  (circles),  $T_\infty = 0.37$  (squares), and  $T_\infty = 0.40$  (triangles). Full lines correspond to Eq. (24). The inset shows the reverse case where the system is instantaneously heated from  $T_0 = 0.35$  to  $T_\infty = 1.0$  so that  $L_0 > L_\infty$ .

## 2. Living Polymers with Monomer-mediated Kinetics

In systems of LP the dynamic response to a temperature quench is characterized by a different mechanism, namely *monomer-mediated* equilibrium polymerization (MMEP) in which only single monomers may participate in the mass exchange. For this no analytic solution, even in terms of MFA, seems to exist yet [70]. Monomer-mediated equilibrium polymerization (MMEP) is typical of systems like poly( $\alpha$ -methylstyrene) [5–7] in which a reaction proceeds by the addition or removal of a single monomer at the active end of a polymer chain after a radical initiator has been added to the system so as to start the polymerization. The attachment/detachment of single monomers at chain ends is believed to be the mechanism of equilibrium polymerization also for certain liquid sulphur systems [8] as well as for self-assembled aggregates of certain dyes [9] where chain ends are thermally activated radicals with no initiators needed.



where we have set  $a = c_1 k_r / k_s$ . One can then easily verify that the resultant distribution of chain lengths for an MMEP system is given by

$$c_l = \frac{k_s}{k_r} a^l, \quad (0 < a < 1) \quad (30)$$

just as in the case of GM scission-recombination kinetics, see Eq. (11). With the equilibrium distribution, Eq. (30), one finds  $N = (k_s/k_r)[a/(1-a)]$  and  $\phi V = (k_s/k_r)[a/(1-a)^2]$ , so that the mean length  $L_{eq} = \phi V/N = (1-a)^{-1}$ , or, for the MWD, one obtains

$$\left. \begin{aligned} c_l &= \frac{k_s}{k_r} \exp(l \ln a) \approx \frac{k_s}{k_r} \exp\left(-\frac{l}{L_{eq}}\right), \\ L_{eq}^{-1} &= \frac{k_s}{2k_r \phi V} \left( \sqrt{1 + \frac{4k_r \phi V}{k_s}} - 1 \right) \approx \sqrt{\frac{k_s}{k_r \phi V}} \end{aligned} \right\} \quad (31)$$

A numerical study of the MMEP kinetics, as described by the system of nonlinear differential equations (26), subject to mass conservation (Eq. (27)), has been carried out [64] for a total number of 1000 monomers and different initial MWDs. As expected, and in contrast to the case of wormlike micelles, it has been found that during relaxation to a new equilibrium state the temporal MWD does not preserve its exponential form.

In Fig. 17(a) is shown the time evolution of a system, consisting initially of only dimers, towards an exponential equilibrium MWD. The non-linear relaxation of  $L(t)$  (see inset) is clearly seen. The variation of  $L(t)$  with time is reasonably interpolated for all times  $t$  by the function  $L(t) = L_\infty - L_0/(1 + 0.27t)$  with  $L_0 = 2$  and  $L_\infty = 5$ . In Fig. 17(b) we replot the data from Fig. 17(a) in terms of  $n_l$  versus  $l$  for several times elapsed after the quench. Evidently, at  $t = 0.10$  s, shortly after the quench, the initial  $\delta$ -like distribution broadens and transforms into a Poisson distribution which later changes into a Gaussian distribution (at  $t = 0.50$  s) and ends eventually as an exponential distribution after  $t = 30$  s. Thus the numerical results for a system without initiator exactly follow the scenario predicted by Taganov [72] for an MMEP *with* initiator. In the latter the total number of chains does not change with time (although  $L(t)$  does) and remains equal to the total number of initiators added at the beginning of the process. It appears indeed that MMEP systems with\* and without initiator undergo qualitatively the same relaxational process.

\* Although the generic equation (26) remains the same for the case with initiator too, that for the active monomers is different:  $\dot{c}_1 = -k_r M c_1 + c_2$ . All other Eqs. (26) retain their form, provided  $c_1$  is replaced there by the concentration of "inert" monomers,  $M$ .



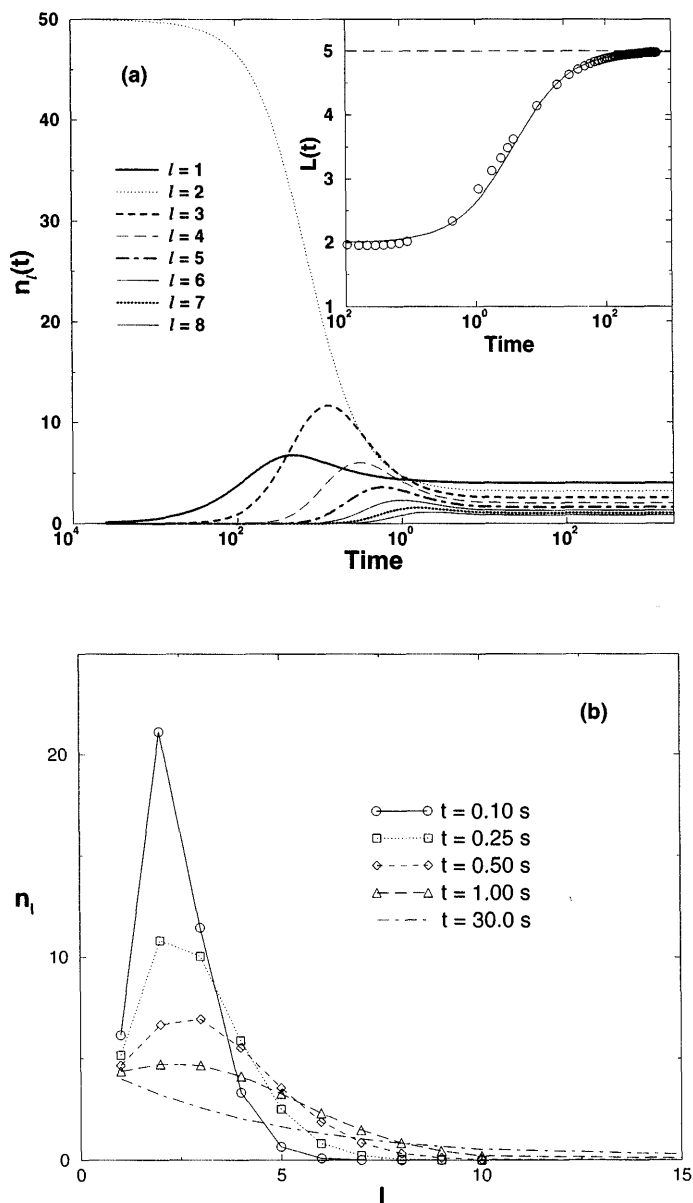


**FIG. 17** (a) Numerical solution [64] for the change in the number of chains of length  $l$  with time after a quench from an initial  $\delta$ -like distribution of chains with  $L = 2$ . In the inset, the variation of the average chain length  $L(t)$  with time is shown (empty circles). The solid line denotes an interpolation by  $L(t) = L_\infty - L_0/(1 + 0.27t)$  with  $L_0 = 2$  and  $L_\infty = 5$ . (b) The same data plotted as  $n_l$  vs  $l$  for different times after the quench.

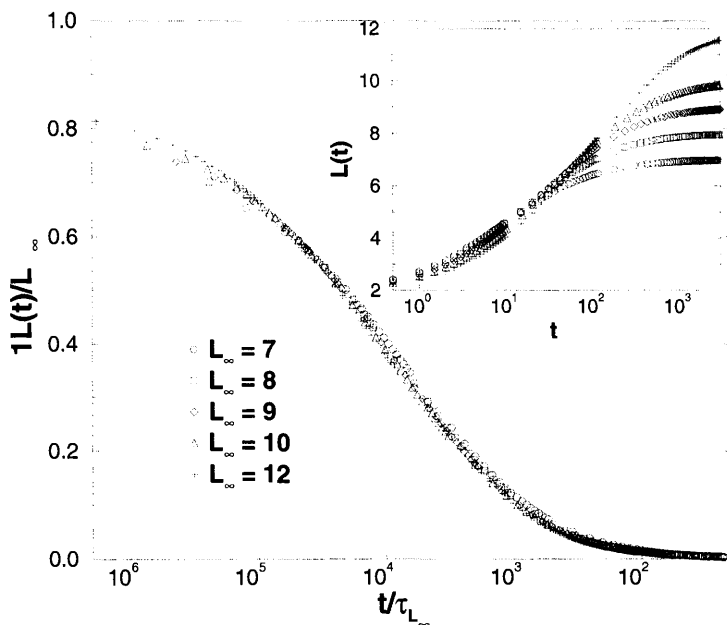


**FIG. 18** Scaling plot of  $L(t)$  from the numerical solution of the rate equations for quenches to different equilibrium states [64] from an initial exponential MWD with  $L = 2$ . The final mean lengths  $L_\infty$  are given in the legend. The inset shows the original  $L(t)$  vs  $t$  data. Here  $\tau_{L_\infty} = (0.33L_\infty)^5$ .

It turns out that a rather simple description of this nonlinear relaxation in terms of a *single* relaxation time,  $\tau_{L_\infty}$ , depending on the final average chain length  $L_\infty$ , is suggested by a scaling plot of  $L(t)$  for different  $L_\infty$ , as shown in Fig. 18 for an initial exponential MWD. It is evident from Fig. 18 that the response curves,  $L_\infty - L(t)$ , for different  $L_\infty$  may be collapsed onto a single “master” curve,  $1 - L(t)/L_\infty = f(t/\tau_{L_\infty})$ , if time  $t$  is measured in units of a single relaxation time  $\tau_{L_\infty}$ . For the case of an exponential initial MWD one finds  $\tau_{L_\infty} = (0.33L_\infty)^5$ . The scaling is also observed for an initial  $\delta$ -distribution, where one obtains  $\tau_{L_\infty} = (1.3L_\infty)^5$ . We also find for the scaling function  $f(x)$ , where  $x = t/\tau_{L_\infty}$ ,  $f(x) \propto x^{-1}$  for  $x \rightarrow \infty$ .

A Monte Carlo simulation of the relaxation kinetics in an MMEP system yields results which agree remarkably well with the MFA treatment in terms of rate equations, suggesting that at higher density transport processes do not significantly limit the relaxation. The behavior of the mean chain length is shown in Fig. 19 as a raw data (inset) and in a scaled form,  $[L(t)/L_\infty - 1]L_\infty^2 = f(t/\tau_{L_\infty})$ , representing a sudden heating of the system from initial temperature  $T_0 = 0.35$  to a series of higher temperatures,

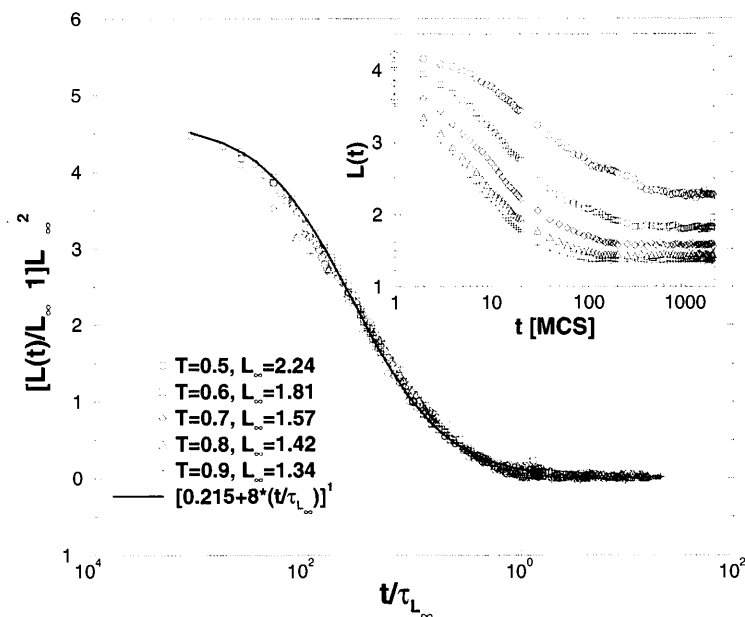


**FIG. 19** Scaling plot for the relaxation of the mean chain length  $L(t)$  after a  $T$ -jump from  $T_0 = 0.35$  to a series of final temperatures, given as a parameter along with the respective  $L_\infty$ 's. The same Monte Carlo results [64] as in Fig. 5 are used. Full line denotes the scaling function  $f(x = t/\tau_{L_\infty}) = (0.215 + 8x)^{-1}$ . In the inset the evolution of  $L(t)$  with time, measured in MCS, is shown.

$T = 0.5, 0.6, 0.7, 0.8$ , and  $0.9$ . Despite some statistical fluctuations at late times after the  $T$ -jump, it is evident from Fig. 19 that the different curves collapse onto a single one if time is scaled by a single  $\tau_{L_\infty}$ . As for the system of rate equations, (26), we again find  $\tau_{L_\infty} = (1.85L_\infty)^5$  where the power 5 is determined with an accuracy of  $\pm 2\%$ . An interpolation formula for the scaling function  $f(x = t/\tau_{L_\infty}) = (0.215 + 8x)^{-1}$  appears to account well for the observed relaxation kinetics.

## B. Transport Properties in Giant Micelles

In contrast to static properties, where LP and GM reveal generally the same behavior as that of conventional polymers, due to the self-assembling nature of the breakdown process the transport properties of GM are much more complex. Like conventional polymers, these materials are highly viscoelastic [73,74] and their novel rheology has been intensively studied recently, both experimentally [75,76] and theoretically [11,31,77–79]. A theoretical model

developed by Cates [31,77], based on the assumption that chain dynamics is predominantly that of reptation, suggests that the relaxational process is governed essentially by two characteristic time scales:  $\tau_{\text{rep}}$ , the reptation time of a polymer of length  $L$ , and  $\tau_{\text{break}}$ , the mean time for such a chain to break into two pieces. If  $\tau_{\text{break}} \gg \tau_{\text{rep}}$ , the dominant stress-relaxation mechanism is simple reptation. Otherwise stress-relaxation is characterized by a new intermediate time scale  $\tau = \sqrt{\tau_{\text{break}}\tau_{\text{rep}}}$ , associated with a process whereby the chain breaks and the relaxation of its “tube” of entanglements occurs before the new chain end is lost by recombination. Thus the relaxational process appears to be very different from that in conventional polymers, and the unique dynamics of wormlike micelles has suggested the possibility of unusual transport properties in such systems, as that of *enhanced* diffusion [35] with diffusion coefficient  $D \propto t^\alpha$ , where  $\alpha > 1$ .

While these model predictions have been confirmed experimentally [11] in a number of cases, significant deviations have been observed [73] in both limits of very low and high salt concentrations in systems of wormlike micelles.

Numeric experiments are scarce. The first computer simulation [60] of GM transport properties has produced results, e.g., for the diffusion constant,  $D \propto \langle L \rangle^{-1}$ , consistent with Rouse dynamics of “dead” chains, although comparatively short chains,  $\langle L \rangle \leq 60$ , have been studied so that reptational dynamics has not been approached even nearly. With the much more powerful algorithm [65,66] investigations are still in progress, but a number of interesting results within intervals covering several orders of magnitude of density, or of chain length variation, have already emerged and offer a test for our theoretical models.

Thus, in order to reproduce the effect of an experimentally existing activation barrier for the scission/recombination process, one may introduce into the MC simulation the notion of “frequency”,  $\omega$ , with which, every so many MC steps, an attempt for scission and/or recombination is undertaken. Clearly, as  $\omega$  is reduced to zero, the average lifetime of the chains, which is proportional by detailed balance to  $\tau_{\text{break}}$ , will grow to infinity until the limit of conventional “dead” polymers is reached. In a computer experiment  $\omega$  can be easily controlled and various transport properties such as mean-square displacements (MSQ) and diffusion constants, which essentially depend on  $\tau_{\text{break}}$ , can be studied.

In Fig. 20 we show the MSQ of a system of GM [66] with different mean chain lengths (depending on  $J$ , cf. Eq. (12)) for three values of  $\omega = 1, 0.1, 0.01$ . Since the individual chains have only transient identity, it is meaningless to discuss their center of mass diffusion. It is evident from Fig. 20 that the MSQ of the segments,  $g(t) = \langle [x(t) - x(0)]^2 \rangle$ , follows an intermediate sub-diffusive regime,  $g(t) \propto t^{0.5}$ , which is later replaced by conventional diffusion at some characteristic crossover time which grows

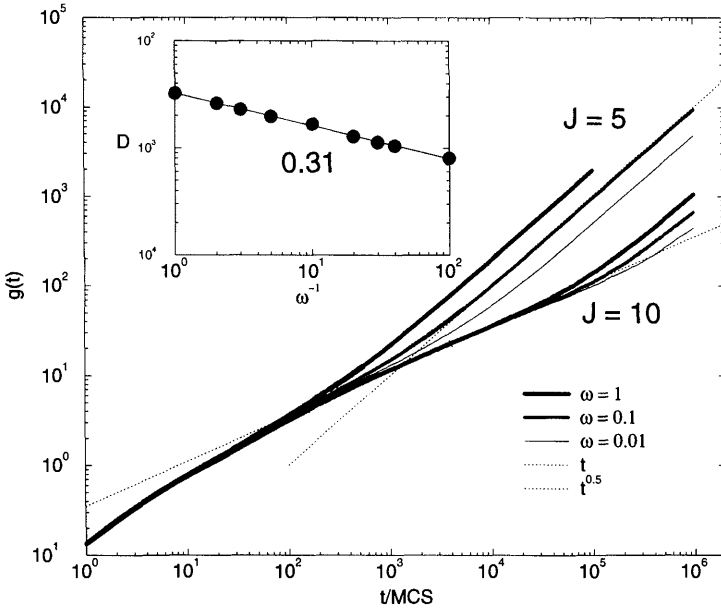


**FIG. 20** Mean square displacement,  $g(t) = \langle [x(t) - x(0)]^2 \rangle$ , averaged over all monomers, for  $J = 5$  (the three upper curves) with  $\langle L \rangle \approx 35$ , and for  $J = 10$  with  $\langle L \rangle \approx 430$ . The frequency  $\omega$  of attempted scissions per MCStep is given as parameter. The inset shows the diffusion coefficient  $D$  vs  $\omega$  scaling relationship [66] with an exponent 0.31.

with decreasing  $\omega$ . The inset in Fig. 20 demonstrates the expected scaling of the diffusion coefficient  $D \propto \omega^{-1/3}$ , which can be understood as follows. Consider normal Rouse dynamics of a polymer of length  $\Lambda$  chosen such that, during its lifetime, the chain MSQ is equal to its gyration radius  $R_g^2$ . Within a time interval  $\tau_{\text{break}} = (k_s \Lambda)^{-1}$ , cf. Eq. (24), where  $k_s = \omega \exp(-J)$  is the rate constant for scission, the polymer travels an MSQ  $\langle x^2 \rangle \approx R_g^2 \approx \Lambda$ . The diffusion coefficient  $D$  is then going to be  $D = \langle x^2 \rangle / \tau_{\text{break}} = k_s \Lambda^2$ . For Rouse diffusion of a chain of length  $\Lambda$  one has generally  $D = D_0 / \Lambda$  ( $D_0$  is the mobility constant), so that eventually  $\Lambda \propto k_s^{-1/3}$ , that is,  $D \propto \omega^{1/3}$ .

The same result follows, however, if the chain dynamics is that of reptation, rather than Rouse. Within time interval  $\tau_{\text{break}}$  a reptating chain of length  $\Lambda$  moves a distance  $\langle x^2 \rangle$  along a *curvilinear* tube formed by entanglements with neighboring chains. However, since the movement of the chain along the contour length is essentially one-dimensional,  $\langle x^2 \rangle \approx \Lambda^2$  so that  $\Lambda^2 \approx D_c \tau_{\text{break}}$  ( $D_c$  is the diffusion coefficient along the tube). The curvilinear diffusion coefficient along the tube does not depend on  $\Lambda$  but rather on

the mean length  $\langle L \rangle$  of the system,  $D_c \propto \langle L \rangle^{-1}$ , since the chain  $\Lambda$  is on the average always within a tube of length  $\langle L \rangle$ . Thus  $\Lambda \propto k_s^{-1/3}$  again, and  $\tau_{\text{break}} = (k_s \Lambda)^{-1} \approx k_s^{-2/3}$ . Using the latter in the relation  $D \approx R_g^2 / \tau_{\text{break}} = \Lambda / \tau_{\text{break}}$ , which still holds for the observable diffusion coefficient  $D$  in the volume, one arrives again at  $D \propto k_s^{1/3}$ . Thus it is not possible from this investigation alone to determine the dominant type of dynamic motion in the system. One should point out, by the way, that, as a matter of fact, the crossover from Rouse to reptational chain dynamics has so far not been unambiguously established in a computer simulation, even in the case of conventional polymers.

The theoretical treatment of GM dynamics, mentioned above, relies entirely on mean-field arguments [31] in the sense that successive breakage and recombination events are uncorrelated. This means that a newly created chain end is not much more likely to recombine with its "partner" from the preceding dissociation than with the end of another chain. It has been suggested recently by O'Shaughnessy and Yu [79] that at short times there should exist another class of recombination kinetics which is *diffusion controlled* and dominated by self-recombinations. As a consequence, instead of the long-time Poisson distribution of chain end lifetimes, the diffusion-controlled regime would imply a short-time power law distribution of the lifetimes of chain ends. And indeed, the computer simulation [66] provides a nice confirmation of the analytic prediction (Fig. 21). It is evident that several distributions of chain end lifetimes  $\Psi(t)$ , sampled at different frequencies  $\omega$  of attempted scissions, reveal a power law deviation from the exponential form at small times (the observed exponent  $\approx -2$ ), marking this diffusion-controlled regime. As the frequency of scission/recombination events is reduced, the chance of self-recombination decreases and the power law portion of  $\Psi(t)$  gradually vanishes. All four distributions are seen to collapse onto a single master curve if time  $t$  is measured in units of the characteristic chain-end lifetime  $\tau_L$  and a similar distribution of the distances, covered by the ends of the chains, yields for the characteristic distance  $\xi_L$  the expected relation  $\xi_L^2 \propto \tau_L^{0.5}$ , consistent with the intermediate regime of anomalous diffusion shown in Fig. 20.

Ending this section, we should like to mention again the MD investigation of GM under shear [54] which finds an increase of the average breaking time  $\tau_{\text{break}}$  as the shear rate of the flow is increased.

## VI. CONCLUSIONS AND OUTLOOK

Living polymers and wormlike micelles suggest an interesting field for basic research in which the constant process of scission and recombination of the

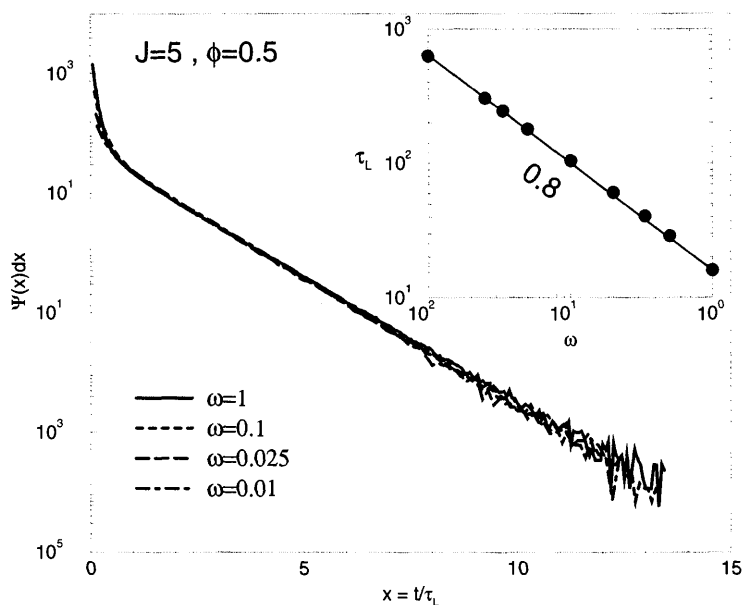


**FIG. 21** Collapse of lifetime distributions [66] for various  $\omega$  at  $J = 5$  and  $\phi = 0.5$ .

chains, and the resulting polydispersity of the system in the state of equilibrium polymerization, provide a challenging background for testing our knowledge of polymer physics. Computer simulations can be viewed as a promising tool for investigation of both static and dynamic properties of these complex systems, especially in cases when the analytical treatment is limited to crude approximations (e.g. MFA) or when laboratory experiments are very difficult.

On the ground of the existing computer experiments it may be concluded that most aspects of the static behavior of living polymers can be understood in terms of the scaling considerations of conventional polymers, namely, that basically a polydisperse solution shows the same behavior as a monodisperse one at least in what concerns the bulk properties of the system. In the presence of geometric constraints like hard wall, pores, etc., the system of LP or GM reveals specific features of its own, depending on the interplay between entropic repulsion and adhesion at the wall, which are sensitive to chain length and may lead to length segregation in the vessel. These effects depend additionally on the degree of flexibility of the polymers. An interesting problem, deserving more investigation, is the impact of shear stress on conformational properties and on the MWD.

In contrast to statics, the relaxational kinetics of living polymers and of giant wormlike micelles is unique (and different in both cases). It is entirely determined by the processes of scission/recombination and results in a non-linear approach to equilibrium. A comparison of simulational results and laboratory observations in this respect is still missing and would be highly desirable.

One of the most interesting aspects of GM is their dynamics. While there already exists a fairly detailed theoretical notion of dynamic behavior and transport properties, experimental results are rather controversial and the first computer experiments are only starting to emerge. The relevance of the reptational mechanism of chain movement among entanglements has not been unambiguously proved so far, although polymers with chain lengths larger than those estimated in a number of laboratory experiments have been simulated. Clearly, much more work is needed in this aspect in order to gain deeper insight into the various details of polymer dynamics and possibly elucidate many laboratory findings.

## ACKNOWLEDGMENTS

The author is indebted to J. Wittmer and Y. Rouault for valuable contributions to this work. This work was supported by the Bulgarian Scientific Foundation, Grant No. X-644/1996, and by the National Science Foundation of USA, Grant No. INT-940518.

## REFERENCES

1. R. L. Scott. *J Phys Chem* 69:261, 1965.
2. J. C. Wheeler, S. J. Kennedy, P. Pfeuty. Equilibrium polymerization as a critical phenomenon. *Phys Rev Lett* 45:1748–1752, 1980.
3. S. J. Kennedy, J. C. Wheeler. Critical and tricritical phenomena in “living polymers”. *J Phys Chem* 78:953–962, 1984.
4. G. Faivre, J. L. Gardissat. Viscoelastic properties and molecular structure of amorphous selenium. *Macromolecules* 19:1988–1996, 1986.
5. K. M. Zheng, S. C. Greer. Living poly(alpha-methylstyrene) near the polymerization line. 1. Mass density and polymerization line for solutions in tetrahydrofuran. *Macromolecules* 25:6128–6136, 1992.
6. S. S. Das, A. Poplis-Andrews, S. C. Greer. Living poly(alpha-methylstyrene) near the polymerization line. 4. Extent of polymerization as a function of temperature. *J Chem Phys* 102:2951–2959, 1995.
7. S. C. Greer. Living polymers. *Comput Mat Sci* 4:334–338, 1995.
8. F. Boue, J. P. Ambroise, R. Bellisent, P. Pfeuty. Equilibrium polymerization of liquid sulfur from small-angle neutron scattering of sulfur solutions. *J Physique I* 2:969–980, 1984.



9. T. K. Attwood, J. E. Lydon, C. Hall, G. L. Tiddy. The distinction between chromonic and amphiphilic lyotropic mesophases. *Liquid Cryst* 7:657–668, 1990.
10. J. Appel, G. Porte. Polymerlike behavior of giant micelles. *Europhys Lett* 12:185–190, 1990.
11. M. E. Cates, S. J. Candau. Statics and dynamics of worm-like surfactant micelles. *J Phys Condens Matter* 2:6869–6892, 1990.
12. F. Oozawa, S. Asakura. *Thermodynamics in the Polymerization of Proteins*. New York: Academic Press, 1975.
13. P. G. De Gennes. Exponents for the excluded volume problem as derived by the Wilson method. *Phys Lett* 38A:339, 1972; J. des Cloiseaux. The Lagrangian theory of polymer solutions at intermediate concentrations. *J Phys* 36:281–291, 1975.
14. J. C. Wheeler, P. Pfeuty. The  $n \rightarrow 0$  vector model and equilibrium polymerization. *Phys Rev A* 24:1050–1062, 1981.
15. P. D. Gujrati, Scaling theory of polydispersity, infinite chain and the Flory–Huggins approximation. *Phys Rev B* 40:5140–5143, 1989.
16. P. J. Flory. *Principles of Polymer Chemistry*. Ithaca, NY: Cornell University Press, 1953.
17. D. Blankschtein, G. Thurston, G. Benedek. Phenomenological theory of equilibrium thermodynamic properties and phase separation of micellar solutions. *J Chem Phys* 85:7268–7288, 1986.
18. R. Zana, C. Weill. Effect of temperature on the aggregation behavior of non-ionic surfactants in aqueous solutions. *J Physique Lett* 46:L953–L960, 1985.
19. W. Brown, R. Johnsen, P. Stilbs, B. Lindman. Size and shape of nonionic amphiphile ( $C_{12}E_6$ ) micelles in dilute aqueous solutions as derived from quasielastic and intensity of light scattering, sedimentation and pulsed-field-gradient nuclear magnetic resonance self-diffusion data. *J Phys Chem* 87:4548–4553, 1983.
20. M. Zulauf, K. Weckström, J. B. Hayter, V. Degiorgio, M. Corti. Neutron scattering study of micelle structure in isotopic aqueous solutions of poly(oxyethylene) amphiphiles. *J Phys Chem* 89:3411–3417, 1985.
21. M. Jaric, K. H. Bennemann. Equilibrium polymerization as an ordering transition. *Phys Rev A* 27:1228–1231, 1983.
22. M. Jaric, G. F. Tothill. Thermodynamic polydispersity and the Flory exponent. *Phys Rev Lett* 55:2891–2894, 1985.
23. G. F. Tothill, M. Jaric. Monte Carlo study of polymerization on a lattice: Two dimensions. *Phys Rev B* 31:2981–2985, 1985.
24. G. F. Tothill, Z. Sui. Chain polymer ensembles by computer simulations. *J Chem Phys* 88:8000–8007, 1988.
25. A. Milchev. Phase transitions in polydisperse polymer melts. *Polymer* 34:362, 1993.
26. S. Livne. A polydisperse polymer solution as a critical system. *Macromolecules* 27:5318–5328, 1994.
27. A. Milchev, D. P. Landau. Monte Carlo study of semiflexible living polymers. *Phys Rev E* 52:6431–6441, 1995.

28. A. Milchev, D. P. Landau. Adsorption of living polymers on a solid surface: A Monte Carlo simulation. *J Chem Phys* 104:9161–9168, 1996.
29. G. I. Menon, R. Pandit, M. Barma. Melts of semi-flexible, living polymers: A lattice model. *Europhys Lett* 24:253–258, 1993.
30. D. Stauffer. Scaling theory of percolating clusters. *Phys Rep* 54:1–74, 1979.
31. M. E. Cates. *J Physique* 49:1593–1600, 1988.
32. L. Schäfer, T. A. Witten. Renormalization field theory of polymer solutions. I. Scaling laws. *J Chem Phys* 66:2121–2130, 1977; A. Knoll, L. Schäfer, T. A. Witten. The thermodynamic scaling function of polymer solution. *J Physique* 42:767–778, 1981.
33. L. Schäfer. Chain length distribution in a model of equilibrium polymerization. *Phys Rev B* 46:6061–6070, 1992.
34. P. van der Schoot. Growth of living polymers in a good solvent. *Europhys Lett* 39:25–30, 1997.
35. J. P. Bouchaud, A. Ott, D. Langevin, W. Urbach. Anomalous diffusion in elongated micelles and its Levy flight interpretation. *J Phys II (France)* 1:1465–1482, 1991.
36. A. Ott, J. P. Bouchaud, D. Langevin, W. Urbach. Anomalous diffusion in “living polymers”: A genuine Levy flight? *Phys Rev Lett* 65:2201–2204, 1990.
37. Y. Rouault. Living polymers in random media: a 2D Monte Carlo investigation. *Europhys J B* 2:483–487, 1998.
38. J. H. Gibbs, E. A. Di Marzio. Nature of the glass transition and the glassy state. *J Chem Phys* 28:373–383, 1958.
39. A. Milchev, I. Gutzow. Temperature dependence of the configurational entropy of undercooled melts and the nature of the glass transition. *J Macromol Sci B* 21:583–615, 1982.
40. G. I. Menon, R. Pandit. Glass formation in a lattice model for living polymers. *Phys Rev Lett* 75:4638–4641, 1995.
41. B. Petroff, A. Milchev, I. Gutzow. Thermodynamic functions of both simple (monomeric) and polymeric melts: MFA approach and Monte Carlo simulation. *J Macromol Sci B* 35:763–794, 1996.
42. G. J. Fleer, M. A. Cohen Stuart, J. M. H. M. Scheutjens, T. Cosgrove, B. Vincent. *Polymers at Interfaces*. London: Chapman & Hall, 1993.
43. M. Tirrell, E. E. Parsonage. In: E. L. Thomas, ed. *Material Science and Technology. Vol. 12; Structure and Properties of Polymers*. Weinheim: VCH, 1993, p. 653.
44. D. Y. Yoon, M. Vacatello, G. D. Smith. In: K. Binder, ed. *Monte Carlo and Molecular Dynamics Simulations in Polymer Science*. New York: Oxford University Press, 1995, Chap. 8.
45. J. A. Marques, K. A. Dill. Solute partitioning into chain molecule interphases: monolayers, bilayer membranes and micelles. *J Chem Phys* 85:434–444, 1986.
46. G. J. Fleer. Chain molecules at interfaces: a versatile self-consistent lattice model. *Colloids Surf* 35:151–167, 1989.
47. V. Schmitt, F. Lequeux, C. M. Marques. Confinement of dilute solutions of living polymers. *J Physique II* 3:891–902, 1993.

48. J. H. van Vliet, G. ten Brinke. Orientation and shape of flexible polymers in a slit. *J Chem Phys* 93:1436–1441, 1990.
49. P. E. Rouse. The theory of nonlinear viscoelastic properties of dilute solutions of scaling polymers. *J Chem Phys* 21:1273–1280, 1953.
50. B. Zimm. Dynamics of polymer molecules in dilute solutions: viscoelasticity, low birefringence and dielectric loss. *J Chem Phys* 24:269–278, 1956.
51. I. Carmesin, K. Kremer. The bond fluctuation method: a new effective algorithm for dynamics of polymers in all spatial dimensions. *Macromolecules* 21:2819–2823, 1988.
52. W. Paul, K. Binder, D. Heermann, K. Kremer. Dynamics of polymer solutions and melts. Reptation prediction and scaling of relaxation times. *J Chem Phys* 95:7726–7740, 1991.
53. See, e.g., K. Binder, ed. *Monte Carlo Methods in Statistical Physics*. Berlin: Springer-Verlag, 1979.
54. M. Kröger, R. Makhlofi. Wormlike micelles under shear flow: A microscopic model studied by nonequilibrium molecular dynamics computer simulations. *Phys Rev E* 53:2531–2536, 1996.
55. J. S. Pedersen, M. Laso, P. Schurtenberger. Monte Carlo study of excluded volume effects in worm-like micelles and semi-flexible polymers. *Phys Rev E* 54:R5917–R5920, 1996.
56. D. J. Evans. *Mol Phys* 37:1745, 1979.
57. A. Milchev, J. Wittmer, D. P. Landau. A Monte Carlo study of equilibrium polymers in a shear flow. *Euro Phys J B* 1999 (in press).
58. Y. Rouault, A. Milchev. Monte Carlo study of living polymers with the bond-fluctuation method. *Phys Rev E* 51:5905–5910, 1995.
59. A. Milchev, Y. Rouault. A Monte Carlo study of thermodynamic relaxation in living polymers. *J Physique II* 5:343–347, 1995.
60. Y. Rouault, A. Milchev. A Monte Carlo study of diffusion in living polymers. *Europhys Lett* 33:341–346, 1996.
61. Y. Rouault, A. Milchev. A Monte Carlo study of living polymers in confined geometries. *Mol Theory and Simul* 6:1177–1190, 1997.
62. Y. Rouault, A. Milchev. Monte Carlo study of molecular weight distribution of living polymers. *Phys Rev E* 55:2020, 1997.
63. Y. Rouault. A Monte Carlo study of living polymers in 2D: Effect of small chains on static properties. *J Physique II* 6:1301–1311, 1996.
64. A. Milchev, Y. Rouault, D. P. Landau. Monomer-mediated relaxation in living polymers. *Phys Rev E* 56:1946–1953, 1997.
65. J. Wittmer, A. Milchev, M. Cates. Computational confirmation of scaling predictions for equilibrium polymers. *Europhys Lett* 41:291–296, 1998.
66. J. Wittmer, A. Milchev, M. Cates. Dynamical Monte Carlo study of equilibrium polymers: Static properties. *J Chem Phys* 109:834–845, 1998.
67. P. G. de Gennes. *Scaling Concepts in Polymer Physics*. Ithaca: Cornell University Press, 1979, Chap. 1.
68. C. M. Marques, M. E. Cates. Nonlinear thermodynamic relaxation in living polymer systems. *J Phys II (France)* 1:489–492, 1991.

69. M. S. Turner, M. E. Cates. The relaxation spectrum of polymer length distributions. *J Physique* 51:307–316, 1990.
70. C. M. Marques, M. S. Turner, M. E. Cates. End-evaporation kinetics in living polymer systems. *J Chem Phys* 99:7260–7266, 1993.
71. M. von Smoluchowski. *Z Phys Chem* 92:129, 1917.
72. N. G. Taganov. *Sov J Chem Phys* 1:2329, 1984.
73. A. Khatory, F. Lequeux, F. Kern, S. J. Candau. Linear and nonlinear viscoelasticity of semidilute solutions of wormlike micelles at high-salt content. *Langmuir* 9:1456–1464, 1993.
74. P. Terech, P. Maldivi, C. Dammer. “Living polymers” in organic solvents: Stress relaxation in bicopper tetracarboxylate/tert-butyl cyclohexane solutions. *J Phys II (France)* 4:1799–1811, 1994.
75. J. F. Berret, J. Appell, G. Porte. Linear rheology of entangled wormlike micelles. *Langmuir* 9:2851–2854, 1993.
76. E. Faetibold, G. Waton. Dynamical properties of wormlike micelles in the vicinity of the crossover between dilute and semidilute regimes. *Langmuir* 11:1972–1979, 1995.
77. M. Cates. Reptation of living polymers: Dynamics of entangled polymers in the presence of reversible chain-scission reactions. *Macromolecules* 20:2289–2296, 1987.
78. R. Granek. Stress relaxation in polymer melts and solutions: Bridging between the breathing and reptation regimes. *Macromolecules* 28:5370–5371, 1995.
79. B. O’Shaughnessy, J. Yu. Rheology of wormlike micelles. *Phys Rev Lett* 74:4329–4332, 1995.

# 12

## Conformational and Dynamic Properties of Polymer Chains Adsorbed on Hard Surfaces

**ANDREY MILCHEV** Institute for Physical Chemistry, Bulgarian Academy of Sciences, Sofia, Bulgaria

I. Introduction and Overview	556
II. Models and Methods	558
A. Static Methods: self-avoiding random walks	559
B. Dynamic Methods	561
III. Adsorption of Single Polymer Chains at Surfaces	569
IV. Single Chain Trapped in a Tube	580
V. Single Polymer Chains in a Slit	587
VI. Polymer Solutions in Slit-like Pores	594
VII. Polymer Chains in Random Porous Media	600
A. Scaling laws in equilibrium	600
B. Polymer chain in a flow through a porous medium	605
VIII. Dewetting of Thin Polymer Films	614
IX. Conclusion and Outlook	623
References	623

## I. INTRODUCTION AND OVERVIEW

The properties of polymers at surfaces and interfaces play an important role in a number of applications in technology (protective coatings, adhesives, lubricants, etc.) and biology (adsorption of biopolymers at cell membranes, etc.) and pose many challenging scientific problems [1–5]. There is an interesting interplay between bulk and surface properties in the interfacial regions between the bulk of a polymer film and the adsorbing substrate on one side, and the polymer solution (or air, respectively) on the other side of the film. A flexible polymer chain experiences a loss of configurational entropy near a wall but this may be outweighed by enthalpic gains due to the wall–monomer interactions. While the static aspects of this behavior have been studied for a long time [2–4], using various experimental and theoretical techniques, the dynamic properties of polymers adsorbed on surfaces are less well understood [5–9]. Thus chains, which are partially adsorbed to the walls and mutually entangled, are very hard to treat by analytical methods, but also they are not easy to study experimentally, since the extent to which polymer films are in thermal equilibrium is rather uncertain [5,10].

In this situation computer simulation is useful, since the conditions of the simulation can be chosen such that full equilibrium is established, and one can test the theoretical concepts more stringently than by experiment. Also, it is possible to deal with ideal and perfectly flat surfaces, very suitable for testing the general mechanisms alluded to above, and to disregard in a first step all the complications that real substrate surfaces have (corrugation on the atomistic scale, roughness on the mesoscopic scale, surface steps, adsorbed impurities, etc.). Of course, it may be desirable to add such complications at a later stage, but this will not be considered here. In fact, computer simulations, i.e., molecular dynamics (MD) and Monte Carlo (MC) calculations, have been extensively used to study both static and dynamic properties [11]; in particular, structural properties at interfaces have been considered in detail [12].

Recently attention has been focused on the dynamics of flexible polymer chains adsorbed from dilute solution [13], confined between hard walls in a tube [14], and in slits [15–19]. Related studies of polymer chain behavior in random porous media [20–22], as well as of the process of polymer film dewetting [23], are also summarized in the present review of coarse-grained models of macromolecules on surfaces. Although it is clearly legitimate to consider the interplay between structure near interfaces and dynamic properties for chemically realistic models [24,25], we do not address properties of specific polymers but rather consider phenomena on larger length scales ( $\geq 1$  nm), where several chemical bonds can be integrated along the backbone of a chain into one effective bond. The solid walls are then treated

as perfectly flat and structureless, rather than representing chemical details of a specific substrate, and crudely simplified potentials between these surfaces and the effective monomers are used [13–23].

Although the properties of specific polymer/wall systems are no longer accessible, the various phase transitions of polymers in confined geometries can be treated (Fig. 1). For semi-infinite systems two distinct phase transitions occur for volume fraction  $\tilde{\phi} = 0$  and chain length  $N \rightarrow \infty$ , namely collapse in the bulk (at the theta-temperature  $\theta$  [26,27]) and adsorp-

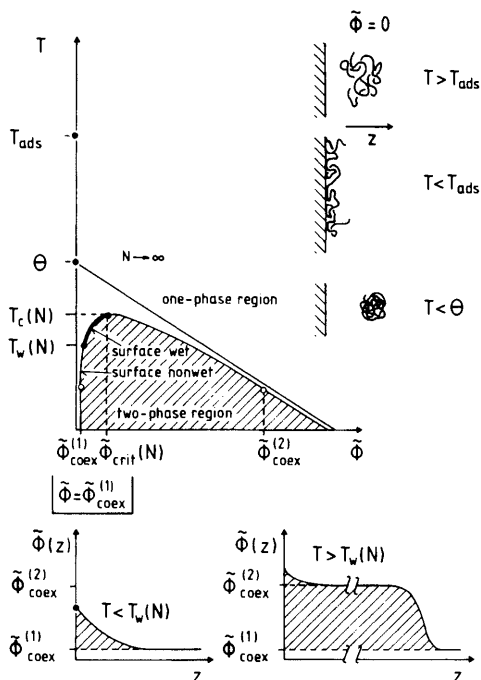


**FIG. 1** Schematic phase diagram of a semi-infinite polymer solution ( $z > 0$ ) with one attractive wall (at coordinate  $z = 0$ ) in the plane of temperature  $T$  and volume fractions  $\tilde{\phi}$  taken by the monomers. (Upper right) The various states of very long ( $N \rightarrow \infty$ ) isolated ( $\tilde{\phi} = 0$ ) chains are shown qualitatively. For  $T > T_{\text{ads}}$ , the adsorption transition temperature, only non-adsorbed three-dimensional (swollen) coils exist. For  $T < T_{\text{ads}}$  these coils, in the bulk of the solution, compete with chains adsorbed at the wall in a two-dimensional configuration. For  $T < \Theta$  the coils in the bulk are collapsed rather than swollen. For nonzero volume fraction an unmixing transition exists for  $T < T_c(N)$ . For  $\tilde{\phi} = \tilde{\phi}_{\text{coex}}^{(1)}$  the surface may exhibit a wetting transition at  $T_w(N)$ , assumed to be a second-order transition. The lower part of the figure shows schematic density profiles for nonwet (left) and wet (right) surfaces [16].

tion to a two-dimensional configuration at the wall [2,35]. For finite chain length, rather distinct transitions occur at non-zero  $\tilde{\phi}$ . For  $T < T_c(N)$  phase separation occurs in the bulk, whereas wetting or drying transitions can occur at the wall if the system takes one of the volume fractions  $\tilde{\phi}^{(1)}$ ,  $\tilde{\phi}^{(2)}$  corresponding to the coexistence curve. For a polymer solution confined between two equivalent walls a distance  $D$  apart, wetting transitions are rounded off [28] and only a single unmixing transition at a shifted critical temperature  $T_c(D)$  remains. But the coexisting phases (at average volume fraction  $\tilde{\phi}^{(1)}(D)$ ,  $\tilde{\phi}^{(2)}(D)$  in the film) are modified in comparison with their bulk counterparts as a result of a precursor of wetting layers at the walls.

In cases when the two surfaces are non-equivalent (e.g., an attractive substrate on one side, an air on the other side), similar to the problem of a semi-infinite system in contact with a wall, wetting can also occur (the term dewetting applies if the homogeneous film breaks up upon cooling into droplets). We consider adsorption of chains only in the case where all monomers experience the same interaction energy with the surface. An important alternative case occurs for chains that are end-grafted at the walls: polymer brushes which may also undergo collapse transition when the solvent quality deteriorates. Simulation of polymer brushes has been reviewed recently [9,29] and will not be considered here.

In the next section we describe briefly some of the principal techniques for simulation of chain macromolecules and elucidate in more detail our off-lattice dynamic Monte Carlo model with which all results presented here have been obtained. The influence of adsorption transition on conformational and dynamic properties of a single chain is reviewed in Sec. III, and the crossover from bulk to quasi one- and two-dimensional behavior of single chains, confined in tubes and slits, is interpreted in terms of scaling concepts in Secs. IV and V. Sec. VI reviews simulations of dense polymer solutions under geometrical constraints, including density and pressure profiles across the slit as well as data on surface tension. In Sec. VII A we show data on equilibrium statics and dynamics of flexible polymer chains in a random host matrix of quenched obstacles, while in Sec. VII B the flow of polymer chains through a random medium due to an external field is considered. Finally, in Sec. VIII we present results of an MC simulation of the early stages of thin polymer film dewetting. The present review then concludes with a brief outlook on unsolved problems.

## II. MODELS AND METHODS

As emphasized in the Introduction, it is advisable to eliminate some of the chemical details and the corresponding small-scale degrees of freedom



(vibrations of bond length and of bond angles, etc.) and deal only with larger scale degrees of freedom, by using a coarse-grained model. It is then possible to vary parameters (chain length, solvent quality, strength of attractive forces between monomers and walls, etc.) over a sufficiently large range and still reach thermal equilibrium. Indeed, for polyethylene, equilibration of chemically realistic models is still possible [11,25,45] at high temperatures (e.g.,  $T = 400$  K) and a small degree of polymerization (e.g.,  $N = 28$ ). Work on chemically realistic models of polymers at lower  $T$  and larger  $N$  can be found, but long wavelength properties clearly are not well equilibrated, and hence questions such as the chain length dependence of relaxation times, etc., cannot be addressed. Therefore work where at best small-scale properties are equilibrated is not included here.

### A. Static Methods: Self-avoiding Random Walks

The simplest model of polymers comprises random and self-avoiding walks on lattices [11,45,46]. These models are used in analytical studies [2,4], in particular in the numerical implementation of the self-consistent field theory [4] and in studies of adsorption of polymers [35,47–50] and melts confined between walls [24,51,52].

Let us consider a simple self-avoiding walk (SAW) on a lattice. The net interaction of solvent–solvent, chain–solvent and chain–chain is summarized in the excluded volume between the monomers. The empty lattice sites then represent the solvent. In order to fulfill the excluded volume requirement each lattice site can be occupied only once. Since this is the only requirement, each available conformation of an  $N$ -step walk has the same probability. If we fix the first step, then each new step is taken with probability  $1/(q-1)$ , where  $q$  is the coordination number of the lattice ( $q = 4$  for a square lattice,  $q = 6$  for a simple cubic lattice, etc.).

In the *simple sampling* procedure of generating chain conformations all successfully generated walks have equal probability. Walks are grown purely stochastically. Each time an attempted new bond hits a site which is already occupied, one has to start at the very beginning. Otherwise different conformations would have different probabilities and this would introduce an effective attraction among the monomers [54]. With this method, each conformation is taken randomly out of the  $q(q-1)^{N-1}$  possible random paths which do not include direct back-folding. However, the total number of SAW on a lattice is known [26] to be:

$$Z(N) = c_0 q_{\text{eff}}^N N^{\gamma-1}, \quad N \gg 1 \quad (1)$$

where  $q_{\text{eff}} < q-1$  and  $c_0$  is a number of the order of unity. The critical exponent  $\gamma$  is purely dimension- but not lattice-dependent ( $\gamma = 1$  ( $d \geq 4$ );

$\gamma \approx 7/6$  ( $d = 3$ );  $\gamma = 43/32$  ( $d = 2$ )). Typical numbers for  $q_{\text{eff}}$  are 2.6385 (square), 2.879 (diamond,  $q = 4$ ) and 4.6835 (simple cubic) [54]. It turns out, therefore, that only a small fraction of all non-reversible random walks (NRRW) are self-avoiding. Thus the probability  $A(N)$  to find a SAW by simply generating a NRRW

$$A(N) = A_0 \left( \frac{q_{\text{eff}}}{q-1} \right)^N N^{\gamma-1} \quad (2)$$

decays exponentially. This attrition has been recognized and discussed very early by Rosenbluth and Rosenbluth [55]. A typical number for  $A$ , is e.g.,  $A(100) = 0.03$  on the diamond lattice.

An improvement of this method—the so-called *biased sampling* [55] (or *inversely restricted sampling*)—suggests to look ahead at least one step in order to overcome the attrition. Consider a SAW of  $i$  steps on a  $q$ -coordination number lattice. To add the  $i + 1$ st step one first checks which of the  $q_0 = q - 1$  neighboring sites are empty. If  $k$  ( $q_0 \geq k \geq 0$ ) sites are empty one takes one of these with equal probability  $1/k$ ; if  $k = 0$  the walk is terminated and one starts from the beginning. This reduces the attrition dramatically. Now each  $N$ -step walk has a probability  $P_N(\{\vec{r}_i\}) = \prod_{i=1}^N k_i^{-1}$ , so that dense configurations are clearly more probable. To compensate for this bias, each chain does not count as 1 in the sample but with a weight

$$W_N(\{\vec{r}_i\}) = \prod_{i=1}^N \frac{k_i}{q_0} \quad (3)$$

so that  $P_N(\{\vec{r}_i\}) W(\{\vec{r}_i\}) = q_0^{-N}$ . In this way one samples exactly the same configurational space as the simple sampling method. In result, especially for  $d = 3$  there appears to be almost no attrition left for  $N \leq 1000$  (diamond lattice) to  $N \leq 10\,000$  (fcc lattice). Thus bias sampling is an appealing method, however, its simplicity involves pitfalls [53,54], e.g., by favoring more compact conformations, and various further improvements have been suggested [47,48]. One should note here also the interesting unbiased method of *dimerization* [56], whereby one attempts to assemble long chains out of successfully generated short chains.

As an illustration of the biased sampling method in application to the problems of polymer chain adsorption on a hard wall we shall recall here briefly the procedure used on a diamond lattice [35]. Starting the chain at the origin, the first bond is fixed at the plane and all the following bonds are determined at random apart from the non-reversal condition. Suppose, after a certain number  $i$  of steps, that the  $(i + 1)$ st monomer reaches the plane at  $z = 0$  again. With  $q = 4$  on the diamond lattice one has the probability  $p = 1/3$  for each new possible choice of a bond. Thus in

2/3 of all attempts one has to start a new chain because two new bonds give negative  $z$  values. Then long chains with many contacts will very seldomly be generated. To improve this aspect, a bias factor  $Q$  is introduced,  $Q > 1$ , and the probability  $p$  is changed as follows

$$\left. \begin{aligned} p \rightarrow p^+ &= p\sqrt{Q}; & z_{i+2} > z_{i+1} = 0, \\ p \rightarrow p^- &= p/\sqrt{Q}; & z_{i+2} < z_{i+1} = 0 \end{aligned} \right\} \quad (4)$$

To normalize the sum of all probabilities to 1, one takes

$$\left. \begin{aligned} p_0^+ &= p^+/(2p^- + p^+) = Q/(2 + Q), \\ p_0^- &= p^-/(2p^- + p^+) = 1/(2 + Q) \end{aligned} \right\} \quad (5)$$

which means that now in  $Q/(2 + Q)$  cases the walk can be continued. To get a correct average now one has to change the statistical weight of the chain generated by this method. Usually one gets a statistical weight  $W = 1$ . Then the number of chains of given length  $N$  divided by the number of attempts to start a walk gives the reduced partition function (i.e., the ratio of SAW and NRRW bulk partition functions). Therefore, in general, each calculated configuration of  $N$  bonds has the statistical weight 1. For conventional simple sampling the NRRW partition function is  $Z(N) = q_0^N$  and one has  $q_0 = 1/p$ . In the biased sampling here the probability of a NRRW might be different, however, and for steps starting in the  $z = 0$  plane this corresponds to a new "theoretical" coordination number  $q' = 1/p_0^+ = (2 + Q)/Q$ . To get the right statistical weight of such a chain with, e.g., one further bond starting at the surface  $W(N, 1)$ , besides the first one, one has to normalize  $q'$  by  $q_0$ :  $W(N, 1) = q'/q_0 = (2 + Q)/q_0Q = (2 + Q)/(3Q)$ . Therefore, by sampling a distribution function one gets, after generating a chain of  $N$  bonds with  $j$  bonds besides the first, starting at the surface, a weight factor  $W(N, j) = (2 + Q)/(q_0Q)^j$  instead of  $W = 1$ . Thus the number of generated chains of length  $N$  with  $j$  reflections at the wall is to be multiplied by  $W(N, j)$  so as to regain the correct "unbiased" probability.

## B. Dynamic Methods

While static Monte Carlo methods generate a sequence of statistically independent configurations, dynamic MC methods are always based on some stochastic Markov process, where subsequent configurations  $\mathbf{X}$  of the system are generated from the previous configuration  $\{\mathbf{X} \rightarrow \mathbf{X}' \rightarrow \mathbf{X}'' \rightarrow \dots\}$  with some transition probability  $W(\mathbf{X} \rightarrow \mathbf{X}')$ . Since to a large extent the choice of the basic move  $\mathbf{X} \rightarrow \mathbf{X}'$  is arbitrary, various methods differ in the choice of the basic "unit of motion". Also, the choice of transition probability  $W(\mathbf{X} \rightarrow \mathbf{X}')$  is not unique: the only requirement is that the principle

of detailed balance with the equilibrium distribution  $P_{\text{eq}}(\mathbf{X})$  should be observed

$$P_{\text{eq}}(\mathbf{X})W(\mathbf{X} \rightarrow \mathbf{X}') = P_{\text{eq}}(\mathbf{X}')W(\mathbf{X}' \rightarrow \mathbf{X}) \quad (6)$$

This means that the probability of selecting a motion  $\mathbf{X} \rightarrow \mathbf{X}'$  must be the same as the probability for the inverse motion,  $\mathbf{X}' \rightarrow \mathbf{X}$ . One has to be very careful to preserve this symmetry in the actual realization of the algorithm, in particular if one has a choice between several types of move.

If there is an additional energy  $\mathcal{H}(\mathbf{X})$  in the problem depending on the configuration  $\mathbf{X}$ , the equilibrium distribution  $P_{\text{eq}}(\mathbf{X}) = (1/Z) \exp[-\mathcal{H}(\mathbf{X})/k_{\text{B}}T]$ , the condition of Eq. (6), leads to a requirement  $\delta\mathcal{H} \equiv \mathcal{H}(\mathbf{X}') - \mathcal{H}(\mathbf{X}) = \text{energy change due to the move}$

$$\frac{W(\mathbf{X} \rightarrow \mathbf{X}')}{W(\mathbf{X}' \rightarrow \mathbf{X})} = \exp[-\delta\mathcal{H}/k_{\text{B}}T] \quad (7)$$

Following Metropolis et al. [57], an attempted move is then accepted if a random number, uniformly distributed between zero and one, is less than  $\exp[-\delta\mathcal{H}/k_{\text{B}}T]$  where  $\delta\mathcal{H} > 0$ , or simply accepted if  $\delta\mathcal{H} < 0$  whereby Eq. (7) is automatically fulfilled. Then the configurations generated in this way are distributed proportionally to the equilibrium distribution  $P_{\text{eq}}(\mathbf{X})$ , provided there is no problem with the *ergodicity* of the algorithm, and the canonical average of any observable is obtained as a simple arithmetic average over the generated configurations. One should keep in mind, however, that the latter does not hold for subsequent configurations which are correlated with each other. Measurements should be performed at intervals comparable to the typical relaxation time of the system. Thus for a simple random walk chain (with no excluded volume interactions) the Rouse model [37] implies that the single chain relaxation time  $\tau_N \propto N^2$ , which indicates the difficulties encountered when sampling of sufficiently long chains is attempted.

One of the most efficient dynamic methods for studying static properties is given by the *pivot* algorithm [58]. In this approach a point of the chain is chosen at random and then one part of the chain is rotated at random. The acceptance rate is then given by the probability that the new configuration has no overlaps. This requires a simple check on a lattice whereas in continuous space the problem is a little more complex. Unfortunately, the efficiency of the pivot algorithm decreases drastically with growing solution density, and even for single chains in confinement existing geometry constraints hamper its implementation.

For semi-dilute and dense solutions the generalized *reptation* (or, “slithering snake”) algorithm [59] is probably among the most efficient ones. In this method one takes at random an end monomer and tries to add it at the other

chain end in a random direction. If the new chain fulfills the SAW condition, the move is accepted, otherwise rejected. In order to overcome some problems with ergodicity,\* however, a combination with *kink-jump* algorithms is recommended [54].

Clearly, both the pivot and the “slithering snake” algorithms are incapable of reproducing true chain dynamics at molecular basis, covering the time range of typical chain relaxation times. Therefore, in the following we focus on two alternative methods, broadly used at present to this end.

### 1. Bond Fluctuation Model

The bond fluctuation model (BFM) [60] has proved to be a very efficient computational method for Monte Carlo simulations of linear polymers during the last decade. This is a coarse-grained model of polymer chains, in which an “effective monomer” consists of an elementary cube whose eight sites on a hypothetical cubic lattice are blocked for further occupation. A polymer chain is made of “effective monomers” joined by bonds. A bond corresponds to the end-to-end distance of a group of 3–5 successive chemical bonds and can *fluctuate* in some range. It is represented by vectors  $\mathbf{l}$  of the set  $P(2,0,0)$ ,  $P(2,1,0)$ ,  $P(2,1,1)$ ,  $P(3,0,0)$ , and  $P(3,1,0)$ , which guarantee that intersections of the polymer chain with other chains, or with itself, are virtually impossible. All lengths are here measured in units of the lattice spacing and the symbol  $P$  stands for all permutations and sign combinations (e.g., 108 bonds in 3d) of the Cartesian coordinates  $(l_x, l_y, l_z)$ . Monomer–monomer interactions can extend over certain range in the lattice and the semi-flexibility of the chains may be accounted for by ascribing some additional energy to certain bond angles. The algorithm displays Rouse behavior for all spatial dimensions and combines typical advantages of the lattice MC methods with those of the continuous Brownian dynamics algorithm. Thus one may increase the density of the system up to that of a melt and still keep the system mobile. The adequacy of the BFM algorithm to describe static and dynamic behavior of polymers has been proven in a number of sensitive investigations [41] on conventional polymer systems.

### 2. Off-lattice Bead–Spring Model

Most of the simulational results described in this chapter have been obtained by using a very efficient dynamic MC method [61,27], so below we shall describe it in more detail. As mentioned earlier, one is not aiming at the explanation of the properties of particular polymers (such as

---

\* E.g., if both ends of the chain are rolled-in like a spiral there is no way out of this situation through reptation.

polyethylene, polypropylene, polycarbonate, etc.), but is rather anxious to contribute to the general understanding of universal properties of flexible polymers. Thus, similar to the BFL model, this is a model of coarse-grained chain macromolecules where coarse-grained monomers are connected by coarse-grained bonds (each bond representing at least  $n \approx 3-6$  chemical bonds along the backbone of a polymer chain). Each coarse-grained bond is described by the so-called FENE (finitely extensible non-linear elastic) potential

$$\left. \begin{aligned} U_{\text{FENE}}(r) &= -\frac{k}{2} R^2 \log [1 - (r/R)^2], \quad \text{for} \quad -R < r - l_0 < R \\ U_{\text{FENE}}(r) &= \infty, \quad \text{otherwise} \end{aligned} \right\} \quad (8)$$

where  $r$  is the distance between two successive beads,  $l_0 = 0.7$  is the unperturbed bond length, the maximal bond extension  $R = l_{\max} - l_0 = 0.3$ , and the elastic constant  $k/2 = 20$  (in our units of energy  $k_B T = 1.0$ ). The FENE potential behaves as a harmonic potential for  $r - l_0 \ll R$ , that is,  $U_{\text{FENE}}(r \approx l_0) \approx -(k/2)(r - l_0)^2$  but diverges logarithmically both for  $r \rightarrow l_{\max}$  and  $r \rightarrow l_{\min} = 2l_0 - l_{\max}$ . We choose our unit of length such that  $l_{\max} = 1$ , and then  $l_{\min} = 0.4$ .

The non-bonded interaction is described by the Morse potential

$$U_{\text{M}}(r) = \epsilon_{\text{M}} \{ \exp [-2a(r - r_{\min})] - 2 \exp [-a(r - r_{\min})] \},$$

$$\text{for } 0 < r - r_{\min} < \infty \quad (9)$$

where  $r_{\min} = 0.8$ ,  $\epsilon_{\text{M}} = 1$ , and the large value of  $a = 24$  makes interactions vanish at distances larger than unity, so that an efficient *link-cell* algorithm [61] for short-range interactions can be implemented. Choosing  $\epsilon_{\text{M}} = 1$  (and units of temperature such that  $k_B = 1$ ), it has been established that the theta temperature for this model occurs at [27]  $\Theta \approx 0.62$  so that at temperature  $T = 1$ , for instance, the system is in the good solvent regime.

The radius of the beads and the interactions, Eqs. (8,9), have been chosen such that the chains may not intersect themselves or each other in the course of their movement within the box. Thus entanglement constraints are obeyed automatically and need not be enforced by extra (time consuming!) control. The chains are treated as fully flexible and a potential for bond angles is not considered, although an extension of the model to allow for semi-flexibility of the chains is straightforward.

A standard Metropolis algorithm is used, whereby an attempted move of a randomly selected particle in a random direction  $\Delta x \in [-1/2, 1/2]$ ,  $\Delta y \in [-1/2, 1/2]$ ,  $\Delta z \in [-1/2, 1/2]$  is accepted according to the standard Metropolis procedure [57] described above. The above displacement widths ensure a reasonably high acceptance rate  $A$  of the moves, of the order of

20%, and even for dense melts at  $T > \Theta$  one has  $A > 5\%$ , and the rate of approach to equilibrium is still reasonable.

As an adsorption geometry one considers a semi-infinite system with an impenetrable wall at  $z = 0$ , such that monomer positions are restricted to the positive half-space  $z > 0$ . At the wall acts a short-range attractive potential, either as a square well

$$U_W(z) = \epsilon, z < \delta; \quad U_W(z) = 0, z > \delta \quad (10)$$

or as a Morse potential again

$$U_W(z) = \epsilon[\exp(-2\alpha z) - 2\exp(-\alpha z)] \quad (11)$$

Using potentials as simple as in Eqs. (10,11), the model is nevertheless useful to elucidate the qualitative features of polymer adsorption. As an example, Fig. 2 presents snapshot pictures of a polymer solution confined between two walls [16]. Fig. 2(a) shows a standard confined melt, similar to that described in Refs. 25,67. In Fig. 2(b) the polymer solution has a high density region in the center of the film with a strong reduction of density near the walls (i.e., precursor of drying layers). In contrast, Fig. 2(c) shows a semi-dilute solution in the center with adsorbed surface layers of high density. In Fig. 2(d) the solution in the bulk would decompose in a dilute solution of collapsed chains coexisting with a concentrated solution (or melt). In the presence of walls, however, all the chains are strongly adsorbed, and apart from a few bridging chains (adsorbed with one end at one wall and the other end at the opposite wall) the central region of the film is free of monomers. From these snapshots it should be clear that the model indeed encompasses the physics alluded to in the Introduction—cf. Fig. 1—by suitably tuning the parameters  $T$  and  $\epsilon/k_B T$ . It is even likely [62] that for high densities and low temperatures glassy phases occur, but these are very hard to simulate with such off-lattice models because the acceptance rate of the attempted moves becomes too low.

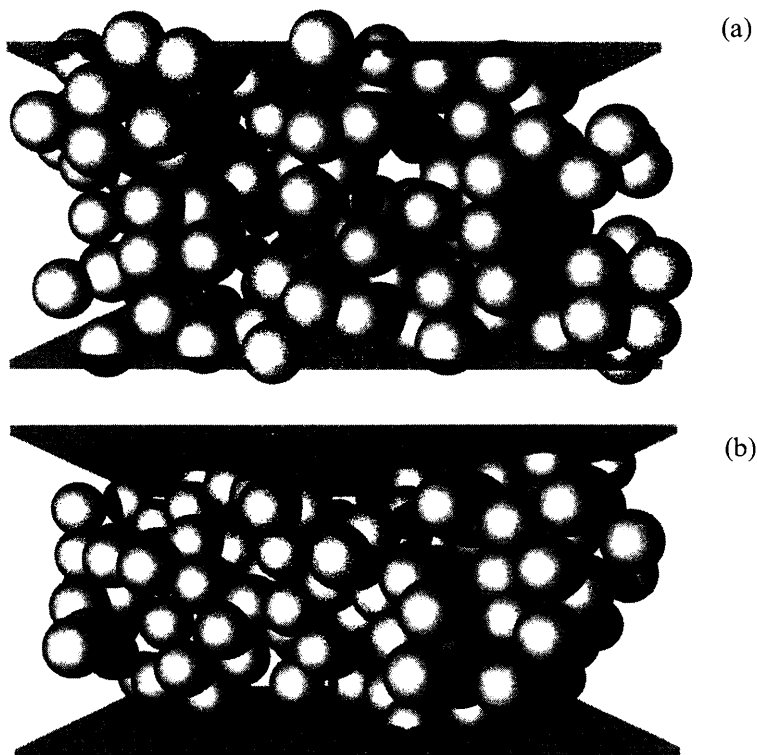
While all aforementioned features of this off-lattice model hardly distinguish it among other off-lattice bead models [63–69]\*, the high efficiency in code performance here is achieved by extensive implementation of integer arithmetic using predominantly bitwise operations with variables. To this end an extremely fine grid of  $2^{16} = 65\,536$  discrete points along each dimension of the container is employed,† whereas the container box size must be

\* As a rule, though, these MC models deal instead with hard bonds between the nearest neighbor monomers in a chain.

† Note that even in a big box of  $64 \times 64 \times 64$  a single cell will thus contain 1024 discrete positions along each side, i.e., the difference between discrete and continuous description almost disappears.

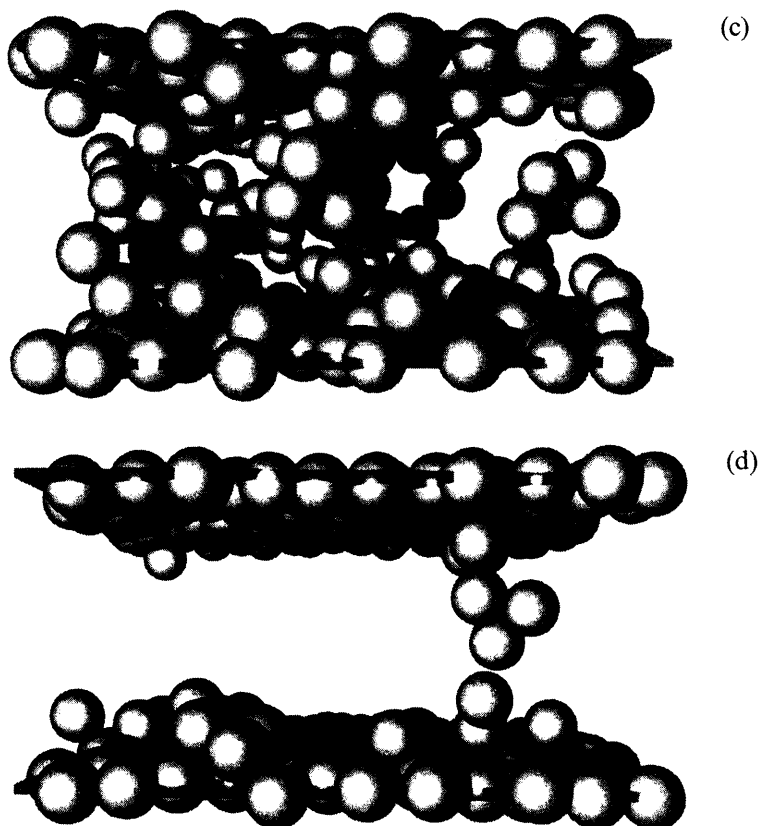
some power of 2, e.g., 8, 16, 32, etc. All coordinates of the particles can then be expressed as *long integers* in the notation of C-language so that, as a consequence, two major advantages are achieved:

- i. the most heavily involved modulo operations which provide periodicity of coordinates are reduced to a single use of the &-operator (bitwise *AND*), and
- ii. the minimum image condition for taking distances between interacting particles is accomplished simply by *type conversion* (or *casting*) of all



**FIG. 2** Snapshot pictures of chains of length  $N = 16$  at a monomer density  $\phi = 1$  in a box of size  $8 \times 8 \times 4$  (i.e., a film of width  $D = 4$ ), for a temperature  $T = 1$  (a, c) above the Theta temperature ( $\theta \approx 0.62$ ), and for a temperature  $T = 0.5$  (below  $\theta$ ) (b, d). Cases (a, b) refer to purely repulsive walls ( $\epsilon = 0$ ) whereas cases (c, d) refer to strongly attractive walls [ $\epsilon/k_B T = -4$  (c)  $-8$  (d)], respectively. Each monomer is represented by a sphere of radius 0.4; walls at  $z = 0$  and  $z = D$  are also shown as shaded planes, effective bonds are not shown [16].



**FIG. 2** Continued.

variables, standing for the coordinates, from *long* into *short* integers, which is probably one of the fastest computational operations.

In order to illustrate these ideas, consider the simplest case of a  $1d$  box containing only  $L = 2^3 = 8$  cells (in “C” numeration starts always with 0) and with periodic boundary conditions:

-4	-3	-2	-1	0	1	2	3	4	5	6	7	8	9	10	11
----	----	----	----	---	---	---	---	---	---	---	---	---	---	----	----

Using binary notation for the coordinates of a given particle, and the definition of the &-operator action on single bits:  $0 \& 0 = 0$ ,  $0 \& 1 = 0$ ,  $1 \& 0 = 0$ ,  $1 \& 1 = 1$ , we demonstrate below that by masking off some sets of bits (i.e.,

setting them to zero) the particle which jumps, say, to cell 9 through the right border of the box automatically lands into its periodic position, that is, in cell 1 (the mask is always equal to  $L - 1$ ):

	sign	$2^{14}$	$2^{13}$	$2^{12}$	$2^{11}$	$2^{10}$	$2^9$	$2^8$	$2^7$	$2^6$	$2^5$	$2^4$	$2^3$	$2^2$	$2^1$	$1^0$
9 =	0	0	0	0	0	0	0	0	0	0	0	0	1	0	0	1
&7 =	0	0	0	0	0	0	0	0	0	0	0	0	0	1	1	1
1 =	0	0	0	0	0	0	0	0	0	0	0	0	0	0	0	1

If the particle leaves the box through the left border, jumping to cell  $-2$ , for instance, then again applying the bitwise *AND* between new coordinate and mask (the mask is given simply by the number of the last cell in the box, 7 in this example) yields the correct new periodic position, i.e., in cell 6.

	sign	$2^{14}$	$2^{13}$	$2^{12}$	$2^{11}$	$2^{10}$	$2^9$	$2^8$	$2^7$	$2^6$	$2^5$	$2^4$	$2^3$	$2^2$	$2^1$	$1^0$
-2 =	1	1	1	1	1	1	1	1	1	1	1	1	1	1	1	0
&7 =	0	0	0	0	0	0	0	0	0	0	0	0	0	1	1	1
6 =	0	0	0	0	0	0	0	0	0	0	0	0	0	1	1	0

The *minimum image* condition in calculating distances is realized by the function **dist2**( $x, y, z$ ) which reads *long* integers as *short*, and then returns the squared distance  $r^2$  as a *long* integer again:

```

unsigned long dist2(x, y, z)
short x, y, z;
{
    unsigned long r;
    r = (long) x * x;
    r += (long) y * y;
    r += (long) z * z;
    return(r);
}

```

Then for the distance  $r = \sqrt{x^2 + y^2 + z^2}$  between any two particles it can be checked that it is the shortest distance allowing for the periodic boundary conditions.

Other binary operations like the  $|$ -operator (bitwise inclusive *OR*), and the right and left shift,  $\gg$  and  $\ll$ , can be used to great effect too, e.g., for recovering the numbers of all neighbor cells to that containing the central particle, but we shall not go into further detail here.

### 3. Molecular Dynamics

Concluding this section, one should mention also the method of molecular dynamics (MD) in which one employs again a bead-spring model [33,70,71] of a polymer chain where each monomer is coupled to a heat bath. Monomers which are connected along the backbone of a chain interact via Eq. (8) whereas non-bonded monomers are assumed usually to exert Lennard-Jones forces on each other. Then the time evolution of the system is obtained by integrating numerically the equation of motion for each monomer  $i$

$$m \frac{d^2 \vec{r}_i}{dt^2} = -\nabla U_i - \Gamma \frac{d\vec{r}_i}{dt} + \eta_i(t) \quad (12)$$

where  $U_i$  denotes the total potential acting on a monomer with mass  $m$ ,  $\Gamma$  is the bead friction which acts to couple the monomer to the heat bath, and  $\eta_i(t)$  describes the random force acting on each bead. It can be considered as a Gaussian white noise with

$$\langle \eta_i(t) \eta_j(t') \rangle = \delta_{ij} \delta(t - t') 6k_B T \Gamma \quad (13)$$

MD runs for polymers typically exceed the stability limits of a micro-canonical simulation, so using the fluctuation-dissipation theorem one can define a canonical ensemble and stabilize the runs. For the noise term one can use equally distributed random numbers which have the mean value and the second moment required by Eq. (13). In most cases the equations of motion are then solved using a third- or fifth-order predictor-corrector or Verlet's algorithms.

## III. ADSORPTION OF SINGLE POLYMER CHAINS AT SURFACES

While the static aspects of the adsorption of single chains at walls have been studied for a long time [2], the dynamic properties of adsorbed polymers have received much less attention [30–32]. Most work considers the kinetics of either adsorption or desorption of polymers at a solid surface [31], or the

collective dynamics of an adsorbed layer of many chains [30], while the dynamics of adsorbed single chains is considered only occasionally [33,34]. We focus here on the behavior of single chains, in the situation where the wall is exposed to a dilute polymer solution in the good solvent case [13]. We study *weakly* adsorbed chains,\* where the fraction of “trains” [4] (sequences of adsorbed monomers attached to the wall) is still small enough so that the fraction of monomers in “loops” and “tails” is still large and the concentration near the wall is at most semi-dilute (Fig. 3).

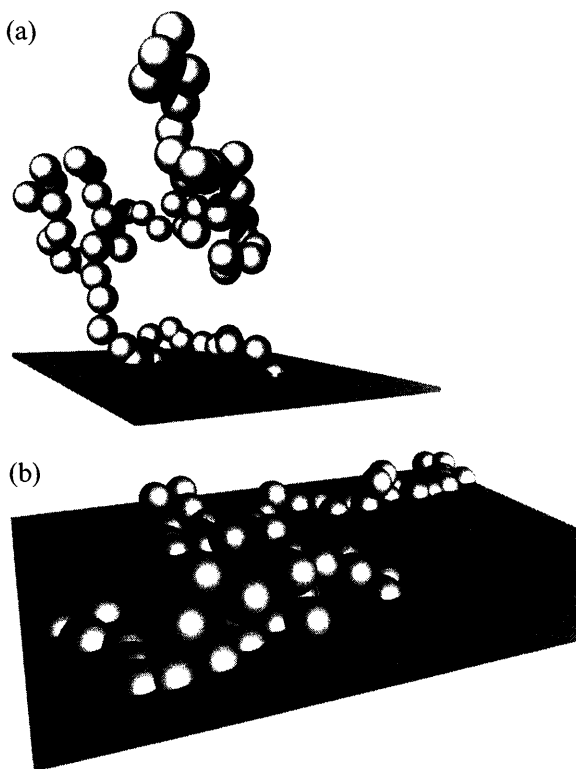


**FIG. 3** Snapshot picture of a bead-spring chain containing  $N = 64$  monomers at  $\epsilon/k_B T = -2.5$  (a, top) and at  $\epsilon/k_B T = -3.0$  (b, bottom). The adsorbing plane  $z = 0$  is shown shaded: there is no repulsion between monomers and wall as long as  $z > 0$ , while no monomers can cross the plane since  $U_W(z < 0) = \infty$  [13].

\* “Weakly” adsorbed does not mean that the adsorption energy  $|\epsilon|$  is small in comparison to  $k_B T$ , since entropic effects are important; rather, it means  $|\epsilon - \epsilon_c| \ll |\epsilon_c|$ ,  $|\epsilon_c|$  being the adsorption energy at the threshold [2].

We use the off-lattice MC model described in Sec. II B 2 with a square-well attractive potential at the wall, Eq. (10), and try to clarify the dynamic properties of the chains in this regime as a function of chain length and the strength of wall-monomer interaction.

In order to get an overview of where the adsorption transition occurs, it is convenient to study the density profile  $n(z)$  as a function of the strength  $|\epsilon|$  of the adsorption potential (Fig. 4). In the non-adsorbed case ( $|\epsilon|/k_B T < |\epsilon_c|/k_B T$ ) the density has a mild maximum near  $z \approx 0.7$ , reflecting the formation of a second layer, while for  $z \gg 1$  it develops to a flat plateau at the value of the bulk solution density. However, when the chain gets adsorbed ( $|\epsilon|/k_B T > |\epsilon_c|/k_B T$ ), the peak at  $z \approx 0.7$  (due to nonadsorbed monomers which are nearest neighbors of adsorbed monomers) grows considerably whereas  $n(z)$  decays essentially to zero for large  $z$ . Further increase of  $|\epsilon|/k_B T$  (the strongly adsorbed case) renders more and more monomers to become part of "trains", rather than being part of "loops" or "tails". Thus the second peak decreases again while  $n(z)$  for

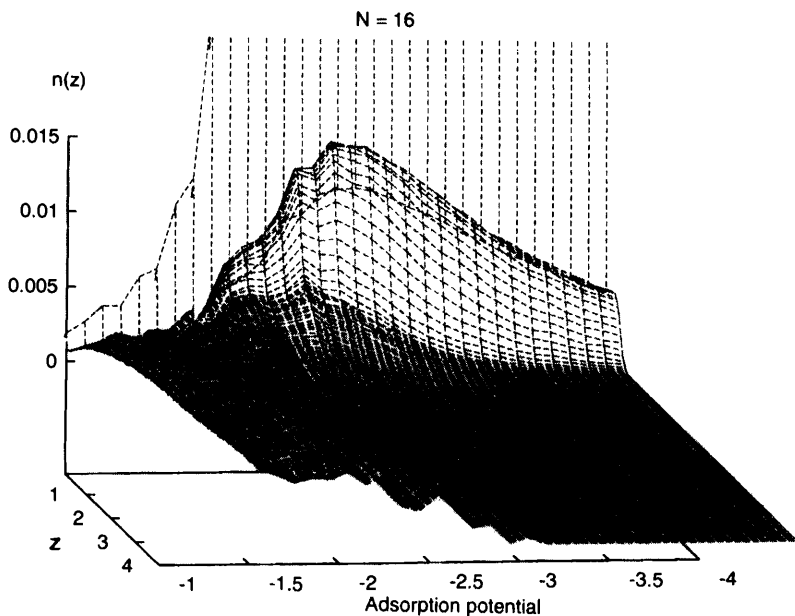


**FIG. 4** Density  $n(z)$  plotted as a function of distance  $z$  from the adsorbing wall and of adsorption strength  $\epsilon/k_B T$  for chain length  $N = 16$ . Vertical dotted lines denote the density of the monomers sticking immediately at the wall: for  $\epsilon/k_B T \geq 2.0$  this density changes dramatically [13].

$z \geq 1$  is essentially zero. This qualitative picture is in full accord with standard theoretical concepts of this problem [2,4,5].

The transition shows up in many other characteristics: the fraction  $f_a$  of adsorbed monomers (Fig. 5(a)), and the average orientation of bonds,

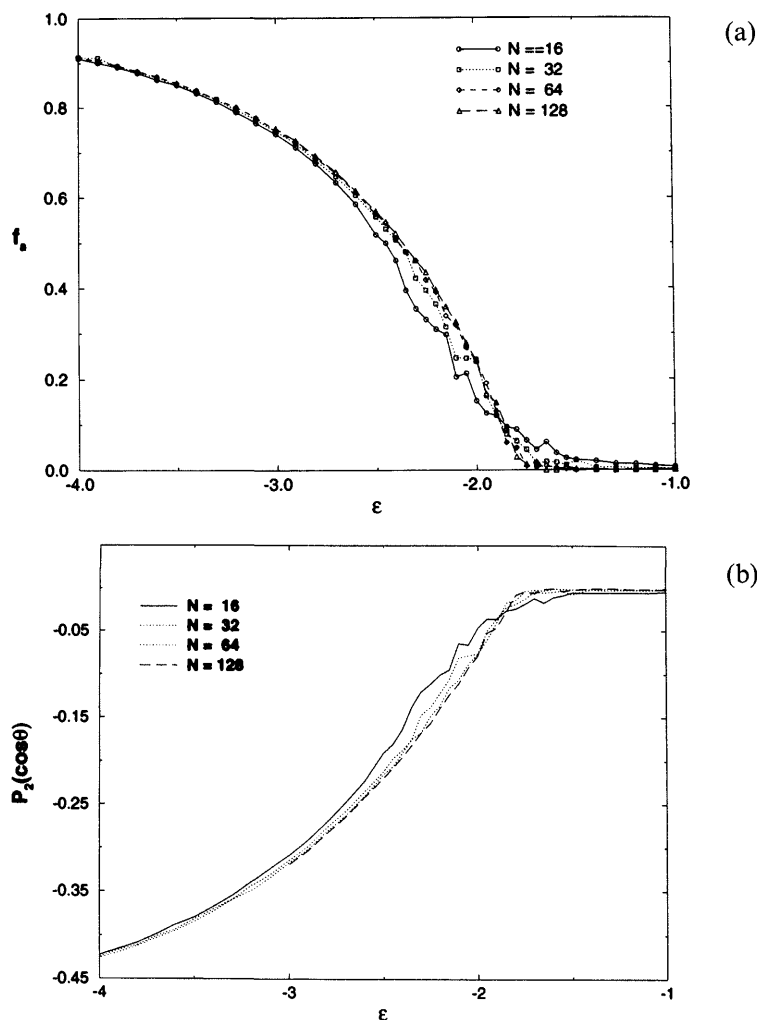


**FIG. 5** (a) Fraction of adsorbed monomers (i.e., those with  $z$ -coordinate less than  $\delta$ ) vs  $\epsilon/k_B T$  for four different chain lengths. (b) The same for the second Legendre polynomial  $P_2(\cos \theta)$ . (c) Scaling plot of  $f_a$  and  $P_2(\cos \theta)$  vs distance from the adsorption threshold, using  $\epsilon_c = -1.9$  [13].

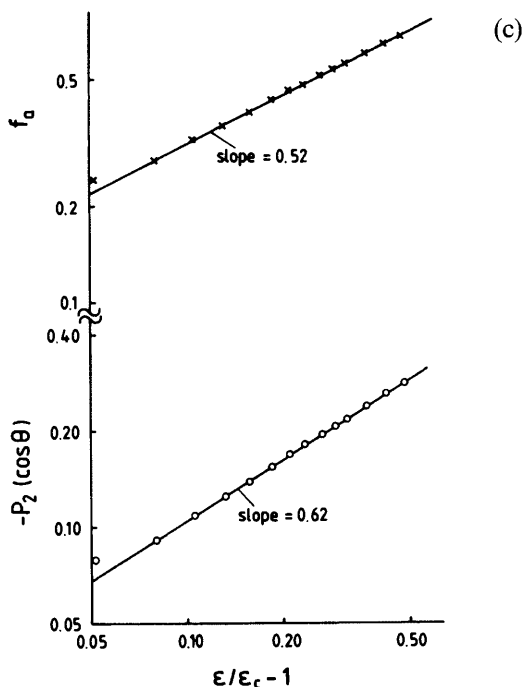


FIG. 5 Continued.

measured by the second Legendre polynomial  $P_2(\cos\theta) = \frac{1}{2}(3\langle\cos^2\theta\rangle - 1)$ , where  $\theta$  measures the angle between an effective bond and the  $z$ -axis. Since  $P_2(\cos\theta) = 1$  if all bonds were oriented perpendicular to the surface,  $P_2(\cos\theta) = -\frac{1}{2}$  if they are parallel to the surface, and  $P_2(\cos\theta) = 0$  for random orientation, the behavior seen in Fig. 5(b) is clear. Thus either  $f_a$  or  $P_2(\cos\theta)$  behaves like an “order parameter” of the adsorption transition, and one can conclude from Figs. 5(a,b) that in our model this transition occurs at  $\epsilon_c = -1.90 \pm 0.05$  (remember, units are chosen everywhere such that  $k_B T = 1$ ).

According to the scaling theory of the adsorption transition [2,35], one expects for  $\epsilon$  near  $\epsilon_c$  in the limit  $N \rightarrow \infty$  a power law behavior

$$f_a \propto -P_2(\cos\theta) \propto \left(\frac{\epsilon}{\epsilon_c} - 1\right)^{1/\varphi-1}, \quad \epsilon \rightarrow \epsilon_c \quad (14)$$

where the so-called crossover exponent  $\varphi$  has been estimated by early MC work [35] as  $\varphi \approx 0.58$ , while second-order renormalization group

expansions [36] yield  $\varphi \approx 0.62$ . Fig. 5(c) demonstrates that our data is roughly compatible with the expected behavior, although as a matter of fact one measures here only effective exponents, and significantly longer chains than  $N = 128$  are needed to be well within the asymptotic regime near  $|\epsilon_c|$ .

The adsorption transition also shows up in the behavior of the chain linear dimension. Fig. 6(a) shows the mean-square gyration radii parallel,  $R_{g\parallel}^2$ , and perpendicular,  $R_{g\perp}^2$ , to the adsorbing plate. While these components do not differ from each other for  $|\epsilon| \ll |\epsilon_c|$ , for  $|\epsilon| \geq |\epsilon_c|$   $R_{g\parallel}^2$  strongly increases whereas  $R_{g\perp}^2$  decreases. In the first case (non-adsorbed chain)  $R_{g\parallel}^2 \propto R_{g\perp}^2 \propto N^{2\nu}$  as a dilute solution in a good solvent in the bulk. For adsorbed chains  $R_{g\perp}^2/N^{2\nu} \rightarrow 0$  for  $N \rightarrow \infty$  because the thickness is finite; it is controlled by the distance  $|\epsilon - \epsilon_c|$  from the adsorption threshold, but does not diverge as  $N \rightarrow \infty$ . The adsorbed chain follows in fact a

**N = 32**

(a)

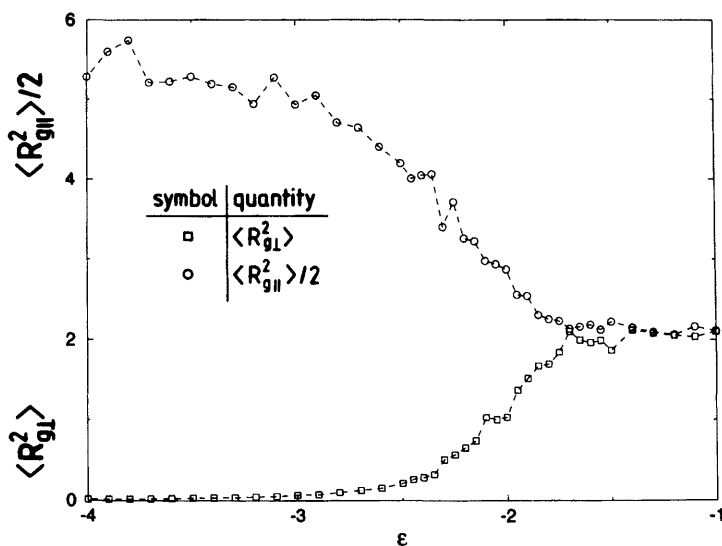


**FIG. 6** (a) Parallel  $R_{g\parallel}^2$  and perpendicular  $R_{g\perp}^2$  components plotted vs  $\epsilon$  for  $N = 32$ . (b) Crossover scaling description of  $R_{g\parallel}^2$  and  $R_{g\perp}^2$  (c) vs the crossover scaling variable  $|\Delta|N^\varphi$ , where  $\Delta \equiv \epsilon/\epsilon_c - 1$  for different chain lengths. The flat branch of each curve refers to  $|\epsilon| < |\epsilon_c|$  while the other branch refers to  $|\epsilon| > |\epsilon_c|$ . Ideally, the slopes of the latter branches should yield the theoretical exponents expected for large  $|\Delta|N^\varphi$ ,  $2(\nu_2 - \nu)/\varphi \approx 0.55$ , and  $-2\nu/\varphi \approx -2.03$ , respectively [13].



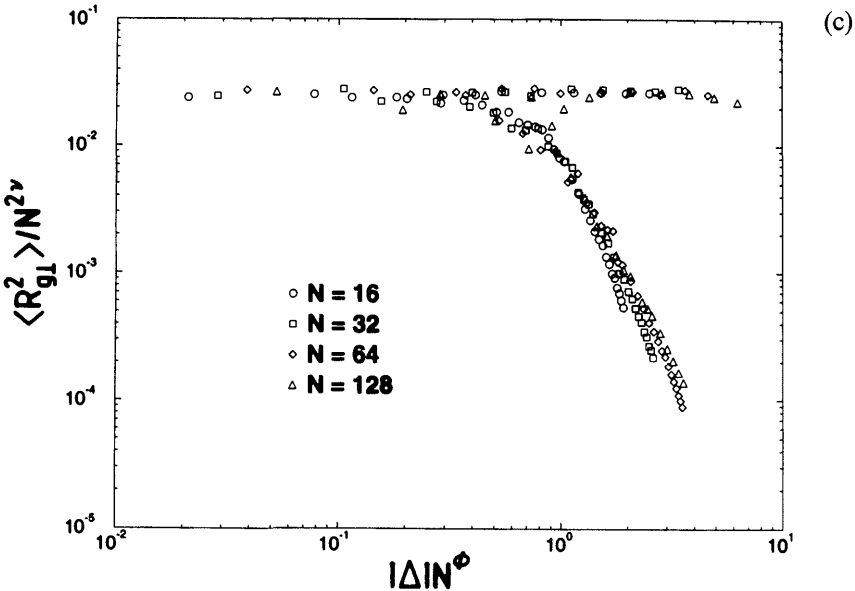
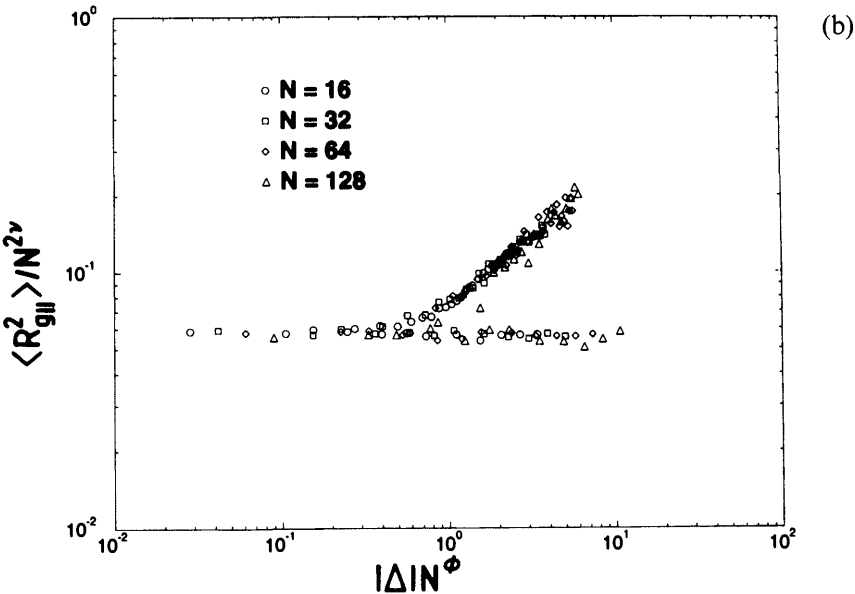


FIG. 6 Continued.

two-dimensional SAW statistics with an exponent  $\nu_2 = 3/4$ , so that  $R_{g\parallel}^2 \propto N^{2\nu_2}$  for  $|\epsilon| \geq |\epsilon_c|$  (Fig. 6 (b,c)).

Before turning to dynamics, we should like to point out that, because no solvent is explicitly included, the Rouse model [37,38] (rather than the Zimm model [39]) results in the dilute limit, as there is no hydrodynamic interaction. The rate of reorientation of monomers per unit time is  $\mathcal{W}$ , and the relaxation time of a chain scales as [26,38]

$$\tau_N \approx \mathcal{W}^{-1} N^Z, \quad Z = 2\nu + 1 \approx 2.18 \quad (15)$$

omitting prefactors of order of unity, assuming good solvents and taking for  $\nu$  the exponent for the 3d SAW,  $\nu_3 \approx 0.59$  [26]. If monomeric reorientations add up randomly, and neglecting correlations, the mean-square displacement of the center of mass is

$$g_3(t) = \langle [\vec{r}_{\text{cm}}(t) - \vec{r}_{\text{cm}}(0)]^2 \rangle \propto \mathcal{W} \left\langle \left( \frac{l}{N} \right)^2 \right\rangle Nt = \mathcal{W} \frac{\langle l^2 \rangle}{N} t \quad (16)$$

because each monomeric motion moves the center of mass by a random displacement of order  $l/N$ ,  $l$  being the bond length. There are  $\mathcal{W}N$  such random motions per unit time. Invoking the Einstein relation  $g_3(t) = 2dD_N t$ , one thus concludes

$$D_N \propto \mathcal{W} \frac{\langle l^2 \rangle}{N} \quad (17)$$

The relaxation time in Eq. (15) and the scaling law  $Z = 2\nu + 1$  for the dynamic critical exponent  $Z$  are then understood by the condition that the coil is relaxed when its center of mass has diffused over its own size  $R_g^2$

$$g_3(\tau_N) \propto \mathcal{W} \frac{\langle l^2 \rangle}{N} \tau_N \propto \langle l^2 \rangle N^{Z-1} \propto R_g^2 \propto \langle l^2 \rangle N^{2\nu} \quad (18)$$

whence Eq. (15) follows. These arguments can be carried over to the mean-square displacement of the inner monomers of the chain as well. We define

$$g_1(t) = \langle [\vec{r}_i(t) - \vec{r}_i(0)]^2 \rangle \propto \langle l^2 \rangle (\mathcal{W}t)^{X_1}, \quad t < \tau_N \quad (19)$$

where we anticipate that the inner monomers exhibit anomalous diffusion, i.e., an exponent  $X_1 < 1$ . For short times  $\mathcal{W}t \leq 1$ , of course, we expect a free diffusion of the single monomer, and thus  $g_1(t)$  for  $\mathcal{W}t \approx 1$  should be of the order of  $\langle l^2 \rangle$ . Requiring now that  $g_1(\tau_N) \approx R_g^2$ , we get a scaling relation

for  $X_1$  [40]

$$g_1(\tau_N) \propto \langle l^2 \rangle (\mathcal{W}\tau_N)^{X_1} \propto \langle l^2 \rangle N^{ZX_1} \propto \frac{\langle l^2 \rangle}{N^{2\nu}} \quad (20)$$

$$X_1 = \frac{2\nu}{Z} = \frac{1}{1 + \frac{1}{2\nu}} \quad (21)$$

For good solvents  $X_1 \approx 0.54$ , whereas for  $\theta$ -solvents ( $\nu = 1/2$ ) [26] one recovers the standard Rouse results

$$Z = 2, \quad X_1 = \frac{1}{2} \quad (\text{Gaussian chains}) \quad (22)$$

Actually, it is also useful to introduce the mean-square displacement of inner monomers measured in the center of mass coordinate system of the chain

$$q_2(t) = \langle [\vec{r}_i(t) - \vec{r}_{\text{cm}}(t) - \vec{r}_i(0) + \vec{r}_{\text{cm}}(0)]^2 \rangle \quad (23)$$

For long chains,  $g_2(t) \approx g_1(t)$  for  $t \ll \tau_N$ , whereas  $g_2(t) \propto R_g^2$  for  $t \gg \tau_N$  (inner monomers cannot travel further from the center of mass than the coil size, of course).

If the dynamics of a strongly adsorbed chain can be described by a two-dimensional Rouse model, with a smaller value of  $\mathcal{W}$  (reflecting the decrease of the acceptance rate of the moves), and using the  $2d$  value  $\nu_2 = 3/4$ , from Eqs. (15–21) one predicts

$$Z = 2\nu_2 + 1 = 5/2, \quad X_1 = \frac{1}{1 + \frac{1}{2\nu_2}} = 3/5 \quad (24)$$

These concepts are tested in Fig. 7(a,b) where one can see that both in the non-adsorbed case (Fig. 7(a)) and in the adsorbed case (Fig. 7(b)) the data is compatible with normal diffusion of the parallel (longitudinal) component,  $g_{3l}(t) = 4D_N t$ . For  $\epsilon = -1.5$ , the chains are freely diffusing in the  $3d$  bulk, far away from the adsorbing wall,  $g_{3l} = 2D_N t$ . For  $\epsilon = -3$  most monomers are bound in positions  $z < \delta = 1/8$  and the transversal mean-square displacement  $g_{3t}(t)$  saturates at early times (not shown here) at a value  $\approx (\delta/2)^2$ .

In order to extract characteristic relaxation times one may apply crossing criteria [41], e.g., in Fig. 7 one looks for intersection points of curves and defines the abscissa of such an intersection as a characteristic time. One is mostly interested in characteristic times for longitudinal motion parallel to the adsorbing wall and may define two times:

$$g_{3l}(\tau_3^l) = \frac{2}{3} R_{gl}^2, \quad g_{2l}(\tau_{23}^l) = g_{3l}(\tau_{23}^l) \quad (25)$$

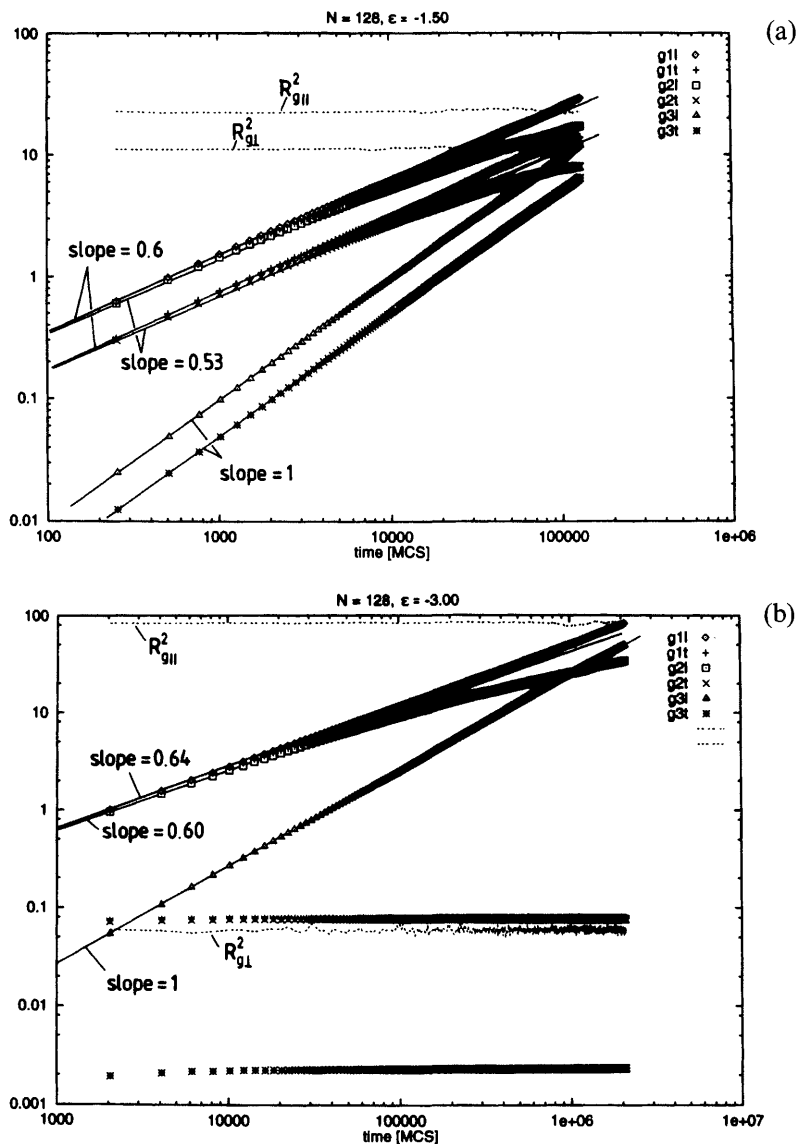


**FIG. 7** Log-log plot of mean-square displacements  $g_{1l}(t)$ ,  $g_{1t}(t)$ ,  $g_{2l}(t)$ ,  $g_{2t}(t)$ ,  $g_{3l}(t)$ ,  $g_{3t}(t)$  plotted vs time  $t$  for a chain length  $N = 128$ ,  $k_B T = 1$  and two choices of the normalized adsorption energy:  $\epsilon = -1.5$  (a) and  $\epsilon = -3$  (b). Fluctuating broken lines indicate the time averages of the parallel  $R_{g||}^2$  and perpendicular  $R_{g\perp}^2$  components of the mean-square gyration radius. Straight lines indicate power laws with effective exponents as indicated [13].

The first equation expresses a scaling idea as in Eq. (18), introducing the arbitrary factor  $2/3$  instead of unity for numerical convenience—the problem of statistical accuracy becomes easier, and numerical prefactors should not matter in statistical considerations.

Fig. 8 shows that the relaxation times can be represented in terms of power laws  $\tau_{23}^I \propto N^{Z_{\text{eff}}}$ , as suggested in Eqs. (15,24), although the effective value  $Z_{\text{eff}}$  is consistently too large:  $Z_{\text{eff}} \approx 2.33$  (instead of 2.18) in the non-adsorbed case,  $Z_{\text{eff}} \approx 2.63$  (instead of 2.5) in the adsorbed case. It is possible that a larger value for  $Z$  could occur for the adsorption transition  $\epsilon = \epsilon_c$  itself, because the static properties of this transition could be mapped to a *multicritical* point [2,35] and are a special case. If at  $\epsilon = \epsilon_c$  a larger value of  $Z$  occurs, one would expect that for finite chain lengths an enhanced value of the effective exponent  $Z_{\text{eff}}$  is seen in a broad environment of  $\epsilon_c$  due to crossover effects. A related disturbing fact concerns the self-diffusion constant  $D_N$  of the chain parallel to the wall: it does not strictly follow the Rouse model,  $D_N \propto N^{-1}$ , but decays slightly faster with an effective exponent of  $\approx 1.1$ . Of course, it is possible that a crossover to Eq. (17) takes place at large enough  $N$ .

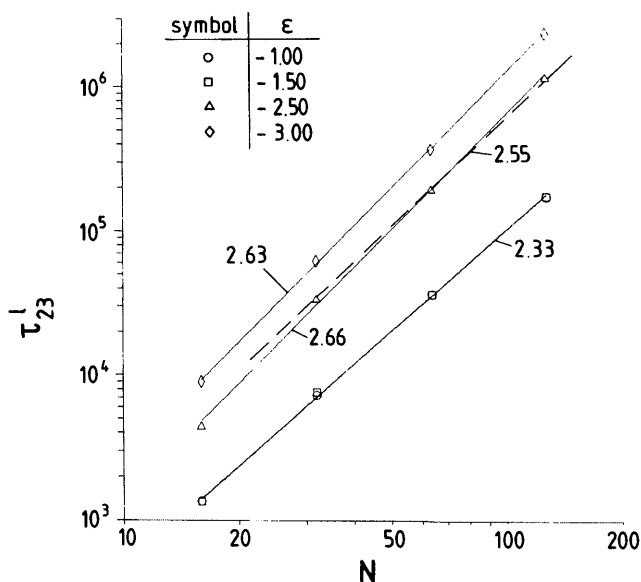


**FIG. 8** Log-log plot of the relaxation time  $\tau_{23}^I$ , Eq. (25), vs chain length  $N$ , for four values of  $\epsilon$ . Full straight lines indicate power-law fits including the shortest chain length  $N = 16$ ; the broken line indicates a fit where  $N = 16$  is excluded. Effective exponents  $Z_{\text{eff}}$  are quoted [13].

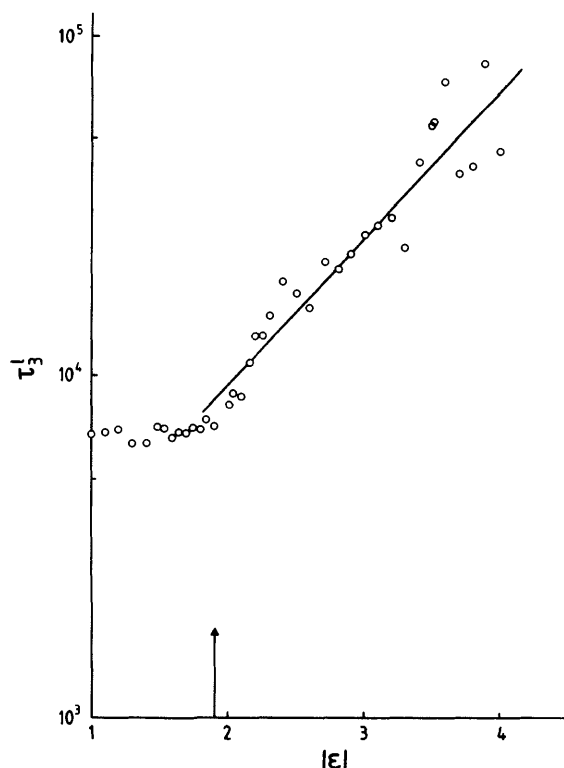


**FIG. 9** Semi-log plot of  $\tau_3^i$  vs  $|\epsilon|$  for chains of length  $N = 32$ ,  $k_B T = 1$ . The straight line indicates a simple Arrhenius-type law; the arrow shows the location of the adsorption transition [13].

In Fig. 9 the relaxation time shows a very smooth variation with  $\epsilon$  (analogously smooth data has been obtained for  $D_N(\epsilon)$ ). In particular, no evidence for a critical anomaly as  $\epsilon \rightarrow \epsilon_c$  is seen. The straight line in Fig. 9 represents a law  $\tau_3^i = \tau_3^i(\epsilon_c) \exp [(\epsilon_c - \epsilon)/k_B T]$ , which indicates a simple thermally activated behavior.

#### IV. SINGLE CHAIN TRAPPED IN A TUBE

The properties of flexible polymer chains moving in porous structures, that is, in structures with geometric constraints such as tubes or slits, apart from their relevance for various applications such as filtration, gel permeation chromatography, oil recovery, etc., pose an exciting problem of statistical

physics since the conformation of the macromolecule in confinement may be severely distorted in comparison with the conformations which the polymer takes in bulk solution. This distortion of the polymer geometry may have two rather different sources: (i) adsorption due to attractive interaction between the monomers and the wall, and (ii) entropic repulsion of random coil from the walls.

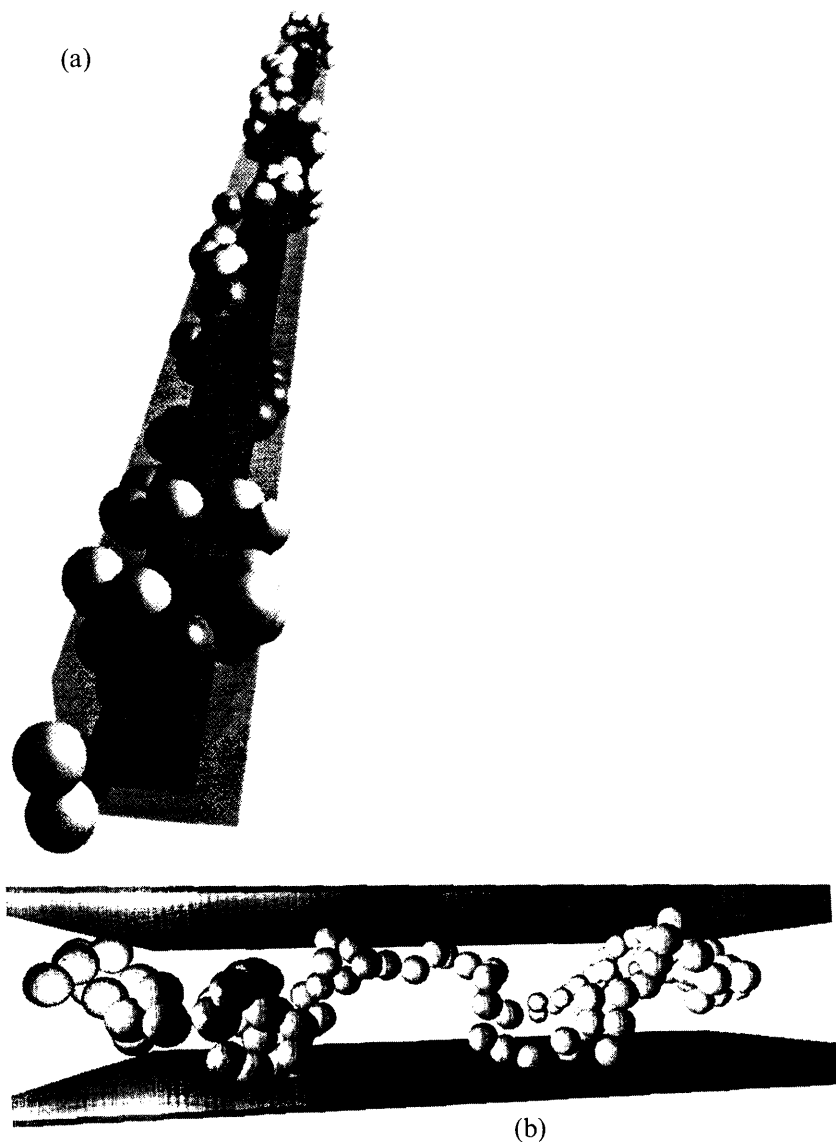
Let us consider briefly the latter for the case of a tube. If the diameter  $D$  of the narrow tube in which the polymer moves is smaller than the average size (or gyration radius  $\sqrt{R_{gb}^2}$ ) of the polymer coil in bulk solution, there is a purely geometric constraining effect due to the excluded-volume interactions between the repeating units of the polymer and the walls of the tube. As a result one expects the random coil in a straight tube to be deformed into a long cigar-shaped object, such that  $R_{g\perp}^2$  is of the order of  $D^2$  and hence fits into the tube, while  $R_{g\parallel}^2$  now is much larger than the bulk radius square  $R_{gb}^2$  (Fig. 10). This structure then can be understood [26,72] as a one-dimensional succession of blobs of size  $D$  containing about  $g$  repeating units of size  $l$ , so that  $D \propto lg^\nu$ . Since there must be  $N/g$  such blobs, the "cigar" length is

$$R_{g\parallel} \propto D \frac{N}{g} \propto D^{1-1/\nu} l^{1/\nu} N \quad (26)$$

The crossover from bulk size,  $R_{gb}^2 \propto N^{2\nu}$ , to Eq. (26) is described by a crossover scaling function  $\mathcal{L}(x)$ , where  $x = lN^\nu/D$ :

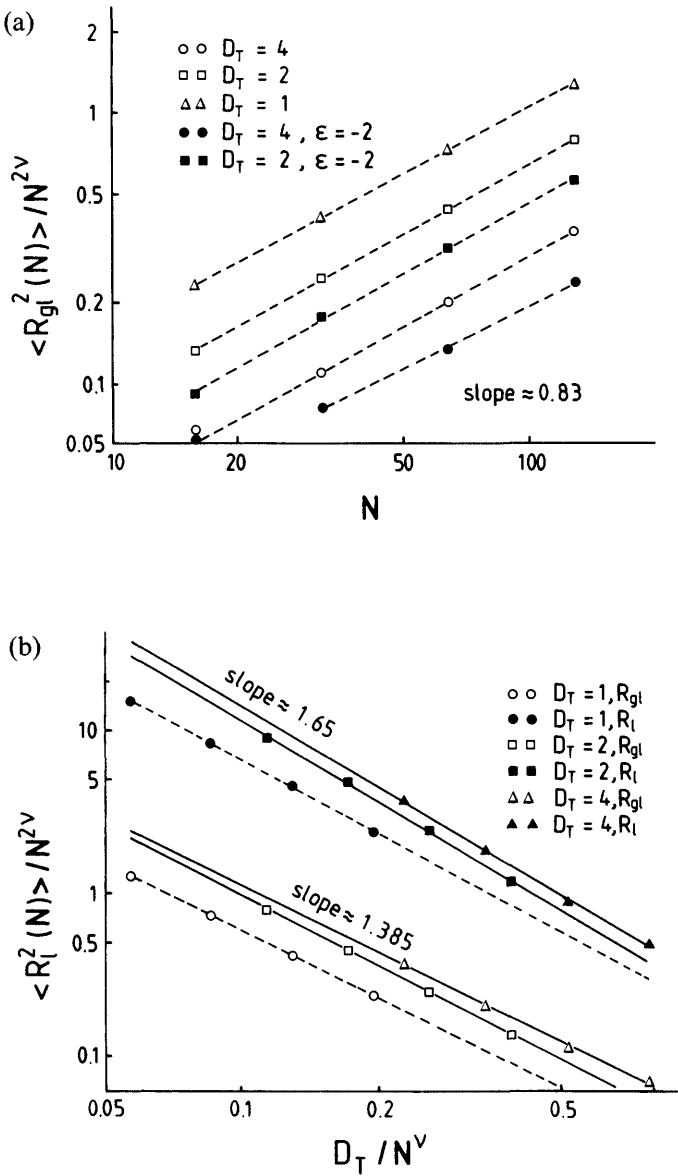
$$R_{g\parallel} = lN^\nu \mathcal{L}\left(\frac{lN^\nu}{D}\right), \quad f(x \rightarrow 0) = \text{const.}, \quad \mathcal{L}(x \gg 1) \propto x^{1/\nu-1} \quad (27)$$

Fig. 11(a) shows a log-log plot of  $R_{g\parallel}^2/N^{2\nu} \propto N^{2(1-\nu)} \approx N^{0.82}$  and, evidently, irrespective of  $D$ , and even for weak attraction  $\epsilon = -2$  at the walls, a very good agreement is found with the theoretical predictions. Thus while the precise value of  $D$  and interaction strength  $\epsilon/k_B T$  affect the prefactor in the relation  $R_{g\parallel} \propto N$ , (Eq. (26)), the exponent of the power law is universal and does not depend on such details of the model (or on details of a real material, of course). However, one cannot push all scaling concepts too far: while Eq. (27) predicts  $R_{g\parallel}^2/N^{2\nu} \approx (lN^\nu/D)^{1.39}$ , it is seen from Fig. 11(b) that the data for  $D = 1, 2, 4$  do not yet scale in this form; in particular, the data points for  $D = 1$  are quite off, but this must be expected since now the tube linear dimension is of the same order as the bond length, and thus scaling must break down. Nevertheless, the exponent predicted in Eq. (27) is already seen for the gyration radius, although for the much more fluctuating end-to-end distance such good agreement is still missing. By using SAW on a lattice [40], rather than the dynamic MC algorithm, good scaling for both quantities has been observed earlier for  $D \geq 10$ .



**FIG. 10** (a) Snapshot picture of a chain with  $N = 128$  monomers confined in a tube with  $D = 2$  for strong wall attraction  $\epsilon/k_B T = -3$  [14]. The inner concentric tube with  $D = 1$  emphasizes that the chain winds itself around along the walls and is thus a guide for the eye—in the actual simulation no inner tube is present. (b) Snapshot picture of the same chain between two repulsive walls [19] at a distance  $D = 4$ . Each bead is represented by a sphere of diameter 0.8; the springs between the beads are not shown.





**FIG. 11** (a) Log-log plot of the longitudinal gyration radius  $R_{gl}^2/N^{2\nu}$  vs  $N$  for several choices of tube diameter  $D_T$  and  $\epsilon/k_B T$  ( $\epsilon/k_B T = 0$  if not otherwise indicated). The four upper dashed straight lines have all the same slope of about 0.83 [14]. (b) Scaling plot of  $R_{gl}^2/N^{2\nu}$  (open symbols) and  $R_l^2/N^{2\nu}$  (full symbols) vs  $D_T/N^\nu$  for  $\epsilon/k_B = 0$ .

The main predictions of the scaling theory [40], concerning the dynamics behavior of polymer chains in tubes, deal with a number of characteristic times: the smallest time  $\tau_{\text{tube}}$  measures the interval of essentially Rouse relaxation before the monomers feel the tube constraints significantly,  $1 \leq \mathcal{W}t \leq \mathcal{W}\tau_{\text{tube}} \equiv (D/l)^{1/(1+1/2\nu)}$ , and diffusion of an inner monomer is anomalous, cf. Eq. (21). The mean-square displacements grow as

$$g_{1\perp} \propto g_{1\parallel} \propto g_{2\parallel} \propto l^2(\mathcal{W}t)^{1/1+(1/2\nu)} \quad (28)$$

Of course, for time  $t = \tau_{\text{tube}}$  the perpendicular displacement is of the order of  $D$  and, hence, the tube constraint is strongly felt. For  $t > \tau_{\text{tube}}$  the perpendicular motions are essentially equilibrated and the dynamics is determined by individual motions along the tube:

$$g_{1\parallel} \propto g_{2\parallel} \propto D^2 \sqrt{\mathcal{W}t} \left( \frac{l}{D} \right)^{1+(1/2\nu)}, \quad t_{\text{tube}} < t < \tau_R \quad (29)$$

where the generalized Rouse time  $\tau_R$

$$\tau_R \equiv \mathcal{W}^{-1} \left( \frac{D}{l} \right)^{2-1/\nu} N^2 \quad (30)$$

is the time needed to equilibrate density fluctuations along the tube. Eqs. (29,30), yield  $g_{2l}(\tau_R) = D^2 N(l/D)^{1/\nu}$ , i.e., a mean-square displacement proportional to  $N$  is reached.

For times  $t > \tau_R$  one expects  $g_{2\parallel}$  to settle down to its saturation value while  $g_{1\parallel}$  continues to grow and crosses over to a diffusive behavior:

$$g_{1\parallel} \propto D_N t, \quad t > \tau_R \quad (31)$$

From the requirement that a smooth crossover between Eqs. (29) and (31) for  $t = \tau_R$  should take place, one can estimate the diffusion constant as  $D_N \propto \mathcal{W}l^2/N$ , i.e., in the scaling limit  $D_N$  does not depend on the tube size  $D$ .

The longest relaxation time of the polymer chain in a tube, however, may be defined as the time needed by the chain to diffuse its own size,  $\tau_D \approx Rg\|^2/D_N = \mathcal{W}N^3(D/l)^{1-1/\nu}$ ; as a matter of fact this is the time revealed by the coherent scattering function of a diffusing chain in a tube [40].

In the result of the simulation one expects the times  $\tau_{23}^l$  to be proportional to  $\tau_R$  and  $\tau_3^l$  to be proportional to  $\tau_D$ , and, indeed, from Fig. 12 the respective power laws are nicely seen in the athermal case of neutral walls,  $\epsilon/k_B T = 0$ . Good agreement with predicted results (not shown graphically here) is obtained also for the scaling of  $D_N$  with  $N$ , and  $\tau_3^l$  with  $D$  [14].

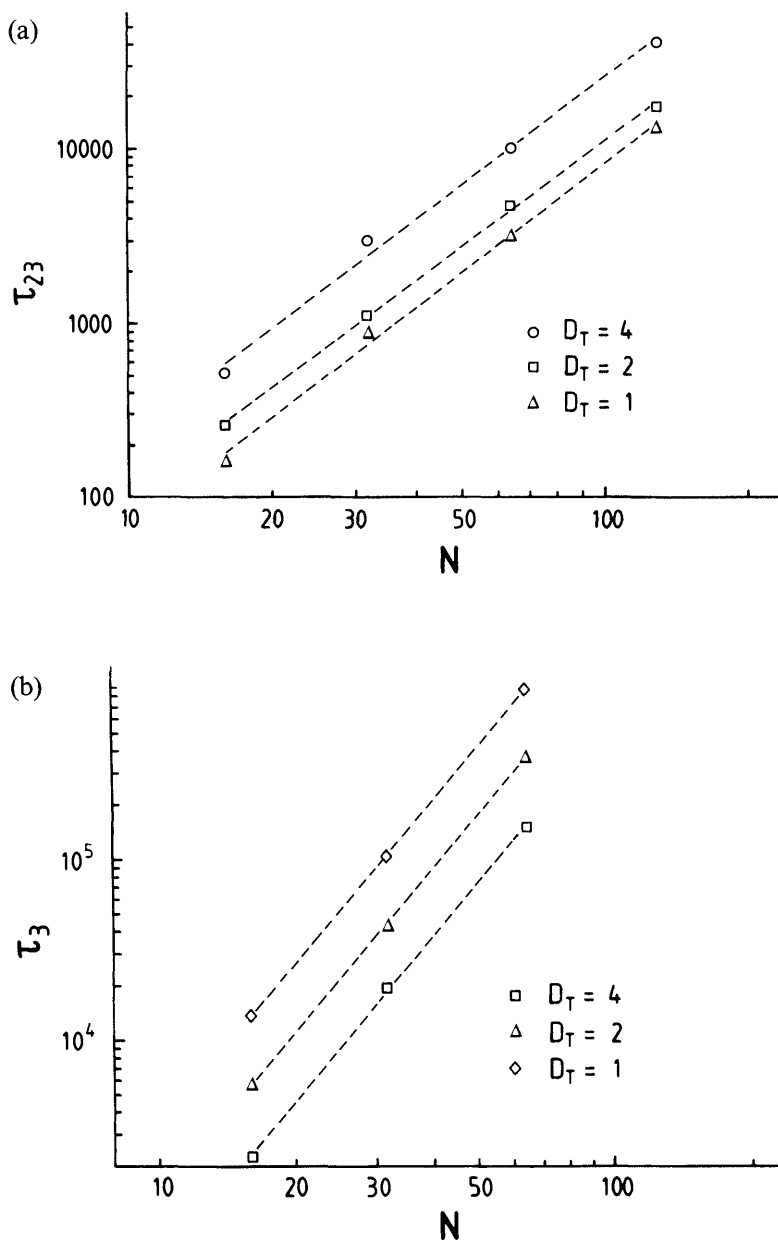


**FIG. 12** Log-log plot of the relaxation times  $\tau'_{23}$  (a) and  $\tau'_3$  (b) vs  $N$  in a tube with neutral walls and  $D = 1, 2, 4$  as indicated. Straight lines show the expected power laws. Parts (c) and (d) show scaling plots for  $\tau_R$  and  $\tau_D$  [14].

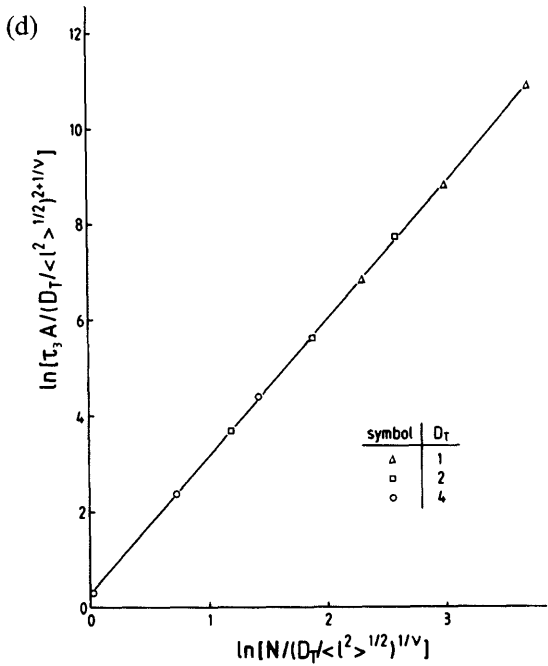
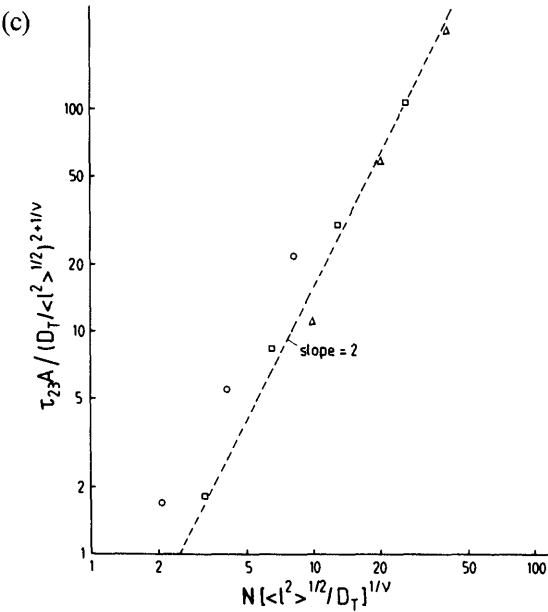


FIG. 12 Continued.

The effect of including attractive interactions with the walls is essentially to reduce the acceptance rate of the algorithm as more monomers get adsorbed on the walls. The relaxation times show an Arrhenius behavior, similar to the result on Fig. 9 in Sec. III.

## V. SINGLE POLYMER CHAINS IN A SLIT

Single chains confined between two parallel purely repulsive walls with  $\epsilon = 0$  show in the simulations the crossover from three- to two-dimensional behavior more clearly than in the case of adsorption (Sec. III), where we saw that the scaling exponents for the diffusion constant and the relaxation time slightly exceeded their theoretical values of 1 and 2.5, respectively. In sufficiently narrow slits,  $D \ll R_{gb}$ , one may see from the density profile in the perpendicular direction ( $z$ ) across the film that the monomers are localized in the mid-plane  $z = D/2$  so that a two-dimensional SAW, cf. Eq. (24), is easily established [15]; i.e., the scaling of the longitudinal component of the mean gyration radius  $R_{g\parallel}^2$ , and also the relaxation times exhibit nicely the  $2d$ -exponent  $\nu_2 = 3/4$  (Fig. 13).

The crossover  $2d \leftrightarrow 3d$  behavior can be described in a similar manner to the case of a tube confinement. For the chain, trapped between two parallel plates a distance  $D$  apart, one again has  $N/g$  blobs but they arrange to a two-dimensional random coil configuration:

$$R_{g\parallel}^2 = \frac{2}{3} R_{gb}^2 \mathcal{L}_{\parallel} \left( \frac{ln^{\nu}}{D} \right) \quad (32)$$

$$R_{g\perp}^2 = \frac{1}{3} R_{gb}^2 \mathcal{L}_{\perp} \left( \frac{ln^{\nu}}{D} \right) \quad (33)$$

where the factors  $2/3$ ,  $1/3$  are arbitrarily chosen in order to have a simple normalization of these scaling functions in the limit  $D \rightarrow \infty$  where one must recover bulk behavior, and hence  $\lim_{x \rightarrow 0} \mathcal{L}_{\parallel}(x) = \mathcal{L}_{\perp}(x) = 1$ . In contrast, in the inverse limit of narrow slits,  $x \gg 1$ ,  $R_{g\perp}$  cannot exceed  $D$  and thus one concludes  $\mathcal{L}_{\perp}(x \gg 1) = c_{\perp}/x^2$  where  $c_{\perp}$  is a universal constant, and the power  $x^{-2}$  ensures that in this limit  $R_{g\perp}^2$  in Eq. (33) cancels out. Most interesting, of course, is the parallel component, since there a crossover to two-dimensional behavior must occur,  $R_{g\parallel}^2 \propto N^{2\nu_2}$ , where the  $2d$  exponent  $\nu_2 = 3/4$ . This behavior implies

$$\mathcal{L}_{\parallel}(x \gg 1) = c_{\parallel} x^{2(\nu_2 - \nu)/\nu} \quad (34)$$

and hence for  $D \ll R_{gb}$  the parallel component of the mean-square gyration

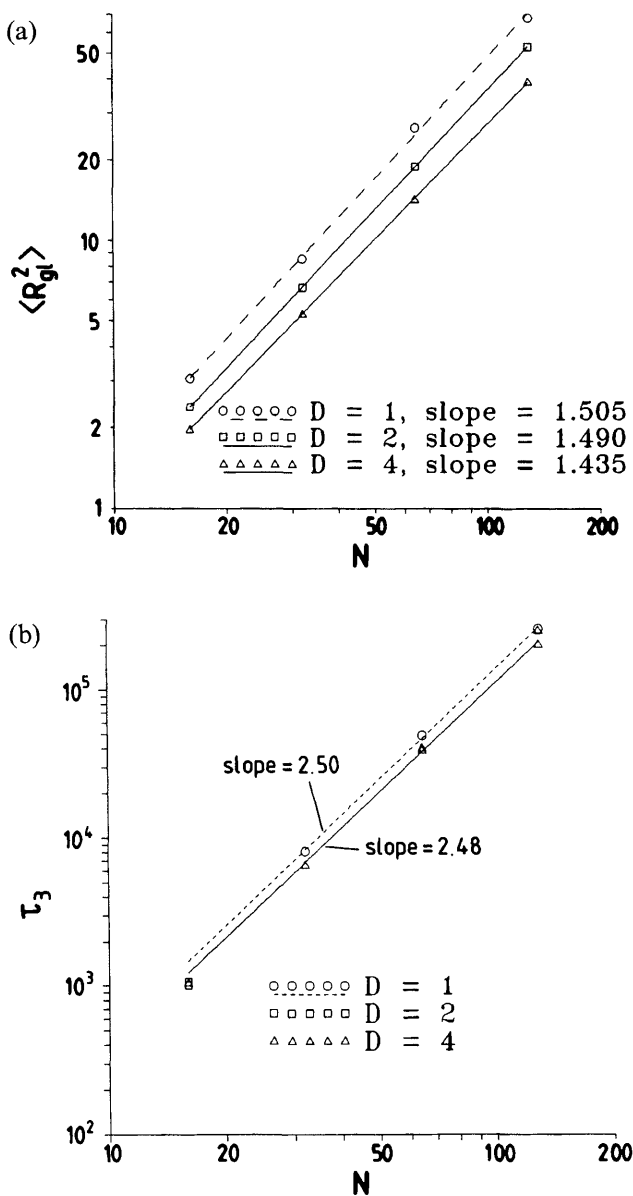


**FIG. 13** (a) Log-log plot of the longitudinal part of the mean gyration radius,  $R_{gl}^2$ , vs chain length  $n$  for the three choices of slit width  $D$ . Straight lines indicate effective exponents  $2\nu_2$ . (b) Log-log plot of  $\tau_3^l$  vs  $N$ . Straight lines show the effective exponent confirming the scaling law  $Z = 2\nu_2 + 1 = 2.5$  [15].

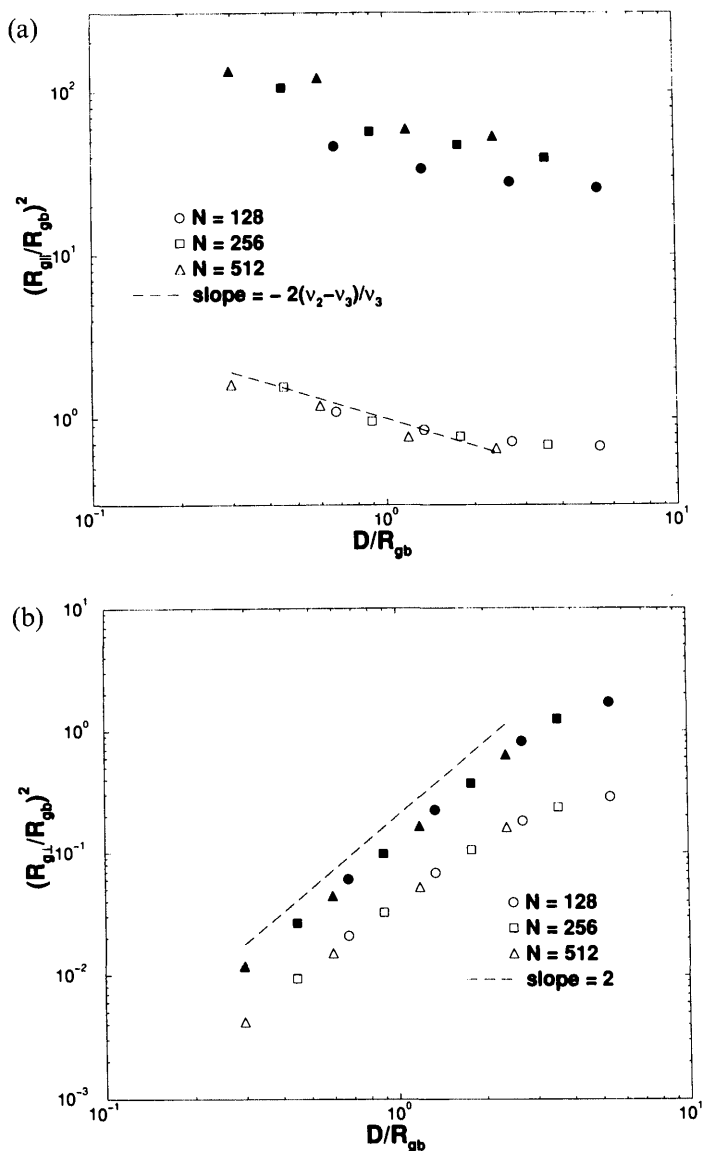


**FIG. 14** (a) Plot of the normalized parallel component of the mean gyration radius  $R_{g||}^2/R_{gb}^2$  (open symbols), and end-to-end distance  $R_{||}^2/R_{gb}^2$  (full symbols), vs the ratio  $D/R_{gb}$  [19] (chain lengths  $N = 128, 256, 512$  are distinguished by different symbols). The dashed straight line indicates the asymptotic slope of the scaling function for small  $D/R_{gb}$ , namely  $-2(\nu_2 - \nu)/\nu$ . (b) The same for the perpendicular components. The asymptotic slope for small  $D/R_{gb}$  (dashed line) is 2.

radius behaves as

$$R_{g\parallel}^2 = \frac{2}{3} D^2 \left( \frac{l}{D} \right)^{2\nu_2/\nu} c_{\parallel} N^{2\nu_2} \quad (35)$$

$c_{\parallel}$  being another universal constant. It should be emphasized, however, that all these relations neglect corrections to scaling and hence are only asymptotically valid in the limit where both  $D \gg l$  and  $R_{gb} \gg l$ . The scaling relations, Eqs. (32,33) have been checked [19] by the OLMC method (Fig. 14). Despite some statistical errors, affecting mainly the parallel components, the general trends of the scaling functions do follow the theoretical predictions sketched above. These findings also agree with those of an earlier simulation work [63].

Theoretical predictions [73,74] concern also the monomer density profile  $\rho(z)$ , which is predicted to scale as

$$\rho(z) = \frac{R_{gb}^{1/\nu}}{D} \mathcal{F} \left( \frac{z}{R_{gb}}, \frac{D}{R_{gb}} \right) \quad (36)$$

with  $\mathcal{F}$  another universal scaling function. In the limit,  $R_{gb} \rightarrow \infty$  at fixed  $D$ ,  $R_{gb}$  should cancel out from the arguments of  $\mathcal{F}$  in Eq. (36):

$$\rho(z) = \frac{R_{gb}^{1/\nu}}{D} \mathcal{F}' \left( \frac{z}{D} \right), \quad R_{gb} \gg D \quad (37)$$

while in the opposite case,  $R_{gb} \ll D$  and  $z \ll D$ , the profile near the plate should approach the characteristic behavior for a semi-infinite system:

$$\rho(z) = \frac{R_{gb}^{1/\nu}}{D} \mathcal{F}'' \left( \frac{z}{R_{gb}} \right), \quad R_{gb} \ll D \quad (38)$$

Considering now the limit  $z/R_{gb} \ll 1$  in Eq. (38), it has been argued that a simple power law  $\rho(z) \propto z^{1/\nu}$  results:

$$\rho(z) = \frac{z^{1/\nu}}{D} \mathcal{F}''' \left( \frac{D}{R_{gb}} \right) \rightarrow \frac{z^{1/\nu}}{D} c_p \quad \text{for} \quad D \rightarrow \infty, \quad (39)$$

with  $\mathcal{F}'''$  and  $c_p$  another universal scaling function and universal constant, respectively.

A simulation test [19] of the power law (39) can be seen in Fig. 15(a). As it is clear from the “raw” data, presented in the insert to Fig. 15(a) the data for  $z/D \ll 1$  settle down to constant values, and a region where  $z/D$  is still small and a power law is seen cannot be easily identified. The scaling theory, however, is expected to hold only for distances  $z$  that are *large on the microscopic scale* [74]. Studying such a regime where  $z$  is very large in



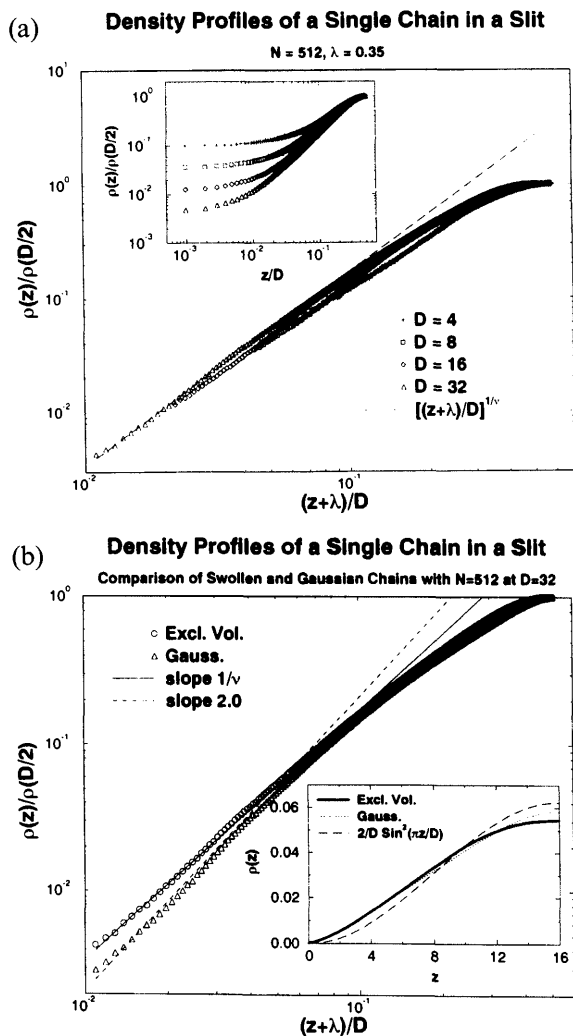


**FIG. 15** (a) Density profiles  $\rho(z)$ , normalized by the density  $\rho(D/2)$  in the center of the slit, on a log-log plot vs the modified relative distance from the wall  $(z + \lambda)/D$ . The extrapolation length  $\lambda = 0.35$ . Four widths of the slit are included, as indicated. The dashed line gives the predicted power law behavior,  $[(z + \lambda)/D]^{1/\nu}$ . Insert shows the same data but plotted vs  $z/D$ , i.e., without taking the extrapolation length into account. Chain length  $N = 512$  [19]. (b) Density profiles for  $N = 512$  and  $D = 32$ , comparing chains with excluded-volume interactions (circles) and without them (triangles). The extrapolation length  $\lambda = 0.35$  for both cases. Insert shows  $\rho(z)$  vs  $z$ , including also the corresponding analytical result  $(2/D) \sin^2(\pi z/D)$  for Gaussian chains with the boundary conditions  $\rho(z = 0) = 0$ .

comparison to microscopic scales, but very small with respect to  $D$  as well as  $R_{gb}$ , is very hard with simulations, it does require both  $N$  and  $D$  to be chosen extremely large. Fortunately, to leading order the effects of the microscopic scale can be incorporated in the treatment by using the concept of the “extrapolation length” [75–77], well known from the theory of surface effects on magnetic phase transitions (which can be mapped [26] to the case of polymers at surfaces [2,35,74] within the framework of the  $n \rightarrow 0$  vector model of magnetism). This means that in Eq. (39) the relation  $z^{1/\nu}$  should be replaced by  $(z + \lambda)^{1/\nu}$ . For  $z \gg \lambda$ , of course, this correction does not alter the description of the scaling behavior. But, as Fig. 15(a) shows, fitting  $\lambda$  such that the horizontal plateaus seen in the insert just disappear gives a straightforward fit to the law  $\rho(z) \propto (z + \lambda)^{1/\nu}$  over a wide parameter range. The value obtained for  $\lambda$ ,  $\lambda = 0.35$ , has an obvious physical interpretation in our OLMC model since this is simply one-half of the preferred bond length,  $l_0 = 0.7$ , cf. Eq. (8), and tests have shown that this value of  $\lambda$  does not depend on mesoscopic parameters like the slit width  $D$  and the chain length  $N$  of the polymers. Fig. 15(b) provides a further test of the concept of the extrapolation length: one simulates Gaussian chains by turning off the Morse potential (9) but keeping the FENE potential (8) between the beads. It is seen from Fig. 15(b) that also in this case the same choice of  $\lambda = 0.35$  is needed in order to verify  $\rho(z) \propto (z + \lambda)^{1/\nu_{MF}} = (z + \lambda)^2$  over a wide range (the mean field value  $\nu_{MF} = 1/2$ ). The asymptotic result for Gaussian chains in a narrow slit where  $\lambda$  is neglected, namely,  $\rho(z) = (2/D) \sin^2(\pi z/D)$  [26], deviates from the observed density profile markedly, even for Gaussian chains as long as  $N = 512$  beads! This observation shows again that for many phenomena of interest it is not only important to consider some asymptotic scaling law, but one should try to understand how effects on short length scales change the picture.

The last quantity that we discuss is the mean repulsive force  $f$  exerted on the wall. For a single chain this is defined taking the derivative of the logarithm of the chain partition function with respect to the position of the wall (in the  $-z$  direction). In the case of a semi-infinite system exposed to a dilute solution of polymer chains at polymer density  $n_b$ , one can equate the pressure on the wall to the pressure in the bulk which is simply given by the ideal gas law ( $n_b k_B T$ ). The conclusion then is that [74]

$$\rho(z)/z^{1/\nu} = Bf/k_B T, \quad z \ll R_{gb}, \quad z \ll D \quad (40)$$

where  $B \approx 2$  is an universal constant. Combining equations (38,40), one obtains in the wide slit limit  $D \gg R_{gb}$ , where  $\mathcal{F}'''$  tends to the constant  $c_p$  for the force  $f/k_B T \approx 1/D$ . In the narrow slit limit, one expects that the

force becomes ultimately proportional to the chain length  $N$  and hence  $\mathcal{F}'''$  for  $D \ll R_{gb}$  must behave as [74]

$$\mathcal{F}''' \left( \frac{D}{R_{gb}} \right) \propto \left( \frac{D}{R_{gb}} \right)^{1/\nu} \quad (41)$$

In a simulation [19] the pressure tensor is obtained from the virial theorem [78]

$$p_{\alpha\beta}(z) = \rho(z)k_B T \delta_{\alpha\beta} - (6V)^{-1} \sum_{i \neq j} (\vec{r}_{ij})_{\alpha} \frac{\partial U(\vec{r}_{ij})}{\partial (\vec{r}_{ij})_{\beta}} [\delta(z_i - z) + \delta(z_j - z)] \quad (42)$$

where  $U(\vec{r}_{ij})$  is the sum of all potentials, (8), (9). In Fig. 16 we show a scaling plot for the force  $f$ , which evidently confirms the predicted behavior (Eq. (40)).

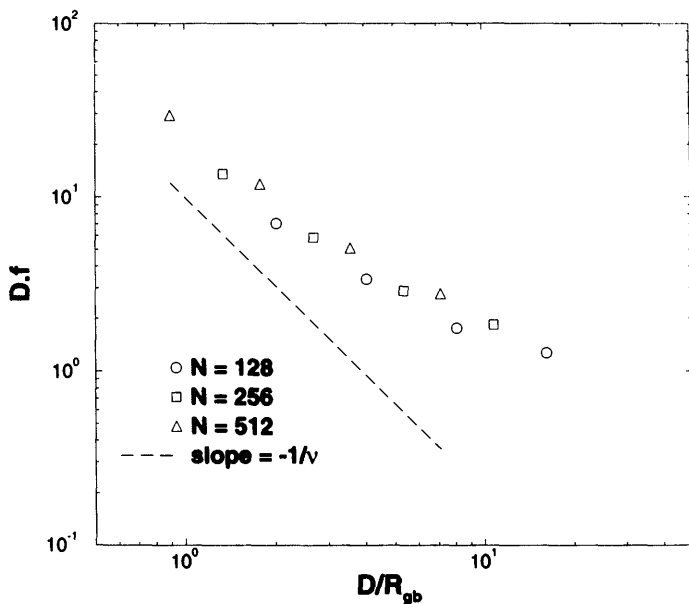


**FIG. 16** Scaling plot for the force,  $Df$ , vs  $D/R_{gb}$  [19]. The dashed straight line indicates the slope that the scaling function should exhibit for small  $D/R_{gb}$ .

VI. POLYMER SOLUTIONS IN SLIT-LIKE PORES

If concentrated polymer solutions confined in thin film geometry are considered, it turns out that the static properties readily match the theoretic expectations (Fig. 17) whereas the problem with dynamics is more complex [16,17]: writing  $Z_{\text{eff}} = 2\nu_{\text{eff}} + 1$ , one expects a corresponding decrease in the effective exponent because of screening, but this is not seen (Fig. 18). The relaxation times seem to increase monotonically with growing  $\phi$  for all  $N$ , and  $Z_{\text{eff}}$  seems to be independent of  $\phi$ . Interestingly, this behavior is accompanied by anomalous diffusion for the chain's center of mass

$$g_3(t) \propto t^{x_3^{\text{eff}}}, \quad x_3^{\text{eff}} \approx 0.84, \quad t < \tau_R \tag{43}$$

A similar anomalous behavior has been detected also in 3d polymer melts but only for rather short chains [41]; for longer chains, several regimes occur because of the onset of entanglement (reptation!) effects. In two dimensions, of course, the topological constraints experienced by a chain from

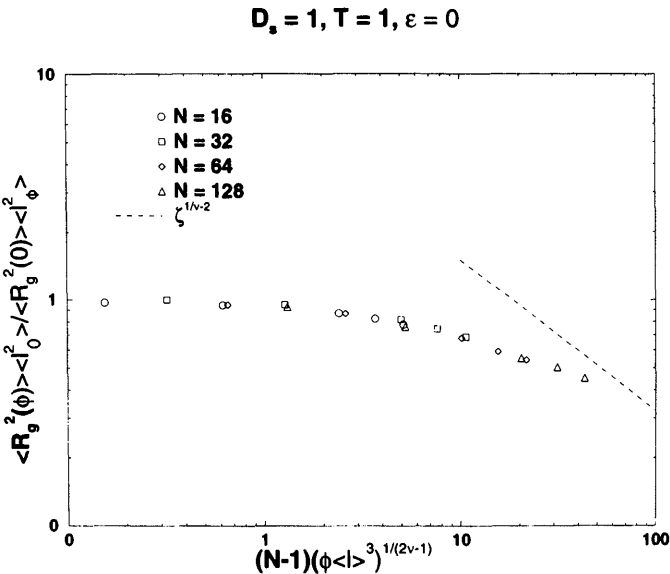


**FIG. 17** Longitudinal part of the mean-square gyration radius in the form of cross-over scaling plot, using the theoretical exponent  $\nu_2 = 3/4$  in  $2d$ . Here  $R_{g\parallel}^2$  is measured in units of the mean-squared bond length  $l^2$  at the corresponding density, and also the dimensionless volume fraction  $\phi l^3$  is used. Broken straight line indicates the slope corresponding to simple RW behavior,  $R_{g\parallel}^2 \propto N$ , expected to hold for large enough  $\phi$  [16].

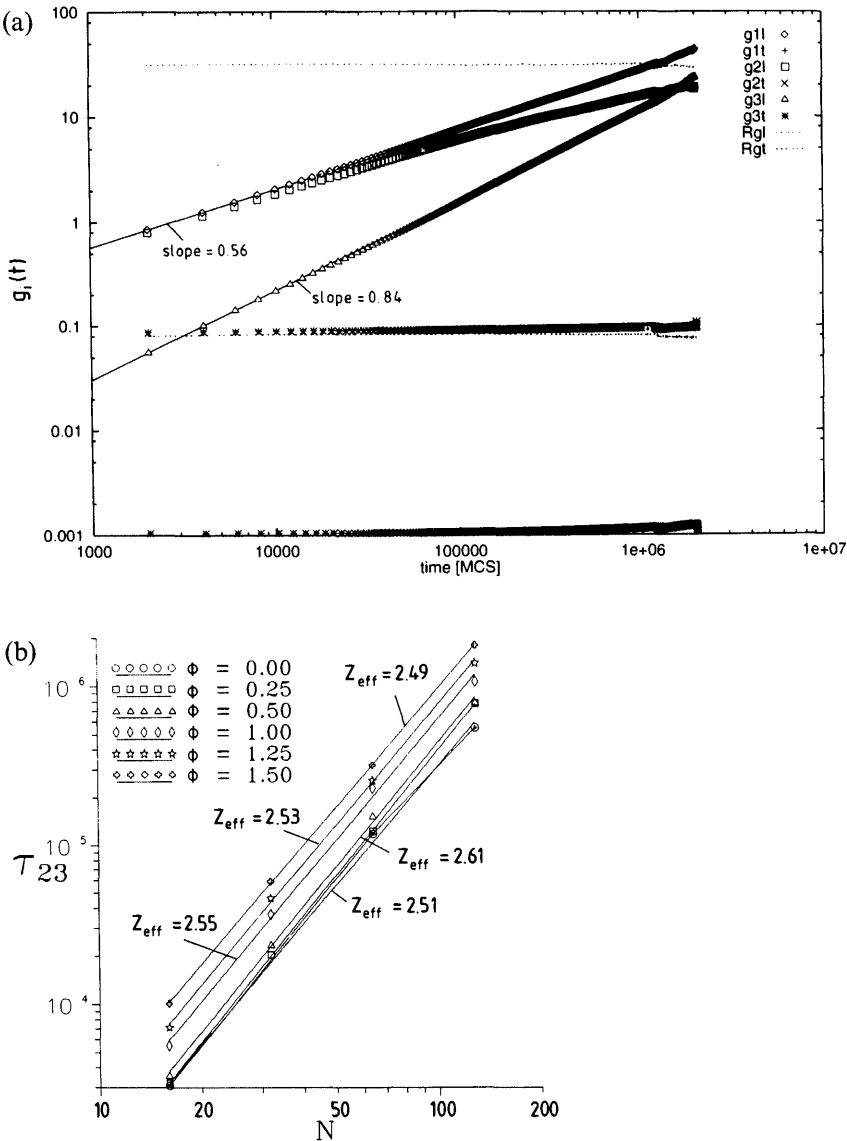


**FIG. 18** Mean-square displacements  $g_i(t)$  vs time for chains with  $N = 128$  in a narrow non-adsorbing slit ( $D = 1, \epsilon = 0$ ) at density  $\phi = 1.5$ . Straight lines show effective exponents  $x_1^{eff} = 0.56$ , and  $x_3^{eff} = 0.84$ , respectively. Broken horizontal lines show  $R_{gl}^2$  (above) and  $R_{gt}^2$  (below). (b) Log-log plot of the relaxation time  $\tau_{23}$  vs  $N$  for the case ( $D = 1, \epsilon = 0$ ) and various densities  $\phi$  as indicated. Straight lines show interpretations in terms of effective exponents  $Z_{eff}$  ( $\tau \propto N^{Z_{eff}}$ ) [16].

the surroundings are more severe because chains cannot pass through each other. In a dense system self-diffusion may require cooperative rearrangements of neighboring chains, and it would not be surprising if anomalous diffusion were the true asymptotic behavior ( $N \rightarrow \infty, t \rightarrow \infty$ ). However, for a strictly  $2d$  model system (the BFL model on a square lattice [60]) it was suggested that even at high densities the simple Rouse model holds. If Eq. (43) were the true asymptotic behavior, it could explain why  $Z_{\text{eff}}$  does not agree with  $2\nu_{\text{eff}} + 1$  because now a different scaling relation applies [17].

It has been found, too, that the relaxation times are compatible with an Arrhenius-like variation with density  $\phi$  (Fig. 19). This suggests that free volume concepts [42] might be useful for the understanding of the dynamics of dense polymeric films.

Apart from the global motions of the chains in the film as a whole, one can consider the local mobility as a function of distance from the plates. While for  $\epsilon = 0$  this mobility is slightly larger near the walls than in the center of the film, the opposite is true for large  $\epsilon$  [16]. This behavior reflects simply the structure of the density profile: for a purely repulsive wall the density is reduced near the wall whereas, for an attractive wall, a layer of enhanced density is found close to the wall. These simulational results are in

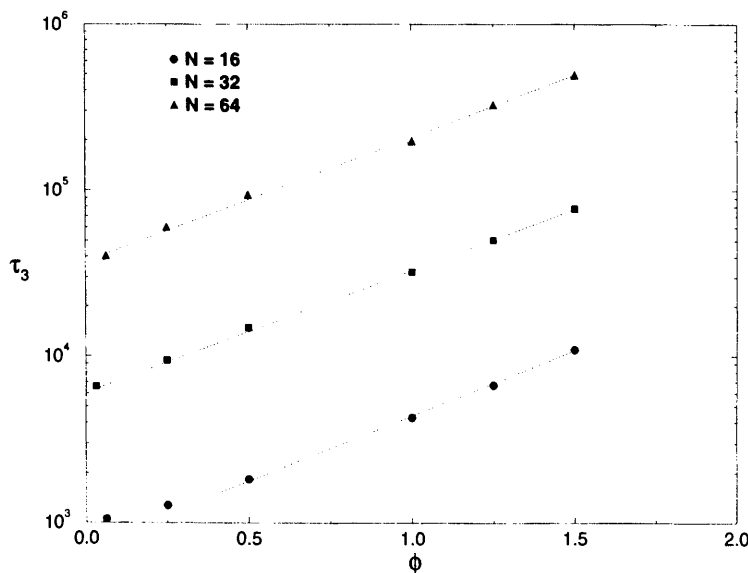


**FIG. 19** Semi-log plot of  $\tau_3$  vs  $\phi$  for the case  $D = 4$ ,  $\epsilon = 0$  and three choices of  $N$ . The dashed straight lines indicate a behavior  $\tau_3(N, \phi) = \tau_3(N) \exp(c\phi)$  with a constant  $c$  independent of  $N$  [16].

agreement with experimental evidence of reduced center of mass mobility near surfaces [43].

Density and pressure profiles as well as data on surface tension have been extensively studied in a slit of thickness  $D$  where one of the walls is attractive, (Eq. (11)), while for the opposite wall a purely repulsive potential of Lennard-Jones type is employed [18]. Choosing a smooth confinement potential rather than the simpler hard core interaction with the confining wall should damp out the density oscillations that one finds in dense systems confined near walls, and facilitate computation from the virial theorem, Eq. (42). It is seen from Fig. 20(a) that density profiles rise steeply within the range of the adsorption potential.\* For higher mean densities  $\phi$  the formation of a second and even a third peak at distances from the wall corresponding to the mean diameter of the beads exhibits a layering structure of the film in the vicinity of the attractive wall. One must be aware, however, that this layering structure does depend on details of our model—neither heights nor wavelengths of these density oscillations are supposed to have universal character. In this respect, therefore, the present coarse-grained model is useful only as a qualitative guidance but not in its quantitative detail.

A useful characteristic of the adsorption is the total amount that is adsorbed on the surface. One may define this surface excess from the density profile as  $\rho_s = \int_0^{D/2} [\rho(z) - \rho_b] dz$ . Fig. 20(b) shows a plot of  $\rho_s$  versus  $\rho_b$ . It is seen that for small  $\rho_b$  and not too strong adsorption ( $\phi \leq 0.5$ ,  $|\epsilon| \leq 2$ )  $\rho_s$  is actually negative: the entropic repulsion of the hard wall at  $z = 0$  is not compensated by the adsorption potential to produce net adsorption. Interestingly, for  $|\epsilon| = 2$  the sign of  $\rho_s$  changes near  $\rho_b = 1$ , i.e., the denser the system the less efficient is the entropic repulsion at the hard wall. For strong adsorption potential ( $|\epsilon| \geq 4$ ) the trend is different:  $\rho_s$  decreases somewhat with growing density  $\rho_b$  because the very high density of the adsorbed monomayer at the wall is little affected by  $\rho_b$ . In all cases, however, the surface excess is of order one, i.e., a thick adsorbed layer is not formed in these good solvent conditions. We believe that this conclusion is of general validity and is not specific to our coarse-grained model.

Since our system in the slit is anisotropic and inhomogeneous, it makes sense to consider the local pressure tensor, Eq. (42), which depends on the distance  $z$  from the adsorbing wall. If one defines  $P_x = p_{xx}$ ,  $P_y = p_{yy}$ , and  $P_z = p_{zz}$ , as well as the "total" pressure  $P_{\text{tot}} = P_x + P_y + P_z$ , then for symmetry reasons  $P_x = P_y$ , and this symmetry holds with good accuracy in our data (Fig. 20(c)). Generally one finds from the simulation that the total pressure follows the density profile. The pressure tensor  $p_{\alpha\beta}(z)$  is very useful

\* The density profiles are normalized so that  $\int_0^D \rho(z) dz / D = \phi$ .

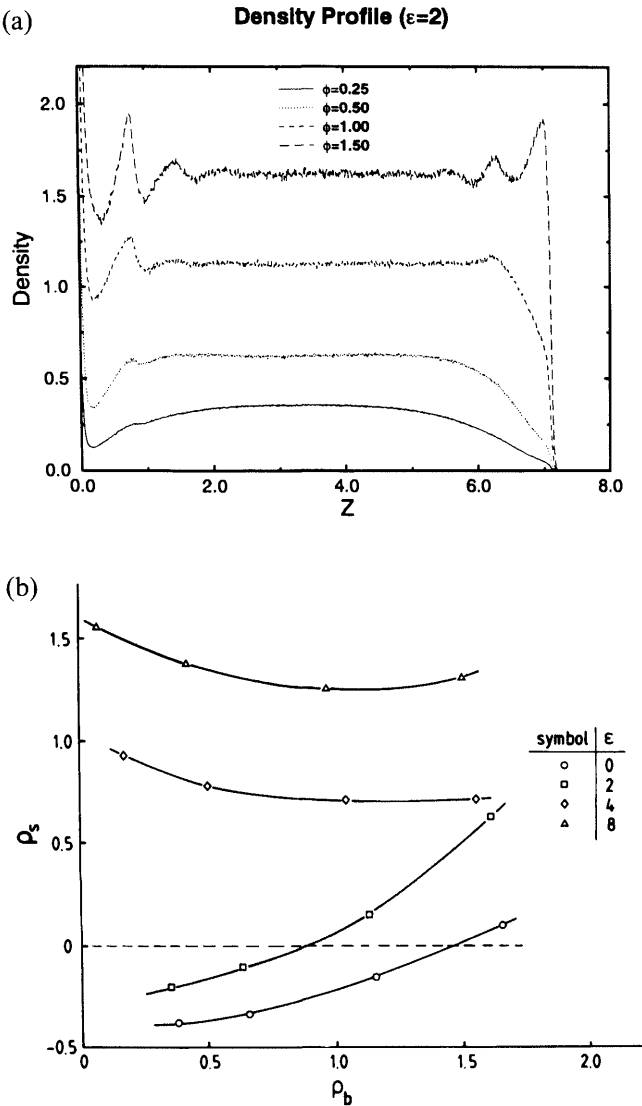


**FIG. 20** (a) Density profiles  $\rho(z)$  vs  $z$  for  $\epsilon = -2$  and four average bulk densities  $\phi$  as indicated. (b) Surface excess vs density in the bulk for four choices of  $\epsilon$ . (c) Profiles for the diagonal components of the pressure tensor and of the total pressure for  $\phi = 1.0$  and  $\epsilon = -2$ . Insert in (c) shows the difference between  $P_z$  and  $P_x$  to show that isotropic behavior in the bulk of the film is nicely obtained. (d) Interfacial tension  $\gamma_I^{\text{rep}}$  between the polymer film and the repulsive wall vs bulk density  $\rho_b$  for all four choices of  $\epsilon$ . Curve is only a guide for the eye [18].



(c) Pressure ( $\epsilon=2, \phi=1.00$ )

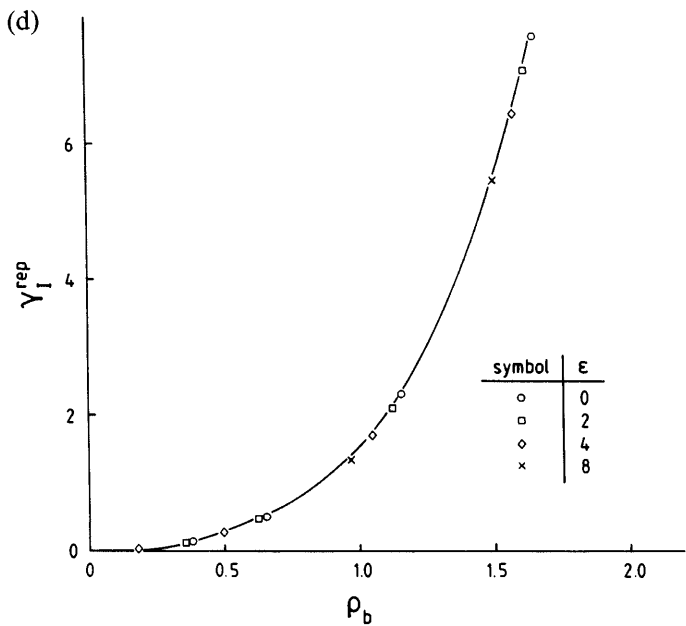
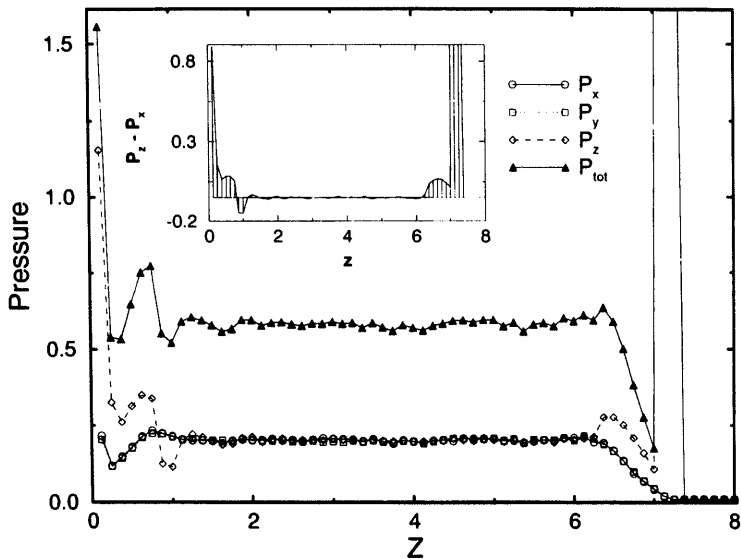


FIG. 20 Continued.

for computing interfacial free energies [44]. Noting that in the center of the film ( $z = D/2$ ) the normal component  $p_{\perp}(z)$  and the parallel component  $p_{\parallel}(z) \equiv (p_{xx} + p_{yy})/2$  are equal and hence there the system shows bulk behavior at the corresponding bulk density  $\rho_b$ , one can obtain interfacial tensions between the polymer solution at density  $\rho_b$  and the repulsive wall as well as the attractive wall as [44]

$$\gamma_I^{\text{rep}} = \int_{D/2}^D dz [p_{\perp}(z) - p_{\parallel}(z)] \quad (44)$$

$$\gamma_I^{\text{att}} = \int_0^{D/2} dz [p_{\perp}(z) - p_{\parallel}(z)] \quad (45)$$

The interfacial energy of the repulsive wall, for instance, should be completely independent of the adsorption energy  $\epsilon$  at the adsorbing wall; one expects  $\gamma_I^{\text{rep}}$  to be a function of the bulk density only (and of temperature, of course, but we consider only  $k_B T = 1$  here). Since different choices of  $\epsilon$  in our geometry with finite thickness do lead to different  $\rho_b$ , we get different results for  $\gamma_I^{\text{rep}}(\phi)$  for the various choices of  $\epsilon$ , albeit all data should be part of a common curve (Fig. 20(d)). As expected,  $\gamma_I^{\text{rep}}$  is a steadily increasing function of density; it reflects the increasing energy cost of confining the chains in the film by the repulsive wall as  $\rho_b$  increases.

In contrast,  $\gamma_I^{\text{att}}$  always stays much smaller and even turns negative for the strongly adsorbing case, indicating that spontaneous adsorption of polymers from the bulk of the film to the attractive wall occurs.

## VII. POLYMER CHAINS IN RANDOM POROUS MEDIA

### A. Scaling Laws in Equilibrium

The statistical properties of polymer chains in a quenched random medium have been the subject of intensive investigations during the last decades, both theoretically [79–89] and experimentally [90–96], because diffusion in such media is of great relevance for chromatography, membrane separation, ultrafiltration, etc.

Due to difficulties and uncertainties in the experimental separation of the porous media [93], and the inevitability of approximations in the analytical treatment [87,89], the nature of the chain movement in a random environment is still far from being well understood, and theoretical predictions are controversial [87,89]. Thus, on the ground of replica calculations within a variational approach, one predicts three regimes [87] in which the chain gyration radius  $R_g^2$  scales with the number of repeatable units  $N$  as  $R_g^2 \propto N^{6/5}$  for low,  $R_g^2 \propto N$  for medium, and  $R_g^2 \propto C_{\text{obs}}^{2/3} N^{2/3}$  for high

density of obstacles  $C_{\text{obs}}$ , so that the porous medium generally shrinks the size of the polymer coil [97–99]. In contrast, a regular expansion in a small parameter [89] predicts a Gaussian statistics for chains shorter than the localization length of the medium, whereas sufficiently long chains are typically distributed over several *entropic* potential wells so that  $R_g^2 \propto N^{6/5}$ , which can be interpreted as a SAW each step of which is equal to the average distance  $l_r$  between the wells,  $l_r \propto C_{\text{obs}}^{1/3}$ . Chains of medium length are expected to stretch out into a string,  $R_g^2 \propto N^2$ .

The scaling dependence of the diffusion coefficient  $D_N$  on  $N$  and  $C_{\text{obs}}$  also poses a number of questions. While the original scaling predictions, based on reptation dynamics [26,38],  $D_N \propto N^{-2}$ , have been verified by some measurements [91,98], significant discrepancies have been reported too [95,96]. Attempts to interpret existing data in terms of alternative models, e.g., by the so-called “hydrodynamic scaling model” [96], fail to describe observations [100,101].

In a simulational study using the OLMC model [20], a number of these problems have been addressed, using as a host matrix an equilibrated dense solution of identical polymer chains of  $N = 16$  which is frozen in different configurations. The behavior of diffusing chains of length  $N = 8, 16, 32, 64$  is then studied in the good solvent regime whereby the concentration of the network  $C_{\text{obs}}$  is varied to up to 3072 chains in a box of  $32^3$ . For longer chains, even at intermediate obstacle densities, it was found that the chains get stuck and practically do not move.

In Fig. 21(a) we plot the variation of  $R_g^2$  with increasing system density  $C_{\text{obs}}$  and, for comparison, also give the respective change for a system of moving medium (dynamic host matrix) of equal density. This result is in good agreement with recent predictions [89]. If one defines an effective Flory exponent  $\nu_{\text{eff}}$  from the scaling relation  $R_g^2 \propto N^{2\nu_{\text{eff}}}$ , it is then evident from Fig. 21(a) that, in contrast to the case of polymer melts where the screening of excluded volume interactions leads to  $\nu_{\text{eff}} \rightarrow 1/2$ , in the porous medium  $\nu_{\text{eff}}$  grows with vanishing free volume. Of course, since the simulation deals generally with rather short chains, one could reformulate this result in terms of growing *persistent* length of the chains as the host matrix becomes denser, rather than in terms of  $\nu_{\text{eff}}$ . One may conclude that in the high density regime of obstacles and long chain lengths the conformations of the chain are governed predominantly by the density fluctuations of the porous medium, i.e., the chain follows the distribution of cavities and channels, formed in the host matrix, and one observes effective renormalization of the Kuhn length of the chain, which becomes equal to the average distance between cavities. This leads to the observed increase of gyration radius (Fig. 21(a)).

A crossover scaling for  $R_g^2$  and  $R^2$  of a polymer chain in a quenched random medium may be developed if one introduces a correlation length

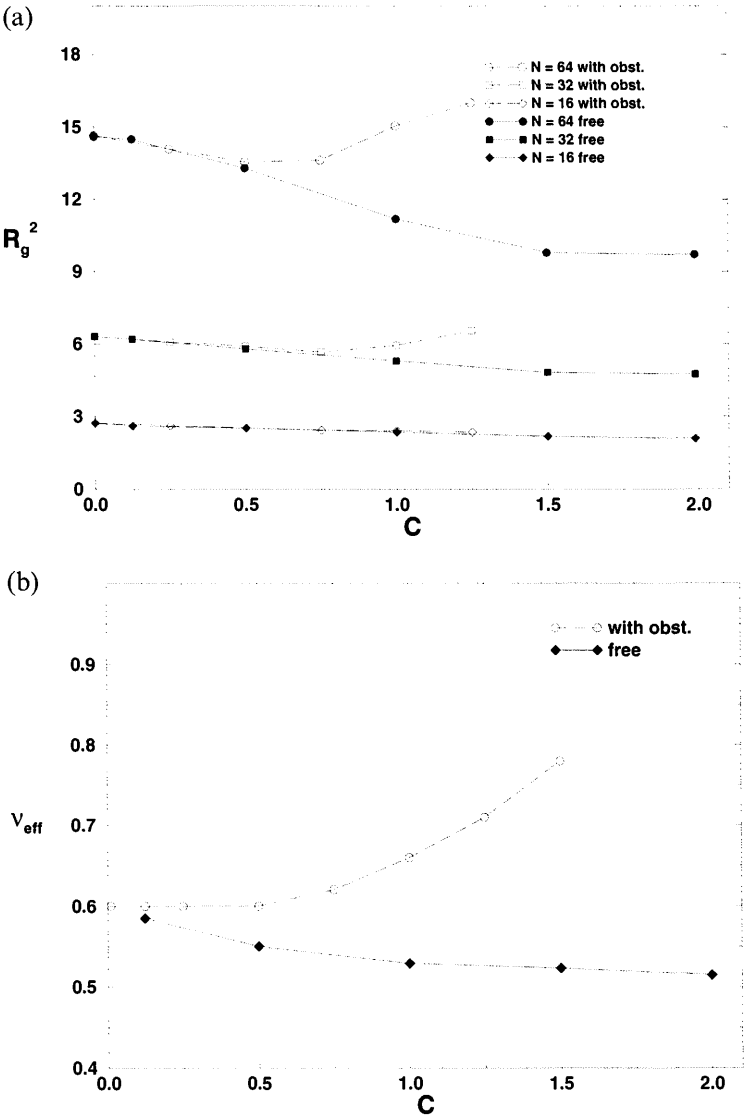


**FIG. 21** (a) Mean square gyration radius  $R_g^2$  vs total density  $C$  of the system for three different chain lengths in the case of equilibrated polymer solution (no fixed obstacles) (full symbols), and for frozen host matrix (empty symbols), at equivalent total density. (b) Variation of the effective Flory exponent  $\nu_{eff}$  with total density  $C$  in a polymer solution (full symbols), and in a porous medium (empty symbols) at equivalent density [20].

$\xi_{\text{obs}}$  which characterizes the volume fraction of the quenched polymer network,

$$\xi_{\text{obs}} \propto C_{\text{obs}}^{-\nu/(3\nu-1)} \quad (46)$$

where  $\nu = 0.588$  is the Flory exponent. In the dilute limit the chain does not feel geometric constraints and

$$R_{g0}^2 \propto N^{2\nu} \quad (47)$$

but in a dense matrix (small  $\xi_{\text{obs}}$ ) or for large enough chain, when  $R_g^2 \gg \xi_{\text{obs}}^2$  Fig. 21 shows that the chain stretches as  $C_{\text{obs}}$  is increased, which could be described as

$$R_g^2 \propto C_{\text{obs}}^x N^{2\nu_{\text{cross}}} \quad (48)$$

with some exponent  $x$  which is still to be determined, and  $\nu_{\text{cross}}$  being the limiting value of Flory's effective exponent at high obstacle density.

The crossover regime occurs at obstacle density  $C_{\text{obs}}^*$  when the size of the random polymer coil becomes equal to the size of the pores,  $R_g^2 = \xi_{\text{obs}}^2$ . From Eqs. (46) and (47) in this regime follows

$$C_{\text{obs}}^* \propto N^{-(3\nu-1)} \quad (49)$$

The exponent  $x$  in Eq. (48) has to be determined from the condition of a smooth matching between (46) and (48) at  $C_{\text{obs}} = C_{\text{obs}}^*$ , which yields

$$x = 2 \frac{\nu - \nu_{\text{cross}}}{1 - 3\nu} \quad (50)$$

Using a new variable,  $\zeta = R_{g0}/\xi_{\text{obs}} = N^\nu C_{\text{obs}}^{\nu/(3\nu-1)}$ , the relative change of gyration radius with obstacle concentration in the system can be expressed by a scaling function  $\mathcal{F}_{\text{obs}}(\zeta)$  as

$$\frac{R_g^2}{R_{g0}^2} = \mathcal{F}_{\text{obs}}(N^\nu C_{\text{obs}}^{\nu/(3\nu-1)}) = \begin{cases} \text{const.} & \zeta < 1 \\ \zeta^{-2(2-(2\nu_{\text{cross}}/\nu))} & \zeta > 1 \end{cases} \quad (51)$$

With  $\nu_{\text{cross}} \approx 0.7 \div 0.78$  (Fig. 21(b)), one gets a power of  $\zeta \approx 0.37 \div 0.64$  in Eq. (51) which is an *increasing* function for  $\zeta > 1$  (in contrast to dense polymer solutions where, with  $\nu_{\text{cross}} = 0.5$ , this exponent is equal to  $-(2 - 1/\nu) \approx -1/3$ ). Nevertheless, a scaling plot of Eq. (51), in terms of  $R_g^2/N^{2\nu}l^2$  versus  $N(Cl^3)^{1/(3\nu-1)}$ , (Fig. 22(a)), looks bad! A good scaling is obtained only if one plots  $R_g^2/N^{2\nu}l^2$  (remember,  $l$  is the size of the beads) against  $N(Cl^3)^{2/(3\nu-1)}$  (Fig. 22(b)). This can be explained if one takes into account the renormalization of the persistent length: a sufficiently long chain can be represented as a sequence of “blobs” with size equal to the mean size

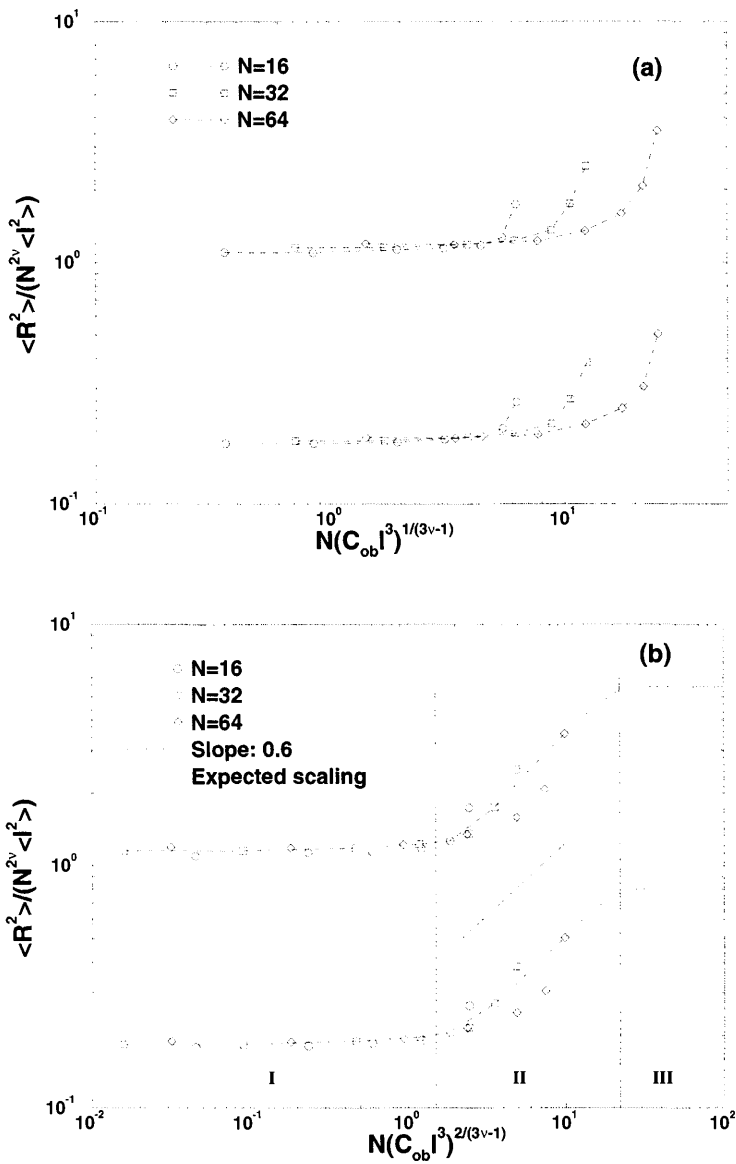


**FIG. 22** (a) Log-log plot of the scaling function  $\mathcal{F}_{\text{obs}}$  vs  $\zeta = N^\nu C_{\text{obs}}^{1/(3\nu-1)}$ . The upper curves refer to the mean-square end-to-end distance,  $R^2$ , while the lower ones show results for  $R_g^2$ . (b) The same vs scaling variable  $N^\nu C_{\text{obs}}^{2/(3\nu-1)}$ . Region I—free chains, II—crossover, and III—renormalized free chains. The slope 0.6 corresponds to  $\nu_{\text{cross}} = 0.78$ . [20]

of the cavities in the host matrix, so that the average number of monomers  $g$  per cavity of size  $\xi_{\text{obs}}$  is:  $g \propto \xi_{\text{obs}}^{1/\nu} \propto C_{\text{obs}}^{1/(3\nu-1)}$ . The number of blobs,  $N_g$ , per chain will be  $N_g = N/g \propto NC_{\text{obs}}^{1/(3\nu-1)}$  so that the renormalized length  $N_g C_{\text{obs}}^{1/(3\nu-1)} \propto NC_{\text{obs}}^{2/(3\nu-1)}$ . Since  $\mathcal{F}_{\text{obs}}(\zeta) = \text{const.}$  for  $\zeta < 1$ , one may formally replace  $N$  by  $N_g$  in  $\zeta$  even in this case.

Typical dynamic properties like the scaling of relaxation times, e.g.,  $\tau_1$ , or diffusion coefficient  $D_N$  with  $N$  are found in the simulation to change systematically from typical Rouse-like behavior ( $D_N \propto N^{-1}$ ,  $\tau \propto N^{2\nu+1}$ ) to reptational behavior [38], ( $D_N \propto N^{-2}$ ,  $\tau \propto N^3$ ) as the free volume of the porous medium decreases (Fig. 23). In a similar way one may analyze the crossover scaling of the diffusion coefficient, assumed as  $D_N \propto C_{\text{obs}}^z N^{-2}$  for the dense medium, by requiring a smooth transition in the crossover regime to Rouse behavior at low density. One obtains the same  $z = -1/(3\nu - 1)$  as for semi-dilute polymer solutions [41] and expects some scaling function  $\mathcal{F}_{\mathcal{D}}(R_g/\xi_{\text{obs}})$  in the relation

$$\frac{D_N}{D_N^0} = \mathcal{F}_{\mathcal{D}}(NC_{\text{obs}}^{1/(3\nu-1)}) \quad (52)$$

The density dependence of  $D_N$ , however, is not trivial since one must take into account the density dependence of the monomeric friction [41] given by the monomer reorientation rate  $\mathcal{W}$ . If a scaling plot of the correct ratio  $D_N/(\mathcal{W}l^2/N)$  is attempted, one again finds poor scaling in terms of the variable  $N(Cl^3)^{1/(3\nu-1)}$  (Fig. 24(a)), and a good collapse of data if instead the variable  $N(Cl^3)^{2/(3\nu-1)}$  is used (Fig. 24(b)). This suggests that the renormalization effects discussed above play an important role in the dynamics too.

## B. Polymer Chain in a Flow through a Porous Medium

A natural extension of the studies in Sec. VII A would be the investigation of the drift of a polymer chain in random environment when a constant external field  $B$  is applied in one direction [21,22].

Again, the OLMC bead-spring model (Sec. II B 2) is used, with a host matrix of an equilibrated dense solution of polymer chains quenched at different concentrations  $C_{\text{obs}}$ . Eq. (7) for the probability  $W$  of a random monomer displacement in direction  $\Delta x$ ,  $\Delta y$ ,  $\Delta z$  is given by

$$W = \begin{cases} \exp[-(E_{\text{new}} - B\Delta x - E_{\text{old}})] & \text{for } E_{\text{new}} - B\Delta x - E_{\text{old}} > 0 \\ 1, & \text{otherwise} \end{cases} \quad (53)$$

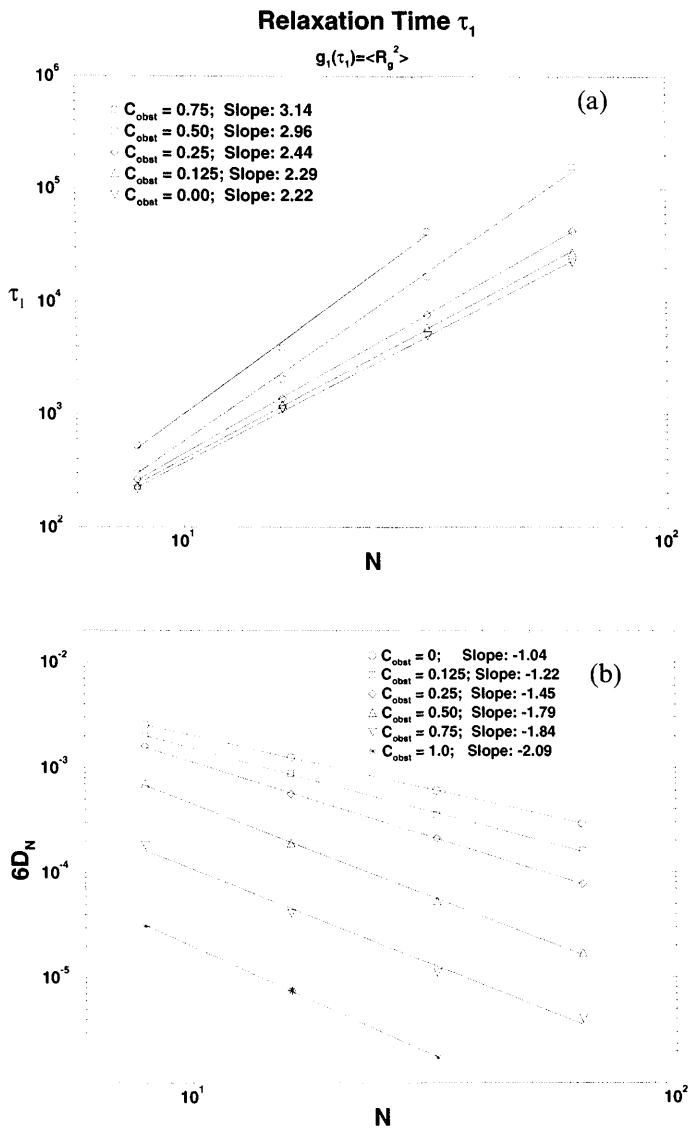


**FIG. 23** (a) Log-log plot of relaxation time  $\tau_1$  vs chain length  $N$  at several obstacle densities. The limiting slopes of 2.22 and 2.96 coincide within statistical error with the values 2.18 and 3.0, characteristic for Rouse and reptational behavior, respectively. (b) Variation of diffusion coefficient  $D_N$  with chain length  $N$ . The change of slopes from  $\approx -1$  at  $C_{\text{obs}} = 0$  to  $\approx -2$  in a porous system with vanishing free volume is given in the legend [20].



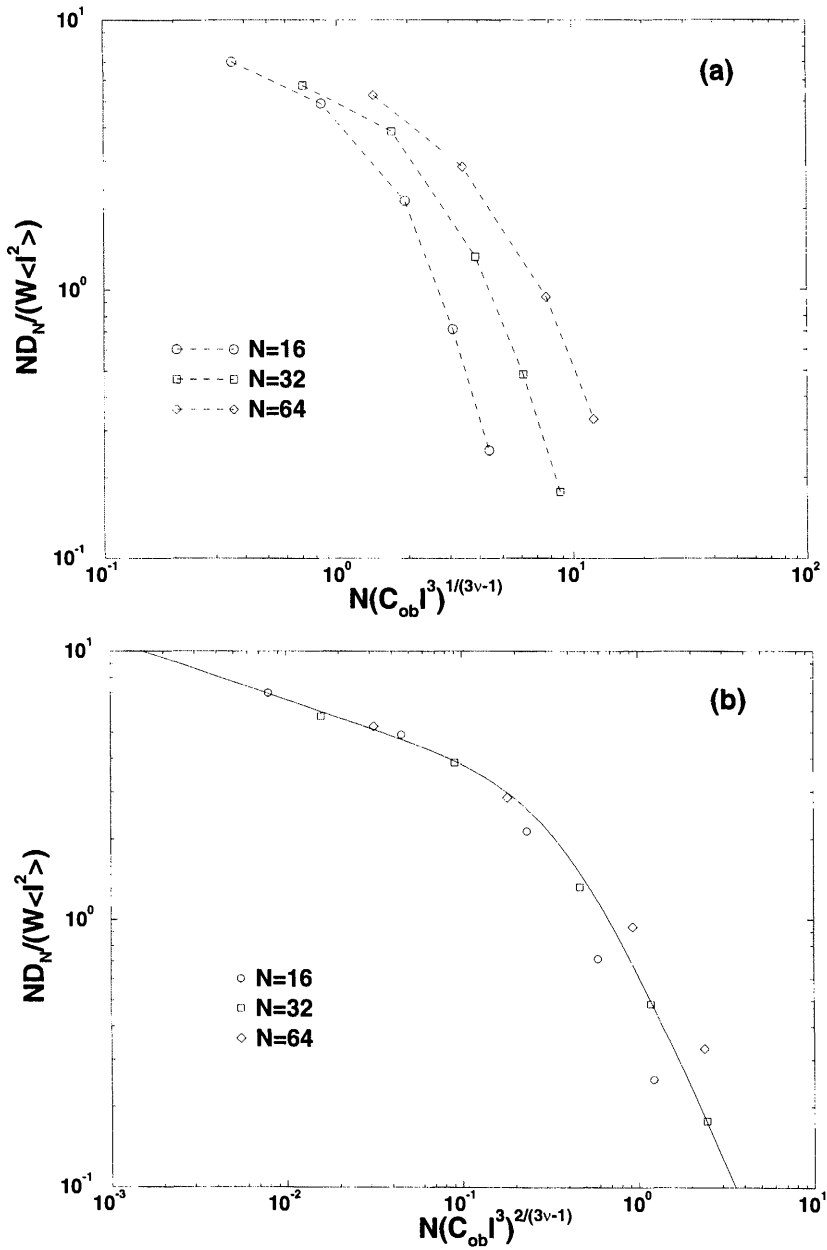


**FIG. 24** (a) Scaling plot of  $D_N/(Wl^2/N)$  vs  $N(CI^3)^{1/(3\nu-1)}$  for several chain lengths indicated in the figure. (b) The same vs  $N(CI^3)^{2/(3\nu-1)}$  [20].

where  $E_{\text{new}}$  and  $E_{\text{old}}$  are the energies of the new and old system configurations and the field  $B$  acts in the  $x$ -direction. In order to get better statistics, several chains “invisible” to each other move simultaneously through the medium, and the direction of the field is changed successively along the  $x$ -,  $y$ -, and  $z$ -axes.

The changes in the conformational properties of the drifting chains with growing bias  $B$  and medium density  $C_{\text{obs}}$  are shown in Fig. 25. Evidently, even a small presence of fixed obstacles,  $C_{\text{obs}} = 0.125$ , leads to a significant increase of the size of the chains at higher drift rates ( $B > 0.5$ ). The ratio between longitudinal  $R_{\text{gl}}^2$  and transversal components  $R_{\text{gt}}^2$ , plotted in Fig. 25(b), indicates that this increase is mainly due to stretching of the polymer along the drift direction. If such stretching is assumed, one must then expect that the ratio  $R_{\text{ee}}^2/R_{\text{g}}^2$  between the chain’s end-to-end distance and its gyration radius should increase in comparison to that of a chain in free space. For a Gaussian coil its theoretical value is 6 and for a fully stretched string it is 12. However, from Fig. 25(c) it is seen that, after a slight increase of up to 6.4, one observes a decrease to values below 5 at intermediate host matrix density. This result may be understood if one assumes that the drifting chain adopts a *hairpin* form with ends directed along the drift—as this is indeed seen on a snapshot (Fig. 26).

It is interesting to note that the typical conformations of the chains, usually observed in our MC simulations, are similar to those reported for polymers in extensional flows [105,106], although we do not consider inhomogeneity of the solvent flow between the obstacles. This is probably due to the fact that the acceptance rate in the simulations is different away from an obstacle and close to it by nearly an order of magnitude. We also observe the predicted elongation of the average square bond length  $l^2$ , based on considerations of a dumbbell model with FENE potential between the beads [102]. These extensions happen for sufficiently strong fields and intermediate densities of the medium.

In order to examine the permeability of the porous medium, it is useful to study the average velocity of the chain

$$V_N^2 = \lim_{t \rightarrow \infty} [g_3(t)/t^2] \quad (54)$$

where  $g_3(t)$  again measures the mean-square displacement of the chain’s center of mass with elapsed time  $t$ . In the case of slow drift through a dilute porous medium, when the conformation of the driven chain is not essentially affected by the drift,  $V_N$  is a linear function of the mobility  $\mu$  of the chain and the total external force  $f_{\text{tot}}$  acting on it [26], which in our case is  $BN$ :

$$V_N = \mu f_{\text{tot}} = \mu BN \quad (55)$$

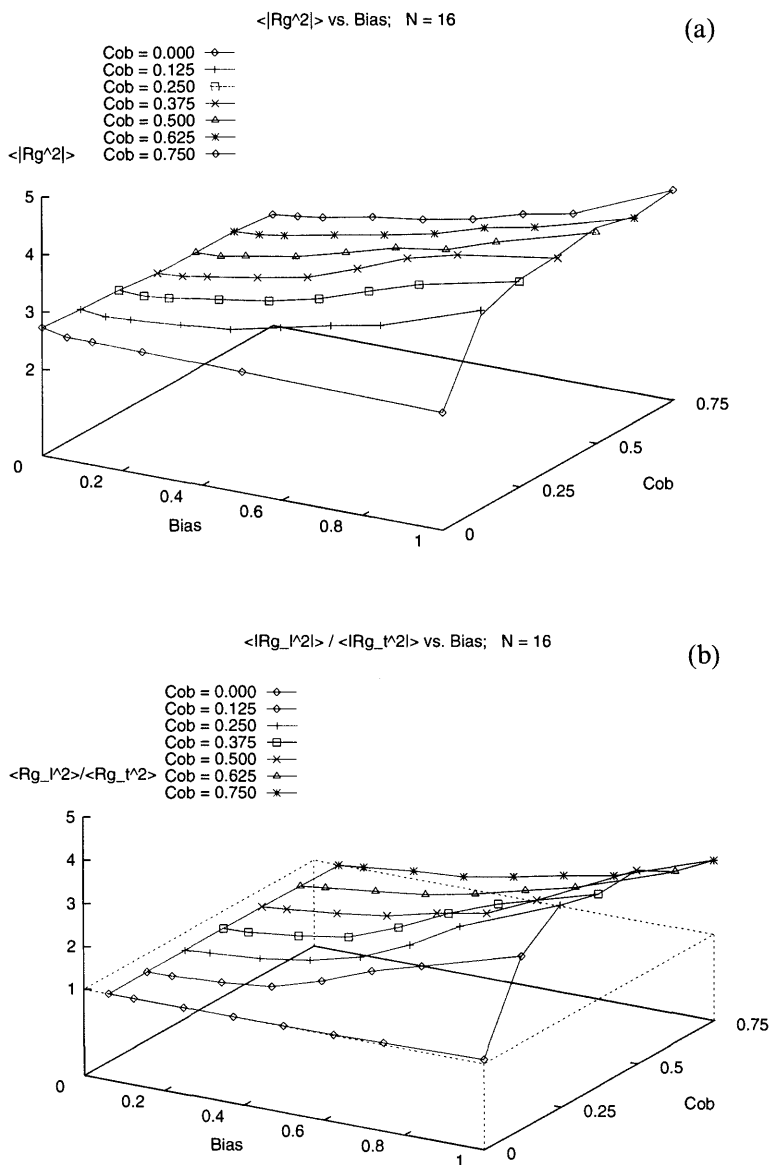


**FIG. 25** (a) Variation of the mean-square gyration radius  $R_g^2$  with the intensity of the field (bias) and with host matrix density  $C_{ob}$ . (b) The same for the ratio of its longitudinal and transversal components  $R_{gl}^2/R_{gt}^2$ . (c) The ratio between the end-to-end distance  $R_{ce}^2$  and gyration radius  $R_g^2$  vs bias for series of densities of the host matrix. [21].

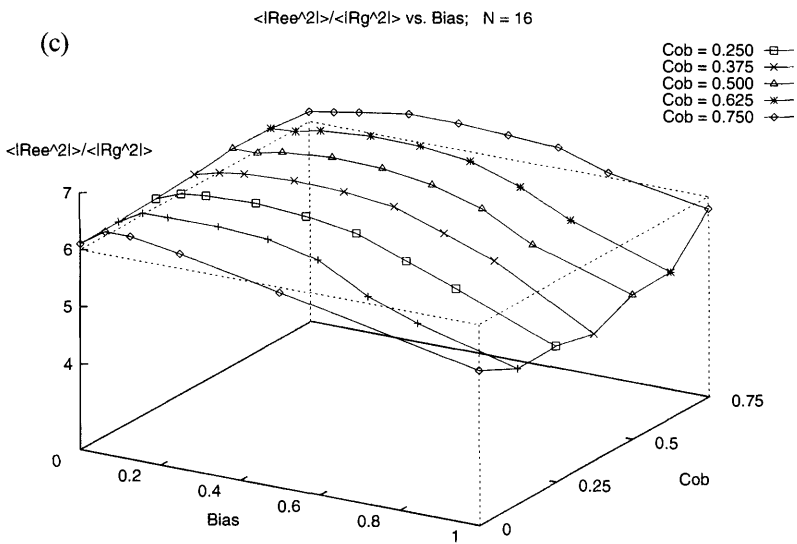


FIG. 25 Continued.

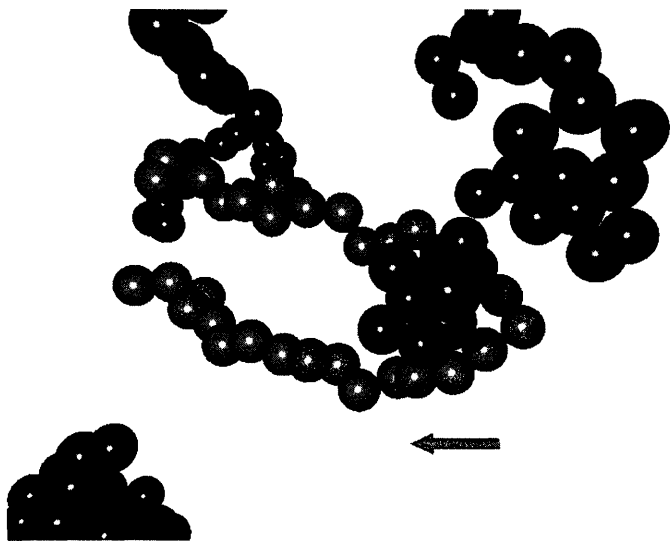


FIG. 26 A snapshot of a typical hoof-like form of a driven 32-bead chain (light beads) at overcritical bias  $B = 0.625$  through a dilute medium of fixed obstacles (dark beads) of density  $C_{\text{obs}} = 0.125$ . The direction of flow is indicated by the arrow. [21]

Applying Einstein's formula, which links  $\mu$  with the diffusion coefficient  $D_N$ ,

$$D_N = \mu k_B T \quad (56)$$

one obtains a relation for the average velocity as a function of the diffusion coefficient and the bias:

$$V_0 = D_0 B N / k_B T \quad (57)$$

Here the index 0 at  $D$  refers to the diffusion coefficient in a system at rest (no bias), and  $V_0$  denotes the "zero" approximation i.e., this relation is applicable for slow drift in dilute medium only.

The simulation data, represented in Figs. 27(a–c), confirms Eq. (57) in the region of weak  $f_{\text{tot}}$  ( $BN < 4$ ) for  $N = 8, 16, 32$  at dilute regimes whereby the values for  $D_0$  have been measured for the same system in equilibrium [20] (cf. Sec. VII B). Substantial discrepancies emerge only for high density of the medium.

For intermediate drift rates ( $4 < BN < 8$ ), when chain conformations are already distorted,  $V_N$  deviates from linear behavior and goes through a maximum at some critical value  $B_c$  of the field, confirming earlier findings by Pandey et al. [103,104]. This critical bias  $B_c$  at which the velocity  $V_N$  starts to decrease depends rather weakly on the density  $C_{\text{obs}}$ , and turns out to be reciprocal to chain length  $N$ , implying that only when the *total* force,  $f_c = B_c N \approx 9$ , acting upon the whole driven molecule, exceeds a certain threshold, which does not depend on the size of the macromolecule, the chains start to get stuck in the medium.

One could assume that this characteristic behavior of the mobility of the polymers is also reflected by the typical relaxation times  $\tau$  of the driven chains. Indeed, in Fig. 28 we show the relaxation time  $\tau_2$ , determined from the condition  $g_2(\tau_2) = R_g^2/3$  in dependence on the field  $B$ : evidently, while for  $B < B_c$   $\tau_2$  is nearly constant (or rises very slowly), for  $B \geq B_c$  it grows dramatically. This result, as well as the characteristic variation of  $V_N$  with  $B$  (cf. Figs. 27(a–c)), may be explained, at least phenomenologically, if the motion of a polymer chain through the host matrix is considered as consisting of (i) nearly free drift from one obstacle to another, and (ii) a period of trapping,  $\tau$ , of the molecule at the next obstacle. If the mean distance between obstacles is denoted by  $\xi$  and the time needed by the chain to travel this distance is  $t_\xi$ , then  $V_N = \xi / (\tau + t_\xi)$ , whereby from Eq. (57)  $t_\xi = \xi / V_0 = \xi k_B T / (D_0 B N)$ . This gives a somewhat better approximation for the drift velocity

$$V_1 = \frac{\xi D_0 B N}{\tau D_0 B N + \xi k_B T} \quad (58)$$

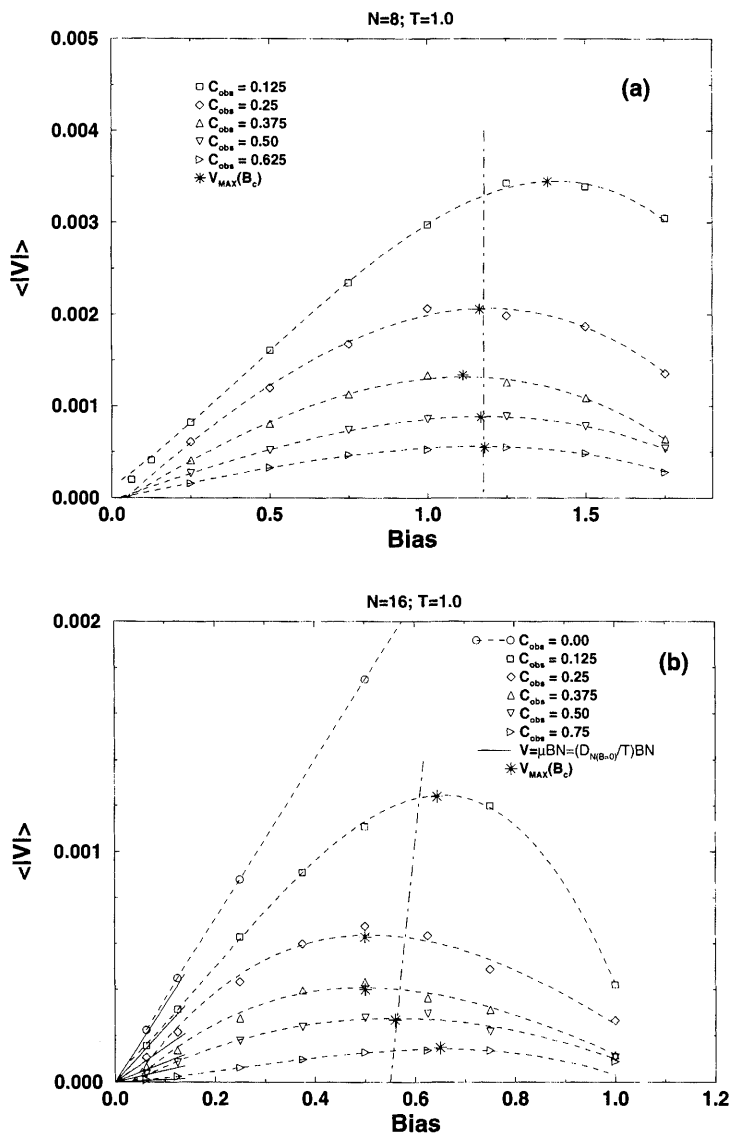


**FIG. 27** Drift mean velocity of polymer chains of length (a)  $N = 8$ , (b)  $N = 16$ , and (c)  $N = 32$  vs bias  $B$  for a series of densities of the medium. Dashed lines are guides for the eye. The vertical long-dashed line on each of the figures indicates the approximate value of the critical bias  $B_c$  for given chain length. The straight solid lines drawn through the origin of the coordinate system present the linear approximation Eq. (57) [21].

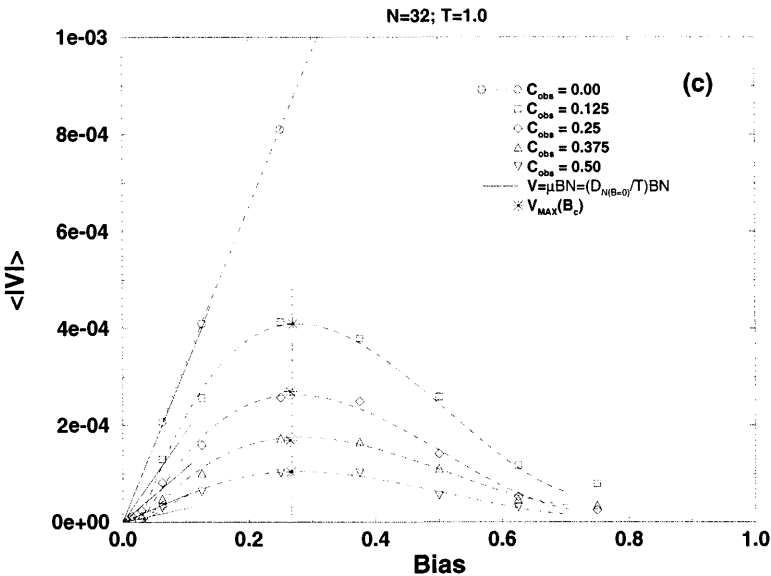


FIG. 27 Continued.

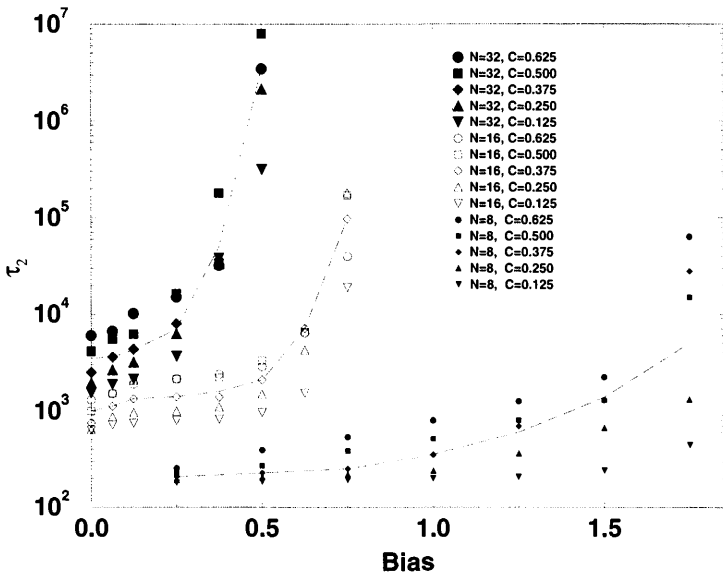
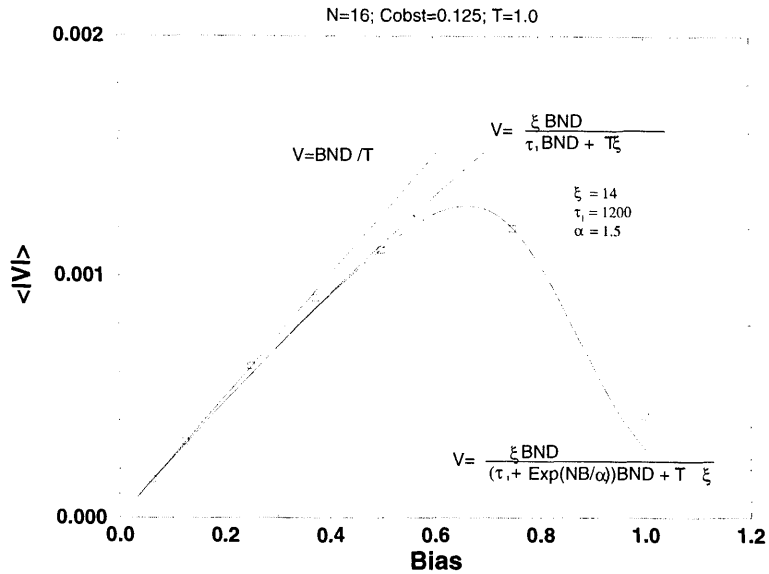


FIG. 28 Log-normal plot of relaxation time  $\tau_2$  vs bias for three different chain lengths (given as a parameter) and a series of medium densities [21].



**FIG. 29** Drift mean velocity for a chain of length  $N = 16$  at small obstacle concentration  $C_{ob} = 0.125$  vs bias  $B$ , fitted with the expressions  $V_0(BN)$ ,  $V_1(BN)$ , and  $V_2(BN)$  [21].

although it still cannot describe even qualitatively the measured data (Fig. 29). One does get a satisfactory description for the drift velocity:

$$V_2 = \frac{\xi D_0 BN}{[\tau_0 \exp(\alpha BN/k_B T)] D_0 BN + \xi k_B T} \tag{59}$$

with a maximum at some critical bias  $B_c$ , only after the mean-stay time (or “capture time”)  $\tau$  is assumed to be of the form  $\tau = \tau_0 \exp(\Delta F/k_B T)$ , where the free energy difference  $\Delta F$  between a free (drifting) state and a “bound” state of the chain is given by the work of the total force,  $f_{tot} = BN$  over a finite displacement of the monomers,  $\alpha$ .

**VIII. DEWETTING OF THIN POLYMER FILMS**

Thin polymeric films have important industrial applications (e.g., as protective coatings, lubricants, adhesives, dielectric or nonlinear optic devices, etc.) and pose many fundamental problems of film stability [1,2,4]. An important question, therefore, is whether these films break up and spontaneously dewett the substrate, resulting in the formation of droplets. The

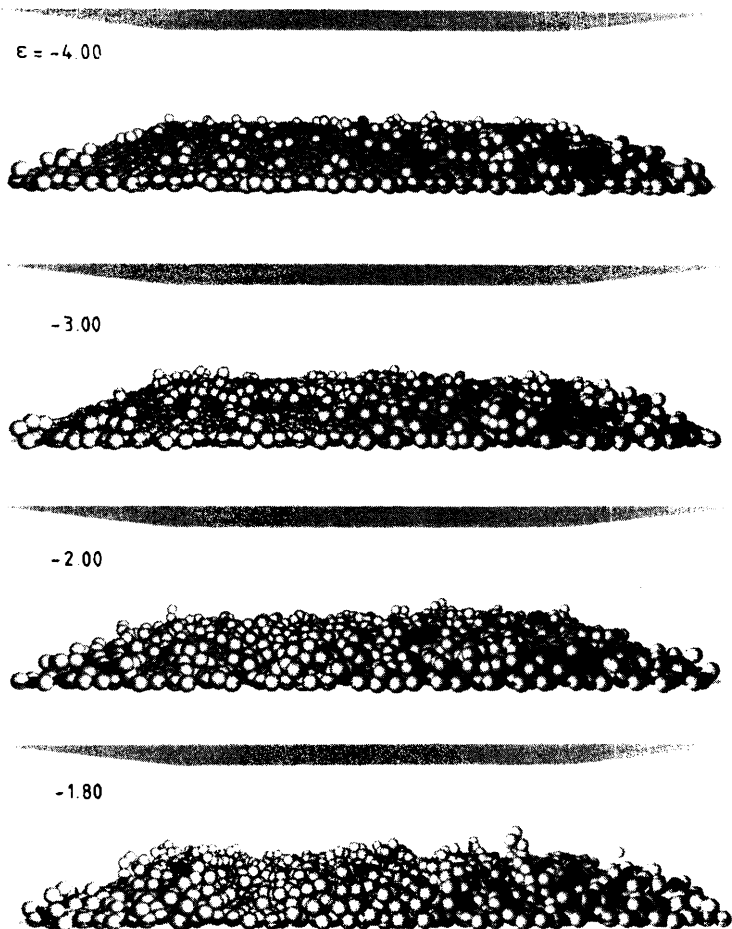


problem has been addressed both theoretically [107–110] and experimentally [111–117].

Often the polymer film is prepared in an unstable homogeneous state that is frozen in (e.g., by cooling the film underneath its glass transition temperature) and one is interested in how the film decays by droplet formation when the temperature is increased [112,113]. Theoretical analysis shows [109] that the local height  $h$  of the polymer–vapor interface becomes unstable against thickness fluctuations around the mean thickness  $\bar{h}$ . The fluctuations are characterized by some wave vector  $\mathbf{q}$  and a relaxation time  $\tau(\mathbf{q})$ . Stability is then controlled by the competition between the disjoining pressure due to van der Waals forces,  $P_d = \mathcal{A}/6\pi h^3$ , where  $\mathcal{A}$  is the Hamaker constant for solid–liquid and liquid–liquid interactions, and the Laplace pressure  $P_L = \gamma_{pv} \nabla^2 h$ , with  $\gamma_{pv}$  being the surface free energy of the film against the vapor. If  $\mathcal{A}$  is positive, fluctuations decay for all wavelengths, but for negative  $\mathcal{A}$  unstable modes develop, reminiscent of spinodal decomposition [118]. These unstable fluctuations then develop into holes, whose radius grows with time following a power law [110].

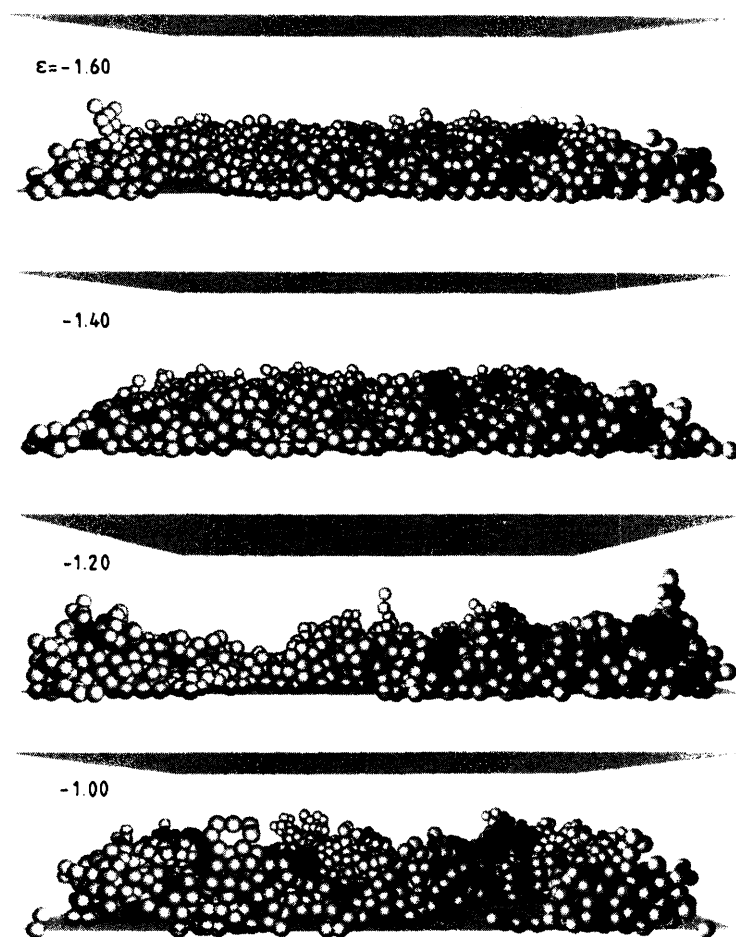
If one is interested in the character of the dewetting process on length and time scales, much smaller than the mesoscopic length scales (i.e., scales much larger than that of an individual monomer) adopted in the theoretical analysis, one can use again a coarse-grained bead–spring type model [23] to derive useful information on the interplay of the various parameters governing this phenomenon. Fig. 30 presents a series of snapshot pictures which demonstrate that in the framework of such models the initial stages of dewetting kinetics may be clearly observed. Of course, one should keep in mind that dynamic MC methods produce purely diffusive dynamics only [45], and thus can never account for hydrodynamic interactions which should be significant in the late stages of dewetting. Similarly to spinodal decomposition in polymer blends [119], where it is again known that hydrodynamic mechanisms control the late stages but are not so important during the early stages, one may expect that the neglect of hydrodynamic mechanisms would be justified for the length and time scales considered in the simulation.

With Eq. (10) as an adsorption potential, and keeping in mind that the model exhibits an adsorption transition for a single chain at  $\epsilon/k_B T_{\text{ads}} \approx -1.90 \pm 0.05$  [13], one can understand the overall distribution of density in the system, shown in Fig. 31. Unlike in a real system, it is obtained by varying the adsorption strength  $\epsilon/k_B T$  while remaining in the “poor solvent” regime  $k_B T = 0.5$ . For small strength of the adsorption potential ( $|\epsilon| \leq 1.2$ ) the density is only weakly enhanced within the range  $\delta < 1/8$ , and for  $z > \delta$  it is reduced in comparison with the center of the film (which is at  $z = 4$ ). However, with growing  $|\epsilon|$  the density of the adsorbed



(a)

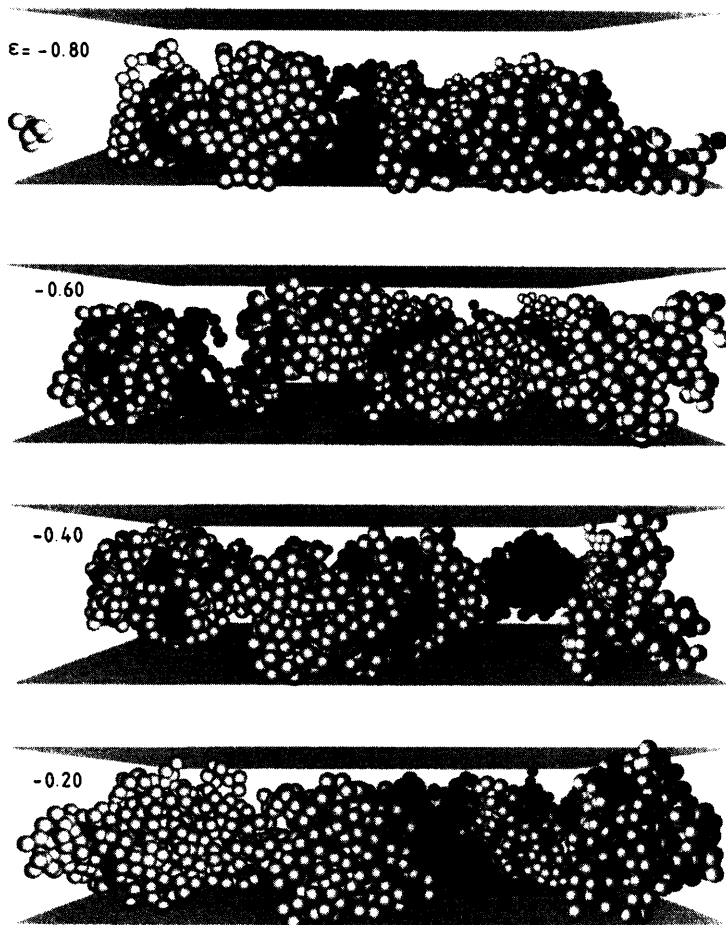
**FIG. 30** Snapshot pictures of the simulated system at thermal equilibrium for several values of the strength  $\epsilon$  of the adsorption potential. The simulation geometry is a  $L \times L \times D$  box with  $L = 32$ ,  $D = 8$ , and the upper plate is repulsive while at the lower plate also an attractive square-well potential of strength  $\epsilon$  and range  $\delta$  acts. The system contains 64 chains, each  $N = 32$  monomers long, at a temperature  $T = 0.5$  (for an intermolecular potential for which the  $\Theta$ -temperature is  $T_\theta \approx 0.62$  in dilute bulk solutions when  $N \rightarrow \infty$ ). Cases shown are: (a)  $\epsilon = -4.0, -3.0, -2.0, -1.8$ , (b)  $\epsilon = -1.6, -1.4, -1.2, -1.0$ , and (c)  $\epsilon = -0.8, -0.6, -0.4, -0.2$ . The systems have been equilibrated for  $2 \cdot 10^6$  MCS at  $\epsilon = -4.0$ , and this configuration was used as an initial state for the other runs [23].



(b)

**FIG. 30** Continued.

layer (for  $z \leq \delta$ ) increases rapidly, and a pronounced peak develops for  $z \approx l_0 = 0.7$ , due to a second layer of effective monomers once the first layer reaches the rather large density  $\phi \approx 2$  typical of melt [61,27,120]. This typical layering structure of fluids near an attractive wall has already been observed in our numeric experiments [16–18] for the good-solvent case where laterally the layer is always homogeneous whereas in the present case (poor solvent) inhomogeneities occur for small  $|\epsilon|$ . A useful quantity to



(c)

**FIG. 30** Continued.

characterize the lateral structure is the radial distribution function  $G(r)$  of the density around an effective monomer, constraining the direction of  $\vec{r}$  to be in the  $xy$ -plane (Fig. 32). Again, the behavior is readily understood: for  $r \leq 0.4$  the function  $G(r)$  is zero, due to repulsive interactions between the monomers. The peak of the nearest-neighbor shell has a double peak structure, the peak at  $r \approx 0.7$  being due to a bonded nearest neighbor (along the backbone of the chain), the peak at  $r \approx 0.8$  due to non-bonded neighbors.

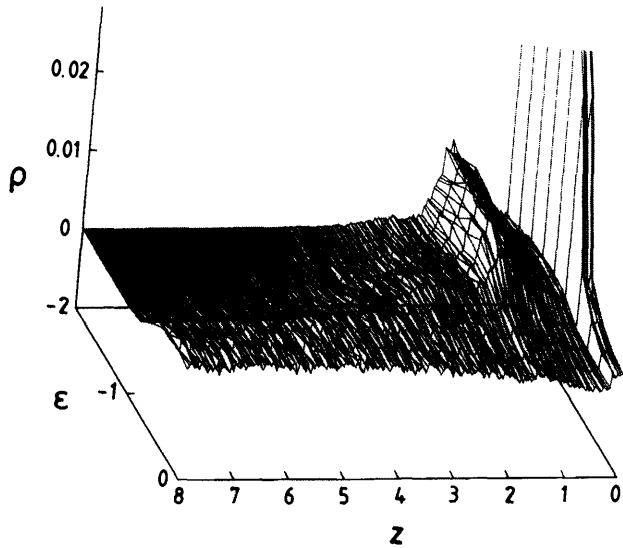


**FIG. 31** Density profile  $\rho(z)$  at the adsorbing wall as a function of  $\epsilon$  for a system of Fig. 30 [23].

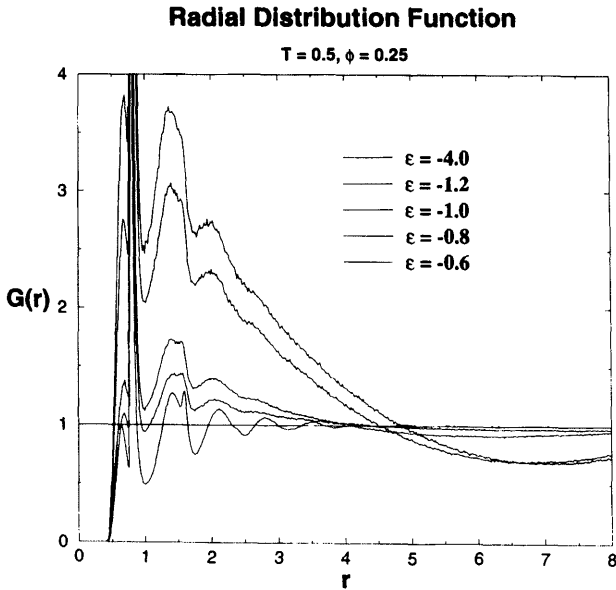


**FIG. 32** Radial density distribution function  $G(r)$  plotted vs  $r$  in the  $xy$ -plane for five choices of  $\epsilon$  [23].

While for strongly adsorbed layers (at  $\epsilon = -4.0$ ) the oscillations indicate regular structure, corresponding to dense packing of spheres, this fine structure is washed out for the less strongly adsorbed layers. Interestingly, for  $|\epsilon| \leq 1.2$ , where the adsorbed fraction of effective monomers is rather small,  $G(r)$  is not oscillating around unity and, after a few neighbor shells, decays monotonically with  $r$ . At a characteristic value  $r_c$ ,  $G(r_c) = 1$ , while for  $r > r_c$  a clearly developed minimum occurs. This is typical for systems which are laterally inhomogeneous on a large length scale  $r_c$ , as in fluids inside the liquid–gas coexistence region where  $r_c$  characterizes the length scale of the fluid drops that have formed. Of course, such a structure is only an intermediate stage of a phase separation process—in the final equilibrium state a macroscopically large fluid region (a huge droplet sitting on the substrate) should form. Such a coarsening process in polymers takes a prohibitively long time for our simulation, however, and the linear dimensions of our system are probably too small to apply quasimacroscopic concepts of wetting theory.

Fig. 33(a,b) shows a series of snapshot pictures as a result of a “computer experiment” probing the kinetics of dewetting. The local darkness of each snapshot indicates the local coverage of the substrate surface. Coverage fluctuations (white spots) appear rather early and get rapidly amplified. The substrate regions, covered with polymer, have very irregular surface initially and are connected with many weak links; later, these links disappear, and the droplets of adsorbed polymer compactify, a pattern similar to spinodal decomposition.

In order to characterize the dewetting kinetics more quantitatively, the time dependence of the average thickness of the film and the decrease of adsorbed fraction  $F_{\text{ads}}(t)$  with time (Fig. 34) are monitored. The standard interpretation of the behavior of such quantities is in terms of power laws,  $F_{\text{ads}}(t) \propto t^{-\alpha}$ , with some phenomenological exponents. From Fig. 34(a), where such power-law behavior is indeed observed, one finds that the exponent  $\alpha$  is about  $2/3$  or  $3/4$  for small  $|\epsilon|$  and then decreases smoothly to a value very close to zero at the critical value  $|\epsilon| \approx -1.2$  where the equilibrium adsorbed fraction  $F_{\text{ads}}^{\text{eq}}(|\epsilon|)$  starts to be definitely nonzero. If, instead, one analyzes the time dependence of  $F_{\text{ads}}(t) - F_{\text{ads}}^{\text{eq}}(|\epsilon|)$ , one observes a collapse of the curves far from the critical adsorption strength with a new exponent,  $F_{\text{ads}}(t) - F_{\text{ads}}^{\text{eq}}(|\epsilon|) \propto t^{-0.39}$ .

Thus one may conclude that the observed behavior resembles qualitatively spinodal decomposition in the bulk, although the power laws describing droplet growth are presumably different. However, these late stages when a description with power laws and universal exponents apply have probably not yet been reached. It is also an open question to what extent the neglect of hydrodynamic interactions would be adequate in these late

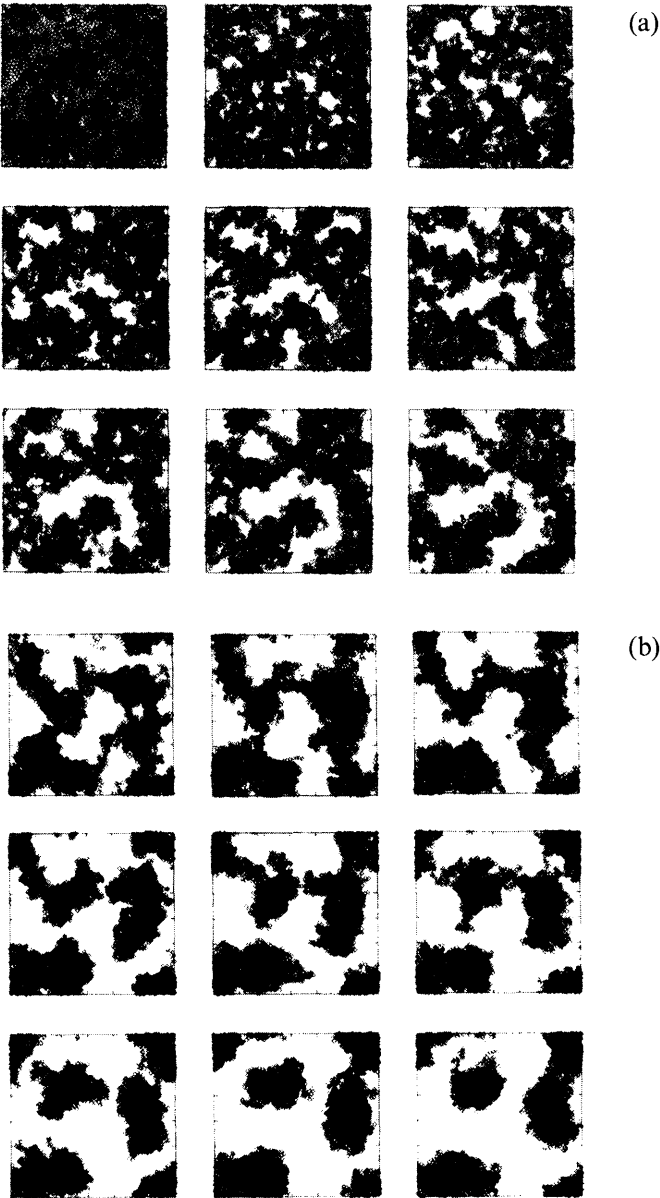


**FIG. 33** (a) Evolution of a system of 128 chains quenched at times  $t = 0$  from a state with  $\epsilon = -4.0$  (upper left corner) to  $\epsilon = -0.4$ . Snapshots are shown in time increments  $\Delta t = 65536$  MCS (in typewriter fashion from left to right). (b) Evolution of the same system but for time increments  $\Delta t = 524288$  MCS [23].

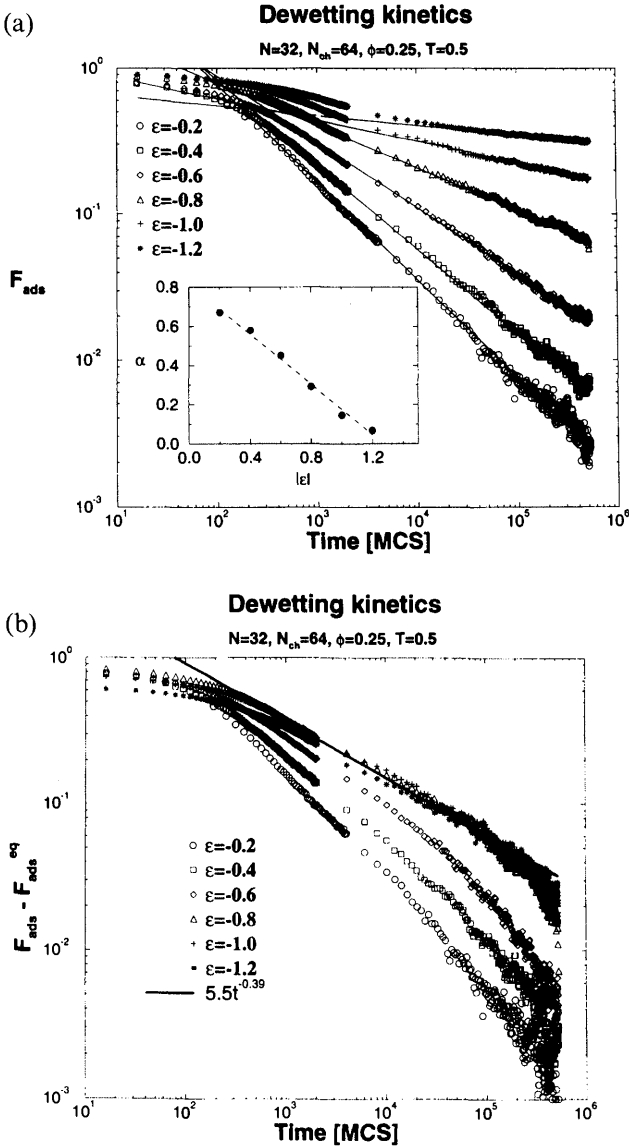


**FIG. 34** (a) Log-log plot of  $F_{ads}(t)$  vs time for an adsorbed layer containing 64 chains ( $\phi = 0.25$ ), where at time  $t = 0$  the adsorption energy strength  $\epsilon$  is reduced from  $\epsilon = -4.0$  to values between  $\epsilon = -1.2$  and  $\epsilon = -0.2$ , as indicated in the figure. Straight lines show a power law  $F_{ads}(t) \propto t^{-\alpha}$  over some intermediate range of times. The inset shows that the (effective) exponent  $\alpha$  can be fitted to a linear decrease with  $|\epsilon|$ . (b) The same data but with the “equilibrium” part  $F_{ads}^{eq}(|\epsilon|)$  subtracted [23].



stages. The answer should be sought probably by MD, requiring much larger systems and computing time.

## IX. CONCLUSION AND OUTLOOK

Polymers at interfaces show a subtle interplay, defined by the competition between enthalpic forces acting between the wall and the monomers, and various entropic contributions due to geometric constraints.

Although experiments always capture only partial aspects of this complex situation, simulations can elucidate this behavior in great detail for well-defined (but, at the present stage, greatly simplified) models. Many aspects of the behavior found in the work reviewed here can be understood in terms of scaling considerations and adaptation of the Rouse model. Even for these simplified models, however, some puzzling features remain, as, e.g., the anomalous diffusion in dense quasi-two-dimensional polymer systems, revealing some interesting interplay of single-chain dynamics with collective modes of many chains and possible failure of the Rouse model in these systems if the observed behavior is substantiated for very long chains. Clearly, faster computers and, possibly, novel, more efficient algorithms could provide essential information in the asymptotic regimes of longer chains, larger slit thicknesses, or denser porous media, where scaling concepts apply.

Future work should consider effects of variable chain stiffness, existence of rough or heterogeneous surfaces, effects of attractive walls on glass transition behavior, etc. Another interesting extension is to add solvent molecules explicitly, carrying out an MD simulation to incorporate effects of hydrodynamic interactions, which have been completely outside the scope of this review. The present simulational approach promises much insight into these problems and may possibly stimulate further experiments and contribute to their interpretation.

## ACKNOWLEDGMENT

This research has been supported by the Deutsche Forschungsgemeinschaft (DFG) under Grant No. 435-BUL-113/45.

## REFERENCES

1. S. Wu. *Polymer Interfaces and Adhesion*. New York: Marcel Dekker, 1982.
2. E. Eisenriegler. *Polymers near Surfaces*. Singapore: World Scientific, 1993.
3. I. C. Sanchez. In: I. Sanchez, ed. *Physics of Polymer Surfaces and Interfaces*. Boston: Butterworth-Heinemann, 1992.

4. G. J. Fleer, M. A. Cohen Stuart, J. M. H. Scheutens, T. Cosgrove, B. Vincent. *Polymers at Interfaces*. London: Chapman & Hall, 1993.
5. M. Tirrell, E. E. Parsonage. Structure and properties of polymers. In: E. Thomas, ed. *Materials Science and Technology*. Weinheim: VCH, 1993, Vol. 12, p. 653.
6. A. Halperin, M. Tirrell, T. P. Lodge. Tethered chains in polymer microstructures. *Adv Polym Sci* 100:31–71, 1992.
7. H. R. Brown. Chain mobility and pull-out effects in lubrication and friction. *Faraday Discuss Chem Sci* 98:47–54, 1994.
8. K. O'Connor, T. McLeish. Entangled dynamics of healing end-grafted chains at solid/polymer interface. *Faraday Discuss Chem Sci* 98:67–78, 1994.
9. K. Binder, P. Y. Lai, J. Wittmer. Monte Carlo simulations of chain dynamics in polymer brushes. *Faraday Discuss Chem Sci* 98:97–109, 1994.
10. L. Leger, H. Hervet, P. Silberzan, D. Frot. Dynamics of polymer chains close to a solid wall. In: D. Beysens, ed. *Dynamical Phenomena at Interfaces, Surfaces and Membranes*. New York: Nova Science, 1993, pp. 499–510.
11. K. Binder. General aspects of computer simulation techniques and their applications in polymer physics. In: K. Binder, ed. *Monte Carlo and Molecular Dynamics Simulations in Polymer Science*. New York: Oxford University Press, 1995, pp. 3–41.
12. D. Y. Yoon, M. Vacatello, G. D. Smith. Simulation studies of polymer melts at interfaces. In: K. Binder, ed. *Monte Carlo and Molecular Dynamics Simulations in Polymer Science*. New York: Oxford University Press, 1995, pp. 433–475.
13. A. Milchev, K. Binder. Static and dynamic properties of adsorbed chains at surfaces: Monte Carlo simulations of a bead-spring model. *Macromolecules* 29:343–354, 1996.
14. A. Milchev, W. Paul, K. Binder. Polymer chains confined into tubes with attractive walls: A Monte Carlo simulation. *Macromol Theory Simul* 3:305–323, 1994.
15. A. Milchev, K. Binder. Dynamics of polymer chains confined in slit-like pores. *J Physique II* 6:21–31, 1996.
16. A. Milchev, K. Binder. Polymer solutions confined in slit-like pores with attractive walls: An off-lattice Monte Carlo study of static properties and chain dynamics. *J Computer-Aided Mater Des* 2:167–181, 1995.
17. K. Binder, A. Milchev, J. Baschnagel. Simulation studies on the dynamics of polymers at interfaces. *Annu Rev Mater Sci* 26:107–134, 1996.
18. R. B. Pandey, A. Milchev, K. Binder. Semidilute and concentrated polymer solutions near attractive walls: Dynamic Monte Carlo simulation of density and pressure profiles of a coarse-grained model. *Macromolecules* 30:1194–1204, 1997.
19. A. Milchev, K. Binder. A polymer chain between two parallel repulsive walls: A Monte Carlo test of scaling behavior. *Europ Phys J B* 3:477–484, 1998.
20. V. Yamakov, A. Milchev. Diffusion of a polymer chain in a porous medium. *Phys Rev E* 55:1704–1712, 1997.

21. V. Yamakov, A. Milchev. Polymer chain in a flow through a porous medium: A Monte Carlo simulation. *Phys Rev E* 56:7043–7052, 1997.
22. V. Yamakov, D. Stauffer, A. Milchev, G. M. Foo, R. B. Pandey. Crossover dynamics for polymer simulation in porous media. *Phys Rev Lett* 79:2356–2358, 1997.
23. A. Milchev, K. Binder. Dewetting of thin polymer films adsorbed on solid substrates: A Monte Carlo simulation of the early stages. *J Chem Phys* 108:1978–1989, 1997.
24. K. F. Mansfield, D. N. Theodoru. Interfacial structure and dynamics of macromolecular liquids: A Monte Carlo simulation approach. *Macromolecules* 22:3143–3152, 1989.
25. T. Matsuda, G. D. Smith, R. G. Winkler, D. Y. Yoon. Stochastic dynamics simulations of *n*-alkane melts confined between solid surfaces: Influence of surface properties and comparison with Schetjens–Fleer theory. *Macromolecules* 28:165–173, 1995.
26. P. G. de Gennes. *Scaling Concepts in Polymer Physics*. Ithaca, NY: Cornell University Press, 1979.
27. A. Milchev, W. Paul, K. Binder. Off-lattice Monte Carlo simulation of dilute and concentrated polymer solutions under theta conditions. *J Chem Phys* 99:4786–4798, 1993.
28. H. Nakanishi, M. E. Fisher. Critical point shifts in films. *J Chem Phys* 7–8:3279–3293, 1983.
29. G. S. Grest, M. Murat. Computer simulations of tethered chains. In: K. Binder, ed. *Monte Carlo and Molecular Dynamics Simulations in Polymer Science*. New York: Oxford University Press, 1995, pp. 476–578.
30. H. Yu. Polymer monolayer dynamics by light scattering. In: *Polymer Interfaces and Adhesion*. Boston: Butterworth–Heinemann, 1992, p. 263.
31. S. Granick. Dynamics of adsorption and desorption at polymer/solid interfaces. In: *Polymer Interfaces and Adhesion*. Boston: Butterworth–Heinemann, 1992, p. 227.
32. A. N. Semenov, J. F. Joanny. Kinetics of adsorption of linear homopolymers onto flat surfaces: Rouse dynamics. *J Physique II* 5:859, 1995.
33. I. Bitsanis, G. Hadzioannou. Molecular dynamics simulations of the structure and dynamics of confined polymer melts. *J Chem Phys* 92:3827–3847, 1990.
34. P. Y. Lai. Statics and dynamics of a polymer chain adsorbed on a surface: Monte Carlo simulation using the bond fluctuation model. *Phys Rev E* 49:5420–5430, 1994.
35. E. Eisenriegler, K. Kremer, K. Binder. Adsorption of polymer chains at surfaces: Scaling and Monte Carlo analysis. *J Chem Phys* 77:6296–6320, 1982.
36. H. W. Diehl, S. Dietrich. Field theoretical approach to static critical phenomena in semi-infinite systems. *Z Phys B* 42:65, 1981.
37. P. E. Rouse. The theory of nonlinear viscoelastic properties of dilute solutions of scaling polymers. *J Chem Phys* 21:1273–1280, 1953.

38. M. Doi, S. F. Edwards. In: R. K. Adair, R. J. Elliott, eds. *The Theory of Polymer Dynamics*. Oxford: Clarendon, 1986.
39. B. H. Zimm. Dynamics of polymer molecules in dilute solutions: Viscoelasticity, flow birefringence and dielectric loss. *J Chem Phys* 24:269–279, 1956.
40. K. Kremer, K. Binder. Dynamics of polymer chains confined into tubes: Scaling theory and Monte Carlo simulations. *J Chem Phys* 81:6381–6394, 1984.
41. W. Paul, K. Binder, D. Heermann, K. Kremer. Dynamics of polymer solutions and melts. Reptation prediction and scaling of relaxation times. *J Chem Phys* 95:7726–7740, 1991.
42. G. B. McKenna. Glass formation and glassy behavior. In: C. Booth, ed. *Comprehensive Polymer Science*. New York: Pergamon, 2:311–362, 1989.
43. J. G. van Alsten, B. B. Sauer, D. J. Walsh. Polymer dynamics at the melt/solid interface: Experimental evidence of reduced center of mass mobility. *Macromolecules* 25:4046–4048, 1992.
44. B. Smit. Molecular dynamics simulations of amphiphilic molecules at liquid–liquid interface. *Phys Rev A* 37:3431–36, 1988.
45. K. Binder. Monte Carlo and molecular dynamics simulations of amorphous polymers. In: J. Bicerano, ed. *Computational Modeling of Polymers*. New York: Marcel Dekker, 1992, pp. 221–295.
46. E. A. Colbourn. *Computer Simulation of Polymers*. London: Longman Group, 1994.
47. S. Livne, H. Meirovitch. Computer simulation of long polymers adsorbed on a surface: I. Corrections to scaling in an ideal chain. *J Chem Phys* 88:4498–4506, 1988.
48. H. Meirovitch, S. Livne. II. Critical behavior of single self-avoiding walks. *J Chem Phys* 88:4507–4515, 1988.
49. F. Van Dieren, K. Kremer. Adsorption of a  $\Theta$ -polymer: Competition between mean field and multicritical behavior. *Europhys Lett* 4:569–576, 1987.
50. R. Hegger, P. Grassberger. Chain polymers near an adsorbing surface. *J Phys A: Math Gen* 27:4069–4081, 1994.
51. G. ten Brinke, D. Ausserre, G. Hadzioannou. Interaction between plates in a polymer melt. *J Chem Phys* 89:4374–4380, 1988.
52. I. Bitsanis, G. ten Brinke. A lattice Monte Carlo study of long chain conformations at a solid polymer-melt interface. *J Chem Phys* 99:3100–3111, 1993.
53. K. Kremer, K. Binder. Monte Carlo simulation of lattice models for macromolecules. *Comp Phys Rep* 7:259–310, 1988.
54. K. Kremer. Computer simulation of polymers. In: M. P. Allen, D. J. Tildesley, eds. *Computer Simulation in Chemical Physics*. Amsterdam: Kluwer, 1993, pp. 397–459.
55. M. N. Rosenbluth, A. W. Rosenbluth. Monte Carlo calculation of the average extension of molecular chains. *J Chem Phys* 23:356–359, 1955.
56. Z. Alexandrovicz. Monte Carlo simulation of chains with excluded volume: A way to evade simple attrition. *J Chem Phys* 51:561, 1969.

57. N. Metropolis, A. W. Rosenbluth, M. N. Rosenbluth, A. N. Teller, E. Teller. Equation of state calculation by fast computing machines. *J Chem Phys* 21:1087, 1953.
58. N. Madras, A. D. Sokal. The pivot algorithm: A highly efficient Monte Carlo method for the self-avoiding walk. *J Stat Phys* 50:109, 1988.
59. F. T. Wall, F. Mandel. Macromolecular dimensions obtained by an efficient Monte Carlo method without sample attrition. *J Chem Phys* 63:4592, 1975.
60. I. Carmesin, K. Kremer. The bond fluctuation method: a new effective algorithm for dynamics of polymers in all spatial dimensions. *Macromolecules* 21:2819–2823, 1988.
61. I. Gerroff, A. Milchev, W. Paul, K. Binder. A new off-lattice Monte Carlo model for polymers: A comparison of static and dynamic properties with the bond fluctuation model and application to random media. *J Chem Phys* 98:6526–6539, 1993.
62. A. Milchev, K. Binder. Anomalous diffusion and relaxation of collapsed polymer chains. *Europhys Lett* 26:671–676, 1994.
63. I. Webman, J. L. Lebowitz, M. H. Kalos. Monte-Carlo studies of a polymer between planes, crossover between dimensionalities. *J Physique* 41:579–583, 1980.
64. R. Dickman, C. K. Hall. High density Monte Carlo simulations of chain molecules: Bulk equation of state and density profile near walls. *J Chem Phys* 89:3168–3174, 1988.
65. S. K. Kumar, M. Vacatello, D. Y. Yoon. Off-lattice Monte Carlo simulations of polymer melts confined between two plates. *J Chem Phys* 89:5206–5215, 1988.
66. S. K. Kumar, M. Vacatello, D. Y. Yoon. Off-lattice Monte Carlo simulations of polymer melts confined between two plates. 2. Effects of chain length and plate separation. *Macromolecules* 23:2189–2197, 1990.
67. A. Yethiraj, C. K. Hall. Monte Carlo simulation of polymers confined between flat plates. *Macromolecules* 23:1865–1872, 1990.
68. C. W. Woodward, A. Yethiraj. Density functional theory for inhomogeneous polymer solutions. *J Chem Phys* 100:3181–3186, 1994.
69. A. Yethiraj. Monte Carlo simulation of confined semiflexible polymer melts. *J Chem Phys* 101:2489–2497, 1994.
70. G. Grest, K. Kremer. Molecular dynamics simulation for polymers in the presence of heat bath. *Phys Rev A* 33:3628–3631, 1986.
71. K. Kremer, G. Grest, I. Carmesin. Crossover from Rouse to reptation dynamics. *Phys Rev Lett* 61:566–569, 1988.
72. M. Daoud, P. G. de Gennes. Statics of macromolecular solutions trapped in small pores. *J Physique* 38:85–93, 1977.
73. J. F. Joanny, L. Leibler, P. G. de Gennes. Effects of polymer solutions on colloid stability. *J Polym Sci Polym Phys Ed* 17:1073–1084, 1979.
74. E. Eisenriegler. Universal density-force relations for polymers near a repulsive wall. *Phys Rev E* 55:3116–3123, 1997.

75. K. Binder. Critical behavior at surfaces. In: C. Domb, ed. *Phase Transitions and Critical Phenomena*. London, Academic Press, 1989, Vol. 8, pp. 2–144.
76. K. Binder, P. C. Hoehenberg. Phase transitions and static spin correlations in Ising models with free surfaces. *Phys Rev B* 6:3461–3487, 1972.
77. D. P. Landau, K. Binder. Monte Carlo study of surface phase transitions in the three-dimensional Ising model. *Phys Rev B* 41:4633–4645, 1980.
78. M. P. Allen, D. J. Tildesley. *Computer Simulations of Liquids*. Oxford: Clarendon Press, 1987.
79. For a recent review, see: I. Teraoka. Polymer solutions in confining geometries. *Prog Polym Sci* 21:89–149, 1996.
80. B. Derrida. Can disorder induce several phase transitions? *Phys Rep* 103:29–39, 1984.
81. A. B. Harris. Self-avoiding walks on random lattices. *Z Phys B* 49:347–349, 1983.
82. M. Kardar, G. Parisi, Y. C. Zhang. Dynamic scaling of growing interface. *Phys Rev Lett* 56:889–892, 1986.
83. M. Kardar, Y. C. Zhang. Scaling of directed polymers in random media. *Phys Rev Lett* 58:2087–2090, 1987.
84. A. K. Roy, B. K. Chakrabarti. Statistics of self-avoiding walks on random lattices. *Z Phys B* 55:131–136, 1984.
85. B. Duplantier, H. Saleur. Exact tricritical exponents for polymers at the  $\Theta$ -point in two dimensions. *Phys Rev Lett* 59:539–542, 1987.
86. A. R. Khokhlov, S. K. Nechaev. Polymer chains in an array of obstacles. *Phys Lett A* 112:156–160, 1985.
87. M. Muthukumar. Localization of a polymer manifold in quenched random media. *J Chem Phys* 90:4594–4603, 1989.
88. O. Lumpkin. Diffusion of a reptating polymer interacting with a random matrix. *Phys Rev E* 48:1910–1915, 1993.
89. S. V. Panyukov. Statistics of polymers in random media. *Zh Eksp Theor Fiz* 103:1287–1304, 1993. (Sov Phys JEPT 76:631–638, 1993.)
90. D. S. Cannel, F. Rondelez. Diffusion of polystyrene through microporous membranes. *Macromolecules* 13:1599–1602, 1980.
91. G. Guillot, L. Leger, F. Rondelez. Diffusion of large flexible polymer chains through model porous membranes. *Macromolecules* 8:2531–2537, 1985.
92. M. P. Bohrer, G. D. Paterson, P. J. Carrol. Hindered diffusion of dextran and ficoll in microporous membranes. *Macromolecules* 17:1170–1173, 1984.
93. M. T. Bishop, K. H. Langley, F. E. Karasz. Diffusion of a flexible polymer in a random porous material. *Phys Rev Lett* 57:1741–1744, 1986.
94. W. W. Graessley. Viscoelastic properties of entangled flexible polymers. *Faraday Symp Chem Soc* 18:7–27, 1983.
95. H. Kim, T. Chang, J. M. Yohanan, L. Wang, H. Yu. Polymer diffusion in linear matrices: Polystyrene in toluene. *Macromolecules* 19:2737–2744, 1986.
96. G. D. J. Phillies. Universal scaling equation for self-diffusion by macromolecules in solution. *Macromolecules* 19:2367–2376, 1986; Dynamics of polymers

- in concentrated solutions: The universal scaling equation derived. *Macromolecules* 20:558–564, 1987.
97. R. M. Briber, X. Lieu, B. L. Bauer. The collapse of free polymer chains in a network. *Science* 268:395–397, 1995.
  98. J. D. Honeycutt, D. Thirumalai. Influence of optimal cavity shapes on the size of polymer molecules in random media. *J Chem Phys* 93:6851–6858, 1990.
  99. D. Wu, K. Hui, D. Chandler. Monte Carlo study of polymers in equilibrium with random obstacles. *J Chem Phys* 96:835–841, 1991.
  100. N. Nemoto, M. Kishine, T. Inoue, T. Osaki. Tracer diffusion of linear polystyrene in entanglement networks. *Macromolecules* 23:659–664, 1990.
  101. N. A. Rotstein, T. P. Lodge. Tracer diffusion of linear polystyrenes in poly-(vinyl methyl ether) gels. *Macromolecules* 25:1316–1325, 1992.
  102. M. S. Jhon, G. Sekhon, R. Armstrong. The response of polymer molecules in a flow. In: I. Prigogine and S. A. Rice, eds. *Advances in Chemical Physics, Vol. LXVI*. New York: Wiley, 1987, p. 153.
  103. R. B. Pandey, J. L. Becklehimer. Computer simulation of the permeability of a porous sediment model. *Phys Rev E* 51:3341–3344, 1995.
  104. G. M. Foo, R. B. Pandey. Computer simulation study of the permeability of driven polymers through porous media. *Phys Rev E* 51:5738–5744, 1995.
  105. D. H. King, D. F. James. Analysis of the Rouse model in extensional flow. *J Chem Phys* 78:4749–4754, 1983.
  106. R. G. Larson. The unraveling of a polymer chain in a strong extensional flow. *Rheol Acta* 29:371–384, 1990.
  107. D. J. Srolowitz, S. A. Safran. Capillary instabilities in thin films. *J Appl Phys* 60:247–260, 1986.
  108. K. Sekimoto, R. Oguma, K. Kawasaki. Morphological stability analysis of partial wetting. *Ann Phys* 176:359–392, 1987.
  109. F. Brochard, J. Daillant. Drying of solids wetted by thin films. *Can J Phys* 68:1084–1088, 1990.
  110. F. Brochard-Wyart, P. G. de Gennes, H. Hervet, C. Redon. *Langmuir* 10:1566, 1994.
  111. C. Redon, F. Brochard-Wyart, F. Rondelez. Dynamics of wetting. *Phys Rev Lett* 66:715–718, 1991.
  112. G. Reiter. Dewetting of thin polymer films. *Phys Rev Lett* 68:75–78, 1992.
  113. G. Reiter. Unstable thin polymer films: rupture and dewetting process. *Langmuir* 9:1344–1351, 1993.
  114. R. Yershalmi-Rozen, J. Klein, L. J. Fetters. Suppression of rupture in thin non-wetting liquid films. *Science* 263:793–795, 1994.
  115. K. R. Shull, T. E. Karis. Dewetting dynamics for large equilibrium contact angles. *Langmuir* 10:334–339, 1994.
  116. A. Faldi, R. J. Composto, K. I. Winey. Unstable polymer bylayers: Morphology of dewetting. *Langmuir* 11:4855–4861, 1995.
  117. G. Henn, D. J. Bucknall, M. Stamm, P. Vanhoorne, R. Jerome. Chain end effects and dewetting of thin polymer films. *Macromolecules* 29:4305–4313, 1996.

118. J. D. Gunton, M. San Miguel, P. S. Sahni. The dynamics of first order phase transitions. In: C. Domb, ed. *Phase Transitions and Critical Phenomena*. London, Academic Press, 1987, Vol. 8, pp. 267–467.
119. K. Binder. Phase transitions in polymer blends and block copolymer melts: some recent developments. *Adv Polym Sci* 112:181–299, 1994.
120. A. Milchev, K. Binder. Osmotic pressure, atomic pressure and the virial equation of state of polymer solutions: Monte Carlo simulations of a bead–spring model. *Macromol Theory Simul* 3:915–929, 1994.



# 13

## Systems Involving Surfactants

**FRIEDERIKE SCHMID** Max-Planck-Institut für Polymerforschung,  
Mainz, Germany

I.	Introduction	631
II.	Simulations in Atomic Detail	640
III.	Idealized Chain Models	642
	A. Lattice models	643
	B. Chain models in continuous space	647
	C. An application: Micelle shapes and size distributions	651
IV.	Lattice Spin Models and Others	655
	A. Bulk systems	656
	B. Bilayer and monolayer models	663
V.	Phenomenological Models	665
	A. Ginzburg–Landau models	666
	B. Random interfaces	667
	C. Conclusions	673
	References	673

### I. INTRODUCTION

Surfactants can be defined very generally as substances which influence the properties of interfaces and surfaces, and which can be used to tune them. Since most materials contain a certain amount of internal interfaces, the study of such substances has attracted longstanding interest. In this chapter, we shall be concerned with a particularly efficient class of surfactants, the amphiphiles

[1,2]. These are molecules which contain both hydrophilic and hydrophobic units (usually one or several hydrocarbon chains), such that they “love” and “hate” water at the same time. Familiar examples are lipids and alcohols. The effect of amphiphiles on interfaces between water and nonpolar phases can be quite dramatic. For example, tiny additions of good amphiphiles reduce the interfacial tension by several orders of magnitude. Amphiphiles are thus very efficient in promoting the dispersion of organic fluids in water and vice versa. Added in larger amounts, they associate into a variety of structures, filling the material with internal interfaces which shield the oil molecules—or in the absence of oil the hydrophobic parts of the amphiphiles—from the water [3]. Some of the possible structures are depicted in Fig. 1. A very rich phase

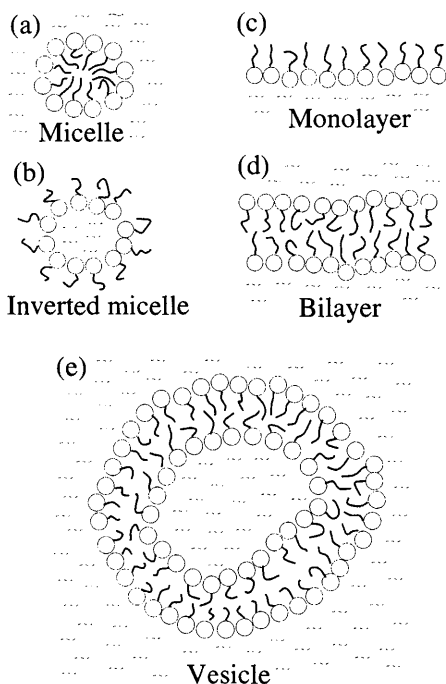


**FIG. 1** Self-assembled structures in amphiphilic systems: micellar structures (a) and (b) exist in aqueous solution as well as in ternary oil/water/amphiphile mixtures. In the latter case, they are swollen by the oil on the hydrophobic (tail) side. Monolayers (c) separate water from oil domains in ternary systems. Lipids in water tend to form bilayers (d) rather than micelles, since their hydrophobic block (two chains) is so compact and bulky, compared to the head group, that they cannot easily pack into a sphere [4]. At small concentrations, bilayers often close up to form vesicles (e). Some surfactants also form cylindrical (wormlike) micelles (not shown).

behavior emerges, including isotropic, but mesoscopically structured micellar and bicontinuous phases, and several ordered anisotropic phases (Fig. 2). Due to their emulsifying and self-organizing qualities, amphiphilic molecules are widely used in technology (salad dressing, detergents, soaps, oil recovery, as coating materials to stabilize colloidal systems, as nanoreactors for the preparation of nanoparticles, etc). as well as by nature (milk, biological membranes, liposomes etc.).

Schematic phase diagrams for binary mixtures of water with a strong amphiphile, and for ternary mixtures containing oil, water, and amphiphile, are shown in Fig. 3 (adapted from Refs. 7,8). Among the many interesting

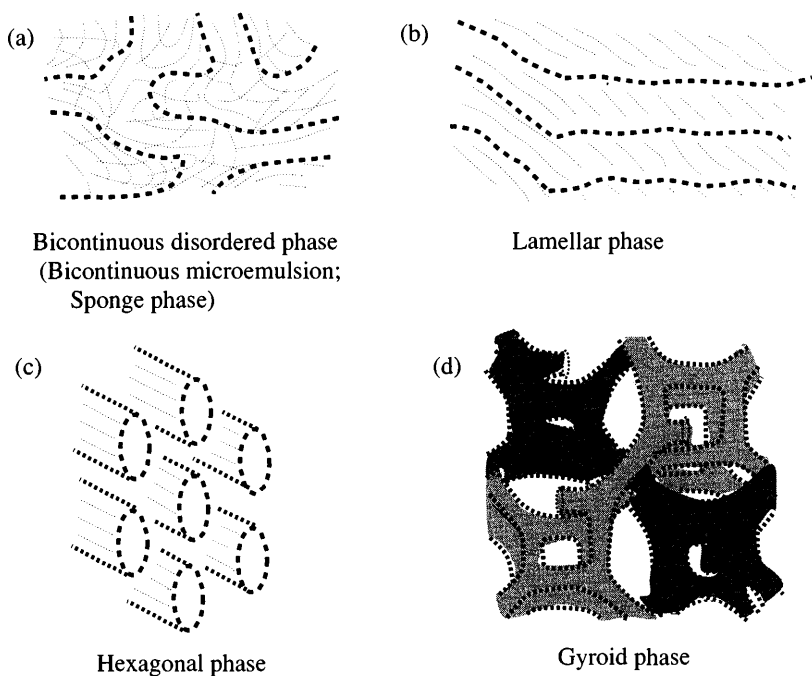


**FIG. 2** Selected structured phases in amphiphilic systems: again, these phases are present in both ternary oil/water/amphiphile mixtures and binary systems of water and amphiphile. In the first case, the dashed lines represent monolayers which separate oil from water domains; in the second case, they represent bilayers in (a) and (b), and surfaces of amphiphile aggregates in (c) and (d). Specifically, we show a macroscopically isotropic but microscopically structured bicontinuous phase, called sponge phase ( $L_3$  structure), in the binary mixture [5] and bicontinuous microemulsion in the ternary mixture [6] (a); the lamellar phase  $L_\alpha$  (b); the hexagonal phase  $H_1$  (c); and the gyroid phase  $G$  (d). The different shading in (d) distinguishes between the two constituting networks of the gyroid. See text for more explanation.

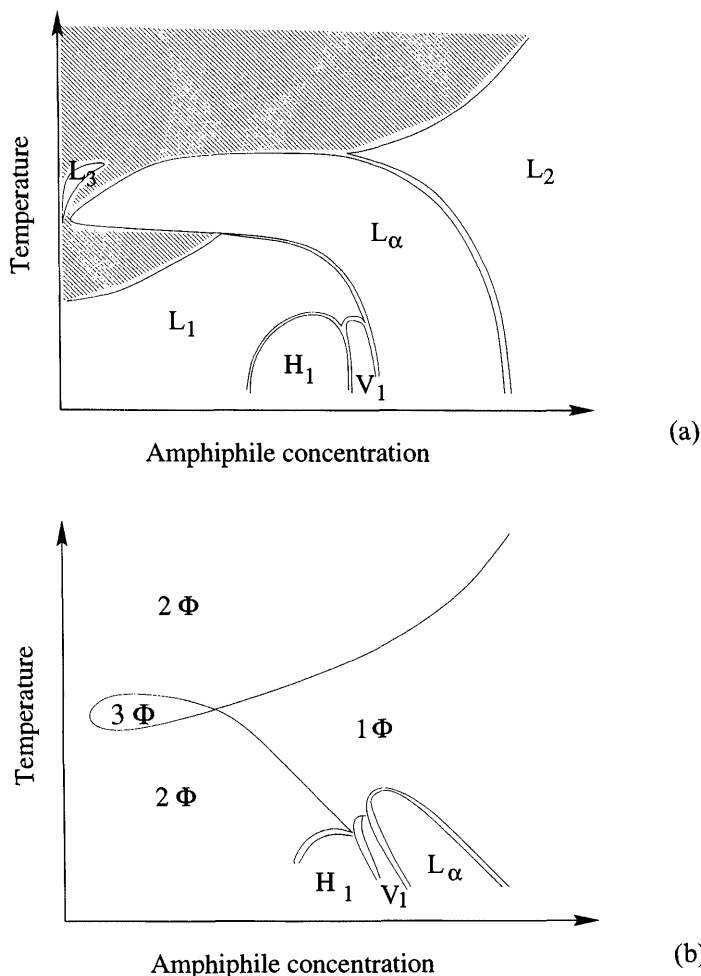


**FIG. 3** Schematic phase diagrams of amphiphilic systems with good anionic amphiphiles (a) for a binary water/amphiphile mixture (adapted from Strey et al. [7]), and (b) for a ternary mixture at an oil/water ratio of 1:1 (adapted from Kahlweit et al. [8]). Here  $L_\alpha$  denotes the lamellar phase,  $H_1$  the hexagonal phase and  $V_1$  a phase with cubic symmetry, presumably a gyroid phase. In the binary system (a),  $L_3$  represents the sponge phase and  $L_1, L_2$  two other isotropic liquid phases. Shading indicates regions of two phase coexistence. In the ternary system, the symbol  $1\Phi$  labels a single-phase region,  $2\Phi$  a region of two-phase coexistence between an oil-rich and a water-rich phase, and  $3\Phi$  a region of three-phase coexistence with an additional amphiphile rich "middle phase". In systems with strong amphiphiles, the coexisting middle phase is usually a structured microemulsion (cf. Fig. 2).

features of these phase diagrams, we mention in particular the existence of phases which are macroscopically isotropic and homogeneous, but structured on a mesoscopic scale. The short-range order can be inferred from the form of the structure functions (obtained, e.g., by small angle neutron scattering). In the case of microemulsions, the best indicator for structure is the water–water structure function. It can be fitted very well by the expression [9]

$$S(q) \propto (a + gq^2 + cq^4)^{-1} \quad (1)$$

For strongly structured microemulsions,  $g$  is negative, and the structure functions show a peak at nonzero wavevector  $q$ . As long as  $g < 2\sqrt{ca}$ , inverse Fourier transform of  $S(q)$  still reveals that the water–water correlation functions oscillate rather than decay monotonically. The lines in phase space where this oscillating behavior sets in are usually referred to as “disorder lines,” and those where the maximum of  $S(q)$  moves away from zero as “Lifshitz lines.”

Another phase which has attracted recent interest is the gyroid phase, a bicontinuous ordered phase with cubic symmetry (space group  $Ia\bar{3}d$ , cf. Fig. 2 (d) [10]). It consists of two interwoven but unconnected bicontinuous networks. The amphiphile sheets have a mean curvature which is close to constant and intermediate between that of the usually neighboring lamellar and hexagonal phases. The gyroid phase was first identified in lipid/water mixtures [11], and has been found in many related systems since then, among other, in copolymer blends [12].

In a somewhat wider sense, one can define amphiphiles as molecules in which chemically very different units are linked together. For example, the structures formed by A:B block copolymers in demixed A and/or B homopolymer melts and their phase behavior are very similar to those of classical amphiphiles in water and/or oil [13,14]. Copolymers are used not only to disperse immiscible homopolymer phases in one another, but also to create new, mesoscopically structured materials with unusual and interesting properties [15].

Another interesting class of phase transitions is that of internal transitions within amphiphilic monolayers or bilayers. In particular, monolayers of amphiphiles at the air/water interface (Langmuir monolayers) have been intensively studied in the past as experimentally fairly accessible model systems [16,17]. A schematic phase diagram for long chain fatty acids, alcohols, or lipids is shown in Fig. 4. On increasing the area per molecule, one observes two distinct coexistence regions between fluid phases: a transition from a highly diluted, “gas”-like phase into a more condensed “liquid expanded” phase, and a second transition into an even denser

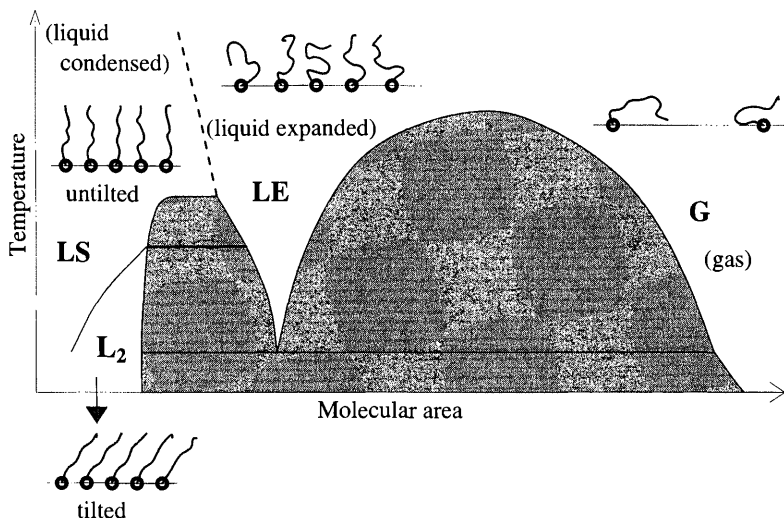


**FIG. 4** Phase diagram of Langmuir monolayers at low and intermediate surface coverage (schematic). Not shown are the various phases on the condensed side at high surface coverage.

“liquid condensed” region. The latter splits into a number of distinct phases which differ in their tilt order, positional order, and orientational order of the backbones of the  $(\text{CH}_2)_n$  chains. In bilayers, the liquid expanded/liquid condensed transition translates into the “main transition” or the “liquid/gel” transition, where the bilayer thickness, the amphiphile mobility, and the conformational order of the chains jump discontinuously as a function of the temperature [18]. On the ordered gel side various different phases exist, among them tilted phases and wavy phases (ripple phases). Bilayer phases are of special interest from a biological point of view, since the structure of biological membranes is coupled to the membrane functions [18].

This rich scenario, together with the wide range of applications of amphiphiles, is reflected by an equally wide range of problems which have been addressed in studies of amphiphilic systems. In particular, the interest has focused on the following rather different classes of topics:

- The influence of amphiphiles on interfacial properties: interfacial tension, wetting behavior, dynamical aspects such as the question of how small amounts of surfactant influence the kinetics of phase separation.
- The reasons for self-assembly and the mechanisms: necessary conditions for the aggregation into micelles, mono- or bilayers, structure of aggregates, distribution of aggregation numbers, etc.

- Mesoscopic structures and phases: vesicles and vesicle shapes, structured phases and phase behavior of amphiphilic systems.
- The inner structure of monolayers and bilayers, the liquid/gel transition, tilt transitions, mixed layers, etc.

A wide range of length scales and time scales is involved in these different problems, and a unified treatment of amphiphilic systems is practically impossible. On the smallest scales (up to 100 Å and 10–100 ns [19]), molecular dynamics simulations in atomic detail are feasible [20,21]. They provide information on the microscopic structure and the short-time dynamics of specific systems and have the big advantage that they allow for a direct, quantitative comparison with experiments. On the other hand, they rely heavily on the quality of the force fields. The choice of the model is the most important and the most critical step in an atomistic simulation. Other limitations come from the short accessible time scales. Phases must usually be preassembled since the times for self-assembly are very large. Hence it is difficult to decide whether a given structure is metastable or really corresponds to a true free energy minimum. Mapping out a phase diagram by a systematic variation of parameters (temperature, pressure) is generally out of reach. However, the force fields are improving, the computer technology is developing, and realistic simulations of amphiphilic systems can be pushed further and further. A large number of studies has dealt with the local properties of micelles, monolayers, and particularly of lipid bilayers. This is a rapidly growing field of research, and enormous progress has been achieved in the last few years. A brief overview over some of the activities will be given in Sec. II.

Nevertheless, large-scale phenomena and complicated phase diagrams cannot be investigated within realistic models at the moment, and this is not very likely to change soon. Therefore, theorists have often resorted to coarse-grained models, which capture the features of the substances believed to be essential for the properties of interest. Such models can provide qualitative and semiquantitative insight into the physics of these materials, and hopefully establish general relationships between microscopic and thermodynamic quantities.

What are the essential features of surfactant systems? An important ingredient is obviously the repulsion between water and nonpolar molecules or molecule parts, the hydrophobic force. This interaction is however highly nontrivial, and its analysis is still an active field of research [4,22,23]. Qualitatively, it is usually attributed to the strong orientational and positional correlations between nonpolar molecules in solution and the surrounding water molecules. The origin of the interaction is therefore entropic: free water forms a network of hydrogen bonds. In the neighborhood

of a nonpolar solute, the water molecules reorient and replace themselves so as to maintain the highest possible number of hydrogen bonds. The associated loss of entropy accounts for the dominant contribution to the hydrophobic interaction. This effect is of course far too involved to be easily included in a simplified model for amphiphilic systems. On the other hand, we have already noted that many characteristics of amphiphilic systems are also found in homopolymer/copolymer mixtures, where the interactions can be of a very different nature. Hence the precise origin of the interactions does not seem to be important for the phenomenology, and they can conceivably be replaced by simpler potentials for most purposes.

The second important attribute of amphiphiles is their affinity to both water and oil. This aspect is retained in the microscopic models, which will be discussed in Sec. III and IV. Oil, water, and surfactant molecules are represented by simplified pseudoparticles.

In some of these models (see Sec. III) the surfactants are still treated as flexible chains [24]. This allows one to study the role of the chain length and chain conformations. For example, the chain degrees of freedom are responsible for the internal phase transitions in monolayers and bilayers, in particular the liquid/gel transition. The chain length and chain architecture determine the efficiency of an amphiphile and thus influence the phase behavior. Moreover, they affect the shapes and size distributions of micelles. Chain models are usually fairly universal, in the sense that they can be used to study many different phenomena.

Models of a second type (Sec. IV) restrict themselves to a few very basic ingredients, e.g., the repulsion between oil and water and the orientation of the amphiphiles. They are less versatile than chain models and have to be specified in view of the particular problem one has in mind. On the other hand, they allow an efficient study of structures on intermediate length and time scales, while still establishing a connection with microscopic properties of the materials. Hence, they bridge between the microscopic approaches and the more phenomenological treatments which will be described below. Various microscopic models of this type have been constructed and used to study phase transitions in the bulk of amphiphilic systems, internal phase transitions in monolayers and bilayers, interfacial properties, and dynamical aspects such as the kinetics of phase separation between water and oil in the presence of amphiphiles.

Finally, when it comes to large scale structures and long-time dynamics, it often proves useful to drop the notion of particles altogether and to resort to phenomenological models (see Sec. V). Here again, one can distinguish between two main lines of approaches. Ginzburg-Landau theories [1,25] characterize the system by smooth "order parameters," which stand for local, coarse-grained averages of microscopic quantities. The coarse-graining



length is usually not specified, but is thought to be of the order of the bulk correlation length, i.e., a few molecular diameters. The order parameter fields are then distributed according to a free energy functional, which is typically constructed from symmetry considerations as an expansion in powers of the order parameter. Generic behavior is obtained as a function of the coefficients in the expansion. Unfortunately, the relation between the model parameters and the “real” parameters such as the pressure and the temperature is usually not obvious. On the other hand, Ginzburg–Landau theories have the advantage that they require relatively little input, which can in part be taken from experiments (e.g., from scattering experiments). Like the simple microscopic models, they have been applied to the study of phase behavior, interfaces, and the phase separation kinetics in amphiphilic mixtures. We will very briefly sketch the approach in Sec. A and refer to chapter 14 for a more detailed discussion.

The other class of phenomenological approaches subsumes the random surface theories (Sec. B). These reduce the system to a set of internal surfaces, supposedly filled with amphiphiles, which can be described by an effective interface Hamiltonian. The internal surfaces represent either bilayers or monolayers—bilayers in binary amphiphile–water mixtures, and monolayers in ternary mixtures, where the monolayers are assumed to separate oil domains from water domains. Random surface theories have been formulated on lattices and in the continuum. In the latter case, they are an interesting application of the membrane theories which are studied in many areas of physics, from general statistical field theory to elementary particle physics [26]. Random surface theories for amphiphilic systems have been used to calculate shapes and distributions of vesicles, and phase transitions [27–31].

We close these introductory remarks with a few comments on the methods which are actually used to study these models. They will for the most part be mentioned only very briefly. In the rest of this chapter, we shall focus mainly on computer simulations. Even those will not be explained in detail, for the simple reason that the models are too different and the simulation methods too many. Rather, we refer the reader to the available textbooks on simulation methods, e.g., Ref. 32–35, and discuss only a few technical aspects here. In the case of atomistically realistic models, simulations are indeed the only possible way to approach these systems. Idealized microscopic models have usually been explored extensively by mean field methods. Even those can become quite involved for complex models, especially for chain models. One particularly popular and successful method to deal with chain molecules has been the self-consistent field theory. In a nutshell, it treats chains as random walks in a position-dependent chemical potential, which depends in turn on the conformational distributions of the chains in

some self-consistent way. A recent survey of the method can be found in Ref. 36. Self-consistent field approaches provide extremely good descriptions of polymer blends (for which they were developed originally), since macromolecules have many contacts with other molecules and therefore show mean-field type behavior almost everywhere in phase space. In the case of short chain surfactants in low molecular weight solvents, the quantitative predictions are not quite as satisfactory. In particular, the stability of self-assembled aggregates can be overestimated by several orders of magnitude [37]. However, the local structure in the aggregates, local density profiles etc., are still in reasonable agreement with Monte Carlo simulations [37,40]. Self-consistent field theories have been used to study micelles [37,38] bilayers [38–40], and monolayers [41–43]. More details on the technique are given in Chapter 12 of this book.

The first step in studying phenomenological theories (Ginzburg–Landau theories and membrane theories) has usually been to minimize the free energy functional of the model. Fluctuations are then included at a later stage, e.g., using Monte Carlo simulations. The latter will be discussed in Sec. V and Chapter 14.

## II. SIMULATIONS IN ATOMIC DETAIL

Even among the so-called realistic simulations, there are still very different levels of coarse-graining. A full quantum chemical and *ab initio* treatment of a system as complex as amphiphilic system is practically impossible. Hence these systems are usually studied by classical molecular dynamics in combination with empirical interaction potentials, which have been optimized by fitting them to experimental data (structural data, latent heat of first-order transitions etc.) and/or to *ab initio* data (substructures of molecules). The functional form of these potentials may have little or nothing to do with the underlying physics of the interactions. For example, the forces between atoms of different chains are usually taken to be pairwise additive, even if the underlying interactions are nonadditive dispersion forces [4]. One has thus some freedom in the choice of the potentials, and many different forms are available. Hydrogen atoms are sometimes not included explicitly, but adsorbed into the more “important” neighbor atoms (united atom models vs full atomic detail). Bond angles and bond lengths are sometimes constrained to take fixed values (constrained models vs fully flexible models). Complicated head groups are sometimes replaced by simpler structures. The models also differ in the way charges and partial charges are treated. Some models do not include electrostatic interactions at all, i.e., they have no  $1/r$  terms in the potentials. Others do, but truncate them at a certain distance,

and still others deal with them in full by Ewald summation methods [44]. Whether or not interactions are truncated obviously makes a difference [45]. One could hope that the long-range character of the interactions is not essential for the physics of amphiphilic systems, in which case one empirical potential is as promising as the other, as long as they all have been optimized independently. Note that long-range interactions are ignored in most of the more idealized treatments of amphiphilic systems. On the other hand, a careful treatment of the electrostatic interactions is crucial to reproduce the peculiarities of water, such as the dielectric properties [46].

After these introductory *caveats*, we review some of the work that has been done in realistic simulations of amphiphilic systems.

Perhaps the first simulation of a system with amphiphiles is due to Kox in 1980 [47], a model of a lipid monolayer. A number of simulations of monolayers at air/substrate interfaces have followed [48–56], which have been able to reproduce cooperative tilt effects of the hydrocarbon chains and tilt transitions as well as backbone ordering and different rotator phases [50,55]. Moreover, they have provided valuable insight on the density profiles and the distribution of defects in the chains [53,55]. The simulations are usually done at constant volume. In one case, the Gibbs ensemble is used to study the phase coexistence between the “gas” phase and the “liquid expanded” phase [56]. (In the Gibbs ensemble, two boxes are simulated in parallel, and particles can be exchanged between the boxes [57]. The two boxes are thus at pressure and chemical potential equilibrium: coexisting phases can be monitored in systems which contain no disturbing interfaces.) In most of the models, the amphiphiles are supported by a uniform continuum substrate, which could be water or any other polarizable material, on the hydrophilic side, and in contact with vacuum (“air”) on the hydrophobic side. The work of Alper et al. [49] focuses on the influence of an amphiphilic layer on a water substrate, therefore the water is treated explicitly. A few recent studies have also probed amphiphiles at oil/water interfaces [58–60] with explicit oil molecules; much work clearly remains to be done here. Rice and coworkers have investigated special systems, such as monolayers of fluorinated amphiphiles [61] and monolayers on Cs [62] and ice [63].

Bilayers have received even more attention. In the early studies, water has been replaced by a continuous medium as in the monolayer simulations [64–67]. Today’s bilayers are usually “fully hydrated”, i.e., water is included explicitly. Simulations have been done at constant volume [68–73] and at constant pressure or fixed surface tension [74–79]. In the latter case, the size of the simulation box automatically adjusts itself so as to optimize the area per molecule of the amphiphiles in the bilayer [33]. If the pressure tensor is chosen isotropic, bilayers with zero surface tension are obtained. Constant

(positive) surface tension can be enforced by choosing an anisotropic pressure tensor, which is smaller in the directions parallel to the bilayer [75,77,78]. A comparison of different simulation methods, different ensembles, different water models, and different hydrocarbon models, has been made recently by Tielemann and Berendsen [78].

Whereas the main challenge for the first bilayer simulations has been to obtain stable bilayers with properties (e.g., densities) which compare well with experiments, more and more complex problems can be tackled nowadays. For example, lipid bilayers were set up and compared in different phases (the fluid, the gel, the ripple phase) [67,68,76,81]. The formation of large pores and the structure of water in these water channels have been studied [80,81], and the forces acting on lipids which are pulled out of a membrane have been measured [82]. The bilayer systems themselves are also becoming more complex. Bilayers made of complicated amphiphiles such as unsaturated lipids have been considered [83,84]. The effect of adding cholesterol has been investigated [85,86]. An increasing number of studies are concerned with the important complex of lipid/protein interactions [87–89] and, in particular, with the structure of ion channels [90–92].

The third class of systems, which have been investigated relatively extensively by simulations in atomic detail, comprises micelles. Again, the first studies have ignored the water molecules and simply considered the conformations of amphiphiles which are confined into a shell of given spherical geometry [93,94]. Later studies focus on the stability of (preassembled) micelles in water, on the structure and mobility of the amphiphiles, and on the degree of water penetration into the hydrophilic shell and the hydrophobic core [73,95–99]. Reverse micelles have also been considered, as well in vacuum as in an explicit oil environment [100,101]. Simulations of more complex self-assembled structures are still in their infancy. Watanabe and Klein have investigated cylindrical hexagonal phases using simulation cells with appropriate boundary conditions [102]. The structure of the cylinders turns out to be comparable with that of spherical micelles in many respects (water penetration, conformational properties etc.). More recently, Kong et al. [103] have employed a simplified amphiphile model (ethoxy head group chains attached to a hydrocarbon continuum) to study the water-induced interactions between lamellae in a lamellar phase. They conclude that water restructuring plays an important part in stabilizing the lamellar phase.

### III. IDEALIZED CHAIN MODELS

In coarse-grained microscopic models, the amphiphiles, oil, and water molecules are still treated as individual particles, but their structure is very much

simplified. Molecular details are largely lost. For reasons of computational efficiency, coarse-grained models are often formulated on a lattice. This obviously introduces the danger of lattice artefacts; as we shall see, lattice models have nevertheless been used successfully in the study of various phenomena and turn out to be extremely powerful. Off-lattice models are computationally more costly but do not impose an *a priori* anisotropy on space, and are attracting growing interest.

## A. Lattice Models

The most complex and powerful coarse-grained models are those which retain the chain character of the amphiphile molecules.

In a class of “realistic” lattice models, hydrocarbon chains are placed on a diamond lattice in order to imitate the zigzag structure of the carbon backbones and the *trans* and *gauche* bonds. Such models have been used early on to study micelle structures [104], monolayers [105], and bilayers [106]. Levine and coworkers have introduced an even more sophisticated model, which allows one to consider unsaturated C=C bonds and stiffer molecules such as cholesterol: a monomer occupies several lattice sites on a cubic lattice, the saturated bonds between monomers are taken from a given set of allowed bonds with length  $\sqrt{5}$ , and torsional potentials are introduced to distinguish between “*trans*” and “*gauche*” conformations [107,108].

Most lattice models, however, abstract from the details of the hydrocarbon chain structure. The “monomers” of the model chains are then conceived as effective monomers, which represent several ( $\text{CH}_2$ ) (or other) units in the molecules. One particularly popular lattice model has been introduced by Larson et al. [24,109]. In this model, oil and water molecules occupy single sites of a cubic lattice, and amphiphiles are chains made of “tail” monomers  $T$  and “head” monomers  $H$ , which are identical to the oil and water particles, respectively. The amphiphile monomers are connected by bonds with one of the 26 nearest or diagonally nearest neighbors. Since the lattice is entirely filled with either oil, water, or amphiphile, one only has one independent (dimensionless) interaction parameter  $w/k_{\text{B}}T$ , the relative repulsion between oil and water particles or between tail and head monomers. The interaction range is chosen such that particles interact with their nearest neighbors and diagonally nearest neighbors, i.e., the coordination number is again 26. The phase behavior of the model is solely controlled by the architecture of the amphiphile. It has been studied for a number of systems by Larson himself and others [109–113] and turns out to be amazingly multifarious. Perhaps the most spectacular achievement of the model is that it seems to exhibit a gyroid phase [112] (cf. Fig. 2(d)). In a narrow concentration region, and if the size of the simulation box matches closely

the preferred spacing of the gyroid unit cell, the amphiphiles self-assemble spontaneously into a gyroid upon cooling. This may not be conclusive evidence that the gyroid is actually the phase with the lowest free energy in an infinitely extended system, but it nevertheless demonstrates impressively the power of simple lattice models. Some phase diagrams [112] for binary water/amphiphile systems are shown in Fig. 5. Their topology resembles that of experimental phase diagrams, i.e., the gyroid phase intrudes between the hexagonal phase and the lamellar phase, as an intermediate between a state where the amphiphilic sheets have high local curvature (the hexagonal phase) and one without local curvature (the lamellar phase).

The Larson model and Larson-type models have been widely used to study micelles [37,111,114–120], amphiphiles at oil/water interfaces [121,122] bilayers [117,123] and various other problems [125–128]. The models differ from each other in the range of the interactions and in the treatment of the amphiphile monomers. Other than in Larson's original model, most authors include only nearest-neighbor interactions, sometimes in combination with a

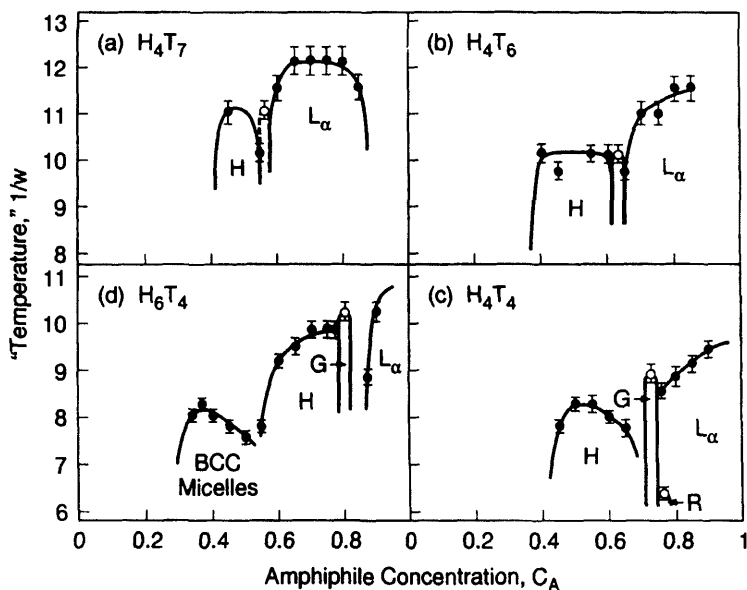


**FIG. 5** Phase diagrams of binary amphiphile/water systems in the Larson model. The amphiphile structures are (a)  $H_4T_7$ , (b)  $H_4T_6$ , (c)  $H_4T_4$ , and (d)  $H_6T_4$ . H denotes the hexagonal phase,  $L_\alpha$  the lamellar phase, G the gyroid phase, BCC a phase with spherical micelles in body-centered cubic arrangement, and R a rhombohedral-like mesh phase. (From Larson [112].)

different underlying lattice [120]. Some models stay with Larson's simplifying assumption that the amphiphile monomers are identical to oil or water particles [37,119,120], but most of them equip the amphiphiles with new types of particle, often even allowing for more than two different monomer species. A popular description, going back to Stauffer and coworkers [114] and to Bernardes and coworkers [115,123], adopts the language of the Ising model and assigns a spin  $S = -1$  to oil particles, a spin  $S = +1$  to water particles, and an integer spin ranging between  $-1$  and  $+2$  to surfactant monomers. The interaction energy is described by a Hamiltonian  $\mathcal{H} = -\epsilon \sum_{\langle ij \rangle} S_i S_j$ , where the sum  $\langle ij \rangle$  runs over nearest-neighbor sites on the lattice. Bernardes has demonstrated, that amphiphiles with the architecture  $(+1, 0, -1, -1, -1, -1)$  or  $(-1, -1, -1, -1, 0, 1, 1, 0, -1, -1, -1, -1)$  (two-tailed amphiphiles) can spontaneously self-assemble into vesicles [125,126]. A snapshot of such a vesicle is shown in Fig. 6.

A particularly simple lattice model has been utilized by Harris and Rice [129] and subsequently by Stettin et al. [130] to simulate Langmuir monolayers at the air/water interface: chains on a cubic lattice which are confined to a plane at one end. Haas et al. have used the bond-fluctuation model, a more sophisticated chain model which is common in polymer simulations, to study the same system [131]. Amphiphiles are modeled as short chains of monomers which occupy a cube of eight sites on a cubic lattice and are connected by bonds of variable length [132]. At high surface coverage, Haas et al. report various lattice artefacts. They conclude that the study

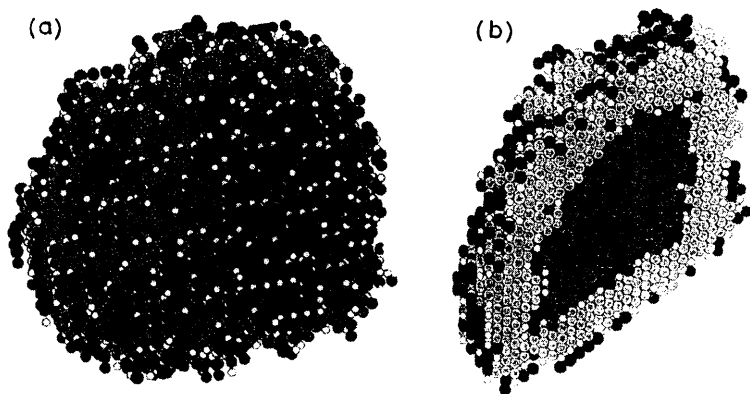


**FIG. 6** Configuration snapshot of a spontaneously formed vesicle from double-tailed amphiphiles in the Larson model: (a) entire vesicle; (b) vesicle cut in half in order to show its inner side. Black circles represent head particles (+1), gray circles tail particles (-1), white circles the neutral connecting particles (0). (From Bernardes [126].)

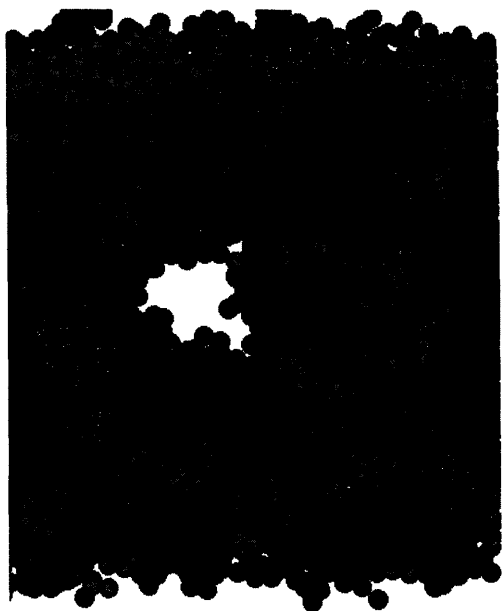


**FIG. 7** Snapshot of a bilayer conformation with a pore in the bond-fluctuation model. The dark spheres represent head particles, the light spheres tail particles. Around the pore, the amphiphiles rearrange so as to shield the bilayer interior from the solvent. (From Müller and Schick [133].)

of dense surfactant monolayers calls for the use of off-lattice models, especially if one is interested in phenomena such as collective tilt etc. Nevertheless, the bond-fluctuation model can be a useful tool in other contexts. For example, Müller and Schick [133] have employed it to study the formation and structure of pores in amphiphilic bilayers. From the bilayer undulations they were able to extract the bilayer tension, and from the distribution of pore sizes they could deduce the line tension of the pore edges. Fig. 7 shows an example of a pore. It is found to be “hydrophilic,” i.e., the amphiphiles around the pore rearrange themselves so as to shield the bilayer core from the unfavorable solvent.

Last in this section on lattice chain models, let us cite the somewhat different approach of Jennings et al. [134], who model the amphiphiles as single-site particles on a lattice but surround them with long hydrophobic chains (of chain length up to  $N = 80$ ). Their study focuses on the influence of amphiphiles on the conformations of nonpolar polymers. They report phenomena such as amphiphile-induced polymer collapse and the stabilization of lamellar phases.



Lattice models have the advantage that a number of very clever Monte Carlo moves have been developed for lattice polymers, which do not always carry over to continuum models very easily. For example, Nelson et al. use an algorithm which attempts to move vacancies rather than monomers [120], and thus allows one to simulate the dense cores of micelles very efficiently. This concept cannot be applied to off-lattice models in a straightforward way. On the other hand, a number of problems cannot be treated adequately on a lattice, especially those related to molecular orientations and nematic order. For this reason, chain models in continuous space are attracting growing interest.

## B. Chain Models in Continuous Space

The usual structure of off-lattice chain models is reminiscent of the Larson models: the water and oil particles are represented by spheres (beads), and the amphiphiles by chains of spheres which are joined together by harmonic springs

$$U_{ij}^b = k_b(|\vec{r}_i - \vec{r}_j| - b)^2/2 \quad (2)$$

Here a hard or smooth cutoff  $b^c$  is sometimes imposed, such that

$$U_{ij}^b = \infty \quad \text{for} \quad b - b^c < |\vec{r}_i - \vec{r}_j| < b + b^c$$

in order to ensure that the beads cannot move arbitrarily far apart from each other. Spheres of type  $i$  and  $j$  often interact via truncated and shifted Lennard-Jones potentials

$$U_{ij}^{\text{LJ}}(r) = \begin{cases} 4\epsilon_{ij}[(\sigma_{ij}/r)^{12} - (\sigma_{ij}/r)^6] + C_{ij} & r < R_{ij}^c \\ 0 & \text{otherwise} \end{cases} \quad (3)$$

where  $C_{ij}$  is chosen such that  $U_{ij}^{\text{LJ}}(r)$  is continuous everywhere. In most cases the interaction parameter  $\epsilon_{ij}$  is chosen species-independent,  $\epsilon_{ij} \equiv \epsilon$ , and the "sign" of the interaction is controlled by the cutoff length  $R_{ij}^c$ : purely repulsive interactions between hydrophilic and hydrophobic units are obtained by choosing  $R_{ij}^c = 2^{1/6}\sigma_{ij}$ . For the attractive interactions,  $R_{ij}^c = 2.5\sigma$  (most common) or  $2\sigma$  is often used. In addition, a bending potential is sometimes introduced which favors chain stretching and makes the chains stiffer. A model of this kind was first introduced by Smit et al. [135] and later employed to explore the interplay of micelle formation and amphiphile adsorption at an oil/water interface [136,137], the self-assembly of micelles in general [138–141], and that of bilayers [141]. In the case of binary systems, the model can be further simplified by ignoring the solvent particles. Even then, one can still observe and study self-assembling micelles very well [142–144].

The different surfactant models vary mostly in details. Karaborni et al. [139] explore the influence of different chain architectures on the micelle shapes. Inserting spacers between hydrophobic tails in a double-tailed amphiphile turns out to transform former spherical micelles into threadlike micelles. (A similar result was observed by Maiti and Chowdhury in the Larson model [118].) Götz and Lipowsky [141] replace the repulsive interactions between hydrophilic and hydrophobic beads by the softer potential  $U = 4\epsilon(\sigma/r)^9$  and introduce spontaneous tilt angles in the bending potential in some of their simulations. Harries and Ben-Shaul [40] and von Gottberg et al. [142] connect the beads by rigid rods, i.e., they choose an infinitely large spring constant  $k_b$ . Bhatthacharya et al. [142] compare nonionic surfactants with ionic surfactants and model the latter by including an additional Yukawa-type electrostatic interaction  $U(r) \propto \exp(-\kappa/r)$  between the head groups. Perhaps not surprisingly, the charged micelles show a much stronger ordering tendency than the neutral micelles.

A few groups replace the Lennard–Jones interactions by interactions of a different form, mostly ones with a much shorter interaction range [144,146]. Since most of the computation time in an off-lattice simulation is usually spent on the evaluation of interaction energies, such a measure can speed up the algorithm considerably. For example, Viduna et al. use a potential in which the interaction range can be tuned

$$U^M(r) = E_{ij}[e^{-2\alpha(r-\sigma)} - 2e^{-\alpha(r-\sigma)}] - C \quad \text{for } r < R_c \quad (4)$$

(Morse potential). The constant  $C$  is defined such that  $U^M(r) = 0$  at the cutoff distance  $R_c$ . The interaction range is determined by the parameter  $\alpha$ , which Viduna et al. choose very large,  $\alpha = 24$ . Hence the cutoff distance can be made small ( $R_c = 1.25\sigma$  in [144]). This model was first used by Gerroff et al. [147] and is discussed in some detail in Chapter 12 of this book.

Bead–spring models without explicit solvent have also been used to simulate bilayers [40,145,146] and Langmuir monolayers [148–152]. The amphiphiles are then forced into sheets by tethering the head groups to two-dimensional surfaces, either via a harmonic potential or via a rigid constraint.

Baumgärtner and coworkers [145,146] study lipid–protein interactions in lipid bilayers. The lipids are modeled as chains of hard spheres with heads tethered to two virtual surfaces, representing the two sides of the bilayer. Within this model, Baumgärtner [145] has investigated the influence of membrane curvature on the conformations of a long embedded chain (a “protein”). He predicts that the protein spontaneously localizes on the inner side of the membrane, due to the larger fluctuations of lipid density there. Sintès and Baumgärtner [146] have calculated the lipid-mediated interactions between cylindrical inclusions (“proteins”). Apart from the

usual depletion interaction at contact, they find that the lipids induce a net attractive force between the inclusions over the much wider range of  $\sigma < r < 6\sigma$ , where  $\sigma$  is the diameter of a lipid bead.

Simulations of monolayers have focused on internal phase transitions, e.g., between the expanded phase and the condensed phases, between different tilted phases, etc. These phenomena cannot be reproduced by models with purely repulsive interactions. Therefore, Haas et al. [148,149] represent the amphiphiles as stiff Lennard–Jones chains, with one end (the head bead) confined to move in a plane. In later versions of the model [150–152], the head bead interactions differ from those of the tail beads: they are taken to be purely repulsive, and the head size is variable.

Stadler et al. [150,151] have performed Monte Carlo simulations of this model at constant pressure and calculated the phase behavior for various different head sizes. It turns out to be amazingly rich. The phase diagram for chain length  $N = 7$  and heads of size  $1.2\sigma$  ( $\sigma$  being the diameter of the tail beads) is shown in Fig. 8. A disordered expanded phase is found as well as

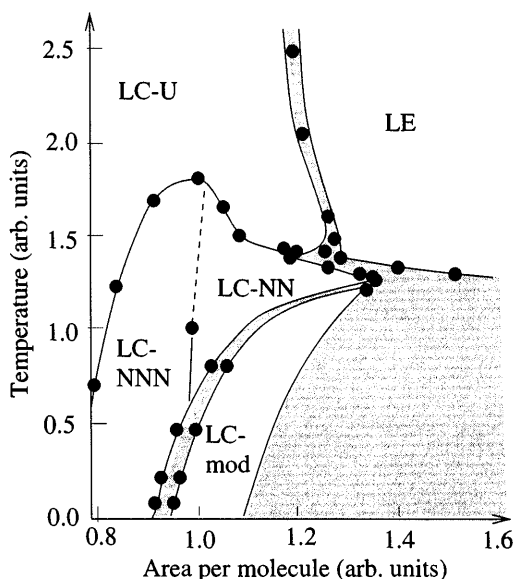


**FIG. 8** Phase diagram of a Langmuir monolayer in a model of grafted stiff Lennard–Jones chains. LE denotes a disordered expanded phase, LC–U a condensed phase with untilted chains, LC–NN and LC–NNN condensed phases with collective tilt towards nearest neighbors and next-nearest neighbors, respectively, and LC–mod a phase which has a superstructure and an intermediate direction of tilt. (From Stadler and Schmid [151].)

several condensed phases with different tilt order—a phase without collective tilt, one with tilt towards nearest neighbors, and one with tilt towards next-nearest neighbors. Particularly unexpected is a phase with a superstructure (LC-mod), where the direction of tilt is modulated and points on average towards an intermediate between nearest neighbors and next-nearest neighbors. The heads in the condensed phases are arranged on a hexagonal lattice, which is distorted in the direction of tilt. In order to avoid shear stress in the system, it is thus crucial to let fluctuate not only the size of the simulation box, but also its shape. Moreover, huge hysteresis effects were observed at some of the phase boundaries, and the free energies of the competing phases had to be calculated by thermodynamic integration methods [35] in order to locate the phase boundaries. Configuration snapshots of the expanded phase and the modulated condensed phase are shown in Fig. 9.

The modulated phase disappears for head sizes smaller than  $1.14\sigma$ . Modulations of this kind have not been observed in experiments so far.

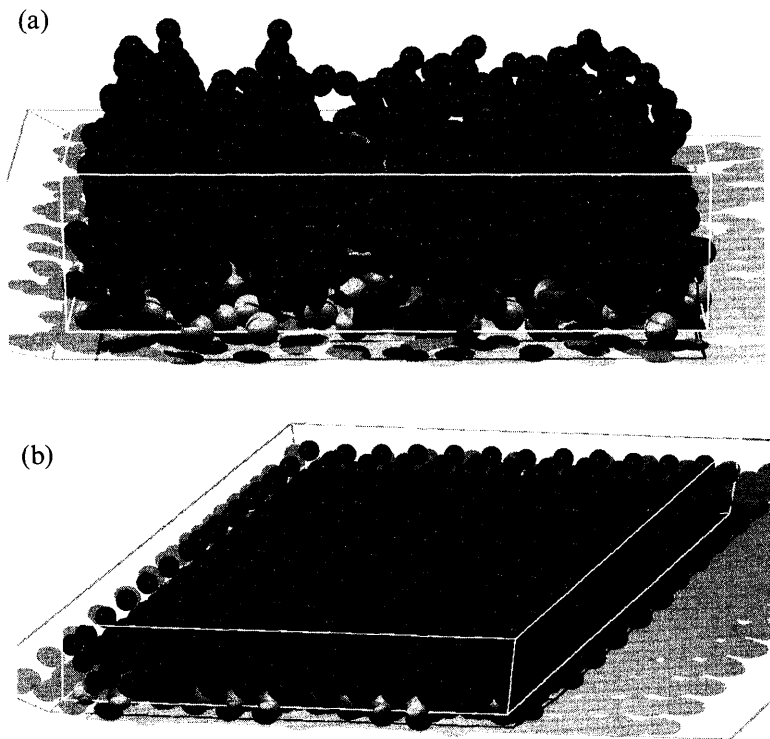


**FIG. 9** Configuration snapshots of the monolayer in Fig. 8(a) in the disordered expanded phase LE; (b) in the condensed modulated phase LC-mod.

However, Stadler et al. argue that the intensity of the satellite peaks which would be indicative of the superstructure is so low that they could not possibly be detected in X-ray measurements with the usual experimental resolution. Phases with intermediate tilt directions have been reported [16,17].

To complete this overview of chain models, we mention the dimer models, which represent the amphiphiles by just two units attached to each other [153–157]. They have been used to study curved bilayers [153], the kinetics of phase separation between oil and water in the presence of surfactants [155], and some aspects of self-assembled micelles [154,157] (see below).

### C. An Application: Micelle Shapes and Size Distributions

As has probably become obvious already, the study of micelles has been one of the big topics in simulations of systems with surfactants. We have cited many of the related publications in the previous sections. Here, we shall discuss some special aspects of micelle simulations in order to illustrate the use of idealized chain models for this type of problem.

The first important step in a micelle simulation obviously consists in defining a “micelle”. In simulations of systems with short-range interactions, this can be done in a relatively straightforward way: molecules are said to form an aggregate if they are in contact with each other, i.e., if they interact. Having set this straight, one can proceed to measure the concentration of *free*, i.e., non-interacting surfactants as a function of the total surfactant concentration. In self-assembling systems, the concentration of free surfactants saturates very soon after a first regime of linear increase, and stays constant or even decreases slightly [142] thereafter. Similarly, the chemical potential of the surfactant as a function of the surfactant concentration exhibits a marked kink, and turns from an initial increase almost into a constant [119,154]. The concentration at which this happens is called the critical micelle concentration (CMC). The sharp changes at the CMC can be understood from the competition between the translational entropy of the free surfactants and the energy which their hydrophobic tails gain in the micelles due to the reduced number of unfavorable water contacts. Let us consider surfactants which are part of an aggregate with the aggregation number  $N$ , and neglect the interactions between aggregates. Since the aggregates are in equilibrium with each other, the chemical potential at temperature  $T$  can be written as [4]

$$\mu = \mu_N^0 + k_B T / N \ln (f_N X_N / N) \quad (5)$$

for all  $N$ , where  $\mu_N^0$  denotes the mean interaction free energy in the aggregate, and the second term describes its translational entropy. Here  $X_N$  is the volume fraction of amphiphiles in an aggregate of size  $N$ , and the activity coefficient  $f_N$  is of order one. From Eqn. (5) one concludes immediately

$$f_N X_N = N [f_1 X_1 e^{(\mu_1^0 - \mu_N^0)/k_B T}]^N \quad (6)$$

Note that  $\mu_1^0 > \mu_N^0$ , since the surfactants gain energy in the aggregates. Large aggregates can therefore be expected to dominate at surfactant concentrations larger than

$$(X_1)_{\text{CMC}} \approx e^{(\mu_N^0 - \mu_1^0)/k_B T} \quad (7)$$

Beyond the CMC, surfactants which are added to the solution thus form micelles which are in equilibrium with the free surfactants. This explains why  $X_1$  and  $\mu$  level off at that concentration. Note that even though it is called "critical," the CMC is not related to a phase transition. Therefore, it is not defined unambiguously. In the simulations, some authors identify it with the concentration where more than half of the surfactants are assembled into aggregates [114]; others determine the intersection point of linear fits to the low concentration and the high concentration regime, either plotting the free surfactant concentration vs the total surfactant concentration  $\Phi$  [115], or plotting the surfactant chemical potential vs  $\ln(\Phi)$  [119].

We turn to the discussion of micelle size distributions and micelle shapes. In order to proceed with the analysis, one needs an expression for the interaction free energy  $\mu_N^0$  of surfactants in aggregates of size  $N$ . Following Israelachvili [4], we assume that the amphiphiles pack closely into aggregates, occupying a fixed volume per amphiphile  $v$ , and that  $\mu_N^0$  is simply given by the surface free energy of the aggregates:

$$\mu_N^0 = \frac{\gamma}{a} (a - a_0)^2 + \bar{\mu}^0 \quad (8)$$

where  $\gamma$  is the interfacial tension,  $a$  the surface area per molecule, and  $a_0$  the optimal head group area. In the case of spherical micelles, the surface area is given by  $a = (36\pi v^2)^{1/3} N^{-1/3}$ . The free energy (8) has a minimum at the aggregation number  $M = 36\pi v^2/a_0^3$ , and can be expanded around this minimum to yield

$$\mu_N^0 = \text{const.} + \frac{\gamma a_0}{9M^2} (N - M)^2 \quad (9)$$

Inserting this into Eq. (6), one obtains a size distribution for spherical micelles which is approximately Gaussian,

$$X_N^S \propto e^{-(N-M)^2/2\sigma^2} \quad \text{with} \quad \sigma = \sqrt{\frac{9k_B T M}{2\gamma a_0}} \quad (10)$$

Hence the sizes of spherical micelles are distributed around a most probable aggregation number  $M$ , which depends only on molecular details of the surfactants in this simplest approximation. Indeed, micelle size distributions at concentrations beyond the CMC have shown a marked peak at a given aggregation number in many simulations [37,111,112,117,119,138,144,154,157].

Larger aggregates seldom have spherical geometry, but tend to form cylindrical micelles. In this case, the diameter of the cylinders can usually be adjusted such that the head groups can cover their optimal head group area  $a_0$ , and the interaction free energy per surfactant reduces to the constant  $\bar{\mu}^0$ . The size distribution for cylindrical micelles is then exponential in the limit of large  $N$ ,

$$X_N^C \propto e^{-N\alpha} \quad \text{with} \quad \alpha = -\ln(f_1 X_1) - (\mu_1^0 - \bar{\mu}^0)/k_B T \quad (11)$$

At small  $N$ , correction terms come into play, which account for the ends of the cylinders. In particular, the aggregation number of cylindrical micelles in this simple picture must always be larger than  $M$ , the most probable aggregation number of a spherical micelle. Putting everything together, the expected size distribution has a peak at  $M$  which corresponds to spherical micelles, and an exponential tail at large  $N$  which is due to the contribution of cylindrical micelles.

That this is indeed so has been demonstrated neatly by Nelson et al. [120] in extensive simulations of the Larson model. Fig. 10 shows an example of a micellar size distribution for  $H_2T_2$  surfactants in an aqueous environment, at 7.5% surfactant volume fraction. The main peak is fitted to a Gaussian distribution (10), and the tail to an exponential distribution of the form (11),  $X_N \propto f(N) \exp(-\alpha N)$ , where the prefactor  $f(N)$  interpolates smoothly between  $f(N) = 0$  at  $N = M$  and  $f(N) = 1$  at  $N \gg M$ . The results confirm clearly the predicted exponential decay at large  $N$ . The shape of the micelles can be studied directly by comparing the different eigenvalues of the radius of gyration tensor of the aggregates. Nelson et al. find that they are approximately equal, as long as the aggregation number is smaller than the most probable size  $M \approx 40$ . Beyond that value, the largest eigenvalue grows linearly to become much larger than the other two. This observation is consistent with the picture that the peak of the distribution is generated by spherical micelles, and the tail by spherically capped cylindrical micelles.

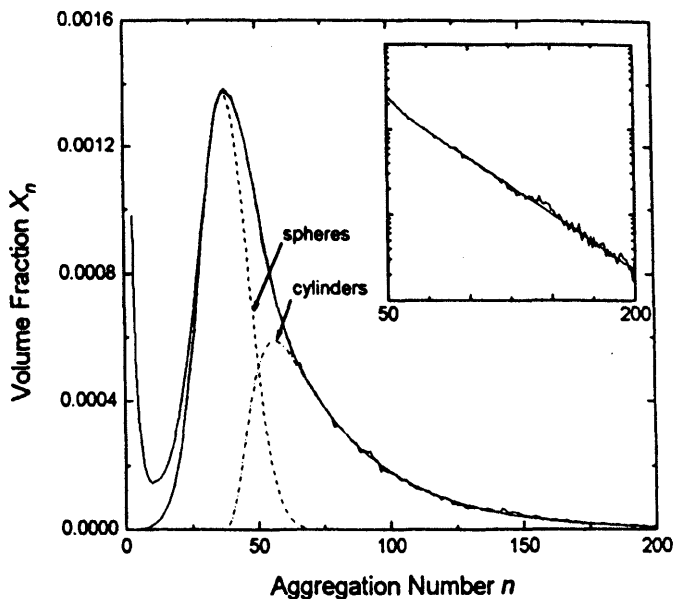


**FIG. 10** Micelle size distribution for  $H_2T_2$  surfactants within the Larson model. The dashed lines show fits to the expected form for spherical micelles (main peak) and cylindrical micelles (tail). Inset shows the tail of the distribution on a semi-logarithmic plot to demonstrate the exponential decay predicted for the cylindrical micelles. (From Nelson et al. [120].)

Whereas the evolution from spherical to cylindrical shapes as a function of aggregation number appears to be gradual in the simulations of Nelson et al., Viduna et al. report a rather dramatic transition at a well-defined aggregation number in their off-lattice simulations of  $H_2T_2$  micelles. The eigenvalues of the radius of gyration tensor are shown as a function of the aggregation number in Fig. 11. At this choice of parameters, the micelle size distribution exhibits a peak at  $N \approx 28$ . The shape parameters seem rather unaffected by this; one barely notices that the largest eigenvalue begins to increase a little bit faster than the other two. In contrast, at  $N \approx 47$ , it rises abruptly and attains a larger value, where it seems to level off again. This interesting “shape transition” clearly deserves further investigation in the future.

Other questions which will have to be studied in more detail refer to the role of micelle interactions. Note that they are not included in the approximate analysis sketched above. Von Gottberg et al. [142] have argued that excluded volume interactions between micelles are responsible for the slight



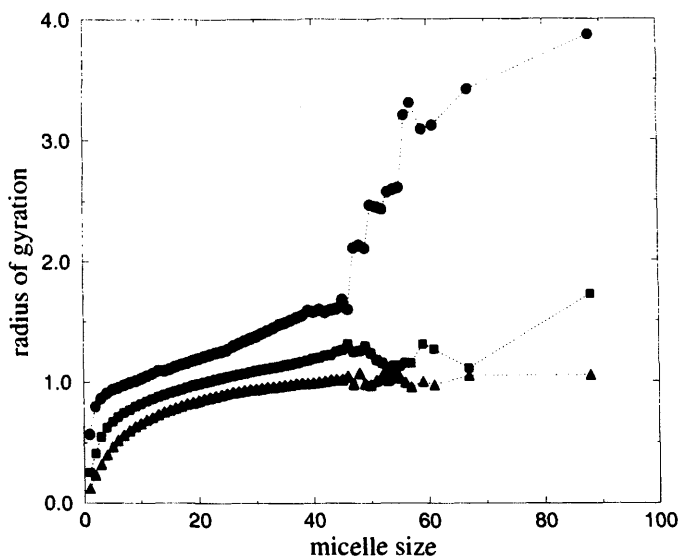


**FIG. 11** Eigenvalues of the radius of gyration tensor (dots: largest, squares: middle; triangles: smallest) of micelles vs aggregation number  $N$  in an off-lattice model of  $H_2T_2$  surfactants. The micelle size distribution for this particular system has a peak at  $N \approx 28$ . (From Viduna et al. [144].)

decrease of  $X_1$  at higher surfactant concentrations, which has been observed in many simulations [119,142,144]. Bolhuis and Frenkel [57] have studied the influence of intermicellar interactions on the micelle size distributions within a simple model, which approximates the micelles as hard spheres of variable size. Their results indicate that the interactions affect the size distribution in a way which is equivalent to shifting the chemical potential to an effectively lower value.

#### IV. LATTICE SPIN MODELS AND OTHERS

Whereas chain models still allow for a relatively unified treatment of various aspects of amphiphilic systems, such as their bulk phase behavior and the properties of monolayers and bilayers, this is no longer true for the even more idealized models at the next level of coarse graining. These usually have to be adapted very specifically to the problem one wishes to study.

One particularly favored class of models has been the models of Ising type, which represent the particles by states on sites or bonds of a lattice. Those intended to describe bulk amphiphilic systems have been reviewed

recently by Gompper and Schick in Ref. 1, and those developed for monolayers and bilayers by Dammann et al. in Ref. 158. Hence we shall only briefly recall their main features here, and focus on the discussion of their use in computer simulations.

## A. Bulk Systems

Lattice models for bulk mixtures have mostly been designed to describe features which are characteristic of systems with low amphiphile content. In particular, models for ternary oil/water/amphiphile systems are challenged to reproduce the reduction of the interfacial tension between water and oil in the presence of amphiphiles, and the existence of a structured disordered phase (a microemulsion) which coexists with an oil-rich and a water-rich phase. We recall that a "structured" phase is one in which correlation functions show oscillating behavior. Ordered "lamellar" phases have also been studied, but they are much more influenced by lattice artefacts here than in the case of the chain models.

The most senior among the lattice models is the Widom model, which was formulated as early as 1968 in its first version by Wheeler and Widom [159]. The water, oil, and amphiphile molecules are represented by (1,1), (-1,-1), and (1,-1) *bonds*, respectively, on a two-state Ising lattice. Hence oil and water are always separated by amphiphiles, by construction. If the particles are taken to be non-interacting otherwise, the model maps directly onto the Ising model with nearest neighbor interactions, where the role of the temperature is assumed by the chemical potential of the amphiphile. The resulting phase diagram is well known; one finds a region of oil/water coexistence and a critical point. In order to obtain more complex phase behavior, interactions between particles have to be added. For example, a penalty is often imposed on amphiphiles which meet at their one end. This introduces additional terms into the equivalent Ising Hamiltonian,

$$\mathcal{H} = -h \sum_i \sigma_i - J \sum_{ij} \sigma_i \sigma_j - 2M \sum_{ij}^I \sigma_i \sigma_j - M \sum_{ij}^{II} \sigma_i \sigma_j \quad (12)$$

where the second sum runs over nearest neighbors, the third over next nearest neighbors, and the fourth over fourth nearest neighbors. The first two terms drive the volume fraction of oil, water, and amphiphile in the system, the third term incorporates some sort of "bending energy" of the amphiphilic sheets, and the last term an interaction between sheets. The model exhibits a region of coexistence between oil- and water-rich phases, a region with various ordered phases, and a disordered structured phase. In the simple version (12), the transition between the oil/water region and the disordered region is continuous, hence the model does not recover three-

phase coexistence. However, this can be remedied by including suitable additional bond interactions [160]. The phase behavior of the model has been investigated in detail in Monte Carlo simulations, in particular by Stauffer and coworkers [160–162]. Chowdhury and coworkers have used it to study various other aspects of amphiphilic systems, such as the effect of confinement on a microemulsion [163], the lifetime, stability, and rupture of Newton black films [164], and the roughness of an amphiphilic film [165].

Even though the basic idea of the Widom model is certainly very appealing, the fact that it ignores the possibility that oil/water interfaces are not saturated with amphiphiles is a disadvantage in some respect. The influence of the amphiphiles on interfacial properties cannot be studied in principle; in particular, the reduction of the interfacial tension cannot be calculated. In a sense, the Widom model is not only the first microscopic lattice model, but also the first random interface model: configurations are described entirely by the conformations of their amphiphilic sheets.

As an alternative, Alexander [166] has proposed a model which places the oil and the water on lattice sites and distributes the amphiphiles on the bonds. The interactions between two neighboring oil and/or water particles depend on whether or not the connecting bond is occupied by an amphiphile. As long as the amphiphiles themselves do not interact with each other, the sum over possible bond states can be carried out independently, and the model turns out to be equivalent to an Ising model with temperature dependent interactions. Hence this simplest version does not capture the specific properties of amphiphilic systems, and additional amphiphile interactions have to be included. A variety of different interaction terms has been implemented: bending energies, edge energies, corner energies, special penalties if amphiphilic sheets meet or cross each other etc. Different versions of the model have been explored in Monte Carlo simulations by Ebner and coworkers [167] and Stockfisch and Wheeler [168]. The model displays lamellar phases and three-phase coexistence between an oil rich, a water-rich, and a disordered phase with intrinsic structure. Moreover, the amphiphiles were shown to reduce the interfacial tension between oil and water by a factor of up to 1000 [168]. The interfacial tension was determined with the histogram method of Binder [169], which will be discussed in more detail below.

More recently suggested models for bulk systems treat oil, water and amphiphiles on equal footing and place them all on lattice sites. They are thus basically lattice models for ternary fluids, which are generalized to capture the essential properties of the amphiphiles. Oil, water, and amphiphiles are represented by Ising spins  $S = -1, 0$  and  $+1$ . If one considers all possible nearest-neighbor interactions between these three types of particle, one obtains a total number of three independent interaction parameters, and

two independent chemical potentials. In Ising language, the most general Hamiltonian then reads

$$\mathcal{H} = - \sum_{ij} [JS_i S_j + KS_i^2 S_j^2 + C(S_i^2 S_j + S_j^2 S_i)] - \sum_i [HS_i - \Delta S_i^2] \quad (13)$$

which is exactly the Hamiltonian of the Blume–Emery–Griffiths model [170]. Balanced systems with intrinsically identical oil and water particles are described by the set of parameters  $C = 0$  and  $H = 0$ .

The first extension of this model, which accounts for the special character of the amphiphiles, has been the three-component model introduced by Schick and Shih in 1987 [171]. They simply add an additional triplet interaction

$$\mathcal{H}_{\text{amp}} = -L \sum_{ijk} S_i (1 - S_j^2) S_k \quad (14)$$

between triplets  $(ijk)$  of sites in a line. At  $L < 0$ , this term imposes a energy penalty if an amphiphile is sitting between two oil or two water particles, and offers an extra energy reward if an amphiphile separates oil from water. The model exhibits a structured disordered phase, which may coexist with an oil-rich and a water-rich phase in three dimensions, and ordered “lamellar” phases. It has been examined in detail by mean-field theories and other analytical methods [1], but relatively seldom by computer simulations [172,174].

In order to illustrate the type of questions which can be addressed within such an idealized lattice model, we show a histogram of the normalized order parameters  $M = \sum_i S_i/N$  and  $Q = \sum_i S_i^2/N$  ( $N$  being the system size) in Fig. 12 [174] for a point in phase space, where oil- and water-rich phases coexist with a structured microemulsion. The peaks corresponding to the three phases are readily identified at  $M \approx \pm 1$  and  $M = 0$ . Moreover, one discerns a broad band at  $Q \approx 0.94$  which extends over nearly the whole range of  $M$ . The story behind this plot is the following. Based on mean-field arguments, Gompper and Schick [173] had made the prediction that a structured microemulsion should not wet the oil/water interface. This is indeed observed in systems with strongly structured microemulsions; however, it is not always true for weakly structured microemulsions [177]. One reason had already been pointed out by Gompper and Schick [173]: long-range van der Waals forces shift the wetting transition beyond the structured side of the disorder line. Other factors which usually influence phase transitions are fluctuations. The Monte Carlo study [174] aimed to elucidate this latter aspect.

Having obtained a set of histograms like Fig. 12 for different system sizes (using histogram reweighting methods [175] in larger systems), the proce-

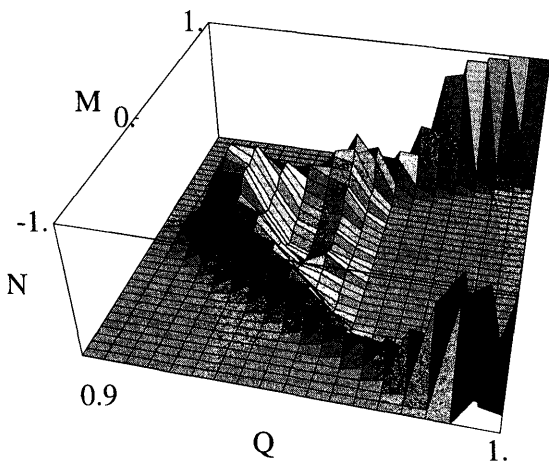


**FIG. 12** Histogram of  $Q$  and  $M$  in the three component model at three phase coexistence. Parameters are  $C = H = 0, K = 0.5, \Delta = -7, L = -5$  in units of  $J$ , and temperature  $k_B T/J = 2.78$ . System size is  $12 \times 12 \times 24$ . See text for further explanation. (From Schmid and Schick [174]. Copyright 1994 APS.)

dure was as follows: Assuming that the main contribution to the valleys between the peaks arises from configurations which contain two interfaces separating one-phase regions, the interfacial tension between these phases is given by [169]

$$\gamma/k_B T = -\frac{1}{2A} \ln(N_{\min}/N_{\max}) \quad (15)$$

where  $A$  is the interfacial area. The interfacial tensions  $\gamma_{om}$  and  $\gamma_{wm}$  between the oil- or water-rich phase and the microemulsion can thus be extracted directly from the valleys between the peaks at  $M = \pm 1$  and  $M = 0$ . Furthermore, one estimates the number of amphiphiles needed to form just two sheets of amphiphiles, and realizes that the corresponding configurations are just those which belong to the band at  $Q = 0.94$ . Hence the direct interfacial tension  $\gamma_{ow}$  between the oil- and the water-rich phase can be calculated from the area under that band. The microemulsion wets the oil/water interface if  $\gamma_{ow} < \gamma_{om} + \gamma_{wm}$ . Note that the numbers obtained for the interfacial tensions with this method are subject to strong finite-size corrections, which have to be analyzed carefully.

For the system studied in [174], it turns out that the oil/water interface is not wetted by the microemulsion, even though the latter is weakly structured. Hence fluctuations do shift the wetting transition beyond the disorder

line. This was explained later by Schmid and Schick as the effect of capillary wave fluctuations of the interface positions [176]. The amphiphiles in [174] are found to reduce the total interfacial tension by a factor of 100, a value which is consistent with experimental results for comparably weak amphiphiles [177].

The example illustrates how Monte Carlo studies of lattice models can deal with questions which reach far beyond the sheer calculation of phase diagrams. The reason why our particular problem could be studied with such success lies of course in the fact that it touches a rather fundamental aspect of the physics of amphiphilic systems—the interplay between structure and wetting behavior. In fact, the results should be universal and apply to all systems where structured, disordered phases coexist with non-structured phases. It is this universal character of many issues in surfactant physics which makes these systems so attractive for theoretical physicists.

After this short intermezzo, we turn back to introduce the last class of lattice models for amphiphiles, the vector models. Like the three-component model, they are based on the three state Ising model for ternary fluids; however, they extend it in such a way that they account for the orientations of the amphiphiles explicitly: amphiphiles (sites with  $S = 0$ ) are given an additional degree of freedom  $\vec{\tau}_i$ , a vector with length unity, which is sometimes constrained to point in one of the nearest neighbor directions, and sometimes completely free. It is set to zero on sites which are not occupied by amphiphiles. A possible interaction term which accounts for the peculiarity of the amphiphiles reads

$$\mathcal{H}_{\text{amph}} = -J \sum_{ij} (\sigma_i \vec{\tau}_i \vec{r}_{ji} + \sigma_j \vec{\tau}_j \vec{r}_{ij}) \quad (16)$$

where  $\vec{r}_{ij}$  denotes the vector which connects the site  $i$  to the site  $j$ . The new interaction thus awards an energy bonus if an amphiphile points towards a water molecule or away from an oil molecule. As long as the  $\tau_i$  do not interact with each other, one can get rid of them by integrating them out exactly. However, this generates a set of temperature-dependent multiplet interactions which are not necessarily easier to handle [1,178]. Probably the first Monte Carlo simulation of such a model (for a binary water/amphiphile system) was performed by Halley and Kolan [179] in 1988. Later, ternary systems were studied in two dimensions by Slotte [178] and Laradji et al. [180], and in three dimensions by Gunn and Dawson [181] Matsen and Sullivan [182] and Linhananta [183]. Fig. 13 shows a phase diagram of Matsen and Sullivan. As in the previously discussed models, vector models display lamellar phases, regions of oil/water coexistence, and a structured microemulsion. Fluctuations are found to have a particularly destabilizing effect on the lamellar phase [180,182] and to increase, in turn, the region of

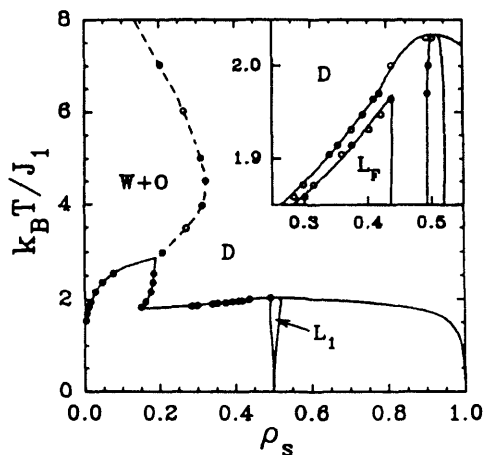


**FIG. 13** Phase diagram of a vector lattice model for a balanced ternary amphiphilic system in the temperature vs surfactant concentration plane. W + O denotes a region of coexistence between oil- and water-rich phases, D a disordered phase,  $L_1$  an ordered phase which consists of alternating oil, amphiphile, water, and again amphiphile sheets, and  $L_F$  an incommensurate lamellar phase (not present in mean field calculations). The data points are based on simulations at various system sizes on an fcc lattice. (From Matsen and Sullivan [182]. Copyright 1994 APS.)

stability of the microemulsion. This has a significant effect on the topology of the phase diagram in both two and three dimensions. In two dimensions, phase coexistence between the lamellar phase and the oil- and water-rich phases is entirely suppressed, and the lamellar phase is separated from the oil/water coexistence region by a microemulsion channel at all temperatures. Matsen [184] has conjectured that this should generally be the case for microemulsion models in two dimensions, and argued that, as a consequence, two dimensional models also fail to produce a triple line of coexistence between an oil-rich, a water-rich, and a disordered phase, as soon as the surfactant is efficient enough to produce a lamellar phase. Hence fluctuations suppress three phase coexistence of oil, water, and microemulsions in two dimensions. In three dimensions, the effect is just the opposite. The mean field phase diagram corresponding to Fig. 13 does not exhibit three-phase coexistence. By stabilizing the microemulsion, the fluctuation unveils a region of three-phase coexistence which would otherwise be covered by the coexistence region between the lamellar phase and the oil/water phases.

Note that Fig. 13 still has little similarity with the experimental phase diagram of ternary amphiphilic systems, Fig. 3b. In particular, the region of

three-phase coexistence is not confined between an upper and a lower critical endpoint, as in the experiments. This is, however, not surprising, since the lower critical endpoint is probably caused by orientational ordering in the water molecules, i.e., the increasing structure of the hydrogen bond network. In order to account for this effect, Matsen et al. [185] have proposed a vector model which attaches vector degrees of freedom to both the amphiphile and the water molecules. They were able to calculate a mean field phase diagram which is indeed remarkably similar to the experimental phase diagram for weak amphiphiles. The model has not been studied in Monte Carlo simulations so far.

A somewhat different type of vector model has been studied by Emerton, Boghosian and coworkers [186] in a set of recent papers. It is a lattice gas model: i.e., the sites of a (triangular) lattice can also be empty. Amphiphiles are assigned a dipole vector, and all particles are given a "velocity"  $\vec{c}_i$ , which points in one of the lattice directions. The dynamics of the system is described by collision processes: particles move along the direction of their velocity, collide, and are redistributed according to a Boltzmann weight under consideration of various conservation laws. The interaction energies are fairly complicated and will not be spelled out here. The basic feature of the model is that it includes hydrodynamic interactions and allows one to study dynamical phenomena under conditions of conserved momentum. At equilibrium, it exhibits the usual phases, lamellae, droplets and bicontinuous structures. It has been used mainly to investigate non-equilibrium phenomena, such as the kinetics of phase separation, shear induced phase transitions, etc.

Before moving on to the bilayer and monolayer models, we briefly discuss a few idealized microemulsion models in continuous space. In general, off-lattice models on this level of coarse graining have attracted much less interest than lattice models. Gunn and Dawson [187] have studied a mixture of Lennard-Jones spheres (water) and Gay-Berne ellipsoids (amphiphile) as a model for a binary amphiphile/water mixture (the Gay-Berne potential is a distorted Lennard-Jones potential). An additional interaction similar to (16) between amphiphiles and water is added in order to mimic the amphiphilic nature. The system is simulated under constant pressure and constant temperature conditions. It exhibits a crystalline lamellar phase, a fluid lamellar phase, and a disordered liquid crystal. Unfortunately, Gunn and Dawson do not seem to have pursued their studies of this model. Drouffe et al. [188] have studied self-assembly into two-dimensional layers using a two-dimensional model of hard spheres which are decorated with interacting intrinsic "orientations"  $\vec{n}$ . Two-dimensional aggregation into ring vesicles has also been examined by Saito and Morikawa [189] within a hard rod model. Recently, de Miguel and Telo da Gama [190] have introduced a



model which borrows elements from Drouffe's model and from the lattice vector models: particles are represented by hard spheres of equal diameter  $\sigma$ , with attractive (species dependent) van der Waals potentials. In addition, amphiphiles are given an extra dipole moment, which interacts with water and oil particles with a potential which is again reminiscent of the vector model potentials (16)

$$V_{\text{ani}} = \pm \epsilon (\sigma/r)^6 (\vec{n} \cdot \vec{r}/r). \quad (17)$$

The model has not been studied very intensely so far; in particular, none of the features which are characteristic for amphiphilic systems have been recovered yet. However, it is close enough to the successful vector models and simple enough that it might be a promising candidate for off-lattice simulations of idealized amphiphilic systems in the future.

## B. Bilayer and Monolayer Models

Whereas microscopic models for bulk systems incorporate the amphiphilic character and often the orientational properties of the surfactants as basic ingredients, models for bilayers and monolayers are constructed to reproduce internal transitions, such as the gel-fluid transition, and therefore concentrate on rather different aspects of the surfactant structure.

For example, Scott et al. [191] take interest in the ripple phase in bilayers and have constructed a lattice model which assigns two integer degrees of freedom to each site ("lipid") on the lattice: one Ising spin  $\sigma = \pm 1$ , which describes possible orientations of the head group, and one integer  $n \in \{0, \pm 1, \pm 2, \dots\}$ , which represents the displacement of the molecules perpendicular to the bilayer plane. Using a complicated Hamiltonian, borrowed from the chiral clock model, they indeed find a ripple phase with properties which are in decent agreement with experimental data. The interplay of head group orientation and ripple formation in lipid bilayers has also been studied by Schneider and Keller within a coarse-grained lipid model [192].

Other studies have been concerned with transitions between condensed phases in Langmuir monolayers. Tilting phase transitions have been studied in some detail within models of grafted rigid rods [193–195]. Swanson et al. [196] study a fluid of up to 4096 particles with fourfold symmetry in order to model rotator phase transitions. These are transitions from a state where the amphiphile tails are locked into each other to a state where they are free to rotate around. Interestingly, a hexatic phase is found in which positional correlations decay exponentially but the correlations between the orientations of the bonds connecting nearest neighbors decay only algebraically. Many condensed monolayer phases are indeed believed to be hexatic [16].

Most monolayer and bilayer studies focus on the gel–fluid transition, where the internal (conformational) degrees of freedom of lipids are important. In the most widely studied lattice model, the ten-state Pink model [197], they are built in as intrinsic degeneracies. The Pink model assigns one of ten states, denoted  $m$ , to every site (lipid) on a triangular lattice. Every state corresponds to a set of conformations: the lowest state  $m = 1$  to the (unique) all-*trans* configuration, the states  $m = 2 - 9$  to almost ordered chains with a few isolated chain defects, and the highest state  $m = 10$  to a completely disordered chain. Every state is characterized by its degeneracy  $D_m$  ( $D_1 = 1$ ,  $D_m \approx 4\text{--}100$  for  $m = 2\text{--}9$ ,  $D_{10} \approx 400,000$ ), its energy  $\epsilon_m$ , and the area  $A_m$  covered by the lipids. The latter is approximated by  $1/d_m$ , the inverse chain length in the state  $m$ . With this identification,  $D_m$ ,  $\epsilon_m$ , and  $A_m$  are single chain properties which can be calculated within an appropriate microscopic chain model. One further defines the occupation variable  $\mathcal{L}_{im}$ , which takes the value 1 if the lipid  $i$  is in the state  $m$ , and 0 otherwise. The Pink Hamiltonian is then written as

$$\mathcal{H}_{\text{Pink}} = \sum_i \sum_{m=1}^{10} (\epsilon_m + \Pi A_m) \mathcal{L}_{im} - \frac{J_0}{2} \sum_{ij} \sum_{m,n=0}^{10} I_m I_n \mathcal{L}_{im} \mathcal{L}_{jn} \quad (18)$$

where  $\Pi$  is an effective lateral pressure,  $J_0$  the strength of the van der Waals interaction between neighbor chains and  $I_m I_n$  an interaction matrix which accounts for the conformations of the chains and the distance between two chains, and can also be calculated from microscopic single chain properties. In practice, the model parameters have often been chosen so as to describe phospholipid monolayers and bilayers. The interactions between the monolayers in bilayer sheets are usually ignored. If one is not interested in a quantitative comparison with experiments, one can choose to study a simplified version of the model. For example, the two-state Doniach model [198] distinguishes between only two states, one ordered state with  $\epsilon_0 = 0$ , and one highly degenerate state with  $\epsilon_1 > 0$ . The interactions are such that only ordered lipids are capable of interacting with each other. A similarly simple model has been studied by Jerala et al. [199].

The Pink model is found to exhibit a gel–fluid transition for lipids with sufficiently long chains, which is weakly first order. The transition disappears in bilayers of shorter lipids, but it leaves a signature in that one observes strong lateral density fluctuations in a narrow temperature region [200,201]. In later studies, the model has been extended in many ways in order to explore various aspects of gel–fluid transitions [202]. For example, Mouritsen et al. [203] have investigated the interplay between chain melting and chain crystallization by coupling a two-state Doniach model or a ten-state Pink model to a Potts model. (The use of Potts models as models for

grain boundary melting has been suggested by Sahni et al. in 1983 [204]: every Potts state is then identified with a different domain orientation.) More recently, Nielsen and coworkers [205] have approached the same problem in a different fashion and placed the lipids on a random lattice rather than on a regular lattice. The random lattice was constructed as a network of hard disks on a plane, tethered to each other such that the tethers cannot exceed a given maximum length. The model has been simulated at constant pressure with a suitably adapted version of the dynamic-triangulation algorithm, which will be discussed in detail in Sec. V B. The interactions between lipids are taken to depend both on their conformational state and on their distance, which introduces very naturally a coupling between the conformation of the lipids and that of the random lattice. If this coupling is weak, the gel–fluid transition takes place at a higher temperature than the crystallization transition. However, the two transitions can be brought to concur if the coupling is chosen large enough.

Note that large density fluctuations are suppressed by construction in a random lattice model. In order to include them, one could simply simulate a mixture of hard disks with internal conformational degrees of freedom. Very simple models of this kind, where the conformational degrees of freedom affect only the size or the shape of the disks, have been studied by Fraser et al. [206]. They are found to exhibit a broad spectrum of possible phase transitions.

Zhang et al. [207] have discussed the effect of intermonolayer coupling on the gel–fluid transition. They find that any kind of coupling usually drives the transition to be more strongly first order. In other studies, the model has been generalized to incorporate hydrogen bonding and hydration in bilayers [208]. Moreover, it has been extended to include several molecular species, such that binary mixtures of lipids [209,210] and mixtures of cholesterol and lipids [203] could be studied. Special attention has been given to lipid–protein interactions [211,213]. Proteins in bilayers have been reviewed recently by Mouritsen [214].

## V. PHENOMENOLOGICAL MODELS

The last class of models, which are widely used to describe amphiphilic systems, comprises the phenomenological models. As opposed to all the previous models, they totally ignore the fact that amphiphilic fluids are composed of particles, and describe them by a few mesoscopic quantities. In doing so, they offer the possibility of clarifying the interrelations between different behaviors on a very general level, and of studying universal characteristics which are independent of the molecular details.

As already mentioned in the Introduction, phenomenological models for amphiphilic systems can be divided into two big classes: Ginzburg–Landau models and random interface models.

## A. Ginzburg–Landau Models

Ginzburg–Landau theories of amphiphiles have been reviewed at various places [1,25], among others, in Chapter 14 of this book. Hence we shall be brief in this subsection.

The basic idea of a Ginzburg–Landau theory is to describe the system by a set of spatially varying “order parameter” fields, typically combinations of densities. One famous example is the one-order-parameter model of Gompper and Schick [173], which uses as the only variable  $\phi$ , the density difference between oil and water, distributed according to the free energy functional

$$\mathcal{F}\{\phi\} = \int d\vec{r} [c(\Delta\Phi)^2 + g(\phi)(\nabla\phi)^2 + f(\phi)] \quad (19)$$

Here the functions  $g(\phi)$  and  $f(\phi)$  are defined in a suitable way to produce the desired phase behavior (see Chapter 14). The amphiphile concentration does not appear explicitly in this model, but it influences the form of  $g(\phi)$ —in particular, its sign. Other models work with two order parameters, one for the difference between oil and water density and one for the amphiphile density. In addition, a vector order-parameter field sometimes accounts for the orientational degrees of freedom of the amphiphiles [1].

The equilibrium phase behavior of models of this kind has been investigated by various methods, including Monte Carlo sampling methods [215,216], since these allow one to account for fluctuation effects in a complete and straightforward way. However, the vast majority of computer simulations which have been dealing with Ginzburg–Landau models have employed them to study nonequilibrium phenomena. In particular, the phase separation kinetics in the presence of surfactants has attracted much interest. It was mostly investigated in two dimensions by Langevin simulations [217–221]. The differences lie in the particular form of the Ginzburg–Landau model and in the dynamical system which is examined. For example, Pätzold and Dawson [218] include hydrodynamic effects and couple the system to Navier–Stokes equations, whereas most other groups consider a simpler relaxation dynamics, with or without conserved order parameters. Kawakatsu et al. take special interest in situations where the surfactant molecule is much larger than the oil or water, i.e., a polymer. Therefore they work with a hybrid model, which treats the surfactants as particles and the difference of oil and water density by a Ginzburg–Landau

field [220]. Related models by the same authors represent all particle densities by continuous fields, but include long range interactions between the surfactants or extend the original hybrid model in other ways [221].

The phase separation process at late times  $t$  is usually governed by a law of the type  $R(t) \propto t^n$ , where  $R(t)$  is the characteristic domain size at time  $t$ , and  $n$  an exponent which depends on the universality class of the model and on the conservation laws in the dynamics. At the presence of amphiphiles, however, the situation is somewhat complicated by the fact that the amphiphiles aggregate at the interfaces and reduce the interfacial tension during the coarsening process, i.e., the interfacial tension depends on the time. This leads to a pronounced slowing down at late times. In order to quantify this effect, Laradji et al. [217,222] have proposed the scaling *ansatz*

$$R(t) = t^n f(\rho_s^x t) \quad \text{with} \quad x = 1/n \quad \text{in two dimensions} \quad (20)$$

The function  $f$  incorporates the screening effect of the surfactant, and  $\rho_s$  is the surfactant density. The exponent  $x$  can be derived from the observation that the total interface area at late times should be proportional to  $\rho_s$ . In two dimensions, this implies  $R(t) \propto 1/\rho_s$  and hence  $x = 1/n$ . The scaling form (20) was found to describe consistently data from Langevin simulations of systems with conserved order parameter (with  $n = 1/3$ ) [217], systems which evolve according to hydrodynamic equations (with  $n = 1/2$ ) [218], and also data from molecular dynamics of a microscopic off-lattice model (with  $n = 1/2$ ) [155]. The data collapse has not been quite as good in Langevin simulations which include thermal noise [218].

Langevin simulations of time-dependent Ginzburg–Landau models have also been performed to study other dynamical aspects of amphiphilic systems [223,224]. An attractive alternative approach is that of the Lattice–Boltzmann models, which take proper account of the hydrodynamics of the system. They have been used recently to study quenches from a disordered phase in a lamellar phase [225,226].

## B. Random Interfaces

Random interface models for ternary systems share the feature with the Widom model and the one-order-parameter Ginzburg–Landau theory (19) that the density of amphiphiles is not allowed to fluctuate independently, but is entirely determined by the distribution of oil and water. However, in contrast to the Ginzburg–Landau approach, they concentrate on the amphiphilic sheets. Self-assembly of amphiphiles into monolayers of given optimal density is premised, and the free energy of the system is reduced to effective free energies of its internal interfaces. In the same spirit, random interface models for binary systems postulate self-assembly into bilayers and intro-

duce an effective interface Hamiltonian to study the conformations of the bilayers.

For fluid membranes, in which neighbor relations are not maintained, the free energy of a membrane is often written in the form [27,30]

$$\beta\mathcal{H} = \int dS [\sigma + \lambda_S H + 2\kappa H^2 + \bar{\kappa} K] \quad (21)$$

Here  $dS$  denotes a surface element,  $H$  the local mean curvature, and  $K$  the local Gaussian curvature. They are derived from the two local radii of curvature  $R_1$  and  $R_2$  via  $H = (1/R_1 + 1/R_2)/2$  and  $K = 1/(R_1 R_2)$ . The parameter  $\sigma$  drives the total amount of interface in the system and is thus, in a sense, related to the chemical potential of the amphiphiles; it can also be interpreted as an interfacial free energy or a negative spreading pressure. The second term  $\lambda_S$  generates a preferred radius of curvature towards one side of the membrane; hence it breaks the symmetry of the two sides. The parameters  $\kappa$  and  $\bar{\kappa}$  denote the bending rigidity and the saddle-splay modulus, respectively. Note that the integral over the last term depends solely on the topology of the interfaces according to the Gauss–Bonnet theorem

$$\int dSK = 2\pi\chi_E, \quad \text{with} \quad \chi_E = 2(c - g) \quad (22)$$

where the Euler characteristic  $\chi_E$  counts the number of closed surfaces  $c$  (including cavities) minus the number of handles  $g$ .

How can one simulate such a system?

A relatively simple approach suggests itself if the interfaces are known to be almost flat. In that case, the interface position can be described by a single-valued function  $z(x, y)$ , where  $(x, y)$  are cartesian coordinates on a flat parallel reference plane. The functional (21) can be approximated by

$$\beta\mathcal{H} = \int dx dy \left[ \frac{\sigma}{2} (\nabla z)^2 + \frac{\kappa}{2} (\Delta z)^2 \right] \quad (23)$$

(Monge representation [1,27]). Due to the underlying cartesian coordinates, the discretization of this Hamiltonian is straightforward. Obviously, the Hamiltonian (23) does not really need to be studied by Monte Carlo simulation since it can be solved exactly. However, things become more interesting if one considers stacks of interacting membranes [227–339], or fluid membranes with locally varying elastic properties [230].

The model (23) is simple to study, but unfortunately not very widely applicable. In general, one is more interested in situations where the interfaces are free to fold around and to assume every possible conformation. A second possible approach is to switch over to a lattice formulation. This has been done by a number of groups [231–233]. The resulting models are very

similar to the Widom or Alexander model. As a first step, random surfaces are composed from plaquettes on a lattice. In models for ternary systems [231,232], these have to be closed, but they may be open in models for binary systems [233] (there is no reason why a bilayer should not end somewhere). Then, a Hamiltonian is introduced for these random surfaces which imposes penalties on plaquettes which meet at a right angle, which share a link with more than one other plaquette, etc.—in the case of open surfaces, also for edges and seams. A particularly elegant form has been used by Likos et al. [232]: they construct the Hamiltonian as a sum over the four Minkowski functionals in three dimensions, i.e., the volume, the area, the total mean curvature, and the Euler characteristic [234]. If the surfaces are closed, the Hamiltonian can then be mapped in a straightforward way onto an Ising model on the dual lattice, which has various pair and multiplet interactions. Since the models are so similar to the lattice models of Sec. III A, their phase behavior is comparable as well. One finds ordered phases, three-phase coexistence and a structured microemulsion in ternary systems, and a sponge phase in the binary system.

Thus random interfaces on lattices can be investigated rather efficiently. On the other hand, much analytical work has concentrated on systems described by Hamiltonians of precisely type (21), and off-lattice simulations of models which mimic (21) as closely as possible are clearly of interest. In order to perform such simulations, one first needs a method to generate the surfaces  $\{S\}$ , and second a way to discretize the Hamiltonian (21) in a suitable way.

A widely used method to generate surfaces is the dynamic random-triangulation algorithm [235,236], which we have already mentioned in Sec. IV B. Surfaces are modeled by triangular networks of spherical beads, linked by tethers of some given maximum length  $l_0$ . The tethers define the neighbor relations on the surface. In order to generate self-avoidance, the beads are equipped with hard core interactions, and the maximum tether length is chosen smaller than  $\sqrt{3}\sigma$ , where  $\sigma$  denotes the bead diameter [237]. The Monte Carlo algorithm involves two different types of step [158]: regular attempts to move single beads or clusters of beads in space, and attempts to change the connectivity of the network, i.e., to redistribute the tethers between the chains [158]. The latter is done by randomly cutting tethers and reattaching them between the four beads which form two neighboring triangles [235,236], as illustrated schematically in Fig. 14. Updates of the bead positions are subject to the constraint that the maximum tether length must not exceed  $l_0$ , and connectivity updates have to comply in addition with the requirement that at least three tethers are attached to one bead, and that two beads cannot be connected to each other by more than one tether. Otherwise, attempted updates are accepted or rejected according to a standard Metropolis prescription.

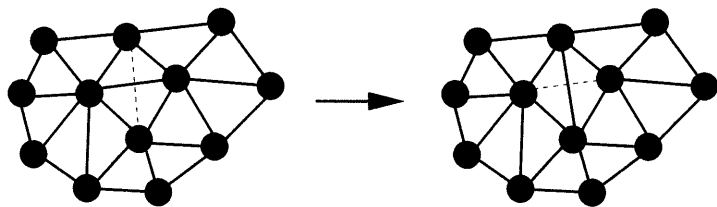


**FIG. 14** Schematic sketch of a connectivity update in the dynamic triangulation algorithm.

The next task is to discretize the surface integral (21). In most simulations, all terms except for the third one are dropped: the average interfacial area is determined by the choice of the number of beads and the maximum tether length; including the first term would only make sense in a “grand canonical” ensemble, where beads can be added and removed. The last term ( $2\pi\chi_E$  according to Eq. (22)) can be evaluated much more accurately by other methods than by an integral over some approximate expression for the Gaussian curvature. Finally, the amphiphilic layers are usually assumed to be intrinsically symmetric, which eliminates the second term. The remaining term is the bending penalty on the mean curvature  $H$ . It is usually approximated by [238]

$$\int dS 2\kappa H^2 \approx \lambda \sum_{\alpha\beta} (1 - \vec{n}_\alpha \vec{n}_\beta) + 2\pi\kappa\chi_E \quad (24)$$

where  $\vec{n}_\alpha$  is the unit normal vector of triangle  $\alpha$ , and the sum runs over all neighbor triangle pairs. This expression is commonly employed in simulations of stiff fluid membranes. However, it has the disadvantage that the relationship between  $\lambda$  and  $\kappa$  is not clear. Comparing ideal spheres, for example, one obtains  $\lambda = \sqrt{3}\kappa$  [240], whereas a similar calculation yields  $\lambda = 2\kappa/\sqrt{3}$  for the case of cylinders. In order to avoid this problem, Gompper and Kroll [241] have recently argued that a more appropriate discretization of the bending free energy should be based directly on the square of the local mean curvature:

$$\int dS 2\kappa H^2 \approx \frac{\tau}{2} \sum_{ij} \frac{1}{\sigma_i} \left[ \sum_{j(i)} \frac{\sigma_{ij}^z}{l_{ij}} (\vec{R}_i - \vec{R}_j) \right]^2 \quad (25)$$

with  $\tau \approx \kappa$ , where  $i$  runs over all sites,  $j$  over all neighbors of  $i$ ,  $\vec{R}_i$  denotes the position of bead  $i$  and  $l_{ij}$  the length of the bond connecting  $i$  with  $j$ . The other quantities are related to the dual lattice, which is created from the intersections of the perpendicular bisectors of the bonds:  $\sigma_{ij}$  is the length of



the dual bond which bisects  $l_{ij}$ , and  $\sigma_i = \sum_{j(i)} \sigma_{ij} l_{ij} / 4$  the area of the dual cell of site  $i$ . Note that  $\sigma_{ij}$  is not necessarily positive.

As yet, models for fluid membranes have mostly been used to investigate the conformations and shapes of single, isolated membranes, or vesicles [237,239–244]. In vesicles, a pressure increment  $p$  between the vesicle's interior and exterior is often introduced as an additional relevant variable. An impressive variety of different shapes has been found, including branched polymer-like conformations, inflated vesicles, dumbbell-shaped vesicles, and even stomatocytes. Fig. 15 shows some typical configuration snapshots, and Fig. 16 the phase diagram for vesicles of size  $N = 247$ , as calculated by Gompper and Kroll [243].

The collapsed polymer-like state is characterized by specific scaling laws, e.g., the average volume of the vesicle is proportional to the number of beads,  $\langle V \rangle \propto N$ . Other scaling laws apply in other regions of the phase diagram. For the case of zero pressure increment,  $p = 0$ , and moderate bending rigidity, a scaling *ansatz* of the form

$$\langle V \rangle = N^{3/2} \theta(\sqrt{A}/\xi) \quad (26)$$

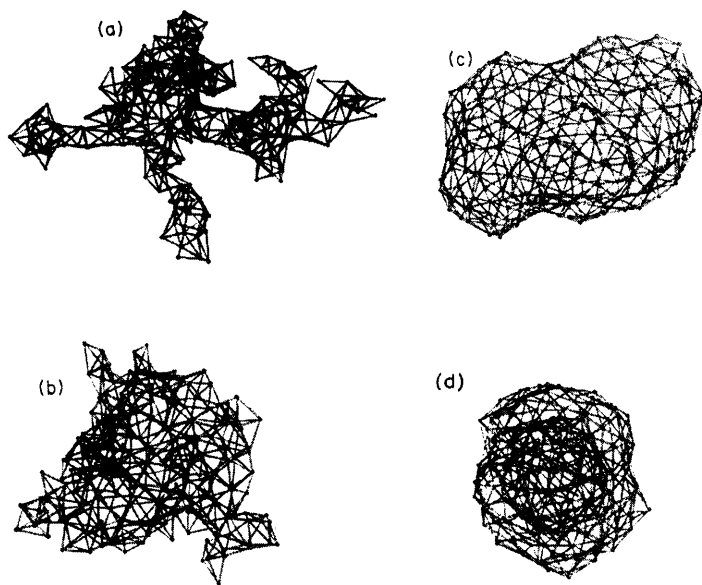


**FIG. 15** Conformations of fluid vesicles for different values of the bending rigidity and pressure increment: (a) branched polymer; (b) inflated vesicle; (c) prolate vesicle; (d) stomatocyte. (From Gompper and Kroll [243]. Copyright 1995 APS.)

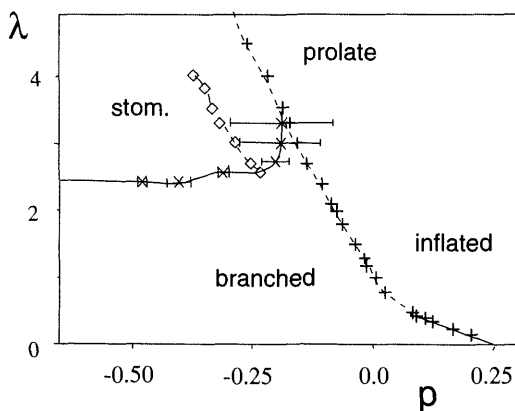


**FIG. 16** Phase diagram of fluid vesicles as a function of pressure increment  $p$  and bending rigidity  $\lambda$ . Solid lines denote first-order transitions, dotted lines compressibility maxima. The transition between the prolate vesicles and the stomatocytes shows strong hysteresis effects, as indicated by the error bars. Dashed line (squares) indicates a “transition” from metastable prolate to metastable disk-shaped vesicles. (From Gompper and Kroll 1995 [243]. Copyright 1995 APS.)

has been proposed [243,244], where  $\sqrt{A} = \sqrt{N}$  is the area of the vesicle and  $\xi \propto \exp(4\pi/3\kappa)$  its persistence length. If the scaling law (26) holds, simulation data for different vesicle sizes  $N$  should collapse on one curve if  $\langle V \rangle N^{-3/2}$  is plotted versus  $\sqrt{N} \exp(-4\pi\kappa/3)$ . This is indeed the case [243,244]. Scaling laws are extremely sensitive tools which allow one to study various phenomena very accurately. For example, it has been predicted [245] that the bending rigidity  $\kappa$  is softened by fluctuations on large length scales  $l$

$$\kappa(l) = \kappa - \frac{\alpha}{4\pi} \ln(l/a_0) \quad (27)$$

where  $a_0$  is a microscopic cutoff length, and  $\alpha$  a universal constant. By a careful scaling analysis of volume fluctuations in the limit of large bending rigidity, Gompper and Kroll have been able to verify this prediction [241].

A number of recent studies consider more complex systems, such as freezing vesicles [246] (freezing can be induced by reducing the tether length) or mixed membranes which contain more than one component [247,248]. The possibility that a membrane may break up and form pores has also been considered [249].

In all of these investigations, the topology of the simulated object was kept fixed (spherical). Current work is devoted to the study of systems with

variable topology, where vesicles can fuse and break up. Such models will probably be very useful in studying bicontinuous states and their evolution into states of isolated vesicles and droplets [250,251].

## VI. CONCLUSIONS

We have attempted to give an overview of the wide spectrum of topics which are currently investigated in amphiphilic systems, and of the multitude of simulation methods and simulation models which have been used to explore them. Amphiphilic systems have been studied on length scales ranging from a few Angstroms to micrometers, and over a similarly wide range of time scales. Hence a whole hierarchy of models has been developed, each of which covering a different length scale, and devised to address a different type of problem. We have also attempted to give a feeling for the many interesting questions which are still open and/or under current investigation. Amphiphilic systems turn out to be an immensely rich playground for researchers, which has something to offer for almost everybody: for the materials scientist, the physical chemist, the biologist, the condensed matter physicist, and the hard core theoretician in statistical physics.

## ACKNOWLEDGMENTS

It is a pleasure to thank Michael Schick, Christoph Stadler, and Harald Lange for enjoyable collaboration, and Kurt Binder for fruitful discussions and encouragement. I have benefitted from stimulating interactions with Mark Matsen, Ralph Blossey, Marcus Müller, Andreas Werner, Frank Haas, and Nigel Wilding. Thanks also go to Gregor Huber for carefully reading this manuscript, and to the Deutsche Forschungsgemeinschaft for financial support through the Heisenbergprogramm.

## REFERENCES

1. G. Gompper, M. Schick. In: C. Domb, J. L. Lebowitz, eds. *Phase Transitions and Critical Phenomena, Vol. 16, Self-assembling Amphiphilic Systems*. London: Academic Press, 1994.
2. V. Degiorgio, M. Corti, eds. *Physics of Amphiphiles: Micelles, Vesicles and Microemulsions*. Amsterdam: North-Holland, 1985; W. M. Gelbart, A. Ben-Shaul, D. Roux, eds. *Micelles, membranes, microemulsions and monolayers*. Berlin: Springer, 1994.
3. For recent reviews on experimental phase diagrams of amphiphilic systems see: K. V. Schubert. *Ber Bunsenges Phys Chemie* 100:190–205, 1996; R. S. Strey. *Curr Opin Coll Interf Sci* 1:402–410, 1996.

4. J. Israelachvili. *Intermolecular and Surface Forces*, 2nd ed. London: Academic Press, 1991.
5. For a recent review on the sponge phase, see: G. Porte. *Curr Opin Coll Interf Sci* 1:345–349, 1996.
6. See Chapter 14 in this book.
7. R. Strey, R. Schomäcker, D. Roux, F. Frederic, U. Olsson. *J Chem Soc Faraday Trans* 86:2253–2261, 1990.
8. M. Kahlweit, R. Strey, P. Firman. *J Phys Chem* 90:671–677, 1986.
9. M. Teubner, R. Strey. *J Chem Phys* 87:3195–3200, 1987.
10. For a recent review on the gyroid phase, see: M. Schick. *Physica A* 251:1–11, 1998.
11. V. Luzzati, P. A. Spegt. *Nature* 215:701–704, 1967; V. Luzzati, A. Tardieu, T. Gulik-Krzywicki, E. Rivas, F. Reiss-Husson. *Nature* 220:485–488, 1968; R. Templer. *Curr Opin Coll Interf Sci* 3:255–263, 1998.
12. D. A. Hajduk, P. E. Harper, S. M. Gruner, C. C. Honeker, G. Kim, E. L. Thomas, L. J. Fetters. *Macromolecules* 27:4063–4075, 1994; M. F. Schulz, F. S. Bates, K. Almdal, K. Mortensen. *Phys Rev Lett* 73:86–89, 1994; F. S. Bates, M. F. Schulz, A. K. Khandpur, S. Förster, J. H. Rosedale. *Faraday Discuss* 98:7–18, 1994.
13. F. S. Bates, G. H. Fredrickson. *Ann Rev Phys Chem* 41:525–557, 1990; M. W. Matsen, F. S. Bates. *Macromolecules* 29:1091–1098, 1996; P. K. Janert, M. Schick. *Macromolecules* 30:3916–3920, 1997.
14. H. Hasegawa. *Curr Opin Coll Interf Sci* 3:264–269, 1998.
15. M. Templin, A. Franck, U. Chesne, H. Leist, Y. Zhang, R. Ulrich, V. Schädler, U. Wiesner. *Science* 278:1795–1798, 1997.
16. H. Möhwald. *Ann Rev Phys Chem* 41:441–476, 1990; H. M. McConnell. *Ann Rev Phys Chem* 42:171–195, 1991; C. M. Knobler, R. C. Desai. *Ann Rev Phys Chem* 43:207–236, 1992; D. Andelman, F. Brochard, C. M. Knobler, F. Rondelez. In: M. Gelbart, A. Ben-Shaul, D. Roux, eds. *Micelles, Membranes, Microemulsions, and Monolayers*. Berlin: Springer, 1994, pp. 599–602.
17. V. M. Kaganer, H. Möhwald, P. Dutta. *Rev Mod Phys* (in press).
18. M. Bloom, E. Evans, O. G. Mouritsen. *Quart Rev Biophys* 24:293–397, 1991.
19. Of course, these numbers are constantly increasing due to the fast progress in computer technology.
20. G. la Penna, S. Letardi, V. Minicozzi, S. Morante, G. C. Rossi, G. Salina. *Nucl Phys B* 63:985–987, 1998.
21. For recent reviews on molecular dynamics simulations of amphiphilic systems, see: D. J. Tobias, K. Tu, M. L. Klein. In: K. Binder, G. Ciccotti, eds. *Monte Carlo and Molecular Dynamics of Condensed Matter Systems*. Bologna: SIF, 1996, pp. 327–344. S. Bandyapadhyay, M. Tarek, M. L. Klein. *Curr Opin Coll Interf Sci* 3:242–246, 1998.
22. C. Tanford. *The Hydrophobic Effect: Formation of Micelles and Biological Membranes*. New York: Wiley, 1980.
23. For a recent review on the hydrophobic effect, see: M. E. Paulaitis, S. Garde, H. S. Ashbaugh. *Curr Opin Coll Interf Sci* 1:376–383, 1996.

24. For a recent review on chain models of amphiphiles, see: T. B. Liverpool. In: D. Stauffer, ed. *Annual Reviews of Computational Physics IV*. Singapore: World Scientific, 1996, pp. 317–358.
25. For a recent review on Ginzburg–Landau theories, see: G. Gompper. *Ber. Bunsenges Phys Chemie* 100:264–271, 1996.
26. D. Nelson, T. Piran, S. Weinberg, eds. *Statistical Mechanics of Membranes and Surfaces*. Singapore: World Scientific, 1989.
27. S. A. Safran. *Statistical Thermodynamics of Surfaces, Interfaces and Membranes*. Reading, Massachusetts: Addison-Wesley, 1994.
28. L. Peliti. In: F. David, P. Ginsparg, J. Zinn-Justin, eds. *Fluctuating Geometries in Statistical Mechanics and Field Theory*. Amsterdam: North-Holland, 1996, pp. 195–285.
29. U. Seifert. *Curr Opin Coll Interf Sci* 1:350–357, 1996; *Adv Phys* 46:130–137, 1997.
30. G. Gompper, D. M. Kroll. *Curr Opin Coll Interf Sci* 2:373–381, 1997; G. Gompper, D. M. Kroll. *J Phys Cond Matt* 6:8795–8834, 1997.
31. O. G. Mouritsen, K. Jorgensen. *Curr Opin Struct Biol* 7:518–527, 1997.
32. K. Binder, D. W. Heermann. *Monte Carlo Simulation in Statistical Physics*. Berlin: Springer, 1990.
33. M. P. Allen, D. J. Tildesley. *Computer Simulation of Liquids*. Oxford: Oxford University Press, 1989.
34. K. Binder, ed. *Monte Carlo and Molecular Dynamics Simulations in Polymer Science*. Oxford: Oxford University Press, 1995.
35. K. Binder, G. Ciccotti, eds. *Monte Carlo and Molecular Dynamics of Condensed Matter Systems*. Bologna: Societa Italiana di Fisica, 1996.
36. F. Schmid. *J Phys: Cond Matt* 10:8105–8138, 1998.
37. C. M. Wijmans, P. Linse. *Langmuir* 11:3748–3756, 1995.
38. A. Ben-Shaul, I. Szleifer, W. M. Gelbart. *J Chem Phys* 83:3597–3611, 1985; 83:3612–3620, 1985; I. Szleifer, A. Ben-Shaul, W. M. Gelbart. *J Chem Phys* 85:5345–5358, 1986.
39. D. R. Fattal, A. Ben-Shaul. *Biophys J* 67:983–995, 1994.
40. D. Harries, A. Ben-Shaul. *J Chem Phys* 106:1609–1619, 1997.
41. F. A. M. Leermakers, J. M. H. M. Scheutjens, J. Lyklema. *Biophys Chem* 18:353–360, 1983; *Biochim et Biophys. Acta* 1024:139, 1990; F. A. M. Leermakers, J. M. H. M. Scheutjens. *J Chem Phys* 89:3264–3274, 1988; 89:6912–6924, 1988; *J Phys Chem* 93:7417–7426, 1989.
42. F. Schmid, M. Schick. *J Chem Phys* 102:2080–2091, 1995; F. Schmid. *Phys Rev E* 55:5774–5784, 1997.
43. J. P. Rieu, M. Vallade. *J Chem Phys* 104:7729–7740, 1996.
44. S. W. de Leeuw, J. W. Perram, E. R. Smith. *Proc Roy Soc London A* 373:27–56, 1980; T. Darden, D. York, L. Pedersen. *J Chem Phys* 98:10089–10092, 1993; U. Essmann, L. Perera, M. L. Berkowitz, T. Darden, H. Lee, L. Pedersen. *J Chem Phys* 103:8577–8593, 1995.
45. S. E. Feller, R. W. Pastor, A. Rojnuckarin, S. Bogusz, B. R. Brooks. *J Phys Chem* 100:17011–17020, 1996.

46. P. H. Hünenberger, W. F. van Gunsteren. *J Chem Phys* 108:6117–6134, 1998.
47. A. J. Kox. *Nature* 285:317–319, 1980.
48. S. H. Northrup, M. S. Curvin. *J Phys Chem* 89:4707–4713, 1985.
49. H. E. Alper, D. Bassolino, T. R. Stouch. *J Chem Phys* 98: 9798–9807, 1993; 99:5547–5559, 1993.
50. J. P. Bareman, G. Cardini, M. L. Klein. *Phys Rev Lett* 60:2152–2155, 1988; G. Cardini, J. P. Bareman, M. L. Klein. *Chem Phys Lett* 145:493–499, 1988; *J Phys Chem* 94:5202–5205, 1990; J. Hautman, M. L. Klein. *J Chem Phys* 91:4994–5001, 1989; 93:7483–7492, 1990.
51. J. Harris, S. A. Rice. *J Chem Phys* 89:5898–5908, 1988.
52. S. B. Clough, X. F. Sun, J. Kumar, S. Tripathy. *Mol Cryst Liq Cryst* 190:155–160, 1990.
53. M. A. Moller, D. J. Tildesley, K. S. Kim, N. Quirke. *J Chem Phys* 94:8390–8401, 1991.
54. P. Ahlström, J. C. Berendsen. *J Phys Chem* 97:13691–13702, 1992.
55. S. Karaborni, S. Toxvaerd. *J Chem Phys* 96:5505–5515, 1992; 97:5876–5883, 1992; S. Karaborni, S. Toxvaerd, O. H. Olsen. *J Phys Chem* 96:4965–4973, 1992; S. Karaborni. *Langmuir* 9:1334–1343, 1993; S. Karaborni, G. Verbist. *Europhys Lett* 27:467–472, 1996.
56. J. I. Siepmann, S. Karaborni, M. L. Klein. *J Phys Chem* 98:6675–6678, 1994; S. Karaborni, J. I. Siepmann. *Mol Phys* 83:345–350, 1994.
57. For an overview of the Gibbs ensemble technique see: B. Smit. In: M. P. Allen, D. J. Tildesley, eds. *Computer Simulations in Chemical Physics*. Kluwer Academic, 1993, pp. 173–209.
58. M. L. Marquez, E. Rogel, I. Reif. *Coll Surf A* 106:135–148, 1996.
59. G. Urbina-Villalba, P. M. Landrove, J. A. Guarega. *Langmuir* 13:1644–1652, 1997.
60. K. J. Schweighofer, U. Essmann, M. Berkowitz. *J Phys Chem B* 101:3793–3799, 1997; 101:10775–10780, 1997.
61. S. Shin, N. Collazo, S. A. Rice. *J Chem Phys* 96:1352–1366, 1991; N. Collazo, S. Shin, S. A. Rice. *J Chem Phys* 96:4735–4742, 1991; S. Shin, N. Collazo, S. A. Rice. *J Chem Phys* 98:3469–3474, 1992; J. Gao, S. A. Rice. *J Chem Phys* 99:7020–7029, 1993; 104:2101–2113, 1996; 104: 2114–2123, 1996.
62. Z. Cai, S. A. Rice. *J Chem Phys* 90:6716–6729, 1989.
63. K.-P. Bell, S. A. Rice. *J Chem Phys* 99:4160–4167, 1993; 104:1684–1692, 1996.
64. P. van der Ploeg, H. J. C. Berendsen. *J Chem Phys* 76:3271–3276, 1982; *Mol Phys* 49:233–248, 1983; O. Edholm, H. J. C. Berendsen, P. van der Ploeg. *Mol Phys* 49:379–388, 1983.
65. P. G. Khalatur, N. K. Balabaev, A. S. Pavlov. *Mol Phys* 59:753–773, 1986.
66. T. Xiang. *Biophys J* 65:1108–1120, 1993; T. Xiang, B. D. Anderson. *Biophys J* 66:561–572, 1994; *J Chem Phys* 103:8666–8678, 1995.
67. T. Taga, K. Masuda. *J Comp Chem* 16:235–242, 1995.
68. E. Egberts, H. J. C. Berendsen. *J Chem Phys* 89:3718–3732, 1988; E. Egberts, S.-J. Marrink, H. J. C. Berendsen. *Eur Biophys J* 22:423–436, 1994; J. J. L.

- Cascales, J. Garcia de la Torr, S. J. Marrink, H. J. C. Berendsen. *J Chem Phys* 104:2713–2720, 1996.
69. K. Niklas, J. Boecker, M. Schlenkrich, J. Brickmann, P. Bopp. *Biophys J* 60:260–272, 1991.
70. A. J. Robinson, W. G. Richards, P. J. Thomas, M. M. Hann. *Biophys J* 67:2345–2354, 1994.
71. M. A. Wilson, A. Pohorille. *J Am Chem Soc* 116:1490–1501, 1994.
72. F. Zhou, K. Schulten. *J Phys Chem* 99:2194–2207, 1995.
73. J. F. Rusling, T. F. Kumosinski. *J Phys Chem* 99:9241–9247, 1995.
74. W. Shinoda, T. Fukada, S. Okazaki, I. Okada. *Chem Phys Lett* 232:308–312, 1995; W. Shinoda, N. Namiki, S. Okazaki. *J Chem Phys* 106:5731–5743, 1996.
75. S.-W. Chiu, M. Clark, V. Balaji, S. Subramaniam, H. L. Scott, E. Jacobson. *Biophys J* 69:1230–1245, 1995.
76. T. Kechuan, D. J. Tobias, M. L. Klein. *Biophys J* 69:2558–2562, 1995; T. Kechuan, D. J. Tobias, J. K. Blasie, M. L. Klein. *Biophys J* 70:595–608, 1996.
77. S. E. Feller, Z. Yuhong, R. W. Pastor. *J Chem Phys* 103:10267–10276, 1995; S. E. Feller. *Biophys J* 71:1350–1355, 1996.
78. D. P. Tieleman, H. J. C. Berendsen. *J Chem Phys* 105:4871–4880, 1996.
79. O. Berger, O. Edholm, F. Jahnig. *Biophys J* 72:2002–2013, 1997.
80. S. J. Marrink, R. M. Sok, H. J. C. Berendsen. *J Chem Phys* 104:9090–9099, 1996; S. J. Marrink, F. Jahnig, H. J. C. Berendsen. *Biophys J* 71:632–647, 1996.
81. W. Shinoda, S. Okazaki. *J Chem Phys* 109:1517–1521, 1998.
82. S.-J. Marrink, O. Berger, D. P. Tieleman, F. Jahnig. *Biophys J* 74:931–943, 1998.
83. M. Hyvonen, M. Ala-Korpela, J. Vaara, T. T. Rantala, J. Jokisaari. *Chem Phys Lett* 246:300–306, 1995; 268:55–60, 1997; M. T. Hyvonen, T. T. Rantala, M. Ala-Korpela. *Biophys J* 73:2907–2923, 1997.
84. S. E. Feller, D. Yin, R. W. Pastor, A. D. Mackerell. *Biophys J* 73:2269–2279, 1997.
85. O. Edholm, A. M. Nyberg. *Biophys J* 63:1081, 1992.
86. A. J. Robinson, W. G. Richards, P. J. Thomas, M. M. Hann. *Biophys J* 68:164–170, 1995.
87. O. Edholm, J. Johansson. *Eur Biophys J* 14:203–209, 1987.
88. K. V. Damodaran, K. M. Merz. *Biophys J* 66:1076–1087, 1994.
89. L. Shen, D. Bassolino, T. Stouch. *Biophys J* 73:3–20, 1997.
90. M. S. P. Sansom. *Eur Biophys J* 22:104–124, 1993; M. S. P. Sansom, I. D. Kerr. *Biophys J* 69:1334–1343, 1995; P. C. Biggin, J. Breed, H. S. Son, M. S. P. Sansom. *Biophys J* 72:627–636, 1997; M. S. P. Sansom, G. R. Smith, C. Adcock, P. C. Biggin. *Biophys J* 73:2404–2415, 1997.
91. T. B. Woolf, B. Roux. *Biophys J* 72:1930–1945, 1997; K. Belohorcova, J. H. Davis, T. B. Woolf, B. Roux. *Biophys J* 73:3039–3055, 1997.
92. D. P. Tieleman, H. J. C. Berendsen. *Biophys J* 74:2786–2801, 1998.
93. J. M. Haile, J. P. O'Connell. *J Phys Chem* 88:6363–6366, 1984; M. C. Woods, J. M. Haile, J. P. O'Connell. *J Phys Chem* 90:1875–1885, 1986.

94. S. Karaborni, J. P. O'Connell. *Langmuir* 6:905–911, 1990; *J Phys Chem* 94:2624–2631, 1990.
95. B. Jönsson, O. Edholm, O. Telemann. *J Chem Phys* 85:2259–2271, 1986.
96. K. Watanabe, M. Ferrario, M. L. Klein. *J Phys Chem* 92:819–827, 1988; K. Watanabe, M. L. Klein. *J Phys Chem* 93:6897–6901, 1989.
97. J. J. Wendoloski, S. J. Kimatian, C. E. Schutt, F. R. Salemme. *Sci* 243:636–638, 1989.
98. L. Laaksonen, J. B. Rosenholm. *Chem Phys Lett* 216:429–434, 1993.
99. A. D. MacKerell. *J Phys Chem* 99:1846–1855, 1995.
100. J. A. Griffiths, D. M. Heyes. *Langmuir* 12:2418–2424, 1996.
101. D. J. Tobias, M. L. Klein. *J Phys Chem* 100:6637–6648, 1996.
102. K. Watanabe, M. L. Klein. *J Phys Chem* 95:4158–4166, 1991.
103. Y. C. Kong, D. Nicholson, N. G. Parsonage, L. Thompson. *Mol Phys* 89:835–865, 1996.
104. S. W. Haan, L. R. Pratt. *Chem Phys Lett* 79:436–440, 1981; B. Owenson, L. R. Pratt. *J Phys Chem* 88:2905–2915, 1984; 88:6048–6052, 1984.
105. M. Milik, J. Skolnick, A. Kolinski. *J Phys Chem* 93:4440–4446, 1990.
106. M. Milik, J. Skolnick, A. Kolinski. *J Phys Chem* 96:4015–4022, 1992.
107. Y. K. Levine, A. Kolinski, J. Skolnick. *J Chem Phys* 98:7581–7587, 1993.
108. D. A. van der Sijs, Y. K. Levine. *J Chem Phys* 100:6783–6791, 1994.
109. R. G. Larson, L. E. Scriven, H. T. Davis. *J Chem Phys* 83:2411–2420, 1985.
110. R. G. Larson. *J Chem Phys* 89:1642–1650, 1988; 91:2479–2488, 1989; *Mol Sim* 13:321–345, 1994.
111. R. G. Larson. *J Chem Phys* 96:7904–7918, 1992.
112. R. G. Larson. *J Physique II* 6:1441–1463, 1996.
113. A. D. Mackie, K. Onur, A. Z. Panagiotopoulos. *J Chem Phys* 104:3718–3725, 1996.
114. D. Stauffer, N. Jan, R. B. Pandey. *Physica A* 198:401–409, 1993; D. Stauffer, N. Jan, Y. He, R. B. Pandey, D. G. Marangom, T. Smith-Palmer. *J Chem Phys* 100:6934–6943, 1994; N. Jan, D. Stauffer. *J Phys I France* 4:345–350, 1994; S. Boyden, N. Jan, T. Ray. *Il Nuovo Cimento D* 16:1439–1445, 1994; D. Stauffer, D. Woermann. *J Physique II* 5:1–3, 1995.
115. A. T. Bernardes, V. B. Henriques, P. M. Bisch. *J Chem Phys* 101:645–650, 1994.
116. D. Brindle, C. M. Care. *Int. J Mod Phys C* 2:284–287, 1991; *J Chem Soc Faraday Trans* 88:2163–2166, 1992.
117. J.-C. Desplat, C. M. Care. *Mol Phys* 87:441–453, 1996.
118. P. K. Maiti, D. Chowdhury. *Europhys Lett* 41:183–188, 1998.
119. C. M. Wijmans, P. Linse. *J Phys Chem* 100:12583–12591, 1996; *J Chem Phys* 106:328–338, 1997.
120. P. H. Nelson, G. C. Rutledge, T. A. Hatton. *J Chem Phys* 107:10777–10781, 1997.
121. D. Chowdhury. *J Physique II* 5:1469–1489, 1995; *Langmuir* 12:1098–1104, 1996; D. Chowdhury, A. T. Bernardes, D. Stauffer. *Int J Mod Phys C* 7:73–88, 1996.



122. P. K. Maiti. *Phys Lett A* 230:369–372, 1997; D. Chowdhury, P. K. Maiti, S. Sabhapandit, P. Taneja. *Phys Rev E* 56:667–679, 1997.
123. T. B. Liverpool, A. T. Bernardes. *J Physique II* 5:1003–1016, 1995; 5:1457–1468, 1995.
124. A. T. Bernardes, T. B. Liverpool, D. Stauffer. *Phys Rev E* 54:R2220–R2223, 1996.
125. A. T. Bernardes. *J Physique II* 6:169–174, 1996.
126. A. T. Bernardes. *Langmuir* 12:5763–5767, 1996.
127. J.-M. Jin, K. Parbhakar, L. H. Dao. *Phys Rev E* 55:721–726, 1997.
128. P. K. Maiti, D. Chowdhury. *Int J Mod Phys C* 8:1335–1343, 1997.
129. J. Harris, S. A. Rice. *J Chem Phys* 88:1298–1306, 1987.
130. H. Stettin, H. J. Mögel, R. Friedemann. *Ber Bunsenges Phys Chem* 97:44–48, 1993; H. Stettin, H. J. Mögel, C. M. Care. *Ber Bunsenges Phys Chem* 100:20–26, 1996.
131. F. M. Haas, P.-Y. Lai, K. Binder. *Makromol Chem Theory Simul* 2:889–899, 1993.
132. I. Carmesin, K. Kremer. *Macromolecules* 21:2819–2823, 1988; *J Physique* 51:915–932, 1990.
133. M. Müller, M. Schick. *J Chem Phys* 105:8282–8292, 1996.
134. D. E. Jennings, Y. A. Kuznetsov, E. G. Timoshenko, K. A. Dawson. *J Chem Phys* 108:1702–1709, 1998.
135. B. Smit, A. G. Schlijper, L. A. M. Rupert, N. M. van Os. *J Phys Chem* 94:6933–6935, 1990.
136. B. Smit, P. A. J. Hilbers, K. Esselink, L. A. M. Rupert, N. M. van Os, A. G. Schlijper. *Nature* 348:624–627, 1990; *J Phys Chem* 95:6361–6368, 1991.
137. S. Karaborni, M. M. van Os, P. A. J. Hilbers. *Langmuir* 9:1175–1178, 1993.
138. B. Smit, P. A. J. Hilbers, K. Esselink. *Int J Mod Phys C* 4:393–400, 1993; B. Smit, K. Esselink, P. A. J. Hilbers, N. M. van Os, L. A. M. Rupert, I. Szleifer. *Langmuir* 9:9–11, 1993; K. Esselink, P. A. J. Hilbers, N. M. van Os, B. Smit, S. Karaborni. *Coll Surf A* 91:155–167, 1994.
139. S. Karaborni, K. Esselink, P. A. J. Hilbers, B. Smit, J. Karthäuser, N. M. van Os, R. Zana. *Science* 266:254–256, 1994.
140. B. J. Palmer, J. Liu. *Langmuir* 12:746–753, 1996; 12:6015–6021, 1996.
141. R. Götz, R. Lipowsky. *J Chem Phys* 108:7397–7409, 1998.
142. F. K. von Gottberg, K. A. Smith, T. A. Hatton. *J Chem Phys* 106:9850–9857, 1997; 108:2232–2244, 1998.
143. A. Bhattacharya, S. D. Mahant, A. Chakrabarti. *J Chem Phys* 108:10281–10293, 1998.
144. D. Viduna, A. Milchev, K. Binder. *Macromol Theory Simul* (in press).
145. A. Baumgärtner. *J Chem Phys* 103:10669–10674, 1995; *Biophys J* 71:1248–1255, 1996.
146. T. Sintes, A. Baumgärtner. *Biophys J* 73:2251–2259, 1997; *Physica A* 249:571–575, 1998.
147. I. Gerroff, A. Milchev, K. Binder, W. Paul. *J Chem Phys* 98:6526–6539, 1993.

148. R. Hilfer, F. M. Haas, K. Binder. *Nuovo Cimento* 16:1297–1303, 1994; F. M. Haas, R. Hilfer, K. Binder. *J Chem Phys* 102:2960–2969, 1995.
149. F. M. Haas, R. Hilfer, K. Binder. *J Phys Chem* 100:15290–15300, 1996; F. M. Haas, R. Hilfer. *J Chem Phys* 105:3859–3867, 1996.
150. F. Schmid, C. Stadler, H. Lange. In: D. P. Landau, K. K. Mon, B. Schüttler, eds. *Computer Simulations in Condensed Matter Vol. 10*, Springer, 1997, pp. 37–51; F. Schmid, C. Stadler, H. Lange. *Coll Surf A* 149:301–306, 1999; C. Stadler, H. Lange, F. Schmid. *Phys Rev E* 59:4248–4257, 1999.
151. C. Stadler, F. Schmid. *J Chem Phys* 110:9697–9705, 1999.
152. S. Opps, B. Yang, C. Gray, D. Sullivan. In preparation, 1998.
153. A. Baumgärtner. *J Chem Phys* 101:9060–9062, 1994.
154. D. R. Rector, F. van Swol, J. R. Henderson. *Mol Phys* 82:1009–1031, 1994.
155. M. Laradji, O. G. Mouritsen, S. Toxvaerd, M. J. Zuckermann. *Phys Rev E* 5:1243–1252, 1994.
156. D. R. Kuespert, V. Muralidharan, M. D. Donohul. *Mol Phys* 86:201–223, 1995.
157. P. G. Bolhuis, D. Frenkel. *Physica A* 244:45–58, 1997.
158. B. Dammann, H. C. Fogedby, J. H. Ipsen, C. Jeppesen, K. Jorgensen, O. G. Mouritsen, J. Risbo, M. C. Sabra, M. M. Sperotto, M. J. Zuckermann. In: D. D. Lasic, Y. Barenholz, eds. *Handbook of nonmedical applications of liposomes, Vol. 1*. CRC Press, 1995, pp. 85–127.
159. J. C. Wheeler, B. Widom. *J Am Chem Soc* 90:3064–3072, 1968; B. Widom. *J Chem Phys* 84:6943–6954, 1986.
160. A. Hansen, M. Schick, D. Stauffer. *Phys Rev A* 44:3686–3691, 1991.
161. D. Stauffer, N. Jan. *J Chem Phys* 87:6210–6211, 1987; N. Jan, D. Stauffer. *J Physique* 49:623–633, 1988; D. Stauffer, H. F. Eicke. *Physica A* 182:29–32, 1992; D. Morawietz, D. Chowdhury, S. Vollmar, D. Stauffer. *Physica A* 187:126–132, 1992.
162. K. A. Dawson, B. L. Walker, A. Berera. *Physica A* 165:320–351, 1990.
163. D. Chowdhury, D. Stauffer. *J Chem Phys* 95:7664–7677, 1991.
164. D. Chowdhury, D. Stauffer. *Phys Rev A* 44:R2247–R2250, 1991; *Physica A* 186:237–249, 1992; 189:70–80, 1992.
165. P. K. Maiti, D. Chowdhury. *J Physique I* 5:671–674, 1995.
166. S. Alexander. *J Physique Lett* 39:L1–L3, 1978.
167. K. Chen, C. Ebner, C. Jayaprakash, R. Pandit. *J Phys C* 20:L361–L366, 1987; *Phys Rev A* 38:6240–6254, 1988; Y. Jiang, C. Ebner. *Phys Rev A* 37:2091–2098, 1988; W. Wenzel, C. Ebner, C. Jayaprakash, R. Pandit. *J Phys: Cond Matt* 1:4245–4250, 1989.
168. T. P. Stockfish, J. C. Wheeler. *J Chem Phys* 99:6155–6171, 1993.
169. K. Binder. *Z Phys B* 43:119–140, 1981; *Phys Rev A* 25:1699–1709, 1982.
170. M. Blume, V. Emery, R. B. Griffiths. *Phys Rev A* 4:1071–1077, 1971.
171. M. Schick, W.-H. Shih. *Phys Rev Lett* 59:1205–1208, 1987.
172. G. Gompper, M. Schick. *Phys Rev A* 42:2137–2149, 1990.
173. G. Gompper, M. Schick. *Phys Rev Lett* 65:1116–1119, 1990.
174. F. Schmid, M. Schick. *Phys Rev E* 49:494–500, 1994.

175. B. A. Berg, T. Neuhaus. *Phys Rev Lett* 68:9–12, 1989.
176. F. Schmid, M. Schick. *Z Phys B* 97:189–192, 1995; *J Chem Phys* 102:7197–7203, 1995.
177. K.-V. Schubert, R. Strey. *J Chem Phys* 95:8532–8545, 1991.
178. P. A. Slotte. *Phys Rev A* 46:6469–6478, 1992.
179. J. W. Halley, A. J. Kolan. *J Chem Phys* 88:3313–3316, 1988.
180. M. Laradji, H. Guo, M. Grant, M. Zuckermann. *Phys Rev A* 44:8184–8188, 1991; M. Laradji, H. Guo, M. Zuckermann. *J Phys: Cond Matt* 6:2799–2812, 1994.
181. J. R. Gunn, K. A. Dawson. *J Chem Phys* 96:3152–3169, 1991.
182. M. W. Matsen, D. E. Sullivan. *Phys Rev E* 51:548–557, 1994.
183. A. Linhananta, D. E. Sullivan. *Phys Rev E* 57:4547–4557, 1998; A. Linhananta, D. E. Sullivan (to be published).
184. M. W. Matsen. *Phys Rev E* 48:2292–2295, 1993.
185. M. W. Matsen, M. Schick, D. E. Sullivan. *J Chem Phys* 98:2341–2352, 1993.
186. B. M. Boghosian, P. V. Coveney, A. N. Emerton. *Proc Roy Soc London A* 452:1221–1250, 1996; A. N. Emerton, P. V. Coveney, B. M. Boghosian. *Phys Rev E* 55:708–720, 1997; *Physica A* 239:373–381, 1997; F. W. J. Weig, P. V. Coveney, B. M. Boghosian. *Phys Rev E* 56:6877–6888, 1997; A. N. Emerton, F. W. J. Weig, P. V. Coveney, B. M. Boghosian. *J Phys: Cond Matt* 9:8893–8905, 1997.
187. J. R. Gunn, K. A. Dawson. *J Chem Phys* 91:6393–6403, 1994.
188. J. M. Drouffe, A. C. Maggs, S. Leibler. *Science* 254:1353–1356, 1991.
189. Y. Saito, V. Morikawa. *J Phys Soc Jpn* 61:4290–4293, 1992.
190. E. de Miguel, M. Telo da Gama. *J Chem Phys* 10:6366–6378, 1997.
191. H. L. Scott. *J Chem Phys* 80:2197–2202, 1984; W. McCullough, H. L. Scott. *Phys Rev Lett* 65:631–634, 1990; W. McCullough, J. H. H. Perk, H. L. Scott. *J Chem Phys* 93:6070–6080, 1990.
192. K. P. Schneider, J. Keller. *Chem Phys Lett* 261:81–85, 1996; 275:63–69, 1997.
193. Z.-Y. Chen, J. Talbot, W. M. Gelbart, A. Ben-Shaul. *Phys Rev Lett* 61:1376–1379, 1988.
194. M. Kreer, K. Kremer, K. Binder. *J Chem Phys* 92:6195–6205, 1990.
195. M. Scheringer, R. Hilfer, K. Binder. *J Chem Phys* 96:2269–2277, 1992.
196. D. R. Swanson, R. J. Hardy, C. J. Eckhardt. *J Chem Phys* 99:8194–8199, 1993; M. D. Gibson, D. R. Swanson, C. J. Eckhardt, X. C. Zeng. *J Chem Phys* 106:1961–1966, 1997.
197. D. A. Pink, T. J. Green, D. Chapman. *Biochemistry* 19:349–356, 1980; A. Caillé, D. Pink, F. de Verteuil, M. Zuckermann. *Can J Physique* 58:581–611, 1980.
198. S. Doniach. *J Chem Phys* 68:4912–4916, 1978.
199. R. Jerala, P. F. F. Almeida, R. L. Biltonen. *Biophys J* 71:609–615, 1996.
200. O. G. Mouritsen, A. Boothroyd, D. Harris, N. Jan, T. Lookman, L. MacDonald, D. A. Pink, M. J. Zuckermann. *J Chem Phys* 79:2027–2041, 1983; O. G. Mouritsen. *Eur Biophys J* 12:75–86, 1985; J. H. Ipsen, K. Jorgensen, O. G. Mouritsen. *Biophys J* 58:1099–1107, 1990.

201. E. Corvera, M. Laradji, M. J. Zuckermann. *Phys Rev E* 47:696–703, 1993.
202. J. Lemmich, J. H. Ipsen, T. Honger, K. Jorgensen, O. G. Mouritsen, K. Mortensen, R. Bauer. *Mod Phys B* 8:1803–1814, 1994.
203. O. G. Mouritsen, M. J. Zuckermann. *Phys Rev Lett* 58:389–392, 1987; M. J. Zuckermann, O. G. Mouritsen. *Eur Biophys J* 15:77–86, 1987; J. H. Ipsen, O. G. Mouritsen, M. J. Zuckermann. *J Chem Phys* 91:1855–1865, 1989.
204. P. S. Sahni, G. S. Grest, M. P. Anderson, D. J. Srolowitz. *Phys Rev Lett* 50:263–266, 1983.
205. M. Nielsen, L. Miao, J. H. Ipsen, O. G. Mouritsen, M. J. Zuckermann. *Phys Rev E* 54:6889–6905, 1996.
206. D. P. Fraser, R. W. Chantrell, D. Melville, D. J. Tildesley. *Liqu Cryst* 3:423–441, 1988; D. P. Fraser, M. J. Zuckermann, O. G. Mouritsen. *Phys Rev A* 43:6642–6656, 1991.
207. Z. Zhang, M. J. Zuckermann, O. G. Mouritsen. *Phys Rev A* 46:6707–6713, 1992.
208. Z. Zhang, J. Topochnik, M. J. Zuckermann, J. Silvius. *Phys Rev E* 47: 3721–3729, 1993; T. Tobochnik, M. J. Zuckermann, Z. Zhang. *Phys Rev E* 51:6204–6212, 1995.
209. J. Risbo, M. M. Sperotto, O. G. Mouritsen. *J Chem Phys* 103:3643–3656, 1995.
210. K. Jorgensen, O. G. Mouritsen. *Biophys J* 69:942–954, 1995.
211. M. M. Sperotto, O. G. Mouritsen. *Biophys J* 59:261–270, 1991; *Eur Biophys J* 19:157–168, 1991; 22:323–328, 1993.
212. T. Heimburg, R. L. Biltonen. *Biophys J* 70:84–86, 1996.
213. T. Gil, M. Sabra, J. H. Ipsen, O. G. Mouritsen. *Biophys J* 73:1728–1741, 1997; M. C. Sabra, O. G. Mouritsen. *Biophys J* 74:745–752, 1998.
214. O. G. Mouritsen. *Curr Opin Coll Interf Sci* 3:78–87, 1998.
215. G. Gompper, M. Kraus. *Phys Rev E* 47:4301–4312, 1993; G. Gompper, J. Goos. *Phys Rev E* 50:1325–1335, 1994.
216. R. Holyst, W. T. Gozdz. *J Chem Phys* 106:4773–4780, 1996; R. Holyst, P. Oswald. *Phys Rev Lett* 79:1499–1502, 1997.
217. M. Laradji, H. Guo, M. Grant, M. J. Zuckermann. *J Phys A* 24:L269–L315, 1991; M. Laradji, H. Guo, M. Grant, M. J. Zuckermann. *J Phys: Cond Matt* 4:6715–6728, 1992.
218. G. Pätzold, K. Dawson. *Phys Rev E* 52:6908–6911, 1995.
219. J. Melenkowitz, S. H. Javadvour. *J Chem Phys* 107:623–629, 1997.
220. K. Kawasaki, T. Kawakatsu. *Physica A* 164:549–563, 1990; T. Kawakatsu, K. Kawasaki. *Physica A* 167:690–735, 1990; *J Coll Interf Sci* 145:413–419, 1991; T. Kawakatsu, K. Kawasaki, M. Furusaka, H. Okabayashi, T. Kanaya. *J Chem Phys* 99:8200–8217, 1993; *J Phys: Cond Matt* 6:6835–6408, 1994.
221. T. Kawakatsu. *Phys Rev E* 50:2856–2862, 1994; T. Kawakatsu, K. Kawasaki, M. Furusaka, H. Okabayashi, T. Kanaya. *J Chem Phys* 102:2247–2253, 1995; T. Kawakatsu. *Mol Sim* 16:47–57, 1996.
222. J. H. Yao, M. Laradji. *Phys Rev E* 47:2695–2701, 1993.

- 223. B. A. C. van Flimmeren, M. Postma, P. Huetz, A. Brisson, J. G. E. M. Fraaije. *Phys Rev E* 54:5836–5839, 1996; B. A. C. van Flimmeren, J. G. E. M. Fraaije. *Comp Phys Comm* 99:21–28, 1996.
- 224. H. Kodama, S. Komura. *J Physique II* 7:7–14, 1997.
- 225. G. Gonnella, E. Orlandini, J. M. Yeomans. *Phys Rev Lett* 78:1695–1698, 1997.
- 226. O. Theissen, G. Gompper, D. Kroll. *Europhys Lett* 42:419–423, 1998.
- 227. R. Lipowsky, B. Zielanska. *Phys Rev Lett* 62:1572–1575, 1989.
- 228. G. Gompper, D. M. Kroll. *Europhys Lett* 9:59–64, 1989.
- 229. R. R. Netz, R. Lipowsky. *Europhys Lett* 29:345–350, 1995; R. R. Netz. *Phys Rev E* 51:2286–2294, 1995; *Phys Rev E* 52:1897–1902, 1995.
- 230. R. R. Netz, P. Pincus. *Phys Rev E* 52:4114–4128, 1995.
- 231. A. Cappi, P. Colangelo, G. Gonnella, A. Maritan. *Nucl Phys B* 370:659–694, 1992; P. Colangelo, G. Gonnella, A. Maritan. *Phys Rev E* 47:411–418, 1993.
- 232. C. N. Likos, K. R. Mecke, H. Wagner. *J Chem Phys* 102:9350–9361, 1995.
- 233. G. I. Menon, R. Pandit, S. Ramoswamy. *Mol Cryst Liq Cryst* 288:93–104, 1996.
- 234. K. R. Mecke. *Int J Mod Phys B* 12:861–899, 1998.
- 235. V. A. Kazakov, I. K. Kostov, A. A. Migdal. *Phys Lett B* 157:295–300, 1985; D. V. Boulatov, V. A. Kazakov, I. K. Kostov, A. A. Migdal. *Nucl Phys B* 275:641–686, 1986.
- 236. A. Billoire, F. David. *Nucl Phys B* 275:617–640, 1986.
- 237. J.-S. Ho, A. Baumgärtner. *Europhys Lett* 12:295–300, 1990; A. Baumgärtner, J.-S. Ho. *Phys Rev A* 41:5747–5750, 1990.
- 238. Y. Kantor, D. R. Nelson. *Phys Rev Lett* 58:2774–2777, 1987; *Phys Rev A* 36:4020–4032, 1997.
- 239. D. H. Boal, M. Rao. *Phys Rev A* 10:R6947–R6950, 1992.
- 240. D. M. Kroll, G. Gompper. *Science* 255:968–971, 1992; *Phys Rev A* 46:3119–3122, 1992; G. Gompper, D. M. Kroll. *Europhys Lett* 19:581–586, 1992; *Phys Rev A* 46:7466–7473, 1992; *Phys Rev Lett* 73:2139–2142, 1994.
- 241. G. Gompper, D. M. Kroll. *J Physique I* 6:1305–1320, 1996.
- 242. B. Dammann, H. C. Fogeby, J. H. Ipsen, C. Jeppesen. *J Physique I* 4:1139–1149, 1994.
- 243. G. Gompper, D. M. Kroll. *Phys Rev E* 51:514–525, 1995.
- 244. J. H. Ipsen, C. Jeppesen. *J Physique I* 5:1563–1571, 1995.
- 245. L. Peliti, S. Leibler. *Phys Rev Lett* 54:1690–1693, 1985.
- 246. G. Gompper, D. M. Kroll. *Phys Rev Lett* 78:2859–2862, 1997; *J Physique I* 7:1369–1390, 1997.
- 247. P. B. S. Kumar, M. Rao. *Mol Cryst Liq Cryst* 288:105–118, 1996; *Phys Rev Lett* 80:2489–2492, 1998.
- 248. T. Koyama. *Phys Rev E* 57:6815–6824, 1998.
- 249. J. C. Shillcock, D. H. Boal. *Biophys J* 71:317–326, 1996; J. C. Shillcock, U. Seifert. *Biophys J* 74:1754–1766, 1998.
- 250. B. Dammann, J. H. Ipsen. *Europhys Lett* 40:99–104, 1997.
- 251. G. Gompper, D. M. Kroll. *Phys Rev Lett* 81:2284–2297, 1998.

# 14

## Ordering in Microemulsions

**ROBERT HOLYST, ALINA CIACH, and WOJCIECH T. GÓŹDŹ** Institute of Physical Chemistry, Polish Academy of Sciences, Warsaw, Poland

I.	Introduction: Microemulsions and Ordered Structures	686
II.	Basic Landau–Ginzburg Model for Microemulsions	690
III.	Minimization of the Basic Functional	692
	A. Analytic minimization	692
	B. Minimization in the Fourier space	693
	C. Minimization in the real space	693
	D. Initial configurations, symmetries and reduction of dependent variables	694
	E. Accuracy of numerical computations	695
IV.	Characterization of Periodic Structures	696
	A. Symmetry	696
	B. Interface surface area, oil–water volume fraction	696
	C. Curvatures	698
	D. Euler characteristic, genus	700
	E. Distribution of the normal vectors	701
V.	Triply Periodic Structures Generated from the Basic Model	702
	A. Structures with interface described by known minimal surfaces	702
	B. New structures generated from the basic functional	706
VI.	Mean-field Bulk Phase Diagram	709
VII.	Computer Simulations of the Basic Landau–Ginzburg Model	711
	A. Topological fluctuations	711

B.	Discretization	712
C.	Euler characteristic in computer simulations	713
D.	Microemulsion–lamellar phase transition	714
VIII.	Extended Landau–Ginzburg Model	720
A.	The CHS model	720
B.	Derivation of the mesoscopic model from the microscopic lattice model	721
C.	The extended model	722
IX.	Bifurcation Analysis of the Extended Model	724
A.	Bifurcation line	724
B.	Tricritical point in the extended model	726
C.	Stability of the cubic phases near the bifurcation line	727
X.	Structure of Microemulsion	730
A.	New structure parameters	731
B.	Structure parameters in ordered phases	732
C.	Structure parameters in microemulsion	734
XI.	Summary	737
	References	740

## I. INTRODUCTION: MICROEMULSIONS AND ORDERED STRUCTURES

Amphiphilic molecules (surfactants) are composed of two different parts: hydrophobic tail and hydrophilic head [1–4]. Due to their chemical structure they self-assemble into internal surfaces in water solutions or in mixtures of oil and water, where the tails are separated from the water solvent. These surfaces can form closed spherical or cylindrical micelles or bicontinuous phases [3,5]. In the latter case a single surface extends over the volume of the system and divides it into separated and mutually interwoven subvolumes.

When comparable amounts of oil and water are mixed with surfactant a bicontinuous, isotropic phase is formed [6]. This bicontinuous phase, called a microemulsion, can coexist with oil- and water-rich phases [7,1]. The range of order in microemulsions is comparable to the typical length of the structure (domain size). When the strength of the surfactant (a length of the hydrocarbon chain, or a size of the polar head) and/or its concentration are large enough, the microemulsion undergoes a transition to ordered phases. One of them is the lamellar phase with a periodic stack of internal surfaces parallel to each other. In binary water–surfactant mixtures, or in

ternary mixtures with a small amount of oil, apart from the lamellar phase hexagonal or cubic phases occur.

In the latter the surfactant monolayer (in oil and water mixture) or bilayer (in water only) forms a periodic surface. A periodic surface is one that repeats itself under a unit translation in one, two, or three coordinate directions similarly to the periodic arrangement of atoms in regular crystals. It is still not clear, however, whether the transition between the bicontinuous microemulsion and the ordered bicontinuous cubic phases occurs in nature. When the volume fractions of oil and water are equal, one finds the cubic phases in a narrow window of surfactant concentration around 0.5 weight fraction. However, it is not known whether these phases are bicontinuous. No experimental evidence has been published that there exist bicontinuous cubic phases with the ordered surfactant monolayer, rather than bilayer, forming the periodic surface.

The period of the lamellar structures or the size of the cubic cell can be as large as 1000 Å and much larger than the molecular size of the surfactant (25 Å). Therefore mesoscopic models like a Landau–Ginzburg model are suitable for their study. In particular, one can address the question whether the bicontinuous microemulsion can undergo a transition to ordered bicontinuous phases.

This chapter is devoted to a description of ternary mixtures of oil, water, and surfactant within the Landau–Ginzburg (LG) approach. In order to introduce the LG functional which correctly describes many different phenomena, at least qualitatively, it is advantageous to study the molecular basis of the underlying properties of such mixtures and to derive the mesoscopic description from the crucial properties of the interparticle interactions. The interactions between the oil or water molecules and amphiphiles strongly depend on the orientations of the latter, since one end of the amphiphile is hydrophilic and the other one is hydrophobic. Therefore, in ternary surfactant mixtures, in addition to the translational degrees of freedom of oil, water, and surfactant molecules, the orientational degrees of freedom of amphiphiles are also important. The dependence of the interactions on orientations is the more significant the stronger the surfactant. In the case of relatively weak surfactants it turns out that a sufficiently accurate description is provided by models in which only translational degrees of freedom of oil and water particles are included and the amphiphilicity of surfactant molecules is taken into account only through the effective interactions between oil and water molecules. The effective attraction between oil and water particles appears when an amphiphile with the head oriented towards water and the tail oriented towards oil is located between them. Once the effective interactions are introduced, the degrees of freedom of amphiphiles do not have to be explicitly taken into account in this type of



approximation. Microscopic lattice models of this kind were introduced in Refs. 8–10. On the mesoscopic level, such simplified or basic description was first introduced in Ref. 11 and extended in Ref. 12.

The description based on the effective, amphiphile-induced interactions between oil and water leads to the “basic” LG functional which depends on a single order parameter (OP), namely the local concentration difference between oil and water,  $\phi(\mathbf{r})$ , which is assumed to be positive in the oil-rich regions and negative in the water-rich regions. It is next assumed that all the surfactant molecules are located between the oil-rich and water-rich domains, i.e., at the surface  $\phi(\mathbf{r}) = 0$ . In addition, it is assumed that this surface is saturated by the surfactant molecules, according to the above discussion concerning the origin of the effective interactions. The basic model very well describes the mixtures with weak surfactants in the limited region of the phase space in which the above assumptions can be satisfied. In particular, the model is suitable only for relatively low surfactant volume fractions  $\rho_s$ . This is, however, a very interesting region in which the microemulsion and the lamellar phase are stable. The great advantage of the basic model is its simplicity. The structure of the system can be described within the model in terms of geometrical and topological properties of surfaces  $\phi(\mathbf{r}) = 0$ . In this chapter we calculate the local geometrical invariants, the mean  $H$  and the Gaussian  $K$  curvatures (Fig. 1). In the case of ordered phases the equation  $\langle \phi(\mathbf{r}) \rangle = 0$  represents various periodic surfaces. We

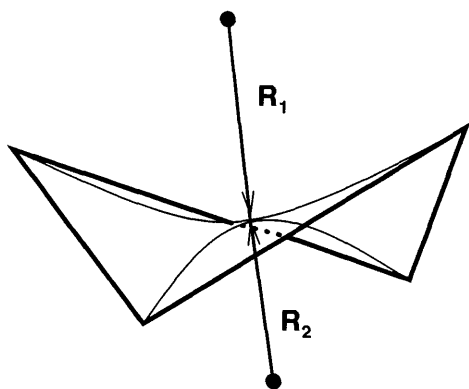


**FIG. 1** The figure illustrates a piece of surface with non-positive Gaussian curvature.  $R_1$  and  $R_2$  are the principal radii. The Gaussian ( $K$ ) and the mean ( $H$ ) curvatures are expressed in terms of the principal radii as follows:  $H = 1/(2R_1) + 1/(2R_2)$ ,  $K = 1/(R_1 R_2)$ . If  $R_1 = -R_2$  at every point, the surface is called minimal. This implies that  $K$  is non-positive at every point.

classify the surfaces corresponding to local minima of the LG functional (metastable states) according to their symmetry properties, surface area in the unit cell, and the mean and Gaussian curvatures averaged over the unit cell of the structure. The global topology of the surface is given by the Euler characteristic  $\chi = 1/2\pi \int dSK$ .

In the case of strong surfactants the dependence of the interactions with amphiphiles on their orientations is more significant and the orientational degrees of freedom become essential. Even for weak surfactants, the assumption that all the surfactant molecules completely saturate the oil-water interfaces cannot be satisfied when  $\rho_s$  is larger than the volume fractions of oil and water, or is very low, and also when the temperature is very high and all the components are uniformly mixed. In such cases the description based on the effective "amphiphile-induced" interactions between oil and water molecules is no longer accurate enough. In particular, in the mixtures with strong surfactants and for rather high  $\rho_s$ , cubic phases with unidentified structure were observed experimentally [13]. A variety of cubic phases was found to be metastable in the basic model [14]. Their structure can be studied within the model, but neither the region of stability nor the dependence of the structure of the cubic phases on temperature and on the strength and volume fraction of the surfactant can be determined.

In order to provide a more general description of ternary mixtures of oil, water, and surfactant, we introduce an extended model in which the degrees of freedom of the amphiphiles, contrary to the basic model, are explicitly taken into account. Because of the amphiphilic nature of the surfactant particles, in addition to the translational degrees of freedom, leading to the scalar OP, also the orientational degrees of freedom are important. These orientational degrees of freedom lead to another OP which has the form of the vector field.

The LG models are usually introduced on symmetry grounds. In the case of several order parameters such an approach has a serious disadvantage: there are many coupling constants (for three OPs, one of which is the vector field, there are as many as 22 [3]). Moreover, the coupling constants are not independent from one another and are not directly related to measurable quantities, or such a relation is not known. Therefore, in Ref. 15, the free-energy functional is derived from a lattice microscopic model (CHS) [16]. With this method all the coupling constants of the mesoscopic model are expressed in terms of parameters of the lattice model, which have direct physical interpretation. In our case the coupling constants are expressed in terms of  $\rho_s$ , temperature, and a single parameter  $\gamma$  measuring the amphiphilicity of the surfactant. We determine the boundary of the stability of the uniform phase and the stability regions of various ordered phases. We also extend the description based on  $H$  and  $K$  to the case of surfactant particles

occupying some extended region in three-dimensional space, not just a mathematical surface. The extensions of  $H$  and  $K$  are related to 3- and 4-point correlation functions of the vector field describing the orientational ordering of the surfactants.

In this chapter we present various computational methods for studying the structure and stability regions of various phases within the basic and the extended LG models of the ternary surfactant mixtures. In particular we use:

- minimization of the LG functionals in the case of structures periodic in space;
- Monte Carlo (MC) simulations;
- bifurcation analysis; and
- perturbation expansion for many-body correlation functions.

## II. BASIC LANDAU–GINZBURG MODEL FOR MICROEMULSIONS

In order to study microemulsion and ordered phases which appear in systems containing surfactants the following Landau–Ginzburg functional was proposed [11,12]:

$$\mathcal{F}[\phi(\mathbf{r})] = \int d^3\mathbf{r} [c|\Delta\phi(\mathbf{r})|^2 + g[\phi(\mathbf{r})]|\nabla\phi(\mathbf{r})|^2 + f[\phi(\mathbf{r})] + \mu\phi(\mathbf{r})] \quad (1)$$

We have used in our calculations the model (1) with the functions  $g[\phi(\mathbf{r})]$ ,  $f[\phi(\mathbf{r})]$  given by

$$g[\phi(\mathbf{r})] = g_2\phi(\mathbf{r})^2 + g_0 \quad (2)$$

$$f[\phi(\mathbf{r})] = \omega(\phi(\mathbf{r}) + \phi_w)^2(\phi(\mathbf{r})^2 + f_0)(\phi(\mathbf{r}) + \phi_o)^2 \quad (3)$$

with the following set of constants:  $\phi_o = -\phi_w = 1$ ,  $c = 1$ ,  $\omega = 1$ ,  $\mu = 0$ .

The values of the field  $\phi(\mathbf{r})$  are proportional to the difference between oil and water concentrations and are negative for water-rich and positive for oil-rich regions. The surface

$$\phi(\mathbf{r}) = 0 \quad (4)$$

describes the interface between oil and water and is assumed to be saturated by surfactant molecules. More precisely, we assume that  $\phi(\mathbf{r}) = 0$  describes the center of the surfactant monolayer. The function  $f[\phi(\mathbf{r})]$  is the bulk free energy.  $\mu$  is the chemical potential difference between oil and water. The surfactant degrees of freedom are considered as being integrated out and the surfactant properties enter the functional (1) through the form of the func-

tions  $g[\phi(\mathbf{r})]$  and  $f[\phi(\mathbf{r})]$ . The functional (1) can also be used to model the sponge phase. In this case the negative values of the order parameter are interpreted as the interior part of the sponge phase, and positive values as the exterior part of the phase.

The function  $f[\phi(\mathbf{r})]$  has three minima by construction and guarantees three-phase coexistence of the oil-rich phase, water-rich phase, and microemulsion. The minima for oil-rich and water-rich phases are of equal depth, which makes the system symmetric, therefore  $\mu$  is zero. Varying the parameter  $f_0$  makes the microemulsion more or less stable with respect to the other two bulk uniform phases. Thus  $f_0$  is related to the chemical potential of the surfactant. The constant  $g_2$  depends on  $g_0$  and  $f_0$  and is chosen in such a way that the correlation function  $G(r) = \langle \phi(\mathbf{r})\phi(\mathbf{0}) \rangle$  decays monotonically in the oil-rich and water-rich phases [12,13]. This is the case when  $g_2 > 4\sqrt{1+f_0} - g_0$ . Here we take, arbitrarily,  $g_2 = 4\sqrt{1+f_0} - g_0 + 0.01$ .

In the Gaussian approximation the water–water structure factor  $S_{ww}(k)$  for (1) is given by

$$S_{ww}(k) \propto \frac{1}{ck^4 + g(\phi_b)k^2 + \frac{1}{2}f''(\phi_b)} \quad (5)$$

where  $\phi_b \in \{\phi_w, \phi_m, \phi_o\}$ , and for the oil-rich phase  $\langle \phi(\mathbf{r}) \rangle \simeq \phi_o$ , for the water-rich phase  $\langle \phi(\mathbf{r}) \rangle \simeq \phi_w$ , for microemulsion  $\langle \phi(\mathbf{r}) \rangle \simeq \phi_m = 0$ . The water–water structure factor  $S_{ww}(k)$  can be measured by experiment. It turns out that Eq. (5) describes very well the data from the scattering experiments [11,17].

The Fourier transform of (5) gives the correlation function

$$G(r) \propto \lambda \exp(-r/\xi) \frac{\sin(2\pi r/\lambda)}{2\pi r} \quad (6)$$

where

$$\lambda = \left[ \left( \frac{\frac{1}{2}f''(0)}{4c} \right)^{1/2} - \left( \frac{g(0)}{4c} \right) \right]^{1/2} \quad (7)$$

$$\xi = \left[ \left( \frac{\frac{1}{2}f''(0)}{4c} \right)^{1/2} + \left( \frac{g(0)}{4c} \right) \right]^{-1/2} \quad (8)$$

In the real space the correlation function (6) exhibits exponentially damped oscillations, and the structure is characterized by two lengths: the period of the oscillations  $\lambda$ , related to the size of oil and water domains, and the correlation length  $\xi$ . In the microemulsion  $2\pi\xi > \lambda$  and the water-rich and oil-rich domains are correlated, hence the water–water structure factor assumes a maximum for  $k = k_{\max} \neq 0$ . When the concentration of surfac-

tants decreases, the ratio  $2\pi\xi/\lambda$  decreases as well and at the Lifshitz line  $2\pi\xi/\lambda = 1$  and  $k_{\max} = 0$ . When the surfactant volume fraction is further decreased, the correlation functions still oscillate but the amplitude decreases rapidly and the oil-rich and water-rich domains become uncorrelated. Eventually  $2\pi\xi/\lambda = 0$  at the disorder line, beyond which the correlation functions decay monotonically.

The model has been successfully used to describe wetting behavior of the microemulsion at the oil–water interface [12,18–20], to investigate a few ordered phases such as lamellar, double diamond, simple cubic, hexagonal, or crystals of spherical micelles [21,22], and to study the mixtures containing surfactant in confined geometry [23].

### III. MINIMIZATION OF THE BASIC FUNCTIONAL

The thermodynamic quantities and correlation functions can be obtained from Eq. (1) by functional integration. However, the functional integration cannot usually be performed exactly. One has to use approximate methods to evaluate the functional integral. The one most often used is the mean-field approximation, in which the integral is replaced with the maximum of the integrand, i.e., one has to find the minimum of  $\mathcal{F}[\phi(\mathbf{r})]$ , which satisfies the mean-field equation

$$\frac{\delta\mathcal{F}[\phi(\mathbf{r})]}{\delta\phi(\mathbf{r})} = 0 \quad (9)$$

#### A. Analytic Minimization

For a certain choice of  $g(\phi)$  and  $f(\phi)$  the above equation can be solved analytically for simple spatially modulated phases, such as lamellar or hexagonal [22]. This is possible for the piecewise parabolic model of  $f(\phi)$ :

$$\omega_w(\phi - \phi_w)^2 \quad \phi_{0+} < \phi \quad (10)$$

$$f(\phi) = \omega_m\phi^2 + f_0 \quad \phi_{0+} < \phi < \phi_{0-} \quad (11)$$

$$\omega_o(\phi - \phi_o)^2 \quad \phi < \phi_{0-} \quad (12)$$

and

$$g_w \quad \phi_{0+} < \phi \quad (13)$$

$$g(\phi) = g_m \quad \phi_{0+} < \phi < \phi_{0-} \quad (14)$$

$$g_o \quad \phi < \phi_{0-} \quad (15)$$

where  $\phi_{0-}$ ,  $\phi_{0+}$  are chosen to make  $f(\phi)$  continuous.  $g_w$ ,  $g_m$ ,  $g_o$  are the values of  $g(\phi)$  in water, oil, and microemulsion respectively. The solution for the full profile is obtained by matching the solution for each parabola. Unfortunately this can be done only numerically. For the spatially modulated phases in only one coordinate this is not a problem, but when the order parameter depends on two or three coordinates the matching points form one- or two-dimensional hypersurfaces which are hard to determine numerically. For these reasons, it is more convenient to minimize the full functional numerically in the Fourier space by expanding the order parameter in the Fourier series or in the real space by discretizing the functional.

## B. Minimization in the Fourier Space

In the Fourier space, the order parameter  $\phi(\mathbf{r})$  for periodic structures is approximated by the Fourier series

$$\phi(\mathbf{r}) = A_0 + \sum_i A_i \sum_{\mathbf{k}^i} \cos(\mathbf{k}^i \cdot \mathbf{r}) + \sum_i B_i \sum_{\mathbf{k}^i} \sin(\mathbf{k}^i \cdot \mathbf{r}) \quad (16)$$

where  $\mathbf{k}^i$  are the reciprocal lattice vectors in the  $i$ th shell,  $A_i$  and  $B_i$  are the amplitudes of the  $i$ th shell. The shell means here a set of reciprocal lattice vectors of the same length related to each other by the symmetry operations characteristic for a given lattice. The approximation by the Fourier series ensures that the function  $\phi(\mathbf{r})$  is continuous at the unit cell boundaries. The quality of the approximation is the better, the larger number of shells included. Next, the functional (1) is minimized with respect to the amplitudes  $A_i$  and  $B_i$ . The advantage of the minimization in the Fourier space is the fact that the solution is already continuous at the boundary of the unit cell, by construction. From the computational point of view the Fourier space approach requires fewer variables than in the real space approach, but the speed of calculations is significantly decreased by the calculation of trigonometric functions.

## C. Minimization in the Real Space

In order to find the local minima of the functional we have to discretize it on the cubic lattice. Thus the functional  $\mathcal{F}[\phi(\mathbf{r})]$  becomes a function  $F(\{\phi_{i,j,k}\})$  of  $N^3$  variables, where  $L = (N - 1)h$  is the linear dimension of the cubic lattice,  $h$  is the lattice spacing, and  $\{\phi_{i,j,k}\}$  stands for the set of all variables of the function. Each variable  $\phi_{i,j,k}$  represents the value of the field  $\phi(\mathbf{r})$  at the point  $\mathbf{r} = (i, j, k)h$ , and  $i, j, k = 1, \dots, N$ . In our calculations we use  $N = 129$ , which results in over 2 million points per unit cell.

All the structures we have investigated are periodic. Thus periodicity has to be incorporated into the functional (1). It is done by periodic boundary

conditions:  $\phi_{1,j,k} = \phi_{N,j,k}$ ,  $\phi_{2,j,k} = \phi_{N+1,j,k}$ ,  $\phi_{3,j,k} = \phi_{N+2,j,k}$ ,  $\phi_{0,j,k} = \phi_{N-1,j,k}$ ,  $\phi_{-1,j,k} = \phi_{N-2,j,k}$ , and similarly in  $y$  and  $z$  directions. The points outside the unit cell, given by the periodic boundary conditions, enter the functional through the calculations of derivatives of points at the boundary and near the boundary of the lattice, i.e., when at least one of the indices  $i, j, k$  is equal to 1, 2,  $N - 1, N$ .

The first and second derivatives in the gradient and Laplacian term of the functional (1) at the point  $\mathbf{r} = (i, j, k)h$  on the lattice are calculated according to the following formulas [24]

$$\frac{\partial \phi(\mathbf{r})}{\partial x} \rightarrow \frac{\phi_{i+1,j,k} - \phi_{i-1,j,k}}{2h} \quad (17)$$

and

$$\frac{\partial^2 \phi(\mathbf{r})}{\partial x^2} \rightarrow \frac{1}{12h^2} (-\phi_{i+2,j,k} + 16\phi_{i+1,j,k} - 30\phi_{i,j,k} + 16\phi_{i-1,j,k} - \phi_{i-2,j,k}) \quad (18)$$

and similarly in  $y$  and  $z$  directions.

The mixed derivatives used in (28) and (29) are calculated according to [24]

$$\begin{aligned} \frac{\partial^2 \phi(\mathbf{r})}{\partial x \partial y} \rightarrow & -\frac{1}{2h^2} (\phi_{i+1,j,k} + \phi_{i-1,j,k} + \phi_{i,j+1,k} + \phi_{i,j-1,k} \\ & - 2\phi_{i,j,k} - \phi_{i+1,j+1,k} - \phi_{i-1,j-1,k}) \end{aligned} \quad (19)$$

## D. Initial Configurations, Symmetries and Reduction of Dependent Variables

To start minimization one needs an initial configuration which should contain the most important features of the investigated structures. This may substantially reduce the computation time. Here we present the initial configurations used in the minimization of structures with  $Im3m$  symmetries.

The initial configuration is set up by building the field  $\phi(\mathbf{r})$  for a unit cell first on a small cubic lattice,  $N = 3$  or 5, analogously to a two-component, AB, molecular crystal. The value of the field  $\phi(\mathbf{r}) = \phi_{i,j,k}$  at the point  $\mathbf{r} = (i, j, k)h$  on the lattice is set to 1 if, in the molecular crystal, an atom A is in this place; if there is an atom B,  $\phi_{i,j,k}$  is set to  $-1$ ; if there is an empty place,  $\phi_{i,j,k}$  is set to 0. Fig. 2 shows the initial configuration used to build the field  $\phi(\mathbf{r})$  for the simple cubic-phase unit cell. Filled black circles represent atoms of type A and hollow circles represent atoms of type B. In this case all sites are occupied by atoms A or B.

The tetrahedron drawn in Fig. 2 with thick solid lines is the kaleidoscopic cell used to build the unit cell. One can easily see now that in order to build

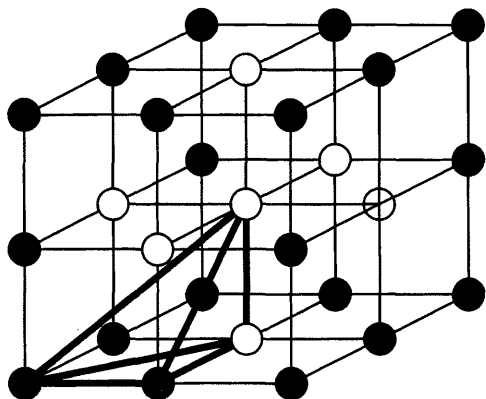


**FIG. 2** The initial configuration used to create structures of symmetry of simple cubic phase.

the field in the unit cell on a small cubic lattice,  $N = 3$ , it is enough to specify the values of the field  $\phi(\mathbf{r}) = \phi_{i,j,k}$  only at the points inside the tetrahedron. The values of the field at the remaining points can be set using the symmetry of the structures. Thus instead of specifying  $3^3 = 27$  values of  $\phi_{i,j,k}$  one has to specify these values at four points of the cubic lattice for the simple cubic structure.

The symmetry of the structure we are looking for is imposed on the field  $\phi(\mathbf{r})$  by building up the field inside a unit cubic cell of a smaller polyhedron, replicating it by reflections, translations, and rotations. Such a procedure not only guarantees that the field has the required symmetry but also enables substantial reduction of independent variables  $\phi_{i,j,k}$  in the function  $F(\{\phi_{i,j,k}\})$ . For example, structures having the symmetry of the simple cubic phase are built of quadrirectangular tetrahedron replicated by reflection. The faces of the tetrahedron lie in the planes of mirror symmetry. The volume of the tetrahedron is  $1/48$  of the unit cell volume.

The small lattice can be enlarged to the desired size by changing the number of points from  $N$  to  $2N - 1$  and finding the values of  $\phi_{i,j,k}$  in the new lattice sites by interpolation. The interpolation done to enlarge the lattice has no influence on the results. It may speed up the calculations but only if it is done appropriately.

## E. Accuracy of Numerical Computations

The conjugate gradient method [25] is used to minimize the function  $F(\{\phi_{i,j,k}\})$ . Minimization is done with respect to  $\{\phi_{i,j,k}\}$  for a given value



of the cell length  $L = (N - 1)h$ . The lattice spacing  $h$  is varied to find the cell length for the lowest value of the free energy functional  $F(\{\phi_{i,j,k}\})$ .

The solution for the discretized model of the continuous functional is obtained with a certain accuracy which depends on the value of the lattice spacing  $h$  and the number of points  $N$ . The accuracy of our results is checked by calculating the free energy and the surface area of  $\phi(\mathbf{r}) = 0$  for a few different sizes of the lattice. The calculation of the free energy is done with sufficient accuracy for  $N = 129$ , which results in over 2 million points per unit cell. The calculation of the surface area of  $\phi(\mathbf{r}) = 0$  is sufficiently accurate even for a smaller lattice size.

The calculation of the free energy by minimization in the Fourier space gives almost the same values of the free energy, but a significant number of shells is necessary [26].

#### IV. CHARACTERIZATION OF PERIODIC STRUCTURES

The surface dividing the components of the mixture formed by a layer of surfactant characterizes the structure of the mixture on a mesoscopic length scale. This interface is described by its global properties such as the surface area, the Euler characteristic or genus, distribution of normal vectors, or in more detail by its local properties such as the mean and Gaussian curvatures.

##### A. Symmetry

The structures we have generated can be, in principle, characterized by space group symmetry [27–29], analogously to molecular crystals. The simple cubic structure has the space group  $Im\bar{3}m$ , double diamond  $Pn\bar{3}m$ , gyroid  $Ia\bar{3}d$ . However, it is not always obvious, even for the structures of a simple topology, which Bravais lattice should be assigned to a given structure [29]. For more complex structures, assigning a Bravais lattice becomes even less clear. Therefore we decided to characterize the symmetry of the structures we have generated by including it in the class of symmetry characteristic of the following structures: simple cubic, double diamond, and gyroid. All these structures belong to the class of cubic symmetry, thus here we generate only the structures belonging to this class.

##### B. Interface Surface Area, Oil–Water Volume Fraction

The order parameter field  $\phi(\mathbf{r})$  characterizes the local structure of the phases we have investigated. The most interesting is the topology of the phases,

described by the surface given by the following equation

$$\phi(\mathbf{r} = (x, y, z)) = 0 \quad (20)$$

separating the regions of positive values of the order parameter (oil) from the regions of its negative values (water). Thus it is crucial in our studies to find the location of the surface  $\phi(\mathbf{r}) = 0$ .

Since the solution of the functional is given as a three-dimensional table of numbers, the position of the surface  $\phi(\mathbf{r}) = 0$  is determined by interpolation between the neighboring points of different sign. It is highly unlikely, because of numerical accuracy, that the value of the field  $\phi(\mathbf{r}) = \phi_{i,j,k}$  at the point  $\mathbf{r} = (i, j, k)h$  on the lattice is exactly zero. Therefore the points of the surface have to be localized by interpolation between the neighboring sites of the lattice. If  $\phi(\mathbf{r}_1 = (i, j, k)h) = \phi_{i,j,k} < 0$  and  $\phi(\mathbf{r}_2 = (i+1, j, k)h) = \phi_{i+1,j,k} > 0$ , then the point  $\mathbf{r}_0$ , for which  $\phi(\mathbf{r}_0) = 0$ , must lie between the points  $\mathbf{r}_1 = (i, j, k)h$  and  $\mathbf{r}_2 = (i+1, j, k)h$ . Moreover, the location of  $\mathbf{r}_0$  depends on the values of the field at the points  $\mathbf{r}_1$  and  $\mathbf{r}_2$  in the following way

$$\mathbf{r}_0 = \left( i + \frac{|\phi_{i,j,k}|}{|\phi_{i,j,k} - \phi_{i+1,j,k}|}, j, k \right) h \quad (21)$$

All points of the surface  $\phi(\mathbf{r}) = 0$  are found by the interpolation of the points located between the neighboring lattice sites. However, to describe the surface it is also necessary to specify the connections between these points. Due to the discretization the unit cell is divided into  $(N-1)^3$  small cubes of the size of the lattice spacing,  $h$ . The surface  $\phi(\mathbf{r}) = 0$  passing through a small cube cuts a polygon out of it. The edges of the polygons are formed by the intersection of the surface and the faces of the small cube. The edges are approximated by straight lines. The possible configurations of the surface  $\phi(\mathbf{r}) = 0$  cutting a small cube are pictured in Fig. 3. The surface  $\phi(\mathbf{r}) = 0$  can cut out only four kinds of polygon: a triangle, a tetragon, a pentagon, and a hexagon. Since the edges of these polygons, except for the triangle, do not lie in a common plane, it is necessary to specify also the connections between the vertices of the polygon in order to characterize the surface unambiguously. It is done in the way shown in Fig. 3 with thick dotted lines in the patches of the surface inside the small cubes. This procedure makes the surface covered only with triangles. The triangulation described above is used to calculate the surface area inside a unit cell by summing up the surface area of all triangles. The triangulation can also be used to calculate the volume ratio of the space occupied by the regions where the order parameter is negative to the region where it is positive. These two regions, are, of course, separated by the surface  $\phi(\mathbf{r}) = 0$ .

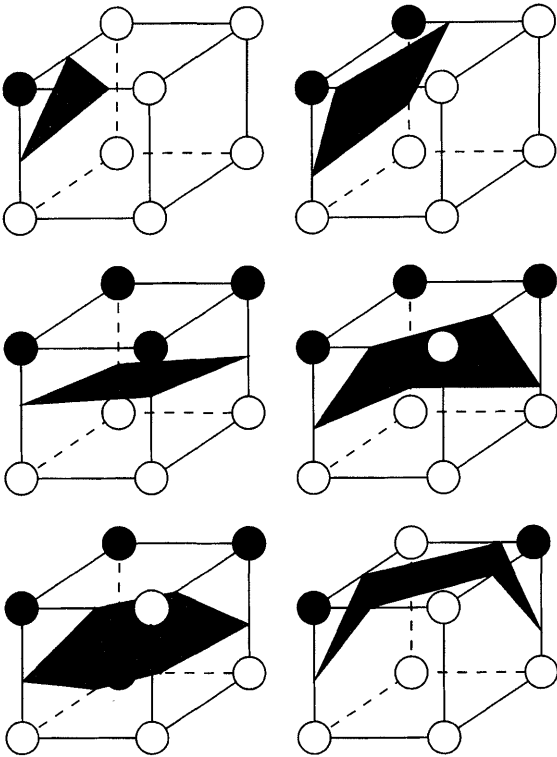


**FIG. 3** The possible configurations of passing the surface  $\phi(\mathbf{r}) = 0$  through the field  $\phi(\mathbf{r})$  discretized on the lattice. Black circles represent  $\phi_{i,j,k} < 0$ , whereas white circles  $\phi_{i,j,k} > 0$ . The cubes represent the smallest pieces of the lattice of linear dimension  $h$ . For smooth surfaces studied here, cases of 3, 4, 5, and 6 vertices of the surface in a small cube are the only ones. The cases of 7, 8, 9, and 12 vertices in a single cube have not been encountered.

**C. Curvatures**

The Gaussian ( $K(\mathbf{r})$ ) and mean curvatures ( $H(\mathbf{r})$ ), see Fig. 1, present another characteristic of internal surfaces. By definition we have

$$H(\mathbf{r}) = \frac{1}{2} \left( \frac{1}{R_1(\mathbf{r})} + \frac{1}{R_2(\mathbf{r})} \right) \tag{22}$$

$$K(\mathbf{r}) = \frac{1}{R_1(\mathbf{r})} \frac{1}{R_2(\mathbf{r})} \tag{23}$$

where  $R_1(\mathbf{r})$ ,  $R_2(\mathbf{r})$  are the principal radii of curvature at point  $\mathbf{r}$ . For minimal surfaces  $H(\mathbf{r}) = 0$  at every point of the surface.

For the surface  $\phi(\mathbf{r}) = 0$  it is more convenient to use formulas expressing the curvatures in terms of the field  $\phi(\mathbf{r})$ . The unit normal to the surface  $\hat{\mathbf{n}}(\mathbf{r})$  at the point  $\mathbf{r}$  is given by the gradient of the field  $\phi(\mathbf{r})$

$$\hat{\mathbf{n}}(\mathbf{r}) = \frac{\nabla\phi(\mathbf{r})}{|\nabla\phi(\mathbf{r})|} \quad (24)$$

The mean  $H$  curvature is given by the divergence of the unit vector [30] normal to the surface at  $\mathbf{r}$ ,

$$H(\mathbf{r}) = -\frac{1}{2}\nabla \cdot \hat{\mathbf{n}}(\mathbf{r}) = -\frac{1}{2}\nabla \cdot \frac{\nabla\phi(\mathbf{r})}{|\nabla\phi(\mathbf{r})|} \quad (25)$$

and the Gaussian curvature  $K$  by the formula [31]

$$K(\mathbf{r}) = \frac{1}{2}(-(\partial_i \hat{n}_j)^2 + (\nabla \cdot \hat{\mathbf{n}}(\mathbf{r}))^2) \quad (26)$$

One can discover a special property of the functional (1) by analyzing the formula for the mean curvature (25) expressed in terms of the three dimensional field  $\phi(\mathbf{r})$ . From the form of Eq. (1) one can realize that for some local minima of (1) the average curvature given by

$$H(\mathbf{r}) = -\frac{1}{2}\nabla \cdot \left( \frac{\nabla\phi(\mathbf{r})}{|\nabla\phi(\mathbf{r})|} \right) = -\frac{1}{2} \frac{\Delta\phi(\mathbf{r})}{|\nabla\phi(\mathbf{r})|} + \frac{\nabla\phi(\mathbf{r})\nabla|\nabla\phi(\mathbf{r})|}{2|\nabla\phi(\mathbf{r})|^2} \quad (27)$$

vanishes at every point of the  $\phi(\mathbf{r}) = 0$  surface. It follows from the second term of that  $|\nabla\phi(\mathbf{r})|$  should have the maximal value for  $\phi(\mathbf{r}) = 0$  (note that  $g_0 < 0$ ) and consequently the second term (which, after some algebra, can be written as  $(\partial|\nabla\phi(\mathbf{r})|/\partial n)/2|\nabla\phi(\mathbf{r})|$ , with  $\partial n$  denoting the derivative along the normal to the surface) in (27) vanishes. Also, for the  $\phi(\mathbf{r})$ ,  $-\phi(\mathbf{r})$  symmetry we know that  $H(\mathbf{r})$  averaged over the whole surface should be zero. This means that either  $\Delta\phi(\mathbf{r})$  is exactly zero at the surface or it changes sign. From the first term of (1) it follows that the former is favored and consequently  $H(\mathbf{r}) = 0$  at every point  $\mathbf{r}$  at the surface  $\phi(\mathbf{r}) = 0$ . Therefore the structures with minimal surfaces should be favored among the local minima of the functional (1). The argument presented here has a local nature and does not rule out other possibilities.

In the numerical calculations of the curvatures the following formulas are

used [30,32]:

$$H = -\frac{1}{2\sqrt{\phi_x^2 + \phi_y^2 + \phi_z^2}} \frac{B}{A} \quad (28)$$

$$K = \frac{1}{\phi_x^2 + \phi_y^2 + \phi_z^2} \frac{C}{A} \quad (29)$$

where  $A$ ,  $B$ , and  $C$  are obtained from

$$\det \begin{pmatrix} (\phi_{xx} - \lambda) & \phi_{xy} & \phi_{xz} & \phi_x \\ \phi_{yx} & (\phi_{yy} - \lambda) & \phi_{yz} & \phi_y \\ \phi_{zx} & \phi_{zy} & (\phi_{zz} - \lambda) & \phi_z \\ \phi_x & \phi_y & \phi_z & 0 \end{pmatrix} = A\lambda^2 + B\lambda + C \quad (30)$$

and are given by

$$A = -(\phi_x^2 + \phi_y^2 + \phi_z^2) \quad (31)$$

$$B = \phi_x^2(\phi_{yy} + \phi_{zz}) + \phi_y^2(\phi_{xx} + \phi_{zz}) + \phi_z^2(\phi_{xx} + \phi_{yy}) \\ - 2\phi_x\phi_y\phi_{xy} - 2\phi_x\phi_z\phi_{xz} - 2\phi_y\phi_z\phi_{yz} \quad (32)$$

$$C = \phi_x^2(\phi_{yz}^2 - \phi_{yy}\phi_{zz}) + \phi_y^2(\phi_{xz}^2 - \phi_{xx}\phi_{zz}) + \phi_z^2(\phi_{xy}^2 - \phi_{xx}\phi_{yy}) \\ + 2\phi_x\phi_z(\phi_{xz}\phi_{yy} - \phi_{xy}\phi_{yz}) + 2\phi_x\phi_y(\phi_{xy}\phi_{zz} - \phi_{xz}\phi_{yz}) \\ + 2\phi_y\phi_z(\phi_{yz}\phi_{xx} - \phi_{xy}\phi_{xz}) \quad (33)$$

The mean and the Gaussian curvatures have to be computed at the points of the surface  $\phi(\mathbf{r}) = 0$ . These points do not lie exactly at the lattice sites. In order to calculate the derivatives of the field  $\phi(\mathbf{r})$  at the point  $\mathbf{r}_0$ , for which  $\phi(\mathbf{r}_0) = 0$ , according to the formulas (17), (18), (19), the values of the field  $\phi(\mathbf{r})$  at the points  $\mathbf{r}_0 + (0, 0, h)$ ,  $\mathbf{r}_0 + (0, h, 0)$ ,  $\mathbf{r}_0 + (h, 0, 0)$ ,  $\mathbf{r}_0 + (0, 0, 2h)$ ,  $\mathbf{r}_0 + (0, 2h, 0)$ ,  $\mathbf{r}_0 + (2h, 0, 0)$ ,  $\mathbf{r}_0 + (0, h, h)$ ,  $\mathbf{r}_0 + (h, h, 0)$ ,  $\mathbf{r}_0 + (h, 0, h)$  have to be interpolated.

## D. Euler Characteristic, Genus

The Euler characteristic for a closed surface is related to the Gaussian  $K$  curvature and genus  $g$  of this surface in the following way [33,29]

$$\chi = \frac{1}{2\pi} \int_S K dS = 2(1 - g) \quad (34)$$

where the integral is taken over the surface  $S$ . The genus is an integer number equal to the number of holes in the closed surface. For example,

the genus for a sphere (or ellipsoid) is zero and for a torus it is one. The structure we investigate are infinite and periodic. The genus for an infinite surfaces is infinite, of course, but for a finite piece of this surface, bounded by the unit cell, it is finite and characterizes the surface. Due to the periodicity, the surface patch in the unit cell can be treated as a closed surface in four dimensions, making calculation of the genus for the infinite periodic surface fully justified [34]. Therefore the genera of the structures are calculated according to  $g = 1 - \chi/2$ , where  $\chi$  is the Euler characteristic for the surface inside a unit cell.

The Euler characteristic for a surface built of polygons is much more conveniently calculated according to the Euler formula [33]

$$\chi = F + V - E \quad (35)$$

where  $F, V, E$  are the numbers of faces  $F$ , vertices  $V$ , and edges  $E$  of the polygons cut out by the surface  $\phi(\mathbf{r}) = 0$  in the small cubes of dimension of the lattice spacing,  $h$ . The fact that each polygon is inside a small cube makes the calculation very easy, because each vertex of the polygon belongs to four polygons since it lies in the edge of the small cube. Therefore, to calculate  $\chi$  one does not need to know the connections between points. It is sufficient to know only how many times the surface  $\phi(\mathbf{r}) = 0$  cuts the edges of the small cube and how many cubes it cuts. The number of faces  $F$  is therefore the number of small cubes cut by the surface  $\phi(\mathbf{r}) = 0$ , that is, the cubes with the values of the field  $\phi(\mathbf{r}) = \phi_{i,j,k}$  of different sign at its vertices. The number of vertices  $V$  is given by the number of intersections of the surface  $\phi(\mathbf{r}) = 0$  with the edges of the small cubes taken with a weight  $1/4$ , because each edge belongs to four cubes. The number of edges  $E$  is the same as the number of vertices, but it has to be taken with a weight  $1/2$  because the polygon edges lie in the faces of small cubes and each face belongs to two cubes. Only the last case shown in Fig. 3 needs a slightly different treatment since one face of the surface lies on the face of the small cube.

## E. Distribution of the Normal Vectors

The distribution of the vectors normal to the surface is particularly interesting since it can be obtained experimentally. The nuclear magnetic resonance (NMR) bandshape problem, for polymerized surfaces, can be transformed into the mathematical problem of finding the distribution function  $f(x)$  of

$$x = (3 \cos^2(\theta_{\mathbf{nB}}) - 1)/2 \quad (36)$$

where  $\theta_{\mathbf{nB}}$  is the angle between the normal  $\hat{\mathbf{n}}$  to the surface, describing the locus of the head groups, and the static NMR magnetic field direction  $\mathbf{B}$

[35,36]. More precisely, the distribution function is the sum of  $f(x)$  and  $f(-x)$  since NMR cannot distinguish between  $x$  and  $-x$ .

In order to compute the distribution function  $f(x)$  the vectors normal to the surface are calculated. Since the surface is given as a set of triangles we can calculate the vectors perpendicular to these triangles and next calculate the angles  $\theta_{\mathbf{nB}}$  between these vectors and the direction of the magnetic field  $\mathbf{B}$ . Once the angles are calculated it is straightforward to calculate the variable  $x$ . In order to get the distribution function  $f(x)$  the histogram of the variable  $x$  is constructed. The domain for the variable  $x$  is divided into bins. The quality of the histograms can be checked by comparing the analytic results of Anderson [29] with our numerical results (see Fig. 6(a)). The triangulated surface is only an approximation of a given surface and the approximation is better when the surface is constructed of a bigger number of triangles. In our calculation the number of triangles building up the surface is limited by the lattice size. The value of the variable  $x$  for a given triangle and the surface area of this triangle,  $S_{\Delta}$ , are calculated. Next, the bin for the corresponding value of the variable  $x$  is updated with the value of  $S_{\Delta}$ . Finally, to obtain the distribution function for the NMR the histograms for  $f(x)$  and  $f(-x)$  are summed.  $f(x)$  integrated over the whole surface in the unit cell gives the total surface area.

## V. TRIPLY PERIODIC STRUCTURES GENERATED FROM THE BASIC MODEL

In this section we characterize the minima of the functional (1) which are triply periodic structures. The essential features of these minima are described by the surface  $\phi(\mathbf{r}) = 0$  and its properties. In 1976 Scriven [37] hypothesized that triply periodic minimal surfaces (Table 1) could be used for the description of physical interfaces appearing in ternary mixtures of water, oil, and surfactants. Twenty years later it has been discovered, on the basis of the simple model of microemulsion, that the interface formed by surfactants in the symmetric system (oil–water symmetry) is preferably the minimal surface [14,38,39].

### A. Structures with Interface Described by Known Minimal Surfaces

The gyroid phase G with the minimal surface has the lowest free energy among all the cubic structures. For a given symmetry of the cubic structures the one with the lowest energy is usually the structure with the minimal surface of the lowest genus. Thus among all the structures of simple cubic symmetry the P structure has the lowest free energy. The structures are

**TABLE 1** Geometrical Properties of the Known Minimal Surfaces Obtained from the Functional (1), for the Parameters  $f_0 = 0.0$ ,  $g_0 = -3.0^a$ 

Name	Cell length	Energy	Surface area	Genus	Volume fraction
P	7.88	-0.181	2.3453 [2.3451068]	3	0.5
D	12.56	-0.188	3.8387 [3.8377862]	9	0.5
I-WP	11.78	-0.180	3.4640 [3.4646016]	7	0.533
G	10.08	-0.190	3.0919	5	0.5
O, C-TO	14.68	-0.162	3.6805	10	0.535

<sup>a</sup> In the square brackets are given the exact values found in the literature. Surface area  $\tilde{S}$ , in the table, is the normalized per face of the unit cube  $L^2$ , surface area  $S$  of the interface in the unit cell,  $\tilde{S} = S/L^2$ ,  $L = (N - 1)h$ . The energy is given per unit volume.

generated independently of the initial configuration, provided that the unit cell length is set close to the minimal length. If the cell length is taken close to a multiple of the length of the unit cell then multiple images of a given structure are formed.

The P, D, G (see Fig. 4(a,b,c)) surfaces are adjoint surfaces and consequently the histograms of the Gaussian curvature for these surfaces are the same. Fig. 5 shows the histograms of the Gaussian and the mean curvatures calculated for the P surface. The histograms for the D and G surfaces are very similar; only small differences result from the numerical accuracy. The mean curvature of the minimal surface is zero at every point, thus its histogram should be a single infinitely sharp peak at  $H = 0$ . Here it is smeared (see Fig. 5(b)) because of the numerical accuracy. In fact it may serve as a good estimate of the errors for curvatures. The oil-water volume fraction for the P, D, G surfaces is the same and equals 0.5.

The distribution function of the vectors normal to the surfaces,  $f(x)$ , for the direction of the magnetic field  $\mathbf{B}$ , in accord with the directions of the crystallographic axis (100) for the P, D, G surfaces, is presented in Fig. 6. The histograms for the P, D, G are practically the same, as they should be; the differences between the histograms are of the order of a line width. The accuracy of the numerical results can be judged by comparing the histograms obtained in our calculation with the analytically calculated distribution function for the P, D, G surfaces [29]. The solid line in Fig. 6(a) represents the result of analytical calculations [35].

The example of the P, D, G surfaces shows that there is no correlation between the symmetry of the structure and its distribution of the normal



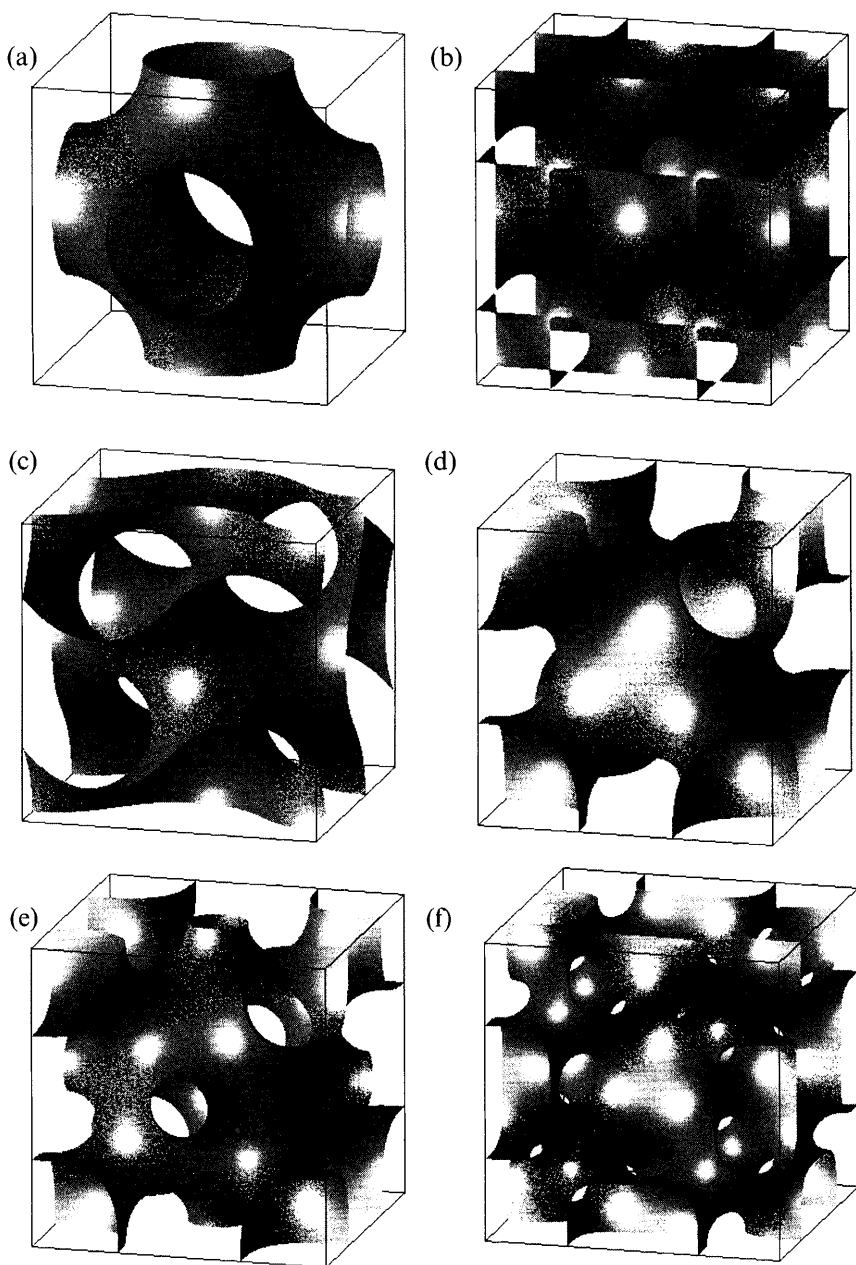


**FIG. 4** Cubic phases generated from the functional (1).

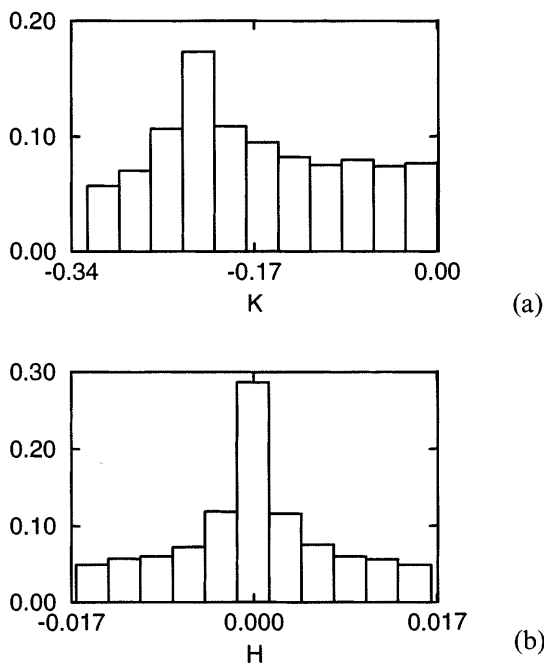


**FIG. 5** Histograms of the Gaussian ( $K$ ) (a) and mean ( $H$ ) (b) curvature for the Schwarz P surface.

vectors. In fact, for the P, D, G surfaces the distribution functions are the same (Fig. 6(a,b,c)). Thus the distribution function itself is not the fingerprint of the structure. However, it does not mean that the NMR bandshape technique is useless. It can be combined with other techniques, for example with X-ray scattering, to give a unique characterization of the structure. It is sufficient to know the symmetry (from X-ray experiments) and the distribution function (from NMR experiments) to distinguish the P, D, G structures. The distribution function will distinguish the P, D, G structures from the other structures, and the X-ray scattering experiment will differentiate the P, D, G structures since they have different symmetry.

The surfaces in Fig. 4(d,e,f,) obtained from the functional (1) are the surfaces already discovered by Schoen [28] and named by him O, C-TO, I-WP, F-RD. O, C-TO is the only structure which cannot be minimized with respect to the cell length. For all the structures except this one we are able to find the minimal cell length; i.e., by varying the cell length we are able to find the length for which the free energy per unit volume (functional (1)) has a minimum. The O, C-TO structure collapses to I-WP when the cell

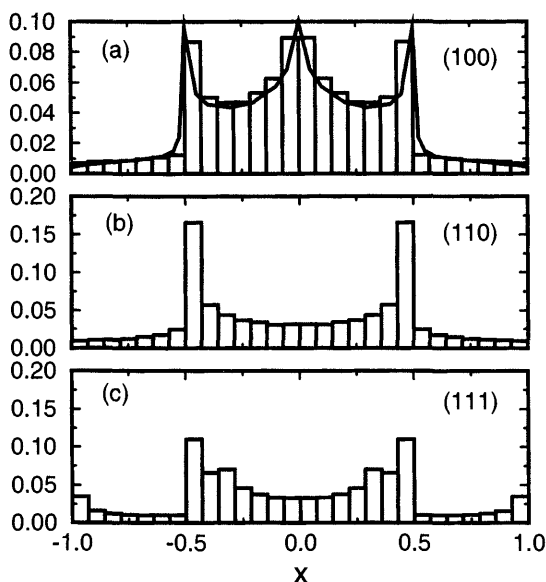


**FIG. 6** Distribution functions for P, D, G surfaces for the following directions of the magnetic field  $\mathbf{B}$ : (a) (100), solid line shows the results of analytic calculations of Anderson [35]; (b) (110); (c) (111).  $x = (3 \cos^2(\theta_{\mathbf{nB}}) - 1)/2$ .

length is varied. Such a behavior suggests that this structure is very unstable and finding it in real systems is problematic. The I-WP surface was found in star block copolymers [40]. The volume fraction for the O, C-TO, I-WP, F-RD structures differs from 0.5.

## B. New Structures Generated from the Basic Functional

The new surfaces BFY, CPD, and GP, Fig. 7(a,b,c), have been found from the minimization of the functional (1). BFY, CPD have the same symmetry as the Schwarz P surface, while GP has the gyroid G symmetry. The BFY surface can be generated from an arbitrary initial configuration if the length of the unit cell is set close to the equilibrium length, i.e., the length of the minimum of the functional (1). The pattern cut out on the face of the unit cell for the BFY surface resembles “butterfly” wings; that is why the symbol BFY is given to this surface. The volume fraction for the BFY structure is 0.5. The volume fraction for the CPD is not equal to 0.5. The CPD surface is very similar to the minimal surface discovered by Neovius [28,29]. The

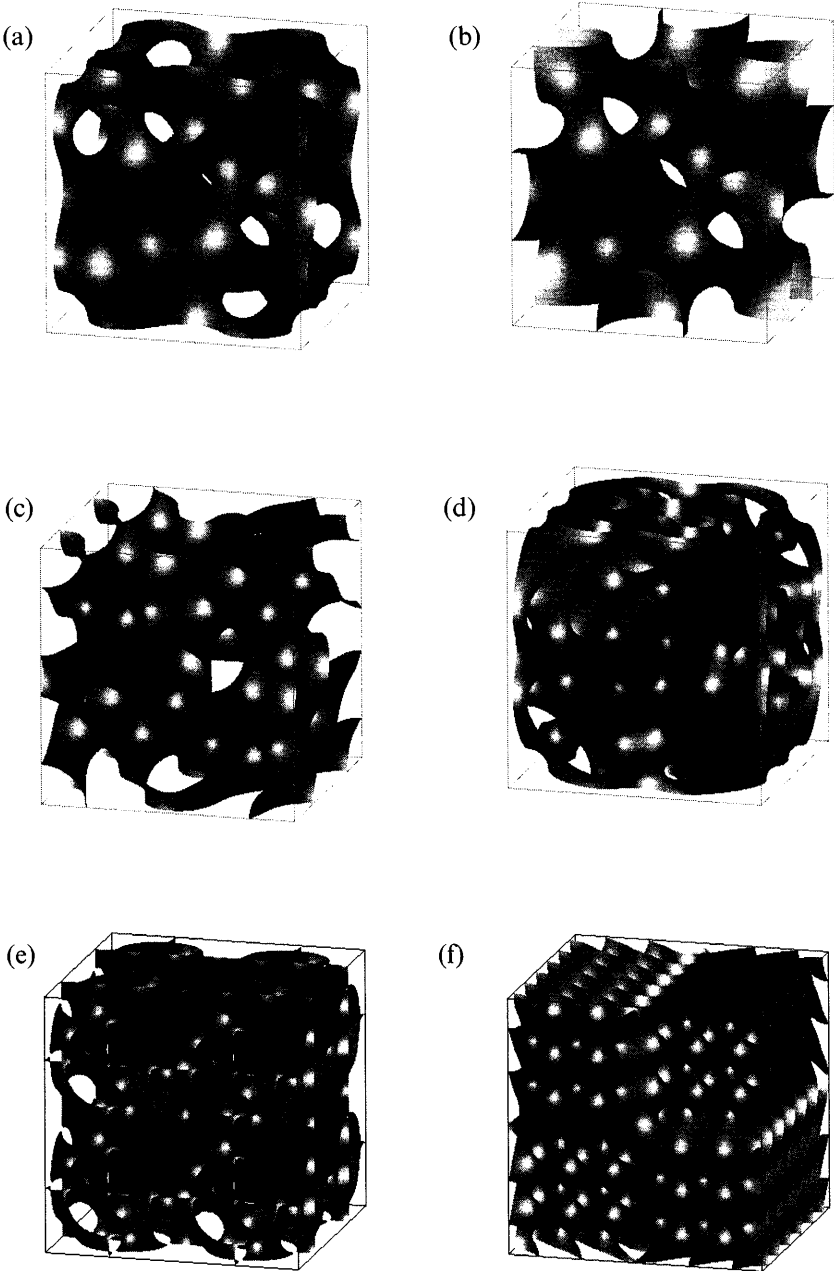


**FIG. 7** New cubic phases generated from the functional (1).

difference is that the CPD surface has a hole inside a unit cell, therefore its genus is bigger.

Fig. 7 shows high genus surfaces. They are most easily generated for the values of the parameters  $f_0$  and  $g_0$  in (1) taken near the phase boundary of the lamellar and microemulsion phases (see the phase diagram) and for the bigger unit cell length,  $L = (N - 1)h$ , than the length of structures of low genus.

The structure SCN1, Fig. 7(d), has the symmetry of the simple cubic phase (Fig. 4(a)), the structure CD, Fig. 7(e), has the symmetry of the double diamond phase (Fig. 4(b)), and the structure GX5, Fig. 7(f), has the symmetry of the gyroid phase (Fig. 4(c)). The existence of such surfaces in real systems has been questioned. The researchers argued that it was impossible to build high genus periodic surface because of large curvatures which could not be accommodated by the displacement of surfactant molecules at the surface [41]. The high genus surfaces have large sizes of the unit cell and therefore their curvatures are similar in magnitude to those of surfaces of low genus. Therefore this argument against the existence of these surfaces does not hold.

The multiply continuous structures of the simple cubic symmetry (SCL1, SCL2) and of the gyroid phase symmetry (GL1, GL2) are presented in Fig. 8. The possibility of the existence of multiply continuous structures has never been discussed for the case of ternary mixtures of oil, water, and surfactant. In the bicontinuous structure the single surface separates the volume into two disjoint subvolumes. In the multiply continuous structures there is more than one periodic surface, which separates the volume into three or more disjoint subvolumes. The multiply continuous structures are most easily generated for the values of the parameters  $f_0$  and  $g_0$  in (1) taken near the boundary of the lamellar and water (oil) phases (see the mean-field phase diagram) and for the bigger unit cell length,  $L = (N - 1)h$ , than the length of the structures of low genus.

The SCL1 structure, Fig. 8(a), is triply continuous, the GL1, SCL2, Fig. 8(b,c), are quadruply continuous, and GL2, Fig. 8(d) is sextuply continuous. For bigger sizes of the unit cell one is able to generate the structures  $n$ -tuply continuous. It is remarkable that the volume fraction of oil and water is 0.5 for all these structures. The genus for every surface in a given  $n$ -tuply continuous structure is the same.

The SCL1 surface is particularly interesting. Although the outer and the inner surface look different in Fig. 8(a), they have the same surface area. In fact they are built of the same piece of the surface. The picture of  $1/8$  of the unit cell, see Fig. 8(b), explains how two different periodic surfaces can be built of the same surface patch.

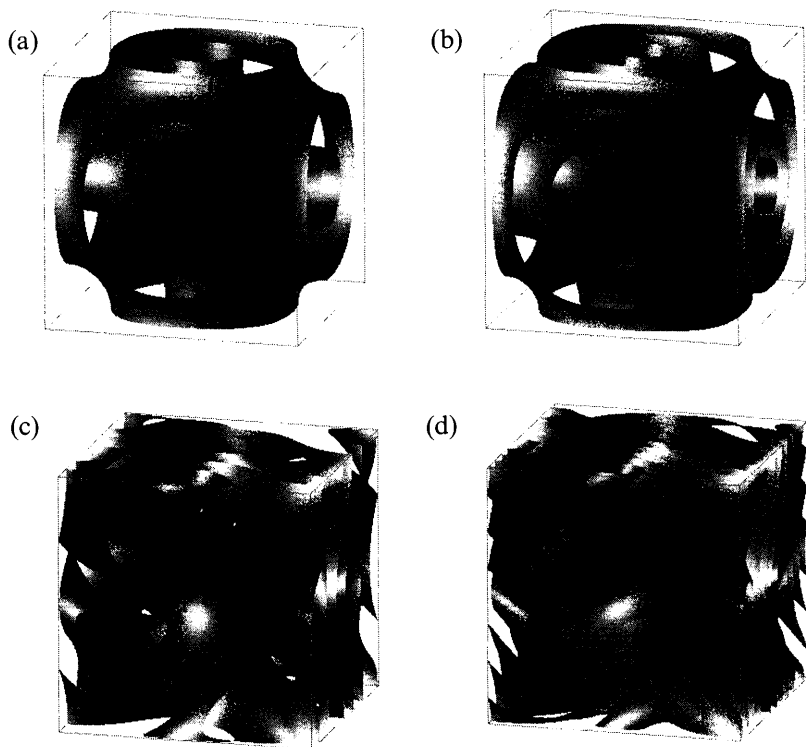


**FIG. 8** Multiply continuous cubic phases generated from the functional (1).

The SCL2 structure is composed of three different embedded periodic surfaces. The middle surface is the Schwarz minimal surface P. Similarly, the middle phase surface in GL1 (Fig. 8(c)) and GL2 (Fig. 8(d)) structures is the Schoen minimal surface G.

The GL2 structure suggests that one can generate arbitrary  $n$ -tuply continuous structures. It is only necessary to set the cell length sufficiently large. We have not attempted to generate such structures because, due to the limits imposed by computer memory and processor speed, the lattice spacing would be too big for a given size of the lattice to obtain a reasonable accuracy.

## VI. MEAN-FIELD BULK PHASE DIAGRAM

We have investigated many bicontinuous phases of different symmetries, genera and dimensions of the unit cell. The bicontinuous phase with the

lowest value of the free energy turned out to be the gyroid, but the only stable liquid crystalline phase in this model is the lamellar phase. The phase diagram for the model (1), in the mean-field approximation, calculated by Gompper and Zschocke [22], is shown in Fig. 9. The value of the free energy in the vicinity of the microemulsion boundary converges to the value of the free energy for the microemulsion. The geometric characteristics such as the genus and the normalized surface area are the same for all phases in different places of the phase diagram.

We have also studied the stability of bicontinuous phases for a different function describing the surfactant,  $g[\phi(\mathbf{r})]$ . We have used the following form of  $g[\phi(\mathbf{r})]$ :

$$g[\phi(\mathbf{r})] = g_2\phi(\mathbf{r})^4 + g_0 \quad (37)$$

We have expected that this form of  $g[\phi(\mathbf{r})]$  would make the interface between oil and water sharper and therefore it would lower the free energy. The interface indeed was sharper, as we expected, but the unit cell length decreased as well. This resulted in higher values of the free energy than before and all the bicontinuous phases were metastable, as in the previous case. We have performed Monte Carlo simulations (next section) in order to find out whether the thermal fluctuations stabilize the cubic structures. Once again we have found that the only stable ordered structure is the lamellar phase. These results suggest that one order parameter functional is not sufficient to describe the behavior of the ordered phases in the system. Indeed, in the multi-parameter Landau–Ginzburg models introduced in recent years [13] stabilization of the various cubic phases has been found. It is called the extended Landau–Ginzburg model, with two scalar and one vector order parameters, and is presented in this chapter.

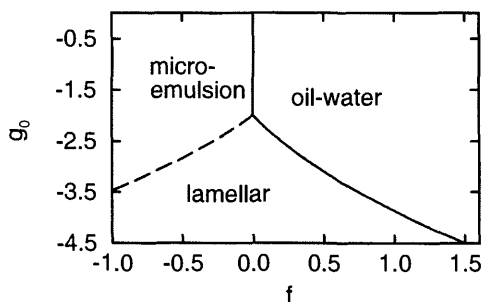


**FIG. 9** The phase diagram for the model (1).

## VII. COMPUTER SIMULATIONS OF THE BASIC LANDAU-GINZBURG MODEL

### A. Topological Fluctuations

Phase transitions between ordered surfaces of different topology should be accompanied by topological fluctuations in the form of passages or droplets between adjacent surfaces. A direct measure of the topological fluctuations is given by the Euler characteristic (described in the previous section) of the system. A flat surface, in a box, with periodic boundary conditions has the topology of the torus; i.e., its genus  $g$  (number of holes in a closed surface) is 1 and its Euler characteristic  $\chi = 2(1 - g)$  is zero. A parallel stack of such surfaces (as in the lamellar phase) is equivalent to the same number of disconnected tori and therefore the Euler characteristic is 0 for the whole lamellar phase. Two layers with a passage between them are topologically equivalent to two tori with a handle joining them and therefore their genus is now  $g = 2$  (two holes) and consequently  $\chi = -2$ . This means that each passage changes the Euler characteristic in the system by  $-2$  and the lamellar phase with many passages has a large and negative Euler characteristic. The Euler characteristic is the direct measure of the number of passages in the system. The passages between surfaces can be considered as topological defects or topological fluctuations, depending on their energy. If the passage is thermally activated it is the topological fluctuation; otherwise it is the defect. Apart from the passages, we may expect different topological fluctuations in the form of small droplets. Each droplet changes the Euler characteristic by  $+2$ .

The passages were first observed in the experimental studies of a lecithin-water system [42] and were formed when the lecithin was swelled in water. They formed between the lecithin bilayers. They were also observed in the aqueous solution of a non-ionic surfactant (hexaethylene glycol dodecyl ether,  $C_{12}E_6$ ) [43,44] and in phospholipid bilayer [45]. In the former system it was reported that the results of spin labeling experiments and optical birefringence revealed the existence of "defects" (fluctuations) whose concentration increased with temperature. These "defects" were characterized by a small radius of curvature (20 nm) and currently we believe that they were pores in the bilayers. In the phospholipid bilayers the process of the fluctuation of two surfaces connected by the passage was observed [45]. Recently it has been observed in computer simulations [46–50] of the binary and ternary mixtures involving surfactants that the passages accompany the phase transitions between structures of different topology as was previously suggested [51,52]. For example, the microemulsion–lamellar phase transition must be accompanied by topological fluctuations, since the microemul-



sion is a bicontinuous disordered structure characterized by a large and negative Euler characteristic, whereas the ideally ordered lamellar phase (consisting of parallel layers) has zero Euler characteristic (in the system with the periodic boundary conditions). Therefore the change of the topology should force the appearance of the passages and/or droplets. The experimental results [53,58], show that pretransitional effects (like the strong topological fluctuations) should be expected, but their precise nature is still unknown.

The passages have been described theoretically in the Helfrich curvature model of membranes [42,59–62]. A first-order approximation for the shape of the passage is the catenoid [42]. Although the catenoid does not satisfy the boundary conditions, the central part of the passage is very well approximated by its shape [61,62]. Two membranes without the passages repel each other with long-range repulsive forces (Helfrich interactions) due to self-avoidance [63]. However, when the membranes are joined by the passages the latter induce long-range attraction which competes at large distances with the repulsive Helfrich interactions, leading to the overall attraction of the membranes [60]. The passages in the lamellar phase should most easily form close to the bicontinuous (sponge or microemulsion) phase boundary. On the other hand, close to the micellar phase boundary the droplets form in the lamellar phase instead of passages [60], as might be expected.

The phase transitions between ordered surfaces of different topology should be accompanied by topological fluctuations in the form of passages connecting surfaces or droplets between them. A the convenient method for studying the topological fluctuations (passages) is the computer simulation [47,49] of the mesoscopic basic Landau–Ginzburg model of the ternary mixtures of oil, water, and surfactant discussed in the preceding sections.

## B. Discretization

The properties of the periodic surfaces studied in the previous sections do not depend on the discretization procedure in the limit of small distance between the lattice points. Also, the symmetry of the lattice does not seem to influence the minimization, at least in the limit of large  $N$  and small  $h$ . In the computer simulations the quantities which vary on the scale larger than the lattice size should have a well-defined value for large  $N$ . However, in reality we work with a lattice of a finite size, usually small, and the lattice spacing is rather large. Therefore we find that typical simulations of the same model may give different quantitative results although qualitatively one obtains the same results. Here we compare in detail two different discretization

schemes [47,49]. Both simulations were performed on the simple cubic lattice with the following discretization for the derivative, e.g., in the  $x$  direction:

$$g(\phi) \left( \frac{\partial \phi(\mathbf{r})}{\partial x} \right)^2 \rightarrow g(0.5(\phi_{i,j,k} + \phi_{i-1,j,k})) \left( \frac{\phi_{i,j,k} - \phi_{i-1,j,k}}{h} \right)^2 \quad (38)$$

$$\frac{\partial^2 \phi(\mathbf{r})}{\partial x^2} \rightarrow \frac{\phi_{i+1,j,k} - 2\phi_{i,j,k} + \phi_{i-1,j,k}}{h^2} \quad (39)$$

in the Gompper and Kraus case [47] and

$$g(\phi) \left( \frac{\partial \phi(\mathbf{r})}{\partial x} \right)^2 \rightarrow g(\phi_{i,j,k}) \left( \frac{\phi_{i+1,j,k} - \phi_{i-1,j,k}}{2h} \right)^2 \quad (40)$$

in the Holyst and Gózdź case, where the same discretization for the Laplacian is used. Additionally some preliminary results have been obtained for the same model on the fcc lattice with the derivatives calculated on the basis of 12 near neighbours (T. Biben, private communication). In this case similar results have been obtained as in the Holyst, and Gózdź [49] discretization scheme on the simple cubic lattice and different from the Gompper and Kraus [47] results. Here we compare in detail the Gompper and Kraus results with those of Holyst and Gózdź.

### C. Euler Characteristic in Computer Simulations

The calculation method of the Euler characteristic presented for smooth surfaces does not work in computer simulations when the mesh size of the lattice is large (in our case  $h = 0.8$ ). One usually finds that a simple surface cutting an elementary cube can have 6 (other cases than those shown in Fig. 3), 7, 8, 9 or 12 vertices (10 and 11 are not possible). The computation of the Euler characteristic becomes ambiguous, namely, different connections between the points lead to different values of the Euler characteristic. Basically in these cases we can have more than a single surface patch (compare with Fig. 3) in a single cube. In order to get rid of such cases we assume that the value of the field  $\phi$  inside the cube can be obtained from the linear interpolation of the values of the field at the vertices of the cube. If we perform this interpolation and divide the cube into  $17 \times 17 \times 17$  smaller cubes we are left with the cases depicted in Fig. 3 in the smallest cubes. For this fine mesh we can use Eq. (35) and the method described below the equation. The procedure is well defined and is used in our simulations. At this point it is interesting to note that in the systems where the topology changes it is natural to expect that for some configurations the computation of the Euler characteristic must be ambiguous due to the discontinuous change of the latter quantity. In the case of the lamellar phase with the

passages, breaking a single channel changes  $\chi$  by 2, whereas the formation of the channel changes  $\chi$  by  $-2$ . The exact moment of the formation or breakage of the passage, especially on the lattice, is not well defined, hence the procedure must break down in these cases. The linear interpolation mentioned above helps to reduce the number of such cases considerably, however, it cannot eliminate them totally due to the physics of the problem. In principle, in the system with very fine discretization the problems mentioned above are not as acute as here, where the linear size of the mesh is  $h = 0.8$ .

#### D. Microemulsion–Lamellar Phase Transition

Monte Carlo simulations have been done on the  $N \times N \times N$  cubic lattice ( $N = 27$ ) with the lattice spacing  $h = 0.8$  [47,49] for a bulk system. The usual temperature factor  $k_B T$  is set to 1, since it only sets the energy scale. The following periodic boundary conditions are used:  $\phi_{1,j,k} = \phi_{N,j,k}$ ,  $\phi_{0,j,k} = \phi_{N-1,j,k}$  and similarly in the  $y, z$  directions. The lattice points are chosen randomly and the field  $\phi$  is changed by the random increment chosen from the interval  $[-s, s]$ . For  $s = 0.3$  one has almost 50% acceptance ratio.

Typical runs consist of 100 000 up to 300 000 MC moves per lattice site. Far from the phase transition in the lamellar phase, the typical equilibration run takes 10 000 Monte Carlo steps per site (MCS). In the vicinity of the phase transitions the equilibration takes up to 200 000 MCS. For the rough estimate of the equilibration “time” one can monitor internal energy as well as the Euler characteristic. The equilibration “time” for the energy and Euler characteristic are roughly the same. For  $g_0 = -10$ ,  $f_0 = 0$ , it takes 10 000 MCS to obtain the equilibrium configuration in which one finds the lamellar phase without passages and consequently the Euler characteristic is zero. For  $g_0 = -3.15$  and  $f_0 = 0$  (close to the phase transition) it takes more than 50 000 MCS for the equilibration and here the Euler characteristic fluctuates around its mean value of  $-48$ .

In order to study phase transition in the system one computes the averages of the internal energy,  $U = \langle F \rangle$  (see Eq. (1) in the discretized form), and the heat capacity,  $C_V = \langle F^2 \rangle - \langle F \rangle^2$ . The averages are taken with respect to the Boltzmann distribution  $\exp(-F)$ , with  $F$  defined by Eq. (1) discretized on the lattice. They are taken for 50 000 (up to 300 000) MCS every 26 steps, so the average is over  $26 \times 26 \times 50\,000$  (up to 300 000) configurations. The averages are taken every 26 steps in order to reduce the correlations between the successive configurations. Changes in the Euler characteristic require changes not only in the field  $\phi$  but also in the surface given by  $\phi = 0$ . That is why the successive configurations used in the computation of  $\langle \chi \rangle$  and  $\langle \chi^2 \rangle - \langle \chi \rangle^2$  are separated by at least 50 MCS. From

our observation it follows that appreciable changes of  $\chi$  are visible after a few MCS. The computation of the Euler characteristic takes much more “time” than computation of the internal energy; therefore we cannot use as many configurations for the averages of  $\chi$  as for  $U$ . Close to the phase transition we use 1000 configurations separated from each other by 300 MCS, so practically the successive configurations used in the averaging are uncorrelated. The results for  $\langle\chi\rangle$  are almost the same as for the averages taken over 100 configurations, with the differences less than 5%. However, 100 configurations are not sufficient to compute  $\langle\chi^2\rangle - \langle\chi\rangle^2$  and in this case we use, in the final results, 1000 configurations (with different runs giving 10% error for this quantity). Only very close to the transition do different runs give an error of 30%. Far away from the lamellar–microemulsion phase transition the lamellar phase is without passages and therefore we have  $\langle\chi\rangle = 0$  and  $\langle\chi^2\rangle - \langle\chi\rangle^2 = 0$ .

The phase diagram is shown in Fig. 10. It encompasses the region of the oil–water coexistence, the microemulsion, and the lamellar phase. The transition from the microemulsion or the lamellar phase to the oil-rich or water-rich phases is strongly first order. The large peak in the heat capacity and the jump in the internal energy clearly mark the transition line, although the metastability effects prevent its exact location. The same observation has been made in Ref 47. The transition from the microemulsion to the lamellar phase is weakly first order. A comparison between the mean-field bulk phase diagram (Fig. 9) and the Monte Carlo phase diagram (Fig. 10) shows that thermal fluctuations extend the stability region of the microemulsion at the expense of the lamellar phase and the oil-rich and water-rich phases. The same results were also obtained in Ref. 47, but there are two differences between their and our results. The stability region of the microemulsion is slightly smaller in our case. For example, the microemulsion is still stable for  $g_0 = -2$  and  $f_0 = 0.75$  in their simulations [47], whereas we find the transition to the lamellar phase at  $g_0 = -2$  and  $f_0 = 0.45$ . Similarly, for  $f_0 = 0$  they find the transition at  $g_0 = -3.25$  and we find it at  $g_0 = -3.05$ . The comparison of their phase diagram (Fig. 3 in [47] and Fig. 10 here) shows that they are very similar. Concluding: qualitatively the phase diagram is not very sensitive to the details of discretization. The phases and shapes of the transition lines are the same; our diagram is shifted with respect to theirs along the  $f_0$  axis towards smaller values of  $f_0$ .

The second difference is related to the structure of the lamellar phase. The Euler characteristic has been assumed zero in the whole lamellar phase by Gompper and Kraus [47], whereas we show that it fluctuates strongly in the lamellar phase between the transition line and the topological disorder line. The notion of the topological disorder line has not appeared in their paper. We think that the topological disorder line is much closer to the transition

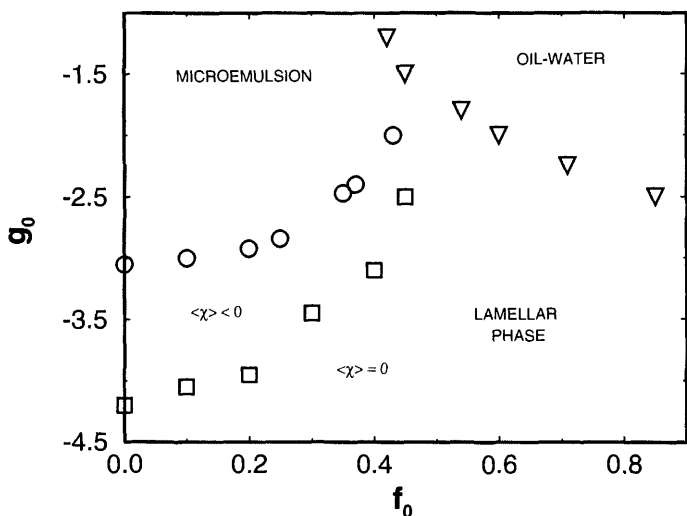


**FIG. 10** Phase diagram for the basic Landau–Ginzburg model obtained in the MC computer simulations (see also Fig. 9) for  $N \times N \times N$  lattice ( $N = 27$ ) in the space of the model parameters  $f_0$  and  $g_0$ . In the rough interpretation,  $g_0$  is the strength of the surfactant (proportional to length of the aliphatic chain or size of the polar head), while  $-f_0$  is proportional to the concentration of the surfactant (or its chemical potential). The triangles mark the line of the strong first-order phase transition from the microemulsion or lamellar phases to the oil and water phases. The circles mark the line of weakly first-order transition from the microemulsion to the lamellar phase. The squares mark the topological disorder line in the stability region of the lamellar phase. On one side of the line, where  $\langle \chi \rangle = 0$ , the topological fluctuations such as wormhole passages do not appear in the system and the lamellar phase consists of a stack of layers separated from one another. On the other side of the line the Euler characteristic fluctuates due to the appearance of passages. The passages proliferate and merge as we approach the transition line to the microemulsion phase. (After Ref. 49.)

line in their case than in ours—presumably so close that on the scale of their phase diagram the latter is indiscernable from the former. The reason for this difference is as follows: the discretization scheme of Gompper and Kraus favors lamellas parallel to the side of the simulation box; in our case the lamellas have oblique orientation with respect to the simulation box. The lamellas in their case are much stiffer than in our case and, since the number of passages decreases exponentially with the increase of the bending rigidity [61] of the lamellas, the location of the topological disorder line is strongly shifted towards the transition line in their case [47]. In fact we

have redone the simulation with the discretization of Gompper and Kraus [47] and found that their lamellar phase forms quicker (10 000 MCS, even close to the transition) than ours (100 000 MCS), when starting from the random configuration. In our case the lamellar phase forms so easily only at very low values of  $g_0$  ( $g_0 = -10$ ), with the rigid layers. These facts suggest that their lamellar phase must be very rigid, while ours is much softer. Concluding: a discretization scheme affects the elastic properties of membranes, topological fluctuations, and the location of the topological disorder line.

From the average Euler characteristic one cannot definitely state what types of topological fluctuations occur in the system. We can see them in the snapshots. The snapshots of lamellar configurations shown in Fig. 11 illustrate the behavior of the lamellar phase between the transition line and the topological disorder line. Close to the topological disorder line the thin passages appear (Fig. 11(a,b)). As we approach the lamellar–microemulsion transition line these passages merge, forming the large passages pierced with holes (Fig. 11(c)). The final configuration of the lamellar phase very close to the transition line is almost indiscernable from configurations of the microemulsion (Fig. 11(d)). The latter fact is certainly responsible for the weakness of the microemulsion–lamellar phase transition (Fig. 12). Namely, due to the passages the lamellar structure is already well adjusted to the bicontinuous structure of the microemulsion before the phase transition occurs.

The behavior of the internal energy, heat capacity, Euler characteristic, and its variance ( $\langle \chi^2 \rangle - \langle \chi \rangle^2$ ) at the microemulsion–lamellar transition is shown in Fig. 12. Both  $U$  and  $\langle \chi \rangle$  jump at the transition, and the heat capacity, and  $\langle \chi^2 \rangle - \langle \chi \rangle^2$  have a peak at the transition. The relative jump in the Euler characteristic is larger than the one in the internal energy. Also, the relative height of the peak in  $\langle \chi^2 \rangle - \langle \chi \rangle^2$  is bigger than in the heat capacity. Conclude: both quantities  $\langle \chi \rangle$  and  $\langle \chi^2 \rangle - \langle \chi \rangle^2$  can be used to locate the phase transition in systems with internal surfaces.

We see from Fig. 11(d) that a typical lamellar configuration close to the transition line is hardly different from a typical configuration of the microemulsion. In order to see that we have a lamellar phase we take the average of the field  $\phi$ . In Fig. 13 the typical configuration of  $\phi(\mathbf{r}) = 0$  is shown together with  $\langle \phi(\mathbf{r}) \rangle = 0$ . Averaging of the field after 250 000 MCS (actually 50 000 MCS is enough) is sufficient to average out all the passages. We have  $\langle \chi(\phi(\mathbf{r}) = 0) \rangle = -86$  but

$$\chi(\langle \phi(\mathbf{r}) \rangle = 0) = 0 \quad (41)$$

In this way, by taking the average over the field  $\phi$  and computing the Euler characteristic for the average surface given by  $\langle \phi \rangle = 0$ , we can easily discern between different ordered phases. In this example (Fig. 13) the snapshot

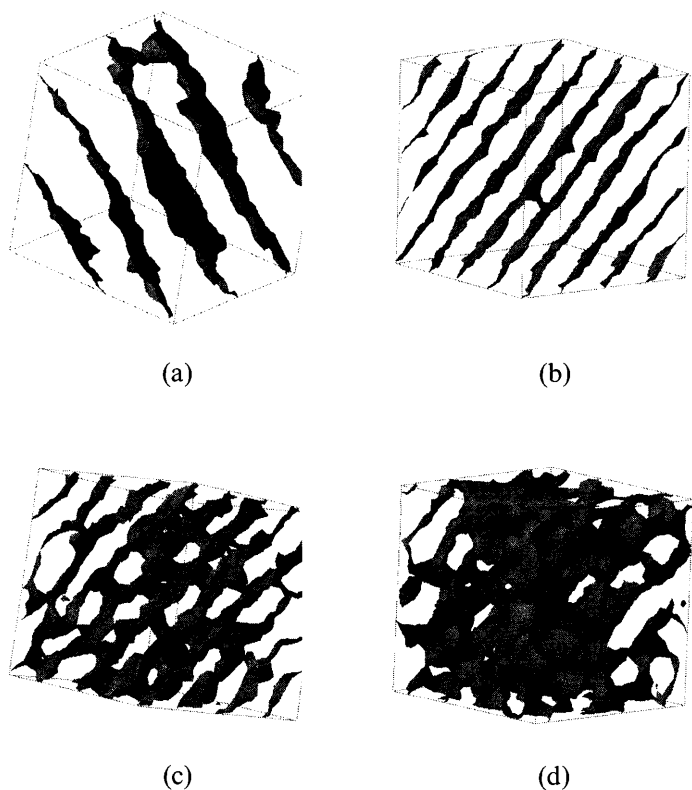


**FIG. 11** Snapshots of the lamellar phase at different points of the phase diagrams. (a,b) show the configuration close to the topological disorder line. Note the appearance of single passages on these figures. (c,d) show the configuration close to the transition line. The configurations were shown for the following parameters: (a)  $g_0 = -2$ ,  $f_0 = 0.5$ ; (b)  $g_0 = -4.05$ ,  $f_0 = 0.1$ ; (c)  $g_0 = -3.15$ ,  $f_0 = 0$ ; and (d)  $g_0 = -3.065$ ,  $f_0 = 0$ . (After Ref. 49.)

does not resemble the lamellar phase at all and only the average gives the stack of flat layers parallel to each other. In this way we can identify other surfaces, e.g., periodic surfaces.

We also observe that the “time scale” for long-range non-topological undulations is separated from the “time scale” of the topological fluctuations. Namely, if we average the lamellar configuration over, say, 50 000 MCS, we obtain the lamellar phase without the wormhole passages, but still the lamellas are not flat but have the shape of the undulating layers.

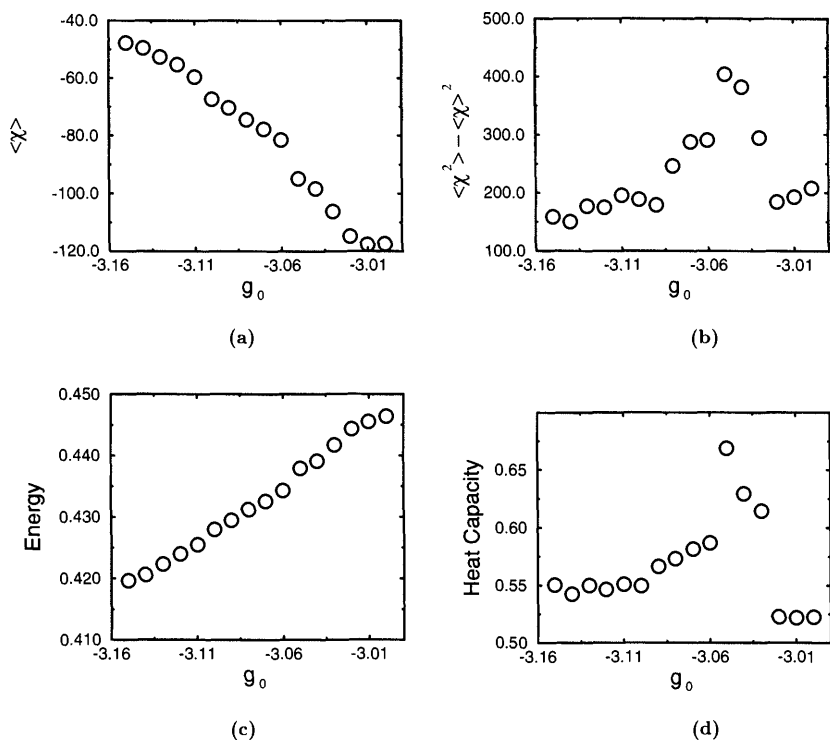


**FIG. 12** The behavior of the internal energy  $U$  (per site), heat capacity  $C_V$  (per site), the average Euler characteristic  $\langle \chi \rangle$  and its variance  $\langle \chi^2 \rangle - \langle \chi \rangle^2$  close to the transition line and at the transition to the lamellar phase for  $f_0 = 0$ . The changes are small at the transition and the transition is very weakly first-order. The weakness of the transition is related to the proliferation of the wormhole passages, which make the lamellar phase locally very similar to the microemulsion phase (Fig. 13). Note also that the values of the energy and heat capacity are not very much different from their values (i.e., 0.5 per site) in the Gaussian approximation of the model [47]. (After Ref. 49.)

The topological fluctuations can also be induced by confinement. It has been found that confinement between parallel walls exhibits topological fluctuations even if they are absent in the bulk system.

Summarizing: the detailed studies of the basic Landau–Ginzburg model presented in the preceding sections and in the present one suggest that this type of simplified model is not sufficient to describe all the effects related to the ordering in microemulsions. In particular, the only stable ordered phase in the model is the lamellar phase and all the cubic phases are only meta-



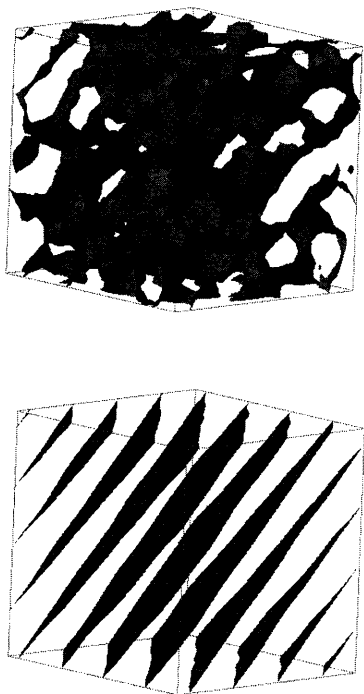


**FIG. 13** Snapshot of the lamellar configuration  $\phi(\mathbf{r}) = 0$  for  $g_0 = -3.065$  and  $f_0 = 0$  and the average configuration  $\langle \phi(\mathbf{r}) \rangle = 0$ . Here  $\chi = 0$  for the average configuration and  $\chi = -88$  for the snapshot configuration. The snapshot configuration of the lamellar phase close to the transition line resembles the microemulsion configuration. (After Ref. 49.)

stable. This observation leads us to the extended Landau–Ginzburg model described in the next section.

## VIII. EXTENDED LANDAU–GINZBURG MODEL

### A. The CHS Model

The basic Landau–Ginzburg model is valid only for relatively weak surfactants and in a limited region of the phase space. In order to find a more general mesoscopic description, valid also for strong surfactants and in a more extended region of the phase space, we derive in this section a mesoscopic Landau–Ginzburg model from the lattice CHS model [16].

In the CHS model only nearest neighbors interact, and the interactions between amphiphiles in the simplest version of the model are neglected. In the case of the oil–water symmetry only two parameters characterize the interactions:  $b$  is the strength of the water–water (oil–oil) interaction, and  $c$  describes the interaction between water (oil) and an amphiphile. The interaction between amphiphiles and ordinary molecules is proportional to a scalar product between the orientation of the amphiphile and the distance between the particles. In Ref. 15 the CHS model is generalized, and  $M$  orientations of amphiphiles uniformly distributed over the sphere are considered, with  $M \rightarrow \infty$ . Every lattice site is occupied either by an oil, water, or surfactant particle in an orientation  $\hat{\omega}_\ell$ ; there are thus  $2 + M$  microscopic states at every lattice site. The microscopic density of the state  $i$  is  $\hat{\rho}_i(\mathbf{r}) = 1(0)$  if the site  $\mathbf{r}$  is (is not) occupied by the state  $i$ . We denote the sum and the difference of microscopic oil and water densities by  $\hat{s}_1$  and  $\hat{s}_2$  respectively and the density of surfactant at a point  $\mathbf{r}$  and an orientation  $\hat{\omega}_\ell$  by  $\hat{\rho}_\ell(\mathbf{r}) = \rho_s(\mathbf{r}, \hat{\omega}_\ell)$ . The microscopic densities assume the values  $\hat{s}_1 = 1, 0$ ,  $\hat{\rho}_\ell = 1, 0$  and  $\hat{s}_2 = \pm 1, 0$ . In the close-packing case the total density of surfactant  $\rho_s(\mathbf{r})$  is related to  $\hat{s}_1$  by  $\rho_s = \sum_{\ell=1}^M \hat{\rho}_\ell = 1 - \hat{s}_1$ . The Hamiltonian of this model has the following form [15]

$$\begin{aligned}
 H[\hat{s}_1, \hat{s}_2, \hat{\rho}_\ell] = & - \sum_{\mathbf{r}} \left\{ \sum_{i=1}^d \left[ \frac{b}{2} (\hat{s}_1(\mathbf{r}) \hat{s}_1(\mathbf{r} + \mathbf{e}^i) + \hat{s}_2(\mathbf{r}) \hat{s}_2(\mathbf{r} + \mathbf{e}^i)) \right. \right. \\
 & + c \sum_{\ell=1}^M \hat{\rho}_\ell(\mathbf{r}) \hat{\omega}_\ell^i \cdot (\hat{s}_2(\mathbf{r} + \mathbf{e}^i) - \hat{s}_2(\mathbf{r} - \mathbf{e}^i)) \left. \right] \\
 & + \mu \hat{s}_1(\mathbf{r}) + \mu_{\text{ow}} \hat{s}_2(\mathbf{r}) \left. \right\}
 \end{aligned} \tag{42}$$

We choose as the length unit the length of the amphiphile, which is about 20, and in this unit the lattice constant is  $a \equiv 1$ . The unit lattice vectors are denoted by  $\mathbf{e}^i$  and  $\hat{\omega}_\ell^i$  denotes the  $i$ th component of the unit vector  $\hat{\omega}_\ell$ , where  $i = 1, \dots, d$ , and  $d$  is the dimension of the system. We concentrate on the symmetric case  $\mu_{\text{ow}} = 0$ . The generalization to  $\mu_{\text{ow}} \neq 0$  is straightforward.

## B. Derivation of the Mesoscopic Model from the Microscopic Lattice Model

The grand thermodynamical potential in the mean-field (MF) approximation is

$$\beta\Omega[s_1, s_2, \rho_\ell] = \beta H[s_1, s_2, \rho_\ell] - S[s_1, s_2, \rho_\ell], \tag{43}$$

where  $H$  is given in (42) and  $S$  is the entropy of the  $M + 2$  component mixture in the lattice gas model in the case of close packing. The fields  $s_1, s_2$ , and  $\rho_\ell$  for which  $\Omega$  (43) assumes a minimum are equal to the average values of the microscopic density operators  $\hat{s}_1, \hat{s}_2$ , and  $\hat{\rho}_\ell$  in the MF approximation [64]. The potential  $\Omega$  is next expanded in a power series of deviations of  $s_1, s_2$ , and  $\rho_\ell$  from their MF-average values. We assume that the fluctuations are small and truncate the expansion after the fourth-order term. In Ref. 15 it is shown that, within the approximation used,  $\Omega$  can be expressed in the limit of  $M \rightarrow \infty$  in terms of three fields:  $\phi, \rho$ , and  $\mathbf{u}$ , instead of  $M + 2$  states.  $\phi$  is proportional to the oil–water concentration difference  $s_2$ ,  $\rho$  is proportional to the deviation of the total surfactant concentration,  $1 - s_1$ , from its average value (denoted by  $\rho_s$ ), and  $\mathbf{u}$  describes the orientational ordering of the surfactant.  $\mathbf{u}$  is related to the deviations of  $\rho_s(\mathbf{r}, \hat{\omega})$  from the average value  $\rho_s/4\pi$  by

$$\delta\rho_s(\mathbf{r}, \hat{\omega}) \equiv \rho_s(\mathbf{r}, \hat{\omega}) - \frac{\rho_s}{4\pi} = \frac{1}{4\pi} \rho(\mathbf{r}) + \frac{\rho_s}{4\pi} \hat{\omega} \cdot \mathbf{u}(\mathbf{r}) \quad (44)$$

The first term in (44) is related to the deviation of the surfactant concentration at point  $\mathbf{r}$  from the average concentration,  $\rho_s$ . The second part is related to the orientational ordering and defines the vector field  $\mathbf{u}$ .

Finally, we assume that the fields  $\phi, \rho$ , and  $\mathbf{u}$  vary slowly on the length scale of the lattice constant (the size of the molecules) and introduce continuous approximation for the thermodynamical-potential density. In the lattice model the only interactions between the amphiphiles are the steric repulsions provided by the lattice structure. The lattice structure does not allow for changes of the orientation of surfactant for distances smaller than the lattice constant. To assure similar property within the mesoscopic description, we add to the grand-thermodynamical potential a term proportional to  $(\nabla \cdot \mathbf{u})^2 + (\nabla \times \mathbf{u})^2$  [15], so that the correlation length for the orientational order is equal to the size of the molecules.

## C. The Extended Model

The resulting functional assumes the form [15]

$$\Omega_{\text{eff}} = (\Omega_2 + \Omega_{\text{int}})b \quad (45)$$

with

$$\begin{aligned} \Omega_2 = \int d\mathbf{r} \left[ \frac{1}{2} a_2 \phi^2 + \frac{1}{2} (\nabla \phi)^2 + \frac{1}{2} \alpha_2 \rho^2 + \frac{1}{2} (\nabla \rho)^2 \right. \\ \left. + \frac{1}{2} [|\mathbf{u}|^2 + (\nabla \cdot \mathbf{u})^2 + (\nabla \times \mathbf{u})^2] - J\mathbf{u} \cdot \nabla \phi \right] \end{aligned} \quad (46)$$

and

$$\Omega_{\text{int}} = \int d\mathbf{r} \left[ \frac{1}{3!} (\alpha_3 \rho^3 + b_3 \phi^2 \rho + c_3 |\mathbf{u}|^2 \rho) + \frac{1}{4!} (a_4 \phi^4 + \alpha_4 \rho^4 + b_4 \phi^2 \rho^2 + c_4 \rho^2 |\mathbf{u}|^2 + A_4 |\mathbf{u}|^4) \right] \quad (47)$$

The grand-thermodynamical potential is, like the temperature, calculated in units of  $b$ . Macroscopically,  $b$  is related to the critical temperature of the oil-water separation by  $kT_c = 3(1 - \rho_s)b$ . The coupling constants of  $\Omega_2$  are

$$a_2 = 2 \left( \frac{\tau}{1 - \rho_s} - d \right) \quad (48)$$

$$\alpha_2 = 2 \left[ \frac{\tau}{\rho_s(1 - \rho_s)} - d \right] \quad (49)$$

$$J = \left( \frac{2\rho_s\gamma}{3\tau} \right)^{1/2} \quad (50)$$

The coupling constants of  $\Omega_{\text{int}}$  used here in the bifurcation analysis are

$$b_3 = \frac{6\sqrt{2}\tau}{(1 - \rho_s)^2} \quad (51)$$

$$c_3 = -\frac{3\sqrt{2}}{\rho_s} \quad (52)$$

$$a_4 = \frac{8\tau}{(1 - \rho_s)^3} \quad (53)$$

$$A_4 = \frac{18}{5\tau\rho_s} \quad (54)$$

The remaining coupling constants are given in Ref. 15. All the coupling constants are expressed in terms of the average surfactant volume fraction  $\rho_s$  and temperature  $\tau = kT/b$ , except for  $J$ , which also depends on  $\gamma = (2c/b)^2$ , describing the amphiphilicity of the surfactant. Recall that in the microscopic model  $c$  and  $b$  are the amphiphile-oil (amphiphile-water) and the oil-oil (water-water) interaction energies respectively, hence  $c/b$  describes the strength of the surfactant. On the mesoscopic level the amphiphilic interactions are described by the single term  $-J\mathbf{u} \cdot \nabla\phi$ . If the amphiphiles are oriented perpendicular to the oil-water interface and point in the appropriate direction, then the term  $-J\mathbf{u} \cdot \nabla\phi$  is large and negative, i.e., such states are favorable. The effect is the stronger, the stronger the

amphiphilic interactions  $c/b$ . This single term is sufficient to account for the amphiphilic interactions if the orientational degrees of freedom are explicitly taken into account. No higher-order derivatives of  $\phi$  are necessary.

The vector field  $\mathbf{u}(\mathbf{r})$  describing the local orientational ordering of amphiphiles is split into two fields  $\mathbf{s}$  and  $\mathbf{t}$

$$\mathbf{u} = \mathbf{s} + \mathbf{t} \quad \text{where} \quad \nabla \times \mathbf{s} = 0 \quad \text{and} \quad \nabla \cdot \mathbf{t} = 0 \quad (55)$$

$\mathbf{s}$  defines a collection of surfaces, the normal vector of which is  $\hat{\mathbf{n}} = \mathbf{s}/s$ , with  $s = |\mathbf{s}|$ . The other part of  $\mathbf{u}$  describes fluctuations of amphiphiles around a common direction  $\hat{\mathbf{n}}(\mathbf{r})$ . Because of the condition  $\nabla \times \mathbf{s} = 0$ , the Fourier transform of  $\mathbf{s}(\mathbf{r})$  is represented by a scalar field  $\tilde{s}_{\parallel}(\mathbf{k})$ ,  $\tilde{\mathbf{s}}(\mathbf{k}) = i\mathbf{k}\tilde{s}_{\parallel}(\mathbf{k})$ , where  $\mathbf{k} = \mathbf{k}/k$ . From (55) and the above it follows that in the Fourier representation the Gaussian part of  $\Omega_{\text{eff}}$  has a simpler form when expressed in terms of  $\tilde{\mathbf{s}}$  and  $\tilde{\mathbf{t}}$ ,

$$\Omega_2 = \int d\mathbf{k} \left[ \frac{1}{2} (a_2 + k^2) |\tilde{\phi}(\mathbf{k})|^2 + \frac{1}{2} (1 + k^2) |\tilde{s}_{\parallel}(\mathbf{k})|^2 - Jk\tilde{s}_{\parallel}(\mathbf{k})\tilde{\phi}(\mathbf{k}) + \frac{1}{2} (\alpha_2 + k^2) |\tilde{\rho}(\mathbf{k})|^2 + \frac{1}{2} (|\tilde{\mathbf{t}}(\mathbf{k})|^2 + |\mathbf{k} \times \tilde{\mathbf{t}}(\mathbf{k})|^2) \right] \quad (56)$$

The field  $\mathbf{t}$  is not coupled to any other fields and plays no role in the formation of ordered structures [15] within the Gaussian approximation.

The structure factor for the density  $\rho$  behaves as  $(\alpha_2 + k^2)^{-1}$ . The structure factors for the fields  $\phi$  and  $s_{\parallel}$  are proportional to  $D(k)^{-1}$ , with

$$D(k) = k^4 + (1 + a_2 - J^2)k^2 + a_2 \quad (57)$$

Hence, the correlation functions for  $\phi$  in the extended and in the basic models are similar.

## IX. BIFURCATION ANALYSIS OF THE EXTENDED MODEL

### A. Bifurcation Line

The uniform phase becomes unstable if there exist fluctuations for which  $\Omega_2$ , given by Eq. (56), vanishes. Since  $\alpha_2 > a_2$  for all temperatures (see (48) and (49)), the instability of the uniform phase is related to fluctuations of the fields  $\phi$  and  $s_{\parallel}$ .  $\Omega_2$  can be written in a diagonal form

$$\Omega_2 = \frac{1}{2} \int d\mathbf{k} \left[ \frac{D(k)}{1 + k^2} |\tilde{\phi}|^2 + (1 + k^2) |\tilde{\psi}|^2 + (\alpha_2 + k^2) |\tilde{\rho}|^2 + |\tilde{\mathbf{t}}|^2 + |\mathbf{k} \times \tilde{\mathbf{t}}|^2 \right] \quad (58)$$

where

$$\tilde{\psi}(\mathbf{k}) = \tilde{s}_{\parallel}(\mathbf{k}) - \frac{Jk}{1+k^2} \tilde{\phi}(\mathbf{k}) \quad (59)$$

and  $D(k)$  is defined in (37). The bifurcation corresponds to  $D(k) = 0$ . There are two possibilities:

- the bifurcation corresponds to instability with respect to uniform fluctuation leading to oil–water separation and is given by

$$a_2 = k = 0 \quad (60)$$

- the boundary of stability of the uniform phase corresponds to the highest temperature for which there exist  $k \neq 0$  such that the equation  $D(k) = 0$  is satisfied. We denote the wave number corresponding to the boundary of stability of the uniform phase by  $k_b$  and, from the conditions  $D(k) = 0$  and  $dT/dk = 0 = -\partial D(k, T)/\partial k / \partial D(k, T)/(\partial T)$ , we find that  $k_b$  and the corresponding bifurcation are given by

$$k_b = a_2^{1/4} \quad \text{and} \quad 1 + a_2 - J^2 + 2\sqrt{a_2} = 0 \quad (61)$$

To find the actual transition we compare the temperatures determined for a given  $\rho_s$  by (60) and (61) and choose the higher one. It turns out that for concentrations lower than at the Lifshitz point [13], in our case given by

$$\rho_s^L = \frac{3d}{2\gamma + 3d} \quad \text{and} \quad \tau^L = d(1 - \rho_s^L) \quad (62)$$

the separation into two uniform phases (60) occurs, and for  $\rho_s > \rho_s^L$  the transition to liquid-crystal phases (61) takes place. At the Lifshitz point the bifurcation line crosses the Lifshitz line.

We define the bifurcation parameter  $\epsilon$  by

$$\text{sgn}(\epsilon)\epsilon^2 \equiv (1 + a_2 - J^2 + 2\sqrt{a_2})/4 \quad (63)$$

and we have

$$\frac{D(k)}{1+k^2} = D_b \text{sgn}(\epsilon)\epsilon^2 \quad \text{with} \quad D_b = \frac{4k_b^2}{1+k_b^2} \quad (64)$$

To determine the position of the tricritical point and the structure of the ordered phases stable below the bifurcation we analyze the asymptotic form of  $\Omega_{\text{eff}}$  for  $\epsilon \rightarrow 0^-$ . At local minima the functional derivative of  $\Omega_{\text{eff}}$  with respect to all the OPs vanishes. From this condition and from (45), (58), (47), and (64) we find that at the metastable states

$$\phi = O(\epsilon), s_{\parallel} = O(\epsilon), \rho = O(\epsilon^2), \psi = O(\epsilon^3), t = O(\epsilon^3) \quad (65)$$

The asymptotic form of  $\Omega_{\text{eff}}$  (corresponding to local minima) is calculated up to  $O(\epsilon^4)$  for  $\epsilon \rightarrow 0^-$ . We thus consistently neglect in our bifurcation analysis all the terms which would lead to contributions to  $\Omega_{\text{eff}}$  of order  $O(\epsilon^6)$ , without further stating this explicitly.

The condition  $\delta\Omega_{\text{eff}}/\delta\tilde{\rho} = 0$  allows us to express  $\tilde{\rho}(\mathbf{k})$  in terms of  $\tilde{\phi}(\mathbf{k})$ , and from (45), (58), (59), (47), and (64) we obtain

$$\Omega_{\text{eff}} = \frac{1}{2} \sum_{\mathbf{k}}' D_b \text{sgn}(\epsilon) \epsilon^2 |\tilde{\phi}(\mathbf{k})|^2 + \Omega_4 + O(\epsilon^6) \quad (66)$$

where

$$\Omega_4 = \frac{1}{4!} \sum_{\mathbf{k}_1, \mathbf{k}_2, \mathbf{k}_3, \mathbf{k}_4}' \delta^{\text{Kr}} \left( \sum_i^4 \mathbf{k}_i \right) [A(\{\hat{\mathbf{k}}_i\}) - G(\{\mathbf{k}_i\})] \prod_i^4 \tilde{\phi}(\mathbf{k}_i) \quad (67)$$

In the above,  $\sum'$  is a summation over vectors such that  $|\mathbf{k}_i| = k_b$  and

$$A(\{\hat{\mathbf{k}}_i\}) = a_4 + A_4 a_2 (\hat{\mathbf{k}}_1 \cdot \hat{\mathbf{k}}_2)(\hat{\mathbf{k}}_3 \cdot \hat{\mathbf{k}}_4) \quad (68)$$

$$G(\{\mathbf{k}_i\}) = \frac{(b_3 - c_3 \mathbf{k}_1 \cdot \mathbf{k}_2)(b_3 - c_3 \mathbf{k}_3 \cdot \mathbf{k}_4)}{3(\alpha_2 + |\mathbf{k}_1 + \mathbf{k}_2|^2)} \quad (69)$$

## B. Tricritical Point in the Extended Model

At the tricritical point (tcp) both  $\epsilon$  and  $\Omega_4$  vanish. When the bifurcation leads to the oil-water separation, i.e.,  $\rho_s < \rho_s^L$ , then the tricritical point is given by  $a_2 = 0$  and  $a_4 = b_3^2/3\alpha_2$ , or explicitly for  $d = 3$  by

$$\rho_s^t = 0.4 \quad \text{and} \quad \tau^t = 1.8 \quad (70)$$

just as in the lattice CHS [65] model, provided that  $\rho_s^t < \rho_s^L$ .

From (62) and (70) it follows that the Lifshitz and tricritical points coincide giving the Lifshitz tricritical point [18,66] for  $\gamma = 27/4$ .  $\gamma = 27/4$  can be considered, as a borderline value between the weak ( $\gamma < 27/4$ ) and the strong ( $\gamma > 27/4$ ) surfactants. For the weak surfactants the tricritical point is located at the transition between the microemulsion and the coexisting uniform oil- and water-rich phases, whereas for the strong surfactants the tcp is located at the transition between the microemulsion and the liquid-crystal phases. The transition between the microemulsion and the ordered periodic phases is continuous for  $\rho_s^L < \rho_s < \rho_s^t$  and first order for  $\rho_s > \rho_s^t$ .

In the case of strong surfactants the tcp corresponds to the lowest value of  $\rho_s$  for which  $\Omega_4$  vanishes at the bifurcation line for some fluctuation  $\tilde{\phi}(\mathbf{k})$ , with  $|\mathbf{k}| = k_b$ . The value of  $\Omega_4$  depends on the form of  $\tilde{\phi}(\mathbf{k})$ . Here we find the approximate position of the tcp, considering a selection of structures

corresponding to the L (lamellar), H (hexagonal), P (simple cubic), G (gyroid), D (diamond), and C (micellar) phases. The C phase is only surfactant-continuous, with oil and water droplets forming a simple-cubic lattice, in which nearest-neighbors are of a different kind and are separated by a surfactant layer. Just below the bifurcation the Fourier amplitudes of the structures listed above can be written in the form

$$\tilde{\phi}(\mathbf{k}) = \Phi \left[ w \sum_j^m \delta^{\text{Kr}}(\mathbf{k} - k_b \hat{\mathbf{p}}_j) + w^* \sum_j^m \delta^{\text{Kr}}(\mathbf{k} + k_b \hat{\mathbf{p}}_j) \right] \quad (71)$$

Here  $w^*$  denotes the complex conjugate to  $w$  and  $|w| = 1$ . For the structures L, H, P, and C,  $w = 1$ ; for D,  $w = (1 + i)/\sqrt{2}$ ; and for G,  $w = i$ . The number  $m$  and orientations of the unit vectors  $\hat{\mathbf{p}}_j$  are different for different structures. For the L phase  $m = 1$  and there is one vector  $\hat{\mathbf{p}}$  in the direction of oscillations. For the H and P phases  $m = 3$  and  $\hat{\mathbf{p}}_j$  for the H phase form an equilateral triangle, whereas for the P phase  $\hat{\mathbf{p}}_j$  are orthogonal to one another. For the D and C phases  $m = 4$  and  $\hat{\mathbf{p}}_j$  form a tetrahedron. For the G phase  $m = 6$  and each unit vector  $\hat{\mathbf{p}}_j$  is parallel to one of the six diagonals of the three adjacent sides of the cube. In the real space the surfaces  $\phi(\mathbf{r}) = 0$  describe the center of the surfactant monolayer, and the maxima and minima of  $\phi(\mathbf{r}) = 0$  describe the centers of the oil- and water-occupied regions. For  $\tilde{\phi}$  given by (71) the surfaces  $\phi(\mathbf{r}) = 0$  are nodal surfaces [67]. They have very similar properties to the corresponding minimal surfaces, except that the mean curvature does not vanish.

After inserting (71) into (66) and some combinatorics we find the value of  $\omega_4(X) = \Omega_4(X)/\Phi^4(X)$ , where by  $X$  we denote one of the phases studied here, i.e.,  $X = \text{L, H, P, G, D, or C}$ . Explicit expressions are given in Ref. 15. It turns out that  $\omega_4$  changes sign for the C structure at the lowest value of  $\rho_s$ . The position of the tcp for  $\gamma = 50$  is shown in Fig. 14(a).

### C. Stability of the Cubic Phases near the Bifurcation Line

To find the stability regions of various phases we determine the value of  $\Phi(X)$  for all the phases  $X = \text{L, H, P, G, D, and C}$  from the condition  $\delta\Omega_{\text{eff}}/\delta\tilde{\phi}(\mathbf{k}) = 0$ , and we obtain

$$\Phi^2(X) = -\frac{m^2}{2} D_b \epsilon^2 \omega_4(X)^{-1} \quad (72)$$

The above and Eqs. (66) and (67) give

$$\Omega_{\text{eff}}(X) = -\left(\frac{m}{2}\right)^2 D_b^2 \epsilon^2 \omega_4(X)^{-1} + O(\epsilon^6) \quad (73)$$



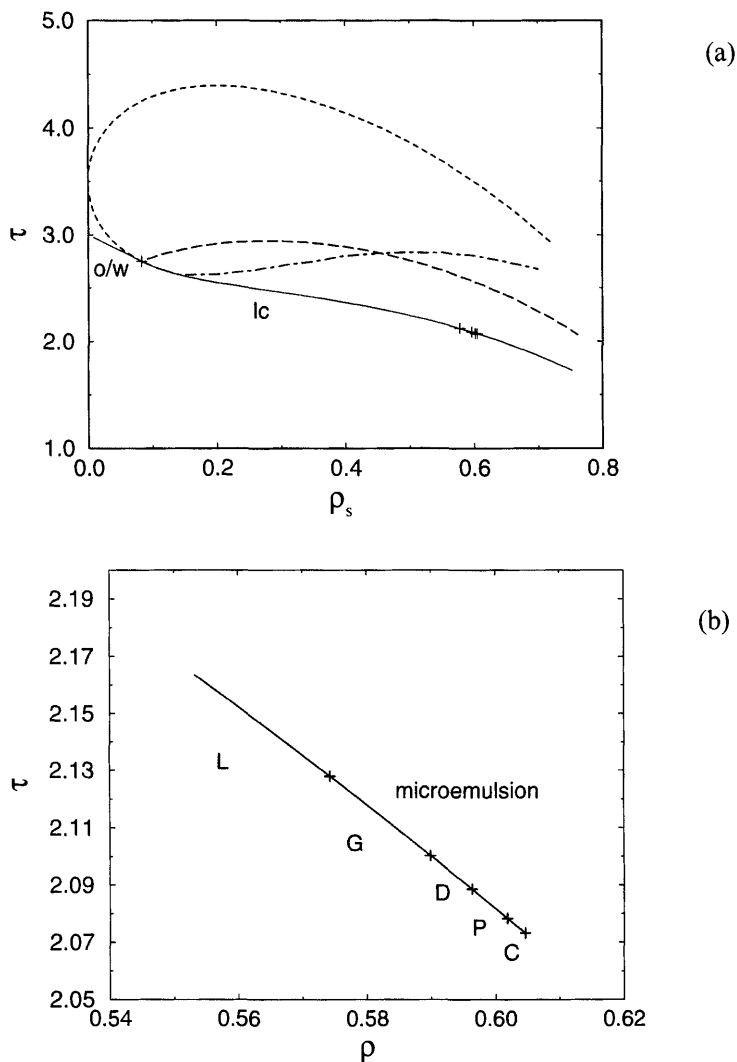


**FIG. 14** (a) Bifurcation (solid), Lifshitz (dashed), disorder (dotted) and  $\bar{K} = 0$  (dash-dotted) lines for  $\gamma = 50$ ;  $\rho_s$  is a surfactant volume fraction and  $\tau$  a dimensionless temperature defined below Eq. (47). Regions of stability of coexisting oil- and water-rich phases and liquid crystals are denoted by "o/w" and "lc" respectively. The Lifshitz point is marked by a cross. The crosses to the right of the Lifshitz point separate different lc phases. (b) The part of the bifurcation line between the microemulsion and the cubic phases. L, G, D, P, and C denote the lamellar, gyroid, diamond, primitive, and cubic micellar structures, respectively.

The lowest value of  $\Omega_{\text{eff}}$  corresponds to different structures for different  $\rho_s$  along the bifurcation line. The sequence of phases is always the same; for various strengths of surfactant (with  $\gamma > 27/4$ ) and for increasing  $\rho_s$  it is:  $L \rightarrow G \rightarrow D \rightarrow P \rightarrow C$ . For  $\gamma = 50$  (strong surfactant, like  $C_{10}E_5$ ) the portion of the phase diagram corresponding to the stable cubic phases is shown in Fig. 14(b). For surfactants weaker than in the case shown in Fig. 14 the cubic phases occur for a lower surfactant volume fraction; for example, for  $\gamma = 16$  cubic phases appear for  $\rho_s \approx 0.45$ .

In the structure with all the surfactant molecules located at monolayers, the volume fraction of surfactant should be proportional to the *average* surface area times the width of the monolayer divided by the volume, i.e.,  $\rho_s \propto Sa/V$ . The proportionality constant is called the surfactant parameter [34]. This is true for a single surface with no intersections. In our mesoscopic description the volume is measured in units of the volume occupied by the surfactant molecule, and the area is measured in units of the area occupied by the amphiphile. In other words, in our model the area of the monolayer is the dimensionless quantity equal to the number of amphiphiles residing on the monolayer. Hence, it should be identified with the area rescaled by the surfactant parameter of the corresponding structure.

In real systems the microscopic configurations of the monolayers can differ from the average configuration. The surfactant density averaged over these configurations is a smooth function, non-vanishing in a region of width comparable to the standard deviation from the average position of the monolayer. In the model considered here within the MF approximation the surfactant-occupied interface is very diffuse close to the second-order transition. For example, in the lamellar phase with modulations of a period  $2\pi/k_b$  in the  $\hat{z}$  direction, and for the surfactant surface located at  $z = 0$ , the density of oriented surfactant is given by  $s_{\parallel} \sim \epsilon \cos(2\pi z/k_b)$  close to the bifurcation (see (59), (71), and (65)). Hence it deviates from zero in an extended region. The “projected” surface corresponds to the average location of the interface between oil-rich and water-rich domains and in our case is given by  $\phi(\mathbf{r}) = 0$ . We expect that the average surface area of the monolayer per unit volume  $S/V$  is larger than the “projected” surface area per unit volume  $\Sigma$ , and that  $\Sigma/\rho_s \leq a^{-1}$ .

The ratio  $\Sigma/\rho_s$ , calculated for different phases below the bifurcation, is shown in Fig. 15. In the special case of the C phase the surface intersects itself; therefore, in the computation of  $\Sigma/\rho_s$  we have subtracted the volume occupied along the lines of intersection, since it would be counted twice otherwise. The surface area per volume is an increasing function of the surfactant volume fraction and it determines the sequence of phases. Moreover, we have found that the effect of broadening of the interface on the value  $\Sigma/\rho_s$  in different phases is different, and we have a quantitative

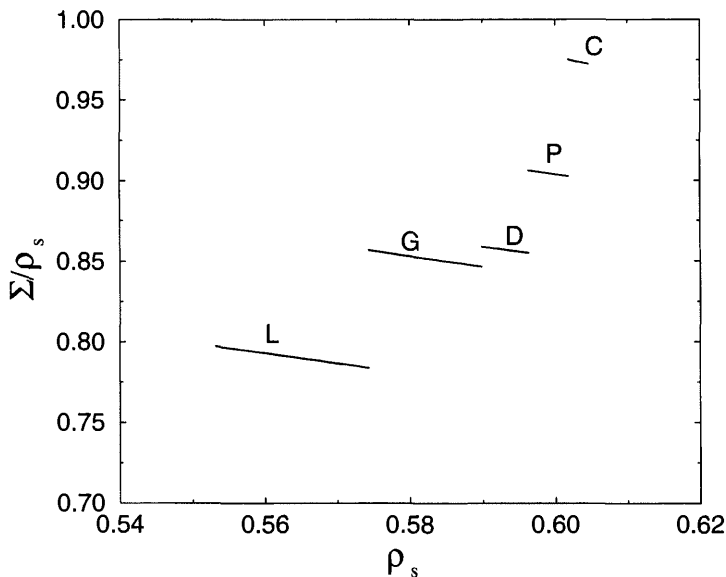


**FIG. 15** The “projected” surface area per unit volume  $\Sigma$ , divided by the surfactant volume fraction for different structures along the bifurcation line as a function of surfactant volume fraction  $\rho_s$ . Note that due to the geometrical constraints this quantity cannot exceed the length of the surfactant  $a$ . Here we set  $a = 1$  for convenience.

measure of its strength through the projected area. As expected, the effect is the stronger, the more independent the surfaces occupied by surfactant. Indeed, in the lamellar phase the difference between the average and the projected surface area is the largest (about 20% of the relative difference). In the C phase the structure is quite stiff due to the intersections of the surface  $\phi(\mathbf{r}) = 0$ , and the effect of broadening of the interface is weaker than in the other structures.

## X. STRUCTURE OF MICROEMULSION

In the standard approaches to the systems in which monolayers or bilayers are formed, one assumes that the width of the film is much smaller than the length characterizing the structure (oil or water domain size, for example). In such a case it is justified to represent the film by a mathematical surface and the structure can be described by the local invariants of the surface, i.e., the mean  $H$  and the Gaussian  $K$  curvatures and by the global (topological)

invariant, the Euler characteristic  $\chi$ , as discussed in the previous sections. In real microemulsions, however, the crucial assumption that the surfactant films are very thin compared to the characteristic length of the structure need not be satisfied. The width of the interface in a microemulsion can be large [49], even comparable with the oil and water domain sizes, as in the ordered phases near the continuous transition to the microemulsion (see the previous subsection).

For diffuse and delocalized interfaces one can still define a mathematical surface which in some way describes the film, for example by  $\phi(\mathbf{r}) = 0$ . A problem arises if one wants to compare the structure of microemulsion and of ordered phases within one formalism. The problem is caused by the topological fluctuations. As was shown, the Euler characteristic averaged over the surfaces,  $\langle \chi(\phi(\mathbf{r}) = 0) \rangle$ , is different from the Euler characteristics of the average surface,  $\chi(\langle \phi(\mathbf{r}) \rangle = 0)$ , in the ordered phases. This difference is large in the lamellar phase, especially close to the transition to the microemulsion.  $\chi(\langle \phi(\mathbf{r}) \rangle = 0)$  is a natural quantity for the description of the structure of the ordered phases. For microemulsion, however,  $\langle \phi(\mathbf{r}) \rangle = 0$  everywhere, and the only meaningful quantity is  $\langle \chi(\phi(\mathbf{r}) = 0) \rangle$ .

## A. New Structure Parameters

Recently an alternative approach for the description of the structure in systems with self-assembling molecules has been proposed in Ref. 68. In this approach no particular assumption about the nature of the internal interfaces or their bicontinuity is necessary. Therefore, within the same formalism, localized, well-defined thin films and diffuse interfaces can be described both in the ordered phases and in the microemulsion. This method is based on the vector field describing the orientational ordering of surfactant,  $\mathbf{u}$ , or rather on its curlless part  $\mathbf{s}$  defined in Eq. (55).

For a particular field  $\mathbf{s}(\mathbf{r})$  we can calculate at every point  $\mathbf{r}$  the mean and the Gaussian curvatures of a corresponding surface passing through  $\mathbf{r}$ , the normal vector of which is  $\hat{\mathbf{n}} = \mathbf{s}/s$ . Using the standard geometrical definitions based on  $\hat{\mathbf{n}}$  and its derivatives we obtain

$$s^3(\mathbf{r})H_s(\mathbf{r}) = \frac{1}{2} \left( s^2 \nabla \cdot \mathbf{s} - \frac{1}{2} \mathbf{s} \cdot \nabla s^2 \right) \quad (74)$$

$$s^4(\mathbf{r})K_s(\mathbf{r}) = \frac{1}{2} \mathbf{s}_i \mathbf{s}_l \epsilon_{ijk} \epsilon_{lmn} \nabla_m \mathbf{s}_j \nabla_n \mathbf{s}_k \quad (75)$$

where the subscript  $s$  means that the related quantity refers to the particular field  $\mathbf{s}$ . For the system characterized by some probability distribution for  $\mathbf{s}$ , average values for the above-defined quantities can be calculated.

In [68] the structure parameters  $\bar{H}$  and  $\bar{K}$  are introduced in the following way

$$\bar{H} = \frac{\int_V d\mathbf{r} \langle s^3 H_s \rangle}{\int_V d\mathbf{r} \langle s^3 \rangle} \quad (76)$$

and

$$\bar{K} = \frac{\int_V d\mathbf{r} \langle s^4 K_s \rangle}{\int_V d\mathbf{r} \langle s^4 \rangle} \quad (77)$$

where, in the numerator, average values of the quantities (74) and (75) are calculated and integrated over the unit cell in the case of ordered structures. The denominator plays the role of normalization with respect to the field  $s$ .

## B. Structure Parameters in Ordered Phases

Consider first the case of the ordered phases. The average distribution  $\langle s(\mathbf{r}) \rangle$  is then periodic in space. If the fluctuations around  $\langle s(\mathbf{r}) \rangle$  are neglected then  $\bar{H}$  and  $\bar{K}$  can be approximated by

$$\bar{H} \approx \frac{\int_V d\mathbf{r} \langle s \rangle^3 H_{(s)}}{\int_V d\mathbf{r} \langle s \rangle^3} \quad (78)$$

$$\bar{K} \approx \frac{\int_V d\mathbf{r} \langle s \rangle^4 K_{(s)}}{\int_V d\mathbf{r} \langle s \rangle^4} \quad (79)$$

For thin surfactant films the integrals in (78) and (79) are restricted to the region of the film, and if  $\langle s(\mathbf{r}) \rangle \approx \text{const}$  across the film then

$$\bar{H} \approx \bar{H}_m = \frac{1}{|S|} \int_V d\sigma H_{(s)} \quad (80)$$

$$\bar{K} \approx \bar{K}_m = \frac{1}{|S|} \int_V d\sigma K_{(s)} \quad (81)$$

where  $S$  denotes the mathematical surface of area  $|S|$  modeling the surfactant film and  $\bar{H}_m$  and  $\bar{K}_m$  denote the mean and Gaussian curvatures of this surface. From the above equations it follows that, in the case of ordered

phases and infinitely thin surfaces, the standard definitions of the average curvatures of the single mathematical surface are recovered. Since  $\bar{H}$  and  $\bar{K}$ , in the case of thin films in the ordered phases, *reduce to the usual geometrical invariants averaged over the surface*, they may be considered as *extensions of the average mean and Gaussian curvatures* to the case of the diffused films, which cannot be represented by just a single surface. By virtue of the Gauss theorem  $\bar{K}_m$  is related to the Euler characteristic by  $\bar{K}_m = 2\pi\chi/|S|$ . Since  $\bar{K}$  reduces to  $\bar{K}_m$ , it may be considered as an extension of the topological invariant per unit surface area.

In order to find the effect of broadening of the surface on the structure parameters  $\bar{H}$  and  $\bar{K}$ , we first study the ordered phases with the diffusive interfaces. The ordered phases can be described by the periodic surfaces  $\langle\phi(\mathbf{r})\rangle = 0$  and we can compare  $\bar{H}_m$  and  $\bar{K}_m$  with  $\bar{H}$  and  $\bar{K}$ . The numerators in the definitions (76) and (77) in the Fourier representation assume the forms [68]

$$\langle s^3 H_s \rangle = -\frac{3}{4} \int \frac{d\mathbf{k}_1}{(2\pi)^d} \cdots \int \frac{d\mathbf{k}_3}{(2\pi)^d} \hat{\mathbf{k}}_1 \cdot \hat{\mathbf{k}}_2 k_3 G_{3s}(\mathbf{k}_1, \mathbf{k}_2, \mathbf{k}_3) \quad (82)$$

$$\langle s^4 K_s \rangle = \frac{1}{2} \int \frac{d\mathbf{k}_1}{(2\pi)^d} \cdots \int \frac{d\mathbf{k}_4}{(2\pi)^d} \frac{|\mathbf{k}_3 \cdot (\mathbf{k}_1 \times \mathbf{k}_2)|^2}{k_1 k_2 k_3 k_4} G_{4s}(\mathbf{k}_1, \mathbf{k}_2, \mathbf{k}_3, \mathbf{k}_4) \quad (83)$$

where the  $n$ -body correlation functions are defined as

$$G_{ns}(\mathbf{k}_1, \dots, \mathbf{k}_n) = \langle s_{\parallel}(\mathbf{k}_1) \dots s_{\parallel}(\mathbf{k}_n) \rangle \quad (84)$$

For the ordered phases we approximate the  $n$ -body functions by

$$G_{ns}(\mathbf{k}_1, \dots, \mathbf{k}_n) \approx \langle s_{\parallel}(\mathbf{k}_1) \rangle \dots \langle s_{\parallel}(\mathbf{k}_n) \rangle \quad (85)$$

Near the bifurcation line, because of (59), we have

$$\langle \tilde{s}_{\parallel}(\mathbf{k}_1) \rangle \approx -J \frac{k_b}{1 + k_b^2} \langle \tilde{\phi}(\mathbf{k}) \rangle + O(\epsilon^3) \quad (86)$$

When (86) and (85) are inserted into (82) and (83), then  $\bar{H}$  and  $\bar{K}$  can be expressed in terms of  $\langle \tilde{\phi}(\mathbf{k}) \rangle$  and calculated for various structures. For illustration, the structures L, H, D, and C (see Eq. (71)) were considered [68]. For the L, H, D, and C phases the signs of  $\bar{H}_m$  and  $\bar{K}_m$  are respectively:  $(\text{sgn}(\bar{H}_m), \text{sgn}(\bar{K}_m)) = (0, 0), (\pm, 0), (0, -), (0, +)$ . The calculations, involving some combinatorics are described in Ref. [68]. In all the cases  $\bar{H}$  and  $\bar{K}$  are of the same sign as  $\bar{H}_m$  and  $\bar{K}_m$  respectively, and their absolute values are smaller by about one-half. Smaller values of  $\bar{H}$  and  $\bar{K}$  result from the fact that the integrals in (76) and (77) are over a continuous set of surfaces and the contribution of each surface is weighted, respectively, by  $\langle s(\mathbf{r}) \rangle^3$  and

$\langle s(\mathbf{r}) \rangle^4$ , whereas  $\bar{H}_m$  and  $\bar{K}_m$  are calculated for a single surface. The same signs of the parameters defined in a different way suggest that either way of defining the structure leads to *the same classification of its type*.

### C. Structure Parameters in Microemulsion

Having determined the effect of the diffusive interfaces on the structure parameters, we now turn to the calculation of  $\bar{H}$  and  $\bar{K}$  in microemulsions. In the case of oil–water symmetry three-point correlation functions vanish and  $\bar{H} = 0$ . In order to calculate  $\bar{K}$  from (77) and (83) we need the explicit expressions for the four-point correlation functions. In the Gaussian approximation

$$\begin{aligned} (2\pi)^{-2d} \left\langle \prod_i^4 s_{\parallel}(\mathbf{k}_i) \right\rangle &= G_{ss}(\mathbf{k}_1) \delta(\mathbf{k}_1 + \mathbf{k}_2) G_{ss}(\mathbf{k}_3) \delta(\mathbf{k}_3 + \mathbf{k}_4) \\ &+ G_{ss}(\mathbf{k}_1) \delta(\mathbf{k}_1 + \mathbf{k}_3) G_{ss}(\mathbf{k}_2) \delta(\mathbf{k}_2 + \mathbf{k}_4) \\ &+ G_{ss}(\mathbf{k}_1) \delta(\mathbf{k}_1 + \mathbf{k}_4) G_{ss}(\mathbf{k}_2) \delta(\mathbf{k}_2 + \mathbf{k}_3) \end{aligned} \quad (87)$$

and  $\bar{K}$  vanishes, since  $\mathbf{k}_1 \cdot (\mathbf{k}_2 \times \mathbf{k}_3) = 0$  for non-vanishing  $\langle \prod_i^4 s_{\parallel}(\mathbf{k}_i) \rangle$  (see (83)). Consider now the perturbation expansion for  $\bar{K}$  in the coupling constants of  $\Omega_{\text{int}}$  about the Gaussian solution. We truncate the expansion at the first-order term. Consistently, the numerator in Eq. (77) is truncated at the first-order term and the denominator at the zeroth-order term. The denominator in (77) has, in the Gaussian approximation (see (87)), the explicit form

$$\begin{aligned} &\langle \mathbf{s}(\mathbf{r}_1) \cdot \mathbf{s}(\mathbf{r}_2) \mathbf{s}(\mathbf{r}_3) \cdot \mathbf{s}(\mathbf{r}_4) \rangle \\ &= \int \frac{d\mathbf{k}_1}{(2\pi)^d} G_{ss}(\mathbf{k}_1) e^{-i\mathbf{k}_1(\mathbf{r}_1 - \mathbf{r}_2)} \int \frac{d\mathbf{k}_3}{(2\pi)^d} G_{ss}(\mathbf{k}_3) e^{-i\mathbf{k}_3(\mathbf{r}_3 - \mathbf{r}_4)} \\ &+ \int \frac{d\mathbf{k}_1}{(2\pi)^d} e^{-i\mathbf{k}_1(\mathbf{r}_1 - \mathbf{r}_3)} \int \frac{d\mathbf{k}_2}{(2\pi)^d} e^{-i\mathbf{k}_2(\mathbf{r}_2 - \mathbf{r}_4)} (\mathbf{k}_1 \cdot \mathbf{k}_2)^2 \frac{G_{ss}(k_1)}{k_1^2} \frac{G_s(k_2)}{k_2^2} \\ &+ \int \frac{d\mathbf{k}_1}{(2\pi)^d} e^{-i\mathbf{k}_1(\mathbf{r}_1 - \mathbf{r}_4)} \int \frac{d\mathbf{k}_2}{(2\pi)^d} e^{-i\mathbf{k}_2(\mathbf{r}_2 - \mathbf{r}_3)} (\mathbf{k}_1 \cdot \mathbf{k}_2)^2 \frac{G_{ss}(k_1)}{k_1^2} \frac{G_s(k_2)}{k_2^2} \end{aligned} \quad (88)$$

In the perturbation expansion [69] the first-order contribution to  $G_{4s}$  consists of two terms which read

$$-(2\pi)^d \frac{a_4}{\tau} \delta \left( \sum_i^4 \mathbf{k}_i \right) \prod_i^4 G_{\phi s}(\mathbf{k}_i) \quad (89)$$

and

$$\begin{aligned}
 & - (2\pi)^d \frac{A_4}{3\tau} \delta\left(\sum_i^4 \mathbf{k}_i\right) \prod_i^4 G_{ss}(\mathbf{k}_i) \\
 & \times (\hat{\mathbf{k}}_1 \cdot \hat{\mathbf{k}}_2 \hat{\mathbf{k}}_3 \cdot \hat{\mathbf{k}}_4 + \hat{\mathbf{k}}_1 \cdot \hat{\mathbf{k}}_3 \hat{\mathbf{k}}_2 \cdot \hat{\mathbf{k}}_4 + \hat{\mathbf{k}}_1 \cdot \hat{\mathbf{k}}_4 \hat{\mathbf{k}}_2 \cdot \hat{\mathbf{k}}_3)
 \end{aligned} \quad (90)$$

The multi-dimensional integrals in the definition of  $\bar{K}$  can be calculated for the denominator (Eq. (88)) or reduced to a one-dimensional integral for the numerator (Eqs. (83), (89) and (90)) with the help of the Fourier-transform method. In Eq. (77) the many-body correlation function is formally calculated at one point. In physical systems, however, the continuous Landau-Ginzburg description is not correct when the characteristic distances of ordering become smaller than the size of molecules. The correlation functions in definition (77) should be calculated at points  $\mathbf{r}_1, \mathbf{r}_2, \mathbf{r}_3, \mathbf{r}_4$  such that the distances from one another are comparable to  $a$  (size of molecules). For shorter distances the correlation functions are calculated for the same molecule and are irrelevant for the determination of the geometrical structure of the film. We thus regularize the integrals with the help of the real-space cutoff  $a \equiv 1$ . Description of the calculation and explicit expressions for the results are given in Ref. 70. The examples of numerical values for  $\bar{K}$  are shown in Fig. 16 for  $\gamma = 50$ .  $\bar{K}$  is negative only in the neighborhood of the liquid-crystal phases, i.e., in a part of the stability region of the microemulsion. We find the line of  $\bar{K} = 0$  in the phase space  $(\rho_s, \tau)$ . Beyond this line, temperatures are too high and/or surfactant volume fractions are too low or too high and the bicontinuous structure cannot be formed in this model. The bicontinuous structure is oil-, water-, and surfactant continuous, with oil and water forming channels of a mesoscopic size and the surfactant separating the two other components. In ordinary binary mixtures with comparable volume fractions (or in the Ising model) the percolating channels of each component (or spins of the same sign) are formed above the critical temperature. Such "bicontinuous" structure is formed on the microscopic scale and should be distinguished from the bicontinuous structure which is formed in the ternary surfactant mixtures. For example, the diffusion, electrical conductivity, etc. are qualitatively different in the two cases.

The line  $\bar{K} = 0$  can be considered as a borderline for applicability of the basic model, in which the Gaussian curvature is always negative. Recall that in the basic model the oil-water interface is saturated by the surfactant molecules by construction of the model. Hence, for equal oil and water volume fractions the Gaussian curvature must be negative, by the definition of the model.



The surface-averaged Gaussian curvature,  $\bar{K}_m$ , introduces the length scale,  $|\bar{K}_m|^{-1/2}$ , describing an average radius of curvature of the single, "central" surface of the film. The extension of  $\bar{K}_m$  to systems with thick surfactant films,  $\bar{K}$ , similarly introduces the length scale  $|\bar{K}|^{-1/2}$ , which represents the average radius of curvature of the collection of surfaces modeling the film.

For ordered periodic structures of a period  $\lambda$  a dimensionless ratio between the two lengths,  $\bar{R}_m = |\bar{K}_m|^{-1/2}/\lambda$ , provides an additional characteristic of the structure. On the basis of the results of Ref. 39, we can estimate this ratio for the periodic minimal surfaces. For simple minimal surfaces, P, D, or G [39], we find respectively  $\bar{R}_m = 0.306$ ,  $\bar{R}_m = 0.195$ , and  $\bar{R}_m = 0.248$ . For more complicated periodic structures [39] its value can be even smaller than 0.1; for example, for the surface labeled GX5,  $\bar{R}_m = 0.073$ .

In the microemulsion the role of  $\lambda$  is played by the period of damped oscillations of the correlation functions (Eq. (7)). The surface-averaged Gaussian curvature  $\bar{K}_m = 2\pi\chi/|S|$  is the *topological* invariant per unit surface area. Therefore the comparison between  $\bar{R}_m = |\bar{K}_m|^{-1/2}/\lambda$  in the disordered microemulsion and in the ordered periodic phases is justified. We calculate here  $\bar{R} = |\bar{K}|^{-1/2}/\lambda$ . Since  $\bar{K}$  differs for diffused films from corresponding  $\bar{K}_m$  related to the "central" surface of the film by about 1/2, the above ratio also has a different value from  $\bar{R}_m$ , with  $\bar{R}_m \approx |\bar{R}|/\sqrt{2}$ . We plot  $1/\sqrt{|\bar{K}|}$  and  $\lambda$  in Fig. 17 for  $\gamma = 50$ . We obtain the ratio  $\bar{R} \sim 0.33$ –0.5 for  $\tau = 2.7$  and for the surfactant concentrations  $\rho_s \sim 0.3$ –0.6. The results for  $\bar{R} \approx \bar{R}_m\sqrt{2}$  show that in the region of negative  $\bar{K}$ , not too close to the line  $\bar{K} = 0$  nor to the bifurcation line, the structure of the microemulsion has features resembling the corresponding features of different simple minimal surfaces for different  $\rho_s$ . For  $\bar{K}$  positive,  $\bar{R}$  decreases when the system becomes less ordered. In the region of a structureless fluid, i.e., in the region of the monotonically decaying correlation functions, we obtain that  $\bar{K}$  is positive and larger than one. This indicates that the surfactant molecules are correlated in such a way that the preferred orientations and positions of four molecules at distances  $\sim a$  from one another are such that they form vectors normal to a sphere with the radius comparable to the size of the molecules.

The above results show that the structure of the system with the molecules self-assembled into the internal films is determined by their correlation functions. In contrast to simple fluids, the four-point correlation functions are as important as the two-point correlation functions for the description of the structure in this case. The oil or water domain size is related to the period of oscillations  $\lambda$  of the two-point functions. The *connectivity* of the oil and water domains, related to the sign of  $\bar{K}$ , is determined by the way four molecules at distances comparable to their sizes are correlated. For  $\bar{K} > 0$  surfactant molecules are correlated in such a way that preferred orientations

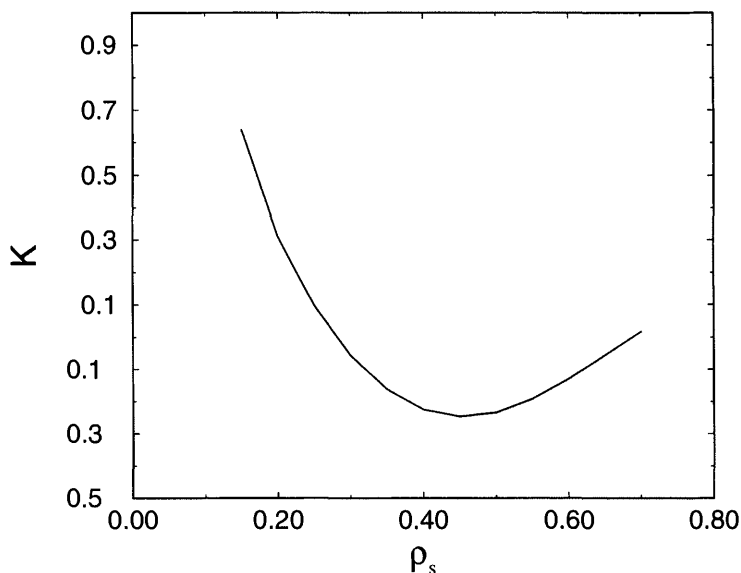


**FIG. 16** Average Gaussian curvature for  $\gamma = 50$  at fixed temperature  $\tau = 2.7$ .  $\rho_s$  is a surfactant volume fraction and a length unit is the size of a surfactant molecule (a bare thickness of the monolayer).

and positions of four molecules at distances  $\sim a$  from one another are such that they form vectors normal to a sphere (or an ellipsoid). For  $\bar{K} < 0$ , four molecules at distances from one another  $\sim a$  are correlated in such a way that their preferred positions and orientations fit a saddle. Moreover, the four-point correlation function determines another important length  $|\bar{K}|^{-1/2}$ , related to the average radius of curvature of the internal film. We propose to consider the dimensionless ratio between the two lengths  $\lambda$  and  $|\bar{K}|^{-1/2}$  as a convenient parameter which allows for comparison between the microemulsion and the different ordered structures.

## XI. SUMMARY

In ternary mixtures of oil, water, and surfactant the ordering properties of the system follow from the vectorial character of the interactions of the surfactant molecules with both the oil and the water molecules. The typical size of the ordered domains, much larger than the molecular size, justifies the application of the mesoscopic Landau–Ginzburg approach to the ordering. In the simplest approach of Gompper and Schick [3,12], which we call here the basic Landau–Ginzburg model, the orientational degrees of free-

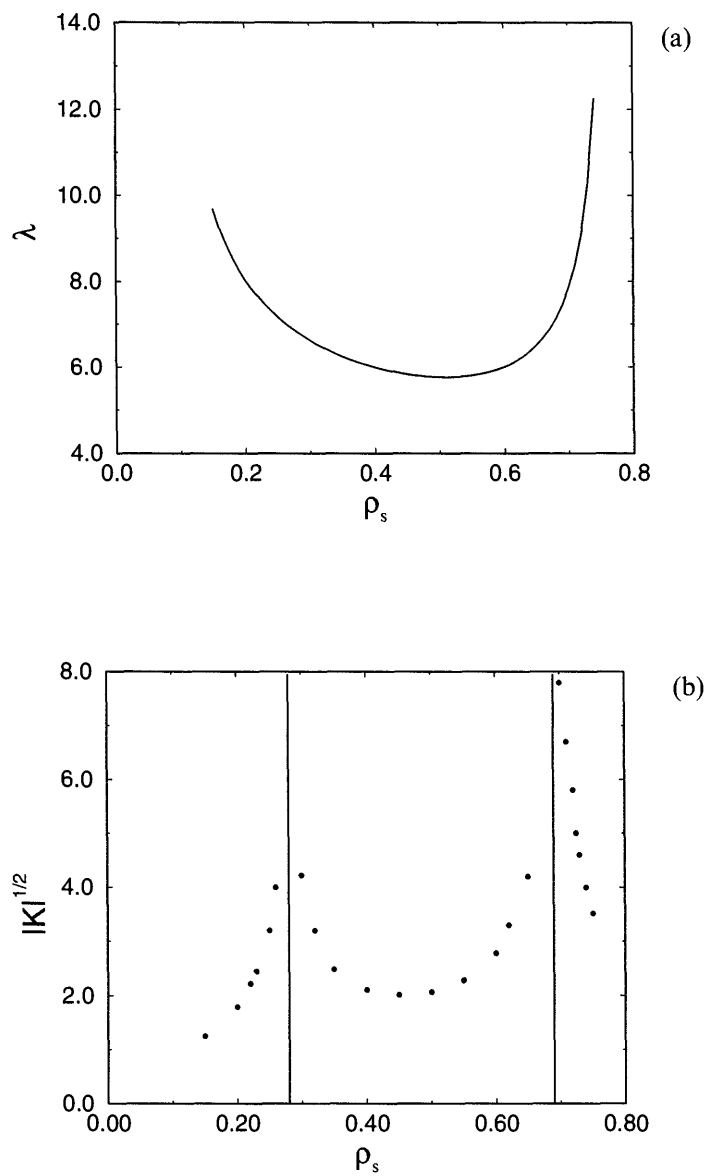


**FIG. 17** (a)  $|\bar{K}|^{-1/2}$  for  $\gamma = 50$  at fixed temperature  $\tau = 2.7$ .  $\rho_s$  is a surfactant volume fraction; a length unit is the size of a surfactant molecule (a bare thickness of the monolayer). (b) Period of damped oscillations of the correlation function for  $\phi$ ,  $\lambda$ , for  $\gamma = 50$  at fixed temperature  $\tau = 2.7$ .  $\rho_s$  is a surfactant volume fraction; a length unit is the size of a surfactant molecule (a bare thickness of the monolayer).

dom of the surfactant are neglected and the vectorial character of the interactions between the molecules is taken into account in terms of the effective coupling between oil and water. This Landau–Ginzburg model with the single scalar order parameter describes very well the scattering intensity in microemulsions, together with a peak at non-zero scattering wave vector, an indication of the correlations between the oil-rich and the water-rich domains. It also describes very well the topological fluctuations which accompany the lamellar–microemulsion phase transition. The minimization of the model leads to the generation of periodic surfaces which appear in the cubic phases, even when they have a very complex topology. As far as we know, this is the most promising method for the generation of new periodic surfaces. However, this model does not allow for studying the stabilization of the periodic cubic structures. All the studied cubic structures are metastable in this model. Therefore, to describe the systems in which the cubic phases are stable we have to include in the effective interactions the vectorial order parameter characteristic for the surfactant molecules.

In order to avoid dealing with numerous unknown coupling constants it has been necessary to derive the Landau–Ginzburg model from the microscopic model of the ternary mixture. We have shown explicitly the pathway from the microscopic lattice CHS model to the mesoscopic Landau–Ginzburg model and expressed the unknown coupling constants in terms of the physical parameters of the system, i.e., the density of surfactant, temperature, and a material parameter describing the strength of the surfactant. Usually the relation between the Landau–Ginzburg phenomenological parameters and physical parameters is not known. In the extended model the bicontinuous cubic phases are stabilized for sufficiently strong surfactants and sufficiently large surfactant density. Moreover, we have shown that locally the structure of microemulsions resembles the structure of the cubic phases with the surfactant forming a periodic surface of low genus. It has been done on the basis of the generalized mean and Gaussian curvatures for the diffusive surfaces in the microemulsion phase.

## ACKNOWLEDGMENTS

We would like to thank Gerhard Gompper, Johann Høye, Andrzej Poniewierski, Michael Schick, and George Stell for fruitful collaboration which led to the results presented in this chapter. This work was partially supported by the Komitet Badań Naukowych under grants 2P03B12516 and 3T09A07316 and by the Maria Skłodowska Curie Joint Fund II.

## REFERENCES

1. R. G. Laughlin. *The Aqueous Phase Behavior of Surfactants*. London: Academic Press, 1994.
2. V. Degiorgio, M. Corti, eds. *Physics of Amphiphiles: Micelles, Vesicles and Microemulsions*. Amsterdam: Italian Physical Society, North-Holland, 1985.
3. G. Gompper, M. Schick. Scattering from internal interfaces in microemulsion and sponge phases. *Phys Rev E* 49:1478–1482, 1994.
4. F. David, P. Ginsparg, J. Zinn-Justin, eds. *Les Houches Session LXII 1994, Fluctuating Geometries in Statistical Mechanics and Field Theory*. Amsterdam: Elsevier Science, 1996.
5. A. Ciach. Statistical mechanics of ternary surfactant mixtures including microemulsions. *Pol J Chem* 66:1347–1387, 1992.
6. M. Kahlweit, R. Stray, D. Haase, H. Kunieda, T. Schmeling, B. Faulhaber, M. Borkovec, H. F. Eicke, G. Busse, F. Eggers, Th. Funck, H. Richmann, L. Magid, O. Söderman, P. Stilbs, J. Winkler, A. Ditrach, W. Jahn. How to study microemulsions. *J Coll Interface Sci* 118:436–452, 1987.
7. M. Kahlweit, R. Strey, P. Firman, D. Haase, J. Jen, R. Schomäcker. General patterns of the phase behavior of mixtures of H<sub>2</sub>O, nonpolar solvents, amphiphiles, and electrolytes. 1. *Langmuir* 4:499–511, 1988.
8. B. Widom. Lattice model of microemulsions. *J Chem Phys* 84:6943–6954, 1986.
9. M. Schick, W. H. Shih. Simple microscopic model of a microemulsion. *Phys Rev Lett* 59:1205–1208, 1987.
10. K. Chen, C. Ebner, C. Jayaprakash, R. Pandit. Microemulsions in oil–water–surfactant mixtures: Systematics of a lattice-gas model. *Phys Rev A* 38:6240, 1988.
11. M. Teubner, R. Strey. Origin of the scattering peak in microemulsion. *J Chem Phys* 87:3195–3200, 1987.
12. G. Gompper, M. Schick. Correlation between structural and interfacial properties of amphiphilic systems. *Phys Rev Lett* 65:1116–1119, 1990.
13. G. Gompper, M. Schick. *Self-assembling amphiphilic systems*. Vol. 16 of *Phase Transitions and Critical Phenomena*. 1st ed. New York: Academic Press, 1994.
14. W. Goźdz, R. Hołyst. From the plateau problem to minimal surfaces in lipids, surfactants and diblock copolymer systems. *Macromol Theory Simul* 5:321–332, 1996.
15. A. Ciach. Bifurcation analysis and liquid-crystal phases in Landau–Ginzburg model of microemulsion. *J Chem Phys* 104:2376–2383, 1996.
16. A. Ciach, J. S. Høye, G. Stell. Microscopic model for microemulsion. I. Ground state properties. *J Chem Phys* 90:1214–1221, 1989.
17. K. V. Schubert, R. Strey. Small-angle neutron scattering from microemulsion near the disorder line in water/formamide–octane–C<sub>1</sub>E<sub>3</sub> systems. *J Chem Phys* 95:8532–8545, 1991.
18. G. Gompper, R. Hołyst, M. Schick. Interfacial properties of amphiphilic systems: the approach to Lifshitz points. *Phys Rev A* 43:3157–3160, 1991.

19. J. Putz, R. Holyst, M. Schick. Nonmonotonic behavior of a contact angle on approaching critical endpoints. *Phys Rev A* 46:3369–3372, 1992. *Phys Rev E* 46:3035, 1993.
20. G. Gompper, M. Hennes. Layering, dewetting, and first-order wetting in ternary amphiphilic systems. *J Chem Phys* 102(7):2871–2880, 1994.
21. G. Gompper, S. Zschocke. Elastic properties of interface in a Ginzburg–Landau theory of swollen micells, droplet crystals and lamellar phases. *Europhys Lett* 16:731–736, 1991.
22. G. Gompper, S. Zschocke. Ginzburg–Landau theory of oil–water–surfactant mixtures. *Phys Rev A* 46:4836–4851, 1992.
23. F. Schmid, M. Schick. Phase transitions of a confined complex fluid. *Phys Rev E* 48:1882–1888, 1993.
24. M. Abramowitz, I. A. Stegun, eds. *Handbook of Mathematical Functions with Formulas, Graphs, and Mathematical Tables*. Vol. 55 of *National Bureau of Standards Applied Mathematics Series*, 9th ed. Washington, DC: US Government Printing Office, 1970, pp. 883–884.
25. W. H. Press, B. P. Flannery, S. A. Teukolsky, W. T. Vetterling. *Numerical Recipes*. Cambridge: Cambridge University Press, 1990.
26. U. Schwarz. Mesoskopische Modellierung amphiphiler Systeme. PhD thesis, Potsdam University, 1998.
27. N. S. M. Henry, K. Lonsdale, eds. *International Tables for X-ray Crystallography, Vol. 1*. Birmingham, UK: Kynoch Press, 1952.
28. A. H. Schoen. Infinite periodic minimal surfaces without self-intersections. *Technical Report TN D-5541*, NASA, May 1970.
29. D. M. Anderson, H. T. Davis, L. E. Scriven, J. C. C. Nitsche. Periodic surfaces of prescribed mean curvatures. *Adv Chem Phys* 77:337–396, 1990.
30. I. S. Barnes, S. T. Hyde, B. W. Ninham. The caesium chloride zero potential surface is not the Schwarz P-surface. *J Physique Colloque* 51 C7:19–24, 1990.
31. A. L. Mackay, J. Klimowski. Towards a grammar of inorganic structure. *Comp Math Appl* 12B:803–824, 1986.
32. M. Spivak. *A Comprehensive Introduction to Differential Geometry, Vol. III*. Berkeley: Publish or Perish, 1979.
33. D. A. Hoffman. Some basic facts, old and new, about triply periodic embedded minimal surfaces. *J Physique Colloque* 51 C7:197–208, 1990.
34. S. T. Hyde. The topology and geometry of infinite periodic surfaces. *Z Kristallogr* 187:165–185, 1989.
35. D. M. Anderson. A new technique for studying microstructures:  $^2\text{NMR}$  band-shapes of polymerized surfactants and counterions in microstructures described by minimal surfaces. *J Physique Colloque* 51:1–18, 1990.
36. W. Gózdź, R. Holyst. Distribution functions for  $^2\text{H}$  nuclear magnetic resonance band shapes for polymerized surfactant molecules forming triply periodic surfaces. *J Chem Phys* 106:9305–9312, 1997.
37. L. E. Scriven. Equilibrium bicontinuous structure. *Nature* 263:123–125, 1976.
38. W. Gózdź, R. Holyst. High genus gyroid surfaces of non-positive gaussian curvature. *Phys Rev Lett* 76:2726–2729, 1996.

39. W. Gózdź, R. Hołyst. Triply periodic surfaces and multiply continuous structures from the Landau model of microemulsions. *Phys Rev E* 54:5012–5027, 1996.
40. D. M. Anderson. PhD thesis, University of Minnesota, 1986.
41. S. T. Hyde. Microstructure of bicontinuous surfactant aggregates. *J Phys Chem* 93:1458–1464, 1989.
42. W. Harbich, R. M. Servuss, W. Helfrich. Passages in lecithin–water systems. *Z Naturforsch* 33a:1013–1017, 1978.
43. L. Paz, J. M. Di Meglio, M. Dvolaitzky, R. Ober, C. Taupin. Highly curved defects in lyotropic (nonionic) lamellar phases. Origin and role in hydration processes. *J Phys Chem* 88:3415–3418, 1984.
44. M. Allain, P. Oswald, J. M. di Meglio. Structural defects and phase transition in a lyotropic system: optical birefringence and order parameter measurements. *Mol Cryst Liq Cryst* 162B:161–169, 1988.
45. X. Michalet, D. Bensimon, B. Fourcade. Fluctuating vesicles of nonspherical topology. *Phys Rev Lett* 72:168–171, 1994.
46. R. G. Larson. Monte Carlo simulations of microstructural transitions in surfactant systems. *J Chem Phys* 96:7904–7918, 1992.
47. G. Gompper, M. Kraus. Ginzburg–Landau theory of ternary amphiphilic systems. II. Monte Carlo simulations. *Phys Rev E* 47:4301–4312, 1993.
48. R. G. Larson. Monte Carlo simulations of the phase behavior of surfactant solutions. *J Phys II France* 6:1441–1463, 1996.
49. R. Hołyst, W. Gózdź. Fluctuating Euler characteristics, topological disorder line, and passages in lamellar phases. *J Chem Phys* 106:4773–4780, 1997.
50. R. Hołyst, P. Oswald. Confinement induced topological fluctuations in a system with internal surfaces. *Phys Rev Lett* 79:1499–1502, 1997.
51. T. Hofsäuss, H. Kleinert. Gaussian curvature in an Ising model of microemulsions. *J Chem Phys* 86:3565–3570, 1987.
52. D. A. Huse, S. Leibler. Phase behavior of an ensemble of nonintersecting random fluid films. *J Phys France* 49:605–621, 1988.
53. S. Ezrahi, E. Wachtel, A. Aserin, N. Garti. Structural polymorphism in a four component nonionic microemulsion. *J Coll Interface Sci* 191:277–290, 1997.
54. P. Sakya, J. M. Seddon, V. Vill. Thermotropic and lyotropic phase behavior of monoalkyl glycosides. *Liq Cryst* 23:409–424, 1997.
55. J. Gustafsson, G. Orädd, G. Lindblom, U. Olsson, M. Almgren. A defective swelling lamellar phase. *Langmuir* 13:852–860, 1997.
56. P. Sakya, J. M. Seddon, R. H. Templer, R. J. Mirkin, G. J. T. Tiddy. Micellar cubic phases and their structural relationships: the nonionic surfactant system C<sub>12</sub>EO<sub>12</sub>/water. *Langmuir* 13:3706–3714, 1997.
57. B. Donnio, D. N. Bruce, H. Delacroix, T. Gulik-Krzywicki. Freeze-fracture electron microscopy of thermotropic cubic and columnar mesophases. *Liq Cryst* 23:147–153, 1997.
58. L. Sallen, P. Sotta, P. Oswald. Pretransitional effects near the hexagonal–micellar phase transition of the C<sub>12</sub>EO<sub>6</sub>/H<sub>2</sub>O lyotropic mixture. *J Phys Chem* 101:4875–4881, 1997.

59. D. C. Morse. Topological instabilities and phase behavior of fluid membranes. *Phys Rev E* 50:R2419–R2422, 1994.
60. L. Golubović. Passages and droplets in lamellar fluid membrane phases. *Phys Rev E* 50:R2419–R2422, 1994.
61. G. Gompper, J. Goos. Fluctuations and phase behavior of passages in a stack of fluid membranes. *J Phys II France* 5:621–634, 1995.
62. T. Charitat, B. Fourcade. Lattice of passages connecting membranes. *J Phys II France* 7:15–35, 1997.
63. J. Charvolin, J. F. Joanny, J. Zinn-Justin, eds. Elasticity and thermal undulations of fluid films of amphiphiles In: *Les Houches, Session XLVIII, 1988, Liquids at Interfaces*. Amsterdam: Elsevier Science, 1990.
64. A. Ciach, J. S. Høye, G. Stell. Microscopic model for microemulsion. II. Behavior at low temperatures and critical point. *J Chem Phys* 90:1222–1228, 1989.
65. A. Ciach. Phase diagram and structure of the bicontinuous phase in a three dimensional lattice model for oil–water–surfactant mixtures. *J Chem Phys* 96:1399–1408, 1992.
66. F. S. Bates, W. Maurer, T. Lodge, M. F. Schulz, M. W. Matsen, K. Almdal, K. Mortensen. Isotropic Lifshitz behavior in block copolymer–homopolymer blends. *Phys Rev Lett* 75:4429–4432, 1995.
67. A. L. Mackay. Periodic minimal surfaces. *Nature* 314:604–606, 1985.
68. A. Ciach, A. Poniewierski. Description of the geometrical properties and topological structure in amphiphilic systems. *Phys Rev E* 52:596–601, 1995.
69. D. J. Amit. *Field Theory, the Renormalization Group and Critical Phenomena*. Singapore: World Scientific Publishing, 1984.
70. A. Ciach. Four-point correlation functions and average Gaussian curvature in microemulsions. *Phys Rev E* 56:1954–1964, 1997.



# 15

## Simulations of Systems with Colloidal Particles

**MATTHIAS SCHMIDT** Institut für Theoretische Physik II, Heinrich-Heine-Universität Düsseldorf, Düsseldorf, Germany

I. Introduction	746
II. Colloids and Their Simulation—A Short Tutorial	750
III. Selected Applications	754
A. Bulk liquid state	754
B. Liquid mixtures	755
C. Liquids near a wall	755
D. Confined liquids	757
E. Bulk freezing	757
F. Freezing: surfaces and confinement	760
G. Two-dimensional systems	761
H. Liquid crystals	762
I. Anisotropic fluids	764
J. Dynamics of colloids	765
K. Shear and rheology	766
L. Aggregation phenomena	767
M. Recent simulation methods	768
IV. Conclusions	769
References	769

## I. INTRODUCTION

Computer simulations are powerful tools for investigating statistical systems. Colloidal suspensions are soft matter systems exhibiting a broad range of fascinating physical phenomena. Computer simulations of colloidal suspensions have increased our understanding and physical insight into these systems enormously and play a vital role as bridges between theory and experiment. The present chapter is devoted to basic and advanced techniques used, and questions addressed by computer simulations. After an introduction to the physics of colloidal suspensions, a tutorial dealing with the most basic computer simulation technique is given. Readers who are familiar with simulations of systems with continuous degrees of freedom may skip this section. In the following section we present examples of simulations with colloidal particles from the recent literature, ranging from homogeneous and inhomogeneous liquids to crystals, the phenomena specific to two-dimensional systems, the physics of colloidal liquid crystals and anisotropic fluids, dynamical properties, shear, rheology, and aggregation phenomena. The chapter finishes with some concluding remarks.

Colloidal suspensions are systems of small mesoscopic solid particles suspended in an atomic liquid [1,2]. We will use the term “colloid” a little loosely, in the sense of colloidal *particle*. The particles may be irregularly or regularly shaped (Fig. 1). Among the regular shapes are tiny spherical balls, but also cylindrical rods or flat platelets. As the particles are solid, fluctuations of their form do not occur as they do in micellar systems. Not all particles in a suspension will, in general, have the same form. This is an intrinsic effect of the mesoscopic physics. Of course in an atomic system, say silicon, all atoms are precisely similar. One is often interested in the con-

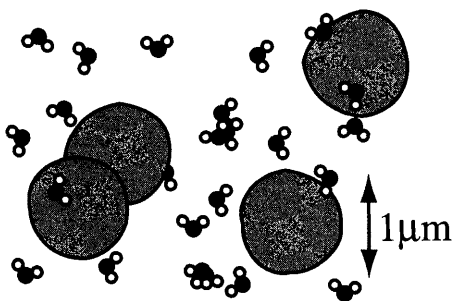


**FIG. 1** Sketch of a colloidal suspension. Mesoscopic particles float in an atomic liquid. Water molecules are drawn schematically. Note the difference in length scales between solvent and solute.

sequences of the disorder introduced by the dissimilarity of the particles. The effect is called polydispersity (Fig. 2). It is quite a surprise that the amount of polydispersity can be made very small in real suspensions of, say, PMMA particles. The spatial extent of the colloids already leads to a highly non-trivial interaction between them, as each particle induces a region of space that cannot be occupied by any other particle. The effect is called excluded-volume or hard-body interaction. It can lead to complex collective phenomena such as freezing! We will discuss that later in detail.

Besides the short-ranged hard-body interaction there are a variety of soft interactions arising from the charges present in the system. These charges lead to an electric polarizability of the material the colloids are made from. Then two particles interact via the van der Waals attraction that stems from fluctuating dipole moments within the particles. The strength of this attraction is determined by the difference of refractive indices of the colloidal material and the surrounding liquid. By index-matching it can be made negligible. One further interaction is electrostatic in nature: the surface of the particles can be prepared to carry an electrical charge. When the colloids are suspended in a polar solvent like water, the surface charges dissolve and become free counterions in the solution (Fig. 3). The resulting repulsion between equally charged particles has a screened Coulomb form.

As a last example we describe the interaction between particles that is caused by other particles. Consider a mixture of small and large particles. The large particles interact with each other through interactions with the small particles. Averaging over many small particles leads to an entropic attractive force between the large species, called the depletion potential. Without having stated orientation-dependent forces, interactions between magnetic dipoles, or many-particle forces, the above brief summary shows that there is a great diversity in the forces present in colloidal systems.

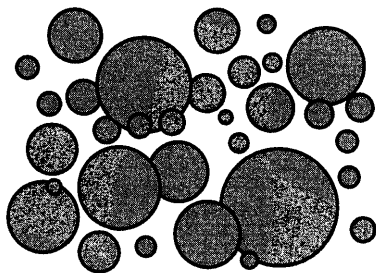


**FIG. 2** A polydisperse suspension consists of particles of different sizes.

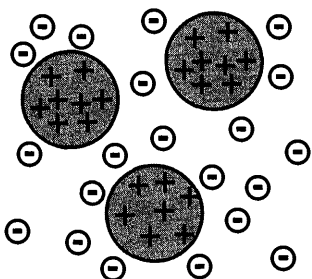


**FIG. 3** Charged colloidal particles and counterions in the solution.

Colloidal suspensions are a wide class of soft matter ranging from biological liquids such as blood and milk to technologically relevant materials such as paint and lubricating material and to chemically tailored suspensions. All these systems possess a structure on a mesoscopic length scale of about  $1\text{ }\mu\text{m}$ . Although the colloidal particles have an internal atomic structure, we regard them as basic building blocks. What makes these systems interesting is the fact that the particles interact with each other in a great variety of ways. These interactions can be very well controlled. This is an advantage from a technological point of view, but it also carries a fundamental aspect: the dependence of collective phenomena on the interactions can be studied. The interactions between colloidal particles are effective interactions in the sense that they arise from atomic interactions of the electrons and ions that build up the particles. Averaging over the many microscopic degrees of freedom leads to interactions between the centers of mass of the particles.

Computer simulations play an important role in modern condensed matter physics. Powerful computers enable us to investigate systems that exhibit interesting and challenging physical phenomena and hence enrich our understanding of nature. In many cases the results of computers simulations are new and surprising, and to understand them can be a challenge. However, the input to a simulation is very precise and clear from a practical as well as from a conceptual point of view. From a conceptual point of view a physical system is specified through a theoretical model. The model consists of a specification of the entities considered, the interactions that are present between them and their relation to the surroundings. Here we adopt the view of soft matter physics, which acts as a bridge between the atomic and the macroscopic world. Individual particles are resolved not on a microscopic but on a mesoscopic scale. This model, often supplemented by a description of its dynamics, is the basic starting point of our consideration.

It may aim at several goals ranging from a conceptual interest to very precise descriptions of experimental systems containing large sets of input parameters and variables. In any case, once we invent a model and decide to study it, we can go ahead using statistical mechanics that tells us how to proceed. The implementation of a model on a computer is often straightforward. Theoretical physics is expressed in mathematical structures and computers are built on similar grounds. So we store the position of a particle as a set of floating point numbers and, once we have many particles, any computer language provides some sort of array to hold a number of similar objects. As long as our starting model is sufficiently simple it makes no big difference how we implement it. However, as the complexity of our models increases, we may be forced to go beyond this naive approach and adopt modern concepts of software design.

But a computer simulation is more than a few clever data structures. We need algorithms to manipulate our system. In some way, we have to invent ways to let the big computer in our hands do things with the model that is useful for our needs. There are a number of ways for such a time evolution of the system: the most prominent is the Monte Carlo procedure that follows an appropriate random path through configuration space in order to investigate equilibrium properties. Then there is molecular dynamics, which follows classical mechanical trajectories. There is a variety of dissipative dynamical methods, such as Brownian dynamics. All these techniques operate on the fundamental degrees of freedom of what we define to be our model. This is the common feature of computer simulations as opposed to other numerical approaches.

So far, we have not considered the question of why we should run a simulation. What is its outcome? What is the purpose of this outcome? The answer to the first question is as diverse as statistical physics is: in principle, any quantity that has an experimental meaning, has a theoretical definition, and makes sense for the simulated model, can be the result. Possible quantities to be simulated are equations of state, free energies, phase diagrams, correlation functions, density profiles, diffusion coefficients, relaxation times, effective interactions, order parameter profiles. Should you have never been interested in at least one of these quantities, you probably should stop reading. In the other case you will also know the answer to the second question above. What is the purpose of the result? Once you know a physical quantity, you learn something about the system. Furthermore, you may want to compare it with your own or your colleagues' experimental data. You also may want to compare it with the outcome of a theory that you or somebody else has invented. This might be enough justification and motivation to dig into the concepts of simulation, develop some computer code and let it run on the nearest machine. In this chapter we will provide

you with the basics to simulate one class of soft matter systems, namely colloidal particles.

## II. COLLOIDS AND THEIR SIMULATION—A SHORT TUTORIAL

We will now go into some detail and explain the physics of colloidal suspensions in parallel with the most basic simulation techniques. Before we start we would like to draw your attention to the literature, namely the books by Frenkel and Smit [3], Allen and Tildesley [4], Rapaport [5], and, for the theoretical background, Hansen and McDonald [6]. A review of simulations of colloids is given by Dickinson and Euston [7].

Suppose we have a physical system with small rigid particles immersed in an atomic solvent. We assume that the densities of the solvent and the colloid material are roughly equal. Then the particles will not settle to the bottom of their container due to gravity. As theorists, we have to model the interactions present in the system. The obvious interaction is the excluded-volume effect caused by the finite volume of the particles. Experimental realizations are suspensions of sterically stabilized PMMA particles, (Fig. 4). Formally, the interaction potential can be written as

$$V(r) = \begin{cases} 0 & \text{if } r \geq \sigma, \\ \infty & \text{if } r < \sigma \end{cases}$$

This means that particle configurations where at least two particles overlap, i.e., have a distance  $r$  smaller than the diameter  $\sigma$ , are forbidden. They are forbidden because the Boltzmann factor contains a term,  $\exp(-\infty) \rightarrow 0$ , that leads to a vanishing statistical weight. Hence we have an ensemble of

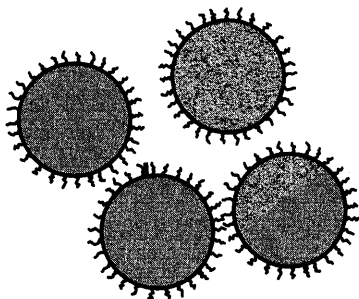


**FIG. 4** Sterically stabilized colloidal particles are coated with short polymer brushes. A hard sphere-like interaction arises.

non-overlapping configurations of particle coordinates. It is governed by only one parameter, a dimensionless density called the packing fraction

$$\eta = \frac{\pi}{6} \frac{N}{V} \sigma^3$$

How do we simulate a system like that on a computer? First of all, we need to be able to store a given microstate of the system. The physical quantities that make up a microstate depend on the situation one wants to investigate. In any case, it is fair to say that one microstate should contain the coordinates of all  $N$  particles. We also need to store the properties of the container the particles are in. To make things easy we assume a cubic box with side length  $L$ . Suppose we are interested in equilibrium properties of the system. Therefore we need to sample the configuration space. This configuration space consists of the spatial part of the classical phase space and has the dimension  $d \cdot N$ , where  $d = 3$  is the dimension of the physical space. The high dimensionality makes direct numerical integration impossible. Nevertheless, one can exploit the fact that typical subsets are very similar to each other. One strategy is to choose a subset sampled *at random*; this is called the Monte Carlo method [8]. Let us see how it works. We start by putting our  $N$  particles randomly inside the simulation box. This is an easy matter at low densities, where we have few particles in a large box. Should an overlap between two particles occur, we simply repeat the procedure until no overlap occurs. In this way we could obtain a set of allowed configurations, each of them carrying equal statistical weight. However, if we increase the density by increasing the number of particles or shrinking the box size, almost all configurations will include overlaps and this simple sampling procedure either becomes inefficient or does not work at all, e.g., in a crystal. How do we simulate the system at intermediate or high density? We exploit the fact that a typical allowed configuration has many other allowed configurations in its neighborhood in phase space. So we proceed in small steps from configuration to configuration.

The hard sphere (HS) interaction is an excellent approximation for sterically stabilized colloids. However, there are other interactions present in colloidal systems that may replace or extend the pure HS interaction. As an example let us consider *soft spheres* given by an inverse power law  $V(r) = V_0(r/\sigma)^{-n}$ . The energy scale  $V_0$  and the length scale  $\sigma$  can be combined to give a parameter  $V_0\sigma^n$  that governs the thermodynamics of the model. The exponent  $n$  governs the softness and range of the interaction, interpolating between the Coulomb case,  $n = 1$ , and the hard sphere case,  $n \rightarrow \infty$ . Let us neglect the long-ranged cases,  $n \leq 3$ , for a moment and suppose that we want to simulate an inverse-power fluid near the hard-sphere limit, say  $n = 12$ . Although the interaction is similar to that of

hard spheres, the configuration space is no longer divided into forbidden and allowed regions. Instead, each configuration carries a statistical weight given by its Boltzmann factor  $Z^{-1} \exp(-V_{\text{pot}}/(k_B T))$ , where the potential energy is given by a sum over all pairs of particles  $V_{\text{pot}} = \sum_{i,j} V(|\mathbf{r}_i - \mathbf{r}_j|)$ . So, in the case of this soft power-law potential, we have configurations that are more or less likely to occur. How can we sample this configuration space with a computer algorithm? Again, as in the case of the ideal gas, we could place the particles randomly inside the simulation box. What will be the typical energy of one of these configurations? The generated configurations will have a very high internal energy, so they will be representative of *high temperature*. How can we simulate the low-temperature behavior of the system? Again, we make use of the Metropolis algorithm, in this case for a soft potential, that works as follows. We start with a randomly generated configuration. Then we select one particle at random and displace its position by a small amount. Let the old position be  $\mathbf{r}_i$  and the new one  $\mathbf{r}'_i = \mathbf{r}_i + \Delta\mathbf{r}$ . The displacement causes changes of the distances between particle  $i$  and all other particles. As the potential energy depends on these distances, a change in the total potential energy also occurs. Let this new energy be  $V'_{\text{pot}}$ . For our algorithm we need to know the *change* in the potential energy  $\Delta E = V_{\text{pot}} - V'_{\text{pot}}$ . Note that the calculation of this quantity does not involve a sum over all pairs of particles, but only involves  $2(N-1)$  contributions and is given by  $\Delta E = \sum_j V(|\mathbf{r}'_i - \mathbf{r}_j|) - V(|\mathbf{r}_i - \mathbf{r}_j|)$ . Next comes the decision criterion whether the new configuration is accepted or discarded. Remember that the new configuration was generated “blindly,” in the sense that the displacement was isotropic without any preferred direction. Hence we need a decision criterion, whether the new configuration is likely for our given temperature. As it is harder to get a new configuration with lower energy, we accept this new configuration with probability one if  $\Delta E < 0$ . If the new configuration has a larger potential energy,  $\Delta E > 0$ , then we accept it with probability  $\exp(-\beta\Delta E)$ . We can put both cases together by stating that the acceptance probability of the randomly chosen new state is given by  $\min\{1, \exp(-\beta\Delta E)\}$ . Now we have finished. All we have to do is to let the computer repeat the above steps with the new configuration: Select one particle at random, displace it, calculate the energy difference, accept or discard it, and so on. We come up with a random walk through configuration space. As typical configurations are visited we can investigate physical quantities that may seem interesting. The above description of the Monte Carlo procedure is from a practical point of view. Of course, it has a solid theoretical footing in the theory of Markov chains, the Master equation and the condition of detailed balance.



Let us comment on the developed schematic Monte Carlo (MC) code. Of course there are many clever ways to improve the execution speed. There is the important concept of neighbor lists, of clever implementation of numerical instructions, and so on. In developing a computer simulation one usually plugs in these enhancing concepts bit by bit.

So far we have implicitly assumed that the particle positions remain homogeneously distributed in space. We had to look for a pair distribution function to see the structure that builds up in the system. As stated earlier, this is the characteristic feature of liquids. From everyday life one knows that liquids freeze into solids upon cooling (or compression). Freezing is a very general phenomenon and is also observable in colloidal suspensions. The macro-particles themselves may arrange to form the constituents of the solid structure, usually some sort of crystalline lattice. To avoid confusion, we stress that the atomic solvent, in which the colloids are suspended, remains liquid. Whether a system is in a fluid or crystalline state is determined by the thermodynamic state point, given by the thermodynamic variables. Hence it is an equilibrium property. So we should be able to observe freezing with the *same* computer code that we built up above (at least in our minds). Let us return to the hard sphere model, where the only thermodynamic variable is the packing fraction  $\eta$ . This system undergoes a freezing transition to a crystalline lattice with a close-packed structure. In Fig. 5 a crystal is shown that is stable for softer potentials.

We have reviewed the basics of computer simulations with colloidal particles and with the physics of colloids. We could only touch on the most basic concepts, that do not lead to highly optimized, rapid code but, nevertheless, lead to working programs.

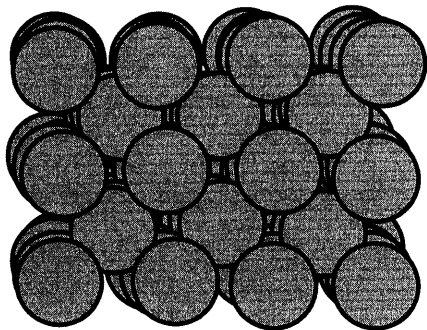


**FIG. 5** A crystalline structure. The particles are located near preferred lattice sites. A body-centered cubic (bcc) structure is shown.

### III. SELECTED APPLICATIONS

Colloidal suspensions are interesting physical systems as they show a large variety of physical phenomena. We will review a selection of applications where simulations have increased our understanding of physical effects. As we will deal with state-of-the-art work, there are a lot of advanced simulation techniques, specifically tailored models, and clever implementations involved. Hence we cannot give the details but merely the general strategies of the reviewed work. The reader should use this section as an overview of the diversity of simulations with colloids. Dealing with one of these problems will require consultation of the original works. As the field is large and rapidly growing we are not able to give a complete account of the literature. The phase transitions encountered are mainly of first order. There are also continuous phase transitions in colloidal systems. However, we do not attempt to review this large field (see, e.g., the review by Wilding [9]). Furthermore, the important and fascinating area of glass transitions in colloidal suspensions is missing. There is a lot more missing and we apologize for the omitted works.

#### A. Bulk Liquid State

The bulk liquid state is a challenge for physicists. It has the trivial translational symmetry of the ideal gas, but the particles are strongly interacting as neighbors are roughly as close to each other as they are in a crystal. For those complex fluids where one has a reliable pair potential between the macro-particles it is usually a standard exercise to simulate the liquid structure. (Remember that we dealt with this problem in our tutorial.) However, this simplified picture is not always justified. Once one has to take into account the solvent degrees of freedom, the simulation becomes a challenge: one is faced with the different length scales of micro- and macro-particles and rapidly encounters the limitations of today's computers. Nevertheless, the pressure of charged spherical macro-ions was investigated by Stevens et al. [10]. A system with an extreme asymmetric charge distribution was considered by Löwen and D'Amico [11]. Simulations of highly asymmetric electrolytes with charge asymmetry up to 20:1 were done by Lobaskin and Linse [12], who found that an effective *repulsive* potential was operating between the macro-ions. Concerning the primitive model, a mechanism for counterion-mediated attraction between the like-charged spherical macro-ions was proposed [13]; this originates from a depletion zone of counterions between nearly touching macro-ions. Also, the effective triplet interactions in charged colloidal suspensions represents a significant attractive correction to the pairwise contributions [14].

Another example is the emergence of a hitherto unknown interaction potential. Due to Likos et al. [15], a solution of star polymers can be viewed as ultra-soft particles interacting with a logarithmic potential at small distances and exponentially decaying at large distances. The form of the interaction potential was validated by Jusufi et al. [16] by taking into account the microscopic structure of the polymeric arms. For this system an anomalous fluid structure factor arises [17], and Watzlawek et al. show that it possesses an interesting phase diagram [18]. For well-known systems one wants to go beyond the knowledge of the famous pair distribution  $g(r)$ . Higher-order correlation functions contain more information. For hard spheres three-body distribution functions have been simulated [19]. A phase transition between two fluid states is the boiling of a liquid or condensation of a gas. This liquid–gas transition also occurs in colloidal suspensions and was investigated recently for the square-well fluid [20].

## B. Liquid Mixtures

Colloidal suspensions are, per definition, mixtures of mesoscopic particles and atomic liquids. What happens if there are several different species of particles mixed in the solvent? One can invent several different sorts of mixtures: small and large particles, differently charged ones, short and long rods, spheres and rods, and many more. Let us look into the literature. One important question when dealing with systems with several components is whether the species can be mixed or whether there exists a miscibility gap where the components macroscopically phase-separate.

Demixing was found in a mixture of small and large hard cubes [21]. As this is a hard-body system the demixing is purely entropy-driven. The binary mixture of small and large hard spheres has attracted a lot of interest; for a sketch (see Fig. 6). The system has three parameters governing its phase behavior, namely the two packing fractions of both species and the ratio of the sphere diameters. Besides the phase diagram that contains a variety of crystal phases, the questions whether there is a demixed region in the phase diagram was only recently solved by Dijkstra et al. [22], who showed that demixing is preempted by freezing (see also [23] and references therein). The depletion potential between two large spheres caused by the pressure of the small ones was studied [24]. A symmetrical square-well mixture [25] was simulated in the so-called semigrand canonical ensemble.

## C. Liquids Near a Wall

The generic inhomogeneity in liquid state theory is the planar wall (Fig. 7). It is relatively simple. First, the position of the wall does not matter, as long

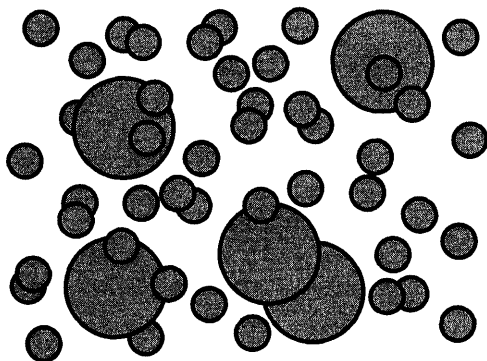


**FIG. 6** A bidisperse system consisting of large and small particles.

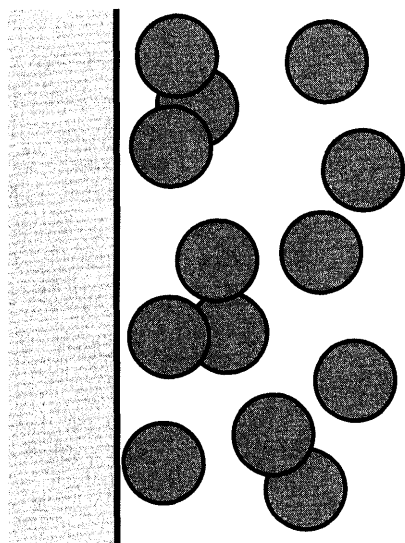


**FIG. 7** A fluid near a single wall.

as all distances are measured relatively to the position of the wall. Second, all one has to specify is the external potential energy  $V_{\text{ext}}(z)$  describing the wall. Last, the limit of large separation from the wall is known: one recovers the bulk case as the surface effect induced by the wall vanishes. One consequence is that the density profile only depends on the coordinate perpendicular to the wall. But the pair correlation function already depends on three coordinates (translational symmetry parallel to the wall and rotational

symmetry around any axis perpendicular to the wall). We note that the simplicity of the inhomogeneity leads neither to simple physical effects nor to simple simulations!

Using grand canonical Monte Carlo the density profile of a Yukawa fluid was simulated and compared with results from integral equation theory [26]. The Derjaguin–Landau–Verwey–Overbeek (DLVO) system was studied in front of a highly repulsive wall [27]. A charged fluid separated by a charged wall of finite thickness was simulated [28]. A related problem is the structure of the hard sphere fluid in wedges [29] (see also Chapter 1, “Structure and phase behavior of confined soft condensed matter”, by M. Schoen).

## D. Confined Liquids

Any real sample of a colloidal suspension has boundaries. These may stem from the walls of the container holding the suspension or from a free interface towards the surroundings. One is faced with *surface* effects that are small compared to *volume* effects. But there are also situations where surface effects are comparable to bulk effects because of strong confinement of the suspension. Examples are cylindrical pores (Fig. 8), porous media filled with suspension (Fig. 9), and thin colloidal films squeezed between parallel plates (Fig. 10). Confined systems show physical effects absent in the bulk behavior of the system and absent in the limit of extreme confinement, e.g., a one-dimensional system is built up by shrinking the size of a cylindrical pore to the particle diameter.

The concentration profiles of colloidal particles [30] and of mixtures [31] in a charged cylindrical pore were considered. A fluid confined in a disordered porous material was simulated [32]. Symmetry-breaking density profiles were found [33]. The static and dynamical properties of hard spherical particles in 2d [34] and in 3d [35] confined to a spherical cavity (see Fig. 11) were investigated by molecular dynamics (MD) simulation. As this situation is also a challenge for theory, simulations were done to compare with density-functional theory [36,37]. For small systems the choice of ensemble matters, whether canonical or grand canonical. The effect of confinement on charge-stabilized colloidal suspensions between two charged plates was investigated [38]. The effective interaction and density profiles of charged colloids between parallel plates [39] was simulated using a model with a space-dependent Yukawa potential.

## E. Bulk Freezing

Freezing is a very general phenomenon. Upon increasing the interaction strength or increasing the density, colloidal suspensions undergo phase

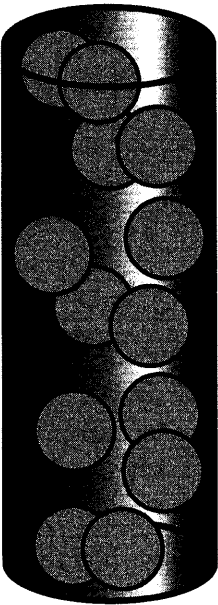


**FIG. 8** A colloidal fluid confined within a cylindrical pore.

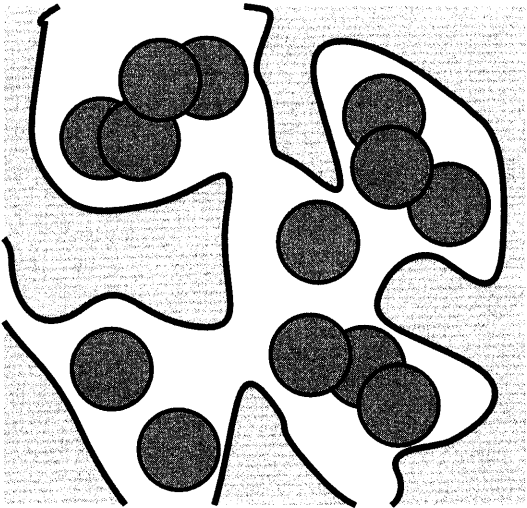


**FIG. 9** A fluid within a random porous medium.

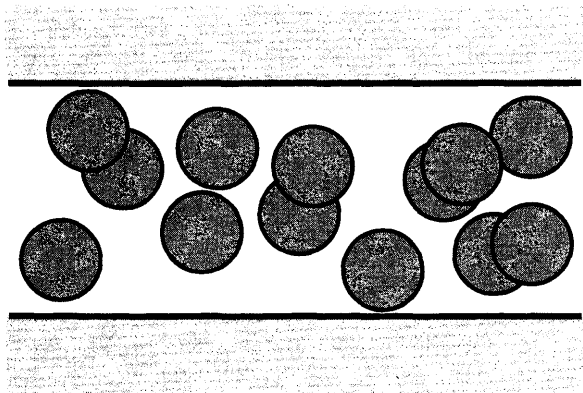


**FIG. 10** A colloidal suspension between two parallel plates. There is strong confinement perpendicular to the plates, but an infinite system in the lateral orientations.

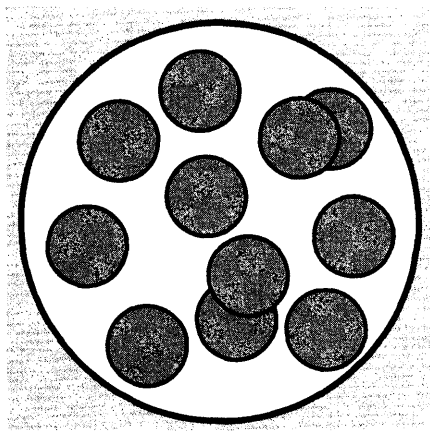


**FIG. 11** Particles inside a spherical cavity. This is the generic case for a strongly confining situation.

transitions to crystals. (This can be suppressed by intrinsic disorder present in the system: size and charge polydispersity.) In fact fluids are expected to freeze, so that it is a big surprise if, in a particular system, freezing does not occur! Facing the variety of interactions and the zoo of crystal lattices, it may become clear that calculating phase diagrams involving solid phases is a delicate task. We review some recent work.

The Yukawa system near its one-component-plasma limit was revisited [40], showing a fluid–solid phase boundary and bcc–fcc phase transition, the latter being well described by quasiharmonic theory. Fluid–solid equilibrium was also investigated for charged hard spheres [41]; this system shows a substitutionally disordered close-packed fcc crystal at high temperature and the cesium chloride structure at low temperature. In the case of inverse-power potentials,  $V(r) \propto r^{-n}$ , it has been shown [42] that for  $1/n < 0.16$ , fcc is the stable crystal, and that bcc is stable for softer potentials. For the freezing of polydisperse hard spheres a “terminal” polydispersity [43] above which there is no fluid–solid coexistence has been found. For monodisperse hard spheres, the disordered, metastable branch of the phase diagram from the freezing point to random close packing was simulated [44–46], and scaling of the pressure near random close packing was found. Besides the possibility of phase transitions between different solid structures, there are also transitions between the same crystal lattice with different lattice constants. These *isostructural* transitions have been found in systems with short-ranged attraction [47] and repulsion [48]. The structure of the hard sphere solid is fcc and not hcp [49]. We will review the lattice-switch method employed by Bruce et al. [49] in Sec. III M. Freezing was also observed in a system of penetrable spheres [50] where the particles interact with a constant repulsive energy once they overlap. Hence the interaction potential is a step function.

## F. Freezing: Surfaces and Confinement

For systems where the bulk freezing transition is well understood, one may want to go one step further and investigate the modifications of the phase transition and the solid phases in the event of external influence on the system. How does freezing happen in a confined situation where external boundaries are present? What is freezing in porous media like? A related question is: What does the interface between solid and liquid look like? This is an intrinsic inhomogeneity that the system builds up by itself (if, as usual, the transition is first order). Let us describe some papers dealing with freezing under external influence.

An intrinsic surface is built up between both phases in coexistence at a first-order phase transition. For the hard sphere crystal–melt interface [51] density, pressure and stress profiles were calculated, showing that the transition from crystal to fluid occurs over a narrow range of only two to three crystal layers. Crystal growth rate constants of a Lennard–Jones (100) surface [52] were calculated from the fluctuations of interfaces. There is evidence for bcc ordering at the surface of a critical fcc nucleus [53].



Concerning external surfaces, crystallization in a gravitational field was investigated [54], finding that a few crystalline layers are spontaneously formed at the bottom of the sample. This crystalline part then grows continuously as the gravitational field is enhanced. The phase diagram of hard spheres between parallel plates was calculated [55–58] and shown to exhibit buckled, rhombic, and layered phases. The effect of an external laser field that induces a spatially modulated external potential was studied, finding reentrant melting [59]. The influence of short-range attractive and repulsive interactions on the phase behavior of model colloidal suspensions was considered in Ref. 60.

## G. Two-dimensional Systems

The dimensionality of a system is one of its major features. Despite the fact that our surrounding space is three-dimensional, one can prepare situations that lead to an effective lowered dimension. A typical example regarding colloids is the surface between the solvent and air. One can prepare the particles to be trapped at that interface, so that they float on top of the solvent, building up a two-dimensional (2d) system. Another realization is strong confinement between parallel plates that leads to an effective 2d system. Concerning simulations, it is very convenient to simulate 2d systems, as one has fewer degrees of freedom to deal with; e.g., plotting snapshots is easier in 2d than it is in 3d. So, besides their experimental realizations, 2d systems are also important from a conceptual point of view.

One prominent feature of two-dimensional systems that has attracted a lot of interest is a different melting scenario due to Kosterlitz, Halperin, Nelson, and Young (KTHNY; see, e.g., Ref. 61 for a review): the 2d solid melts via a continuous phase transition into a so-called hexatic phase that possesses long-ranged orientational order but only short-ranged positional order. A further continuous transition from the hexatic phase leads to the true isotropic phase where the bond-orientational order also is short-ranged. The question is whether a given system follows this KTHNY scenario or the more conventional first-order melting. As large scales are involved, one needs large systems to get reliable results.

For the  $r^{-12}$  repulsive potential [62] and for Lennard–Jones particles [63] a hexatic phase was found to be stable. Up to 102 400 particles were simulated [64] and a metastable phase was found. For a 2d Coulomb gas of opposite charges interacting with a logarithmic potential, the phase diagram was simulated [65]. The dispersity-driven melting transition was considered [66] and a phase diagram in the dispersity–density parameter space calculated. The melting scenario of the hard disk fluid is very controversial. For a recent study see Ref. 67, where a local structure analysis near melting is

done. Jaster [68] analyzes the bond orientational order parameter and correlation length of a system with 65 536 disks and finds consistency with the KTHNY scenario. Dislocation-unbinding exists in dense 2d crystals, where the phase diagram exhibits a solid–solid critical point [69]. From that the stability of a hexatic phase can be concluded. The phase separation of 2d fluid mixtures [70] shows that diffusive coalescence of clusters is the primary mechanism of growth.

## H. Liquid Crystals

Liquid crystals are formed by colloidal particles with non-spherical shapes. They are intermediate between the pure fluid and the pure solid state. As the particles carry both positional and orientational degrees of freedom, freezing of these degrees of freedom can occur in a *sequential* manner. Starting from the least ordered, isotropic fluid (Fig. 12), there is the freezing of the orientational order leading to a nematic phase (Fig. 13), where the particles are aligned along a preferred direction called the nematic director. There is a large variety of additional liquid crystalline phases: smectic, columnar, plastic, crystal, and more, that we cannot go into here. Nevertheless, we compile some recent work.

### 1. Hard Bodies

Let us enter the world of liquid crystals built by the purely entropic forces present in hard body systems. The phase diagram of hard spherocylinders (HSC) shows a rich variety of liquid crystalline phases [71,72]. It includes the isotropic, nematic, smectic A, plastic, and solid phases [73]. In a plastic crystal the particle centers lie on lattice sites, but the orientations of the

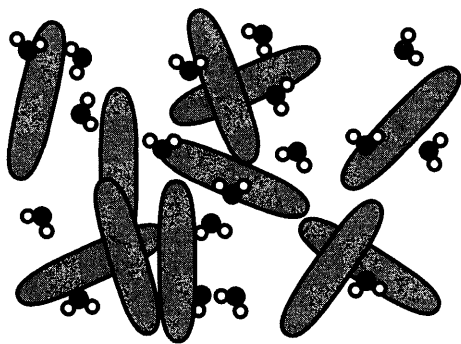


**FIG. 12** A colloidal suspension of rodlike particles. The orientations of the rods are uniformly distributed.

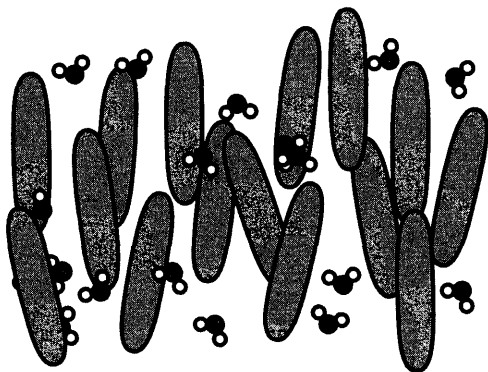


**FIG. 13** A colloidal liquid crystal. The rod-like particles point to a preferred direction, called the nematic director. The solvent is disordered.

particles are random. Ordering of the orientations leads to a true crystal phase [74]. In the limit of infinite aspect ratio the HSC model has an analytical solution, due to Onsager, for the first-order isotropic–nematic transition. Resulting from the simulations by Polson and Frenkel [75], the nematic–smectic transition is also of first order in this so-called Onsager limit. For ellipsoidal particles the isotropic–nematic transitions of the uniaxial case [76] and the phase diagram for the biaxial case [77] were resolved by simulations.

Besides rods, there is another important case of non-spherical particles, namely disks. For reasons of simplicity one may consider infinitely thin disk. Although these particles have no physical volume, they do interact, as one disk induces an excluded volume to its surrounding. For this system a first-order nematic–columnar transition was found [78]. A further challenge is mixtures of different species of non-spherical particles. Extensive immiscibility was found in mixtures of thin and thick rods [79–81]. Dijkstra and van Roij [82] have investigated how the demixing behaves in the range from spherocylinders to spheres. Demixing has also been found in rod–plate mixtures [83]. Dimerizing HSC have been considered in Ref. 84 (see the beautiful snapshots of configurations). In reality colloidal particles are not completely rigid, but may change their shapes slightly. The nematic transition of bendable ellipsoids was investigated [85]. Simulation and theory for hard dumbbells near a hard wall were compared [86]. The microscopic structure of topological defects in nematic droplets is currently being investigated [87] by MC simulation. Influence of polydispersity on the phase behavior of colloidal liquid crystals in the Onsager limit was considered [88].

## 2. Soft Interactions

One prominent example of rods with a soft interaction is Gay-Berne particles. Recently, elastic properties were calculated [89,90]. Using the classical Car-Parrinello scheme, the interactions between charged rods have been considered [91]. Concerning phase transitions, the solid-fluid equilibria for hard dumbbells that interact additionally with a quadrupolar force was considered [92], as was the nematic-isotropic transition in a fluid of dipolar hard spherocylinders [93]. The influence of an additional attraction on the phase behavior of hard spherocylinders was considered by Bolhuis et al. [94]. The gelation transition typical for clays was found in a system of infinitely thin disks carrying point quadrupoles [95,96]. In confined liquid-crystalline films tilted molecular layers form near each wall [97]. Chakrabarti has found simulation evidence of critical behavior of the isotropic-nematic phase transition in a porous medium [98].

## I. Anisotropic Fluids

These are colloidal particles with an orientation-dependent interaction despite their spherical shape. This happens through dipole moments carried by the particles. One distinguishes between electric and magnetic dipoles. As the suspensions exhibit unusual flow behavior they are called electrorheological (ER) and magnetorheological (MR) fluids or ferrofluids, respectively. These substances are very sensitive to external fields that align the dipoles, as the interaction between aligned dipoles differs markedly from free ones. One can trigger the rheological behavior through external fields. There are orientation-dependent forces, external fields in a non-equilibrium flow situation. Hence simulations are a challenge.

The structure formation in an ER fluid was simulated [99]. The characteristic parameter is the ratio of the Brownian force to the dipolar force. Over a wide range of this ratio there is rapid chain formation followed by aggregation of chains into thick columns with a body-centered tetragonal structure observed. Above a threshold of the intensity of an external aligning field, condensation of the particles happens [100]. This effect has also been studied for MR fluids [101]. The rheological behavior of ER fluids [102] depends on the structure formed: chainlike, shear-string, or liquid. Coexistence in dipolar fluids in a field [103], for a Stockmayer fluid in an applied field [104], and the structure of soft-sphere dipolar fluids were investigated [105], and ferroelectric phases were found [106]. An island of vapor-liquid coexistence was found for dipolar hard spherocylinders [107]. It exists between a phase where the particles form chains of dipoles in a nose-to-tail

configuration and a phase for longer rods where antiparallel side-by-side ordering is observed.

## J. Dynamics of Colloids

Colloidal particles experience kicks from the surrounding atoms or molecules of the solvent. This leads to Brownian dynamics in colloidal suspensions (Fig. 14). The study of dynamics is challenging as, of course, first the equilibrium of the system has to be understood. One often knows the short-time dynamics that govern the system and is interested in long-time properties.

Short-time Brownian motion was simulated and compared with experiments [108]. The structural evolution and dynamics [109] and the translational and bond-orientational order [110] were simulated with Brownian dynamics (BD) for dense binary colloidal mixtures. The short-time dynamics was investigated through the velocity autocorrelation function [111] and an algebraic decay of velocity fluctuation in a confined liquid was found [112]. Dissipative particle dynamics [113] is an attempt to bridge the gap between atomistic and mesoscopic simulation. Colloidal adsorption was simulated with BD [114]. The hydrodynamic forces, usually friction forces, are found to be able to *enhance* the self-diffusion of colloidal particles [115]. A novel MC approach to the dynamics of fluids was proposed in Ref. 116. Spinodal decomposition [117] in binary fluids was simulated. BD simulations for hard spherocylinders in the isotropic [118] and in the nematic phase [119] were done. A two-site Yukawa system [120] was studied with

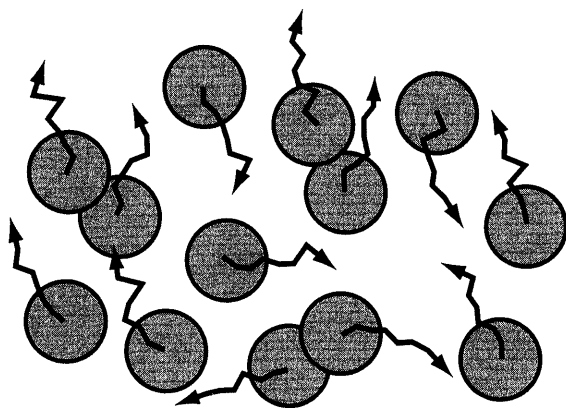


**FIG. 14** Brownian dynamics. The arrows indicate that the particle trajectories show diffusive behavior.

BD. Dynamical correlations in suspensions of charged rod-like particles were simulated [121].

## K. Shear and Rheology

Liquids are able to flow. Complicated stream patterns arise, dependent on geometric shape of the surrounding of the liquid and of the initial conditions. Physicists tend to simplify things by considering well-defined situations. What could be the simplest configurations where flow occurs? Suppose we had two parallel plates and a liquid drop squeezed in between. Let us keep the lower plate at rest and move the upper plate at constant velocity in a parallel direction, so that the plate separation distance keeps constant. Near each of the plates, the velocities of the liquid and the plate are equal due to the friction between plate and liquid. Hence a velocity field that describes the stream builds up, (Fig. 15). In the simplest case the velocity is linear in the spatial coordinate perpendicular to the plates. It is a *shear* flow, as different planes of liquid slide over each other. This is true for a simple as well as for a complex fluid. But what will happen to the mesoscopic structure of a complex fluid? How is it affected? Is it destroyed or can it even be built up? For a review of theories and experiments, see Ref. 122. Let us look into some recent works.

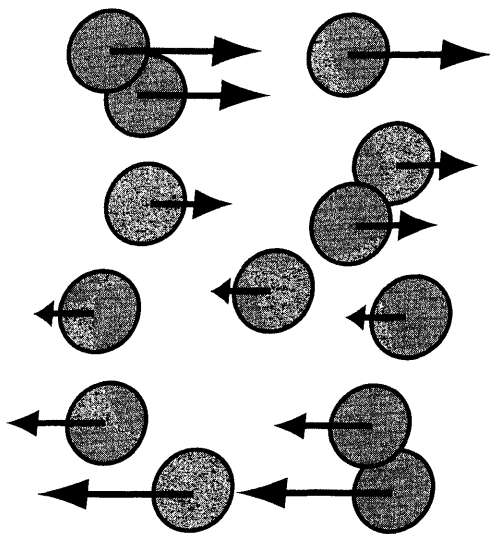


**FIG. 15** A colloidal suspension subject to shear flow. The arrows indicate the mean particle velocities.

In simulations of shear-induced melting and ordering [123] it was found that fcc and bcc phases shear by layer-over-layer shearing. There is also a first-order shear-melting transition [123]. Using MD, one has investigated oscillatory shear [124,125], finding shear-induced melting at low frequency and shear-induced freezing at high frequency of shearing. The DLVO potential and the action of Brownian motion have a Newtonian regime (like an ordinary liquid) at low volume fraction [126]. At high volume fractions a slip layer is observed [126]. Disordering [127] and ordering transitions [128] have been reported. Shear-induced ordering of hard spheres was investigated [129]. By massively parallel non-equilibrium BD, charged colloids were investigated [130]. Using dissipative particle dynamics the rheology of spheres, rods, and disks was simulated [131], as well as the shear viscosity of hard ellipsoids [132].

## **L. Aggregation Phenomena**

So far we have dealt with stable colloidal suspensions where the particles are suspended freely in the surrounding liquid. However, one needs experimental expertise to stabilize a colloidal suspension against aggregation of the particles. Once particles stick together they no longer remain suspended but form aggregates that fall out of the suspension (Fig. 16). The attraction that drives this mechanism is the van der Waals force of fluctuating dipoles. (See the discussion of forces between colloids above.) Aggregation is a dynamical process that happens in non-equilibrium. Usually one starts with a suspended state and removes the stabilizing effect (e.g., adding salt to a charge-stabilized suspension). Then particles that come close to each other become trapped and, as this process goes on, larger and larger structures emerge. There is interest in the growth laws that govern the aggregation dynamically as well as in the statistics of the resulting aggregates.

Lach-hab et. al [133] have investigated the concentration dependence in colloidal aggregation and how the fractal dimension of the emerging aggregates depends on the concentration of the suspension. Once a suspension is fully flocculated one can break up the aggregates by shear flow [134]. For two-dimensional aggregation one has found a local six-fold symmetry at late times [135]. Using Brownian dynamics, gelation and aging were investigated for Lennard-Jones particles [136]. One finds aggregation of particles to clusters, and, on a larger length scale, cluster-cluster aggregation. Pair-drag simulation of aggregated systems was carried out [137]. A theoretical approach based on a modified Smoluchowski-Debye approach was compared with BD simulations for coagulation in charged colloidal suspensions finding reasonable agreement [138].

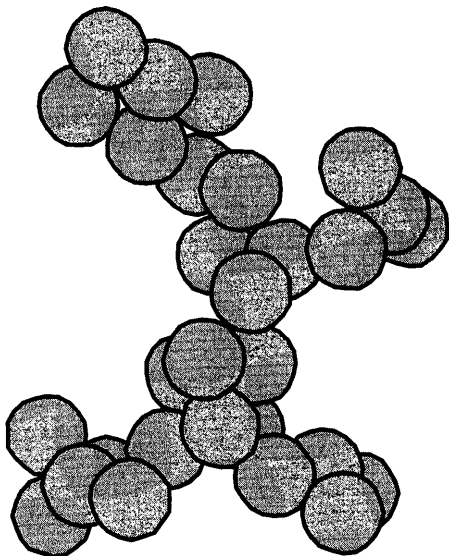


**FIG. 16** An aggregated colloidal structure. Neighboring particles touch each other and a complicated network builds up.

## M. Recent Simulation Methods

So far we have considered computer simulations as a tool to investigate the physics of colloids. In this section we mention work that, besides its physical content, is important because of this tool has been sharpened by the invention of new techniques.

Grand canonical simulations require mechanisms to insert particles into and remove particles from the system. Successful insertion strategies at high densities are challenging, as it is not likely that a cavity that can accommodate a particle appears in a dense fluid. Attard [139] solved this problem by coupling the system size to the chemical potential. (See the references in [139] for more strategies.) The “bicanonical” ensemble consists of systems with  $N$  and  $N - 1$  particles [140]. It leads to high success rates for insertion and deletion of particles. A procedure to trace coexistence lines by combining the Clausius–Clapeyron integration technique with free energy difference calculations has been suggested [141]. Chemical equilibrium between surface and bulk has been used as a key to local free energy calculations [142].

The structure of the hard sphere crystal has been shown to be fcc rather than hcp by Bruce et al. [49]. Their lattice-switch Monte Carlo method allows the crystal to change its lattice during the course of the simulation.



This is achieved by coupling the system to a suitably defined order parameter that is sensitive to the crystal order (the stacking sequence of 111 planes in this case), and doing umbrella sampling with this quantity. The result of the simulation is the free energy difference between both candidate structures—and the winner is fcc!

#### IV. CONCLUSIONS

The world of colloidal particles is large and fascinating. Basic simulation techniques rapidly lead to challenging questions and new things to be discovered. Computer simulations are close enough to experiments to allow intellectual inspiration as well as a quantitative comparison of the results. We have reviewed the basic simulation techniques and their principal implementation but could only briefly mention advanced techniques and results. A survey of the recent literature shows the variety of physical effects present in colloidal systems and accessible to computer simulations.

#### ACKNOWLEDGMENTS

The author wishes to thank Hartmut Löwen for his useful advice and Małgorzata Borówko for her repeated encouragement.

#### REFERENCES

1. H. Löwen. *Phys Rep* 237:249, 1994.
2. H. Löwen. *Phys Bl* 51:165, 1995.
3. D. Frenkel., B. Smit. *Understanding Molecular Simulation*. San Diego: Academic Press, 1996.
4. M. P. Allen, D. J. Tildesley. *Computer Simulation of Liquids*. Oxford: Oxford University Press, 1987.
5. D. C. Rapaport. *The Art of Molecular Dynamics Simulation*. Cambridge: Cambridge University Press, 1995.
6. J. P. Hansen, I. R. McDonald. *Theory of Simple Liquids*, 2nd ed. London: Academic Press, 1986.
7. E. Dickinson, S. R. Euston. *Adv Coll Interface Sci* 42:89, 1992.
8. N. Metropolis, A. Rosenbluth, M. Rosenbluth, A. Teller, E. Teller. *J Chem Phys* 21:1087, 1953.
9. N. B. Wilding. *J Phys: Condens Matter* 9:585, 1997.
10. M. J. Stevens, M. L. Falk, M. O. Robbins. *J Chem Phys* 104:5209, 1996.
11. H. Löwen, I. D'Amico. *J Phys: Condens Matter* 9:8879, 1997.
12. V. Lobaskin, P. Linse. *J Chem Phys* 109:3530, 1998.
13. E. Allahyarov, I. D'Amico, H. Löwen. *Phys Rev Lett* 81:1334, 1998.
14. H. Löwen, E. Allahyarov. *J Phys: Condens Matter* 10:4147, 1998.

15. C. N. Likos, H. Löwen, M. Watzlawek, B. Abbas, O. Jucknischke, J. Allgaier, D. Richter. *Phys Rev Lett* 80:4450, 1998.
16. A. Jusufi, M. Watzlawek, H. Löwen. *Macromolecules* 32:4470, 1999.
17. M. Watzlawek, H. Löwen, C. N. Likos. *J Phys: Condens Matter* 10:8189, 1998.
18. M. Watzlawek, H. Löwen, C. N. Likos. Phase diagram of star polymer solutions (submitted for publication, 1999).
19. D. Ben-Amotz, A. Stamatopoulou, B. J. Yoon. *J Chem Phys* 107:6831, 1997.
20. N. V. Brilliantov, J. P. Valleau. *J Chem Phys* 108:1115, 1998.
21. M. Dijkstra, D. Frenkel. *Phys Rev Lett* 72:298, 1994.
22. M. Dijkstra, R. van Roij, R. Evans. *Phys Rev Lett* 81:2268, 1998.
23. A. Buhot, W. Krauth. *Phys Rev Lett* 80:3787, 1998.
24. T. Biben, P. Bladon, D. Frenkel. *J Phys: Condens Matter* 8:10799, 1996.
25. E. de Miguel, E. M. del Rio, M. M. Telo da Gama. *J Chem Phys* 103:6188, 1995.
26. W. Olivares-Rivas, L. Degrevè, D. Henderson, J. Quintana. *J Chem Phys* 106:8160, 1997.
27. P. González-Mozuelos, J. Alejandre. *J Chem Phys* 105:5949, 1996.
28. L. Degrevè, M. Lozada-Cassou. *Phys Rev E* 57:2978, 1998.
29. M. Schoen, S. Dietrich. *Phys Rev E* 56:499, 1997.
30. M. Chávez-Páez, H. Acuña-Campa, L. Yeomans-Reyna, M. Valdez-Covarrubias, M. Medina-Noyola. *Phys Rev E* 55:4406, 1997.
31. M. Chávez-Páez, E. Urrutia-Bañuelos, M. Medina-Noyola. *Phys Rev E* 58:681, 1998.
32. K. S. Page, P. A. Monson. *Phys Rev E* 54:6557, 1996.
33. M. Merkel, H. Löwen. *Phys Rev E* 54:6623, 1996.
34. Z. T. Németh, H. Löwen. *J Phys: Condens Matter* 10:6189, 1998.
35. Z. T. Németh, H. Löwen. *Phys Rev E* 59:6824, 1999.
36. A. Gonzalez, J. A. White, F. L. Román, S. Velasco, R. Evans. *Phys Rev Lett* 79:2466, 1997.
37. A. González, J. A. White, F. L. Román, R. Evans. *J Chem Phys* 109, 3637, 1998.
38. J. Chakrabarti, H. Löwen. *Phys Rev E* 58:3400, 1998.
39. A. M. Denton, H. Löwen. *Thin Solid Films* 330:7, 1998.
40. S. Hamaguchi, R. T. Farouki, D. H. E. Dublin. *J Chem Phys* 105:7641, 1996.
41. C. Vega, F. Bresme, J. L. F. Abascal. *Phys Rev E* 54:2746, 1996.
42. R. Agrawal, D. A. Kofke. *Phys Rev Lett* 74:122, 1995.
43. P. G. Bolhuis, D. A. Kofke. *Phys Rev E* 54:634, 1996.
44. M. D. Rintoul, S. Torquato. *J Chem Phys* 105:9258, 1996.
45. M. D. Rintoul, S. Torquato. *Phys Rev Lett* 77:4198, 1996.
46. M. D. Rintoul, S. Torquato. *Phys Rev E* 58:532, 1998.
47. P. Bolhuis, M. Hagen, D. Frenkel. *Phys Rev E* 50:4880, 1994.
48. P. Bolhuis, D. Frenkel. *J Phys: Condens Matter* 9:381, 1997.
49. A. D. Bruce, N. B. Wilding, G. J. Ackland. *Phys Rev Lett* 79:3002, 1997.
50. C. N. Likos, H. Löwen, M. Watzlawek. *Phys Rev E* 58:3135, 1998.

51. R. L. Davidchack, B. B. Laird. *J Chem Phys* 108:9452, 1998.
52. W. J. Briels, H. L. Tepper. *Phys Rev Lett* 79:5074, 1997.
53. P. R. ten Wolde, M. J. Ruiz-Montero, D. Frenkel. *Phys Rev Lett* 75:2714, 1995.
54. T. Biben, R. Ohnesorge, H. Löwen. *Europhys Lett* 28:665, 1994.
55. M. Schmidt. *Freezing in Confined Geometry*. Aachen: Shaker-Verlag, 1997.
56. H. Löwen, M. Schmidt. *Prog Col Polym Sci* 107:81, 1997.
57. M. Schmidt, H. Löwen. *Phys Rev E* 55:7228, 1997.
58. M. Schmidt, H. Löwen. *Phys Rev Lett* 76:4552, 1996.
59. J. Chakrabarti, H. R. Krishnamurthy, A. K. Sood, S. Sengupta. *Phys Rev Lett* 75:2232, 1995.
60. A. R. Denton, H. Löwen. *J Phys: Condens Matter* 9:8907, 1997.
61. K. J. Strandburg. *Rev Mod Phys* 60:161, 1988.
62. K. Bagchi, H. C. Andersen, W. Swope. *Phys Rev Lett* 76:255, 1996.
63. F. L. Somer Jr, G. S. Canright, T. Kaplan, K. Chen, M. Mostoller. *Phys Rev Lett* 79:3431, 1997.
64. K. Chen, T. Kaplan, M. Mostoller. *Phys Rev Lett* 74:4019, 1995.
65. G. Orkoulas, A. Z. Panagiotopoulos. *J Chem Phys* 104:7205, 1996.
66. M. R. Sadr-Lahijany, P. Ray, H. E. Stanley. *Phys Rev Lett* 79:3206, 1997.
67. A. C. Mitus, H. Weber, D. Marx. *Phys Rev E* 55:6855, 1997.
68. A. Jaster. *Europhys Lett* 42:277, 1998.
69. P. Bladon, D. Frenkel. *Phys Rev Lett* 74:2519, 1995.
70. G. Leptoukh, B. Strickland, C. Roland. *Phys Rev Lett* 74:3636, 1995.
71. P. Bolhuis, D. Frenkel. *J Chem Phys* 106:666, 1997.
72. S. C. McGrother, D. C. Williamson, G. Jackson. *J Chem Phys* 104:6755, 1996.
73. H. Graf, H. Löwen, M. Schmidt. *Prog Col Polym Sci* 107:177, 1997.
74. C. Vega, P. A. Monson. *J Chem Phys* 107:2696, 1997.
75. J. M. Polson, D. Frenkel. *Phys Rev E* 56:R6260, 1997.
76. P. J. Camp, C. P. Mason, M. P. Allen, A. A. Khare, D. A. Kofke. *J Chem Phys* 105:2837, 1996.
77. P. J. Camp, M. P. Allen. *J Chem Phys* 106:6681, 1997.
78. M. A. Bates, D. Frenkel. *Phys Rev E* 57:4824, 1998.
79. R. P. Sear, D. Frenkel. *J Chem Phys* 105:10632, 1996.
80. R. P. Sear, B. M. Mulder. *J Chem Phys* 105:7727, 1996.
81. R. P. Sear, B. M. Mulder. *J Chem Phys* 106:3827, 1997, Erratum.
82. M. Dijkstra, R. van Roij. *Phys Rev E* 56:5594, 1997.
83. P. J. Camp, M. P. Allen, P. G. Bolhuis, D. Frenkel. *J Chem Phys* 106:9270, 1997.
84. S. C. McGrother, R. P. Sear, G. Jackson. *J Chem Phys* 106:7315, 1997.
85. G. T. Evans. *J Chem Phys* 104:6654, 1996.
86. D. Henderson, J. Quintana, S. Sokołowski. *J Chem Phys* 102:4991, 1995.
87. J. Dzubiella, M. Schmidt, H. Löwen. Microstructure of topological defects in nematic droplets (submitted).
88. M. A. Bate, D. Frenkel. *J Chem Phys* 109:6193, 1998.
89. J. Stelzer, L. Longa, H.-R. Trebin. *J Chem Phys* 103:3098, 1995.

90. M. P. Allen, M. A. Warren, M. R. Wilson, A. Sauron, W. Smith. *J Chem Phys* 105:2850, 1996.
91. H. Löwen. *Phys Rev Lett* 72:424, 1994.
92. C. Vega, P. A. Monson. *J Chem Phys* 102:1361, 1995.
93. D. C. Williamson, F. del Rio. *J Chem Phys* 107:9549, 1997.
94. P. G. Bolhuis, A. Stroobants, D. Frenkel, H. N. W. Lekkerkerker. *J Chem Phys* 107:1551, 1997.
95. M. Dijkstra, J. P. Hansen, P. A. Madden. *Phys Rev Lett* 75:2236, 1995.
96. M. Dijkstra, J. P. Hansen, P. A. Madden. *Phys Rev E* 55:3044, 1997.
97. G. D. Wall, D. J. Cleaver. *Phys Rev E* 56:4306, 1997.
98. J. Chakrabarti. *Phys Rev Lett* 81:385, 1998.
99. R. Tao, Qi Jiang. *Phys Rev Lett* 73:205, 1994.
100. M. Sancho, V. Giner, G. Martinez. *Phys Rev E* 55:544, 1997.
101. M. Mohebi, N. Jamasbi, J. Liu. *Phys Rev E* 54:5407, 1996.
102. H. X. Guo, Z. H. Mai, H. H. Tian. *Phys Rev E* 53:3823, 1996.
103. M. J. Stevens, G. S. Grest. *Phys Rev Lett* 72:3686, 1994.
104. M. J. Stevens, G. S. Grest. *Phys Rev E* 51:5976, 1995.
105. M. J. Stevens, G. S. Grest. *Phys Rev E* 51:5962, 1995.
106. J. J. Weiss, D. Levesque. *Phys Rev E* 48:3728, 1993.
107. S. C. McGrother, G. Jackson. *Phys Rev Lett* 76:4183, 1996.
108. P. N. Segrè, O. P. Behrend, P. N. Pusey. *Phys Rev E* 52:5070, 1995.
109. S. Sanyal, A. K. Sood. *Phys Rev E* 52:4154, 1995.
110. S. Sanyal, A. K. Sood. *Phys Rev E* 52:4168, 1995.
111. C. P. Lowe, D. Frenkel. *Phys Rev E* 54:2704, 1996.
112. M. H. J. Hagen, I. Pagonabarraga, C. P. Lowe, D. Frenkel. *Phys Rev Lett* 78:3785, 1997.
113. R. D. Groot, P. B. Warren. *J Chem Phys* 107:4423, 1997.
114. M. R. Oberholzer, N. J. Wagner, A. M. Lenhoff. *J Chem Phys* 107:9157, 1997.
115. K. Zahn, J. M. Méndez-Alcaraz, G. Maret. *Phys Rev Lett* 79:175, 1997.
116. P. B. S. Kumar, M. Rao. *Phys Rev Lett* 77:1067, 1996.
117. M. Laradji, S. Toxvaerd, O. G. Mouritsen. *Phys Rev Lett* 77:2254, 1996.
118. H. Löwer. *Phys Rev E* 50:1232, 1994.
119. H. Löwen. *Phys Rev E* 59:1989, 1999.
120. A. C. Brańka, D. M. Heyes. *Phys Rev E* 50:4810, 1994.
121. Th. Kirchhoff, H. Löwen, R. Klein. *Phys Rev E* 53:5011, 1996.
122. A. Onuki. *J Phys: Condens Matter* 9:6119, 1997.
123. M. J. Stevens, M. O. Robbins. *Phys Rev E* 48:3778, 1993.
124. H. Komatsugawa, S. Nosé. *Phys Rev E* 51:5944, 1995.
125. H. Komatsugawa, S. Nosé. *Phys Rev E* 53:2588, 1996.
126. N. Olivi-Tran, R. Botet, B. Cabane. *Phys Rev E* 57:1997, 1998.
127. S. Butler, P. Harrowell. *J Chem Phys* 103:4653, 1995.
128. S. Butler, P. Harrowell. *J Chem Phys* 105:605, 1996.
129. J. F. Lutsko. *Phys Rev Lett* 77:2225, 1996.
130. S. R. Rastogi, N. J. Wagner, S. R. Lustig. *J Chem Phys* 104:9234, 1996.

131. E. S. Boek, P. V. Coveney, H. N. W. Lekkerkerker, P. van der Schoot. *Phys Rev E* 55:3124, 1997.
132. S. Tang, G. T. Evans, C. P. Mason, M. P. Allen. *J Chem Phys* 102:3794, 1995.
133. M. Lach-hab, A. E. González, E. Blaisten-Barojas. *Phys Rev E* 54:5456, 1996.
134. A. H. L. West, J. R. Melrose, R. C. Ball. *Phys Rev E* 49:4237, 1994.
135. J. C. Earnshaw, M. B. J. Harrison, D. J. Robinson. *Phys Rev E* 53:6155, 1996.
136. M. T. A. Bos, J. H. J. van Opheusden. *Phys Rev E* 53:5044, 1996.
137. L. E. Silbert, J. R. Melrose, R. C. Ball. *Phys Rev E* 56:7067, 1997.
138. S. Sauer, H. Löwen. *J Phys: Condens Matter* 8:L803, 1996.
139. P. Attard. *J Chem Phys* 107:3230, 1997.
140. W. C. Swope, H. C. Andersen. *J Chem Phys* 102:2851, 1995.
141. E. J. Meijer, F. El Azhar. *J Chem Phys* 106:4678, 1997.
142. M. J. Vlot, J. P. van der Erden. *J Chem Phys* 106:2771, 1997.

# 16

## Fluids in Contact with Semi-permeable Membranes

**SOHAIL MURAD** Department of Chemical Engineering, University of Illinois at Chicago, Chicago, Illinois

**JACK G. POWLES** Physics Laboratory, University of Kent, Canterbury, Kent, England

I.	Introduction	775
A.	Semi-permeable membranes	775
B.	Reverse osmosis membrane technology	778
II.	Selected Computational Techniques	779
A.	Continuum hydrodynamics theories	779
B.	Monte Carlo methods for osmotic equilibrium	780
C.	Molecular dynamics methods	782
III.	Selected Applications	786
A.	Electro-osmosis in polar (nonionic) and ionic solutions	786
B.	Osmosis and reverse osmosis in aqueous electrolyte solutions	790
IV.	Conclusions	794
	References	795

### I. INTRODUCTION

#### A. Semi-permeable Membranes

Semi-permeable membranes are quasi-two-dimensional barriers which, given a fluid mixture of two or more species of particles (usually two different molecular species, mixed or in solution) on one side, allow the passage either way through the membrane of one or more, but not all, of the molecular species, in either direction. This gives the possibility of separating, at

least partially, the two or more species provided a resultant flow of the permeating species can be produced. This flux of molecules is achieved by application of a differential mechanical pressure on the fluids on either side of the membrane or as a result of a spontaneous tendency to thermodynamic equilibrium.

In the following we shall consider only binary mixtures (solutions), but generalization to multi-component mixtures on one or both sides of the membrane is straightforward. There are many reasons why only one component of the mixture will pass through the membrane whereas the other cannot, or only does so with a vanishing or negligible flow rate. The most common case, and the simplest reason, is the difference in size of the particles. If one species is "larger" than the "holes" in the membrane it will not pass through the membrane in practical times—even with the help of quantum fluctuations. But if the other component is "smaller" than the "holes" it can pass through the membrane rather easily, either way. This is a sort of molecular-scale filtration. In practice the reasons for the difference in permeability of the membrane to different sorts of molecules can be complex and subtle. So the design and manufacture of such semi-permeable membranes is also complex and difficult. It currently involves a fair element of engineering judgement, i.e., intelligent but empirical guesswork. In fact, available membranes work remarkably well. One of the problems is the osmotic pressure generated. This may well be tens if not hundreds of atmospheres and is a real force per unit area acting on the membrane, which is often thin, even molecularly thin, and is fragile. It must therefore be mounted on a porous but sufficiently permeable substrate which makes the device more complex.

In general, the rate of permeation of the permeating species is difficult to calculate. It is a complex matter which intimately involves a knowledge of the structure and dynamics of the membrane and the structure and dynamics of the complex fluid mixture in contact with it on one side and the solvent on the other side. Realistic membranes with realistic fluids are beyond the possibilities of theoretical treatment at this time. The only way of dealing with anything at all realistic is by computer simulation. Even then one is restricted to rather simplified models for the membrane.

The process described above is usually called osmosis and this usually implies a flow of fluid in one direction or the other. If the permeating species, usually called the solvent, flows from the pure compartment to the mixture compartment then it is called osmosis pure and simple. This seems the natural process since the solvent dilutes the solution and this involves an increase in entropy and/or a decrease in free energy, so the resultant flow is spontaneous and the system tends to equilibrium. However, the starting conditions may be such that the difference of pressure

is greater than the ultimate osmotic pressure and the flow of solvent is then from the solution to the solvent, but the free energy still falls. This process is called reverse osmosis. Medical osmosis is usually osmosis as is the traditional molecular weight measurement of big molecules in small-molecule solvents. Desalination is reverse osmosis and the entropy increase comes from degradation of the work done by the external pressure difference, which must be provided. If the flow occurs in the presence of an applied electric field, the flow is affected and this is called electro-osmosis.

If we consider only equilibrium situations we have a "static" thermodynamic problem, which is much simpler. The result is totally independent of the properties of the semi-permeable membrane!—provided only that it is semi-permeable. The resulting configuration depends only on the properties of the two fluids, the mixture and the pure component. In equilibrium the chemical potential of the permeating component is equal on either side of the membrane. The two chemical potentials to be equalized require only knowledge of the thermodynamic properties of the mixture and the pure bulk fluids as a function of temperature, pressure, and mole fraction. The structure of the fluids near the membrane is irrelevant, as they are involved only in the rate at which the system comes to equilibrium. The chemical potential of the non-permeating species in the mixture is irrelevant once the equilibrium has been attained. In this sense osmotic equilibrium systems are investigations of the properties of mixtures and in particular of the chemical potential of the components in the mixture. Several tricks can be played, of varied utility. Pressure applied to the solution usually results in reverse osmosis and the solution becomes more concentrated and more pure solvent is produced, one or both of which may be desirable. There need not be a pure solvent in the other compartment at all! If the pure solvent spontaneously produced in this situation is continually removed we have a long-established process called pervaporation. One can have a series of permeable membranes, which may be all the same or may differ from one another in judicious and desirable ways, which serve to separate, concentrate or eliminate certain chosen components. Clearly there is room for ingenuity in the use of osmotic effects which await exploitation. Osmotic processes often occur at constant density and temperature of the pure fluid phase, i.e., at constant chemical potential of the permeating species. This is not, of course, necessary but it does simplify the process and often aids our understanding of it. It is usually achieved by keeping the density and temperature constant in the solvent compartment by pressure servos and thermostats, or by use of a large reservoir of solvent whose density is hardly changed by the resultant transfer of solvent from one phase to the other.

Clearly, however, there are many ways of changing the experimental setup depending on the aim of the procedure. There are many opportunities



for inventiveness and the use of new configurations. For instance, moveable or moving membranes have been suggested [1], but not yet used as far as we are aware. The use of multiple compartments is a promising novelty [2]. Microscopic molecular modeling using molecular dynamics and computer simulation is clearly the currently most profitable avenue of advancement in this field.

Semi-permeable membranes are used for a wide range of applications. Those based on pressure and/or concentration difference across the membrane include microfiltration, ultrafiltration, and reverse osmosis separation. Pervaporation is also included in this category but, in addition, involves two phases as well. Other uses of semi-permeable membranes include dialysis, electro-dialysis, and electro-osmosis. The pore size of the membrane in microfiltration applications varies from one to several hundred nanometers. They are widely used for applications such as water purification cartridges, where they remove products such as micro-organisms, molds, fibers, as well as small organic molecules [3–5]. They are made using several different materials by processes such as stretching polymeric films such as polyethylene, or irradiating polycarbonate plastic films. Ultrafiltration involves pore sizes in the range 1–100 nm. They are often used to separate large molecules such as colloids from solutions. These membranes are generally made from polymeric materials such as cellulose, or inorganic materials such as alumina.

The most important application of semi-permeable membranes is in separations based on reverse osmosis. These membranes generally have pores smaller than 1 nm. The pressure across the semi-permeable membranes for reverse osmosis is generally much larger than those for ultrafiltration, for example. This is because reverse osmosis is usually used for small molecules which have a much higher osmotic pressure, because of the higher number density, than the colloids separated in ultrafiltration. As a result reverse osmosis membranes have to be much more robust than ultrafiltration membranes. Since the focus of our discussion in this chapter will be on reverse osmosis based separations, we will describe these membranes in greater detail.

## **B. Reverse Osmosis Membrane Technology**

The semi-permeable membrane is the heart of the reverse osmosis separation process. Semi-permeable membranes for reverse osmosis are broadly divided into two types. The earliest practical membrane was of the “asymmetric type” [3–6]. It consisted of an osmotically active surface layer with very small pores (less than 1 nm) with a thickness of 30–100 nm. This layer was physically supported on a porous substructure, whose porosity increased with distance from the surface layer. In such a membrane, the

thickness of the surface layer should ideally be as thin as possible to minimize the resistance to solvent flow, since the rejection of solute molecules is a surface phenomenon. Asymmetric membranes are generally manufactured by applying a solution consisting of a polymer, a solvent and an additive to a suitable fabric carrier. The solvent can then be removed by immersing the membrane in water. This also coagulates the polymer into a porous film.

The other widely used membrane structure is referred to as a “composite membrane” [3–6]. In these membranes, a thin layer of solute-rejecting composite layer is formed by coating or polymerizing a suitable polymer on a physical support that usually consists of an asymmetric polysulfone membrane. The composite membrane offers more flexibility with regard to the solute-rejecting layer. Substances that cannot be dissolved to form a coating can still be used by interfacial polymerization, for example. Membrane rejection of solute molecules or ions can be classified into two broad categories. Steric rejection describes the case where an ion (together with its partially bound cluster of molecules) is physically unable to fit inside a very fine pore. Charge exclusion refers to the electrostatic repulsion of metal ions by pores (which may be significantly larger than the ion size) by overlapping electrical double layers between opposing pore walls [7].

The most significant application of reverse osmosis has been in the field of desalination to produce drinking water. Other important applications include the treatment of industrial waste water, concentration of fruit juices, and concentration of weak solutions such as aqueous ethanol [3–6]. The rest of the chapter will focus almost entirely on semi-permeable membranes used for reverse osmosis based applications. We chose this focus in view of the importance of reverse osmosis as a rather efficient separation technique for separating a wide range of solutions, especially very dilute solutions—which are usually notoriously difficult to handle using conventional techniques such as distillation.

## **II. SELECTED COMPUTATIONAL TECHNIQUES**

### **A. Continuum Hydrodynamics Theories**

Most theoretical studies of osmosis and reverse osmosis have been carried out using macroscopic continuum hydrodynamics [5,8–13]. The models used include those that treat the wall as either nonporous or porous. In the nonporous models the membrane surface is assumed homogeneous and nonporous. Transport occurs by the molecules dissolving in the membrane phase and then diffusing through the membrane. Mass transfer across the membrane in these models is usually described using the solution–diffusion

model [5]. In its simplest form, this model can be described by the two equations

$$J_w = A_w(\Delta P - \Delta \Pi) \quad (1)$$

$$J_s = B_s(C_{s,m} - C_{s,p}) \quad (2)$$

where  $J_w$  and  $J_s$  are the solvent and solute flux,  $\Delta P$  and  $\Delta \Pi$  the hydraulic and osmotic pressure differences across the membrane,  $C_{s,m}$  and  $C_{s,p}$  the concentrations of the solute at the membrane interface and the permeate, and  $A_w$  and  $B_s$  the solvent permeability and mass transfer coefficient of the solute, respectively. Eqs. (1) and (2) are somewhat contradictory. Eq. (1) assumes perfect semi-permeability of the membrane, yet Eq. (2) assumes diffusion (Fickian) for the solute on the permeate side. An alternative form, which is more consistent, is to write them as [6–13]

$$J_w = A_w(\Delta P - \sigma_0 \Delta \Pi) \quad (3)$$

$$J_s = A_d \Delta \Pi + \langle C_s \rangle J_w (1 - \sigma_f) \quad (4)$$

Here the permeability of the membrane to the solute is defined in terms of reflection coefficients  $\sigma_0$  and  $\sigma_f$ , for osmosis and filtration respectively. When  $\sigma_0 = 1$ , then perfect semi-permeability results.  $A_w$  in Eq. (4) is the diffusive permeability of the membrane, while  $\langle C_s \rangle$  is the average composition of the solute in the membrane.

Irreversible thermodynamics has also been used sometimes to explain reverse osmosis [14,15]. If it can be assumed that the thermodynamic forces responsible for reverse osmosis are sufficiently small, then a linear relationship will exist between the forces and the fluxes in the system, with the coefficients of proportionality then referred to as the phenomenological coefficients. These coefficients are generally notoriously difficult to obtain, although some progress has been made recently using approaches such as cell models [15].

## B. Monte Carlo Methods for Osmotic Equilibrium

The first Monte Carlo study of osmotic pressure was carried out by Panagiotopoulos et al. [16], and a much more detailed study was subsequently carried out using a modified method by Murad et al. [17]. The technique is based on a generalization of the Gibbs-ensemble Monte Carlo (GEMC) method applied to membrane equilibria. The Gibbs ensemble method has been described in detail in many recent reports so we will only summarize the extension of the method to membrane equilibria here [17]. In the case of two phases separated by semi-permeable membranes

only, there is no direct constraint on the chemical equilibria of the non-permeating species—only the chemical potential of the permeable species are to be equal. In addition, either the osmotic pressure, the pressure difference between the two phases referred to as  $\Pi$ , can be fixed, as was done by Panagiotopoulos et al. [16], or the volume of the two phases can be fixed and the osmotic pressure allowed to develop naturally to satisfy the constraints on the chemical potentials, as was done by Murad et al. [17]. If the osmotic pressure of the system is fixed (and the volume of the two phases allowed to rearrange as is usual in GEMC), the probability of accepting a “move” is given by  $\min(1, P_{\text{vol}})$ , where

$$P_{\text{vol}} = \exp(-\beta[\Delta E^I + \Delta E^{II} - N^I kT \ln(V^I + \Delta V)/V^I - N^{II} kT \ln(V^{II} - \Delta V)/V^{II} - \Pi \Delta V]) \quad (5)$$

$E$ ,  $V$ ,  $T$ , and  $N$  refer to the energy, volume, temperature, and number of particles in a phase, respectively, while the superscripts identify the phases.  $\Delta$  refers to the changes as a result of the change in volume  $\Delta V$ .

Panagiotopoulos et al. [16] studied only a few ideal LJ mixtures, since their main objective was only to demonstrate the accuracy of the method. Murad et al. [17] have recently studied a wide range of ideal and nonideal LJ mixtures, and compared results obtained for osmotic pressure with the van't Hoff [17a] and other equations. Results for a wide range of other properties such as solvent exchange, chemical potentials and activity coefficients [18] were compared with the van der Waals 1 (vdW1) fluid approximation [19]. The vdW1 theory replaces the mixture by one fictitious pure liquid with judiciously chosen potential parameters. It is defined for potentials with only two parameters, see Ref. 19. A summary of their most important conclusions include:

- (i) For solutions that are not highly nonideal and with low concentrations the van't Hoff approximation is given by

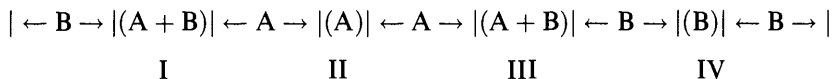
$$\Pi \simeq C_i RT \quad (6)$$

Here  $C_i$  is the solute concentration and  $R$  the gas constant. This is in fact obeyed over a rather wide range of concentrations, almost up to solute mole fractions of 0.61, with an error of only 25 percent. This is remarkable, since the van't Hoff equation is rigorous only in the infinitely dilute limit. Even in the case of highly nonideal solutions, for example a solution with  $\sigma$  ratios of 1.5 and  $\varepsilon$  ratios of 4, the van't Hoff equation is still obeyed quite well for concentrations up to about 6 mole percent. It appears from these results that the van't Hoff approximation is much more sensitive to the nonideality of the solutions, and not that sensitive

to the concentration of the solution, although both requirements are mandatory for it to be a good approximation at other than vanishingly small concentrations.

- (ii) For almost all solutions we studied, the van der Waals 1 fluid theory was found to be remarkably accurate. Even for highly nonideal solutions, vdW1 reproduced all the qualitative features and was in substantial agreement with the exact GEMC results. This was found to be the case for osmotic pressure, extent of osmosis, chemical potential as well as the activity coefficients. These results clearly show that, perhaps, the value of the vdW1 theory is often underestimated.

The chemical potential of associating systems has also been studied more recently by Bryk et al. [2]. They have extended the usual GEMC method for studying osmotic equilibrium by including four simulation cells in series, rather than the usual two compartments, but with osmotic equilibrium established between only two adjacent compartments (e.g. I and II, II and III, or IV and I). Each semi-permeable membrane was made permeable to only one species as shown and described below:



The arrows indicate a semi-permeable membrane and the species allowed to permeate is shown within the arrows. The parentheses show a GEMC phase (or region) and the species it contains. The first and the last region are also connected to each other. Using such a scheme, Bryk et al. showed that osmotic Monte Carlo can be successfully used to study the association of two different molecular species when an associating intermolecular potential is included in the simulation. The results agreed well with the more traditional grand-canonical Monte Carlo methods.

### C. Molecular Dynamics Methods

The first molecular dynamics [20,21] of osmosis was carried out by Murad and Powles [22]. The simulation method is based on the usual microcanonical (NVE) algorithm, with the equations of motion solved using any suitable method, such as the predictor-corrector or leap frog method. The semi-permeable membrane was formed by tethering a subset of the simulation particles at appropriate sites [23] corresponding to the geometry of the desired membrane and its realistic flexibility and mobility, using a simple harmonic potential (although others could just as well be used if desired)

$$\Phi = 1/2K\delta^2 \quad (7)$$

$K$  in Eq. (7) is the spring constant, while  $\delta$  is the scalar distance between the actual position of a tethered molecule and the tethering site. The strength of the method lies in the atomic nature of the membrane, rather than a homogeneous barrier. This makes it possible to study the dynamics of solvent permeation across the membrane, as well as the effect of a range of molecular forces that can affect it. These include the more obvious forces such as the solvent-membrane interactions, as well as less obvious ones such as, the solute-membrane, solvent-solvent, and solute-solvent interactions, which also affect the permeation rate indirectly due to solvation, adsorption, etc. In its simplest implementation, the simulation could be started with all particles in an fcc configuration. All particles at  $x = L_x/4$  or  $3L_x/4$  could then be designated as the membrane, and then tethered to their initial fcc sites using the tethering potential given by Eq. (7).  $L$  is the size of the simulation system, with the subscript designating the coordinate along which the size is measured. For a cubic simulation consisting of 256 molecules, for example, each membrane would consist of 32 molecules in such a scheme. If a membrane more than one molecule thick were desired, then two adjacent fcc layers of particles could be tethered [23].

Another method has also been suggested for tethering [23]. This would require all the molecules designated as the membrane molecules to be tethered to some or all of their neighbors, that are also part of the membrane. Fig. 1 shows the typical structure of a semi-permeable membrane while Fig. 2 shows a typical MD simulation system for osmosis with each membrane one molecular layer thick. In addition, as can be seen from Fig. 2, it is not necessary for the simulation system to be a cube. In fact it is desirable for  $L_x$

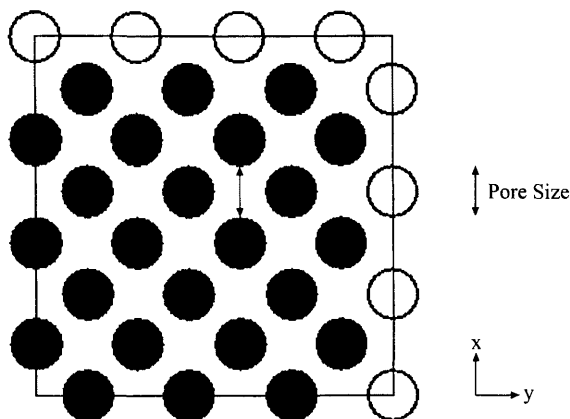


**FIG. 1** Structure of a section of a membrane wall.

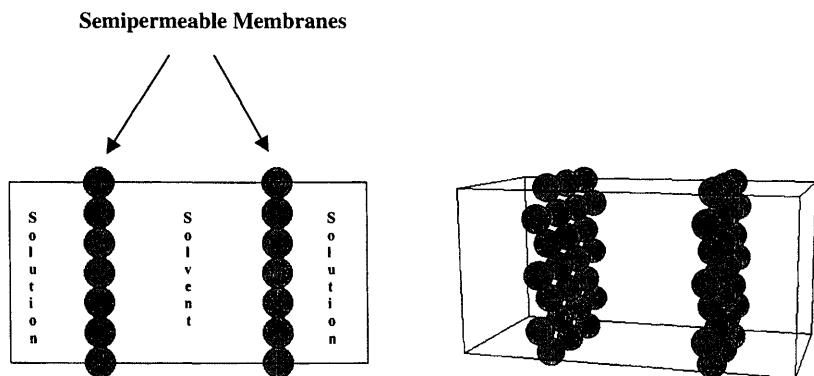


**FIG. 2** The  $xy$  and a 3D projection of a typical osmotic MD simulation system. The semi-permeable membrane walls are in the  $yz$  plane. Periodic boundary conditions automatically generate an infinite pair of walls, infinite in the  $yz$  (transverse) directions, with alternating solution and solvent cells, each of thickness half the system width.

to be larger than  $L_y$  or  $L_z$ , as this increases the distance between the two semi-permeable membranes in the infinitely replicated system, thus minimizing the relative size of the region whose homogeneity is being perturbed by the semi-permeable membranes. In most simulations it would be desirable to have the fraction of molecules so affected to be as small as possible, to obtain better statistics for osmosis and reverse osmosis. The permeability of the membrane can be fixed either by adjusting the molecular parameters of the particles that constitute the membrane (most notably the size and energy interaction parameters), or the constant  $K$  of the simple harmonic tethering potential. At smaller values of  $K$ , the tethered particles oscillate with low frequencies and large amplitudes, thus creating larger holes for longer periods to allow fluid particles to permeate fairly easily. At larger values of  $K$ , the tethered particles oscillate at a higher frequency and smaller amplitude. This does not provide large holes long enough to allow as many fluid particles to permeate. The parameters of the membrane can be fixed so that the membrane is permeable to the particular solvent molecules, and impermeable to the particular solute molecules. This method was then used to study solutions, ranging from simple LJ mixtures to aqueous and methanolic electrolyte solutions [24,25]. The method was also used to investigate the role of various solvent-solvent, solvent-membrane, and other related forces on the permeation rate of the solvent molecules across the membrane, which, as should be obvious, is of great fundamental as well as practical interest in separation processes. By varying the density (or pressure) and

composition of the solution and solvent cells, the dynamics of both osmosis and reverse osmosis can be studied using this simulation method. More recent extensions of the method include its application to investigating electro-osmosis and related phenomena [26] in both polar and ionic solutions. This involves introducing an external electric field in the simulation cell. In addition in the case of ionic solutions, it is necessary to vary the direction of the electric field periodically (alternating electric field), as indeed must also be done experimentally, to avoid fouling of the semi-permeable membrane by ions accumulating near the membrane because of the external electric field [27].

An alternative scheme for osmotic molecular dynamics has been suggested by Rowley et al. [28]. It differs from the method of Murad and Powles [22] in the model used for the semi-permeable membrane, the overall scheme being quite similar. In addition it has been geared more towards calculating the chemical potential of pure fluids and mixtures accurately, using a single MD simulation. It contains two cells within the simulation system separated by a semi-permeable membrane. Cell A contains both components 1 (solvent) and 2 (solute), and cell B contains only component 1. The semi-permeable membrane is simply declared in this method to be invisible to the solvent molecules. For the solute molecules (which it is supposed to prevent from permeating), a repulsive WCA-type potential [28a], which includes only the shifted repulsive part of the LJ potential, is used as a potential barrier. In its reduced form it is given by

$$\left. \begin{aligned} \Phi_{\text{solute-membrane}} &= 4(x^{-12} + x^{-6}) + 1 & x < 2^{1/6} \\ \Phi_{\text{solute-membrane}} &= 0 & x > 2^{1/6} \end{aligned} \right\} \quad (8)$$

$x$  is the scalar distance between the solute molecule and the center of the imaginary membrane, with the LJ parameters of the solute used as reducing parameters. The residual chemical potential for a pure fluid (which would correspond to component 2 in its pure state at the state conditions of cell A) can then, for example, be found using the expression

$$\mu^{\text{res}} = kT \ln x_A + kT \ln \rho^A / \rho^B \quad (9)$$

For this expression to be valid, in cell A components 1 and 2 must be identical in all respects, so it is a rather special case of an ideal mixture. They are however, allowed to interact differently with the membrane, as described above.  $x_A$  is the mole fraction of the solute in cell A, while  $\rho^A$  and  $\rho^B$  are the number densities of cells A and B respectively. The method was extensively tested against both Monte Carlo and equations of state for LJ particles, and the values of the chemical potential were found to be satisfactory. The method can also be extended to mixtures [29] by making



components 1 and 2 have different molecular parameters and using appropriate thermodynamic relationships for the chemical potential of mixtures instead of Eq. (9), which is valid only for pure fluids. More recently the method has also been extended to structured molecules like butane [30].

### III. SELECTED APPLICATIONS

#### A. Electro-osmosis in Polar (Nonionic) and Ionic Solutions

Electro-osmosis has been defined in the literature in many indirect ways, but the simplest definition comes from the *Oxford English Dictionary*, which defines it as “the effect of an external electric field on a system undergoing osmosis or reverse osmosis.” Electro-osmosis is not a well-understood phenomenon, and this especially applies to polar non-ionic solutions. Recent literature and many standard text and reference books present a rather confused picture, and some imply directly or indirectly that it cannot take place in uniform electric fields [31–35]. This assumption is perhaps based on the fact that the interaction of an external electric field on a polar molecule can produce only a net torque, but no net force. This therefore appears to be an ideal problem for molecular simulation to address, and we will describe here how molecular simulation has helped to understand this phenomenon [26]. Electro-osmosis has many important applications in both the life and physical sciences, including processes as diverse as water desalination, soil purification, and drug delivery.

The simulations to investigate electro-osmosis were carried out using the molecular dynamics method of Murad and Powles [22] described earlier. For nonionic polar fluids the solvent molecule was modeled as a rigid homonuclear diatomic with charges  $q$  and  $-q$  on the two active LJ sites. The solute molecules were modeled as spherical LJ particles [26], as were the molecules that constituted the single molecular layer membrane. The effect of uniform external fields with directions either perpendicular to the membrane or along the diagonal direction (i.e.  $E_x = E_y = E_z$ ) was monitored. The simulation system is shown in Fig. 2. The density profiles, mean squared displacement, and movement of the solvent molecules across the membrane were examined, with and without an external field, to establish whether electro-osmosis can take place in polar systems. The results clearly established that electro-osmosis can indeed take place in such solutions.

Simulations were carried out in which the solution compartment contained 80 solvent molecules and 20 solute molecules, while the solvent compartment was initially empty. The parameters used ( $\epsilon$  and  $\sigma$  are the solute

parameters) were  $\sigma_{\text{wall}} = 1.0\sigma$ ,  $\sigma_{\text{solvent}} = 0.7\sigma$  (for both sites). The molecular weight and  $\epsilon$  for all molecules were assumed identical. For the solvent molecules, the bond length was  $l = 0.384\sigma$ , and  $q = \pm 8(\epsilon\sigma)^{1/2}$ . An external electric field with  $E = 2$  was used, irrespective of the direction of field (see above). For cross-interactions, Lorentz–Berthelot rules were used with the binary interaction parameters fixed at 1.0, except for the solvent–wall interactions in which for  $\sigma$  a value of 1.25 was used. This was done to ensure that the no solute molecules permeate the wall.

Results for the net number of solute molecules permeating the wall as a function of time with and without an external electric field are shown in Fig. 3. It is clear from the results that an external electric field increases the rate of reverse osmosis. It is also significant that the increase takes place for both the directions of the electric fields studied. It could have been argued that since linear molecules were being investigated, an electric field perpendicular to the membrane would tend to align solvent molecules perpendicular to the membrane thus making it easier for the solvent molecules to permeate the membrane. This can be seen in Fig. 4, which shows the fraction of the solvent molecules with an orientation perpendicular to the membrane (this has been defined to be for all molecules with  $|e_x|$ , the  $x$  component of the unit vector, between 0.9 and 1.0). For the case of no electric field it fluctuates around 0.1 (as it should be for random orientations). In the case of an electric field perpendicular to the membrane it is 0.18, which means that more molecules are aligned in an orientation more favorable for

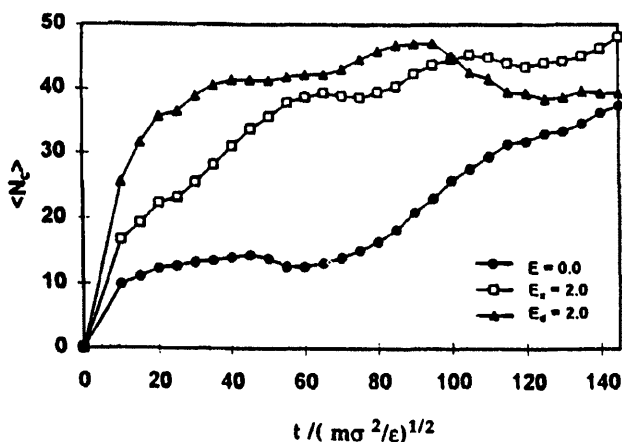


**FIG. 3** The resultant number of solvent molecules permeating the membrane  $\langle N_c \rangle$ , plotted against time for three different applied fields. The lines here and in subsequent figures are shown to guide the eye [26].

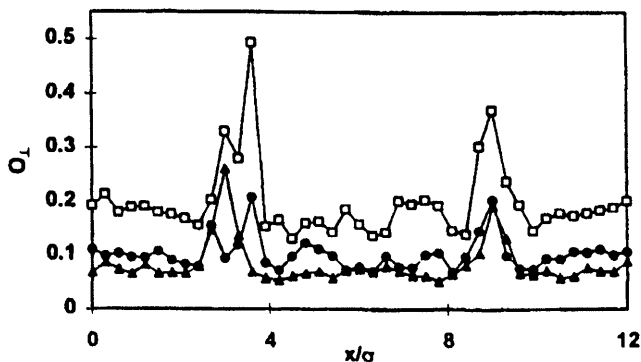


**FIG. 4** Fractional distribution  $O_{\perp}$  of solvent molecules oriented in a direction perpendicular to the plane of the wall across the length of the parallelepiped. Applied field as in Fig. 3 [26].

permeating the membrane than random. However, in the case of the diagonal field, this number appears to be smaller than the no field case, but *even* in this case the rate of permeation was higher, as shown in Fig. 3. This then shows that the increase in permeation rate is not merely an orientation effect, but rather electro-osmosis. This is also confirmed in Fig. 5, which shows the effect of the electric field on the mean-squared displacements of the solvent molecules. An increase in the mean squared displacement is seen

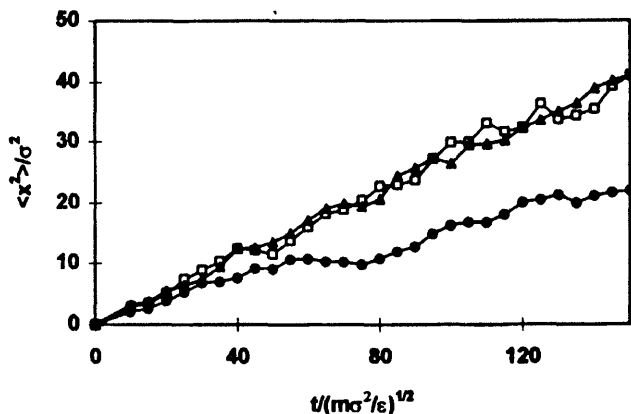


**FIG. 5** Mean squared displacement of solvent molecules in a direction perpendicular to the plane of the membrane plotted against time [26].

due to the external electric field. The cause of electro-osmosis in such systems is thought to be the ability of the external field to make clusters of the highly polar solvent molecules less energetically favorable, which leads to larger permeation rates by the consequently smaller clusters across the membrane.

The case where the solute molecule was charged and the solvent diatomic molecules had no charge distribution was also examined. In this case there is no interaction at all between the external electric field and the solvent molecules. Despite this, as is seen in Fig. 6, there is an increase in the rate of solvent permeation when an alternating (periodically reversed) external electric field is present. The field must be reversed periodically to prevent the charged solute molecules from fouling (blocking) the membrane by accumulating adjacent to it. In this case it is believed that electro-osmosis is due to the solvent molecules getting dragged along as the solute molecules move due to their interaction with the electric field. If the electric field is not reversed then as can be seen from Fig. 6, electro-osmosis is not observed. The reversing of electric fields is also used experimentally to enhance the rate of electro-osmosis [27].

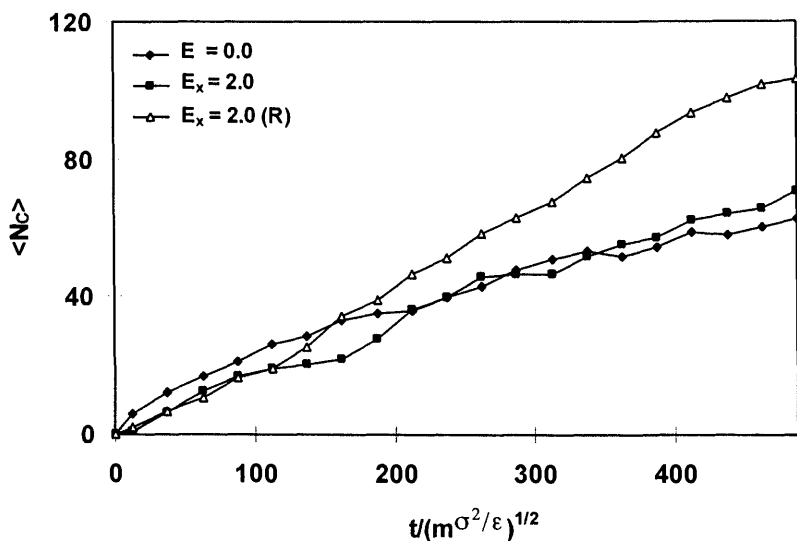


**FIG. 6** Effect of an electric field on the resultant number of solvent molecules permeating the membrane as a function of time for the case of charged solute molecules, and nonpolar homonuclear solvent molecules. R refers to the field being periodically reversed [26].

## B. Osmosis and Reverse Osmosis in Aqueous Electrolyte Solutions

Reverse osmosis separations of electrolyte solutions (such as the desalination process) is a rather interesting problem, because it is not an obvious case of separations enabled by differences in molecular sizes. In the case of an aqueous NaCl solution, for example, the size of  $\text{Na}^+$  is certainly considerably smaller than that of a water molecule. Despite this it is well known that membranes used for desalination, such as those described earlier, allow water molecules to permeate quite easily, yet smaller ions such as  $\text{Na}^+$  are prevented from permeating them. Since permeation in this case could not be explained as a result of size difference, it was generally accepted that this was due to surface interactions between the membrane surface and the solute and solvent molecules. Molecular simulations could thus be a useful tool for understanding these molecular forces. This problem has been examined in considerable detail recently using the molecular dynamics method, and has led to a significant improvement in our understanding of the forces that play a significant role in the reverse osmosis based separation of electrolyte solutions, as described below.

The simulations were carried out using previously developed intermolecular potential models for both the water and the ions. For water, the simple point charge (SPC) model was used, while for the ions the primitive model was used [36,37]. These models are known to provide a realistic picture of these systems for a wide range of properties and state conditions [36]. Long-range forces were accounted for by using the reaction field method [38]. The membrane, which consisted of uncharged one molecular layer LJ particles, was designed to have pore sizes of up to 0.3 nm diameter (see Fig. 2). This compares well with the pore size distribution in industrial membranes used in these separations. Thus these studies can be expected to provide a correct qualitative if not quantitative picture of the reverse osmosis phenomenon in such systems.

One of the most remarkable results from the molecular simulation studies of aqueous electrolyte solutions was that no additional molecular forces needed to be introduced to prevent the much smaller ions ( $\text{Na}^+$  has a molecular diameter of less than 0.2 nm) from permeating the membrane, while permitting the larger water molecules (about 0.3 nm in diameter) to permeate the membrane. This appeared to be due to the large ionic clusters formed. The ions were surrounded by water molecules, thus increasing their effective size quite considerably to almost 1 nm. A typical cluster formed due to the interaction between the ions and a polar solvent is shown in Fig. 7. These clusters were found to be quite stable, with a fairly high energy of desolvation. The inability of the ions to permeate the membrane is also shown

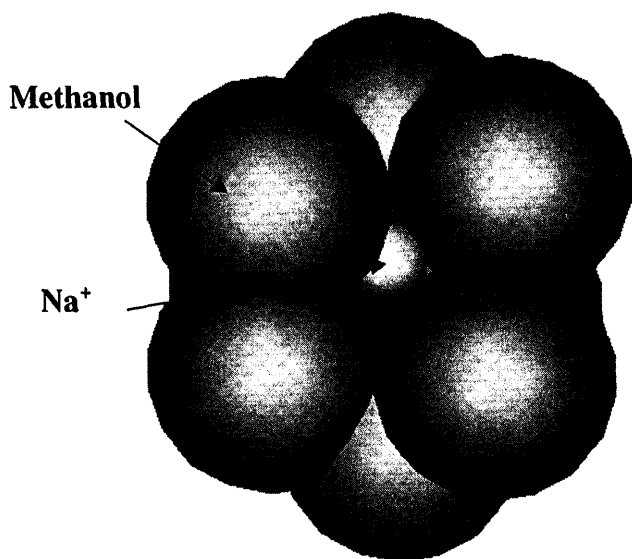


**FIG. 7** Example of an ionic cluster formed by ions being surrounded by molecules of a polar solvent (methanol) [25].

by the density profile for a 4 M NaCl solution at 25 °C given in Fig. 8. It is clear from the figure that not only are there no ions in the solvent compartment (the two membranes are at roughly 5 and 15), but the ions are even kept away from the two membranes by a layer of water molecules adjacent to the membranes. In addition to the clusters of the type shown in Fig. 7, larger clusters involving more than one ion were also observed. Fig. 9 shows

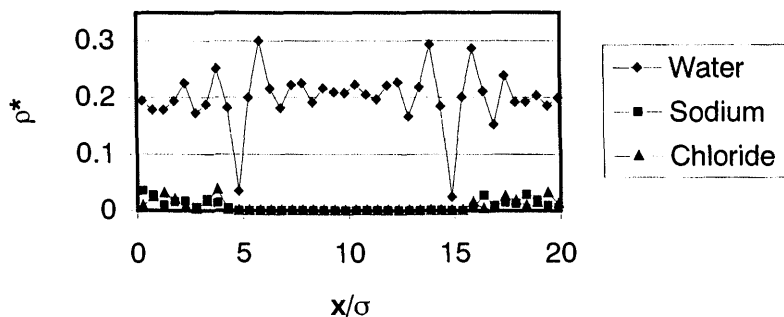


**FIG. 8** Density profiles in a 4 M aqueous NaCl solution at 25°C. The semi-permeable membranes are at about 5 and 15 [25].

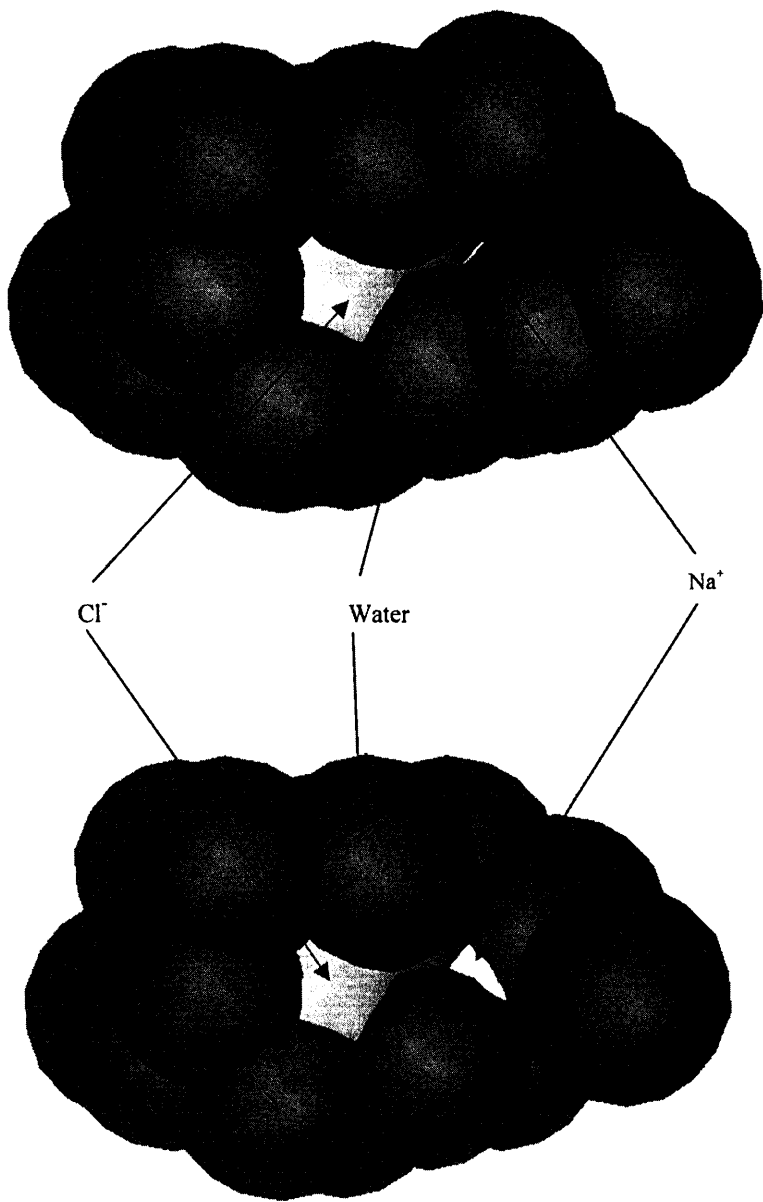


**FIG. 9** Example of a two-ion cluster: the cluster contains sodium and chloride ions surrounded by water molecules to form a two ion cluster. The bottom cluster shows the sodium ion more clearly, after some water molecules in front of it have been removed [25].

two ions separated by a layer of water molecules forming one such large cluster. By increasing the temperature of the solution, it was possible to make ions permeate the membrane. This effectively made the larger ionic clusters less stable, and the ions were able to break away from the clusters; the “bare” ions could then permeate the membrane. This was also found to be the case when an external electric field was included in the simulation system. The electric field weakened the ionic clusters and again allowed ions then to permeate the membrane. These simulations thus showed that the solvation of ions is at least *partly* responsible for these separations, and in the very least these forces must be taken into account as part of the design in reverse osmosis based separations of aqueous electrolyte solutions.

The ionic clusters observed are not limited to aqueous electrolyte solutions only. In fact very similar results were obtained for methanolic solutions as well [25]. This shows that sufficiently large and stable ionic clusters are a fairly common occurrence whenever ions are dissolved in polar solvents. The clusters are an essential factor in the facilitation of reverse osmosis purification. Since many industrially important solutions include ions in polar solvents, it is important to account for them in separation involving such solvents.

The molecular simulations also showed that electro-osmosis is also observed in aqueous electrolyte solutions, as long as the external electric field is reversed periodically to prevent the ions from accumulating near the membrane. An example of this is shown in Fig. 10, which shows the effect of an electric field on a 4.67 mole percent aqueous LiCl solution at 25°C. It is quite clear that the mobility of the solvent molecules increases as a result of

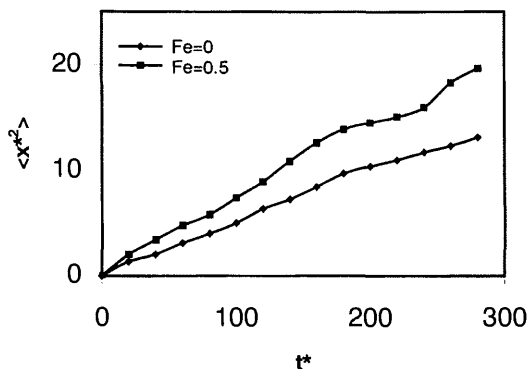


**FIG. 10** Effect of an electric field ( $F_e$ ) on the mean-squared displacement perpendicular to the plane of the membrane for a 4.67 mole percent aqueous LiCl solution at 25°C and 1 bar [25].



the external electric field. This increase is related to the effect of the external electric field on the stability (or energy of desolvation) of the ionic clusters in these systems, which tends to make such clusters less energetically favorable. Thus the solvent molecules that were immobilized by the clusters can break away from them more easily, and move around. In addition there are weaker clusters also present that only involve solvent molecules in both the solution and solvent compartments. These clusters also become less stable in the presence of an electric field, and this also contributes to electro-osmosis. Another more extreme example of the effect of an electric field on such clusters can be seen when very high field strengths are used in the simulation. Not only is the mobility of the solvent molecules increased considerably, but the ions usually bound to clusters also begin to break away from them and are able to permeate the relatively large pores in the membrane, since they are no longer as restricted by the solvent molecules surrounding them.

#### IV. CONCLUSIONS

Osmosis is a general phenomenon which has not often been studied from a fundamental point of view despite its considerable industrial importance. The mechanism of selective permeability of membranes to component molecules of mixtures is not well understood. It is an important and complex subject because there are all sorts of different membranes and all sorts of fluid mixtures.

For any even vaguely realistic atomically constituted membrane it is unlikely that any theory will become available in the near future which will properly or reasonably describe the dynamic properties of the membrane, the fluids near it, and their passage, or selective passage, through it. Nevertheless, one should continue trying with simple models and simple theories [39–43], which show the way forward and can, as usual, be tested by the virtually exact results of molecular dynamics simulation.

The only feasible procedure at the moment is molecular dynamics computer simulation, which can be used since most systems are currently essentially controlled by classical dynamics even though the intermolecular potentials are often quantum mechanical in origin. There are indeed many intermolecular potentials available which are remarkably reliable for most liquids, and even for liquid mixtures, of scientific and technical importance. However potentials for the design of membranes and of the interaction of fluid molecules with membranes on the atomic scale are less well developed.

There is still great scope then for the design of more realistic membranes and for the development of more realistic atomic potentials

for the interaction of the component molecules of the mixtures with atomic membranes. We are at the stage that the present models have roughly the observed, or known, behavior. But they need considerable refinement to give explicit design data for the practical construction and manufacture of better conventional membranes. We must also consider new configurations and novel designs of membrane which will have the desired properties of permeability, robustness, reliability, and cheapness. As always, the more computer power deployed, the better and more realistic the model!

The industrialist should take note of the utility of molecular dynamics computer simulation in this field and of the rapid developments in progress.

## ACKNOWLEDGMENTS

Some of the work reported here was supported by grants from the Chemical Sciences Division, US Department of Energy, and the National Science Foundation.

## REFERENCES

1. J. G. Powles, B. Holtz, W. A. B. Evans, S. Murad. Can osmotic pressure be negative? *Mol Phys* 90:665, 1997.
2. P. Bryk, A. Patrykiewicz, O. Pizio, S. Sokołowski. The chemical potential of Lennard-Jones associating fluids from osmotic Monte Carlo simulations. *Mol Phys* 92:949, 1997; A method for the determination of chemical potential for associating liquids. *Mol Phys* 90:665, 1997.
3. T. Matsuura. *Synthetic Membranes and Membrane Separation Processes*. Boca Raton: CRC Press, 1994; P. Hoornaert. *Reverse Osmosis*. Oxford: Pergamon, 1984.
4. A. F. Turbak, ed. *Synthetic Membranes*. Washington, DC: American Chemical Society, 1981; S. Sourirajan and T. Matsuura (eds.). *Reverse Osmosis and Ultrafiltration*. Washington, DC: American Chemical Society, 1985.
5. B. S. Parekh, ed. *Reverse Osmosis Technology*. New Jersey: Noyes, 1988.
6. S. Sourirajan. *Reverse Osmosis*. New York: Academic Press, 1970.
7. A. Yarshuk, E. Staude. Charged membranes for low pressure reverse osmosis properties and applications. *Desalination* 86:115, 1992.
8. C. S. Slater, C. A. Brooks. Development of a simulation model predicting performance of reverse osmosis batch systems. *Sep Sci Tech* 27:1361, 1992.
9. S. Kimura. New trends of membrane separation technology. *Makromol Chem Macromol Symp* 70-71:397, 1993.
10. H. Mehdizadeh, J. M. Dickson. Theoretical modifications of the finely porous model for reverse osmosis. *J Appl Polym Sci* 42:1143, 1991.
11. J. L. Anderson, D. M. Malone. Mechanisms of osmotic flow in porous membranes transport. *Biophys* 14:957, 1974.

12. W. M. Deen. Hindered transport of large molecules in liquid filled pores. *AIChE J* 33:1409, 1987.
13. D. C. Guell, H. Brenner. Physical mechanism of membrane osmotic phenomena. *Ind Eng Chem Res* 35:3004, 1996.
14. A. E. Yaroshchuk, S. S. Durkhin. Phenomenological theory of reverse osmosis in macroscopically homogeneous membranes and its specification for the capillary charged model. *J Memb Sci* 79:133, 1993.
15. H. O. E. Karlsson, G. Tragadh. Pervaporation of dilute organic waters mixtures: A literature review on modeling studies and applications to aroma recovery. *J Membr Sci* 76:121, 1993.
16. A. Z. Panagiotopoulos, N. Quirke, M. Stapleton, D. J. Tildesley. Phase equilibria in the Gibbs ensemble. Alternate derivation, generalization and application to mixture and membrane equilibria. *Mol Phys* 63:527, 1988.
17. S. Murad, J. G. Powles, B. Holtz. Osmosis and reverse osmosis in solutions: Monte-Carlo simulations and van der Waals one-fluid theory. *Mol Phys* 86:1473, 1995.
- 17a. J. H. van't Hoff. Die rolle des osmotische Drücke in der Analogie Zwischen Lösungen und Gasen. *Z Physik Chemie* 1:481, 1887.
18. J. G. Powles, S. Murad, B. Holtz. A novel osmotic pressure route to the activity coefficient of a molecule in a solution. *Chem Phys Lett* 245:178, 1995.
19. T. W. Leland, J. S. Rowlinson, G. A. Sather. Statistical mechanics of mixtures of different sizes. *Trans Faraday Soc* 64:1447, 1968.
20. J. M. Haile. *Molecular Dynamics: Elementary Methods*. New York: Wiley, 1992.
21. M. P. Allen, D. J. Tildesley. *Computer Simulation of Liquids*. Oxford: Clarendon, 1987.
22. S. Murad, J. G. Powles. A computer simulation of the classic experiment on osmosis and osmotic pressure. *J Chem Phys* 99:7271, 1993.
23. S. Murad, P. Ravi, J. G. Powles. A computer simulation study of fluids in model slit, tubular and cubic micropores. *J Chem Phys* 98:9771, 1993.
24. S. Murad, J. G. Powles. Computer simulation of osmosis and reverse osmosis in solutions. *Chem Phys Lett* 225:437, 1994; S. Murad. Molecular dynamics of osmosis and reverse osmosis in solutions. *Adsorption* 2:95, 1996.
25. F. Paritosh, S. Murad. Molecular simulation of osmosis and reverse osmosis in aqueous electrolyte solutions. *AIChE J* 42:2984, 1996; S. Murad, K. Oder, J. Lin. Molecular simulation of osmosis, reverse osmosis, and electro-osmosis in aqueous and methanolic electrolyte solutions. *Mol Phys* 95:401, 1998; J. G. Powles, S. Murad. The molecular simulation of semi-permeable membranes—osmosis, reverse osmosis and electro-osmosis. *J Mol Liq* 78:225, 1998.
26. S. Murad, R. Madhusudan, J. G. Powles. A molecular simulation to investigate the possibility of electro-osmosis in non-ionic solutions with uniform electric fields. *Mol Phys* 90:671, 1997; R. Madhusudan, J. Lin, S. Murad. Molecular simulations of electro-osmosis in fluid mixtures using semi-permeable membranes. *Fluid Phase Equil* 150:97, 1998.

27. P. Zumbusch, W. Kulcke, G. Brunner. Use of alternating electric fields as anti-fouling strategy in ultrafiltration of biological suspensions. Introduction of a new experimental procedure for crossflow filtration. *J Memb Sci* 142:75 (1998).
28. R. L. Rowley, T. D. Shupe, M. W. Schuck. A direct method for determination of chemical potential with molecular dynamics simulations. 1. Pure components. *Mol Phys* 82:841, 1994.
- 28a. J. D. Weeks, D. Chandler, H. C. Andersen. Role of repulsive forces in determining the equilibrium structure of simple liquids. *J Chem Phys* 54:5237, 1971.
29. R. L. Rowley, M. W. Schuck, J. Perry. A direct method for determination of chemical potential with molecular dynamics simulations. 2. Mixtures. *Mol Phys* 86:125, 1995.
30. R. L. Rowley, M. Henriksen. Calculation of chemical potential for structured molecules using osmotic molecular dynamics simulations. *Fluid Phase Equil* 137:75, 1997.
31. K. P. Tikhomolova. *Electro-osmosis*. New York: Horwood, 1993.
32. H. A. Pohl. *Dielectrophoresis*. Cambridge: Cambridge University Press, 1978.
33. S. Glasstone. *Textbook of Physical Chemistry*. London: Macmillan, 1956.
34. D. H. Everett. *Basic Principles of Colloid Science*. London: Royal Society of Chemistry, 1988.
35. A. K. Jain, R. K. Srivastava, M. K. Gupta, S. K. Das. A novel technique in membrane separation processes: Electroosmotic separation of benzene in ethanol solution. *J Memb Sci* 78:53, 1993.
36. C. R. A. Catlow, S. C. Parker, M. P. Allen, eds. *Computer Modeling of Fluids, Polymers and Solids*. Boston: Kluwer, 1990.
37. R. O. Watts. Monte-Carlo studies of liquid water. *Mol Phys* 28:1069, 1974.
38. I. G. Tironi, R. Sperb, P. E. Smith, W. F. van Gunsteren. A generalized reaction field method for molecular dynamics simulations. *J Chem Phys* 102:5451, 1995.
39. J. G. Powles, M. J. D. Mallett, G. Rickayzen, W. A. B. Evans. Exact analytical solutions for diffusion impeded by an infinite array of partially permeable barriers. *Proc Royal Soc London* 437:391, 1992.
40. J. G. Powles, M. Pogoda. A flexible model for the simulation of fluids in infinite porous systems. *Mol Phys* 78:757, 1993.
41. P. Marsh, G. Rickayzen, M. Calleja. The structure of a hard sphere fluid restricted by permeable walls. *Mol Phys* 84:799, 1995.
42. N. Margaritis, G. Rickayzen. The structure of a fluid confined by permeable walls. *Mol Phys* 90:189, 1997.
43. M. Borówko, P. Bryk, O. Pizio, S. Sokołowski. Fluids in contact with periodic semi-permeable walls; an integral equation approach. *Mol Phys* 94:867, 1998.

# 17

## Double Layer Theory: A New Point of View

**JANUSZ STAFIEJ** Department of Electrode Processes, Institute of Physical Chemistry, Polish Academy of Sciences, Warsaw, Poland

**JEAN BADIALI** Structure et Réactivité des Systèmes Interfaciaux, Université P. et M. Curie, Paris, France

I. Introduction	800
II. Short Overview of the State of the Art	803
A. An example of electrified interface	803
B. Short overview concerning the electrical double layer theory	803
III. A Field-theoretic Approach to the Electrified Interfaces	805
A. Field theory and standard statistical mechanics	806
B. Field theory and density functional theory	807
C. The mean-field approximation	807
IV. Construction of the Effective Hamiltonian	808
A. Construction of the Hamiltonian step by step	808
B. Global construction of the Hamiltonian	812
V. A Field-theoretic Approach to Ionic Solutions	812
A. Local approximation	814
B. Non-local approximation	815
VI. Charged Interfaces in a Linear Regime	817
VII. The Role of the Specific Interaction in the Nonlinear Regime	821
A. Nonlinear Gouy–Chapman theory	821
B. Role of the specific interaction	823

VIII. The Role of Non-locality in the Nonlinear Regime	835
A. Numerical results: profiles, center of gravity, and capacitance	836
B. Lie group description and trajectories	842
IX. Conclusions	846
References	846

I. INTRODUCTION

In conducting media, the screening of electric charges is one of the most important phenomena. In particular, it determines the behavior of these systems when they are submitted to an electrical perturbation. At thermodynamic equilibrium, as a consequence of the screening, the net electric field vanishes in bulk conductive systems. The field may survive only in thin layers surrounding inhomogeneities. For example, when two conductive systems are put into contact their interface gives rise to the electrical double layer, so named because it implies the formation of two charge distributions of opposite sign located on each side of the interface. As the electrostatic attraction opposes charge separation in the electrical double layer, its structure results from the competition between electrostatic and non-electrostatic interactions.

The existence of a double layer determines the properties of many systems in electrochemistry, in colloidal sciences, in biology, etc. [1–4]. Owing to their importance, electrical double layers have long been and remain a subject of intense research on both experimental and theoretical aspects. This is covered by some recent textbooks and review articles [3,5–10].

In this paper we have in mind a theoretical description of the electrical double layer formed at the ideally polarizable interface, i.e., without charge transfer between the two phases. A great simplification of these systems is that they can be treated by equilibrium thermodynamics and statistical mechanics over a wide range of potential difference polarizing the interface. The best known example is the mercury–solution interface. It has been perhaps the most extensively investigated system since the first studies by Helmholtz, more than one century ago [2]. After Helmholtz, the basic tools in the theory of electrified interfaces were built up by Gouy, Chapman, and Stern [2]. A large contribution to this field of investigation came from the comparison between theory and experiments performed by Grahame [11]. During the last twenty years, the theoretical advancements in the liquid state theory have been applied to the description of the electrolyte structure at

charged interfaces. In parallel, progress in surface science has led to the model of the metal surface accounting for the electron spillover traditionally considered as an ideal charged plane [12,13]. New spectroscopic methods and the use of the scanning tunnel microscope have opened a large field of new investigations [5].

From the experimental results and theoretical approaches we learn that even the simplest interface investigated in electrochemistry is still a very complicated system. To describe the structure of this interface we have to tackle several difficulties. It is a many-component system. Between the components there are different kinds of interactions. Some of them have a long range while others are short ranged but very strong. In addition, if the solution side can be treated by using classical statistical mechanics the description of the metal side requires the use of quantum methods. The main feature of the experimental quantities, e.g., differential capacitance, is their nonlinear dependence on the polarization of the electrode. There are such sophisticated phenomena as ionic solvation and electrostriction invoked in the attempts of interpretation of this nonlinear behavior [2].

However, instead of focusing on more and more sophisticated phenomena in this article we should like to identify the main ingredients which determine the gross features of the interfacial properties. We have two main goals. First, we want to select very simple ingredients present at any charged interface and to show that they are already able to produce a large class of behaviors. We focus on the solution side. The opposite side, called "*the wall*" hereafter, is considered as an ideal charged plane. The solvent is reduced to a dielectric continuum. Only ions and their distributions at the interface are relevant for us this time. We assume that there is an effective non-electrostatic interaction between the ions themselves as well as between the ions and the wall in addition to the electrostatic interaction. Just on the basis of these simple facts, we would like to answer some fundamental questions such as:

- (i) what is the result of the competition between electrostatic energy and entropy?
- (ii) how is the interfacial structure influenced by the competition between electrostatic and non-electrostatic interaction?
- (iii) can we describe in a simple way how the interfacial structure is modified when the charge on the wall is changed?

Our second goal is to introduce these simple phenomena in a statistical mechanical scheme such that the calculations keep a transparent significance at each step. Nowadays, the predictions of theoretical approaches depend on approximations of a high level of technicality in the domain of liquid state theory. These approximations seem to have a mathematical rather than

a physical origin. It appears difficult for non-specialists to develop intuitions on their nature and validity and, despite their successes, these approximations have hardly been used in the analysis of experimental data. For instance, in order to describe the structure of an ionic solution formed of point ions immersed in a dielectric continuum we can use the hypernetted chain approximation or the Poisson–Boltzmann theory [10]. Compared to Monte Carlo results, the first approach is more exact than the latter although both may lead to the same results, at least qualitatively, up to moderate charge densities and concentrations. However, the combination of the Boltzmann factor with the Poisson equation leads to a very transparent approach commonly preferred in the analysis of experimental data.

To describe the simple phenomena mentioned above, we would like to have only transparent approximations as in the Poisson–Boltzmann theory for ionic systems or in the van der Waals theory for non-coulombic systems [14]. Certainly there are many ways to reach this goal. Here we show that a field-theoretic approach is well suited for that. Its advantage is to focus on some aspects of charged interfaces traditionally paid little attention; for instance, the role of symmetry in the effective interaction between ions and the analysis of the profiles in terms of a transformation group, as is done in quantum field theory.

This paper is organized as follows. Having in mind an example of ideal polarizable interface, in Sec. II we introduce the main experimental quantities that we try to interpret and a short overview on the evolution of the double layer theory. In Sec. III we present the main aspects of our field-theoretic description of electrified interfaces. This approach is compared with standard statistical mechanics and with the density functional theory. Then the mean-field theory is introduced. In Sec. IV we present a step-by-step construction of the Hamiltonian and then a more global construction is introduced. To check the validity of the Hamiltonian and illustrate how the theory works, a short presentation of recent results for bulk ionic solutions is given in Sec. V. Then we analyze the case when the charge density on the wall and the adsorption potential located on the wall are small enough to have a linear regime and a simpler Hamiltonian for which the interfacial properties can be derived exactly. In the last two sections we consider highly charged interfaces in the presence of an adsorbing potential, not necessarily small. In Sec. VII we consider a Hamiltonian which introduces a renormalization of the Debye length and leads to results very different from the nonlinear Gouy–Chapman theory. The last section is devoted to the analysis of a more complete system in which a new length of non-electrostatic origin is present in addition to the Debye length. Finally, we conclude and give some perspectives.



## II. SHORT OVERVIEW OF THE STATE OF THE ART

### A. An Example of Electrified Interface

A typical example of an ideal polarizable interface is the mercury–solution interface [1,2]. From an experimental point of view it is characterized by its electrocapillary curve describing the variation of the interfacial tension  $\gamma$  with the potential drop across the interface,  $\phi$ . Using the thermodynamic relation due to Lippmann, we get the charge of the wall  $\sigma$  ( $-\sigma$  is the charge on the solution side) from the derivative of the electrocapillary curve:

$$\sigma = -\left(\frac{\partial\gamma}{\partial\phi}\right)_{\rho_+, \rho_-, T} \quad (1)$$

In this partial derivative the temperature  $T$  and the ionic concentrations  $\rho_+$  and  $\rho_-$  in the bulk phase are kept constant. Hereafter we assume that we have a 1:1 electrolyte,  $\rho_+ = \rho_- = \rho_b/2$ . Taking the derivative of (1) relative to  $\phi$  we get

$$C = -\left(\frac{\partial^2\gamma}{\partial\phi^2}\right)_{\rho_+, \rho_-, T} = \left(\frac{\partial\sigma}{\partial\phi}\right)_{\rho_+, \rho_-, T} \quad (2)$$

which defines  $C$  as the differential capacitance of the electrode. Because of the thermodynamic stability conditions, differential capacitance is positive. Then Eq. (1) shows that the charge density on both sides of the interface is a reversible function of the applied potential and vanishes for the potential  $\phi_0$  at the maximum of the electrocapillary curve. Experimentally, differential capacitance  $C$  can be obtained from the zero frequency, zero amplitude limit of the measured impedance. This is the path used in the case of solid electrodes. From the Gibbs isotherm we can also get the adsorption of ions [1]. We select ionic adsorption,  $\phi_0$ , and  $C$  as the experimental quantities that we try to interpret.

### B. Short Overview Concerning the Electrical Double Layer Theory

Since the interface behaves like a capacitor, Helmholtz described it as two rigid charged planes of opposite sign [2]. For a more quantitative description Gouy and Chapman introduced a model for the electrolyte at a microscopic level [2]. In the Gouy–Chapman approach the interfacial properties are related to ionic distributions at the interface, the solvent is a dielectric medium of dielectric constant  $\epsilon$  filling the solution half-space up to the perfect charged plane—the wall. The ionic solution is considered as formed

of point ions submitted only to coulombic interactions. The interface is described by the following Hamiltonian

$$H_{GC}(\mathbf{p}, \mathbf{r}) = \sum_i \frac{\vec{p}_i^2}{2m_i} + \frac{1}{4\pi\epsilon} \sum_{i>j} \frac{e^2}{|\vec{r}_i - \vec{r}_j|} + \frac{\sigma}{\epsilon} \sum_i z_i q_i \quad (3)$$

where the summations run over all ions in the system,  $\vec{p}_i$  is the momentum and  $\vec{r}_i = (x_i, y_i, z_i)$  is the position of the  $i$ th ion with a mass  $m_i$ . The wall is placed at  $z = 0$ . No image potential is considered. From (3) the thermodynamic properties of the interface can be calculated via the partition function  $Z$ , and by the usual methods we can calculate the ionic profiles. In standard statistical mechanics we have [15]

$$Z = \frac{1}{h^{3(N_+ + N_-)} N_+! N_-!} \int \exp[-\beta H_{GC}(\mathbf{p}, \mathbf{r})] d\Gamma \quad (4)$$

where  $\Gamma$  refers to the position of one point in the phase space; as usual,  $\beta$  is  $1/(k_B T)$  and  $h$  is the Planck constant. The free energy of the interface is given by:

$$F = -k_B T \ln Z \quad (5)$$

Instead of an exact calculation, Gouy and Chapman have assumed that (4) can be approximated by combining the Poisson equation with a Boltzmann factor which contains the mean electrical potential existing in the interface. (This approximation will be rederived below). From this approach the distribution of the potential across the interface can be calculated as the function of  $\sigma$  and from (2) we get a differential capacitance  $C_{GC}$ . It has been shown by Grahame that  $C_{GC}$  fits very well the measurements in the case of low ionic concentrations [11]. For higher concentrations another capacitance in series,  $C_i$ , had to be introduced. It is called the inner layer capacitance and it was first considered by Stern [1,2]. Then the experimental capacitance  $C_{exp}$  is analyzed according to:

$$\frac{1}{C_{exp}} = \frac{1}{C_i} + \frac{1}{C_{GC}} \quad (6)$$

In some cases, e.g., the Hg/NaF<sub>aq</sub> interface,  $C_i$  is charge dependent but concentration independent. Then it is said that there is no specific ionic adsorption. In order to interpret the charge dependence of  $C_i$  a standard explanation consists in assuming that  $C_i$  is related to the existence of a solvent monolayer in contact with the wall [16]. From a theoretical point of view this monolayer is postulated as a subsystem coupled with the metal and the solution via electrostatic and non-electrostatic interactions. The specific shape of  $C_i$  versus  $\sigma$  results from the competition between these interactions and the interactions between solvent molecules in the monolayer. This description of the electrical double layer has been revisited by

introducing the recent progress in statistical mechanics [7,8]. First, at the MacMillan–Mayer level of description of the electrolyte the solvent is formally eliminated by introducing the effective potentials of mean force describing interactions of the ions with themselves and with the wall in presence of the solvent. At this level, instead of considering point ions, more realistic potentials of mean force have been introduced. As an example of such potentials we can consider the primitive electrolyte model, i.e., charged hard spheres embedded in a dielectric continuum. The primitive model required a more sophisticated approach than Poisson–Boltzmann theory for pointlike ions. Several approximation schemes have been introduced and their results compared with computer simulations. These new approaches show that the Gouy–Chapman theory retains the major facts which determine the gross features of the interfacial properties, at least for moderate charge and concentrations.

Secondly, the solvent has been introduced on the same footing as the ions. For low values of the charge the mean spherical approximation (MSA) has been extensively used, whereas some more complicated approximations are needed to describe the nonlinear behavior versus  $\sigma$  or  $\phi$ .

Another progress in our understanding of the ideally polarizable electrode came from theoretical works showing that the metal side of the interface cannot be considered just as an ideal charged plane. A simple quantum-mechanical approach shows that the distribution of the electron gas depends both on the charge of the electrode and on the metal–solution coupling [12,13].

Certainly these approaches represent a progress in our understanding of the interfacial properties. All the phenomena taken into account, e.g., the coupling with the metal side, the degree of solvation of ions, etc., play a role in the interfacial structure. However, it appears that the theoretical predictions are very sensitive to the details of the interaction potentials between the various species present at the interface and also to the approximations used in the statistical treatment of the model. In what follows we focus on a small number of basic phenomena which, probably, determine the interfacial properties, and we try to use very transparent approximations to estimate the role of these phenomena.

### **III. A FIELD-THEORETIC APPROACH TO THE ELECTRIFIED INTERFACES**

In this section we introduce the basic ingredients of a field-theoretic approach to electrified interfaces and compare it with both the standard method of statistical mechanics and the density functional theory.

## A. Field Theory and Standard Statistical Mechanics

In the previous section we saw on an example the main steps of a standard statistical mechanical description of an interface. First, we introduce a Hamiltonian describing the interaction between particles. In principle this Hamiltonian is known from the model introduced at a microscopic level. Then we calculate the free energy and the interfacial structure via some approximations. In principle, this approach requires us to explore the overall phase space which is a manifold of dimension  $6N$  equal to the number of degrees of freedom for the total number of particles,  $N$ , in the system.

Instead of starting from particles, we assume that the interfacial properties can be described in terms of fields [17]. We characterize the state of the interface by specifying two fields which give us the distributions of anions,  $\rho_-(\vec{r})$ , and cations,  $\rho_+(\vec{r})$ , or a combination of them such as the charge,  $q(\vec{r})$ , and density,  $s(\vec{r})$  distributions which are defined as [18,19]

$$q(\vec{r}) = \rho_+(\vec{r}) - \rho_-(\vec{r}) \quad (7)$$

$$s(\vec{r}) = \rho_+(\vec{r}) + \rho_-(\vec{r}) \quad (8)$$

We assume that exploring all possible forms for the fields corresponds to exploring the overall usual phase space. To determine the partition function  $Z$  the contributions from all the  $\rho_+(\vec{r})$  and  $\rho_-(\vec{r})$  distributions are summed up with a statistical weight, dependent on  $\rho_+(\vec{r})$  and  $\rho_-(\vec{r})$ , put in the form analogous to the Boltzmann factor:  $\exp[-\beta\mathcal{H}^{\text{eff}}[\rho_+(\vec{r}), \rho_-(\vec{r})]]$ , where the effective Hamiltonian  $\mathcal{H}^{\text{eff}}[\rho_+(\vec{r}), \rho_-(\vec{r})]$  is a functional of the fields. The partition function is obtained by a functional integral

$$Z = \int \mathcal{D}\rho_+(\vec{r}) \mathcal{D}\rho_-(\vec{r}) \exp[-\beta\mathcal{H}^{\text{eff}}[\rho_+(\vec{r}), \rho_-(\vec{r})]] \quad (9)$$

This expression has a formal character and has to be complemented with a prescription for its evaluation. *A priori*, we can vary the values of the fields independently at each point in space and then we deal with uncountably many degrees of freedom in the system, in contrast with the usual statistical thermodynamics as seen above. Another difference with the standard statistical mechanics is that the effective Hamiltonian has to be created from the basic phenomena that we want to investigate. However, a description in terms of fields seems quite natural since the average of fields gives us the actual distributions of particles at the interface, which are precisely the quantities that we want to calculate. In a field-theoretical approach we are closer to the problem under consideration than in the standard approach and then we may expect that a simple Hamiltonian is sufficient to retain the main features of the charged interface. *A priori*, we have no insurance that it

is effectively so. However, we know that such an argument explains for a large part why the density functional theory is so popular nowadays [14,20]. Bearing in mind this point, it seems natural to compare these two kinds of approach.

## B. Field Theory and Density Functional Theory

Let us underline some similarities and differences between a field theory (FT) and a density functional theory (DFT). First, note that for either FT or DFT the standard microscopic-level Hamiltonian is not the relevant quantity. The DFT is based on the existence of a unique functional of ionic densities  $\tilde{\Omega}[\rho_+(\vec{r}), \rho_-(\vec{r})]$  such that the grand potential  $\Omega$  of the studied system is the minimum value of the functional  $\tilde{\Omega}$  relative to any variation of the densities, and then the trial density distributions for which the minimum is achieved are the average equilibrium distributions. Only some schemes of approximations exist in order to determine  $\tilde{\Omega}$ . In contrast to FT no functional integrations are involved in the calculations. In FT we construct the effective Hamiltonian  $\mathcal{H}^{\text{eff}}[\rho_+(\vec{r}), \rho_-(\vec{r})]$  which never reduces to a thermodynamic quantity that we can associate with the system under investigation. We see from Eq. (9) that a functional integration has to be performed to obtain the partition function  $Z$ . As we shall see on an example, the functional integration produces a mixture between the various contributions to the effective Hamiltonian. Instead of the optimization condition which exists in DFT, in FT we have the following relation [21]

$$\left\langle \frac{\delta \mathcal{H}^{\text{eff}}[\rho_+(\vec{r}), \rho_-(\vec{r})]}{\delta \rho_i(\vec{r})} \right\rangle = 0 \quad (10)$$

where  $i$  represents  $+$  or  $-$ . In this equation  $\rho_i(\vec{r})$  is a field—that is to say, a fluctuating quantity not necessarily having the symmetry of the equilibrium system. For instance, in a planar geometry the field may vary parallel to the wall. A discussion of some differences between DFT and FT is given by Evans [20].

## C. The Mean-field Approximation

For a given Hamiltonian the calculation of the partition function can be done exactly in only few cases (some of them will be presented below). In general the calculation requires a scheme of approximations. Mean-field approximation (MFA) is a very popular approximation based on the steepest descent method [17,22]. In this case it is assumed that the main contribution to  $Z$  is due to fields which are localized in a small region of the functional space. More crudely, for each kind of particle only one field is

taken into account for which  $\mathcal{H}^{\text{eff}}[\rho_+(\vec{r}), \rho_-(\vec{r})]$  is minimum. Since we try to find the minimum keeping the total number of particles of each species constant, the relevant profiles in the MFA are given by

$$\frac{\delta \mathcal{H}^{\text{eff}}}{\delta \rho_i(\vec{r})} = \mu_i \quad (11)$$

where  $\mu_i$  is the Lagrange multiplier associated with the field  $\rho_i$ . We have to make sure that Eq. (11) yields a minimum, not a maximum or an inflexion point, e.g., considering the second derivative. In MFA,  $\mathcal{H}^{\text{eff}}[\rho_+(\vec{r}), \rho_-(\vec{r})]$  has to be a sort of free energy that we note  $\mathcal{F}^{\text{MFA}}$ . Eq. (11) can be rewritten as

$$\frac{\delta(\mathcal{H}^{\text{eff}} - \sum_{i=\pm} \mu_i \int \rho_i(\vec{r}) d\vec{r})}{\delta \rho_i(\vec{r})} = \frac{\delta \Omega^{\text{MFA}}}{\delta \rho_i(\vec{r})} = 0 \quad (12)$$

where we have defined  $\Omega^{\text{MFA}}$  as the grand potential in the MFA. This result is reminiscent of the DFT, but it is important to point out that this is an approximation in contrast to the exact minimization condition derived in the DFT.

Finally, before constructing  $\mathcal{H}^{\text{eff}}[\rho_+(\vec{r}), \rho_-(\vec{r})]$  we can note that we have introduced a field-theoretic approach on a heuristic basis where the fields have a clear physical meaning. For the point particle coulomb gas there is a rigorous transformation of the usual statistical mechanics to a field-theoretic formulation in which, however, the field has no apparent physical meaning (see, e.g., [23,24]).

#### IV. CONSTRUCTION OF THE EFFECTIVE HAMILTONIAN

To obtain  $\mathcal{H}^{\text{eff}}[\rho_+(\vec{r}), \rho_-(\vec{r})]$  or shortly  $\mathcal{H}^{\text{eff}}$  we start with a step-by-step construction and we then consider a more global approach.

##### A. Construction of the Hamiltonian Step by Step

To obtain  $\mathcal{H}^{\text{eff}}$  we may try to elaborate several rules, taking into account what is already known in the literature relative to the construction of the Landau Hamiltonian [25] or at the level of quantum field theory [17,22,26].

First, there are some general constraints on the global Hamiltonian. Obviously  $\mathcal{H}^{\text{eff}}$  must contain the physics which is assumed to be essential for the problem under consideration. In our case the coulombic interaction and the ideal entropy play this role. Another requirement is that  $\mathcal{H}^{\text{eff}}$  leads

to a well defined physics. In particular, the partition function should be finite for the fields of the form constrained by the physics of the system. In our case the global electroneutrality condition is an example of the constraint. Secondly, in the construction of  $\mathcal{H}^{\text{eff}}$  we distinguish the contributions by the scale on which they act. We may consider local terms focusing on one point in contrast to non local terms with a coupling between one point and its neighborhood. The coulombic interaction creates a long-range coupling between separated parts of the system. Thirdly, as in the quantum field theory [22], we may demand that the MFA already gives an acceptable description of the system. The MFA cannot produce the exact behavior of the system but it must retain some ingredients in a realistic form.

In our  $\mathcal{H}^{\text{eff}}$  we first introduce two basic ingredients which are expected to exist for any coulombic system. Then we consider more specific terms.

### 1. The Basic Ingredients

The first basic ingredient in our description of the electric double layer is the coulombic interaction. It seems quite natural to assume that the fields are coupled according to a coulombic Hamiltonian  $\mathcal{H}^{\text{coul}}$  of the same form as the Hamiltonian coupling the densities defined at a microscopic level [15]:

$$\mathcal{H}^{\text{coul}} = \frac{e^2}{8\pi\epsilon} \int \frac{[q^{\text{ext}}(\vec{r}) + q(\vec{r})][q^{\text{ext}}(\vec{r}') + q(\vec{r}')] }{|\vec{r} - \vec{r}'|} d\vec{r}d\vec{r}' \quad (13)$$

where  $e$  is the electronic charge,  $q(\vec{r})$  has been defined in (7) and  $eq^{\text{ext}} = \sigma\delta(z)$  is the charge distribution on the wall. Due to  $\mathcal{H}^{\text{coul}}$  all the points of the interface are coupled. If we assume that  $\mathcal{H}^{\text{eff}}$  is reduced to  $\mathcal{H}^{\text{coul}}$  given by Eq. (13) then in the MFA there is only one field  $q(\vec{r})$  to be determined from the minimum condition (11) taking the form

$$\frac{\delta\mathcal{H}^{\text{eff}}}{\delta q(\vec{r})} = \frac{1}{4\pi\epsilon} \int \frac{q^{\text{ext}}(\vec{r}') + q(\vec{r}')}{|\vec{r} - \vec{r}'|} d\vec{r}' = V(\vec{r}) = (\mu_+ - \mu_-) \quad (14)$$

where  $V(\vec{r})$  is the electrostatic potential. This equation shows that  $V(\vec{r})$  must be constant everywhere in the interface. Then the charge on the solution side must be given by  $eq(\vec{r}) = -\sigma\delta(z)$ , showing that we have a perfect screening of the charge on the wall. In a real system we expect that entropy destroys this ideal behavior.

We have seen that  $\mathcal{H}^{\text{eff}}$  has to behave like a free energy in the MFA, and then in addition to the interaction an entropy term has to be introduced into  $\mathcal{H}^{\text{eff}}$ . Since the ideal entropy is a functional of the particle distributions we will assume that there is the same kind of functional in terms of fields. Thus

we introduce  $\mathcal{H}^{\text{ideal}}$  according to

$$\beta\mathcal{H}^{\text{ideal}}[\rho_+(\vec{r}), \rho_-(\vec{r})] = \beta\mathcal{H}^{\text{ideal}} = \int \left\{ \rho_+(\vec{r}) \left[ \ln \frac{\rho_+(\vec{r})}{\rho_{\text{ref}}} - 1 \right] + \rho_-(\vec{r}) \left[ \ln \frac{\rho_-(\vec{r})}{\rho_{\text{ref}}} - 1 \right] \right\} d\vec{r} \quad (15)$$

where  $\rho_{\text{ref}}$  is a reference density. In a recent paper this formula has been derived by using a lattice model and a coarse graining procedure [19].

If we assume that  $\mathcal{H}^{\text{eff}} = \mathcal{H}^{\text{coul}} + \mathcal{H}^{\text{ideal}}$  the following simple and interesting result is obtained in MFA:

$$\frac{\delta\beta\mathcal{H}^{\text{eff}}}{\delta\rho_i(\vec{r})} = \beta eV(\vec{r}) + \ln \frac{\rho_i(\vec{r})}{\rho_{\text{ref}}} - \mu_i = 0 \quad (16)$$

Both entropic and coulombic contributions are bounded from below and it can be verified that the second variation of  $\mathcal{H}^{\text{eff}}$  is positive definite so that the above equations correspond to a minimum [27]. Using conditions in the bulk we can eliminate  $\mu_i$  from the equations. Then we get the Boltzmann equation in which the electric potential verifies the Poisson equation by construction. Hence  $\mathcal{H}^{\text{eff}} = \mathcal{H}^{\text{coul}} + \mathcal{H}^{\text{ideal}}$  is equivalent within MFA to the nonlinear Gouy–Chapman theory. In this subsection we have introduced two contributions which have a universal form for any charged interface. A realistic  $\mathcal{H}^{\text{eff}}$  must also contain more terms which should be specific for a given electrolyte.

## 2. Specific Contributions

In addition to the entropy term we assume that there is an extra local coupling between the fields via  $\mathcal{H}^{\text{loc}}$  and, in addition to the coulombic coupling which is long range, we assume the existence of a short-range non-local coupling via  $\mathcal{H}^{\text{nonloc}}$ . We can choose several functional forms to represent these two new terms. In the spirit of our main goals presented in the Introduction we will try the most simple functional forms. For  $\mathcal{H}^{\text{loc}}$  we consider a quadratic form while for  $\mathcal{H}^{\text{nonloc}}$  we introduce a square-gradient term already suggested by van der Waals in the last century [14]. The combination of these two Hamiltonians reproduces the so-called “Gaussian model” largely used in the literature [17].  $\mathcal{H}^{\text{loc}}$  is explicitly defined according to [28]

$$\beta\mathcal{H}^{\text{loc}} = \frac{1}{2} \int [\tilde{a}_{++}\rho_+^2(\vec{r}) + 2\tilde{a}_{+-}\rho_+(\vec{r})\rho_-(\vec{r}) + \tilde{a}_{--}\rho_-^2(\vec{r})] d\vec{r} \quad (17)$$

$$= \frac{1}{2} \int [\tilde{a}_{qq}q^2(\vec{r}) + 2\tilde{a}_{qs}q(\vec{r})s(\vec{r}) + \tilde{a}_{ss}s^2(\vec{r})] d\vec{r} \quad (18)$$



The phenomenological coefficients:  $\tilde{a}_{++}$ ,  $\tilde{a}_{+-}$ , and  $\tilde{a}_{--}$  are related to  $\tilde{a}_{qq}$ ,  $\tilde{a}_{qs}$ , and  $\tilde{a}_{ss}$  by a simple linear transformation

$$\tilde{a}_{qq} = \frac{\tilde{a}_{++} + \tilde{a}_{--} - 2\tilde{a}_{+-}}{4} \quad (19)$$

$$\tilde{a}_{ss} = \frac{\tilde{a}_{++} + \tilde{a}_{--} + 2\tilde{a}_{+-}}{4} \quad (20)$$

$$\tilde{a}_{qs} = \frac{\tilde{a}_{++} - \tilde{a}_{--}}{4} \quad (21)$$

We may give a meaning to the coupling constants  $\tilde{a}_{ij}$  in  $\mathcal{H}^{\text{loc}}$  by considering the MFA for the effective Hamiltonian  $\mathcal{H}^{\text{eff}} = \mathcal{H}^{\text{coul}} + \mathcal{H}^{\text{ideal}} + \mathcal{H}^{\text{loc}}$ . From the MFA equations we find for cations:

$$\beta e V(\vec{r}) + \ln \frac{\rho_+(\vec{r})}{\rho_{\text{ref}}} + [\tilde{a}_{++}\rho_+(\vec{r}) + \tilde{a}_{+-}\rho_-(\vec{r})] = \mu_+ \quad (22)$$

The structure of this equation suggests that we associate  $\mu_+$  with the chemical potential of cations and  $[\tilde{a}_{++}\rho_+(\vec{r}) + \tilde{a}_{+-}\rho_-(\vec{r})]$  with the logarithm of the activity coefficient relative to cations in the MFA. In addition to their thermodynamic significance, these coefficients characterize the symmetry of the interactions between ions. For example, if  $\tilde{a}_{++} = \tilde{a}_{--}$  then  $\tilde{a}_{qs}$  vanishes and there is no coupling between charge and density distribution at the interface.

The non-local contribution  $\mathcal{H}^{\text{nonloc}}$  is defined by [28]

$$\beta \mathcal{H}^{\text{nonloc}} = \frac{1}{2} \sum_{i,j} \int \tilde{b}_{ij} [\nabla \rho_i(\vec{r}) \nabla \rho_j(\vec{r})] d\vec{r} \quad (23)$$

where  $i, j = +, -$  in the ionic densities frame and  $i, j = q, s$  in the charge-overall density frame. The transformations from  $\tilde{b}_{++}$ ,  $\tilde{b}_{+-}$  and  $\tilde{b}_{--}$  to  $\tilde{b}_{qq}$ ,  $\tilde{b}_{qs}$  and  $\tilde{b}_{ss}$  are similar to those for  $\tilde{a}_{ij}$ . Hereafter we consider a simplified version in which  $\tilde{b}_{++} = \tilde{b}_{+-} = \tilde{b}_{--} = \tilde{b}$ , i.e., the ions are totally symmetric with respect to the non-local interaction introduced with the square gradient form. In the other representation it means that  $\tilde{b}_{qq} = 0$  and  $\tilde{b}_{qs} = 0$ . Thus the non-locality introduced acts only on the overall ionic density,  $\beta \mathcal{H}^{\text{nonloc}} = \frac{1}{2} \int \tilde{b} [\nabla \tilde{s}(\vec{r})]^2$ , and does not interfere directly with the non-locality introduced by the coulombic interaction.

Till this point an electric coupling with the wall is assumed. More generally, we may assume the existence of a short-range potential located at the wall. The following form will be used:

$$\beta \mathcal{H}^{\text{surf}} = \int (\tilde{h}_+\rho_+(\vec{r}) + \tilde{h}_-\rho_-(\vec{r}))\delta(z)d\vec{r} \quad (24)$$

Similar surface terms are commonly used in the description of interfacial systems. They correspond to the idea of a localized interaction with the wall. This has been used in the description of adsorption (see, e.g., [29]), wetting phenomena [30] and interfacial criticality [31].

## B. Global Construction of the Hamiltonian

In a recent publication [32] a more global approach of  $\mathcal{H}^{\text{eff}}$  has been suggested to describe the bulk properties of ionic solutions. We write

$$\mathcal{H}^{\text{eff}} = \mathcal{H}^{\text{coul}} + \mathcal{H}^0 \quad (25)$$

and assume that  $\mathcal{H}^0$  is the Hamiltonian for an uncharged system. For bulk phases the MFA leads to  $\mathcal{F}^{\text{MFA}} = \mathcal{H}^0$ , i.e., there is no electrostatic contribution to  $\mathcal{F}^{\text{MFA}}$ . To describe the charged system we assume that  $\mathcal{H}^0$  can be approximated by the actual free energy of a real uncharged system. Correlations in this system are assumed to be short ranged. When  $\mathcal{H}^{\text{eff}}$  is considered, the coulombic interaction creates charge and density distributions in the system. Then we may replace  $\mathcal{H}^0$  by the functional that we can calculate, at least in principle, by the standard methods of statistical mechanics [15]. Note that  $\mathcal{H}^0$  is not the functional of the density appearing in the DFT. In the calculation of the free energy several levels of approximation can be used. For example, a functional expansion of  $\mathcal{H}^0$  in terms of fields can be performed and stopped at a given order. Since  $\mathcal{H}^0$  is a real free energy, the coefficient in the expansion can be related to the correlation functions of the uncharged system. If we focus only on the long-range behavior an expansion in terms of the wave vector  $\vec{k}$  can be considered.

We can use  $\mathcal{H}^{\text{eff}}$  to investigate both the bulk and surface properties of ionic systems. Although this paper is essentially devoted to the double layer, in the next section we summarize some results obtained for bulk phases. On this example we can check the construction of the Hamiltonian and illustrate how this approach works. In addition, in the simplest case we can go beyond the MFA and do an exact calculation.

## V. A FIELD-THEORETIC APPROACH TO IONIC SOLUTIONS

A field-theoretic approach has been already introduced in order to describe the structure and thermodynamics of charged systems (see, e.g., [33–38]).

Here we start from the generating functional

$$Z[J] = \int \mathcal{D}\rho_+(\vec{r}) \mathcal{D}\rho_-(\vec{r}) \exp \left[ -\beta \mathcal{H}^{\text{eff}}[\rho_+(\vec{r}), \rho_-(\vec{r})] + \sum_{i=\pm} \int J_i(\vec{r}) \rho_i(\vec{r}) d\vec{r} \right] \quad (26)$$

in which  $J_i$  is an external field. The correlation functions can be calculated according to [22]

$$g_{ij}(\vec{r}_1, \vec{r}_2) = \frac{\delta^2 Z[J]}{\delta J_i(\vec{r}_1) \delta J_j(\vec{r}_2)} \bigg|_{J_i=0} \quad (27)$$

When the MFA is used in absence of the external field ( $J_i = 0$ ) the Lagrange multipliers  $\mu_i$  are assumed to give the actual density,  $\tilde{\rho}_i$ , known by construction. In presence of the field the MFA gives a correction  $\delta\tilde{\rho}_i$  to the density  $\tilde{\rho}_i$ . By using the linear response theory we can establish a linear functional relation between  $J_i$  and  $\delta\tilde{\rho}_i$ . The fields  $\rho_i(\vec{r})$  can be expressed in term of a new field  $\delta\rho_i(\vec{r})$  defined according to  $\rho_i(\vec{r}) = \tilde{\rho}_i + \delta\tilde{\rho}_i + \delta\rho_i(\vec{r})$ . Now, we may perform a functional expansion of  $\mathcal{H}^{\text{eff}}$  in terms of  $\delta\rho_i(\vec{r})$ . If this expansion is limited to a quadratic form in  $\delta\rho_i(\vec{r})$  we get the following result [32]

$$Z[J] = Z^{\text{MFA}} (\det \beta \mathcal{A})^{-1/2} \exp \left[ \int \sum_{i,j} J_i(\vec{r}_1) \mathcal{A}_{ij}^{-1}(\vec{r}_1, \vec{r}_2) J_j(\vec{r}_2) d\vec{r}_1 d\vec{r}_2 \right] \quad (28)$$

where the matrix  $\mathcal{A}$  is defined by

$$\mathcal{A}_{ij}(\vec{r}_1, \vec{r}_2) = \frac{\delta^2 \beta \mathcal{H}^{\text{eff}}}{\delta \rho_i(\vec{r}_1) \delta \rho_j(\vec{r}_2)} \bigg|_{\tilde{\rho}_i} \quad (29)$$

and its inverse  $\mathcal{A}^{-1}$  verifies the relation

$$\sum_k \int \mathcal{A}_{ik}^{-1}(\vec{r}_1, \vec{r}) \mathcal{A}_{kj}(\vec{r}, \vec{r}_2) d\vec{r} = \delta_{ij} \delta(\vec{r}_1 - \vec{r}_2) \quad (30)$$

in which  $\delta_{ij}$  is the Kronecker delta. The quantity  $(\det \mathcal{A})^{-1/2}$  is given by

$$\begin{aligned} (\det \mathcal{A})^{-1/2} &= \int \mathcal{D}\delta\rho_+(\vec{r}) \mathcal{D}\delta\rho_-(\vec{r}) \\ &\times \exp \left[ -\frac{1}{2} \sum_{i,j} \int \delta\rho_i(\vec{r}_1) \mathcal{A}_{ij}(\vec{r}_1, \vec{r}_2) \delta\rho_j(\vec{r}_2) d\vec{r}_1 d\vec{r}_2 \right] \end{aligned} \quad (31)$$

The bilinear form in the argument of the exponential must be definite positive to have a well defined physics. This leads to constraints on the elements of the matrix  $\mathcal{A}$ , as we shall see below.

### A. Local Approximation

First we consider the following approximation:  $\mathcal{H}^{\text{eff}} = \mathcal{H}^{\text{coul}} + \mathcal{H}^{\text{ideal}} + \mathcal{H}^{\text{loc}}$ . The matrix  $\mathcal{A}$  can be calculated in the Fourier space

$$\mathcal{A} = \frac{1}{\rho_b} \begin{pmatrix} \bar{a}_{++} + \frac{\kappa_D^2}{k^2} & \bar{a}_{+-} - \frac{\kappa_D^2}{k^2} \\ \bar{a}_{+-} - \frac{\kappa_D^2}{k^2} & \bar{a}_{--} + \frac{\kappa_D^2}{k^2} \end{pmatrix} \quad (32)$$

where  $\rho_b = \tilde{\rho}_+ + \tilde{\rho}_-$ ,  $\kappa_D$  is the reverse of the Debye wavelength,  $\kappa_D^2 = \beta e^2 \rho_b / \varepsilon$  and we have introduced the following notation:  $\bar{a}_{ij} = (\rho_b \tilde{a}_{ij} + 2\delta_{ij}) = a_{ij} + 2\delta_{ij}$ . The quadratic form is definite positive if the determinant of  $\mathcal{A}$  and the diagonal terms are positive for physical real values of  $k$ . It leads to the following relations:

$$\bar{a}_{++}\bar{a}_{--} - \bar{a}_{+-}^2 \geq 0 \quad (33)$$

$$\bar{a}_{++} + \bar{a}_{--} + 2\bar{a}_{+-} \geq 0 \quad (34)$$

From Eqs. (28) and (31) it is seen that the free energy is given by

$$\mathcal{F} = \mathcal{F}^{\text{MFA}} + \frac{1}{2} k_B T \ln(\det \beta \mathcal{A}) \quad (35)$$

This calculation shows explicitly the correction to the MFA. With the quadratic form considered for  $\mathcal{H}^{\text{eff}}$  and the local approximation, the calculation of  $\frac{1}{2} k_B T \ln(\det \beta \mathcal{A})$  can be performed exactly [39]. The change in the free energy by unit of volume,  $\Delta \mathcal{F}_{\text{charging}}$ , when we switch on the charge is given by

$$\beta \Delta \mathcal{F}_{\text{charging}} = -\frac{1}{12\pi} \left( \frac{\bar{a}_{++} + \bar{a}_{--} + 2\bar{a}_{+-}}{\bar{a}_{++}\bar{a}_{--} - \bar{a}_{+-}^2} K_D^2 \right)^{3/2} \quad (36)$$

If the coefficients  $\tilde{a}_{ij}$  vanish,  $\bar{a}_{ij} = 2\delta_{ij}$ , we recover the exact Debye-Hückel limiting law and its dependence on the power 3/2 of the ionic densities. This non-analytic behavior is the result of the functional integration which introduces a sophisticated coupling between the ideal entropy and the coulomb interaction. In this case the conditions (33) and (34) are verified and the

system is stable as expected. If we accept other fluctuations than those due to the ideal entropy we may expect a change in the screening. This is shown in Eq. (36) where we can see that the Debye length is renormalized. We can show that the same change of the Debye length also appears when we consider the correlation functions. Note that  $\mathcal{K}_D$  is unmodified if all the  $\bar{a}_{ij}$  are identical. In this case, there is no change in the electrical properties of the system but the distribution of densities is changed. It is interesting to note that the correction to  $\mathcal{K}_D$  appears as a ratio, as shown by (36). If the numerator goes to zero then the denominator becomes negative and, from (34), we can see that the system becomes unstable.

In the global approach the coefficient in Eq. (36) due to  $\bar{a}_{ij}$  can be related to the thermodynamics of an uncharged system [32]:

$$\frac{\bar{a}_{ss}}{\det \bar{\mathbf{A}}} = \frac{1}{x_i} \left( \frac{\beta \partial \mu_i}{\partial x_i} \right)_{p,T}^{-1} \quad (37)$$

where  $\det \bar{\mathbf{A}} = \bar{a}_{qq}\bar{a}_{ss} - \bar{a}_{qs}^2$ . The transformation from the  $(+-)$  frame of ion densities to the  $(qs)$  frame of the charge and overall ion density for  $\bar{a}_{ij}$  is analogous to Eqs. (19–21) for  $\tilde{a}_{ij}$ . Then  $\bar{a}_{ss} = (\bar{a}_{++} + \bar{a}_{--} + 2\bar{a}_{+-})/4$  is the reverse of the isothermal compressibility for the uncharged system [39]. The ratio  $\bar{a}_{ss}/\det \bar{\mathbf{A}}$  characterizes a demixion. A new behavior can be expected in the case where the uncharged system is near a demixion. This aspect has been illustrated recently by a Brownian dynamic simulation in two dimensions. It has been shown that the liquid exhibits two structures [40]. First, we observe the existence of domains formed by alternated chains of ions of the same sign (Fig. 1). The different domains present a different global orientation for the chains. Secondly, if we only focus on the particles, whatever their sign, we observe a mesoscopic organization having a global hexagonal structure.

The predictions of the theory are obtained for a one-phase system in which the isothermal compressibility for the uncharged system is finite ( $\bar{a}_{ss} > 0$ ). In order to investigate a system with  $\bar{a}_{ss} = 0$ , a more sophisticated Hamiltonian has to be considered in order to stabilize the system.

## B. Non-local Approximation

In this part we consider the effective hamiltonian  $\mathcal{H}^{\text{eff}} = \mathcal{H}^{\text{coul}} + \mathcal{H}^{\text{ideal}} + \mathcal{H}^{\text{loc}} + \mathcal{H}^{\text{nonloc}}$  with the simplified form  $\beta \mathcal{H}^{\text{nonloc}} = \frac{1}{2} \int \tilde{b} [\nabla \tilde{s}(\vec{r})]^2 d\vec{r}$  used to represent  $\mathcal{H}^{\text{nonloc}}$ . With this Hamiltonian the structure and the thermodynamics are well defined if  $\bar{a}_{ss} = 0$ , provided that  $\mu^2 = a_{qs}^2/(b^2 \mathcal{K}_D^2) < 1$  where  $b^2 = \rho_b \tilde{b}$  and  $b$  has a dimension of length. In this case the exact charge–charge,  $h_{qq}(\vec{r})$ , density–density,  $h_{ss}(\vec{r})$ , and charge–density,  $h_{qs}(\vec{r})$ , correlation functions associated with  $\mathcal{H}^{\text{eff}}$  are

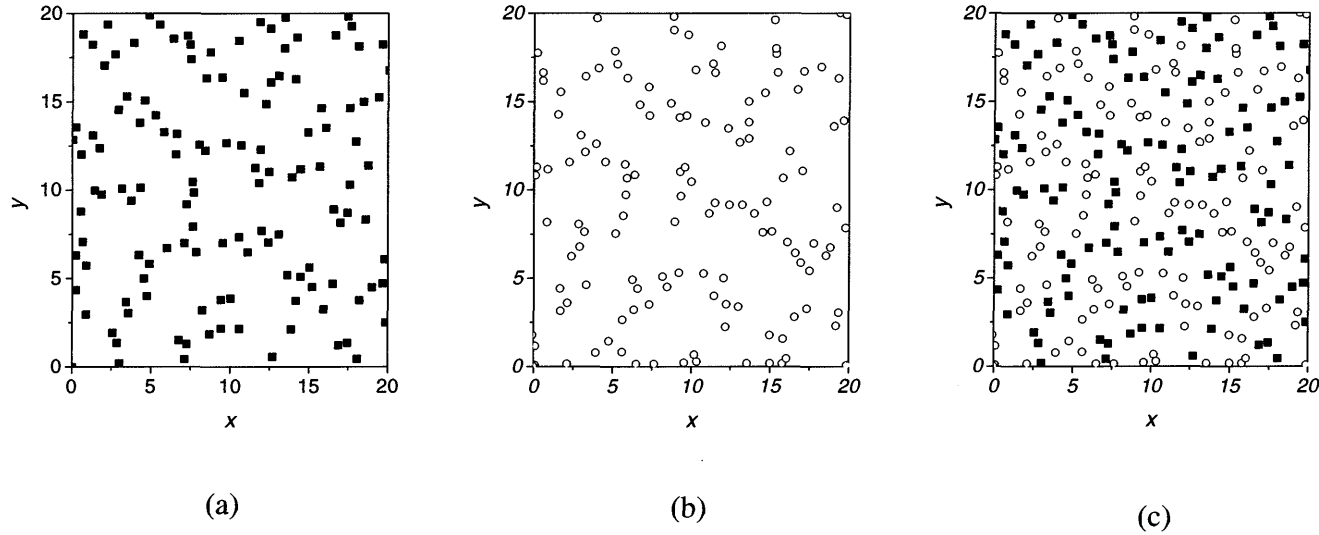


**FIG. 1** Results of a Brownian dynamic simulation for a two-dimensional coulombic system with specific interactions [40]. (a) Positions of ions of one sign (squares); (b) positions of ions of the opposite sign (circles); (c) positions of ions from (a) and (b) together.

given by [39]

$$h_{qq}(\vec{r}) = g_{qq} - 1 = \frac{1}{a_{qq}} \left( \delta(\vec{r}) - K_R^2 \frac{\exp(-K_R|\vec{r}|)}{4\pi|\vec{r}|} \right) \quad (38)$$

$$h_{ss}(\vec{r}) = g_{ss} - 1 = \frac{1}{b^2(1-\mu^2)4\pi|\vec{r}|} - \frac{\mu^2}{b^2(1-\mu^2)} \frac{K_R^2 \exp(-K_R|\vec{r}|)}{4\pi|\vec{r}|} \quad (39)$$

$$h_{qs}(\vec{r}) = g_{qs} - 1 = \frac{-a_{qs}}{a_{qq}b^2} \frac{\exp(-K_R|\vec{r}|)}{4\pi|\vec{r}|} \quad (40)$$

where  $K_R$  is the renormalized reciprocal Debye length defined by  $K_R^2 = (1 - \mu^2)\mathcal{K}_D^2/\bar{a}_{qq}$ . The above results are exact consequences of the model Hamiltonian. Out of criticality, when  $\bar{a}_{ss} > 0$ , the correlation function  $g_{qq}$  verifies the first and second Stillinger–Lovett conditions [39] which characterize a conducting medium [15,41]. At criticality,  $\bar{a}_{ss} = 0$ , only the first Stillinger–Lovett condition is verified in all cases. The second Stillinger–Lovett condition is not verified when  $\bar{a}_{qs} \neq 0$ . It can be considered formally to verify this condition if we accept that the effective concentration of charge carriers is  $\rho_i(1 - \mu^2)$ , lower than  $\rho_i$ . This is an interesting result in view of the experimental data on critical ionic systems with highly asymmetric ions [42]. The problem of asymmetry of ions has been considered by Stell [43].

## VI. CHARGED INTERFACES IN A LINEAR REGIME

In this section we will consider the same Hamiltonian as above, in which we add a surface Hamiltonian  $\mathcal{H}^{\text{surf}}$  to account for a specific interaction with the wall. Our Hamiltonian is then given by  $\mathcal{H}^{\text{eff}} = \mathcal{H}^{\text{coul}} + \mathcal{H}^{\text{ideal}} + \mathcal{H}^{\text{loc}} + \mathcal{H}^{\text{nonloc}} + \mathcal{H}^{\text{surf}}$ . Instead of (24) we will consider a simpler form in which  $h_+ = h_- = h$ . For this Hamiltonian the exact result (10) leads to

$$\begin{aligned} \beta e \langle V(\vec{r}) \rangle + \left\langle \ln \frac{\rho_+(\vec{r})}{\rho_{\text{ref}}} \right\rangle + \tilde{a}_{++} \langle \rho_+(\vec{r}) \rangle + \tilde{a}_{+-} \langle \rho_-(\vec{r}) \rangle \\ - \tilde{b} \Delta [\langle \rho_+(\vec{r}) \rangle + \langle \rho_-(\vec{r}) \rangle] \\ + \delta(z) \left[ \tilde{h} - \tilde{b} \frac{\partial}{\partial z} [\langle \rho_+(\vec{r}) \rangle + \langle \rho_-(\vec{r}) \rangle] \right] = 0 \end{aligned} \quad (41)$$

A similar equation holds for the field  $\rho_-(\vec{r})$ . To derive the above equation we use the relation  $\delta/\delta\rho \int \Theta(z) [\nabla \rho(\vec{r})]^2 d\vec{r} = -\Theta(z) \Delta \rho(\vec{r}) - \delta(z) \vec{n} \nabla \rho(\vec{r})$ , where  $\vec{n}$  is a unit vector normal to the surface  $z = 0$ . The presence of brackets

means that we have to take an average. Hereafter this equation will be separated into a regular part and a singular one corresponding to

$$\tilde{h} = \tilde{b} \frac{\partial}{\partial z} [\langle \rho_+(\vec{r}) \rangle + \langle \rho_-(\vec{r}) \rangle] \Big|_{z=0} \quad (42)$$

It is seen that the symmetry of the non-coulombic non-local interaction in the bulk phase forces the symmetry of the localized interaction with the wall. If we omitted the surface Hamiltonian and set  $h = 0$  we would still obtain the boundary condition setting the gradient of the overall ionic density to zero. The boundary condition due to electrostatics is given by

$$-\frac{\partial}{\partial z} \langle V(\vec{r}) \rangle = \frac{\sigma}{\varepsilon} \quad (43)$$

If we subtract from equation (42) the corresponding equation for the bulk phase we get for the regular part

$$\begin{aligned} \beta e [\langle V(\vec{r}) \rangle - \langle V(\infty) \rangle] + \left\langle \ln \frac{\rho_+(\vec{r})}{\rho_+} \right\rangle \\ + \tilde{a}_{++} [\langle \rho_+(\vec{r}) \rangle - \rho_+] + \tilde{a}_{+-} [\langle \rho_-(\vec{r}) \rangle - \rho_-] \\ - \tilde{b} \Delta [(\langle \rho_+(\vec{r}) \rangle - \rho_+) + (\langle \rho_-(\vec{r}) \rangle - \rho_-)] = 0 \end{aligned} \quad (44)$$

Let us assume that both  $\sigma$  and  $\tilde{h}$  are small enough and we can write

$$\ln \frac{\rho_+(\vec{r})}{\rho_+} = \ln \left( 1 + \frac{\rho_+(\vec{r}) - \rho_+}{\rho_+} \right) \simeq \frac{\rho_+(\vec{r}) - \rho_+}{\rho_+} \quad (45)$$

Eq. (41) can be rewritten as

$$\beta e \rho_b \delta V(\vec{r}) + \bar{a}_{++} \delta \rho_+(\vec{r}) + \bar{a}_{+-} \delta \rho_-(\vec{r}) = b^2 \Delta [\delta \rho_+(\vec{r}) + \delta \rho_-(\vec{r})] \quad (46)$$

in which we have defined:  $\delta V(\vec{r}) = [\langle V(\vec{r}) \rangle - \langle V(\infty) \rangle]$  and  $\delta \rho_i(\vec{r}) = \langle \rho_i(\vec{r}) \rangle - \rho_i$ .

Now, combining the equations for both kinds of ion, and using the Poisson equation for the average potential  $\delta V(\vec{r})$ , we can write our equations in the following matrix form [28]:

$$\Delta \begin{pmatrix} \delta q(\vec{r}) \\ \delta s(\vec{r}) \end{pmatrix} = \frac{1}{b^2 a_{qq}} \begin{pmatrix} b^2 \mathcal{K}_D^2 - \bar{a}_{qs}^2 & -\bar{a}_{qs} \bar{a}_{ss} \\ \bar{a}_{qq} a_{qs} & \bar{a}_{qq} \bar{a}_{ss} \end{pmatrix} \begin{pmatrix} \delta q(\vec{r}) \\ \delta s(\vec{r}) \end{pmatrix} \quad (47)$$

with the boundary condition

$$\frac{\partial}{\partial z} \begin{pmatrix} \delta q(\vec{r}) \\ \delta s(\vec{r}) \end{pmatrix} \Big|_{z=0} = \frac{1}{b^2 a_{qq}} \begin{pmatrix} b^2 \mathcal{K}_D^2 \sigma - \bar{a}_{qs} h \\ \bar{a}_{qq} h \end{pmatrix} \quad (48)$$



The solution of the differential equation (46) is a linear combination of terms in the form  $\exp[-\kappa_i z]$ , where  $\kappa_i = \pm \lambda_i^{1/2}$ . The coefficients  $\lambda_i$  are the eigenvalues of the matrix  $\mathcal{B}$  which appears in (47); they are the roots of the characteristic polynomial

$$\lambda^2 + \lambda \text{Tr } \mathcal{B} + \det \mathcal{B} = 0 \quad (49)$$

We find

$$\lambda_{\pm} = \frac{(b^2 \mathcal{K}_D^2 + \det \bar{\mathbf{A}}) \pm [(b^2 \mathcal{K}_D^2 + \det \bar{\mathbf{A}})^2 - 4b^2 \mathcal{K}_D^2 \bar{a}_{qq} \bar{a}_{ss}]^{1/2}}{2b^2 \bar{a}_{qq}} \quad (50)$$

The physical solutions for the profiles have to relax to their finite bulk values far from the wall. Because of this the real part of  $\kappa_i$  has to be positive. By virtue of arguments analogous to those developed in the previous section, the matrix

$$\frac{1}{2\rho_b} \begin{pmatrix} \bar{a}_{qq} + \frac{\mathcal{K}_D^2}{k^2} & \bar{a}_{qs} \\ \bar{a}_{qs} & \bar{a}_{ss} + b^2 k^2 \end{pmatrix} \quad (51)$$

has to be positive definite for real values of  $k$ . Hence it follows that

$$\bar{a}_{qq} > 0 \quad \text{and} \quad \bar{a}_{ss} > 0 \quad \text{and} \quad b^2 > 0 \quad (52)$$

and for  $|\vec{k}| \neq 0$

$$\bar{a}_{qq} b^2 |\vec{k}|^4 + (b^2 \mathcal{K}_D^2 + \det \bar{\mathbf{A}}) |\vec{k}|^2 + \bar{a}_{ss} \mathcal{K}_D^2 > 0 \quad (53)$$

If  $(b^2 \mathcal{K}_D^2 + \det \bar{\mathbf{A}})^2 \geq 4b^2 \mathcal{K}_D^2 \bar{a}_{qq} \bar{a}_{ss}$  all the  $\kappa_i$  are positive and the solutions are well behaved. Otherwise we may find oscillatory profiles, as shown in Fig. 2. The stability conditions (52) and (53) are sufficient to assure that the real part of  $\kappa_i$  is positive, as we can see from (50).

These results reduce to the linear Gouy–Chapman theory if all the  $\bar{a}_{ij}$  vanish. In the case of symmetrical ions,  $\bar{a}_{++} = \bar{a}_{--}$  or  $\bar{a}_{qs} = 0$ , we can see immediately that  $\delta q(\vec{r})$  and  $\delta s(\vec{r})$  are decoupled. The density profile  $\delta s(\vec{r})$  is proportional to the surface field  $h$  and its characteristic length is  $b/\sqrt{\bar{a}_{ss}}$ . Note that this length is just  $b$  in the absence of specific interactions,  $\bar{a}_{ij} = 0$ . The charge profile  $\delta q(\vec{r})$  is proportional to  $\sigma$  and has a characteristic length  $\sqrt{\bar{a}_{qq}}/\mathcal{K}_D$ . In this case the potential of zero charge vanishes and the capacitance is given by  $C = \epsilon \mathcal{K}_D / \sqrt{\bar{a}_{qq}}$ . If we introduce an asymmetry between ions ( $\bar{a}_{qs} \neq 0$ ) in the case of a local model ( $b = 0$ ) then, in contrast to the linear Gouy–Chapman theory, a non-trivial density profile is introduced. Both  $\delta q(\vec{r})$  and  $\delta s(\vec{r})$  are proportional to the charge but there is only

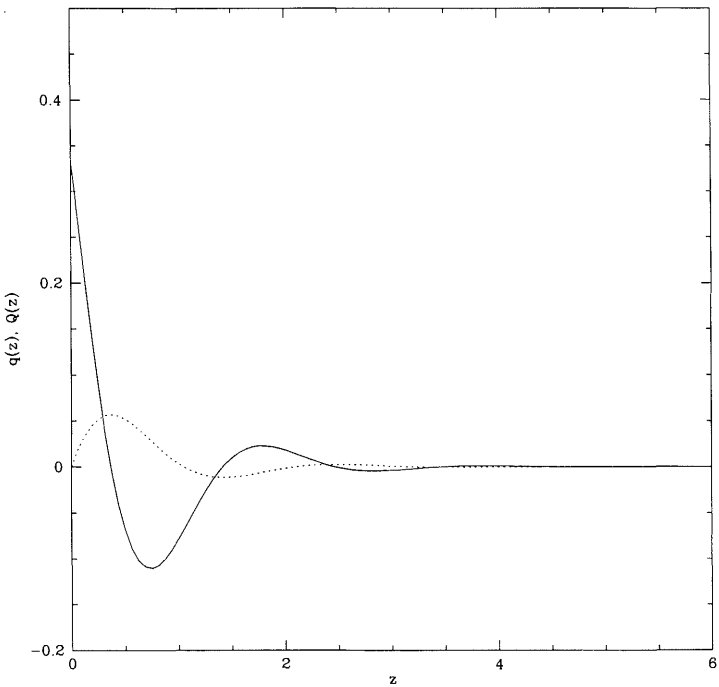


**FIG. 2** Charge density  $q(z)$  (solid line) with its integral  $Q(z) = \int_0^z q(z')dz'$  (dashed line) in presence of an adsorption potential  $h \neq 0$  and, in the case of asymmetrical ions,  $a_{qs} \neq 0$ . The decay constants are  $\kappa_1 = 1 + 2i$  and  $\kappa_2 = 1 - 2i$ . (Reprinted from Ref. 19 with permission from Elsevier Science.)

one characteristic length. Its inverse is given by  $\mathcal{K}_D \sqrt{\bar{a}_{ss}/\det \bar{\mathbf{A}}}$  and the differential capacitance is simply:

$$C = \varepsilon \mathcal{K}_D \sqrt{\frac{\bar{a}_{ss}}{\det \bar{\mathbf{A}}}} \tag{54}$$

An interesting case corresponds to  $\sigma = 0$  but  $h \neq 0$  and  $\bar{a}_{qs} \neq 0$ . Then the charge profile is not monotonic, a surface dipole is created, and the potential of zero charge does not vanish. In the general case we can calculate the differential capacitance. It is given by a complicated formula which involves all the ingredients except  $h$ . The model described in this section is exactly solvable and we have seen the consequence of the presence of two length scales in the system using analytical formulas.

## VII. THE ROLE OF THE SPECIFIC INTERACTION IN THE NONLINEAR REGIME

Eq. (44) is an exact relation for a system described by  $\mathcal{H}^{\text{eff}} = \mathcal{H}^{\text{coul}} + \mathcal{H}^{\text{ideal}} + \mathcal{H}^{\text{loc}} + \mathcal{H}^{\text{nonloc}} + \mathcal{H}^{\text{surf}}$ . If  $\mathcal{H}^{\text{eff}}$  is reduced to  $\mathcal{H}^{\text{eff}} = \mathcal{H}^{\text{coul}} + \mathcal{H}^{\text{ideal}}$  then we have

$$\left. \begin{aligned} \beta e[\langle V(\vec{r}) \rangle - \langle V(\infty) \rangle] + \left\langle \ln \frac{\rho_+(\vec{r})}{\rho_+} \right\rangle &= 0 \\ -\beta e[\langle V(\vec{r}) \rangle - \langle V(\infty) \rangle] + \left\langle \ln \frac{\rho_-(\vec{r})}{\rho_-} \right\rangle &= 0 \end{aligned} \right\} \quad (55)$$

These equations are different from the MFA conditions (16). The MFA equations are obtained if we assume that

$$\langle \ln(\rho_+(\vec{r})/\rho_+) \rangle \sim \ln\langle(\rho_+(\vec{r})/\rho_+)\rangle = \ln\langle(\rho_+(z)/\rho_+)\rangle$$

Since the potential verifies the Poisson equation the nonlinear Gouy–Chapman theory is recovered. In what follows we summarize some results of the nonlinear Gouy–Chapman (NLGC) theory that are useful for the subsequent part of this work.

### A. Nonlinear Gouy–Chapman Theory

To simplify the equations we introduce the following reduced quantities:

$$\hat{z} = K_D z \quad (56)$$

$$g_{\pm}(\hat{z}) = \frac{\langle \rho_{\pm}(z) \rangle}{\rho_{\pm}} \quad (57)$$

$$\hat{q}(\hat{z}) = 2 \frac{q(z)}{\rho_b} = g_+(\hat{z}) - g_-(\hat{z}) \quad (58)$$

$$v(\hat{z}) = 2\beta e[\langle V(z) \rangle - \langle V(\infty) \rangle] \quad (59)$$

$$\hat{\sigma} = \frac{2\beta e}{\epsilon K_D} \sigma \quad (60)$$

We will use the hatted symbols without a hat as, in practice, it does not lead to confusion. With these notations we have  $g_{\pm}(z) = \exp(\mp v(z)/2)$  and the Poisson equation is

$$\frac{d^2 v(z)}{dz^2} = g_+(z) - g_-(z) \quad (61)$$

with the boundary condition  $-(dv(z)/dz)|_{z=0} = \sigma$ . The solutions of the NLGC theory are [1]

$$g_+(z)g_-(z) = 1 \quad \text{or} \quad \ln(g_+(z)g_-(z)) = 0 \quad (62)$$

$$\sigma = 4 \sinh \frac{v(0)}{4} \quad (63)$$

$$\tanh \frac{v(z)}{8} = \tanh \frac{v(0)}{8} e^{-z} \quad (64)$$

$$\frac{C}{\varepsilon \mathcal{K}_D} = \frac{d\sigma}{dv(0)} = \cosh \frac{v(0)}{4} = \sqrt{1 + \frac{\sigma^2}{16}} \quad (65)$$

$$g_+(z) = g_-^{-1}(z) = \left( \frac{1 - a \exp(-z)}{1 + a \exp(-z)} \right)^2 \quad (66)$$

where  $a = \tanh[\operatorname{arcsinh}(\sigma/4)/2] = \tanh(v(0)/8)$ . Thus we see that for high values of  $\sigma$  the capacitance behaves like  $C \simeq (\varepsilon \mathcal{K}_D \sigma/4)$ ; in this case there is no limitation for the potential on the wall. The profiles are monotonic and their product is unity. To characterize the profiles  $g_{\pm}(z)$  in a simple way we consider their lowest-order momenta defined according to

$$\Gamma_q = \int_0^{\infty} [g_+(z) - g_-(z)] dz = -\sigma \quad (67)$$

$$\Gamma_s = \int_0^{\infty} [g_+(z) + g_-(z) - 2] dz = 4 \left( \sqrt{1 + \frac{\sigma^2}{16}} - 1 \right) \quad (68)$$

$$M_q = \int_0^{\infty} [g_+(z) - g_-(z)] z dz = -4 \operatorname{arcsinh}\left(\frac{\sigma}{4}\right) = -v(0) \quad (69)$$

$$M_s = 4 \ln \left[ \frac{1}{2} \left( \sqrt{1 + \frac{\sigma^2}{16}} + 1 \right) \right] \quad (70)$$

For the charge distribution these momenta have a well defined meaning. The zeroth order momentum  $\Gamma_q$  is just the net charge on the wall while the first momentum  $M_q$  is the potential drop across the interface. To  $\Gamma_s$  and  $M_q$  we can associate a length  $z_q = M_q/\Gamma_q = v/\sigma$  which is just the reverse of the integral capacitance of the interface in reduced units.  $z_q$  is a complicated function of  $\sigma$  which tends to one when the charge goes to zero. Then integral and differential capacitance are both equal to  $\varepsilon \mathcal{K}_D$ . For the density

distribution its momentum does not have a simple and absolute meaning.  $\Gamma_s$  gives us the excess of density relatively to the plane  $z = 0$ . To  $\Gamma_s$  and the first momentum we may associate the length  $z_s = M_s/\Gamma_s$  which characterizes the effective position of the adsorption plane. It can be seen that  $z_s \rightarrow 1/2$  when  $\sigma \rightarrow 0$ .

Because the NLGC theory can be solved exactly, a lot of properties can be elucidated by analytical formulas. One of them requires a greater emphasis as, in our opinion, it has not been pointed out sufficiently. The charge  $\sigma$  is a monotonic function of the potential  $v(0)$ , the profiles are monotonic and defined by  $\sigma$  or  $v(0)$ . When the wall changes its charge from  $\sigma$  to  $\sigma_1$  it also acquires a new potential  $v_1(0)$ . Provided that the sign of the electrode charge remains unchanged, the two potential drops can be related by  $\tanh(v(0)/8) = \tanh(v_1(0)/8) \exp z_0$ , where  $z_0$  is uniquely defined. Now the profiles can be written according to

$$g_+(z) = g_-^{-1}(z) = \left( \frac{1 - \left( \tanh \frac{v(0)}{8} \right) \exp(-z)}{1 + \left( \tanh \frac{v(0)}{8} \right) \exp(-z)} \right)^2$$

$$= \left( \frac{1 - \left( \tanh \frac{v_1(0)}{8} \right) \exp(-(z - z_0))}{1 + \left( \tanh \frac{v_1(0)}{8} \right) \exp(-(z - z_0))} \right)^2 \quad (71)$$

There is a universal behavior for the profile. If the profile is known for a given charge on the wall, then the profile is known for every other charge of the same sign by translating the origin of the coordinate system. This mathematical structure is due to the existence of a group of transformations. As we are going to see below, some properties can be deduced without explicit solving of the differential equations.

## B. Role of the Specific Interaction

In this part we consider a mean-field approach restricted to the case  $h = 0$  and  $b = 0$ . Then Eq. (10) leads to [27]

$$v(z) + 2 \ln g_+(z) + a_{++}g_+(z) + a_{+-}g_-(z) = a_{++} + a_{+-} \quad (72)$$

$$-v(z) + 2 \ln g_-(z) + a_{+-}g_+(z) + a_{--}g_-(z) = a_{--} + a_{+-} \quad (73)$$

where  $a_{ij} = \rho_b \tilde{a}_{ij} = \tilde{a}_{ij} - 2\delta_{ij}$ . Instead of these two equations we can write the

following system of equations

$$\frac{dg_+(z)}{dz} = \frac{\frac{2}{g_-(z)} + a_{--} + a_{+-}}{\left(\frac{2}{g_+(z)} + a_{++}\right)\left(\frac{2}{g_-(z)} + a_{--}\right) - a_{+-}^2} \sigma(z) \quad (74)$$

$$\frac{dg_-(z)}{dz} = \frac{\frac{2}{g_+(z)} + a_{++} + a_{+-}}{\left(\frac{2}{g_+(z)} + a_{++}\right)\left(\frac{2}{g_-(z)} + a_{--}\right) - a_{+-}^2} \sigma(z) \quad (75)$$

$$\frac{d}{dz} \sigma(z) = g_+(z) - g_-(z) \quad (76)$$

### 1. Analytical Results Based on a Lie Group Description

For a given interface the charge on the wall is a fixed quantity. At any point of the interface we can define the net charge located between  $z$  and the bulk phase. We can define the quantity  $\sigma(z)$  in this way. We can also adopt another point of view. As an intermediate step in the calculations, we consider an arbitrary wall located at a given  $z_0$  and we assume that the charge on this wall is small enough to be in the linear regime. Since the linear problem can be solved exactly and, for  $z \geq z_0$ , matches the solution of Eqs. (74–76) in this case, in  $z_0$  we know  $g_+(z_0)$ ,  $g_-(z_0)$ , and  $\sigma_0 = \sigma(z_0)$  for a given ionic solution. Now, we can consider the previous system of equations with the boundary conditions fixed in  $z_0$ . This system of equations does not contain the position  $z$  on the right-hand side. It can be considered as a system of canonical equations of a one-parameter Lie group, where  $z$  plays the role of the parameter [44]. A Lie group is a transformation group; in our case it establishes an equivalence between translation in space of the wall position and rescaling the charge of the electrode as noted in the NLGC theory. It implies that with different boundary conditions we have only one profile to calculate. If we stop the calculation at the point  $z$ , then  $g_+(z)$  and  $g_-(z)$  are the contact values and  $\sigma(z)$  is the charge on the wall in this case. Since our problem can also be reformulated as a Cauchy problem we know that there is a unique solution. In addition to density profiles we also consider the profile  $\sigma(z)$  of the electric field in reduced units.

A group of transformations can be characterized by its invariants, if any. There are two invariants for one parameter group with three variables. The first invariant is found by adding Eqs. (72) and (73) to eliminate the

potential

$$2 \ln[g_+(z)g_-(z)] + (a_{++} + a_{+-})g_+(z) + (a_{--} + a_{-+})g_-(z) = a_{++} + 2a_{+-} + a_{--} \quad (77)$$

This result is a simple generalization of the result (75) obtained in the case of the NLGC theory. The second invariant can be obtained by summing derivatives  $d/dz$  of Eqs. (72) and (73) multiplied by  $g_+(z)$  and  $g_-(z)$  respectively and using Eq. (76)

$$2(g_+(z) + g_-(z)) + \frac{1}{2}[a_{++}g_+^2(z) + 2a_{+-}g_+(z)g_-(z) + a_{--}g_-^2(z)] - \frac{1}{2}\sigma^2(z) = 4 + \frac{a_{++} + 2a_{+-} + a_{--}}{2} \quad (78)$$

When all the  $a_{ij}$  vanish we find  $(g_+(z) - 1) + (g_-(z) - 1) = \sigma^2/4$ , which is known as the contact theorem [45]. It describes the mechanical equilibrium of the interface. The second invariant is then a generalization of this theorem to our case. In principle, our problem is solved in terms of the two invariants. We can use them as implicit equations for the functions  $g_+(\sigma)$  and  $g_-(\sigma)$ . We can obtain the  $z$  dependence of the profiles from

$$z - z_0 = \int_{\sigma_0}^{\sigma} \frac{d\sigma}{g_+(\sigma) - g_-(\sigma)} \quad (79)$$

Eqs. (77 and (78) are transcendental and we cannot obtain the solutions in a closed form. Nevertheless, they are convenient for obtaining some exact results.

For any quantity  $f = f(g_+, g_-, \sigma)$  we have, from the equivalence between changing the position and charging of the electrode

$$\frac{df}{dz} = (g_+ - g_-) \frac{df}{d\sigma} \quad (80)$$

The above rule applied to potential  $v$  yields for the differential capacitance

$$C = - \frac{g_+(\sigma) - g_-(\sigma)}{\sigma} \quad (81)$$

To our knowledge this is quite a new formula for the differential capacitance. It is valid whenever charging is equivalent to a shift in space of the position of the wall. We can verify that it is fulfilled for the Gouy–Chapman theory. One physical content of this formula is to show that for a positive charge on the wall we must have  $g_-(\sigma) \geq g_+(\sigma)$  in order to have a positive capacitance.

To investigate the charge dependence of the capacitance we have to calculate the dependence of the profile contact values on the charge density.

From Eqs. (80) and (81) we get

$$\frac{dg_{\pm}}{d\sigma} = -\frac{1}{C\sigma} \frac{dg_{\pm}}{dz} \quad (82)$$

The above formulas combined with Eqs. (74) and (75) taken at zero charge density yield Eq. (54) for the differential capacitance. Eq. (82) can be used recursively to generate the derivatives of the differential capacity at zero charge density to an arbitrary order, though the calculations become rather tedious already for the second derivative. Thus, in principle at least, we can develop capacitance in the Taylor series around the zero charge density. The calculations show that the capacitance exhibits an extremum at the point of zero charge only in the case of symmetrical ions, as expected. In contrast with the NLGC theory, this extremum can be a maximum for some values of the parameters. In the case of symmetrical ions the capacitance is maximum if  $a_{++} + a_{+-} = a_{--} + a_{-+} \leq 1$ . We can understand this result by the following reasoning. The contact values can be expanded according to  $g_{\pm} = 1 + a_{\pm}\sigma + b_{\pm}\sigma^2 + c_{\pm}\sigma^3 + \dots$ . To find whether the extremum is a maximum or a minimum we have to determine the sign of  $c_{\pm}$ . In the case of nonlinearized Gouy–Chapman theory we have  $g_{\pm} = 1 \mp a\sigma + b\sigma^2 \mp c\sigma^3$ , leading, to  $C = 2a + 2c\sigma^2$  with  $c > 0$ . This shows that by increasing the charge we increase the contact value. For  $\sigma \approx 0$  and  $\sigma > 0$  we have  $\phi - \phi_0 = (\sigma/2a) - (c\sigma^3/6a^2)$  and we can see immediately that the third-order term decreases the potential change when  $c > 0$ . When the specific interactions are such that  $c < 0$  it is harder to concentrate ions at the contact with the wall, the third-order term increases the potential drop, and the capacitance exhibits a maximum.

There is another difference between our local model and the NLGC theory. From the second invariant (78), it is easy to see that for  $\sigma \rightarrow \infty$  we have  $a_{--}g_{-}(z)^2 = \sigma(z)^2$  and then, using the expression of the capacitance (81), we immediatly get  $C = \epsilon K_D / \sqrt{a_{--}}$ . This shows that the behavior of capacitance for high values of  $\sigma$  results from a competition between electrostatic energy and the specific interactions. Both effects are proportional to  $\sigma^2$ . We can give a simple picture of this result [46]. The coefficient  $a_{--} = \rho_b \tilde{a}_{ij}$  can be written as  $a_{--} = \rho_b \beta U_{--} \lambda_{--}^3$ , where  $U_{--}$  can be identified as the magnitude of the effective potential between anions and  $\lambda_{--}$  as its range. Then the capacitance can be written as

$$C = \frac{\epsilon}{\lambda_{\text{eff}}} \quad \text{or} \quad C = \frac{\epsilon_{\text{eff}}}{\lambda} \quad (83)$$

This shows that the system behaves like a capacitor in which the two planes are separated by  $\lambda_{\text{eff}} = \lambda \sqrt{U_{--}/(e^2/\epsilon\lambda)}$  or by two planes separated by  $\lambda$  but filled with a medium of dielectric constant  $\epsilon_{\text{eff}} = \epsilon / \sqrt{U_{--}/(e^2/\epsilon\lambda)}$ . In



any case the ratio between electrostatic and non-electrostatic energy is important. A totally different behavior characterizes the NLGC theory. It results from the competition between electrostatic contribution which varies as  $\sigma^2$  and the entropy with a weaker dependence on  $\sigma$ . Consequently the capacitance increases as the charge and is given by  $C = \beta \sigma e^2 / 2$ .

## 2. Numerical Results

To calculate the profiles and the differential capacitance of the interface numerically we have to choose a differential equation solver. However, the usual packages require that the problem is posed on a finite interval rather than on a semi-infinite interval as in our problem. In principle, we can transform the semi-infinite interval into a finite one, but the price to pay is a loss of translational invariance of the equations and the point mapped from that at infinity is singular, which may pose a problem on the solver. Most of the solvers are designed for initial-value problems while in our case we deal with a boundary-value problem. To circumvent these inconveniences we follow a procedure strongly influenced by the Lie group description.

For an arbitrarily selected point  $z_0$  we assume a value of the electric field  $\sigma_0$  sufficiently small to linearize Eqs. (74) and (75) around the bulk values  $g_{\pm} = 1$ . The linearized equations are exactly solvable and in the region  $z \geq z_0$  we obtain a set of consistent values of  $(g_+(z), g_-(z), \sigma(z))$  to start a backward integration. We impose the matching condition at  $z = z_0$  and start integrating the equations with the initial values  $(g_+(z_0), g_-(z_0), \sigma(z_0))$ , moving away from the bulk solution to more negative values of  $z$  in the region  $z < z_0$ . At each integration step we obtain a new, more positive or more negative value of  $\sigma$ , the corresponding values of profiles, differential capacitance and electric potential. The two latter quantities are calculated from the formulas (81) and (72) or (73) respectively. We need only two runs—one for positive and one for negative charge densities—to obtain the capacitance curve in a given charge density range. The values at  $z_0$  should correspond with a sufficient accuracy to zero charge density. The solver we used to obtain the results discussed in this paper is LSODI by Painter and Hindmarsh, downloaded from the website [www.netlib.org](http://www.netlib.org) in the Internet.

We can test the accuracy of the procedure for  $a_{++} = a_{--} = a_{+-} = 0$  corresponding to the Gouy–Chapman theory. The accuracy is such that there is no noticeable difference between the numerically and analytically calculated curves presented in Fig. 3(a), where the shape of Gouy–Chapman capacitance curves is recalled. In all other cases discussed in this section the accuracy is better as the profiles are steepest for the Gouy–Chapman theory.

To estimate the values of coefficients  $a_{ij}$  we write  $a_{ij} = \rho_b \beta U_{ij} \lambda_{ij}^3$  as above. For a 1 M solution we have  $\beta U_{ij} \lambda_{ij}^3 \simeq 1500 a_{ij}$ . Thus for  $\beta U_{ij} \simeq 1$  and a radius of solvated ions of 0.5 nm  $a_{ij}$  must be of the order of unity. In what follows

we assume that  $\tilde{a}_{ij}$  is roughly concentration independent, leading to  $a_{ij}$  having a linear dependence on  $\rho_b$ . We will quote the values of  $a_{ij}$  for a 1 M solution. For other concentrations this coefficient is multiplied by  $\rho_b$  expressed in moles per liter. In Fig. 3(b) we consider the totally symmetrical case with  $a_{++} = a_{--} = a_{+-} = 2$ . At low concentrations and at the potential of zero charge (pzc) we observe the formation of the well-known diffuse layer minimum described by the Gouy–Chapman theory but for large  $\sigma$  the capacitance reaches a finite value as predicted above. At higher concentrations, the coefficients  $a_{ij}$  increase and the capacitance exhibits a maximum at the point of zero charge and then decreases to meet the common limit with the curves for other concentrations. This behavior is different from that in NLGC theory.

In Fig. 3(c) we present an asymmetric case in which  $a_{++} = 8$ ,  $a_{--} = 2$ ,  $a_{+-} = 4$ . As in the symmetric case at low concentration and weak charge densities, the results are described by the Gouy–Chapman theory. At higher charge densities the results for various concentrations converge, as in the

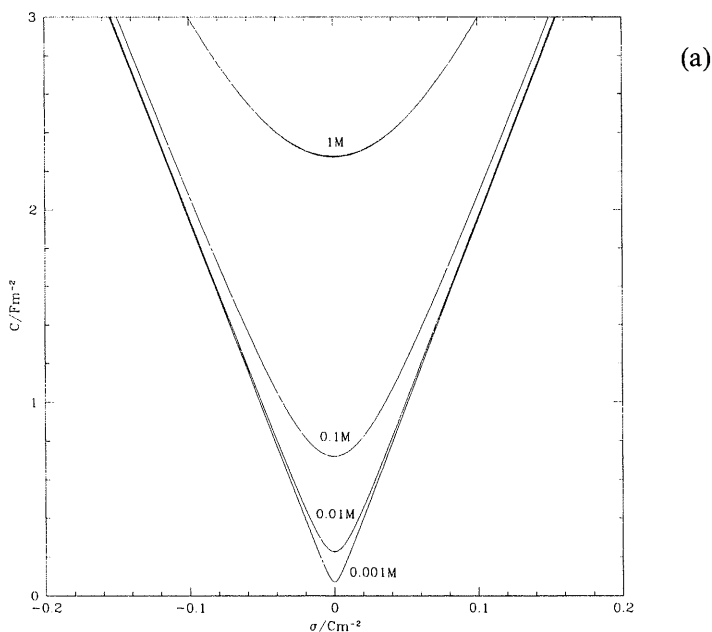


**FIG. 3** Differential capacitance  $C$  as a function of  $\sigma$  for several values of parameters. The parameters are given for 1 M aqueous solution and are rescaled proportionally for other concentrations. (a)  $a_{++} = a_{--} = a_{+-} = 0$  (NLGC theory). (b) Symmetrical case  $a_{++} = a_{--} = a_{+-} = 2$ . (c) Asymmetrical case  $a_{++} = 8$ ,  $a_{--} = 2$ ,  $a_{+-} = 4$ . (From Ref. 27.)

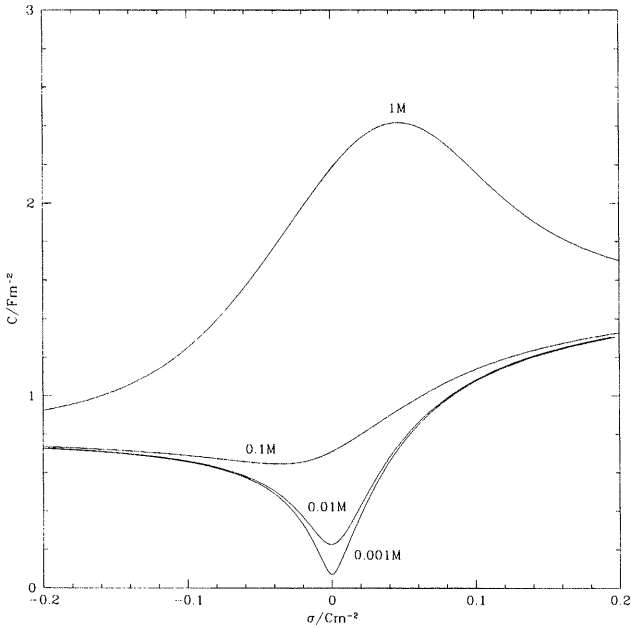
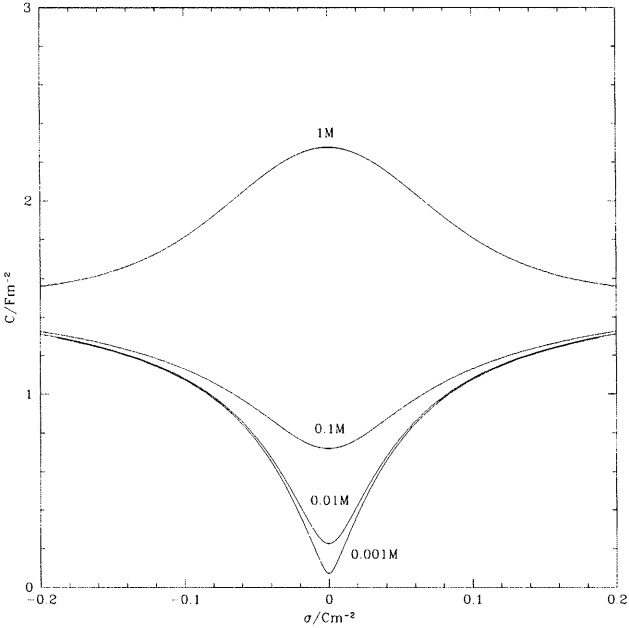
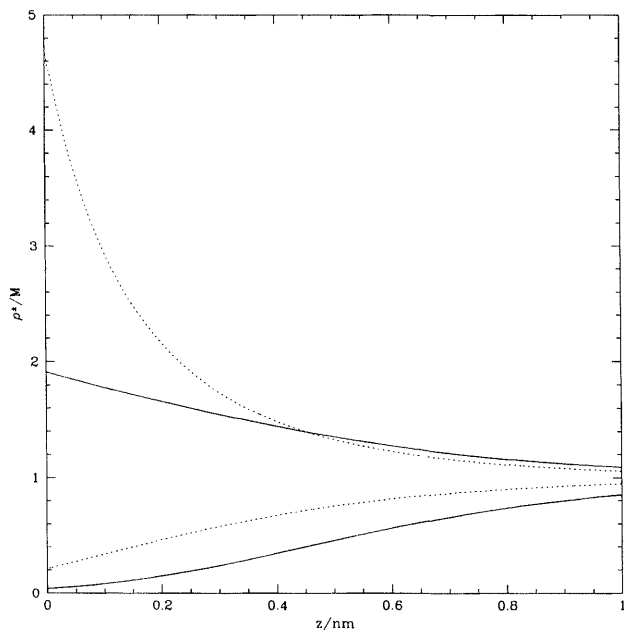


FIG. 3 Continued.

symmetric case, but the limits for positive and negative charge densities are different now, making the overall appearance of the curves asymmetric with respect to zero charge density. The maximum appearing at the highest concentration is shifted towards those charge densities where it is easier to concentrate the counterion. In Fig. 4 we compare ionic profiles for the Gouy–Chapman theory with those calculated for the values of parameters corresponding to the asymmetric case shown in Fig. 3(c). The profiles are monotonic, as in the Gouy–Chapman theory. They are less steep as the non-coulombic interaction prevents concentration of the counterion more than the entropic contribution. This is also clear from the asymptotic behavior in which the contact value of counterion profiles is like  $\sigma^2$  in the case of the Gouy–Chapman theory and like  $|\sigma|$  in the case when  $a_{++} > 0$  and  $a_{--} > 0$ .

The model just presented describes what electrochemists call the diffuse part of the double layer and no account is made of the inner layer effects such as the plane of the closest approach. To have an idea what the impact of the effects predicted by this model on the measured capacitance could be, we assume the traditional inner and diffuse layer separation. However, we



**FIG. 4** Ionic profiles  $\rho_+(z)$  and  $\rho_-(z)$  calculated for 1 M aqueous solution and  $\sigma = -0.1 \text{ C m}^{-2}$ . Dotted lines correspond to NLGC theory, solid lines correspond to  $a_{++} = 8$ ,  $a_{--} = 2$ ,  $a_{+-} = 4$ . (From Ref. 27.)

describe the diffuse layer with our model and for the inner layer we take a simplified form

$$C_i/1\text{ F m}^{-2} = \frac{1.1}{1.0 + 10.0(\sigma/1\text{ C m}^{-2})^2} \tag{84}$$

The total capacitance calculated according to the formula

$$\frac{1}{C_t} = \frac{1}{C_i} + \frac{1}{C_D} \tag{85}$$

is presented in Fig. 5(a-c), corresponding respectively to the three cases in which the diffuse layer capacitance is the capacitance presented in Fig. 3(a) for the Gouy–Chapman theory, 3(b) for the symmetric case, and 3(c) for the asymmetric case. The symmetric case and the Gouy–Chapman theory are similar. For the asymmetric case we see that the asymmetry induced by the asymmetric diffuse layer theory appears at intermediate concentrations (0.1 M). Let us emphasize that this behavior results from interionic interactions

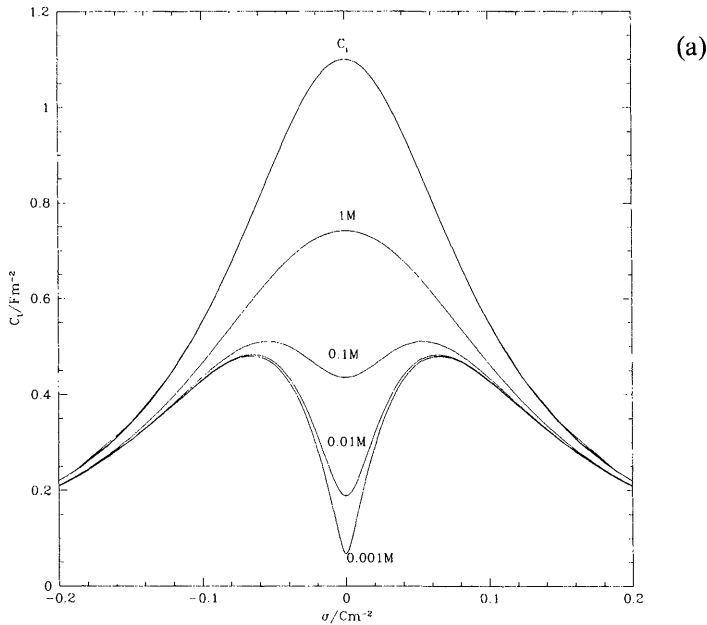
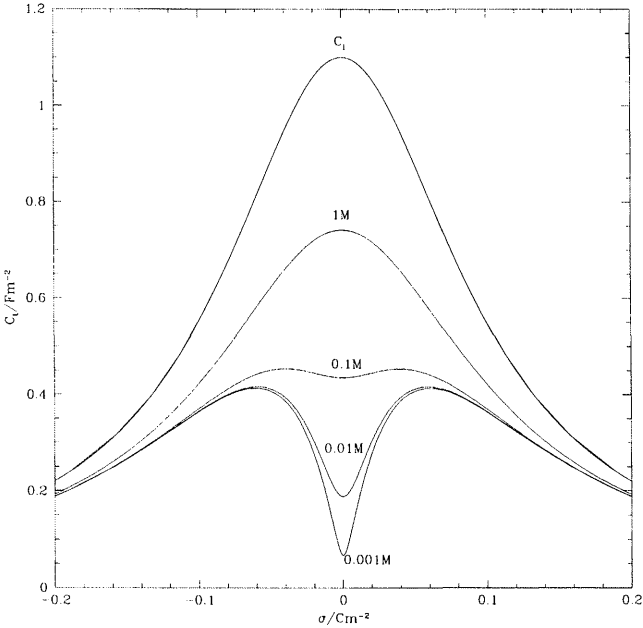
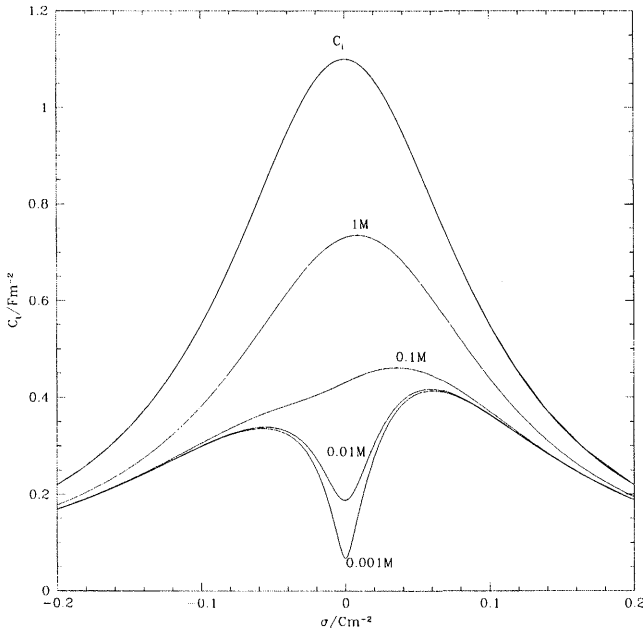


**FIG. 5** Variation of the total capacitance  $C_t$  given by Eq. (85). The inner layer capacitance is given by Eq. (84). (a), (b), and (c) correspond to a diffuse layer capacitance given in Figs. 3(a), (b), and (c), respectively. (From Ref. 27.)



(b)



(c)

FIG. 5 Continued.

and, as such, is different in nature from what is understood to be specific adsorption.

The problem of specific and non-specific adsorption has been central to the analysis of experimental data on electric double layers at the interfaces of inert electrode materials in electrolyte solutions. As a criterion the so-called Parsons–Zobel plot is used [47]. In this plot the experimental reciprocal differential capacitance is given against the reciprocal Gouy–Chapman capacitance for the same charge density and concentration. The plot is formed by varying the concentration and therefore the Gouy–Chapman capacitance and it is a straight line for non-specifically adsorbed electrolytes according to Eq. (6), the intercept of which with one of the axes yields the concentration-independent inner-layer capacitance. The plot is most sensibly used for zero charge density as then the variation of the reciprocal Gouy–Chapman capacitance with concentration is most significant. Let us consider the totally symmetric case first,  $a_{++} = a_{--} = a_{+-} = a$ . For this case  $a_{ss}/\det A = 1$  and there is no renormalization of the Debye length as discussed in Sec. 5 and we have at the pzc  $\tilde{C}_0 = \epsilon K_D$ . It follows

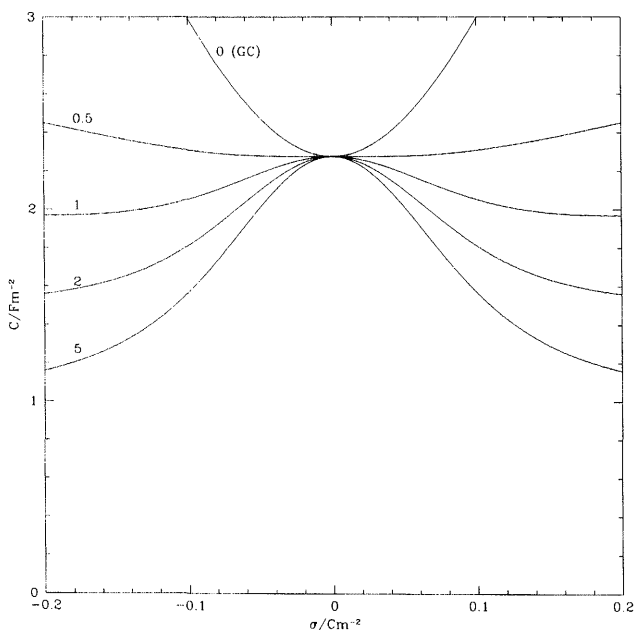


**FIG. 6** Capacitance curves  $C$  vs  $\sigma$  for 1 M aqueous solution for totally symmetrical ions and several values of the common interaction parameter  $a_{++} = a_{--} = a_{+-} = x$ . (From Ref. 50.)

that the interfacial capacitance is independent of the interaction parameter but only at the zero charge potential (see Fig. 6). The physical interpretation of this result is the following. At zero charge density the main mechanism by which the interface is charged is a substitution of the coion by the counterion. For the totally symmetric interaction there is no effect of such a substitution. At higher charge densities the prevailing mechanism of charging is concentration of counterions and then the opposition of non-coulombic interaction becomes important. Independently of the value of  $a$  the case of symmetric ions is therefore represented by the straight line with unit slope in the Parsons–Zobel plot, as for non-specifically adsorbed electrolyte, and in the other cases we can have two types of deviation from the linear Zobel–Parsons plot, as illustrated in Fig. 7.

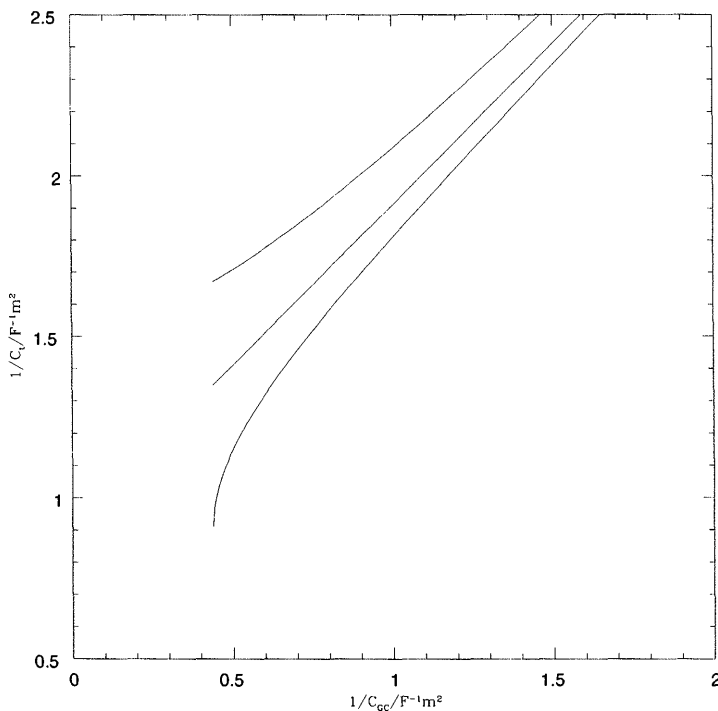


**FIG. 7** Parsons–Zobel plot of  $1/C_t$  as a function of the inverse Gouy–Chapman capacitance  $1/C_{GC}$ . The plot is calculated analytically from Eqs. (54) and (85) at zero charge density. The straight line represents the case  $a_{++} = a_{--} = a_{+-}$ . For the upper line we assumed  $a_{++} = a_{--} = 10$  and  $a_{+-} = 6$  while for the lower line  $a_{+-} = 12$ . (From Ref. 27.)



To conclude this section let us note that already, with this very simple model, we find a variety of behaviors. There is a clear effect of the asymmetry of the ions. We have obtained a simple description of the role of the major constituents of the phenomena—coulombic interaction, ideal entropy, and specific interaction. In the Lie group invariant (78) Coulombic attraction leads to the term  $-\sigma^2/2$ . Ideal entropy yields a contribution proportional to the kinetic pressure  $2(g_+ + g_-)$  and the specific part yields a contribution which retains the bilinear form  $\frac{1}{2}a_{++}g_+^2 + a_{+-}g_+g_- + \frac{1}{2}a_{--}g_-^2$ . At high charge densities the asymptotic behavior is determined by the opposition of the coulombic and specific non-coulombic contributions. At low charge densities the entropic contribution is important and, in the case of a totally symmetric electrolyte, the effect of the specific non-coulombic interaction is cancelled so that the behavior of the system is determined by coulombic and entropic contributions.

## VIII. THE ROLE OF NON-LOCALITY IN THE NONLINEAR REGIME

In the previous section we have combined the ingredients of the Gouy-Chapman theory with a simple, bilinear, and local contribution containing some ionic specificities. In this section we add a non-local contribution in the simple squared gradient form already introduced in Sec. 4. Our main goal is to investigate the modifications of the interfacial properties due to the introduction of a second characteristic length having a non-electrostatic origin. To have a simpler Hamiltonian we assume that  $\mathcal{H}^{\text{loc}} = 0$  and consider

$$\mathcal{H}^{\text{eff}} = \mathcal{H}^{\text{coul}} + \mathcal{H}^{\text{ideal}} + \mathcal{H}^{\text{nloc}} + \mathcal{H}^{\text{surf}} + \mathcal{H}^{\text{ext}} \quad (86)$$

For  $\mathcal{H}^{\text{nloc}}$  and  $\mathcal{H}^{\text{surf}}$  we use the simplest form in which only one parameter is used for each contribution. It is convenient to use two more reduced variables:  $\hat{b} = b\mathcal{K}_D$  and  $h = 2\tilde{h}\mathcal{K}_D$ . We omit the hat over  $b$ , keeping in mind that now the length  $b = \sqrt{\rho_b \tilde{b}}$  is expressed taking the Debye length. In the MFA we have the following equations [48]:

$$\left. \begin{aligned} v(z) + 2 \ln g_+(z) - b^2 \frac{d^2}{dz^2} [g_+(z) + g_-(z)] &= 0 \\ -v(z) + 2 \ln g_-(z) - b^2 \frac{d^2}{dz^2} [g_+(z) + g_-(z)] &= 0 \end{aligned} \right\} \quad (87)$$

We put it into a form showing the Lie group structure of the problem:

$$\frac{d}{dz} g_+(z) = \frac{g_+(z)g_-(z)\sigma(z) + h(z)g_+(z)/b^2}{g_+(z) + g_-(z)} \quad (88)$$

$$\frac{d}{dz} g_-(z) = \frac{-g_+(z)g_-(z)\sigma(z) + h(z)g_-(z)/b^2}{g_+(z) + g_-(z)} \quad (89)$$

$$\frac{d}{dz} \sigma(z) = g_+(z) - g_-(z) \quad (90)$$

$$\frac{d}{dz} h(z) = \ln[g_+(z)g_-(z)] \quad (91)$$

In comparison with the previous section a new variable,  $h(z)$ , is introduced, defined by

$$h(z) = b^2 \frac{d}{dz} (g_+(z) + g_-(z)) \quad (92)$$

## A. Numerical Results: Profiles, Center of Gravity, and Capacitance

To solve Eqs. (88)–(91) we use the same numerical method as in the previous section. At a given point  $z_0$  for which both  $\sigma_0 = \sigma(z_0)$  and  $h_0 = h(z_0)$  are very weak, the profiles are determined in the region  $z \geq z_0$  from the linear theory. The values thus found at the point  $z_0$  serve as the initial conditions for the numerical integration performed with the same solver as before.

Selecting the values of the parameters for the calculations we have in mind a 1:1 aqueous 1 M solution at a room temperature for which the Debye length is 0.3 nm. We assume that the non-local term has the same characteristic length, leading to  $b = 1$ . For the adsorption potential parameter  $h$  we select its value so that it has a similar value to the other contributions to the Hamiltonian. To illustrate, a wall potential with  $h = 1$  corresponds to a square well 0.1 nm wide and 3.0  $kT$  high or, conversely, a 3.0 nm wide square well of height 1.0  $kT$ .

In Fig. 8 density profiles are presented for several values of charge density  $\sigma$  on the wall and for the wall potential  $h = -1$  and  $h = 1$ . Fig. 9 contains the corresponding ionic charge density profiles. For the adsorptive wall potential ( $h < 0$ ) the profiles  $q(z)$  in Fig. 9(a) and  $s(z)$  in Fig. 8(a) are monotonic, as in the Gouy–Chapman theory. For a wall which is neutral relative to the adsorption  $h = 0$  the density profiles are monotonic with a maximum at the wall position. This maximum also appears on the charge

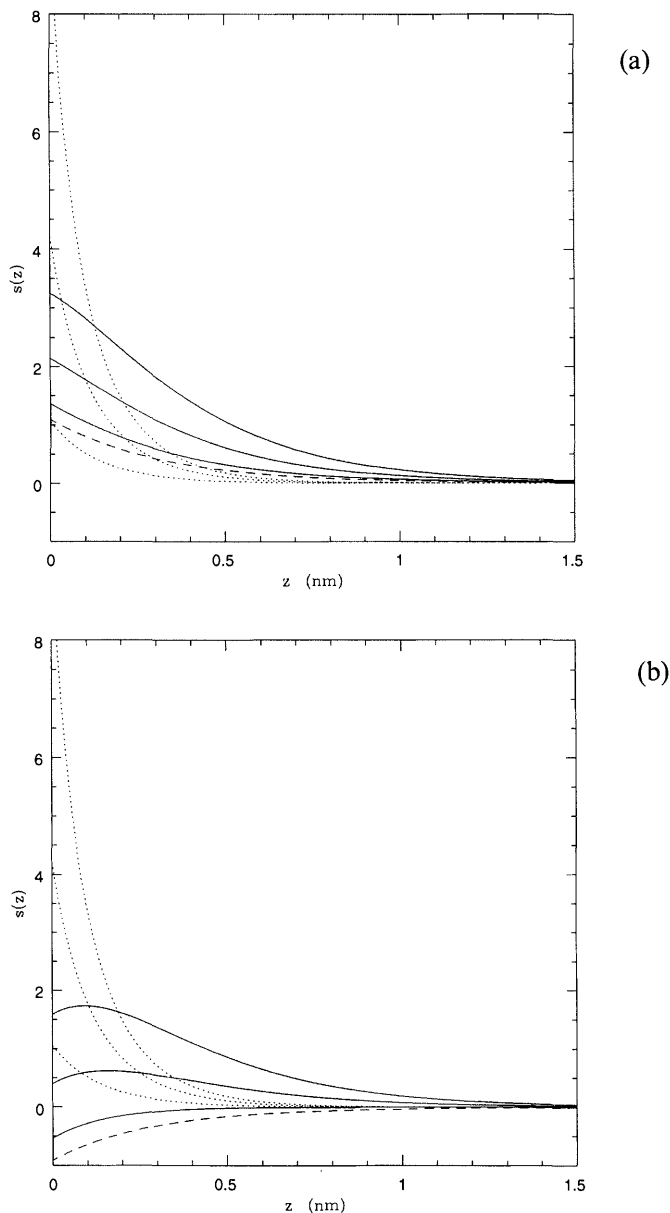
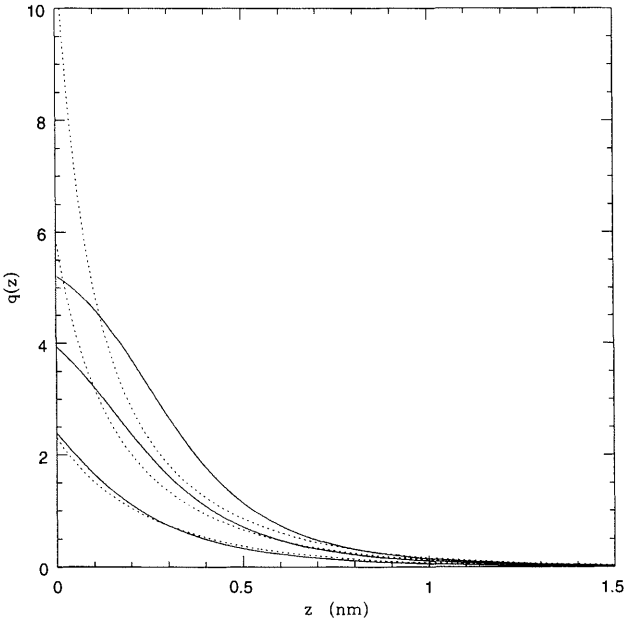
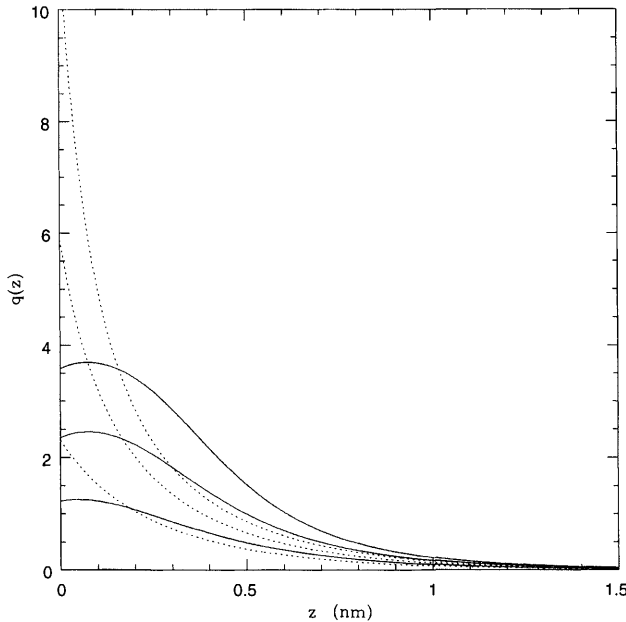


**FIG. 8** Ionic density profiles at a charged wall for (a) the adsorptive wall potential  $h = -1$  and (b) the desorptive wall potential  $h = 1$ . The solid lines correspond to  $\sigma = -0.06, -0.12, -0.18 \text{ C m}^{-2}$  from the lowermost to the uppermost curve. The dashed line indicates  $\sigma = 0$  and the dotted lines the NLGC profiles. (From Ref. 49.)



(a)



(b)

**FIG. 9** Charge density profiles for the same cases as in Fig. 8. (From Ref. 49.)

profiles provided the charge becomes large enough that only one component is in contact with the wall. For a desorptive surface  $h > 0$  we have monotonically increasing profiles  $s(z)$  at weakly charged electrodes while a maximum is formed at a certain distance from the wall for higher charges on the wall (Fig. 8(b)). Such a maximum is also visible on charge profiles  $q(z)$  (Fig. 9(b)). In order to characterize the profiles quantitatively we can introduce their first momenta [49]. From the density profiles we can plot the adsorption  $\Gamma_s$  (Fig. 10). It increases from  $h = 1$  to  $h = -1$ , as expected. In the case  $h = 1$  the adsorption is first negative and crosses the value zero when the charge is increased. Consequently, the center of gravity of the density profile  $s(z)$  is singular in this case, as shown in Fig. 11. We can see that the presence of another length drastically changes the structure of the interface in comparison with the NLGC theory. For  $h = 0$  or  $h = -1$  the center of gravity is pushed away from the electrode while it is attracted to the electrode in the NLGC theory. For the charge

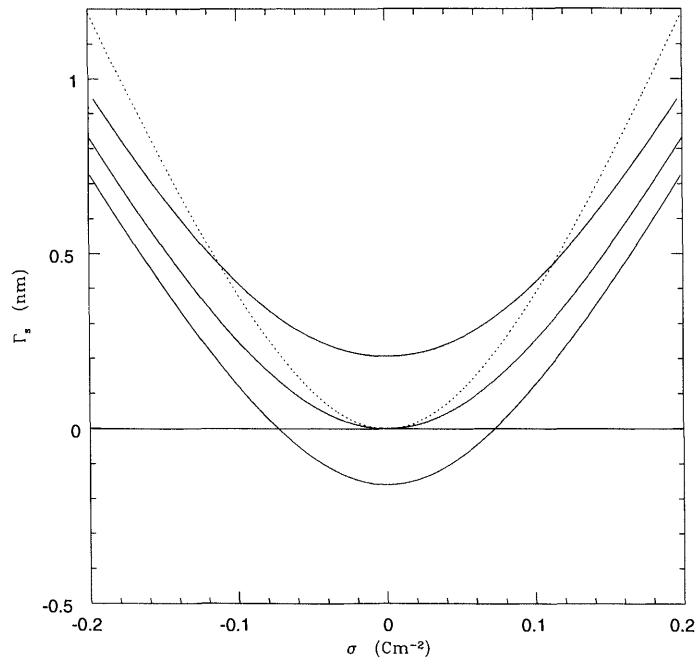


**FIG. 10** Adsorption of ions  $\Gamma_s$  as a function of  $\sigma$  for  $h = 1$  (uppermost curve),  $h = 0$ , and  $h = -1$  (lowermost curve). The dotted line is for NLGC theory. (From Ref. 49.)

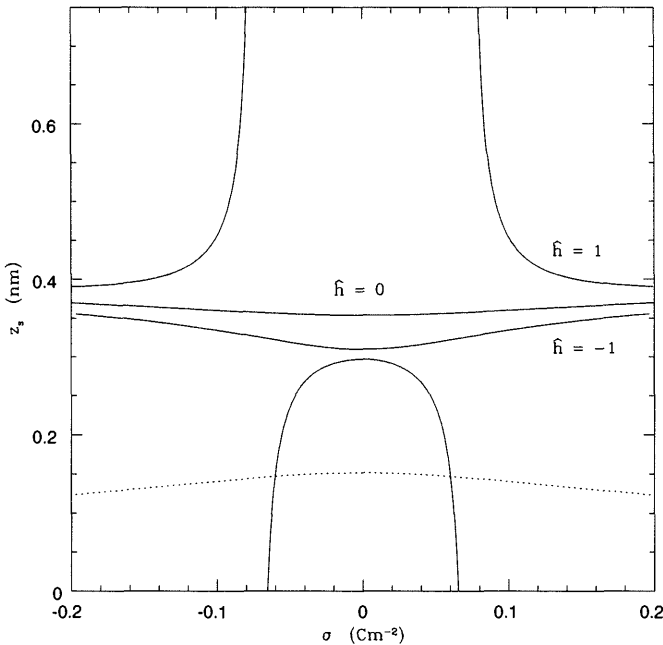


**FIG. 11** The effective distance  $z_s$  as a function of  $\sigma$  for the wall potential values  $h = -1, 0, 1$  (solid lines), and for the NLGC theory (dotted line). (From Ref. 49.)

distribution the first momentum is identical to the potential drop plotted in Fig. 12.

The differential capacitance  $C$  has been calculated according to the formula

$$C = \left( \frac{\partial \sigma}{\partial v} \right)_h \quad (93)$$

It is natural to consider the case when the surface affinity  $h$  to adsorb or desorb ions remains unchanged when charging the wall but other cases could be considered as well. In Fig. 13 the differential capacitance  $C$  is plotted as a function of  $\sigma$  for several values of  $h$ . The curves display a maximum for non-positive values of  $h$  and a flat minimum for positive values of  $h$ . At the pzc the value of the Gouy–Chapman theory and that for  $h = 0$  coincide and the same symmetry argument as in the previous section for the totally symmetric local interaction can be used to rationalize this result.

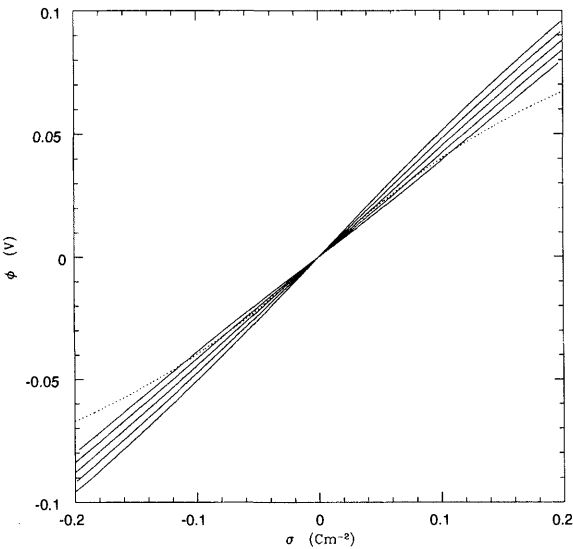


**FIG. 12** Electric potential  $\phi(0)$  as a function of  $\sigma$  for  $h = -1, -0.5, 0, 0.5, 1$  (solid lines). The NLGC case is indicated by a dotted line. (From Ref. 49.)

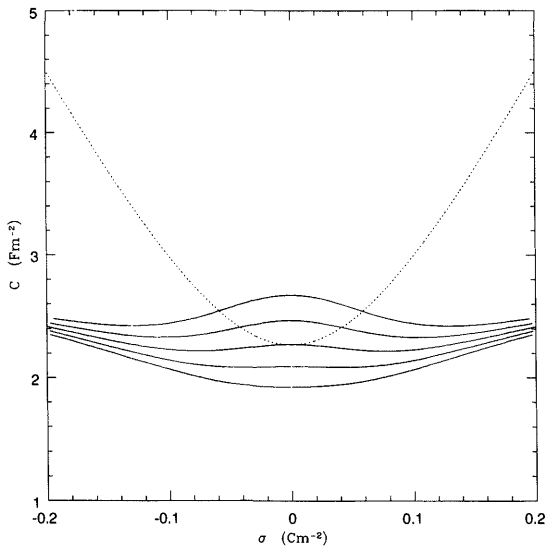


**FIG. 13** Differential capacitance  $C$  as a function of  $\sigma$  for  $h = -1, -0.5, 0, 0.5, 1$  (solid lines). The NLGC case is indicated by a dotted line. (From Ref. 49.)

## B. Lie Group Description and Trajectories

The results of the previous section can be presented in a different way associated with the existence of a one-parameter Lie group in four variables  $(g_+, g_-, \sigma, h)$ . There are three invariants of this group. The values of two of them are set by the boundary condition of the bulk solution far from the wall. We can use the two invariants to eliminate two of the four variables, for instance to calculate  $g_+(\sigma, h)$  and  $g_-(\sigma, h)$ . This is a natural choice since  $\sigma$  and  $h$  determine the properties of the system. Selecting a point  $(\sigma_0, h_0)$  near the origin of the  $(\sigma, h)$  coordinate system as an initial condition we find a unique trajectory  $h = f(\sigma, \sigma_0, h_0)$ . There can be no crossing point between two trajectories. Quite surprisingly, these trajectories stop at a given border (Fig. 14). In the region above the border line there is another regime of solutions. The nature of the terminal points becomes clear when we plot the corresponding trajectories in the  $(g_+, g_-)$  plane (Fig. 15) and the ionic profiles starting from the terminal point (Fig. 16). As can be guessed from

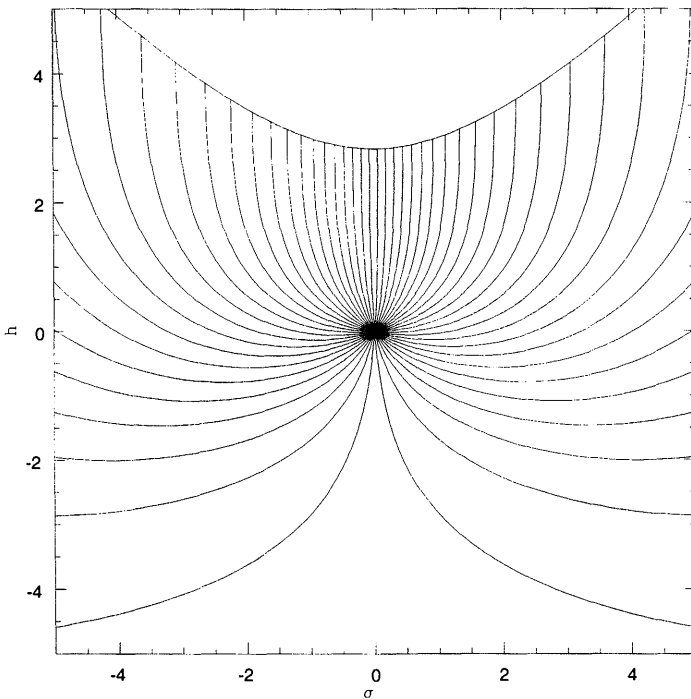


**FIG. 14** Trajectories in the  $(\sigma, h)$  planes for  $a_{ij} = 0$  and  $b = 1$ , and 1 M solution. (From Ref. 44)



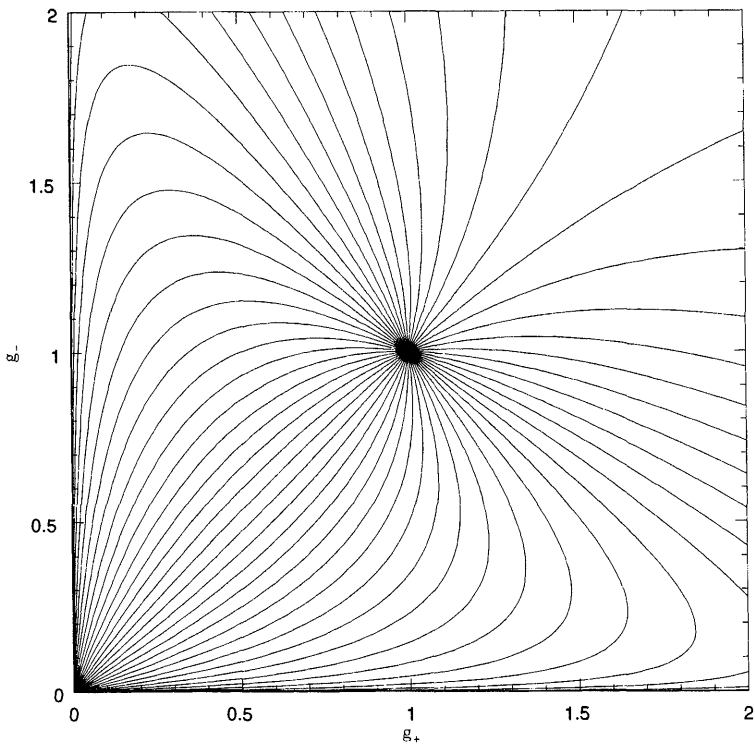


**FIG. 15** Trajectories in the  $(g_+, g_-)$  planes for  $a_{ij} = 0$  and  $b = 1$ , and 1 M solution. (From Ref. 51)

Fig. 15, almost all trajectories join two focal points. One of the focal points corresponds to the bulk solution  $(1, 1)$  and the origin of the  $(\sigma, h)$  plane. The other focal point,  $(0, 0)$  in the  $(g_+, g_-)$  plane, corresponds to the limiting curve in the  $(\sigma, h)$  plane formed by the terminal points. The trajectories terminate when the profiles  $g_+(z)$  and  $g_-(z)$  vanish.

To understand the physical background behind these results we have tried to find and analyze the three invariants predicted by the Lie group analysis. Clearly there is a local Lie group symmetry when  $g_+ > 0$  and  $g_- > 0$  but not when  $g_+ = 0$  and  $g_- = 0$  at the terminal point. We have managed to find only one of the three invariants. It is related to the pressure balance in the system

$$[2 - \ln g_+(z)g_-(z)][g_+(z) + g_-(z)] + \frac{h^2}{2b^2} - \frac{\sigma^2}{2} = 4 = p \tag{94}$$

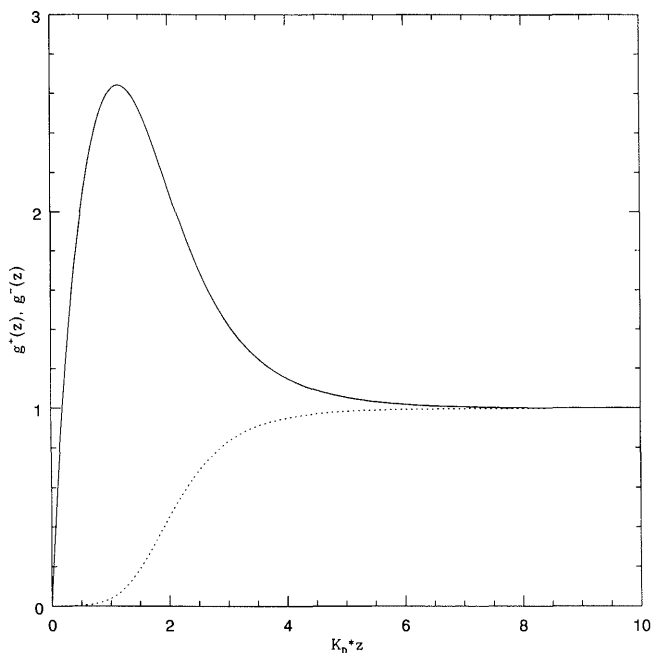


**FIG. 16** Ionic profiles  $g_+(z), g_-(z)$  corresponding to one of the trajectories of Figs. 14 and 15. The origin  $z = 0$  corresponds to the borderline in Fig. 14 and the focal point at the origin in Fig. 15. (Reprinted from Ref. 48 with permission from Elsevier Science.)

where  $p$  is the bulk pressure in reduced units. For  $g_+ = g_- = 0$  it reduces to

$$\frac{h^2}{2b^2} - \frac{\sigma^2}{2} = 4 = p \quad (95)$$

and then its physical meaning is very simple. The repulsion from the wall outweighs the kinetic and electrostatic pressure and disjoins the wall from the electrolyte. The contact value of the ionic profiles vanishes. The limiting curve turns out to be a hyperbola and we can test the accuracy of the solver by imposing this curve on the pattern of trajectories and checking the position of the terminal points—they all lie on the hyperbola. Assuming that the position of the terminal point corresponds to  $z = 0$ , we obtain the following asymptotic relations next to it

$$R = \lim_{z \rightarrow 0} \frac{g_+(z)}{g_-(z)} = \exp(-v_0) \quad (96)$$

where  $v_0$  is the electric potential and is finite. To the leading order we have, from (88–91) for  $z \approx 0$ , that profiles are proportional to  $z$  but the lower-order correction is non-analytic

$$Rg_-(z) \approx g_+(z) \approx \frac{R}{R+1} \left( \frac{h_0}{b^2} z + z^2 \left( \ln z - \frac{1}{2} \right) \right) \tag{97}$$

For  $z \approx 0$  we have also that the trajectory in the  $(\sigma, h)$  plane is given by a scaling law of the form  $|h - h_0| \propto |\sigma - \sigma_0|^{1/2} \ln |\sigma - \sigma_0|$ . Similar scaling relations can be found for other pairs of variables:  $g_{\pm} \propto |\sigma - \sigma_0|^{1/2}$  and  $|h - h_0| \propto g_+ \ln g_+$ . It is fairly straightforward to extend the above results to the case when  $a_{ij} \neq 0$ . An example of an asymmetric system is shown in Fig. 17. Although the pattern of the trajectories is changed the form of the limiting curve remains the same, as well as the form of the scaling relations near the terminal point.

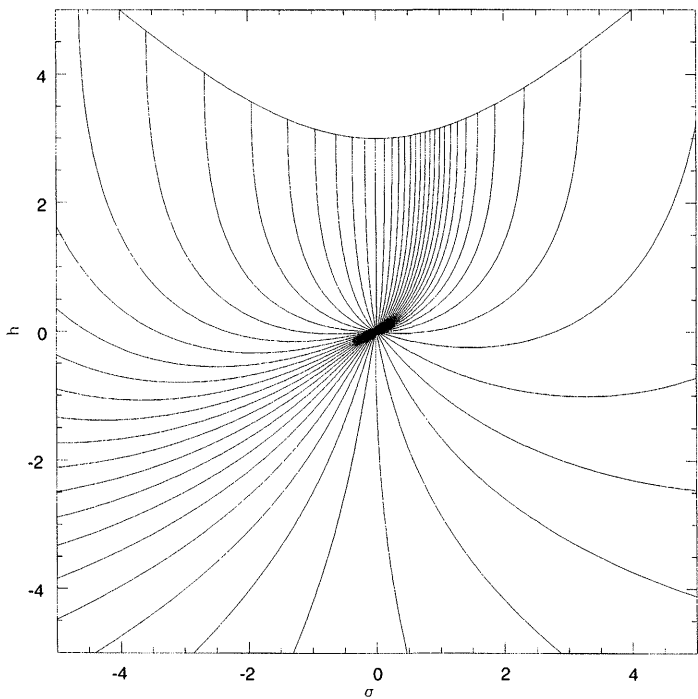


**FIG. 17** Trajectories in the  $(\sigma, h)$  planes for  $a_{++} = 0.2$  and  $a_{--} = 0.8$ ,  $a_{+-} = 0$ , and  $b = 1$ , and 1 M solution. (From Ref. 51)

## IX. CONCLUSIONS

The Gouy–Chapman theory remains up to now one of the basic theoretical tools used to investigate the properties of charged interfaces. In this paper we have shown how it is possible to go beyond this theory by using, systematically, a field-theoretical approach. Among the large number of phenomena that take place at the charged interfaces, we have selected a small number of them which are common for these systems. The results can be obtained in a simple and transparent manner. Some of them are the exact consequence of the Hamiltonian while others are obtained in the mean field approach. For each problem considered we try to answer some questions like, e.g.: what is the consequence of the competition between electrostatics and entropy? what is the role of the symmetry of interaction between ions? The concept of a group of transformations, commonly used in quantum field theory, has been introduced to describe some properties of the interface. We have shown that the small number of phenomena taken into account is already sufficient to produce a large number of behaviors qualitatively different from those predicted by the Gouy–Chapman theory.

In the future it should be interesting to perform more sophisticated descriptions of the nonlinear regime. For instance, it should be interesting to see how the fluctuation of charge and density in the direction parallel to the wall may change the mean field result. It should also be interesting to introduce a simple Hamiltonian in order to investigate both sides of the interface on the same footing.

## ACKNOWLEDGMENTS

The authors are grateful to Zofia Borkowska and Dung di Caprio for helping us during preparation of this work. This work also results from the long cooperation between our laboratories in the framework of the agreement between the Centre National de la Recherche Scientifique in France and the Polish Academy of Sciences.

## REFERENCES

1. P. Delahay. *Double Layer and Electrode Kinetics*. New York: Interscience, 1965, pp. 1–12.
2. M. J. Sparnaay. *The Electrical Double Layer*. Glasgow: Pergamon Press, 1972.
3. R. Parsons. Electrical double layer: recent experimental and theoretical developments. *Chem Rev* 90:813–826, 1996.
4. J. Israelachvili. *Intermolecular and Surface Forces*. 2nd ed. London: Academic Press, 1992.

5. W. Schmickler. *Interfacial Electrochemistry*. New York: Oxford University Press, 1996.
6. A. Sanfeld. *Introduction to the Thermodynamics of Charged and Polarized Layers*. Bath (UK): Wiley-Interscience, 1968.
7. L. Blum. Structure of the electric double layer. In: I. Prigogine, S. A. Rice, eds. *Advances in Chemical Physics*, Vol. 78, New York: Wiley, 1990, pp. 171–222.
8. L. Blum. The electric double layer—a comprehensive approach. In: C. A. Croxton, ed. *Fluid Interfacial Phenomena*. New York: Wiley, 1986, pp. 391–436.
9. A. Watts, T. J. VanderNoot. The electrical double layer at liquid–liquid interfaces. In: A. G. Volkov, D. W. Deamer, eds. *Liquid–Liquid Interfaces. Theory and Methods*. Boca Raton: CRC Press, 1996, pp. 77–102.
10. S. L. Carnie, G. M. Torrie. The statistical mechanics of the electrical double layer. In: I. Prigogine, S. A. Rice, eds. *Advances in Chemical Physics*, Vol. 56. New York: Wiley, 1984, pp. 141–253.
11. D. C. Grahame. Thermodynamic properties of the electrical double layer. *Chem Rev* 41:441–443, 1947.
12. S. Amokrane, J. P. Badiali. Analysis of the capacitance on the metal–solution interface: role of the metal and metal–solvent coupling. In: J. O'M. Bockris, B. E. Conway, R. E. White, eds. *Modern Aspects of Electrochemistry*, Vol. 22. New York: Plenum Press, 1992, pp. 1–96.
13. W. Schmickler, D. Henderson. New models for the electrochemical interface. *Prog Surf Sci* 22:323–420, 1986.
14. J. S. Rowlinson, B. Widom. *Molecular Theory of Capillarity*. Oxford: Clarendon Press, 1982.
15. J. P. Hansen, I. R. McDonald. *Theory of Simple Liquids*. London: Academic Press, 1986, pp. 365–387.
16. W. R. Fawcett. Molecular models for the solvent structure at polarizable interfaces. *Israeli J Chem* 18:3–16, 1979.
17. G. Parisi. *Statistical Field Theory*. Redwood City: Addison Wesley, 1988.
18. J. Stafiej, Z. Borkowska, J. P. Badiali. A description of electrified interfaces based on methods of statistical field theory. *J Electroanal Chem* 395:1–14, 1995.
19. J. Stafiej, J. P. Badiali. On a new theoretical approach of electrified interfaces. *J Electroanal Chem* 409:73–78, 1996.
20. R. Evans. The role of capillary wave fluctuations in determining the liquid–vapor interface. Analysis of the van der Waals model. *Mol Phys* 42:1169–1196, 1981.
21. R. P. Feynman, A. R. Hibbs. *Quantum Mechanics and Path Integrals*. New York: McGraw Hill, 1965.
22. J. Zinn-Justin. *Quantum Field Theory and Critical Phenomena*. Oxford: Clarendon Press, 1990.
23. D. Brydges, P. Federbush. Debye screening in classical Coulomb systems. In: G. Velo, A. S. Wightman, eds. *NATO Advanced Science Institutes. Series No. B 74*. New York: Plenum Press, 1981, pp. 371–385.
24. T. Kennedy. Debye–Hückel theory for charge symmetric Coulomb systems. *Commun Math Phys* 92:269–294, 1983.

25. L. Landau, E. Lifshitz. *Statistical Physics*. Oxford: Pergamon, 1958.
26. D. J. Amit. *Field Theory, the Renormalization Group, and Critical Phenomena*. Singapore: World Scientific, 1984.
27. J. Stafiej, A. Ekoka, Z. Borkowska, J. P. Badiali. New theoretical description of electrified interfaces. *J Chem Soc, Faraday Trans* 92:3677–3682, 1996.
28. J. Stafiej, M. Dymitrowska, J. P. Badiali. Field theoretic approach of electrified interfaces. *Electrochim Acta* 41:2107–2113, 1996.
29. J. P. Badiali, L. Blum, M. L. Rosinberg. Localized adsorption at solid–liquid interface: the sticky site hard wall model. *Chem Phys Lett* 129:149–154, 1986.
30. D. E. Sullivan, M. M. Telo da Gama. Wetting transition and multilayer adsorption at fluid interfaces. In: C. A. Croxton, ed. *Fluid Interfacial Phenomena*. New York: Wiley, 1986.
31. K. Binder. Critical behaviour at surfaces. In: C. Domb, J. L. Lebowitz, eds. *Phase Transitions and Critical Phenomena, Vol. 8*. London: Academic Press, 1983, pp. 1–144.
32. D. di Caprio, J. Stafiej, J. P. Badiali. A field theory study of the effect of specific ionic interactions in ionic systems. *J Chem Phys* 108:8572–8583, 1998.
33. V. M. Nabutovskii, N. A. Nemov, Yu. G. Peisakhovich. Charge-density and order-parameter waves in liquid and solid electrolytes in the vicinity of the critical point. *Phys Lett* 79A:98–100, 1980.
34. V. M. Nabutovskii, N. A. Nemov, Yu. G. Peisakhovich. Correlation functions for the electrolyte near the critical point of pure solvent. *Mol Phys* 54:979–987, 1985.
35. A. L. Kholodenko, A. L. Beyerlein. Theory of symmetric electrolyte solutions: Field theoretic approach. *Phys Rev A* 34:3309–3324, 1986.
36. A. L. Kholodenko, A. L. Beyerlein. Critical versus tricritical phase transitions in symmetric electrolytes. *Phys Lett A* 175:366–369, 1993.
37. A. M. Walsh, R. D. Coalson. Lattice field theory for spherical macroions in solution: Calculation of equilibrium pair correlation function. *J Chem Phys* 100:1559–1566, 1994.
38. R. D. Coalson, A. Duncan. Systematic ionic screening theory of macroions. *J Chem Phys* 97:5653–5661, 1992.
39. J. Stafiej, J. P. Badiali. A simple model for Coulombic systems. Thermodynamics, correlation functions and criticality. *J Chem Phys* 106:8579–8586, 1997.
40. D. di Caprio, A. Filippov, J. Stafiej, J. P. Badiali (accepted in *J Mol Liq*).
41. F. H. Stillinger Jr, R. Lovett. General restriction on the distribution of ions in electrolytes. *J Chem Phys* 49:1991–1994, 1968.
42. M. L. Japas, J. M. H. Levelt Sengers. Critical behavior of a conducting ionic solution near its consolute point. *J Chem Phys* 94:5361–5368, 1994.
43. G. Stell. Criticality and phase transitions in ionic fluids. *J Stat Phys* 78:197–221, 1995.
44. L. V. Ovsiannikov. *Group Analysis of Differential Equations*. New York: Academic Press, 1982.

45. D. Henderson, L. Blum, J. L. Lebowitz. An exact formula for the contact value of the density profile of a system of charged hard spheres near a charged wall. *J Electroanal Chem* 102:315–319, 1979.
46. J. Stafiej, Z. Borkowska, J. P. Badiali. A simple description of the structure of ionic solutions at electrified interfaces. *Cond Matt Phys (Ukraine)* 12:51–61, 1997.
47. R. Parsons, F. G. R. Zobel. The interphase between mercury and aqueous sodium dihydrogen phosphate. *J Electroanal Chem* 9:333–348, 1965.
48. J. Stafiej, D. di Caprio, J. P. Badiali. Theoretical analysis of the competition between coulombic and specific interactions at charged interfaces. *Electrochim Acta* 43:2947–2955, 1998.
49. J. Stafiej, D. di Caprio, J. P. Badiali. A simple model to investigate the effects of non-Coulombic interactions on the structure of charged interfaces. *J Chem Phys* 109:3607–3618, 1998.
50. Z. Borkowska, J. Stafiej, J. P. Badiali. Simple description of ionic solution at electrified interfaces. Proceedings of the Symposium on the Electrochemical Double Layer, Montreal, 1997, pp. 120–130.
51. J. Stafiej, D. di Caprio, J. P. Badiali. *Phys Rev (submitted)*.

# 18

## Crystal Growth and Solidification

**HEINER MÜLLER-KRUMBHAR** Institut für Festkörperforschung,  
Forschungszentrum Jülich, Jülich GMBH, Germany

**YUKIO SAITO** Department of Physics, Keio University, Yokohama,  
Japan

I. Introduction	852
A. Simulation methods	853
B. Crystals and solids	854
C. Equilibrium form of crystals	855
II. Basic Models	856
A. Quantum-mechanical models	856
B. Atomistic models in continuous space	858
C. Lattice models	858
D. Roughening transition	859
E. Kinetic roughening, KPZ equation and variations	861
III. Interface Kinetics	863
A. Master equation formalism and Monte Carlo simulation	863
B. Mean-field dynamics	864
C. Nucleation	866
D. Growth and Ostwald ripening	867
E. Wilson–Frenkel growth law	869
F. Surface steps and spiral growth	871
G. Sharp interface model	875
H. Phase-field model	877
I. Elastic effects on growth processes	879
IV. Growth Under Surface Diffusion	880
A. Fluctuations and diffusion	880
B. Adsorption, desorption, and step motion	881



C.	Cluster growth and molecular beam epitaxy	884
D.	RHEED oscillations	886
E.	Fractal growth	886
V.	Growth Under Bulk Diffusion	888
A.	Basic model equations	889
B.	Growth patterns: dendrites and seaweed	891
C.	Surface dewetting as a diffusional growth process	895
D.	Fractal structures in diffusional growth	896
E.	Directional solidification	898
F.	Multicomponent and eutectic growth	900
VI.	Growth Under Hydrodynamical Flow	902
A.	Hydrodynamical effects on interface advancement	902
B.	Bridgman and Czochralski growth	903
VII.	Growth of Crystals of Complex Materials	904
A.	Polymer crystals	905
B.	Protein crystals	906
C.	Quasi-crystals	906
VIII.	List of Keywords	906
	References	915

I. INTRODUCTION

The growth of crystals has always fascinated scientists [1]. The past two decades have brought a significantly renewed interest into the scientific community for a better understanding of crystal-growth processes. Two obvious reasons are the strong impact of semiconductor-based computer-technology in all fields of everyday life, and simultaneously the dramatic improvement of experimental techniques such as high-resolution transmission electron microscopy and scanning-tunneling microscopy and derivatives. Formerly unexpected direct insights into the fine structure of materials and surface processes now can be achieved. A third reason is the related increase in computational power, which allows a widespread application of computer simulation techniques in materials science.

Currently there are about 200 publications per year related to the simulation of crystal growth. Clearly it is impossible to give a complete survey of what is being achieved in this field. Our aim, therefore, can be only to show

some recent trends and to give a guide to the exploding literature, necessarily somewhat guided by personal scientific interests.

The goal of any simulation is a better understanding of the physical process represented by a specific model. In the following sections of this article we therefore give short introductions into the physical processes and to their model concepts together with references to analytical work. Clearly, our article cannot substitute for textbooks (see, for example, [2,3]) on any of the subjects touched here, nor can it substitute for the reading of the original references. We can only hope that it may help the newcomer to catch some of the flavor of the field, and help the specialist in finding cross-references between the many physical mechanisms, the modelling concepts and the simulation results.

## A. Simulation Methods

The simulation of crystal growth and solidification requires a set of different methods, each one with specific strengths and weaknesses on certain scales of length and time. On the subatomic or electronic scale the currently available quantum methods are not yet capable of describing macroscopic growth phenomena. The possibility of calculating the characteristic  $7 \times 7$  reconstruction of the Si surface is just about the coming state of the art. On the next larger scale, up to a few 10 000 atoms, molecular dynamics and Monte Carlo methods are showing their worth. Molecular dynamics is best for treating defect formation in continuous space, but is restricted to rather short time scales in the nanoseconds range. Monte Carlo simulation runs best on a lattice, and then has the advantage that the intrinsic time scale need not be shorter than the shortest time scale relevant for the process of interest. It is good for growth of a crystal from the gas phase, but not ideal for solidification of a dense liquid. Again, on larger scales, one goes over to continuum description in the form of nonlinear partial differential equations. Typical examples are the sharp-interface models or the phase-field models, where some kind of diffusion equation can be used. The last regime concerns convective flow on large scales, again being treated mostly with partial differential equations.

All of these methods are not really specific for crystal growth, but the problem of crystal growth simulations poses some specific difficulties, so it is a good testing ground for the development of new methods. Particularly promising are combinations of the methods mentioned above: Quantum-mechanical pseudopotential methods with molecular dynamics or "Car-Parrinello" methods [4], combinations of partial differential equations for diffusion fields with Monte Carlo methods for interface kinetics [5,6], and multigrid-multipole methods combined with particle methods to treat long-

range interaction potentials between the particles [7]. Possibly the most characteristic feature of crystal growth and solidification with respect to modeling is the aspect of the moving-boundary problem. There is some analogy in the fluid dynamics of non-miscible two-fluid systems, but the solidification aspect additionally brings anisotropy into play. One aspect, finally, which will become more important in the future, is the parallelization [8] of computer programs. For the present purpose, however, we considered this a bit too technical, so we leave a discussion of this aspect to the future.

## B. Crystals and Solids

Crystals are solids. Solids, on the other hand can be crystalline, quasi-crystalline, or amorphous. Solids differ from liquids by a shear modulus different from zero so that solids can support shearing forces. Microscopically this means that there exists some long-range orientational order in the solid. The orientation between a pair of atoms at some point in the solid and a second (arbitrary) pair of atoms at a distant point must on average remain fixed if a shear modulus should exist. Crystals have this orientational order and in addition a translational order; their atoms are arranged in regular lattices.

There has been great progress in the theory of phase transitions during the last three decades. Surprisingly, the theory of freezing and melting (in three dimensions) has remained more or less on a level of "mean-field approximation." A more fundamental understanding is still lacking as far as the solid-liquid transition is concerned. In two dimensions, the solid-liquid transition can be understood by the formation of dislocation-disclination networks [9]. The formation of crystal lattices in any dimension is more easily described by a theory if one can assume *a priori* that a lattice will form.

The reason for the formation of a lattice can be the isotropic repulsive force between the atoms in some simple models for the crystallization of metals, where the densely packed structure has the lowest free energy. Alternatively, directed bonds often arise in organic materials or semiconductors, allowing for more complicated lattice structures. Ultimately, quantum-mechanical effects are responsible for the arrangements of atoms in the regular arrays of a crystal.

The theory of crystal growth accordingly starts usually with the assumption that the atoms in the gaseous, diluted, or liquid mother phase will have a tendency to arrange themselves in a regular lattice structure. We ignore here for the moment the formation of polycrystalline solids. In principle we should start with the quantum-mechanical basis of the formation of such lattice structures. Unfortunately, however, even with the computational effort of present computers with a performance of about 100 megaflops

per processor one is hardly able to treat more than about 100 atoms by first-principles calculations. One generally tries to employ fully quantum-mechanical computations only to achieve some effective forces between atoms or small groups of atoms. One then constructs effective potentials of the Stillinger–Weber type [10] or of some “embedded atom method” (EAM) [11], with which one then performs molecular-dynamics simulations of typically some thousand atoms over timescales of about  $10^{-9}$  s real time.

These apparent restrictions in size and length of simulation time of the fully quantum-mechanical methods or molecular-dynamics methods with continuous degrees of freedom in real space are the basic reason why the direct simulation of lattice models of the Ising type or of solid-on-solid type is still the most popular technique to simulate crystal growth processes. Consequently, a substantial part of this article will deal with scientific problems on those time and length scales which are simultaneously accessible by the experimental STM methods on one hand and by Monte Carlo lattice simulations on the other hand. Even these methods, however, are too microscopic to incorporate the boundary conditions from the laboratory set-up into the models in a realistic way. Therefore one uses phenomenological models of the “phase-field” or “sharp-interface” type, and finally even finite-element methods, to treat the diffusion transport and hydrodynamic convections which control a realistic crystal growth process from the melt on an industrial scale.

### C. Equilibrium Form of Crystals

The growth of crystals—or more generally the solidification of a solid from a fluid phase—is definitely not an equilibrium problem. Why, therefore, should we discuss here equilibrium thermodynamics, instead of treating directly, for example the coagulation of two atoms and then simply following the growth of the cluster by adding more particles with time?

The reason is that thermodynamics describes the system in equilibrium as a *state*, i.e., the question of the initial conditions for the trajectories of all shared particles is unimportant. This means an enormous simplification for the theory! To be precise: we do not need the system to be in equilibrium, but small parts of the system (each one containing a few atoms) should be describable by at least some local equilibrium, so that we can speak of a local temperature, for example.

Clearly, there are situations where we have to give up this assumption. A typical case is molecular beam epitaxy (MBE) (see [3,12–14] and [15–19]), where particles are shot onto the surface of a crystal rather than condensing slowly from a thermally equilibrated vapor-phase. In this case we will have to be very specific about all the experimental boundary conditions and

eventually we will have to consider the trajectories of the impinging atoms explicitly. For other aspects of this problem and for many other situations, however, thermodynamical equilibrium conditions are a very good starting point for theoretical considerations.

Therefore, we first look at the question of how a crystal looks in thermodynamical equilibrium. Macroscopically, this is controlled by its anisotropic surface (free) energy and the shape can be calculated via the Wulff construction.

Crystals have spatially preferred directions relative to their internal lattice structure with consequences for orientation-dependent physico-chemical properties; i.e., they are anisotropic. This anisotropy is the reason for the typical formation of flat faceted faces. For the configuration of the facets the so-called Wulff theorem [20] was formulated as: "in a crystal in equilibrium the distances of the facets from the centre of the crystal are proportional to their surface free energies."

To find the equilibrium form of a crystal, the following Wulff construction [20] can be used, which will be explained here, for simplicity, in two dimensions. Set the centre of the crystal at the origin of a polar coordinate system  $\{r, \theta\}$ . The radius  $r$  is assumed proportional to the surface tension  $\gamma(\theta)$ , where  $\theta$  defines the angle between the coordinate system of the crystal lattice and the normal direction of a point at the surface. The anisotropy here is given through the angular dependence. A cubic crystal, for example, shows in a two-dimensional cut a clover-leaf shape for  $\gamma(\theta)$ . Now draw everywhere on this graph the normals to the radius vector  $\vec{r} = \{r, \theta\}$ . The area in the centre of the coordinate system untouched by these lines then defines the form of the crystal.

The line which defines the crystal surface can have straight pieces ("facets") as well as curved ones. The latter correspond to a "rough" surface, as explained in the next section. The point at which straight and curved pieces meet can be either a sharp corner or a smooth tangential connection like  $z \approx x^{3/2}$  [21], where  $x$  is the deviation from the contact point in the direction of the facet and  $z$  is the distance orthogonal to this facet ( $z = 0$  on the facet). Alternatively, curved pieces can adjoin with a kink, and there then exist forbidden orientations of crystal surfaces. A generalization to three dimensions is straightforward and will not be further discussed here.

## II. BASIC MODELS

### A. Quantum-mechanical Models

The macroscopic appearance of crystals, with their polygonal facets and the underlying lattice structure, is the consequence of quantum mechanical

interactions between the atoms. The actual forces are the Coulomb forces between electrons and between electrons and ions, and the quantum-mechanical selection rules of this many-body system. A first-principles calculation of crystallization therefore has to start with quantum-mechanical many-body theory. Unfortunately, the calculations on this level cannot be made exactly. Even with the help of computers one has to resort to approximation and even those can be performed for relatively small systems only, if no specific symmetry can be used to reduce the number of degrees of freedom.

Quantum-mechanical density functional theory [22], based on the local density approximation, has led to rather satisfactory results for infinite periodic crystal lattices and for atomic clusters up to about 100 atoms. The methods are able to calculate with reasonable accuracy the ground-state properties of these systems. For the understanding of crystal growth processes one wants to know the resulting lattice structure, the adsorption energies at arbitrary places on the crystal surface, and potential barriers between the various low-energy sites for an additionally adsorbed atom. What makes the calculation complicated is the fact that the resulting energies for an additional atom on a surface are not simply additive since the additional atom changes the whole electronic structure of the crystal. In other words, the "bonds" between the atoms will have preferred directions, lengths, and strengths, depending on the number of atoms in the neighborhood and on their local arrangement. The presently available results relevant to crystal growth processes are still rather limited, but continuing efforts and increasing computer capacities will definitely improve the situation in the future.

For semiconductor crystals the "pseudopotential" methods [23–25] have proven to be most successful. Recent examples are the calculation of the energy barriers for surface diffusion by a complicated hopping and exchange process for Si on an As-decorated Si surface [26]. For metals, and in particular for the transition metals with incompletely filled inner electronic shells, the "Kohn–Korringa–Rostocker" (KKR) methods seem to give the most precise results for crystal structures and layered systems. Recent developments make the calculation of layered systems very efficient, even including adatoms and surface defects as basic ingredients for the crystal growth process [27].

A full-scale treatment of crystal growth, however, requires methods adapted for larger scales on top of these quantum-mechanical methods, such as effective potential methods like the "embedded atom method" (EAM) [11] or Stillinger–Weber potentials [10] with three-body forces necessary. The potentials are obtained from quantum mechanical calculations and then used in Monte Carlo or molecular dynamics methods, to be discussed below.

## B. Atomistic Models in Continuous Space

The simplest atomistic model for the formation of a crystal in continuous space requires the definition of some effective attractive potential between any two atoms, which is defined independently of the other atoms in the cluster or crystal. The most frequently studied potential is the Lennard-Jones potential

$$U(r) = U_0 \{1/r^{12} - 1/r^6\} \quad (1)$$

Here  $r$  is the distance between the centers of two atoms in dimensionless units  $r = R/\sigma$ , where  $R$  is the actual distance and  $\sigma$  defines the effective range of the potential.  $U_0$  sets the energy scale of the pair-interaction. A number of crystal growth processes have been investigated by this type of potential, for example [28–31]. An alternative way of calculating solid-liquid interface structures on an atomic level is via classical density-functional methods [32,33].

## C. Lattice Models

In the analysis of crystal growth, one is mainly interested in macroscopic features like crystal morphology and growth rate. Therefore, the time scale in question is rather slower than the time scale of phonon frequencies, and the deviation of atomic positions from the average crystalline lattice position can be neglected. A lattice model gives a sufficient description for the crystal shapes and growth [3,34,35].

The simplest model is the lattice-gas or Ising model. The whole space is divided into a lattice of  $N$  sites, and on each site two different states are possible: a crystalline state denoted by the variable  $s_i = 1$  and a gaseous state by  $s_i = -1$ . The variable  $s$  denotes the degree of crystalline order. The cohesion of nearest-neighboring solid atoms leads to the following interaction energy

$$\mathcal{H} = -J \sum_{\langle i,j \rangle} s_i s_j - \frac{\Delta\mu}{2} \sum_i s_i \quad (2)$$

$\Delta\mu$  is the chemical potential difference between solid and gas. Also, from the equivalence of the system to an Ising spin system, one often uses the terminology *spin* for the variable  $s$ , although it has nothing really to do with a quantum-mechanical spin.

If one is interested in the configuration of a singular surface or a vicinal surface close to the singular orientation, the surface is better characterized by the local height  $h_i$ . The description assumes that there should be no vacancy in the crystal, no floating-solid atoms in the ambient phase, nor

overhangs at the surface. Therefore, the model is called solid-on-solid (SOS) model. A broken solid-solid bond causes an energy increase in proportion to the height difference between the neighboring sites,  $i$  and  $j$ . The interaction energy is expressed by the following Hamiltonian

$$\mathcal{H} = J \sum_{\langle i,j \rangle} |h_i - h_j| - \frac{\Delta\mu}{2} \sum_i h_i \quad (3)$$

There are cases where non-regular lattices may be of advantage [36,37]. The computational effort, however, is substantially larger, which makes the models less flexible concerning changes of boundary conditions or topological constraints. Another direction, which may be promising in the future, is the use of hybrid models, where for example local attachment kinetics are treated on a microscopic atomistic scale, while the transport properties are treated by macroscopic partial differential equations [5,6].

## D. Roughening Transition

A one-dimensional phase-boundary line between two coexisting phases is always “rough”; i.e., its mean position does not lock into the lattice but can fluctuate freely in thermodynamical equilibrium. A physical representation of such a phase boundary line between two phases would be the edge or the step of a terrace on a crystal surface, where on one side of the step there is one additional atomic layer deposited on the crystal surface. The step follows the atomic structure of the lattice in atomically sharp turns or “kinks.” A single kink represents a sideways displacement of an originally straight step by one lattice unit. A slip of the kink along the step, in consequence, moves the average position of the step in the normal direction virtually continuously. The mean width  $w$  of the step increases due to the existence of kinks along the step as a function of the length  $L$  of the step (in the sense of random fluctuations around the average) as  $w \approx \sqrt{L}$ . Therefore, the width of the fluctuating step diverges when the length  $L$  of the step goes to infinity (see Sec. III F 1).

One now wonders whether these two phenomena are to be observed also for the whole two-dimensional surface of a crystal: non-locking of the crystal surface in spite of lattice periodicity, and divergence of the fluctuation-induced thickening of the interface (or crystal surface), and in consequence the absence of facets. The last seems to contradict experience: crystals almost by definition have their charm simply due to the beautifully shining facets which has made them jewelry objects since ancient times.

By the end of the 1940s, however, there existed the presumption that a roughening transition could possibly occur at a crystal surface with increasing temperature [20]. Although the original idea pursued in this still



impressive paper was not completely correct, the existence of the phenomenon is now accepted. The fundamental consideration goes as follows.

We have argued above, that a surface-step at all temperatures above absolute zero fluctuates and that its width diverges with the square root of the length of the step. The reason for this is the non-zero density  $n_k$  of kinks along the step, which is approximately proportional to  $n_k \approx \exp(-U/kT)$ , where  $U$  is the kink energy. The total number of kinks  $N_k$  is obviously proportional also to the length  $L$  of the step. The number of possible configurations  $N_C$  of such a step increases exponentially with the total number of kinks:  $N_C \approx 2^{C N_k}$ , with some trivial combinatorial constant  $C$ . In consequence, the logarithm of the total number of configurations of the step increases in proportion to its length:  $\log N_C \sim L$ . But this is just the entropy  $S_s$  of the step! On the other hand, the energy  $U_s$  of the step is also directly proportional to the length. Since the free energy of the step  $F_s = U_s - T S_s$  is then proportional to the length of the step, one sees immediately that, for low temperatures, steps will cost free energy while, for high temperatures,  $T > T_R \approx U_s/S_s$ , long surface steps become favorable, for entropy reasons. The temperature  $T_R$ , where the first surface step of infinite length appears on the surface, is called the "roughening temperature" since the average position of the two-dimensional surface may then freely shift up and down due to a lateral shift of the surface step at no cost of energy.

These arguments have of course ignored the formation of other clusters and holes on the surface which interact with the long step, but these details only modify the precise position of the transition point (and the precise nature of the singularity), not the general mechanism of the roughening-transition [9,38]. Note that this transition is a long-range effect and has very little to do with atomically rough or smooth structures observed on any restricted region of the crystal surface [3]. The essential effect of the roughening transition of a crystal facet is that the facet disappears. It loses its singular character, although a crystalline anisotropy will remain even above  $T_R$ . The remaining question, whether this roughening temperature occurs below the melting temperature (or the triple point junction), must be considered separately for each material. The consequences of surface roughening for the kinetics of crystal growth are rather important: below the roughening transition a nucleation barrier must be overcome for a crystal to grow, whereas above the roughening transition the already existing surface steps of arbitrary length can advance with a speed proportional to the "driving force." Therefore, all kinetic properties of crystal surfaces will be affected by the roughening transition [39,40,42].

## E. Kinetic Roughening, KPZ Equation and Variations

In the previous sections, we briefly introduced a number of different specific models for crystal growth. In this section we will make some further simplifications to treat some generic behavior of growth problems in the simplest possible form. This usually leads to some nonlinear partial differential equations, known under names like Burgers, Kardar–Parisi–Zhang (KPZ), Kuramoto–Sivashinsky, Edwards–Anderson, complex Ginzburg–Landau equation and others.

In particular we would like to treat some essential effects of fluctuations where we assume that, for example, thermal fluctuations exist and are localized in space and time. The effects on large lengths and long times are then of interest where the results are independent of local details of the model assumptions and therefore will have some *universal* validity. In particular, the development of a rough surface during growth from an initially smooth surface, the so-called effect of kinetic roughening, can be understood on these scales [42,44].

We first make an ansatz for a one-dimensional rough phase boundary (the edge of a surface-step, for example), with respect to its energy:

$$\tilde{F} \sim \int dx \frac{1}{2} (\nabla h(x))^2 \quad (4)$$

where  $h(x)$  is the local height of the phase boundary relative to some reference level. The integrand allows for a displacement of the interface by a constant value, but suppresses ripples.

The next step is the formulation of an equation of motion. We assume for this moment that  $h(x)$  can only vary by surface diffusion, i.e., by peripheral diffusion of  $h$  along  $x$ . The classical conservation law holds that  $(\partial/\partial t)h + \text{div } j_h = 0$ . For the current  $j_h$ , the constitutive equation is, according to classical thermodynamics,  $j = -D_s \nabla \mu$ ;  $\mu = \delta \tilde{F} / \delta h = -\nabla^2 h$ , and  $\delta \tilde{F} / \delta h$  is the functional derivative. From this follows the equation of motion:

$$\frac{\partial}{\partial t} h = -D_s \nabla^2 (\nabla^2 h), \quad (5)$$

giving a spatial derivative of fourth order, where  $D_s$  is the coefficient of surface diffusion.

If we allow for exchange with the gas phase, then  $h(x)$  does not obey a conservation condition and we have the simple Ginzburg–Landau equation:

$$\frac{\partial}{\partial t} h = -D_v \frac{\delta \tilde{F}}{\delta h} = D_v \nabla^2 h \quad (6)$$

which looks like a diffusion equation with a kinetic coefficient  $D_v$ .

Furthermore, we introduce additionally external forces  $f(x, t)$  and fluctuating forces  $\eta(x, t)$ , and assume  $\delta$ -correlations for the fluctuations:  $\langle \eta \rangle = 0$ ;  $\langle \eta(x, t) \eta(x', t') \rangle = 2\Gamma \delta(x - x') \delta(t - t')$ .

Since all these processes listed here can work independently of each other, they can also occur combined in an equation of motion for the phase boundary:

$$\frac{\partial}{\partial t} h = D_v \nabla^2 h - D_s \nabla^2 \nabla^2 h + f + \eta \tag{7}$$

This is the general linear equation of motion for an almost planar and rough one-dimensional phase boundary. The fourth-order term in the spatial derivative acts as a stabilizer just like the second-order term, and is not really crucial here.

These considerations have so far been restricted to small-amplitude deviations of  $h(x)$  from a straight horizontal line. Since a phase boundary typically advances in the normal direction, we must make a correction for the case of an inclined interface:

$$\frac{\partial}{\partial t} h = V_{\perp} \sqrt{1 + (\nabla h)^2} \approx V_{\perp} (1 + \frac{1}{2} (\nabla h)^2) \tag{8}$$

Keeping the pre-factor of this new nonlinear term free, we can summarize:

$$\frac{\partial}{\partial t} h = D_v \nabla^2 h + \frac{\lambda}{2} (\nabla h)^2 + \eta. \tag{9}$$

This is the Burgers equation with supplementary fluctuation term  $\eta$ , and it became famous in this form as the KPZ equation according to Kardar, Parisi, and Zhang [43,44]. It is the generic equation for the motion of a phase boundary under influence of noise. If one adds the term of fourth-order in the spatial derivative again, as in Eq. (7), then one can admit the case  $D_v < 0$ . The resulting equation is known as the Kuramoto–Sivashinsky equation and has become famous, since it produces deterministic spatio-temporal chaos even in the absence of noise [42,45]. The relevance of the  $\lambda$ -term in both cases can be understood by the fact that a small gradient  $\nabla h$  does not give any contribution to the second- or the fourth-order term, whereas it immediately enters the nonlinear  $\lambda$  term. An important result of the KPZ equation is that fluctuations of the interface grow laterally on average as  $t^{2/3}$  and in amplitude as  $t^{1/3}$ . This is the result in one dimension, while for two-dimensional interfaces one has only approximate results so far [44]. These “critical exponents” are useful tools to describe generic features of growing interfaces, since they do not depend on fine details of the specific

materials or experimental arrangements. Further generalizations of such macroscopic growth models have been made recently [46].

### III. INTERFACE KINETICS

#### A. Master Equation Formalism and Monte Carlo Simulation

The relaxation of a thermodynamic system to an equilibrium configuration can be conveniently described by a master equation [47]. The probability of finding a system in a specific state increases by the incoming jump from adjacent states, and decreases by the outgoing jump from this state to the others. From now on we shall be specific for the lattice-gas model of crystal growth, described in the previous section. At the time  $t$  the system will be found in the state  $\{s_i\}$  with a probability density  $P(\{s_i\}; t)$ , and its evolution is governed by the master equation

$$\begin{aligned} \frac{\partial}{\partial t} P(\{s_i\}; t) = & \sum_{i=1}^N \{P(s_1, s_2, \dots, s_i, \dots; t) W(s_i \rightarrow -s_i) \\ & - P(s_1, s_2, \dots, -s_i, \dots; t) W(-s_i \rightarrow s_i)\} \end{aligned} \quad (10)$$

The transition probability  $W(s_i \rightarrow -s_i)$  represents the rate of state-change per unit time such that the state at a site  $i$  changes from  $s_i$  into  $-s_i$  while those of all other sites  $s_j (j \neq i)$  remain unchanged. The transition probabilities contain the actual information of the physical process.

This master equation is the basis for the Monte Carlo simulation. It creates the configuration  $\{s_i\}$  with the probability  $P(\{s_i\}, t)$  and alters it according to the master equation (10). A computer simulation of the master equation can be simply carried out as follows. A site  $i$  is chosen randomly and the transition probability  $W(s_i \rightarrow -s_i)$  is calculated from the energies involved (see below) if this local change were to take place. A random number  $R$  from a set distributed uniformly between 0 and 1 is then produced. If it is smaller than the transition probability  $W$ , the configuration is altered to the new state with  $-s_i$ . Otherwise, the configuration remains the same. After  $N$  trials, the time increases by unity. Thermodynamic expectation of a macroscopic variable  $A(\{s_i\})$  can then be defined as usual:

$$\langle A(\{s_i\}, t) \rangle = \sum_{\{s_i\}} P(\{s_i\}; t) A(\{s_i\}). \quad (11)$$

Concerning the choice of the transition probabilities  $W$ , one has ample freedom to select the most appropriate one for a specific physical process.

The basic requirement is that the time variation of Eq. (10) should vanish in the thermodynamic equilibrium. A sufficient condition for this is the principle of the "detailed balance," which means that each term in the sum on the right-hand side of Eq. (10) vanishes for an equilibrium probability density  $P(\{s_i\}; t)_{\text{eq}}$

$$P(\{s_i\}; t)_{\text{eq}} W(s_i \rightarrow -s_i) = P(\{-s_i\}; t)_{\text{eq}} W(-s_i \rightarrow s_i). \quad (12)$$

Since the equilibrium probability  $P(\{s_i\}; t)_{\text{eq}}$  contains the Boltzmann factor with an energy  $\mathcal{H}(\{s_i\})$ , the condition (12) leads to the ratio of transition probabilities of the forward and backward processes as

$$\frac{W(s_i \rightarrow -s_i)}{W(-s_i \rightarrow s_i)} = \exp\left(\frac{\mathcal{H}(s_1, s_2, \dots, s_i, \dots) - \mathcal{H}(s_1, s_2, \dots, -s_i, \dots)}{T}\right). \quad (13)$$

As long as the condition (13) is satisfied, any choice of the transition probability is possible. For the lattice-gas model with the Hamiltonian (2), a simple choice is the following:

$$W(s_i \rightarrow -s_i) = \frac{1}{2\tau} [1 - s_i \tanh(H_i/T)] \quad (14)$$

with the local field

$$H_i = J \sum_{j(i)} s_j - \Delta\mu/2 \quad (15)$$

The summation in Eq. (15) is taken over the sites  $j$  next to the site  $i$ .

## B. Mean-field Dynamics

Before trying to solve the master equation for growth processes by direct stochastic simulation it is usually advisable to first try some analytical approximation. The mean-field approximation often gives very good results for questions of first-order phase transitions, and at least it provides a qualitative understanding for the interplay of the various model parameters.

For a macroscopic variable  $A(s_i)$ , the time evolution of the expectation value, Eq. (11), is obtained by the master equation explicitly as

$$\begin{aligned} \frac{\partial}{\partial t} \langle A \rangle = & \sum_{i=1}^N \{ A(s_i) P(s_1, s_2, \dots, s_i, \dots; t) W(s_i \rightarrow -s_i) \\ & - A(s_i) P(s_1, s_2, \dots, -s_i, \dots; t) W(-s_i \rightarrow s_i) \} \end{aligned} \quad (16)$$

If the variable  $A$  is antisymmetric as  $A(\{s_i\}) = -A(\{-s_i\})$ , the time

evolution can be simplified:

$$\frac{\partial}{\partial t} \langle A \rangle = -2 \langle A(s_i) W(s_i \rightarrow -s_i) \rangle \quad (17)$$

With the specific choice of the transition probability, Eq. (14), the evolution (17) of the average of  $s_i$  is written in a simple form as

$$\tau \frac{\partial}{\partial t} \langle s_i \rangle = -[\langle s_i \rangle - \langle \tanh(H_i/T) \rangle]. \quad (18)$$

For crystal growth from the vapor phase, one better chooses the transition probability appropriate to the physical situation. The adsorption occurs ballistically with its rate dependent only on the chemical potential difference  $\Delta\mu$ , while the desorption rate contains all the information of local conformation on the surface [35,48]. As long as the system is close to equilibrium, the specific choice of the transition probability is not of crucial importance.

For an analytical treatment of Eq. (18) we make a mean-field approximation in layers, where the index  $i$  is now decomposed into the layer index  $k$  and lattice position  $j$  within the layer:  $s_i \rightarrow s_k^j$ . The mean-field approximation in the layer leads to the layer order parameter:  $\langle s_k^j \rangle \equiv \sigma_k$ . Its evolution is obtained from (18) as

$$\tau \frac{\partial}{\partial t} \sigma_k = -\{\sigma_k - \tanh([J(4\sigma_k + \sigma_{k+1} + \sigma_{k-1}) - \Delta\mu/2]/T)\} \quad (19)$$

Eq. (19) describes the directional growth of a crystal. The homogeneous and stationary state for  $\Delta\mu = 0$  represents the equilibrium state. For temperatures lower than the critical temperature, we find three different solutions:  $\sigma_0 = 0, \sigma_+ = -\sigma_- \neq 0$ . The state  $\sigma_- > 0$  corresponds to the crystal phase and the state  $\sigma_+ < 0$  to the vapor phase. If the boundary conditions are chosen such that at the end  $k \rightarrow -\infty$  one has a crystal ( $\sigma_k = \sigma_- > 0$ ) and at the other end is a gaseous phase ( $\sigma_k = \sigma_+ < 0$ ), then a steady-state solution has a tanh-profile of crystalline order with an interface between the crystal and gas phases.

With a finite value of  $\Delta\mu \neq 0$ , the interface starts to move. In the mean-field approximation of a similar model, one can obtain the growth rate  $v$  as a function of the driving force  $\Delta\mu$  [49]. For  $\Delta\mu$  smaller than the critical value  $\Delta\mu_c$  the growth rate remains zero: the system is metastable. Only above the critical threshold, the velocity increases as  $v \approx \sqrt{\Delta\mu - \Delta\mu_c}$ , and finally reaches the linear growth  $v \approx \Delta\mu$ . In the metastable region the nucleation process takes place, which will be explained in the next section.

The result is valid below the roughening temperature, but above the roughening temperature this mean-field approximation is not sufficient

since it does not describe the roughening. Above the roughening temperature, one characterizes the crystal surface better by a local height  $h_{i,j}$  where the indices  $i, j$  label the two-dimensional position. Resultant mean-field dynamics then gives [50] at sufficiently high temperatures

$$\tau \frac{\partial}{\partial t} \langle h_j \rangle = \frac{J}{T} (h_{i,j+1} + h_{i+1,j} - 4h_{i,j} + h_{i,j-1} + h_{i-1,j}) + \frac{\Delta\mu}{T} \quad (20)$$

This equation describes not only the crystal growth, but with an additional noise term it also describes the evolution of the surface width and is called the Edward–Wilkinson model. An even better treatment has been performed by renormalization methods and other techniques [44,51–53].

In the variational [3] or renormalization group treatment [51] of the surface roughening, a linear growth law  $v \propto \Delta\mu$  is obtained above the roughening temperature, whereas below the roughening a finite threshold  $\Delta\mu_c$  is expected to drive the crystal growing. In the case of sufficiently large driving forces  $\Delta\mu > \Delta\mu_c$  the numeric solution of Eq. (19) reveals an *oscillatory* growth: If half a layer is filled, the interface becomes rough and the remaining half will be filled quickly. After this the formation of a new half layer requires slow nucleation. This might be related to the RHEED experiments, to be described later.

## C. Nucleation

At a temperature below the roughening temperature, the crystal surface is flat. In order for a new crystal layer to grow on this faceted surface, a so-called “nucleus” should be created. Let us assume that it has a circular shape of a tablet with radius  $R$ . It costs a supplementary free energy  $\tilde{F} = -\Delta\mu\pi R^2 + \gamma_s 2\pi R$ . Here  $\gamma_s$  is the free energy density of a surface step and  $\Delta\mu$  is the chemical potential difference which drives crystallization. Since the probability of the occurrence of a fluctuation depends exponentially on its free energy cost according to general thermodynamic principles, the nucleation rate  $P_{\text{nuc}}$  is given as [54,55]

$$P_{\text{nuc}} \sim \exp(-\tilde{F}(R_c)/T) \quad (21)$$

Here  $R_c$  is a critical radius for nucleation [20,56] on a faceted surface

$$R_c = \frac{\gamma_s}{\Delta\mu} \quad (22)$$

Note that this result is independent of dimension, apart from some constant prefactor, while the nucleation rate depends on dimension. The

two-dimensional nucleation rate is then explicitly given as

$$\nu_{\text{nuc}} \sim \nu_a \exp\left(-\frac{\pi\gamma_s^2}{\Delta\mu T}\right) \quad (23)$$

A pre-factor  $\nu_a \sim 1/\tau$  contains a time scale  $\tau$  or a frequency which for instance corresponds to the “hard” phonon or to an atomic frequency. The growth rate of the crystal is proportional to this rate (23). As will be shown later, the nucleus once formed expands in a time scale shorter than the one necessary for nucleation. If the process consists of a series of sequential subprocesses, the global velocity is governed by the slowest one. Therefore, this nucleation process determines the growth rate of a faceted surface.

At higher temperatures, other degrees of freedom than the radius  $R$  must also be considered in the fluctuation. However, this becomes critical only near the “critical point” where the system goes through a phase transition of second order. The nucleation arrangement described here is for *heterogeneous* or two-dimensional nucleation on a flat surface. In the bulk, there is also the formation of a three-dimensional nucleation, but its rate is smaller:

$$\nu_{\text{nuc}}^{3\text{D}} \sim \nu_a \exp\left(-\frac{C\gamma^3}{\Delta\mu^2 T}\right) \quad (24)$$

since the energy barrier is proportional to  $(\Delta\mu)^{-2}$  instead of  $(\Delta\mu)^{-1}$  in the case of surface nucleation, or more generally  $\sim \gamma^d/\Delta\mu^{d-1}$  with  $d$  being the spatial dimension. Nucleation theory was constructed for small supersaturations only, but it seems to work in principle also for rather strong deviations from equilibrium. For example, the assumption that the process of nucleation is locally isothermal [57] seems to be quite good despite the latent heat generated during freezing.

## D. Growth and Ostwald Ripening

After a supercritical nucleus has formed by some thermodynamical fluctuations the nucleus will then continue to grow in an essentially deterministic way, since it gains free energy during growth. The various possible growth mechanisms will be further discussed below in some detail. For the moment we will only anticipate the phenomenon of the so-called Ostwald ripening, giving a very simple derivation of a scaling form.

Assume that a sudden change in the system parameters initiates a phase transition. After a set of clusters of different size has been generated by a nucleation process, the smaller clusters will shrink again and disappear,



while the larger clusters will grow. This is the ripening or coarsening process. It can be understood by the following scaling argument, which goes back to the theory of Lifshitz and Slyozov [58]. We are interested in a system with conserved order-parameter, so that structure formation associated with a two-phase system requires transport of material (or energy) via a diffusion process.

First we look at the simpler case of the shrinking of a single cluster of radius  $R$  at two-phase coexistence. Assume that the phase inside this cluster and the surrounding phase are at thermodynamic equilibrium, apart from the surface tension associated with the cluster surface. This surface tension exerts a force or pressure inside the cluster, which makes the cluster energetically unfavorable so that it shrinks, under diffusive release of the conserved quantity (matter or energy) associated with the order parameter.

The rate of change of the cluster volume  $R^{d_v}$  can then be written as

$$\frac{\partial}{\partial t} R^{d_v} \sim R^{d_s} j \quad (25)$$

where  $d_v$  is the dimension of the cluster volume,  $d_s$  is the dimension of the surface area through which the material or energy current  $j$  enters or leaves the cluster. To be specific: assume that we have a hemispherical cluster sitting on a substrate of different (inert) material. The cluster can lose its content by a surface diffusion current. The cluster volume then has dimension  $d_v = 3$ , the current  $j$  on the surface of the substrate itself is two-dimensional, but the surface of the cluster, through which the current goes, is basically just a ring of area  $2\pi Ra$ , where  $a$  is the atomic length. Accordingly, the relevant surface dimension is not two but only  $d_s = 1$  here!

The current density  $j$  is, according to linear nonequilibrium thermodynamics, proportional to the gradient of a chemical potential difference

$$j \sim \text{grad } \Delta\mu; \quad \Delta\mu \sim 1/R \quad (26)$$

and the chemical potential difference between the inside and outside of the cluster is proportional to the curvature, according to Eq. (22).

The crucial assumption, to close these equations, is now that there exists only one relevant length scale in the system! This scale of course is  $\sim R$  and consequently  $\text{grad } \Delta\mu \sim \Delta\mu/R$ . With this assumption we have for the current, finally,

$$j \sim -1/R^2 \quad (27)$$

Combining now Eqs. (25) and (27), we arrive, after integration, at the scaling result

$$R \sim (t_0 - t)^{1/(2+d_v-d_s)} \quad (28)$$

with some integration constant  $t_0$ . For our specific example of a three-dimensional shrinking cluster on a substrate with surface diffusion ( $d_v = 3$ ,  $d_s = 1$ ) this gives obviously  $R \sim (t_0 - t)^{1/4}$ . We assume now of course that this cluster is the cluster of “typical size”, representing actually a large number of clusters on average.

The arguments here are immediately generalized from shrinking to growth: instead of having only  $\Delta\mu$  in the expressions we should consider the modifications given for the example in Eq. (52), which can be written as  $\Delta\mu(1 - R_c/R)$  for  $R$  now larger than  $R_c$ . However, this is not really necessary. Our crucial assumption was that there exists only one length scale in the problem, the typical cluster size  $R$ .  $R$  should therefore still be proportional to  $R_c$ . As a consequence, the scaling result, Eq. (28), is almost the same as for the case of growth, apart from a sign change:

$$R \sim t^{1/(2+d_v-d_s)} \quad (29)$$

where we now can ignore the integration constant  $t_0$  for long times. This is the fundamental scaling result for coarsening.

The well-known result  $R \sim t^{1/3}$  is of course also recovered for the usual situation where three-dimensional nuclei grow and compete in free space ( $d_v = 3$ ,  $d_s = 2$ ) [58]. Since the generalized scaling result (29) does not depend on any details of the underlying process, it is encountered in almost all coarsening processes in materials science. As an example, the thermal relaxation of a fractal cluster (see Sec. IV E) is governed by a similar scaling with an exponent depending on the fractal structure and the kinetic processes [59].

## E. Wilson–Frenkel Growth Law

The movement of a surface step around a two-dimensional supercritical nucleus (a nucleus whose radius is greater than the critical  $R_c$ ) occurs according to the so-called Wilson–Frenkel law [20,56]. We assume that the radius of the growing cluster is already so large that we can neglect the effect of curvature. How does a step move over the crystal surface on average? When we look at a step closely, there is always a certain number of “kinks” available in the step at any temperature on account of thermal fluctuations (Fig. 1). If an atom is inserted into a kink, the kink is maintained and only moves itself along the step. In thermal equilibrium, however, a kink will not move on average. At a kink site, adsorption and desorption rates must be balanced in equilibrium:

$$\nu_a = \nu_d \sim \nu_0 \exp(-\mu_0/T). \quad (30)$$

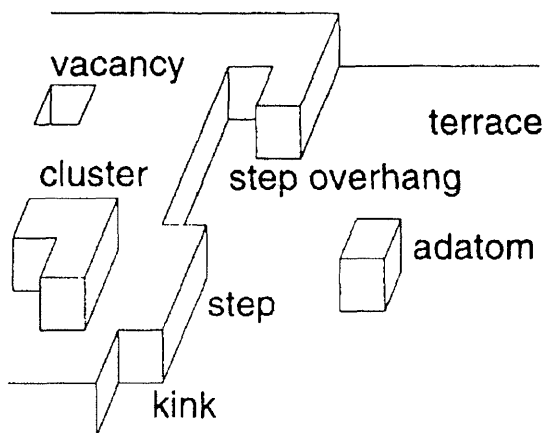


**FIG. 1** Sketch of step structure on the surface with kinks. The surface also shows clusters and holes.

The desorption rate  $\nu_d$  contains an exponential factor with a chemical potential  $\mu_0$  for desorption into the vapor phase, since it is a thermally excited process. In a nonequilibrium situation, the chemical potential increases by  $\Delta\mu$  and increases the adsorption rate  $\nu_a$ . The rate difference is given as

$$\nu_{WF} = \nu_a - \nu_d = \nu_d [\exp(\Delta\mu/T) - 1] \quad (31)$$

This is the Wilson–Frenkel rate. With that rate an individual kink moves along a step by adsorbing more atoms from the vapour phase than desorbing. The growth rate of the step is then simply obtained as a multiple of  $\nu_{WF}$  and the kink density. For small  $\Delta\mu$  the exponential function can be linearized so that the step on a crystal surface follows a linear growth law

$$v_{st} \sim \Delta\mu/T \quad (32)$$

This Wilson–Frenkel law is in fact valid even more generally: the essential assumption for the derivation was that the surface structure of the growing interface does not change from the equilibrium one. Every rough surface should then be able to grow on average according to this Wilson–Frenkel law:

$$V_{WF} \sim \Delta\mu \quad (33)$$

A linear law is valid above the roughening temperature and the Wilson–Frenkel rate is an upper limit to the growth rate which is achieved in the case of very fast surface diffusion. This is illustrated in Fig. 2.

F. Surface Steps and Spiral Growth

At a surface-step the height of the crystal surface changes. Above the roughening transition temperature the surface is rough and full of hills and valleys encircled by steps. Below the roughening transition the singular surface has very few steps in equilibrium. But for the surface to grow one needs steps and kinks which incorporate adsorbed atoms. For a vicinal surface, steps are provided geometrically. From all these relations it is obvious that knowledge about surface-steps and their morphology is very important for the control of crystal growth, especially for epitaxial growth with a smooth surface.

1. Equilibrium Steps

Since atomic bonds are broken at the step edge, a surface-step costs an energy  $J$  per atomic length. At very low temperatures, where the step

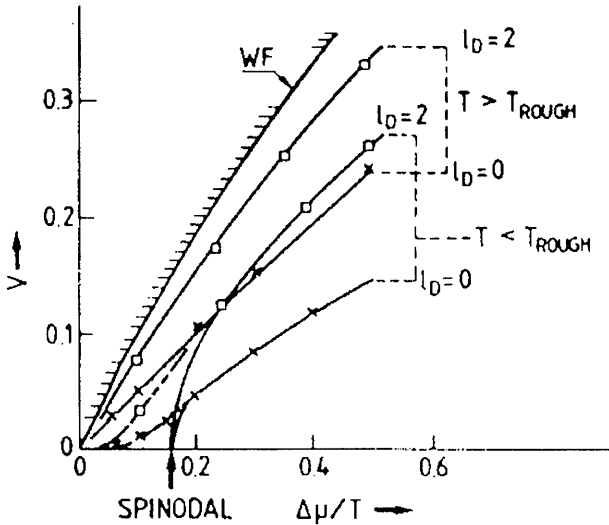


**FIG. 2** Growth rates as a function of the driving force  $\Delta\mu$ . Comparison of theory and computer simulation for different values of the diffusion length  $\ell_D$  and at temperatures above and below the roughening temperature. The *spinodal* value corresponds to the metastability limit  $\Delta\mu_c$  of the mean-field theory [49]. The Wilson–Frenkel rate WF is the upper limit of the growth rate.

fluctuation is negligible, a straight step of length  $La$  costs an energy  $JL$ . At high temperature  $T$ , a step fluctuates and is no longer straight. A place along a step where the step makes a turn is called a "kink." A kink of an atomic size  $a$  costs an energy  $J$ , and therefore the probability of kink formation at a single site is estimated as  $n_{\text{kink}} \approx \exp(-J/T)$ . There are two types of kink, positive and negative. The entropy is then given as  $S = k_B \ln[L!/(Ln_{\text{kink}})!(Ln_{\text{kink}})!(L(1 - 2n_{\text{kink}}))!]$ . The free energy is given by  $F = E - TS = L\gamma$  and this determines the step free energy  $\gamma$ .

We now regard the step as a flexible linear object with a line tension  $\gamma$ . Its deformation  $h(x)$  at a position  $x$  costs an energy

$$H = \int \gamma(\theta) [\sqrt{1 + (\partial h / \partial x)^2} - 1] dx \approx \frac{1}{2} \int \tilde{\gamma} (\partial h / \partial x)^2 dx \quad (34)$$

where  $\gamma(\theta)$  is now an orientation-dependent step tension and  $\tilde{\gamma} \equiv \gamma + \partial_\theta^2 \gamma$  is the step stiffness (see Sec. III G). From the equipartition one can easily get the step width characterizing its fluctuation as [3]

$$w_{\text{eq}}^2 = \langle (x)^2 \rangle_{\text{eq}} = \frac{T}{12\tilde{\gamma}} L \quad (35)$$

An isolated step of length  $L$  fluctuates wildly with its width  $w_{\text{eq}} \sim \sqrt{L}$  diverging with increasing length  $L$ .

## 2. Step-Step Interaction

On a so-called vicinal face there are many steps running in parallel with almost the same separation or terrace width in between. At a finite temperature, these steps also fluctuate. But due to the high energy cost for the formation of overhangs on the crystal surface, steps cannot cross each other. This non-crossing condition suppresses the step fluctuation.

For a step train, two neighboring steps collide when the fluctuation  $w_{\text{eq}}$  determined in (35) becomes the average step separation  $\ell$ . Therefore, the collision takes place for each step length  $L_{\text{coll}} \approx \tilde{\gamma} \ell^2 / T$ . To realize a large fluctuation, all the steps meander simultaneously. The step fluctuation for a long step ( $L \gg L_{\text{coll}}$ ) is reduced to the logarithmic form [3]

$$w_{\text{eq}}^2 = \frac{\ell^2}{2\pi^2} \ln L \quad (36)$$

The result can be derived by assuming a harmonic interaction between consecutive steps, with the strength of interaction  $K_{\text{eff}} = \pi^2 \tilde{\gamma} / L_{\text{coll}}^2$ .

An elastic interaction between steps can also be approximated by a harmonic potential when the deviation of the steps from a straight line is small [18]. Even though steps fluctuate with a diverging width, Eq. (36), the separation between neighboring steps or the terrace width fluctuates a little

around the average value  $\ell$ . Since the terrace width distribution function reflects the step-step interactions, there are intensive theoretical, numerical, and experimental studies on it in order to estimate the elastic step interaction constant [61–63].

### 3. Time-dependent Step Width

If the step is initially prepared to be straight, it relaxes to its fluctuating shape in the due course of time. This time evolution of step width depends on the relaxation kinetics, and can be used to determine the values of various kinetic coefficients [3,16–18,64–66]. For example, if the attachment and detachment kinetics of adsorbed atoms at a step is rate limiting, the step width increases as [65]

$$w^2(t) = \frac{T}{\sqrt{\pi\tilde{\gamma}}} [2(\nu_+ + \nu_-)\Gamma t]^{1/2} \quad (37)$$

where  $\nu_+$  and  $\nu_-$  are the kinetic coefficients for incorporating the adatom into the step from the terrace above and below, respectively, and  $\Gamma = c_{\text{eq}}^0 \Omega^2 \tilde{\gamma} / T$  is the renormalized step stiffness.  $\Omega$  is the atomic area,  $c_{\text{eq}}^0$  is the equilibrium concentration of adatoms for a straight step.

If the kinetics is fast enough and the diffusion of adatoms along the step edge or perimeter is rate limiting, then the width increases slowly as [66]

$$w^2(t) = \frac{1.22T}{\pi\tilde{\gamma}} [2\Omega\Gamma_e\tilde{\gamma}t]^{1/4} \quad (38)$$

where  $\Gamma_e$  is the mobility of the adatom along the step.

If the terrace diffusion with the diffusion constant  $D_s$  is rate limiting, the width relaxation is intermediate as [67]

$$w^2(t) = \frac{1.35T}{\pi\tilde{\gamma}} [4D_s\Gamma t]^{1/3} \quad (39)$$

In this case, however, if the step separation  $\ell$  is small, the consecutive steps are coupled via the terrace diffusion field, and the width cannot increase as fast as  $t^{1/3}$  but increases slowly, like the edge-diffusion-limited growth, as [68]

$$w^2(t) = \frac{1.22T}{\pi\tilde{\gamma}} [2D_s\Gamma\ell t]^{1/4} \quad (40)$$

### 4. Spiral Growth

So far we have discussed the surface of a perfect crystal. But for an imperfect crystal there is another possibility to provide a step source. This is due to the screw dislocation. Assume that one cuts a crystal half-way from one side into the center, and slides the freshly created two faces against each other in

the opposite direction parallel to the central line. Then a screw dislocation is created. On a surface perpendicular to the screw dislocation line, a mono-atomic step appears which runs from the center to the boundary. If crystal-line material is attached along this step, the step advances in the normal direction over the crystal surface. But since the centre cannot move, the step winds itself around the centre to form a spiral [20]. There are plenty of experimental observations and Monte Carlo studies. Theoretical analysis is based on using the interface evolution equation to be derived in the next section [34].

For a fixed driving force  $\Delta\mu$ , the step far away from the center moves faster than the center because of the large radii of curvature and the surface tension creates only a small effect of a backward pointing force. At first sight the spiral seems to wind itself up more and more tightly at the center. However, this is not possible to continue forever. If the radius of curvature at the center falls below the critical radius  $R_c$  given by (22), a retardation of the step sets in. Therefore,  $R_c$  is the smallest possible radius of curvature at the center of the spiral. Since there is no further length scale in this system, the step separation  $\ell$  away from the centre ought to satisfy a relation  $\ell = cR_c$  with a dimensionless constant  $c$ . A more precise analysis confirms this presumption and gives [20,56,69]

$$\ell \approx 19R_c \quad (41)$$

This is an important relation for the growth of an isotropic spiral. It actually also holds for anisotropic spirals, but with a different prefactor  $\ell \approx 8R_c$ .

One can now immediately deduce the normal growth rate of a crystal due to the screw dislocation. Whenever a step edge passes by a fixed point on the crystal surface, this point gains the height of a lattice unit. The normal growth rate  $V$  of the crystal is then

$$V = \frac{a}{\ell} v_{st} \quad (42)$$

By combining the result (32) for the step velocity ( $v_{st} \sim \Delta\mu$ ) with results (22) and (41) for the step separation far away from the center ( $\ell \sim 1/\Delta\mu$ ), the normal velocity is determined as

$$V \sim \Delta\mu^2 \quad (43)$$

For a small driving force  $\Delta\mu$ , this growth law is indeed slower than the Wilson–Frenkel law (33) with  $V_{WF} \sim \Delta\mu$ , but incomparably much larger than that of the nucleation process on faceted surfaces, (24), with  $V \sim \exp(-c/\Delta\mu)$ , where  $c \approx \pi\gamma_s^2/T$  is a positive constant. Therefore, the spiral growth mechanism provides a dominant growth mechanism for a faceted crystal surface [20,56].

### G. Sharp Interface Model

For the explanation of macroscopic phenomena, the thickness of the phase boundary (interface) often plays no important role. As an example, we describe the movement of a phase boundary in two dimensions or the movement of a step edge on a crystal surface. We start with a Ginzburg–Landau equation [69]

$$v_{\perp} \equiv \frac{\partial}{\partial t} \xi(S, t) = -\kappa(\theta) \frac{\delta \tilde{F}}{\delta \xi(S)} \quad (44)$$

where  $\xi(S)$  represents the normal displacement at the point identified through the arclength  $S$  on the step edge, as is sketched in Fig. 3. The kinetic coefficient  $\kappa(\theta)$  might depend on the orientation  $\theta$  of the step edge relative to the crystal lattice. We must now define the free energy  $\tilde{F}$  of the two-phase system consisting of the step edge separating the region of a crystallized adsorbed layer on the surface from that not yet crystallized.

The variation of the free energy  $\delta \tilde{F}$  by a displacement of the edge  $\delta \xi(S)$  can be formally written as

$$\delta \tilde{F} = \delta \left[ \int_S dS \gamma(\theta) \right] - \int_S dS \delta \xi(S) \Delta \mu \quad (45)$$

$\Delta \mu$  is the chemical potential difference between the regions behind and before the step edge,  $S$  is the integration path along the step. The first integral must be transcribed such that it contains  $\delta \xi(S)$  as a product in

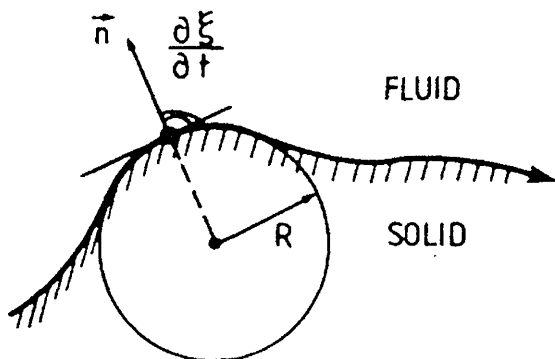


**FIG. 3** Schematic sketch of an interface between fluid and solid, or alternatively a surface step. The interface (or surface step) is characterized locally through the surface tension, the orientation  $\vec{n}$ , and the radius of curvature  $R$ .



the integrand. For this purpose, we split the functional derivative according to the chain rule

$$\delta \left[ \int_S dS \gamma(\theta) \right] = \int_S \gamma \delta(dS) + \int_S dS \delta\gamma \quad (46)$$

The first integral on the right-hand side in (46) describes the change of a length element  $dS$  during the normal displacement. A straight portion does not apparently change the length, but a curved part becomes longer or shorter depending on the sign of the radius of curvature  $R$ :

$$\int \gamma \delta(dS) = \int \gamma \frac{1}{R} dS \delta\xi \quad (47)$$

The second integral on the right-hand side in (46) gives

$$\int dS \delta\gamma = \int dS \frac{1}{R} \frac{d^2\gamma}{d\theta^2} \delta\xi \quad (48)$$

This has to do with the change in orientation of a small straight piece of the step during advancement. It is derived from the following transformations

$$\left. \begin{aligned} \delta\gamma(\theta) &= \frac{d\gamma}{d\theta} \delta\theta \\ \delta\theta &= \frac{d(\delta\xi)}{dS} = \frac{d\theta}{dS} \frac{d}{d\theta} \delta\xi \\ \frac{d\theta}{dS} &= -\frac{1}{R} \end{aligned} \right\} \quad (49)$$

Consequently the variation of  $\gamma$  is written as:

$$\delta\gamma(\theta) = \frac{d\gamma}{d\theta} \frac{d\theta}{dS} \frac{d}{d\theta} \delta\xi = -\frac{d^2\gamma}{d\theta^2} \frac{d\theta}{dS} \delta\xi \quad (50)$$

To obtain the last equality one uses a partial integration so that the derivative by  $\theta$  is now taken on  $d\gamma/d\theta$  instead of on  $\delta\xi$ . Consequently, the variational derivative gives the free energy variation as

$$\delta\tilde{F} = \int_S dS \left[ \frac{1}{R} \gamma + \frac{1}{R} \frac{\partial^2\gamma}{\partial\theta^2} \right] \delta\xi(S) - \int_S dS \Delta\mu \delta\xi(S) \quad (51)$$

and the equation of motion follows from (44) as

$$\frac{\partial}{\partial t} \xi(S, t) = -\kappa(\theta) \left\{ \Delta\mu - \frac{1}{R} (\gamma + \partial_\theta^2 \gamma) \right\} \quad (52)$$

where we use the abbreviation  $\partial_\theta \equiv d/d\theta$ . The result can be easily extended to three-dimensional space as [69]

$$\frac{\partial}{\partial t} \xi(S, t) = -\kappa(\vec{\theta}) \left\{ \Delta\mu - \frac{1}{R_1} (\gamma + \partial_1^2 \gamma) - \frac{1}{R_2} (\gamma + \partial_2^2 \gamma) \right\} \quad (53)$$

where  $R_1, R_2$  are the two principal radii of curvature and the angles  $\theta_1, \theta_2$  are the associated orientational changes.

By putting the right-hand side in Eqs. (52) and (53) equal to zero, one receives the equilibrium value of local radius of curvature  $R$  (or  $R_1, R_2$ ), which is nothing but the Wulff construction. For an anisotropic step tension  $\gamma(\theta)$ , there is a local “critical” radius defined as

$$R_c = \frac{\gamma + \partial_\theta^2 \gamma}{\Delta\mu} = \frac{\tilde{\gamma}}{\Delta\mu}. \quad (54)$$

Here  $\Delta\mu$  is the chemical potential difference between the crystalline and non-crystalline phases.

From Eq. (52) we obtain the following qualitative behavior: when the adsorbed layer on the surface takes the form of a small island with a radius of one critical nucleus size, then the growth will be determined by the anisotropy of surface tension. The important combination of surface tension and second angular derivative is sometimes called “stiffness”:  $\tilde{\gamma} \equiv \gamma + \gamma''$ . When the adsorbed island is already very large, so that all radii of curvature  $R(S)$  are large, then further growth is determined by the anisotropy of the kinetic coefficient  $\kappa(\theta)$  alone. These sharp interface models have recently received substantial attention in the development of hierarchical grid systems for the simulation of surface-tension-driven moving-interface problems [37,70]. The sharp-interface models are generally more efficient numerically than the phase-field models described in the next section, but they are substantially more difficult to program, particularly in three dimensions.

## H. Phase-field Model

It is not an easy task to develop computer codes which correctly treat the advancement of a folding interface as a boundary condition to a diffusion or flow field. In addition, the interface between a solid and a liquid, for example, is usually is not absolutely sharp on an atomic scale, but varies over a few lattice constants [32,33]. In these cases, it is sometimes convenient to treat the interface as having a finite non-zero thickness. An order parameter is then introduced, which for example varies from the value zero on one side of the interface to the value one on the other, representing a smooth transition from liquid to solid across the interface. This is called the phase-field

model, and is equivalent to the time-dependent Ginzburg–Landau theory [54], which is today a standard theory for phase transitions.

We will use it here in order to derive an analytical form for a crystal profile with a rough interface as an explicit example. An order parameter  $\phi$  is defined such that it discriminates between the crystalline phase with  $\phi > 0$  and the gaseous (or liquid) one with  $\phi < 0$ .

We start from the time-dependent Ginzburg–Landau equation for a non-conserved order parameter  $\phi$

$$\frac{\partial}{\partial t} \phi(x, t) = -\kappa \frac{\delta \tilde{F}}{\delta \phi} \quad (55)$$

This says that the variable  $\phi$  changes so that the free energy always decreases towards a minimum value.  $\kappa$  is a kinetic coefficient which depends on the system's characteristics. The free energy can be described as

$$\tilde{F} = U \int dx \left\{ \frac{1}{2} r \phi^2(x) + \frac{1}{4} \phi^4 + \frac{1}{2} a^2 (\nabla \phi)^2 - \phi(x) \tilde{h}(x) \right\} \equiv \int \hat{F} dx \quad (56)$$

with the free energy density  $\hat{F}$ . In the homogeneous case,  $\hat{F}(\phi)$  has a double minimum structure, one corresponding to the liquid and one to the solid phase. This form is obtained as an expansion both with respect to  $\phi$  around  $\phi = 0$  and to its spatial derivative  $\nabla \phi$ . The fourth-order term in  $\phi$  was introduced in order that the model remains stable. The external field  $\tilde{h}$  breaks the symmetry  $\phi \leftrightarrow -\phi$  of the system. For simplicity, we consider here a variation only in one space dimension  $x$ . The energy scale and the length scale are given by  $U$  and  $a$ , but we choose the units such that  $U = 1$  and  $a = 1$ . The remaining parameter  $r (< 0)$  determines the thickness of the interface. In the case of a homogeneous system without field,  $\phi$  is constant and space-independent and thus the gradient is zero. Obviously the functional (56) then has two valleys for  $r < 0$  at

$$\phi_0 = \pm [-r]^{1/2} = \{\phi_+, \phi_-\} \quad (57)$$

In equilibrium, this describes the coexistence of two different phases (solid and liquid), just as in the case of the Ising model (hising) with the “up and down” magnetization phases. When  $\tilde{h} \neq 0$ , one of these two phases has a priority. Therefore, a sign change of  $h \rightarrow -h$  induces a first-order phase transition. (Note that for modeling reasons  $h(T)$  may be assumed to depend on temperature.)

When the solid phase  $\phi_+$  at  $x = +\infty$  coexists with the gas phase  $\phi_-$  at  $x = -\infty$ , the stationary profile of the phase field is determined so as to minimize the free energy functional  $\tilde{F}$  (56). The functional derivative gives

the steady state

$$0 = \frac{\delta}{\delta\phi} \tilde{F} \equiv \frac{\partial}{\partial\phi} \hat{F} - \frac{d}{dx} \left( \frac{\partial}{\partial(\nabla\phi)} \hat{F} \right) = -\nabla^2\phi + r\phi + \phi^3 - \tilde{h} = 0 \quad (58)$$

where  $\hat{F}$  represents the energy density in the integral of (56). We limit ourselves here to the equilibrium case of  $\tilde{h} = 0$ . Then the solution which connects the two phases  $\phi(x = \pm\infty) = \phi_{\pm}$  (57) is given as

$$\phi(x) = \phi_0 \tanh\left(\frac{x}{\xi}\right) \quad (59)$$

with the correlation length or interface thickness

$$\xi = \sqrt{2}[-r]^{-1/2} \quad (60)$$

This profile of the phase boundary determined here looks very similar to that obtained by the mean-field approximation (19), but the result here only applies to the profile above the roughening temperature. Since this is a mean-field theory, fluctuations are also not considered correctly.

The phase-field model and generalizations are now widely used for simulations of dendritic growth and solidification [71–76] and even hydrodynamic flow with moving interfaces [78,79]. One can even use the phase-field model to treat the growth of faceting crystals [77]. More details will be given later.

## I. Elastic Effects on Growth Processes

We have assumed so far, implicitly, that the interactions are strictly local between neighboring atoms and that long-ranged forces are unimportant. Of course the atom–atom interaction is based on quantum mechanics and is mediated by the electron as a Fermi particle. Therefore the assumption of short-range interaction is in principle a simplification. For many relevant questions on crystal growth it turns out to be a good and reasonable approximation but nevertheless it is not always permissible. For example, the surface of a crystal shows a superstructure which cannot be explained with our simple lattice models.

In addition to these direct long-range forces there may also exist effective long-range forces, produced by some medium or substrate. An especially drastic effect is expected for epitaxial growth on a semiconductor. If adsorbate atoms are different from the substrate, the adsorbed layers have a lattice constant different from that of the substrate. In the case of thick adsorbate layers, an instability then appears on the surface of the crystal such that the surface undergoes wavy deformation, which might even lead to

cracks [80]. This effect has been known under the name of Asaro–Tiller–Grinfeld instability [81] for a long time (or even longer in Frenkel–Kontorova models [82]) but has received large interest recently. The effect can be easily understood qualitatively as follows.

Assume for the moment that the surface of the solid has developed into a wavy structure of relatively large amplitude, by reshuffling masses of atoms into rows like a field for growing asparagus-vegetables. It is obvious that this structure offers a reduced resistance against a force parallel to the surface but perpendicular to the direction of the waves. A compression parallel to the interface of that structure therefore costs less energy than a compression with the interface staying flat. On the other hand, the wavy surface has a larger area than the flat surface and therefore has more surface energy. The balance of these two types of energies on the corrugated surface, reduced elastic stress energy and increased surface energy, leads to the above-mentioned instability. Note in particular that the wrinkling of the surface is due to displacements of atoms out of their local environment, and not just bending as in elastic deformation. Elastic stresses of course also influence the other structure formation mechanisms [83] such as Mullins–Sekerka instability, etc.

Another effect of elastic deformation is that it causes a long-range interaction between steps. From the continuum elasticity theory, two steps separated by a distance  $\ell$  have a repulsive interaction proportional to  $\ell^{-2}$  for homo- and to  $\ln \ell$  for hetero-epitaxial cases, respectively [84]. This interaction plays an important role, for example, in step fluctuations, terrace width distribution, step bunching, and so forth [7,85–88].

## IV. GROWTH UNDER SURFACE DIFFUSION

### A. Fluctuations and Diffusion

We have so far assumed that the atoms deposited from the vapor phase or from dilute solution strike randomly and ballistically on the crystal surface. However, the material to be crystallized would normally be transported through another medium. Even if this is achieved by hydrodynamic convection, it must nevertheless overcome the last displacement for incorporation by a random diffusion process. Therefore, diffusion of material (as well as of heat) is the most important transport mechanism during crystal growth. An exception, to some extent, is molecular beam epitaxy (MBE) (see [3,12–14] and [15–19]) where the atoms may arrive non-thermalized at supersonic speeds on the crystal surface. But again, after their deposition, surface diffusion then comes into play.

Diffusion is a stochastic process associated with the Brownian motion of atoms. For simplicity we assume a one-dimensional Brownian motion where a particle moves a lattice unit  $a$  in a short time period  $\tau_D$  in a direction either forward or backward. After  $N$  timesteps the displacement  $\ell$  of the particle from the starting point is

$$\ell = \sum_{i=1}^N a\epsilon_i \quad (61)$$

where  $\epsilon_i = \pm 1$  is a uniformly distributed random number as in a coin toss. It of course makes no sense to worry about the individual  $\epsilon_i$  here. We are only interested in the expectation values, for which we make the natural assumption  $\langle \epsilon_i \rangle = 0$ ,  $\langle \epsilon_i \epsilon_j \rangle = \delta_{i,j} = \{0, 1\}$ , and consequently  $\langle \ell \rangle = 0$ ,  $\langle \ell^2 \rangle = a^2 \sum_{i,j} \delta_{i,j} = Na^2$ . In a time  $t \equiv N\tau_D$  the particle travels on average a distance  $\bar{\ell} \equiv \sqrt{\langle \ell^2 \rangle}$  in a positive or negative direction, given by

$$\frac{\bar{\ell}(t)^2}{t} = \frac{a^2}{\tau_D} \equiv 2D_c \quad (62)$$

represented in a scale independent of  $N$ . Here  $D_c$  is the chemical diffusion coefficient. Therefore, to double the separation from the origin requires fourfold time. This relation is also valid in higher dimensions since the fluctuations in the different spatial directions are mutually independent. The method used to derive Eqs. (61) and (62) is frequently used in physics to characterize random processes and disordering. It is essentially based on the assumption that there remains *no correlation* between the random variables  $\epsilon_i$  outside the time  $\tau_D$ .

From this consideration one can derive the macroscopic diffusion equation for the concentration  $c(\vec{x}, t)$  of the chemical component as

$$\frac{\partial}{\partial t} c(\vec{x}, t) = D_c \nabla^2 c(\vec{x}, t) \quad (63)$$

with the Laplace operator  $\nabla^2$ . The diffusion coefficient  $D_c$  defined in Eq. (62) has the dimension  $[\text{cm}^2/\text{s}]$ . (For correct derivation of the Fokker-Planck equation see [89].) If atoms are initially placed at one side of the box, they spread as  $\langle |x|^2 \rangle \sim t$ , which follows from (62) or from (63).

## B. Adsorption, Desorption, and Step Motion

In addition to the adsorption and desorption explained in Sec. II A, we can also include the diffusion process within our master-equation formalism (10) [47]. For this purpose, we must only include the supplementary channel of the diffusive transition into the right-hand side of Eq. (10). A diffusion jump

on the surface or at the volume of a crystal is simply taken into account via a two-particle exchange process as

$$W_2(s_i, s_j \rightarrow -s_i, -s_j) \sim \frac{1}{\tau_D} \delta_{s_i, -s_j} g(\mathcal{H}(s_i, s_j)) \quad (64)$$

with a function  $g$  that depends on the local configuration and is chosen to satisfy the detailed balance condition

$$\frac{W(s_i, s_j \rightarrow -s_i, -s_j)}{W(-s_i, -s_j \rightarrow s_i, s_j)} = \exp(\{\mathcal{H}(s_i, s_j) - \mathcal{H}(-s_i, -s_j)\}/T) \quad (65)$$

Here the lattice positions  $i$  and  $j$  should be adjacent and the  $\delta$ -function assures that one of the two lattice positions is occupied and the other one is free.  $\tau_D$  is a characteristic time scale for a diffusion jump. The time-dependence of the average  $\langle s_i \rangle$  is calculated by approximating the higher moments  $\langle s_i s_j \rangle$  [49]. In practice the analysis is rather involved, so we do not give further details here. An important result, for example, is the correction to the Wilson–Frenkel rate  $V_{WF}$  (33) at high temperatures:

$$V = V_{WF} \left\{ 1 - \frac{zJ}{2T(2\pi)^2} \int d^2q \frac{f(\vec{q})}{1 + \ell_D^2 f(\vec{q})} \right\} \quad (66)$$

with  $f(\vec{q}) = 1 - z^{-1} \sum_{nn} \exp(i\vec{q}\vec{R}_{nn})$ . Here  $\vec{R}_{nn}$  means the nearest neighbor vector in the the surface,  $z = 4$  is the coordination number,

$$\ell_D = \sqrt{D_c \tau} \quad (67)$$

is the diffusion length, or the mean displacement that the adsorbed atom can migrate on the surface before it is again desorbed, and  $\tau$  is the time for an adsorption–evaporation process (14).  $J$  is the energy of an atomic bond between two neighboring atoms. One sees explicitly that the Wilson–Frenkel rate is attained in the limiting cases of either a very high temperature or a very large diffusion length  $\ell_D$ . In both cases the growing surface has a structure close to the equilibrium structure. In [49] a comparison is given between this theory and the Monte Carlo simulation. As a result, a combination of the nucleation theory for very small driving forces and the pair approximation made here for large  $\Delta\mu$  is sufficient to describe the diffusion effect on the growth process on homogeneous dislocation-free surfaces.

If spiral growth occurs due to the existence of screw dislocations, the results depend upon whether the diffusion length  $\ell_D$  is smaller or larger than the typical separation of the spiral arms  $\ell$ . In the first case the situation hardly changes from the purely kinetic situation without diffusion, but in the second case interaction between steps comes into effect [90] and phenomena such as step bunching [91] take place. We can estimate qualitatively the

effect of diffusion onto a parallel train of surface steps as they appear far away from the center of a spiral in the form of the so-called *Schwoebel effect* [92].

We assume that the atoms adsorbed on the crystal surface diffuse on a terrace between two steps. They are accepted either by the rear or by the front step limiting the terrace, being incorporated into a kink and built into the crystal. If the incorporation into the rear step occurs with preference, the rear step runs slowly in the case of a small terrace width, whereas it runs fast for a large terrace width. Therefore, the rear step runs to keep the terrace width constant and at the same velocity as the front step. If incorporation at the front step has preference, it will run faster in the case of a large terrace width; therefore, the terrace width increases even more. This is a locally unstable situation. In practice, however, the first case is by far the more frequent, and therefore one observes beautiful growth spirals winding uniformly on many crystal surfaces (Fig. 4). But the same instability can be induced by electromigration and the direct current is then shown to cause a step bunching instability [65,66].

In the case where an infinite step-train would be stable, the surface can still become bumpy [12,13,56,93]. A step-train remains stable within itself when a step is basically fed from the terrace below. Assume now that on a surface two step-trains move against each other. Then it is clear that the steps from different trains will slow down when they approach each other,

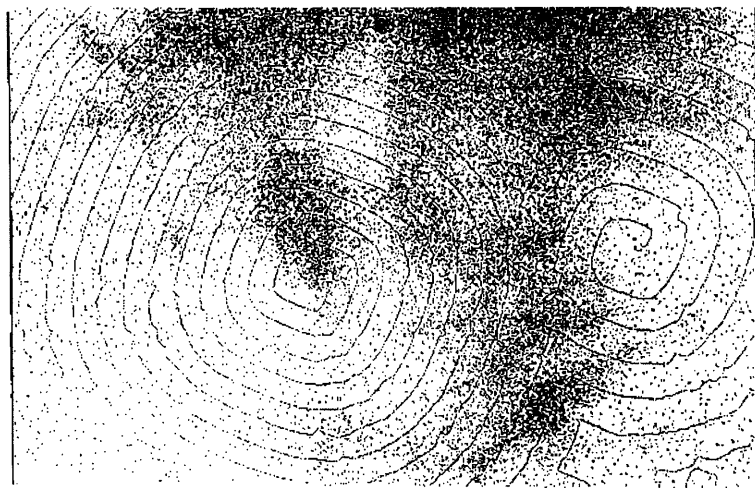


**FIG. 4** Experimental observation of growth spirals on a salt crystal. (Courtesy of K. Reichelt, Jülich.)



since the terraces, which feed the step movement, become smaller and smaller when the two steps come close to each other. In other words, the step advancement in the troughs of the crystal surface is almost stopped, the troughs deepen in relation to the growing surface. This is of course a slightly idealized picture, since two step-trains are hardly ever exactly parallel, but it explains the principle. Note, furthermore, that the diffusion on the terraces between the steps can introduce an instability along the step [15]. These processes will be elaborated upon in the next section.

### C. Cluster Growth and Molecular Beam Epitaxy

An important method for producing semiconductor layers is the so-called “molecular beam epitaxy” (MBE) (see [3,12–14] and [15–19]). Here, atoms of the same or of a different material are deposited from the vapor source onto a faceted crystal surface. The system is always far from thermal equilibrium because the deposition rate is very high. Note that in this case, in principle, every little detail of the experimental setup may influence the results.

By assuming a ballistic delivery of material (e.g., from the vapor phase or through directed evaporation) we obtain at least a qualitative picture for the various growth forms of a faceted crystal surface. We assume that the adsorbed material (“A”) behaves differently from the crystalline substrate (“S”).

We first consider the energetic situation, assuming a regular lattice structure to be given. If energetically it is more favorable for “A on A” than for “A on S,” then three-dimensional islands of the adsorbates “A” will grow, in preference. If “A on S” is favorable, then first a monoatomic layer of A develops before the homogeneous thick layers of A material grow. Here, however, elastic effects may still be important, as is sketched in Sec. III I.

Afterwards, kinetic effects determine whether many small islands are formed on a new layer, or only a few large islands develop there [12,19,81,94]. One must take into account many different length and time scales for the interface processes. The typical residential time of an adsorbed atom on the surface might be

$$\tau \sim \tau_0 \exp(E_s/T) \quad (68)$$

which was already used in (14). Here  $E_s$  is the adsorption energy of an atom on the surface. From  $\tau_D$  of Eq. (64) the diffusion constant on the surface is obtained as  $D_s \approx a^2/\tau_D$ , and then the diffusion length of an atom adsorbed on the surface is

$$\ell_a \approx \sqrt{D_s \tau} \quad (69)$$

At a specific density  $\rho_1$  of adsorbed monomers, a capture time can be defined as

$$\tau_c \approx 1/(D_s \rho_1) \quad (70)$$

Furthermore, assuming a constant deposition rate  $\mathcal{J}$  (particles per area and time) during MBE, we can define a further length scale, namely the free diffusion length or the capture length

$$\ell_c = (D_s/\mathcal{J})^{1/4} \quad (71)$$

This length is apparently related to the capture time  $\tau_c$  by the relation  $\rho_1 \sim \mathcal{J}\tau_c$  and  $\ell_c^2 \sim D_s\tau_c$ . A physical meaning of the free diffusion length  $\ell_c$  is that the maximum size of a *stable* adsorbed two-dimensional nucleus on a facet cannot essentially exceed this free diffusion length. If the nucleus is smaller, all atoms depositing on the surface can still find the path to the boundary of a nucleus in order to be incorporated there. If the nucleus is larger, a new nucleus can develop on its surface.

A flat surface may under certain conditions develop an instability by nucleation. From a completely flat faceted surface, growth must start by nucleation of two-dimensional islands. We assume now, again, the existence of a Schwoebel barrier [93]; i.e., such an island grows preferentially by incorporating atoms from the lower side of the surrounding step, not allowing atoms to jump down over its edge. During growth of this island, there will be a depletion zone of reduced concentration around the island, while the concentration on top of the island increases continuously. As a consequence, the probability of nucleating a second nucleus on top of the first island is significantly higher than the probability for nucleation in the immediate neighborhood of the island. In other words, a first nucleus favors the nucleation on top of itself, which is a positive feedback, characteristic of an instability.

The secondary and ternary islands will keep growing in approximately concentric fashion, thereby producing a conical structure above the original nucleation centers. This process of kinetic roughening supported by the Schwoebel effect makes a rather bumpy surface structure. Looking finally at a vicinal surface, this will grow rather smoothly when the width of the terraces is smaller than the typical distance between nucleation centers  $\ell_{cl}$  (see below), and becomes bumpy in the opposite case [12,93].

All points on the boundary of a growing nucleus are coupled by the diffusion field, and the nucleus can differ from its initial compact form as is shown in Fig. 5. This will be explained further in Secs. IVE and V [7,15,17,101].

A further remark may be useful, concerning the typical distance between different clusters or nuclei growing on the surface [12,14,19]. A generalized

scaling ansatz for this cluster distance  $\ell_{cl}$  is  $\ell_{cl} \sim a(D/a^4\mathcal{J})^\alpha$  with a scaling exponent  $\alpha$ , which is, under a certain approximation, supposed to be about  $\alpha \approx 1/6$ . Here the fractal nature of the cluster seems to play an important role. Furthermore, the fractal structure of the cluster again is influenced by elastic effects [7,85].

The interaction among the clusters via the common diffusion field leads in general to a coarsening of the clusters with time  $t$ . One denotes this by *Ostwald* ripening [58,96] (see Sec. III D). According to the Lifshitz–Slyozov theory [58] on this process, the typical cluster radius  $R$  increases as

$$R \sim t^{1/3} \quad (72)$$

which is meanwhile confirmed by many experiments.

## D. RHEED Oscillations

In the process of MBE, the surface structure can be investigated by reflected high energy electron diffraction (RHEED). During MBE growth, one often observes an oscillation in the intensity of the specular reflected beam as a function of time. This is interpreted to be due to the layer-by-layer growth of a two-dimensional island.

The electron beam is reflected specularly by the initially flat surface. While two-dimensional islands are growing under the flux of the molecular beam, the crystal surface becomes rough when half of the layer is covered. The reflection of the electron beam becomes diffuse and the intensity of the specular reflection decreases. Under continuing deposition islands grow further to fill a monolayer completely, and then the interface almost recovers to its original flat surface structure: the intensity of the specular beam increases again almost to the initial level. The coverage by one monolayer thus corresponds to the oscillation of the specularly reflected RHEED intensity. There are many simulations showing the oscillation of the surface roughness during MBE growth [97,98]. One should note, however, that this behavior is only transient since the nucleation at far distances cannot be correlated and eventually the surface becomes really rough dynamically. The dynamical aspects of this roughening are studied by various models, for example, the Kardar–Parisi–Zhang model and generalizations [43,44,52].

## E. Fractal Growth

So far we have described the growth of a compact cluster. But, as we have seen in Fig. 5, some clusters show more filamental structures under specific circumstances, and this type of form is called *fractal*. The simplest growth process leading to fractal structures is the so-called diffusion-limited

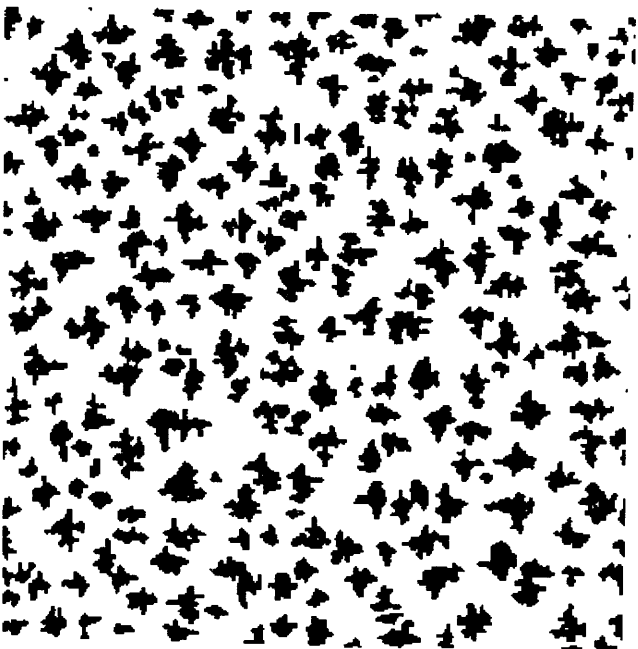


**FIG. 5** Simulation of the growth of adsorbed clusters [19]. On the left the ratio  $D/\mathcal{J}$  was  $10^8$  and on the right  $10^{13}$ . The coverage is 0.25 in both cases.

aggregation (DLA) [99,100]. Hereby a single atom is assumed to be fixed somewhere on the substrate, and a second atom wanders (from infinity) so long over the surface until it hits the first atom where it sticks. A third atom then is released at infinity and wanders until it sticks to the thereby growing cluster, and so on. The structure of the cluster obtained after thousands or millions of particles have aggregated is found to be *fractal*.

Actually, this is not really *diffusion*-limited, but rather *Laplacian* growth, since the macroscopic equation describing the process, apart from fluctuations, is not a diffusion equation but a Laplacian equation. There are some crucial differences, which will become clearer below. In some sense DLA is diffusion-limited aggregation in the limit of zero concentration of the concentration field at infinity.

One characterizes a fractal cluster by its fractal dimension  $D_f$  which can be determined from the integration of the radius-dependent mass density  $\rho(r)$  from the center up to a large radius  $R$  as follows:

$$R^{D_f} \sim \int_a^R dr^d \rho(r) \quad (73)$$

where  $d$  is the embedding dimension. A cluster with a constant density gives  $D_f = d$ , and is called compact. If  $D_f < d$ , one speaks of a fractal cluster. In two dimensions fractal clusters typically give the fractal dimension  $D_f \approx 1.71$  [99] (see also [44]).

A normal diffusion process, however, runs at a finite concentration of particles different from zero. In this situation it was found [101] that a fractal character (73) of the resulting structure is restricted to an interval  $a < R < \ell_D$ , where  $\ell_D$  is the diffusion length (67). Larger clusters have a constant density on a length scale larger than  $\ell_D$ . They are no longer fractal there. These observations have various consequences for crystal growth, and will be discussed in the next section.

## V. GROWTH UNDER BULK DIFFUSION

In this section we discuss the basic mechanisms of pattern formation in growth processes under the influence of a diffusion field. For simplicity we consider the solidification of a pure material from the undercooled melt, where the latent heat  $L$  is emitted from the solidification front. Since heat diffusion is a slow and rate-limiting process, we may assume that the interface kinetics is fast enough to achieve local equilibrium at the phase boundary. Strictly speaking, we assume an infinitely fast kinetic coefficient.

## A. Basic Model Equations

To be specific, we consider the two-dimensional growth of a pure substance from its undercooled melt in about its simplest form, where the growth is controlled by the diffusion of the latent heat of freezing. It obeys the diffusion equation and appropriate boundary conditions [95]

$$\frac{\partial U}{\partial t} = D \nabla^2 U \quad (74)$$

$$v_n = D \vec{n} \cdot (\nabla U_S|_{\text{int}} - \nabla U_L|_{\text{int}}) \quad (75)$$

$$U|_{\text{int}} = \Delta - d(\Theta) K \quad (76)$$

Here  $U = (T - T_\infty)c_p/L$  is the appropriately rescaled temperature field  $T$  measured from the imposed temperature  $T_\infty$  of the undercooled melt far away from the interface. The indices  $L$  and  $S$  refer to the liquid and solid, respectively, and the specific heat  $c_p$  and the thermal diffusion constant  $D$  are considered to be the same in both phases.  $L$  is the latent heat, and  $\vec{n}$  is the normal to the interface. In terms of these parameters,

$$\Delta = (T_M - T_\infty)c_p/L \quad (77)$$

is the dimensionless undercooling of the melt from the melting temperature  $T_M$ .

The physics underlying Eqs. (74–76) is quite simple. A solidifying front releases latent heat which diffuses away as expressed by Eq. (74); the need for heat conservation at the interface gives Eq. (75); Eq. (76) is the local equilibrium condition at the interface which takes into account the Gibbs–Thomson correction (see Eq. (54));  $K$  is the two-dimensional curvature and  $d(\Theta)$  is the so-called anisotropic capillary length with an assumed fourfold symmetry,

$$d(\Theta) = d_0(1 - \epsilon \cos 4\Theta) \quad (78)$$

Here  $d_0 = \gamma T_M c_p / L^2$  is a capillary length proportional to the isotropic part of the surface energy  $\gamma$ ;  $\Theta$  is the angle between the normal  $\vec{n}$  to the interface and some fixed crystallographic direction at which  $d(\Theta)$  is minimal;  $\epsilon$  is the strength of the anisotropy.

In Eq. (76) we neglect the kinetic effects, that is, the dependence of the interface temperature on the growth velocity  $v_n$ . The approximation holds at sufficiently small undercoolings and velocities.

Our main interest here is concerned with patterns which can grow at constant speed even at low undercoolings  $\Delta < 1$ , because if they exist they will dominate the system's behavior. A two-phase structure must then exist behind the growth front, filling the space uniformly on sufficiently

large scales. The fraction  $\eta$  of solid inside this two-phase region should be equal to  $\Delta$ , due to global conservation,

$$\eta = \Delta \quad (79)$$

One may define an envelope over the front of this complex two-phase structure, calling this suitably averaged envelope the *average front* in contrast to the local interface separating the solid from the liquid. This average front can be considered as the real growth front in the sense that a two-phase mixture, solid plus liquid, grows into a one-phase region originally consisting of liquid only. These two-phase structures are developed from initially smooth interfaces by the well-known Mullins–Sekerka instability [102].

Eqs. (74–78) contain two dimensional parameters,  $d_0$  and  $D$ , and two dimensionless parameters,  $\Delta$  and  $\epsilon$ . This means that any characteristic length scale  $\ell$  and growth velocity  $v$  of the possible structures can be presented in the form

$$\ell = d_0 f(\Delta, \epsilon), \quad v = \frac{D}{d_0} \varphi(\Delta, \epsilon) \quad (80)$$

The aim is to predict, for given undercooling  $\Delta$  and anisotropy  $\epsilon$ , the type of the two-phase structure and its characteristic length scales and velocity; that is, to calculate the functions  $f$  and  $\varphi$  in the relation (80). The results will be summarized in the morphology diagram shown in Fig. 6. As it turns out,

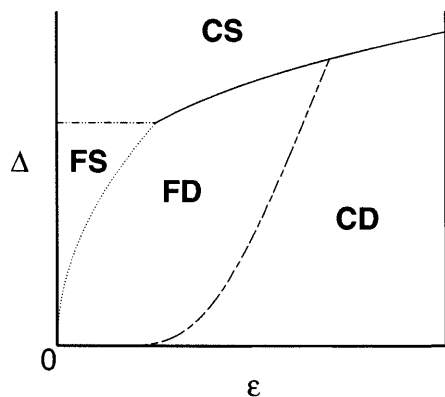


**FIG. 6** Morphology diagram. Plotted is the dimensionless supercooling  $\Delta$  versus the crystalline anisotropy  $\epsilon$ . Compact dendritic (CD) and compact seaweed (CS) structure comprise most of the diagram, under the influence of noise, fractal seaweed (FS) and fractal dendrites (FD) are encountered. For details see text and Ref. 108.

these functions have scaling forms for small  $\Delta$  and  $\epsilon$ , thus showing power law dependences on  $\Delta$  and  $\epsilon$ .

At this point it should be clear that this representation (Eq. (80)) is not restricted to thermal diffusion, but may equally well be formulated in a completely analogous way for the case of chemical diffusion.

Furthermore, it turns out that noise, which always exists in the system (for example, the thermodynamic noise), appears to play a crucial role in the formation of fractal structures but is not so important for compact patterns.

## B. Growth Patterns: Dendrites and Seaweed

At small driving forces a completely flat interface cannot move at a constant speed. This is basically a result of the inherent scaling property of the diffusion equation, which scales lengths proportional to the square-root of time, so an advancing interface would slow down with time.

We have explicitly assumed that the liquid ahead of the advancing interface is supercooled. This means that the liquid is trying to undergo a nucleation process into the solid state and is in principle unstable (or at best metastable). Assume that one makes a sinusoidal rippling perturbation on the interface. The “hills” on this interface landscape are more exposed to the supercooled liquid than the “valleys,” and consequently they will grow even faster into the supercooled melt, increasing hereby the amplitude of the wave surface deformations. This is the famous “Mullins-Sekerka” instability [102]. Intuitive and quantitative analysis shows that perturbations with wavelengths larger than about

$$\ell_{MS} \approx \sqrt{d_0 \ell_D}; \quad \ell_D = D/v \quad (81)$$

are all unstable, while shorter wavelengths are stable. This result can be interpreted such that the characteristic patterns generated by this Mullins-Sekerka instability are characterized by a wavelength  $\ell_{MS}$  which is the result of a competition of a cohesive force characterized by the capillary length  $d_0$  and a dissipative force characterized by the diffusion length  $D/v$ . After this instability has developed, individual spikes will peak out from the rest of the wavy structures. These individual spikes are called “dendrites”. They have an approximately parabolic tail and develop sidebranches [103].

Dendrites can grow at constant speed at arbitrarily small undercooling  $\Delta$ , but usually a non-zero value of the anisotropy  $\epsilon$  is required. The growth pattern evolving from a nucleus acquires a star-shaped envelope surrounding a well-defined backbone. The distances between the corners of the envelope increase with time. For small undercooling we can use the scaling relation for the motion of the corners as for free dendrites [103–106] with tip



radius  $\rho_t$  and velocity  $v$ . These two relations come from the Ivantsov formula [107]

$$P \equiv \frac{v\rho_t}{2D} \sim \Delta^2 \quad (82)$$

and from the selection condition for the stability parameter  $\sigma$

$$\frac{1}{\sqrt{\sigma}} \equiv \frac{\rho_t}{\sqrt{d_0 D/v}} \sim \epsilon^{-7/8} \quad (83)$$

It is quite remarkable that Eq. (82) was obtained in 1947 but it took about 40 years to derive the very non-trivial relation (83). One can find the details in [103–106]. From Eqs. (82–83) follow the dependencies of  $\rho_t$  and  $v$  on the parameters  $\Delta$  and  $\epsilon$ :

$$\rho_t \sim d_0 \epsilon^{-7/4} \Delta^{-2}, \quad v \sim \frac{D}{d_0} \epsilon^{7/4} \Delta^4 \quad (84)$$

Eq. (87) really describes a needle crystal which, without noise, has no side branches. The corresponding star structure then cannot fill the space with constant density and the amount of material solidified in parabolic form increases with time, only like  $t^{3/2}$  rather than like  $t^2$  for a truly compact (initially finite) object in two dimensions.

A small amount of noise, however, cures this problem. The tip of the dendrite is still stable against small noise but has a “convective” instability which produces side branches (Fig. 7). These branches continue to grow until they become independent primary branches a distance  $D/v$  away from the corners of the star. The global shape then consists of an envelope of diamond type over the dendrite tips which appear a distance  $D/v$  apart from each other. The velocity scales like Eq. (84). The relative space filling by primary dendrites and side branches must of course be equal to  $\Delta$ . The two basic length scales in this pattern accordingly are the diffusion length  $D/v$  and the tip radius  $\rho_t$  of a typical dendrite. On length scales larger than  $D/v$  the dendritic structure appears to be “compact” (CD) in contrast to “fractal” with mean density  $\eta = \Delta$ .

Not much is known about the interaction of a multitude of dendrites growing out of individual nuclei in three-dimensional space. A recent simplified model gave some first results on this problem [135].

Compact dendritic (CD) structures formally exist at arbitrarily small anisotropy  $\epsilon$  but their velocity goes to zero with  $\epsilon \rightarrow 0$ . It was only recently discovered that there is another structure, compact seaweed (CS), which is favorable for smaller  $\epsilon$  and larger  $\Delta$  [94].

The compact-seaweed morphology [108] was originally introduced on the basis of experimental observations under the name *dense branching*

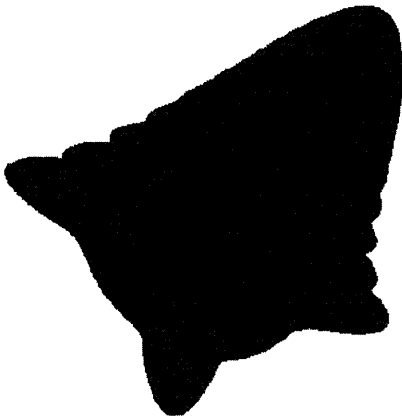


**FIG. 7** Three-dimensional dendrite calculated analytically [119].

morphology [109]. At that time, however, its introduction as a morphological “phase” distinct from the well-known dendritic morphologies was rather speculative. Computer simulations also were inconclusive at that time.

It has been discovered recently that the spectrum of solutions for growth in a channel is much richer than had previously been supposed. Parity-broken solutions were found [110] and studied numerically in detail [94,111]. A similar solution exists also in an unrestricted space which was called “doublon” for obvious reasons [94]. It consists of two fingers with a liquid channel along the axis of symmetry between them. It has a parabolic envelope with radius  $\rho_l$  and in the center a liquid channel of thickness  $h$ . The Peclet number,  $P = v\rho_l/2D$ , depends on  $\Delta$  according to the Ivantsov relation (82). The analytical solution of the selection problem for doublons [112] shows that this solution exists for isotropic systems ( $\epsilon = 0$ ) even at arbitrary small undercooling  $\Delta$  and obeys the following selection conditions:

$$h \sim \rho_l, \quad \frac{1}{\sqrt{\sigma}} \equiv \frac{\rho_l}{\sqrt{d_0 D/v}} \sim P^{-5/4} \tag{85}$$

Eqs. (82) and (85) give

$$\rho_l \sim h \sim d_0 \Delta^{-7}, \quad v \sim \frac{D}{d_0} \Delta^9 \tag{86}$$

If one includes finite anisotropy  $\epsilon$ , doublon solutions exist only above the solid line in Fig. 6, for which

$$\Delta \sim \epsilon^{1/4} \quad (87)$$

For  $\epsilon$  smaller than the value given by Eq. (87) the doublons obey the same scaling law as given by Eq. (86) [112].

It should be noted that doublons, in the range of their existence (Eq. (87)), grow faster than dendrites at the same parameters  $\Delta$  and  $\epsilon$ . This statement is confirmed by numerical calculations [94].

The numerical calculations also show that the double-fingering structure is stable against a competition between the two fingers which belong to the doublon. It means that the axis of symmetry and the direction of growth are at least marginally stable. Of course these directions are arbitrary in isotropic systems. It is not completely clear at the moment whether the stability of the free doublon pair follows precisely the scaling law (87). In any case this line represents a lower bound on  $\Delta$  for a given  $\epsilon$ .

We suppose that the doublons seem to represent a key point in the growth of compact-seaweed morphology (Fig. 8). The formation of a full CS structure evolving from a growing nucleus is possible only due to noise, which triggers side branches, as it is in the CD structure. The resulting two-phase structure has an almost isotropic circular envelope which moves with approximately the same velocity (Eq. (86)) as a free doublon. The structure is fractal with  $D_f = 1.5$  in the intermediate length scale between  $\rho_t$  and  $D/v$ , and it becomes compact with mean density  $\eta = \Delta$  at the length scale larger than  $D/v$ . The region above the solid line,  $\Delta \sim \epsilon^{1/4}$  (Fig. 6), corresponds to the CS structure where doublons exist and grow faster than dendrites. This line represents the discontinuous transitions between CD and CS structures, with a jump in velocities.



**FIG. 8** Compact seaweed originating from the simulation of an isotropic phase by a phase-field model [120]. A doublon structure is just about to emerge from the chaotic background.

### C. Surface Dewetting as a Diffusional Growth Process

The theory of seaweed formation does not only apply to solidification processes but in fact to the completely different phenomenon of a wetting-dewetting transition. To be precise, this applies to the so-called "partial wetting" scenario, where a thin liquid film may coexist with a dry surface on the same substrate. These equations are equivalent to the one-sided model of diffusional growth with an effective diffusion coefficient which depends on the viscosity and on the thermodynamical properties of the thin film.

We assume a surface tension  $\gamma$  to exist between the liquid and the vapor. The free energy of the film can then be written as

$$G = \int \left\{ g(h(x, y)) + \frac{\gamma}{2} |\nabla h|^2 \right\} dx dy \quad (88)$$

Here  $h$  is the thickness of the wet film on the substrate. In equilibrium a double-tangent construction to  $g(h)$  gives two solutions,  $h_-$  for the dry part and  $h_\infty(p)$  for the wet part of the surface. This leads to the evolution equation [113,114] for the film-variable  $h(x, y; t)$ :

$$\frac{\partial h}{\partial t} = \nabla \cdot \left[ \frac{h^3}{3\eta} \nabla \left[ \frac{dg(h)}{dh} - \gamma \nabla^2 h \right] - \alpha \left[ \frac{dg(h)}{dh} - \gamma \nabla^2 h - \mu(p) \right] \right]. \quad (89)$$

Here  $\eta$  is the viscosity of the dewetting liquid. Note that a relaxational term proportional to  $\alpha$  has been added, with  $\mu(p)$  being the chemical potential of the vapor. This term alone guarantees that a homogeneous liquid film will relax to its equilibrium value  $h_\infty(p)$  by evaporation or condensation. For  $h = h_\infty(p)$  this term vanishes.

The first part of Eq. (89), proportional to the inverse viscosity  $\eta^{-1}$  of the liquid film, describes a creeping motion of a thin film flow on the surface. In the (almost) dry area the contributions of both terms to the total flow and evaporation of material can basically be neglected. Inside the wet area we can, to lowest order, linearize  $h = h_\infty [1 + u(x, y)]$ , where  $u$  is now a small deviation from the asymptotic equilibrium value for  $h_\infty(p)$  in the liquid. Since  $\nabla h_\infty(p) \equiv 0$  the only surviving terms are linear in  $u$  and its spatial derivatives  $\nabla u$  and  $\Delta u$ . Therefore, inside the wet area, the evolution equation for the variable part  $u$  of the height variable  $h$  becomes

$$\frac{\partial u}{\partial t} = D_{\text{eff}} \Delta u - \lambda_{\text{eff}} u \quad (90)$$

We have dropped here the terms  $\sim \gamma \Delta^2 u$  since the effective diffusion constant  $D_{\text{eff}} = (h_\infty^3/3\eta) \{d^2 g/dh^2\} + \alpha\gamma$  is positive and dominates the

long-wavelength behavior over the fourth-order term. The relaxation coefficient is  $\lambda_{\text{eff}} = \alpha \{d^2 g / dh^2\}$ . Derivatives are taken around the equilibrium value  $h = h_{\infty}$ . Note that the dewetting equation (90) is now precisely the equation of motion for diffusional growth studied in [115], generalizing the basic model (74).

## D. Fractal Structures in Diffusional Growth

For the compact structures described above noise is important only as the trigger of side branches. It has been supposed that the tips (of dendrites or doublons) remain undestroyed. However, the strength of noise may be large enough not only to trigger the side branches but also to destroy the tips. In order to estimate the parameters for which this happens, let us look at the theory of side-branch formation more carefully. According to the result of Langer [116] the root-mean-square amplitude  $\langle \zeta^2 \rangle^{1/2}$  of the side branches on the underlying parabolic interface generated by thermal fluctuations depends on the distance from the tip  $z$  as

$$\frac{\langle \zeta^2 \rangle^{1/2}}{\rho_t} \sim \Gamma \exp \left[ \frac{2^{7/4}}{3\sqrt{3}\sigma} \left( \frac{z}{\rho_t} \right)^{1/4} \right] \quad (91)$$

Here the stability parameter  $\sigma$  is given by Eqs. (83) and (85) for dendrites and doublons respectively;  $\Gamma$  is the relative noise strength ( $\Gamma \ll 1$ )

$$\Gamma = (T/T_o) \left( \frac{2Dd_0^3}{v\rho_t^4} \right)^{1/2}, \quad T_o = \left( \frac{L^2 d_0^3}{k_B c_p} \right)^{1/2} \quad (92)$$

where  $k_B$  is the Boltzmann constant. The tip becomes destroyed if the amplitude of the side branches is of the order of  $\rho_t$  at the distance  $z \sim \rho_t$  down the shaft. Thus we obtain from Eq. (91) the following condition

$$\frac{1}{\sqrt{\sigma^*}} \sim |\ln \Gamma| \quad (93)$$

The tips of structures will be destroyed if the stability parameter  $\sigma$  becomes smaller than the critical value  $\sigma^*$  given by Eq. (93). Using the value  $\sigma \sim \epsilon^{7/4}$  (Eq. (83)), one obtains from (93) a line of smooth transition from CD to FD structures in Fig. 6:

$$\epsilon^* \sim |\ln \Gamma|^{-8/7} \quad (94)$$

The analogous line which separates CS and FS structures in Fig. 6 can be obtained using Eqs. (82), (85), and (93):

$$\Delta^* \sim |\ln \Gamma|^{-2/5} \quad (95)$$

Eq. (93) has the following physical meaning. Let us rewrite this relation, using the definition of  $\sigma = d_0 D / (v \rho_t^2)$  (Eq. (83)), which gives the following condition for a stable tip radius

$$\rho_t \leq \ell_{\text{MS}} |\ln \Gamma| \quad (96)$$

where  $\ell_{\text{MS}} \sim \sqrt{d_0 D / v}$  is the Mullins–Sekerka length (81) describing the instability of a planar interface. One can think of the right-hand side of Eq. (96) as the characteristic length scale,  $a_\Gamma$ , of the instability set by noise

$$a_\Gamma = \ell_{\text{MS}} |\ln \Gamma| \sim \sqrt{d_0 D / v} |\ln \Gamma| \quad (97)$$

The tip is stable if  $\rho_t < a_\Gamma$  and it becomes destroyed if  $\rho_t > a_\Gamma$ . Using a self-consistent scaling theory, explicit formulas can be obtained for the dependence of growth rates and characteristic scales of the pattern [108]. There is still a substantial need for numerical support of these results [60].

The scaling arguments given here for two-dimensional growth patterns can be extended formally in a straightforward fashion to three dimensions. For dendritic structures this seems to be perfectly permissible since the basic growth laws are rather similar in two and three dimensions [117,118]:

$$\rho_t \sim d_0 \epsilon^{-7/4} |\ln \Delta| / \Delta, \quad v \sim \frac{D}{d_0} \epsilon^{7/4} (\Delta / \ln \Delta)^2 \quad (98)$$

(compare with Eq. (84) for 2D). There is, however, a crucial difference between the 3D and the 2D case. In the latter, small anisotropy implies that the shape of the selected needle crystal is close to the Ivantsov parabola everywhere; in the former, strong deviations from the Ivantsov paraboloid appear for any anisotropy. This shape, in units of the tip radius of curvature, depends mostly on the crystalline symmetry and is almost independent of the material and growth parameters. The shape of the 3D dendrite has been described analytically [118], together with side branching activity [119].

For the seaweed patterns in three dimensions without anisotropy much less is known since our preliminary results are mostly numerical ones [120]. Instead of “doublons” one now obtains “tripbons” in three dimensions, spikes with a threefold cut in their tip. The crucial point here is that this self-organized triplet structure is not imposed by the symmetry of the calculation box and it consists of three cooperating symmetry-broken fingertips. A hexagonal or triplet structure should be expected to occur under free growth conditions from basic symmetry considerations, since these growth problems do not have reflection symmetry about some average interface position. The resulting multiplets, consisting of symmetry-broken cooperating fingers of the growing phase, finally seem to be the basic building blocks for the compact-seaweed morphology; in particular the triplet structure appears to be characteristic for free growth. We expect these

triplons even to appear in systems with convection, driven by surface tension, provided the growth rate is faster than the convection rate defined as the ratio of surface tension divided by viscosity. At present, however, there is still a need for detailed experiments in this region of low crystalline anisotropy but rather high driving force.

## E. Directional Solidification

Directional solidification (see [121–123,125] and [126–129]) is the most frequent way in which a material changes its state from solid to liquid. The necessary removal of the latent heat of freezing usually occurs in a direction prescribed by the location of heat sinks: For a freezing lake it is the cold atmosphere above it; in casting iron in a foundry it is the cold sand-form into which the heat flow is directed.

The basic difference to the case of free growth is the fact that the orientation of the solid–liquid interface is prescribed by the experimental conditions. The interface then typically consists of an array of dendrites or cellular structures growing in parallel. An important question from an engineering point of view is the prediction of the fine structure resulting in this growth process. Suppose we know all the material parameters and the experimentally controllable parameters like thermal gradient and pulling speed for a directional solidification process; can we then predict the characteristic scale of that fine structure or, in other words, of the distance between the cells and dendrites which form at the moving interface? The importance of this question comes from the fact that the mechanical and chemical properties of the resulting alloy are usually improved with a decrease of that primary cell spacing [121,122].

A natural mechanism for the local reduction of cell spacings (or creation of a new cell) is either a nucleation in one of the grooves (the liquid is supercooled) or, even more likely, the formation of a new cell out of a side branch in such a groove. Alternatively, tip-splitting of a cell may give the same result [121].

The opposite mechanism, for the increase of cell spacings (or annihilation of an existing cell), could occur through the competition of neighboring cells for the diffusion field, such that finally one cell moves at a slightly lower speed than the neighboring cells and consequently will be suppressed relative to the position of the moving front.

The initial development of a cellular structure from an originally flat interface has been at least partially understood [130]. Let us look only at the large-wavelength  $\lambda$  limit (for more details see [122]). In the numerical calculations it was found [123] that for fixed cell-spacing  $\lambda$  at increasing velocity a *tail instability* occurs. A side branch in the groove between two

dendrites hereby splits off a ternary branch which then moves so fast in the strong supersaturation in the groove that it finally becomes a new primary branch. In fact, this is also observed experimentally (see the references in [121,122]), in particular when the solid consists of slightly misaligned regions separated by grain boundaries, such that the growth direction of two neighboring dendrites is slightly divergent. Our basic assumption now is that this tail instability occurs when the intersection of parabolic envelopes over neighboring dendrites occurs at a point  $z \lesssim 0$  where  $\Delta > 1$  theoretically. In that case, namely, there is no need for long-range diffusion around a side branch and its dynamics becomes local. Of course, this ignores geometrical competition between neighboring side branches to a certain extent, but for the moment there seems no better argument at hand.

Taking the point seriously that neighboring parabolas with tip position at  $z_{\text{tip}} > 0$  cannot intersect further down the cold side than at  $z = 0$ , we can use the parabolic relation  $z_{\text{tip}} = \lambda^2/8R$  for the intersection of two parabolas of radius  $R$  at  $z = 0$ , being a distance  $\lambda$  apart from each other. The result for the tail instability to occur is

$$\lambda \gtrsim \sqrt{\ell_T \ell_D} \quad (99)$$

with a prefactor roughly of order unity. The scaling with the inverse growth rate  $\ell_D$  follows the neutral stability curve at velocities safely in between the two critical values at high and low velocities. The result (99) seems to be in agreement with experiments (see references in [121,122]) concerning the scaling with respect to diffusion length  $\ell_D$  and thermal length  $\ell_T$ . (The treatment of the limit  $k \rightarrow 0$  for the segregation coefficient  $k$  as a singular point would require more effort.)

The previously given relation [121]  $\lambda \sim \ell_D^{1/4}$  seems to be valid in an intermediate velocity region where  $\Delta$  does not vary significantly, such that one may set  $z_{\text{tip}}/\ell_T \approx 1/2$  approximately.

A serious point is the neglect of surface tension and anisotropy in these derivations. In the experiments analyzed so far the relation  $V\lambda^2 \approx \text{const.}$  seems to hold approximately, but what happens when the capillary anisotropy  $\epsilon$  goes to zero? Numerically, tip-splitting occurs at lower velocities for smaller  $\epsilon$ . Most likely in a system with anisotropy  $\epsilon = 0$  (and zero kinetic coefficient) the structures show seaweed patterns at velocities where the diffusion length  $\ell_D$  is smaller than the short wavelength limit of the neutral stability curve, as discussed in Sec. VB.

Arguing, finally, whether the tail instability (large  $\lambda$ ) or the competition mechanism (small  $\ell_D$ ) will dominate in casting processes, we tend to favor the first option. If the solidification front consists of groups of dendrites slightly misoriented against each other due to small angle grain boundaries,



cells will disappear at points where the local growth directions are converging and new cells appear through the tail instability at diverging points at the front.

To summarize, the most likely scaling behavior of the primary cell spacing  $\lambda$ , depending on pulling velocities, follows Eq. (99) as a consequence of the arguments presented in this section supported by a number of recent experiments (Billia et al., Somboonsuk, Kurowsky, Esaka, and Kurz, cited in [122]).

A different problem of spacing, which is closely related to directional solidification but has some additional degrees of freedom, is electrocrystallization. We would like to mention at least one example of greater significance, namely the production of porous silicon [131], which is still not very well understood today.

## F. Multicomponent and Eutectic Growth

In our treatment of directional solidification above, only one diffusion field was treated explicitly, namely the compositional diffusion. If a simple material grows dendritically (thermal diffusion) one may worry about small amounts of impurities. This was reconsidered [132], confirming a qualitative previous result [133] that impurities may increase the dendritic growth rate. Recently some direct simulation results have been obtained with two coupled diffusion fields, one for heat and one for matter, but due to long computing times they are not yet in the state of standard applications [120,134].

A specific, but in some sense crucial, question concerns the high-speed limit in two- or more-component systems. Assume that a typical binary mixture is solidifying at such high speed that the alloy atoms in front of the advancing solid-liquid interface cannot rearrange themselves, but are being incorporated into the solid in exactly the same local arrangement as they were in the liquid. In this case the local disorder of the mixture plays a crucial role, as the advancing interface may suffer from *pinning* by impurities [136].

Eutectic growth is a special mode of solidification for a two-component system. Operating near a specific point in the phase diagram, it shows some unique features [121,137].

The phase-diagram (temperature vs concentration) for a eutectic two-component alloy shows at low temperatures a central two-phase region and two solid one-phase regions at low and high relative concentrations. At the eutectic temperature  $T_E$  the liquid phase at an intermediate concentration  $C_E$  can all of a sudden coexist with the two solid phases. Upon further increase of temperature, the liquidus lines open up a V-shaped liquid

region, and consequently two regions of two-phase coexistence remain at fixed temperature, one for the coexistence of a low-concentration solid with the liquid and one of a high-concentration solid with the liquid.

When one starts with a liquid of concentration  $C_E$  at a high temperature, and cools it down to a temperature slightly below  $T_E$ , a solid will grow which consists of two phases, which appear alternatively as lamellae or as fibers of one phase in a matrix of the other phase.

The eutectically growing material must be cooled by a small amount  $\Delta T$  below the eutectic temperature  $T_E$ . This supercooling is the driving force needed to grow the lamellar structure against two competing forces. One is the curvature of the interface between each lamellar region and the liquid, which acts as a backdriving force. The other one is due to the fact that in the liquid just ahead of a growing lamella, let's say of phase A, there is an excess of concentration of material "B", acting as a hindering impurity for the growth of phase A, and vice versa. This is a diffusion barrier for the phase separation of material in the liquid just in front of the solid. The capillary force can be characterized by a capillary length  $d$  (proportional to the surface tension); the diffusive force can be characterized by the diffusion length  $\ell = D/V$  with diffusion constant  $D$  and growth rate  $V$ . The driving force for the lamella-producing growth is then related to these two length scales as

$$\Delta T \approx T_E \left\{ \frac{\lambda}{\ell} + \frac{d}{\lambda} \right\} \quad (100)$$

The length scale  $\lambda$  is the wavelength of the lamellar structure. Minimization of Eq. (100) with respect to  $\lambda$  gives

$$\lambda \sim \sqrt{\ell d} \quad (101)$$

which is the fundamental scaling law for eutectics.

The diffusion field just ahead of the solid front can be thought of as containing two ingredients: a diffusion layer of thickness  $\tilde{\ell}$  associated with global solute rejection, and modulations due to the periodic structure of the solid of extent  $\lambda$  ( $\lambda \ll \tilde{\ell}$ ). When the amplitude of the front deformations is small compared to these lengths the averaging approximation by Jackson and Hunt [137] seems justified.

This point was taken up by Caroli et al. [138] who found that only in the limit of large thermal gradient is this approximation safe, which appears difficult to reach experimentally.

In an attempt to shed some light on the wavelength selection Datye and Langer [139] considered finite amplitude perturbations of the local wavelength. This type of approach was used in a somewhat refined version by

Brener et al. [140]. They derived an approximate potential function for wavelengths  $\lambda$  and argued, that under finite amplitude of noise the wavelength selected is defined on average, by a balance in the creation and annihilation rates of lamellae. In other words, if lamellae disappear through suppression by neighboring lamellae and appear through nucleation, then an equal rate of these processes leads to a selection of an average spacing  $\bar{\lambda}$ , as both depend on  $\ell$ . The operating point was hereby found in a limited interval near the wavelength corresponding to minimal supercooling (or maximal velocity in an isothermal process), and accordingly scales like (101).

More recent extensions of the theory (see citations in [122]) gave indications that the orientation of the lamellae (under isotropic material parameters) is not necessarily parallel to the growth direction of the front but may be tilted so that the lamellae travel sideways at some specific angles [138]. Finally it was found that the standard model of eutectic solidification has an intrinsic scaling structure [141–147]

$$\lambda \sim \sqrt{\ell} df(\ell/\ell_T) \quad (102)$$

with a scaling function  $f$  depending only on  $\ell/\ell_T$ , such that  $\lambda \sim V^{-1/2}$  for  $4\ell \lesssim \ell_T$  or for high enough velocities, while at smaller velocities the exponent should be smaller:  $\lambda \sim V^{-0.3}$ . This is quite in agreement with the arguments given for ordinary directional solidification. In addition to this more general scaling structure a host of new grow-modes was discovered by semi-analytical investigations [142–147], such as tilted lamellae and lamellar superstructures.

Periodic oscillations have been observed as a morphological instability in several systems grown under various conditions [148]. The correspondence of the observed structures with results of theoretical modelling [139,149] is striking.

We expect more insight from simulations in the future, particularly in situations where these multicomponent systems show effects of coupling between the different degrees of freedom, surface tensions depending on temperature and concentration, hydrodynamic flow induced by concentration gradients in addition to thermal buoyancy.

## VI. GROWTH UNDER HYDRODYNAMICAL FLOW

### A. Hydrodynamical Effects on Interface Advancement

In many crystal growth phenomena, transportation of material occurs not only via diffusion but also via hydrodynamic convection. We assume

as an example that a crystal should be grown from a solution or a multi-component melt. At some distance of the crystal, we then have a homogeneous liquid which is continuously mixed on account of natural thermal convection or by continuous stirring. When silicon single crystals are grown by the Czochralski method, the cylindrical crystal body is rotated in order to achieve steady flow rates in the neighborhood of the crystal. Within a boundary layer of thickness  $\delta_b$  near the crystal the convection current is reduced due to the no-slip boundary condition. Diffusion is then limited to the thickness of this layer.

We cannot deal here with the details of the hydrodynamic Navier–Stokes equations and their consequences. For dimensional reasons one can derive the following expression [150] for the thickness of the boundary layer when the crystal rotates with angular frequency  $\omega$

$$\delta_b \approx c \sqrt{\frac{\nu_{\text{visc}}}{\omega}}; \quad c = \text{Min} \left\{ \left( \frac{D}{\nu_{\text{visc}}} \right)^{1/3}; 1 \right\} \quad (103)$$

Here,  $D$  is the diffusion constant for heat or material and  $\nu_{\text{visc}}$  the kinematic viscosity of the liquid. A consequence of the existence of such a diffusive surface barrier is that the diffusion length  $\ell_D \equiv D/V$  is to be replaced by  $\delta_b$  in all formulas, as soon as  $\delta_b \ll \ell_D$ . Therefore, the smaller the growth rate  $V$  the more important become the hydrodynamic convection effects.

Another velocity finally appears in a system where a liquid is in contact with an interface. The interface energy  $\gamma$  then works as a static driving force. This can trigger a current which is damped by a dynamic force, the viscous friction, in the case of density difference between crystal and liquid. Taking the ratio

$$v_c \sim \frac{\gamma}{\nu_{\text{visc}} \rho} \frac{\Delta \rho}{\rho} \quad (104)$$

with density difference  $\Delta \rho$  and liquid density  $\rho$ , this has the dimension of a velocity. This convective velocity becomes relevant if it is larger than the growth rate of the crystal defined by other effects. In this case it sets the length or time scale of the growth process.

## B. Bridgman and Czochralski Growth

Hydrodynamic convection can modify the shape and the dynamics of a growing solidification front [151–153]. The growth of large single crystals is often achieved by pulling them out of a melt. This implies strong thermal gradients, free surfaces, and in consequence convective flow in the melt. Again, there are so many aspects like geometry and material of the crucibles

etc. coming into play that we can only sketch some basic concepts here and leave the rest to the literature.

In Bridgman growth [155], a boat or vessel filled with the melt is slowly cooled from one side, so that the crystal forms from that side. In Czochralski growth [156,157] a cylindrical crystal sits on the surface of the melt and is slowly pulled upward. In both cases the hydrodynamical flow of the melt is an important factor in the chemical composition and fine structure of the resulting crystal.

The basic model equations for a description of hydrodynamical flow are the Navier–Stokes equations, representing momentum conservation in the fluid

$$\frac{\partial}{\partial t} \hat{v} + (\hat{v} \nabla) \hat{v} = -\rho^{-1} \nabla p + \nu \Delta \hat{v} + \hat{f} \quad (105)$$

Here  $\hat{v}$  is the space- and time-dependent velocity field,  $\rho$  is the density of the fluid,  $p$  is the local pressure,  $\nu$  is the kinematic viscosity, and  $\hat{f}$  is some arbitrary body-force acting on each small element of the fluid (gravitation, for example).

The numerical solution of these equations is not trivial, since for reasonably low viscosities the flow becomes turbulent. A popular method of treating these equations (together with the equations of energy and mass conservation) is the MAC method [156,157]. For the case of immiscible fluids or moving internal interface a phase-field-type approach seems to be successful [78,158,159]. Because of the enormous requirements of computing resources the development in this field is still relatively slow. We expect, however, an impact from the more widespread availability of massively parallel computers in the near future.

## VII. GROWTH OF CRYSTALS OF COMPLEX MATERIALS

In this section we briefly summarize a few modern applications of simulation techniques for the understanding of crystal growth of more complex materials. In principle, liquid crystals and colloids also belong to this class, but since the relative length of their basic elements in units of their diameter is still of order about unity in contrast to polymers, for example, they can be described rather well by the more conventional models and methods as discussed above.

## A. Polymer Crystals

A polymer such as polyethylene is a long-chain molecule with repetitions of the same monomer. Due to topological constraints, the crystallization process of polymer chains is expected to be different from that of simple molecules as discussed so far [160].

With the first successful growth of a polymer single crystal in the 1950s it was found that the polymer chains are folded back and forth many times inside the crystal [161].

The single crystal of a polymer is a lamellar structure with a thin platelet-like form, and the chain runs perpendicular to the lamella. The crystal is thinner than the polymer chain length. The chain folds back and forth on the top and bottom surfaces. Since the fold costs extra energy, this folded chain crystal (FCC) should be metastable with respect to the thermodynamically more stable extended chain crystal (ECC) without folds.

The main questions in polymer crystallization are:

- Why and how are the chains folded during the polymer crystallization?
- How does the polymer chain sneak out from the entangled random coil state and how does it order into a crystalline state?
- How can the FCC relax to ECC, if this happens?

For the first problem, Lauritzen and Hoffman [162] explained the thickness of the lamella in terms of a secondary nucleation model. The lateral growth of the lamella requires the formation of a secondary nucleus on the rim of the crystal plate. According to that model the nucleation process consists of a series of stem attachments on the rim of the lamella. The height of the stem is assumed to remain the same for consecutive lateral growth, and the fastest process was assumed to determine the critical fold length. In the original theory, there was a problem of so-called “ $\delta\ell$  catastrophe,” and many modifications followed [160]. When crystals with curved faces were observed, a new model with rough surfaces and nucleation-free growth was proposed by Sadler and Gilmer [163]. The apparent activation barrier in the growth rate is attributed to entropic origin. There are various molecular dynamics and Monte Carlo simulations to clarify the problem of lamellar thickness [164].

Whenever the polymer crystal assumes a loosely packed hexagonal structure at high pressure, the ECC structure is found to be realized. Hikosaka [165] then proposed the sliding diffusion of a polymer chain as dominant transport process. Molecular dynamics simulations will be helpful for the understanding of this sliding diffusion. Folding phenomena of chains are also studied intensively by Monte Carlo methods and generalizations [166,167].

## **B. Protein Crystals**

Proteins are molecules vital for supporting and sustaining life. A protein is a long linear chain of groups of atoms, but in contrast to the polymers discussed in the previous subsection proteins consist of 20 different amino acids. Therefore the complexity increases if the molecules are entangled. The folding and crystallization of macromolecules such as proteins are often called the ternary and quarternary structure. Experimentally, protein crystallization is performed from a very dilute solution and each protein molecule assumes its ternary conformation during incorporation into the crystal. The main difficulty in protein crystallization lies in the weak molecular interactions and their dependence on mutual orientations. The growth is controlled by various factors such as temperature, solution, pH, etc. Especially, membrane proteins are insoluble in water, and it is therefore difficult to crystallize them until the appropriate amphiphilic medium is found to make the protein soluble. Because of the complexity of these processes computer simulation studies [166,168–171] of protein folding and crystallization are still on a somewhat preliminary level. The field, however, is very active and will also profit from progress in polymer simulations.

## **C. Quasi-crystals**

A peculiar solid phase, which has been discovered not too long ago [172], is the quasi-crystalline phase. Quasi-crystals are characterized by a fivefold or icosahedral symmetry which is not of crystallographic type and therefore was assumed to be forbidden. In addition to dislocations which also exist in normal crystals, quasi-crystals show new types of defects called phasons. Computer simulations of the growth of quasicrystals [173] are still somewhat scarce, but an increasing number of quasi-crystalline details are studied by simulations, including dislocations and phasons, anomalous self-diffusion, and crack propagation [174,175].

We finally think it is fair to say that simulation techniques will play an increasingly important role in predicting properties of new materials in all areas of materials science.

## **VIII. LIST OF KEYWORDS**

Computer simulation applied to problems of crystal growth and solidification is a very strongly growing field at present. There are currently over two hundred publications per year appearing on these subjects. Clearly, it is impossible to give a completely fair review of all the ideas emerging over a period of several years. To facilitate the orientation of the reader, we have

checked some 1000 references, and include here some three hundred over the past few years, together with older significant material. The references after [175] could not be discussed in the main part of this article, but these references will appear in the following list of keywords. The numbers following the keywords indicate the corresponding reference in our list.

**activation energy:** [185] [189] [248]

**adsorption:** [185] [249] [261] [300] [235] [237] [270] [294] [312] [317]

**aggregate:** [183] [261] [271]

**alloy:** [128] [136] [151] [152] [154] [179] [189] [206] [213] [214] [215] [219] [220] [225] [227] [230] [233] [234] [235] [253] [259] [264] [266] [271] [275] [279] [282] [283] [284] [298] [316] [321]

**anisotropy:** [72] [73] [123] [124] [176] [179] [182] [207] [211] [227] [232] [266] [268] [282] [300] [306] [308] [314] [320]

**austenite:** [321]

**band:** [189] [190] [191] [215] [219] [262] [267]

**bond:** [11] [168] [188] [189] [249] [258] [306] [313] [314] [320]

**boundary:** [37] [70] [73] [123] [124] [158] [178] [181] [192] [198] [200] [208] [211] [213] [225] [229] [233] [235] [239] [245] [252] [259] [278] [283] [284] [291] [296]

**boundary layer:** [233] [235] [283] [284]

**boundary element:** [37] [123] [124] [252]

**Brownian:** [182] [262] [282] [287] [294] [303] [317]

**bunch:** [91] [184] [207] [308]

**buoyancy:** [212] [239] [243] [244] [246] [269] [290] [296]

**capillary:** [177] [209] [239] [272] [296] [301] [322]

**Car-Parinello:** [26]

**casting:** [135] [154] [259] [264] [298] [316] [321]

**cellular:** [122] [126] [180] [205] [224] [225] [232] [233] [235] [283] [292]

**chaos:** [127]

**cluster:** [82] [7] [195] [214] [249] [270] [271] [279] [303] [315] [195] [204] [261] [270]

**coating:** [294]

**coherent:** [220] [230] [254] [316]

**compact:** [298] [321]

**concentration:** [179] [180] [185] [188] [189] [202] [208] [222] [223] [224] [227] [228] [229] [232] [235] [236] [238] [247] [253] [266] [292] [300] [301] [304] [305] [317] [321]

**conduction:** [25] [76] [176] [181] [185] [186] [188] [189] [191] [200] [202] [204] [208] [209] [215] [216] [218] [219] [221] [223] [228] [229] [232] [237] [239] [240] [243] [245] [246] [247] [251] [253] [257] [263] [267] [271] [275] [276] [277] [283] [289] [290] [291] [296] [300] [304] [305] [307] [310] [313] [320]



- convection:** [151] [153] [154] [184] [186] [202] [206] [208] [209] [211] [217] [225] [233] [235] [238] [239] [240] [241] [243] [244] [245] [246] [247] [252] [259] [263] [269] [272] [280] [283] [290] [296] [302] [304] [308] [318] [322]
- correlation:** [199] [228] [284] [289]
- coulomb:** [9] [38]
- crack:** [80] [174] [179] [201] [205] [241] [251] [254] [264] [271]
- crystal morphology:** [180] [184] [194] [195] [207] [222] [227] [257] [261] [283] [286] [295] [320] [322]
- crystallizer:** [187] [286] [318]
- curvature:** [37] [238] [243] [252] [263] [265] [266] [291]
- CVD:** [236] [237] [257] [236] [237] [257]
- cyclic:** [179] [180] [222]
- defect:** [87] [185] [188] [189] [199] [201] [205] [221] [228] [249] [266] [270] [291]
- dendritic:** [71] [74] [123] [135] [180] [206] [222] [225] [252] [263] [283] [303] [316]
- deposition:** [185] [189] [194] [196] [204] [236] [237] [248] [249] [250] [257] [261] [270] [272] [274] [282] [287] [294] [295] [312]
- desorption:** [12] [235] [237] [287] [312]
- diamond:** [205] [257] [289] [313]
- dilute:** [234]
- directional:** [83] [122] [124] [126] [127] [128] [143] [151] [152] [206] [209] [233] [235] [259] [262] [265] [298] [302]
- disclination:** [9]
- dislocation:** [174] [189] [192] [218] [268] [271] [274] [285] [289]
- dispersion:** [190] [262]
- EAM:** [11] [12] [16] [93] [185] [189] [196] [204] [211] [245] [250] [261] [270] [303]
- Eden model:** [85]
- Ekman:** [217]
- elasticity:** [83] [85] [7] [87] [154] [220] [254] [272] [311]
- electrochemical:** [228] [229] [317]
- electrodeposition:** [282]
- electromigration:** [251] [288]
- electrostatic:** [317]
- embedded atom:** [294] [11] [12] [16] [93] [185] [189] [196] [204] [211] [245] [250] [261] [270] [303]
- enthalpy:** [189] [245] [283] [302]
- entropy:** [189] [192] [197] [220] [269] [279] [282] [285] [302] [311] [313]
- epitaxy:** [16] [93] [185] [189] [193] [194] [195] [196] [204] [236] [237] [248] [249] [250] [257] [261] [270] [272] [274] [275] [276] [282] [287] [294] [295] [312] [315]
- equiaxed:** [135]

- equilibrium:** [13] [18] [19] [20] [21] [5] [6] [53] [65] [66] [106] [180] [185] [213] [222] [227] [228] [249] [253] [261] [267] [270] [275] [279] [280] [283] [286] [287] [289] [300] [303] [311] [314] [317] [321]
- experimental observation:** [220] [230] [235] [271] [311]
- eutectic:** [122] [137] [140] [141] [142] [143] [144] [145] [146] [147] [149] [233] [283] [321]
- evaporation:** [185] [195] [203] [235] [237] [257] [261] [312] [318]
- facet:** [179] [180] [232] [262] [285] [289]
- fcc:** [214] [279]
- film:** [88] [185] [189] [193] [194] [195] [196] [204] [205] [236] [237] [248] [249] [250] [251] [257] [261] [270] [272] [274] [282] [287] [288] [294] [295] [312] [315]
- finite element:** [37] [212] [213] [218] [236] [239] [240] [242] [243] [245] [247] [254] [276] [290] [298] [302]
- first principles:** [194] [225] [319]
- flow:** [37] [128] [150] [153] [155] [157] [158] [177] [179] [184] [199] [202] [204] [206] [207] [208] [209] [211] [212] [216] [217] [225] [234] [235] [236] [237] [238] [239] [240] [241] [243] [244] [245] [246] [263] [265] [269] [272] [276] [286] [290] [296] [301] [302] [307] [308] [318]
- fluctuation:** [15] [17] [182] [244] [262] [269] [280] [282] [283] [287] [292] [294] [303] [307] [317]
- Fokker–Planck:** [89] [229]
- fractal:** [44] [7] [99] [260] [292]
- fracture:** [80] [86] [179] [201] [215] [241] [251] [254] [264] [271]
- gas:** [38] [179] [203] [236] [237] [243] [257] [267] [280] [300]
- Gauss:** [50] [190] [235]
- gel:** [25] [26] [275] [276] [301] [322]
- Gibbs:** [189] [197] [263] [281]
- Gibbs–Thomson:** [197]
- grain:** [178] [179] [192] [197] [198] [213] [227] [230] [235] [271] [278] [279] [281] [282] [284] [288] [291] [294] [298] [311] [312] [320] [321]
- gravity:** [177] [209] [223] [224] [238] [263] [307]
- Grinfeld:** [81]
- Green function:** [123] [124]
- growth morphology:** [6] [180] [184] [194] [195] [207] [220] [227] [257] [261] [286] [295] [322]
- heat:** [181] [186] [188] [198] [202] [209] [212] [217] [218] [229] [230] [233] [235] [238] [239] [240] [241] [243] [244] [245] [246] [252] [259] [263] [267] [269] [278] [280] [282] [283] [284] [285] [289] [293] [295] [296] [302] [304] [313] [316] [318] [322]
- hydrodynamic:** [150] [158] [177] [199] [202] [206] [216] [234] [246] [269] [272] [296] [318]

- ice:** [176] [179] [180] [185] [191] [194] [198] [199] [202] [212] [213] [219] [221] [227] [228] [229] [237] [239] [243] [244] [246] [259] [266] [268] [269] [274] [281] [289] [300] [306] [319] [320] [322]
- impurity:** [180] [188] [189] [207] [208] [219] [222] [247] [304] [305] [27] [180] [189] [207]
- instability:** [15] [122] [177] [184] [202] [205] [207] [244] [252] [257] [308] [317]
- interdendritic:** [316]
- iron:** [27] [230] [239] [241] [245] [267] [271] [276] [280] [282] [321]
- Ising model:** [253] [275] [277] [285] [300]
- island:** [195] [204] [261] [270] [82] [7] [195] [214] [249] [270] [271] [279] [303] [315]
- isotherm:** [57] [231] [263] [277] [284] [285] [316]
- Ivantsov:** [107] [263]
- Kardar–Parisi–Zhang:** [43]
- kinetic:** [50] [52] [53] [56] [69] [74] [122] [124] [183] [194] [197] [199] [205] [207] [213] [218] [220] [222] [223] [227] [230] [231] [235] [237] [251] [257] [277] [278] [279] [287] [291] [300] [303] [306] [308] [311] [312] [320]
- kinetic coefficient:** [207]
- kinetic roughening:** [52] [53]
- kinetic transition:** [52] [199] [222] [235]
- kink:** [262] [275]
- KPZ:** [43]
- KS:** [28] [35] [37] [38] [45] [48] [51] [137] [179] [186] [201] [215] [232] [236] [237] [238] [239] [240] [241] [242] [243] [244] [245] [246] [247] [251] [253] [254] [262] [264] [271] [275] [305] [309] [316] [318]
- Kuramoto–Sivashinsky:** [44] [45]
- Landau:** [54] [220] [227] [278] [291] [293] [220] [227] [278] [291]
- laser:** [280] [293]
- latent heat:** [186]
- lattice:** [180] [185] [194] [213] [227] [266] [268] [274] [281] [289] [300] [319] [320]
- layer:** [87] [176] [178] [181] [185] [189] [194] [196] [204] [209] [219] [233] [235] [246] [248] [249] [257] [258] [259] [261] [272] [274] [283] [284] [289] [295] [296] [300] [306] [312] [315] [317]
- Lennard–Jones:** [28] [31] [258] [279] [281] [315]
- Liesegang:** [190]
- linear stability:** [207] [211] [257] [308]
- liquid:** [30] [32] [33] [152] [176] [178] [190] [197] [199] [205] [206] [207] [209] [222] [223] [225] [227] [231] [233] [235] [243] [244] [246] [253] [258] [259] [261] [265] [272] [273] [274] [275] [276] [280] [282] [283] [284] [286] [292] [296] [298] [301] [302] [318] [321]

**liquid crystal:** [152] [176] [199] [205] [206] [207] [209] [222] [223] [225] [227] [231] [235] [243] [244] [246] [253] [258] [261] [272] [273] [274] [275] [280] [284] [286] [301] [302] [318]

**long range:** [214] [278]

**LPE:** [274]

**MAC:** [14] [169] [184] [212] [232] [233] [277] [295] [298] [310] [322]

**magnet:** [157] [181] [185] [202] [206] [208] [216] [234] [244] [246] [296] [307]

**Marangoni:** [202] [208]

**mass crystallization:** [186] [223] [292]

**MBE:** [16] [17] [93] [182] [185] [187] [188] [189] [191] [196] [199] [202] [204] [208] [216] [223] [242] [244] [246] [248] [252] [258] [259] [260] [261] [262] [263] [269] [270] [273] [279] [294] [296] [301] [303] [308]

**melt:** [9] [157] [176] [177] [181] [188] [202] [206] [208] [209] [212] [216] [217] [218] [221] [225] [227] [228] [229] [234] [235] [238] [239] [240] [241] [242] [243] [244] [245] [246] [247] [252] [253] [263] [272] [273] [274] [275] [276] [277] [280] [282] [285] [290] [293] [296] [298] [302] [304] [305] [306] [307] [310] [320] [321]

**membrane:** [224]

**microgravity:** [223] [263] [307]

**microstructure:** [178] [179] [192] [195] [197] [198] [203] [213] [215] [220] [225] [227] [230] [232] [233] [235] [254] [264] [265] [271] [278] [279] [282] [283] [284] [288] [291] [294] [309] [310] [311] [316] [320] [321]

**mobility:** [82] [178] [191] [192] [198] [219] [254] [300]

**modeling:** [71] [74] [135] [154] [155] [169] [170] [202] [237] [242] [245] [277] [280] [294] [302] [311] [125] [178] [181] [186] [191] [206] [215] [217] [225] [230] [232] [236] [237] [238] [239] [240] [241] [242] [243] [244] [245] [246] [247] [251] [267] [279] [290] [298] [301] [302] [316] [318]

**molecular beam epitaxy:** [16] [17] [93] [182] [185] [187] [188] [189] [191] [196] [199] [202] [204] [208] [216] [223] [242] [244] [246] [248] [252] [258] [259] [260] [261] [262] [263] [269] [270] [273] [279] [294] [296] [301] [303] [308]

**morphology:** [5] [6] [108] [170] [180] [184] [194] [195] [207] [215] [220] [222] [227] [257] [261] [271] [283] [286] [294] [295] [320] [322]

**Mullins–Sekerka:** [102]

**multi-component:** [215] [225] [227] [237] [283]

**multi phase:** [75] [76] [227] [237] [237] [242] [272] [276] [277]

**mushy:** [206] [259] [284]

**nanocrystal:** [282] [303]

**nanosstructure:** [195] [279] [282]

**Navier–Stokes:** [79] [209] [212] [217] [237] [245] [246] [263] [296]

**needle:** [100] [247]

**nematic:** [199]

**noise:** [235]

- nucleation:** [55] [57] [178] [182] [187] [188] [192] [204] [213] [223] [229] [230] [231] [254] [262] [268] [273] [282] [286] [292] [301] [309] [311] [313] [317] [318] [321]
- nucleation growth:** [57] [178] [182] [187] [188] [192] [204] [213] [223] [230] [231] [262] [268] [273] [301] [309] [311] [313] [317] [318] [321]
- ordering:** [14] [38] [214] [266] [279]
- orientation:** [178] [180] [184] [192] [194] [195] [207] [220] [227] [257] [258] [268] [275] [278] [286] [291] [294] [307] [311] [315] [320] [322]
- oscillatory:** [196] [244] [250] [270]
- parallel:** [8] [199] [206] [207] [212] [242] [250] [258] [275] [276] [290] [296] [308]
- parity:** [142] [143] [144] [145]
- pattern:** [146] [199] [200] [214] [235] [248] [252] [288] [311] [320] [322]
- pattern formation:** [200] [252] [320]
- Peclet:** [263]
- peritectic:** [76]
- phase diagram:** [30] [200] [230] [231] [265] [267] [309] [321]
- phase field:** [72] [73] [74] [75] [149] [154] [227] [232] [265] [277] [278] [283] [310]
- phase transition:** [14] [76] [176] [180] [182] [185] [186] [192] [195] [204] [213] [222] [227] [230] [231] [254] [261] [262] [273] [283] [289] [292] [301] [309] [313] [317] [318] [321]
- polymer:** [160] [163] [164] [165] [166] [167]
- porous:** [131] [198] [286]
- potential:** [23] [169] [191] [213] [227] [242] [258] [279] [281] [315] [317]
- powder:** [186] [267]
- power:** [186] [196] [203] [216] [240] [243] [246] [251] [252] [260] [278] [301] [302] [321]
- protein:** [166] [168] [169] [170] [171] [183] [223] [224] [268] [301] [308] [322]
- preroughening:** [289] [313]
- primary arm:** [206]
- pseudo-potential:** [23]
- quantum:** [25] [26] [27] [250] [295]
- quasi-crystal:** [115] [172] [174] [175] [176] [180] [252]
- rapid:** [178] [207] [253] [269] [270]
- recrystallization:** [192] [205] [267]
- renormalization:** [292]
- RHEED:** [196] [250] [270]
- rough:** [9] [14] [28] [38] [51] [52] [53] [99] [179] [180] [182] [194] [196] [200] [203] [205] [210] [213] [241] [252] [257] [258] [259] [260] [264] [266] [268] [278] [286] [289] [294] [300] [303] [306] [309] [312] [313] [321]
- roughening:** [9] [14] [38] [51] [52] [53] [196] [289] [303] [313]

**scaling:** [195] [199] [203] [232] [261] [269] [278] [279] [310]

**Schroedinger:** [250]

**Schwoebel:** [92] [93]

**segregation:** [152] [178] [180] [188] [190] [194] [197] [198] [205] [208] [213] [220] [229] [230] [233] [234] [247] [248] [249] [253] [257] [261] [275] [283] [287] [292] [300] [305] [312] [316] [318] [320]

**selection:** [225] [233]

**semiconductor:** [25] [185] [186] [188] [189] [191] [202] [204] [208] [216] [218] [219] [221] [228] [229] [237] [239] [240] [243] [245] [246] [247] [251] [253] [257] [267] [275] [276] [289] [290] [304] [305] [307] [313]

**sharp interface:** [265] [291]

**silica:** [210]

**silicon:** [131] [186] [188] [208] [218] [219] [221] [228] [229] [245] [247] [253] [264] [267] [275] [289] [290] [305] [307] [321]

**singularity:** [264]

**smectic:** [258]

**solution:** [91] [177] [178] [180] [184] [187] [190] [192] [201] [205] [207] [211] [223] [224] [231] [235] [236] [237] [239] [242] [250] [254] [259] [263] [268] [269] [272] [274] [278] [282] [285] [286] [291] [292] [296] [300] [301] [302] [308] [317] [318] [322] [238] [284]

**SOS model:** [135] [287] [303]

**spacing:** [122] [206] [225] [235] [258] [284]

**specific heat:** [289] [313]

**spherulite:** [283] [284]

**spiral:** [90]

**stability:** [15] [73] [122] [128] [131] [153] [177] [184] [188] [202] [205] [207] [208] [211] [225] [244] [252] [257] [267] [272] [308] [317]

**steady state:** [187] [191] [240] [269] [290] [305]

**steel:** [215] [271]

**step:** [15] [16] [18] [65] [66] [67] [68] [184] [204] [207] [212] [252] [262] [289] [294] [295] [308] [315] [317] [321]

**Stillinger-Weber:** [10]

**STM:** [225]

**stochastic:** [185] [189] [197] [198] [204] [213] [262] [282] [283] [287] [294] [303] [311]

**strain:** [179] [189] [201] [211] [219] [220] [221] [272] [274] [311]

**stress:** [80] [83] [86] [175] [179] [192] [201] [215] [220] [241] [243] [254] [264] [272] [274] [288] [296]

**striation:** [208] [304]

**succinonitrile:** [235] [263]

**superconduction:** [76] [232] [277] [310] [320]

**supercooling:** [231] [321]

**surface anisotropy:** [123] [124]  
**surface diffusion:** [122] [123] [124] [184] [194] [196] [198] [205] [220] [248] [249]  
 [257] [261] [287] [294] [300] [312]  
**surface kinetic:** [183] [257] [287] [303]  
**surface tension:** [122] [123] [124] [177] [208] [211] [296]  
**symmetry:** [157] [227] [289] [314] [319]  
**terrace:** [262]  
**thermocapillary:** [177] [209] [239] [296]  
**thin film:** [88] [185] [189] [193] [194] [195] [196] [204] [205] [236] [237] [248]  
 [249] [250] [251] [257] [261] [270] [272] [274] [282] [287] [294] [295] [312]  
 [315]  
**thin layer:** [87] [178] [259] [295]  
**three dimensions:** [74] [293]  
**topological:** [199] [279]  
**translation:** [176] [222] [272] [315]  
**twin:** [178] [192] [197] [198] [235] [279] [281] [291] [311]  
**two dimensions:** [9] [74] [182] [227]  
**undercooling:** [263] [273] [321]  
**unidirectional:** [151] [152] [262]  
**unidirectional solidification:** [151] [152]  
**vapor:** [185] [186] [195] [203] [203] [236] [237] [249] [257] [261] [275] [276] [294]  
 [312] [318] [185] [186] [203] [236] [237] [249] [250] [257] [261] [267] [294]  
 [303] [314] [318]  
**vibration:** [280] [289]  
**vicinal:** [16] [17] [18] [65] [66] [184] [204] [308]  
**viscosity:** [209] [217] [212] [290]  
**wave:** [52] [158] [184] [189] [244] [250] [301] [308]  
**YBaCuO:** [76] [232] [277] [310] [232] [310]  
**zone:** [70] [177] [181] [206] [208] [240] [242] [247] [254] [284] [286] [294]  
**zone melting:** [177] [208] [247]

## ACKNOWLEDGMENTS

We would like to thank Deutsche Forschungsgemeinschaft and Volkswagenstiftung for supporting us by a research grant. Y.S. acknowledges the support by the Japan Society for the Promotion of Science through a grant on Research for the Future Program in the Area of Atomic-scale Surface and Interface Dynamics. We appreciate many discussions with our colleagues E. Brener, C. Misbah, and D. Temkin.

## REFERENCES

1. J. Kepler. *The Six-Cornered Snowflake*, translated by C. Hardie. Oxford: Clarendon Press, 1966. Originally published as: *Seu de Nive Sexangula*. Frankfurt am Main: Godfrey, Tampach, 1611).
2. D. Hurlé, ed. *Handbook of Crystal Growth*. Amsterdam: Elsevier, 1994.
3. Y. Saito. *Statistical Physics of Crystal Growth*. Singapore: World Scientific, 1996.
4. D. Hohl, R. O. Jones, R. Car, M. Parrinello. *J Chem Phys* 89:6823, 1988.
5. O. Shochet, K. Kassner, E. Ben-Jacob, S. G. Lipson, H. Müller-Krumbhaar. Morphology transitions during non-equilibrium growth: I. Study of equilibrium shapes and properties. *Physica A* 181:136, 1992.
6. O. Shochet, K. Kassner, E. Ben-Jacob, S. G. Lipson, H. Müller-Krumbhaar. Morphology transitions during non-equilibrium growth: II. Morphology diagram and characterization of the transition. *Physica A* 187:87, 1992.
7. J. Steinbrecher, H. Müller-Krumbhaar, E. Brener, C. Misbah, P. Peyla, Fractal growth of epitaxial surface clusters with elastic interaction. *Phys Rev E* 59:5600, 1999.
8. J. Stadler, R. Mikulla, H.-R. Trebin. IMD: a software package for molecular dynamics studies on parallel computers. *Int J Mod Phys C* 8:1131, 1997.
9. Y. Saito, H. Müller-Krumbhaar. Roughening and melting in two dimensions. In: K. Binder, ed. *Applications of the Monte Carlo Method*, Berlin: Springer, 1987.
10. F. Stillinger, T. Weber. *Phys Rev B* 31:5262, 1985.
11. D. G. Pettifor. *Bonding and Structure of Molecules and Solids*. Oxford: Oxford University Press, 1995.
12. J. Villain, A. Pimpinelli. *Physique de la croissance cristalline*. Paris: Editions Eyrolles, 1995 (in French); J. Villain. Continuum models of crystal growth from atomic beams with and without desorption. *J Phys (France)* 1 1:19, 1991.
13. J. Krug, M. Schimschak. *J Phys (France)* I 5:1065, 1995; J. Krug. In: A. McKane, M. Droz, J. Vannimenus, D. Wolf, eds. *Scale Invariance, Interfaces and Nonequilibrium Dynamics*. New York: Plenum Press 1995.
14. R. Jullien, J. Kertesz, P. Meakin, D. Wolf, eds. *Surface Disordering: Growth, Roughening and Phase Transitions*. Commack: Nova Science, 1993.
15. Y. Saito, M. Uwaha. Fluctuation and instability of steps in a diffusion field. *Phys Rev B* 49:10677, 1994.
16. O. Pierre-Louis, C. Misbah, Y. Saito, J. Krug, P. Politi. New nonlinear evolution equation for steps during molecular beam epitaxy on vicinal surfaces. *Phys Rev Lett* 80:4221, 1998.
17. O. Pierre-Louis, C. Misbah. Dynamics and fluctuations during MBE on vicinal surfaces. I. Formalism and results of linear theory. *Phys Rev B* 58:2259, 1998; II. Nonlinear analysis. *Phys Rev B* 58:2276, 1998.
18. T. Ihle, C. Misbah, O. Pierre-Louis. Equilibrium step dynamics on vicinal surfaces revisited. *Phys Rev B* 58:2289, 1998.



19. D. Wolf. In: A. McKane, M. Droz, J. Vannimenus, D. Wolf, eds. *Scale Invariance, Interfaces and Nonequilibrium Dynamics*. (New York, Plenum Press, 1995).
20. W. Burton, N. Cabrera, F. Frank. The growth of crystals and the equilibrium structure of their surfaces. *Phil Trans Roy Soc London A* 243:299, 1951.
21. P. Nozieres. In: C. Godreche, ed. *Solids Far from Equilibrium*. Cambridge: Cambridge University Press, 1992.
22. R. O. Jones, O. Gunnarson. The density functional formalism, its applications and prospects. *Rev Mod Phys* 61:689, 1989.
23. W. Pickett. Pseudopotential methods in condensed matter applications. *Comput Phys Rep* 9:115, 1989.
24. J. Ihm. Total energy calculations in solid state physics. *Rep Prog Phys* 51:105, 1988.
25. Ph. Ebert, B. Engels, P. Richard, K. Schroeder, S. Bluegel, C. Domke, M. Heinrich, K. Urban. Contribution of surface resonances to scanning tunneling microscopy images: (110) surfaces of III–V semiconductors. *Phys Rev Lett* 77:2997, 1996.
26. K. Schroeder, B. Engels, P. Richard, S. Bluegel. Reexchange controlled diffusion in surfactant-mediated epitaxial growth: Si on As-terminated Si(111). *Phys Rev Lett* 80:2873, 1998.
27. B. Nonas, K. Wildberger, R. Zeller, P. H. Dederichs. Energetics of 3d impurities on the (001) surface of iron. *Phys Rev Lett* 80:4574, 1998.
28. J. Broughton, G. Gilmer, K. Jackson. Crystallization rates of a Lennard Jones fluid. *Phys Rev Lett* 49:1496, 1982.
29. M. J. Vlot, J. P. v. d. Eerden. Local free energy calculations in simulations. *J Chem Phys* 106:2771, 1997.
30. M. J. Vlot, S. Claassen, H. E. Huitema, J. P. v. d. Eerden. Monte Carlo simulation of racemic liquid mixtures: thermodynamic properties and local structures. *Mol Phys* 91:19, 1997; M. J. Vlot, J. C. v. Miltenburg, H. A. Oonk, J. P. v. d. Eerden. Phase diagrams of scalemic mixtures. *J Chem Phys* 107:10102, 1997.
31. M. J. Vlot, H. E. Huitema, A. d. Vooys, J. P. v. d. Eerden. Crystal structures of symmetric Lennard–Jones mixtures. *J Chem Phys* 107:4345, 1997.
32. B. Laird, D. Kroll. Freezing of soft spheres: a critical test for weighted density functional techniques. *Phys Rev A* 42:4810, 1990; D. Kroll, B. Laird. Comparison of weighted density functional theories for inhomogeneous liquids. *Phys Rev A* 42:4806, 1990.
33. S. Dietrich. Fluids in contact with structured substrates. In: C. Cacamò, ed. *Proceedings of the NATO–ASI, New Approaches to Old and New Problems in Liquid State Theory*, Messina, 1998. (Dordrecht: Kluwer, 1999).
34. H. Müller-Krumbhaar. Monte Carlo simulation of crystal growth. In: K. Binder, ed. *Topics in Current Physics, Vol. 7*. Heidelberg: Springer Verlag, 1986.

35. J. D. Weeks, G. Gilmer, K. A. Jackson. *J Chem Phys* 65:712, 1976; J. D. Weeks, G. H. Gilmer. Dynamics of crystal growth. *Adv Chem Phys* 40:157, 1979.
36. K. Kassner. Numerical simulation of crystal growth. In: D. Krönig, M. Lang, eds. *Physik und Informatik—Informatik und Physik. Informatik-Fachbericht Bd.\*306*. Berlin: Springer 1992, p. 259.
37. G. Dziuk. A boundary element method for curvature flow. Application to crystal growth. In: J. E. Taylor, ed. *Computational Crystal Growers' Workshop, AMS Selected Lectures in Mathematics*. Providence, Rhode Island: American Mathematical Society, 1992, p. 34; A. Schmidt. Computation of three dimensional dendrites with finite elements. *J Comput Phys* 125:293, 1996.
38. S. T. Chui, J. D. Weeks. *Phys Rev B* 14:4987, 1976; J. D. Weeks. The roughening transition. In: T. Riste, ed. *Ordering in Strongly Fluctuating Condensed Matter Systems*. New York: Plenum Press, 1980, p. 293; J. M. Kosterlitz. The  $d$ -dimensional Coulomb gas and the roughening transition. *J Phys C* 10:3753, 1977.
39. P. M. Duxbury, W. Selke. Surface profile evolution above roughening. *Z Physik B* 94:311–318, 1994; P. M. Duxbury, W. Selke. Equilibration of crystal surfaces. *Phys Rev B* 52:17468–17479, 1995.
40. J. P. van der Eerden, A. Roos, J. M. van der Veer. Surface roughening versus surface melting on Lennard–Jones crystal surfaces. *J Cryst Growth* 99:77, 1990.
41. N. Georgiev, A. Pavlovska, E. Bauer. Surface disordering without surface roughening. *Phys Rev B* 52:2878, 1995.
42. I. Procaccia, M. H. Jensen, V. S. L'vov, K. Sneppen, R. Zeitak. Surface roughening and the long-wavelength properties of the Kuramoto–Sivashinsky equation. *Phys Rev A* 46:3220, 1992.
43. M. Kardar, G. Parisi, Y. Zhang. *Phys Rev Lett* 56:889, 1986.
44. A. L. Barabasi, H. E. Stanley. *Fractal Concepts in Surface Growth*. New York: Cambridge University Press, 1996.
45. C. Misbah, H. Müller-Krumbhaar, D. Temkin. *J. Physique I (France)* 1:585, 1991 (and references therein).
46. A. Valance, C. Misbah, P. Peyla. *Physica D* (to appear).
47. K. Binder, ed. *Monte Carlo Methods in Statistical Physics*. Berlin: Springer, 1986.
48. G. Gilmer, P. Bennema. *J Appl Phys* 43:1347, 1972; G. Gilmer, K. A. Jackson. In: E. Kaldis, H. J. Scheel, eds. *Crystal Growth and Materials*. Amsterdam: North-Holland, 1977.
49. Y. Saito, H. Müller-Krumbhaar. *J Chem Phys* 70:1078, 1979.
50. H. Müller-Krumbhaar. Kinetic Gaussian model. *Z Physik B* 25:287, 1976.
51. S. T. Chui, J. D. Weeks. Dynamics of the roughening transition. *Phys Rev Lett* 40:733, 1978.
52. T. Emig, T. Nattermann. Disorder-driven roughening transition of charge-density waves and flux-lines. *Phys Rev Lett* 79:5090, 1997; T. Emig, Th.

- Nattermann. Roughening transition of interfaces in disordered systems. *Phys Rev Lett* 81:1469 (1998).
53. J. Krug, H. Spohn. Kinetic roughening of growing surfaces. In: C. Godreche, ed. *Solids Far from Equilibrium*. Cambridge: Cambridge University Press, 1991.
  54. L. Landau, E. Lifshitz. *Statistical Physics*. Berlin: Akademie-Verlag, 1970.
  55. A. Zettlemoyer. *Nucleation II*. New York: Dekker, 1976.
  56. A. A. Chernov. The kinetics of the growth forms of crystals. *Sov Phys Crystallog* 7:728, 1963; A. A. Chernov. *Sov Phys Uspekhi* 4:116, 1961.
  57. K. Ohno, H. Trinkaus, H. Müller-Krumbhaar. Simulation of non-isothermal nucleation. *J Cryst Growth* 99:68, 1990.
  58. I. M. Lifshitz, V. V. Slyozov. *J Phys Chem Solids* 19:35, 1961.
  59. T. Irisawa, M. Uwaha, Y. Saito. Scaling laws in thermal relaxation of fractal aggregates. *Europhys Lett* 30:139, 1985.
  60. E. Brener, T. Ihle, H. Müller-Krumbhaar, Y. Saito, K. Shiraishi. Fluctuation effects on dendritic growth morphology. *Physica A* 200:96, 1994.
  61. N. C. Bartelt, T. L. Einstein, E. D. Williams. The influence of step-step interactions on step wandering. *Surf Sci Lett* 240:L591, 1990.
  62. B. Joós, T. L. Einstein, N. C. Bartelt. Distribution of terrace width on a vicinal surface within the one-dimensional free-fermion model. *Phys Rev B* 43:8153, 1991.
  63. N. C. Bartelt, J. L. Goldberg, T. L. Einstein, E. D. Williams. The equilibration of terrace width distributions on stepped surfaces. *Surf Sci* 273:252, 1992.
  64. W. Selke. Relaxation of surface steps towards equilibrium. In: P. M. Duxbury, T. Pence, eds. *Dynamics of Crystal Surfaces and Interfaces*. New York: Plenum Press, 1997, p. 147.
  65. T. Ihle, C. Misbah, O. Pierre-Louis. Equilibrium step dynamics on vicinal surfaces revisited. *Phys Rev E* (to appear).
  66. C. Misbah, Y. Saito. Vicinal surfaces at, and out of, equilibrium. *Phys Rev E* (to appear).
  67. N. C. Bartelt, T. L. Einstein, E. D. Williams. Measuring surface mass diffusion coefficients by observing step fluctuation. *Surf Sci* 312:411, 1994.
  68. A. Pimpinelli, J. Villain, D. E. Wolf, J. J. Métois, J. C. Heyraud, I. Elkinani, G. Uimin. Equilibrium step dynamics on vicinal surfaces. *Surf Sci* 295:143, 1993.
  69. T. Burkhardt, H. Müller-Krumbhaar, D. Kroll. A generalized kinetic equation of crystal growth. *J Cryst Growth* 38:13, 1973.
  70. E. Bänsch, B. Höhn. Numerical treatment of the Navier-Stokes equations with slip-boundary condition. Preprint 9-98, Mathematische Fakultät Freiburg. *SIAM J Sci Comput* (submitted).
  71. R. Kobayashi. Modeling and numerical simulations of dendritic crystal growth. *Physica D* 63:410, 1993; R. Kobayashi. A numerical approach to three-dimensional dendritic solidification. *Exp Math* 3:59, 1994.
  72. A. A. Wheeler, B. T. Murray, R. J. Schaefer. Computation of dendrites using a phase field model. *Physica D* 66:243, 1993; G. McFadden, A. Wheeler, R.

- Braun, S. Corriell, R. Sekerka. Phase field models for anisotropic interfaces. *Phys Rev E* 48:2016, 1993.
73. A. Boesch, H. Müller-Krumbhaar, O. Shochet. Phase field models for moving boundary problems: Controlling metastability and anisotropy. *Z Physik B* 97:367, 1995.
74. A. Karma, W.-J. Rappel. Phase field method for computationally efficient modeling of solidification with arbitrary interface kinetics. *Phys Rev E* 53:R3017, 1996; A. Karma, W.-J. Rappel. Quantitative phase field modeling of dendritic growth in two and three dimensions. *Phys Rev E* 57:4323, 1998.
75. I. Steinbach, F. Pezzola, B. Nestler, M. Seesselberg, M. Prieler, G. J. Schmitz, J. L. L. Rezende. A phase-field concept for multiphase systems. *Physica D* 94:135, 1996.
76. J. Tiaden, B. Nestler, H. J. Diepers, I. Steinbach. *Physica D* 115:73, 1998; G. J. Schmitz, B. Nestler. Simulation of phase transitions in multiphase systems, peritectic solidification of YBaCuO-superconductors. *Mater Sci Eng B* 53:23, 1998.
77. R. Gonzalez-Cinca, L. Ramirez-Piscina, J. Casademunt, A. Hernandez-Machado, L. Kramer, T. Toth Katona, T. Börzsönyi, A. Buka. Phase field simulations and experiments of faceted growth in liquid crystals. *Physica D* 99:359, 1996.
78. R. Gagniol, P. Seppecher. Modelisation of fluid–fluid interfaces with material properties. *Journal de Mécanique Théorique et Appliquée, Numéro Spécial*, 1986, pp. 225–247.
79. M. Rieber, A. Frohn. Navier–Stokes simulation of droplet collision dynamics. In: Proceedings of the 7th ISCFD in Beijing, China, 1997 (to be published).
80. K. Kassner, C. Misbah. Nonlinear evolution of a uniaxially stressed solid: a route to fracture? *Europhys Lett* 28:245, 1994.
81. R. J. Asaro, W. A. Tiller. *Metall Trans* 3:1789, 1972; M. A. Grinfeld. *Sov Phys Dokl* 31:831, 1986.
82. J. Frenkel, T. Kontorova. *J Phys USSR* 1:137, 1939; E. Allroth, H. Müller-Krumbhaar. *Phys Rev A* 27:1575, 1983; S. Stoyanov, H. Müller-Krumbhaar. Resonance-induced cluster mobility: Dynamics of a finite Frenkel–Kontorova model. *Surf Sci* 159:49, 1985.
83. I. Durand, K. Kassner, C. Misbah, H. Müller-Krumbhaar. Strong coupling between diffusive and elastic instabilities in directional solidification. *Phys Rev Lett* 76:3013, 1996; I. Cantat, K. Kassner, C. Misbah, H. Müller-Krumbhaar, Directional solidification under stress. *Phys Rev E* 58:6027, 1998.
84. K. H. Lau, W. Kohn. *Surf Sci* 65:607, 1977; V. I. Marchenko, A. Y. Parshin. *Sov Phys JETP* 52:129, 1980.
85. Y. Saito, H. Müller-Krumbhaar. Eden model with elastic interactions. *J Phys Soc Jpn* 67:3661, 1998.
86. E. A. Brener, S. V. Iordanskii, V. I. Marchenko. Elastic effects on the kinetics of a phase transition. *Phys Rev Lett* 82:1506, 1999.
87. P. Peyla, A. Vallat, C. Misbah, H. Müller-Krumbhaar. Elastic interaction between surface defects in thin layers. *Phys Rev Lett* 82:787, 1999.

88. G. Indiveri, A. C. Levi, A. Gliozzi, E. Scalas, H. Möhwald. *Thin Solid Films* 284:106, 1996.
89. H. Risken. *The Fokker-Planck Equation*. Berlin: Springer, 1989.
90. J. P. v. d. Eerden. In: A. A. Chernov, H. Müller-Krumbhaar, eds. *Modern Theory of Crystal Growth, Vol I*. Heidelberg: Springer, 1983.
91. A. A. Chernov. Formation of crystals in solutions. *Contemp Phys* 30:251, 1989; J. P. v. d. Eerden, H. Müller-Krumbhaar. Dynamic coarsening of crystal surfaces. *Phys Rev Lett* 57:2431, 1986.
92. R. Schwoebel. *J Appl Phys* 40:614, 1969.
93. M. D. Johnson, C. Orme, A. W. Hunt, D. Graff, J. Sudijono, L. M. Sander, B. G. Orr. Stable and unstable growth in molecular beam epitaxy. *Phys Rev Lett* 72:116, 1994.
94. T. Ihle, H. Müller-Krumbhaar. *Phys Rev Lett* 70:3083, 1993; *Phys Rev E* 49:2972, 1994.
95. J. S. Langer. *Rev Mod Phys* 52:1, 1980.
96. K. Binder. Spinodal decomposition. In: P. Haasen, ed., *Materials Science and Technology, Vol. 5*. Weinheim: VCH-Verlag, 1990.
97. S. Clake, D. D. Vvedensky. Origin of reflection high-energy electron-diffraction intensity oscillations during molecular-beam epitaxy: a computational modeling approach. *Phys Rev Lett* 58:2235, 1987.
98. T. Irisawa, Y. Arima, T. Kuroda. Periodic changes in the structure of a surface growing under MBE conditions. *J Cryst Growth* 99:491-495, 1990.
99. T. Witten, L. Sander. *Phys Rev Lett* 47:1400, 1981; B. Kaye. *A Random Walk through Fractal Dimensions*. Weinheim: VCH-Verlag, 1989.
100. J. Krug, K. Kassner, P. Meakin, F. Family. Laplacian needle growth. *Europhys Lett* 24:527, 1993.
101. M. Uwaha, Y. Saito. *Phys Rev A* 40:4716, 1989.
102. W. Mullins, R. Sekerka. *J Appl Phys* 34:323, 1963.
103. E. A. Brener, V. I. Mel'nikov. *Adv Phys* 40:53, 1991.
104. J. S. Langer. In: J. Souletie, J. Vannimenus, R. Stora, eds. *Chance and Matter*. Amsterdam: Elsevier, 1987.
105. D. A. Kessler, J. Koplik, H. Levine. *Adv Phys* 37:255, 1988.
106. Y. Pomeau, M. Ben Amar. In: C. Goldrèche, ed. *Solids Far from Equilibrium*. Cambridge: Cambridge University Press, 1992.
107. G. P. Ivantsov. *Dokl Acad Nauk SSSR* 58:567, 1947.
108. E. Brener, H. Müller-Krumbhaar, D. Temkin. *Europhys Lett* 17:535, 1992; Structure formation and the morphology diagram of possible structures in two-dimensional diffusional growth. *Phys Rev E* 54:2714, 1996.
109. E. Ben-Jacob, G. Deutsch, P. Garik, N. Goldenfeld, Y. Lereah. *Phys Rev Lett* 57:1903, 1986.
110. E. Brener, H. Müller-Krumbhaar, Y. Saito, D. Temkin. *Phys Rev E* 47:1151, 1993.
111. R. Kupfermann, D. Kessler, E. Ben-Jacob. *Physica A* 213:451, 1995.
112. M. Ben Amar, E. Brener. *Phys Rev Lett* 75:561, 1995.
113. A. Sharma, A. T. Jameel. *JCIS* 161:190, 1993; 164:416, 1994.

114. N. Samid-Merzel, S. G. Lipson, D. S. Thannhauser. *Physica A* (in press).
115. T. Ihle, H. Müller-Krumbhaar. *J Phys I (France)* 6:949, 1996.
116. J. S. Langer. *Phys Rev A* 36:3350, 1987.
117. M. Ben Amar, E. Brener. *Phys Rev Lett* 71:589, 1993.
118. E. Brener. *Phys Rev Lett* 71:3653, 1993.
119. E. Brener, D. Temkin. *Phys Rev E* 51:351, 1995.
120. E. Brener, H. Müller-Krumbhaar, D. Temkin, T. Abel. *Physica A* 249:73, 1988; T. Abel. Phasensfeldmodelle für Wachstumsprozesse. Berichte des Forschungszentrums Jülich, Nr. 3477, 1998. (in Germany).
121. W. Kurz, D. J. Fisher. *Fundamentals of solidification*. Adermannsdorf: TransTech Publications, 1984.
122. H. Müller-Krumbhaar, W. Kurz. P. Haasen, ed. *Solidification in Phase Transformation in Materials*. Weinheim: 1991.
123. G. Goldbeck-Wood, Y. Saito, H. Müller-Krumbhaar. Numerical simulation of dendritic growth. *Phys Rev A* 38:2148, 1988.
124. A. Classen, C. Misbah, H. Müller-Krumbhaar, Y. Saito. Kinetics in directional solidification. *Phys Rev A* 43:6920, 1991.
125. T. Zacharia, J. Vitek, J. Goldak, T. Debroy, M. Rappaz, H. Bhadeshia. *Model Simul Mater Sci Eng* 3:265, 1995.
126. K. Kassner, J.-M. Debierre, B. Billia, N. Noël, H. Jamgotchian. Cellular structures in three-dimensional directional solidification: simulation and analysis. *Phys Rev E* 57:2849, 1998.
127. K. Kassner, C. Misbah, H. Müller-Krumbhaar. Transition to chaos in directional solidification. *Phys Rev Lett* 67:1551, 1991.
128. L. Bühler, S. H. Davis. Flow induced changes of the morphological stability in directional solidification: localized morphologies. *J Crystal Growth* 186:629, 1998; Y.-J. Chen, S. H. Davis, Directional solidification of a binary alloy into a cellular convective flow (unpublished). Applied Math Technical Report No. 9708, Northwestern University, Evanston, IL 60208.
129. K. Brattkus, S. H. Davis. *J Cryst Growth* 89:423, 1988.
130. J. A. Warren, J. S. Langer. Prediction of dendritic spacings in a directional solidification experiment. *Phys Rev E* 47:2702, 1993.
131. A. Valance. Porous silicon formation: Stability analysis of the silicon-electrolyte interface. *Phys Rev B* 52:8323, 1995.
132. M. Ben Amar, P. Pelce. *Phys Rev A* 39:4263, 1989.
133. A. Karma, B. Kotliar. *Phys Rev A* 31:3266, 1985.
134. J. A. Warren, W. J. Boettinger. *Acta Mat* 43:689, 1995.
135. I. Steinbach, B. Kauerauf, C. Beckermann, J. Guob, Q. Lib. Threedimensional modeling of equiaxed dendritic growth on a mesoscopic scale. In: B. G. Thomas, C. Beckermann, eds. Proceedings of the Eighth International Conference on Modeling of Casting and Welding Processes, San Diego, June 7-12, 1998.
136. X. Feng, E. A. Brener, D. E. Temkin, Y. Saito, H. Müller-Krumbhaar, Creep motion of a solidification front in a two-dimensional binary alloy. *Phys Rev E* (to appear); X. Feng, E. A. Brener, D. E. Temkin, Y. Saito, H. Müller-

- Krumbhaar. Solidification in the one-dimensional model for a disordered binary alloy under diffusion. *Eur Phys J. B* 5:663, 1998.
137. K. A. Jackson, J. D. Hunt. Lamellar and rod eutectic growth. *Trans Met Soc of AIME* 236:1129, 1966.
  138. B. Caroli, C. Caroli, B. Roulet, K. Brattkus. *J Phys (France)* 51:1865, 1990.
  139. V. Datye, J. S. Langer. *Phys Rev B* 24:4155, 1981.
  140. E. A. Brener, M. B. Geilikman, D. E. Temkin. *Sov Phys JETP* 67:1002, 1987.
  141. K. Kassner, C. Misbah. Similarity laws in eutectic growth. *Phys Rev Lett* 66:445, 1991.
  142. K. Kassner, C. Misbah. Parity breaking in eutectic growth. *Phys Rev Lett* 65:1458, 1990; *Phys Rev Lett* 66:522(E), 1991.
  143. K. Kassner, C. Misbah. Spontaneous parity-breaking transition in directional growth of lamellar eutectic structures. *Phys Rev A* 44:6533, 1991.
  144. K. Kassner, A. Valance, C. Misbah, D. Temkin. New broken-parity state and a transition to anomalous lamellae in eutectic growth. *Phys Rev E* 48:1091, 1993.
  145. A. Valance, C. Misbah, D. Temkin, K. Kassner. Analytic theory for parity breaking in lamellar eutectic growth. *Phys Rev E* 48:1924, 1993.
  146. R. Baumann, K. Kassner, C. Misbah, D. E. Temkin. Spatial subharmonics, irrational patterns, and disorder in eutectic growth. *Phys Rev Lett* 74:1597, 1995.
  147. K. Kassner, C. Misbah, R. Baumann. Eutectic dynamics: a host of new states. *Phys Rev E* 51:R2751, 1995.
  148. M. Zimmermann, A. Karma, M. Carrard. *Phys Rev B* 42:833, 1990.
  149. A. Karma. Phase field model of eutectic growth. *Phys Rev E* 49:2245, 1994.
  150. J. Burton, R. Prim, W. Slichter. *J Chem Phys* 21:1987, 1953.
  151. S. Coriell, M. Cordes, W. Boettinger, R. Sekerka. Convective and interfacial instabilities during unidirectional solidification of a binary alloy. *J Cryst Growth* 49:13, 1980.
  152. S. Coriell, R. Boisvert, R. Rehm, R. Sekerka. Lateral solute segregation during unidirectional solidification of a binary alloy with a curved solid-liquid interface. *J Cryst Growth* 54:167, 1981.
  153. S. Coriell, R. Sekerka. Effect of convective flow on morphological stability. *Physico-Chem Hydrodyn* 2:281, 1981.
  154. H.-J. Diepers, C. Beckermann, I. Steinbach. Modeling of convection-influenced coarsening of a binary alloy mush using the phase-field method. In: B. G. Thomas, C. Beckermann, eds. *Proceedings of the Eighth International Conference on Modeling of Casting and Welding Processes*, San Diego, June 7-12, 1998.
  155. W. Shyy, H. S. Udaykumar, M. M. Rao, R. W. Smith. *Computational Fluid Dynamics with Moving Boundaries in Series in Computational and Physical Processes in Mechanics and Thermal Sciences*. Washington, DC: Taylor & Francis, 1995; W. Shyy. *Computational Modeling for Fluid Flow and Interfacial Transport*. Amsterdam: Elsevier, 1994.

156. H. Kopetsch. A numerical method for the time-dependent Stefan-problem in Czochralski crystal growth. *J Crystal Growth* 88:71, 1988; H. Kopetsch. *Physico-Chem Hydrodyn* 11:357, 1989; H. Kopetsch. *J Cryst Growth* 102:500, 1990.
157. M. Mihelcic, K. Wingerath. Threedimensional simulations of the Czochralski bulk flow in a stationary transverse magnetic field and in a vertical magnetic field: Effects on the asymmetry of the flow and temperature distribution in the Si-melt. *J Cryst Growth* 82:318, 1987.
158. J. Vieceili. *J Comput Phys* 8:119, 1971.
159. D. Anderson, G. McFadden, A. Wheeler. Diffuse-interface methods in fluid mechanics. *Ann Rev Fluid Mech* 30:130, 1998.
160. K. Armitstead, G. Goldbeck-Wood. Polymer crystallization theories. *Adv Polym Sci* 100:219–312, 1992.
161. A. Keller. *Phil Mag* 2:21, 1957.
162. J. I. Lauritzen, J. D. Hoffman. *J Res Nat Bur Stand A* 64:73–102, 1960.
163. D. M. Sadler, G. H. Gilmer. *Polymer* 25:1446–1452, 1984.
164. J. P. K. Doye, D. Frenkel. Mechanism of thickness determination in polymer crystals. *Phys Rev Lett* 81:2160–2163, 1998.
165. M. Hikosaka. *Polymers* 28:1257, 1987.
166. P. Grassberger, G. T. Barkema, W. Nadler, eds. *Monte Carlo Approach to Biopolymers and Protein Folding*. Singapore: World Scientific, 1997.
167. P. Grassberger. Pruned-enriched Rosenbluth method: Simulations of theta-polymers of chain-length up to 1,000,000. *Phys Rev E* 56:3682, 1997.
168. A. M. Mathiowetz, A. Jain, N. Karasawa, W. A. Goddard III. Protein simulations using techniques suitable for very large systems: the cell multipole method for nonbond interactions and the Newton–Euler inverse mass operator method for internal coordinate dynamics. CN 8921. *Proteins* 20:227, 1994.
169. A. D. MacKerell Jr., D. Bashford, M. Bellott, R. L. Dunbrack Jr., J. D. Evanseck, M. J. Field, S. Fischer, J. Gao, H. Guo, S. Ha, D. Joseph-McCarthy, L. Kuchnir, K. Kucsera, F. T. K. Lau, C. Mattos, S. Michnick, T. Ngo, D. T. Nguyen, B. Prodhom, W. E. Reiher III, B. Roux, M. Schlenkerich, J. C. Smith, R. Stote, J. Straub, M. Watanabe, J. Wiorkiewicz-Kucsera, D. Yin, M. Karplus. All-atom empirical potential for molecular modeling and dynamics studies of proteins. *J Phys Chem B* 102:3586–3617, 1998.
170. R. Docherty, K. J. Roberts. Modeling the morphology of molecular crystals: Applications to anthracene, biphenyl and B-succinic acid. *J Cryst Growth* 88:159, 1988.
171. S. J. Weiner, P. A. Killman, D. A. Case, U. Chandra Singh, C. Ghio, G. Alagona, S. Profeta, P. A. Weiner. A new force field for molecular mechanical simulation of nucleic acids and proteins. *J Am Chem Soc* 106:765–784, 1984.
172. D. Shechtman, I. Blech, D. Gratias, J. W. Cahn. *Phys Rev Lett* 53:1951, 1984.
173. V. E. Dmitrienko, S. B. Astaf'ev. *Phys Rev Lett* 75:1538–1541, 1995.
174. R. Mikulla, F. Krul, P. Gumbsch, H.-R. Trebin. Numerical simulations of dislocation motion and crack propagation in quasicrystals. In: A. Goldmann,



- ed. *New Horizons in Quasicrystals: Research and Applications*. Singapore: World Scientific, 1996, p. 200.
175. Ch. Dilger, R. Mikulla, J. Roth, H.-R. Trebin. Simulation of shear stress in icosahedral quasicrystals. *Phil Mag A* 75:425, 1997.
176. Y. Furukawa, H. Nada. Anisotropic surface melting of an ice crystal and its relationship to growth forms. *J Phys Chem B* 101:6167, 1997.
177. E. Chenier, C. Delcarte, G. Labrosse. Multiple thermocapillary solutions in floating zone at zero gravity. *Eur Phys J Appl Phys* 2:93, 1998.
178. V. Yu. Novikov. Abnormal grain growth: computer simulation. *Interf Sci* 6:77, 1998.
179. W. J. Evans. Optimising mechanical properties in alpha + beta titanium alloys. *Mater Sci Eng A* 243:88, 1998.
180. L. M. Martiouchev, V. D. Seleznev, S. A. Skopinov. Computer simulation of nonequilibrium growth of crystals in a two-dimensional medium with a phase-separating impurity. *J Stat Phys* 90:1413, 1998.
181. S. Boschert, P. Dold, K. W. Benz. Modelling of the temperature distribution in a three-zone resistance furnace: influence of furnace configuration and ampoule position. *J Cryst Growth* 187:140, 1998.
182. T. Pusztai, L. Granasy. Monte Carlo simulation of first-order phase transformations with mutual blocking of anisotropically growing particles up to all relevant orders. *Phys Rev B* 57:14110, 1998.
183. S. C. Ke, L. J. DeLucas, J. G. Harrison. Computer simulation of protein crystal growth using aggregates as the growth unit. *J Phy D* 31:1064, 1998.
184. S. Y. Potapenko. Formation of solution inclusions in crystal under effect of solution flow. *J Cryst Growth* 186:446, 1998.
185. S. Muthuvenkatraman, S. Gorantla, R. Venkat, D. L. Dorsey. Theoretical study of antisite arsenic incorporation in the low temperature molecular beam epitaxy of gallium arsenide. *J App Phys* 83:5845, 1998.
186. S. G. Mueller, R. Eckstein, D. Hofmann, L. Kadinski, P. Kaufmann, M. Koelbl, E. Schmitt. Modelling of the PVT-SiC bulk growth process taking into account global heat transfer, mass transport and heat of crystallization and results on its experimental verification. *Mater Sci Forum* 0:57, 1998.
187. K. C. Lim, M. A. Hashim, B. Sen Gupta. Monte Carlo simulation of transient crystal size distribution in a continuous crystallizer using the ASL model. *Cryst Res Technol* 33:249, 1998.
188. J. Vanhellemont, E. Dornberger, J. Esfandyari, G. Kissinger, M. A. Trauwaert, H. Bender, D. Graef, U. Lambert, W. von Ammon. Defects in as-grown silicon and their evolution during heat treatments. *Mater Sci Forum* 0:341, 1997.
189. A. N. Larsen. Defects in SiGe. *Mater Sci Forum* 0:83, 1997.
190. N. Curtis, D. G. Leaist. Interdiffusion of aqueous silver nitrate and potassium chromate and the periodic precipitation of silver chromate Liesegang bands. *Ber Bunsen-Ges—Phys Chem, Chem Phys* 102:164, 1998.

191. F. Dessenne, D. Cichocka, P. Desplanques, R. Fauquembergue. Comparison of wurtzite and zinc blende III–V nitrides field effect transistors: a 2D Monte Carlo device simulation. *Mater Sci Eng B* 50:315, 1997.
192. R. D. Doherty, D. A. Hughes, F. J. Humphreys, J. J. Jonas, D. J. Jensen, M. E. Kassner, W. E. King, T. R. McNeley, H. J. McQueen, A. D. Rollett. Current issues in recrystallization: a review. *Mater Sci Eng A* 238:219, 1997.
193. A. Chame, F. Lancon, P. Politi, G. Renaud, I. Vilfan, J. Villain. Three mysteries in surface science. *Int J Mod Phys B* 11:3657, 1997.
194. Ming Jiang, Yu-Jun Zhao, Pei-Lin Cao. Surfactant-mediated layer-by-layer homoepitaxial growth of Cu/In/Cu(100) and Ag/Sb/Ag(111) systems: A theoretical study. *Phys Rev B* 57:10054, 1998.
195. P. Jensen, H. Larralde. Experiments in a perfect world: computer simulations of growth. *Int J Mod Phys B* 11:3635, 1997.
196. H. Kallabis, L. Brendel, J. Krug, D. E. Wolf. Damping of oscillations in layer-by-layer growth. *Int J Mod Phys B* 11:3621, 1997.
197. V. Tikare, J. D. Cawley. Application of the Potts model to simulation of Ostwald ripening. *J Am Ceram Soc* 81:485, 1998.
198. V. Tikare, E. A. Holm. Simulation of grain growth and pore migration in a thermal gradient. *J Am Ceram Soc* 81:480, 1998.
199. J. Fukuda. Effect of hydrodynamic flow on kinetics of nematic–isotropic transition in liquid crystals. *Eur Phys J B* 1:173, 1998.
200. G. Schulz, M. Martin. Computer simulations of pattern formation in ion-conducting systems. *Solid State Ionics, Diffusion and Reactions* 101–103:417, 1997.
201. D. N. Dai, D. A. Hills, G. Harkegard, J. Pross. Simulation of the growth of near-surface defects. *Eng Fract Mech* 59:415, 1998.
202. K. Kakimoto, H. Ozoe. Heat and mass transfer during crystal growth. *Comput Mater Sci* 10:127, 1998.
203. J. Soderlund, L. B. Kiss, G. A. Niklasson, C. G. Granqvist. Lognormal size distributions in particle growth processes without coagulation. *Phys Rev Lett* 80:2386, 1998.
204. Z. Sh. Yanovitskaya, I. G. Neizvestny, N. L. Shwartz, M. I. Katkov, I. P. Ryzhenkov. Desynchronization mode of 2D-island creation on the vicinal surface during MBE growth. *Appl Surf Sci* 0:729, 1998.
205. S. Mourachov, V. P. Poliakov. Analysis of diamond crystal growth stability from graphite through a film of the metal solvent. *Diamond Rel Mater* 7:309, 1998.
206. P. Lehmann, R. Moreau, D. Camel, R. Bolcato. A simple analysis of the effect of convection on the structure of the mushy zone in the case of horizontal Bridgman solidification. Comparison with experimental results. *J Cryst Growth* 183:690, 1998.
207. S. R. Coriell, A. A. Chernov, B. T. Murray, G. B. McFadden. Step bunching: generalized kinetics. *J Cryst Growth* 183:669, 1998.
208. T. Kaiser, K. W. Benz. Floating-zone growth of silicon in magnetic fields. III. Numerical simulation. *J Cryst Growth* 183:564, 1998.

209. Q. S. Liu, B. Roux, M. G. Velarde. Thermocapillary convection in two-layer systems. *Int J Heat and Mass Transf* 41:1499, 1998.
210. V. V. Murashov, I. M. Svishchev. Quartz family of silica polymorphs: comparative simulation study of quartz, moganite, and orthorhombic silica, and their phase transformations. *Phys Rev B* 57:5639, 1998.
211. D. S. Noh, Y. Koh, I. S. Kang. Numerical solutions for shape evolution of a particle growing in axisymmetric flows of supersaturated solution. *J Cryst Growth* 183:427, 1998.
212. D. Givoli, J. E. Flaherty, M. S. Shephard. Parallel adaptive finite element analysis of viscous flows based on a combined compressible-incompressible formulation. *Int J Numer Meth Heat and Fluid Flow* 7:880, 1997.
213. P. Franke, G. Inden. Diffusion controlled transformations in multi-particle systems. *Z Metallkd* 88:917, 1997.
214. S. Hata, H. Fujita, C. G. Shlesier, S. Matsumura, N. Kuwano, K. Oki. Monte Carlo study of ordering processes in fcc-based Ni-Mo alloys. *Mater Trans JIM* 39:133, 1998.
215. T. Hoshide, K. Kusuura. Life prediction by simulation of crack growth in notched components with different microstructures and under multiaxial fatigue. *Fatigue Fract Eng Mater Struct* 21:201, 1998.
216. Y. Y. Khine, J. S. Walker. Thermoelectric magnetohydrodynamic effects during Bridgman semiconductor crystal growth with a uniform axial magnetic field. *J Cryst Growth* 183:150, 1998.
217. L. Juncheng, J. Wanqi. Modelling Ekman flow during the ACRT process with marked particles. *J Cryst Growth* 183:140, 1998.
218. N. Miyazaki, S. Okuyama. Development of finite element computer program for dislocation density analysis of bulk semiconductor single crystals during Czochralski growth. *J Cryst Growth* 183:81, 1998.
219. S. Kal, N. B. Chakrabarti. Strained silicon-SiGe devices using germanium implantation. *IETE J Res* 43:185, 1997.
220. D. Y. Li, L. Q. Chen. Morphological evolution of coherent multivariant TiNi precipitates in Ti-Ni alloys under an applied stress—a computer simulation study. *Acta Mater* 46:639, 1998.
221. S. Iida, Y. Aoki, K. Okitsu, Y. Sugita, H. Kawata, T. Abe. Microdefects in an as-grown Czochralski silicon crystal studied by synchrotron radiation section topography with aid of computer simulation. *Jpn J Appl Phys Pt1* 37:241, 1998.
222. L. M. Martyushev, V. D. Seleznev, S. A. Skopinov. Reentrant kinetic phase transitions during dendritic growth of crystals in a two-dimensional medium with phase stratification. *Tech Phys Lett* 23:495, 1997.
223. F. Otalora, J. M. Garcia-Ruiz. Crystal growth studies in microgravity with the APCF. I. Computer simulation of transport dynamics. *J Cryst Growth* 182:141, 1997.
224. J. Hong. Crystal growth in high gravity. *J Cryst Growth* 181:459, 1997.
225. Q. Han, J. D. Hunt. Numerical modelling of the growth of a cellular/dendritic array in multi-component alloys. *Mater Sci Eng A* 238:192, 1997.

- 226. C. Charbon, S. Swaminarayan. Modeling the microstructural evolution of thermoplastic composites. *Mater Sci Eng A* 238:166, 1997.
- 227. M. K. Venkitachalam, L.-Q. Chen, A. G. Khachaturyan, G. L. Messing. A multiple-component order parameter phase field model for anisotropic grain growth. *Mater Sci Eng A* 238:94, 1997.
- 228. T. Sinno, R. A. Brown, W. Van Ammon, E. Dornberger. Point defect dynamics and the oxidation-induced stacking-fault ring in Czochralski-grown silicon crystals. *J Electrochem Soc* 145:302, 1998.
- 229. H. Takeno, T. Otagawa, Y. Kitagawara. Practical computer simulation technique to predict oxygen precipitation behavior in Czochralski silicon wafers for various thermal processes. *J Electrochem Soc* 144:4340, 1997.
- 230. F. Soisson, C. Pareige, M. Athenes, G. Martin, D. Blavette. Kinetics of phase transformations in metallic alloys: Monte-Carlo simulations versus experiments. *Ann Phys* 22:3, 1997.
- 231. V. Palumbo-Romand, M. Ferriol, M. T. Cohen-Adad, N. Clavaguera. Nucleation and crystallization phenomena in stoichiometric monomethylhydrazine-water mixtures. *J Cryst Growth* 180:238, 1997.
- 232. G. J. Schmitz, F. Pezzola, R. Prieler, H. J. Diepers, I. Steinbach. Numerical modelling of YBCO growth using the phase field method. 1995 International Workshop on Superconductivity, Controlled Processing of High-temperature Superconductors: Fundamentals and Applications. (Tokyo: International Superconductivity Technology Center, 1995, Program and Extended Abstracts. pp. 313–314.
- 233. M. D. Dupouy, B. Drevet, D. Camel. Influence of convection on the selection of solidification microstructures at low growth rates. *J Cryst Growth* 181:145, 1997.
- 234. T. Alboussiere, A. C. Neubrand, J. P. Garandet, R. Moreau. Segregation during horizontal Bridgman growth under an axial magnetic field. *J Cryst Growth* 181:133, 1997.
- 235. N. Noel, H. Jamgotchian, B. Billia. In situ and real-time observation of the formation and dynamics of a cellular interface in a succinonitrile-0.5 wt. % *J Cryst Growth* 181:117, 1997.
- 236. W. Y. Chung, D. H. Kim, Y. S. Cho. Modelling of Cu thin film growth by MOCVD process in a vertical reactor. *J Cryst Growth* 180:691, 1997.
- 237. A. Ern, V. Giovangigli, M. D. Smooke. Detailed modeling of three-dimensional chemical vapor deposition. *J Cryst Growth* 180:670, 1997.
- 238. J. Holuigue, O. Bertrand, E. Arquies. Solutal convection in crystal growth: effect of interface curvature on flow structuration in a three-dimensional cylindrical configuration. *J Cryst Growth* 180:597, 1997.
- 239. M. C. Liang, C. W. Lan. Three-dimensional thermocapillary and buoyancy convections and interface shape in horizontal Bridgman crystal growth. *J Cryst Growth* 180:587, 1997.
- 240. H. Weimann, J. Amon, T. Jung, G. Mueller. Numerical simulation of the growth of 2" diameter GaAs crystals by the vertical gradient freeze technique. *J Cryst Growth* 180:560, 1997.

241. T. Tsukada, K. Kakinoki, M. Hozawa, N. Imaishi, K. Shimamura, T. Fukuda. Numerical and experimental studies on crack formation in  $\text{LiNbO}_3$  single crystal. *J Cryst Growth* 180:543, 1997.
242. W. K. Chui, J. Glimm, F. M. Tanagerman, H. Zhang, V. Prasad. A parallel algorithm for multizone, multiphase systems with application to crystal growth. *J Cryst Growth* 180:534, 1997.
243. J. Fainberg, H.-J. Leister, G. Mueller. Numerical simulation of the LEC-growth of GaAs crystals with account of high-pressure gas convection. *J Cryst Growth* 180:517, 1997.
244. Y.-S. Lee, C.-H. Chun. Experiments on the oscillatory convection of low Prandtl number liquid in Czochralski configuration for crystal growth with cusp magnetic field. *J Cryst Growth* 180:477, 1997.
245. J. Jaervinen, R. Nieminen, T. Tiihonen. Time-dependent simulation of Czochralski silicon crystal growth. *J Cryst Growth* 180:468, 1997.
246. L. Davoust, R. Moreau, M. D. Cowley, P. A. Tanguy, F. Bertrand. Numerical and analytical modelling of the MHD buoyancy-driven flow in a Bridgman crystal growth configuration. *J Cryst Growth* 180:422, 1997.
247. A. Muehlbauer, A. Muiznieks, J. Virbulis. Analysis of the dopant segregation effects at the floating zone growth of large silicon crystals. *J Cryst Growth* 180:372, 1997.
248. H. Kallabis, D. E. Wolf. Growth of patterned surfaces. *Phys Rev Lett* 79:4854, 1997.
249. V. Chirita, E. P. Munger, J.-E. Sundgren, J. E. Greene. Enhanced cluster mobilities on Pt(111) during film growth from the vapor phase. *Appl Phys Lett* 72:127, 1998.
250. A. Daniluk, P. Mazurek, K. Paprocki, P. Mikolajczak. RHEED intensity oscillations observed during the growth of  $\text{YSi}_{2-x}$  on Si(111) substrates. *Surf Sci* 391:226, 1997.
251. V. C. Lo, X. T. Dam. Simulation of electromigration failure by variable resistance model. *Model and Sim in Mater Sci and Eng* 5:563, 1997.
252. K. X. H. Zhao, H. Power, L. C. Wrobel. Numerical simulation of dendritic crystal growth in a channel. *Eng Anal Bound Elem* 19:331, 1997.
253. K. A. Jackson, K. M. Beatty, M. V. Minke. Monte Carlo simulation of non-equilibrium segregation during crystal growth. *J Non-Cryst Solids* 219:100, 1997.
254. V. I. Levitas, A. V. Idesman, E. Stein. Finite element simulation of martensitic phase transitions in elastoplastic materials. *Int J Solids Struct* 35:855, 1998.
255. C. C. Battaille, D. J. Srolvitz, J. E. Butler. A kinetic Monte Carlo method for the atomic-scale simulation of chemical vapor deposition: application to diamond. *J App Phys* 82:6293, 1997.
256. Y. Shimomura. Point defects and their clusters in f.c.c. metals studied by computer simulations. *Mater Chem Phys* 50:139, 1997.
257. P. Mahalingam, D. S. Dandy. Simulation of morphological instabilities during diamond chemical vapor deposition. *Diamond Rel Mater* 6:1759, 1997.

258. M. R. Wilson. Molecular dynamics simulations of flexible liquid crystal molecules using a Gay-Berne/Lennard-Jones model. *J Chem Phys* 107:8654, 1997.
259. J. S. Wettlaufer, M. G. Worster, H. E. Huppert. Natural convection during solidification of an alloy from above with application to the evolution of sea ice. *J Fluid Mech* 344:291, 1997.
260. T. Matsuyama, K. Honda. Dynamics of rough surfaces growing on fractal substrates. *J Phys Soc Jpn* 66:2533, 1997.
261. P. Jensen, B. Niemeyer. The effect of a modulated flux on the growth of thin films. *Surf Sci* 384:9999, 1997.
262. D. J. Gates. Surface angle transitions and facets in a solvable TSK model of steady crystal growth. *J Cryst Growth* 180:136, 1997.
263. R. Ananth, W. N. Gill. Dendritic growth in microgravity and forced convection. *J Cryst Growth* 179:263, 1997.
264. T. Kobayashi, H. Toda. Toughness enhancement based on fracture mechanical simulation of Al-SiC composite. *Mater Sci Forum* 242:193, 1997.
265. M. Benes. On a computational comparison of phase-field and sharp-interface model of microstructure growth in solidification. *Acta Technica CSAV* 41:597, 1996.
266. M. Porta, C. Frontera, F. Vives, T. Castan. Effect of the vacancy interaction on antiphase domain growth in a two-dimensional binary alloy. *Phys Rev B* 56:5261, 1997.
267. S. Yu Karpov, N. Yu Makarov, M. S. Ramm. Simulation of sublimation growth of SiC single crystals. *Physica Status Solidi B* 202:201, 1997.
268. A. M. Kierzek, W. M. Wolf, P. Zielenkiewicz. Simulations of nucleation and early growth stages of protein crystals. *Biophys J* 73:571, 1997.
269. D. Maynes, J. Klewicki, P. McMurty, H. Robey. Hydrodynamic scalings in the rapid growth of crystals from solution. *J Cryst Growth* 178:545, 1997.
270. E. Chason, B. K. Kellerman. Monte Carlo simulations of ion-enhanced island coarsening. *Nucl Instrum and Meth in Phys Res B* 0:225, 1997.
271. T. Hoshida. Simulation of microstructural effects on cracking behavior in biaxial fatigue. *Mater Sci Res Int* 3:119, 1997.
272. R. K. Akchurin, D. V. Komarov. Formation of multilayer strained-layer heterostructures by liquid epitaxy. I. Theoretical aspects of the problem and mathematical model. *Tech Phys* 42:755, 1997.
273. M. J. Uttormark, J. W. Zanter, J. H. Perepezko. Repeated nucleation in an undercooled aluminum droplet. *J Cryst Growth* 177:258, 1997.
274. K. Kaigawa, T. Kawaguchi, M. Imaeda, H. Sakai, T. Fukuda. Crystal structure of LPE-grown LiNbO<sub>3</sub> epitaxial films. *J Cryst Growth* 177:217, 1997.
275. K. M. Beatty, K. A. Jackson. Orientation dependence of the distribution coefficient obtained from a spin-1 Ising model. *J Cryst Growth* 174:28, 1997.
276. D. Givoli, J. E. Flaherty, M. S. Shephard. Parallel adaptive 3D finite element analysis of CZ melt flows. *J Cryst Growth* 174:1, 1997.

277. M. Seesselberg, G. J. Schmitz, B. Nestler, I. Steinbach. Macroscopic and microscopic modeling of the growth of YBaCuO bulk material. *IEEE Trans Appl Supercond* 7:1739, 1997.
278. D. Fan, L.-Q. Chen. Diffusion-controlled grain growth in two-phase solids. *Acta Mater* 45:3297, 1997.
279. Y. Saito. The Monte Carlo simulation of microstructural evolution in metals. *Mater Sci and Eng A* 99:114, 1997.
280. G. W. Young, J. A. Heminger. Modeling the time-dependent growth of single-crystal fibers. *J Cryst Growth* 178:410, 1997.
281. S. D. Fleming, G. M. Parkinson, A. L. Rohl. Predicting the occurrence of reflection twins. *J Cryst Growth* 178:402, 1997.
282. H. Li, F. Czerwinski, J. A. Szpunar. Monte-Carlo simulation of texture and microstructure development in nanocrystalline electrodeposits. *Nanostruct Mater* 9:673, 1997.
283. T. Kraft, H. E. Exner. Numerical simulation of solidification. III. Prediction of microstructure. *Z Metallk* 88:278 (1997).
284. M. Rettenmayr, O. Pompe. Interface instabilities on solidifying globulitic particles. *J Cryst Growth* 173:182, 1997.
285. P. D'Ambra. Numerical simulation of polyhedral crystal growth based on a mathematical model arising from nonlocal thermomechanics. *Contin Mech Thermodyn* 9:97, 1997.
286. M. Belcu, D. Turtoi. Simulation of the fluidized-bed crystallizers (I). Influence of parameters. *Cryst Res Technol* 31:1015, 1996.
287. A. C. Levi, U. Tartaglino. Simulation of growth with diffusion in the kinetic BCSOS model. *Physica A* 238:172, 1997.
288. B. D. Knowlton, J. J. Clement, C. V. Thompson. Simulation of the effects of grain structure and grain growth on electromigration and the reliability of interconnects. *J Appl Phys* 81:6073, 1997.
289. D. L. Woodraska, J. A. Jaszczak. A Monte Carlo simulation method for [111] surfaces of silicon and other diamond-cubic materials. *Surf Sci* 374:319, 1997.
290. D. Givoli, J. E. Flaherty, M. S. Shephard. Simulation of Czochralski melt flows using parallel adaptive finite element procedures. *Model Simul Mater Sci Eng* 4:623, 1996.
291. D. Fan, L.-Q. Chen. Diffuse-interface description of grain boundary motion. *Phil Mag Lett* 75:187, 1997.
292. S. Mourachov. Cellular automata simulation of the phenomenon of multiple crystallization. *Comput Mater Sci* 7:384, 1997.
293. M. J. P. Nijmeijer, P. Landau. Simulation of optical fiber growth in three dimensions. *Comput Mater Sci* 7:325, 1997.
294. Y. G. Yang, R. A. Johnson, H. N. G. Wadley. A Monte Carlo simulation of the physical vapor deposition of nickel. *Acta Mater* 45:1455, 1997.
295. D. Schmicker, T. Hibma, K. A. Edwards, P. B. Howes, J. E. MacDonald, M. A. James, M. Breeman, G. T. Barkema. Low-temperature growth of thin Pb layers and the quantum size effect. *J Phys: Condens Matt* 9:969, 1997.

296. H. B. Hadid, D. Henry. Numerical study of convection in the horizontal Bridgman configuration under the action of a constant magnetic field. 2. Three-dimensional flow. *J Fluid Mech* 333:57, 1997.
297. Seung Jae Moon, Charn-Jung Kim, Sung Tack Ro. Effects of buoyancy and periodic rotation on the melt flow in a vertical Bridgman configuration. *Int J Heat and Mass Transf* 40:2105, 1997.
298. N. Hofmann, S. Olive, G. Laschet, F. Hediger, J. Wolf, P. R. Sahm. Numerical optimization of process control variables for the Bridgman casting process. *Model Simula Mater Sci Eng* 5:23, 1997.
299. J. C. Carrano, P. A. Grudowski, C. J. Eiting, R. D. Dupuis, J. C. Campbell. Very low dark current metal-semiconductor-metal ultraviolet photodetectors fabricated on single-crystal GaN epitaxial layers. *Appl Phys Lett* 70:1992, 1997.
300. O. E. Braun, M. V. Paliy, M. Peyrard. Growth of ordered domains in a highly anisotropic two-dimensional system. *Phys Rev B* 55:4797, 1997.
301. F. Otalora, J. M. Garcia-Ruiz. Computer model of the diffusion/reaction interplay in the gel acupuncture method. *J Cryst Growth* 169:361, 1996.
302. M. Yao, D. H. Matthiesen, A. Chait. Numerical simulation of heat transport and fluid flow in directional crystal growth of GaAs. *Numer Heat Transf A* 30:685, 1996.
303. A. C. Levi, M. Kotrla. Theory and simulation of crystal growth. *J Phys Condens Matt* 9:299, 1997.
304. T. Jung, G. Mueller. Amplitudes of doping striations: comparison of numerical calculations and analytical approaches. *J Cryst Growth* 171:373, 1997.
305. Zhang Weilian, Yan Shuxia, Ji Zhijiang. Effective segregation coefficient and steady state segregation coefficient of germanium in Czochralski silicon. *J Cryst Growth* 169:598, 1996.
306. H. Nada, Y. Furukawa. Anisotropic growth kinetics of ice crystals from water studied by molecular dynamics simulation. *J Cryst Growth* 169:587, 1996.
307. J. Baumgartl, G. Mueller. The use of magnetic fields for damping the action of gravity fluctuations (g-jitter) during crystal growth under microgravity. *J Cryst Growth* 169:582, 1996.
308. S. R. Coriell, B. T. Murray, A. A. Chernov, G. B. McFadden. Step bunching on a vicinal face of a crystal growing in a flowing solution. *J Cryst Growth* 169:773, 1996.
309. L. E. Levine, K. Lakshmi Narayan, K. F. Kelton. Finite size corrections for the Johnson-Mehl-Avrami-Kolmogorov equation. *J Mater Res* 12:124, 1997.
310. G. J. Schmitz, B. Nestler, M. Seesselberg. YBCO melt-processing development by numerical simulation. *J Low Temp Phys* 105:1451, 1996.
311. Y. Wang, A. G. Khachaturyan. Three-dimensional field model and computer modeling of martensitic transformations. *Acta Mater* 45:759, 1997.
312. R. W. Smith. A kinetic Monte Carlo simulation of fiber texture formation during thin-film deposition. *J Appl Physics* 81:1196, 1997.



- 313. D. L. Woodraska, J. A. Jaszczak. Roughening and preroughening of diamond-cubic [111] surfaces. *Phys Rev Lett* 78:258, 1997.
- 314. Hua Li, Nai-Ben Ming. Significance of many-body interactions in Monte Carlo simulation of crystal-vapour interface. *Solid State Commun* 101:351, 1997.
- 315. A. A. Katsnel'son, A. E. Moroz, O. S. Trushin, V. S. Stepanyuk. Molecular dynamics simulation of growth of thin metal films. *Moscow Uni Phys Bull* 50:38, 1995.
- 316. S. Olive, U. Grafe, I. Steinbach. The modelling of Ostwald-ripening during non-isothermal heat treatments resulting in temperature dependent matrix solubility of the precipitate forming elements: a further development of the LSW-theory. *Comput Mater Sci* 7:94, 1996.
- 317. A. Tadano, M. Asanuma, R. Aogaki. Electrochemical nucleation induced by nonequilibrium fluctuations. *J Cryst Growth* 166:1111, 1996.
- 318. H. J. M. Kramer, J. W. Dijkstra, A. M. Neumann, R. O'Meadhra, G. M. van Rosmalen. Modelling of industrial crystallizers, a compartmental approach using a dynamic flow-sheeting tool. *J Cryst Growth* 166:1084, 1996.
- 319. F. J. J. Leusen. Ab initio prediction of polymorphs. *J Cryst Growth* 166:900, 1996.
- 320. R. Cloots, N. Vandewalle, M. Ausloos. Simulations of the kinetic growth of YBaCuO grains. *J Cryst Growth* 166:816, 1996.
- 321. O. Yanagisawa, A. Almansour, K. Matsugi, T. Hatayama. Computer simulation for solidified microstructure prediction of spheroidal graphite cast iron of the Fe-C-Si system. *J Jpn Inst Met* 60:1101, 1996.
- 322. F. Otalora, J. M. Garcia-Ruiz, A. Moreno. Protein crystal quality studies using rod-shaped crystals. *J Cryst Growth* 168:93, 1996.

# Index

## Adsorption

- at aqueous interfaces, 362, 365–367, 369, 377
- on charged surfaces, 803, 812, 833, 839
- contact, 365, 366, 367
- in disordered porous media, 293–343
- dissociative, 377, 440, 441, 443
- isotherm of, 225, 230, 231, 246, 247, 255, 256, 263–265, 267, 306, 313, 318, 322, 441, 532, 533, 803
- isosteric heat of, 263, 441, 445, 446, 453
- nondissociative, 463–470
- of polymers, 532–537, 555–558, 565, 569–581, 587
- at solid surfaces, 57–60, 245–280, 388, 389, 392, 395, 398, 401, 404, 405, 407, 415, 532–537, 569–580, 851, 865, 869, 870, 881, 907
- of associating fluids, 168, 170, 171, 182–186, 207, 208, 211, 219, 220, 225, 228, 230, 231, 238
- kinetics of, 439–477

## [Adsorption]

- precursor mediated, 441, 470–472
- quantum effects, 77–123
- Adsorption energy distribution
  - function (AEDF), 246, 247, 251–254, 257, 260, 278
- Adsorption transition, 558, 571–574
- Aggregation, 510, 636, 651, 745, 746, 767
  - diffusion-limited (ADL), 886, 888
  - number, 636, 651, 653, 654
- Alexander model, 657, 669
- Alloys, 88, 907
- Amphiphiles (*see also* Surfactants), 631–673, 686–688, 721–724
- Associating fluids, 168–238, 342
- Association, 168–238, 321
  - constant, 197
  - degree, 180
- Associative potentials, 167, 171, 194
- Ballone–Pastore–Galli–Gazillo
  - approximation (BPGG), 149
- Bead-spring model, 495, 496, 563–569, 605
- Bifurcation analysis, 686, 724–730
- Bifurcation line, 686, 724–726

- Bond fluctuation model (BFM), 495, 496, 515, 517, 519, 563, 646
- Born–Green–Yvon hierarchy (BGY), 139, 140, 142, 145, 151, 294, 330, 332, 333
- Born–Oppenheimer approximation, 82
- Born–Oppenheimer potential surface energy, 348, 485
- Bose–Einstein condensation, 94
- Bose statistics (*see* Quantum statistics)
- Brownian dynamics, 3, 343, 563, 749, 765–767, 815, 907
- Butler–Volmer law, 368
- Capacitance
  - differential, 801, 803, 804, 820, 822, 825–827, 831, 833, 834, 840
- Capillary condensation
  - association effects on, 167, 171, 222–228
- Carnahan–Starling equation, 144, 150, 153, 198, 213, 218, 234, 320, 336
- Car–Parinello method, 82, 853, 907
- Catalytic reactions, 387–430
- Cavity function, 141, 142, 173, 176, 199–201, 214, 331
  - generalized, 151
- Chaos, 907
- Chapman–Kolmogoroff equation, 24
- Chemically reacting fluids (*see* Associating fluids)
- Clausius’ virial, 30
- Coarse-grained models, 482, 515, 556, 563, 597, 637, 643
- Coarse-grained thermodynamics, 14–16
- Colloidal suspensions (*see* Colloids)
- Colloids, 3, 154, 294, 295, 308, 309, 311, 342, 745–769
- Compressibility
  - equation, 215
  - isothermal, 264, 266, 267, 301, 513, 815
  - transverse, 16, 44
- Computed adsorption energy
  - distribution in monolayers (CAEDMON), 247
- Computer simulation (*see* Monte Carlo method and Molecular dynamics)
- Convolution integrals, 141
- Correlation functions, 19–21, 41–42, 139, 155, 174–176, 177, 179, 195, 196, 201, 206, 293, 300, 301, 331, 332, 336, 338, 350, 441, 749, 756
  - blocking, 301, 302, 308, 321
  - connected, 301, 322
  - direct (DCF), 100, 139, 150, 155, 156, 159, 171–175, 177, 179, 190, 196, 302, 308, 321, 322, 332
  - indirect, 139
  - partial, 195, 196, 201, 205
- Critical exponents, 63, 84, 112, 267, 394, 397, 422, 429, 521–523, 530, 532, 862
- Critical micelle condensation (CMC), 651–653
- Critical phenomena, 78, 388, 393, 510
- Crossover exponent, 573
- Crystal growth, 851–906
  - Bridgman, 852, 903, 904
  - cluster, 852, 884
  - Czochralski, 852, 903, 904
  - diffusional, 852, 895, 896
  - diffusion-limited aggregation, 888
  - epitaxial, 82, 871, 879
  - eutectic, 852, 900, 901
  - fractal, 886
  - of ice, 376
  - kinetics of, 851, 860, 863
  - phenomenological models of, 855
  - spiral, 871, 873, 882
- Cummings–Stell theory, 178, 184, 186
- Cumulant analysis (*see also* Scaling), 84–85
- Cumulants, 84–86, 88, 120, 121
- Curvatures
  - Gaussian, 668, 670, 688–690, 696, 698–700, 730–737
  - mean, 668, 670, 688–690, 696, 698–700, 703, 730–737

- Debye–Hückel law, 814
- Debye length, 367, 802, 814, 815, 817, 833, 835
- Density-alignment distribution, 36, 37, 40, 41
- Density functional theory, 9, 99–101, 477, 487, 757, 807, 857, 858
  - of associating fluids, 167, 168, 171, 190, 211–228
- Depletion forces, 9
- Derjaguin approximation, 8–11
- Derjaguin–Landau–Verwey–Overbeek theory (DLVO), 148, 157, 567, 757
- Desorption, 389, 392, 404, 405, 417, 418, 421, 439–477, 851, 869, 881, 908
- Dewetting, 555, 556, 558, 614–623, 852, 895
- Diffuse layer, 367, 828, 830, 831
- Diffusion, 391, 392, 400, 408, 412, 413, 416, 429, 430, 444, 463, 468, 474, 489, 490, 491, 495, 496, 502, 545–547, 576, 577, 584, 600, 765, 779, 780, 852, 853, 855, 868, 877, 880–885, 888, 903
  - coefficient, 350, 372, 487, 489, 502, 545–547, 605, 611, 749, 861, 895
  - constant, 482, 496, 545, 579, 587, 873, 895, 901
  - equations, 399, 402, 853, 862, 891
  - self-diffusion coefficient, 361, 362, 369, 376
  - sliding, 905
  - surface, 398, 399, 414, 439, 441, 469, 475, 851, 861, 868, 871, 880, 914
  - terrace, 873
- Disordered porous systems (*see* Random porous media)
- Double layer, 348, 358, 365, 367, 799–846
- Duh–Haymet–Henderson approximation (DHH), 146, 160, 161, 162
- Dynamic exponents, 396, 397
- Elastic modulus, 493, 497
- Electrical double layer (*see* Double layer)
- Electrocapillary curve, 803
- Electrochemical double layer (*see* Double layer)
- Electrolyte solutions (*see also* Ionic fluids), 365–368, 790–794, 802, 803, 805, 812–817
- Electro-osmosis, 775, 778, 785–789, 793, 794
- Embedded atom method (EAM), 855, 857, 908
- Epidemic analysis, 395, 397
- Equilibrium theory of confined phases, 3–21
- Euler characteristic, 668, 669, 689, 696, 700, 701, 711–717, 731
- Fermi statistics (*see* Quantum statistics)
- Field theory (FT), 805–807, 846
  - of ionic solutions, 812–817
- Finitely extendible nonlinear elastic potential (FENE), 519, 564, 592, 608
- Finite-size scaling theory (*see* Scaling)
- Flory exponent, 528, 531, 603
- Fluctuations, 44, 53, 300, 361, 394, 395, 401, 423, 658, 660, 661, 665, 672, 861, 862, 866, 872, 880, 896, 909
  - quantum, 112, 116, 776
  - topological, 685, 711–712
- Fluid lamella, 5
- Force expressions, 31, 49
- Force field, 485–487
- Fourier–Bessel transform, 83
- Fourier transform, 141, 155, 156, 215, 635, 691
- Fractal, 397, 398, 852, 869, 886, 888, 892, 896, 909
  - dimension, 888

- Freezing, 98, 99, 140, 376, 672, 745, 747, 753, 757, 760, 767, 854, 867, 898  
surface-induced, 49
- Gay-Berne fluid, 35–37, 40, 41, 662
- Genus, 700, 701, 708
- Gibbs–Duhem equation, 12, 14, 16
- Gibbs' fundamental relation, 6
- Ginzburg–Landau models, 631, 638–640, 666–667, 685–739, 878  
equation, 861, 875, 878  
extended, 686, 720–724
- Ginzburg–Landau theories (*see* Ginzburg–Landau models)
- Glass, 373–375, 499–505
- Gouy–Chapman theory, 358, 367, 799, 800, 803–805, 819, 825–828, 830, 831, 833, 836, 840, 846  
nonlinear (NLGC), 799, 802, 821–827, 839, 840
- Growth exponent, 398, 526
- Hamiltonian, 92, 95, 98, 100, 101, 110, 113–115, 255, 269, 272, 277, 443, 448, 470, 473, 512, 645, 656, 658, 660, 664, 802, 804, 806–812, 815, 817, 818, 835, 836, 846, 858, 859, 864
- Hard-sphere fluids, 3, 35, 140, 144, 161, 211, 234, 294, 305–307, 312, 319–322  
associating, 178, 197, 216
- Hard-sphere potential, 137, 179, 321, 750
- Henderson–Abraham–Barker equation (HAB), 158–160  
associative extension, 170
- Heterogeneity Investigation at Loughborough by a Distribution Analysis (HILDA), 247
- Homogeneity of thermodynamic potentials, 11
- Hydrogen bonds, 348–350, 354, 355, 357, 361, 362, 368, 369, 371, 373, 379, 493, 637, 638, 662
- Hypernetted chain approximation (HNC), 9, 141, 142, 144, 146, 149, 157, 159–162, 303, 305, 321, 322, 325, 326, 330, 802  
first-order (HNC1), 172, 173, 175–177, 180–182, 187, 190, 191  
hydrostatic (HHNC1), 191  
reference (RHNC), 149  
second-order (HNC2), 175, 186, 333, 336, 802
- Inhomogeneous fluids, 158–160  
associating, 167–238  
partly quenched, 293, 330–337
- Integral equations, 9, 135–163  
for associating fluids, 171–211  
geometrically based hierarchy, 151–154  
for partly quenched systems, 293–346
- Interfaces  
aqueous, 355–378  
charged, 802, 805–808, 817–846  
electrochemical, 358–369  
electrified (*see* Interfaces, charged)
- Interfacial tensions, 7, 18, 266, 284, 285, 600, 636, 652, 659, 803
- Ionic clusters, 790, 791, 793
- Ionic solutions (*see* Electrolyte solutions)
- Irreversible phase transitions (*see* Surface chemical reactions)
- Ising model, 89, 150, 265, 266, 272, 283, 428, 655, 660, 855, 858, 910
- Kardar–Parisi–Zhang model (KPZ), 398–401, 406–408, 412, 416, 418, 421–424, 851, 861, 862, 910
- Kierlik–Rosinberg theory, 211, 212
- Kinetics  
of adsorption, desorption, 439–477  
of crystal growth, 851, 860, 861, 863–888  
of dewetting, 620  
of living polymer, 539–544

**[Kinetics]**

- of phase separation, 636, 638, 651, 662
- of shear-induced phase transitions, 662

Landau–Ginzburg models (*see*  
Ginzburg–Landau models)

Langmuir kinetics, 465, 466

Langmuir monolayers, 645, 648, 663

Langmuir–Hinshelwood mechanism,  
392, 415, 419, 421, 423

Larson model, 643–645, 647, 653

Layering, 277–279, 314

Lennard–Jones fluids, 30, 31, 42, 100,  
107, 146, 161, 191, 307, 761,  
767, 781, 786, 790  
associating, 199, 201–204, 219–233,  
235–237

Lennard–Jones potentials, 31, 82, 83,  
107, 115, 137, 144, 199, 200,  
219, 229, 230, 255, 306,  
354–356, 365, 369, 373, 486,  
496, 519, 647, 648, 760, 785,  
858, 910

Lévy exchange mechanism, 428, 429

Lie group, 800, 835, 836, 842, 843

Lifshitz line, 692

Lipid bilayers, 642, 648

Liquid bridge, 60, 64

Liquid crystal, 29, 35, 911

Lovett–Mou–Buff–Wertheim equation  
(LMBW), 160, 200, 201, 330,  
331

Macroscopic director, 28

Markov process, 21–26, 440, 463, 474,  
561, 752

Martynov–Sarkisov approximation  
(MS), 149

Mathieu equation, 117, 118

Maximum entropy method, 102, 104

Mean-field approximation (MFA), 63,  
99, 100, 103, 104, 107, 119, 120,  
248, 285, 296, 306, 307, 390, 509,  
510, 511, 520–522, 526, 530

**[Mean-field approximation (MFA)]**

- 390, 531, 539, 543, 548, 658,  
661, 685, 692, 709, 710, 721–  
722, 729, 802, 807–814, 821,  
835, 846, 854, 864, 865, 879

Mean spherical approximation (MSA),  
146, 148, 160, 306, 307, 338, 805

extended (EMSA), 180–182

site-site extended (SSEMSA), 180

Membranes, 712

biological, 535, 578, 633, 636

permeable, 311, 312, 341

semi-permeable, 233–237, 775–795

Metropolis method, 25, 349, 503, 512,  
514, 517, 562, 564, 669, 752

Micelles, 509–549, 636–638, 642, 647,  
651–654, 686

critical condensation of (CMC),  
651–653

giant wormlike (GM), 509–511, 517,  
519, 526, 529, 531, 537, 538,  
544, 547–549

Microemulsions, 635, 668, 659, 661,  
685–743

structure of, 730–737

Microporous matrices (*see* Random  
porous media)

Microscopic director, 28, 29

Microscopic reversibility, 24

Modified Meister–Kroll theory, 167,  
214–216

Modified Verlet approximation (MV),  
146, 149, 154, 159, 160, 162

Molecular beam epitaxy (MBE), 855,  
880, 884–886, 911

Molecular dynamics, 22, 249, 260, 268,  
348, 349, 355, 377, 378,  
485–505, 519, 556, 569, 637,  
749, 757, 767, 853, 855  
nonequilibrium (NEMD), 51  
osmotic, 782–786

Molecular weight distribution (MWD),  
510, 511, 514, 519, 522–526,  
528, 537, 541, 548

Monte Carlo simulations, 1, 21–29, 53,  
60, 77, 78, 84–91, 97, 98, 153,

- [Monte Carlo simulations]
  - 167–169, 171, 191, 211, 216,
  - 228–233, 249, 268, 269, 273,
  - 279, 312–320, 333–336, 342,
  - 348, 349, 355, 377, 378,
  - 391–430, 412, 440, 476, 481,
  - 488, 499–505, 511–519, 529,
  - 531, 532, 535, 545, 556, 558,
  - 559–569, 573, 581, 608, 615,
  - 640, 647, 649, 657, 658, 660,
  - 662, 668, 669, 690, 710–721,
  - 749, 751–753, 757, 763, 765,
  - 802, 853, 857, 863, 874, 882, 905
- osmotic, 233–237, 780–782, 785
- path integral (PIMC), 78, 80, 91–99,
  - 102–106, 113, 114, 117,
  - 119–123
- Morse potential, 564, 565, 592
- Navier–Stokes equations, 666, 903,
  - 904, 911
- Nonuniform fluids (*see*
  - Inhomogeneous fluids)
- Nucleation, 273, 851, 865–867, 902,
  - 912
- Order parameters, 84, 115, 116, 119,
  - 393, 394, 510, 513, 638, 639,
  - 666, 688–740
- passim, 749, 762, 769, 865, 868
- Orientational bias, 28
- Ornstein–Zernike equations (OZ) (*see*
  - also* Replica Ornstein–Zernike
  - equations), 141, 148, 150, 154,
  - 155, 158, 160, 162, 308, 313,
  - 321
- inhomogeneous (IOZ), 160, 174,
  - 178, 179, 190
- multidensity, 169, 194–196, 200, 201,
  - 205, 207
- second-order (OZ2), 161, 162, 331
- Oscillatory behavior in reactions (*see*
  - Surface reactions)
- Osmosis, 775–779
  - reversed, 775, 777–779, 784–786,
  - 790, 793
- Osmotic pressure, 776, 780, 781
- Ostwald-ripening, 867, 886
- Pair distribution functions, 20, 58,
  - 138–140, 199, 202, 214, 300,
  - 303, 331
- Pairwise additivity, 136, 138, 640
- Partly quenched systems (*see also*
  - Random porous media),
  - 293–346
- ionic, 293, 337–341
- Path integral Monte Carlo (*see* Monte
  - Carlo method)
- Percolation, 394, 422, 428–430
- Percus–Yevick approximation (PY),
  - 103, 142, 144–146, 148, 149,
  - 151, 157, 160, 162, 179, 197,
  - 190, 206, 207, 214, 215, 302,
  - 303, 305, 308, 313, 314, 318,
  - 319, 321, 322, 325, 330, 332
- first-order (PY1), 173, 175, 176,
  - 180–183, 187, 188, 190
- second-order (PY2), 175, 186, 188,
  - 333, 336
- Phase
  - bicontinuous, 633, 686, 687, 709
  - columnar, 762, 763
  - cubic, 687, 692, 696
  - diamond, 692, 696, 727
  - ferromagnetic, 98–104, 106
  - gyroid, 633, 635, 643, 644, 696, 702,
  - 706, 708, 710, 727
  - hexagonal, 633, 635, 644, 687, 692,
  - 727
  - lamellar, 633, 635, 642, 644, 646,
  - 660–662, 686, 687, 692, 714,
  - 716, 720, 727
  - nematic, 29, 35, 762, 763, 911
  - paramagnetic, 98–104, 106
  - smectic, 40, 762, 763, 913
  - tilted, 636
- Phase diagrams, 64, 78, 81, 98, 101,
  - 106, 119, 228, 269–271,
  - 633–636, 644, 649, 660–662,
  - 671–672, 685, 709, 710, 749,
  - 755, 759, 900, 912

- Phase-field models, 851, 853, 855,  
877–879, 904, 912
- Phase transitions, 1, 3, 49–66, 78–82,  
84–88, 98–123, 261–286, 295,  
304, 359, 364, 557, 635–639,  
658, 662, 665, 686, 712,  
714–720, 755, 760, 763, 764,  
854, 878, 912
- commensurate-incommensurate, 5,  
79, 81, 261, 262, 273–276
- herringbone, 78, 110
- microemulsion-lamellar, 714–720
- shear-induced, 49–56, 662
- Pink model, 664
- Poisson–Boltzmann theory, 802,  
805
- Poisson equation, 361, 802, 804, 810,  
818, 821
- Polydisperse fluids, 154–157
- Polydispersity, 154, 157, 548, 747, 759,  
760, 763
- Polymer crystals, 905
- Polymer glasses, 481, 499–505
- Polymer melts, 481, 493–499, 511
- Polymer networks, 481, 493–499
- Polymerization (*see* Polymers, living)
- Polymers, 481–623, 905, 912
- dense, 481–506, 905
- equilibrium (EP), 509–549
- living (LP), 509–511, 526, 529,  
532–537, 539, 544, 548,  
549
- in random porous media, 600–614
- in solutions, 492–493, 555, 558,  
594–600
- Potential of mean force (PMF), 308,  
309, 311, 805
- Potts model, 512, 664, 665
- Prewetting, 219–228, 230, 233, 278
- Principle of detailed balance, 24, 28,  
464, 752, 864, 882
- Quantum dynamics, 102–107
- Quantum effects, 77, 78, 80, 97–122
- Quantum statistics, 94, 105
- Quasistatic process, 51
- Radial distribution function (*see* Pair  
distribution function)
- Ramakrishnan–Yussouff theory, 99
- Random interface theories, 639,  
667–673
- Random porous media, 293–343, 556,  
600–614
- Random walk, 22, 428, 494, 536
- non-reversible (NRRW), 560, 561
- self-avoiding (SAW), 559–561, 563,  
576, 581, 587, 601
- Reflection coefficients, 780
- Registry parameter, 6
- Renormalization group method, 265,  
573, 866
- Replica method, 293, 298
- Replica Ornstein–Zernike equations  
(ROZ), 293, 294, 297, 302,  
304, 306–307, 311, 314, 318,  
319, 321, 326, 337, 338, 341,  
342
- inhomogeneous (IROZ), 330, 331
- Rogers–Young approximation (RY),  
149, 157, 330
- Roughening, 866, 914
- kinetic, 861, 885, 910
- transition, 851, 859–860, 871
- Roughness exponent, 398
- Rouse model, 494, 504, 545–547,  
562, 576, 577, 579, 596, 605,  
623
- Scaling, 77, 78, 84, 85, 88, 98, 120,  
266–269, 283, 391, 398, 399,  
403, 404, 496, 509, 520–522,  
528–532, 555, 558, 573–593,  
596, 600–605, 623, 868, 869,  
891, 899, 913
- Schrödinger equation, 117, 485
- Segura–Chapman–Shukla theory,  
211–214
- Sharp-interface model, 851, 853, 855,  
875–877
- Shear, 745, 746, 766
- modulus, 49, 50, 854
- stress, 4, 12, 49–53, 512



- Solidification (*see also* Crystal growth),  
831, 853, 854, 895, 898  
directional, 898–900
- Solid-on-solid model, 855, 859
- Solution diffusion model, 779–780
- Solvation forces, 2, 9, 10, 31, 33, 35, 40
- Sticking, 388, 389  
coefficient 389, 407, 424, 441–443,  
457, 465, 469, 471, 476
- Stick-slip transitions, 51–53
- Stillinger–Weber potential, 855, 857,  
913
- Stratification, 31–35, 61
- Stochastic process (*see also* Markov  
process), 1, 22–24, 409, 416,  
427, 881, 913
- Stress-strain ensembles, 1, 16–19, 22,  
24–26
- Stress tensor, 6, 35
- Structure factor, 503, 635, 691, 755
- Structure function (*see* Structure factor)
- Substrates  
atomically smooth, 11–12  
chemically heterogeneous, 60–66  
nonplanar, 1, 45–49
- Superfluidity, 78, 94
- Superposition approximation, 140
- Surface charge density, 365–367,  
370–372
- Surface chemical reactions, 388–430  
irreversible phase transitions (IPTs)  
in, 388, 400, 401, 409, 416,  
417, 420–430  
phase diagram, 393, 395, 408, 421,  
424  
kinetics of, 472–476  
passim  
oscillatory behavior in, 388,  
404–415
- Surface-forces apparatus (SFA), 2–5,  
8, 11, 16, 32, 35, 49–51
- Surface heterogeneity, 245–286  
passim  
models of, 250–261  
patchwise, 248, 252, 254  
random, 251, 254
- Surfaces (*see also* Substrates), 158  
adsorption at, 77–123, 168–238,  
439–477, 556–623  
of catalyst, 392, 423, 425  
of clay, 348, 377  
heterogeneous, adsorption on,  
245–286  
homogeneous, 245  
hydrophilic, 348  
hydrophobic, 35, 348  
of ionic salts, 376  
of metals, 365, 801  
nonpolar, 355  
of oxides, 347, 377  
reactions on (*see* Surface chemical  
reactions)
- Surface tension (*see also* Interfacial  
tensions), 280, 558, 597, 641,  
642, 856, 868, 877, 895, 913
- Surfactants, 510, 631–673, 686–692,  
696, 702, 720–723, 726, 727,  
729, 731, 738, 739
- Tarazona weighted density  
approximation, 212, 213
- Taylor-expansion algorithm, 1, 26–28
- Tethering, 782, 783
- Thermodynamic perturbation theory,  
167, 196–200, 213
- Thommes–Findenegg experiment, 56,  
57, 59
- Transfer matrix method, 439, 446–452,  
460, 462, 476
- Transverse structure, 41
- Trotter dimensions, 107, 114
- Trotter path, 117
- Trotter product formula, 91, 92, 107
- van't Hoff equation, 781
- Virial expression, 30, 31, 49
- Wedge, 45–49
- Week–Chandler–Anderson  
approximation, 199, 212, 785
- Wertheim theory, 169, 192–200, 294,  
321

- Wetting, 45, 245, 276–286, 558,  
658–660, 812, 895  
    association effects on, 225, 229–233  
    roughness-induced, 284, 286
- Widom model, 656, 657, 667, 669
- Widom–Rowlison models, 78, 86, 123
- Wilson–Frenkel growth law, 851,  
869–871, 874
- Wulff construction, 856, 877
- Yield point, 4, 50, 53
- Yukawa potential, 137, 146, 148–150,  
307, 648, 757, 765
- Ziff–Gulari–Barshad model (ZGB),  
392, 393, 395, 397, 399–401,  
404, 406–409, 412, 416, 418,  
421–423, 425, 427